Saint Petersburg OPEN 2022
9th International School and Conference
May 24-27, 2022

OPEN CONFERENCE

BOOK of ABSTRACTS

9th International School and Conference on Optoelectronics, Photonics, Engineering and Nanostructures

May, 24-27, 2022
Saint-Petersburg, Russia

9 th International School and Conference “Saint Petersburg OPEN 2022” on Optoelectronics, Photonics, Engineering and Nanostructures carries on the tradition of annual conferences and schools organized at St Petersburg Academic University for students, PhD students and young scientists. More detailed information on the School and Conference is presented on https://spb.hse.ru/spbopen/ The Book of Abstracts includes abstracts of contributed works accepted for presentation at the Conference. The volume was composed by HSE University - St. Petersburg from electronic files submitted by the authors. Only minor technical corrections were made by the composers.

Chief Editor: A. E. Zhukov Published by HSE University - St. Petersburg, Soyuza Pechatnikov 16, 190121, St Petersburg, Printed in Russian Federation

Head of Program Committee

Alexey E. Zhukov corr. member of the RAS, HSE University, Russia

Program Committee

Aleksandr V. Omelchenko (HSE University- St.Petersburg)
Andrey A. Lipovskii (Peter the Great St.Petersburg Polytechnic University, Russia) George E. Cirlin (Alferov University, Russia)
Valentina V. Zhurikhina (Peter the Great St.Petersburg Polytechnic University, Russia)
Natalia V. Kryzhanovskaya (HSE University- St.Petersburg)

Head of Organizing Committee

Alexey E. Zhukov (HSE University- St.Petersburg)

Organizing Committee

Mikhail V. Maximov (Ioffe Institute, Alferov University, Russia)
Andrey A. Lipovskii (Peter the Great St.Petersburg Polytechnic University, Russia)
Valentina V. Zhurikhina (Peter the Great St.Petersburg Polytechnic University, Russia)
Vladimir V. Korenev (Alferov University, Russia)
Eduard I. Moiseev (HSE University- St.Petersburg)
Anna S. Dragunova (Alferov University, Russia)
Svetlana A. Kadinskaya (Alferov University, Russia)
Anastasia Baryshnikova (HSE University- St.Petersburg)

1. Nanophotonics, Spectroscopy, Microcavities, Optics, Plasmonics

1-1	Адам	Юрий	Александрович	Университет ИТМО	Modulation and demodulation process of the vortex beam under the condition of additional phase modulation
1-2	Ашарчук	Илья	Михайлович	Институт нанотехнологий микроэлектроники РАН	Up-conversional luminescence particles based on NaYF4 matched with passive optical devices
1-3	Бабич	Екатерина	Сергеевна	Академический университет им. Ж.И. Алфёрова	Optical absorption and Raman scattering mapping of nanoparticles patterns formed in glass by nanosecond laser in UV, VIS and IR
1-4	Бабухин	Данила	Валерьевич	Qrate LLC	Adaptive eavesdropping on the BB84 quantum key distribution protocol with distinguishable photons
1-5	Бакина	Ксения	Андреевна	СГУ им. Питирима Сорокина / ФИЦ Коми НЦ УрО РАН	X-ray spectral studies of doped bismuth-magnesium and bismuth-zinc tantalates
1-6	Барышникова	Ксения	Владимировна	Университет ИТМО	Silicon nanoantenna for efficient control of single-photon source emission
1-7	Бастракова	Марина	Валерьевна	Нижегородский государственный университет им. Н.И. Лобачевского	Generation of correlated photons and single photon detection processes in an array of qubits in a microwave transmission line
1-8	Бондарева	Полина	Игоревна	Московский Педагогический Государственный Университет	Investigation of graphene photodetectors for next generation communication systems
1-9	Бородина	Любовь	Николаевна	Университет ИТМО	Laser microscopy of periodic holographic structures with quantum dots
1-10	Бузин	Даниил	Сергеевич	ИФ СО РАН	Hybrid Tamm-microcavity optical modes with tunable Q-factor
1-11	Ведерникова	Анна	Александровна	Университет ИТМО	Luminescent properties of carbon dots from o-phenylenediamine under excitation at 800 nm
1-12	Венедиктов	Илия	Олегович	МИЭМ НИУ ВШЭ	Fabrication of diffraction gratings for generation of OAM light
1-13	Викторов	Евгений	Александрович	Санкт-Петербургский Государственный Университет	Modulation of quantum beat signals under photoionization of Xe isotopes
1-14	Гаврилович	Арина	Альбертовна	МФТИ	State preparation intensity fluctuations in QKD
1-15	Галкин	Максим	Леонидович	Сколковский институт науки и технологий, Российский квантовый центр	On whispering gallery mode crystalline microresonators polishing techniques
1-16	Глебов	Никита	Вячеславович	Университет ИТМО	Atomic force lithography for fabrication of high-Q planar perovskite polaritonic cavities
1-17	Гольдберг	Артемий	Александрович	СПБПУ Петра Великого	Исследование характера распространения лазерного излучения в дифференциальной кювете Андерсона
1-18	Гречанинова	Евгения	Вадимовна	Университет ИТМО	Photoluminescence from lead halide perovskite superlattices
1-19	Давыдов	Максим	Николаевич	СПБПУ Петра Великого	Development of compact NMR relaxometer for express control of the state of liquid media
1-20	Дорогов	Александр	Евгеньевич	Московский физико-технический институт	Application of a broadband Josephson parametric amplifier

1-21	Дрязгов	Михаил	Александрович	НИУ ВШЭ	New design of a waveguide integrated photon number resolving superconducting detector with micron-wide strips
1-22	Ершов	Александр	Александрович	Санкт-Петербургский государственный электротехнический университет «ЛЭТИ»	Investigation of optical waveguide properties of SOI integrated circuits
1-23	Ибрагимов	Алишер	Ахмад Угли	МГУ им. Ломоносова	Light modulation by semiconductor metasurfaces upon electric injection of free carriers.
1-24	Кашапов	Артем	Ильясович	Самарский университет	Broadband light absorber based on a multilayer metal-insulator-metal structure
1-25	Кондратьев	Валерий	Игоревич	Университет ИТМО	Experimental study of all-van-der-Waals waveguide polaritons at room temperature
1-26	Константинова	Ирина	Юрьевна	Московский физико-технический институт	
1-27	Кошелев	Александр	Владимирович	ФНИЦ "Кристаллография и фотоника" РАН	Enhancement of luminescent efficiency of a-NaREF4:Er3+ (RE= Y, Yb, Lu) nanocrystals through multi-doping strategy
1-28	Красников	Виктор	Викторович	МГУ им. М.В. Ломоносова	Neuromorphic photoelectric synapses based on metal oxides nanocrystallites
1-29	Краснов	Алексей	Ильдарович	ИФ СО РАН	All-dielectric photonic crystal microcavity with electrically tunable Q-factor
1-30	Кузин	Алексей	Юрьевич	Сколковский институт науки и технологий/ (МПГУ)	Thermo-optical effect in a Mach-Zehnder interferometer on a silicon nitride platform for quantum photonic applications
1-31	Курилова	Анастасия	Владимировна	Университет ИТМО	Synthesis and properties of nanostructure composites based on barium titanate and 3d metal
1-32	Лебедева	Елизавета	Сергеевна	Московский Педагогический Государственный Университет	Detection of orbital angular momentum by forked diffraction method
1-33	Лосев	Антон	Вадимович	ООО "КуРэйт"	Optimization of gating signal parameters of sine-gated single-photon detector based on InGaAs/InP single-photon avalanche diodes
1-34	Макеев	Сергей	Сергеевич	Санкт-Петербургский политехнический университет Петра Великого	Method for constructing NMR signal spectra using the discrete Fourier transform
1-35	Малеева	Ксения	Андреевна	Университет ИТМО	Chemical Stability of the SERS Substrate Based on Gold Nanoparticles Self-Assembling Films
1-36	Мало	Дана	.	Московский физико-технический институт	Aluminum nanostructures produced by aerosol dry printing for ultraviolet photoluminescence enhancement
1-37	Махлуф	Мазен	Мамдух	НИУ ВШЭ	FPGA-Based Time-to-Digital Converter for Time-of-Flight Photon Counting LiDAR measurement
1-38	Машарин	Михаил	Алексеевич	Университет ИТМО	Temperature-dependent exciton-polaritons in perovskite photonic crystal slab
1-39	Медведева	Светлана	Сергеевна	Университет ИТМО	Dynamics of the uncertainty value of quadratures for bosonic quantum states
1-40	Миропольцев	Максим	Андреевич	Университет ИТМО	Fabrication of SERS-Active Structures via Electrostatic Deposition of Colloidal Gold Nanoparticles on Polymer Microspheres

1-41	Михайловский	Михаил	Сергеевич	Университет ИТМО	Collective states with high quality factors in chains of dielectric resonators
1-42	Мязин	Никита	Сергеевич	Санкт-Петербургский политехнический университет Петра Великого	On improvements of nuclear magnetic resonance magnetometer to study magnetic mid-fields variations
1-43	Набиуллина	Резида	Даниловна	Университет ИТМО	Optical properties of nanoporous alumina activated by pseudoisocyanine molecular nanoclusters
1-44	Наболь	Степан	Васильевич	Институт физики им. Л. В. Киренского СО РАН	Fabry-Perot type bound state in the continuum in an anisotropic photonic crystal
1-45	Наумова	Виктория	Викторовна	Санкт-Петербургский политехнический университет Петра Великого	A new method of processing measurement results of tissue oxygen saturation abnormalities.
1-46	Никитина	Анастасия	Дмитриевна	Университет ИТМО	Nonlinear circular dichroism in dielectric nanoparticle dimers and trimers
1-47	Певцов	Дмитрий	Николаевич	МФТИ / ИПХФ РАН	Förster resonance energy transfer in thin layers of indium phosphide quantum dots
1-48	Перетокин	Артём	Викторович	ННГУ им. Н.И. Лобачевского / ИФМ РАН	Experimental Study of Luminescent Properties and Band Structure of Two-Dimensional Photonic Crystals with Ordered Ge(Si) Nanoislands
1-49	Петров	Иван	Витальевич	QRate	Phase-time-encoding MDI QKD tolerant to detector imperfections
1-50	Пономарев	Роман	Сергеевич	ПГНИУ, Молодежная лаборатория интегральной фотоники	Lensed optical fiber production technology using optical glue (Технология производства линзованного оптического волокна с использованием оптического клея)
1-51	Проводин	Даниил	Сергеевич	Санкт-Петербургский политехнический университет Петра Великого	Новая методика контроля состояния жидких сред оптическим методом в экспресс-режиме
1-52	Проскурин	Алексей	Алексеевич	Университет ИТМО	Perfect absorption of a focused beam by a single nanoparticle
1-53	Рахманова	Гульназ	Раифовна	Университет ИТМО	Electron-spectrum and transport phenomena in two-dimensional Dirac Semimetals
1-54	Романенко	Гавриил	Александрович	ИФ СО РФН им. Киренского	Metal-dielectric optical microcavity with tunable Q-factor.
1-55	Рябцев	Илья	Александрович	Санкт-Петербургский государственный электротехнический университет «ЛЭТИ»	Towards Passive Silicon Micro-Ring Memories Using Nonlinear Free Carrier Dispersion Effect
1-56	Савельев	Дмитрий	Андреевич	Самарский национальный исследовательский университет им. академика С.П. Королева	The investigation of the optical vortices diffraction on silicon ring gratings with variable height using high-performance computer systems
1-57	Сахно	Денис	Игоревич	Университет ИТМО	Describing topological transitions in subwavelength metamaterials via effective material parameters
1-58	Седых	Ксения	Олеговна	Национальный исследовательский технологический	Generation of different orbital angular momentum modes via array of computer-generated holograms.

				университет «МИСиС»	
1-59	Сектаров	Эдуард	Саитович	НИУ ВШЭ/ИСАН	Control of color centers charge states in crystals by using X-Ray radiation
1-60	Селиверстов	Сергей	Валерьевич	Московский педагогической государственный университет	Simulation of terahertz photonic integrated antenna
1-61	Серая	Олеся	Валерьевна	Московский физико-технический институт	Synthesis of silver nanoparticles by spark discharge
1-62	Слюсаренко	Нина	Викторовна	Сибирский федеральный университет	Förster Resonance Energy Transfer from colloidal quantum dots to xanthene dye in polymer film
1-63	Смолина	Екатерина	Олеговна	ИПФ РАН	Edge states and modulation instability in nonlinear photonic topological lattices
1-64	Студзинский	Виталий	Михайлович	Санкт-Петербургский Политехнический Университет Петра Великого	Ion-beam-induced formation of gold nanostructures on polymethyl methacrylate film.
1-65	Терещенко	Иван	Борисович	ФТИ им. А.Ф. Иоффе	Исследование устойчивости серебряных зеркал с защитными покрытиями к условиям высокой влажности и термоциклирования
1-66	Титова	Надежда	Андреевна	Московский Педагогический Государственный Университет	Thermal relaxation mechanisms in CVD monocrystalline boron-doped diamond microstructures
1-67	Толкач	Никита	Михайлович	Национальный исследовательский университет «МИЭТ»	Investigation of crystallinity degree for Ge2Sb2Te5 films by reflection and transmission photometry
1-68	Тонкаев	Павел	Андреевич	Университет ИТМО	Photoluminescence from lead halide perovskite superlattices
1-69	Трофимов	Павел	Игоревич	Университет ИТМО	Phase-change periodic surface structures for engineering of excitonic photoluminescence in WS2 monolayers
1-70	Фоминых	Никита	Андреевич	НИУ ВШЭ - Санкт-Петербург	The Investigation of Optical Coupling of Microlasers with Tapered Fiber
1-71	Харисова	Руфина	Даниловна	Университет ИТМО	Luminescent properties of mixed CsPb(BrxI1-x)3 perovskite nanocrystals in borogermanate glass
1-72	Цимоха	Мария	Александровна	Университет ИТМО	Classification and multipolar content of the eigenmodes of acoustic resonators with different symmetries
1-73	Цыкарева	Юлиана	Витальевна	ФГАОУ ВО "САФУ имени М.В. Ломоносова"	Simple expressions for the quantum entanglement of non-monochromatic photons on a waveguide beam splitter
1-74	Шеин	Кирилл	Вячеславович	МИЭМ НИУ ВШЭ/Лаборатория радиофизики МПГУ	Terahertz response in superconducting niobium diselenide
1-75	Щербак	Сергей	Александрович	Академический университет им. Ж.И.Алферова	Optical second-harmonic response of an axially-symmetric medium under radially polarized excitation
1-76	Эннс	Яков	Борисович	Академический университет им. Ж.И.Алферова	Modification of the optical and electrical properties of NiO films by thermal annealing

1-77	Mikhailova	Tatiana	Vladislavovna	Крымский федеральный университет имени В.И. Вернадского	Investigation of interference patterns by scanning near-field optical microscopy
1-78	Shkoldin	Vitaliy	Alekseevich	Академический университет им. Ж.И.Алферова	Precision formation of hybrid Au/Si nanoantennas by STM lithorgaphy
1-79	Макарова	Ксения	Алексеевна	Северный федеральный университет им.М.В. Ломоносова	Nanoscale waveguide beam splitter in quantum technologies

2. Lasers, solar cells and other optoelectronic devices

2-1	Альхалил	Джордж	-	Университет ИТМО	Polarization entanglement-enhanced optical gyroscope
2-2	Ачева	Полина	Павловна	МИИГАиК/ РКЦ	Automated setup for testing Single-Photon Detectors countermeasures with bright-light attacks
2-3	Бадильо	Пабло Даниэль	-	СПбГЭТУ «ЛЭТИ»	New challenges for 3D scanning over flat surfaces applied in Cultural Heritage: The tombstone of the bishop Vasilije Petrović (Negosh) in Saint Petersburg
2-4	Богданова	Милана	Владимировна	Академический университет им. Ж.И.Алферова	Optimization of the contact grid for the GaP/Si solar cells
2-5	Ведь	Михаил	Владиславович	Научно-исследовательский физико-технический институт ННГУ	Spin light-emitting diode with intensity modulation
2-6	Вовк	Николай	Александрович	НИУ ВШЭ/ ИНМЭ РАН	Development of technological methods for fabrication high-density luminescent structures based on up-conversion NaYF4:Yb3+,Er3+ particles.
2-7	Гафуров	Эльдар	Маратович	РФЯЦ-ВНИИТФ	Reliability of 808nm QCW Laser Diode Arrays
2-8	Герасин	Илья	Сергеевич	МФТИ, QRate	Simple method for preparing highly-indistinguishable coherent states
2-9	Голтаев	Александр	Сергеевич	Академический университет им. Ж.И.Алферова	Epitaxial lift-off GaAs/AlGaAs solar cells for flexible devices
2-10	Грязнова	Екатерина	Михайловна	Санкт-Петербургский политехнический университет Петра Великого	Application of a fiber-optic communication line for transmitting RF-signal in system formeasuring parameters of active phased antenna arrays
2-11	Дмитриева	Диана	Сергеевна	Санкт-Петербургский государственный университет телекоммуникаций им. проф. М. А. Бонч-Бруевича	Development of the radiation situation monitoring system based on fiber-optic sensors for pools of nuclear power plants
2-12	Драгунова	Анна	Сергеевна	НИУ ВШЭ	Analysis of characteristics of InGaAs/GaAs microdisk lasers bonded onto silicon board.
2-13	Дуплинский	Алексей	Валерьевич	НИУ ВШЭ / QRate	
2-14	Еремеев	Андрей	Игоревич	СПбГЭТУ "ЛЭТИ"	Modelling of electromagnetic wave spectra of integrated optical waveguides

2-15	Заводиленко	Владимир	Владимирович	ООО "КуРэйт"	Evaluation of the operational parameters of single-photons detectors in quantum key distribution devices
2-16	Иванов	Антон	Евгеньевич	СПбГЭТУ "ЛЭТИ"	A comprehensive study of electroluminescence and temperature distribution of UX:3 AlInGaN LED
2-18	Казакин	Алексей	Николаевич	Академический университет им. Ж.И.Алферова	Fabrication and investigation of UV photodiode based on n-GaN/p-NiO heterojunction
2-19	Калентьева	Ирина	Леонидовна	НИФТИ ННГУ им. Н.И. Лобачевского	Effect of ion radiation on the characteristics of InGaAs/GaAs/Al2O3/CoPt spin light-emitting diodes.
2-20	Корепанова	Анна	Георгиевна	Университет ИТМО	Radiometric performance model of the near-infrared spectrometer for hydrocarbon analysis
2-21	Куркова	Александра	Дмитриевна	Санкт-Петербургский политехнический университет Петра Великого	Veracity a method of detecting scattered laser radiation for content measuring of particulate matter in the air.
2-22	Логунов	Семён	Эдуардович	Санкт-Петербургский политехнический университет Петра Великого	Development of a fiber-optic system for monitoring the state of oxygen activity in the current flow of the coolant
2-23	Макаров	Михаил	Эрнстович	АО НИИМЭ	Optimization of optical signal routing in the photonic tensor processor
2-24	Максимова	Елизавета	Игоревна	Санкт-Петербургский Политехнический Университет Петра Великого / ООО «КуРэйт»	Quantum noise extraction from polarization swapping in a gain-switched VCSEL
2-25	Мерзлинкин	Виталий	Евгеньевич	ООО «КуРэйт»	Polarization compensation design for free-space quantum communication transmitter
2-26	Мехтиев	Эл	Эльчин	QRate	Posterior laser-locking technique for MDI-QKD
2-27	Можайко	Анна	Анатольевна	Санкт-Петербургский политехнический университет Петра Великого	Laser surface treatment of aluminium: Correlation between thermal modeling and experimental study
2-28	Моисеев	Эдуард	Ильмирович	НИУ ВШЭ	Investigation of the far-field emission pattern of microdisk lasers
2-29	Нестеров	Дмитрий	Андреевич	Самарский национальный исследовательский университет имени академика С.П. Королева	Structures of porous silicon doped with erbium for optoelectronics
2-30	Поповский	Никита	Игоревич	Санкт-Петербургский государственный университет телекоммуникаций им. проф. М.А. Бонч-Бруевича	Features of the construction of fiber-optic communication lines with orthogonal frequency-division multiplexing
2-31	Пчелкин	Григорий	Александрович	СПбГУТ / АО «НПО ГОИ им. С.И. Вавилова»	Study of the characteristics of few-mode microstructured optical fibers with 6 cores made of highly doped GeO2 silica, step profile and induced chirality

2-32	Реутов	Алексей	Алексеевич	МФТИ / ООО «КуРэйт»	QKD and phase modulator imperfections
2-33	Родин	Сергей	Алексеевич	Санкт-Петербургский государственный университет телекоммуникаций им. проф. М.А. Бонч-Бруевича	Optical communication channel for multifunctional ecological monitoring complex
2-34	Рудавин	Никита	Владимирович	НИУ ВШЭ	Synchronization protocol for MDI-QKD systems
2-35	Самарцев	Илья	Владимирович	ННГУ им. Н.И. Лобачевского	Metamorphic InGaAs photodiode with low dark current grown on GaAs substrate
2-36	Сёмкин	Валентин	Андреевич	МФТИ	Gate- and polarization-dependent graphene-metal junction for polarization resolution
2-37	Синицкая	Олеся	Алексеевна	Академический университет им. Ж.И.Алферова	Development of ultraviolet photodetectors based on ultrathin GaN epitaxial layers grown on c-Al2O3
2-38	Таценко	Иван	Юрьевич	СПбГЭТУ "ЛЭТИ"	Investigation of optoelectronic oscillator without microwave and optical amplifiers
2-39	Тишин	Павел	Дмитриевич	Самарский национальный исследовательский университет имени академика С.П. Королева	Investigation of the degradation of the characteristics of photosensitive structures with porous silicon
2-40	Тойкка	Андрей	Сергеевич	СПБГЭТУ "ЛЭТИ"/ НИЦ Курчатовский институт - ПИЯФ	The development of ITO-based orienting coatings for Nematic Liquid Crystal Devices
2-41	Уваров	Александр	Вячеславович	Академический университет им. Ж.И.Алферова	Study of recombination and transport properties of a-Si:H(i)/a-Si:H(n) contact system for crystalline silicon solar cells
2-42	Филоненко	Елена	Михайловна	ФГУП "РФЯЦ-ВНИИТФ им. академ. Е.И. Забабахина"	The effect of mesa-stripe design parameters on the 975 nm laser diode output characteristics
2-43	Филяев	Александр	Александрович	Национальный исследовательский технологический университет МИСиС	Afterpulse effects simulation of InGaAs/InP single-photon avalanche diodes for applying in quantum key distribution systems
2-44	Фролов	Илья	Владимирович	УФИРЭ им.В.А.Котельникова РАН	Measurement of the internal quantum efficiency of emission in the local region of the LED chip
2-45	Харламова	Анастасия	Александровна	Северный федеральный университет имени М.В.Ломоносова	Peculiarity of electron density calculation during interaction of ultrashort laser pulse with nitrogenous base of DNA molecule adenine
2-46	Хыдырова	Селби	-	МГТУ имени Н.Э. Баумана	Temperature rate equations for a semiconductor laser
2-47	Шурупов	Дмитрий	Николаевич	Санкт-Петербургский политехнический университет Петра Великого	Hollow-core antiresonant optical fiber activated with YAG:Yb3+
2-48	Boudjemila	Linda	Linda	Санкт-Петербургский политехнический университет Петра Великого	Electrical Characteristics of CsPbI3 and CsPbBr3 Lead Halide Perovskite Nanocrystal Films Deposited on Si-C Solar Cells for High Efficiency
2-49	Ignatev	Andrey	Nikolaevich	FSUE «RFNC-VNIITF named after Academ. E.	Wavelength stabilized laser module for pumping high-power fiber lasers

				I. Zababakhin»	
2-50	Артеев	Дмитрий	Сергеевич	ФТИ им. А.Ф.Иоффе	Optimization of InGaN-based luminescent heterostructures by genetic algorithm
2-51	Кудряшов	Игорь	Сергеевич	МФТИ/QRATE	SIMLAD: A General Simulation Program For Semiconductor Laser Dynamics

3. Nanobiotechnology, Biophysics and Biophotonics
May 25, 2022

3-1	Абелит	Анна	Андреевна	Академический университет им. Ж.И.Алферова	Adaptive filtering revealed a new way for single living cells high-resolution electro- and optical research
3-2	Аникина	Виктория	Алексеевна	ФГБУН Институт теоретической и экспериментальной биофизики РАН	Исследование ранозаживляющих свойств нанокомпозита на основе диоксида церия в модели протон-индуцированного радиационного дерматита на мышах
3-3	Антипенко	Владимир	Викторович	Пензенский государственный университет	Development of a bioimpedance instrument and study of the interaction of electrodes with a biological object in bioimpedance diagnostics
3-4	Волков	Денис	Андреевич	Политехнический университет Петра Великого/ФТИ имени А.Ф. Иоффе	The study of NADH conformations in water-ethanol solutions using molecular dynamics simulations.
3-5	Голощапов	Дмитрий	Леонидович	ФГБОУ ВО "Воронежский государственный университет	Study of biomimetic composite dental materials based on nanocrystalline hydroxyapatite and light-curing adhesive.
3-6	Градусов	Илья	Андреевич	Политехнический университет Петра Великого	Fluorescence kinetics of biological coenzyme FAD in water-propylene glycol solutions excited by picosecond laser pulses
3-7	Григорьев	Виталий	Владимирович	Политехнический университет Петра Великого	Long-term storage of freeze-dried qPCR reagents in microfluidic devices
3-8	Гулин	Александр	Андреевич	ФИЦ ХФ РАН	Oxidative destruction of human RPE cells melanosomes induced by superoxide radicals leads to the formation of reactive aldehydes and ketones
3-9	Гуреева	Ирэна	Михайловна	Санкт-Петербургский Политехнический университет Петра Великого	A new technique for researching the absorption signal fronts of laser radiation on blood vessels
3-10	Демина	Полина	Андреевна	ФНИЦ «Кристаллография и фотоника» РАН	Nanobioreagents based on upconversion nanoparticles and hyaluronic acid for bioimaging
3-11	Добрецов	Родион	Кириллович	Санкт-Петербургский Политехнический университет имени Петра Великого	Creation of a device for detecting fluorescence from microfluidic chips
3-12	Емельянова	Анна	Андреевна	Воронежский Государственный	Microramanspectroscopy and laser-induced contrast visualisation for

				Университет	analysing incipient and clinically unrecorded enamel fissure caries
3-13	Замятина	Елизавета	Александровна	Институт теоретической и экспериментальной биофизики РАН	Effect of controlling the synthesis parameters by the Stöber method on the physicochemical characteristics of mesoporous silica nanoparticles
3-14	Зубик	Александра	Николаевна	Институт аналитического приборостроения Российской академии наук (ИАП РАН)	Applicability of domestic production glues for adhesive bonding microfluidic chips for polymerase chain reaction
3-15	Иванов	Александр	Сергеевич	СПбПУ им. Петра Великого / СПбАУ им. Ж.И. Алфёрова	Computer analysis of erythrocyte deformability in microfluidic devices
3-16	Калганова	Анастасия	Игоревна	Академический университет им. Ж.И.Алферова	Evaluation of different viability assays for studying the course of multidrug resistant infections in C. elegans
3-17	Камалов	Алмаз	Маратович	Санкт-Петербургский политехнический университет Петра Великого	Activation of polylactide films by cold plasma dielectric barrier discharge to improve the interaction of fibroblasts
3-18	Клименко	Дарья	Юрьевна	Санкт-Петербургский политехнический университет Петра Великого	Processing of qPCR signals obtained on microfluidic chips in the measurement sequence disorder event
3-19	Кубенко	Варвара	Георгиевна	Санкт-Петербургский государственный университет	Tetrahydrobiopterin and 5,10 –Methenyltetrahydrofolate Excited States Dynamics
3-20	Кулагина	София	Юрьевна	Самарский национальный исследовательский университет имени академика С.П. Королева	Investigation of solubility of porous silicon nanocomposite with hydroxyapatite
3-21	Минаева	Екатерина	Дмитриевна	НИЯУ МИФИ/ ИФТ РАН	Laser-induced forward transfer method adaptation for cell spheroids
3-22	Михайлова	Олеся	Александровна	Санкт-Петербургский политехнический университет Петра Великого	Development of a device for picoampere currents measuring
3-23	Можаева	Вера	Александровна	ИОФ РАН/ИБХ РАН	Surface-enhanced Raman spectroscopy to distinguish between similar peptides
3-24	Насиров	Павел	Денисович	Государственный университет "Дубна"	Исследование процесса конъюгации антител с квантовыми точками для создания иммунохроматографических тест-систем на их основе
3-25	Осыченко	Алина	Анатольевна	ФИЦ ХФ РАН	Oocyte enucleation by 795 nm femtosecond laser is a precise and effective method of recipient cytoplast preparation
3-26	Перепелица	Елизавета	Сергеевна	Санкт-Петербургский государственный технологический институт	Colloidal stability of iron oxide nanoparticle clusters in biologically relevant fluids
3-27	Плешаков	Павел	Сергеевич	СПбАУ РАН им. Ж.И. Алфёрова	Study of hydrogel microparticles with cells in microfluidic chips for 3D bioprinting
3-28	Рудных	Сергей	Константинович	Государственный университет "Дубна"	Application of computer modeling in study of quantum dots-antibody conjugates
3-29	Сенотрусова	Софья	Андреевна	Московский государственный	Microsphere optical microscopy for biological objects

				университет имени М.В. Ломоносова	
3-30	Серов	Егор	Денисович	Санкт-Петербургский политехнический университет Петра Великого	Development of a control algorithm for a fluid flow monitoring system in a microfluidic system
3-31	Сырчина	Мария	Сергеевна	ФИЦ ХФ РАН	Comparison of femtosecond laser, hydrothermal and microwave synthesis of fluorescent products from L-lysine
3-32	Терешенкова	Ольга	Алексеевна	БГТУ "ВОЕНМЕХ" им. Д.Ф. Устинова / АО "Лазерные системы"	Research of the method of optical spectral real-time laser ablation estimation during endoscopic surgeries
3-33	Точило	Ульяна	Алексеевна	ФИЦ ХФ РАН	Фемтосекундный лазер - эффективный инструмент в энуклеации зигот
3-34	Трифанова	Екатерина	Максимовна	ИФТ ФНИЦ «Кристаллография и фотоника» РАН	Photoluminescent nanoparticles β-NaYF4:Yb3+Er3+Ce3+ for multipurpose bioimaging
3-35	Хакимова	Анастасия	Алексеевна	Саратовский национальный исследовательский государственный университет имени Н.Г. Чернышевского	TEM use for the study of chitosan microspheres and nanospheres obtained from its salts with several acids
3-36	Чуйко	Яна	Владимировна	Санкт-Петербургский государственный университет	Colorimetric detection of tyrosine with silver nanoparticles and tyrosinase
3-37	Шиповская	Анна	Борисовна	Саратовский национальный исследовательский государственный университет имени Н.Г. Чернышевского"	Comparative analysis of nanosized structures in thin hydrogel plates of chitosan L- and D-ascorbate–hydrochloride
3-38	Шишкина	Дарья	Александровна	Самарский национальный исследовательский университет имени академика С.П. Королева	Porous silicon nanocontainers for targeted drug delivery
3-39	Яшков	Дмитрий	Владимирович	СПБПУ	Исследование флуоресцентных свойств NADH-ADH в смеси естественных ферментативных комплексов методом флуоресцентной поляризационной спектроскопии с высоким временным разрешением
3-40	Васин	Александр	Александрович	ФИЦ ХФ РАН	Physicochemical analysis of bisretinoid A2E photooxidative destruction products

4. Electric, Magnetic and Microwave Devices

4-1	Аринушкина	Ксения	Геннадьевна	Санкт-Петербургский политехнический университет Петра Великого	Improving the electrical characteristics of a frequency standard based on cesium atoms
4-2	Багров	Александр	Романович	ССАУ	Magnetic field in a magneto-optical system

					of solenoids and magnetic quadrupole lenses
4-3	Белозеров	Игорь	Александрович	Ярославский государственный университет им. П. Г. Демидова	Оптимизация рабочих характеристик МЭМС-переключателя на основе кантилевера
4-4	Брюшинин	Анатолий	Алексеевич	Санкт-Петербургский политехнический университет Петра Великого	Synchronization systems of time scales and frequencies in polar latitudes by meteor radio channel
4-5	Булатов	Никита	Олегович	МФТИ	RFID-based sensor for insect detection
4-6	Бурмистров	Олег	Ильич	Университет ИТМО	Wireless power transfer using higher-order eigenmode a birdcage coil in MRI-bore
4-7	Бурцев	Владимир	Денисович	Московский физико-технический университет	Additive Manufacturing of An Antenna Array
4-8	Ван	Дин		Санкт-Петербургский политехнический университет Петра Великого	Possibility of using atomic clocks on mercury-199 ions in satellite navigation systems
4-9	Васильев	Илья	Владимирович	Samara University	Modelling of ion transfer processes in ion-plasma generator with discrete flow compaction
4-10	Герасименко	Владислав	Сергеевич	Университет ИТМО	Higher spectral harmonics generation in an unamplified fiber ring resonator with electro-optical phase modulator
4-11	Дмитриев	Роман	Алексеевич	АО "РИРВ"	Features of the formation of the frequency of the microwave excitation signal in the quantum frequency standard
4-12	Елисов	Максим	Вячеславович	Самарский национальный исследовательский университет имени академика С.П. Королева	Lithium ions with energy 250-360 keV in the system of solenoidal and quadrupole magnetic fields
4-13	Исаева	Алина	Сергеевна	Южный федеральный университет	Rail condition monitoring using LSTM recurrent neural networks
4-14	Исупова	Екатерина	Васильевна	Санкт-Петербургский политехнический университет Петра Великого	Improvement of the characteristics of the frequency synthesizer in the quantum frequency standard on caesium atoms
4-15	Кенесбай	Рамазан	-	Санкт-Петербургский Политехнический Университет Петра Великого	Low-induction integral heater for temperature control of MEMS vapor cell
4-16	Кожевников	Василий	Юрьевич	Институт сильноточной электроники СО РАН	The kinetic simulation in vacuum electronics: uncovering the fundamental nature of non-Maxwellian distribution function effects
4-17	Листюхин	Владислав	Аександрович	ФГБОУ ВО "Пензенский государственный университет"	Monitoring of overhead power lines parameters in real time
4-18	Литвинов	Кирилл	Андреевич	Ульяновский государственный технический	Algorithm and installation for measuring the current lacing voltage in high-power RF and microwave bipolar and heterojunction

				университет	bipolar transistors
4-19	Лукашев	Никита	Александрович	Санкт-Петербургский государственный университет телекоммуникаций им. проф. М.А. Бонч-Бруевича	New optic system for low mass 199Hg ion clock
4-20	Любчак	Анастасия	Николаевна	НИУ ВШЭ	A mmWave Rod Antenna Array Compatible with a PCB Prototyping Technology
4-21	Макаров	Павел	Андреевич	ФМИ ФИЦ КНЦ УрО РАН	Transmission of Electromagnetic Waves Through Disordered Multiphase Composite Media
4-22	Пермякова	Ольга	Олеговна	МФТИ (НИУ) / ФТИАН им. К.А. Валиева РАН	Analysis of STDP characteristics of HfO2-based memristor
4-23	Приходько	Анатолий	Николаевич	НИУ ВШЭ	Millimeter Wave Photonic Crystal Waveguides Fabricated via Direct Machining
4-24	Рыжова	Дарья	Александровна	Санкт-Петербургский политехнический университет Петра Великого	Monitoring of radioactive contamination in the atmosphere using radar systems
4-25	Савин	Данила	Дмитриевич	Санкт-Петербургский политехнический университет Петра Великого	Generator of highly stable SHF signals with low phase noise
4-26	Солдатенкова	Мария	Дмитриевна	МИЭМ НИУ ВШЭ/лаборатория квантовых детекторов МПГУ	Voltage noise and fluctuation mechanisms in ultrathin NbN nanowires.
4-27	Стручков	Николай	Сергеевич	НИУ МИЭТ	On the mechanism of CNT network resistive response to NH3
4-28	Ткаченко	Алексей	Вячеславович	Южный федеральный университет	Manufacturing of the RF MEMS switch for 5G mobile network transceivers
4-29	Тризнова	Александра	Даниловна	Московский педагогический государственный университет	
4-30	Уваров	Илья	Владимирович	Ярославский филиал Физико-технологическо го института имени К.А. Валиева РАН	A seesaw-type MEMS switch with Pt and Ru contacts
4-31	Усачев	Антон	Сергеевич	Московский Физико-Технический Институт	Non-mechanical steering of GHz waves by diffraction grating
4-32	Чижиков	Сергей	Владимирович	МГТУ им. Н.Э. Баумана	Optimization of heterostructural transistor parameters for the MIC of the amplifying path of a medical radiothermograph
4-33	Чуканова	Ольга	Борисовна	НИУ МИЭТ, НТИ "Сенсорика"	GaN IC E-mode p-channel and n-channel transistors simulation
4-34	Шавшин	Артём	Владимирович	Санкт-Петербургский политехнический университет Петра Великого	Development of automatic gain control for the rubidium-87 frequency standard
4-35	Шлепаков	Павел	Сергеевич	ЯФ ФТИАН им. К.А. Валиева РАН	Fabrication of a micropump based on the fast electrochemical actuator with the PDMS membrane

4-36	Шугуров	Константин	Юрьевич	Академический университет им. Ж.И. Алфёрова РАН	Microwave Schottky diodes based on single GaN nanowires
4-37	Rudyk	Nikolay	Nikolaevich	Southern Federal University	Resistive type gas sensor based on carbon nanotubes
4-38	Shlepakov	Pavel	Sergeevich		Ruthenium as an electrode material for the fast electrochemical actuator

5. Other Aspects of Nanotechnology

5-1	Алымов	Георгий	Вадимович	МФТИ	Impact of the current pulse width on the speed of metal-insulator transition in VO2 nanobeams
5-2	Миронюк	Владислав	Николаевич	Саратовский национальный исследовательский государственный университет имени Н.Г.Чернышевского	Self-organization of quantum dots and porphyrin Langmuir monolayers on the surface of water subphase
5-3	Денисенко	Марк	Анатольевич	Южный федеральный университет	Design of the Two-Axis MEMS Gyroscope-Accelerometer
5-4	Дронова	Мария	Александровна	МГТУ им. Н. Э. Баумана/ "НИИграфит"	Electrical conductivity and optical properties of water-based graphene/AgNWs hybrid inks for flexible electronics
5-5	Еуров	Даниил	Александрович	ФТИ им. А.Ф. Иоффе	TEM contrast enhancement by adsorption of erbium ions on the inner surface of micro-mesoporous silica particles
5-6	Журина	Ангелина	Евгеньевна	ФГБОУ ВО "Пензенский государственный университет"	STUDY OF PIEZOCERAMIC MATERIALS POLARIZATION
5-7	Захаров	Родион	Константинович	Самарский национальный исследовательский университет	Entanglement between isolated atom and Jaynes-Cummings atom in a cavity with Kerr media
5-8	Исокжанов	Шахбоз	Шокиржон угли	Национальный исследовательский университет "МИЭТ"	Features of the formation Super C45-RuO2 based planar supercapacitor structures
5-9	Кесслер	Илария	Олеговна	Южный федеральный университет	Investigation of the use of combined plasma to create nanostructures on the surface of semiconductor wafers
5-10	Козловский	Александр	Валерьевич	ФГБОУ ВО "СГУ имени Н.Г. Чернышевского"	Dependence of light-addressable potentiometric sensor sensitivity on photo-induced processes in Si
5-11	Комаров	Иван	Александрович	АО "НИИ Графит"	Multicomponent graphene oxide suspensions for spin-coated thin films
5-12	Кондратьев	Валерий	Михайлович	Алфёровский	Study of quasi 1-D silicon nanostructures

				университет	adsorption properties
5-13	Леоненко	Екатерина	Сергеевна	НИУ МИЭТ	Study of the Al/CuOx thermite material combustion initiation process using a thin film Ni/Cr heating element
5-14	Лепаев	Александр	Николаевич	Чебоксарский институт (филиал) Московского политехнического университета	Transformation of dispersed particles in a pyrotechnical flame
5-15	Литовченко	Наталья	Александровна	"Московский Институт Электронной Техники"	Features of electrophoretic deposition of nanostructured cathode material based on NCA and Super C45.
5-16	Ломакин	Андрей	Игоревич	МИЭМ ВШЭ	Inelastic scattering in ultra-thin Nb films
5-17	Мастюкова	Алена	Сергеевна	МФТИ, РКЦ	Quantum convolutional neural networks for multiclass classification
5-18	Миронюк	Владислав	Николаевич	Саратовский национальный исследовательский государственный университет имени Н. Г. Чернышевского	Investigation of Langmuir floating layers by capacitive methods
5-19	Мирошниченко	Анна	Сергеевна	ИТМО, СПБАУ РАН	Low-adhesive functionalized silicone rubbers for flexible light-emitting devices
5-20	Морозова	Екатерина	Владимировна	ФГБОУ ВО Ульяновский государственный университет	Modeling of thermoelectric properties of graphenylene nanotubes encapsulated with fullerenes
5-21	Мурашко	Альбина	Максимовна	МГУ им. М.В. Ломоносова	Resorbable materials of complex shape based on calcium pyrophosphate for bone tissue regeneration
5-22	Науменко	Данил	Валерьевич	Южный федеральный университет	Characterization of MEMS gyroscope sensor by nanoindentation
5-23	Николаева	Анастасия	Сергеевна	Российский квантовый центр	Multi-qubit gate decomposition using photonic qutrits
5-24	Нугманова	Алсу	Галимовна	ИФХЭ РАН им. А.Н. Фрумкина	Size-selective hybrid photocatalysts based on porphyrin SURMOFs and graphene oxide
5-25	Миронюк	Владислав	Николаевич	Саратовский национальный исследовательский государственный университет имени Н. Г. Чернышевского	On the compression modulus of floating Langmuir layers
5-26	Романов	Никита	Сергеевич	РХТУ им. Д.И. Менделеева / АО "НИИграфит"	Exfoliation of h-BN for silicone-based thermal pads - effective heat management material in electronics
5-27	Ромашкин	Алексей	Валентинович	Национальный исследовательский университет «МИЭТ»	Thin WO3/Pt layer with top spray deposited carbon nanotubes to form structure with heterojunctions for selective gas sensor
5-28	Семенов	Александр	Алексеевич	ФТИ им. Иоффе	Local elastic moduli of amorphous nanostructures (Локальные упругие модули аморфных наноструктур)
5-29	Смирнова	Мария	Александровна	ЯрГУ им. П.Г. Демидова	Influence of the initial surface state on the ripple formation induced by O2+ sputtering of Si
5-30	Соболева	Ольга	Игоревна	Южный Федеральный Университет	Investigation of the Stability of Current Generation in Nitrogen-Doped Carbon

					Nanotubes
5-31	Соколов	Максим	Римович	МГУ им. М.В. Ломоносова	Self-assembly of porphyrin-based symbimetic hybrid material on layered europium hydroxide
5-32	Старовойтов	Сергей	Олегович	Университет ИТМО	Effect of the ratio of intensities of the reference and object beams on the performance of computer-generated holograms designed for extreme ultraviolet lithography
5-33	Терещенко	Иван	Борисович	ФТИ им. А.Ф. Иоффе	Durability silver coating for Second Mirrors optical diagnostic ITER to high humidity and thermal cycling
5-35	Харитонова	Полина	Геннадьевна	ФГБОУ ВО «Саратовский национальный исследовательский государственный университет имени Н.Г. Чернышевского»	Langmuir-Blodgett technology to obtain semi-magnetic photosensitive materials
5-36	Шарапов	Андрей	Анатольевич	МФТИ (НИУ) / АО "НИИМЭ"	Sidewall roughness model for optical losses calculation in photonic integrated circuits
5-37	Ширяев	Максим	Евгеньевич	Национальный исследовательский университет «МИЭТ»	Features of the combustion initiation process of Al-CuOx multilayer thermite structures

6. Crystal growth and structural properties of semiconductor materials and nanostructures

6-1	Авилов	Вадим	Игоревич	Южный федеральный университет	Cross-bar memristor nanostructures array for neural network layout
6-2	Арефина	Ирина	Александровна	Университет ИТМО	Optical properties of carbon dots covalently bonded with plasmonic nanoparticles
6-3	Белов	Ярослав	Дмитриевич	ЯрФТИАН им. Валиева	Formation of Pb-Sn Janus particles on the surface of lead-tin telluride films during ion-plasma sputtering
6-4	Бесполудин	Владислав	Валерьевич	Южный федеральный университет	Gas-sensitive properties of cobalt oxide films formed by RTA
6-5	Большин	Даниил	Сергеевич	МГУ им. М.В. Ломоносова/НИЦ "Курчатовский институт"	Influence of the applied voltage on electrophysical properties of conductive hydrogel studied by Raman spectroscopy
6-6	Бондаренко	Дарья	Николаевна	СПбАУ РАН им. Ж.И. Алфёрова	Design of LEDs based on GaN/InGaN nanowires on Si substrates
6-7	Вакулов	Захар	Евгеньевич	Федеральный исследовательский центр Южный научный центр Российской академии наук	Ferroelectric films for renewable energy
6-8	Васин	Сергей	Вячеславович	УФИРЭ им. В.А. Котельникова РАН	Шумовые характеристики пленок поливинилового спирта с магнито-чувствительными многостенными

					углеродными нанотрубками
6-9	Вовк	Илья	Александрович	Университет ИТМО	Lattice reconstruction in finite-size MoSe2-WSe2 heterostructures
6-10	Волкова	Мария	Геннадьевна	Южный федеральный университет	The effect of the seed layer on the TiO2 nanotubes coatings quality grown on the glass substrates by hydrothermal synthesis
6-11	Горелов	Илья	Кириллович	МГУ	Research of microresonator characteristics with carbon nanotubes
6-12	Гридчин	Владислав	Олегович	СПбАУ РАН им. Ж.И. Алфёрова	InGaN nanostructures on Si substrate: PA-MBE growth and properties
6-13	Грушевский	Егор	Алексеевич	ЯрГУ им. П. Г. Демидова	The plasma assistant cathodic electro-chemical exfoliation of graphite.
6-14	Гуляева	Ирина	Александровна	ИТА ЮФУ	Investigation of the surface properties of thin nanocomposite films of TiO2-SnO2 composition
6-15	Дададжанова	Антонина	Ивановна	Университет ИТМО	The properties of magneto-luminescent nanocomposites in a liquid flow
6-16	Данилина	Элеонора	Михайловна	Федеральный исследовательский центр Южный научный центр Российской академии наук	The effects of epitaxial strain on the thermodynamic parameters of III-V bismuth-containing alloys
6-17	Ерёменко	Михаил	Михайлович	Южный федеральный университет	Effect of pregrowth annealing temperature on the subsequent epitaxial growth of GaAs on Si
6-18	Звягина	Александра	Игоревна	ИФХЭ РАН	Self-assembly of recyclable semiconductor nanowires from lutetium bis-phthalocyanine on solids
6-19	Золотухин	Дмитрий	Сергеевич	ФГБОУ ВО «ВГУ»	AlGaN/GaN heterostructures grown on hybrid SiC/porSi substrates
6-20	Иванов	Андрей	Юрьевич	Университет ИТМО	Heteroepitaxial growth of κ-Ga2O3 films by halide vapor phase epitaxy
6-21	Кадинская	Светлана	Алексеевна	Академический университет им. Ж.И. Алфёрова	Study of hydrothermal zinc oxide nanostructures photovoltaic properties
6-22	Киндюшов	Иван	Константинович	Академический университет им. Ж.И. Алфёрова	Study of narrow-band UV radiation sources based on zinc oxide
6-23	Кириченко	Данил	Владимирович	Южный Федеральный Университет	Multistage droplet epitaxy for the fabrication of InAs/GaAs quantum dots with ultra-low density
6-24	Комаревцев	Иван	Михайлович	Академический университет им. Ж.И. Алфёрова	Effect of noble metal nanoparticles in transition metal oxide magnetron sputtering
6-25	Кондратьева	Анастасия	Сергеевна	Академический университет им. Ж.И. Алфёрова	Surface modification of magnetron sputtered metal oxide films with plasmonic nanoparticles
6-26	Косолапова	Ксения	Дмитриевна	Университет ИТМО	Control of optical properties by change in surface chemistry of carbon dots based on citric acid and ethylenediamine
6-27	Краснов	Алексей	Галинурович	Институт химии ФИЦ Коми НЦ УрО РАН	New bismuth titanates heterostructures as Vis-photocatalysts: DFT and experimental insight
6-28	Крюков	Руслан	Николаевич	ННГУ им. Н.И. Лобачевского	Efficiency of GaOx nanoclusters formation in SiO2 and Al2O3 dielectric layers subjected to O+ and Ga+ ion implantation

6-30	Кузнецов	Юрий	Михайлович	Нижегородский государственный университет им. Н.И. Лобачевского	Method of GexSi1-x doping with phosphorus in the spark plasma sintering process
6-31	Кутепов	Максим	Евгеньевич	Южный Федеральный университет	Optimizing deposition regimes to fabricate vanadium dioxide film for active metasurfaces
6-32	Лахина	Екатерина	Александровна	Южный федеральный университет	Independent control of size and shape of GaAs nanostructures during droplet epitaxy using ultra-low arsenic flux
6-33	Лендяшова	Вера	Вадимовна	СПбАУ РАН им. Ж.И. Алфёрова	InAs quantum dots in Si: MBE growth and optical properties
6-34	Максимова	Алина	Андреевна	СПбГЭТУ ЛЭТИ	Plasma Deposited Indium Phosphide and its Electrophysical Properties
6-35	Мартынова	Ирина	Константиновна	НИУ МИЭТ	Effect of thermal annealing on catalytic properties of Ge-Co nanostructure obtained by electrochemical deposition
6-36	Махмуд-Ахунов	Марат	Юсупович	ФГБОУ ВО "Ульяновский государственный университет"	Titanium oxide nanotubes for high capacity systems
6-37	Мельниченко	Иван	Алексеевич	СПбГЭТУ "ЛЭТИ"/НИУ ВШЭ	Optical studies of InP nanostructures monolithically integrated in Si (100)
6-38	Морозова	Юлия	Викторовна	Южный Федеральный Университет	Creation of a sensitive element of a gas sensor based on a graphene-like film
6-39	Низамеева	Гулия	Ривалевна	ФИЦ КазНЦ РАН	Cetyltrimethylammonium bromide as a soft template for the synthesis conductometric gas sensor active substance
6-40	Никитина	Лариса	Сергеевна	Южный Федеральный Университет	Study of FIB-modified silicon areas by AFM
6-41	Османов	Себастьян	Вадимович	КФУ им. В.И. Вернадского	Topological features of nanoplasmonic structures based on Bi-substituted iron garnets
6-42	Резник	Родион	Романович	СПбГУ/СПбАУ им Ж.И. Алфёрова	III-V hybrid nanostructures on silicon: molecular-beam epitaxy growth and physical properties
6-43	Рыбин	Владислав	Витальевич	ГОУ ВО "Ульяновский государственный университет"	Thermal and mechanical properties of a metal-matrix composite with ceramic inclusions
6-44	Трошкина	Наталья	Николаевна	Государственный университет "Дубна"	Investigation of the properties of quantum dots depending on the nature and number of additional semiconductor layers
6-45	Фаттахов	Илья	Сергеевич	ЯрГУ им. П.Г. Демидова	Growth of nanostructured cobalt film at oblique angle deposition
6-46	Федотов	Артем	Владимирович	НИУ ВШЭ	Grain structure of LPCVD polycrystalline silicon
6-47	Харин	Никита	Юрьевич	ФГАОУ ВО СПбПУ	"Development of the design of a THz radiation source based on tunnel-coupled quantum wells"
6-48	Черненко	Наталия	Евгеньевна	Южный Федеральный Университет	Experimental study of nanoholes formation using local droplet etching of FIB-modified GaAs (001) surface

6-49	Чистиков	Илья	Евгеньевич	Академический университет им. Ж.И.Алферова	The development of the method for temperature-resolved measuring of local Raman and photoelectric response
6-50	Шандыба	Никита	Андреевич	Южный Федеральный Университет	Effect of FIB-modification of Si(111) surface on GaAs nanowire growth
6-51	Шишкин	Иван	Александрович	Самарский университет/ООО "Бетавольтаика"	Formation of porous silicon layers in a «universal» type electrochemical cell
6-52	Шугабаев	Талгат	Маратович	Академический университет им .Ж.И. Алферова	
6-53	Юшков	Вячеслав	Владиславович	Московский государственный университет имени М.В. Ломоносова	Semiconductor metasurfaces for Fourier filtering of an optical signal
6-54	Гуляева	Ирина	Александровна	ЮФУ	Study of photoconductivity of thin films Co3O4 – ZnO

Adaptive filtering revealed a new way for single living cells high-resolution electro- and optical research

A A Abelit, N A Boitsova, and D D Stupin

[1] Alferov University, Khlopina 8/3, 194021 St. Petersburg, Russia
E-mail: anna.abelit@gmail.com, Stu87@ya.ru

Abstract. In our study, we propose to combine the study of HeLa cells using confocal microscopy and adaptive filtering based electrical impedance spectroscopy using. As a result, we have found that in contrast to the Fourier transformation impedance spectroscopy, adaptive filtering has a greater noise immunity, which made it possible for us to observe individual cells using microelectrodes. Moreover, this method is high-speed and high-resolution. Combining the methods of electrical impedance spectroscopy and confocal microscopy allowed us to observe in real time the proliferation of cells under the action of trypsin-Versene, as well as their subsequent death when a solution of the detergent Triton x114 was added to them.

1. Introduction

Nowadays the interface of the biological and physical experimental techniques has become a birthplace of the new significant breakthroughs in biotechnologies [1]. In the framework of this paradigm combining of the laser-pumped confocal microscopy – a state-of-the-art technique for high-resolution studying single cells lateral morphology [2] – with single-cell electrical impedance sensing method (SCIS), which is significantly sensitive to the variation in cells morphology in out-of-plane direction [3], represents a way for high-informative investigation of the living cells. However, despite both CM and SCIS methods are working perfectly apart, their simultaneous application face with the problem of the influence of the microscope hardware noise interferences on the impedance measurements. To overcome this issue, in present paper we have applied the adaptive-filtering based impedance spectroscopy (AF-IS) measurement protocol during cells CM investigation and compared it with standard Fourier impedance spectroscopy (Fourier-IS) method.

2. Materials and methods

For study single cells with CM and SCIS methods multielectode array MED P5155 with transparent (Pt-black free) electrodes was used (Panasonic, 50×50 μm^2, ITO). During experiment, cells were seeded on multielecrode array and then for their CM investigation was used Zeiss Observer. Z1 microscope (Zeiss, Germany) and DiBAC dye (XXX, membrane visualisation), and for their for SCIS research was used setup, discussed in Ref. [4], and AF-IS and Fourier-IS protols. As an investigated cells line was used HeLa cells. As a model stimuli were used trynsin-Versene solution (de-adhesion agent, Biolot, Russia) and Triton X-114 detergent (membrane distortion agent).

3. Results and discussion

The obtained results are presented on Figure 1. As can be seen from panels (a)-(c) after addition of trypsin-Versene solution the cells change their shape from fusiform to spherical, and after Triton X-114 addition cells membrane became drastically distorted. In the same time, on the AF-IS impedance evolution we can resolve the logistic $\tanh(t/7\text{min})$-shaped region, which corresponds to cells- de-adhesion process under trypsine-Versene action, and 10-s decay exponential region, which reflect the Triton X-114 induced cells membrane distortion process. However, contrary to AF-IS data the impedance evolution, obtained with Fourier-IS, is highly overlapped by noise interference produced by microscope hardware, and no useful information can be extracted from it. This significant difference between AF-IS and Fourier-IS is explained by noise immunity of the AF-IS, which automatically cancel high-level noise in the input data and extract from it useful signal, which being in agreement with CM photographs and include not only qualities, but also quantitive information about biophysical processes which take place in the single living cells.

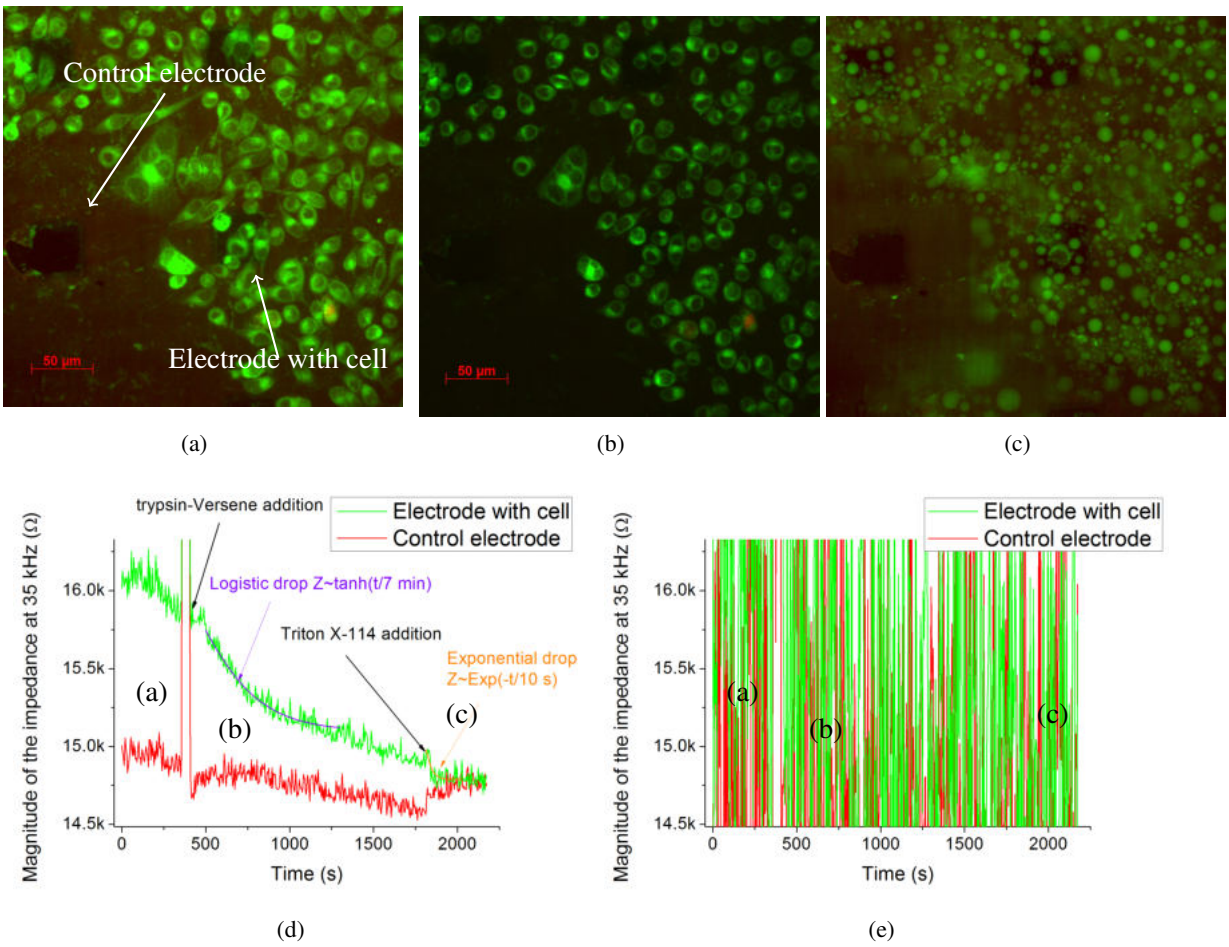

Figure 1. Demonstration of the simultanious optical- (a-c) and electro- (d,e) investigation of the living HeLa cells *invitro*. (a), (b), and (c) are photographs of the multielectrode array with cells before experiment, after trypsin-Veresne addition, and after Triton X-114 treatment respectively, (d) and (e) are AF-IS and Fourier-IS specra respectively.

4. Conclusion

In this paper, we have shown that combination of the AF-IS and CM represents a high-informative electro- and optical technique for single cells investigation, which allows studying cells lateral morphology as well as cells membrane properties in Z-direction in parametric manner. We believe that results of our study found an applications for solving a wide range of actual medical and cytological problems.

Acknowledgements

Author express their gratitude Knyazev N.A., Verlov N.A., Kazantsev V.B., Blinova M.I, and Dubina M.V. for comprehensive assistance and support. The setup creation for CM and SCIS was funded by the Russian Science Foundation (20-13-00303), the study of the trypsin-Versene and Triton X-114 action on the cells was founded by the Ministry of Education and Science of the Russian Federation (FSRM-2020-0006).

References

[1] Gather M C and Yun S H 2011 *Nature Photonics* **5** 406–410

[2] Brian Matsumoto 2002 *Cell Biological Applications of Confocal Microscopy* 2nd ed Methods in Cell Biology 70

[3] Stupin D D, Kuzina E A, Abelit A A, Koniakhin S V, Emelyanov A E, Nikolaev D M, Ryazantsev M N and Dubina M V 2020 *ACS Biomaterials science and engineering*

[4] Stupin D D, Koniakhin S V, Verlov N A and Dubina M V 2017 *Phys. Rev. Applied* **7**(5) 054024

Study of Cerium Dioxyde Based Wound-Healing Properties of a Nanocomposite in a Proton-Induced Radiation Dermatitis Model on Mice

V A Anikina[1], N R Popova[1], S S Sorokina[1], E A Zamyatina[1], A E Shemyakov[2]

[1]Institute of Theoretical and Experimental Biophysics of RAS, Institutskay 3, 142290 Pushchino, Russia
[2]LPI Physico-technical Centre, 142281 Protvino, Russia

E-mail: viktoriya.anikina@list.ru, nellipopovaran@gmail.com, sorokinasvetlana.iteb@gmail.com

Abstract. Radiodermatitis is the most common side effect of radiotherapy. Currently, there is no specific way to prevent or treat radiation-induced skin damage. In this article, a nanocomposite based on cerium dioxide (CeO_2) was investigated as a promising prophylactic and therapeutic agent in a proton-induced dermatitis model in SHK mice.

1. Introduction

In the last decade, different types of ionizing radiation (gamma, X-ray and hadron therapy) have been used to increase the effectiveness of oncological disease therapy, depending on the type and localization of the tumor. However, irrespective of the type of radiation used, 95% of patients develop a side effect as radiation dermatitis [1].

The main reason for the pathogenesis of radiodermatitis is the oxidative stress induced by radiation. During radiotherapy, ionizing radiation causes the molecules and intracellular structures to be directly and indirectly ionized. As a result there is the generation of free radicals, active oxygen forms (AFCs), the formation of nuclear and mitochondrial DNA double-strand breaks, and the activation of genes and proteins of early inflammatory response. Subsequent to this cascade of biochemical reactions, basal keratinocytes, fibroblasts, endothelial cells and hair follicle stem cells are damaged, leading to the development of radiation dermatitis [2].

Thus, an important task of modern radiation biomedicine is the research for new specific means for the radiation dermatitis therapy. One such agent is nanocrystalline cerium dioxide (nanocerium). Nanocerium is considered to be the most promising nanomaterial for biomedical applications due to its physicochemical properties. It is in the nanoscale state that CeO_2 exhibits unique antioxidant properties due to high degree of oxygen non-stechiometry, auto regenerative potential, catalazo-, superoxide dismutase- and peroxidase-like activity. In addition, cerium dioxide nanoparticles have been shown to be capable of participating in biological processes as a regulator of AFC and an acceptor of free radicals both in vitro and in vivo [3].

2. Materials and methods

Our laboratory team as well as the LPI Physico-technical Centre medical physicists on the synchrotron proton ("Prometheus", Protvino) have for the first time received a radiation dermatitis model on male SHK colony mice. One day prior to the irradiation of the animal, the rear hairs were removed and then irradiated locally once on the proton synchrotron. The estimated dosage at the surface of the animal is 50 Gy. The uniform coverage area (95%) at a given dose is 15x15mm. Beam energy from the accelerator outlet - 88.5 MeV. Irradiation pulse, with a cycle of 2 seconds. Radiation time is 2.5 min.

The assessment of the local radiation lesion of the skin was carried out daily for the purpose of fixing the clinical manifestations of radiation dermatitis, using photofixation, visual evaluation (according to the RTOG classification) and measuring the area of the affected skin with a caliper.

As a therapeutic agent, we synthesized a stabilised triethylene glycol nanocomposite based on CeO2 using a unique technique developed in collaboration with Kurnakov Institute of General and Inorganic Chemistry of the Russian Academy of Sciences (IGIC RAS).

3. Results and discussion

In this study, a post-radiotherapy scheme for radiotherapy dermatitis was developed, when the use of nanocomposite as an experimental therapeutic agent started with the formation of erythema, peeling and skin oedema, which corresponds to three degrees of radiodermatitis according to the RTOG classification. This degree of radiodermitis was found in all mice irradiated on day 11 of the experiment. The average area of formed radiation damage to the skin was 5.4 cm^2, which was 2.4 times the area of the proton beam at the source (beam area 2.25 cm^2), which may indicate progressive inflammation at both the local and systemic level.

Laboratory animals were divided into three groups: non-irradiated mice using nanocomposites, irradiated with nanocomposites and irradiated without treatment. A strictly defined quantity of the test nanocomposite was applied to the skin twice daily from a sterile vial with no further dressing. No skin reactions were found in non-irradiated animals using nanocomposites.

The therapeutic wound-healing effect of the CeO_2-based nanocomposite was estimated to reduce the area of radiation dermatitis in an experimental group relative to the control group of irradiated animals without the use of therapy. It was assumed that the mean radiation-induced dermatitis zone was 100% for all irradiated mice.

Treatment duration was 90 days, which corresponds to the time during which acute dermatitis is diagnosed. At the end of the experiment, the control group of animals showed incomplete healing of radiation dermatitis with severe erythema, scar tissue formation and partial alopecia at the centre of the wound. The 90-day test group also showed incomplete healing, mild erythema and partial alopecia at the centre of the wound, but the area of the affected skin decreased by 10% relative to the control group.

Thus, in this experimental design, the nanocomposite under study has a moderate healing effect in the radiation dermatite model in mice, and can be considered a prospective active ingredient in developing a treatment for preexisting skin irradiation.

Acknowledgments

The authors express their gratitude to the staff of the Laboratory of Functional Materials Synthesis and Mineral Raw Materials Processing IGIC RAS Ivanov V.K., Baranchikov A.E. and Kozlova T.O. for help in the conduct of this research.

References

1. Wei J., Meng L., Hou X. et al. 2019 *Cancer Management and Research*. **2** 167–177
2. Kim J.H., Kolozsvary A. J.J., Jenrow K.A. and Brown S.L. 2013 *International Journal of Radiation Biology*. **89(5)** 311-318
3. Shcherbakov A.B., Zholobak N.M. and Ivanov V.K. 2020 *Cerium Oxide (CeO_2): Synthesis, Properties and Applications.* **Chapter 8** 279-358

Development of a bioimpedance instrument and study of the interaction of electrodes with a biological object in bioimpedance diagnostics

V V Antipenko[1], E A Pecherskaya[1], S A Antipenko[2], A I Levin[1], O A Safronova[1] and V S Alexandrov[1]

[1]Department of Information and measuring equipment and metrology, Penza State University, Penza 440026, Russia
[2]JSC PO Elektropribor, Penza 440011, Russia

v.antipenko7@yandex.ru

Abstract. In diagnostic medicine, in order to monitor physiological parameters that characterize the composition of the human body, the state of the respiratory system, in oncology and other areas, one of the informative parameters is bioimpedance. At the moment, when measuring bioimpedance parameters, much attention is paid to the methods and measurement accuracy. The biological object in contact with the electrodes under the influence of alternating current demonstrates a complex behavior of the impedance. This article discusses the electrode-bioobject contact, ways to reduce the impact on the accuracy of impedance measurements, and proposes a model of a bioimpedance instrument.

1. Introduction

Over the past two years, many areas, including science, technology, and medicine, have faced changes in development priorities due to the spread of the coronovirus infection. From year to year, the trend of improvement in the field of health care is increasing, and in the medicine of the future, a large role is assigned to the prevention and prognosis of the treatment of diseases. This will make it possible to diagnose diseases at an early stage, increase the chances of recovery and significantly save on the treatment of the patient [1, 2].

The method of bioimpedance analysis (BIA) is based on measuring the conductivity of a biological object under the action of an external electric field, which makes it possible to assess a wide range of morphological and physiological parameters of an organism. This BIA method is non-invasive, its main advantage is to preserve the integrity of the structure of the biological object and the comfort of the measurement procedure. In bioimpedance analysis, the active and reactive impedances of the human body or its segments are measured at various frequencies. Based on the measured data, body composition characteristics are calculated.

There are many bioimpedance measuring devices in the world today, but all of them have the main problems associated with measurement error [3]. In this paper, we consider the electrode-bioobject contact and ways to reduce the influence of electrodes and their attachment methods on the accuracy of impedance measurements. A model of a bioimpedance instrument for measurements is proposed.

2. Processes of electrode-tissue interaction

The device that measures bioimpedance parameters interacts with a biological object through electrodes. In the area of electrode-tissue contact, complex physical and chemical processes occur that affect the measurement results. When the electrode contacts the electrolyte, an equilibrium potential difference is established between them, and a double electric layer is formed near the interface. This is due to the fact that in metal electrodes the current is formed by electrons, and in a biological object - by ions. It is important that the electrode material does not dissolve during measurements; therefore, inert materials are used.

The skin consists of three main layers: the outer layer - the epidermis, the dermis and the subcutaneous layer. The main problems are associated with the application of electrodes to the surface of the skin. This is due to the fact that a thin layer of the epidermis (10 - 20 microns) in a dry state at direct current has a very high resistivity, 10^4 - 10^5 Ohm·m. On alternating current, with increasing frequency, the resistivity gradually decreases to $\approx 10^2$ Ohm·m per 1 MHz. To overcome them, it is necessary, firstly, to clean the skin in the places where the electrodes are applied and, secondly, to apply a special conductive gel or saline solution to the skin.

The specific classification of the electrode system of the material depends on the number and arrangement of the electrodes. A model of a bioimpedance instrument (Figure 1) with a more reliable contact of the electrode with the biological object and an optimal electrode surface area is proposed.

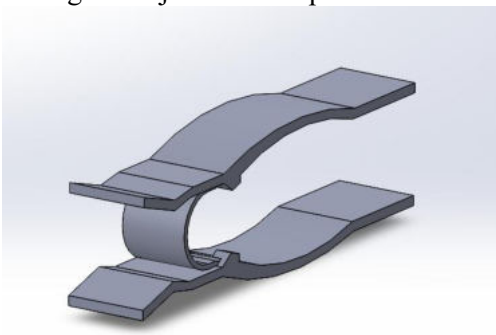

Figure 1. Model of the bioimpedance instrument.

The total contact impedance consists of the electrode-gel contact impedance connected in series, the gel impedance, and the epidermal impedance reduced by gel impedance. In general, the modulus of the contact impedance noticeably decreases with increasing frequency. When using electrodes with a small surface area, non-linear distortions can be more significant.

Conclusion

In this paper, a model of a bioimpedance instrument is proposed that allows measurements to be made on individual parts of a biological object and its segments, as well as ways to reduce the methodological errors in bioimpedance measurement due to the influence of electrodes.

References

[1] Buendía R, Bogónez-Franco P, Nescolarde L and Seoane F 2012 Influence of electrode mismatch on Cole parameter estimation from Total Right Side Electrical Bioimpedance Spectroscopy measurements *Medical Engineering & Physics* **34** (7)

[2] Antipenko V V, Pecherskaya E A, Zinchenko T O, Artamonov D V, Spitsina K Yu and Pecherskiy A V 2020 Development of an automated bioimpendance analyzer for monitoring the clinical condition and diagnosis of human body diseases *J. Phys. Conf. Ser.* **1515** (5)

[3] Antipenko V V, Pecherskaya E A, Zinchenko T O, Melnikov O A and Fimin A V and Zaryvahina S A 2020 Analysis of methodological errors in measuring a digital automated bio-impedance meter *J. Phys.: Conf. Ser.* **1695** 012051

Physicochemical analysis of bisretinoid A2E photooxidative destruction products

A.A. Vasin[1*], M.A. Yakovleva[2], A.E. Dontsov[2], A.A. Gulin[1], A.V. Aybush[1], T.B. Feldman[2,3], M.A. Ostrovsky [2,3]

[1] N.N. Semenov Federal Research Center for Chemical Physics, Russian Academy of Sciences, Moscow 119991, Russia
[2] Emanuel Institute of Biochemical Physics, Russian Academy of Sciences, Kosygin st. 4, Moscow 119334, Russia
[3] Department of Biology, Lomonosov Moscow State University, Leninskiye Gory 1, Moscow 119234, Russia

* a2vasin@yandex.ru

Abstract. A2E is a product of visual cycle whose accumulation is associated with degenerative diseases. In this study A2E were photooxidezed and 2D fluorescence spectra were obtained. Time-of-flight secondary ion mass spectrometry (ToF-SIMS) and Fourier transform infrared spectroscopy (FTIR) revealed chemical changes during the process of photooxidation. Aldehydes accumulation was observed and some new structures of the resulting compounds were proposed. It was shown the products of the photooxidative destruction of A2E cause modification of hemoglobin.

1. Introduction

Lipofuscin granule accumulation in the retinal pigment epithelium (RPE) cells is associated with various eye degenerative diseases. The main bisretinoid of RPE lipofuscin A2E is the side product of the visual cycle. It is known, that A2E is able to damage cellular structures in situ. In addition, as we demonstrated earlier [1], the photooxidative destruction of A2E results in the formation of toxic water-soluble TBA-reactive products. The main goal of this work is to characterize the A2E oxidation products using the 2D fluorescence spectroscopy, IR-spectroscopy, ToF-SIMS and HPLC analyses.

2. Methods

A2E photooxidation was carried out at room temperature under constant stirring using a 150 W incandescent lamp with a heat filter (KGM 24–150, 400–700 nm, 80 mWm/m^2). Nonirradiated A2E was as control sample. The A2E samples were irradiated during 120 minutes. For each sample fluorescence spectra were obtained (Horiba Fluoromax). Mass-spectra and FTIR-spectra were collected by time-of-flight secondary ion mass spectrometry (ION-TOF TOF-SIMS 5) and Fourier transform infrared spectroscopy (Bruker Lumos II). The ability of A2E oxidized products to modify proteins was studied by high performance liquid chromatography (HPLC) (Knauer).

3. Results and discussion

2D fluorescence map spectra were accumulated for nonirradiated and irradiated A2E (Fig.1). There is a general shift of fluorescence maximums to the short wavelength region. This is probably due to A2E photooxidation and the destruction of the original A2E conjugated structure that is result in the accumulation of oxidation products with a shorter conjugated structure. A large Stokes shift upon excitation with UV light was found. It could be associated either with fluorescence overlapping of different oxidized products or with charge transfer in pyridinium ring. Changes were detected in all spectral area after photooxidation.

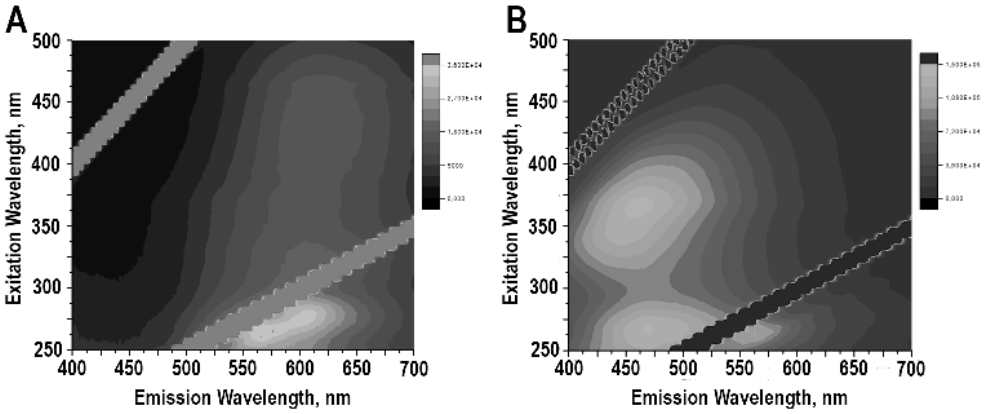

Figure 1. Fluorescence profiles of nonirradiated A2E (**A**) and photooxidized A2E (**B**). The color map represents fluorescence intensity from blue (low fluorescence signal) to red (high fluorescence signal).

Carbonyls group signal accumulation was confirmed by ToF-SIMS and FTIR spectroscopy during irradiation. Using FTIR-spectroscopy, an increase in intensity of carbonyl bands (1750 cm^{-1}, 1450 cm^{-1}, 1350 cm^{-1}) in oxidized samples was also detected. An intensity growth of ions with m/z = 29 (CHO^+), m/z = 43 ($C_2H_3O^+$), m/z = 60 ($C_2H_4O_2^+$) and m/z = 69 ($C_4H_7O^+$) was observed in oxidized samples by ToF-SIMS. Moreover, several secondary ions showing monotone growth during irradiation were revealed. Based on the exact masses and assumed mechanisms of oxidation, chemical structures have been proposed (Fig.2).

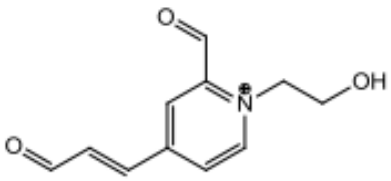

Chemical Formula: $C_{11}H_{12}NO_3^+$
Molecular Weight: 206,22

Figure 2. Propoused structure of A2E photooxidation product. Chemical formula and molecular weight are given.

The ability of A2E oxidized products to modify proteins was studied by HPLC. The hemoglobin from bovine erythrocytes was used as a target protein. It was shown that the products of the photooxidative destruction of A2E cause modification of hemoglobin with the formation of fluorescent Schiff bases. This result was compared with hemoglobin glycation by methylglyoxal and fructose. It was found that both A2E oxidation products and methylglyoxal and fructose caused an increase in the fluorescence signal in the total spectrum of samples, which was accompanied by the appearance and growth of fluorescent peaks in the chromatogram.

Thus, it was shown that during photooxidation of A2E, reactive aldehydes and ketones are formed, which exhibit a toxic effect on hemoglobin molecules, causing their modification by the glycation mechanism, and can be considered as an aggravating factor in the degenerative diseases progression. Some new structures of the resulting compounds were also proposed.

4. Acknowledgments
This research was funded by Russian Science Foundation (№ 22-24-00549)

References

1. Alexander Dontsov, Marina Yakovleva, Natalia Trofimova, Natalia Sakina, Alexander Gulin, ArsenyAybush, Fedor Gostev, Alexander Vasin, Tatiana Feldman, Mikhail Ostrovsky. Water-Soluble Products of Photooxidative Destruction of the Bisretinoid A2E Cause Proteins Modification in the Dark // *Int. J. Mol. Sci.* 2022, *23*(3), 1534; https://doi.org/10.3390/ijms23031534

The study of NADH conformations in water-ethanol solutions using molecular dynamics simulations.

D A Volkov[1,2], I A Gorbunova[1], M E Sasin[1], O S Vasyutinskii[1]

[1]Ioffe Institute, Saint-Petersburg, 195251, Russia
[2]Peter the Great St.Petersburg Polytechnic University, Saint-Petersburg, 195251, Russia

dinvol99@gmail.com

Abstract. Conformation dynamics of reduced nicotinamide adenine dinucleotide (NADH) in water-ethanol solutions was studied by means of molecular dynamics calculations. The number of trajectories of NADH were acquired. Distances between centres of mass of nicotinamide (NA) and adenine (AD) rings and relative concentration of NADH folded conformations were calculated and analysed as a function of ethanol concentration.

1. Introduction

Computer modelling of biological fluorescent molecules (biological fluorophores) in various environmental condition is often used nowadays in biological engineering and science for obtaining information on molecular structural dynamics. A coenzyme reduced nicotinamide adenine dinucleotide (NADH) is an important natural biological fluorophore that plays a significant role in redox reactions in living cells. Through redox reactions NADH endures great conformation changes, therefore the investigation of NADH conformational distribution at various microenvironmental conditions are very important for monitoring of redox reactions. The main aim of this work is the study of NADH conformational dynamics in water-ethanol mixtures at various concentration by means of molecular dynamics calculations and comparison of the theoretical results obtained with experimentally determined NADH conformational distribution in solutions.

2. Method

All molecular dynamics (MD) simulations of NADH were performed using GROMACS 2020.1 software with the CHARMM36-jul2021 force field. NADH structure was obtained from charm-gui library. NADH modelling was performed at temperature of 300 K and pressure of 1 atm. For NVT equilibration velocity-rescale (Bussi) temperature coupling and for NPT equilibration Berendsen pressure coupling were used. Molecular dynamics calculations were performed for 300 ns with a time step of 2 fs, V-rescale and Parrinello-Rahman algorithms were used for temperature and pressure coupling, long-range electrostatic interactions were computed with the particle mesh Ewald method (PME) and cutoff range of 12 Å.

3. Results and discussion

A set of molecular trajectories of NADH at six ethanol concentrations were obtained by MD simulations and distances between adenine and nicotinamide rings were acquired. The histograms of the number of

NADH states (N_s) with particular distances between the NA and AD centers of mass (R) are shown in figure 1 (a).

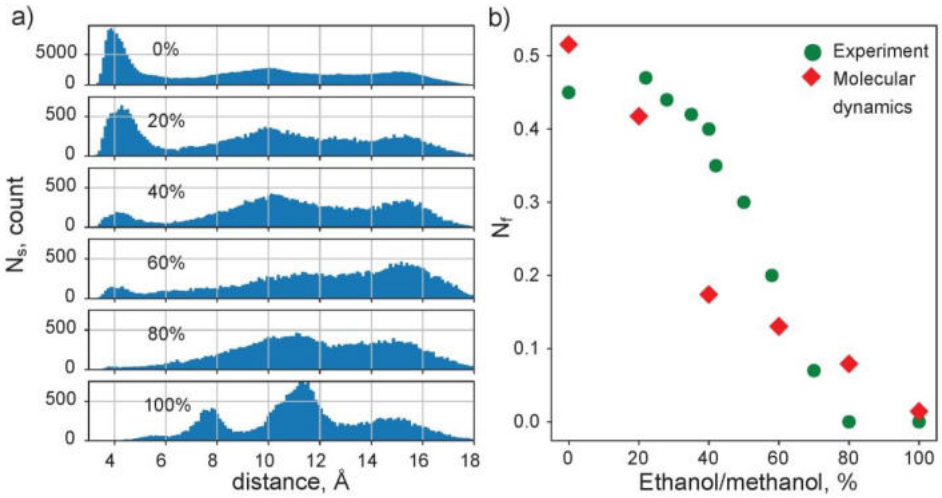

Figure 1. a) Number of states (N_s) with certain distances between centers of mass of NA and AD rings for six ethanol concentrations. Calculated relative concentration of folded conformations (N_f) as a function of ethanol concentration are given in 1 b) with red squares. Experimental N_f values as a function of methanol concentration determined in ref [3] are shown in 1 b) with green dots.

As can be seen in figure 1 (a) NADH conformations can be separated into three main groups: folded conformations (R < 5 Å), unfolded conformations (R > 12 Å), and intermediate conformations (5 Å < R < 12 Å). The relative concentration of folded conformations (N_f) determined using the histograms in figure 1 (a) is shown in figure 1 (b) with red squares, only folded and unfolded conformations were considered in calculation. Relative concentration of NADH conformation determined experimentally by means of polarized TCSPC technique [3] is also presented in figure 1 (b) with green dots. As expected, the folded conformations were found to be more stable in water than in ethanol. As can be seen in figure 1 (b) about 50% of folded conformations N_f exist in pure water while when ethanol concentration rise N_f decreases. As can be seen in figure 1 (b) the dependence of N_f on ethanol concentration determined theoretically differs somehow from the experimentally determined one in water-methanol mixtures [3]. The discrepancy can be due to different types of solvents: methanol and ethanol used in this paper and in ref. [3]. The relative number of the folded NADH conformations in water experimentally determined by other groups (see references in ref. [3]) varied from 25% to 55%. Based on the trajectory calculations we also analysed the angle α between the NA and AD planes. This planes are always non-parallel to each other: there are two stable conformation states with α =15-25º and α = 160-170º that can be determined by the NA ring rotation around ribose bond

The results obtained can be useful in future experimental and theoretical studies of microenvironmental effects on NADH configurations and lead to the development of new examination methods of important processes in living cells.

References

[1] Radoszkowicz L. et al. Sampling the Conformation Space of FAD in Water− Methanol Mixtures through Molecular Dynamics and Fluorescence Measurements //The Journal of Physical Chemistry A. – 2010. – Т. 114. – №. 2. – С. 1017-1022.

[2] Formoso E. et al. Aluminum and its effect in the equilibrium between folded/unfolded conformation of NADH //Journal of Inorganic Biochemistry. – 2015. – Т. 152. – С. 139-146.

[3] Gorbunova I. A. et al. Two-Photon Excited Fluorescence Dynamics in NADH in Water–Methanol Solutions: The Role of Conformation States //The Journal of Physical Chemistry B. – 2020. – Т. 124. – №. 47. – С. 10682-10697

Рамановская спектроскопия наночастиц пористого кремния, функционазированного 4,4’-(пропандиамидо)дибензоатом натрия

М. Ш. Сатторов[1], А. Ю. Гагарина[1], Ю. М. Коцур[2], А. Кузнецов[3], Ю.М. Спивак[1], Е.В. Флисюк[2], В.А. Мошников[1]

[1] Санкт-Петербургский государственный электротехнический университет «ЛЭТИ» им. В.И. Ульянова (Ленина), Санкт-Петербург
[2] Санкт-Петербургский государственный химико-фармацевтический университет
[3] Санкт-Петербургский национальный исследовательский Академический университет имени Ж. И. Алфёрова Российской академии наук

Пористые наночастицы, включая пористый кремний (por-Si), являются перспективными нанобъектами для адресной доставки лекарств и тераностики [1-3]. Применение в качестве носителя микро-мезо-макропористых наночастиц позволяет объединять на едином носителе (дисперсной транспортной системе для адресной доставки лекарств) несколько видов лекарственных средств разной природы. Современным трендом в области создания систем направленного лекарственного транспорта является использование интеллектуальных гибридных наноплатформ, состоящих из сложным образом спроектированных многослойных наносистем из нескольких типов наноматериалов [4, 5]. Сложный дизайн таких структур придает новые («интеллектуальные») свойства наноносителям за счет их функционализации (физической, химической и др.). При этом специфические заданные свойства таких систем (физические, химические или биологические) могут быть чувствительными как к внешним, так и к внутренним воздействиям. Другим важным достоинством таких систем доставки ожидается эффект пролонгированного высвобождения лекарственных субстанций и возможность моделирования кинетики высвобождения лекарственной субстанции (ЛС). При этом свойства поверхности пористых наночастиц будут во многом определять их характер взаимодействия с инкорпорируемыми и инкапсулирующими материалами. Актуальной проблемой является исследование взаимодействия пористой матрицы с лекарственными субстанциями разной природы и влияния на кинетику высвобождения [6].

Целью данной работы является исследование характера взаимодействия 4,4’-(пропандиамидо)дибензоатом натрия с наночастицами por-Si методом рамановской спектроскопии.

Выбор модельной субстанции для инкорпорирования обусловлен ее антистеатозным, гепатопротекторным и антиоксидантным действием [7, 8]. Наночастицы por-Si получены методом электрохимического анодного травления кремния марки КЭФ-4,5(111) в водно-спиртовом растворе HF при плотности тока анодирования 80 мА/см^2 с последующим измельчением

пористого слоя ультразвуком. Инкорпорирование наночастиц por-Si 4,4'-(пропандиамидо)дибензоатом натрия осуществлялось методом импрегнации наночастиц por-Si из водного раствора. Также в качестве образцов сравнения были подготовлены механические смеси кристаллической субстанции и наночастиц por-Si. В работе обсуждаются результаты рамановской спектроскопии (Horiba LabRAM 800) полученных образцов.

1. Korolev D. et al. The Combination of Solid-State Chemistry and Medicinal Chemistry as the Basis for the Synthesis of Theranostics Platforms. *Biomolecules* 2021, *11*, 1544.
2. Osminkina L. et al. Antiviral adsorption activity of porous silicon nanoparticles against different pathogenic human viruses // Bioactive Materials, KeAi Commun.,2022, 7, 39-46. .
3. Spivak Y. M. et al. Porous silicon nanoparticles for target drag delivery: structure and morphology //JP: Conf. Ser., 2015, 643, 1, 012022.
4. Duan W. et al. A co-delivery platform for synergistic promotion of angiogenesis based on biodegradable, therapeutic and self-reporting luminescent porous silicon microparticles // Biomaterials, 2021, 272, 120772.
5. Hossen S. et al. Smart nanocarrier-based drug delivery systems for cancer therapy and toxicity studies: A review // J. Adv. Research, 2019, 15, 1-18.
6. М. Сатторов и др. Особенности адсорбции органических молекул в пористом кремнии по данным ИК-спектроскопии // Сб. матер. VII науч.-тех. конф. с межд. уч. «Наука настоящего и будущего» для студ., асп. и мол. уч. 2019, 3, 128-131.
7. Власов Б.Я. и др. Экспериментальное обоснование возможности применения малоновой кислоты для коррекции психоэмоционального стресса // Бюллетень ВСНЦ РАМН. 2011. 1 (77), Ч. 1, 216-218.
8. Белых М. А. и др. Влияние нового производного малоновой кислоты на массу жировой ткани мышей с57бь/6 при экспериментальном стеатозе // Инновации в здоровье нации. - 2017. - С. 112-116.

Study of biomimetic composite dental materials based on nanocrystalline hydroxyapatite and light-curing adhesive.

P V Seredin[1], D L Goloshchapov[1], N S Builov[1], Yu.A. Ippolitov [2] and J Vongsvivut[3]

[1]Voronezh state uniberisity, Universitetskaya pl. 1, Voronezh, Russian Federation, paul@phys.vsu.ru
[2]Department of Pediatric Dentistry with Orthodontia, Voronezh State Medical University, Voronezh, Studentcheskaya st. 11, 394006, Russian Federation
[3] ANSTO-Australian Synchrotron, 800 Blackburn Road, Clayton, Victoria 3168 Australia

Abstract. With the use of light-curing Bis-GMA (Bis-phenol-A glycidylmethacrylate) adhesive and nanocrystalline carbonate-substituted calcium hydroxyapatite (nano-cHAp), corresponding by an aggregate set of characteristics to the apatite of human enamel and dentin obtained from the biogenic source of calcium – egg's shell of birds biomimetic Bis-GMA/nano-cHAp adhesives were synthesized.

In summary, for the specified nanofiller concentration increased values of Vicker hardnesses (VH) and degree of conversion were attained simultaneously while light curing of Bis-GMA/nano-cHAp adhesive.

1. Introduction

Numerous innovations with the application of biomimetic strategies and nanotechnologies (nanodentology) provided a considerable impetus in the area of engineering of the new class related with a new class of modern adhesion restoration materials [1]. It was repeatedly shown that the enhancement of trophic, mechanical (hardness and strength), physicochemical and performance properties of adhesive polymer matrix can be attained due to the introduction of various inorganic micro- and nanofillers into its composition [2]. One of the applied fillers for dental materials and bonds is calcium hydroxyapatite (HAp). The main task of our work was the determination of the proper adaptive composition and molecular properties of biomimetic adhesive based on Bis-GMA (bis-phenol -A glycidylmethacrylate), filled with nanocrystalline carbonate-substituted hydroxyapatite (nano-cHAp), providing a high degree of polymerization and mechanical hardness.

2. Materials and methods of their investigations

To obtain the samples of biomimetic samples in our work we used bisphenol-A-glycidyl methacrylate -based commercial adhesive. Nanocrystalline carbonate-substituted calcium hydroxyapatite (nano-cHaP) corresponding to the aggregate number of features in the human enamel and dentin was applied as a filler for light-curing Bis-GMA aadhesive. Samples of nano-cHAp were obtained using the wet chemistry method. The raw calcium hydroxide was obtained by thermal annealing from the hen's eggshells [3]. Mixing of nano-cHAp component and adhesive was performed with the use of ultrasound homogenizer QSonica Q55 for 30 s. To solve the problems stated in the work and

connected with the determination of the adaptive composition and molecular properties of biomimetic nano-filled adhesives the following samples were obtained with different content of the raw components (0.01 – 0.2g of nano-cHaP per 250 ml of Bis-GMA).

The obtained samples were investigated with the use of Fourier transform infrared (FTIR) spectroscopy technique, including the application of Synchrotron FTIR microspectroscopy at the Infrared Microspectroscopy beamline (Australian Synchrotron, Victoria, Australia). Microhardness of the synthesized biomimetic adhesive samples after their photopolymerization was determined using Vicker's technique and employing optical microscope-hardness testing instrument.

3. Experimental results and their discussion

Measuring of microhardness in the samples of biomimetic Bis-GMA/nano-cHAp adhesives was performed by Vicker's technique. From the analysis of obtained data one can see that microhardness of biomimetic Bis-GMA/nano-cHAp adhesive begins at the addition of nanocrystalline hydroxyapatite and it attains maximum at the content of ~0,16 g nano-cHAp in 250 ml of Bis-GMA adhesive. After that a decay of microhardness value is observed. Non-linear behavior of the dependence of microhardness values on nano-cHAp content is due to the changes that occur in molecular composition of the samples.

A degree of conversion for the adhesive material was determined with the use of FTIR data [4].

Simultaneous graphical analysis of the degree of conversion and microhardness makes it possible to determine the range of the optimal compositions for bioadhesive providing maximal value of as microhardness as the value of the degree of conversion during polymerization. From the calculations it follows that the content of nanocrystalline hydroxyapatite with characteristic morphological characteristics should be within the vicinity of the value ~0.125 – 0.135 g per 250 ml of Bis-GMA.

Unlike of the number of the previous similar investigations where HAp nanoparticles and other inorganic nanomaterials were applied for the filling of adhesion system, in our work used nanocrystals of carbonate-substituted hydroxyapatite with the mean sizes of 20x20x50 nm obtained according to our elaborated technology [3]. Uniform distribution of nano-cHAp filler in the adhesive matrix as well the interaction with the filler molecular groups favors the changes in molecular bonds that is confirmed by FTIR data; as a result, this considerably improved mechanical characteristics of the material.

4. Conclusion

Introduction and distribution of nano-cHAp filler in the adhesive matrix as well as its interaction with molecular groups of the latter one resulted in the change of chemical bonds that was evidenced by the data of Fourier transform infrared spectroscopy. In summary, for the specified nanofiller concentration increased values of Vicker hardnesses (VH) and degree of conversion were attained simultaneously while light curing of Bis-GMA/nano-cHAp adhesive.

Funding

This work was supported by the grant of Russian Science Foundation, grant number 21-15-00026 and support of the Ministry of Science and Higher Education of Russia, Agreement N 075-15-2021-1351.

References

[1] Zafar M S, Amin F, Fareed M A, Ghabbani H, Riaz S, Khurshid Z and Kumar N 2020 Biomimetic Aspects of Restorative Dentistry Biomaterials *Biomimetics* **5** 34

[2] Alhenaki A M, Attar E A, Alshahrani A, Farooq I, Vohra F and Abduljabbar T 2021 Dentin Bond Integrity of Filled and Unfilled Resin Adhesive Enhanced with Silica Nanoparticles—An SEM, EDX, Micro-Raman, FTIR and Micro-Tensile Bond Strength Study *Polymers* **13** 1093

[3] Seredin P V, Goloshchapov D L, Prutskij T and Ippolitov Yu A 2017 *Results Phys.* **7** 1086–94

[4] Daood U, Swee Heng C, Neo Chiew Lian J and Fawzy A S 2015 In vitro analysis of riboflavin-modified, experimental, two-step etch-and-rinse dentin adhesive: Fourier transform infrared spectroscopy and micro-Raman studies *Int. J. Oral Sci.* **7** 110–24

Fluorescence kinetics of biological coenzyme FAD in water-propylene glycol solutions excited by picosecond laser pulses

I A Gradusov[1,2], V P Belik[2], D M Beltukova[2], M K Danilova[2], O S Vasyutinskii[2]

[1]Peter the Great St.Petersburg Polytechnic University, 195251, Russia
[2]Ioffe Institute, St.Petersburg, 195251, Russia

gradusov.ia@edu.spbstu.ru

Abstract. The polarized fluorescence of intracellular coenzyme FAD was studied using time-correlated single-photon counting (TCSPC) technique. Fluorescence decay times, anisotropy coefficient and rotational diffusion time were determined as a function of propylene glycol concentration and analyzed.

1. Introduction

Flavin-adenine-dinucleotide (FAD) is an intracellular coenzyme widely used as a natural fluorescent biomarker of cellular biochemical processes, so this is important for biology and medicine. As known FAD exists in folded and unfolded conformations that can affect the fluorescence decay characteristics [1]. The distribution of folded and unfolded conformations depends on the solution properties, in particular, on its polarity and pH [1-3]. Fluorescence decay in FAD in an aqueous solution is double-exponential, with typical decay times of about 4 and 2 ns [1-3]. In water-alcohol solutions FAD solvation increases and the number of unfolded conformations grows up, at the same time the proportion of FAD molecules with a long fluorescence decay time increases [1-3]. Therefore, the investigation of polarized fluorescence parameters as a function of alcohol concentration can be used for understanding of the conformation distribution. In this paper we present the results of the study of fluorescence decay times, anisotropy, and rotational diffusion time in FAD as a function of propylene glycol concentration in aqueous solutions.

2. Experiment

The scheme of the experimental setup used was already reported in our recent publication [3]. A solution of FAD with the concentration of 60 μM in a mixture of distilled water with propylene glycol was used. Propylene glycol concentrations ranged from 0% to 98%. The solution was placed in a quartz cuvette and irradiated with a pulsed Nd:YAG laser (355 nm, 400 ps, 4 kHz). To prevent FAD photobleaching in solution and saturation effects, the laser intensity was reduced using an optical wedge. A polarizing cube was placed in front of the cuvette, providing vertical polarization of laser beam. The fluorescence signal was collected in the direction perpendicular to the excitation laser beam by a lens to the entrance slit of a monochromator (MDR-12, LOMO). A thin film polaroid was installed in front of the monochromator entrance slit with the transmission axis set alternately in the vertical and horizontal directions. The monochromator was tuned to the maximum fluorescence band intensity at 530 nm. The fluorescence was recorded by a photomultiplier tube (Hamamatsu H10682-01). A TCSPC module (PicoHarp 300, PicoQuant) was used to process the experimental data.

3. Results

The polarized fluorescence decay kinetics were observed, and the experimental data was processed following the procedure described in our recent paper [3]. As a result, the fluorescence decay times τ_i, fluorescence anisotropy r_0, and rotational diffusion time τ_{rot} were determined depending on the propylene glycol concentration. The results obtained are presented in Table 1.

Table 1. Polarized fluorescence parameters of FAD.
α_i are weighting coefficients which depict the contribution of the i-th exponent to the fluorescence intensity.

PG%	τ_1	α_1	τ_2	α_2	r_0	τ_{rot}
0%	4,46±0,19	0,30	2,17±0,04	0,70	0,24±0.02	0,15±0.05
20%	3,93±0,20	0,69	2,33±0,12	0,31	0,23±0.01	0,38±0.05
40%	4,39±0,09	0,80	2,30±0,10	0,20	0,23±0.01	0,75±0.05
60%	4,78±0,04	0,84	2,01±0,09	0,16	0,22±0.02	1,80±0.21
80%	5,13±0,19	0,83	2,23±0,19	0,18	0,24±0.01	3,42±0.60
98%	5,53±0,18	0,78	1,77±0,18	0,22	0,22±0.01	7,22±0.76

As can be seen in Table 1 the anisotropy coefficient r_0 was independent of the propylene glycol concentration in the solution and the change in the rotational diffusion time τ_{rot} was directly proportional to the solution viscosity in accordance with the Stokes-Einstein-Debye equation [3]:

$$\tau_{rot} = fC\frac{\eta V_M}{kT},$$

where parameter $f \geq 1$ is a shape factor accounting for the shape of solute molecules, C signifies the extent of coupling between the solute and solvent, η is the macroscopic solvent viscosity, V_M is a Van der Waals solute molecule volume, k is Boltzmann constant, and T is the absolute temperature.

Also, the weighting coefficient α_1 of the component with a longer fluorescence decay time τ_1 increased with an increase in the propylene glycol concentration. This founding can be associated with the increase of the relative concentration of the unfolded FAD conformation. At the same time, the weighting coefficient α_2 of the component with a shorter decay time, was likely related with the folded conformation. The decay time τ_1 increased at high propylene glycol concentrations, and the decay time τ_2 was practically constant within the experimental error bars.

Acknowledgments
This work funded by the Russian Science Foundation, Grant No. 21-72-10044.

References

[1] Nakabayashi, T., Md. Islam, S., Ohta, N. Fluorescence Decay Dynamics of Flavin Adenine Dinucleotide in a Mixture of Alcohol and Water in the Femtosecond and Nanosecond Time Range // J. Phys. Chem. B – 2010. – Vol. 114(46) – Pp. 15254– 15260.

[2] Sengupta, A., Gavvala, K., Koninti, R. K., Chaudhuri, H., Hazra, P. Folding dynamics of flavin adenine dinucleotide (FAD) inside non-aqueous and aqueous reverse micelles // Chem. Phys. Let. – 2013. – Vol. 584 – Pp. 67–73.

[3] M. K. Krasnopevtceva, M. E. Sasin, I. A. Gorbunova, D. P. Golyshev, A. G. Smolin, V. P. Belik, O. S. Vasyutinskii. Anisotropic fluorescence decay kinetics in FAD in water-methanol solutions under excitation at 355 and 450 nm// Proc. SPIE 11900, Optics in Health Care and Biomedical Optics XI, 119003H (9 October 2021); doi: 10.1117/12.2602467

Long-term storage of freeze-dried qPCR reagents in microfluidic devices

V V Grigorev[1], N A Esikova[2], A A Evstrapov[2], A S Bukatin[2,3]

[1]Peter the Great St. Petersburg Polytechnic University, St. Petersburg 195251, Russia
[2]Institute for Analytical Instrumentation of the RAS, St. Petersburg 198095, Russia
[3]Alferov Saint Petersburg National Research Academic University of the RAS, St. Petersburg 194021, Russia

E-mail: grigorjewitalij@yandex.ru

Abstract. Acceleration, automatization, and accuracy enhancement of a routine qPCR analysis is notably increased during the emerged COVID-19 pandemics. Besides, the indicated technique has much broader area of applications. At the same time, there are some difficulties (incl. low-temperature storage, contamination risks), which should be taken in account. We propose an integration between microfluidic approach and freeze-drying technology to overcome automatization problem, improve the detection accuracy, and allow room temperature storage, that enables to perform qPCR by just adding a sample into a device inlet and set up a thermocycler. Our results show that microfluidic devices with immobilized reagents are stable and ready to use for at least 6 months.

1. Introduction

The real-time or quantitative polymerase chain reaction (qPCR) allows to detect the presence and the amount of nucleic acids with definite sequence what is necessary in very different applications (disease or mutation detection, GMO-control etc.) [1–4]. Hence, qPCR analyses are in high demand. Everything related to the reagents volume reduction, automatization and accuracy enhancement of this process arouse interest. First two problems could be resolved by using microfluidic devices instead of conventional qPCR [4]. While the immobilization of reagents inside the chip lets to minimize the number of components needing to be added, and therefore improves the accuracy.

For several years different research groups and reagents supplier companies proposed several technologies for immobilizing qPCR reagents in microfluidic devices. That could be encapsulation or gel-immobilization, but incomparably more often is used freeze-drying (lyophilization) [5–7]. Freeze-dried reagents could be stored at a room temperature at least 1–2 years (with use of different stabilizers) and redissolved by adding a sample within seconds [7].

2. Results

We developed a microfluidic chip that works with relatively small amounts of the reagents and sample (20 μl and 5 μl respectively). The lower heat capacity and high surface-to-volume ratio of the reaction chamber allows faster and more accurate temperature cycling. The chips are made of biocompatible and transparent polycarbonate and polypropylene, what makes the fluorescence detection (incl. multiplex) possible and does not inhibit the reaction. Pressure moulded planar channel network is

subsequently sealed by PCR plate sealing film, what is a well-established, scalable manufacturing process [8].

We also have developed a freeze-drying protocol (so far without using stabilizers), that allows to store premixed qPCR reagents for at least 6 months inside the developed microfluidic chip. Every month the reagents in three chips (9 chambers) were redissolved for performing qPCR. The absence of amplification efficiency decline was controlled by the constancy of quantification cycle (qC) value. By the time significant value change was not detected neither for different chip materials, nor different fluorescent dye.

The future integration of “thermocycling” chip and the “extraction and purification” chip into comprehensive device will enable to perform rapid automated qPCR diagnostics in resource-limited areas as well as in major laboratories.

Acknowledgments

The work was supported by the Ministry of Higher Education and Science of Russian Federation (project No 122031000265-6).

References

[1] Setterquist R.A., Smith G.K. Encapsulated pcr reagents: pat. WO1996000301A1 USA. 1996.

[2] Xu J. et al. Transferable, easy-to-use and room-temperature-storable PCR mixes for microfluidic molecular diagnostics // Talanta. 2021. Vol. 235. P. 122797.

[3] Chat-Uthai N. et al. Development of ultra-short PCR assay to reveal BRAF V600 mutation status in Thai colorectal cancer tissues // PLoS One. 2018. Vol. 13, № 6. P. e0198795.

[4] Safiabadi Tali S.H. et al. Tools and Techniques for Severe Acute Respiratory Syndrome Coronavirus 2 (SARS-CoV-2)/COVID-19 Detection // Clin Microbiol Rev. 2021. Vol. 34, № 3. P. e00228-20.

[5] Naegeli H. et al. Assessment of genetically modified maize 1507 × MIR162 × MON810 × NK603 and subcombinations, for food and feed uses, under Regulation (EC) No 1829/2003 (application EFSA-GMO-NL-2015-127) // EFSA J. 2021. Vol. 19, № 1. P. e06348.

[6] Есикова Н.А., Гермаш Н.Н., Евстрапов А.А. ОПЕРАТИВНОЕ ИЗГОТОВЛЕНИЕ МИКРОЧИПОВ ДЛЯ ПЦР-АНАЛИЗА ИЗ ПОЛИМЕРНЫХ МАТЕРИАЛОВ В ЛАБОРАТОРНЫХ УСЛОВИЯХ: 4 // Научное приборостроение. Россия, Санкт-Петербург: ФГБУН «Институт аналитического приборостроения РАН», 2020. Vol. 30, № 4. P. 21–26.

[7] Strizhkov B.N. et al. PCR Amplification on a Microarray of Gel-Immobilized Oligonucleotides: Detection of Bacterial Toxin- and Drug-Resistant Genes and Their Mutations // BioTechniques. 2000. Vol. 29, № 4. P. 844–857.

[8] Wulff-Burchfield E. et al. Microfluidic Platform versus Conventional Real-time PCR for the Detection of Mycoplasma pneumoniae in Respiratory Specimens // Diagn Microbiol Infect Dis. 2010. Vol. 67, № 1. P. 22–29.

Oxidative destruction of human RPE cells melanosomes induced by superoxide radicals leads to the formation of reactive aldehydes and ketones

Alexander Gulin[1*], Alexander Dontsov[2], Marina Yakovleva[2], Natalia Trofimova[2], Arseny Aybush[1], Alexander Vasin[1], Mikhail Ostrovsky[2,3]

[1] N.N. Semenov Federal Research Center for Chemical Physics, Russian Academy of Sciences, Moscow 119991, Russia
[2] Emanuel Institute of Biochemical Physics, Russian Academy of Sciences, Kosygin st. 4, Moscow 119334, Russia
[3] Department of Biology, Lomonosov Moscow State University, Leninskiye Gory 1, Moscow 119234, Russia
* aleksandr.gulin@phystech.edu

Abstract Oxidative destruction of the natural pigment melanin leads to a decrease in its antioxidant activity and to the accumulation of its photodegradation products. In this work absorption and fluorescence spectroscopy, high performance liquid chromatography, and time-of-flight secondary ion mass spectrometry (ToF-SIMS) were applied for the analysis of melanosomes from the retinal pigment epithelium (RPE) cells of the human eye. It was shown for the first time the active carbonyl compounds namely aldehydes and ketones are formed from oxidative destruction of melanosomes. Oxidative destruction of melanosomes was induced by the action of potassium superoxide. Water-soluble products of melanosomes oxidative degradation induce modification of proteins with the formation of fluorescent Schiff bases. It was suggested that carbonyl products of melanosomes oxidative destruction can have a toxic effect on RPE cells, which is important for understanding the mechanisms of aging and the development of degenerative diseases of the retina.

1. Introduction

Natural pigment melanin undergoes oxidative modification in the presence of hydrogen peroxide in an alkaline medium with the formation of free monomeric tricarboxylic acids PDCA and PTCA [1, 2]. We have previously shown that the action of superoxide radicals on various natural and synthetic melanins results in the formation of a mixture of water-soluble fluorescent products [3] containing PDCA, PTCA, and other compounds. The aim of this work was to study the nature and physicochemical properties of compounds formed during the oxidative degradation of melanin in melanosomes obtained from RPE cells of the human eye. During aging, as well as under conditions of development of pathologies associated with oxidative stress, a significant decrease in the number of melanosomes (melanin-containing granules) occurs in human RPE cells. This leads to a decrease in the antioxidant status of RPE cells. In addition, the products accumulated as a result of melanin destruction are photoactive and may be involved in the development of photosensitized stress in RPE cells. We suggested that during the oxidative destruction of melanosomes, reactive carbonyls can also be formed, which are extremely toxic for the cell and can damage cell structures in the darkness. In the present work we analyzed the water-soluble fractions obtained before and after the chemical oxidation of melanosomes of RPE with potassium superoxide in order to test this assumption.

2. Methods

Melanosomes were obtained from RPE cells of the human eye. Cadaveric eyes were obtained from the ophthalmic tissue bank of S.N. Fedorov NMRC "MNTK "Eye Microsurgery"[4]. Oxidative destruction of melanosomes was carried out by incubation with dry potassium superoxide in the dark at room temperature for 1-2 hours, followed by separation of water-soluble degradation products by centrifugation (10000g, 20 min). The content of carbonyl compounds was determined by reaction with thiobarbituric acid (TBA) and ToF-SIMS. Serum albumin modification by water-soluble products of melanosomes oxidative degradation was carried out at 37 °C for 1-2 days, followed by dialysis in order to remove low molecular weight substances. Modified albumin fluorescence intensity was measured on a Shimadzu spectrofluorimeter at excitation wavelength 365 nm.

3. Results and discussion

Fig. 1A shows that under normal physiological conditions, potassium superoxide causes the destruction of melanin with the formation of fluorescent degradation products with an emission maximum at 520–525 nm. Time-of-flight mass spectrometry was performed to determine the presence

of aldehydes in water-soluble fractions of melanosomes of RPE cells from human eye. As can be seen from the diagram (Fig. 1C), there is a significant increase in carbonyl ions (m/z = 29 – CHO^+ ion, m/z = 60 – $C_2H_4O_2^+$ ion, m/z = 69 – $C_4H_7O^+$ ion) after exposure of superoxide. The ion with m/z = 60 shows the largest increase (about 1.5 times). The results indicate the presence of aldehydes in the water-soluble degradation products formed after the oxidation of melanosomes by superoxide radicals. These results are related to experiments on the content of carbonyl compounds reacting with thiobarbituric acid (TBA-reactive products) (Fig. 1B). One can see the supernatants of oxidized samples contain significantly more TBA-active products than the supernatants of control samples and the higher the dose of KO_2 the more TBA-active products are formed (Fig. 1B). It was found for the first time that the products of melanosomes oxidative destruction cause modification of serum albumin (Fig. 1D). Albumin incubation at 37°C for 48 hours and in the presence of water-soluble melanosome degradation products (curve 2) leads to a significant increase in the albumin fluorescence intensity. The obtained results indicate the toxicity of oxidative destruction products of melanosomes RPE. The accumulation of carbonyl products in the cell can lead to the increase of carbonyl stress, inflammatory processes and be of great importance in the pathogenesis of senile eye pathologies.

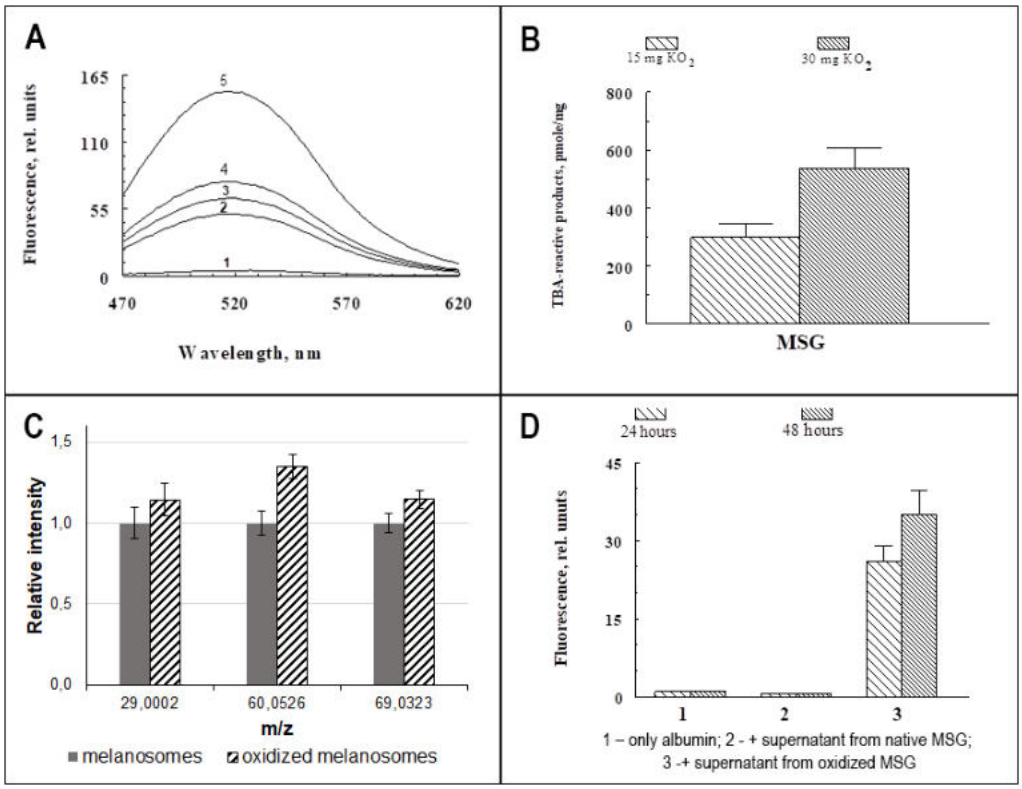

Рис. 1. A – Fluorescence spectra at different incubation times with KO_2 (curves 1-5 correspond incubation during 0 min, 30 min, 60 min, 90 min and 180 min, respectively). Excitation wavelength was 450 nm. **B** – Histogram of the content of TBA-active products in melanin at different amounts of KO_2. **C** – Histogram of carbonyl ion signals in melanin samples under the destructive effect of KO_2. **D** – Histogram of integrated fluorescence signal from albumin and modified albumin.

4. Acknowledgement
This research was funded by Russian Science Foundation (№ 075-15-2020-773).

References

[1]. Shosuke Ito1, Yukiko Nakanishi1, Robert K. Valenzuela2, Murray H. Brilliant3, Ludger Kolbe and Kazumasa Wakamatsu. Pigment Cell Melanoma Res. 24; 605–613
[2]. Kazumasa Wakamatsu, Yukiko Nakanishi, Narimi Miyazaki, Ludger Kolbe, Shosuke Ito. Pigment Cell Melanoma Res. 2012, 25; 434–445
[3]. A. E. Dontsov, N. L. Sakina, and M. A. Ostrovsky. Biochemistry (Moscow), 2017, Vol. 82, No. 8, pp. 916-924.
[4]. Feldman T.B., Yakovleva M.A., Arbukhanova P.M., Borzenok S.A., Kononikhin A.S., Popov I.A., Nikolaev E.N., Ostrovsky M.A. Anal. Bioanal. Chem. 2015. V. 407 (4). P. 1075-1088.

A new technique for researching the absorption signal fronts of laser radiation on blood vessels

I M Gureeva[1] and V V Davydov[1, 2]

[1]Peter the Great Saint-Petersburg Polytechnic University, Saint Petersburg, Russia, 195251
[2]All-Russian Research Institute of Phytopathology, Moscow Region 143050, Russia

e-mail: irena-gureeva@mail.ru

Abstract. The necessity of developing express diagnostic methods for monitoring human health in various situations is substantiated. The prospects for the development of pulse oximetry as a method that has not exhausted all the possibilities for obtaining additional information about the state of human health are noted. It is noted that modern pulse oximeter designs and pulse wave signal processing methods have a number of disadvantages. This leads to a significant measurement error and an unreliable interpretation of the data. It is established that to describe the rising and falling fronts, as well as the ridges (maxima) of the pulse wave, it is necessary to use various dependencies. Techniques have been developed to study the fronts of the rise, fall and ridges of the pulse wave. Pulse waves of various people and the results of their processing are presented.

1. Introduction

In conditions of environmental degradation, acceleration of the rhythm of life and increased stress levels, people began to actively monitor their health [1-3]. One of the elements of such control is rapid diagnostics in real time [3]. It is important that a person can perform this diagnosis independently. For this reason, both traditional criteria (temperature, blood pressure) and pulse oximetry have become widespread among express diagnostics [3]. The advantages of pulse oximetry include non-contact measurements when receiving data on pulse and oxygen content in the blood

Note that modern methods of pulse wave signal processing have a number of disadvantages. This leads to large measurement errors and inaccurate interpretation of data. Hence, problems arise that do not allow obtaining information about the presence or absence of pathologies in full with the help of blood flow analysis.

Therefore, the development of new pulse wave processing techniques to obtain additional information about the state of human health is still an urgent task. One of its possible solutions is presented in our work.

2. Pulse wave front processing technique

Numerous studies have shown that transmission pulse oximetry using a laser radiation absorption signal has the greatest advantages for personal use at the right time. The shape of the absorption signal recorded using a CCD array from laser radiation transmitted through blood vessels and soft tissues is shown in Fig. 1.

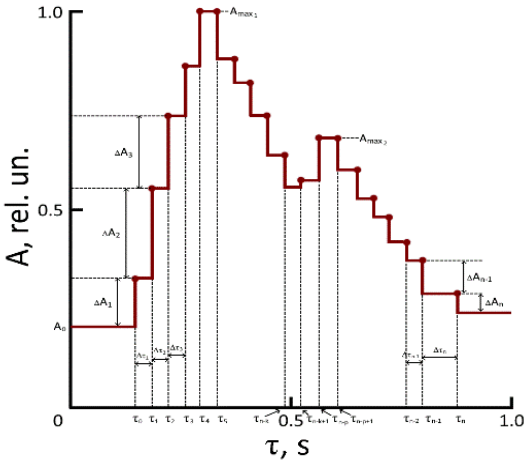

Figure 1. Pulse wave shape for transmission pulse oximetry. The absorption signal was registered on the finger.

The presented signal has a pronounced maximum (peak). The pulse value per minute is determined by the distance between the peaks and their number. Comparing the peak amplitude with the A0 level (the amplitude of the absorption signal transmitted through soft tissues), the oxygen content in the blood is determined.

3. Results of experimental studies and discussion

Figure 2 shows, for example, registered pulse wave signals from two people of the same age with typical possible deviations at the moment (COVID-19 disease and high pulse due to stress load).

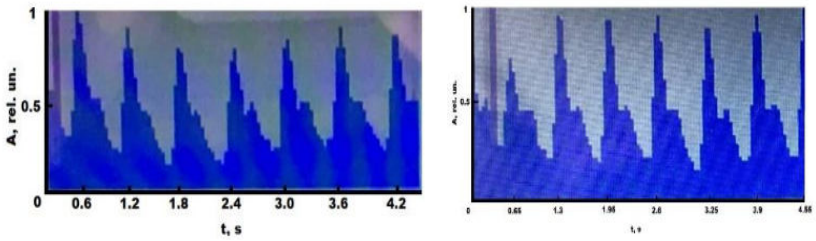

Figure 2. Pulse waves registered in people aged 22 years

The analysis presented in Fig. 2 pulse waves allows you to notice minor deviations in the waveforms, which are quite difficult to interpret with diseases. Therefore, we carried out a study of the "crest" and the fronts of the rise and fall of these pulse waves using the developed techniques and functions.

4. Conclusion

The obtained research results show the expediency of using the methods developed by us to obtain additional information about the nature of changes in the "crests" and fronts of the rise and fall of pulse waves.

References

[1] Mazing M, Zaitceva A, Kislyakov Y and Avdyushenko S 2020 *International Journal of Pharmaceutical Research* **12** 1974-1978

[2] Luo J, Guo S, Cao S 2016 *Evidence-based Complementary and Alternative Medicine* **201(6)** 2468254

[3] Guo R, Wang Y, Yan H, Liu G and Xu W 2015 *Evidence-based, Complementary and Alternative Medicine* **201(5)** 895749

Nanobioreagents based on upconversion nanoparticles and hyaluronic acid for bioimaging

P.A. Demina[1,2*], A.V. Sochilina[1,2], S.A Morozova.[2], E.V. Utushev[2], A.N. Generalova[1,2], E.V. Khaydukov[1,2,3]

[1]FSRC "Crystallography and Photonics" of RAS, 119333, Moscow, Russia

[2]Shemyakin-Ovchinnikov Institute of Bioorganic Chemistry of RAS, 117997, Moscow, Russia

[3] I.M. Sechenov First Moscow State Medical University, Moscow, 119991, Russia

*Corresponding author, e-mail: polidemina1207@yandex.ru

Abstract. Early diagnostics of cancer tumors determines the correct patient treatment strategy. To date, non-invasive optical visualization of pathological tissues are the most promising methods. Currently, upconversion nanoparticles (UCNP) excited by near infrared irradiation are a perspective nanoplatform for bioimaging. The nanoscale range of UCNPs and biopolymer surface modification make it as a tool for assessing real time accumulation in a tumor *in vivo*. Although, there is great issue for development of one-step easily reproducible methods of UCNP surface modification with biopolymers.

1. Introduction

Pathological tissue visualization with UCNPs has a number of advantages over the classical bioimaging agents for photoluminescent diagnostics. However, the immune response evolution, the adsorption of blood plasma proteins should be prevented in order to exclude the rapid removal of nanobioreagents from the circulatory system and to promote their effective accumulation in tumor tissues due to the EPR (enhanced permeability and retention) effect. The great potential to create a nanobioreagent based on UCNPs has their modification with endogenous biopolymers. Among them, hyaluronic acid (HA) can be highlighted, which is a negatively charged polysaccharide composed of repeating disaccharides D-glucuronic acid and N-acetyl-D-glucosamine. HA exhibits excellent physical and chemical properties: high level association with water molecules, non-toxicity, biodegradability, biocompatibility and non-immunogenicity. These features define great interest in the development of HA-based nanobioreagents for various biomedical applications, including optical imaging.

2. Results and discussion

The nanobioreagents based on UCNPs are powerful tool for highly sensitive cancer tumor visualization. UCNPs represent an inorganic host matrix $NaYF_4$ doped with rare earth elements ions (Yb^{3+} as a sensitizer and Tm^{3+} as an activator). UCNP excitation is carried out by near-IR light (975 nm) and, due to multistage nonlinear optical processes, UCNPs generate photons with shorter wavelength in the UV, visible and near-IR spectral ranges [1]. Nanobioreagents on the platform of

UCNPs allow deeper visualization with minimal scattering and absorption along with photostability, photosensitivity and high spatial resolution.

The successful UCNP application for biovisualization is usually associated with the multistep surface modification in order to obtain biocompatible nanobioreagents. This is laborious, time consuming and usually hardly reproducible process. We developed one-step reproducible UCNP surface modification method based on the cross-linking of methacrylated hyaluronic acid [2] triggered by either temperature or light exposure. The obtained nanobioreagents retained colloidal stability for more than 3 weeks. They were characterized with spectrophotometry, DLS and zeta potential measurements. UCNP-HA *in vivo* behavior is greatly influenced by protein corona formation on the surface. The large protein corona formation means the immune response and leads to rapid cleaning from the circulatory system. In order to demonstrate the successful surface modification, we simulated protein corona formation by protein adsorption on the UCNP-HA surface.

Acknowledgments
The reported study was funded by RSF, project number 18-79-10198-П.

References
[1] Generalova A N, Chichkov B N, Khaydukov E V. 2017 *Adv. Colloid Interface Sci.* **245** 1
[2] Sochilina A. V., Savelyev A. G., Akasov R. A., Zubov V. P., Khaydukov E. V, Generalova A. N. 2021 *Russ J Bioorganic Chem* **47** 828

EXPRESSION AND INTRACELLULAR LOCALIZATION OF TRANSCRIPTION FACTOR E2F1 IN THE PERIPHERAL NEURONS OF RATS AND CRAYFISH AFTER NEUROTRAUMA BY IMMUNOFLUORESCENCE MICROSCOPY

V.A. Dzreyan, S.V. Rodkin, M.A. Pitinova, M. Eid
Laboratory of Molecular Neurobiology, Academy of Biology and Biotechnology,
Southern Federal University, Rostov-on-Don, Russia
✉ dzreyan@sfedu.ru

Abstract. In this work, by immunofluorescence microscopy showed for the first time intracellular localization of E2F1 in various model objects: in axotomized mechanoreceptor neurons (MRN) and ventral nerve cord ganglia (VNC) of crayfish, as well as in the dorsal root ganglia (DRG) of the rat spinal cord in the early stages after axotomy. It is determined in which cells, neurons, or glia cells, this protein is expressed. This work showed the rabbit antibodies against mammalian E2F1 used in this work perfectly recognized the corresponding epitopes in the homologous crayfish protein. Axotomy causes overexpression of E2F1 as early as 4 hours and even 1 hour after axotomy of MRN and ganglia of crayfish VNC, as well as rat DRG. The level of E2F1 expression increased both in the cytoplasm and the nuclei of neurons. It was interesting to note that E2F1 was expressed exclusively in neurons, but not in the glial cells of the rat DRG ganglia and the crayfish MRN. Thus, we studied the expression of E2F1 in three models of neurotrauma in vertebrates and invertebrates. It has been demonstrated that E2F1 is present not only in the nervous system of invertebrates, but also in crustaceans, confirming the conservative nature of this protein. Our novel date by immunofluorescence microscopy indicate that E2F1 can be potential biomarker in the in the early stages after neurotrauma, suggesting that inhibitors of E2F1 can be considered for therapeutic approaches in this period.

Keywords: immunofluorescence microscopy, E2F1, crayfish neuron, dorsal root ganglion, nerve injury

Funding: This study was funded by a grant from the Ministry of Education and Science of the Russian Federation No. 0852-2020-0028 and a stipend from the President of the Russian Federation for young researchers.

АНАЛИЗ ЭКСПРЕССИИ И ВНУТРИКЛЕТОЧНОЙ ЛОКАЛИЗАЦИИ ТРАНСКРИПЦИОННОГО ФАКТОРА E2F1 В ПЕРИФЕРИЧЕСКИХ НЕЙРОНАХ КРЫСЫ И РАКА ПОСЛЕ НЕЙРОТРАВМЫ МЕТОДОМ ИММУНОФЛУОРЕСЦЕНТНОЙ МИКРОСКОПИИ

В.А. Дзреян ✉, С.В. Родькин, М.А. Питинова, М. Ид
Лаборатория «Молекулярная нейробиология», Академия биологии и биотехнологии,
Южный федеральный университет, Ростов-на-Дону, Россия
✉ dzreyan@sfedu.ru

Аннотация. Мы изучали экспрессию фактора транскрипции E2F1 на трех моделях нейротравмы позвоночных и беспозвоночных животных. Показано, что E2F1 присутствует не только в нервной системе беспозвоночных, но и у ракообразных, что подтверждает консервативную природу этого белка. Наша новые данные по иммунофлуоресцентной микроскопии указывают на то, что E2F1 может быть потенциальным биомаркером на ранних стадиях нейротравмы.

Ключевые слова: иммунофлуоресцентная микроскопия, E2F1, нейрон рака, спинномозговой ганглий, повреждение нерва

Финансирование: Работа выполнена при поддержке гранта Министерства науки и высшего образования РФ № 0852–2020–0028 и стипендии Президента Российской Федерации для молодых ученых.

Introduction

Neurotrauma is among the main causes of human disability and mortality. However, the mechanisms that mediate the survival and death of cells in the peripheral nervous system are still not fully understood [1]. The transcription factor E2F1 - one of the key proteins that determine the fate of cells, including DNA repair, cell cycle, metabolism, and apoptosis [2]. But the involvement of E2F1 in the regulation of survival and death of the peripheral nerve cells after axotomy has not been previously studied. Immunofluorescence microscopy was used for to study axotomy-induced changes in the expression and localization of E2F1 in mechanoreceptor neurons (MRN) and ganglia of the crayfish ventral nerve cord (VNC) as well as the dorsal root ganglia (DRG) of the rat spinal cord after axotomy.

Materials and Methods

For the detection of E2F1 by immunofluorescence microscopy we used the anti-rabbit E2F1 (SAB2103144) antibody recognized the N-terminal domain of E2F1 (N-terminal). We used the antibody anti-E2F1 according to the Producer‘s recommendations: https://www.sigmaaldrich.com/RU/en/product/sigma/sab2103144. The average (by area) fluorescence of the cytoplasm and nucleus for each cell was estimated and the obtained values were averaged. The data obtained on crayfish ganglia were expressed in relative units: the average fluorescence (by area) of the nucleus and perikaryon was estimated, the background was subtracted, and divided by the background (the point most distant from the object). Crayfish stretch receptor preparations and rat DRG samples were photographed using an Olympus BX-51 fluorescent microscope equipped with an OrcaFlash 4.0 V3 digital camera (Hamamatsu, Japan) at approximately 535 nm excitation wavelengths for Anti-Mouse IgG1 (γ1) labeled with CF555, 488 nm for anti-rabbit IgG (H+L) labeled with CF488A and 365 nm for Hoechst-33342. Fluorescence was recorded at wavelengths >580 nm and >460 nm, respectively. E2F1 level was analyzed by fluorescence intensity using the ImageJ software (http://rsb.info.nih.gov/ij/, accessed on October 4, 2021).

Results and Discussion

Immunofluorescence microscopy revealed overexpression of E2F1 as early as 4 hours and even 1 hour after axotomy of mechanoreceptor neurons and ganglia of crayfish VNC, as well as rat DRG. These results are consistent with the data of previous experiments with proteomic microarrays and western-blott assay, in which a 1.8-fold increase in E2F1 expression in axotomized ganglia of crayfish VNC was observed as early as 1 and 3 hours after axotomy [3,4]. It can be seen that the dynamics of E2F1 expression in axotomized ganglia and MRN, reaching its maximum by 4 hours after axotomy, gradually decreases. This suggests an early E2F1-dependent response in neurons that develops under stress. It is important to note here the fact that 7 days after transection of the sciatic nerve, the expression of E2F1 is significantly lower compared to earlier periods. Moreover, this was observed both in the damaged ganglia and in the control. These results also speak in favor of the fact that E2F1 is directly involved only in the initiation of apoptosis, after which its content in the cell tends to a minimum.

An important observation is that the level of E2F1 expression in our experiments increased both in the cytoplasm and the nuclei of neurons, as evidenced by immunofluorescence microscopy. In the case of cytoplasmic localization, one of the possible functions of E2F1 is its interaction with mitochondria and regulation of their functions, for example, by direct interaction with the Bcl-xL protein on the outer mitochondrial membrane and regulation of its permeabilization [5].

In this regard, it was also important for us to determine in which cells, neurons or glia, this protein is expressed. It was interesting to note that E2F1 was localized both in DRG neurons and the glial cells. Thus, increased expression of E2F1 in axotomized ganglia is associated with

increased protein expression in neurons, but not in DRG glial cells. But in the crayfish stretch receptor E2F1 was expressed exclusively in neurons, but not in the glial cells. It is possible that such features of the distribution of this protein can explain the different reactions of neurons and glial cells in response to axon transection.

Conclusion

This work showed the rabbit antibodies against mammalian E2F1 used in this work perfectly recognized the corresponding epitopes in the homologous crayfish protein. Axotomy causes overexpression of E2F1 as early as 4 hours and even 1 hour after axotomy of MRN and ganglia of crayfish VNC, as well as rat DRG. The level of E2F1 expression increased both in the cytoplasm and the nuclei of neurons. It was interesting to note that E2F1 was expressed exclusively in neurons, but not in the glial cells of the rat DRG ganglia and the crayfish MRN. Thus, we studied the expression of E2F1 in three models of neurotrauma in vertebrates and invertebrates. It has been demonstrated that E2F1 is present not only in the nervous system of invertebrates, but also in crustaceans, confirming the conservative nature of this protein. Our novel date by immunofluorescence microscopy indicate that E2F1 can be potential biomarker in the in the early stages after neurotrauma, suggesting that inhibitors of E2F1 can be considered for therapeutic approaches in this period.

Acknowledgments

This study was funded by a grant from the Ministry of Education and Science of the Russian Federation No. 0852-2020-0028 and a stipend from the President of the Russian Federation for young researchers.

REFERENCES

1. **Martin, S. L., Reid, A. J., Verkhratsky, A., Magnaghi, V., & Faroni, A.** (2019). Gene expression changes in dorsal root ganglia following peripheral nerve injury: roles in inflammation, cell death and nociception. Neural regeneration research, 14(6), 939–947. https://doi.org/10.4103/1673-5374.250566

2. **Engelmann, D., & Pützer, B. M.** (2012). The dark side of E2F1: in transit beyond apoptosis. Cancer research, 72(3), 571–575. https://doi.org/10.1158/0008-5472.CAN-11-2575

3. **Demyanenko, S., Dzreyan, V., & Uzdensky, A.** (2019). Axotomy-Induced Changes of the Protein Profile in the Crayfish Ventral Cord Ganglia. Journal of molecular neuroscience: MN, 68(4), 667–678. https://doi.org/10.1007/s12031-019-01329-5

4. **Dzreyan, V., Rodkin, S., Nikul, V., Pitinova, M., & Uzdensky, A.** (2021). The Expression of E2F1, p53, and Caspase 3 in the Rat Dorsal Root Ganglia After Sciatic Nerve Transection. Journal of molecular neuroscience: MN, 71(4), 826–835. https://doi.org/10.1007/s12031-020-01705-6

5. **Ma, L., Yu, H. J., Gan, S. W., Gong, R., Mou, K. J., Xue, J., & Sun, S. Q.** (2017). p53-Mediated oligodendrocyte apoptosis initiates demyelination after compressed spinal cord injury by enhancing ER-mitochondria interaction and E2F1 expression. Neuroscience letters, 644, 55–61. https://doi.org/10.1016/j.neulet.2017.02.038

THE AUTHORS

DZREYAN Valentina I.
Laboratory of Molecular Neurobiology, Academy of Biology and Biotechnology, Southern Federal University
Rostov-on-Don, prospect Stachki 194/1, 344090, Russia
dzreyan@sfedu.ru
ORCID: 0000-0003-3249-5020

RODKIN Stanislav II.
Laboratory of Molecular Neurobiology, Academy of Biology and Biotechnology, Southern Federal University
Rostov-on-Don, prospect Stachki 194/1, 344090, Russia
rodkin_stas@mail.ru
ORCID: 0000-0003-4036-5410

PITINOVA Maria III.
Laboratory of Molecular Neurobiology, Academy of Biology and Biotechnology, Southern Federal University
Rostov-on-Don, prospect Stachki 194/1, 344090, Russia
maria.pitinova@mail.ru
ORCID: 0000-0003-3958-7331

EID Moez IV.
Laboratory of Molecular Neurobiology, Academy of Biology and Biotechnology, Southern Federal University
Rostov-on-Don, prospect Stachki 194/1, 344090, Russia
moez1995.mae@gmail.com
ORCID: 0000-0002-3554-3529

Creation of a device for detecting fluorescence from microfluidic chips

R K Dobretsov[1] and V V Davydov[1, 2]
[1]Peter the Great Saint-Petersburg Polytechnic University, Saint Petersburg, Russia, 195251
[2]All-Russian Research Institute of Phytopathology, Moscow Region 143050, Russia

e-mail: rodya99@gmail.com

Abstract. In this paper, we consider the creation and testing of a prototype for recording fluorescence from microfluidic chips during the polymerase chain reaction (PCR). The paper presents the characteristics of the main elements used to create the layout of the device for fluorescence detection. The results of experiments in testing the performance of mock-up elements and microfluidic chips are presented. The operability of the assembled layout was demonstrated during the real-time PCR reaction.

1. Introduction

Currently, the leading tool for chemical and biological research is PCR. With PCR, specific sequences in a DNA or cDNA template can be copied or "amplified" a thousand or a million times using sequence-specific oligonucleotides, thermostable DNA polymerase, and thermal cycling techniques. Real-time PCR is a type of PCR method that is commonly used to quantify DNA or RNA in a sample. Using sequence-specific primers, the copy number of a particular DNA or RNA sequence can be determined. Quantification is possible by measuring the amount of amplified product at each step of the PCR cycle.

Most current PCR assay devices use tubes or microtiter plates and have several serious drawbacks. Disadvantages: uneven heating/cooling of volumetric systems, analysis speed does not meet the requirements of modern medicine, biology, environmental services, etc., namely, the requirement for rapid analysis. The solution to this problem is microfluidic chips since they are planar systems. Using microfluidic chips, more samples can be analyzed in less time. Thus, the development and creation of devices for real-time PCR analysis using microfluidic technologies is essential for extremely important [1, 2].

2. Mock-up of a device for detecting fluorescence

The light source 1 (Fig. 1) in this device is an SMD LED with a wavelength of emitted light of 480 nm, a power of 3 W, with a maximum control current of 700 mA and a luminous flux of up to 70 lm. From the source, the light enters the system of plano-convex lenses 2 and 3 (Fig. 1) and excitation filter 3 (Fig. 1) with a wavelength of 490 nm. Further, the light enters the triple optical fiber 12 (Fig. 1., fiber-optic bundle of type O-BKh-I-3-250). One channel is excitation, the other two are registration of a fluorescence/emission signal. Light, passing through the fiber, falls into the solution located in the chip 10 (Fig. 1), and excites fluorescence. The chip is located in the thermal cycler 11 (Fig. 1), with which the PCR reaction is carried out. The thermal cycler also has a device for fixing the optical fiber, which

allows not only to fix the lighting bundle in the thermal cycler, but also to control the distance from it to the chip.

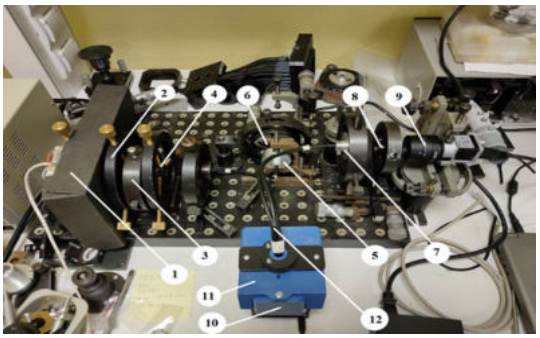

Figure 1. Mock-up of the device for registration of fluorescence: 1 - source (LED); 2, 4, 6, 8 - lenses; 3 - excitation filter; 5, 7 - emission filters; 9 - photodetector; 10 - location of the chip; 11 - thermal cycler; 12 - optical fiber (optical fiber bundle).

Fluorescence is detected using a photo application 9 (Fig. 1., Basler ace acA720-520um cameras with a quantum efficiency of 63.2%), on which light enters after passing through an emission filter 5 or 7 (Fig. 1) with a wavelength of 520 nm and plano-convex lenses 6 and 8 (Fig. 1).

3. Results of experimental studies on the created mock-up

When conducting experimental studies, a set of reagents for the detection of plant DNA in food, food raw materials, seeds, and feeds by real-time polymerase chain reaction "Plant universal" was used to fill the microfluidic chip. Cy5 dye was used.

A graph of the dependence of the signal level on the PCR time was obtained, shown in Fig. 2.

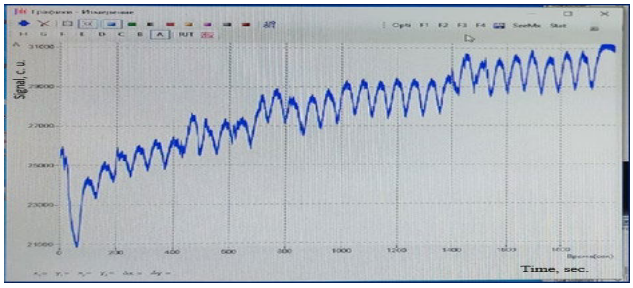

Figure 2. Graph of the dependence of the signal level on the PCR time.

As a result of the experiments, graphs were obtained that adequately reflect the processes of thermal cycling, that is, the growth of the product in the chip. The task of recording the real-time amplification process was successfully completed.

4. Conclusion

As a result of experimental studies on the assembled layout, graphs were obtained reflecting the processes of thermal cycling, amplification and reaching a plateau in real time, that is, the real-time PCR process was recorded. Thus, the assembled device layout can be further used for biological and medical research on microfluidic chips during real-time PCR.

References

[1] Esikova N A, Germash N N and Evstrapov A. A 2020 *Scientific instrument-making* **30(4)** 21-26
[2] Reznik V S and Kruglov V A 2021 *Journal of Physics: Conference Series* **2086(1)** 012120

Microraman spectroscopy and laser-induced contrast visualisation for analysing incipient and clinically unrecorded enamel fissure caries

P V Seredin[1,2], D L Goloshchapov[1], V M Kashkarov[1], A A Emelyanova[1], N S Builov[1], Y.A. Ippolitov [3] and T. Prutskij[4]

[1]Voronezh state unibersity, Universitetskaya pl. 1, Voronezh, Russian Federation, paul@phys.vsu.ru
[2]Ural federal university named after the first President of Russia B.N. Yeltsin, Yekaterinburg, ul. Mira, 19, 620002, Russian Federation
[3]Department of Pediatric Dentistry with Orthodontia, Voronezh State Medical University, Voronezh, Studentcheskaya st. 11, 394006, Russian Federation
[4]Sciences Institute, Autonomous University of Puebla (BUAP), Puebla 72570, Mexico

Abstract. Our current work is concerned with the use of a laser-induced contrast visualisation technique and microRaman spectroscopy to the measuring system enables reliable detection of the transformation of the organic–mineral component in the dental tissue as well as the spread of bacterial microflora in the affected region.

1. Introduction

Although some modern achievements in therapeutic dentistry have shown progress in this area [1], early and precise diagnostics of carious lesions remains a top priority. Spatial-spectroscopic visualisation with a high resolution within the regions of caries development at the micro- and nano-scale is a key challenge in the search for new methods in caries prevention and treatment [2]. The advantages of simultaneously employing fluorescence and Raman microspectroscopy to detect caries development in teeth have been demonstrated in [3–5]. However, these reports did not involve comparing and analysing the light-scattering and autofluorescence of dental tissues at the initial stages of the pathology used to visualise the boundaries of carious lesion microregions and the applicability of such a diagnostic instrument in clinical practice. Our current work is concerned with these problems.

2. Materials and methods of their investigations

In our work, we studied dental tissue samples extracted from patients aged 20–25 years. Five human teeth with different degrees of carious lesions were collected.

Segments of teeth were prepared for examination. The prepared slices and samples of biomimetic composites were analysed with a laser-induced fluorescence and non-contact microRaman and luminescence spectroscopy. The laser-induced contrast imaging setup was designed to visualise the caries-induced changes in the tooth tissue. The cut section of a tooth was illuminated by the parallel beam of a solid-state laser with a wavelength of 532 nm. The signal reflected by the sample was collected and registered with a Canon EOS camera with the Canon lens EF and a CMOS-sensor.

Raman and luminescence spectra were obtained with a Raman-luminescence microscope RamMix M532 (EnSpectr, Russia) combined with an Olympus optical microscope.

3. Experimental results and their discussion

The analysis of the results of investigating samples of dental tissue with different degrees of carious lesions (1–6 ICDAS), with the use of laser-induced contrast visualisation (LICV) and microRaman scattering, enabled the understanding of the correspondence between the regions of the fluorescent images of the samples and the changes of the mineral and organic components of the dental tissue under caries attack, accompanied by the spread of bacterial microflora.

Using a wavelength in the green spectral range for the excitation provides deeper penetration into a tooth and thus enhances the qualitative and quantitative analysis of the signal emitted by the dental tissue. For both the deep and incipient carious lesions, LICV with the notch filter allows the precise separation of the regions in the hard-dental tissue undergoing changes. Visualisation of the carious lesions obtained without the filter shows that for the deep carious lesions, anatomically different areas provide a certain fluorescence. There is also a specific gradation of colours in the images that allows the visualisation of the bacterial invasion. The incipient stage of caries (ICDAS 1–2) requires additional analysis of the near-surface layers, where maximal contrast is observed using LICV. This task can be successfully completed by introducing Raman microspectroscopy into the exploratory scheme. Different products of the bacteria in the oral cavity, including porphyrins and pentosidine, provide a characteristic set of bands in the spectrum of infected dental tissue [3]. The observed spectral emission profile demonstrates more energy features representing the specific character of the microbiota in the carious region than in previous works. This can be used to improve screening techniques.

4. Conclusion

This work presents a practical approach to detecting and visualising the initial forms of caries that are not clinically registered. As a result, further personalised medical treatment could be specified.

Acknowledgement

Financing

This work was funded by a grant from the Russian Science Foundation, grant number 21-75-10005.

Conflict of interests

Authors declare no conflict of interests.

References

[1] Hayashi M, Haapasalo M, Imazato S, Lee J I, Momoi Y; Murakami S; Whelton H and Wilson N 2014 International Dental Journal **64** 333

[2] Besnard C, Harper R A; Moxham T E J; James J D, Storm M, Salvati E, Landini G, Shelton M and Korsunsky A M 2021 Materials Today Communications **27** 102418

[3] Slimani A, Nouioua F, Panayotov I, Giraudeau N, Chiaki K, Shinji Y, Cloitre T, Levallois B, Gergely C and Cuisinier F 2016 Int. Journal of Experimental Dental Science **5** 10029

[4] Goloshchapov D L, Kashkarov V M, Ippolitov Y A, Prutskij T and Seredin P V 2018 *Results in Physics* **10** 346

[5] Al-Obaidi R, Salehi H, Collart-Dutilleul P-Y, Jacquot B, Tassery H, Cuisinier F J G, Gergely C and Cloitre T 2020 *CRE* **54** 144

Effect of controlling the synthesis parameters by the Stöber method on the physicochemical characteristics of mesoporous silica nanoparticles

E A Zamyatina[1], N R Popova[1], V A Anikina[1], M P Shevelyova[2]

[1]Institute of Theoretical and Experimental Biophysics of RAS, Pushchino 142290, Russia
[2]Institute of Biological Instrumentation of RAS, Pushchino 142290, Russia

Email: sonyoru162@gmail.com

Abstract. Mesoporous silica nanoparticles (MSN) were obtained from 100 to 800 nm by the Stöber method. Synthesis parameters such as the precursor concentration, catalyst concentration, temperature, and stirring rate significantly affect the physicochemical characteristics of nanocarriers. It is possible to obtain MSN with specified parameters that satisfy the conditions for their use in biomedical purposes by changing the synthesis parameters.

1. Introduction

Mesoporous silica nanoparticles (MSN) have proven to be promising and widely used nanocarriers for therapeutic agent delivery systems since they have some advantages over other types of nanoparticles. MSN have a high surface-to-volume ratio, providing the possibility of wide surface functionalization while maintaining high porosity, which makes it possible to achieve a high degree of load capacity [1]. One of the most common methods for the synthesis of nanoparticles is the Stöber method. It makes it possible to obtain monodisperse nanoparticles from 50 to 2000 nm and control the pore size [2].

This method is based on the hydrolysis of tetraethoxysilane (TEOS) catalyzed by ammonia (NH_4OH) in an aqueous-alcoholic solution [3]. The Stöber method makes it to vary the physicochemical characteristics to synthesize nanostructures for use as targeted drug delivery systems. The analysis of changing the synthesis parameters by the Stöber method on the physicochemical characteristics of nanoparticles seems to be a topical issue in biomedicine.

2. Experiment and results

In this work, the synthesis of MSN was carried out with a change in the TEOS concentration, NH_4OH concentration, temperature, and stirring rate of the reaction solution. The hydrodynamic radius, polydispersity index and ζ-potential were studied by dynamic light scattering and electrophoretic light scattering using a Zetasizer Nano ZS nanoparticle characterization system (Malvern Panalytical, UK). The shape of the nanoparticles was measured by transmission electron microscopy using a JEM-1011 electron microscope (JEOL, Japan).

Nanoparticles were obtained at mixing rate of the reaction solution at 300, 500, 750, and 900 rpm. In most studies this parameter is omitted, but we have established the direct effect on the physicochemical characteristics of nanoparticles. With an increase in the mixing rate, the size of nanoparticles decreased from 244 to 100 nm, while the polydispersity index decreased from 1 to 0.2,

respectively. Oval-shaped nanoparticles were formed at a low mixing rate, while at 500, 700, and 900 rpm the nanoparticles had a spherical shape. Therefore, the mixing speed of 500 rpm was a threshold value below which the synthesis of nanoparticles of a regular oval shape is not possible.

The ζ-potential is an important parameter for determining the stability of a nanoparticle suspension. The ζ-potential of +30 or -30 mV is regarded as a characteristic value in which nanoparticles are electrostatically stable. The obtained nanoparticles had a ζ-potential value from -32 to -63 mV, which indicates that the suspensions were not subjected to aggregation and were stable.

In the range of TEOS concentration from 0.5M to 1.2M, there was a significant increase in the size of nanoparticles in the range from 100 to 800 nm. With the increasing of TEOS concentration, an increase in the number of hydrolyzed silicic acid monomers occurred, which ultimately affected the increase in the size of nanoparticles. At TEOS concentration close to 1.2M, the polydispersity of nanoparticles increased.

There was also an increase in the size of nanoparticles from 120 nm to 425 nm in the range of NH_4OH concentration from 0.2 to 1.2M. At higher concentration of NH_4OH, hydrolyzed silanol monomers were formed, which increased the degree of polymerization and increased the size of nanoparticles.

When the system temperature increased from 25 to 65°C, the synthesis rate of nanoparticles increased. With an increase in temperature, the rapid formation of silicic acid monomers occurred, which immediately reached critical saturation levels necessary for the formation of nanoparticle seeds. A large number of monodisperse particles of small size were formed in a shorter period. Accordingly, when temperature conditions are controlled, the synthesis time of nanoparticles can vary from 3 to 12 hours.

3. Conclusion

The Stöber method makes it possible to synthesize MSN with various physicochemical characteristics. Therefore, it is necessary to plan and control the synthesis parameters to achieve the best size and polydispersity of nanosystems for their application in biomedicine.

Acknowledgments

The results were obtained using the equipment of the Institute of Biological Instrumentation of RAS and the Kurnakov Institute of General and Inorganic Chemistry of the RAS.

References

[1] Manzano M, Vallet-Regi M 2019 *Advanced Functional Materials* **30**, 2.

[2] Beltrán-Osuna Á A, Gómez Ribelles J L. & Perilla J E 2017 *J Nanopart Res* **19**, 381.

[3] Ren G, Su H & Wang S 2020 *J Sol-Gel Sci Technol* **96**, 108–120.

Applicability of domestic production glues for adhesive bonding microfluidic chips for polymerase chain reaction

T A Lukashenko, A N Zubik and G E Rudnitskaya

Laboratory of Bio-&Chemosensors microsystems, Institute for Analytical instrumentation RAS, Saint Petersburg 190103, Russia

tunix@yandex.ru

Abstract. The microfluidic chip for PCR is a key element of a portable system for molecular diagnostics. Previously, imported glue Permabond® UV630 was used for the adhesive bonding of polymer microchips, but now the search for Russian analogues is becoming relevant. Experiments have shown that Mastix UV glue inhibits PCR. SM Chemie 301 glue does not inhibit PCR and it can be used to bonding microchips for polymerase chain reaction.

1. Introduction

In recent years, miniature devices for molecular diagnostics have become in demand [1]. The use of a microfluidic chip or cartridge makes it possible to automate complex analysis schemes and implement the storage and dosage of reagents inside the chip [2, 3]. Quantitative polymerase chain reaction (qPCR) is the most popular method of molecular diagnostics. This reaction takes place at an elevated temperature, while it is important to maintain the tightness of the microstructures in order to avoid evaporation of the reagents. Previously, the IAI RAS developed a technology for adhesive bonding (gluing) microchips by introducing adhesive (glue) between the channelized (with microstructures) and protective plates of the microchip due to capillary forces [4]. This bonding technique is suitable for both glass and polymer microchips. The peculiarity of the gluing is the presence of a layer of cured glue between the parts, which in the case of a microchip is part of the wall of its reaction chamber and is in contact with the reaction mixture. Therefore, it is necessary to check the effect of glue on the reaction carried out in the microchip.

In a previous work [5], Permabond® UV630 (Engineering Adhesives) photocurable acrylic adhesive made in the UK was used for adhesive bonding polymethylmethacrylate (PMMA) microchips for PCR. This is medium-viscosity glue (200-300 mPa·c), which has adhesion to polymers (including polycarbonate (PC)), glass, and metals [6]. We ascertained that Permabond® UV630 does not inhibit qPCR [7].

The objective of this work is to study the effect of Russian single-component photocurable acrylic adhesives SM Chemie 301 (SM Chemie) [8] and Mastix UV (Mastix LLC) [9] on qPCR. SM Chemie 301 glue is designed for bonding plexiglass (PMMA), has adhesion to PC, and its viscosity (90-170 mPa·c) is comparable to that of its foreign analogue Permabond® UV630. Mastix UV glue (TU 2257-024-90192380-2012) is designed for bonding glass with glass, plastic, metal, etc.

2. Experiment results

Analytical scales with a margin of error of ± 0.5 mg were used to weigh the glue samples. Samples of cured glue weighing ~ 3 mg were kept at room temperature for at least two weeks (to remove volatile compounds traces). Then each sample was placed in a 0.2 ml test tube and 25 µl of the finished mixture for qPCR was added. The synthesized GAPDH fragment was used as a DNA target, the final concentration of which in the test tube was 4000 or 200 copies / µl. The thermal cycling mode was as follows: preheating at 95 °C for 5 minutes and 50 cycles according to the program – 60 °C for 60 seconds, 95 °C for 20 seconds. An increase in the threshold cycle of qPCR (C_t) by one unit corresponds to a halving of the reaction yield. A material was considered to inhibit quantitative PCR if the difference (ΔC_t) between C_{tx} in sample tubes and C_{t0} in tubes without sample was +1.0 or greater.

Preliminary experiments have shown that Mastix UV glue is suitable for adhesive bonding polymer chips, but it cannot be recommended for PCR chips, since the glue completely inhibits this reaction. The results of experiments with SM Chemie 301 glue are presented in table 1. The ΔC_t value is less than +1.0 cycle PCR. Thus, domestic production SM Chemie 301 glue does not inhibit qPCR and it can be recommended for adhesive bonding microfluidic chips intended for polymerase chain reaction.

Table 1. The effect of SM Chemie 301 glue on qPCR at different concentrations of the target DNA.

Duration of storage of glue sample (week)	C_{tx} with glue sample (PCR cycle)	C_{t0} without glue sample (PCR cycle)	ΔC_t (PCR cycle)
at a concentration of 4000 copies / µl			
2	25.4±0.1(n=5)	25.4±0.2(n=5)	0.0
20	25.3±0.2(n=5)		– 0.2
at a concentration of 200 copies / µl			
3	32.0±0.1 (n=3)	32.1±0.2 (n=4)	+ 0.1
21	32.1±0.2 (n=3)		0.0

3. Conclusions

The microfluidic chip for PCR is a key element of a miniature system for molecular diagnostics. Previously, UK manufactured Permabond® UV630 glue was chosen for adhesive bonding PMMA microchips. However, at present, the search for similar adhesives (glues) of Russian manufactured is becoming relevant. When choosing glue for bonding PCR chips, it is necessary to check whether the glue used inhibits this reaction. In this work, we show that SM Chemie 301 glue does not inhibit qPCR and it can be recommended for adhesive bonding polymeric microchips for polymerase chain reaction.

Acknowledgments

The research was carried out within the state assignment of Ministry of Science and Higher Education of the Russian Federation (theme No. 075-00761-22-00).

References

[1] Harpaldas H, Arumugam S, Campillo Rodriguez C, Kumar B A, Shi V and Sia S K 2021 *Lab Chip* **21** (23) 4517-48
[2] Yang J, Brooks C, Estes M, Hurth C and Zenhausern F 2014 *Forensic Sci Int-Gen* **8** 147-58
[3] Chen D et al. 2010 *Biomed Microdevices* **12** (4) 705-19
[4] Lukashenko T A, Tupik A N, Rudnitskaya G E, Bulyanitsa A L, Tsimbalov A I and Evstrapov A A 2016 *"Nauchnoe Priborostroenie" (in Russ.)* **26** (2) 64-74
[5] Zubik A N, Rudnitskaya G E, Bulyanitsa A L, Lukashenko T A and Evstrapov A A 2021 *J Phys Conf Ser* **2086** 012124
[6] https://permabond.ru/catalog/uf/Permabond-UV630.htm
[7] Tupik A N, Rudnitskaya G E, Lukashenko T A and Evstrapov A A 2020 *Tech Phys* **65** 1510-5
[8] https://smchemie.ru/SMChemie301
[9] http://mastiks.ru/catalog/klei-i-germetiki/klej-dlya-stekla-uv-odnokomponentnyj-fotootverzhdaemyj

Computer analysis of erythrocyte deformability in microfluidic devices

A.S. Ivanov[1,2,*], N.A. Besedina[1], E.A. Skvechinskaya[1,3], A.S. Bukatin[1,4]

[1]Alferov Saint Petersburg National Research Academic University of the Russian Academy of Sciences, 194021 Saint-Petersburg, Russia

[2]Institute of Physics and Mechanics, Peter the Great Saint-Petersburg Polytechnic University, 195251 Saint-Petersburg, Russia

[3]Sechenov Institute of Evolutionary Physiology and Biochemistry, Russian Academy of Sciences, 194223 Saint-Petersburg, Russia

[4]Institute for Analytical Instrumentation of the RAS, 190103 Saint-Petersburg, Russia

*a.s.ivanov@mail.ru

Abstract. Simulation of cell movement in the microcapillaries of the circulatory system using biomimetic microfluidic devices is a relevant and powerful method for studying the functional properties of erythrocytes, which change both as a result of the development of various diseases, such as malaria or sickle cell anemia, and as a side effect of drugs chemotherapy in cancer patients [1]. In this study proposed improvement of the analysis method based on computer vision and machine learning algorithms, which can multiply the volume of data.

1. Introduction

Erythrocytes (red blood cells, RBCs) are the main part of circulatory system. They are response for gas exchange throughout the body, occurring mainly in microcapillaries. The efficiency of gas exchange depends on RBC's ability to adapt their shape to dynamic flow conditions. Disfunction of RBC's deformability leads to deterioration of gas exchange in tissues and organs and to the occurrence of anemia [3]. To date, several methods that directly assess the deformability of RBCs have been developed, such as micropipette, optical stretching, and atomic force microscopy. However, these methods have low productivity and high labor intensity, which does not allow their use in clinical practice. Microfluidic devices make it possible to directly simulate blood microcirculation in vitro with a high rate of statistics collection [4].

2. Used materials

In this study, a microfluidic chip with an array of 16 channels with a cross section of 1.5x8 μm was used [1]. The movement of cells along the microchannels was recorded using a Leica DM4000 B LED optical microscope with a XIMEA MC023MG-SY digital camera (400 fps).

Simulation of oxidative stress conditions was performed by incubation of tert-Butyl hydroperoxide (tBH).

3. Motion analysis software

We can estimate erythrocyte deformability and adhesion by calculating their velocity in microchannels. For this purpose, a motion analysis software was developed on MATLAB (The MathWorks). This software is separated in two parts: cell tracking [2], used for normalization velocity data and microchannel velocity calculation algorithm. The normalization shows, how much lower erythrocyte's velocity than flow rate, so we can compare influence of different concentrations of tBH.

4. Form classification

In addition to stiffness and adhesion, an important parameter of erythrocytes is the shape of RBCs in the stream. In case of deviations from the norm, the area of contact of the cell with the tissues of the capillary decreases, which makes gas exchange difficult and can cause anemia even with a sufficient number of cells. By this reason on Python was developed a classification algorithm, based on neural network from TensorFlow package. The main idea of the algorithm is to separate cell images to different classes by form and estimate diversity of forms. The more deformed cells, the worse they perform their physiological functions, so this classification complements visual analysis of erythrocyte behavior in microfluidic chip.

On test arrays of images, the division of cells into 6 classes according to the shape was obtained:

1) Non-deformed discoid cells;
2) Strongly deformed, almost flat, cells;
3) Medium-deformed parachute-shaped cells;
4) Weakly deformed elliptical cells;
5) Outliers;
6) Medium-deformed, with very curved border, cells.

In summary, based on the results of clustering, we can say that the developed algorithm makes it possible to create clusters of normal and transformed cells, which will allow us to determine the proportion of affected by oxidative stress RBCs. In the future, it is planned to create a dataset of images for the classification of erythrocytes in various pathologies.

Acknowledgments

The study was supported by a grant from the Russian Science Foundation (project No. 22-24-00998).

References

[1] Tsai C. H. D. et al. https://doi.org/10.1039/C4RA08276A
[2] Crocker J.C. et al, https://doi.org/10.1006/jcis.1996.0217
[3] Huisjes, R. et al, https://doi.org/10.3389/fphys.2018.00656
[4] Besedina N.A. et al, https://doi.org/10.3390/cells10123552

Evaluation of different viability assays for studying the course of multidrug resistant infections in *C. elegans*

Anastasya I. Kalganova, Anna D. Mikushina, Igor E. Eliseev

Alferov University, St. Petersburg 194021, Russia

eliseev@spbau.ru

Abstract. New effective platforms are urgently needed to discover new antimicrobials active against multidrug-resistant pathogens, biofilms, and intracellular pathogens. In this work, we evaluate the capabilities of the whole-animal *C. elegans* system for screening drugs and microorganisms *in vivo*. We aim to use infected nematodes to study the *in vivo* activity of combinations of antimicrobial peptides and antibiotics against multidrug-resistant pathogens. This technology will make it possible to study the course of an infection in a living animal and explore various aspects of the organism-pathogen interaction: the effect of antimicrobial peptides on pathogens, the interaction of resistance and virulence factors in bacteria and the formation of biofilms.

1. Introduction

The spread of bacterial resistance to existing antibiotics is a major public health challenge. Antibiotic resistance (AR) not only carries an obvious risk of incurable infectious diseases, but also complicates many medical technologies, such as conventional surgery, organ transplantation, and cancer therapy. Existing approaches to finding and testing new therapeutics have not kept pace with the evolution of microbial resistance development. Antimicrobial activity is predominantly assessed in cultures of pathogens in vitro, which does not allow studying the interaction between the organism and the pathogen. Testing on traditional laboratory animals is too laborious and expensive and therefore is used for preclinical studies of already selected candidates, but not for primary screening. This approach does not favor the selection of molecules with low toxicity and does not allow the identification of therapeutic molecules that act on virulence factors.

2. Results and Discussion

Microscopic nematodes *C. elegans* develop infections after feeding on Petri dishes with all ESKAPE pathogens [1, 2]. Therefore, we plan to study the activity of various combinations of antimicrobial peptides and conventional antibiotics in an infection model in this organism. We first have established the previously published laboratory protocols for the infection of nematodes [3] with opportunistic pathogens *P. aeruginosa* and *S. aureus*, both standard laboratory strains (ATCC 27853 and ATCC 25923) and clinical isolates with multiple antibiotic resistance (*P. aeruginosa* MDR 522/17 and *S. aureus* MDR 1399/2017 from Institute of experimental medicine, St. Petersburg). Then we compared the infections caused by laboratory *P. aeruginosa* and *S. aureus*, and their multidrug resistant clinical isolates. The kinetics of ongoing infection were analysed by measuring survival curves of infected

nematodes in 96-well plates over the course of one week after contact with pathogen. We compared different methods for determining infected/healthy and live/dead animals using image analysis, fluorescent signal from a vital dye, as well as real-time experimental observation of a degree of motility [4].

Having worked out the platform for *C. elegans* infection, we moved to their "treatment". In the experiments with laboratory drug susceptible strains, we observed efficient treatment with ampicillin, kanamycin and tetracycline. The antibiotic-treated animals showed lifespan almost indistinguishable from controls and also resumed reproduction. Nematodes infected with drug-resistant pathogens did not respond to treatment and died within 2-5 days. We next plan to investigate the synergy between antimicrobial peptides and classical antibiotics in the developed in vivo model, which we have recently shown in vitro [5]. It is expected that this synergy may manifest itself even more clearly, since in the in vivo system one can observe alternative mechanisms of action that are not associated with the direct killing of bacteria, which is typical for protective peptides.

Acknowledgments

This study was funded by the Russian Science Foundation (grant № 22-24-20120, https://rscf.ru/project/22-24-20120/) and co-funded by the city of St. Petersburg.

References

[1] Powell, Jennifer R., and Frederick M. Ausubel 2008. Methods in Molecular Biology. vol 415 p 403-427

[2] Balla, K. M., & Troemel, E. R. 2013. Cellular microbiology.15(8) p 1313-22

[3] Moy, Terence I., et al. 2009. ACS chemical biology.vol 4 No 7 (2009) p 527-533

[4] Moy, Terence I., et al. 2006. Proceedings of the National Academy of Sciences. vol 103 No 27 (2006) p 10414-19

[5] Zharkova, Maria S., et al. 2019. Frontiers in cellular and infection microbiology. vol 9 (2019) p 128.

Activation of polylactide films by cold plasma dielectric barrier discharge to improve the interaction of fibroblasts

Kamalov A.M.[1], Kolbe K.A. [2], Pavlov A.A. [1], Borisova M.E. [1], Yudin V.E.[2]

1-Peter the Great St.Petersburg Polytechnic University, St.Petersburg, Russia, Polytechnicheskaya, 29
2-Institute of Macromolecular Compounds Russian Academy of Sciences, St. Petersburg, Russia, Bolshoy Prospekt, 31

spb.kamalov@gmail.com

Abstract. This work focuses on the surface modification of PLA films. The films were treated in a dielectric barrier discharge in order to optimize their biological properties and interaction with human dermal fibroblasts. The optimal properties of the dielectric barrier discharge, which improve cell proliferation the most, were found.

1. Introduction

Polylactides are weakly hydrophilic materials; so, it is necessary to increase the hydrophilicity of the surface of a PLA-based material in order to use it as a film scaffold in cell cultivation. This may be achieved by activation of the surface by dielectric barrier discharge plasma at high frequencies (higher than 1 kHz) at atmospheric pressure. Usually, the main goal of plasma treatment is the accumulation of functional groups on a polymer surface. As a result, surface properties of a polymer (including wettability, biocompatibility, and chemical composition of a surface) improve. Activation of a polymer with cold plasma makes it possible to modify surface properties of a film while maintaining its geometrical parameters. Besides, unlike the traditional wet chemical etching, no potentially cytotoxic chemical substances are used during plasma activation [1].
The goal of the present work was to optimize the technique of surface modification of PLA films in dielectric barrier discharge in air at atmospheric pressure; this modification was designed to improve the biocompatibility and bioactivity of the materials during interaction with human dermal fibroblasts.

2. Materials and methods

The objects of this study are samples of polylactide films, which thickness was 30±5 μm. The samples were produced using a DSM Xplore micro-extruder and a DSM Film Device Machine.
A dielectric barrier discharge (DBD) was created in an ionization cell, which consists of ceramic plates with electrodes divided by an air gap (1 mm thick). The method of DBD film surface treatment was shown in the previous work [2].
The water contact angles of the PLA samples were obtained using the sessile drop method (Kruss DSA30) Distilled water was used as the probe liquid.

3. Results

The water contact angle measurements of the PLA samples show that after 1 minute of DBD treatment the contact angle decreases to 43.5°, with the increase of treatment time the angle starts to return to its initial value (55°). It is known fact that crystallization temperature of PLA is 70-130 °C. Therefore, the surface of the sample reaches the crystallization temperature after 3 minutes of treatment; the supramolecular structure of the sample starts to change. To reduce the impact of the surface temperature, the chosen sample treatment time was from 0 to 3 minutes (figure 1, I).

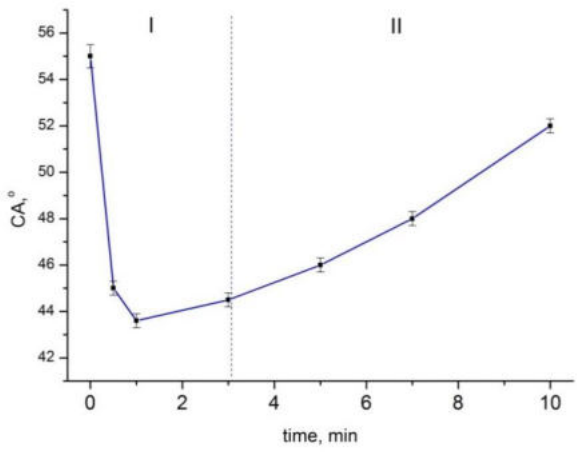

Figure 1. Water contact angle versus DBD treatment time

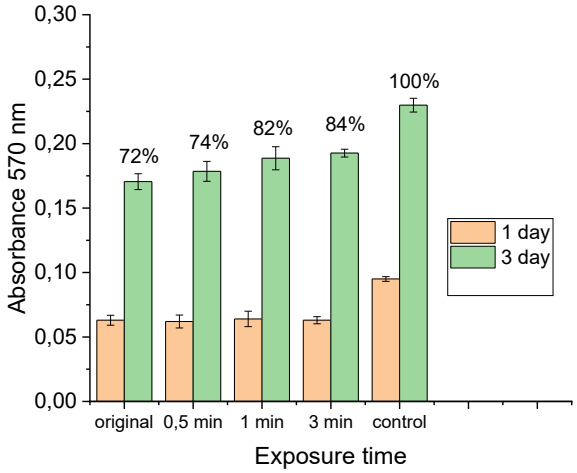

Figure 2. MTT assay on the cell viability of human dermal fibroblasts on the surface of the PLA samples (1 and 3 days).

Human dermal fibroblasts were observed *in vitro* in order to determine the biological properties of the PLA films. After 24 h of cell cultivation on the surfaces of PLA films and plastic culture substrate, which was used as a control sample, the MTT assay on cell adhesion was done. The results suggest that all PLA samples are biocompatible, support cell adhesion on the sample surface. PLA surface modification does not lead to any drastic changes in cell adhesion levels (Fig. 2). The MTT assay shows that after 72 hours of cell cultivation the optimal surface properties for equal sell distribution and high cell proliferative activity were achieved. After 3 minutes of the DBD treatment the film samples have the best biocompatibility (Fig. 2).

4. Conclusion

The results of this work suggest that the optimal time of the DBD treatment, which provides the optimal surface microrelief for cell proliferative activity, is 3 minutes.

After 3 minutes of the DBD treatment the cell proliferative activity on the treated sample is 12% better than on the initial sample. This can be caused by oxygen-containing functional groups appearing on the surface of a sample after the treatment. They interact with the cells and improve their proliferative activity.

Acknowledgments

Grant for young scientists the Ministry of Education and Science Russia MK-4346.2022.4

Reference

[1] T Jacobs et al. 2013 Mater Sci Mater Med;24(2):469.

[2] A M Kamalov *et al* 2021 *J. Phys.: Conf. Ser.* 2103 012051

Processing of qPCR signals obtained on microfluidic chips in the measurement sequence disorder event

D Yu Klimenko[1], A Yu Tryastsyn[2], N A Esikova[3], A L Bulyanitsa[1, 3], R V Davydov[1, 4] and D A Belov[3]

[1] Peter the Great Saint-Petersburg Polytechnic University, Saint Petersburg, 195251, Russia
[2] St. Petersburg State Institute of Technology, 190013, Russia
[3] Institute of Analytical Instrumentation of the Russian Academy of Sciences, 198095, Russia
[4] All-Russian Research Institute of Phytopathology, Moscow Region 143050, Russia

e-mail: onoff_10@mail.ru

Abstract. New methods for automatically processing of qPCR signals distorted by the formation and movement of bubbles in microfluidic chips were developed. Methods make it possible to obtain satisfying RMS values in determining the quantification cycle values C_q and to successfully perform a quantitative PCR analysis when developing new microfluidic chips.

1. Introduction

The rapid development of microfluidics and, as a result, the widespread use of devices that reproducibly control the flow of nano- and picoliter volumes of liquid in microsized channels is due to their high sensitivity, compact size and low consumption of reagents and samples [1].

The Institute for Analytical Instrumentation of the Russian Academy of Sciences (IAI RAS) develops and improves microfluidic chips for real-time quantitative polymerase chain reaction (qPCR) analysis [2]. qPCR is one of the most popular genetic analysis methods, which makes it possible to quantify the target nucleotide sequence content in a sample. The number of sequences increases with each PCR cycle and is accompanied by fluorescence signal growth. The determination of quantification cycle value C_q and the efficiency of PCR when using various parameters of chips, reagents and reaction conditions is difficult due to the bubbles appearance and movement from the detection zone and the fluorescence intensity decrease over several cycles. Bubbles are one of the main microfluidic chips problems, they can appear due to many factors, and it is not always possible to prevent their occurrence [3]. An urgent task is to develop methods for processing of qPCR signals distorted by the formation and movement of bubbles, which leads to a discord in the informative signal sequential measurement and erroneous results of quantitative analysis.

2. Description of methods

Two qPCR signal processing methods were developed and implemented in the MATLAB software package. Both are based on the approximation of qPCR curves by a known sigmoid function (1) [4]. In method No. 1 the measurement with the largest deviation of the experimental curve from the model is assigned a value corresponding to a point on the approximating dependence. In method No. 2, the above-described value of the maximum deviation is excluded from the experimental sample.

$$F_c = \frac{F_m}{1 + e^{\frac{C_q - C}{k}}} + f_0 \ , \quad (1)$$

where F_c — the fluorescence signal at cycle C, RFU; F_m — maximal reaction fluorescence, RFU; C_q — fractional cycle at which reaction fluorescence reaches half of F_m; k is related to the slope of the curve, f_0 — fluorescence background, RFU.

Thus, a change in the level of fluorescence caused by the formation of a bubble is excluded. The developed methods do not take into account the possible decrease in the efficiency of the PCR reaction due to the appearance of a bubble, research in this area is a separate task.

3. Approbation of methods

The analysis of the soybean DNA samples and its dilutions by 1-3 orders of magnitude in 3-fold repetition for each concentration were carried out in polypropylene and polycarbonate microfluidic chips. The convenience of using the developed methods on experimental data were revealed, however, in order to evaluate their effectiveness, a decision was made to test them on simulation curves. The use of traditional methods for random errors processing, calculated in the experimental signals sections with a conditionally determined form, made it possible to draw the following conclusions:

- the mathematical expectations of the errors are close to zero;
- distribution of errors to a greater extent corresponds to the normal law: Kullback–Leibler divergence score [5] of the interference real distribution histogram of over 6 intervals with a uniform law of 0,0710 nat, with a normal one — 0,0422 nat, excess coefficient — 3,07;
- the error is close to multiplicative with a standard deviation (SD) proportional to the signal value.

It was created 10000 simulation curves with parameters $F_m = 1000$, $C_q = 30$, $k = 1$, $f_0 = 600$, the law of the dependence of normally distributed errors SD on the signal value $\sigma = 0{,}0024 \cdot F_c + 1{,}1368$, bubble durations from 2 to 7 cycles, the uniform distribution value of the bubble beginning and the intensity of the signal fall $(0{,}22 \div 0{,}24) \cdot F_c$ when the bubble occurs.

4. Results and discussion

As a result of the method No. 1 application on simulation curves, the average value of $C_q = 30{,}24 \pm 0{,}60$, 19,4 % curves have significant deviations (more than 0,1). As a result of using method No. 2, the average value of $C_q = 30{,}22 \pm 0{,}70$, 15,5 % curves have significant deviations. In both methods, criteria are formulated that automatically determine such analysis results as false. Significant deviations were obtained when bubbles more than 5 cycles occurred on cycles corresponding to the exponential growth region of PCR curves.

5. Conclusion

As a result of this work, two methods have been developed that make it possible to obtain satisfying RMS values in determining the C_q and to successfully perform a quantitative analysis of qPCR in microfluidic chips in the event of bubbles. The authors consider method No. 2 to be preferable due to fewer number of significant deviations and closer to true C_q value.

Acknowledgments

The work was carried out within the framework of the state task of the Ministry of Science and Higher Education of the Russian Federation No. 075-00761-22-00. Science theme code FFZM-2022-9910.

References

[1] Evstrapov A A 2011 *Russian Chemical Journal* **55**(2) 99-110
[2] Esikova N A, Germash N N, Evstrapov A A 2020 *Science Instrumentation* **30**(4) 21-6
[3] Sung J H, Shuler M L 2009 *Biomed. Microdevices* **11**(4) 731-8
[4] Rutledge R G, Stewart D A 2008 *BMC Biotechnology* 8:47
[5] Kullback S, Leibler R A 1951 *Annals of Mathematical Statistics* **22**(1) 79–86

Processing of qPCR signals obtained on microfluidic chips in the measurement sequence disorder event

D Yu Klimenko[1], A Yu Tryastsyn[2], N A Esikova[3], A L Bulyanitsa[1, 3] and D A Belov[3]

[1] Peter the Great Saint-Petersburg Polytechnic University, Saint Petersburg, 195251, Russia
[2] St. Petersburg State Institute of Technology, 190013, Russia
[3] Institute of Analytical Instrumentation of the Russian Academy of Sciences, 198095, Russia

e-mail: onoff_10@mail.ru

Abstract. New methods for automatically processing of qPCR signals distorted by the formation and movement of bubbles in microfluidic chips were developed. Methods make it possible to obtain satisfying RMS values in determining the quantification cycle values C_q and to successfully perform a quantitative PCR analysis when developing new microfluidic chips.

1. Introduction

The rapid development of microfluidics and, as a result, the widespread use of devices that reproducibly control the flow of nano- and picoliter volumes of liquid in microsized channels is due to their high sensitivity, compact size and low consumption of reagents and samples [1].

The Institute for Analytical Instrumentation of the Russian Academy of Sciences (IAI RAS) develops and improves microfluidic chips for real-time quantitative polymerase chain reaction (qPCR) analysis [2]. qPCR is one of the most popular genetic analysis methods, which makes it possible to quantify the target nucleotide sequence content in a sample. The number of sequences increases with each PCR cycle and is accompanied by fluorescence signal growth. The determination of quantification cycle value C_q and the efficiency of PCR when using various parameters of chips, reagents and reaction conditions is difficult due to the bubbles appearance and movement from the detection zone and the fluorescence intensity decrease over several cycles. Bubbles are one of the main microfluidic chips problems, they can appear due to many factors, and it is not always possible to prevent their occurrence [3]. An urgent task is to develop methods for processing of qPCR signals distorted by the formation and movement of bubbles, which leads to a discord in the informative signal sequential measurement and erroneous results of quantitative analysis.

2. Description of methods

Two qPCR signal processing methods were developed and implemented in the MATLAB software package. Both are based on the approximation of qPCR curves by a known sigmoid function [4]:

$$F_c = \frac{F_m}{1 + e^{\frac{C_q - C}{k}}} + f_0 \ , \tag{1}$$

where F_c — the fluorescence signal at cycle C, RFU; F_m — maximal reaction fluorescence, RFU; C_q — fractional cycle at which reaction fluorescence reaches half of F_m; k is related to the slope of the curve, f_0 — fluorescence background, RFU.

In method No. 1 the measurement with the largest deviation of the experimental curve from the model is assigned a value corresponding to a point on the approximating dependence. In method No. 2, the above-described value of the maximum deviation is excluded from the experimental sample. Thus, a change in the level of fluorescence caused by the formation of a bubble is excluded. The developed methods do not take into account the possible decrease in the efficiency of the PCR reaction due to the appearance of a bubble, research in this area is a separate task.

3. Approbation of methods

The analysis of the soybean DNA samples and its dilutions by 1-3 orders of magnitude in 3-fold repetition for each concentration were carried out in polypropylene and polycarbonate microfluidic chips. The convenience of using the developed methods on experimental data were revealed, however, in order to evaluate their effectiveness, a decision was made to test them on simulation curves. The use of traditional methods for random errors processing, calculated in the experimental signals sections with a conditionally determined form, made it possible to draw the following conclusions:

- the mathematical expectations of the errors are close to zero;
- distribution of errors to a greater extent corresponds to the normal law: Kullback–Leibler divergence score [5] of the interference real distribution histogram of over 6 intervals with a uniform law of 0,0710 nat, with a normal one — 0,0422 nat, excess coefficient — 3,07;
- the error is close to multiplicative with a standard deviation (SD) proportional to the signal value.

It was created 10000 simulation curves with parameters $F_m = 1000$, $C_q = 30$, $k = 1$, $f_0 = 600$, the law of the dependence of normally distributed errors SD on the signal value $\sigma = 0{,}0024 \cdot F_c + 1{,}1368$, bubble durations from 2 to 7 cycles, the uniform distribution value of the bubble beginning and the intensity of the signal fall $(0{,}22 \div 0{,}24) \cdot F_c$ when the bubble occurs.

4. Results and discussion

As a result of the method No. 1 application on simulation curves, the average value of $C_q = 30{,}24 \pm 0{,}60$, 19,4 % curves have significant deviations (more than 0,1). As a result of using method No. 2, the average value of $C_q = 30{,}22 \pm 0{,}70$, 15,5 % curves have significant deviations. In both methods, criteria are formulated that automatically determine such analysis results as false. Significant deviations were obtained when bubbles more than 5 cycles occurred on cycles corresponding to the exponential growth region of PCR curves.

5. Conclusion

As a result of this work, two methods have been developed that make it possible to obtain satisfying RMS values in determining the C_q and to successfully perform a quantitative analysis of qPCR in microfluidic chips in the event of bubbles. The authors consider method No. 2 to be preferable due to fewer number of significant deviations and closer to true C_q value.

Acknowledgments

The work was carried out within the framework of the state task of the Ministry of Science and Higher Education of the Russian Federation No. 075-00761-22-00. Science theme code FFZM-2022-9910.

References

[1] Evstrapov A A 2011 *Russian Chemical Journal* **55**(2) 99-110
[2] Esikova N A, Germash N N, Evstrapov A A 2020 *Science Instrumentation* **30**(4) 21-6
[3] Sung J H, Shuler M L 2009 *Biomed. Microdevices* **11**(4) 731-8
[4] Rutledge R G, Stewart D A 2008 *BMC Biotechnology* 8:47
[5] Kullback S, Leibler R A 1951 *Annals of Mathematical Statistics* **22**(1) 79–86

Tetrahydrobiopterin and 5,10 –Methenyltetrahydrofolate Excited States Dynamics

Kubenko V. V.[1], Reveguk Z.V.[1], Buglak A.A.[1], Kononov A. I.[1]

[1]Department of Molecular Biophysics and Polymer Physics, Saint Petersburg State University, 199034 Saint Petersburg, Russia
varvara.kubenko@mail.com

Abstract. Ultrafast fluorescence decay curves of tetrahydrobiopterin (H4Bip) coenzyme and 5,10 –Methenyltetrahydrofolate (MTHF) photoantenna were recorded and analyzed. Fast and slow components were found and evaluated.

1. Introduction

Pterins are low molecular weight heterocyclic compounds widely distributed in the human organism, mainly in the form of reduced coenzymes. They are divided into two large groups: folic acid derivatives (folates) and pterin derivatives. Depending on the redox state pterins are divided into tetrahydro-, dihydropterins, and oxidizedpterins. H_4pterins play the role of key biological coenzymes. Probably, the most significan pterin coenzyme is tetrahydrobiopterin (H_4Bip). The biological role of H_4Bip is to participate in the renzymatic reactions of NO synthases, alkylglycerol monooxygenases, and aromatic amino acid hydroxylases[1].

Folates cofactors are also involved in a wide variety of biological processes. 5,10 - Methenyltetrahydrofolate and its photodegradation product 5,10-methylenetetrahydrofolate are associated with the light-controlled DNA repair protein DNA photolyase and its homologues [2]. The ubiquitous presence of pterins in cellular processes and pathologies, as well as their rich photochemistry and photophysics in solutions, suggests that a detailed knowledge of the properties of these molecules is essential for understanding both the biological and photobiological processes in which these chromophores are involved.

2. Experiment

H_4Bip was dissolved under nitrogen atmosphere to avoid oxidation, then it was diluted by 0.01 M TRIS-HCl pH 7.5 buffer to 1 OD in a rotating 0.25 mm quartz cuvette. MTHF was dissolved in 0.1 M HCl. The absorbance spectra were recorded with a Specord 210 plus spectrophotometer (AnalyticJena). The fluorescence time-resolved measurements were performed with a FOG 100-DX fluorescence up-conversion spectrometer (CDP System Corp., Moscow, Russia). The excitation was performed using the third harmonic (266 nm) of a Ti:sapphire laser (TISSA, CDP Corp.) at 80 MHz. Fluorescence decay traces were analyzed using DecayFit software [3].

3. Results and discussion

3.1. H4Bip excited states dynamics.

Fluorescence decay trace of H4Bip in 0.01 M TRIS-HCl pH 7.5 buffer is shown in Fig. 1. They were fitted with two exponents (fit: a1*exp(-tau1)+(1-a1)*exp(-tau2)). The results of fitting are shown in table1.

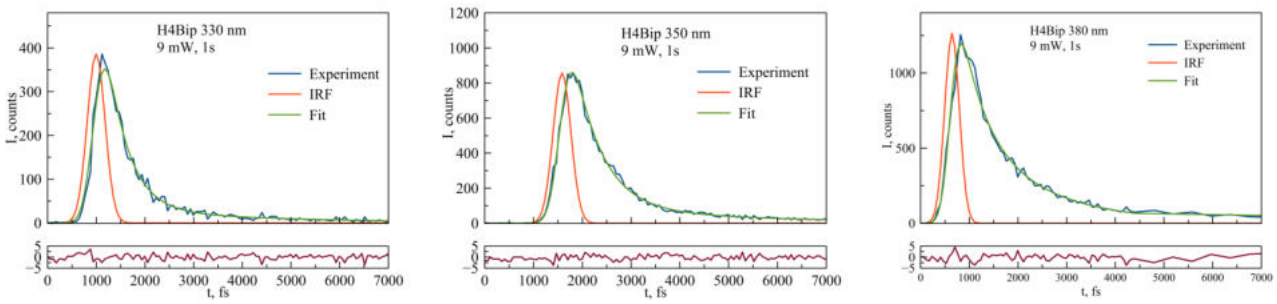

Figure 1. Fluorescence decay trace of H4Bip in 0.01 M TRIS-HCl pH 7.5 buffer at 330 nm (left), 350 nm (middle) and 380 nm (right).

Table1. Intensities, decay times and amplitudes for H4Bip.

Wavelength	a1	tau1	tau2	I, counts
330 nm	0.94	430 fs	3050 fs	380
350 nm	0.93	745 fs	3400 fs	850
380 nm	0.63	230 fs	1400 fs	1250

3.2. *MTHF excited states dynamics.*

Fluorescence decay trace of H_4Bip in 0.01 M TRIS-HCl pH 7.5 buffer and the corresponding were recorded at the same conditions and fitted: a1*exp(-tau1) + a2*exp(-tau2) + (1-a1-a2)*exp(-tau3)). The results of fitting are shown in Table 2.

Table2. Intensities, decay times and amplitudes for MTHF.

Wavelength	a1	tau1	a2	tau2	tau3	I, counts
330 nm	0.69	195 fs	0.24	2.3 ps	1.4 ns	320
350 nm	0.41	395 fs	0.25	4.2 ps	0.13 ns	540
370 nm	0.33	611 fs	0.27	12ps	0.43 ns	690

4. Conclusion

Ultrafast fluorescence decay curves were recorded and analysed for H4Bip and 5,10 – Methenyltetrahydrofolate (MTHF).

Acknowledgments The work was supported by the Russian Science Foundation Grant No. 20-73-10029.

References

1. Fitzpatrick P.F. Mechanism of Aromatic Amino Acid Hydroxylation // Biochemistry. 2003. Vol. 42, № 48. P. 14083–14091.
2. Tyagi A. et al. Thermal degradation of (6R,S)-5,10-methenyltetrahydrofolate in aqueous solution at pH 8 // Chemical Physics. 2009. Vol. 358, № 1–2. P. 132–136.
3. http://www.fluortools.com/software/decayfit (last available 01.04.2022).

Investigation of solubility of porous silicon nanocomposite with hydroxyapatite

Kulagina S. Y., Latukhina N. V.

Samara National Research University, 443086 Samara, Russia

kulagina4@ya.ru

Abstract. In this work, a porous silicon nanocomposite (por-Si) with hydroxyappatite (HAP) was studied as the basis of a promising biomaterial for osteoplasty, since HAP is the mineral phase of bone tissue, and silicon contributes to faster and stronger bone formation.

1. Biomaterials based on porous silicon and its nanocomposites in medical applications, namely for use in osteoplasty.

The task lies in the field of targeted delivery of hydroxyapatite to bone areas damaged as a result of injury or disease using porous nanoparticles [1]. To deliver HAP to the affected areas of the bone, it is necessary to use water-soluble transport porous particles saturated with the substance, since pure HAP is practically insoluble in blood and plasma [2]. The purpose of this work was to test the solubility of the por-Si nanocomposite with HAP, since the por-Si itself is completely dissolved. When filling the pores of a soluble por-Si with insoluble HAP, it is important to obtain soluble porous nanocomposite particles [3]. This is extremely important for the creation of biodegradable biovectors.

2. Experimental part

Porous silicon was obtained by electrochemical etching in HF:H2O:C2H5OH solution. Samples with a polished and grinded surface were etched for 20 minutes at current and voltage values of 120 mA and 40 V. Porosity was assessed using the gravimetric analysis [4]. The largest porosity values were obtained on a polished surface, which allowed the bulk of the HAP to penetrate into the pores of silicon. Alloying was performed by applying a solution of HAP in alcohol with a total mass of 33.8 mg + 1.5 ml to the surface of the plates. After evaporation of alcohol and removal of excess HAP, the total increase in the mass of the plates was about 0.2-0.5 percent. Dissolution in distilled water was carried out for 1.5 months. According to the results of the study, samples with a polished surface dissolved by 0.25 percent. Samples with a polished surface dissolved by 0.5 percent. It can be concluded that PCs with a HAP with a polished surface are more suitable for creating a soluble nanocomposite.

References

[1] A. S. Lenshin, Formirovanie I funkcional'nye svoictva nanostructur na osnove poristogo kremniya. Diss. kand. fiz.–mat. nauk [Formation and functional properties nanostructures based on porous silicon. Cand. phys. and math. sci. diss.], Voronezh, 2020

[2] R. S. Gonzalo, J. P. Ramon, Porous silicon: An attractive material for biomedical uses, Inorganic Frameworks as Smart Nanomedicines, 3 (2018) 789–797

[3] Jeffery L Coffer, Porous silicon-based scaffolds for tissue engineering and other biomedical applications, Phys. Stat. Sol. (a), 202(8) (2005) 1451–1455

[4] Chuan Lai, Improvement in gravimetric measurement for determining the porosity and thickness of porous silicon using an optimized solution, Materials Science in Semiconductor Processing 26(1) (2014) 1451–1455

Genetically encoded labels for non-invasive tumor cells tracking

Anna N. Gabashvili [1], Stepan S. Vodopyanov [1,2], Nelly S. Chmelyuk [1,3], Vera V. Oda [1], Maria K. Leonova [4], Alevtina S. Semkina [3,5], Anna V. Ivanova [1] and Maxim A. Abakumov [1,3]

[1] Laboratory "Biomedical Nanomaterials", National University of Science and Technology "MISiS", Leninskiy Prospect, 4, 119049 Moscow, Russia
[2] Biology Faculty, Lomonosov Moscow State University, Leninskiy Gory, 119234, Moscow, Russia
[3] Department of Medical Nanobiotechnology, Pirogov Russian National Research Medical University, Ostrovityanova st, 1, 117997 Moscow, Russia;
[4] National University of Science and Technology "MISiS", Leninskiy Prospect, 4, 119049 Moscow, Russia
[5] Department of Basic and Applied Neurobiology, Serbsky National Medical Research Center for Psychiatry and Narcology, Kropotkinskiy Per. 23, 119991 Moscow, Russia
* Correspondence: gabashvili.anna@gmail.com

Abstract. According to World Health Organization, breast cancer is the most common oncological disease worldwide. There are multiple animal models for different types of breast carcinoma allowing the research of tumor growth, metastasis, and angiogenesis. When studying these processes, it is crucial to visualize cancer cells for a prolonged time via a non-invasive method, for example MRI. In this study, we present a new genetically encoded label based on *Quasibacillus thermotolerans* (*Qt*) encapsulin, stably expressed in mouse 4T1 cells. The label consists of a protein shell containing an enzyme called ferroxidase. When adding Fe^{2+}, a ferroxidase oxidizes Fe^{2+} to Fe^{3+}, followed by magnetic nanoparticles formation. Besides, genes encoding mZip14 metal transporter, enhancing the iron transport, were inserted into the cells via lentiviral transduction. The expression of transgenic sequences does not affect cell viability, and the presence of magnetic nanoparticles formed inside encapsulins allows visualizing *4T1-Qt* cells by MRI.

1. Introduction

As a rule, tumor cells *in vivo* visualization is carried out using fluorescent dyes, as well as MRI and PET methods [1,2]. A common disadvantage of fluorescent labels is a small penetration depth (about 2 mm), which makes their use only possible for surface tissues in small animals. A significant disadvantage of MRI and PET contrast agents is the decrease in the signal intensity associated with cell proliferation, and also toxicity. Developing a stable and non-toxic label that allows the non-invasive tracking of tumor cells remains highly relevant. Here we present *Qt* encapsulin-based genetic label, which is stably expressed in 4T1 mouse carcinoma cells. The diameter of the *Qt* encapsulin shell is 42 nm. The accumulation of iron inside the encapsulin shell results from a catalytic activity of IMEF (Iron-Mineralizing Encapsulin-Associated Firmicute) cargo protein. *Qt* encapsulin accumulating up to 30 000 iron atoms [3], which makes it a promising label for MRI cell tracking. To obtain a 4T1 cell line with a stable expression of *Qt* encapsulins genes (4T1-Qt), lentiviral transduction was performed using two viral vectors that carry genes encoding encapsulin shell and cargo protein ($QtEnc^{FLAG}$-QtIMEF), as well as genes encoding the divalent metal transporter (mZip14). We used ferrous ammonium sulfate (FAS) as a source of Fe^{2+}. The entire system works as follows: Fe^{2+} ions from FAS are transported into cells via mZip14 and enter the encapsulin nanocompartments. There, under the

action of IMEF, Fe^{2+} is oxidized, resulting in iron oxide nanoparticles, which further allow 4T1-Qt cell tracking by MRI.

2. Materials and Methods

The 4T1 mammary mouse carcinoma cells were cultured in RPMI 1640 media (Gibco) supplemented with antibiotics (100 U/ml penicillin, 100 mg/ml streptomycin, Gibco), GlutaMax Supplement (2 mM, Gibco), and 10 % fetal bovine serum (HyClone). Cells were grown under standard culture conditions. HEK293T cells were used for lentiviral particle production. Transfection with Lipofectamine 3000 (Thermo Fisher) was performed according to the manufacturer's protocol. Transduction of the cells with the lentiviral vectors was done according to standard protocol in DMEM growth medium supplemented with 10 % heat-inactivated FBS and polybrene. The transduced cells were cultured until 90 % of monolayer confluence. Total RNA was extracted by Extract RNA reagent (Evrogen) according to the manufacturer's instructions. cDNA was synthesized with Invitrogen SuperScript III Reverse Transcriptase (Thermo Fisher) and oligo-DT and random primers. The cDNA and negative control (RNA sample without reverse transcriptase added) were used for classical PCR with Taq polymerase (Fermentas) and corresponding buffer. PCR products were separated with electrophoresis in 1 % agarose gel. The desired fragments were identified by their length. MTS-assay was performed with CellTiter 96 AQueous One Solution Cell Proliferation Assay (Promega) after 24 h of incubation of 4T1 and 4T1-Qt cells with FAS in a various concentrations. Cell viability (%) = $(A_s - A_b) / (A_c - A_b) \times 100$ where A_s – mean optical density in sample wells, A_b – mean optical density in blank wells, A_c – mean optical density in positive control wells. Magnetic-activated cell sorting (MACS) of 4T1-Qt cells after 24 h of incubation with 2 mM FAS was performed using a magnetic separation kit (Miltenyi Biotech). Prussian Blue Staining was performed using Iron Stain Kit (Sigma-Aldrich), according to the manufacturer's instructions. Images of 4T1 and 4T1-Qt cells were taken with an inverted microscope Primo Vert (Zeiss). Ultrathin (70 nm) cell sections were obtained with an EM UC6 ultramicrotome (Leica). Imaging was performed with a JEOL JEM 1400 electron microscope. Iron concentration was determined using an Agilent 4200 MP-AES atomic emission spectrometer. For T2 relaxometry measurement, 4T1 and 4T1-Qt cells were incubated with 2 mM and 1 mM FAS for 24 h. MRI images were acquired on ClinScan 7T system (Bruker Biospin) in Spin Echo sequence.

3. Results

The expression of encapsulin genes was validated with a reverse transcription-polymerase chain reaction. Protein expression of $QtEnc^{FLAG}$ protomer was confirmed by using Western blot analysis. We also performed direct immunofluorescence staining of 4T1-Qt cells using primary labeled anti-FLAG Tag antibodies that bind to the FLAG sequence coexpressed with $QtEnc^{FLAG}$. We hypothesized that when FAS is added to wild-type 4T1 cells, excess iron may have a toxic effect due to accumulation of free iron in the cytoplasm. In genetically modified 4T1-Qt, part of the iron ions will be sequestered into encapsulins, which may reduce toxicity. Our hypothesis was confirmed in the 0.25 - 4 mM FAS concentration range. AES data indicate that iron accumulation in 4T1-Qt cells is dose-dependent. The iron accumulation in 4T1-Qt cells is significantly higher than the same value in wild-type 4T1 cells. The intracellular iron concentrations per cell for 4T1 and 4T1-Qt cells after the incubation with 2 mM FAS are almost an order of magnitude different. For a 4T1-Qt line obtained in this study, the maximum concentration of FAS allowing the saturation of encapsulins with iron while maintaining the cell viability is 2 mM. MRI data have shown lower T2 relaxation times for MACS-separated 4T1-Qt cells after 24 h incubation with FAS at 1 mM and 2 mM concentrations (120 ± 14 ms and 134 ± 15 ms, respectively) in comparison with 4T1 cells (294 ± 53 ms).

4. Conclusion

In this work, we describe the 4T1 mouse carcinoma cell line stably expressing *Qt* encapsulin genes for the first time. The latter do not alter the viability and proliferation of 4T1-Qt cells; moreover, *Qt* encapsulins have a protective effect against high concentrations of iron ions, at the same time

providing a dose-dependent iron accumulation in 4T1-Qt cells. Finally, *in vitro* MRI study showed a decrease in T2 relaxation time for magnetically sorted 4T1-Qt cells compared to wild-type 4T1 cells. We believe that this is an essential step towards the future *in vivo* MRI monitoring of malignant cells.

Funding
This research was funded by RSF grant number 21-75-00096.

References
[1] Hoffman, R. M. In Vivo Imaging with Fluorescent Proteins: The New Cell Biology. Acta Histochem. 2004, 106 (2), 77–87.
[2] Spira, D.; Bantleon, R.; Wolburg, H.; Schick, F.; Groezinger, G.; Wiskirchen, J.; Wiesinger, B. Labeling Human Melanoma Cells With SPIO: In Vitro Observations. Mol. Imaging 2016, 15.
[3] Giessen, T. W.; Orlando, B. J.; Verdegaal, A. A.; Chambers, M. G.; Gardener, J.; Bell, D. C.; Birrane, G.; Liao, M.; Silver, P. A. Large Protein Organelles Form a New Iron Sequestration System with High Storage Capacity. Elife 2019

The efficiency increase of two-cell embryos femtosecond laser induced fusion with the use of fluorescent dye

D. Yu. Martirosyan[1*], A. D. Zalessky[1], A. A. Osychenko[1], U. A. Tochilo[1] and V. A. Nadtochenko[1]

[1]N.N. Semenov Federal Research Center of Chemical Physics, Russian Academy of Sciences, Kosygina 4, Moscow, Russia

*e-mail: petrosyan359@gmail.com

Abstract. Femtosecond laser-induced cell fusion is a novel and highly low-invasive technic which was recently intensively developed. The main advantage of this approach is high localisation of laser impact on the cell adhesion area. In order to increase the fusion efficiency we propose to use lipophilic carbocyanine membrane fluorescent dye. We have shown that efficiency of femtosecond laser induced cell fusion could be increased with the use of BioTracker 400 Blue Cytoplasmic Membrane fluorescent dye.

1. Introduction

Laser-induced cell fusion is a promising method for medical and biomedical applications, e.g., somatic cell nuclear transfer in mammals and mitochondrial replacement therapy in humans. Namely, femtosecond laser-induced cell fusion could be more safe method of donor nucleus introduction in compare to microinjection or electrofusion. In our recent research we have shown that we could increase femtosecond laser induced fusion efficiency with the use of lipophilic carbocyanine membrane fluorescent dye. We used two-cell mouse embryos as a model system. Fluorescent dye incorporated in cytoplasmic membrane is able to act like a photosensitizer, lowering the laser energy required for the cytoplasmic membrane breakdown. This way, we managed to make the laser impact better controlled and more precise. More, taking into consideration the wavelength dependence of the fluorescent dye absorbance, the fine tuning of laser impact efficiency become possible.

2.1. Embryos collection

The female mice were superovulated by the standard scheme [1] and subsequently were coupled with males. Two-cell embryos were flushed from the oviducts by M2 (M7167, Sigma) medium 48 h after hCG injection and cultivated in M2 during the experiment.

2.2. Laser parameters

The detailed scheme of the cell fusion is described here [1]. Femtosecond laser pulses (80 MHz repetition rate; up to 25 nJ) were generated by the tunable femtosecond laser (Chameleon Discovery, Coherent), which could be tuned from 660 to 1300 nm. The average laser power before the objective lens was up to 800 mW and tuned by polarizing cube and half-wave plate. Femtosecond laser was coupled to microscope (Olympus IX71) by dielectric filter (Thorlabs FESH0750) mounted at 45^0 and then focused by the objective lens (UPlanFLN 60x 0.75NA, Olympus) on a sample (embryos were placed onto a cover glass in a 50 µl drop of M2 medium and placed at the 3-d stage). The pulse duration

was 100 fs, which was measured in the focal plane of the microscope by the autocorellator (Avesta AA-M). Pulse train, consisted of femtosecond pulses at fixed 80 MHz repetition rate, was applied to the sample. Pulse train length was set by the opening of a mechanical shutter (SH05, Thorlabs) unblocking the femtosecond laser beam (for a time up to 100 ms). The bright-field imaging was performed by a XIMEA xiQ MQ013MG-ON or by XIMEA xiD MD061CU-SY camera, mounted on the microscope.

2.3. BioTracker 400 Blue Cytoplasmic Membrane staining

Embryos were stained according to staining protocol of BioTracker 400 Blue Cytoplasmic Membrane Dye (SCT109, Sigma-Aldrich), provided by Sigma-Aldrich (Fig. 1).

3. Results.

Laser induced cell fusion was performed with the use of femtosecond laser pulse trains (pulse energy 0.8 nJ, train duration 30 ms) focused on the cell`s contact. Pulse trains were repeated until gas-vapor bubble occurred. After the laser action 4 possible outcomes could be realized: a) blastomeres of embryo were fused; b) blastomeres were not fused, and no morphological changes occurred; c) one blastomere was destroyed; d) finally, both blastomeres were destroyed. The series of experiments were performed for the femtosecond laser wavelength of 730, 760 and 790 nm, the outcome`s statistic is summarized in Table 1. We can see wavelength dependence of femtosecond laser induced two-cell embryo fusion efficiency. We suppose that it could be interpreted as a dependence of overlapping laser two-photon excitation with the fluorescent dye absorption spectrum: as the overlap becomes greater efficiency growth (from 790 nm to 760 nm), but further growth of absorbed laser power (from760 nm to 730 nm) results in fusion efficiency decay.

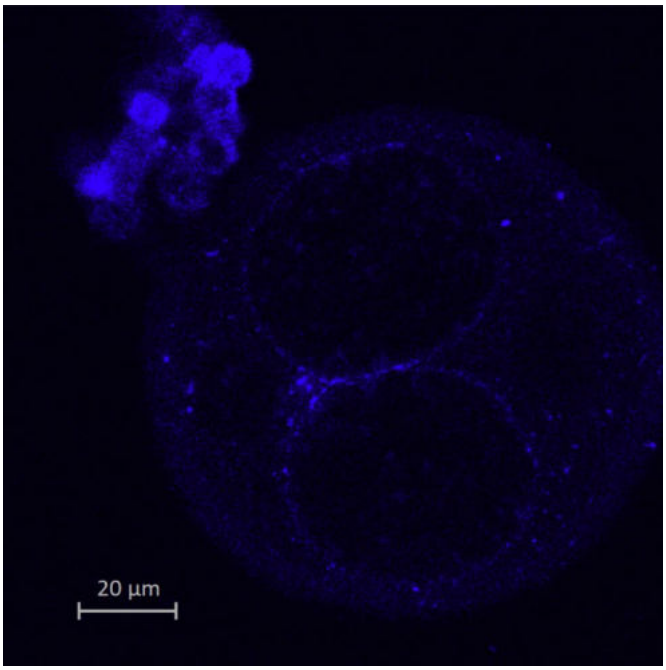

Figure 1. Confocal image of the two-cell embryo before the laser induced fusion.

Table 1. Outcome`s statistics after laser action with different wavelength.

Wavelength	Total number	Fused	Not fused
730 nm	41	17 (41%)	19
760 nm	43	24 (55%)	23
790 nm	50	24 (48%)	22
790 nm (not stained)	70	21 (30%)	19

Acknowledgments
This work is supported by the Russian Science Foundation under grant № 21-75-10155. The work was performed on facilities of ACBS Centre of the Collective Equipment (no. 506694, FRCCP RAS) and large-scale research facilities № 1440743.

References

1. Alina A. Osychenko, Alexandr D. Zalessky, Andrey N. Kostrov, Anastasia V. Ryabova, Alexander S. Krivokharchenko, Viktor A. Nadtochenko, "Femtosecond laser surgery of two-cell mouse embryos: effect on viability, development, and tetraploidization," J. Biomed. Opt. 22(12), 125006 (2017), doi: 10.1117/1.JBO.22.12.125006

Laser-induced forward transfer method adaptation for cell spheroids

E.D. Minaeva [1,2], A.A. Antoshin [1,3], N.V. Kosheleva [3], P.I. Koteneva [3], P.S. Timashev[3,4,5], N.V. Minaev [1]

[1] Institute of Photon Technologies of FSRC «Crystallography and Photonics» RAS, Troitsk, Moscow, 142190, Russia
[2] National Research Nuclear University MEPhI (Moscow Engineering Physics Institute), Moscow, 115409, Russia
[3] Institute for Regenerative Medicine, Sechenov University, 8-2 Trubetskaya st., Moscow, 119991, Russia
[4]World-Class Research Center "Digital Biodesign and Personalized Healthcare", Sechenov University, 119991 Moscow, Russia
[5]Chemistry Department, Lomonosov Moscow State University, 119991 Moscow, Russia

E-mail: minaeva.e.d@bk.ru

Abstract. Materials contain experimental results of laser-induced forward transfer of gel microdroplets with living cell aggregates – cell spheroids. The parameters of the laser interaction were customized and the shape of the laser beam profile was changed to non-Gausses to fine-tune the bioprinting process. The survival rate of cell spheroids due to laser-induced forward transfer with different energy distribution in the laser spot was analyzed. This method allows living cell spheroids to be bioprinted without critical damage.

1. Introduction

Regeneration of damaged organs or tissues fragments is one of the urgent tasks of regenerative medicine. Tissue engineering is a novel approach, when the regeneration of a biological tissue fragment is implemented using artificial tissue engineering constructions. A biocompatible scaffold (matrix) is populated with recipient' cells and implanted into the defect area to restore the damaged tissue. This approach is an alternative to the "classical" transplantology.

In this study, we present the adaptation of the bioprinting method - laser-induced forward transfer (LIFT) – to seed artificial scaffolds with living cell aggregates - cell spheroids. LIFT is non-contact method, provides high cell survival [1], and also it gives the possibility of precise positioning of single transferred cell microobjects. This approach allows to realize non-contact bioprinting process with gel microdroplets containing living cells inside with a high percentage of survival using the laser pulses energy [2]. Usually, pulsed laser irradiation is focused through the volume of a transparent donor ribbon onto its lower surface on absorbing metal layer while implementing the LIFT process. A thin layer of gel with living cells is preliminarily applied to this surface. The energy absorption of a focused laser pulse leads to the evaporation of a section of the absorbing metal layer, then to local increase in pressure, and finally the ejection of a gel microjet with living cells is happening. As a result, the gel microdroplet is transferred to the collector substrate.

It is necessary to use a laser spot comparable to the linear size of the spheroid. That's why focused laser radiation difficult to be used to transfer cell spheroids. Focused laser radiation has a smaller diameter than linear size of the spheroid and a Gaussian energy distribution in the laser spot profile. Therefore, laser exposure with such parameters can lead to damage to the spheroid central region. In this regard, the laser interaction scheme was modified.

The aim of this work is adaptation of the LIFT method for the transfer of large cell aggregates - cell spheroids.

2. Materials and methods

The LIFT setup is based on a previously assembled scheme for the living cellular and microbial objects transfer [3]. The irradiation source in the current setup is a pulsed solid-state laser Tech-1053 (Laser-Compact, Russia) with a wavelength of 1053 nm and a pulse duration of 7 ns. A telescopic objective with a magnification of 2.0x - 8.0x and a motorized beam expander with a magnification of 1.0x - 3.0x were used to increase the diameter of the laser beam. The use of the beam shaper Pi-Shaper (AdlOptica, Lithuania) [4] is an important feature of current setup version to redistribute the laser irradiation energy in the laser beam profile. It is possible to transform a Gaussian beam into beams with a different energy distribution in a spot such as "donut", "small flat-top", "flat-top" and others using Pi-Shaper. Such an adaptation of the scheme will make it possible to change the transfer process parameters for large cell objects and to increase the survival of the transferred spheroids. A glass plate with 100 nm absorbing titanium layer is used as a donor ribbon, and a cover slide is used as an acceptor plate. The positions of the donor and acceptor plates are independently controlled by microcontrollers using two motorized sliders. The transfer process was realized inside a sterile Petri dish. There was a donor ribbon with a hydrogel and spheroids suspension on it, and an acceptor plate.

3. Results and discussion

The laser-induced transfer process was realized with an energy density of 0.35 and 0.6 J/cm^2. The distance from donor ribbon to acceptor plate was ~500 μm. The spheroids diameter was ~300 μm.

The laser pulse induced the spatial transfer process of a small gel amount containing a cell spheroid from the donor ribbon to the acceptor plate. Holes were formed in the absorbing titanium layer as a result of laser interaction can be used to control the profile of the laser beam. The characteristic sizes of the obtained holes were in the range of 160 – 270 μm in diameter.

Survival rate of transferred spheroids was almost the same at all energy densities and significantly exceeded the survival rate while using a Gaussian beam energy distribution in the laser spot. The transfer process was accompanied by precise positioning of transferred cell aggregates (~20 μm), which allowed printing the simplest objects, such as three spheroids in a row, a square and a triangle.

Acknowledgments

This work was supported by the Ministry of Science and Higher Education as part of the fulfilment of the State Assignment of the Federal Research Centre for Crystallography and Photonics of the Russian Academy of Sciences (development of laser technologies).

References

[1] Antoshin A.A. et al. LIFT-bioprinting, is it worth it? // Bioprinting. Elsevier Ltd, 2019. Vol. 15. P. e00052.

[2] Ovsianikov A. et al. Laser printing of cells into 3D scaffolds // Biofabrication. 2010. Vol. 2, № 1. P. 014104

[3] Minaev N. V, Epifanov E.O., Yusupov V.I. An Apparatus for Laser Engineering of Microbiological Systems // Instruments Exp. Tech. 2021. Vol. 64, № 3. P. 464–467.

[4] Laskin A. Achromatic refractive beam shaping optics for broad spectrum laser applications / ed. Forbes A., Lizotte T.E. 2009. P. 743003.

Surface-enhanced Raman spectroscopy to distinguish between similar peptides

V A Mozhaeva[1,2], **D S Kudryavtsev**[2], **M R Tagirova**[2] **and K A Prokhorov**[1]
[1] Prokhorov General Physics Institute of the Russian Academy of Sciences, 38 Vavilova Street, Moscow, Russian Federation
[2] Shemyakin–Ovchinnikov Institute of bioorganic chemistry of the Russian Academy of Sciences, 16/10 Miklukho-Maklaya Street, Moscow, Russian Federation

Veramozhaev@yandex.ru

Abstract. Currently, the use of surface-enhanced Raman spectroscopy (SERS) for the peptide or protein analysis is very popular. In this work, we analyzed SERS and normal (conventional) Raman spectra of two peptides, which differ by one amino acid residue, in order to evaluate the effect of such a single substitution on the spectra. The SERS spectra of these two samples differed significantly, while the conventional spectra were extremely similar. We explain this diversity by the different affinity of the peptides to the SERS substrate. The result obtained demonstrates the possibility of using SERS to distinguish between similar peptides and also the role of the affinity of the peptide to the substrate in such studies.

1. Introduction

Currently, the surface-enhanced Raman spectroscopy (SERS) method is widely used as an alternative to conventional Raman spectroscopy for the analysis of protein structural elements. Molecular vibrations localized as close as possible to the enhancing surface (nanostructured) are subject to a larger enhancement factor. In turn, the region of the molecule, which in contacts with the nanostructured surface, is determined by its affinity to this surface (due to both electrostatic and hydrophobic/hydrophilic interactions). Therefore, modifications of a molecule leading to a change in its charge or hydrophobicity/hydrophilicity can lead to significant changes in the SERS spectrum.

In this work, we analyzed conventional Raman spectra and SERS spectra (recorded on a substrate functionalized with gold nanoparticles) of extremely similar peptide toxins SIA and [D12K]SIA (K-SIA), which differ by only one amino acid residue in the sequence. The SERS spectra of SIA and K-SIA differed significantly, which we explained by the difference in affinity of these molecules to the substrate surface used for enhancement.

2. Results

At the first stage of the study we obtained Raman spectra of the SIA toxin and its “mutant” K-SIA without the effect of signal enhancement and these spectra were extremely similar. At the second stage, SERS spectra of samples were obtained. The SERS substrate was cetrimonium bromide (CTAB)-modified Au nanoparticles (NPs) on silicon wafer. The SERS spectra of SIA and its mutant are shown in Figures 1(a) and (b) (red lines), respectively. Black lines in the same figure show Raman

spectra of the SIA (Figure 1(a)) and K-SIA (Figure 1(b)) without signal enhancement, for comparison. All spectra in the figure were normalized.

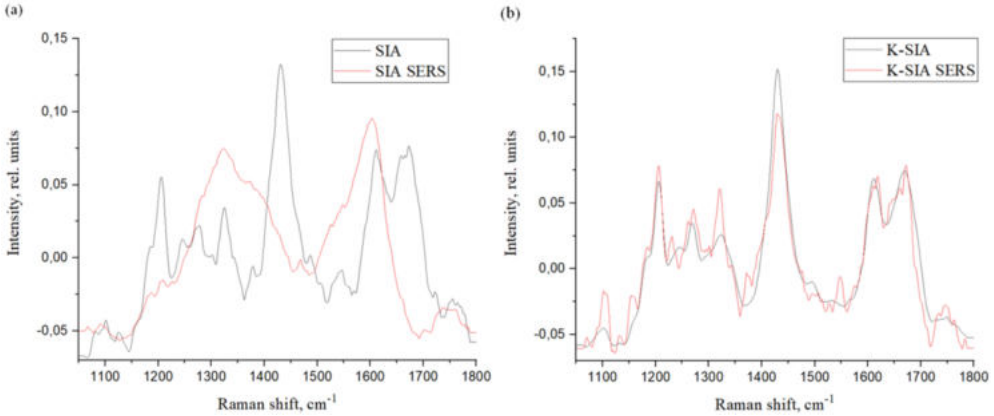

Figure 1. (a) The SER (red line) and Raman spectra without signal enhancement (black line) of SIA; (b) the SER (red line) and Raman spectra without signal enhancement (black line) of K-SIA

From the spectra obtained we can conclude that we managed to obtain enhancement for the SIA toxin spectrum, since the relative intensities of the peaks in the spectrum are different for the two spectra obtained on different substrates (with and without the enhancement effect). The enhancement of the peaks accompanied by their broadening. The maximally enhanced peaks ~1605 cm^{-1} and ~1320 cm^{-1} probably reflect vibrations of the phenylalanine residue. At the same time, the spectra of K-SIA on two different substrates are very similar in terms of the peaks shape and relative intensities, which means that the signal enhancement for this sample was not obtained.

A single mutation in the modified toxin corresponds to the replacement of a negatively charged aspartic acid residue by a positively charged lysine residue. With this in mind, it can be assumed that aspartic acid in the SIA sequence causes an increased affinity of SIA to the nanostructured surface, thereby allowing the peptide molecule approximate to the NPs surface at a sufficiently close (for enhancing effect) distance. This fact can be explained by the electrostatic attraction of the negatively charged side group of aspartic acid and the positively charged “head” of CTAB (Figure 2).

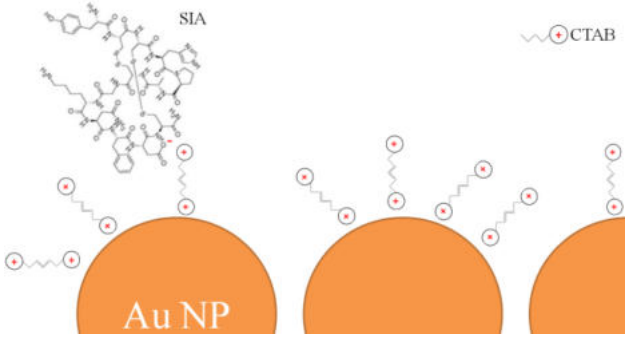

Figures 2. Schematic representation of the proposed model of the interaction of SIA with NPs on the SERS substrate surface

3. Conclusion

The possibility of distinguishing similar peptides using SERS was demonstrated. We can conclude that the affinity to the SERS substrate has an extremely significant effect on the SERS spectrum. So, it is important to taking into account the type of the interaction with the SERS surface.

Acknowledgments

The study was carried out at the expense of Russian Science Foundation grant № 22-24-01051, https://rscf.ru/project/22-24-01051/.

Study of quantum dots conjugation with antibodies to be used in a lateral flow immunochromatographic assay

Nasirov P., Sidorov E., Kryger V., Novikova S., Gribova E., Gladyshev P., Mukhina I.

141982, Moscow region, Dubna, st. Universitetskaya, 19, Dubna State University

e-mail: chembios.lne@gmail.com

Abstract. In this study, the conjugation of QDs with antibodies was conducted by the carbodiimide-succinimide method. The conjugation of specific molecules (antibodies) with a fluorescent label is an essential part of Lateral flow immunoassay. In the work was established the parameters of the conjugation which are the most optimal for orientation of antibodies on the QD's surface. There are polymers for modifying the QD's surface were proposed based on theoretical and experimental analysis and also the conjugation process conditions were optimized.

1. Introduction

Lateral flow immunoassay (LFIA) is the most common format of rapid immunochemical methods for detection and quantification of viral diseases. Such test systems are based on the highly selective interaction of biomolecules which immobilized on the nanoparticles with the biological components in the sample. LFIA widely used due to express of analysis (about 10-30 minutes), its reproducibility, minimum number of instruments and devices also it is suitable for directly using on the spot of sampling. There are a lot of labels for visualize complexes of biomolecules. The most common labels are colloidal gold nanoparticles (NPs), fluorescent organic molecules, magnetic and latex particles. It should be noted that the test systems with fluorescent labels have the highest sensitivity. Nowadays one of the most perspective areas is the use of colloidal quantum dots (QDs) as labels. QDs possesses a number of unique properties including a narrow symmetrical fluorescence peak, high fluorescence brightness, a wide excitation band, and high photostability. Due to these properties, it is possible to decrease detection limits and increase the sensitive of LFIA. It is causes practical interest for their application in bioanalysis.

The conjugation of specific molecules (antibodies) with a fluorescent label is an essential part of this method of analysis and provides the possibility of monitoring the performance of the system, as well as the possibility of identifying the target analyte in the sample. A necessary condition for the conjugation of proteins with a label is the saving of their specific activity, since this factor determines the reliability of the analysis result. Violation of the ability of antibodies to form a complex with the antigen directly affects the result of the analysis. Important parameters affecting the result of conjugation of protein molecules are the nature of the surface of the label and protein and the method of conjugation.

For binding of antibodies to a fluorescent label, it is preferable that the Fab regions are not involved in the immobilization process so that the antibodies do not lose their antigen binding domains. Since antibodies are asymmetric molecules, they can take on different dimensional orientations upon conjugation with the surface of nanoparticles [1]. Some of the protocols used for the functionalization of NPs are based on the attachment of antibodies to the surface of nanoparticles in random orientation, which includes limiting the ability of the antibody to recognize the antigen [2]. Thus, the development of site-specific strategies that to be attached antibodies is a key challenge to overcome the reduction of randomly immobilized antibodies.

The orientation of antibodies on QDs can be controlled by changing the pH values of antibodies solution, thereby affect on the ionization amino and carboxyl groups on their surface. Two-stage

approaches to oriented conjugation are prospect. They are based on a combination of electrostatic adsorption and covalent bonding. Since electrostatic adsorption is a multipoint interaction, the orientation of antibodies will depend on the number of positively or negatively charged regions on the surface of the protein molecule. A region with a higher density of charged residues will have a higher adsorption rate and, as a result, antibodies will be adsorbed on the carrier predominantly through it, providing the desired orientation on the surface.

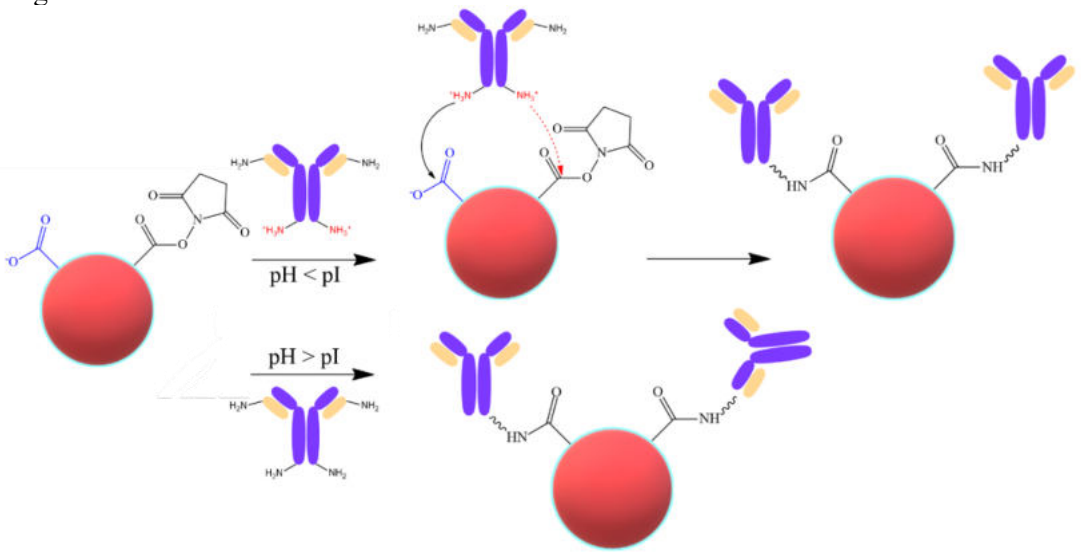

Fig. 1 - Orientation of antibodies on nanoparticles depending on the pH of the medium

2. Results and discussion

In this study, the conjugation of QDs with antibodies was conducted by the carbodiimide-succinimide method. By controlling the immobilization conditions, the carboxyl-activated matrix can demonstrate the advantages of fast reversible electrostatic adsorption and covalent bonding. Also, the activating reagent has a significant effect on the orientation of bound biomolecules. In the work was established the parameters of the conjugation which are the most optimal for orientation of antibodies on the QD's surface. There are polymers for modifying the QD's surface were proposed based on theoretical and experimental analysis and also the conjugation process conditions were optimized.

References

[1] Johnson B., Mutharasan R. Effect pH on Protein G Orientation on Gold Surfaces and Characterization of Adsorption Thermodynamics // Langmuir. – 2012. T. 28, № 17. – C. 6928-6934.

[2] Xu Y., Ma B., Chen E., Yu X., Ye Z., Sun C., Zhang M. Dual fluorescent immunochromatographic assay for simultaneous quantitative detection of citrinin and zearalenone in corn samples // Food Chemistry. – 2021. – T. 336. C. 2–5.

Oocyte enucleation by 795 nm femtosecond laser is a precise and effective method of recipient cytoplast preparation

A A Osychenko[1], A D Zalessky[1], U A Tochilo[1], D Yu Martirosyanv[1] and V A Nadtochenko[1]

[1]N.N. Semenov Federal Research Center of Chemical Physics, Russian Academy of Sciences, Kosygina 4, Moscow, Russia

*e-mail: alina.chemphys@gmail.com

Abstract. Oocyte enucleation by femtosecond laser pulses is low-invasive and effective method of recipient cytoplast preparation. We are able to destroy the metaphase plate without significant oocyte impairment. In this work we studied the remains of the metaphase plate by super resolution confocal microscopy. We have shown that after the 795 nm femtosecond laser enucleation the metaphase plate remains could become undetectable.

1. Introduction

Removing the DNA from the living cell is of relevance for medical and biomedical applications, including somatic cell nuclear transfer (SCNT) in animals and mitochondrial replacement therapy (MRT) in humans. In particular for these purposes, DNA removing commonly performed by nucleus or metaphase plate aspiration with a needle, which inevitably leads to the loss of reprogramming factors. In our recent research we have shown that near-infrared femtosecond laser effectively destroys the metaphase plate but does not affect oocyte viability and development by itself. Double fluorescent staining as well as the disability to develop parthenogenetically after the laser exposure confirm the lack of DNA in enucleated oocytes [1]. However, the question of enucleation quality still needed to be answered. In this work we have studied the remains of the metaphase plate by super resolution confocal microscopy. Our results have shown that under the careful laser exposure the remains of DNA could become undetectable.

2. Methods

2.1. Oocyte collection

To obtain oocytes at metaphase II stage, C57Bl/6 female mice were induced to superovulate by the standard scheme [1]. Mice were sacrificed and the oviducts were removed. Cumulus-oocyte complexes were purified from cumulus by 0.1% hyaluronidase (H4272, Sigma-Aldrich) in M2 culture medium (M7167, Sigma-Aldrich). For the metaphase plate visualization, the oocytes were stained with 5 μg/ml Hoechst 33342 dye (B2261, Sigma-Aldrich) for 15 minutes in M2 medium and then washed twice. During the experiment the oocytes were cultured in M2 medium.

2.2. Laser parameters and enucleation process

The detailed scheme of the oocyte enucleation is described here [1]. Briefly, in these experiments we used following parameters for the irradiation of the metaphase plate: λ = 795 nm, υ = 80 MHz, pulse

energy 0,5 nJ (40 mW power); 100 fs pulse duration, pulse train duration 60 ms. Laser radiation was focused by 60× objective lens (NA = 0.7). Before the enucleation, the metaphase plate visualization by UV illumination. Then the metaphase plate were exposed to laser. The exposure were repeated multiple times until the DNA luminescence stopped.

2.3. Confocal imaging

Fluorescence imaging was performed using a laser scanning confocal microscope Zeiss LSM 980 (Carl Zeiss Microscopy, Jena, Germany), 63x Plan-Apochromat objective (NA = 1.4, oil immersion). The oocytes were placed in M2 medium drop on a 0.17 mm cover glass (Zeiss). Hoechst 33342 luminescence excitation were performed by 405 nm laser, detection range 410-479 nm. Super resolution was obtained by Airyscan 2 with 5 AU pinhole (251 μm).

3. Results.

Figure 1 represents the oocytes before and after the femtosecond enucleation. Clearly visible at the left image (A), DNA luminescence is almost undetectable at the right image, obtained after the laser exposure. The remains of the metaphase plate are slightly visible in super resolution mode (Figure 1, B). A single peak of the luminescence, shown at right B image, could be easily eliminated by more careful laser exposure and control. The rest of the laser-exposured area has practically zero luminescence signal.

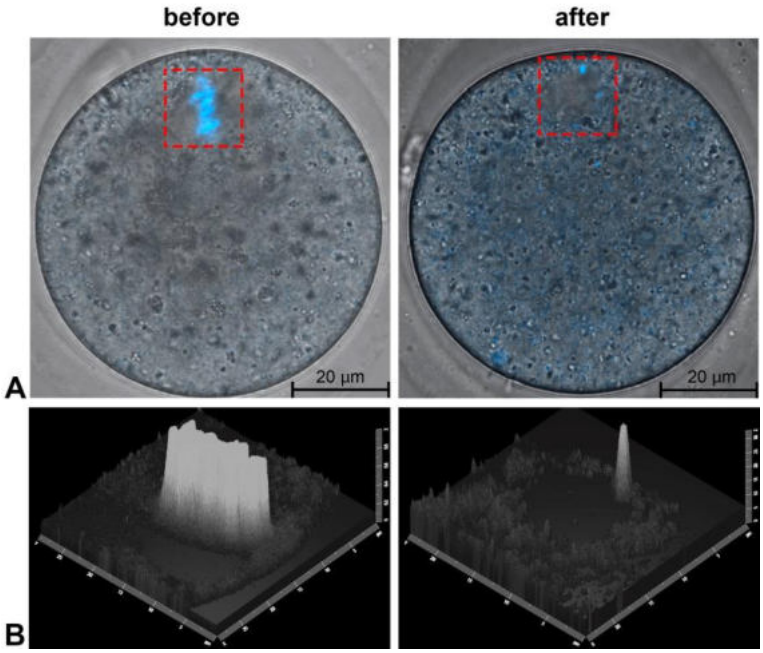

Figure 1. Confocal images of the oocytes before and after the laser enucleation. A – brightfield + luminescence images. The red square shows an area containing the metaphase plate. These areas were further investigated by Airyscan 2. B – super resolution image, presented in 2,5 D mode. X and Y axes show the distance (5 μm scale), Z axe shows the intensity.

Acknowledgments

This work is supported by the Russian Science Foundation under grant № 21-75-10155. The work was performed on facilities of ACBS Center of the Collective Equipment (no. 506694, FRCCP RAS) and large-scale research facilities № 1440743.

References

[1] Osychenko A A, Zalessky A D, Tochilo U A, Martirosyan D Yu, Silaeva Y Yu and Nadtochenko V A 2022 *Biomed. Opt. Express* **13**(3)1447–1456

Colloidal stability of iron oxide nanoparticle clusters in biologically relevant fluids

E.S. Perepelitca[1], L.Yu. Yakovleva[2], V.S. Fedorov[1], B.P. Nikolaev[2], N.M. Yudintceva[2], M.A. Shevtsov[2]

[1] Saint Petersburg State Institute of Technology, St. Petersburg 190013, Russia
[2] Institute of Cytology Russian Academy of Science, St. Petersburg 194064, Russia

e-mail: ross8marquise@gmail.com

Abstract. Colloidal stability of iron oxide magnetic nanoparticles coated with dextran and carboxymethyldextran has been studied via a temperature-stress test. The state of the dispersed system was monitored by the particle size distribution. Both types of MNPs have been shown to sustain their stability practically to the same extent.

1. Introduction

As of now, iron oxide based magnetic nanoparticles (MNPs) are being widely researched as a novel therapeutic carrier for many biomedical applications, such as MRI or targeted drug delivery.

Colloidal stability of MNPs suspensions is measured by ability to sustain the degree of dispersion over time, i.e., particle size distribution in the media, as well as the ability to withstand processes leading to a decrease in the free energy of interaction between particles in the dispersion medium. While being in biological media, MNPs tend to form aggregates which can lead to their recognition and uptake by macrophages. This can reduce the efficacy and the prospects of biomedical application. This fact places emphasis on research of the colloidal stability of MNPs based agents in biologically relevant media

2. Experiment

Iron oxide MNPs were obtained by co-precipitation from Fe^{2+}/Fe^{3+} salt solutions, stabilized by either dextran or carboxymethyldextran as described before [1]. Dextran and carboxymethyldextran were chosen as biocompatible nontoxic coating materials that provide steric and electrostatic stabilization.

MNPs suspensions are usually administrated intravenously. MNPs circulate in the blood stream (pH 7,4) and get rapidly taken up by the cells via endocytosis. The particles reside in the endosomes (pH 5,5) and then migrate to the lysosomes (pH 4,5) where the shell material and the iron core get degraded. To simulate these biological conditions, three phosphate buffer solutions with corresponding pH levels were used.

To shorten the time of estimation of the MNPs colloidal stability, a temperature-stress test was used according to ICH Q1A requirements towards drug substances or products as described in [2]. MNPs (50 μg/ml) suspensions in different buffer media were sterile filtered (0,22 μm) and incubated at 70 °C for 2 h. For each set of test subjects, a sample that was not heated and resided at room temperature for 2 h was prepared. After the incubation, DLS was used to assess the size distribution of the MNPs in the

samples. Samples were further centrifuged at 12,000 rpm for 5 min. Supernatant was collected to estimate the iron concentration via thiocyanate specthrophotometric method.

3. Results and discussion

Characteristics of obtained MNPs suspensions are presented in Table 1.

Table 1. Characteristics of obtained MNPs

Coating	Iron content, mg/ml	Mean hydrodynamic diameter, nm	ζ-potential, mV
Dextran	6,39 ± 0,01	96,6 ± 1,8	-4,9 ± 0,5
Carboxymethyldextran	6,22 ± 0,01	108,7 ± 2,7	-19,9 ± 0,9

3.1. MNPs size distribution

The DLS size distributions by intensity were mostly monomodal, with no single core particles or large aggregates registered. For MNPs@dextran, during the temperature-stress test mean hydrodynamic diameter increased with time in all media except the pH 4,5 one. Size of MNPs slightly decreased over time in the buffer pH 4,5. This can be seen more clearly the size distributions by volume. The graphs show two peaks that merge into one with smaller size. For MNPs@carboxymethyldextran, mean hydrodynamic diameter slightly (8-10%) decreased with time in all media.

3.2. Iron concentration of supernatants

Iron content in supernatants of MNPs@dextran and MNPs@carboxymethyldextran mostly decreased over time. The highest decline was registered for pH 4,5 in both cases, while iron content was mostly stagnant in pH 5,5.

4. Conclusion

A temperature-stress test method was chosen as a mean to save time for estimation of colloidal stability. It was shown to be reliable for magnetic nanosuspensions of iron oxide nanoclusters.

MNPs with dextran and carboxymethyldextran were shown to be able to maintain colloidal stability over time. This is evident by the fact that MNPs suspensions retained their cluster size without forming large aggregates. Suspensions of MNPs stabilized by dextran and carboxymethyldextran have different rate of sedimentation which can be explained by different surface charge.

MNPs size and iron content data can be used to calculate approximate shelftimes for MNPs suspensions for different storage temperatures. To verify and adjust the calculated shelftimes of both samples, a long-term storage experiment is being conducted.

Acknowledgments

This work was supported by RFBR grant № 19-58-45012.

References

[1] M. Shevtsov, S. Stangl et al., Small, 15 (2019).
[2] M. Rabel, P. Warncke et al., Nanomedicine, 14, 1681-1706 (2019).
[3] GPM.1.1.0009.15. Shelflives of Medicinal Products. State Pharmacopoeia of Russian Federation. XIII ed. (2015).

Determination of absorption cross section spectra dependence of natural biopolymers in the range NEXAFS C1s edge

Petrova O.V.[1,2], **Bakina K.A.**[1,2]

[1]Komi Science Centre of Urals Branch, RAS, 167982, Syktyvkar, Russia
[2]Pitirim Sorokin Syktyvkar State University, 167001, Syktyvkar, Russia
teiou@mail.ru

Abstract. Using Near Adge X-ray Absorption Fine Structure spectroscopy (NE spectroscopy) absorption cross sections spectral dependence in arbitrary units and os strength distributions as well as absorption cross section in the NEXAFS C1s-spectra o and bacterial cellulose were determined and interpreted using building block concep NEXAFS spectra of investigated material were studied by Total Electron Yield (TEY) with usage of 150 nm Titanium film filter for suppression and estimation of nonmonochr stray and high order background radiation in incident synchrotron beam and measured signal.

Cellulose and chitin are the most abundant biopolymers on the earth. The first is the constituent of plants, serving to maintain their structure, and is also present in bacteria, fungi, and even in invertebrate animals like tunicates [1]. The second is known to occur as a compon the cell wall in fungi and diatoms, and is also found in diverse skeletal structures of at least 19 a phyla. The monomers of cellulose and chitin are β-glucose and N-Acetyl-D-glucosamine (1 respectively (see Fig.1).

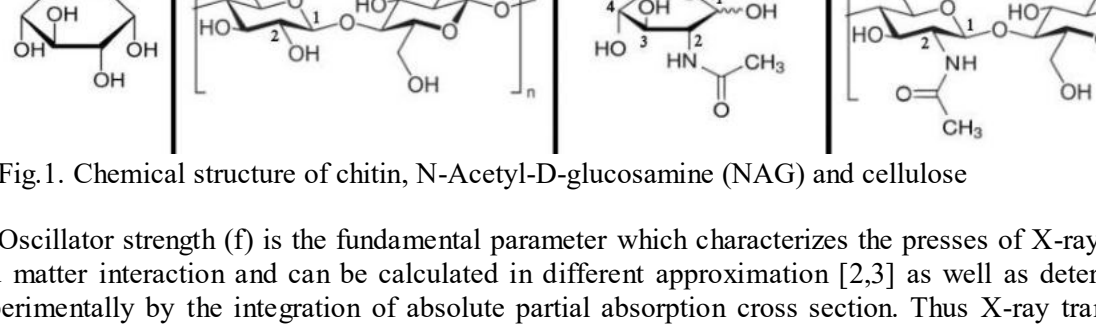

Fig.1. Chemical structure of chitin, N-Acetyl-D-glucosamine (NAG) and cellulose

Oscillator strength (f) is the fundamental parameter which characterizes the presses of X-ray and matter interaction and can be calculated in different approximation [2,3] as well as deter experimentally by the integration of absolute partial absorption cross section. Thus X-ray tra oscillator strength distribution is used for testing theoretical models which describe X-ray absorption process.

The main aim of this work is to carry out for the first time experimental determinati fundamental parameters: absolute X-ray absorption cross section and oscillator strength distribu the NEXAFS C1s-spectra of the chitin and bacterial cellulose and their interpretation in building concept. For this purpose the specific multi-stage procedure of spectra processing were ap according the procedure described in [4, 5].

The NEXAFS studies were carried out at the Berliner Elektronenspeicherrin

first narrow peak (285.38eV) in NEXAFS C1s-spectra of HOPG [7]. All spectra were normali the incident photon flux determined by a clean Au-plate.

In the scope of current work:

- Absolute partial absorption cross sections spectral dependence in (Mb) and osc strength distributions in NEXAFS C1s-spectra of chitin was estimated for the first time;
- Partial absorption cross section in arbitrary units in NEXAFS C1s-spectra of NAG, ba and plant cellulose was estimated (see Fig 2.);
- Interpretation of NEXAFS C1s-spectra of chitin, NAG, bacterial and plant cellulose building block concept was performed.

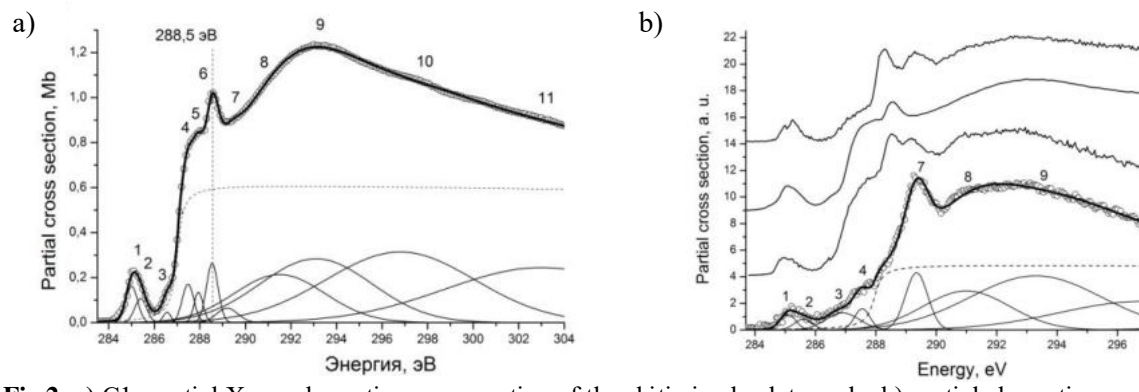

Fig.2. a) C1s partial X-ray absorption cross section of the chitin in absolute scale; b) partial absorption cro sections in NEXAFS C1s-spectra of chitin (2'), NAG (3'), plant (1') and bacterial (black heavy line) cellul arbitrary units along with decomposition of bacterial cellulose spectra into separate peaks (1-9 lines) and c step (dash line).

peak number	1	2	3	4	5	6	7	8	9	10	11
Chitin											
E, eV	285	285,4	286,6	287,5	287,9	288,5	289,2	291,5	293,1	296,8	303
dE, eV	0,6	0,6	0,4	0,6	0,5	0,6	1,1	4,7	5,8	7,7	10,0
f(exp) · 10^{-3}	0,9	0,6	0,2	1,0	0,6	1,5	0,7	9,7	15,9	23,4	23,7
Bacterial cellulose											
E, eV	285,1	285,6	286,9	287,6	—	—	289,4	291	293,3	296,8	

Tabl.1 f (exp) – experimentally determined oscillator strengths of X-ray transition from C1s-level to free s chitin structural element, E – peak energy position, dE – width at half-height of separated peaks of chitin a bacterial cellulose absolute absorption cross section.

Acknowledgments

This work was supported by the Bilateral Program of the Russian-German Laboratory at BES and grant of the President of Russian Federation No MK-3796.2021.1.2.

References

[1] O'Sullivan A.C., Cellulose, 1997. V.4. P.173–207.
[2] J .Stor, NEXAFS Spectroscopy // Springer, Berlin, 1992.
[3] U. Fano and J. W. Cooper, Rev.Mod. Phys., 1968. V.40. P.441.
[4] D.V. Sivkov, O.V. Petrova, S.V. Nekipelov et al., Nanomaterials 2021, 11, 2993
[5] D.V. Sivkov, S.V. Nekipelov, O.V. Petrova et al., Appl. Sci. 2020, 10, 4736
[6] S. I. Fedoseenko, D. V. Vyalikh, I. E. Iossifov et al., Nucl. Instrum. Methods Phys. Res. A, V. 505. P.718.

Low cost microscopy imaging system for microfluidics and other applications

M B Pechin,[1] N A Filatov,[1] A C Bukatin[1,2]

[1]Alferov University, Khlopina 8/3, 194021 St. Petersburg

[2]Institute for Analytical Instrumentation of the Russian Academy of Sciences, St Petersburg, Russian Federation

E-mail: ahsima1@gmail.com

Abstract. Imaging in microfluidic devices is typically performed using expensive motorized microscopy instrumentation from mainline manufacturers. Often this slows down the spread of new technologies for conventional laboratories and creation of compact devices, for example, Point-of-care test systems. In this work, the imaging system consisting of a 3D-printed motorized stage and an optics module based on a low-cost monochrome global shutter camera was characterized in several imaging modes, including bright-field transmission, and reflection.

1. Introduction

Light microscopy is a primary way of observing microfluidic experiments. High cost of microscopes from established manufacturers, limits the applicability and scalability of microfluidic research, especially when experiments require motorized sample positioning or observation modes different from bright-field transmission. There are several projects, which address high cost of microscopy equipment, including the OpenFlexure project [1]. Most of those projects are using the Raspberry Pi microcomputer and Raspberry Pi camera module due to a wide availability and a low cost. However, said camera module may not be well suited for microfluidic experiments due to its relatively low framerate and rolling shutter, which may produce artifacts when imaging fast-moving cells or droplets inside microfluidic chips. In this work, we constructed and characterized the microscopy system consisting of the 3D-printed motorized delta stage and the optics module based on the low-cost monochrome global shutter camera. The optical resolution was measured using the USAF-1951 target.

2. Materials and methods

The microscope body is the 3D-printed flexure-based stage [2], printed from the PLA (polylactide) plastic using FDM (fused deposition modeling) 3D-printer Picaso Designer X Pro or Tenlog TL-D3 Pro. Motion was provided by 28BYJ-48 stepper motors and controlled by the Arduino Uno microcontroller. Both the regular stage and the delta-geometry based stage were constructed and tested. Several optical systems were evaluated. The low-cost optical system was made from the 3D-printed case and the inverted plastic lens, extracted from the Raspberry Pi camera module. The advanced optics module, capable of using RMS-threaded infinite conjugate objectives, was constructed. Components of this module included the objective, the achromatic doublet plano-convex lens with 400-700nm AR (antireflection) coating (d=12.7mm, fl=50mm) and the optional 3D-printed filter cube, required for fluorescence and epi-illumination. Two camera modules were tested, both compatible with a Raspberry Pi single-board computer and connected through a MIPI-CSI interface. The first

module was Raspberry Pi camera module V2, a board-level camera module based on color 1/4" Sony IMX219 sensor with 3280x2464 resolution. The second camera was a board-level camera, based on monochrome 1/4" Omnivison OV9281 sensor with 1280x800 resolution. Image acquisition and control of the motorized stage were performed from a Raspberry Pi 4 microcomputer. For the Raspberry Pi camera module, the OpenFlexure software[3] was used. For the OV9281 camera module, several image acquisition software options were explored, including VLC, OpenCV and yavta.

3. Results and discussion

As a result, the optical resolution of 228.1 lp/mm was obtained when using the 10x objective with both camera modules, suggesting that the resolution is optically limited and the lower pixel count of the OV9281 camera module does not reduce image quality with the current optical system. Full 144fps framerate video was successfully captured with the OV9281 camera module when using the yavta software. In low-light conditions, the OV9281 sensor showed significantly better performance and was able to provide a usable image, while the IMX219 sensor was providing no image at all. A fluorescence imaging remains a challenge for now due to a lack of affordable optical filters with sufficient performance, however some sourcing options are currently being explored.

Acknowledgments

The study was supported by a grant from the Russian Science Foundation (project No. 20-74-10117)

References

[1] J. Collins, J. Knapper, J. Stirling, J. Mduda, C. Mkindi, V. Mayagaya, G. Mwakajinga, P. Nyakyi, V. Sanga, D. Carbery, L. White, S. Dale, Z. Jieh Lim, J. Baumberg, P. Cicuta, S. McDermott, B. Vodenicharski, and R. Bowman 2020, Biomed. Opt. Express 11, 2447-2460.

[2] J. Sharkey, D. Foo, A. Kabla, J. Baumberg, and R. Bowman 2016, Review of Scientific Instruments 87, 025104

[3] J. Collins, J. Knapper, S. McDermott, F. Ayazi, K. Bumke, J. Stirling and R. Bowman 2021, R. Soc. open sci. 8211158211158

The use of optical and scanning electron microscopy to study the effect of needle type on the risk of postoperative complications during epidural and spinal anesthesia

E V Pimakhina[1, *], A A Pimakhin[1], N V Vishnyakov[2], N B Rybin[2] and N M Tolkach[2]

[1] Ryazan State Medical University named after I. P. Pavlov, 9, Vysokovol'tnaya Street, Ryazan, 390026, Russian Federation
[2] Ryazan State Radio Engineering University named after V.F. Utkin, 59/1, Gagarina Street, Ryazan, 390005, Russian Federation

[*]elenapim@yandex.ru

Abstract. Electron microscopy makes it possible to explain the influence of the type of needles for epidural or spinal anesthesia on the risks of complications in the form of post-operative headache in anesthesiological practice.

1. Introduction

Quincke and Whitacre pencil point needles are most commonly used in epidural and spinal anesthesia. [1]

The Quincke needle has a medium length cutter type sharpening with a hole at the end. The popularity of the needle is explained by simplicity of production. [2]

The Whitacre pencil point needle has a Pencil-type point. The needle is equipped with a side window near the tip for targeted drug administration. [3]

Spinal and epidural anesthesia women giving birth using needles with the studied types of sharpening revealed different rates of postpuncture complications. Anesthesia with cutting needles in 30% of cases leads to complications in the postoperative period in the form of postpuncture headache. [4]

The size and shape of the spinal dura mater defect has been found to determine the rate of loss of cerebrospinal fluid from the spinal canal. This is crucial in the development of postpuncture complications. [5]

1. Methods and experiments

Differences in the structure of the cutting edge of Quincke and Whitacre pencil point needles were studied by optical microscopy. Fresh preparation slides of T6-L1 dura of Porculasalvania were obtained by anterior laminectomy. No pre-puncture treatment was performed. 25G (0.525 mm) needles of both types were punctured through parallel dura mater fibers. A scanning electron microscope JSM-6610LV (JEOL, Japan) was used to study the diameter, area, puncture shape on the

external and internal sides of the sample, and the degree of fiber damage in correlation with the shape of the incision and the injury trajectory.

Without removing the needle from the sample, we dried the preparation in a desiccator at 46.5 °C for 4 hours. Needles were removed from the preparations and the characteristics of the defects caused by needles of different sharpening shapes were determined in the tissues.

2. Results and Discussion

Microscopy of dura mater sections of needles with a cutting edge and needles without a cutting edge revealed tissue differences.

The presence and nature of a dura mater defect at the needle puncture site depended on the structure of the cutting edge. The absence of a cutting edge causes minimal changes in the structure of the dura mater when a needle passes through it.

The Quincke needle leaves a incised hole in the dura mater after puncture. The Whitacre needle does not pierce but rather expands the dura mater fibers due to the conical shape of the tip without cutting edges, which facilitates atraumatic puncturing. After extraction of the needle, the dura mater fibers are fused and the tightness of the spinal canal is restored.

The pathogenesis of post-puncture headache is revealed. Puncture needle puncturing the dura mater violates its integrity, leading to liquor leakage. The puncture cross-sectional area was determined by electron microscopy. At the puncture area of 300 μm the loss of cerebrospinal fluid of 32.1±6.2 ml leads to a cerebrospinal fluid pressure drop to 65±15. This increase the intensity of cerebral blood flow, cause dilatation of intracranial veins, irritation of dura mater, activation of pain receptors.

3. Conclusion

Based on the results of optical and scanning electron microscopy of sections of biological tissue for spinal and epidural anesthesia, it is proposed to use Whitacre needles with pencil tips that do not cause a defect at the puncture site of the dura mater. To reduce complications, the author's method of treatment was proposed [3].

Acknowledgments

Electron microscopy was performed with JSM-6610LV scanning electron microscope (JEOL, Japan) in the electron microscopy laboratory of the Regional Center of Probe Microscopy for Collective Use in the Ryazan State Radio Engineering University named after V.F. Utkin.

References

[1] Ovechkin A M 2014*Regional anesthesia and treatment of acute pain***8(1)** 5-13

[2] Safin R R, et al 2013*Practical medicine***1-2(69)**133-134

[3] Parker R K, White P F 1997*Anesthesia& Analgesia***85(5)**1101-1104

[4] Ozerov AV, Waghulde N, Pimachina EB, Ershov NG 2018 *Science of the Young–EruditioJuvenium***6(3)** 388-393

[5] Shifman E M, et al2014 *Regional anesthesia and treatment of acute pain***8(1)** 31-46

Electron microscopy of needles for spinal and epidural anesthesia

Study of hydrogel microparticles with cells in microfluidic chips for 3D bioprinting

P S Pleshakov,[1] N A Filatov,[1] A C Bukatin[1,2]

[1]Alferov University, Khlopina 8/3, 194021 St. Petersburg

[2]Institute for Analytical Instrumentation of the Russian Academy of Sciences, St Petersburg, Russian Federation

E-mail: avekipp@gmail.com

Abstract. Effective drug development requires high-quality models of artificial organs and tissues. For such purposes, it is rational to create 3D bioprinters that print with high-resolution 3D bioinks. Droplet microfluidics methods for the formation of emulsion microdroplets are one of the promising tools for creating inks. In this work, we studied a formation of hydrogel microparticles from sodium alginate in microfluidic microchips. The CT26 mouse colon carcinoma cell line expressing green fluorescent protein was used for encapsulation. As a result, methods for the formation of microparticles with a diameter in range of 50–300 μm have been obtained. Dependences of the emulsion droplet diameters and the generation frequencies on the pressures ratio of working liquids were obtained. Methods for packing cells into microparticles inside a microchip and their further cultivating inside microparticles within 7 days were also studied.

1. Introduction

One of the most promising areas for creating artificial organs is currently 3D bioprinting. This technology allows layer-by-layer formation of an organ or tissue using bioinks [1]. Typically, bioinks are made up of hydrogels that contain cells. It should be noted that monodisperse hydrogel microparticles with sizes of 100–500 μm have a number of advantages [2–3]. They make it possible to form an organ in more detail than modern bioinks on spheroids due to their smaller size and the ability to encapsulate different types of cells in different microparticles or layers. Biocompatible hydrogel microparticles may contain cells and excipients [4–5], such particles may have different sizes and physicochemical characteristics. Also, individual microparticles can be manipulated and their position controlled. In this direction, droplet microfluidics technologies have great potential, which provide control of liquid flows at the micro level in special microchips, which allow the formation of monodisperse water-in-oil drops (macroemulsion) of a given size. In this work, we studied methods for the formation of hydrogel microparticles in microfluidic microchips, which can be used as the basis of an in vitro system for 3D cell cultivation inside such microparticles.

2. Results and discussion

For the formation of microparticles, microfluidic chips with macroemulsion generators by the type of flow focusing were used. They had 4 inputs: 1 – central, dispersed phase (culture medium with fluorescent cells), 2 – hydrogel flow, dispersed phase (aqueous solution of sodium alginate and Ca-

EDTA), 3 – oil flow, continuous phase, in which microparticles are formed (fluorocarbon oil with surfactant), 4 – additional flow of continuous phase (fluorocarbon oil with the addition of acetic acid). Microchips were fabricated using the soft lithography technology [6] from polydimethylsiloxane (PDMS). A vacuum pump was used to operate the microfluidic chip. The CT26 mouse colon carcinoma cell line expressing green fluorescent protein (GFP) was used for encapsulation. Sodium alginate was used as a hydrogel. The central aqueous phase was flowed with the aqueous phase stream of the alginate-calcium-EDTA solution. The combined aqueous phase stream was emulsified into monodisperse droplets using a microfluidic generator with flow focusing, then fell into the last stream – the continuous phase with the acetic acid. Hydrogen ions from the acetic acid lower the pH and cause the Ca-EDTA complex to dissociate, followed by the release of calcium ions, leading to crosslinking of the alginate. After gelation, the microparticles were transferred into an aqueous solution of CaCl2 to impart greater mechanical strength. Hydrogel microparticles were transferred to the culture medium and incubated at 37°C and 5% CO2. Cell viability was assessed by the fluorescence of GFP in them. To confirm the possibility of using microparticles to form complex cellular structures, we studied the control of the arrangement of microparticles with cells on microstructured hydrogel (e.g. gelatin) substrates. The application of microparticles was carried out using a three-coordinate micromanipulator.

3. Conclusions

As a result, methods were studied for the formation of monodisperse alginate microparticles with a diameter in range of 50–300 μm in PDMS/PDMS or PDMS/glass microfluidic chips. Dependences of the emulsion microdroplets diameter and the frequencies of generation on the pressures ratio of work liquids were obtained. Methods for packing cells into microparticles inside the microchip and their further cultivating inside microparticles were studied. The data show that the developed microfluidic platform can be used to form cellular structures in hydrogel microparticles, which in the future can be used as a bioink in 3D printing of tissues and organs.

Acknowledgments

The study was supported by a grant from the Russian Science Foundation (project No. 20-74-10117)

References

[1] Gungor-Ozkerim, P. Selcan, et al. \"Bioinks for 3D bioprinting: an overview.\" Biomaterials science 6.5 (2018): 915-946.

[2] Pataky, Kris, et al. \"Microdrop printing of hydrogel bioinks into 3D tissue-like geometries.\" Advanced Materials 24.3 (2012): 391-396.

[3] Gudapati, H., Dey, M., & Ozbolat, I. (2016). A comprehensive review on droplet-based bioprinting: Past, present and future. Biomaterials, 102, 20-42.

[4] Marquis, Melanie, et al. \"Microfluidic encapsulation of pickering oil microdroplets into alginate microgels for lipophilic compound delivery.\" ACS Biomaterials Science & Engineering 2.4 (2016): 535-543.

[5] Collins, David J., et al. \"The Poisson distribution and beyond: methods for microfluidic droplet production and single cell encapsulation.\" Lab on a Chip 15.17 (2015): 3439-3459.

[6] Bukatin A. S., Mukhin I. S., Malyshev E. I., Kukhtevich I. V., Evstrapov A. A., Dubina M. V. Tech. Phys. 2016. 61. 1566-1571.

Application of computer modeling in study of quantum dots-antibody conjugates

S K Rudnykh[1], E D Gribova[1], A A Popova[1], P P Gladyshev[1]

[1]Dubna State University, Moscow region, Universitetskaya 19, Dubna 141980, Russia.

E-mail: rudnih@yandex.ru

Abstract. In recent years, quantum dots (QDs) have found wide application in biomedical diagnostics. However, the process of antibodies conjugation to nanoparticles (NPs) leads to random orientation, and it reduces their ability to recognize antigens. Existing approaches to orientation of antibodies commonly are expensive and labor-intensive. Computer modeling makes it possible to predict basic mechanisms of the protein systems interaction with NPs based on the construction of models and their comprehensive analysis. Using this method, it is possible to determine a number of parameters that are critical for oriented conjugation. This study aims to consider the possibility of using computer modeling to predict optimal conditions for oriented conjugation of proteins.

1. Introduction

Quantum dots (QDs) play an indispensable role in the diagnostics of several diseases as a fluorescent label [1]. The use of nanoparticles (NPs) significantly affects test systems detection limit, which can be improved by adjusting of conjugation conditions. During the conjugation process, the orientation of antibodies is important [2]. Antibodies, an asymmetric protein macromolecule with (Y)-shape, can be immobilized with four possible orientations (head-on, side-on, bottom-on and flat-on) which may demonstrate distinct antigen-binding accessibilities [Fig. 1].

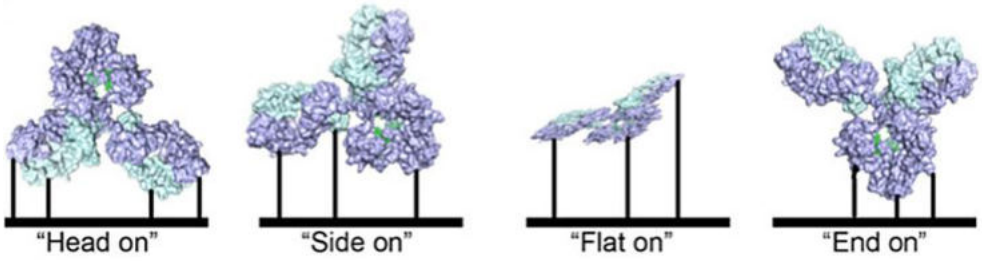

Figure 1. Four possible orientations for conjugation of antibodies with solid carrier [3]

According to modern concepts, as a result of conjugation the spatial structure of a protein can be changed significantly [3]. The disordered orientation of antibodies through direct attachment causes the lower signal-to-noise ratio, reduced antigen-binding activity. Therefore, it reduces the detection limit of the analysis system [4]. To preserve the activity of antibodies in the test-system it is necessary to carry

out covalent binding of the antibody and QDs, controlling protein orientation. Currently various attempts are known to bind antibodies while maintaining high biological activity [5]. Nevertheless, for each new specific case, depending on properties of proteins and NPs, it is necessary to reselect conditions of conjugation. The selection of conditions is expensive due to large consumption of reagents; moreover, special laboratory equipment is required. Based on the construction of models and their comprehensive analysis, computer simulation makes it possible to predict basic mechanisms of the interaction between protein systems and NPs. It can significantly reduce the duration of the experiment.

2. Methods

The application of molecular dynamics (MD) for comprehensive modeling of macromolecules mobility was considered. The applied method effectively describes electrostatic interactions and immobilization through covalent binding. The interaction between proteins and NPs surface can be described by the following potentials: the Lennard-Jones potential models Van der Waals interactions, electrostatic interaction can be represented through Goui-Chapman potential, potential representing covalent bonds.

3. Result and conclusions

Conformational changes of antibodies during conjugation can be studied not only by physico-chemical methods, but also by computer modeling. MD method makes it possible to modeling mobility of macromolecules, for example proteins. Thus, pH of solution most significantly affects conformation and binding of protein. It determines the surface charge of protein and quantum dots. Evaluation of these parametric dependencies by MD method can considerably simplify the approach to rational orientation of proteins for designing of diagnostic systems. Modeling allows us to predict suitable conditions for protein immobilization, select optimal binding method for protein, achieve specifically recognize and capture analytes with high sensitivity without resorting to expensive equipment. Resulting methods can be used for designing of test systems with advanced analytical characteristics.

Acknowledgments

This study was carried out with the financial support of The Foundation for Assistance to Small Innovative Enterprises in Science and Technology (No. 16271ГУ/2021).

References

[1] Farias P. M. A., Fontes A., Galembeck A., Figueiredo R., Santos B. S. Fluorescent II-VI semiconductor quantum dots: Potential tools for biolabeling and diagnostic // Journal of the Brazilian Chemical Society. – 2008. – Т. 19, № 2. – С. 352-356.

[2] Matsuda Y., Mendelsohn B. A. An overview of process development for antibody-drug conjugates produced by chemical conjugation technology // Expert Opinion on Biological Therapy. – 2021. – Т. 21, № 7. – С. 963-975.

[3] Gao S. P., Rojas-Vega F., Rocha-Martin J., Guisan J. M. Oriented immobilization of antibodies through different surface regions containing amino groups: Selective immobilization through the bottom of the Fc region // International Journal of Biological Macromolecules. – 2021. – Т. 177. – С. 19-28.

[4] Akinshina Y. A., Mardanly S. S., Kiseleva V. A. Immunochromatographic test for differentiation detection of IgM and IgG to SARS-CoV-2 // Klinicheskaia laboratornaia diagnostika. – 2020. – Т. 65, № 11. – С. 688-692.

[5] Cerofolinia L. Orientation of immobilized antigens on common surfaces by a simple computational model: Exposition of SARS-CoV-2 Spike protein RBD epitopes / Fragaia M., Luchinata C., Raveraa E. // Biophysical Chemistry. – 2020. Т. 64, № 3. С. 559–567.

Microsphere optical microscopy for biological objects

Senotrusova S.A.[1], Akhmetova A.I.[1], Yaminsky I.V.[1]

[1]Lomonosov Moscow State University, Faculty of Physics

sofsen@mail.ru

Abstract. The resolution of modern conventional optical microscopes is limited by the diffraction limit. To overcome this limitation, it is proposed to use microlenses — optically transparent, micrometer-size spherical particles. The method was developed by a team of researchers led by Zengbo Wang at the University of Massachusetts. Placed between the sample and the microscope objective lens, the microlens is an optical amplifier that increases the resolution of the optical microscope.

This paper presents the results of studies using transparent microlenses made of such materials as $BaTiO_3$, TiO_2 and polymethylacrylate. Samples investigated were both biological objects, e.g. erythrocytes, and topologies of various chips, coated samples with structures ranging in size from 1 to 20 microns. As a result, a resolution of over 150 nm was obtained using microlenses and the diffraction limit was overcome.

1. Introduction

Optical microscopy is a well-known and widely used tool for optical imaging. However, the far-field imaging resolution of conventional microscope is limited by the diffraction of optical waves [1]. It is expressed by the formula: $d = 0.61\lambda/NA$, where NA is the numerical aperture of the objective lens, and λ is the wavelength of the source of light by which the sample is illuminated.

In modern microscopy numerous efforts are made to overcome this diffraction limit in order to obtain images with super-resolution and investigate objects on the nano-scale. There are many non-optical ways to achieve this resolution. For example, atomic force microscopy (AFM), magnetic force microscopy (MFM), scanning electron microscopy (SEM), transmission electron microscopy (TEM), etc. The use of these methods provides high lateral resolution, but they are expensive and may also require sample preliminary preparation.

There are many interesting developments in optical microscopy as well. For example, near-field scanning optical microscopy (SNOM), using non-linear effects of fluorophores (STED, STORM), using solid immersion lenses (SIL) as well as microscopy using near-field structures (microspheres, cylindrical microlenses). The last method listed is called 'microsphere optical microscopy'.

The use of this method was first demonstrated by a team of researchers at the University of Manchester, led by Zengbo Wang [2]. The main idea was the following: microspheres of SiO_2 with refractive index $n = 1.46$ and sizes ranging from 2 to 9 μm were placed on top of the surface of the investigated object. A halogen lamp was used as a source of white light, the wavelength of the emitted light was 600 nm. The microsphere lenses gather information about the object in the near field, magnify

it to form virtual images, and then collect it with an objective of microscope (objective used: Olympus MD Plan ×80, NA = 0.9). A gold coated anodic aluminium oxide membrane was used as a sample. The pores were 50 nm in diameter and spaced 50 nm apart. The optical microscope with microspheres resolved these tiny pores, although their size was much smaller than the diffraction limit.

The imaging mechanism of the microspheres consists of the following: the spheres collect the near-field object information and form virtual images that can be captured by the conventional lens. Placed between the sample and the microscope objective, the microlens is an optical amplifier increasing the microscope's resolution. The imaging resolution and magnification of the microsphere superlenses are fundamentally related to their properties: the size and refractive index of the microsphere and its environment.

2. Materials

In this paper, results are shown with transparent microlenses made of such materials as $BaTiO_3$ (diameter between 20 μm and 100 μm), TiO_2 (diameter between 10 and 60 μm) and polymethylacrylate (diameter 9 μm). Measurements were performed in both air and immersion environments (silicone oil and immersion oil were used). Both reflected light mode and transmitted light mode were used. Using microlens optical microscopy, images of erythrocytes, chip topologies, and coated samples with hollow structures from 1 to 20 μm were acquired. As a result, the use of microlenses has allowed the resolution of over 150 nm and the diffraction limit has been overcome [3].

3. Conclusion

Microlens optical microscopy is a convenient, simple and inexpensive way to achieve nanometer resolution. The use of microlenses in combination with a standard optical microscope allows for sub-diffraction-limited optical imaging in air and liquid conditions under real-time white light illumination. Many sensitive biological samples often require liquid conditions, so they can be explored directly without chemical treatment, fluorescence, vacuum and similar. The possibilities offered by microsphere microscopy can facilitate the understanding of the mechanisms and interactions of viruses, bacteria and cells by examining these objects at nanometer resolution.

References

[1] Betzig, E., Trautman, J. K., Harris, T. D., Weiner et al. Breaking the diffraction barrier: optical microscopy on a nanometric scale. Science, (1991), 251(5000), 1468-1470.

[2] Wang Z., Guo W., Li L., Luk'yanchuk B., Khan A. et al. Optical virtual imaging at 50 nm lateral resolution with a white-light nanoscope, Nature Communications, (2011), 2, 218.

[3] Yaminsky I.V., Akhmetova A.I., Senotrusova S.A. Optical microscopy with the use of microlenses, Nanoindustry, (2021), 14 (3-4): 22-25.

Development of a control algorithm for a fluid flow monitoring system in a microfluidic system

E D Serov[1], A I Kavaler[1], V A Kruglov[2], V S Reznik[2], A S Saraev[2] and V V Davydov[1, 3]

[1]Peter the Great Saint-Petersburg Polytechnic University, St. Petersburg, Russia, 195251

[2]Institute of Analytical Instrumentation of the Russian Academy of Sciences, St. Petersburg, 190103, Russia

[3]All-Russian Research Institute of Phytopathology, Moscow Region 143050, Russia

e-mail: egorserov22021998@gmail.com

Abstract. Microfluidic systems are widely used in the preparation and analysis of liquid samples in biology, pharmacology and medicine. Each individual device using microfluidic systems differs in structure from others, and the accuracy of fluid control inside is an important factor. In this paper, we will consider the microfluidic system of a DNA analyzer. An algorithm that reads information from flow sensors in real time and transfers it to microcontroller STM32 has been developed for it. The received information was further processed, and on the basis of the received data, a conclusion was drawn about the correctness of the work performed by the device. The error handler, in case of deviation from the process, made the necessary adjustments by sending an error code to the necessary part of the device.

1. Introduction

The sequencing method of DNA is currently extremely demand for solving the different tasks in medicine and biology [1-3]. This method has no replacement because of several advantages in terms of informativeness of research in comparison with other methods, for example, optical spectroscopy [4, 5] or nuclear magnetic spectroscopy.

In sequencing devices, it is necessary to transfer a given volume of liquid at a given speed for the correct analysis.

The performance of microfluidic systems depends on monitoring and adjusting the fluid flow in them. This tusk performing by fluid flow sensor. Information from the sensor must be read and processed during the entire operation of the hydraulic system.

Thus, it is important to create an optimal algorithm that is able to carry out the task throughout the entire sequencing process. This algorithm serves not only as a way to control and adjust the hydraulic system, but also to collect data for post-processing of the experiment.

2. The structure of the algorithm

The fluid in the microfluidic system of the sequencer moves through thin capillaries using a pump. The pump, having received a command from the control algorithm, adjusts the direction and speed of the fluid supply. To check the correctness of its operation, a liquid flow sensor is installed in front of the element in which the direct process of growing clusters takes place (the main stage of sequencing).

The sensor detects the presence of a stream in a specified place and sends a command via the I2C exchange protocol to the board responsible for processing data from the sensors. The block diagram of the signal processing algorithm is presented in Figure 1.

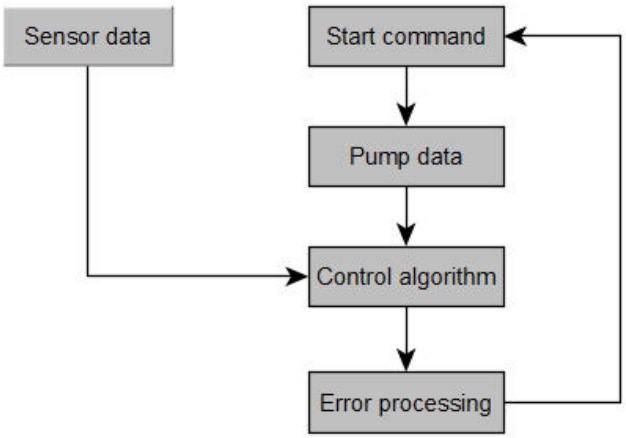

Figure 1. Flowchart of data processing algorithm.

The data exchange between the sensor control board and the fluid flow sensor is carried out using the symbols of the binary system, where the unit corresponds to the state of the sensor in which the fluid flow is fixed, and to zero, the state in which the sensor does not observe the flow. To control the operation this data comparing with the received information from the pump about necessary time of observing the fluid flow. In case of discrepancy between the expected and accepted values from the flow sensor, this data goes through the error processing process. Further, the processor can continue the operation of the device, if the error was not critical, or suspend the experiment by calling the user's dialog box with a choice of further actions.

The entire process of polling the sensor and the operation of the hydraulic system is logged with time stamps. Thus, if necessary, it could be determined the cause of the failure by examining the relevant documentation.

3. Conclusion

The developed algorithm allows to control correct operation of the hydraulic system of the sequencing device and has the ability to suspend operation of the entire device and notify user to get the further instructions. If necessary, the algorithm has the ability to suspend the operation of the entire device, or a specific part thereof, notifying the user at the same time, and will wait for further instructions.

References

[1] Esikova N A, Germash N N and Evstrapov A. A 2020 *Scientific instrument-making* **30(4)** 21-26
[2] Reznik V S and Kruglov V A 2021 *Journal of Physics: Conference Series* **2086(1)** 012120
[3] Belov Yu V, Petrov A I, Ivanov V V and Kurochkin V E 2011 *Scientific instrumentation* **21(1)** 44-49
[4] Alekseev Ya I, Belov Yu V, Malyuchenko O P, Monakhova Yu A, Natyrov A N, Orekhov V A, Konovalov S V, Kurochkin V E ans Petrov A I 2012 *Scientific instrumentation* 22(4) 86-92
[5] Antonova O S, Rudnidskya G E, Tupik A N, Bylianitsa A L and Evstrapov V E 2011 *Scientific instrumentation* **21(4)** 5-21

Genetically encoded tool with time-resolved fluorescence read-out for the calcium concentration measurement

T R Simonyan[1#*], E A Protasova[2#], A V Mamontova[1], E G Maksimov[2], K A Lukyanov[3] and A M Bogdanov[3]

[1] Center of Life Sciences, Skolkovo Institute of Science and Technology, Moscow 121205, Russia;
[2] Faculty of Biology, M.V. Lomonosov Moscow State University, 119992, Moscow, Russia;
[3] Shemyakin-Ovchinnikov Institute of Bioorganic Chemistry, Moscow 117997, Russia;
[#]These authors contributed equally to the study;
[*]Corresponding author: tatiana.simonyan7@gmail.com

Abstract. Here, we describe two variants of the calcium indicators based on the GCaMP sensitive core and BrUSLEE fluorescent protein (GCaMP-BrUSLEE and GCaMP-BrUSLEE-145). In contrast to the conventional GCaMP6-family indicators, these fluorophores are characterized by the well-marked responsiveness of their fluorescence decay kinetics to external calcium concentration both *in vitro* and *in cellulo*. Specifically, we show that the purified GCaMP-BrUSLEE and GCaMP-BrUSLEE-145 exhibit three-component fluorescence decay kinetics, with the amplitude-normalized lifetime component (t3*A3) of GCaMP-BrUSLEE-145 changing four-fold (500-2000 a.u.) in response to a Ca^{2+} concentration shift in the range of 0—350 nM. Time-resolved fluorescence microscopy of live cells displays the two-fold change of the GCaMP-BrUSLEE-145 mean lifetime upon histamine-stimulated calcium release. Aforementioned Ca^{2+}-dependence calls considering the GCaMP-BrUSLEE-145 as a prospective Ca^{2+}-indicator with the signal read-out in the time domain.

1. Introduction

The cloning of the avGFP gene in the early 1990s marked the beginning of the triumphant march of fluorescent proteins (FPs) as indispensable tools in biology [1]. Visualization of molecular indicator signals stands out among the key methods of fluorescence analysis using FPs. A significant number of genetically encoded indicators based on fluorescent proteins, have been engineered, allowing detecting changes in various parameters, such as membrane voltage, pH, concentrations of hydrogen peroxide, lactate, pyruvate, NAD^+/NADH, ATP, calcium cations, etc. [2]. The fundamental limitation of most fluorescent indicators is that they are able to assess only a relative change in the studied parameter in the cell. The nature of this drawback is rooted in the difficulty to uniformly and reproducibly connect an absolute value of the measured parameter with the detected fluorescent signal. Quantitative measurements thus impose an additional requirement on the indicator's signal: it must be independent of the technical features of the experiment (such as the level of protein expression, type and power of the excitation source, set of fluorescent filters, etc.). A possible way to fulfill this requirement is to detect the indicator's signal in the time domain, where its read-out relies on the measurement of fluorescence lifetime, an intrinsic fluorophore's property. Time-resolved imaging mode, in turn, imposes its own limitations on the behavior of the indicator's fluorescent core. Specifically, its fluorescence lifetime should be responsive to the changes in the

chromophore's environment and thus able to shift proportionally to the target analyte [3].

Calcium ions (Ca^{2+}) are among the essential compounds in live cells, which are deeply involved in their physiology and biochemistry. These ions play an important role in intracellular signaling [4,5], where they act as secondary messengers, in the release of neurotransmitters from neurons, in a contraction of all muscle cell types [6], and in fertilization. Many enzymes require calcium ions as a cofactor, including several blood coagulation factors [7]. Extracellular calcium is important for maintaining the transmembrane voltage in electrically excitable cells as well as for proper bone formation. Calcium fluctuations during neuronal activity are of particular interest. A number of fluorescent indicators have been designed to measure Ca^{2+} concentration, including the GCaMP family of genetically encoded calcium indicators (GECIs) based on the green fluorescent protein [8,9]. Although these molecules functioning in the spectral domain can only monitor the relative changes in calcium concentration, they have become a basis for the first GECIs with time-resolved read-out, e.g., recently described indicator built on the Turquoise 2 cyan FP [10] and the constructs based on the BrUSLEE protein, which we represent here.

The BrUSLEE green fluorescent protein is an EGFP mutant containing T65G/Y145M/F165Y substitutions [11]. It combines a high fluorescence brightness (~80% of EGFP) and short mean lifetime (820 ps). Such a set of properties, which is quite unique among the FPs described to date, makes BrUSLEE an attractive probe for fluorescence lifetime imaging microscopy (FLIM). Earlier, we demonstrated the BrUSLEE performance in the FLIM experiments, where its time-resolved signal was effectively unmixed from those of several spectrally similar FPs [11]. Moreover, as we have recently shown, the fluorescence lifetime of the BrUSLEE circular permutants is sensitive to the protein's environment (specifically, pH), and can smoothly change within the 0.5–3 ns range [12]. This probably indicates a high conformational mobility of the chromophore, which is important for the indicator's signal acquisition in the time domain. In contrast, little is known about the lability of fluorescence lifetime of the enhanced GFP (eGFP), which is used as a fluorescent core in a number of fluorescent indicators including the GCaMPs.

2. Results and discussion

The original GCaMP6s is a circular permutant of the eGFP protein fused with two calcium-sensitive domains, calmodulin and the M-13 peptide [9]. We engineered two variants of GCaMP6s with the circularly permuted BrUSLEE protein as a fluorescent core. The BrUSLEE permutation point remained homologous to that in the original indicator (the site includes residues 144–149 according to avGFP numbering). At the same time, we proposed two alternative variants of the permutants' primary structure: with the removal (cpBrUS-145) and with the preservation (cpBrUS) of the methionine residue at position 145 (the Met145 residue is an important determinant of the BrUSLEE fluorescent properties [13]).

At the first stage, we compared the GCaMP6s, GCaMP6s-BrUSLEE, and GCaMP6s-BrUSLEE-145 indicators in the spectral domain (using steady-state fluorescence spectroscopy) *in vitro* (aqueous solutions of

the purified proteins) in the physiological range of calcium concentration 0-350 nM (Calcium Calibration Buffer kit, Invitrogen). The results are presented in Figure 1.

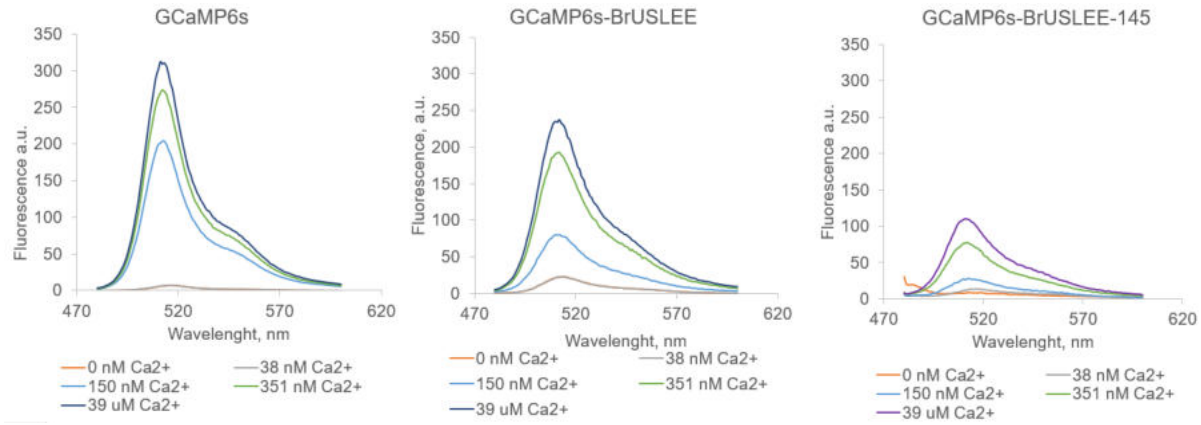

Figure 1. Fluorescence emission spectra of the GCaMP6s, GCaMP6s-BrUSLEE and GCaMP6s-BrUSLEE-145 at five Ca^{2+} concentration points.

We observed significant changes in the fluorescence intensity of all three indicators starting from 38 nM Ca^{2+}. The parental GCaMP6s showed an increase in fluorescence intensity from 5 to 300 a.u., while GCaMP6s-BrUSLEE and GCaMP6s-BrUSLEE-145 - from 25 to 250 a.u. and from 10 to 100 a.u., respectively. The dynamic ranges of the response (calculated in the 38-351 nM range) of GCaMP6s-BrUSLEE and GCaMP6s-BrUSLEE-145 turned out to be 6 times lower than that of the response of the original indicator.

Further, similar *in vitro* experiments were carried out in the time domain using time-resolved fluorescence spectroscopy upon fluorescence excitation by a single-photon picosecond laser at a 450 nm central wavelength (see Figure 2).

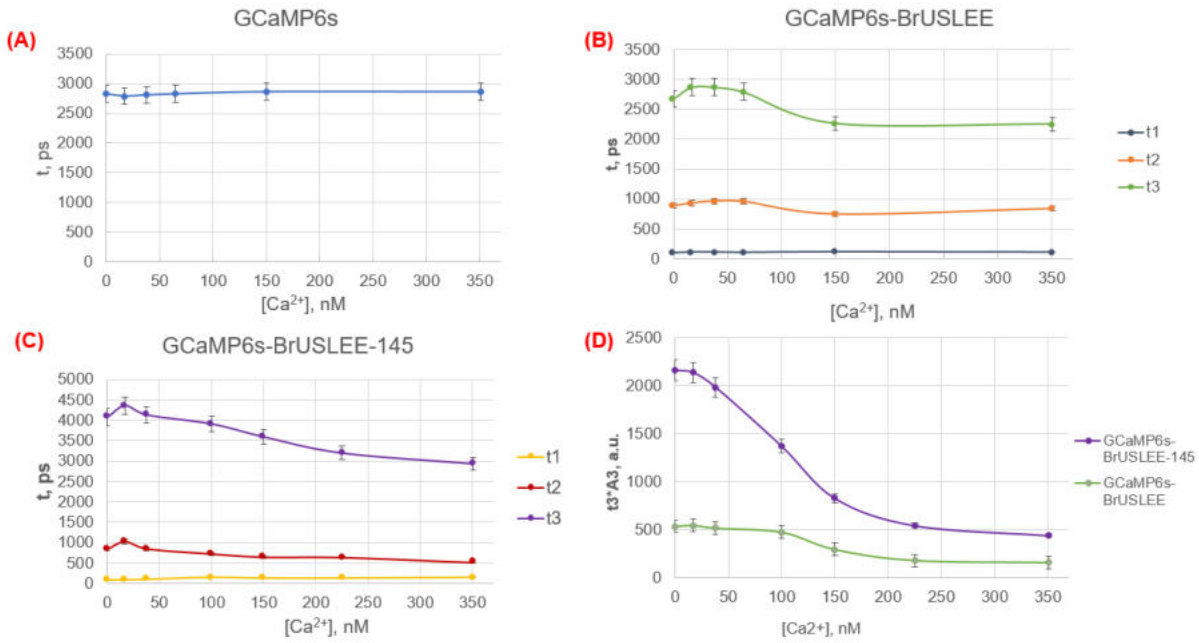

Figure 2. Curves showing [Ca^{2+}]/fluorescence lifetime dependence measured in vitro on a purified protein for: (A) GCaMP6s fluorescence decay fitted by a single-exponential function; (B) GCaMP-BrUSLEE, (C) GCaMP-BrUSLEE-145 fluorescence decays, both fitted by a three-component exponential model; (D) comparison of the GCaMP-BrUSLEE and GCaMP-BrUSLEE-145 time-resolved fluorescence signals represented as a [t3*A3]—an amplitude-normalized lifetime of the third fluorescent component.

As one can see, GCaMP6s was characterized by a single-exponential fluorescence decay with a lifetime of ~2.8 ns, which was almost insensitive to a change in calcium concentration (Figure 2A). In contrast to it, GCaMP6s-BrUSLEE and GCaMP6s-BrUSLEE-145 showed a complex fluorescence decay fitted best by the three exponential (lifetime) components (Figure 2B,C). Two of them (t2 and t3) responded to the calcium concentration shift. The amplitude-normalized lifetime of the third component (i.e., a product of the lifetime value by its relative contribution; t3*A3) shows nearly linear dependence on calcium concentration within the range of 10-150 nM with a twofold contrast (250-500 a.u.) for GCaMP6s-BrUSLEE and fourfold contrast (500-2000 a.u.) for GCaMP6s-BrUSLEE-145 (see Figure 2D). Since the fluorescence response of GCaMP-BrUSLEE-145 is generally characterized by a wider dynamic range, this construct would be more reliable for the subsequent quantitative analysis of the calcium concentration.

The GCaMP-BrUSLEE-145 coding sequence was cloned into a DNA vector (pEGFP-N1 backbone) for expression in mammalian cells for further *in cellulo* testing using FLIM. After transfection, we studied the fluorescence lifetime dynamics of GCaMP-BrUSLEE-145 in live HEK293T cells upon stimulation with a 200 µM histamine solution (addition of histamine causes calcium release from the endoplasmic reticulum, ER; see Figure 3).

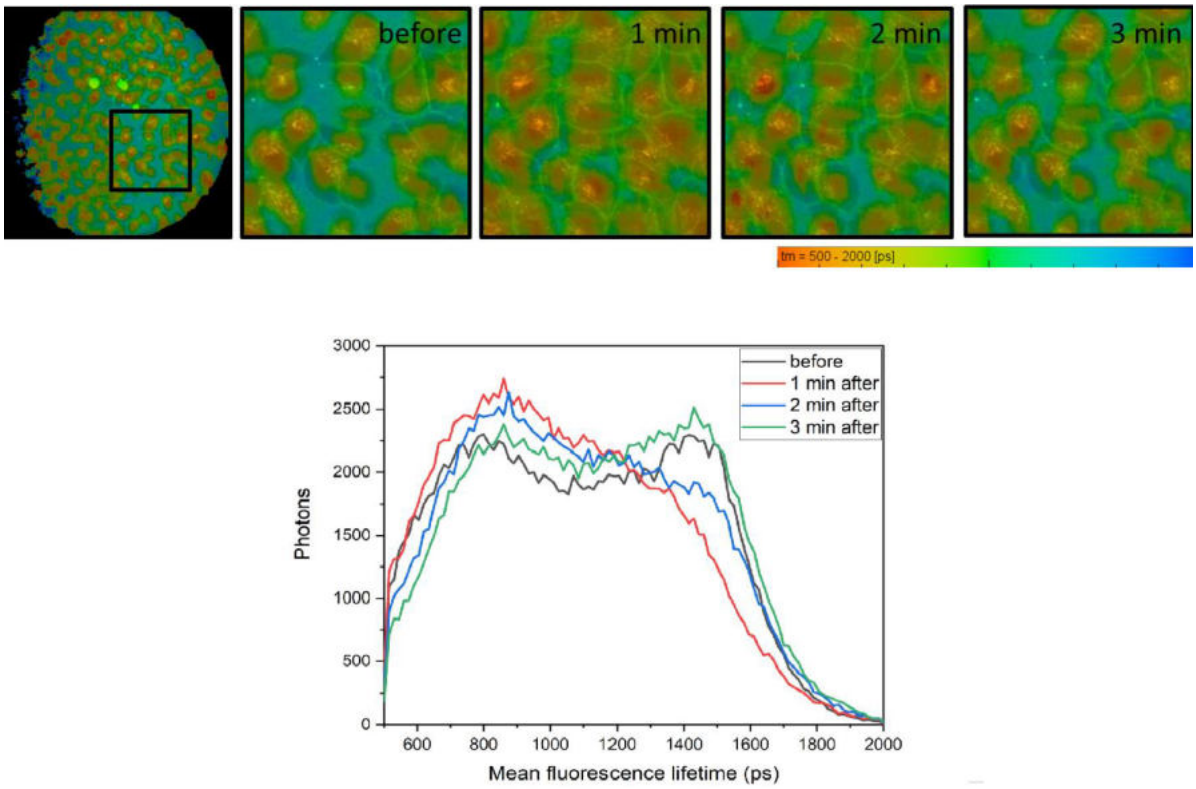

Figure 3. The fluorescence lifetime dynamics of GCaMP-BrUSLEE-145 in cellulo upon addition of histamine to live HEK293T cells. Above are the FLIM images of the cells pseudocolored according to the mean fluorescence lifetime, before and after the addition of 200 μM histamine. Below is a histogram showing the distribution of the mean fluorescence lifetime quantified on a basis of the FLIM images' data.

These preliminary data show that the histamine-stimulated calcium release from ER the cytoplasm results in the shortening of the GCaMP-BrUSLEE-145's mean fluorescence lifetime from 1600 ps to 800 ps. Importantly, after the calcium reuptake (∼2 min of the post-stimulation incubation), the indicator lifetime's recovery to 1600 ps is observed, indicating the reversibility of the GCaMP-BrUSLEE-145's response and its potential suitability for long-term experiments where Ca^{2+} concentration can change many times.

3. Conclusions

We designed two variants of the GCaMP indicator for time-resolved fluorescence imaging with the circularly permuted BrUSLEE as a fluorescent core. In the spectral domain, both BrUSLEE-based molecules demonstrated narrower response range than the parental indicator but in contrast to GCaMP6s, their fluorescence lifetimes were shown to be sensitive to the ambient Ca^{2+} concentration. GCaMP-BrUSLEE-145 displayed a greater lifetime shift in response to calcium addition than GCaMP-BrUSLEE that probably indicates the role of the Met145 residue in limiting the conformational flexibility of the chromophore. Upon live cell time-resolved fluorescence microscopy, GCaMP-BrUSLEE-145 showed a twofold change in the mean fluorescence lifetime after histamine-induced calcium release with the ability to further restore an initial state of the chromophore upon

calcium reuptake. Taken together, these results indicate that GCaMP-BrUSLEE-145 can function as a Ca^{2+} fluorescent indicator with a time-resolved read-out. In further experiments, we aim to determine the absolute values of the calcium concentration using GCaMP-BrUSLEE-145 FLIM imaging.

Acknowledgments

The project was supported by RFBR (Project 19-34-60019).

References

1. Chalfie M, Tu Y, Euskirchen G, Ward W W, Prasher D C, Green Fluorescent Protein as a Marker for Gene Expression. *Science* **1994**, *263*, 802–805, doi:10.1126/science.8303295.
2. Sanford L, Palmer A, Recent Advances in Development of Genetically Encoded Fluorescent Sensors. In *Methods in Enzymology*; Elsevier, 2017; Vol. 589, pp. 1–49 ISBN 978-0-12-805406-2.
3. Berezin M Y, Achilefu S, Fluorescence Lifetime Measurements and Biological Imaging. *Chem. Rev.* **2010**, *110*, 2641–2684, doi:10.1021/cr900343z.
4. Brini M, Ottolini D, Calì T, Carafoli E, Calcium in Health and Disease. *Met. Ions Life Sci.* **2013**, *13*, 81–137, doi:10.1007/978-94-007-7500-8_4.
5. Brini M, Calì T, Ottolini D, Carafoli E, Intracellular Calcium Homeostasis and Signaling. *Met. Ions Life Sci.* **2013**, *12*, 119–168, doi:10.1007/978-94-007-5561-1_5.
6. Szent-Györgyi A G, Calcium Regulation of Muscle Contraction. *Biophys. J.* **1975**, *15*, 707–723, doi:10.1016/S0006-3495(75)85849-8.
7. Garland C J, Hiley C R, Dora K A, EDHF: Spreading the Influence of the Endothelium. *Br. J. Pharmacol.* **2011**, *164*, 839–852, doi:10.1111/j.1476-5381.2010.01148.x.
8. Nakai J, Ohkura M, Imoto K, A High Signal-to-Noise Ca(2+) Probe Composed of a Single Green Fluorescent Protein. *Nat. Biotechnol.* **2001**, *19*, 137–141, doi:10.1038/84397.
9. Chen T-W, Wardill T J, Sun Y, Pulver S R, Renninger S L, Baohan A, Schreiter E R, Kerr R A, Orger M B, Jayaraman V, et al. Ultrasensitive Fluorescent Proteins for Imaging Neuronal Activity. *Nature* **2013**, *499*, 295–300, doi:10.1038/nature12354.
10. van der Linden F H, Mahlandt E K, Arts J J G, Beumer J, Puschhof J, de Man S M A, Chertkova A O, Ponsioen B, Clevers H, van Buul J D, et al. A Turquoise Fluorescence Lifetime-Based Biosensor for Quantitative Imaging of Intracellular Calcium. *Nat. Commun.* **2021**, *12*, 7159, doi:10.1038/s41467-021-27249-w.
11. Mamontova A V, Solovyev I D, Savitsky A P, Shakhov A M, Lukyanov K A, Bogdanov A M, Bright GFP with Subnanosecond Fluorescence Lifetime. *Sci. Rep.* **2018**, *8*, 13224, doi:10.1038/s41598-018-31687-w.
12. Mamontova A V, Simonyan T R, Lukyanov K A, Bogdanov A M, Circular Permutants of BrUSLEE Protein as Fluorescent PH Indicators. *Russ. J. Bioorganic Chem. in press*.
13. Mamontova A V, Shakhov A M, Lukyanov K A, Bogdanov A M, Deciphering the Role of Positions 145 and 165 in Fluorescence Lifetime Shortening in the EGFP Variants. *Biomolecules* **2020**, *10*, 1547, doi:10.3390/biom10111547.

Comparison of femtosecond laser, hydrothermal and microwave synthesis of fluorescent products from L-lysine

A A Astafiev[1], A M Shakhov[1], M S Syrchina[1], D V Shepel[1] and V A Nadtochenko[1]

[1]N.N. Semenov Federal Research Center of Chemical Physics, Russian Academy of Sciences, Kosygina 4, Moscow, Russia

Abstract. Femtosecond laser synthesis of fluorescent products from essential amino acids in living cells and tissues can be exploited in fluorescent bioimaging. To gain insight into reaction mechanism and a role of thermal processes we examine synthesis of fluorescent products from L-lysine by femtosecond laser irradiation, hydrothermal and microwave synthesis and perform comparative analysis of reaction products. Our results indicate that compared with purely thermal synthetic routes femtosecond laser synthesis favours formation of carbon dots-type fluorescent nanomaterials.

1. Introduction

Production of fluorescent species from biomolecules in living cells and tissues in situ by femtosecond laser irradiation offers many unique advantages in fluorescent bioimaging [1-2]. We demonstrated that femtosecond laser synthesis of fluorescent carbon dots from essential amino acid L-lysine provides a potential route of fluorescent species formation in living cells [3]. Laser-induced heating can be one of mechanisms responsible for carbon dots synthesis and fluorescent carbon dots can be also produced from amino acids, including L-lysine, by a more conventional thermal-driven reactions using solvothermal or microwave synthesis [4]. In order to gain a better understanding of the role of thermal mechanisms and peculiarities of femtosecond laser synthesis we analysed optical properties, morphology and chemical composition of products obtained from L-lysine aqueous solution by three different routines: femtosecond laser, hydrothermal and microwave synthesis (hereafter samples **Lys-FS**, **Lys-HT** and **Lys-MW** respectively).

2. Methods

2.1. Synthesis and purification of products.

Lys-FS: 2 ml of L-lysine aqueous solution (0.1 g/mL) in a quartz cuvette was irradiated with trains of femtosecond laser pulses focused by a spherical lens (f=8 mm, 0.5NA). Central wavelength of laser pulses was 800 nm, repetition rate - 1 kHz, duration - 50 fs, pulse energy - 1.4 mJ. **Lys-HT**: 10 ml of 0.5 g/mL L-lysine solution in a PTFE container was heated in an oven for 30 hours at 220 ^{0}C. **Lys-MW**: 5 ml of 0.1 g/mL L-lysine solution in a glass vial was heated in a domestic microwave oven for 1 min at 800 W. For chemical analysis samples were dialyzed for 72 hours in 2,000 MWCO dialysis units.

2.2. Samples characterization

Absorption of photoluminescence spectra of samples in water were recorded with Shimadzu spectrophotometer (UV-3600) and spectrofluorometer (RF-5031 PC). Fluorescence quantum yield (356 nm excitation) was estimated with the slope method using ethanol solution of anthracene as a standard. Effective hydrodynamic volumes were estimated from anisotropy decay kinetics (excitation at 360 nm and emission at 450 nm). Infrared absorption spectra were collected using Bruker Lumos II FTIR microscope-spectrometer. High resolution transmission electron microscopy (HRTEM) images were recorded on a JEM 2100F high-resolution transmission electron microscope (JEOL Co. Ltd., Japan)

3. Results

All the samples exhibited strongest optical absorption in UV range and visible fluorescence with excitation maximum near 350 nm and emission maximum at 430-440 nm (**Figure 1**). Fluorescence spectra were excitation-dependent and demonstrated a red shift with increase of the excitation wavelength, revealing multicomponent emission. Measurements of effective hydrodynamic volumes and dialysis demonstrated that **Lys-FS** contained fluorescent products of the largest sizes with nanometer-scale dimensions, i.e. carbon dots. HRTEM images confirmed presence of nanoparticles with onion-like structure in **Lys-FS**. Infrared absorption spectra of the samples exhibited strong amide bands attributed to polymerization of L-lysine, at the same time revealing presence of unsaturated fragments, which can form chromophore groups.

Our results indicate that whereas all the three synthetic routes yield products with multicomponent and excitation-dependent visible emission from L-lysine, femtosecond laser synthesis is the most effective for obtaining carbon dots-type fluorescent nanoparticles albeit with a relatively small fluorescence quantum yield.

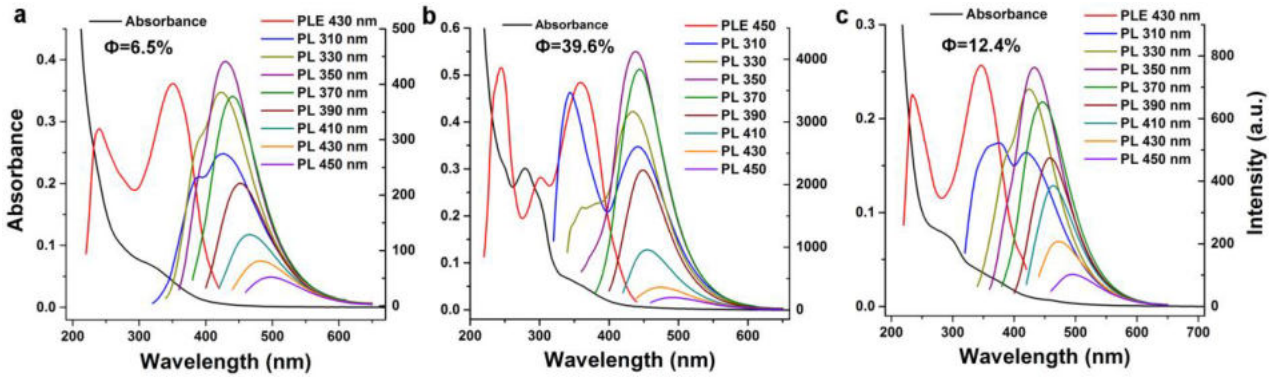

Figure 1. UV-Vis absorbance, photoluminescence emission (PL) and excitation (PLE) spectra of (a) **Lys-FS**, (b) **Lys-HT** and (c) **Lys-MW**. Φ – fluorescence quantum yield.

Acknowledgments

The work has financial support from the Russian Scientific Foundation grant No.21-72-20169. The work was performed on facilities of ACBS Center of the Collective Equipment (no. 506694, FRCCP RAS).

References

[1] Sun Q, Qin Z, Wu W, Lin Y, Chen C, He S, Li X, Wu Z, Luo Y and Qu J 2018 *Biomed. Opt. Express* **9** 581-90

[2] Astafiev A A, Shakhov A M, Osychenko A A, Syrchina M S, Karmenyan A V, Tochilo U A and Nadtochenko V A 2020 *ACS OMEGA* **5** 21 12527-38

[3] Astafiev A A, Shakhov A M, Gulin A A, Vasin A A, Gubina M V, Syrchina M S and Nadtochenko V A 2021 J. Phys: Conf. Ser. 2086 012121

[4] Sahiner H, Sunner S S, Sahiner M, Silan C 2019 J. Fluorescence 29 1191-1200

Research of the method of optical spectral real-time laser ablation estimation during endoscopic surgeries

A.A. Kim[1,2], O.A. Tereshenkova[1,2]

[1] BALTIC STATE TECHNICAL UNIVERSITY «VOENMEH» named after D.F.Ustinov, St, Petersburg, 190005, Russia
[2] Laser Systems JSC, Saint Petersburg, 198515, Russia

E-mail: tereshenkova_oa@mail.ru

Abstract. This scientific paper presents the results of research of the method of dynamic estimation of the laser ablation exposure to biological tissues during endoscopic surgeries. Described method is based on the dynamic estimation of the ablation process by the spectral characteristics of the tissue's area on which laser radiation is applied. In the article is given the description of the system prototype, which realizes the proposed method, and the results of preformed experiments.

1. Introduction

The progress of science and technology in the 1990s was an impetus for the development of minimally invasive surgery that have made it possible to reduce surgical intervention in some operations and achieved more target exposure to needed field [1]. Nowadays, minimally invasive surgeries are used in phlebology, cardiology and oncology with use of laser, radiofrequency and low-temperature radiations for applying exposure [2, 3, 4]. Each of these spheres of medicine employs different methods of estimating the operation's results that mostly are made after the operation and have no possibility to measure the exposure degree during the operation. We have proposed the method of dynamic estimation of the laser ablation that may be used for operations with another type of radiations.

2. Description of the proposed method

The proposing method is based on continuous real-time registration of the optical spectral characteristics of the tissue's field to which the radiation is applied. The developed prototype for realization of the proposing method combines the laser ablative radiation and the broadband visible radiation of illumination by the optical system of light combining. Both radiations come into optical fiber, which is inside the catheter and which performs ablation. Back reflected radiation, which consist information about spectral characteristic of the tissue’s surface, comes through the optical fiber and optical system of light division to the spectrometer. By information about changes of spectral characteristic during the exposure from the spectrometer is realized the estimation of result of laser ablation.

3. Experiments

As a part of this research was made several experiments where we performed laser exposure to the pig's cardiac muscle *ex vivo*. The purpose of the experiments was to study the characteristic course of the ablative process of tissues and to determine the permissible exposure capacities (operating modes)

for exposure times no greater than 40 seconds. We made three types of experiments: experiments in air; experiment where the tissue's sample was in the saline solution; experiment where the tissue's sample was in a combination of blood and saline solution. The power of laser radiation was from 5W to 10W with different durations of exposure, which were varied depending on results of exposure. During the experiments we were recording obtained spectral characteristics. One of recorded spectral characteristics is on the Fig.1(a). The result of laser ablation is on the Fig.1(b).

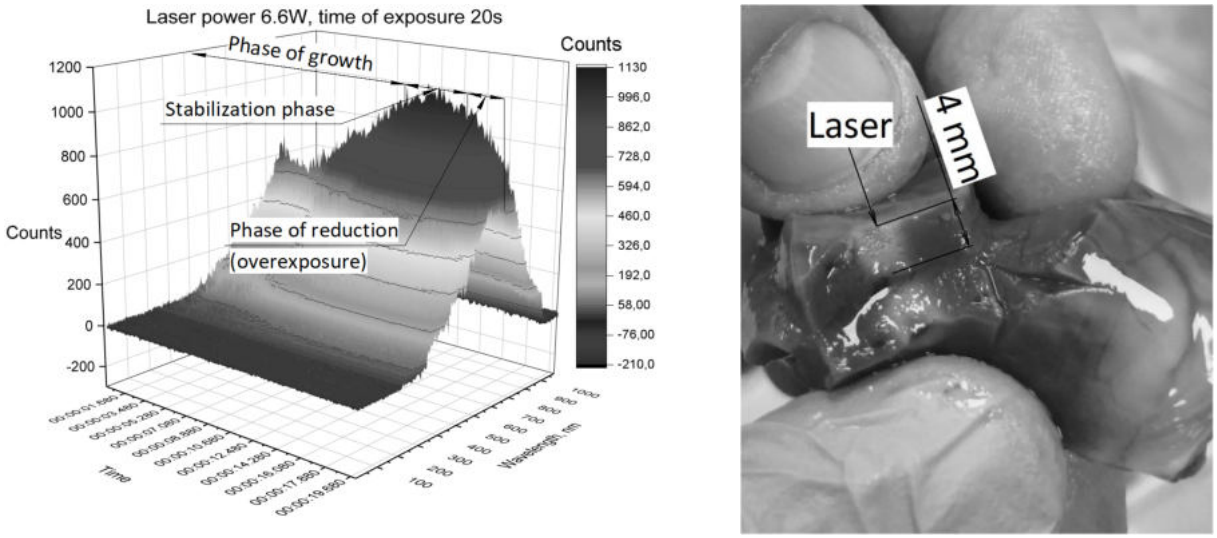

(a) (b)

Figure 1. Results of experiment with laser power 6.6W and time of exposure 20s: **(a)** recorded three-dimensional spectrum development during the exposure; **(b)** test tissue sample of pig's cardiac muscle after laser ablation

In this experiment, the sample of tissue was in the saline solution. Three-dimensional spectral characteristic in Fig.1(a) shows that there are three parts of a characteristic course of ablation to biological tissue: increase, stabilization and reduction. The growth of spectrum corresponds to gradual development of ablative necrosis which on the stabilization phase extends deep into tissue. The decrease of the spectrum indicates that small local area of dark, which further extends to charring. has appeared on the surface of biological tissue. As shown in Fig.1(b) the depth of achieved exposure is about 4mm. The surface of the test sample tissue got small but acceptable damage. The spectrum in Fig.1(a) was used for control of ablation during the experiment. As soon the reduction was noticed on the spectral characteristic, the laser exposure was stopped.

4. Conclusion

At this stage of research, can be made preliminary conclusions about efficiency of the proposed method as a high performance system of feedback control of ablative exposure to biological tissues, including endoscopic surgery with using catheter. Results of research show that achieved sensibility of estimations is enough for monitoring of ablation dynamic and timely determination of the occurrence of the critical tissue's damage. This allows preventing development of excessive damage. It is also shown that the proposed method can be used to determine and control the required operating modes (time and intensity of exposure).

Acknowledgments

This research is funded by Foundation for Assistance to Small Innovative Enterprises (FASIE) within the program "UMNIK" contract №16517ГУ/2021. The results were obtained using equipment of BALTIC STATE TECHNICAL UNIVERSITY «VOENMEH» named after D.F. Ustinov, Laser

Systems JSC and Federal State Budgetary Institution “Almazov National Medical Research Centre” of the Ministry of Health of the Russian Federation.

References

[1] St. Peter, Shawn & Holcomb, George, History of minimally invasive surgery. Endoscopic Surgery in Infants and Children. (2009) 1-5.

[2] H. Weber, L. Schmitz, A. Heinze, L. Ruprecht, M. Sagerer-Gerhardt, The Development of a laser catheter with improved monitoring of lesion formation during arrhythmia ablation. Nova Science Publishers, Inc., (2017) 4-49.

[3] L.I. Moskvicheva, L.O. Petrov, D.V. Sidorov, Vozmozhnosti sovremennykh metodov abli͡atsii pri nerezektabel’nom mestno-rasprostranennom rake podzhludochnoĭ zhelezy [Possibilities if modern ablation methods for unresectable locally advanced pancreatic cancer], Research and practice in medicine, 2 (2018) 86-99.

[4] E.S. Katanov, T.N. Erëmima, A.V. Semënov, Ėndovaskuliarnai͡a lazernai͡a koaguliatsii͡a i fizioterapii͡a pri lechenii varikoznoĭ bolezni ven nizhnikh konechnosteĭ [Endovascular laser coagulation and physiotherapy in the treatment of varicose veins of the lower extremities], Newsletter of the Chuvash University, 2 (2014) 251-256.

Femtosecond laser is an effective instrument to remove DNA in pronuclei of mouse zygotes

U A Tochilo1, A A Osychenko1, A D Zalessky1, D Yu Martirosyan1 and V A Nadtochenko1

1N.N. Semenov Federal Research Center of Chemical Physics, Russian Academy of Sciences, Kosygina 4, Moscow, Russia

e-mail: yanulyana@gmail.com

Abstract. We show the possibility of removing pronuclei in the zygote by a femtosecond laser irradiation. We suppose this method is more effective than mechanical removal with a micromanipulator. Cytoplasts prepared with a laser are more viable and suitable for further biotechnological manipulations.

1.Introduction

Triploidy is the most common anomaly of the chromosome set in the process of embryogenesis. Usually these embryos do not develop, or in the case of IVF, they are automatically considered as abortive material. We have an assumption that when the pronucleus is removed, normal development will be able for embryo. In the classical method, DNA removal is carried out mechanically, using aspiration by a microinjector. This can damage cell and the chances of normal development are sharply reduced. Previously [1], we showed that the removal of the metaphase plate in oocytes at the MII stage using a femtosecond laser is possible and quite effective. In this work, we show that the same method is also suitable for the destruction of pronuclei.

2.Methods

2.1. Oocyte collection

C57Bl/6 female mice aged eight- to ten weeks were mated with males of the same strain. Mice were sacrificed and the oviducts were removed. Fertilized oocytes with two pronuclei were washed and then cultured in KSOM culture medium (MR-101-D, EmbryoMax). The zygotes were stained with 5 μg/ml Hoechst 33342 dye (B2261, Sigma-Aldrich) for 15 minutes in KSOM medium in the incubator and then washed twice. During the experiment the zygotes were placed onto a cover glass in a 50 μl drop of M2 (M7167, Sigma) medium.

2.2. Laser parameters and enucleation process

In our experiments we used following parameters for the irradiation of the pronuclei: λ = 795 nm, υ = 80 MHz, pulse energy 0,5 nJ (40 mW power); 100 fs pulse duration, pulse train duration 60 ms. Laser radiation was focused by 60× objective lens (NA = 0.7). Pronuclei are easily visualised, we exposed laser on one of them. We repeated the exposure multiple times, until the DNA luminescence stopped.

2.3. Confocal imaging

Fluorescence imaging was performed using a laser scanning confocal microscope Zeiss LSM 980 (Carl Zeiss Microscopy, Jena, Germany), 63x Plan-Apochromat objective (NA = 1.4, oil immersion). The oocytes were placed in M2 medium drop on a 0.17 mm cover glass (Zeiss). Hoechst 33342 luminescence excitation were performed by 405 nm laser, detection range 410-479 nm.

3.Results.

Figure 1 shows the zygote (A) before and after irradiation, as well as the control zygote (B), which we did not irradiate. In sample A, we were able to focus the irradiation on one of the pronuclei and achieved the

complete absence of DNA luminescence in it. We measured the luminescence level, it also showed a decrease in the indicator by about a twice. In the non-irradiated zygote, we placed for the same time on the microscope stage as the irradiated one, the level of DNA luminescence practically did not decrease. It proves, that our routine manipulations, except laser radiation, did not affect on the DNA removal.

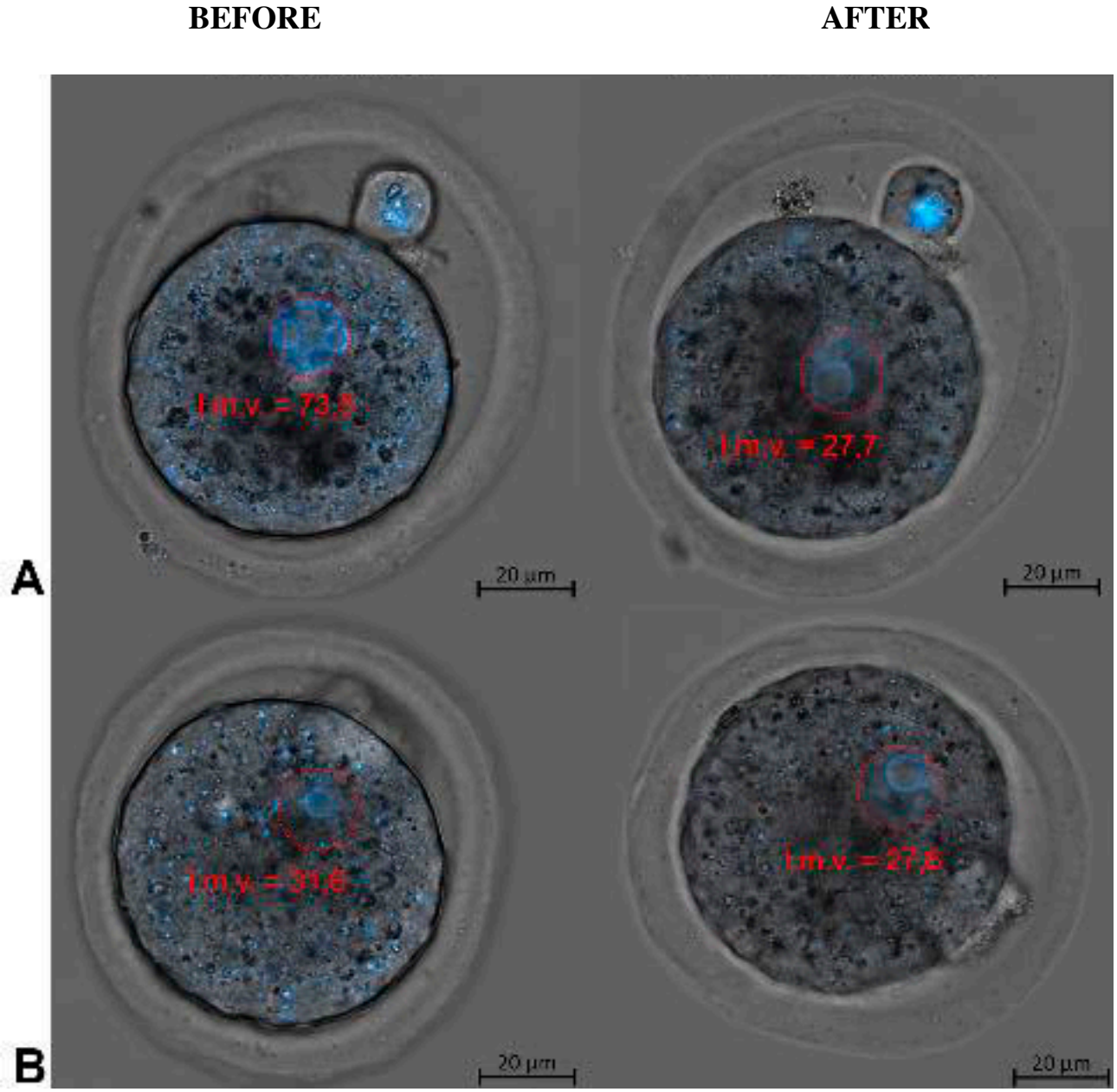

Fig.1 In zygote A after irradiation by a femtosecond laser we can observe decreasing of DNA luminescence, while in zygote B we don't notice significant changes

Acknowledgments

This work is supported by the Russian Science Foundation under grant № 21-75-10155. The work was performed on facilities of ACBS Center of the Collective Equipment (no. 506694, FRCCP RAS) and large-scale research facilities № 1440743.

References

[1] Osychenko A A, Zalessky A D, Tochilo U A, Martirosyan D Yu, Silaeva Y Yu and Nadtochenko V A 2022 *Biomed. Opt. Express* **13**(3)1447–1456

Photoluminescent nanoparticles β-$NaYF_4$:$Yb^{3+}Er^{3+}Ce^{3+}$ for multipurpose bioimaging

E M Trifanova, K V Khaydukov, A V Koshelev, I V Krylov, V K Popov.

Federal Scientific Research Center "Crystallography and Photonics" RAS, Moscow, 119333, Russia
e-mail: katikin@mail.ru

Abstract. Photoluminescent nanoparticles doped with Yb^{3+}, Er^{3+}, Ce^{3+} that can perform emission in different regions of the spectrum are very promising for biological tissue visualization. In order to show their possibilities β-$NaYF_4$:$Yb^{3+}Er^{3+}Ce^{3+}$ nanoparticles were characterized and had narrow luminescent lines. Visualization experiments with phantoms of biotissue both 3.5% fat milk and distilled water showed that nanoparticles can be used for multipurpose bioimaging.

1. Introduction

Noninvasive optical technologies are very perspective for bioimaging due to their safety and high spatial and time resolution [1]. Usually three biotissue transparency windows (BTW): I-BTW (650–950 nm), II-BTW (1000–1350 nm), III-BTW (1500–1870 nm) are used in bioimaging because of higher light penetration depths according to local minimum of extinction coefficient [2]. Generally I-BTW and III-BTW attract significant interest due to low signal-to-noise ratio and low autoluminescence [3]. The design of photoluminescent nanomarkers capable of excitation and luminescence in all three BTW ranges is a challenge. From this point of view, fluoride nanoparticles (NPs) doped with lanthanide ions (Ln^{3+}), generating photoluminescence in a wide spectral range, have a huge potential. We demonstrate the possibility of using Ln^{3+}-doped β-$NaYF_4$ NPs, which exhibit high intensity up- (~650 nm) and down-conversion (~1530 nm) luminescence under λ = 976 nm irradiation, as imaging instrument. Our experiments display broad perspective in multipurpose visualization with fluoride NPs and recommendations on the choice of the detected range depending on specificity of the application.

2. Experimental

β-$NaYF_4$:$Yb^{3+}Er^{3+}Ce^{3+}$ NPs with average diameter 30 nm, perform intense photoluminescence in the I-BTW range (650 and 670 nm) and III-BTW (1530 nm) upon excitation by λ = 976 nm radiation. For the imaging experiment two pieces (0.1x10 mm) of white paper were covered with the NPs. The paper pieces were placed on a quartz cuvette with a 0.7 mm gap between them. Two visualization experiments were carried out: imaging through a strongly scattering medium – 3.5% fat milk [4] – and distilled water aiming to imitate scattering and absorption coefficient of biotissue. For visualization in the visible range, we used homebuild imaging system with CCD camera. For visualization in the NIR range, we performed time-gated luminescence imaging. This method allows the laser excitation signal to decay and autoluminescence with a short lifetime before the signal from the NPs with a long lifetime is received [5].

On the images obtained through a 1 mm layer of milk in the visible range (fig. 1a) gap between the pieces is not observed, two bands merge into one. On the image at a wavelength of 1530 nm (fig. 1b),

on the contrary, the two photoluminescent bands are clearly visible. This can be explained by the Mie scattering effect – the greater the wavelength, the less light is scattered [6].

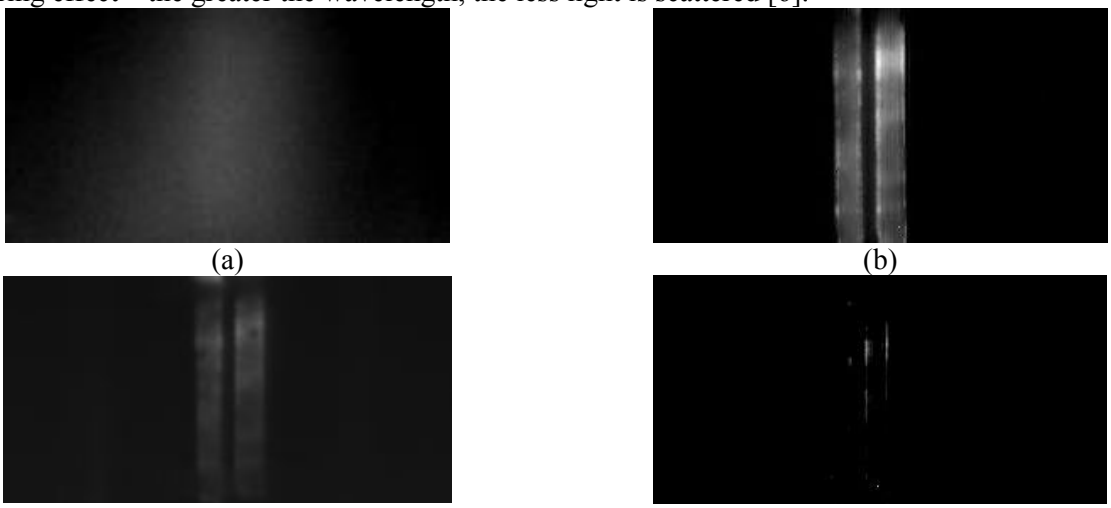

(a) (b) (c) (d)

Figure 1. Images of the two paper pieces were covered with the NPs obtained through a 1 mm layer of 3.5% fat milk in a – visible and b – NIR region of the spectrum and through a 3 mm layer of water in c – visible and d – NIR region of the spectrum.

In the experiment with distilled water, optical cuvettes of different thicknesses from 1 to 11 mm were used. With a water layer thickness of 1-2 mm, we can observe bands and a gap in between in both visible and NIR region of the spectrum. However, as the layer thickness increases, the image in NIR deteriorates and disappears completely at a thickness greater than 3 mm, which does not occur in the visible range as shown in figure 2. This is because the absorption coefficient of water is higher at a wavelength of 1530 nm [7].

3. Conclusion

The β-$NaYF_4$:$Yb^{3+}Er^{3+}Ce^{3+}$ NPs can be used as multipurpose photoluminescent nanomarkers both in I-BTW and III-BTW region of the spectrum. We obtained sharp images of the photoluminescent bands through 1 mm layer 3.5% fat milk using time-gated luminescence imaging in near IR region of the spectrum. However, this method cannot be used through thick (more 3 mm) layer media with high absorption coefficient. While visualization can be carried out in visible of the spectrum. Each visualization method has its own advantages determined by specific application and experimental conditions.

Acknowledgments

The study was funded by the Ministry of Science and Higher Education within the State assignment FSRC 'Crystallography and Photonics' RAS and RFBR according to the project №20-32-90218.

References

[1] del Rosal B and Jaque D 2019 *Methods Appl. Fluoresc.* **7** 022001

[2] Hemmer E, Venkatachalam N, Hyodo H, Hattori A, Ebina Y, Kishimoto H and Soga K 2013 *Nanoscale* **5** 11339

[3] Hemmer E, Benayas A, Légaré F and Vetrone F 2016 *Nanoscale Horizons* **1** 168–84

[4] Fajardo C and Solarte E 2020 *J. Phys. Conf. Ser.* **1547** 012026

[5] Khaydukov EV., Boldyrev KN, Khaydukov KV., Krylov IV., Asharchuk IM, Savelyev AG, Rocheva VV., Karimov DN, Nechaev AV. and Zvyagin AV. 2019 *Opt. Spectrosc.* **126** 95–101

[6] Mie G 1908 *Ann. Phys.* **331** 597–614

[7] Beć KB and Huck CW 2019 *Front. Chem.* **7** 1–22

Structure of supramers formed by glycan-containing Function-Spacer-Lipid constructs: a SAXS study.

Polina Troitskaya[1,5] , Ivan Vaskan[1,2] , Maxim Petoukhov[4], Milena Shestopalova[1,3], Nicolai Bovin[1], Ivan Ryzhov[1], Eleonora Shtykova[4], Vladimir Oleinikov[1,3,] and Anton Zalygin[1]

1 Shemyakin-Ovchinnikov Institute of Bioorganic Chemistry Russian Academy of Sciences, 16/10 Miklukho-Maklaya str., Moscow, 117997, Russian Federation;
2 Moscow Institute of Physics and Technology, 9 Institutskiy per., Dolgoprudny, 141701, Russian Federation
3 National Research Nuclear University MEPhI (Moscow Engineering Physics Institute), Kashirskoe shosse 31, Moscow, 115409, Russian Federation
4 Shubnikov Institute of Crystallography of Federal Scientific Research Centre 'Crystallography and Photonics' of Russian Academy of Sciences, Moscow, 119333, Russian Federation;
5 Moscow State University, Ulitsa Kolmogorova, 1, Moscow, 119991

Abstract. Development of multivalent biocompatible molecular instruments capable of forming stable nanoparticles with desired morphology and surface properties is of high importance as they will offer efficient therapeutic, diagnostic, and research tools towards personalized medicine. In this work, the structure of supramers formed by neoglycolipid containing A(type 2) blood group glycan is studied by SAXS technique. Since interaction with each other is usually a concentration-dependent process, studies were performed at a range of SAXS-applicable concentrations. Obtained results indicate that self-assembly process leads to formation of monodisperse nanoparticles with micelle-like architecture, which is maintained regardless of concentration. Such structure suggests that nanoparticles do not interact with each other by carbohydrate parts, which makes them suitable tools to study drug delivery research.

• Introduction

Synthetic glycolipids and similar amphiphiles with other functional “head” (peptide, label, etc.) instead of glycol-part known as Function-spacer-lipid (FSL) constructs [1] have been designed for labeling cells [2], membrane viruses and hard surfaces using a number of biological and nonbiological markers [3] under physiological conditions. In contrast to other lipids, FSLs are easily dispersed in water, saline, and biological media. They can integrate into the cell membrane without compromising functionality or viability [1]. Based on the described properties, we can conclude that Function-spacer-lipid constructs are powerful tools for a wide range of studies of the biological functions of glycans on the cell surface [4].
Recently, we found that FSL constructs are able to self-assemble into micelle-like particles that are homogeneous in shape, size and internal structure [5]. Nanoparticles with biotin as a functional head showed a low critical aggregation concentration. This design is attractive from the viewpoint of development of biomimetic nanoparticles which can serve as models in biomedical research [6,7].

However, the structural properties and architecture of such nanoparticles can depend on spacer and functional head moieties, hence for each synthetized conjugate structure it is necessary to identify these dependencies and establish nanoparticle properties in each case.

The basic structure of the FSL construct is usually consist of (Figure 1): a hydrophilic functional head (1); biologically inert spacer (2), which helps the structure to disperse in water and separates the functional head from the surface; and a lipid tail (3) that renders the construct amphipathic and drives spontaneous self-assembly and incorporation into lipid membranes.

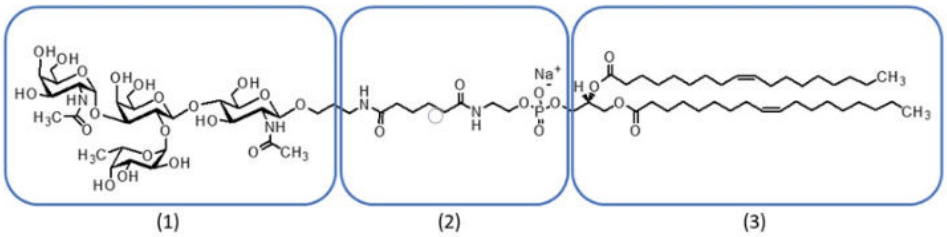

Figure 1. Structure of the FSL construct A(type2)-Ad-DE. Ad, adipoyl; DE, di-oleoylphosphatidyl ethanolamine.

- **Results and Discussion**

SAXS experimental curves with corresponding sample concentration values are shown in Figure 2a. Such curve patterns are typical for micelle-like structures. Positions of maxima and minima peaks of the curves leads to a conclusion that there are no fluctuations along the scattering vector relative to the positions of the peaks, which means that supramers size, shape and architecture are maintained at the SAXS-applicable concentration range from 0.60 to 3.35 mg/ml. This result indicates that self-assembled nanoparticles are not clustering in large aggregates upon increase of concentration. In turn, this suggests that supramers do not interact with each other by their surface glycan moieties. Thus, these moieties represent "a free valence" that enables application of such nanoparticles as a model systems for investigation of carbohydrate-carbohydrate, carbohydrate-protein, carbohydrate-surface interactions and in drug delivery research.

Kratky plot (Figure 2b) allows to qualitatively assess the flexibility or degree of unfolding in samples. This type of curve is characteristic of spherical micelles with the changing electron density for different lairs which can be obtained by the high amplitude of the curve. The bell-shaped curve with a rise on the right side is inherent in a folded well-structured part of the supramer. The bend of the curve means that there are unfolded parts on the surface.

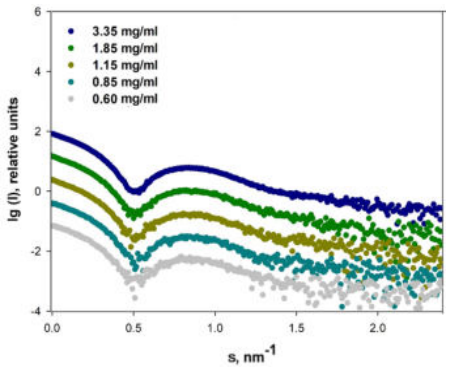

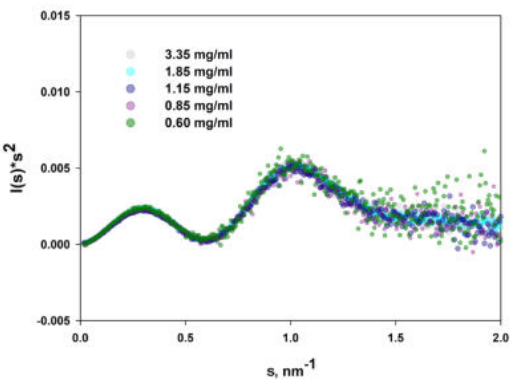

Figure 2 (a). SAXS data: the experimental curves corresponding to the range of sample concentrations 0.60-3.35 mg/ml.

Figure 2 (b). SAXS data: Kratky plot corresponding to the range of sample concentrations 0.60-3.35 mg/ml.

- **Conclusion**

In present work we applied SAXS technique to characterize the structure of nanoparticles formed by self-assembly of glycan-containing FSL construct A(type2)-Ad-DE and to estimate its dependence on FSL concentration. From experimental data, it was found that nanoparticles have micelle-like architecture that is maintained in selected concentration range. For more details, we applied ab initio modeling that showed a good agreement with experimental data, and found that nanoparticles have ellipsoidal shape with monodisperse size about 14 nm in which glycan moieties are prone to clustering on nanoparticle surface where the clusters localization tends to octahedral symmetry.

The obtained results demonstrated that, like FSL in which biotin is a functional group [5], the studied A(type2)-Ad-DE molecules also self-assemble into well-structured nanoparticles. The studies performed by the SAXS technique provided an experimental basis for constructing a computational model of such nanoparticles. As a result, their architecture was determined. It has been shown that this micelle-like architecture is maintained in a range of concentrations. Due to the presence of glycan moieties on the nanoparticle surface, such nanoparticles can serve as a convenient research tool for studying drug delivery research.

Acknowledgments

The research was supported by the Ministry of Education and Science of the Russian Federation, Goszadanie 2019-1080 and 0101-2019-0012. In the part of computer calculations and the design of nanoparticles the research was funded by the project number 075-15-2020-773.

References

[1] Blake, D. A., Bovin, N. V., Bess, D., Henry, S. M. FSL Constructs: A Simple Method for Modifying Cell/Virion Surfaces with a Range of Biological Markers Without Affecting their Viability. J. Vis. Exp. 2011, (54), e3289

[2] Gallo J, García I, Genicio N, Padro D, Penadés S. Specific labelling of cell populations in blood with targeted immuno-fluorescent/magnetic glyconanoparticles. Biomaterials. 2011, 32(36), pp.9818-9825.

[3] Maron E, Nutt D. Biological markers of generalized anxiety disorder. Dialogues Clin Neurosci. 2017, 19(2), pp.147-158.

[4] Yuan B, Chen Y, Sun Y, et al. Enhanced Imaging of Specific Cell-Surface Glycosylation Based on Multi-FRET. Anal Chem. 2018, 90(10), pp.6131-6137.

[5] Zalygin A., Solovyeva D., Vaskan I., Henry S., Schaefer M., Volynsky P., Tuzikov A., Korchagina E., Ryzhov I., Nizovtsev A., Mochalov K., Efremov R., Shtykova E., Oleinikov V., and Bovin N., Structure of Supramers Formed by the Amphiphile Biotin‐CMG‐DOPE. ChemistryOpen, 2020, 9(6), pp.641–648.

[6] Zhou, J., Kroll, A. V., Holay, M., Fang, R. H., & Zhang, L. Biomimetic Nanotechnology toward Personalized Vaccines. Advanced Materials, 2019, 1901255

[7] Chen, H.-Y., Deng, J., Wang, Y., Wu, C.-Q., Li, X., & Dai, H.-W. Hybrid cell membrane-coated nanoparticles: a multifunctional biomimetic platform for cancer diagnosis and therapy. Acta Biomaterialia. 2020, 112, pp.1-13

TEM use for the study of chitosan microspheres and nanospheres obtained from its salts with several acids

Khakimova A.A., Pominov V.V., Babicheva T.S., Shmakov S.L., and Shipovskaya A.B.

Chair of Polymers, Institute of Chemistry, Saratov State University, 83 Astrakhanskaya St., Saratov 410012, Russian Federation

e-mail: konduktorova.anastasiya@gmail.com

Abstract. Chitosan nanospheres and microspheres obtained by neutralizing the salt form (glycolate and tartrate) of the polymer with triethanolamine in emulsion were studied by transmission electron microscopy. The size of spherical structures is estimated from 50 nm to 115 μm. The effect of the acid nature o on the formation of microspheres and nanospheres is shown.

1. Introduction

Currently, much attention is paid to obtaining materials to become matrices for biologically active and medicinal substances. The biocompatibility of chitosan, its low toxicity and biodegradability make this polymer attractive for medical applications [1, 2]. The use of biologically active acids in combination with chitosan will allow us to expect a synergistic effect and expand the scope of spherical structures of microsizes and nanosizes. However, it is necessary to control both the size of the resulting spheres and the structure of their walls, which transmission electron microscopy (TEM) can be successfully applied for. In this work, this method was used to examine the effect of the acid nature on the formation of microspheres and nanospheres obtained in the process of the interfacial reaction of the polymer-analogous salt→base transformation of chitosan.

2. Experimental methods

Microspheres and nanospheres obtained from chitosan solutions in aqueous glycolic and tartaric acids were chosen as objects of our study. An aqueous triethanolamine solution served as a neutralizing agent. Samples were obtained by coacervation in two stages. First, an emulsion was prepared by mixing vegetable (sunflower) oil with a chitosan solution in aqueous glycolic or tartaric acid under stirring (1,000 rpm), and the system was kept on a stirrer for 3 min. At the second stage, the neutralizing agent (TEA) was added and the system was kept for an hour on the stirrer until dispersion was formed. The mass ratio of all three liquids was varied. The size of solid objects was estimated by TEM using a MIRA\\LMU microscope at an accelerating voltage of 30 kV and a conducting current of 400 pA with a dark and bright field detector (TED/TEB). To do this, the resulting dispersion was centrifuged (12,000 rpm) for 5 min, the upper part of the oil phase was removed and dispersed in water. The procedure was repeated 5 times. Next, the aqueous dispersion was applied to an aluminum substrate coated with formvar and dried under vacuum on a K450X Carbon Coater for 5 min.

3. Results

The studied dispersions of the chitosan-containing system with variable mass oil:chitosan salt:TEA ratios were unstable and delaminated into few layers, namely: oil layers without and with a small fraction of dispersed particles, and a layer of solid white sediment. The use of chitosan tartrate made it possible to obtain more stable systems, especially at a mass oil:chitosan salt:TEA ratio = 1:2:1. The size of the obtained spherical chitosan structures depended on the volume ratio of the aqueous (chitosan solution and TEA solution) and oil media. TEM made it possible to establish that the size of solid-phase spherical structures varied within ~50 nm–115 μm and ~2.7–33 μm for chitosan tartrate and glycolate, respectively. These sizes are comparable with currently known analogs obtained with the use of chitosan acetate and NaOH (~0.5–10 μm) [3].

Thus, the spherical structures obtained from a chitosan solution in tartaric acid had a larger range of sizes, in contrast to those obtained in glycolic acid. TEM was used to find a relationship between the size of the obtained chitosan microspheres and nanospheres and the ratio of the aqueous (chitosan solution and TEA solution) and oil media, which would make it possible to obtain capsules of a given size in the future.

References

[1] Butstraen C., Salaün F. 2014. Carbohydrate Polymers. **99**. *608-616*.

[2] Valente J.F.A., Gaspar V.M., Antunes B.P., Countinho P., Correia I.J. 2013. Polymer. **54**. *1. 5-15*.

[3] Tokumitsu H., Ichikawa H., Fukumori Y., Block L.H. 1999. Chemical and pharmaceutical bulletin. **47**, *6*, *838–842*.

Colorimetric detection of tyrosine with silver nanoparticles and tyrosinase

Chuiko Ya. V.[1], Reveguk Z.V.[1], Buglak A.A.[1], Kononov A. I.[1]

[1]Department of Molecular Biophysics and Polymer Physics, Saint-Petersburg State University, 199034 Saint-Petersburg, Russia
mareckawert@gmail.com

Abstract. A new, simple and rapid colorimetric technique of tyrosine (Tyr) detection was developed. It is based on the oxidation of Tyr to L-dioxyphenylalanine (L-DOPA) with subsequent reduction of Ag^+ ions leading to silver nanoparticles (Ag NPs) formation. Ag NPs have strong plasmonic band visible by naked eye and easily detected using a UV-vis spectrophotometer.

1. Introduction

Tyrosine is one of the essential amino acids in the human body, and it is used for the synthesis of neurotransmitters and melanin. The lack of tyrosine is an attribute of nervous system diseases, phenylketonuria and vitiligo. Consequently, a simple, cost-effective quantitative assay for Tyr detection is necessary. In this study, we developed a novel, method of colorimetric Tyr detection based on Ag NPs synthesis using L-dioxyphenylalanine. L-DOPA is the product of Tyr hydroxylation by tyrosinase (TR) enzyme which is used by multiple Tyr detection methods [1].

2. Experiment

A typical protocol of silver NPs was as follows: L-Tyr was dissolved in water (C = 50 μM) at pH=8.5, controlled with NaOH. Then TR (10 U/mL), $CuSO_4$, $AgNO_3$ (100 μM) were added. The samples were kept at 20 °C in a thermostat. The absorbance spectra were recorded with Specord210 plus after 15 min. Values of pH were measured using Hanna HI220 pH-meter equipped with Hanna microelectrode.

3. Results and discussion

3.1. Synthesis of silver nanoparticles.

Figure 1 shows the absorbance spectra of two samples containing L-Tyr, TR and $CuSO_4$ with and without $AgNO_3$ at pH 8.5. Blue curve has a plasmonic band at 400 nm typical of Ag NPs of spherical shape and small sizes [2]. The green curve has an absorbance maximum at 475 nm which refers to dopachrome [3]. The formation of dopachrome was observed in the case of silver absence.

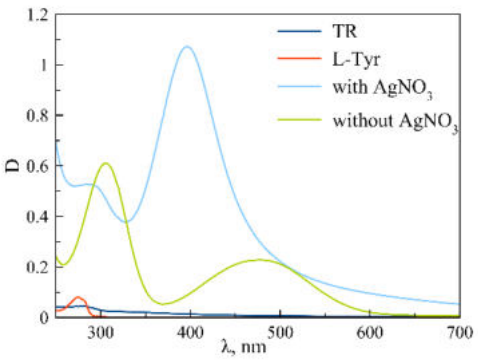

Figure 1. Absorption spectra of Tyr/TR solutions with and without silver nitrate

3.2. Ag NPs synthesis optimization: $CuSO_4$ concentration and pH.

Figure 2 shows the absorbance spectra of solutions at pH 8.5 containing different amount of $CuSO_4$. It was found that the $CuSO_4$ concentration of 2.5 μM is optimal. And these conditions were used for further experiments. Also, the dependence of the absorbance maximum on pH is shown in Fig. 3. At pH 8-11, silver nanoparticles demonstrate a noticeable absorption band. It appeared that the method was not selective at pH > 9. Therefore, we chosen pH 8.5 for further experiments.

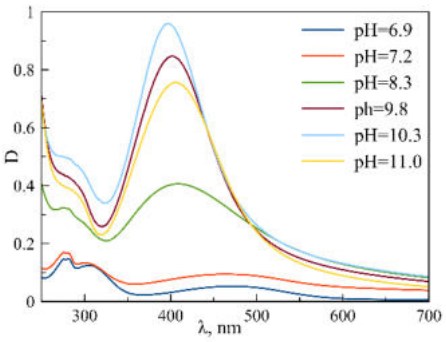

Figure 2. Absorption spectra of L-DOPA - Ag NPs complexes with different concentrations of $CuSO_4$

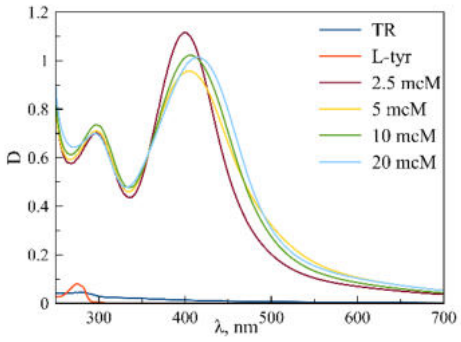

Figure 3. Absorption spectra of L-DOPA - Ag NPs complexes at different pH values.

4. Conclusion

The colorimetric method of Tyr detection has been developed. 2.5 μM $CuSO_4$ and 8.5 pH are found to be the optimal conditions. In further, we are planning to determine the limit of detection and test the method with human serum.

Acknowledgments The work was supported by the Russian Science Foundation grant No. 20-73-10029.

References

[1]Chen H.-Y., Yeh Y.-C. Detection of tyrosine and monitoring tyrosinase activity using an enzyme cascade-triggered colorimetric reaction // RSC Adv. 2020. Vol. 10, № 50. P. 29745–29750.

[2]Rubira R.J.G. et al. Designing Silver Nanoparticles for Detecting Levodopa Using SERS // Sensors. 2019. Vol. 20, № 1. P. 15.

[3]Aroca P. et al. A new spectrophotometric assay for dopachrome tautomerase // Journal of Biochemical and Biophysical Methods. 1990. Vol. 21, № 1. P. 35–46.

Comparative analysis of nanosized structures in thin hydrogel plates of chitosan L- and D-ascorbate–hydrochloride

A B Shipovskaya, N O Gegel, and T S Babicheva

Department of Polymers, Saratov State University, Saratov State University 83 Astrakhanskaya St., Saratov 410012, Russian Federation

Shipovskayaab@yandex.ru

Abstract. Transmission electron microscopy (TEM) and small-angle X-ray scattering (SAXS) were used to explore the supramolecular structure of thin hydrogel plates of chitosan L- and D-ascorbate–hydrochloride. A comparative analysis of the morphology and average size of phase inhomogeneities and their bulk distribution in the material depending on the ascorbic acid isomer (L or D) was carried out.

In recent years, along with the dynamically developing biomedical lead of using the aminopolysaccharide chitosan, there is great interest in obtaining thin-film nanocomposite materials based thereon for solving applied problems of optoelectronics and optosensorics, in particular, for designing highly sensitive and highly selective planar waveguides, SPR and GRS detectors, and optical sensors for analytical applications [1, 2].

In this work, the structure of thin hydrogel plates of chitosan L- and D-ascorbate–hydrochloride was explored by TEM and SAXS. It has been established that the materials differ in supramolecular ordering and dimensional characteristics of phase inhomogeneities. The intensity curves of small-angle X-ray scattering have no Bragg peaks to indicate the amorphous structure of the samples. The average sizes of macromolecular domains calculated therefrom were 15–168 Å and 25–188 Å for plates obtained from chitosan solutions in L- and D-ascorbic acid, respectively. The TEM images of plates made from chitosan L-ascorbate–hydrochloride reveal more branched supramolecular structures with a smaller branch width than those made from chitosan D-ascorbate–hydrochloride. For both plates, a bimodal character of the bulk size distribution of phase aggregates with two maxima is observed. The first peak shows the presence of nanoscale structures, whose scale for chitosan L- and D-ascorbate–hydrochloride lies in the range of 20–80 nm and 25–70 nm, respectively. The relative contribution of nanosized aggregates to the phase polydispersity is significantly higher for samples made from chitosan D-ascorbate–hydrochloride.

Acknowledgments

The study was supported by a grant from the Russian Science Foundation № 22-23-00320.

References

[1] Yoon S H, Jeong W T, Kim K C, Kim K J, Oh M C, Lee S M 2011 *J Surf Eng Mater Adv Technol* **1**(2) 56.

[2] Voznesenskiy S S, Sergeev A A, Mironenko A Y, Bratskaya S Y, Kolchinskiy V A 2012 *Tech Phys Lett* **38**(3) 228.

Porous silicon nanocontainers for targeted drug delivery

D A Shishkina, I A Shishkin, A V Shishkin

Samara National Research University, Samara, 443086, Russia

daria.lizunkova@yandex.ru

Abstract. Nanocontainers based on solid materials have great potential for drug delivery. Nanodelivery systems typically improve the biodistribution of drugs, resulting in reduced side effects and improved therapeutic efficacy. In this paper, we study the issue of using porous silicon produced by electrochemical etching to create nanocontainers for targeted drug delivery. The functional composition of the surface of the synthesized samples is controlled depending on the anodization current density. The effect of etching modes on the characteristics of porous structures is shown - the thickness of the porous layer, porosity. Nanocontainers containing the broad-spectrum antibiotic Ceftriaxone have been created.

1. Introduction

Nanotechnology has provided new tools to address unresolved clinical situations, especially in the treatment of complex diseases such as oncology. The development of "smart" nanocarriers capable of delivering chemotherapeutic agents specifically to diseased cells and releasing them in a controlled manner offers a huge advantage over conventional therapy. Among the types of nanoparticles that can be used for this purpose, much attention is paid to inorganic porous materials due to their unique properties, such as high load capacity, chemical and physical stability, low toxicity, and ease and low cost of production.

To create nanocontainers based on porous silicon, it is necessary to take into account a number of its characteristics, namely, the pore size, the chemical composition of the surface, porosity, and the electronic state of the por-Si surface [1]. The chemical composition and electronic state of the por-Si surface are important for studying the mechanisms of loading a drug into nanocontainers, as well as possible chemical interactions and features of drug action. It is difficult to take into account all the parameters of obtaining porous silicon at once, since there are many uncontrollable factors of the source material: the type of conductivity, the concentration of the dopant, structural defects, etc. In addition, the etching modes, the composition of the etchant have a strong influence on the parameters of the porous layer. In this work, the dependence of porosity on the etching time and current density is considered.

2. Experiment

To create nanostructures, silicon p-type with a crystallographic orientation (100) was used. The silicon structures were preliminarily purified in an ammonia peroxide solution, after which they were subjected to electrochemical etching in a vertical cell [2]. Etching modes are presented in Table 1. The morphology of the samples was studied using a NEOPHOT 21 optical microscope.

Table 1. Etching modes

№	t, min	j, mA/cm^2	electrolyte composition
2	30	30	HF+C_2H_5OH
3	30	30	HF+C_2H_5OH
4	30	20	HF+C_2H_5OH
5	30	30	HF+C_2H_5OH
7	30	30	HF+C_2H_5OH
15	30	30	HF+C_2H_5OH
17	30	20	HF+C_2H_5OH
19	30	20	HF+C_2H_5OH
20	30	20	HF+C_2H_5OH
21	30	30	HF+C_2H_5OH
22	30	20	HF+C_2H_5OH
23	30	20	HF+C_2H_5OH

3. Results

Figure 1 shows the image of porous structure cleavage.

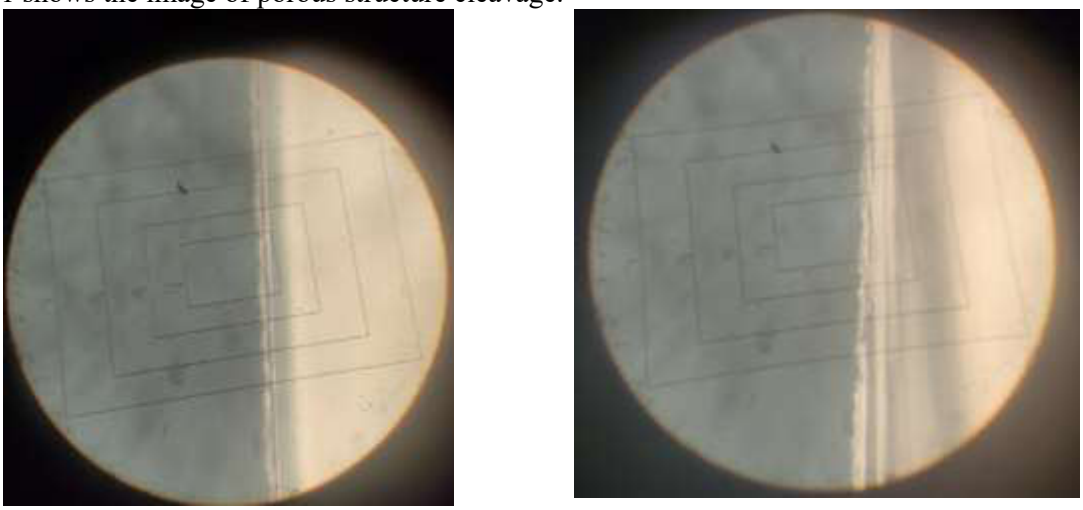

Figure 1. Image of transverse cleavage of structures fabricated with a current density of 20 mA/cm^2 (a) and 30 mA/cm^2 (b).

The figures show a noticeable effect of the current density on the thickness of the porous layer. The porous layer thickness of the obtained structures varied from 25 to 38 μm. The porosity of such structures ranged from 5 to 10%. Next, the nanocontainers were filled with the broad-spectrum antibiotic Ceftriaxone. Further study of the structures will include the manufacture of nanocontainers of various sizes in an ultrasonic bath for 30-60 minutes, as well as the study of their optical and physical properties.

Next, the samples were subjected to saturation with the drug from an aqueous solution, after which the upper layer of pores with the drug was scraped off the surface with a scalpel. The resulting powder was subjected to grinding in an ultrasonic bath from 10 to 50 minutes with a step of 10 minutes. One of the preparations acted as a control. Images obtained from an optical microscope are shown in figure 2.

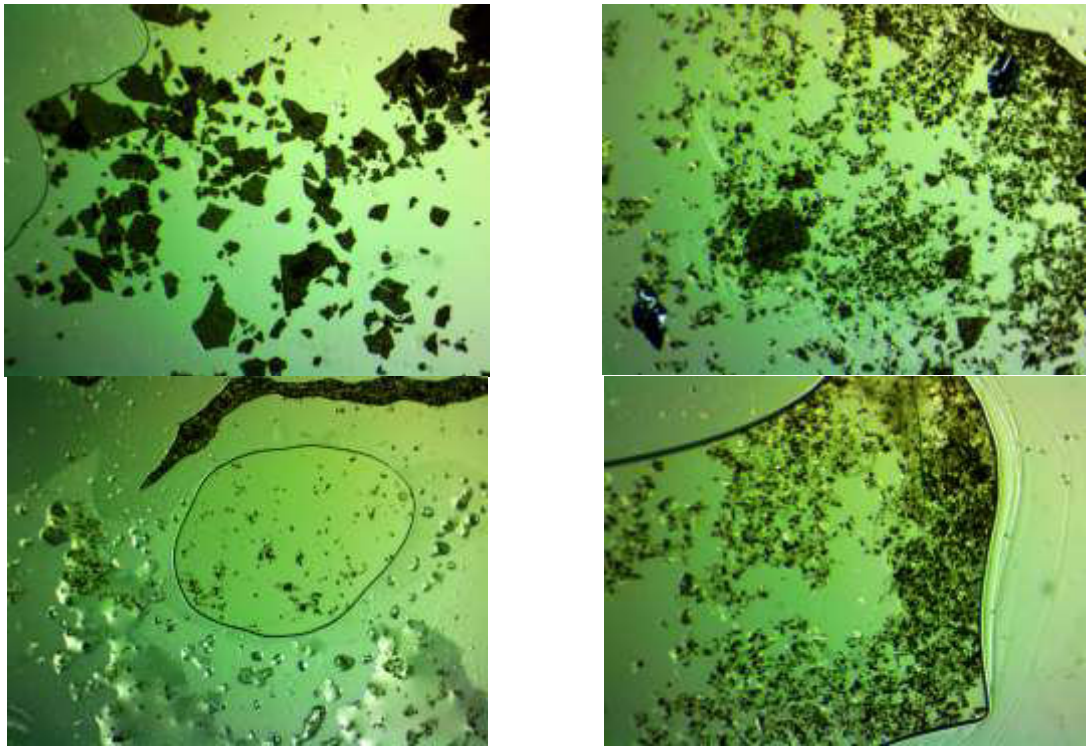

Figure 2. Image of porous silicon nanocontainers, initial (a) after 10-minute treatment with ultrasonic waves (b); after 40 minutes of treatment with ultrasonic waves (c); after 50 minutes of ultrasonic treatment (d).

From the analysis of the figures it can be seen that there is a dependence of the impact of ultrasonic waves on time. This method allows to obtain particles of smaller size, which can already be used depending on the specific application.

4. Conclusion

In the course of the work, the morphology of porous silicon samples was studied. Based on the main regularities of the formation of por-Si, the conditions for etching porous silicon were chosen to ensure the production of por-Si with the required characteristics. Nanoparticles have been created to load a wide range of drugs.

References

[1] Abramova E N, Khort A M, Yakovenko A G, Lvovsky A I, Slipchenko E A, Prokhorov D I, Shvets V I 2018 *IOP Conf. Series: Materials Science and Engineering* 347 **012048**

[2] Shishkin I A, Lizunkova D A, Latukhina N V 2020 *Information technologies and nanotechnologies (ITNT-2020): Sat. tr. Based on the materials of the VI Intern. conf. and youth. school (Samara, May 26-29): in 4 volumes - Tek / Ministry of Science and Education Ros. Federation, Samar. nat. research un-t im. S. P. Koroleva (Samar. Univ.), Institute of Systems Processing. fig. RAS - Phil. FSRC "Crystallography and Photonics" RAS. At* **1** pp. 27-30

Investigation of fluorescent properties of NADH-ADH complex in presence of natural enzymes by means of time-resolved polarization spectroscopy.

D.V. Yashkov[1], I.A. Gorbunova[2], M.E. Sasin[2], A.D. Vedyaykin[1] and O.S. Vasutinskii[2].

[1]Ioffe Institute, Russian Academy of Sciences, St. Petersburg, Russia.
[2]Peter the Great St.Petersburg Polytechnic University, St. Petersburg, Russia.

yashkovddd@gmail.com

Abstract. This paper presents the results of the studies of polarized fluorescence in NADH-alcohol dehydrogenase (ADH) complex in a mixture of natural enzymes. Fluorescence spectra and fluorescence decay signals in ADH solution was observed under two-photon excitation at 720 nm and 840 nm. As a result of analysis of the fluorescence decay signals, fluorescence decay times τ_i and weighting coefficients a_i were determined.

1. Introduction

Nowadays the study of spectral properties of natural intracellular fluorophores in solutions and in living cells using fluorescence polarization spectroscopy with high temporal resolution has found wide applications in biomedical technologies. Reduced nicotinamide adenine dinucleotide (NADH) is an important intracellular fluorophore that regulates ~~of~~ oxidation-reduction reactions in living cells. As reported recently [1, 2] fluorescent properties of NADH: decay times, anisotropy, ets are very sensitive to the changes of microenvironment conditions. In particular, blue shift in NADH fluorescence maximum and increase in fluorescence decay times were observed [2 - 4] upon NADH binding with ~~the~~ enzymes in the course of redox reactions. However, despite a number of studies performed the problem of separation of NADH fluorescence signals in the presence of other natural fluorophores still has to be addressed.

2. Experimental method

A femtosecond Ti:Sapphire oscillator tunable in the spectral range of 690-1040 nm, with a pulse duration of 100 fs and a repetition rate of 80 MHz was used as excitation source. The average power of the laser beam focused onto the cuvette was at about 600 mW. The fluorescence was collected in the direction perpendicular to the excitation beam and then passed through a narrow-band filter to isolate the fluorescence at 436 nm or 470 nm. The orthogonal fluorescence components were separated by a Glan prism, and then recorded simultaneously by two avalanche photodiodes operating in the photon counting mode. The electrical signals from the photodiodes were processed by a time-correlation single photon counting system TCSPC with a time bin of 4 ps.

3. Results and discussion

The fluorescence spectra of the ADH measured under two-photon excitation at 720 nm and 840 nm are shown in figure 1 (a).

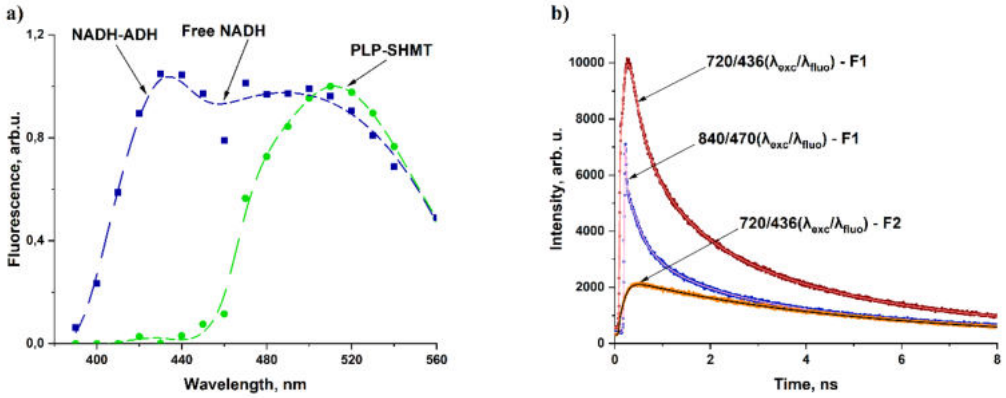

Fig. 1. a) The fluorescence spectra of the ADH under two-photon excitation at 720 nm (blue squares) and 840 nm (green circles). The arrows indicate the estimated fluorescence maxima of substances contained in the reagent ADH. b) Polarization-independent (isotropic) fluorescence decay signals of ADH fractions.

As can be seen in Fig. 1 (a) under excitation at 720 nm two fluorescence maxima at 425 ~~nm~~ and 510 nm were observed while under excitation at 840 nm only the second maximum remained. We suggest that the fluorescence maximum at 510 nm arose due to existence of others fluorescing enzymes in the initial ADH reagent. To analyze the enzymatic composition of the initial ADH reagent chromatograph purification was carried and then the obtained ADH fractions were analyzed by means of mass spectrometry analysis. The fluorescing enzymes serine hydroxymethyl transferase (SHMT) and isocitrate dehydrogenase (ICDH) were identified through the analysis. Then polarized fluorescence decay signals of the pure ADH fraction (F1) and ADH fraction containing SHMT and ICDH (F2) were studied at various excitation and emission conditions. The fluorescence decay signals observed are shown in Fig. 1 (b). The fluorescence decay times τ_i and weighting coefficients a_i were determined from the experimental data in Fig. 1 (b). The fluorescence decay signals from the sample F2 were well fitted only by the sum of four exponentials and the fluorescence decay signal from the sample F1 was found to be a single exponential under excitation at $\boldsymbol{\lambda_{exc}}$ = 720 nm and did not fluoresce at all under excitation at 840 nm. Thus, in this paper the fluorescence from the NADH-NADH complex was isolated from a mixture of others fluorescent enzymes. According to the results of mass spectrometry, all the enzymes under study had almost the same weights that complicated their purification without the loss of activity.

References

[1] Gorbunova I. A., Sasin M. E., Rubayo-Soneira J., Smolin A. G. and Vasyutinskii O. S. "Two Photon Excited Fluorescence Dynamics in NADH in Water–Methanol Solutions: The Role of Conformation States" J. Phys. Chem. B 124(47), 10682–10697 (2020).

[2] Blacker T.S., Duchen M.R." Investigating mitochondrial redox state using NADH and NADPH autofluorescence" Free Radic. Biol. Med., 100, 53–65 (2016).

[3] Konig K., Berns M. W. and Tromberg B. J. "Time-resolved and steady-state fluorescence measurements of ¨ βnicotinamide adenine dinucleotide-alcohol dehydrogenase complex during UVA exposure" J. Photochem. Photobiol. B 37(1-2), 91–95 (1997).

[4] Gorbunova I. A., Sasin M. E., Golyshev D. P., Semenov A. A., Smolin A. G., Beltukov Y. M. and Vasyutinskii O. S. "Two-Photon Excited Fluorescence Dynamics in Enzyme-Bound NADH: the Heterogeneity of Fluorescence Decay Times and Anisotropic Relaxation" J. Phys. Chem. B 125(34), 9692–9707 (2021).

Development of a device for picoampere currents measuring

O A Mikhailova[1], I E Antifeev[2], D G Petrov[2] and R V Davydov[1, 3]
[1]Peter the Great Saint-Petersburg Polytechnic University, Saint Petersburg, Russia, 195251
[2] Institute of Analytical Instrumentation of the Russian Academy of Sciences, 198095, Russia
[3]All-Russian Research Institute of Phytopathology, Moscow Region 143050, Russia

e-mail: lesya101201@gmail.com

Abstract. One of the actual topics in microelectronics is the problem of measuring small currents. This paper shows the circuit design of a device for measuring picoampere currents. We proposed the principle of measuring currents, based on the amplifier circuit with differential inputs. As a result of the experiments, the range of values of the measured current was determined: 500pA – 1nA.

1. Introduction

The problem of measuring small currents remains relevant in modern science. For this task, various circuit solutions can be used. One of the most widely used is the use of a resistive current sensor [1] [2] [4]. The principle is based on the dependence of voltage on the current passing through the measuring resistor. The advantage of this method of current measurement is the ease of use in DC circuits.

An alternative way to solve the above problem is to use Hall effect microcircuits [3]. The principle of operation is based on the occurrence of an electric voltage on a magnetically sensitive element under the influence of a forming magnetic field, which appears as a result of the passage of an electric current through a nearby conductor. The main advantage of this measurement method is the absence of a resistive shunt, which leads to the absence of unwanted release of thermal energy during measurement. Circuits based on the use of current transformers were not considered by us, since they are designed for measurement in alternating current circuits, which does not correspond to our tasks. Both of the measurement methods discussed above have proven themselves in industry and household appliances and can be applied to solve the problem of analyzing small currents, but these solutions will lead to complex technical and technological solutions. Thus, the purpose of this work is to create a circuit solution that allows you to measure picoampere currents with high accuracy. We have proposed a method for measuring currents based on the use of an amplifier with differential inputs. The advantage of this circuit is that the high-resistance measuring resistance is divided between two identical elements, which are physically mounted in the same orientation and at the same distance from the source of magnetic interference. Interference induced on two resistors, in this case, create the same signals, which are suppressed at the output of the amplifier [4].

2. Materials and methods for solving the problem

To solve this problem, we have developed a stand for testing the device for measuring picoampere currents. The test bench consists of measuring block, D/A. Converter Module and Special software.

The measuring unit consists of a differential amplifying stage, followed by a signal amplification circuit on an operational amplifier. The input nodes of the differential amplifying stage are implemented on AD8641AK operational amplifiers, which allow measuring picoampere currents. The digital-to-analogue converter module is implemented on the basis of an external input-output module L-CARD E20-10. This is a high-speed four-channel ADC module with a USB interface for connecting to a PC. FPGA-based architecture with one ADC, switch and input buffer amplifiers in sequentially polled channels completely eliminates switching noise, third-order active low-pass filters in each channel improve the signal-to-noise ratio. Of the advantages of this ADC, among others, one can note the galvanic isolation of each channel, which provides high noise immunity.
To register, visualize, and process the analog signal, special software LGraph 2(program) was used, adapted to work with an external ADC L-CARD E20-10.

3. Measurement results

The measuring stand created in the course of this work has the following characteristics:

Table 1. Measured and calculated parameters.

	Calculated value	Experimental value
Range of measured currents	10pA-10nA	500pA-1nA
Measuring frequency range	0Hz – 10κHz	0Hz – 1κHz
Maximum measurable resistance	100MOm	10MOm

The experimentally obtained frequency values fall within the analytical calculated range of values, the experimental values of resistance and current do not satisfy the values obtained analytically.

4. Conclusion

As a result of the data obtained, we were convinced that the proposed circuit design solution corresponds to the specified characteristics. The measuring stand allows measuring picoampere currents with an accuracy of +-50pA, and the results obtained correlate with the theoretical parameters of the circuit. A significant disadvantage of the measuring unit is the large leakage currents associated with the relatively low, compared with the analyzed samples, the resistance of the insulating material. In the manufacture of the measuring unit, a printed circuit board based on FR4 insulating material was used, which does not allow achieving a high electrical resistance. This parameter can be improved by using a separator based on polytetrafluoroethylene (PTFE).

References

[1] Salakhov R F and Miskov D N 2015 *Tests. Quality control and management* **3** 59-62
[2] Wenn D 2011 *Components and technology* **7** 156-158
[3] Sakharov K Y, Turkin V A, Mikheev O V, Sukhov A V, Ugolev V L and Denisov M Y 2020 *EMC Technologies* **1 (72)** 63-70
[4] Hobbs P 2009 *Components & Technologies* **3** 48-49

Electrical Characteristics of $CsPbI_3$ and $CsPbBr_3$ Lead Halide Perovskite Nanocrystal Films Deposited on Si-C Solar Cells for High Efficiency

L Boudjemila[1], V V Davydov[1, 2, 3], A N Aleshin[2], V M Malyshkin[4,] and E I Terukov[4]

[1]Peter the Great Saint-Petersburg Polytechnic University, Saint Petersburg, Russia, 195251
[2]The Bonch-Bruevich Saint-Petersburg State University of Telecommunications, Saint Petersburg 193232, Russia
[3]All-Russian Research Institute of Phytopathology, Moscow Region 143050, Russia
[4]Ioffe Institute, St. Petersburg, Russia

e-mail: lariessai21@gmail.com

Abstract. The high efficiency of hybrid solar cells based on nanoparticles to improve optical and electrical performances is the subject of much current research. For this purpose, the results of the following research, nanoparticles of perovskite $CsPbI_3$ and $CsPbBr_3$ are used, their optical properties provided a good interaction with crystallin silicon (Si-c), absorption coefficient (α) is significantly high in different ranges which increases the generation of photocurrent in the range 370-900nm. Degradation factor reduces fast the efficiency and for precise results, it requires developed equipment. $CsPbI_3$ showed a textured surface while $CsPbBr_3$ is smooth according to this all results showed a better measurement for iodine.

1. Introduction

A recent study of tandem solar cells at Oxford found that the best way to improve Si-c efficiency at present is to apply additional perovskite films. To this end, the interest of our work is mainly focused on how to improve the optical and electrical properties of a solar cell by depositing films of iodine and bromine perovskite nanoparticles having significant absorption/emission and higher photoluminescence quantum yields. This is due to the large exciton binding energies and longer lifetimes (diffusion lengths) compared to bulk crystals. [1].

The lead halide (Ncs) perovskite nanoparticles $CsPbI_3$ and $CsPbBr_3$ used in subsequent work were deposited on a crystalline silicon substrate coated with a conductive ITO layer. They are characterized by a respectively tunable band gap between 2.85 eV and 2.34 eV [2], while silicon has a band gap of 1.2 eV, which creates a diverse heterostructure with a wider overall band gap.

2. Materials and Methods

The structure of the perovskite solar cells is ITO/(n)a-Si:H(p)/a-Si:H/ITO/$CsPbI_3$ or $CsPbBr_3$ main fabrication procedure is shown in Figure 1(a). The Si-c substrates were provided by Research and development center for thin-film technologies in energetics **R&D Center TFTE LLC** conserved under vacuum condition to avoid any contamination. A compact $CsPbI_3$ and $CsPbBr_3$ precursor solution provided by chemistry lab of LETI university. This last was spin-coated on the textured conductive

ITO/Si-c substrates at 2000 rpm for 30s and subsequently in the oven at 120 °C for 10 min. Finally, an 80 nm ITO electrode was deposited on the top of the device using thermal evaporation. The morphological properties of the samples were characterized by scanning probe microscopy atomic force microscopy (AFM) whose measurement of the surface roughness is carried out by the fluctuation of cantilever. Photocurrent current-voltage (IV) curves of solar cells were measured with a Keithley 2400 source meter under simulated handmade lamp illumination at a calibrated solar simulator intensity of 50 mW/cm^2 at room temperature in the air, and the scan direction is from open circuit at 0.5V to short circuit at -0.5V. Steady-state photoluminescence (PL) spectroscopy was measured with an excitation wavelength of 375 nm [3].

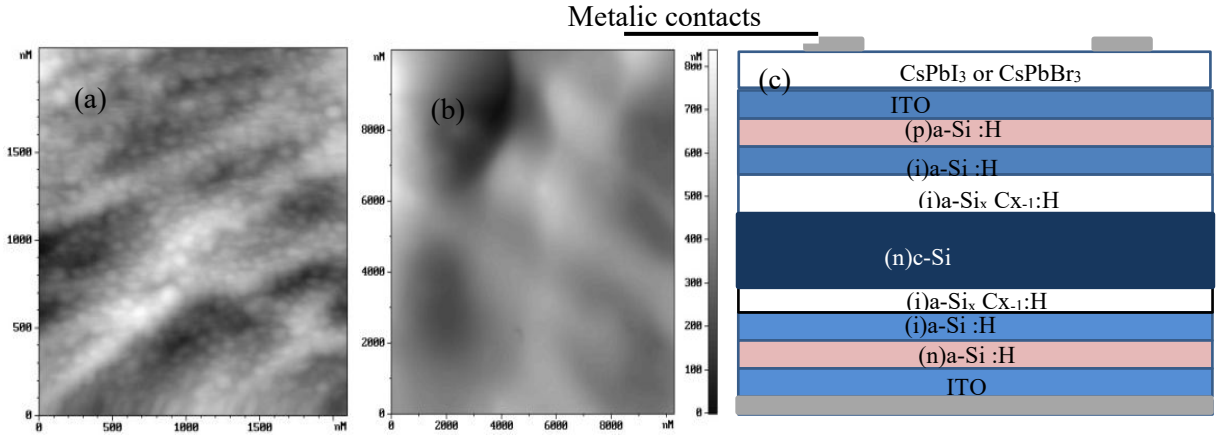

Figure 1. Surface morphologies of Atomic Force Microscopy (AFM) images of the with $CsPbI_3$ and $CsPbBr_3$ to (a) (b) respectively. Illustration of device structure labeled (c).

3. Results of experimental measurements

The morphological characterization was examined using an atomic force microscope (AFM) on two types of Ncs. A noticeable difference in the texture of the surfaces for $CsPbBr_3$, which is smooth and flat with a complete absence of any spherical structure, unlike $CsPbI_3$, a spherical shape with different sizes was present with a random distribution, with an RMS value of: Sq = 10.32 nm and 12. 8 nm, respectively. Such a significant difference in RMS and average roughness can be explained by an increase in the size and density of $CsPbI_3$ crystals.

Reflection measurements also indicate this. For $CsPbI_3$, the absorption coefficient (α) is high in the range of 370–600 nm, while for bromine Ncs (α) it is lower, but in a different range from 530 to 900 nm. At the same time, the PL intensity of the Iodine Ncs films at ambient temperature is observed with a maximum peak of about 740 nm, and the PL intensity of the Bromine Nc film has a maximum of about 550 nm,

4. Conclusion

Thus, the light trapping caused by the textured surface after $CsPbI_3$ deposition, helps to provide an appropriated management for optical optimization of perovskite solar cells. Also, $CsPbI_3$ and $CspbBr_3$ interact differently with Si-c, which leads to different absorption peaks in different ranges, this improves the absorption of our heterostructure (before PNC fast degradation), for $CsPbI_3$ it is 350-450nm, and for $CsPbBr_3$ 530-850nm, which together can perfectly complement the absorption range. Further studies are planned to explore this latter in more depth. Also, $CsPbI_3$ exhibits better optical and electrical properties than $CsPbBr_3$.

References

[1] Jung S et al. 2020 *Nanomaterials* **10(4)** 710
[2] Giovanni. M 2020 *J. Phys. Chem. Lett.* **11(7)** 2490–2496
[3] Pan D, Fu Y, Chen J, Czech K J, Wright J C and Jin S 2018 *Nano Letters* **18** 1807

Wavelength stabilized laser module for pumping high-power fiber lasers

A. N. Ignatev, A. V. Fomin, S. R. Usmanov.
FSUE «RFNC-VNIITF named after Academ. E. I. Zababakhin», 456770, Snezhinsk, Russia

Polarization entanglement-enhanced optical gyroscope

George Alkhalil[1*], Andrei Gaidash[1,2], Anton Kozubov[1,2]

[1]Laboratory of Quantum Processes and Measurements, ITMO University, Saint Petersburg, Russia
[2]Department of Mathematical Methods for Quantum Technologies, Steklov Mathematical Institute of Russian Academy of Sciences, Moscow, Russia

[*]Gorg.kalel@yahoo.com

Abstract. In this work we propose a theoretical design of a polarization entanglement enhanced fibre optic gyroscope. This scheme uses polarization entangled states PES instead of path-entangled NOON-states. The advantages of using PES states over NOON states is that it eliminates the birefringent effect of a single-mode fibre coil. Another advantage of the suggested design is the reciprocal configuration which ensures that paths of both opposite photons travelling through all the optical components are perfectly equalized.

1. Introduction

Gyroscopes are devices used for measuring the angular velocity in navigation systems. Fiber optic gyroscopes (FOGs) are based on sagnac effect. Sagnac effect is the phase shift induced between two light waves moving in closed counterpropagating directions in a rotating frame [1].

Recently, it has been reported on the experimental realization of quantum-enhanced FOGs using path-entangled NOON-states [2] and via injection of squeezed vacuum [3].

Although theoretically using quantum measurements one can approach the Heisenberg limit, practically there are various sources of noise that degrade the system performance. For FOGs the birefringent, backscattering, and Kerr effects are three dominant noise sources that lower the gyroscope performance [4,5]. In this work we will discuss the birefringent effect and propose a scheme for quantum FOGs in which the birefringent effect can be eliminated.

2. Birefringent effect

The birefringent effect is the effect when the refractive index of a material depends on the polarization of light propagating through the material. In a FOGs, counterpropagating waves in single-mode fibres (SMF) having different state of polarization, they acquire different phase accumulation. This nonreciprocal phase accumulation results in a noisy signal and phase errors at the output [4].

For classical FOGs several techniques can be used to compensate for the birefringent effect [6,7], however, for quantum FOGs this problem requires a different approach. In the suggested scheme instead of using NOON state which consists of photons with different polarizations propagating in opposite directions, we have a dual-polarization counterpropagating photons figure 1. This scheme results in a suppression of the polarization nonreciprocity.

In the scheme in figure 1 the coincidence counts at ports 5 and 6 is

$$\langle \psi_{in} | a_5^+ a_6^+ a_6 a_5 | \psi_{in} \rangle = \frac{1}{2}(1 + cos4\varphi_s)$$

Where φ_s is Sagnac shift.

On the other hand, using NOON states in FOGs results in measurements proportional to $\sim(1 + \cos 4(\varphi_s - \beta))$ where β represents the change in the ellipticity of the input state of polarization.

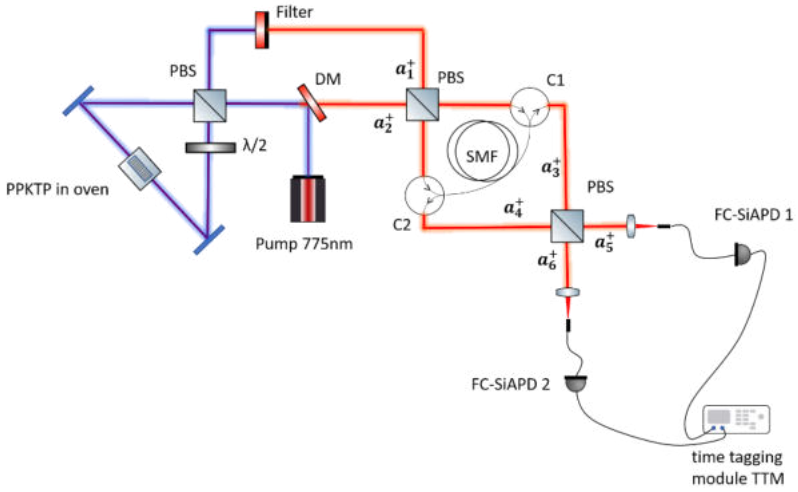

Figure 1 Schematic diagram of the optical setup for a polarization entanglement enhanced fibre optic gyroscope.

Comparing these two results we notice that our scheme totally suppresses the birefringent effect induced by the nonreciprocal phase shift.

Moreover, other advantage of this scheme is its symmetricity which eliminates any possible nonreciprocal phase shift experienced by the counterpropagating beams traveling through different paths.

Acknowledgments

This work was supported by the Ministry of Science and Education of the Russian Federation (Passport No. 2019-0903).

References

[1] Culshaw, Brian. "The optical fibre Sagnac interferometer: an overview of its principles and applications." Measurement Science and Technology 17.1 (2005).

[2] Matthias Fink, Fabian Steinlechner, Johannes Handsteiner, Jonathan P. Dowling, Thomas Scheidl, and Rupert Ursin. Entanglement-enhanced optical gyroscope. New Journal of Physics, 21(053010), (2019).

[3] Moritz Mehmet, Tobias Eberle, Sebastian Steinlechner, Henning Vahlbruch, and Roman Schnabel. Demonstration of a quantum-enhanced fiber Sagnac interferometer. Optics Letters, 35(10):1665, (2010).

[4] Pavlath, G. A., and Herbert J. Shaw. "Birefringence and polarization effects in fiber gyroscopes." Applied Optics 21.10 1752-1757 (1982).

[5] Seth W. Lloyd, Michel J.F. Digonnet, and Shanhui Fan. Modeling coherent backscattering errors in fiber optic gyroscopes for sources of arbitrary line width. Journal of Lightwave Technology, 31(13):2070{2078, (2013).

[6] Lin, Chu-En, and Chih-Jen Yu. "Heterodyne interferometry to eliminate the polarization effect in a fiber optic gyro." IEEE Photonics Technology Letters 26.19 1897-1899 (2014).

[7] Yang, Yi, Zinan Wang, and Zhengbin Li. "Optically compensated dual-polarization interferometric fiber-optic gyroscope." Optics Letters 37.14 2841-2843 (2012).

Optimization of InGaN-based luminescent heterostructures by genetic algorithm

D S Arteev[1], A V Sakharov[1], A E Nikolaev[1], E E Zavarin[1], A F Tsatsulnikov[2], V M Ustinov[3]

[1] Ioffe Institute, 194021, St. Petersburg, Russia
[2] Submicon Heterostructures for Microelectronics, Research & Engineering Center, RAS, 194021, St. Petersburg, Russia
[3] Peter the Great St. Petersburg Polytechnic University, 195251, St. Petersburg, Russia

e-mail: ArteevDS@mail.ioffe.ru

Abstract. A genetic algorithm was employed to optimize the doping profile of luminescent InGaN-based heterostructures. It was shown that a "parasitic" luminescence from GaN barriers could be suppressed while the efficiency remained the same as that of the best uniformly doped structure. Moreover, the optimized structure had lower total dopant concentration, what could be beneficial in terms of crystal quality.

1. Introduction

Optimization of the design of semiconductor structures for achieving a better performance has been a hot topic from the earliest days of semiconductor industry. Computer simulation is a very helpful tool in that process. However, it can be very difficult to find an optimal design of complex heterostructures due to enormous parameter space, especially when different parameters strongly affect each other, so conventional methods could be inefficient.

A very promising approach to overcome the so called 'curse of dimensionality' is a genetic algorithm (GA). It is inspired by the process of the natural selection and rely on such operators as crossover, mutation and selection [1]. This simple but power method is suitable for optimization tasks in different areas of science. It is not widely used in semiconductor device design yet, however, there are several works demonstrating its efficiency [2, 3, 4].

In this study, we employ a GA to optimize a Si doping profile of the GaN barrier layer in multiple-quantum-well (MQW) InGaN/GaN luminescent heterostructures.

2. Simulation details

The structure consists of three 1.5 nm $In_{0.11}Ga_{0.89}N$ quantum wells (QWs) separated with 31 nm GaN quantum barrier (QB) layer. The QB is divided to 10 sub-layers of different Si dopant concentration, representing a 'genotype' of the sample. Simulation was carried out using 1D-DDCC simulation software [5] for drift-diffusion part together with Python scripting for GA part. Doping-dependent carrier mobilities, lifetimes and dopant activation energy models were implemented.

3. Results

Obviously, internal quantum efficiency (IQE) is wanted to be high. It is also preferable to keep "parasitic" luminescence from QB low. Therefore, we chose the following fitness function:

$$F = IQE^{1.5} r = IQE^{1.5} \frac{R_{QW}}{R_{barrier}}$$

where, R_{QW} and $R_{barrier}$ is the radiative recombination rates in the QWs and Bs, respectively.

In order to calibrate the model, a set of samples with uniformly doped QBs, grown by MOVPE was investigated by photoluminescence, and the structures of the corresponding design were simulated. The maximum value F achieved is 6.3 (IQE=0.323, r=34.3) for Si doping of $2.2 \cdot 10^{18}$ cm^{-3}. Then, GA optimization, started with 21 structures with randomly assigned Si density in each sub-layer, was performed. After 100 generations, the best F achieved is 7.665 with the same IQE=0.333 and r=39.954, i.e. parasitic signal from GaN QB is suppressed. Figure 2 shows the total and ionized dopant concentrations in the best uniformly doped structure and in the optimized structure. As one can see, they differ significantly – there is a highly doped region just under the QW (i.e. near 0 at figure 2) that serve as a source of electrons for an upper QW, while the rest of the barrier is not highly doped to reduce radiative recombination in the barrier and enhance carrier transport. The total silicon concentration is reduced by 2.6 times, what could be beneficial in terms of crystal quality (and, as a result, in terms of non-radiative recombination, carrier transport and efficiency as well).

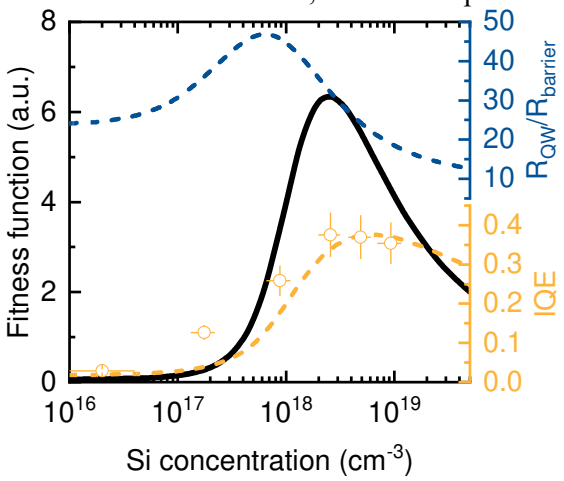

Figure 1. F, r and IQE vs. uniform Si doping concentration. Symbols are experimental PL intensities (in arb. unit).

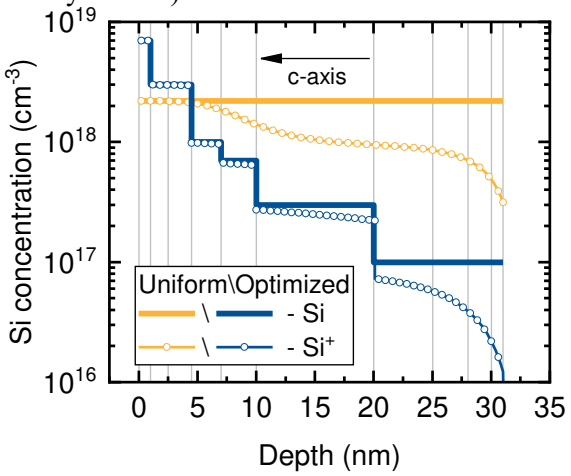

Figure 2. Total and ionized silicon concentrations in the barrier layer for uniformly doped and optimized structures.

Acknowledgments

The research is partially funded by the Ministry of Science and Higher Education of the Russian Federation as part of Strategic Academic Leadership program "Priority-2030" (contract No. 075-15-2021-1333 dated 30.09.2021)

References

[1] https://en.wikipedia.org/wiki/Genetic_algorithm

[2] Zhu D, Schubert M F, Cho J, Schubert E F, Crawford M H, Koleske D D, Shim H and Sone C 2012 *Appl. Phys. Express* **5** 012102

[3] Kim D Y, Lin G-B, Hwang S, Park J H, Meyaard D, Schubert E F, Ryu H-Y and Kim J K 2015 *IEEE Photonics J* **7** 1–9.

[4] Passaro A, Tanaka R Y, Muraro A, Vieira G S and Abe N M 2010 *IEEE Transactions on Magnetics* **46** 2759–62

[5] http://yrwu-wk.ee.ntu.edu.tw/index.php/ddcc-1d/

New challenges for 3D scanning over flat surfaces applied in Cultural Heritage: The tombstone of the bishop Vasilije Petrović (Negosh) in Saint Petersburg

P D Badillo[1], **V A Parfenov**[1], **R Raspopović**[2] **and V O Tishkin**[3]

[1] Saint Petersburg Electrotechnical University (SPbETU "LETI"), St. Petersburg, 197376, Russia
[2] University of Montenegro, Podgorica, 81000, Montenegro
[3] ITMO University, St. Petersburg, 197101, Russia

pbadillo@gmail.com

Abstract. 3D laser and optical scanning techniques are widely employed in Cultural Heritage for creating documentation of pieces of different sizes and shapes. However, due to limitations of the methods available today, the results obtained vary according to different characteristics of the object under study. External surfaces showing very smooth features make the capturing process and the posterior processing a more elaborate task, requiring special attention and additional retouching to improve the final model. Tombstones are a good example of this type of objects, combining both flat external contours and refined outlines. In this work the procedure of creation of the digital model of the tombstone of the bishop Vasilije Petrović (Negosh) is described, a piece of art which combines both technical and historical importance.

1. Introduction

3D laser and optical scanning devices are now more intensively used in everyday tasks when high precision and repeatability are required. Together with these two features, their non-destructive working principle make them invaluable tools in different fields in which to keep the conservation state of the object under study is the top priority, which is the case of Cultural Heritage (CH) field. Nowadays, the use of 3D laser and optical scanning devices in CH field is very widespread [1], being used in multiple tasks for pieces of different sizes, materials and shapes. The good results obtained and their relatively low cost allow to apply them in new and challenging applications in the area.

However, the results obtained in the scanning procedure vary according to some factors like the technology used, ambient light, material and color of the object and others [2-3]. In particular, the capture presents some issues when the surface under study is very flat, requiring special attention in both the capturing procedure and the post-processing tasks. These problems become more apparent when they are combined with very delicate details on the exterior, like the ones seen in carved stone, being the case of most of the tombstones where the effect of environmental agents [4] along the time made their inscriptions and drawings barely noticeable in extreme cases.

In this article, we present a case study of 3D scanning procedure of the tombstone of the bishop Vasilije Petrović (Negosh), established in 1766 in Saint Petersburg, Russia. The 3D scanning procedure and the creation of a virtual model of it has two main features: one technical and the other

historical. The first one, from the technical point of view, to evaluate the use of 3D optical and laser scanning techniques applied for documentation of CH objects can also be used in pieces with very smooth surfaces with good results and the challenges that the practitioners faced in their employment. The second characteristic of the work comes from its historical importance, as this tombstone is a landmark of the shared history between the city of Saint Petersburg and the country of Montenegro.

2. Object under analysis and post-processing tasks description

The 3D scan set obtained for this task corresponds to a procedure done at Alexander Nevsky Lavra (Saint Petersburg, Russia) on June 2021. The scanned object was the tombstone of bishop Vasilije Petrović (Negosh). It is made in limestone and its dimensions are about 220 x 108 cm. The front part of it is carved showing a coat of arms and inscriptions. The tombstone was established on 1766 and in 1783 the construction of the building was finished, protecting it from external agents. The coat of arms shows some deterioration and some parts of the material are missing. The scanning procedure was done with a handheld structured-light based 3D optical scanning device developed by Artec 3D (Artec 3D, Luxemburg), model Artec Eva Lite. Light conditions where interior light without any special additional lighting. Two scanning procedures were done over the object, paying special attention to the coat of arms and the inscriptions. The first scanning procedure is composed by 22 shots (around 300.000 vertices and 650.000 faces each) and the second procedure contains 43 shots (around 200.000 vertices and 400.000 faces each). The format used to store the captures is proprietary, developed by the manufacturer and was exported to STL format for further processing in different programs.

For the post-processing tasks different tools were used, among them Geomagic Design X (3D Systems corporation, USA), ZBrush (Maxon Computer GmbH, Germany) and Photoshop (Adobe Inc., USA). The first stage required a careful selection of the scans to be employed, cleaning of the surfaces for capture errors and noise, alignment of the different shots (rough alignment and automatic adjustment) and hole filling. After that, the coat of arms was digitally improved to increase the texture and obtain a clearer inscription; some missing parts were restored. Finally, an image of the model was used as a texture to give a photorealistic effect to the work.

3. Historical importance of the object under analysis

Vasilije III Petrović Negosh (Njeguši, 1709 – Saint Petersburg, 1766) was the metropolitan bishop of Cetinje (Prince-Bishop of Montenegro) and ruler of Montenegro from 1750 until his dead together with his cousin, Sava Petrović. He is the author of the History of Montenegro, published in 1754, the first book dedicated to this matter. He traveled several times to Russia and in particular to Saint Petersburg, where he met with empress Elizabeth Petrovna and other important political figures, looking to establish political and diplomatic alliances between the states. He died during one of his trips in 1766 in Saint Petersburg.

References

[1] Parfenov V, Igoshin S, Masaylo D, Orlov A and Kuliashou D 2022 *Quantum Beam Sci*. **6** 11

[2] Gupta M, Agrawal A, Veeraraghavan A and Narasimhan S G 2011 *Proc. of the 2011 IEEE Conf. on Computer Vision and Pattern Recognition (Colorado Springs)* (Washington: IEEE Computer Society) pp 713–20

[3] Zaimović-Uzunović N and Lemeš S 2010 *IMEKO Conf. Proc.: 10th Int. Symp. on Measurement and Quality Control* (Osaka) ed Y Takaya (Tokyo: Japan Society for Precision Engineering) pp 408–11

[4] Vlasov D Yu, Frank-Kamenetskaya O V, Manurtdinova V V and Zelenskaya M S 2019 *The Effect of the Environment on Saint Petersburg's Cultural Heritage: Results of Monitoring the Historical Necropolis Monuments* ed V O Frank-Kamenetskaya, D Yu Vlasov and V V Rytikova (Cham: Springer Nature) chapter 4 pp. 75–96

Optimization of the contact grid for the GaP/Si solar cells

M V Bogdanova[1], A V Uvarov[1], A S Gudovskikh[1,2]

[1]St. Petersburg Academic University of RAS, 194021 St. Petersburg, Russia
[2]St. Petersburg Electrotechnical University ("LETI"), 197376 St. Petersburg, Russia

Abstract. In this paper, the calculation of electrical properties for (n)GaP-p(Si) solar cells was performed for different contact grid design. The influence of annealing temperature on the current-voltage curves of solar cells was shown via the Hall measurements and the simulation respectively. For calculations were used 200 μm width contact bars, which could be appropriate for mass-scalable screen-printing metallisation technique. According to the results, the thermal annealing at 700˚C was the most suitable condition from point of view calculated conversion efficiency.

1. Introduction

The formation of contact systems is an important technological process in the design of solar cells. Materials, structure, and geometry of contacts affect the distribution of currents.

Depending on the contact position relative to the propagation of light (front or rear), they have different requirements. In the front contact system, an optimum must be observed between the shading effect and the contact resistance losses. If the contact grid area is small, then the optical losses associated with shading will decrease, but the electrical resistance will increase. Therefore, in industrial solar cells, one can often find a configuration of mutually perpendicular current-carrying bars and strips. It is the optimal ratio between light and electrical losses.

In this work, we will calculate contact systems for the (n)GaP/(p)Si structure, we will search for the optimal distance between contacts at fixed annealing temperatures.

2. Materials and methods

In our simulations, we varied the distance between contact bars and estimated its influence on the conversion efficiency. We calculated the electrical properties of GaP/Si solar cells using Silvaco software. For calculation we used spectra in the wavelength range from 0.3 μm to 1.2 μm, the spectral density distribution corresponds to the AM1.5G standard. For numerical calculations, we divided this range into 50 bands of equal width. The radiation propagated along the normal on the sample, while we considered the condition of complete bleaching with GaP (there is no reflection at the interface with GaP). For electrical calculation the Shockley-Read-Hall model was used.

The influence of the thermal annealing on electrical properties was analyzed using experimental data obtained for (n)GaP/(p)Si structures. Various annealing temperature was applied in range from 500 °C to 800°C. Via the Hall method, we measured the concentration and the mobility of charge carriers in the (n)GaP layer and inversion layer at the (n)GaP/(p)cSi interface. Using the database [1] the lifetime was taken as a parameter for further calculations. Further, the influence of annealing temperature and the searching of the optimal distance between the contacts was considered.

3. Results

The Hall measurement results are shown below.

Table 1. The electrical properties of inversion layer

Annealing temperature, ˚C	Without	500	600	700	750	800
Concentration, cm^{-3}	$8 \cdot 10^{17}$	$1 \cdot 10^{19}$	$8 \cdot 10^{19}$	$5 \cdot 10^{20}$	$3 \cdot 10^{21}$	$7 \cdot 10^{22}$
Mobility, $cm^2 \cdot V^{-1} \cdot s^{-1}$	108	25	29	26	30	0.5
Lifetime, s	$5 \cdot 10^{-5}$	$1 \cdot 10^{-7}$	$1 \cdot 10^{-8}$	$1 \cdot 10^{-8}$	$1 \cdot 10^{-9}$	$1 \cdot 10^{-9}$

The thicknesses and electrical properties of the remaining layers are given in the table below. The GaP-Si junction is designed to generate and spatially separate electron-hole pairs and the BSF (back surface field) is used to reduce the surface recombination of charge carriers.

Table 2. Electrical properties of layers in tandem GaP/Si solar cell

Parameter	(n)GaP	(p)c-Si	BSF
Thickness, μm	0.05	300	1
Concentration, cm^{-3}	10^{18}	10^{16}	10^{19}
Mobility, $cm^2 \cdot V^{-1} \cdot s^{-1}$	1	holes: 300; electrons: 1000	holes: 300; electrons: 1000
Lifetime, s	10^{-6}	10^{-4}	10^{-4}

We will focus on the contact widths of 200 μm, which is preferred for screen printing technology.

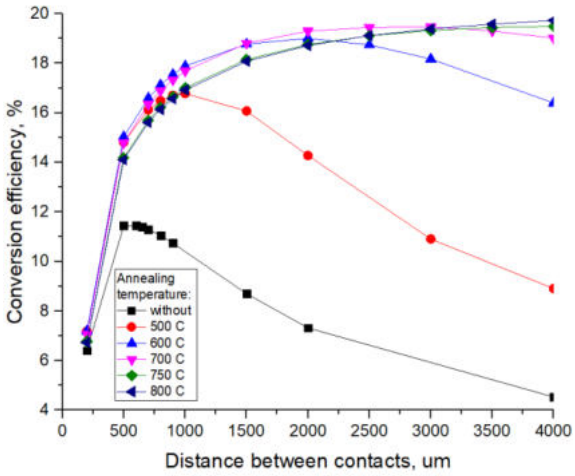

Figure 1. Dependence of the simulated conversion efficiency of a solar cell on the distance between the contacts for a contact width of 200 μm for GaP/Si structures annealed at different temperatures

The maximum efficiency under these conditions is about 19%. Of particular note are the results that correspond to an annealing temperature of 700 ˚C. In this case, with lengths between contacts from 2 to 3.5 mm, it is possible to maintain efficiency of 19%. This allows the use of screen printing, taking into account inhomogeneities in the application of contacts.

Acknowledgments

This work was supported by Ministry of Science and Higher Education of the Russian Federation (research project FSRM-2020-0004).

References

[1] Electrical properties of Silicon // New Semiconductor Materials. Biology systems. Characteristics and Properties. URL: http://www.matprop.ru/Si_electric

Spin light-emitting diode with intensity modulation

M Ved, M Dorokhin, A Zdoroveishchev, P Demina, D Zdoroveishchev, Yu Dudin, V Kotomina

Research Institute for Physics and Technology of UNN, Gagarina ave., 23/3, Nizhny Novgorod, 603950

mikhail28ved@gmail.com

Abstract. The operation of new spintronic device is discussed. This device is a magnetoresistive spin light-emitting diode, in which the intensity and circular polarization degree can be independently controlled by applying longitudinal and transverse magnetic fields respectively. The device is a combination of spin LED based on an InGaAs/GaAs quantum well heterostructure with a CoPd spin injector and a spin valve consisting of $Cr/Co_{90}Fe_{10}/Cu/Co_{90}Fe_{10}$ layers connected in series. It is shown that in such a device a 100% change in electroluminescence intensity can be obtained, whereas the degree of circular polarization is 0.4%.

1. Introduction

The functional combination of the basic elements of spintronics (a magnetoresistive element and a spin light-emitting diode) is an urgent task. This will allow obtaining one of the four stable states for one cell, which will at least double the information capacity of spintronic devices. In the field of research of a combined magnetoresistive element and a light-emitting diode, several works can be mentioned. Some examples are refs [1,2], in which structures that combine various elements of electronics and spintronics were studied. The structures studied in the cited papers are the schemes of a low integration level with the intensity of the optical signal be controlled by an external magnetic field. In this paper, we report on a device with an independent variation of both the emission intensity and degree of circular polarization carried out by applying external magnetic fields.

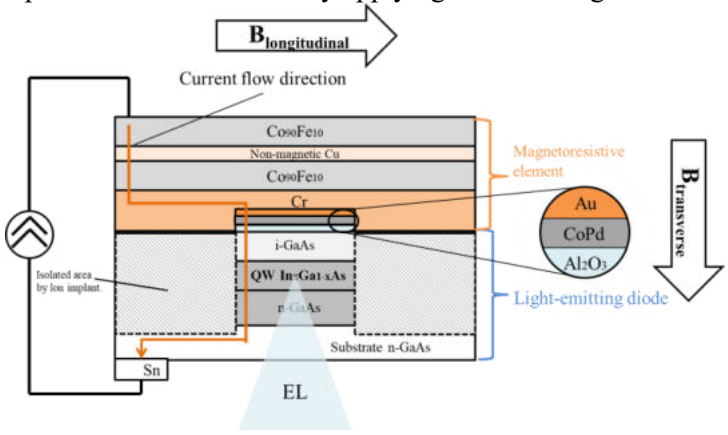

Figure 1. Combined device scheme.

2. Experimental technique

A magnetoresistive spin light-emitting diode is a combination of an emitting part based on a heterostructure with an InGaAs/GaAs quantum well with a CoPd spin injector and a spin valve consisting of $Cr/Co_{90}Fe_{10}/Cu/Co_{90}Fe_{10}$ layers connected in series. The base contact to the substrate was formed by sparking of Sn foil. The device was powered in the current source mode. Fig. 1 shows a scheme of a combined device. For the electrical insulation of the semiconductor structure around the mesa contacts, the parts of the structure, uncovered by the contacts, were bombarded with He^{++} ions before applying magnetoresistive layers [3].

3. Results and discussion

Fig. 2 shows the magnetic field dependence of the relative electroluminescence intensity of the device. The observed modulation of the EL intensity is due to a change of the resistance for the magnetoresistive contact layer. It should be noted that at a current of 36 mA, the structure operates in the key mode: in a magnetic field of ±50 mT, the relative intensity takes on maximum values; in zero magnetic field, as well as in a field above 100 mT it is zero. The most probable mechanism for increasing the EL intensity in the longitudinal magnetic field for combined devices is presented in [4].

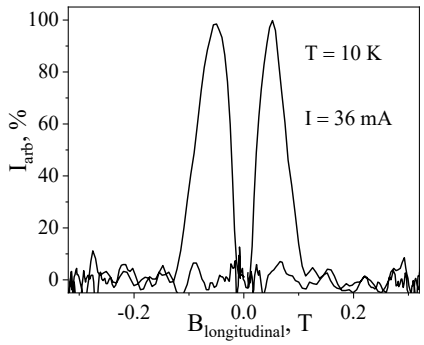

Figure 2. Magnetic field dependence of the relative emission intensity for a combined device.

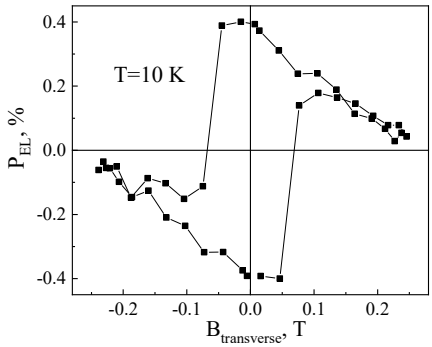

Figure 3. Magnetic field dependence of P_{EL} for a combined device.

When the combined device is placed in a transverse magnetic field, the emission becomes partially circularly polarized. Figure 3 shows the magnetic field dependence of the circular polarization degree of EL (P_{EL}). The maximum P_{EL} value was 0.4%. The linear slope in magnetic fields greater than 0.1mT (in absolute value) is presumably related to the Zeeman splitting of energy levels in the QW.

As a result, we have fabricated a laboratory sample that operates not in two controlled states corresponding to a logical zero and one (high and low intensity or right- and left-circularly polarized emission), but four independently variable states (high intensity with right- and left-circularly polarized emission and low intensity with right- and left-circularly polarized emission).

Acknowledgments

The work was supported by the Ministry of Science and Higher Education of the Russian Federation (the federal academic leadership program “Priority 2030” and the basic part of the state assignment No. 0729-2020-0060).

References

[1] Appelbaum I, Russel K, Monsma D, Narayanamurti V, Marcus C, Hanson M, Gossard A 2003 *Appl. Phys. Lett.* **83** 4571.

[2] Saha D, Basu D, Bhattacharya P 2008 *Appl.Phys.Lett.* **93** 194104.

[3] De Souza J, Danilov I, Boudinov H 1996 *Appl. Phys. Lett.* **68**(4) 535.

[4] Ved M, Danilov Yu, Demina P, Dorokhin M, Dudin Yu, Kotomina V, Kudrin S, Kuznetsov Yu, Zdoroveyshchev S, Zdoroveyshchev D 2021 *Appl.Phys.Lett.* **118** 092402.

Reliability of 808nm QCW Laser Diode Arrays

E. M. Gafurov, E. V. Smirnov
FSUE «RFNC-VNIITF named after Academ. E.I. Zababakhin», Snezhinsk, 456770, Russia

E-mail: dep5@vniitf.ru

Abstract: This work provides the results of researches of dependence of radiating characteristics for 808 nm high power QCW laser diode arrays (LDAs) and heat-sink temperature. According to the offered method of the accelerated resource tests researched long term stability of power output and wavelength of radiation of LDAs with the duty factor of impulses of 6% exceeding rated value by 2.5 times, and also at two values of temperature of the junction temperatures 65ºC and 82.5ºC. Accumulated life-test duration of LDAs in the accelerated mode made more than 7.2•10^8 impulses that allows to predict a resource of work of LDAs at nominal mode during 1.9•10^10 of impulses (more than 65 600 hours or slightly less than 7.5 years of continuous work with a frequency of impulses of 100 Hz).

1. Introduction

Within creation and production of diode-pumped solid-state laser (DPSSL), the big research directed to development of construction and manufacturing techniques of powerful laser on the basis of the laser diodes bar (LDB) was carried out in RFNC-VNIITF. Application of the developed technical solutions allowed to produce the laser diode arrays (LDAs) with the characteristics which not be of a lower quality to world analogs [1].

The major stage in production of LDAs and any other laser diodes, is determination of reliability at the required modes of operation. In turn, the speed of change of output characteristics laser diodes, allowing to estimate reliability of products, depend on presence of different mechanisms of degradation of laser devices which can be set in the course of carrying out resource tests [2].

2. Method

As on average the resource of high power QCW laser diode arrays exceed 10^9 impulses [3], in this work the technique of accelerated tests was applied. In a general view Arrhenius model describes influence on a resource of work not only temperatures, but also a pumping current and radiant power. On the basis of the presented coupling equation of Arrhenius it is possible to define acceleration coefficient $\tau_{T,P}$ between service life at nominal modes and service life under modes of carrying out resource tests:

$$\tau_{T,P} = \frac{\tau_1}{\tau_0} = \exp\left(\frac{E_a}{K}\left(\frac{1}{T_1} - \frac{1}{T_0}\right)\right)\left(\frac{P}{P_0}\right)^{-n}\left(\frac{I}{I_0}\right)^{-m} \quad (1)$$

where T_0 and T_1 – values of heat-sink temperature under nominal working modes and heat-sink temperature when carrying out accelerated test; τ_1 and τ_0 – respectively a work resource in the conditions of carrying out accelerated test and under nominal modes. The value of activation energy E_a is usually provided by the manufacturer of a semiconductor crystal or is defined from results of the accelerated resource tests.

3. Experimental

Within this work is conducted the research of dependence of output characteristics of high power QCW laser diode arrays from time of carrying out resource tests (Fig. 1).

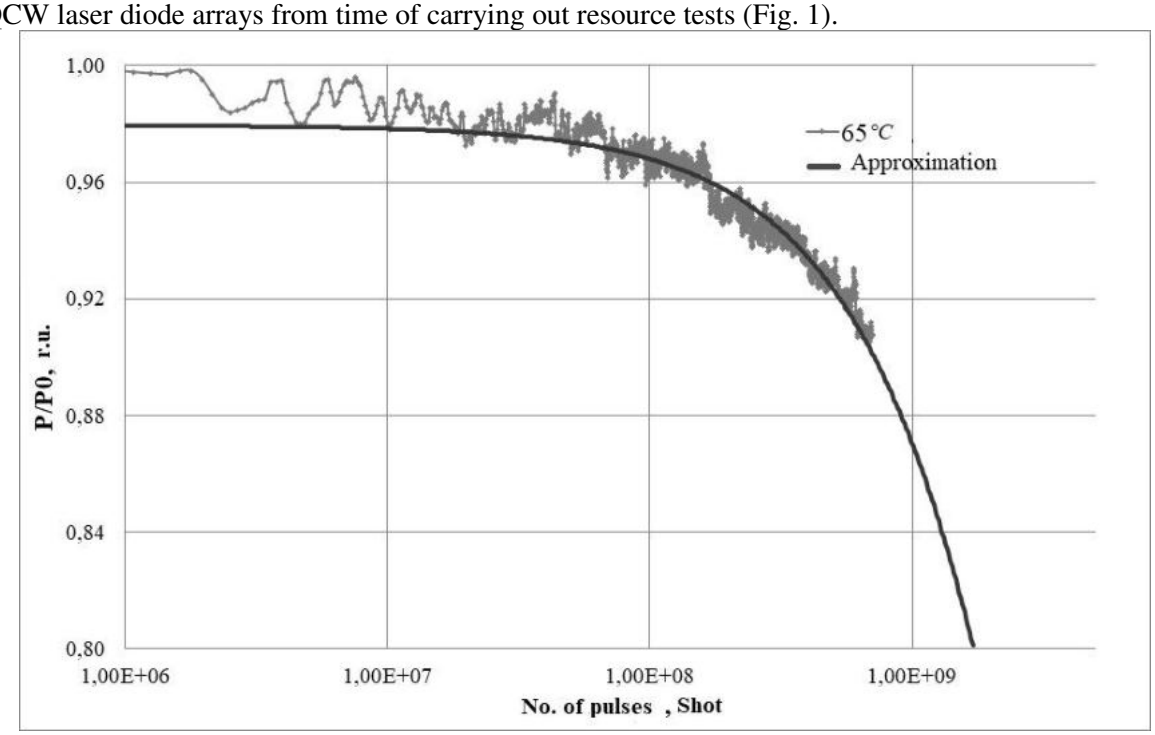

Figure. 1. Results of the accelerated resource tests of LDA at values of temperature of the LDB junction temperatures 65 °C.

In this work for assessment of service life at rated values of heat-sink temperature the method of the accelerated resource tests of LDAs at the increased values of temperature is offered. On the basis of the received results according to Arrhenius's model, found and calculation speed of degradation of the studied LDAs and of value activation energy of degradation processes. Besides, calculated value of coefficient of acceleration between service life at nominal operating modes (120A, 100 Hz, 240 ms, 25 °C) and the modes created in the course of the accelerated resource tests (120A, 200 Hz, 300 ms, 65 °C), equal 0.032 and (120A, 200 Hz, 300 ms, 82.5 °C) 0.012 respectively.

4. Conclusions

The available experimental data of the accelerated resource tests allow to predict a resource of work of LDAs at the nominal modes of operation during not less than 1.9•10^10 impulses. Gradual falling of quantum efficiency of emitters is a probable cause of falling of emitting power LDAs eventually. Further studies of resource characteristics of LDAs will be continued. It is expected that these researches will allow to specify values of activation energy of degradation processes and the coefficient of acceleration of power for the LDAs specific type developed and made in RFNC-VNIITF.

References:

[1] Fomin A V, Smirnov E V, Milovidov N I 2013 *Pat.2544875 Russia*
[2] Ter-Martirosyan A.L. 2014 *Semiconductor devices* **45**
[3] Jing Zhu et al. 2016, *Photonics* **73** 6 / 60

Simple method for preparing highly-indistinguishable coherent states

I S Gerasin[1,2,3,4], E E Mekhtiev[1,2,3,4], E L Maksimova[1,5], N V Rudavin[1,6], A V Duplinsky[1,3,4] and Y V Kurochkin[1,2,3,4]

[1]QRate, Novaya av. 100, Moscow, Russia
[2]Moscow Institute of Physics and Technology, 9 Institutskiy per., Dolgoprudny, Moscow Region, 141701, Russian Federation
[3]NTI Center for Quantum Communications, National University of Science and Technology MISiS, Leninsky prospekt 4, Moscow 119049, Russia
[4]Russian Quantum Center, Bolshoy Boulevard 30, bld. 1, Skolkovo, Moscow 121205, Russia
[5]Peter the Great St. Petersburg Polytechnic University, 29 Polytechnicheskaya str., St. Petersburg 194064, Russia
[6]HSE University, 20 Myasnitskaya ulitsa, Moscow 101000, Russia

i.gerasin@goqrate.com

Abstract. The preparation of indistinguishable quantum states by remote users is one of the crucial tasks in MDI-QKD. To solve this problem, laser injection techniques or modulation of the CW laser on the transceiver side are used. These techniques require a complex setup or a pair of modulators. Here we present a different setup for generating coherent states, using one modulator and one gain-switched laser per transceiver, to find a balance between the complexity of the setup and its cost. The level of indistinguishability achieved allows our scheme to be used in high-speed MDI-QKD protocols.

1. Preparing of indistinguishable coherent states

Quantum interference is one of the key experiments in quantum information technologies. It is useful for quantum teleportation, quantum computing, and quantum cryptography. Usually, the visibility of interference at the beamsplitter (Hong-Ou-Mandel interference) serves as a measure of indistinguishability of quantum states. In particular, measured device independent quantum key distribution (MDI-QKD) protocols require the interference at the central untrusted node of two weak coherent states with random phase (WCSRP) prepared by two remote users [1]. There are two main approaches to generate such indistinguishable states by remote users: (a) modulating a CW laser with an intensity modulator (IM) and a phase modulator, (b) using a gain-switched semiconductor laser. The first approach allows to easily prepare almost indistinguishable states by two remote users in cost of additional optical devices and lasers with high stability [2]. The second approach implies only semiconductor lasers, however the states produced by two users are more distinguishable due to the temporal and spectral properties of two different laser diodes [3]. To increase mode match, in recent work the laser injection technique was adopted to prepare WCSRP by two remote users [4]. On the one hand, laser injection allows to achieve better mode overlap between independent gain switch laser

sources, but on the other hand, it increases the complexity of the setup and one needs to drive laser with high stability current. In our work, we propose a novel method to prepare WCSRP using gain-switched lasers without injection and only one modulator.

2. Experimental setup

The main idea of our preparation scheme is to generate sufficiently long laser pulses and open IM when the transition process associated with chirp is stabilized. We drive two DFB-lasers with a repetition rate of 312 MHz. Each laser generates optical pulses with a length of 1 ns. The bias current and temperature settings are optimized to have nearly the same spectra. After each laser the IM is located to suppress the onset of the optical pulse. At the IM output the beam splitter is located to monitor the average output power of the pulses and adjust the bias setting of each IM. The output of each preparation block is connected to the input of the 50/50 beamsplitter to interfere. An optical filter and a photodetector are installed at one of the outputs of the beam splitter to observe the interference result on the oscilloscope. Using the collected statistics, we calculate the second order correlation function to measure the indistinguishability of the prepared states.

3. Experimental results

By configuring our experimental setup, we can observe the interference of different preparation schemes. First, we consider the **GS-laser** scheme, where IM is turned off and the filter bandwidth is opened to its maximum value (3 nm) around the central peak of the lasers. In this mode, we calculate the indistinguishability of two directly modulating semiconductor lasers. The second setup is **GS-laser + filter**. Also in this case IM is not driven, however the filter bandwidth has its narrowest value (0.05 nm). Another setup **GS-laser + IM** is to drive IM with opened filter. The last scheme **GS-laser + filter + IM** includes the driving of IM and the filter with its narrowest bandwidth. The results of the measured second order correlation function are presented in Table 1. The results show that the proposed scheme with proper time and frequency filtering achieves values close to the theoretical minimum ½ and can be used to prepare states in high-speed MDI-QKD setups. Moreover, the same intensity modulator can be used to make decoy states in MDI-QKD.

Table 1. Experiment results.

Setup	$g^2(0)$
GS-laser	0.728
GS-laser + filter	0.588
GS-laser + IM	0.534
GS-laser + filter + IM	0.508

References

[1] Lo, Hoi-Kwong, Marcos Curty, and Bing Qi. "Measurement-device-independent quantum key distribution." *Physical review letters* 108.13 (2012): 130503.

[2] Tang, Zhiyuan, et al. "Experimental demonstration of polarization encoding measurement-device-independent quantum key distribution." *Physical review letters* 112.19 (2014): 190503.

[3] Yuan, Z. L., et al. "Interference of short optical pulses from independent gain-switched laser diodes for quantum secure communications." *Physical Review Applied* 2.6 (2014): 064006.

[4] Comandar, L. C., et al. "Near perfect mode overlap between independently seeded, gain-switched lasers." *Optics express* 24.16 (2016): 17849-17859.

Epitaxial lift-off GaAs/AlGaAs solar cells for flexible devices

A S Goltaev, A V Vorobyev, D M Mitin, Y S Berdnikov and A M Mozharov

Alferov University, Khlopina 8/3, 194021 St. Petersburg, Russia
e-mail: AKBAPNYM@yandex.ru

Abstract: The new demand for highly efficient, flexible, lightweight solar cells (SCs) requires a modern approach to solving the problem of technology for obtaining lift-off SCs. In this work, to implement a flexible solar cell based on GaAs/AlGaAs, a AlInP release layer was used. Based on numerical calculation the nanoheterostructure was grown by molecular beam epitaxy. Photovoltaic characteristics SCs on rigid substrate were obtained.

1. Introduction

Rapid development of wearable electronics, mobile devices and autonomous vehicles has generated a new demand for highly efficient, yet flexible, low-weight SCs [1]. The already existing photovoltaic technology uses GaAs layers [2] with a thickness of several microns due to their flexibility and high absorption coefficient. Promising approach here is flexible single-junction SCs based on GaAs heterostructures with thickness of several micrometers and lifted off the growth substrate. To obtain flexible SCs structures, the methods of separating GaAs/AlGaAs nanostructures from the growth substrate using wet-etched release layer [3] within an improved post-growth processing. The implementation of the work involves numerical calculation of the optical and electronic properties of SCs to search for the optimal design of nanostructures (morphology and composition of layers, doping profile) for subsequent epitaxial synthesis. Thus, the approaches used in the implementation of the work will make it possible to achieve progress at each of the steps to create highly efficient flexible SCs based on GaAs/AlGaAs nanoheterostructures and release layer.

2. Experiment

Numerical calculation was made to determine the optimal design of a GaAs/AlGaAs based thin film lift-off SCs and AlInP sacrificial layer, corresponding to a maximum energy conversion efficiency. Based on numerical calculation GaAs/AlGaAs nanoheterostructure SCs were synthesized by molecular beam epitaxy on 2-inch diameter (100) GaAs wafers. AlInP epitaxial layer lattice-matched with GaAs were used as the material for the wide-gap window and the rear potential barrier, which also act as a release layer during liquid etching. After growth, first the n-side AuGe (300 nm) metal rear contact was deposited by vacuum evaporation and annealed at 400°C to ensure low contact resistivity. Next, the front side of the cell structure was accessible for the deposition of the p-side Cr/Au (5/100 nm) grid contact. Contact layer was removed by wet etching in citric acid. After that, the I-V characteristics were measured, as well as the efficiency (under AM1.5 spectrum) and external quantum efficiency.

3. Conclusion

In this work, numerical calculation of the lift-off solar cell with an AlInP core layer was carried out. The GaAs/AlGaAs nanoheterostructure was synthesized by molecular beam epitaxy. The main photo-electrical characteristics of the solar cell were measured.

Acknowledgements

The reported study was funded by RFBR, project number 19-38-60008 (metal contacts deposition, I-V measurement), D M Mitin thanks the MK-3031.2021.1.2. for supporting research in the field of epitaxial growth.

Y S Berdnikov thanks the Russian Science Foundation (project number 21-79-00281) for supporting research in the field of numerical calculation.

References

[1] Pagliaro M, Ciriminna R and Palmisano G 2008 Flexible solar cells *ChemSusChem: Chemistry & Sustainability Energy & Materials* **1-11** 880-891

[2] Yablonovitch E, Gmitter T, Harbison J P and Bhat R 1987 Extreme selectivity in the lift‐off of epitaxial GaAs films *Appl. Phys. Lett.* **51-26** 2222-2224

[3] Cheng C W et al 2013 Epitaxial lift-off process for gallium arsenide substrate reuse and flexible electronics *Nat. Commun* **4-1** 1-7

Application of a fiber-optic communication line for transmitting RF-signal in system formeasuring parameters of active phased antenna arrays

E M Gryaznova[1], **V V Davydov**[1,2] **and K Y Malanin**[3]

[1]Peter the Great St.Petersburg Polytechnic University, St.Petersburg, Russia
[2]All-Russian Research Institute of Phytopathology, Moscow Region, Russia
[3]JSC "Zaslon", St.Petersburg, Russia

katya.gryaznova@mail.ru

Abstract. The necessity of using fiber-optic communication lines (FOCL) for transmitting microwave signals in radar complexes is substantiated. The advantages of the use of FOCL when working with microwave signals and testing various antennas are noted. A system with a fiber optic system has been developed to measure the parameters of an active phased array antenna (APAA) in the far zone. The choice of the components of the system is justified and their characteristics are measured. The results of research on the operation of the developed system are presented.

1. Introduction

The development of efficient high-speed optoelectronic devices has aroused great interest in the use of optoelectronic and optical technologies in microwave technology [1]. Various developments of laser systems also contributed to the emergence of the direction of radiophotonics [2]. Radiophotonics makes it possible to create devices and systems of the microwave range with parameters unattainable by traditional electronic means. The main advantages of radiophotonics devices and systems are related to the properties of optical fiber: ultra-low losses during transmission of a microwave signal, a wide frequency band, immunity to electromagnetic interference, complete galvanic isolation, mechanical flexibility, low weight and dimensions. When solving various tasks in radar, the use of FOCL allows obtaining the necessary results. It should be noted that the transmission of microwave signals is carried out mainly at distances less than 1000 m. In this case, different types of dispersion do not have time to form in the fiber and affect the transmitted signal. This greatly simplifies the design of the FOCL.

2. Design of fiber-optic information transmission system

Figure 1 shows a block diagram of a system for measuring APAA parameters in the far zone in the "on transmission" mode. The principle of operation of the microwave path of the FOCL is as follows: the microwave signal received by the horn goes to a broadband low-noise amplifier, then the amplified microwave signal goes to an optical modulator and modulates the light beam coming from the laser module. From the modulator, the modulated optical signal is transmitted via a fiber-optic line to the optoelectronic receiving module, in which the light signal is converted back into a microwave signal with minimal distortion.

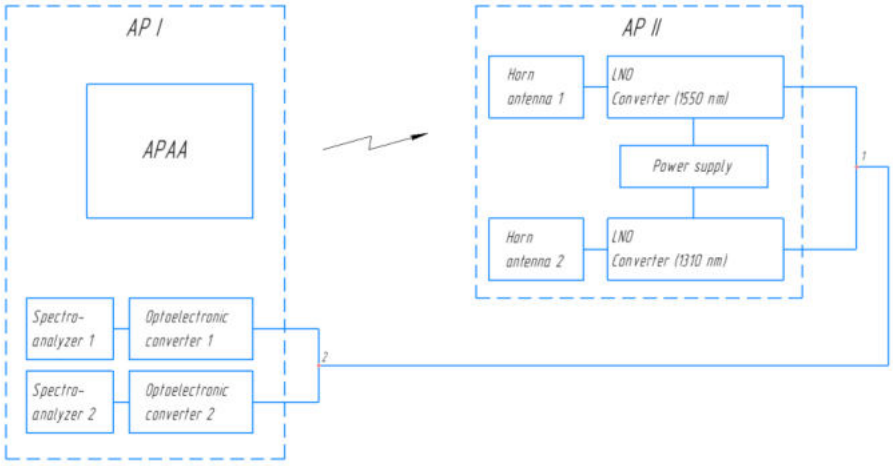

Figure 1. Block diagram of the system.

Then the converted microwave signal is sent to the measuring receiver for further processing, after which it is sent to the spectroanalyzer

3. Results of FOCL performance and its discussion

In Figure 2 shows, as an example, the APAA directional diagrams in a rectangular coordinate system, taken using a coaxial cable and a FOCL developed by us in landfill conditions.

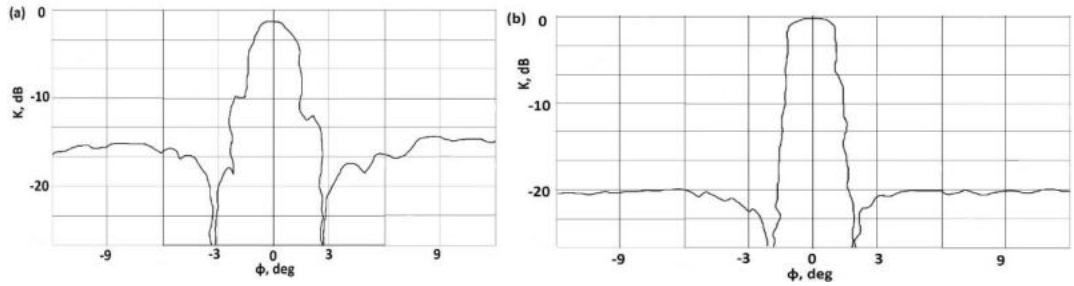

Figure 2. AFAR directional pattern: (a) - a coaxial cable is used to transmit the microwave signal, (b) - FOCL is used to transmit the microwave signal.

An analysis of experimental studies shows that the obtained radiation pattern using the FOCL allows an approximation to be performed to assess the stable APAA radar survey zone. Allows you to adjust the APAA to the maximum suppression of the side lobes in order to reduce the impact on the accuracy of determining the coordinates, for example, of a moving object, repeatedly reflected microwave signals.

4. Conclusion

The results obtained show that the use of the FOCL developed by us makes it possible to make insignificant the effect of distortion when transmitting a microwave signal over the territory of the landfill over long distances to the equipment for subsequent processing. This also makes it possible to identify various defects in the design of APAA elements that cannot be established when using feeder paths for transmitting a microwave signal.

References

[1] Davydov R, Antonov V and Moroz A 2019 *IEEE International Conference on Electrical Engineering and Photonics (EExPolytech-2019).* Saint-Petersburg, **vol. 8906791**, p. 295-297

[2] Kozlova E S and Kotlyar V V 2014 *Computer Optics* **38(1)** 132-138

Development of the radiation situation monitoring system based on fiber-optic sensors for pools of nuclear power plants

D S Dmitrieva[1]and V V Davydov[2, 3]

[1]The Bonch-Bruevich Saint-Petersburg State University of Telecommunications, Saint Petersburg 193232, Russia
[2]Peter the Great Saint Petersburg Polytechnic University, Saint Petersburg 195251, Russia
[3]All-Russian Research Institute of Phytopathology, Moscow Region 143050, Russia

dmitrievadiana1405@gmail.com

Abstract. The necessity of development of the remote monitoring system of the radiation situation based on fiber-optic sensors for pools of nuclear power plants is substantiated. New design of fiber-optic sensor is suggested, its functional capabilities are identified. Experimental results are presented.

1. Introduction

Nowadays the using of radioactive materials in different fields of industry is only increasing, the amount of nuclear power plants has increased [1]. Despite the large number of protective screens and ceilings, has increased the number of radioactive releases, the consequences of which cannot be eliminated for a long time. In addition to the reactors, the spray pools used for continuous cooling of NPP equipment pose a danger. In the case of leakage, spray pools also often become sources of releases into the atmosphere due to the ingress the liquid radioactive waste into the water. Due to the presence of a nozzles system, some of drops containing radionuclides are carried by the wind outside the spray pools. Moreover, the natural water evaporation from the pool surface also leads to a change in radiation situation in the atmosphere. So, this is the reason, why the great attention is paid to possibility if control the radiation level in pools of nuclear power plants.

The great attention is paid to possibility of remote control the radiation situation in pools of NPP. This control must be carried out continuously in real time. Most dosimetry devices cannot cope with this task. Devices often go off, and communication systems, which are used for transmitting information about radiation level to monitoring center, are out of order because of radiation accumulation [2].

Thus, the perspective direction for solving this problem is the use of high-speed fiber-optic sensors with fiber optic communication line. However, sensors developed nowadays, cannot provide measurements at a high values of exposure dose of radiation because of prolong relaxation process of optical fiber and impossibility of using more powerful radiation sources in sensors. Therefore, the development of a system for monitoring radiation situation based on the fiber-optic sensors and be capable of withstanding high levels of exposure dose, is extremely actual.

2. Design of fiber-optic sensor design for the radiation situation monitoring system.

As a design of the fiber-optic sensor based on the experimental results obtained earlier [3] is proposed to use an optical fiber 200 m long with a SiO_2 – GeO_2 core with alloying 20%, which connects to an optical fiber with a pure quartz core through optical connectors. To accelerate the relaxation process (this process can take 10^6 s and more) in this construction is used the method of E'-centers formation control developed earlier for trunk FOCL's. The research of velocity of the optical properties recovery after γ-radiation influence with a dose of 100 G was provided for checking the reliable of the proposed design. In this research was used pulsed laser radiation with λ=1310 nm and a duration of 0.1 s during 10 s. Measurements were provided with various powers of laser radiation. Experimental results are presented at the fig.1.

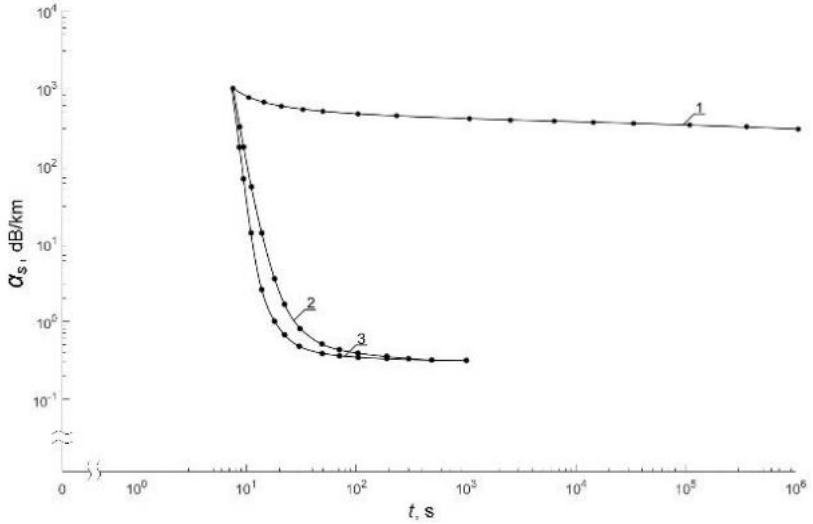

Figure 1. Dependence of the change in losses α_s with time t at a wavelength λ = 1550 nm for a single-mode fiber with a SiO_2 – GeO_2 core (alloying 10.0 %) and polymer cladding at T = 294.3 K. Charts 1, 2 and 3 are correspond to different laser radiation powers in mW: 0; 40; 80.

Analysis of the obtained results confirmed the possibility of increasing the relaxation velocity when using the additional laser radiation. Optical properties recover in less 10s.

3. Conclusion

Obtained results showed a reliable work of developed sensor in continuous mode. Its use makes it possible to control an exposure dose from 0.1 to 1000 G in real time at pools of NPP.

References

[1] Davydov V V, Myazin N S and KiryukhinA V 2020 *Atomic Energy***127(5)**274–279

[2] Khan P W, Abbas K, Shaiba H,Abuarqoub A and Khayyat M 2020 *Electronics***9(6)** 1–20

[3] Dmitrieva D, Pilipova V, Andreeva E and Dudkin V, 2020 In *Proceedings of ITNT 2020 - 6th IEEE International Conference on Information Technology and Nanotechnolog* (Samara< Russia), vol. 9253348, p. 13-17

Analysis of characteristics of InGaAs/GaAs microdisk lasers bonded onto silicon board.

A S Dragunova[1,2], N V Kryzhanovskaya[1,2], E I Moiseev[1], F I Zubov[1,2], N. A. Kalyuzhnyy[3], S. A. Mintairov[3], Yu.A.Guseva[3], M. M. Kulagina[3] and A E Zhukov[1]

[1]National Research University Higher School of Economics, 16 Soyuza Pechatnikov, St. Petersburg 190008, Russia
[2]St. Petersburg National Research Academic University, Russian Academy of Sciences, St. Petersburg, 194021, Russia
[3]Ioffe Physical Technical Institute of RAS, Politehnicheskaya 26, St Petersburg, 194021, Russia
E-mail: anndra@list.ru

Abstract. In this work we study characteristics of the III-V microdisk lasers bonded onto silicon board. The bonding of microdisk lasers to a silicon substrate reduces their thermal resistance. Here we show improvement in lasing threshold, output power, dynamic characteristics and energy consumption in microdisk lasers with diameters of 19 μm and 31 μm by comparison of the characteristics obtained before and after bonding. Also estimation of energy-to-data ratio was performed for a microdisk lasers after bonding.

1. Introduction

In recent years, much attention has been paid to the development of microlasers based on III-V materials, which could be placed on a silicon substrate and thus allow the integration of light emitting devices with elements of silicon microelectronics and/or silicon photonics [1]. Whispering gallery mode (WGM) microlasers, such as microdisk and microring lasers, are one of the promising microlasers due to the simplicity of their manufacture, high quality factor and low optical losses. It is known [2-4], that thermal resistance increases with decreasing laser cavity size. This effect is quite critical for small devices such as microdisk lasers (MDL), because it has a great influence on their characteristics and performance due to various temperature-dependent processes [5]. It was shown in work [6] that the bonding of microdisk lasers to a silicon substrate improve thermal resistance.

In this work we analyze the effect of reducing thermal resistance on output power, high-frequency characteristics, modulation properties and energy-to-data ratio (EDR) in microdisk lasers.

2. Methods

The laser heterostructure was grown by metalorganic vapour-phase epitaxy on an n+-GaAs substrate misoriented by 6° toward [111] direction. The laser active region consists of 6 InGaAs/GaAs quantum well-dot layers separated from each other with 40 nm thick GaAs spacer layers.Microdisk lasers were formed by photolithography and dry etching. The thermocompression bonding of microdisk lasers on the silicon surface was performed using a Finetech FINEPLACERlambda2. Electroluminescence was collected with a x50 Mitutoyo M Plan Apo NIR objective and detected by a Yokogawa AQ6370C

optical spectrum analyzer or by Thorlabs FDG1010 1 × 1 cm^2 photodiode. Dynamic characteristics were carried out using a New Focus 1434 photodetector with the range from 50 MHz to 20 GHz and an Agilent E8364B network analyzer.

3. Results and discussion

Characteristics of the microdisk lasers with a diameter of 19 and 31 μm were compared before and after bonding. Thermal resistance of bonded MDL decreases in a 2.3 and 1.8 times for 19 μm and 31 μm, respectively. The threshold current after bonding decreased from 9.4 to 7.6 mA for 19 μm microdisk and from 21.4 to 17.4 for 31 μm microdisk (fig. 1(a)). Better heat removal from the active region results in the higher output optical power, slope of dependence of optical power on bias current and thermal roll-over.

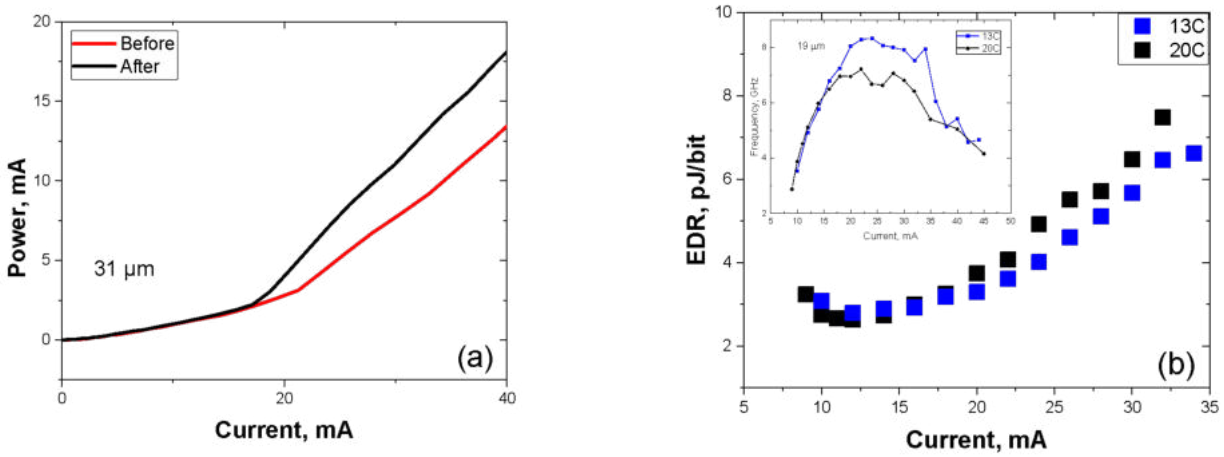

Figure 1. The output power versus the injection current of 31 μm MDL before and after bonding (a). The dependence of EDR on the bias current for 13ºC and 20ºC and the 3dB bandwidth versus the pumping current (inset) for 19 μm MDL (b). .

We also observe improvement in dynamic characteristics of the bonded lasers. The 3dB modulation bandwidth (f_{3dB}) of 6.9 GHz and 8 Ghz for 19 μm in diameter device was 20ºC and 13ºC degrees, respectively (inset in Fig.1, b). To estimate the energy efficiency of the microdisk laser intended for optical data transmission one can use energy-to-data ration (EDR), e.g. the electrical energy consumed per bit of transmitted information, EDR = UI/B, where U – is voltage, I- is bias current, B – is the bit rate [7]. The value of bit rate (B) can be estimate from twice the modulation bandwidth $B = 2f_{3dB}$. The smallest EDR value of 2.5 pJ/bit is achieved in 10-15 mA bias current range. At the current of maximum f_{3dB} (25mA) for 13ºC degrees the EDR value is 4 pJ/bit.

Acknowledgments This study was supported by Russian Science Foundation grant 18-12-00287, https://rscf.ru/project/18-12-00287/.

References

[1] Cornet C, L´eger Y, Robert C, Integrated lasers on silicon 2016 ISTE Press

[2] Kryzhanovskaya N. V. *et al* 2016 Semicond., **50(3)**, 390
[3] Moiseev E. *et al*, Opt. Lett., 2018, **43(19)**, 4554
[4] Zhukov A. E. *et al*, 2020, IEEE J. Quantum Electron., **56(5)**, 2000908
[5] Joyce W. B. and Dixon R. W., 1975 J. Appl. Phys., **46(2)**, 855
[6] Zubov F. *et al,* 2021, Optics Letters.. **46 (16)**, 3853
[7] Moser P. *et al* , 2011 Appl. Phys. Lett., **98 (23)**, 231106

Influence of polarization reference frame rotation on ground-receiver error rate in satellite quantum key distribution

A V Duplinsky[1,2,6], A V Khmelev[1,2,4], V E Merzilkin[2,3], V L Kurochkin[1,2,3,4], and Y V Kurochkin[1,2,3,4,5]

[1]QSpace Technologies, Lugovaya st. 4, Moscow, Russia
[2]QRate, Novaya av. 100, Moscow, Russia
[3]NTI Center for Quantum Communications, National University of Science and Technology MISiS, Leninsky prospekt 4, Moscow, Russia
[4]Russian Quantum Center, Bolshoy Boulevard 30, bld. 1, Skolkovo, Moscow, Russia
[5]Moscow Institute of Physics and Technology, 9 Institutskiy per., Dolgoprudny, Moscow Region, Russia
[6]HSE University, Myasnitskaya ulitsa 20, Moscow, Russia

{al.duplinsky, a.khmelev, v.merzlinkin, v.kurochkin, yk}@goqrate.com

Abstract. Quantum key distribution in Space-Earth communication link is a complicated technical task. To precise mutual guidance of the optical axes during a session on a satellite QKD, it is also necessary to ensure the best possible angular bases positions coincidence of the satellite and the receiving station, since during the flight the satellite has its own rotation, and this displacement makes a great contribution to error rate depending on time.

1. Introduction

Quantum key distribution (QKD) in Space-Earth communication link is a complicated technical task [1]. The development of equipment requires a solution of many issues including as the precise pointing of optical axes of a ground station and a satellite payload, but also the highly necessary polarization reference frame coincidence of them. The problem of a pointing and tracking was successfully solved and reported in our previous articles [2,3].

The satellite reference frame has a time dependent rotation relatively at the ground station, even when satellite system is stabilized along nadir axis [4]. Such angular movement creates a shift in the angles of the polarization bases in time during a QKD communication session with a satellite, which increases the error rate when decoding quantum states.

In this work we consider an effect a time dependent rotation of polarization basis during and describe the method which help to actively compensate of this polarization deviation.

2. Compensation unit

As we wrote earlier [2], the main optical part of our ground-based receiver for quantum key distribution with a satellite consists of a mirror telescope, an optical signal processing unit, and a polarization analyzer that acts as a free-space decoder that allows using the BB84 protocol for key distribution. The optical signal analysis and processing system (APS) includes a motorized half-wave plate, whose

rotation can be controlled in accordance with a time-dependent function in order to make it possible to compensate the angular shift of the bases.

Such a unit makes it possible to align the analysis angles of the decoder bases with the changed angular coordinates of the satellite bases by shifting the phase on the half-wave plate.

3. Operating mode simulation

In order to test the operation of compensating system we performed experiment that allows to simulate the rotation of the satellite during the QKD session. A laser source with a polarizer is installed in front of our receiving ground station, output is a strong 850 nm optical signal with linear polarization (PER > 1:4000). This source is mounted in a high-precision rotary holder, which allows to change the angle of the output linear polarization.

The first step is to find the zero point of our receiver. |H⟩ polarization is set on the source and by rotating the half-wave plate of the compensation system in APS we find its angular position corresponding to the largest number of clicks on the SPD connected to the |H⟩ channel of decoder.

Next, we rotate the polarization at the source in ± 90 degrees range with the compensation system turned on, while fixing the dependence of the extinction coefficient within one basis on time. Such a measurement must be carried out for all |H⟩, |V⟩, |D⟩, |A⟩ decoder channels. The average value of a reciprocal PER for our setup from the residual error in the operation of the compensation system turned out to be less than 0.5%.

Acknowledgments

This work was supported by The Russian Science Foundation (Grant No. 17-71-20146)

References

[1] Han, Xuan, et al. Polarization design for ground-to-satellite quantum entanglement distribution. Optics Express 28.1, 369-378 (2020).

[2] Khmelev, A. V., et al. Recording of a Single-Photon Signal from Low-Flying Satellites for Satellite Quantum Key Distribution. Technical Physics Letters, 1-4 (2021).

[3] Kurochkin, V. L., et al. Elements of satellite quantum network. International Conference on Micro-and Nano-Electronics 2021, Vol. 12157 SPIE (2022).

[4] Ming Zhang, Liang Zhang, Jincai Wu, Shiji Yang, Xiong Wan, Zhiping He, Jianjun Jia, D. S. Citrin, and Jianyu Wang, "Detection and compensation of basis deviation in satellite-to-ground quantum communications," Opt. Express 22, 9871-9886 (2014).

Modelling of electromagnetic wave spectra of integrated optical waveguides

A I Eremeev[1], **M A Gordienko**[1], **A V Bagautdinov**[1], **A B Ustinov**[1]

[1]Saint Petersburg Electrotechnical University "LETI", St. Petersburg 197022, Russia

e-mail: andrey-eremeev1999@mail.ru

Abstract. The main element of integrated circuits is a rectangular integrated optical waveguide. Its spectrum is calculated in various ways, among which the method of Marcatili and Goell. The simulation was carried out for the parameters of optical waveguides, which are most often encountered in practice.

1. Introduction

Interest in the research and development of integrated optical circuits has been growing rapidly in recent decades. The main element of such schemes is an integrated optical waveguide. It is a basis for elaboration of such circuit components as ring resonators, interferometers, etc. [1-3].

The aim of this work is numerical simulation of the spectra of electromagnetic waves propagating in rectangular integrated optical waveguides by the Marcatili method [4] and the Goell method [5], as well as a comparison of the calculation results.

2. Results

The simulation was carried out for geometrical parameters of optical waveguides most often encountered in practice. Such waveguides include rectangular waveguides made of silicon or silicon nitride surrounded by silicon oxide [6]. In the simulation, the width and thickness of the waveguides were varied from 200 to 1000 nm.

Consider the results obtained for the silicon waveguide with the following topology: width 500 nm, thickness 220 nm, refractive index of the waveguide layer 3.476, refractive index of the environment 1.444. The simulation results showed that for the wavelength of 1.55 microns (corresponding to the frequency of 193.414 THz), the deviation of the frequency calculated by the Marcatili method and the Goell method is approximately 0.58% (Figure 1a).

The results obtained for a waveguide made of silicon nitride with a refractive index of 1.9963, but with the other parameters given above, showed that for the wavelength of 1.55 microns, the deviation of the frequency calculated by the Marcatili method and the Goell method is approximately 3.52% (Figure 1b). Similar values given for other values of width and thickness also showed a small discrepancy in the results of calculations using two methods. The results obtained allow us to conclude that for the case of silicon waveguides, the calculation method does not play a significant role, and for silicon nitride waveguides, it is preferable to use the Goell method.

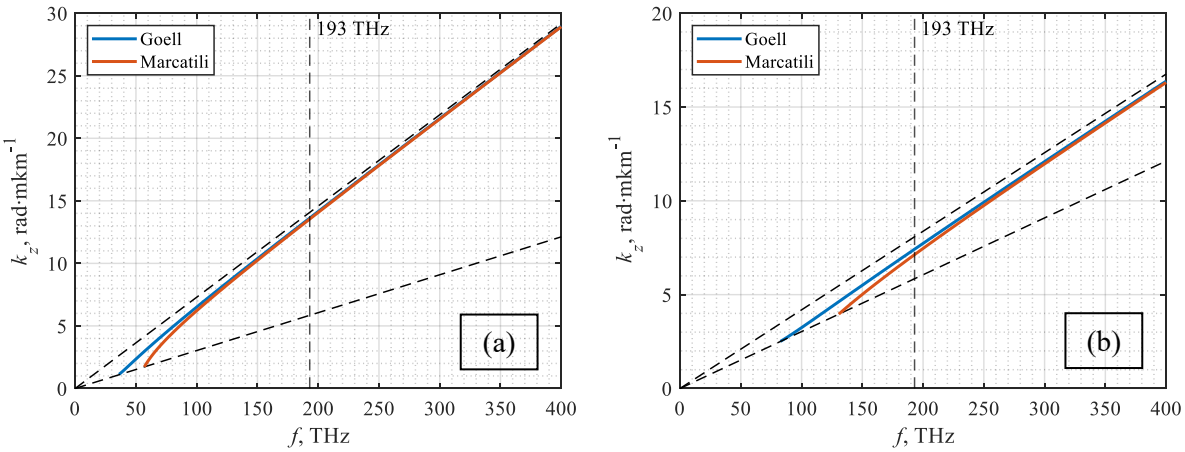

Figure 1. Dispersion characteristics calculated by methods of Marcatili and Goell for silicon waveguide (a) and for silicon nitride waveguide (b).

Acknowledgments

The work was partially supported by the Ministry of Science and Higher Education of the Russian Federation (project "Goszadanie", grant No. FSEE-2020-0005).

References

[1] A. A. Nikitin et. al. «Carrier-induced optical bistability in the silicon micro-ring resonators under continuous wave pumping» Optics Communications. Vol. 480. pp. 126456. 2021.

[2] A. B. Ustinov et. al. «Principles of Constructing Optoelectronic Microwave Oscillators» Photonics Russia. Vol. 15, №3. pp. 228-237. 2021.

[3] A. A. Nikitin et. al. «Optical bistable SOI micro-ring resonators for memory applications» Optics Communications. Vol. 511. pp. 127929. 2022.

[4] E. A. Marcatili «Dielectric rectangular waveguide and directional coupler for integrated optics». Bell System Technical Journal. Vol. 48, №7. pp. 2071-2102. 1969.

[5] J. E. Goell «A circular-harmonic computer analysis of rectangular dielectric waveguides». Bell System Technical Journal. Vol. 48, №7. pp. 2133-2160. 1969.

[6] D. J. Blumental et. al. «Silicon nitride in silicon photonics». Proceedings of the IEEE. Vol. 106, №12. pp. 2209-2231. 2018.

A comprehensive study of electroluminescence and temperature distribution of UX:3 AlInGaN LED

A E Ivanov[1,2*], A V Aladov[1], A E Chernyakov[1] and A L Zakgeim[1]

[1] SHM R&E Center, RAS, St. Petersburg 194021, Russia
[2] St.-Petersburg State Electrotechnical University "LETI", St. Petersburg 197376, Russia
*a-e-ivano-v@yandex.ru

Abstract. Comprehensive analysis of current spreading, temperature distribution and near-field electroluminescence of high-power "UX:3" AlInGaN LED has been performed by combination of different experimental methods. A thermal resistance evaluation was based on transient electrical processes in the diode under heating by direct current and analysis of thermal equivalent circuit (the Cauer model). Thanks to the applied method, thermal resistances of internal elements of the LED were determined. At the same time high resolution mapping of EL and thermal radiation was obtained by optical microscope and infrared images technique. It has been established distribution pattern of light and temperature mapping.

1. Introduction

The scope of application of light-emitting diodes (LEDs) keeps expanding. The study of the operation of LEDs in pulsed mode to exclude self-heating at high excitation levels is of great interest to reveal the injection and recombination mechanisms and identifying the reasons that limit the energy capabilities of devices [1-4].

2. Experimental

The object of study in this work was the most advanced AlInGaN LEDs of the "UX:3" design [5] with a distributed system of reflective contacts located on the back side of the emitting chip (produced by Osram [6]). In this regard, chip had an unilateral arrangement of contacts and the light output through the n-area. LEDs had a chip with area of 1500x1200 μm^2 and were mounted by "flip-chip" method on the AlN substrate.

As has been shown previously [2], the near field of electroluminance (EL), as a first approximation, correlated with the current density distribution in the active region. Current spreading uniformity can be evaluated by the uniformity of the near field EL.

The near-field EL was mapped by a Mitutoyo optical microscope equipped with a digital camera (12 Mpxl CMOS matrix) and Avantes AvaSpec-2048 spectrometer. Profiles of EL intensity is shown in Fig.1b. In addition, for revealing the mechanisms of current redistribution with an excitation, the dependence light output and thermal resistances on current was measured. Light-current characteristics were obtained using the automated OL 770-LED Test and Measurement System [7]. The thermal resistance was measured by the forward-voltage relaxation method with Thermal tester T3Ster.

Study of thermal resistance generally gives an average temperature distribution on the area of chip. To obtain the temperature distribution across the area of chip, the infra-red (IR) thermal radiation in the spectral range of 2.5-3 μm was mapped by a specially designed IR microscope. Using of the relatively short-wavelength IR radiation allowed reduction of the diffraction blurring and, consequently, improvement of the spatial resolution of IR mapping down to ~3 μm [5].

3. Results and discussion

Temperature distributions in the active region of the LED chip (insert 1 to fig. 1) have been obtained by mapping the IR thermal radiation at operating current. Fig. 1 curve 1 plots corresponding temperature distributions in the cross-section A of the LED chip with forward current switched on. At the bias applied, i.e. at the current of 3 A (current density of 170 A/cm^2), the temperature distributions remain to be nearly

uniform. On the other hand, some tendency to a concave temperature profile can be recognized in the distributions. It can be explained by the fact that the heat transfer from the center of the chip to the ambient environment is worse than at the periphery.

The distribution map of near-field EL intensity (insert 2 to fig. 1) on the chip surface at operating currents was obtained by optical microscopy. One can see from fig.1 curve 2 that at operating current (I=3 A) uniform distribution of LED emission takes place. The minimum of curve indicate the *n* - contacts, which pass through the *p*-*n*-junction and made of metal.

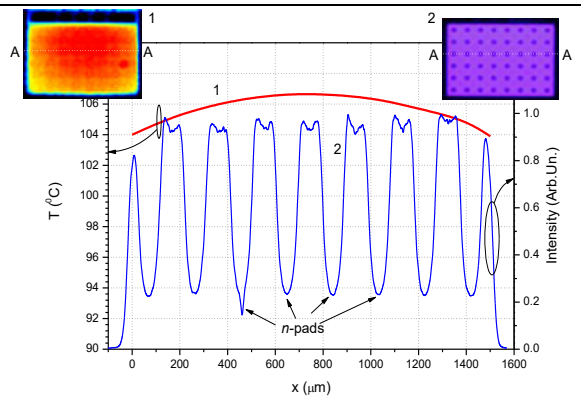

Figure 1. Temperature distributions (curve 1), profile of EL intensity (curve 2) in the cross-section A LED at I=3 A. Insert shows IR-mapping (1), EL-mapping (2)

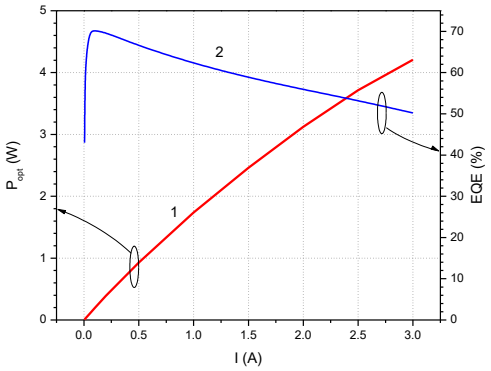

Figure 2. Optical power (curve 1) and external quantum efficiency (curve 2) of the LED chip dependences on current.

4. Conclusion

High-power AlInGaN blue LED of "UX:3" design have been studied by advanced experimental techniques including: optical power and external quantum efficiency (EQE) dependences on current, high-resolution mapping of EL and IR radiation (thermal imaging) and transient thermal analysis.

For the LED chip was established maximum EQE (70%) and low effect of efficiency droop which obtained by better design of chip.

It was investigated variation EL and temperature distribution as well as thermal resistance for high-power LED with the driving current. The total thermal resistance of the LED is found 4 K/W.

For LED chip was established uniform temperature distribution of the central. The little temperature gradient $\Delta T \sim 3$ K of distribution in cross-section associated with the deterioration of the conditions of heat removal from the center to the periphery.

Acknowledgments

This work was carried out at the Center of Multi-User Facilities «Element Base of Microwave Photonics and Nanoelectronics: Technology, Diagnostics, and Metrology».

References

[1] Yadaev A, Titkov I, Socolovskii G, Karpov S, Dudelev V, Soboleva K, Pietzonka I, Lugauer H-J and Rafailov E 2016 *SPIE Proceedings* **9768**

[2] Karpov S, Galler B, Strabburg M and Rafailov E 2014 *IEEE J. Quantum Electron* **50** 911-20

[3] Aladov A, Chernyakov A, Ivanov A and Zakgeim A 2020 *ICLO* **1109**

[4] Chernyakov A, Zakgeim A, Bulashevich K and Karpov S 2015 *16th Int. Conf. on Thermal, Mechanical and Multi-Physics Simulation and Experiments in Microelectronics and Microsystems,* 1-5, DOI: 10.1109/EuroSimE.2015.7103132

[5] Laubsch A, Sabathil M, Baur J, Peter M and Hahn B 2010 *IEEE Transaction on Electron Devices* **57** (1) 79-87 DOI: 10.1109/TED.2009.2035538

[6] Osram Datasheet LE B Q8WP, https://www.osram.com/ecat/OSRAM%20OSTAR%C2%AE%20Projection%20Compact%20LE%20B%20Q8WP/com/en/class_pim_web_catalog_103489/prd_pim_device_2191200/

[7] Zakgeim A and Chernyakov A 2013 *LIGHT & ENGINEERING* **21** Iss 4 64-70

Wavelength stabilized laser module for pumping high-power fiber lasers

A N Ignatev, A V Fomin, S R Usmanov
FSUE «RFNC-VNIITF named after Academ. E. I. Zababakhin», 456770, Snezhinsk, Russia

Abstract. The paper presents the results of the development of wavelength stabilized laser modules using volume Bragg gratings with a center wavelength of 976 nm. A stabilization scheme with the placement of volume Bragg gratings after collimating lenses of a laser module is considered. The characteristics of laser diodes have been studied using volume Bragg gratings with different reflection coefficients, the spectral and power characteristics of wavelength stabilized laser modules have been measured.

1. Introduction

The important characteristics of laser modules (LMs) used for pumping fiber lasers include pumping efficiency, determined, among other things, by the spectral characteristics of the used LM. For pumping ytterbium fiber lasers, LMs of the spectral ranges 915 nm, 940 nm, 975 nm are required, while pumping modules of the spectral range 975 nm are especially important, as corresponding to the absorption peak with a maximum absorption coefficient of ytterbium-doped fibers [1]. At the same time, the width of the absorption peak in this region is quite narrow, which imposes certain restrictions on the pumping modules based on high-power laser diodes (LDs) since the spectral width can reach values up to 6 nm, the typical wavelength shift from temperature is 0.3 nm/°C. One of the ways to narrow the spectral width of the LD, as well as the temperature stabilization of the central wavelength, is the implementation of an external LD resonator by using volume Bragg grating as an output mirror [1,2].

2. Wavelength stabilized laser module

In this work, an LM was used as a pumping source with a spatial combination of the radiation of several LDs, followed by coupling into a silica fiber with a core diameter of 105 μm and a numerical aperture of 0.15 [3]. The typical wavelength shift from the pump current in the LM used didn't exceed 1.1 nm/A, the spectral width amounted to 5 nm (Figure 1a). The LM design allowed to implement a scheme for stabilizing the wavelength of LD radiation by placing volume Bragg grating after collimating lenses of LM.

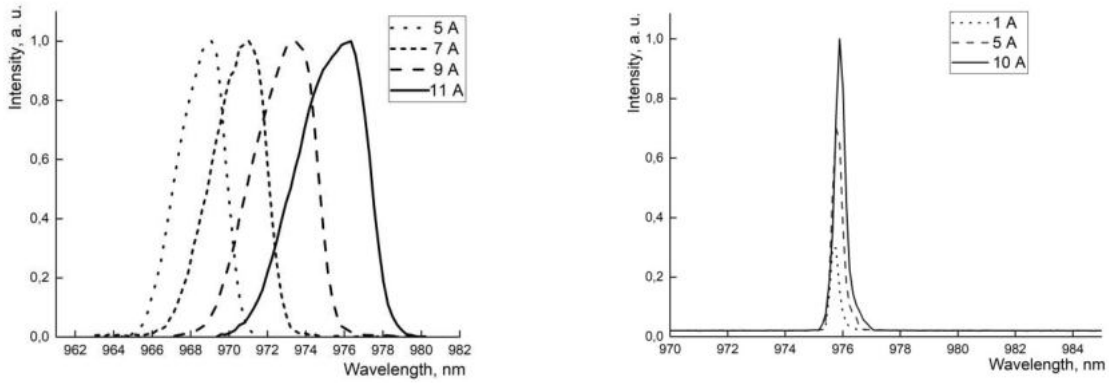

a) b)

Figure 1. Dependence of the LM's spectral characteristics on the pumping current: a) without stabilization of the wavelength b) with stabilization of the wavelength.

3. Results

In this work, the influence of volume Bragg gratings with different reflection coefficients on the spectral and power characteristics of the LD was investigated. The use of volume Bragg gratings with a reflection coefficient of 8% made it possible to achieve stabilization of the wavelength of LM radiation for the entire range of operating temperatures and pumping currents (Figure 1 b) with minimal losses of LM's radiation power. The spectral width of the LM's radiation was narrowed to 0.5 nm, the wavelength shift from the pump current decreased to ~ 0.03 nm/A. The power of the manufactured LMs exceeded 40 W in continuous operation with a pumping current of 10 A.

References

[1] Kohler B., Brand T., Haag M. 2009 *Proc. of SPIE* **7198**
[2] Volodin B. L., Dolgy S. V., Melnik E. D., Downs E., Shaw J., Ban V. S. 2004 *Optics Letters* **2** 16
[3] Fomin A. V., Usmanov S. R., Ignatev A. N., Kadigrob E. V. 2022 *J. of Technical Physics* **92** 4

Fabrication and investigation of UV photodiode based on n-GaN/p-NiO heterojunction

A Kazakin[1,2], Y Enns[1,2], A Uvarov[1], E Nikitina[1]

[1]Alferov University, St. Petersburg, Russia
[2]Peter the Great Saint-Petersburg Polytechnic University, St. Petersburg, Russia

Abstract. This paper presents the experimental results of the study of n-GaN/p-NiO heterojunction for a UV photodiode. Synthesis of n-GaN films was carried out using the method of molecular beam epitaxy with plasma nitrogen activation on template substrates GaN/c-Al_2O_3. The p-type layers were formed by DC magnetron sputtering of NiO films followed by annealing. The optical and electrical characteristics of individual semiconductor layers and diode structures were studied. The study of the diode current-voltage characteristics under light and dark conditions showed the selective sensitivity of the diode structure to UV radiation.

1. Introduction

Improvement in technologies for the epitaxial growth of gallium nitride (GaN) contributed to the successful application of this material in high-frequency electronics and optoelectronic devices, such as light-emitting diodes and lasers [1, 2]. In addition, the high band gap of GaN makes this material promising for the development of selective UV photodetectors (wavelength $\lambda < 365$ nm). To create such devices, various photodiode structures based on homo- or heterojunctions can be used [3, 4]. However, due to numerous technological difficulties that arise during the synthesis of high-quality p-type GaN epitaxial layers [5], the use of homojunctions for UV photodiodes is less preferable compared to heterojunctions based on n-type GaN and another wide-gap p-type semiconductor. Among various p-type materials, nickel oxide (NiO) is most compatible with GaN in terms of such parameters as band gap and lattice parameter [6]. In addition, NiO is a direct gap semiconductor, has excellent chemical stability, and is easy to deposit with current microelectronics technologies. Therefore, the n-GaN/p-NiO heterostructure can be used in the future to create cheap and efficient UV photodiodes.

In this work, we analyze the possibility of creating a selective UV photodetector based on the n-GaN/p-NiO heterojunction.

2. Results

The synthesis of GaN layers was carried out on a Veeco Gen 200 industrial type installation by the PA MBE method. The growth of the epitaxial layer was carried out on GaN/c-Al2O3 template substrates, where 2 μm thick GaN sublayer was obtained by metal-organic vapor phase epitaxy. The subsequent growth of Si-doped GaN layers was carried out at constant substrate temperatures Ts = 700°C, a gallium flow of ~0.25 μm/h, and an activated nitrogen flow of ~0.05 μm/h. The silicon flow used in the experiments made it possible to obtain an electron concentration in the GaN layers of $\sim 3.7\times10^{18}$ cm^{-2}.

The formation of NiO films was carried out using DC magnetron sputtering from a nickel target Ni (99.95%) in a mixture of working gases 25%O_2 / 75%Ar at a working pressure of 3 mTorr. The deposition was carried out both on the surface of the GaN epitaxial film and on the glass for optical and electrical measurements of the obtained layer. The thickness of the NiO layer was 300 nm. The resulting NiO films had high conductivity and low transparency. Subsequent annealing of the films at a temperature of 550°C and a duration of 60 min led to an increase in the resistivity and optical transmission of the film.

To form contacts, Cr/Au and Ni layers were used for contact to GaN and NiO, respectively. Contact metallization to the NiO layer was made in the form of a grid structure with an aperture of 3 mm, where the width of the grid band was 5 μm with a period of 100 μm.

In this work, optical transmission and reflection spectra of GaN and NiO layers were obtained using an AvaSpec-ULS2048XL-EVO-RS spectrometer and a xenon radiation source. The photoluminescence (PL) spectra of the structures were measured using an Accent RPM Sigma setup with 266 nm lasers. Based on the measurement results, the values of the optical band gap for the photodetector layers were obtained. Measurement of current-voltage characteristics was carried out using UV LEDs with a wavelength of 365 nm and a halogen radiation source. The results of the studied characteristics of the light and dark current showed the selective sensitivity of the diode structure to UV radiation.

Acknowledgments
The work was supported by the Ministry of Education and Science (grant №FSRM-2020-0008).

References
[1] Wasisto H S, Prades J D, Gülink J, Waag A 2019 *Appl. Phys. Rev.* **6**
[2] Ueda T 2019 *J. Appl. Phys*. **58** 0804
[3] Lee C-R, Seol K-W, Yeon J-M, Choi D-K and Ahn H-K 2001 *J. Cryst. Growth* **222** 459–64
[4] Alivov Y I, Van Nostrand J E, Look D C, Chukichev M V and Ataev B M 2003 *Appl. Phys. Lett.* **83** 2943–5
[5] Enatsu Y, Gupta C, Keller S, Nakamura S, Mishra U K 2017 *Semicond. Sci. Technol.* **32** 1–6
[6] Irwin M D, Buchholz D B, Hains A W, Chang R P H and Marks T J 2008 *Proc. Natl Acad. Sci*. **105** 2783–7

Effect of ion radiation on the characteristics of InGaAs/GaAs/Al_2O_3/CoPt spin light-emitting diodes

I.L. Kalentyeva, P.B. Demina, M.V. Dorokhin, O.V. Vikhrova, A.V. Zdoroveyshchev, Yu.A. Dudin

Research Institute for Physics and Technology of UNN, Gagarina Avenue, 23/3, Nizhny Novgorod, 603950

istery@rambler.ru

Abstract. The influence of ion implantation on the characteristics of InGaAs/GaAs/Al_2O_3/CoPt spin light-emitting diodes has been studied. It has been established that under ion irradiation of He^+ with a fluence of 1×10^{12} cm^{-2} it can be preserved the emitting properties of the InGaAs/GaAs quantum well. In this case, an increase in the degree of circular polarization of electroluminescence is also observed, up to approximately 4 times, depending on the thickness of the GaAs cap layer.

1. Introduction

InGaAs/GaAs based heterostructures with a CoPt ferromagnetic injector are used to fabricate spin light emitting diodes (SLEDs) exhibiting circularly polarized radiation. In this case, the degree of circular polarization of electroluminescence in such diodes depends both on the efficiency of spin injection from the magnetized CoPt layer and on spin relaxation and precession that occur during the transfer of spin-polarized carriers from the ferromagnetic injector to the active region of the SLED [1]. This paper presents the results of studying the effect of ion implantation on the characteristics of InGaAs/GaAs/Al_2O_3/CoPt SLEDs.

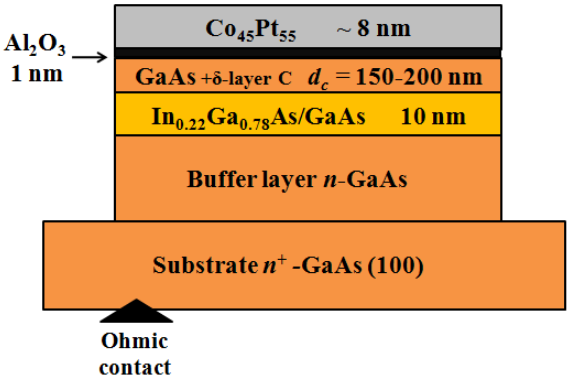

Figure 1. Scheme of a spin light emitting diode with a CoPt ferromagnetic injector.

2. Experimental technique

The semiconductor part of the light-emitting diodes was formed by MOCVD on *n*-GaAs (100) substrates: an *n*-GaAs buffer layer, an $In_{0.22}Ga_{0.78}As$ quantum well (10 nm), and a GaAs cap layer

d_c = 150–200 nm thick containing delta layer of carbon. Then, by the method of electron beam evaporation in vacuum at 300°C, a ferromagnetic injector based on the $Co_{45}Pt_{55}$ alloy ~8 nm thick was formed [2]. A schematic representation of the formed SLEDs is shown in fig.1.

Using photolithography and chemical etching, mesastructures of diodes with a diameter of 500 μm were fabricated. The resulting SLEDs were irradiated at the ILU-3 accelerator with He^+ ions with a fluence of 1×10^{12} cm^{-2} and an energy of 20 keV. The influence of ion irradiation on the *I-V* characteristics, electroluminescence intensity (I_{EL}), and the degree of circular polarization of electroluminescence (P_{EL}) of SLEDs data was investigated.

3. Results and discussion

It has been established that, under ion irradiation with the indicated fluence, it is possible to preserve the radiative properties of the InGaAs/GaAs quantum well, however, the I_{EL} of such diodes decreases by more than an order of magnitude due to the penetration of defects into the active region. At the same time, according to *I-V* characteristics, a decrease in the reverse current by an order of magnitude to values of 1×10^{-7} A at a voltage of 2 V was observed.

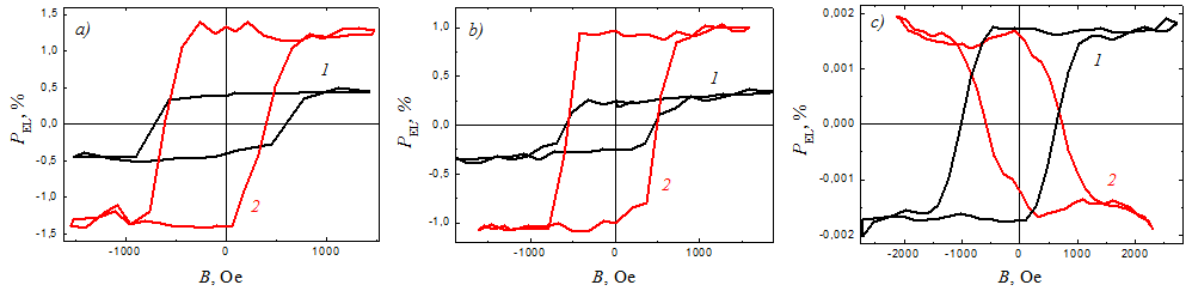

Figure 2. P_{EL} magnetic field dependences for InGaAs/GaAs/Al_2O_3/$Co_{45}Pt_{55}$ SLEDs with different coating layer thickness d_c, nm: *a*) 150, *b*) 175, *c*) 200 before (*1*) and after implantation (*2*) at a temperature of 10 K.

An increase in the degree of circular polarization of electroluminescence by about 4 times is observed for structures with a coating layer thickness of 150 and 175 nm (up to 1% and 1.3%, respectively) (fig.2*a*,*b*). In the case of a diode with d_c = 200 nm, a change in the sign of P_{EL} = - 0.17 % is observed (fig.2*c*). It is assumed that the increase and reversal of the sign of the degree of circular polarization after exposure to low fluencies of ion irradiation is associated with a change in the magnetic field of the inhomogeneously magnetized CoPt contact that "twirls" spin-polarized injected carriers with a different oscillation period. A change in such an "internal" magnetic field may be associated with an increase in the homogeneity of the alloy due to the mixing of the components under the influence of high-energy ions. Apparently, the change in the P_{EL} value is also influenced by the change in the recombination time (τ_R). Thus, when radiation defects are introduced, the value of τ_R decreases at a constant spin relaxation time (τ_S), and the value of $P_{EL} \sim 1/(1+\tau_R/\tau_S)$ increases [3]. The achieved results may be of interest for the technology of spin optoelectronic devices.

Acknowledgments

This work was supported by the Russian Science Foundation (project no. 21-79-20186).

References

[1] M.V. Dorokhin et al. Physics of the Solid State, **59**, 2155 (2017).

[2] A.V. Zdoroveyshchev et al. Physics of the Solid State, **58**, 2267 (2016).

[3] G. Salis et al. //Appl. Phys. Lett., **87**, 262503 (2005).

Radiometric performance model of the near-infrared spectrometer for hydrocarbon analysis

A G Korepanova[1], A S Bobe[1,2], A O Voznesenskaya[1]

[1]ITMO University, Grivtsova Ln. 14-16, Saint Petersburg, 190031, Russia
[2]Geophotonica LLC, Aptekarsky Pr. 4, Saint Petersburg, 197022, Russia

korepanova@niuitmo.ru

Abstract. The paper describes the simulated radiometric performance of the near-infrared (1.45–2.05 μm) spectrometer for hydrocarbon analysis. This simulation allows to estimate the signal-to-noise ratio as a function of the wavelength. The model results of the optoelectronic system with commercial photodetectors are also presented.

1. Introduction

Near-infrared (NIR) spectroscopy is a powerful tool for quantitative and qualitative analysis and process control. Furthermore, downhole fluid analysis (DFA) by NIR spectroscopy is an important and effective method to understand the composition in hydrocarbon fluid [1, 2]. The implementation of DFA spectrometer is a very challenging engineering task. Hence, an accurate radiometric performance model is essential for designing new devices.

The aim of the present work is to develop the optoelectronic system model of the NIR spectrometer (Fig. 1) and estimate the signal-to-noise ratio (SNR) properties. With understanding of these properties a way of optimizing the optical system and improving the device can be identified.

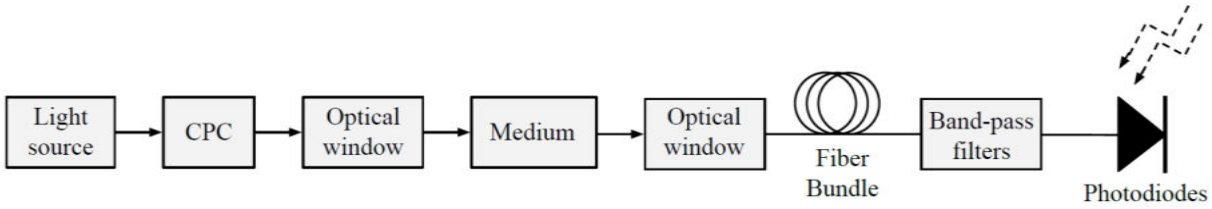

Figure 1. Block diagram of the spectrometer optical system.

2. Spectral radiance modeling

The optical system light transmittance and spectral radiance of the light source are wavelength dependent. To calculate irradiance output non-sequential Zemax model have been developed. Non-sequential ray trays allow to define spectral data of the source and medium and analyze stray or scattered light effects.

Figure 1 shows a block diagram of the spectrometer optical system. The energy is emitted by a gallogen lamp and concentrate by a compound parabolic collector (CPC). Then it is transmitted, scattered, and reflected by the medium and optical components. After passing through the optical system the transmitted light is distributed to photodiodes.

3. Radiometric performance

Data from calculated radiometric performance are presented in Table 1 with the wavelength channels. To calculate the irradiance Zemax model was used. The SNR of the photodiode (Hamamatsu G12182) was calculated according to the formula SNR = (mean of signal)/(r.m.s. of the noise).

Table 1. Irradiance and signal-to-noise ratio performance

Wavelength, μm	1.45	1.60	1.65	1.67	1.69	1.73	1.76	1.80	1.93	1.98	2.01	2.05
Irradiance, W/(m^2·nm)	0.64	0.53	0.38	0.35	0.39	0.35	0.24	0.32	0.24	0.28	0.19	0.21
SNR	612	595	506	487	512	509	422	484	416	453	368	389

4. Conclusion

Radiometric performance models can be used to determine optimal system design to achieve the required specifications. A model of the of the NIR spectrometer for hydrocarbon analysis has been developed.

Acknowledgments

The study is funded by RPMA grant of School of Physics and Engineering of ITMO University.

References

[1] Sarkodie K, Fergusson-Rees A, Diaz P 2018 *J. Comput. Multiph. Flows* **10(1)** 43-56

[2] Mullins C, Pomerantz A, Zuo J, Dong C 2014 *Annu. Rev. Chem. Biomol. Eng.* **5** 325-345

Veracity a method of detecting scattered laser radiation for content measuring of particulate matter in the air

A D Kurkova[1] and V V Davydov[1, 2, 3]
[1]Peter the Great Saint-Petersburg Polytechnic University, Saint Petersburg, Russia, 195251
[2]The Bonch-Bruevich Saint-Petersburg State University of Telecommunications, Saint Petersburg 193232, Russia
[3]All-Russian Research Institute of Phytopathology, Moscow Region 143050, Russia

e-mail: kurkova.ad@edu.spbstu.ru

Abstract. The problem of measuring the parameters of dust particles in the environment is currently relevant for residents of densely populated cities. Measurements of the size and size distribution function of dust particles are carried out using instruments based on the method of laser radiation scattering. An analysis of the measurement method based on the spherical particle model and the Mie diffraction theory is carried out. The possibility of erroneous indication of measurement results by widely used portable measuring devices for dust parameters is shown.

1. Introduction

In recent years, industrial production in the world is rapidly gaining momentum. Along with this, the importance of solving the problem of measuring the parameters of dust particles in the environment is growing. This is most relevant for residents of densely populated cities, as transport, industrial emissions and smog from thermal power plants are the main source of dust particles. Particularly important are solid particles with a size of 25 microns, the same PM 2.5. They overcome our natural protective barriers, penetrating the body through the mucous surface of the respiratory organs, and then spreading inside, overcoming the protective membranes of the body and penetrating directly into the cell. The essence of the problem lies in the fact that the accuracy of commercial portable measuring instruments for dust parameters is low (± 15%), since the device registers particles larger than 2.5 μm, while in fact the size of the registered particles is less than 2.5 μm [1]. They have a negative impact on human health.

2. Method

The measurements were carried out based on the Mie diffraction theory [2]. This theory is a complex electromagnetic theory describing the scattering of light by spherical particles. The radiation scattering pattern on a particle can be described over the entire angular range from 0° to 360° depending on the amplitude and wavelength. To use this theory, the optical properties of this system must be known, i.e. complex refractive index, its real and imaginary parts. For quartz dust particles in ambient air, this value is typically 1.6–0.05i, where «i» is the imaginary unit. Knowing the value of the imaginary part is necessary to take into account the specific structure of the particle surface, for example, roughness.

3. Results

Curves of the angular distribution of scattered light intensity for atmospheric dust were obtained. For small particles, the scattering indicatrix of radiation is concentrated in a sufficiently large scattering

angle, and for large particles, on the contrary, in a small angle. At large scattering angles for very small particles, the intensities of the scattered radiation are very small, and at small angles little scattering is observed. For particles smaller than 2.5 μm, it cannot be established that the scattering intensities are extremely low compared to particles larger than 2.5 μm. The selection of small particles by scattering angles is based precisely on this fact. On Figure 1 shows the calculated dependences of the scattered light intensity s on the scattering angle θ for silica particles with sizes of 2.5 and 10 μm.

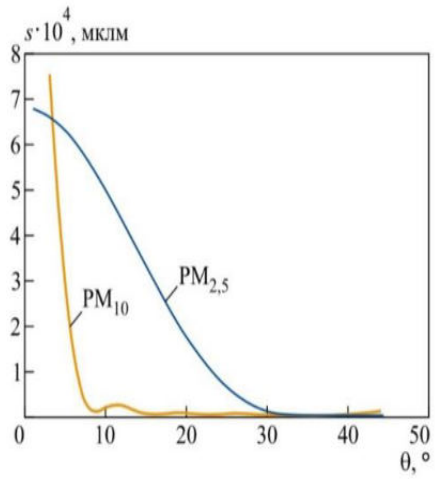

Figure 1. The intensity of the scattered light calculated from the Mie scattering equations as a function of the scattering angle for particles of sizes 2,5 and 10 μm.

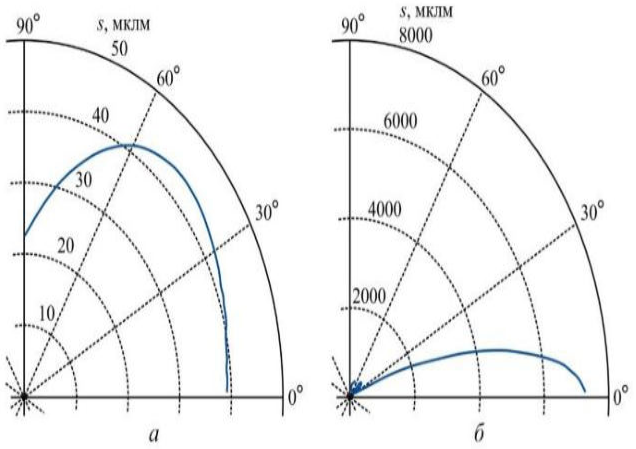

Figure 2. A polar graph of the scattering intensity *for particles of size 2 (a) and 8 μm (b).*

A during developing simple devices for estimating particle concentration, information about the scattering angles described above is taken into account. Dependences of the scattered light intensity on the scattering angle can be depicted on a polar diagram (Fig. 2). For particles with a size of 2.5 μm, the intensity is maximum at an angle of 45°, but for particles of large sizes, 10°. Simple estimates of the number density of particles from the measured scattering intensity are based on the choice of selective angles between 10° and 45° for fixing photodetectors.

4. Conclusion

The detected measurement errors are inherent in both simple and complex instruments for determining the countable concentration of particles. The measurement error of devices, the principle of which is based on a simple correspondence of a specific angle to the particle size value, can be 100%, in particular, for PM2.5 particles. Particle size distribution is easy to obtain from the readings of several photodetectors at selected scattering angles. In addition, there are other errors due to the size of the angle, the finiteness of the size of the aperture in the working gap, as well as changes in the nature of the particles. The analysis carried out indicates that the readings of portable devices with both one and several photodetectors do not correspond to reality.

References

[1] Mariselvam A K, Padmanabhan K and Sivanesan S 2020 *Measurement Techniques* **63(4)** 266-272

[2] Borghi F, Spinazzè A, Campagnolo D, Rovelli S, Cattaneo A and Cavallo D M 2018 *Sensors* **18(9)** 1–21

Development of a fiber-optic system for monitoring the state of oxygen activity in the current flow of the coolant

S E Logunov[1, 2], R V Davydov[2] and V V Davydov[2, 3]

[1]The Bonch-Bruevich Saint-Petersburg State University of Telecommunications, Saint Petersburg 193232, Russia
[2]Peter the Great Saint Petersburg Polytechnic University, Saint Petersburg 195251, Russia
[3]All-Russian Research Institute of Phytopathology, Moscow Region 143050, Russia

sema-logunov@ya.ru

Abstract. The necessity of developing an optical system for remote monitoring of the state of the coolant in the current flow in the first circuit of the nuclear reactor of a nuclear power plant has been substantiated. A method for monitoring the state of the coolant by changing the nature of the evolution of oxygen activity is presented. A fiber-optic system has been developed to study the nature of the change in the evolution of the oxygen activity of the coolant in the current flow. The results of the study of the evolution of oxygen activity in the current flow of the coolant are presented. The nature of the change in the evolution of oxygen activity in the event of the ingress of foreign particles into the coolant (carbon steel particles from welded joints) is determined.

1. Introduction

In the context of increasing consumption of electrical energy with a reduction in the reserves of natural resources for its production, one of the tasks of applied physics is to conduct research to develop new and modernize existing technologies to increase its production [1]. The need to improve methods and devices for controlling chain reactions, in the development of new devices for monitoring the operation of nuclear reactors and much more required research evolution of oxygen activity in the flow of various liquid media used as a coolant in nuclear reactors [2]. The oxygen activity $^{16}O(n,p)^{16}N$ is associated with the interaction of oxygen nuclei that are part of one of the parts of the coolant - water with neutrons with an energy greater than 9 MeV, which are present in the reactor zone due to the flow of a chain reaction. As a result of this interaction, the core $^{\text{of } 16N}$ is formed. which is extremely unstable. After the formation of the nucleus, immediately, the process of its decay begins. The half-life is about 7.1 s. Decay of ^{16}N is accompanied by γ radiation with an energy of $E_{\gamma} \approx 6.2$ MeV. It has been established that this activity occurs only when a nuclear reactor is operating at high capacities and subsides immediately after the end of the chain reaction. Therefore, during its research, very great difficulties arise.

2. Fiber-optic system for monitoring oxygen activity and the results of its study

To study the oxygen activity in the current flow of the coolant, we developed a fiber-optic system in which a special optical fiber with a high degree of doping of the core with germanium oxide (SiO_2 - GeO_2) is used to register the γ radiation. As a result of the research, it was determined that it is most expedient to use optical fiber with a dop of 20% in the developed system. In this case, the maximum sensitivity to the growth of losses in the optical fiber of the amplitude of laser radiation is achieved due

to the formation of color centers and "electronic" connections. This makes it possible to record minimal changes in variations in the intensity of oxygen activity in the coolant, which is characterized by the emission of γ - quanta. Fig. 1 presents the results of the study of the change in the number of emitted γ - quanta N from time t for various values of the flow rate of the coolant q. A solution ($H_20 + H_3BO_3$) with plutonium nitride filling at a temperature *of* $T_G = 960$ K was used as a coolant.

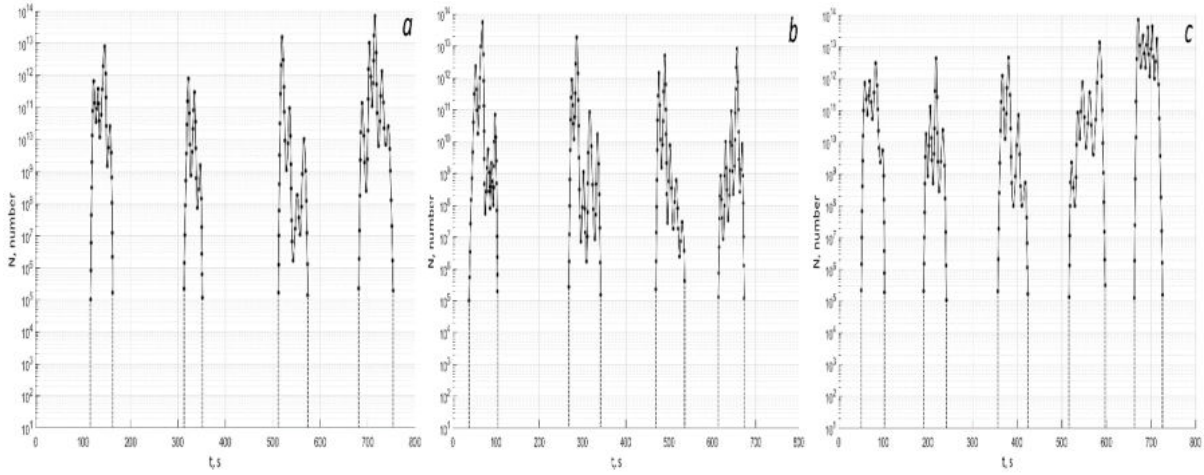

Figure 1. The dependence of change N on time t. Graphs on a), b) and c) corresponds to q in m^3/s: 0.169; 0.339; 0.678.

Analysis of the results obtained in Fig. 1 results show that oxygen activity in the coolant is randomly distributed over time. The maximum time interval between the occurrence of these bursts in the fixed zone of the pipeline is less than 250 s. Therefore, the study of the evolution of oxygen activity requires the provision of long-term studies (for example, for a time of 1800 s or more).

By adjusting the flow rate of the coolant q, it is possible to partially control the N distribution function in the registration area of γ - quanta coils with optical fiber.

3. Conclusion

The results obtained showed the reliable operation of the developed design of the fiber-optic system to monitor the state of oxygen activity in the current flow of the coolant. In the case of additional calibration, it is possible to use the developed fiber-optic system to control the radiation level in the central zone of the reactor. This is necessary for ensuring the independence of measurements when using photomultipliers (PMTs) to solve these problems.

References

[1] Gulevich A V, Dekusar V M, Chebeskov A N, Kuchinov V P and Voloshin N P 2020 *Atomic Energy* **127(3)** 192–195

[2] Davydov V V , Myazin N S and Kiryukhin A V 2020 *Atomic Energy* **127(5)** 274–279

Optimization of optical signal routing in the photonic tensor processor

M E Makarov [1], **A A Sapegin** [1,2] **and R T Minnullin** [1,2]
[1]JSC Molecular Electronics Research Institute, Moscow 124460, Russia
[2]Moscow Institute of Physics and Technology, Dolgoprudny 141701, Russia

Abstract. This paper shows an approach to the reduction of optical loss in a matrix-vector multiplication unit (MVMU) of a photonic tensor processor. The operation principle and spectral characteristics of the device are presented.

1. Introduction

The development and widespread use of the artificial neural networks, computer vision, speech recognition, Internet of Things and other digital technology sectors lead to the exponential growth in data volumes and increasing demand for high-speed data processing devices. Major technology companies offer various electronic AI accelerators [1] to meet these challenges. However, the future prospects of these devices are limited [2, 3]. There is another approach to speed up the calculations presented in [4, 5]. This approach involves the creation of a photonic tensor processor with a similar or better operating speed (10^{12} – 10^{15} multiply–accumulate operations (MAC) per second) and power consumption (17 fJ per MAC).

In this paper we proposed a modified MVMU of the photonic tensor processor [4]. The aim of the modification is to reduce energy consumption and simplify output signal processing.

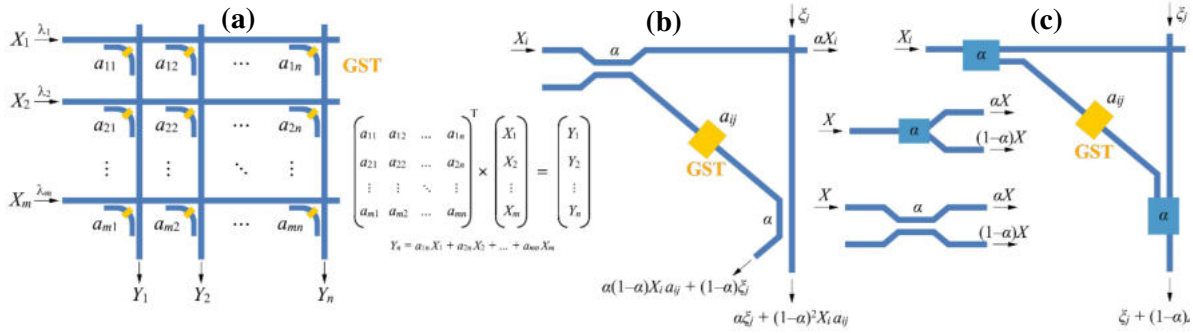

Figure 1. (a) Schematic view of the MVMU and its operation principle; **(b)** MVMU routing node with DC; **(c)** MVMU routing node with 1x2 splitter/combiner.

2. Matrix-vector multiplication unit

MVMU is a plane waveguide structure (Figure 1a) consisting of routing nodes with integrated photonic non-volatile memory cells based on $Ge_2Sb_2Te_5$. The cells store a_{ij} elements of the multiplied matrix. The multiplied vector components are amplitudes X_i of the input optical signals at different wavelengths λ_i. The directional couplers (DC) route input optical signals through specific memory cells. The components Y_j of the resulting vector are given by the following equation:

$$Y_j = (1 - \alpha)^2 \sum_{i=1}^{m} a_{ij} X_i \alpha^{m+j-i-1} \quad (1)$$

where α is a DC splitting ratio, m is a number of the matrix rows.

3. Optimization

As it was mentioned before, DCs route the optical signals (Figure 1b) in the original MVMU structure [4]. We assume that DCs were used in [4] to obtain direct access to the states of individual optical memory cells, i.e., to check the specific values of a_{ij} elements. However, the final industrial version of the photonic tensor processor does not require such verification. Therefore, we propose to replace DCs with 1x2 splitters/combiners (Figure 1c). Such modification will reduce excessive losses during the propagation of the optical signals through the routing nodes.

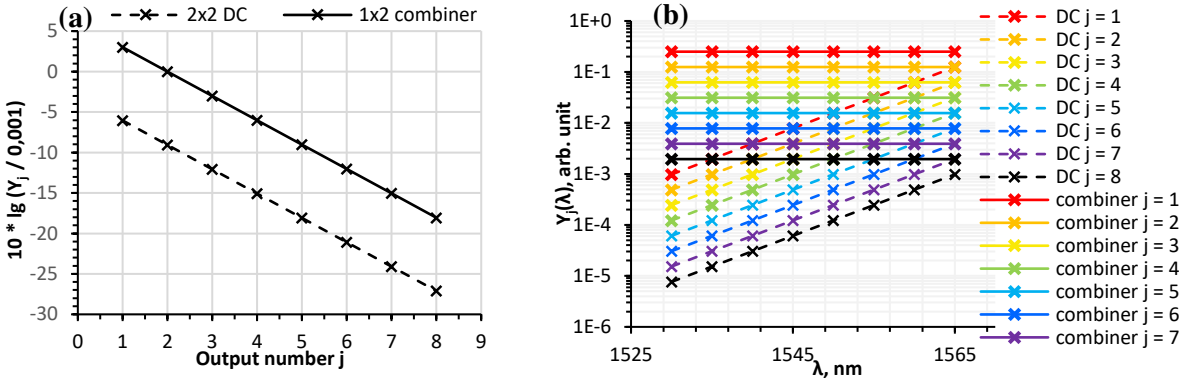

Figure 2. (a) The amplitude distribution of the output signals Y_j; **(b)** the spectral distribution of the output signals Y_j. The results were obtained for the ideal case with $a_{ij} = 0.5$, $\alpha = 0.5$ and zero waveguide losses for two variants of MVMU: with DCs and with 1x2 splitters/combiners.

These losses are caused by splitting of the input optical signal by DC between its 'cross' and 'bar' outputs and further use of only one of the output signals ('cross' in case of a signal traveling from the routing node and 'bar' in case of a vertical multispectral line signal). The use of the 1x2 splitters/combiners according to the numerical simulation will ensure complete transfer of optical signals to multispectral vertical lines and thus reduce losses by several times (Figure 2a). In addition, such modification simplifies the post-processing of the output signals Y_j, since the spectral distribution of these signals becomes uniform (Figure 2b) and is given by the following equation:

$$Y_j = (1 - \alpha)\alpha^{j-1} \sum_{i=1}^{m} a_{ij} X_i \quad (2)$$

4. Conclusion

This paper states that the described modification of the MVMU based on 1x2 splitter/combiners allows reducing optical losses and has enhanced output signal characteristics. Further work should be devoted to the development and verification of a more accurate model of the MVMU.

Acknowledgments

This study was supported by the Russian Foundation for Basic Research, project 19-29-03040.

References

[1] A. Reuther, P. Michaleas, M. Jones, V. Gadepally, S. Samsi and J. Kepner 2021 *Proc. IEEE High Performance Extreme Computing Conf.* (virtual)

[2] D. A. B. Miller 2017 *Journal of Lightwave Technology* **35** 346

[3] G. Y. Krasnikov, N. A. Zaytsev *et al.* 2015 *Journal of nano- and microsystem technique* **4** 63

[4] J. Feldmann, N. Youngblood, M. Karpov, H. Gehring, X. Li *et al*. 2021 *Nature* **589** 52

[5] B. J. Shastri, A. N. Tait, Ferreira de Lima *et al.* 2021 *Nat. Photonics* **15** 102

Quantum noise extraction from polarization swapping in a gain-switched VCSEL

R Shakhovoy[1,2,3], E Maksimova[1,4*], V Meshkov[1], and Y Kurochkin[1,2,5,6]

[1]QRate, 100 Novaya str., Skolkovo, Russia
[2]NTI Center for Quantum Communications, National University of Science and Technology MISiS, 4 Leninsky prospekt, Moscow, Russia
[3]Moscow Technical University of Communications and Informatics, 8A Aviamotornaya, Moscow, Russia
[4]Peter the Great St. Petersburg Polytechnic University, 29 Polytechnicheskaya str., St. Petersburg, Russia
[5]Russian Quantum Center, 45 Skolkovskoye Shosse, Moscow, Russia
[6]Moscow Institute of Physics and Technology, 9 Institutskiy per., Dolgoprudny, Russia

[*]e.maksimova@goqrate.com

Abstract. We propose an implementation of a quantum random number generator (QRNG) on polarization swapping in a gain-switched vertical cavity surface emitting laser (VCSEL) and a method for quantum noise extraction in assumption that the main source of classical noise are signal fluctuations on the photodetector.

Keywords: quantum random number generator, VCSEL, quantum noise extraction

A simplified scheme of the proposed QRNG is shown in figure 1. A gain-switched VCSEL is driven by a high-frequency laser driver, which is, in turn, controlled by the computer or FPGA. Laser output is followed by the polarization filter (PF) that allows obtaining polarization-resolved optical pulses. The latter are converted into the electrical signal via a broadband photodetector (PD). Random bits are obtained by digitizing pulses with a comparator. A threshold of the comparator is calculated by FPGA, which also performs post-processing algorithms including randomness extraction.

In figure 2, we simulated the process of digitizing polarized laser pulses. (The PF is assumed to pass the x-linear polarization.) Laser pulses were simulated with VCSEL rate equations [1]; the calculated signal was then processed with a low-pass digital filter (30 GHz bandpass) to simulate the finite bandwidth of the photodetector. The level of the comparator threshold (V_{th}) is shown by the green line; red circles correspond to the moments of the comparator latch actuation. The result of digitization ('0'-s or '1'-s) is shown in the corresponding frames in figure 2 (the frames are filled by the light blue color).

Generally, a laser pulse at the VCSEL output contains both polarization components (x and y), such that polarization state of a given pulse can be referred to as "quasi-elliptical". Relative contribution of orthogonal components is a random quantity; however, it depends on the width of pulse and the rate of relaxation processes (transients). To demonstrate this, we calculated probability density function (PDF) of the normalized integral signal S_x at three different repetition rates (figure 3). In the ideal case,

we would get two peaks at the values $S_x = 0$ and $S_x = 1$, which means that all optical power goes into one particular linear polarization (y and x respectively). However, due to the finiteness of transients, S_x could take intermediate values between 0 and 1. The influence of transients becomes more prominent when decreasing the pulse width, which is clearly seen in figure 3, where the area under the PDF curve in the middle of the histogram is increased when increasing the pulse repetition rate from 2.5 to 7 GHz. Polarization-resolved laser pulses (x-pulses in our case) that fall into this intermediate region are the most affected by classical (non-quantum) noises of the photodetector; therefore, '0'-s and '1'-s resulted from digitization of such pulses can be considered as "untrusted" bits. The proportion of these bits can be thought of as a quantum reduction factor G, whose value determines how much the raw random sequence should be "compressed" using the randomness extractor. We propose the following formula to find G:

$$G = \frac{1}{H_r (1 - P)} \tag{1}$$

where H_r is the min-entropy of the raw random sequence, and P is the probability to obtain the pulse with the S_x value inside some "window" around the middle of the probability distribution, whose width is proportional to the r.m.s. value of the photodetector noise.

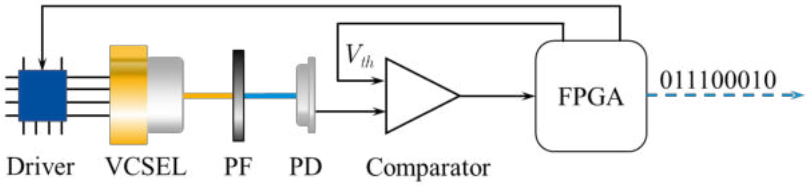

Figure 1. A simplified scheme of a VCSEL-based QRNG.

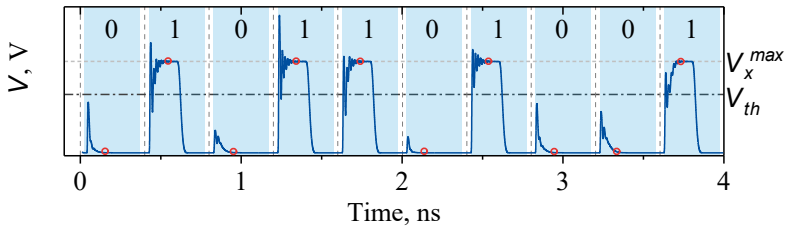

Figure 2. Pulses at the comparator input and the results of digitization.

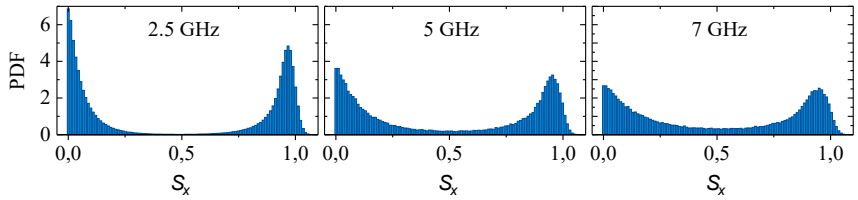

Figure 3. Probability density of the normalized integral signal S_x.

References

[1] Shakhovoy R, Maksimova E, Sharoglazova V, Puplauskis M, and Kurochkin Y 2021 Fast and compact VCSEL-based quantum random number generator *Journal of Physics: Conference Series* **1984** pp 1 – 5.

Polarization compensation design for free-space quantum communication transmitter

V E Merzlinkin[1,2,3], A V Khmelev[1,2,4,5], A V Duplinsky[1,2,6], V L Kurochkin[1,2,3,4], and Y V Kurochkin[1,2,3,4,5]

[1]QSpace Technologies, Lugovaya st. 4, Moscow, Russia
[2]QRate, Novaya av. 100, Moscow, Russia
[3]NTI Center for Quantum Communications, National University of Science and Technology MISiS, Leninsky prospekt 4, Moscow, Russia
[4]Russian Quantum Center, Bolshoy Boulevard 30, bld. 1, Skolkovo, Moscow, Russia
[5]Moscow Institute of Physics and Technology, 9 Institutskiy per., Dolgoprudny, Moscow Region, Russia
[6]HSE University, Pokrovsky Boulevard 11, Moscow, Russia

{v.merzlinkin, a.khmelev, al.duplinsky, v.kurochkin, yk}@goqrate.com

Abstract. Quantum communication is a transmission technology that allows you to share a secret key. The BB84 protocol uses 4 linear states for encoding, but the optical elements affect the polarization, which leads to errors. The polarization controller was added to the optical circuit to correct these errors. An algorithm was written to find the angles of the wave plates of the polarization controller. It was possible to increase the polarization extinction rate for the optical system.

1. Introduction

Quantum communication is studied by a large number of scientific groups as one of the reliable and promising methods in the information security[1,2]. Significant progress has been achieved in the development of systems and their theoretical analysis for the quantum key distribution (QKD) since the first concept was proposed[3]. However, practical realisation of quantum key distribution systems are imperfect, and this fact opens up many opportunities for eavesdropping[4]. To achieve a high-secure communication, researchers propose different protocols and optical schemes to share secret key[5].

The high losses of single photons that propagates across a medium are also one of the main problem for the quantum cryptography implementation for a long distances. Nowadays, cutting-edge QKD experiment provides an adequate key rate at distance up to 250 km in an optical fiber[6]. To perform a long-distance quantum key distribution, the most preferable realisation is a free-space system using polarization coding method of photon states[7]. Commonly, the BB84 decoy-state protocol is the most practically useful for free-space quantum communication based on the linear polarization states: $|\mathrm{H}\rangle$, $|\mathrm{V}\rangle$, $|\mathrm{D}\rangle = \frac{1}{\sqrt{2}}(|\mathrm{H}\rangle + |\mathrm{V}\rangle)$, $|\mathrm{A}\rangle = \frac{1}{\sqrt{2}}(|\mathrm{H}\rangle - |\mathrm{V}\rangle)$.

The transmitter using polarization encoding has to provide high linearity and unbiased bases output photon states. However, the polarization light can be affected by the imperfection of the optical elements and their dependence on incident angle of the polarization light. Therefore, polarization

compensation of photons is one of the essential technology to decrease the level of errors while decoding quantum states.

We report the results of polarization characteristics of designed transmitter for free-space quantum communication. The polarization properties of optical elements in transmitter have been investigated and algorithm for a polarization controller made up of one half-wave plate (HWP) and two quarter-wave plate (QWP) has been developed.

2. Numerical analysis and laboratory experiment

Optical systems can introduce dissipative and phase losses. Dissipative polarization losses are the rotation of one of the bases relative to the other, for example due to the large absorption of ”s“ or ”p" polarization. Phase loss is the phase shift between the ”s“ or ”p" of polarization, which leads to ellipticity of polarization in the diagonal basis[8]. Dissipative losses are insignificant in our QKD optical systems, therefore, as part of the work, measures were taken to eliminate the phase error.

It is also possible to get rid of the phase shift with the help of a polarization controller consisting of three wave plates – two QWP and one HWP. Such a system makes it possible to change both degrees of freedom of polarization (azimuth angle and ellipticity angle), which makes it possible to convert an arbitrary polarization into another arbitrary one.

The first experiment was done on a system consisting of a beam splitter and a dichroic mirror. These elements are part of the QKD transmitter and the dichroic mirror introduces the most phase error. The polarization extinction ratio (PER) before the correction was equal to 15000:1 for horizontal and vertical polarization and 22:1 in the diagonal basis. After that a polarization controller was added to the system and a computer algorithm found the angles for the plates. The algorithm is an optimization of the value of a function that describes the work of the optical scheme and the polarization controller. With the controller it was possible to compensate for the polarization to a value of 10000:1 for both bases. Such values are suitable for conducting quantum communication with a protocol based on polarization. After such results, the PER value was measured for the entire QKD optical scheme of the transmitter as part of this work.

Acknowledgments

This work was supported by The Russian Science Foundation (Grant No. 17-71-20146)

References

[1] Dowling, Jonathan P., and Gerard J. Milburn. Quantum technology: the second quantum revolution. Philosophical Transactions of the Royal Society of London. Series A: Mathematical, Physical and Engineering Sciences 361.1809, 1655-1674 (2003).

[2] Sidhu, J.S., et al. Advances in space quantum communications. IET Quant. Comm. 2(4), 182–217 (2021).

[3] C. H. Bennett and G. Brassard. Quantum cryptography: public key distribution and coin tossing, Proceedings of the IEEE International Conference on Computers, Systems & Signal Processing, 175–179 (1984).

[4] Sun, Shihai, and Anqi Huang. A Review of Security Evaluation of Practical Quantum Key Distribution System, Entropy 24.2, 260 (2022).

[5] Bedington, Robert, Juan Miguel Arrazola, and Alexander Ling. Progress in satellite quantum key distribution. npj Quantum Information 3.1, 1-13 (2017).

[6] Zhang, Yichen, et al. Long-distance continuous-variable quantum key distribution over 202.81 km of fiber. Physical review letters 125.1, 010502 (2020).

[7] Toyoshima, Morio, et al. Polarization-basis tracking scheme in satellite quantum key distribution. International Journal of Optics 2011 (2011).

[8] Wu, Jincai, et al. Polarization study about a telescope-based transmitter for quantum communication. Applied Optics 56.30, 8501-8506 (2017).

Posterior laser-locking technique for MDI-QKD

E E Mekhtiev, [1,2,5] **I S Gerasin,** [2,3,5] **N V Rudavin,** [3,4]
A V Duplinsky, [1,2,3] **and Y V Kurochkin** [2,3,5]

[1] QRate, Novaya av. 100, Moscow, Russia
[2] Russian Quantum Center, Bolshoy Boulevard 30, bld. 1, Skolkovo, Moscow 121205, Russia
[3] NTI Center for Quantum Communications, National University of Science and Technology MISiS, Leninsky prospekt 4, Moscow 119049, Russia
[4] 6HSE University, 20 Myasnitskaya ulitsa, Moscow 101000, Russia
[5] Moscow Institute of Physics and Technology, 9 Institutskiy per., Dolgoprudny, Moscow Region, 141701, Russian Federation

E-mail: e.mekhtiev@goqrate.com

Abstract. We present a novel soft-ware based method to ensure independent lasers mutual coherence required for practical realization of advanced MDI-QKD protocols. Proof of principle experiment has proved validity of the method, providing mutual coherence time ~ 10 μs while upper bound dictated by uncontrollable phase drift in optical fiber being ~ 100 μs.

1. Introduction

Recently have been proposed so-called Asynchronous MDI-QKD protocols [2, 3]. The main feature of this protocol is a drastic improvement of the secure key rate over longer distances. However, Asynchronous MDI-QKD requires high degree of senders lasers mutual coherence. Usually this problem is solved via various hard-ware based laser-locking techniques [4]. In this work we present easy soft-ware based approach to solve this problem.

2. Setup and method

2.1. Setup

We investigate interference of two independent continuous light beams. Central wavelength of the two lasers adjusted so that mean mutual beat frequency $\langle \Delta\omega_{\mathrm{AB}} \rangle \sim 250$ MHz. We use two fiber-coupled photodetectors at Charlie's side to register interference pattern. Interference traces are captured by oscilloscope. We investigate communication links of L = 0, 25, 50 and 75 km lengths to test robustness of a proposed method.

2.2. Method

We aim to use frequency beat measured on $\mathrm{PD_c}$ to post-compensate phase difference on detector $\mathrm{PD_s}$ arising from lasers wavelength difference. Intensities on $\mathrm{PD_s}$ and$\mathrm{PD_c}$ are respectively:

$$J_{\mathrm{s}}(t) \sim e^{i[\Delta\varphi^0_{\mathrm{AB}} + \Delta\varphi_{\mathrm{fs}} + \Delta\omega_{\mathrm{AB}}(t-t_{\mathrm{s}})\cdot t]} \tag{1}$$

$$J_{\mathrm{c}}(t) \sim e^{i[\Delta\varphi^0_{\mathrm{AB}} + \Delta\varphi_{\mathrm{fc}} + \Delta\omega_{\mathrm{AB}}(t-t_{\mathrm{c}})\cdot t]}, \tag{2}$$

where $\Delta\varphi^0_{\mathrm{AB}}$ is initial phase difference between two laser sources; $\Delta\varphi_{\mathrm{fs}}$, $\Delta\varphi_{\mathrm{fc}}$ are random phase differences induced by optical fibers of signal and compensating channels; $\Delta\omega_{\mathrm{AB}}(t - t_{\mathrm{s}})\cdot t$, $\Delta\omega_{\mathrm{AB}}(t - t_{\mathrm{c}}) \cdot t$ are phase differences on detectors $\mathrm{PD_s}$ and $\mathrm{PD_c}$ at time t due to lasers mutual incoherence; $|t_{\mathrm{c}} - t_{\mathrm{s}}| \cdot c$ is path difference between signal and compensating channels. The proposed method works as follows:

1. Collect interference traces with detectors $\mathrm{PD_s}$ and $\mathrm{PD_c}$
2. Find $\Delta\omega_{\mathrm{AB}}(t)$ from $J_{\mathrm{c}}(t)$ with Fast Fourier Transform
3. Subtract $\Delta\omega_{\mathrm{AB}}(t)$ from the phase of $J_{\mathrm{s}}(t)$
4. Search to find delay $|t_{\mathrm{c}} - t_{\mathrm{s}}|$ minimizing final phase error $\Delta\varphi_{\mathrm{err}}(t)$

3. Results and discussion

Table 1 shows phase error rate of the two posteriorly-locked lasers. For detection node remote at 25 km mutual lasers coherence of ~ 10 μs is achieved with 0.15 rad certainty. We note that the upper time limit for Lasers A and B mutual coherence, imposed by random phase noise in optical fiber, ~ 100 μs [5].

Table 1. Phase error rate against communication link length.

L, km	$\Delta\dot{\varphi}_{err}$, rad$\cdot\mu$s^{-1}
0	0.004
25	0.015
50	0.027
75	0.059

Further improvement can be achieved with using higher sample rates on oscilloscope and greater lasers detuning. Altogether the degree of mutual coherence provided with new technique looks promising for effective realisation of asynchronous MDI-QKD protocols.

$$|\gamma_1\rangle = |r_1\rangle \otimes |t_1\rangle \otimes |\omega_1\rangle \otimes |p_1\rangle$$
$$|\gamma_2\rangle = |r_2\rangle \otimes |t_2\rangle \otimes |\omega_2\rangle \otimes |p_2\rangle$$

$$g^2(0) = \frac{\langle I_1 I_2\rangle}{\langle I_1\rangle\langle I_2\rangle} = |\langle I_1\rangle = \langle I_2\rangle; I_2 = I_0 - I_2| = 1 - \frac{\langle I_1^2\rangle}{\langle I_1\rangle^2} = \left(\frac{\sigma_{I_1}}{\langle I_1\rangle}\right)^2$$

4. References

[1] Lo H K, Curty M and Qi B 2012 *Physical review letters* **108** 130503
[2] Xie Y M, Lu Y S, Weng C X, Cao X Y, Jia Z Y, Bao Y, Wang Y, Fu Y, Yin H L and Chen Z B 2021 *arXiv preprint arXiv:2112.11635*
[3] Zeng P, Zhou H, Wu W and Ma X 2022 *arXiv preprint arXiv:2201.04300*
[4] Khabarova K Y, Kudeyarov K S, Vishnyakova G A and Kolachevsky N N 2017 *Quantum Electronics* **47** 794
[5] Fang X T, Zeng P, Liu H, Zou M, Wu W, Tang Y L, Sheng Y J, Xiang Y, Zhang W, Li H *et al.* 2020 *Nature Photonics* **14** 422–425

Laser surface treatment of aluminium: Correlation between thermal modeling and experimental study

A A Mozhayko[1, 2], D A Gerashchenkov[2] and V V Davydov[1, 3]
[1]Peter the Great Saint-Petersburg Polytechnic University, Saint Petersburg, Russia, 195251
[2]NRC "Kurchatov Institute" - CRISM "Prometey", St. Petersburg, Russia, 191015
[3]All-Russian Research Institute of Phytopathology, Moscow Region 143050, Russia

e-mail: annaanna-1996@mail.com

Abstract. In recent years, laser surface treatment was widely used to improve the properties of aluminum coatings. This paper implements a thermal model to simulate the laser treatment effects on a cold-sprayed aluminum coating and St3 substrate. As a result of the work, a model has been developed to evaluate the thermal fields and the melt pool during the laser surface treatment process, and laser treatment modes have been identified, with the help of which a high-alloyed aluminum layer on the surface of steel has been obtained.

1. Introduction

The laser surface treatment of metals enables the production of a surface layer with a thickness of under a millimeter to several millimeters and with special functional properties: high hardness and wear resistance, while maintaining the properties of the substrate material. Laser power and speed conditions the structure and properties of the surface layer [1].

An important step in laser surface treatment is the mode selection, namely, the laser speed and power, the laser spot diameter, and the hatch spacing. The mismatch of the process parameters leads to various adverse outcomes, such as inefficient processing, in which the conditions necessary for the formation of intermetallides are not met, and damage to the processed sample [2].

It is advantageous to select the modes of the laser surface treatment process using computer modeling. With the help of modern numerical simulation packages, it is possible to calculate thermal fields in a sample during surface treatment. This significantly saves time and production resources.

The aim of the study was to better understand the behavior of aluminum deposited by gas dynamic spraying during laser treatment. At the modeling stage, treatment modes are identified in which the conditions for the formation of intermatallic compounds are fulfilled. For this purpose, a thermal finite element model of laser processing was implemented to evaluate the thermal fields occurring in the deposited coating. Using the selected modes, heat treatment of aluminum deposited by gas-dynamic spraying on a steel substrate is carried out.

2. Modeling laser surface treatment

In general, heat transfer can be described by the heat conduction equation. The laser source is represented by a heat source with a Gaussian distribution. When the laser interacts with the material, heat losses due to convection and radiation are taken into account. The phase transition of melting and evaporation is considered in the equation of heat capacity.

The Comsol Multiphysics package and 3D finite element method are used to model thermal effects.

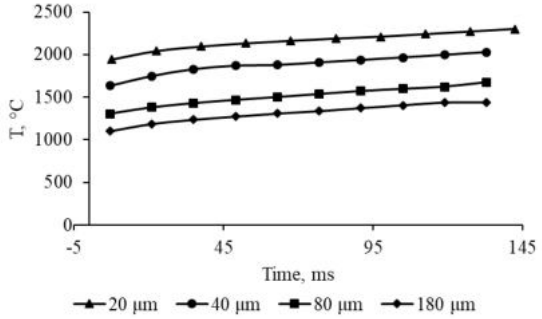

Figure 1. Dependence of the maximum surface temperature on the scanning time for different coating thicknesses

Ten laser beam passes were simulated for samples made of St3 steel with different thickness of aluminum coating. The maximum temperatures for each pass of the laser beam are found (Fig. 1). It is established that at a laser speed of 400 mm/s, 800 mm/s and a power of 180 W, there is no mixing of components in the laser exposure zone, since energy input is insufficient.

3. Experiment results

For the coating of aluminum, the technology of gas-dynamic spraying was used [3], after which the surface was treated with a laser to improve the mechanical properties of the coating. As a result of the study, the dependence of the melt mixing zone size on the scanning mode was established (Table 1).

Table 1. Comparison of the melt pool depth obtained from simulation and experimental study for a scanning speed of 100 mm/s

	20 μm	40 μm	80 μm	180 μm
d, μm (modeling)	70	58	80	180
d, μm (experiment)	63.3	62.9	74.2	230.3

It was found that for a coating thickness of 20 μm and 40 μm, a scanning speed of 100 mm/s, and a power of 180 W, intermetallic compounds are formed in the mixing zone of the components.

The discrepancies with the simulation results when comparing the values in Table 1are caused by the uneven distribution of the precursor coating over the substrate, as well as the presence of corundum in the coating, which was not taken into account in the simulation.

3. Conclusion

As a result of the work, a model was developed for estimating thermal fields in an aluminum coating deposited by gas-dynamic spraying during laser treatment. It was found that for a coating thickness of 20 microns and 40 microns, a scanning speed of 100 mm/s, and a power of 180 W, intermetallic compounds are formed in the mixing zone of the components.

References

[1] Dobrzański L A, Tański T, Dobrzańska-Danikiewicz A D , Jonda E, Bonek M, Drygała A 2015 *Laser Surface Engineering* **1** 3-32

[2] Rubino F, Astarita A and Carlone P 2018 *Coatings* **8(6)** 219

[3] Geraschenkov D A, Vasiliev A F, Farmakovsky B V and Mashek A Ch 2014 *Materials Science* **1** 87–96.

Investigation of the far-field emission pattern of microdisk lasers

E I Moiseev[1], N V Kryzhanovskaya[1], F I Zubov[2], A V Nahorny[3], B D Urmanov[3], S A Mintairov[4], N A Kalyuzhnyi[4], M M Kulagina[4], M V Maximov[2], A E Zhukov[1]

[1] HSE University, St Petersburg, 190008 Russia
[2] Alferov University, St Petersburg, 194021 Russia
[3] Institute of Physics of NAS of Belarus, 220072 Belarus
[4] Ioffe Institute, St Petersburg, 194021 Russia

Abstract. We studied a far-field emission pattern for microlasers with InGaAs/GaAs quantum well-dots in the active region. Angular-resolved electroluminescence spectra measurement revealed various far-field patterns depending on current and resonance mode.

1. Introduction

Whispering-gallery microdisk semiconductor lasers are of interest for a wide range of fundamental and applied studies[1-4]. The advantages of such lasers are simple design, small size, low threshold currents, etc. However, the absence of directional light output from the microdisk lasers prevent collecting high optical power and hampers their applications. In this work, we study the far-field emission pattern of microdisk lasers with quantum well-dots (QWDs).

2. Experiment

The epitaxial structure p-$Al_{0.39}Ga_{0.61}As$/GaAs/QD/GaAs/n-$Al_{0.39}Ga_{0.61}As$ was grown by the MOCVD on n-doped GaAs (100) substrates. Microdisk lasers were formed by photolithography and dry etching methods. AgMn/NiAu (AuGe/Ni/Au) metallization was used to form ohmic contacts to p+ GaAs cap layer (n+ substrate, respectively).

A gold 17.5 μm thick wire was soldered to a 30 μm in diameter microdisk laser. The other end of the wire was welded to the contact pad on the ceramic plate. The emission was collected through a collimator and coupled into a multimode optical fiber. To control the spatial resolution, the collimator aperture was limited by a pinhole. The coupled optical power was measured by a power meter. The spectra were recorded by Yokogawa AQ6370C optical spectrum analyzer. The collimator was moved around the laser using a rotary station. Azimuthal acquisition angle (φ) is the angle in the plane of the p-n junction, the polar angle (θ) is the angle perpendicular to the plane of the p-n junction (counting from the normal to the plane of the p-n junction). The angular resolution of the far-field measurement was 0.6° in the azimuthal and polar direction.

3. Results

The emission spectrum of MD laser above threshold contains a narrow lasing whispering gallery mode line superimposed to a broad spontaneous emission spectrum. Figure 1 shows electroluminescence spectra obtained at the same injection current for different azimuthal angles at the same polar angle. The lasing wavelength, the intensity of spontaneous emission, and the value of threshold current (figure 2) are the same for both cases, however, the intensity of the lasing line (inset in figure 1) varied significantly for different azimuthal angles.

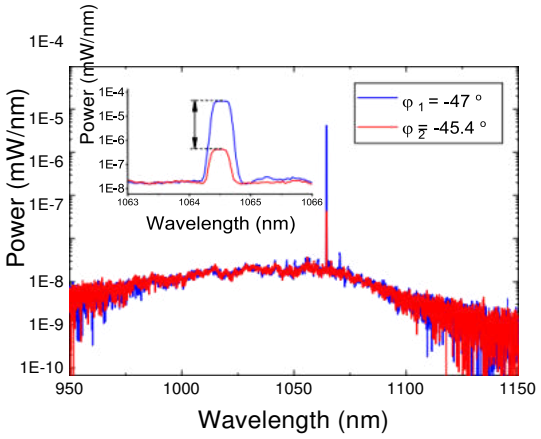

Figure 1. Electroluminescence spectra obtained at different azimuthal angles.

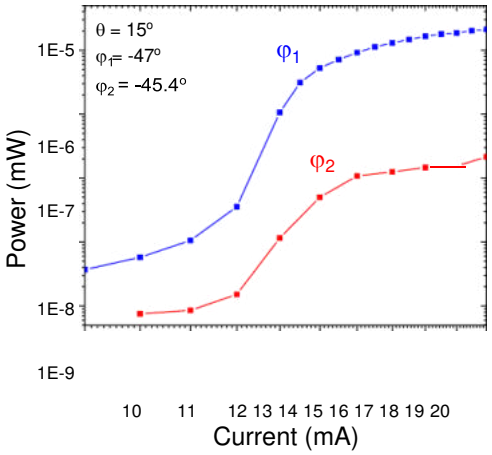

Figure 2. Output power as a function of injection current for different azimuthal angles.

In the polar direction, the output beam is distributed over a relatively narrow angle of about 20°. A far-field pattern narrowing effect is consistent with a previous study of a similar disk published in [6].

4. Conclusion

We studied a far-field emission pattern for microlasers with InGaAs/GaAs quantum well-dots in the active region as a function of the injection current The results obtained may be useful for the development of efficient methods for light outcoupling from microcavities.

Acknowledgments

The reported study was funded by RFBR and BRFBR, project number 20-52-04016. N.V.K, E.I.M, and A.E.Zh gratefully acknowledge support from the Basic Research Program of the National Research University Higher School of Economics.

References

1. Peter E. et al. Exciton-Photon Strong-Coupling Regime for a Single Quantum Dot Embedded in a Microcavity // Phys. Rev. Lett. 2005. Vol. 95, № 6. P. 067401.
2. Stock E. et al. On-chip quantum optics with quantum dot microcavities // Adv. Mater. 2013. Vol. 25, № 5. P. 707–710.
3. Kiraz A. et al. Quantum Dot Single Photon Source // Coherence and Quantum Optics VIII. Boston, MA: Springer US, 2003. Vol. 14. P. 165–170.
4. He L. et al. Detecting single viruses and nanoparticles using whispering gallery microlasers // Nat. Nanotechnol. 2011. Vol. 6, № 7. P. 428–432.
5. Peter E. et al. Highly directional radiation pattern of microdisk cavities // Appl. Phys. Lett. 2007. Vol. 91, № 15. P. 151103.

Structures of porous silicon doped with erbium for optoelectronics

Nesterov D. A., Latukhina N. V.

Samara National Research University, 443086 Samara, Russia

nesand2606@mail.ru

Abstract. In this work, silicon plates doped with erbium were studied. As a promising basis for creating more efficient solar panels that transform with up-conversion that part of the spectrum that passes through conventional solar cells.

1. Erbium-doped silicon as a material for adding up-conversion properties to solar cells.

The structures of porous silicon (Por-S) doped with erbium are of significant interest for the creation of an infrared emitter on a silicon substrate and an solar cells up-conversion coating [3]. The effect of up-conversion is that materials can absorb several infrared photons in the part of the spectrum, followed by luminescence in the visible region [1,2].

In this study, the structures of Por-S doped with erbium are considered to create more efficient solar cells.

2. The experimental part

Samples of textured and polished p-type silicon were selected for the study. Samples of porous silicon were obtained by chemical etching in an alcoholic solution of hydrofluoric acid HF: C2H5OH. Etching occurred at a constant current density of 10 mA/cm^2. The etching time is 5, 10 and 15 minutes. The porosity of the samples was evaluated using the gravimetric method. Alloying was carried out by applying an aqueous-alcohol solution of erbium to the surface of the samples. After that, annealing was carried out at a temperature of 950 degrees for 30 minutes. Ohmic contacts were applied by thermal evaporation of aluminum in vacuum.

The volt- capacitance characteristics were measured (see Fig. 1). And volt-Siemens characteristics were measured (see Fig. 2).

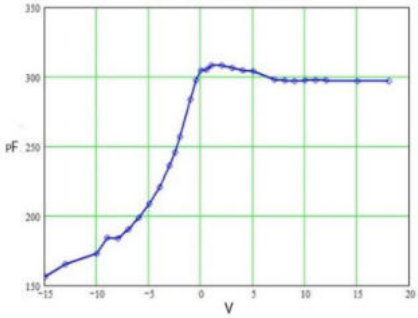

Figure 1. Volt-capacitance curve.

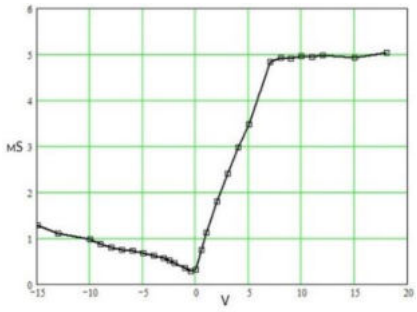

Figure 2. Volt-siemens curve

The graphs C(V) and G(V) have a form characteristic of the MOS structures, which indicates the dielectric properties of porous silicon doped with erbium.

References

[1] A. D. Kozyurov, Ap-konversionnaya lyuminescenciya monokristalla LiYbF4:Ho3+, [Up-conversion luminescence of single crystals LiYbF4:Ho3+], Coherent Optics and Optical Spectroscopy, Kazan, Kazan University Press, 18 (2014) 125-129

[2] G. Algun, An Investigation of Electrical Properties of Porous Silicon, Tr. J. of Physics, 23 (1999) 789–797

[3] L. F. Biana, C.G. Zhang, Interface effect on emission properties of Er-doped Si nanoclusters embedded in prepared by magnetron sputtering, J. of Applied Physics, 99.094302 (2006)

Investigation of volt-ampere characteristic of photosensitive structures with contact tracks obtained by laser radiation

N A Poluektova[1], D A Shishkina[1], A M Holstein[1] , I A Shishkin[1]

[1]Samara National Research University, Samara, 443086, Russia

daria.lizunkova@yandex.ru

Abstract. In this paper, a technology for manufacturing contact tracks for photosensitive structures based on porous silicon using laser radiation is proposed. The analysis of the volt-ampere characteristics of the obtained structures is presented.

1. Introduction

Currently, scientific work on improving the energy characteristics of photosensitive structures is quite relevant. For example, [1] presents a literature review of methods for creating silicon nanostructures on solar cells to improve their output characteristics. It was shown in [2] that porous layers really increase the characteristics of photosensitive structures, however, there is a possibility of current loss due to uneven deposition of metal contacts on the pores. In this paper, it is proposed to treat the surface of photosensitive structures with laser radiation before spraying to create grooves for contact tracks, which should help reduce losses.

2. Experiment

Before creating photosensitive structures, the samples were washed in peroxide-ammonia solution to remove mechanical impurities from their surface.

Then a diffusant was applied to the samples: boron for p-type conductivity, phosphoric for n-type. After drying the diffusants, the structures were annealed in a diffusion furnace for 40 minutes at 1000 ° C to create a p-n transition.

Further, a porous layer was formed on the n-type by the method of anodic electrochemical etching. Etching was carried out in a solution of hydrofluoric acid and ethyl alcohol in a ratio of 1:1. The current density was j = 15 mA/ cm^2 and 20 mA/cm^2 and the etching time was 10 and 15 minutes.

To identify the best way to create grooves for contacts, photosensitive structures were divided into two groups: one part was irradiated in air, the other in a solution of ethyl alcohol and glycerin in a ratio of 1:1. The grooves were created using a CO2 laser. In both groups, the samples were irradiated with laser radiation with a frequency of f = 20 kHz and a power of P = 10 w.

Before applying the contacts, the resistivity was measured in different areas of the plate: before etching, on porous silicon and on tracks. After that, aluminum contacts were applied by thermal evaporation in vacuum.

Volt-ampere characteristics were measures for both groups of samples. A photosensitive structure without a porous layer and contact tracks was used as a control sample.

3. Results and discussions

Table 1 shows the results of measurements of the specific and surface resistance of structures.

Table 1. Specific and surface resistance of photosensitive structures.

№	Processing environment	Surface Type	Resistivity, Ω*cm	Surface resistance, kΩ/cm^2
2	glycerin: ethyl alcohol	por-Si area after scribing	0,214	0,0095
8	air	por-Si area after scribing	0,133	5,4
1	initial porous surface		0,199	0,010

The influence of the medium on the specific and surface resistance of structures is noticeable. Processing in glycerine retained the parameters of specific and surface resistance relative to the original ones. At the same time, this type of processing makes it possible to obtain less defective structures.

Figure 1 shows the results of measurements of the volt-ampere characteristics of photosensitive structures, the contact paths of which are made in various media: in an alcoholic solution of glycerin (a) and in air (b).

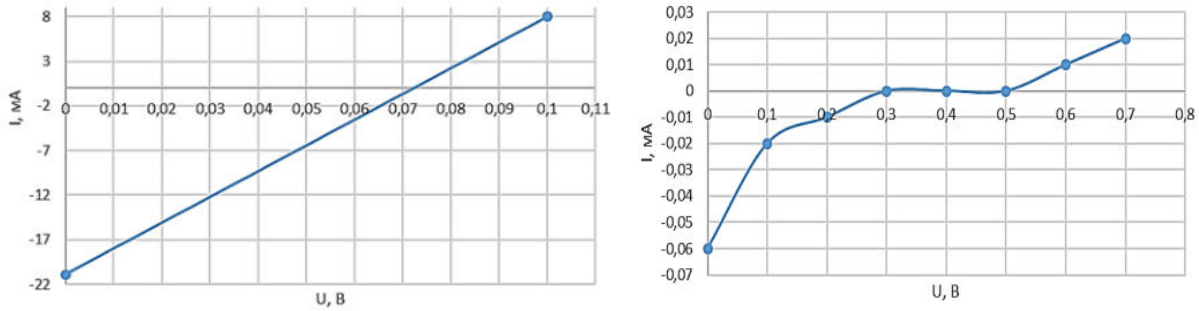

Figure 1. Volt-ampere characteristic of photosensitive structures with a porous layer, the contact paths of which are made in an alcoholic solution of glycerin (a) and in air (b).

It can be seen from the graphs that the sample whose contact tracks were obtained by laser irradiation in a solution of glycerin and alcohol demonstrates higher current values, however, the sample obtained by laser irradiation in air has higher values of the no-load voltage.

Figure 2 shows the results of measurements of the volt-ampere characteristics of a photosensitive structure, the contact tracks of which are made without the use of laser radiation.

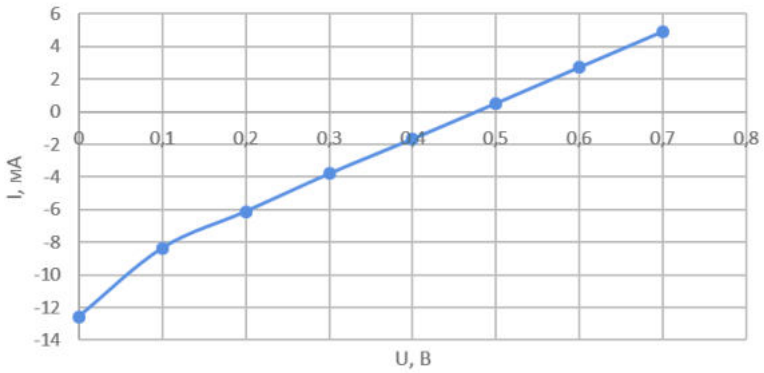

Figure 2. Volt-ampere characteristics of a photosensitive structure, the contact paths of which are made without the use of laser radiation.

When comparing the graphs from Figures 1 and 2, it can be seen that the no-load voltage of the samples with contacts made using a laser in an air environment (Fig.1 (b)) is the same as the voltage of the sample made without using a laser. And the short-circuit current of a sample made using a laser in a solution of glycerin and alcohol has a lower short-circuit current.

4. Results and discussions

Analysis of the graphs shows that the manufacture of photosensitive structures using a laser in a solution of glycerin and alcohol can improve the characteristics of the structures, but the manufacturing technology needs to be refined.

References

[1] Huo C, Wang J, Fu H, Li X, Yang Y, Wang H, ..., Peng K Q 2020 *Advanced Functional Materials* ***30*** p 2005744

[2] Latukhina N V, Lizunova D A, Shishkin I A, Erofeev A S 2019 *Science of the Present and the Future* **3** pp 19-22

Features of the construction of fiber-optic communication lines with orthogonal frequency-division multiplexing

N I Popovskiy[1], V V Davydov[2, 3] and V Yu Rud[3, 4]

[1] The Bonch-Bruevich Saint-Petersburg State University of Telecommunication, Saint Petersburg 195251, Russia
[2] Peter the Great Saint Petersburg Polytechnic University, Saint Petersburg 195251, Russia
[3] All-Russian Research Institute of Phytopathology, Moscow Region 143050, Russia
[4] A.F. Ioffe Physicotechnical Institute, St. Petersburg, 195152, Russia

nikitanikita24@mail.ru

Abstract. The article investigates the features of the construction of fiber optic communication lines with multiplexing using orthogonal frequency channel separation. Block diagrams of transmitters and receivers of signals of fiber optic communication lines with this type of multiplexing are presented. The properties and operational characteristics of the main platforms and technological nodes are considered. The necessity of developing such systems for future use in optical transport networks, cloud and high-performance computing systems is substantiated.

1. Introduction

Recently, interest has grown in the transmission of orthogonal frequency-multiplexed (OFDM - Orthogonal Frequency-Division Multiplexing) signals along the optical path, since the method has a well-developed hardware and software implementation of the signal and high spectral efficiency. The features of the formation of the OFDM signal lead to large signal outliers, and as a consequence, the output of signal amplitudes from the linear section of the transmission characteristics of the optoelectronic components of the optical path and to the transition of these devices to a nonlinear mode of operation. Consequently, nonlinear distortions occur that fall into the frequency bandwidth of the subcarrier channels of the OFDM signal and worsen the signal-to-noise ratio.

2. Optical Communication Systems

The purpose of this work is to study the effect on subcarrier channels of nonlinear distortions that occur during electro-optical or optoelectronic conversion of the OFDM signal during optical modulation and/or photodetection. Such components of the optical path as a laser diode (LD), an optical modulator based on a Mach-Zander interferometer with two electrodes (MZI – Mach-Zehnder Interferometer) and a photodiode (PD) are considered. To achieve these goals, modeling programs have been developed that simulate the processes of modulation and photodetection of the OFDM signal.

In Figure 1 shows the relative spectrum of LD radiation when modulated by an OFDM signal in the frequency band from 4096 MHz to 8192 MHz (the frequency interval is 64 MHz, the number of subcarriers is 64).

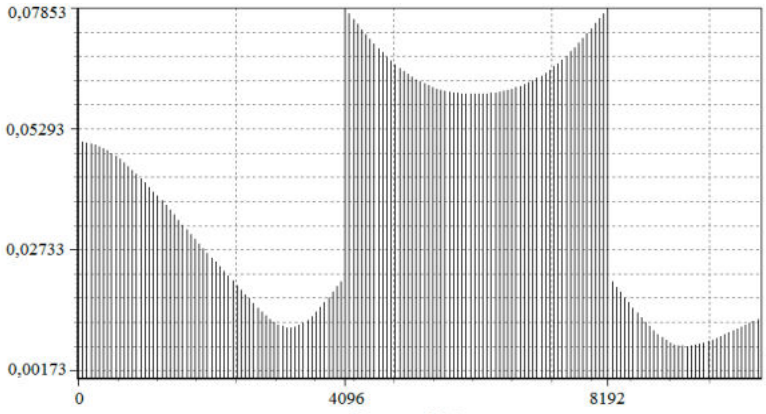

Figure 1. The spectrum at the output of the laser diode.

As can be seen from Fig.1, the OFDM signal is distorted due to interference falling into the bandwidth of subcarrier channels. The source of such interference is clipped pulses that occur when the level of the OFDM signal exceeds the threshold value of the modulation current. In addition, Figure 1 shows second-order combinational frequency components having a low-frequency (LF) spectrum (from 0 to 4096 MHz). It is possible to avoid these interferences and improve the energy budget of access networks by using external modulation of the optical carrier with an OFDM signal. An even greater increase in spectral efficiency can be achieved by using single-band external modulators, for example, based on MZI. Modeling of the modulation process by the OFDM signal of such a modulator leads to the fact that there will be no combinational frequency components occupying the low frequency region of the spectrum in the output spectrum.

The influence of the quadrature nonlinearity of the PD (relative to the field) during the conversion of an optical signal into an electric one was also studied. By analogy with Fig.1, when the OFDM signal is photodetected, noises also appear in the low frequency region in the photocurrent spectrum, these noises are caused by beats between subcarriers.

On the other hand, when using this method when constructing the fiber optic design, a number of features arise that must be taken into account when transmitting information in communication channels.

3. Conclusion

Simulation results show that high-frequency subcarrier channels are most susceptible to distortion due to chromatic dispersion. These distortions manifest themselves in the form of a decrease in the signal level in these channels. It is shown that the limiting factors of bandwidth are the total frequency band occupied by the OFDM signal and the value of the coefficient of specific chromatic dispersion of the optical fiber at the operating wavelength. The results of the modeling showed that for access networks where a standard optical fiber with a length of 20 km is used in the optical infrastructure, the total frequency band of the OFDM signal at a wavelength of 1.55 microns should not exceed 8 GHz. Based on this simulation model, it is possible to create measuring equipment for measuring the bandwidth of fiber-optic transmission systems with direct photodetection.

References

[1] Karanov B and Chagnon M 2018 *J. Lightwave Technol* **36 (20)** 4843-4855

[2] Popovskiy N I and Davydov V V and Rud V Yu 2021 *Journal of Physics: Conference Series* **2086(1))** 012163

Study of the characteristics of few-mode microstructured optical fibers with 6 cores made of highly doped GeO2 silica, step profile and induced chirality

G A Pchelkin[2,3], V V Demidov[2], E V Ter-Nersesyants[2], V V Davydov[1], A V Bourdine[1,2,3]

[1]Peter the Great Saint-Petersburg Polytechnic University, Saint Petersburg, Russia, 195251

[2]JSC "Research and Production Association Vavilov State Optical Institute", Saint Petersburg, Russia, 192171

The Bonch-Bruevich Saint Petersburg State University of Telecommunications, Saint Petersburg, Russia, 193232

e-mail: beegrig@mail.ru

Abstract. The necessity of using low-mode microstructured optical fibers with induced chirality is experimentally substantiated. The case with a 6-core structure for constructing the cross section of an optical fiber is considered. Prototypes of microstructured optical fibers were fabricated and studied to study the quasi-annular distribution of the optical field in the cross section. The results of experimental studies of an optical element with 6 cores made on the basis of germanosilicate glass with a stepped refractive index profile are presented, and an assessment is made of the dependence of the basic characteristics on the parameters of the technological cycle of its production.

1. Introduction

At present, the need to transfer large amounts of information in various communication systems is constantly increasing . Increasing requirements for speed and quality of information processing. The fiber optic communication lines are one of the most reliable ways to implement these tasks, especially in difficult conditions. For example, in the presence of a large number of electromagnetic interferences in the coverage areas of radar stations or outer space. In modern designs of single-mode optical fibers for trunk communication lines, the limit has almost been reached in terms of the possibilities for transmitting large amounts of information using various seals and compressions. Therefore, research is constantly underway to find new solutions. One of the possible solutions to this problem is associated with the use of low-mode microstructured fibers.

Nowadays, twisted microstructured optical fibers (MOFs) are considered as novel fiber optic elements with great potentiality for various applications in both fiber optic sensors/sensor networks and telecommunications. At the present time, there are known published works (both theory and containing practice implementation), declaring twisted MOFs as polarization-maintaining fiber optic devices with generation optical activity, fiber optic probes for strain and twist sensing as well as for current and magnetic field sensing, spectral and mode filters, optical tweezers, and optical angular orbital momentum (OAM)-based telecommunications.

This work presents fabricated twisted silica MOF with special six GeO_2-doped core geometry (6-core-MOF), refractive index step profile, an outer diameter of 125 μm, operating in a few-mode regime, and induced chirality with twisting of 1000 revolutions per minute.

2. Result of experimental investigations

To detect quasi-annular (vortex) distributions of the optical field in low-mode microstructured optical fibers with 6 cores made of high-doped GeO2 quartz glass, a measuring bench was modified. The previously used optical scheme had large dimensions, excessive losses during radiation transmission, and increased requirements for temperature stabilization.

In Figure 1 shows the topologies of low-mode microstructured optical fibers, for which the distribution of optical radiation at the output was studied at different twisting frequencies and other parameters of the technological cycle.

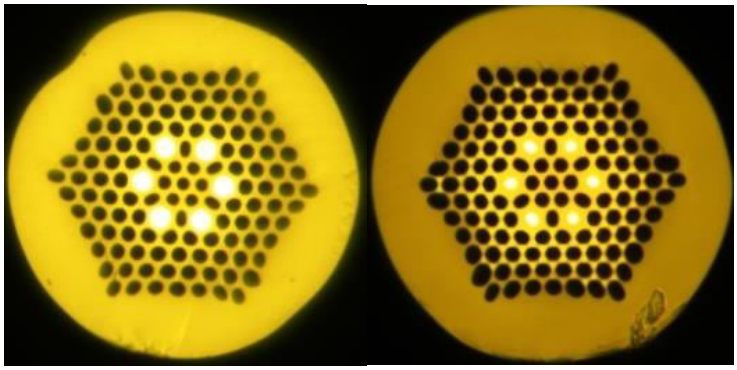

Figure. 1. The fiber of 6-core-MOFs: cross-section view of the fabricated MOF with step profile, 50 rpm and 100 rpm twist

Analysis of the presented data shows that the distribution of optical radiation is quasi-annular and uneven. This distribution can be controlled.

3. Conclusion

This work presents designed and fabricated samples of new 125-μm silica microstructured optical fiber with special six GeO2-doped core geometry, refractive index step profile, an outer diameter of 125 μm, operating in a few-mode regime, and induced chirality with twisting of 1000 revolutions per minute. Some results of tests, performed with pilot samples of designed and manufactured microstructured optical fibers, including their geometrical parameters, basic transmission characteristics, as well as measurements of far-field laser beam profiles are represented. Detailed research of the 6-core-MOF properties underutilization in various applications in measurements/sensors or/and laser systems, telecommunications etc. require an additional series of tests and experiments in future works.

References

[1] V.A. Burdin, M.V. Dashkov, V.V. Demidov, A.E. Zhukov, A.V. Bourdine, “New silica laser-optimized multimode optical fibers with extremely enlarged 100-μm core diameter for gigabit onboard and industrial networks,” Fibers, vol. 8(3), p. 18, 2020.

[2]

QKD and phase modulator imperfections

Aleksei Reutov[1,2] **and Andrey Tayduganov**[1,2]

[1] QRate, Skolkovo, Moscow 143025, Russia

[2] NTI Center for Quantum Communications, National University of Science and Technology MISiS, Moscow 119049, Russia

E-mail: aleksey.reutov@phystech.edu

Abstract. Very often in practical schemes of quantum key distribution various realistic device imperfections are usually neglected. In this work we consider the imperfect phase-modulation encoding that might lead to a potential information leakage and study its effect on the secret key generation rate.

1. Introduction

The quantum key distribution (QKD) is based on fundamental laws of quantum physics and theoretically provides security regardless eavesdropper's potential resources. However, the practical QKD implementations suffer from imperfections of realistic devices [1]. One of the sources of potential information leakage in practical BB84 [2] schemes is the imperfect state preparation by a phase modulator (PM) used for the qubit state encoding. This imperfection leads to an asymmetry between the bases, that can provide more efficient strategies for an eavesdropper [3]. In this work we consider the general quantum state description and introduce two possible phase modulation uncertainties. Using the density matrix formalism, we provide a metrics of distinguishability between the BB84 bases in our model and estimate its effect on the secret key rate.

2. Theory and methods

In our setup the linearly polarized light is brought to the Alice's PM at an angle of 45° with respect to the crystal axes of the modulator. In general, there is some phase difference φ between the field amplitudes along the ordinary and extraordinary axes. By applying an electric voltage along one of the axes, an additional phase difference $\varphi_{\text{bit}}^{\text{basis}}$ (with some uncertainty $\delta\varphi_{\text{bit}}^{\text{basis}}$) is created, which determines the basis and bit states. The general polarization state, prepared by Alice in X' and Y' bases, can be described on the Bloch sphere (see Fig. 1) in the following form,

$$|\psi_{\text{bit}}^{\text{basis}}\rangle = \cos(\pi/4 - \delta\theta/2)\,|\leftrightarrow\rangle + e^{i(\varphi+\varphi_{\text{bit}}^{\text{basis}}+\delta\varphi_{\text{bit}}^{\text{basis}})}\sin(\pi/4 - \delta\theta/2)\,|\updownarrow\rangle \tag{1}$$

where $\delta\theta$ represents the deviation from the xy–plane on the Bloch sphere caused by e.g. the 45° fiber input error, $|\leftrightarrow\rangle$ and $|\updownarrow\rangle$ are the standard horizontal and vertical polarization states.

To describe the distinguishability between the states in two bases, the metric Δ called the *imbalance of "quantum coin"* [4] is used. It can be expressed in terms of *fidelity* F [5]:

$$\Delta \equiv \frac{1 - \sqrt{F(\rho^{X'}, \rho^{Y'})}}{2}, \quad F(\rho^{X'}, \rho^{Y'}) \equiv \left(\text{Tr}\sqrt{\sqrt{\rho^{Y'}}\rho^{X'}\sqrt{\rho^{Y'}}}\right)^2 \tag{2}$$

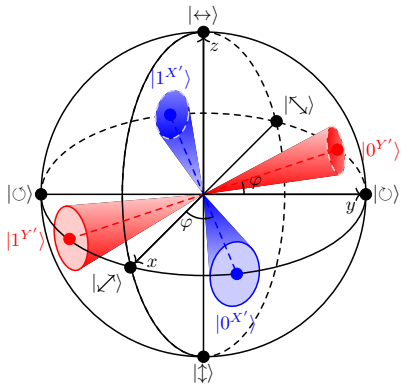

Figure 1. Physical polarization states on the Bloch sphere. Experimental phase uncertainties are schematically depicted as red and blue cones.

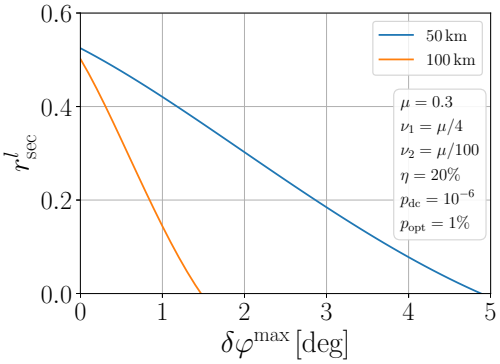

Figure 2. Minimized secret key rate (per bit) lower bound as function of maximum phase modulation error $\delta\varphi^{\max}$.

where the density matrices $\rho^{X',Y'}$ are given by $\rho^{\mathrm{basis}} = (|\psi_0^{\mathrm{basis}}\rangle\langle\psi_0^{\mathrm{basis}}| + |\psi_1^{\mathrm{basis}}\rangle\langle\psi_1^{\mathrm{basis}}|)/2$.

3. Results and discussion

Using the explicit state parametrization (1) we provide the analytical computation of fidelity and estimate the single-photon phase error rate correction according to Ref. [4]

$$E_1^{\mathrm{phase}} = E_1^{\mathrm{bit}} + 4\Delta'(1-\Delta')(1-2E_1^{\mathrm{bit}}) + 4(1-2\Delta')\sqrt{\Delta'(1-\Delta')E_1^{\mathrm{bit}}(1-E_1^{\mathrm{bit}})}\,, \quad \Delta' = \frac{\Delta}{Y_1} \tag{3}$$

where the single-photon yield Y_1 and bit error rate E_1^{bit} are determined via decoy-state technique taking into account the finite-key-size effects [6]. Then we use E_1^{phase} for the secret key rate calculation [7],

$$r^l_{\mathrm{sec}} = \frac{Q_1}{Q_\mu}[1 - h_2(E_1^{\mathrm{phase}})] - f_{\mathrm{ec}}h_2(E_\mu) \tag{4}$$

and study the effects of $\delta\theta$ and $\delta\varphi^{\mathrm{basis}}_{\mathrm{bit}}$ uncertainties on r^l_{sec}.

Our main result is presented in Fig. 2. One can see that for the 100 km–long optical line the critical (i.e. when $r^l_{\mathrm{sec}} \leq 0$ no secret key can be distributed) value of a phase disturbance is about 1.5°. For the length of 50 km our result is more promising – the key rate vanishes only for the phase error greater than 5°.

References

[1] Xu F, Ma X, Zhang Q, Lo H K and Pan J W 2020 *Rev. Mod. Phys.* **92**(2) 025002
[2] Bennett C H and Brassard G Quantum cryptography: Public-key distribution and coin tossing *Proc. of the IEEE Int. Conf. on Comp. Sys. and Sign. Process. (IEEE, 1984)* pp 175–179
[3] Gottesman D, Lo H K, Lüttkenhaus N and Preskill J 2004 *Quant. Inf. Comput.* **4** 325–360
[4] Lo H K and Preskill J 2007 *Quantum Info. Comput.* **7** 431–458
[5] Jozsa R 1994 *Journal of Modern Optics* **41** 2315–2323
[6] Trushechkin A, Kiktenko E and Fedorov A 2017 *Phys. Rev. A* **96**(2) 022316
[7] Lo H K, Ma X and Chen K 2005 *Phys. Rev. Lett.* **94**(23) 230504

Optical communication channel for multifunctional ecological monitoring complex

D I Isaenko[1], S A Rodin[1], B K Reznikov[1], K A Kovaleva[1] and V V Davydov[2,3]

[1]The Bonch-Bruevich Saint-Petersburg State University of Telecommunications, Saint-Petersburg 191186, Russia
[2]Peter the Great Saint-Petersburg Polytechnic University, Saint-Petersburg 195251, Russia
[3]All-Russian Research Institute of Phytopathology, Moscow Region 143050, Russia

Email: psnp.174.sut@gmail.com

Abstract. The necessity of transmitting information from a multifunctional complex for environmental monitoring located on a high-voltage power line via a fiber-optic communication line is substantiated. The features of the transmission of this information are noted. A fiber-optic communication line has been developed to transmit information over distances up to 200 km without the use of optical amplifiers. The results of the study of its main characteristics are presented. The prospects for further use of this type of FOCL are determined.

1. Introduction

Currently, on the occasion of environmental degradation, much attention is paid to careful environmental monitoring [1]. A large number of systems and complexes have been developed for its implementation. One of these complexes is formed on the upper parts of high-voltage power lines, since there are a lot of benefits from its location and operation (for example, constant power supply, inaccessibility, control of air flow over the earth's surface, etc.). On the other hand, there is a problem with the transmission of information from such multifunctional complexes in conditions of increased activity of electromagnetic interference. One of the solutions may be the use of export-optical communication lines (FOCL), which are resistant to reflection deviation and can transmit information over long distances [2].

2. Design of fiber-optic communication line

A feature of the information transfer from the multifunctional complex of environmental monitoring is that the information must be transmitted only in one direction (to the user). The reverse channel for the transmission of information is not needed. Information is a set of values from various sensors, which are measured at intervals of 3-5 s. Therefore, it is possible to use one optical channel with time division of signals for transmission. Such a time interval (information transmission frequency) makes it possible to refuse the use of an electro-optical modulator in the design (direct modulation is used). This simplifies the design of the FOCL and reduces its cost. The structural diagram of the fiber-optic communication channel is shown in figure 1. The developed design uses a transmitting laser module with direct modulation with $\lambda = 1550$ nm, the radiation power is adjustable from 1 to 20 mW. This allows in some cases to increase the range of information transmission over FOCL.

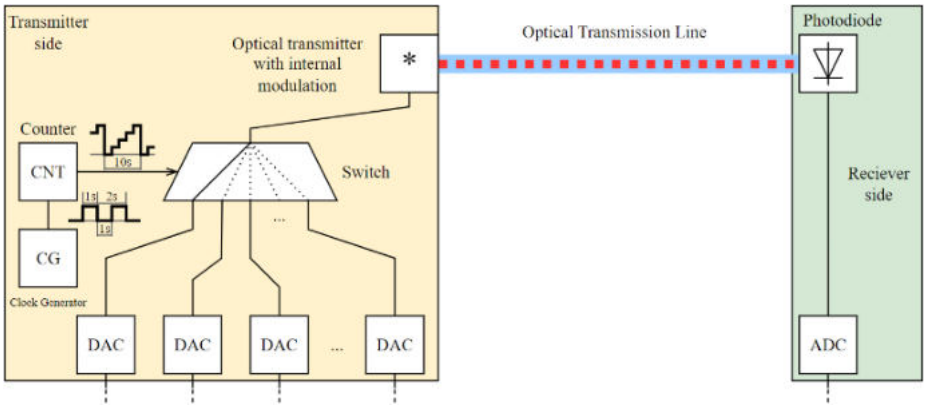

Figure 1. Structural diagram of fiber-optic transmission system.

The modulated optical signal is recorded by a photodiode. This signal is then sent to an analog-to-digital converter. The most important characteristic in this case is the dynamic range of the developed optical communication channel, are presented in figure 2.

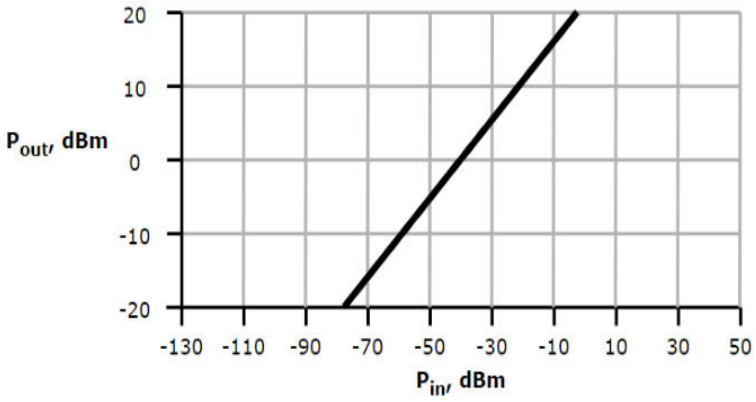

Figure 2. Dynamic range of the optical communication channel.

Analysis of the obtained results shows that the dynamic range is more than 120 dBm, which is sufficient for stable information transmission. In addition, the system developed by us is highly reliable in terms of the element base used.

3. Conclusions

In this work the multifunctional complex for environmental monitoring with an optical communication channel concept has been developed. The selection of components for the designed complex was made. The developed concept can be used by organizations working in the environmental safety area.

References

[1] Grevtseva A, Diuldin M, Savchenko I, Druzhinina Gand Valov A 2020 *IOP Conference Series: Earth and Environmental Science* **578(1)** 012058

[2] Dmitrieva D, Pilipova V, Andreeva E, Dudkin V and Davydov V 2020 *In Proceedings of ITNT 2020 - 6th IEEE International Conference on Information Technology and Nanotechnology*, vol. **9253348**, p. 34-39

Synchronization protocol for MDI-QKD systems

N V Rudavin[3,5], I S Gerasin[2,3,4], E E Mekhtiev[1,2,4], A V Duplinsky[1,3,4] and Y V Kurochkin[1,2,3,4]

[1]QRate, Novaya av. 100, Moscow, Russia
[2]Moscow Institute of Physics and Technology, 9 Institutskiy per., Dolgoprudny, Moscow Region, 141701, Russian Federation
[3]NTI Center for Quantum Communications, National University of Science and Technology MISiS, Leninsky prospekt 4, Moscow 119049, Russia
[4]Russian Quantum Center, Bolshoy Boulevard 30, bld. 1, Skolkovo, Moscow 121205, Russia
[5]HSE University, 20 Myasnitskaya ulitsa, Moscow 101000, Russia

n.rudavin@goqrate.com

Abstract. Commercial fiber quantum key distribution systems require the implementation of a protocol for synchronizing the frequency synthesizers of the transmitter and receiver nodes. Frequency mismatch may be due to temperature fluctuations, mechanical effects and imperfections in the technological processes. In this work, an algorithm for automatically adjusting Alice's and Bob's frequency to Charlie's frequency is proposed. After optimizing the algorithm parameters, it was tested on optical lines of different lengths.

1. Introduction

Nowadays, the commercial implementation of fiber quantum key distribution (QKD) systems use crystal oscillators and several frequency multipliers as frequency synthesizers to generate the operating frequency. At the same time, the existing technological production process does not allow obtaining frequency synthesizers with identical output parameters. Moreover, modern crystal oscillators do not have high stability over long periods of time due to temperature fluctuations or mechanical stress. The discrepancy between the frequencies of the synthesizers is crucial for key generation. So, it is necessary to organize frequency synchronization system for experimental measurement-device-independent QKD protocol (MDI-QKD) fiber setup.

There are two main approaches to organize the synchronization protocol in QKD systems. The first method is based on computing the cross-correlation of transmitted and received qubit sequences [1]. The disadvantage of this approach is the necessity to use single photon detectors (SPD), which are the most technologically complex node of modern QKD systems. The second approach is to use high energy optical pulses sent by Alice through a quantum channel [2] or an additional fiber [3] to transmit the frequency of Alice's synthesizer. The use of a second fiber imposes additional requirements on the integration of the QKD system into existing telecommunication networks and increases the cost of the system.

2. Protocol description

In the MDI-QKD protocol the secret key is distributed between the two transmitters (Alice and Bob) using the untrusted central node (Charlie). Since SPDs are located at Charlie's node, we cannot use qubit-based synchronization method. Therefore, for experimental MDI-QKD fiber setup we suggest to use quantum channel to transmit the synchronization signal. Since Alice and Bob are not connected by an optical fiber, we use a laser and a 50/50 beamsplitter to generate a synchronization signal on Charlie. The wavelengths of the synchronization laser and the signal laser are in different DWDM channels. In this configuration the sync pulses propagate in the opposite direction through the quantum channel. To eliminate their influence on the quantum signal and the SPDs, we use time-division multiplexing and WDM optical filters.

From the point of view of the theory of control of technical systems, the task of adjusting the frequency of one synthesizer to the frequency of another synthesizer can be considered as the task of designing and implementing an industrial control system (ICS). A phase-locked loop system (PLL) system was chosen as the ICS. We use photodetectors to register the optical synchronization signal and to convert it into an electrical signal.

To obtain a synchronization error value between the synthesizers, the synchronization signal is sent to one of the inputs of the phase detector (PD). The signal from Charlie's synthesizer is sent to the second PD input. Then we tune the frequency by changing the voltage supplied to Alice's (Bob's) synthesizer. The value of the control signal is calculated using a proportional– derivative controller (PD controller). In general, the integral term is also used to calculate the correction, but during the experiments it was decided not to use it to simplify the optimization process of the gain coefficients. By using third and fifth order derivative terms we can achieve a high frequency tuning rate even if the initial frequencies of the synthesizers are very different.

3. Experimental results

The proposed synchronization protocol has four hyperparameters – the gain coefficients of the terms of the controller. Using the method of experimental tuning with different sets of coefficients, their optimal values were found. For proof of principle experiment we built experimental setup, consisting of Alice and Charlie.

To estimate the accuracy of the synchronization, we have measured the frequency ratio of Alice's and Charlie's synthesizers with 0 and 75 km of fiber. During the tests with optimal coefficients, we were able to achieve stable synchronization with accuracy up to the eleventh decimal place, regardless of the length of the optical line. The experiment confirmed that the proposed protocol can be used in MDI-QKD experimental setups.

References

[1] Cochran R. et al. "Qubit-based clock synchronization for QKD systems using a Bayesian approach." Entropy 23.8 (2021): 988.

[2] Walenta, Nino, et al. "A fast and versatile quantum key distribution system with hardware key distillation and wavelength multiplexing." New Journal of Physics 16.1 (2014): 013047.

[3] Korzh, Boris, et al. "Provably secure and practical quantum key distribution over 307 km of optical fibre." Nature Photonics 9.3 (2015): 163-168.

Metamorphic InGaAs photodiode with low dark current grown on GaAs substrate

I.V. Samartsev*, S.M. Nekorkin, B.N. Zvonkov, A.B. Chigineva, K.S. Zhidyaev

Research Institute of Physics and Technology, Nizhny Novgorod State University, Nizhniy Novgorod 603950, Russia
*woterbox@mail.ru

Abstract. The results of studies aimed for creation of photodiodes formed on GaAs substrates for the spectral range above 1 μm are shown. The epitaxial growth technique of InGaAs photodiode structures based on a digital InGaAs/GaAs metamorphic buffer layer by metalorganic chemical vapor deposition (MOCVD) has been developed. The spectral dependence of the photocurrent of photodiodes based on the produced structures has a maximum at the 1.16 μm wavelength. The photosensitivity range at 10% of peak at room temperature is 0.99 - 1.33 μm. The current-voltage characteristics in the temperature range 9–300 K. The dark current density at room temperature was 8×10^{-5} A/cm^2 with a reverse bias of -5 V.

1. Introduction

Photodiodes operating in the short infrared range (up to 3 μm) grown on GaAs substrates are interest as a replacement for devices currently used for this range grown on InP substrates. One of the directions of creating such photodiodes is the use of metamorphic buffers (MB) [1, 2]. The practical implementation of metamorphic heterostructures on GaAs, the characteristics which would not be low to those of heterostructures on InP, is hindered by incomplete suppression of the intergrowth of dislocations into active layers of the structure and the appearance of surface micro relief. Thus, it is current task to search for and optimize the MB design in order to improve the crystal quality of the obtained heterostructures. In this work, we present the results of the study of photosensitive GaAs heterostructures and photodiodes based on them, obtained by MOCVD on GaAs (100) substrates using digital MB.

2. Experimental samples

The investigated heterostructures were produces by the MOCVD method at atmospheric pressure in a horizontal reactor. The 0.18 μm thick n-GaAs buffer layer doped with silicon (10^{18} cm^{-3}) was grown on an n^+-GaAs substrate. Next, a digitally-graded buffer with a total thickness of 1.3 μm doped with Si up to 10^{18} cm^{-3} and a p-i-n $In_{0.3}Ga_{0.7}As$ structure were formed. The p-i-n structure consisted of 1.68 μm thick Si-doped n-layer with doping level of 10^{18} cm^{-3}, 15 nm undoped layer, and 1.4 μm thick p-layer doped with Zn up to 7×10^{17} cm^{-3}. The thickness of layers was calculated based on the growth rate and time.

The formation of a digitally-graded buffer is in changing the thicknesses of alternating layers of GaAs and $In_{0.3}Ga_{0.7}As$ in opposite directions as the buffer layer grows, while the composition remains the same. The thicknesses of GaAs and InGaAs layers at the initial stage of growth were 62 nm and 3

nm, respectively. The GaAs layer thickness decreased and the $In_{0.3}Ga_{0.7}As$ thickness increased during the growth of the buffer with the total of 38 GaAs and InGaAs layers. The GaAs layer thickness at the final stage of buffer growth was 3 nm, and the InGaAs thickness was 62 nm. Thus, the digitally-graded MB consisted of many GaAs/$In_xGa_{1-x}As$ pairs of various thicknesses, in which the propagation of dislocations at heterointerfaces is blocked. A schematic representation of the heterostructure is shown in Figure 1.

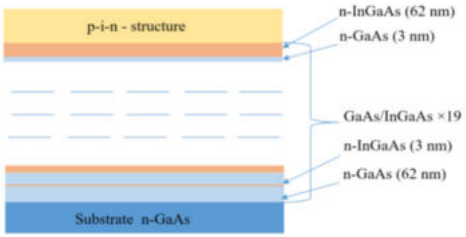

Figure 1. The scheme of the photodetector heterostructure with a digitally-graded MB.

3. Results and discussion

The surface roughness was studied using atomic force microscopy. The root mean square deviation (RMS) was 20 nm. The dislocation density can be estimated from the density of etching pits, which was calculated using optical microscopy and amounted to 10^6 cm^{-2}.

Photodiodes were fabricated on the basis of the investigated heterostructures. Figure 2 shows a typical spectrum of photocurrent measured at room temperature. The photodiodes had a photosensitivity range of 0.99 - 1.33 μm at the 10% level of the maximum at a wavelength of 1.23 μm. This indicates that these photodiodes are promising for applications in the telecommunications range. In addition, the small width of the photosensitivity spectrum (0.34 μm) makes it possible to use such photodiodes for detecting weak signals in atmospheric signal transmission without the use of

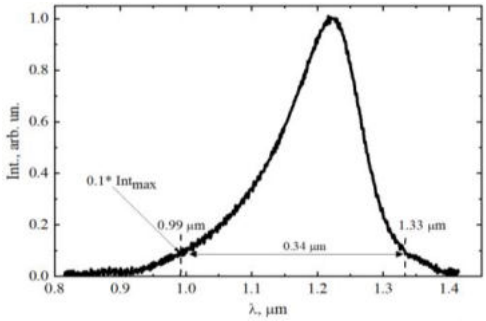

Figure 2. Photocurrent spectrum of photodiodes at room temperature.

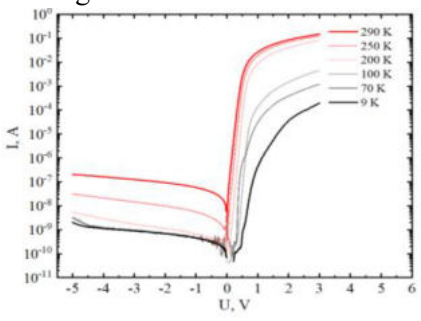

Figure 3. Typical I–V curves of the obtained photodiodes at range of 9–290 K.

appropriate filters. Figure 3 shows current-voltage characteristics typical for the investigated photodiodes, measured in the temperature range 9 – 290 K. For photodiodes with a mesa structure with 560 μm diameter dark current was 2×10^{-7} A at room temperature and reverse bias of -5 V, which corresponds to a current density of 8×10^{-5} A/cm^2.

Thus, new photodiode InGaAs structures with a digitally-graded MB on a GaAs substrate were formed by MOCVD. The use of a new design of the MB layer allowed us to create photodiodes with a low dark current. Thus, the proposed design of a digitally-graded MB is promising for the production of photosensitive structures for wavelengths over 1 μm.

By the support of the federal academic leadership program «Priority 2030» of Ministry of Science and Higher Education of the Russian Federation.

References

[1] K. Swaminathan, L.-M. Yang, T. J. Grassman, et. al., Opt. Express. 19 (2011) 7280-7288.
[2] P. Jurczak, K.A. Sablon, M. Gutiérrez, et. al., Infrared Physics & Technology, 81 (2017) 320-324.

Gate- and polarization-dependent graphene-metal junction for polarization resolution

Valentin Semkin*, Dmitry Mylnikov, Elena Titova, Sergey Zhukov and Dmitry Svintsov

Center for Photonics and 2D Materials, Moscow Institute of Physics and Technology, Dolgoprudny, Russia

*semkin.va@phystech.edu

Abstract. Nowadays, there is still a devices necessity for fast reading of the light polarization state, which cannot be satisfied with common solutions based on movable polarizers. Here, we propose a simple graphene-based mid-IR detector with polarization sensitivity. Moreover, the unusual pattern of this sensitivity makes it possible to use it as an electrically-calibrated on power detector with polarization resolution.

1. Introduction

Radiation polarization is an independent channel for encoding and transmitting information, alongside intensity, frequency and phase. The ability to select radiation components with the electric field vector orientation of interest allows to see details that are hidden in the polarization. The presented work introduces a detector for the mid-IR range based on CVD graphene with contacts made of dissimilar metals, which can resolve the detected radiation polarization [1].

2. Devices and experiments

We investigated the photodetectors of transistor geometry. The channel in them is consist of CVD graphene, which is transferred on a silicon substrate with 300 nm silicon oxide. The substrate also acts as an electrical gate. We have studied devices with pairwise metallization of contacts from Au, Cr and Ti. The device with an Au-Ti pair turned out to be the most efficient for photodetection purposes. Optical measurements of the detectors were carried out with synchronous detection at a wavelength of 8.6 um.

3. Polarization-resolving detector

In this work, the photovoltage dependencies on polarization and carrier concentration of the graphene-metal junction are measured and studied (Fig. 1). A strong polarization sensitivity of the detector was observed because of the electric field amplification due to the lightning rod effect. And the unusual features in the dependencies - polarization-independent points and ranges of the photovoltage sign-flipping with the polarization rotation, are explained by the presence of at least two photovoltage generation mechanisms in the device: isotropic and anisotropic. As a result, a method for polarization determining with a single device based on strong polarization sensitivity and polarization-independent point is proposed. In order to resolve polarization in the full π-range, only two detectors are needed instead of common three.

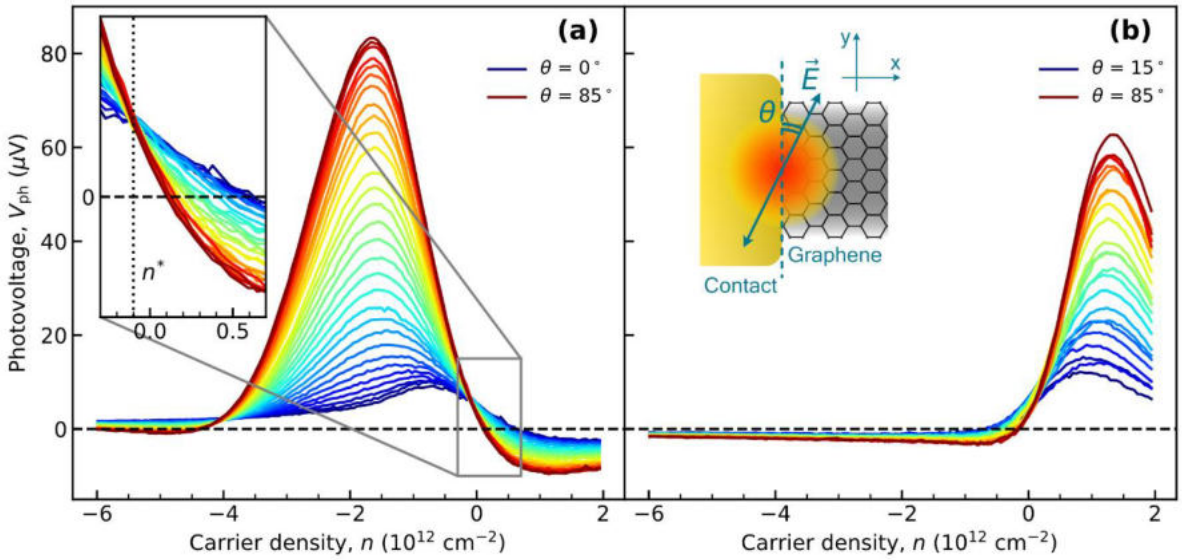

Figure 1. Dependencies of photovoltage on carrier density and polarization angle at graphene-Ti (a) and graphene-Au (b) junctions. The polarization angle θ is counted from the direction that parallel to the graphene-metal junction (right inset) and varies with 3° step. Inset in (a) magnifies the vicinity of carrier density n^* where the photoresponse becomes polarization-independent [1].

4. Conclusion

To conclude, we have fabricated, measured and proposed a physical 'backend' of the detector based on a graphene-metal junction. And the features of its sensitivity such as polarization-independence and strong polarization dependence at various gate voltages allowed it to be used as a polarization-resolving detector.

Acknowledgments

This work was supported by the grant 21-72-00078 of the Russian Science Foundation (optical and electronic measurements) and by Ministry of Science and Higher Education of the Russian Federation (No. FSMG-2021-0005) (device fabrication). The devices were fabricated using the equipment of the MIPT Center of Shared Research Facilities.

References

[1] Semkin, V., Mylnikov, D., Titova, E., Zhukov, S. & Svintsov, D. Polarization-resolving graphene-based mid-infrared detector. *arXiv:2203.12423* (2022).

Development of ultraviolet photodetectors based on ultrathin GaN epitaxial layers grown on c-Al_2O_3

O A Sinitskaya, K Yu Shubina, D V Mokhov, A V Uvarov, V V Filatov, A M Mizerov, S N Timoshnev

Alferov University, St. Petersburg 194021, Russia

E-mail: olesia-sova@mail.ru

Abstract. In this work, metal-semiconductor-metal photodetectors based on GaN/c-Al_2O_3 epitaxial structures were created. By studying their current-voltage and spectral characteristics, it was found that these devices can be used for near-range UV detection.

1. Introduction

In recent years, the development of ultraviolet (UV) photodetector (PD) technology has sparked interest in generating innovative ideas to improve these devices and create efficient visible-blind UV PDs. These devices are used in environmental, industrial, military and biological fields [1]. One of the most popular PD designs is metal-semiconductor-metal (MSM) structure due to the ease of fabrication, low noise level and high detection capability [2]. UV PDs can be fabricated based on various semiconductor materials, such as Si, SiC, ZnO and others. Among them wide bandgap semiconductors, especially (Al,Ga)N, are one of the most prospective materials for this purpose. The advantages of (Al,Ga)N are: a wide band gap corresponding to the UV spectral range (E_g ~ 3.4 - 6.2 eV), high mobility of charge carriers, high breakdown voltage, as well as excellent mechanical, thermal and chemical stability [3].

In this work, MSM UV photodetectors based on epitaxially grown on c-Al_2O_3 substrates undoped GaN layers were developed and their characteristics were studied.

2. Experimental details

The 300 nm thick GaN layers were grown by plasma-assisted molecular beam epitaxy (PA MBE) using Veeco GEN 200 industrial type MBE setup on annealed and nitrided c-Al_2O_3 substrates (see figure 1, a, b).

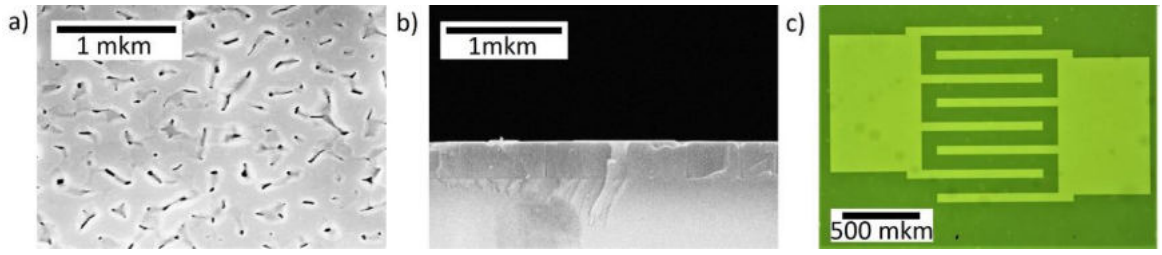

Figure 1. SEM image of the GaN/c-Al_2O_3 epitaxial structure: plan view (a) and cross-section (b). Photomicrograph of metal electrodes (c)

Using Hall measurements it was found that the undoped GaN epitaxial layers have n-type conductivity with a carrier concentration of $n \sim 1.5 \times 10^{18}$ cm^{-3} and mobility of $\mu \sim 40$ cm^2/(V×s).

The MSM structure with semitransparent Ni/Au (15 nm thick) interdigitated electrodes (see figure 1, c) was obtained using standard laser lithography technique, e-beam and thermal vacuum evaporation and standard lift-off process. The Ni/Au contact metallization was chosen because of its low imperfection factor, large Schottky barrier height (SBH, 1.02 eV), and simple fabrication process.

The UV PD I–V characteristics were obtained both in the dark and under visible range and 365 nm UV LED illumination (see figure 2, a).

3. Results and discussion

As it can be seen from figure 2 a, the I–V curves coincided in the dark and under normal illumination. Thus, visible radiation indeed has little effect on the operation of the fabricated UV PD. The appearance of additional photocurrent was observed under 365 nm LED illumination. At the same time, as can be seen from spectral characteristics (figure 2, b) the highest photoresponse was observed at wavelength range of 350 – 360 nm, that corresponds to GaN bandgap (3.4 eV) and confirms the reliability of the obtained I-V curves. However, obtained photodetectors have a high dark current (6 mA at a bias of 2 V). It can be explained by both high dislocation density in the ultrathin epitaxial GaN layer grown on mismatched substrate and imperfection of contact formation procedure. The GaN crystal quality can be improved by using different types of templates for epitaxial growth of ultrathin GaN layers (SiC/substrate, GaN/substrate etc.). In addition, the improving of PD fabrication technology through the use of mesa structures or passivating surface with dielectric coatings (SiO_2, Al_2O_3, etc.) also can drastically reduce the dark current. Moreover, high-temperature annealing of the grown structures can increase the height of the Schottky barrier, and thus also reduce the level of dark current.

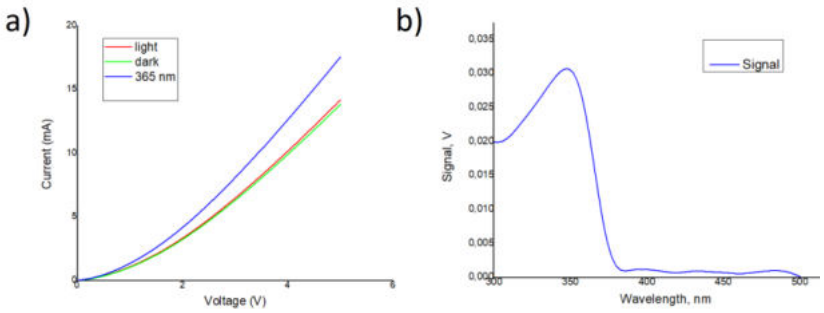

Figure 2. I–V characteristics (a) and spectral characteristics (b) of the obtained PD based on GaN/c-Al_2O_3

4. Conclusion

In this work, MSM PDs based on GaN epitaxial layers were fabricated. The I-V and spectral characteristics of the PDs were investigated. It was found that the devices respond to near UV radiation. However, the obtained PDs have a high dark current, which adversely affects the detectivity of the device. Therefore, it is necessary to improve the fabrication technology of such devices (for example, mesa etching and surface passivation with dielectric coatings, high-temperature annealing).

Acknowledgments

The work was supported by the Ministry of Education and Science (grant №FSRM-2020-0008).

References

[1] Munoz E, Monroy E, Pau1 J L, Calle1 F, Omnes F, Gibart P 2001 *J. Phys.: Condens. Matter* **13**, 7115–37

[2] Shi L, Chen K, Zhai A, Li G, Fan M, Hao Y, Zhu F, Zhang H, Cui Y 2021 *Laser Photonics Rev* **15**, 2000401

[3] Wengang B 2017 *Handbook of GaN semiconductor materials and devices (*Boca Raton: Taylor & Francis, CRC Press)

Investigation of optoelectronic oscillator without microwave and optical amplifiers

I Yu Tatsenko, A B Ustinov

Saint Petersburg Electrotechnical University "LETI", St.Petersburg, 197022, Russia

e-mail: abitur.tatsenko@mail.ru

Abstract. Optoelectronic oscillator without microwave and optical amplifier was proposed. Microwave photonic link with positive transmission coefficient was investigated. Microwave oscillation in range of 3.5-7.5 GHz was observed. A phase noise of -135 dBc/Hz at the frequency offset 10 kHz was obtained.

1. Introduction

During last two decades optoelectronic oscillator (OEO) is one of the most studied subjects in microwave photonics [1-5]. The main advantage of OEO is low phase noise, which makes it possible to use in radar and telecommunication systems.

OEO presents an active ring resonator with positive feedback and consists of two main parts: optical path and electrical part. The optical path represents a microwave photonic link (MPL) which includes laser, electro-optical modulator, optical fiber and photodetector. Electrical path usually includes a microwave amplifier to compensate losses the in ring and a microwave filter for mode selection.

Purpose of the present work is investigation of optoelectronic oscillator based on a high-power laser. The main difference of such OEO is the absence of a microwave amplifier in electrical path. Oscillation in such system occurs due to the positive transmission coefficient in MPL, thus, there is no need to compensate losses in the ring.

2. Results

In the first part of this work a MPL based on a high-power laser was studied. Transmission characteristics of the MPL were measured at various laser powers. Optical radiation wavelength of the laser was 1550 nm. Half-wave voltage of electro-optical modulator was 1.6 V. Optical losses of electro-optical modulator was 4.5 dB. Sensitivity of photodetector was 0.8 A/W in the range of 0-12 GHz.

Performed experiments showed that increasing of the laser power up to 28 dBm (630 mW) makes it possible to obtain a positive gain of MPL (more than 2.3 dB in 0-10 GHz range). Therefore, MPL provides positive feedback, which is necessary to obtain microwave oscillation.

Based on the described microwave photonic link an OEO was constructed. Microwave oscillation in the range of 3.5-7.5 GHz was observed. Phase noise of the proposed OEO is about -35 dBc/Hz at 10 Hz frequency offset and -135 dBc/Hz at an offset of 10 kHz. Thus, the obtained results show the possibility of developing an OEO without a microwave or an optical amplifier, which simplifies its design and potentially improve phase noise characteristics.

Acknowledgments
This work was supported by Ministry of Education and Science of Russian Federation (Project "Goszadanie").

References
[1] Yao X S, Maleki L 1996 *JOSA B* **13(8)** 1725-1735
[2] Bánky T, Horváth B, Berceli T 2006 *JOSA B* **23(7)** 1371-1380
[3] Chembo Y K, Brunner D, Jacquot M., Larger L 2019 *Reviews of Modern Physics* **91(3)** 035006
[4] Ustinov A B, Kondrashov A V, Nikitin A A, Lebedev V V, Petrov A N, Shamrai A V, Kalinikos B A 2019 *Journal of Physics: Conference Series* **1326(1)** 012015
[5] Hao T, Liu Y, Tang J, Cen Q, Li W, Zhu N, Dai Y, Capmany J, Yao J, Li M 2020 *Advanced Photonics* **2(4)** 044001

Investigation of the degradation of the characteristics of photosensitive structures with porous silicon

A Shishkina[1,2], **I A Shishkin**[1], **P D Tishin**[2]

[1]Department of Physics, Samara National Research University, Samara, 443086, Russia
[2]Institute of Informatics and Cybernetics, Samara National Research University, Samara, 443086, Russia

daria.lizunkova@yandex.ru

Abstract. High-efficiency solar cells, as power sources for aircraft, are of great interest to the developers of space technology, since for most spacecraft solar batteries are practically an uncontested source of energy. Increasing their efficiency is a promising direction. To increase the efficiency of solar cells for space, it is proposed to use silicon nanostructures, namely porous silicon. This paper presents a review of the results on the prospects for the use of silicon nanostructures in a hard radiation environment. Silicon nanostructures have good radiation resistance, which manifests itself in improving the characteristics of photosensitive structures based on them, which is associated with "radiation doping". Moreover, if we analyze their change over a long period of time, the parameters of solar cells remain at the same level. Degradation processes in these structures are not observed, or they are very insignificant.

1. Introduction

Currently, solar cells are one of the most promising areas in science and technology. They are used for both terrestrial and space purposes. To work in space, solar cells need a special approach, since outer space is an extremely dangerous environment. One of the most obvious threats is cosmic radiation, which includes solar, galactic and magnetospheric energy particles [1]. The impact of cosmic radiation can lead to a gradual deterioration of the properties of materials and characteristics [2], thus, the service life of solar cells decreases, which adversely affects the performance of the spacecraft (SC), which can lead to its premature exit from standing. Thus, one of the urgent tasks today is to increase the resistance of solar cells to radiation exposure to ensure a minimum decrease in work efficiency. In this paper, the prospects of silicon nanostructures for the creation of solar cells with silicon nanostructures are considered.

2. Radiation-resistant structures with porous silicon

Promising materials for such elements are photosensitive structures containing silicon nanoscale structures [3]. Compared to single-crystal silicon solar cells, such structures exhibit a high efficiency of radiation conversion, as well as a higher radiation resistance [4].

Most semiconductor materials and devices are very sensitive to cosmic radiation. The cause of radiation effects in semiconductors is, as a rule, the appearance of structural defects, and sometimes the appearance of new impurities in crystals. Ionization also leads to significant changes, i.e., the

appearance of charge carriers—electrons and holes as a result of the absorption of radiation energy by the crystal [5]. Radiation defects manifest themselves in semiconductors as recombination centers, changing the lifetime of minority charge carriers, as capture centers, reducing the concentration of majority carriers, and as scattering centers, reducing mobility. Thus, by introducing certain strictly dosed concentrations of thermally stable radiation defects into semiconductors and semiconductor device structures, one can sometimes control their properties and characteristics with an accuracy that is unattainable when using the diffusion of chemical impurities. This is the basis for the developed radiation technologies for specific types of semiconductor devices.

Structures using nanoscale elements are more promising for space applications, because exhibit higher radiation resistance. This is due, firstly, to an increase in the working surface, which facilitates the recombination of emerging radiation defects on the surface. Secondly, it is thermodynamically unfavorable for nanostructures to have defects.

The reason for the increased radiation resistance of silicon nanostructures is their extremely developed porous silicon surface (up to 600 m^2/cm^3), which can act as a region of effective sink and subsequent annihilation of radiation defects. When high-energy ions interact with elements of such a structure, energy can be transferred not only to individual atoms, but also to clusters or parts of silicon filaments. Such a "collective" reception of energy is possible due to the change in the phonon spectrum in nanometer silicon structures [6]. The energy received by groups of atoms in por-Si nanostructures will obviously be less than the value taken by individual atoms, which will reduce the destructive effect.

When exposed to cosmic radiation, several processes will occur. On the one hand, this is an increase in the concentration of free charge carriers due to the formation and ionization of point defects (radiation doping), on the other hand, it is a decrease in the concentration of free charge carriers due to the formation of surface recombination centers. The influence of the latter factor weakens with time, since the concentration of surface centers decreases, returning to the equilibrium one.

Comparison of ground and flight tests on small spacecraft AIST-2D showed that solar cells based on porous silicon can be more resistant to cosmic radiation than solar cells based on traditional semiconductor materials [7, 8].

3. Conclusion

Thus, the results show the promise of using silicon nanomaterials to create radiation-resistant solar cells.

References

[1] Kuznetsov V 2014 *Space technology and technology*. **3** (6). pp. 3-13

[2] Novikov LS 2010 *Radiation effects on spacecraft materials. Tutorial* 192 p.

[3] G.P. Yarovoy, N.V. Latukhina, A.S. Rogozhin, A.S. Gurtov, S.V. Ivkov, S.I. Minenko 2012 *Izvestiya SNTs RAN* **14** 1 (2) pp. 521 – 524

[4] Gerasimenko N Smimov D Medetov N 2008 *Abstracts of 16th International Conference on Ion Beam Modification of Materials* p 202

[5] Vavilov V S Ukhin I A 1969 *Atomizdat* p 3-30

[6] Reshina I I Hook E G 1993 Semiconductors **27** 728

[7] Gurtov A.S., Ivkov S.V., Lizunkova D.A. et al. 2017 *International Youth Scientific Conference "XIV Royal Readings", dedicated to the 110th anniversary of the birth of S.P. Korolev, to the 75th anniversary of the KuAI-SGAU-SamGU-Samara University and the 60th anniversary of the launch of the first artificial Earth satellite* **1** p 503-504

[8] Latukhina NV Gurtov A S Ivkov S V et al 2017 *V All-Russian scientific and technical conference with international participation Actual problems of rocket and space technology "V Kozlov Readings"* 2017 **2** p 323-326

The development of ITO-based orienting coatings for Nematic Liquid Crystal Devices

A S Toikka[1,2,3,4]**, N V Kamanina**[1,2,3,4]
[1]Lab for Photophysics of media with nanoobjects, Vavilov State Optical Institute, 199053 St. Petersburg, Russia
[2]Department of Photonics, St. Petersburg Electrotechnical University ("LETI"), 197376 St. Petersburg, Russia
[3]Advanced Development Division, Petersburg Nuclear Physics Institute, 188300 Gatchina, Russia
[4]Photophysics Co., 199004, St. Petersburg, Russia

e-mail: atoikka@obraz.pro

Abstract. In the current paper, the influence of laser oriented deposited (LOD) multi-wall carbon nanotubes on the roughness of indium tin oxides was considered. During the deposition of nanotubes, the average electrical field strength in range 100-600 V/cm was used. Via the atomic force microscopy was shown the rise of root-mean square roughness from 1.7-2.4 nm (for pure ITO) to 7.9-27.4 nm in the case for nanotubes deposition. The correlation of electrical strength during the LOD and roughness of surface has shown. The received surface of ITO with CNTs performs the orienting functions for nematic liquid crystals. The contact angle of water drops is in the range 75-105˚ for pure ITO and 115-129˚ for ITO with CNTs.

1. Introduction

Nematic liquid crystals (NLC) – is an electrically and optically tunable anisotropy medium, what could provide the temporal, spatial, phase and intensity modulation of the optical beam. It allows to use these devices in display technologies, laser techniques, biomedicine and cryptography [1-2].

The properties of LC media strongly correlate with the distribution of dipole orientation. The mean value of LC molecule orientation is called the director of LC θ. It should be mentioned, that θ is a function versus coordinate and field in the normal direction relative to electrical contact. The basis LC cell consists on mesophase, orienting layers, electrical contacts and substrates. In order to improve the switching properties of devices, the sensibilization of mesophase and the structurization of orienting layers or contacts is used [3-4]. In this paper, we consider ITO coating with the deposited multi-wall carbon nanotubes (MWCNTs) as orienting surface for LC molecules orientation.

2. Materials and methods

On quartz substrates through the laser-oriented deposition method were deposited indium-tin oxide films. The methodology of deposition and metrology of pure ITO was described in more details in the article [5]. Then using the same technique, the MWCNTs were deposited under the various average electrical strength range from 100-600 V/cm. For surface characterization was used atomic-force microscope Solver Next (NT-MDT) in contact mode with scan area 30μm×30μm and with scan rate 2 Hz. For macro-parameter description, the contact angle in lying drop method was measured by the OCA 15EC instrument.

3. Results

The root-mean square roughness of pure ITO is in range R_q=1.7-2.4 nm. The length of LC molecule is approximately 1.5 nm and the thickness of operational LC mesophase layers is in μm-scale range. Due to the viscosity of this media and due to collective collision between the LC dipoles, the relief of pure ITO doesn't provide the orienting functions and the reproducible in the formation of boundary conditions for director (Figure 1(a-b)).

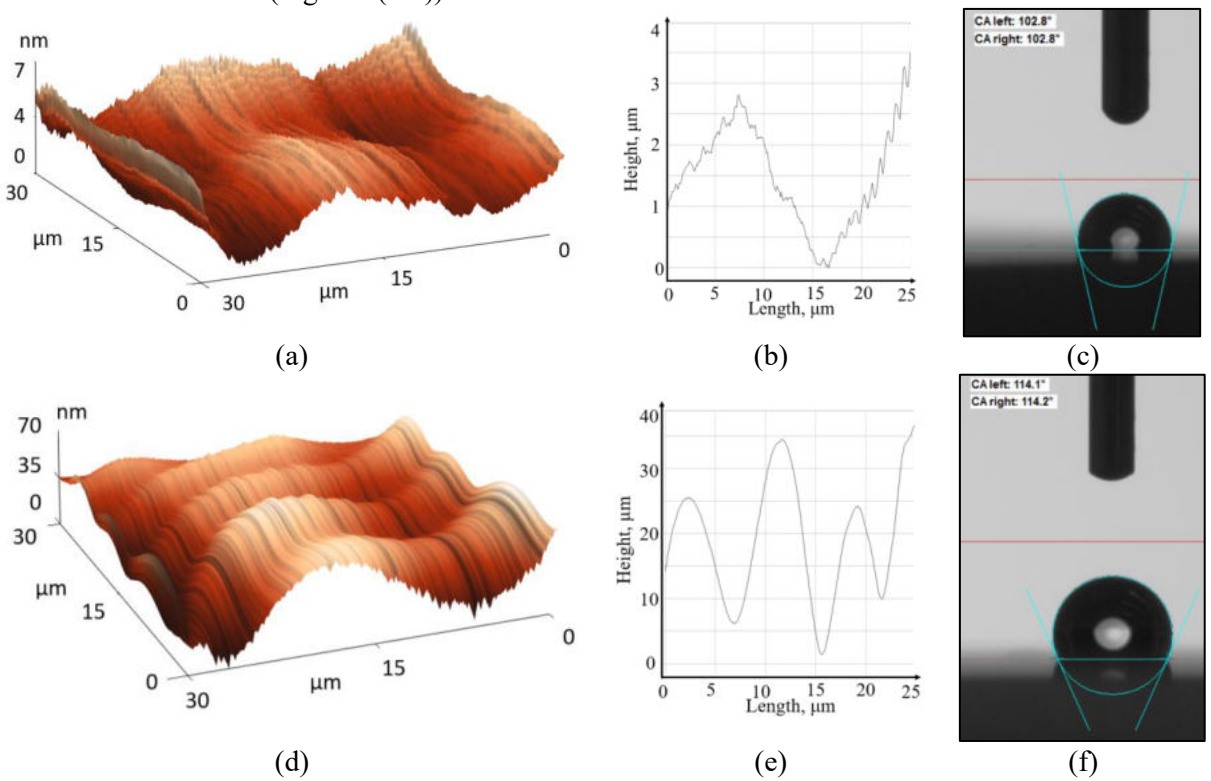

Figure 1. The relief properties of ITO-based coatings: **(a)** AFM image of pure ITO, **(b)** AFM profile of pure ITO, **(c)** contact angle of pure ITO, **(d)** AFM image of ITO with CNTs, **(e)** AFM profile of ITO with CNTs, **(f)** contact angle of ITO with CNTs.

The deposited MWCNTs increase the roughness of the surface and it depends on the applied electric field strength (Figure 1(d-e)). For E=100 V/cm the RMS roughness is equal to 7.9 nm, for E=200 V/cm and E=600 V/cm, R_q=12.2 and R_q=27.4 nm respectively. Thus, the surface of modified ITO with CNTs has enough roughness for LC alignment. The measurements of contact angle represent the significant rise from 75-105˚ for pure ITO to 115-129˚. Using the received comparison and the results from papers [3-5], we can conclude, that the alignment properties of ITO coatings with CNTs could be tuned via the supplied electrical field during the LOD deposition.

References

[1] Wu Z., Zhou X., Wu S., Yan Z., Li Y., He G, *IEEE Photonics Journal*, 13(6), 5200106 (2021). DOI: 10.1109/JPHOT.2021.3121266

[2] Shen C., Sun J., Qi Y., Lv S., Wei S., *IEEE Photonics Journal*, 13(4), 4600205(2021). DOI:10.1109/JPHOT.2021.3092052More references

[3] Toikka A.S., Lomova L.S., Kamanina N.V. *Journal of Optical Technology*, 88(8), 460 (2021) DOI: 10.1364/JOT.88.000460

[4] Kamanina N., Toikka A., Barnash Y., Zak A., Tenne R. *Crystals*, 12(391), 1(2022) DOI: 10.3390/cryst12030391

[5] Toikka A.S., Kamanina N.V. Technium, 3(7), 154(2021) DOI: 10.47577/technium.v3i7.4594

Study of recombination and transport properties of a-Si:H(i)/a-Si:H(n) contact system for crystalline silicon solar cells

A V Uvarov[1,2], A I Baranov[1,2], A A Maksimova[1,2], E A Vyacheslavova[1,2], A S Gudovskikh[1,2]

[1]St. Petersburg Academic University, St. Petersburg 194021, Russia
[2]St. Petersburg Electrotechnical University "LETI", St. Petersburg 197376, Russia

Abstract. This article is devoted to the study of the contact and recombination properties of the combination of a-Si:H(i)/a-Si:H(n) layers. Numerical modeling of the band diagram as well as experimental study of the contact system with a silicon substrate has been carried out. The optimal values of the thicknesses of the contact layers are determined, which make it possible to obtain a low rate of carrier recombination and contact resistance.

1. Introduction

Silicon-based solar photovoltaic converters are an asymmetric diode structure with a heavily doped emitter and a lightly doped base. When such a structure is irradiated with optical radiation with a photon energy greater than the band gap of the base material, electron-hole pairs appear, which are separated by the field of the p-n junction. However, the reverse process of recombination of electron-hole pairs also takes place, which occurs most intensively in the presence of defects in the volume and at the boundaries of the silicon substrate. This process leads to the transition of the energy of the absorbed radiation into heat losses. Volume recombination is relatively small and mainly depends on the addition of dopants during the production of silicon wafers. To reduce surface recombination, it is necessary to apply special passivating layers during the formation of contact and emitter layers of a solar cell. The contact to the silicon substrate should have a low specific contact resistance and good surface passivation. The quality of surface passivation is determined by the effective lifetime τeff of nonequilibrium charge carriers by the limited rate of bulk and surface recombination [1]. To form highly efficient silicon photovoltaic converters, contact layers with low values of both the recombination current and the specific contact resistance are required. The method of forming such contacts is also important, which should be high-performance and scalable. In this paper, we study the a-Si:H(i)/a-Si:H(n) contact system, which is characterized by the lowest recombination current at acceptable values of contact resistance [2].

2. Experimental study

To study the specific contact resistance and recombination rate of nonequilibrium charge carriers contacts with different configurations of a-Si:H(i) and a-Si:H(n) layers were deposited on n-type Si substrates by plasma-enhanced chemical vapor deposition at the temperature of 250 °C. We used phosphorus doped silicon substrates produced by the Czochralski method with a thickness of 380 μm and resistivity 5 – 10 Ohm*cm. The effective lifetime of nonequilibrium charge carriers in the obtained structures was studied using the photoluminescence decay (PLD) method. Based on the

results of the study, a map of the lifetime distribution over the substrate surface was formed. After studying the effective lifetime on the existing structures by magnetron sputtering, a 100 nm thick ITO layer was deposited in the form of TLM test contacts. According to the obtained dependences of the resistance R on the distance between the contacts, the values of the specific contact resistance were determined. To evaluate the band structure of the contacts, numerical simulation was carried out using the Afors-HET 2.4.1 software package. This model shows the effect of the thickness of the a-Si:H(i) layer on the shape of the I-V curve at a fixed concentration of dangling bonds.

3. Conclusion

The effect of the layer thickness in the a-Si:H(i)/a-Si:H(n) system on the contact and recombination parameters of the obtained structures was evaluated. It was noted that at a distance of 7-12 mm from the edges of the substrate, a decrease in the effective lifetime is observed. The maximum effective lifetime of nonequilibrium charge carriers in a substrate with a-Si:H 2.5nm/μc-Si:H 10nm contacts is 3250 μs, which is close to the value of the volume lifetime for these silicon substrates. Passivating contact layers were formed to crystalline silicon substrates with a minimum resistivity of 4.42 $\Omega*cm^2$. It was shown that a high concentration of dangling bonds in the i-layer (insufficient hydrogenation) can lead to electric-field screening of the n-contact and the formation of a barrier in the substrate, which significantly increases the specific contact resistance. These results can be used in the formation of highly efficient photovoltaic converters based on amorphous and crystalline silicon.

Acknowledgments

This work was supported by Ministry of Science and Higher Education of the Russian Federation (research project 0791-2020-0004)

References

[1] Richter, S. W. Glunz, F. Werner, J. Schmidt, and A. Cuevas, “Improved quantitative description of Auger recombination in crystalline silicon,” Physical Review B, vol. 86, no. 16. American Physical Society (APS), Oct. 09, 2012. doi: 10.1103/physrevb.86.165202

[2] S. Y. Herasimenka, W. J. Dauksher, and S. G. Bowden, “>750 mV open circuit voltage measured on 50 μm thick silicon heterojunction solar cell,” Applied Physics Letters, vol. 103, no. 5. AIP Publishing, p. 053511, Jul. 29, 2013. doi: 10.1063/1.4817723.

Fast Electro-optic Beam steering with Acousto-optic Deflector

A S Usachev[1,2,*], M A Talalaev[2], K A Makhnyr[2], V V Atepalikhin[2], Tatyana Vosheva[1], Anton Khudykin[3], and Dmitry Filonov[1]

[1]Center for Photonics and 2D Materials, Moscow Institute of Physics and Technology, 141701 Moscow, Russia
[2]Outdoor Lasers, ltd., 141701 Moscow, Russia
[3]Telecom R&D Center, Moscow Institute of Physics and Technology, Dolgoprudny 141700, Russia

E-mail: * usachev.anton@phystech.edu

Abstract. Here we demonstrate a new solution for acousto-optically controlled beam steering, where the array is driven with an acousto-optic deflector. This device is capable of projecting optical patterns in three-dimensional space and prompt interchange between them – this is the key to fast antenna pattern reconfigurability. Our architecture encompasses antenna elements, PIN diodes, and photodiodes, activated by light. Projected patterns change antenna impedances with the aid of photocurrents, and, as a result, propagation of GHz electromagnetic radiation is controlled in real-time. Fast electronic responses and interchangeable light holograms allow for beam steering on the sub-microsecond scale, fitting the demands of 5G wireless communications

1. Introduction

Electromagnetic tunable metamaterials recently emerged as a novel type of matter [1] At microwave frequencies, it is easy to design a tunable nonlinear meta-atom as a SRR loaded with a varactor diode that operates in either continuously variable or switching mode. [2,3]. Three-dimensional metamaterials based on a meta-atom are proposed and studied for different applications [4]. The key issue is the compensation of electromagnetic interference [5,6] and the speed of the beam steering [7]. By controlling the intensity of the light incident on the photodetector of each meta-atom, we can personalize its resonance shift over a wide range. And from the metamaterial (SRR array) [8], create radio lenses of the required parameters and change the radiation pattern of the metamaterial in a time of up to 1200 ns.

We present details of our work which has been focused on the efficiency and scan rate of the acousto-optic deflector. This approach presents a viable low-cost solution for non-mechanical beam steering, suitable for many applications at sm-wave and (sub) mm-wave frequencies that require rapid beam steering capabilities in order to meet their technological goals, such as imaging, surveillance and remote sensing. This method has the advantage of being comparatively low-cost, is based on a simple and flexible architecture, enabling rapid and precise arbitrary beam forming, and which is scalable to higher frame-rates and higher submm-wave frequencies.

2. Experimental setup

The experimental setup consists of a 561 nm fiber optic laser, an acousto-optical deflector (AOD), peripheral equipment for controlling the operation. Our test device is an array of 4 antenna elements (here we use split ring resonators). The performances were assessed with an oscilloscope to test the time response of antenna elements and spectrum analyzer RigExpert A230 for impedance and frequency response measurement. Figure 1 summarises the installation setup to control the AOD.

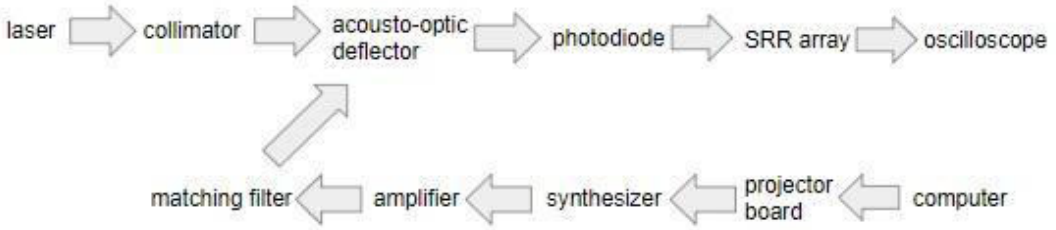

Figure 1. Circuit diagram of the installation.

A photograph of the experimental setup is shown in Figure 2. A fiber-optic laser, a collimator, an acoustic-optical deflector manufactured by Outdoor Lasers, an output zoom lens, and an SRR array are installed on the laboratory table on one optical axis.

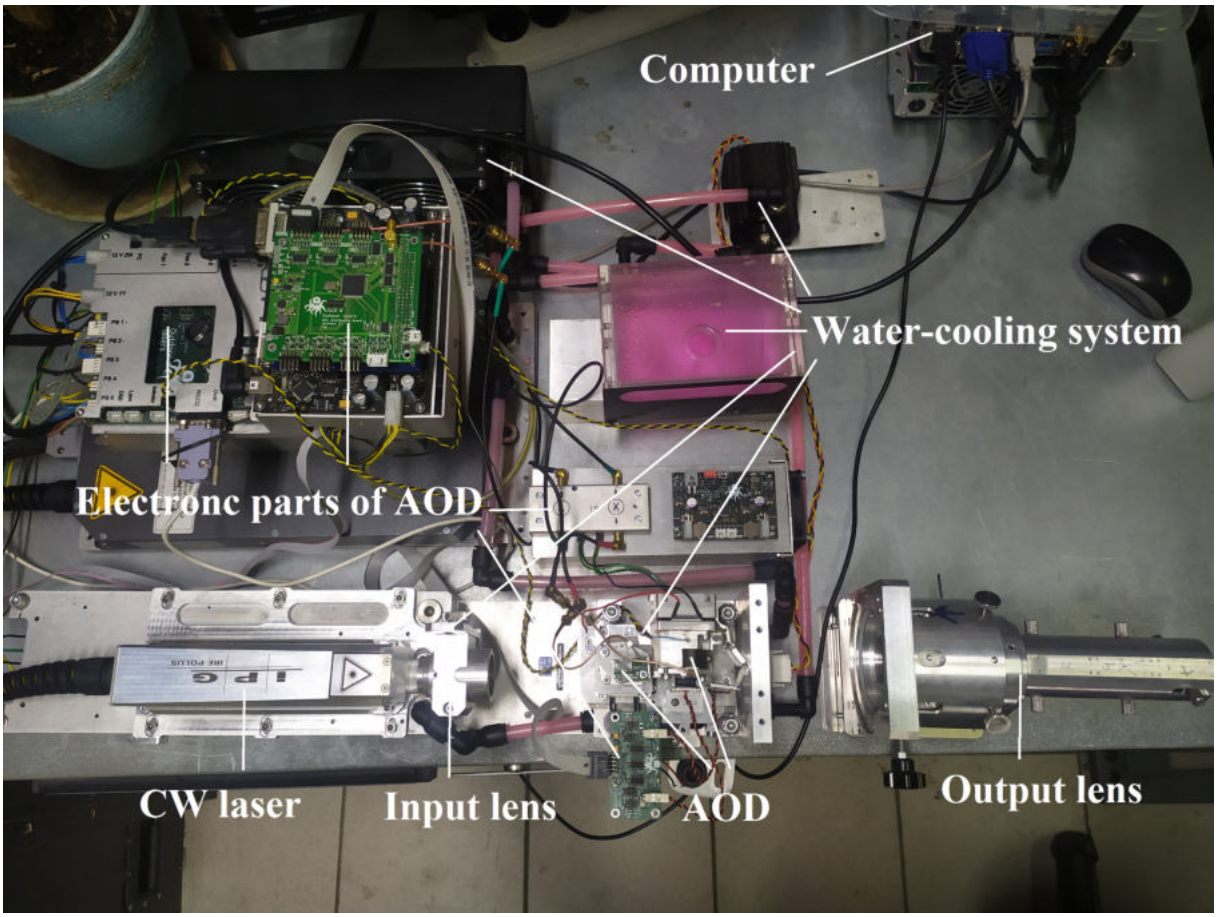

Figure 2. A photograph of the experimental setup.

A photo and diagram of the SRR meta-atom is shown in Figure 3. In our design [3], we mount a Skyworks SMV1233 varactor diode in the bottom split in the outer ring. Two chip inductors with the

self-resonant frequency around 2,27 GHz and a BPW-34-S photodiode from Osram. Overall dimensions of the inner ring thickness 4mm, diameter 40mm, gap size 4mm. Outer ring diameter 6mm. All elements of the system: photodiode, varactor diode and SRR circuit are matched to a frequency of 2,27 GHz to minimise losses.

a) b)

Figure 3. a) photo of SRR meta-atom. b) diagram of the SRR meta-atom

The laser beam entering the acousto-optic deflector at the Bragg angle to the volumetric phase acoustic diffraction grating is deviated by 1 order of diffraction. By changing the period of the diffraction grating, we scan with a deflector. The radiation pattern of the acousto-optic deflector is shown in Figure 4. The deflector creates a pattern of 4 points in 1200 ns. The photodetector of the oscilloscope is placed in the 0 order of diffraction, we can see on the oscilloscope screen the time to create a pattern of 4 points.

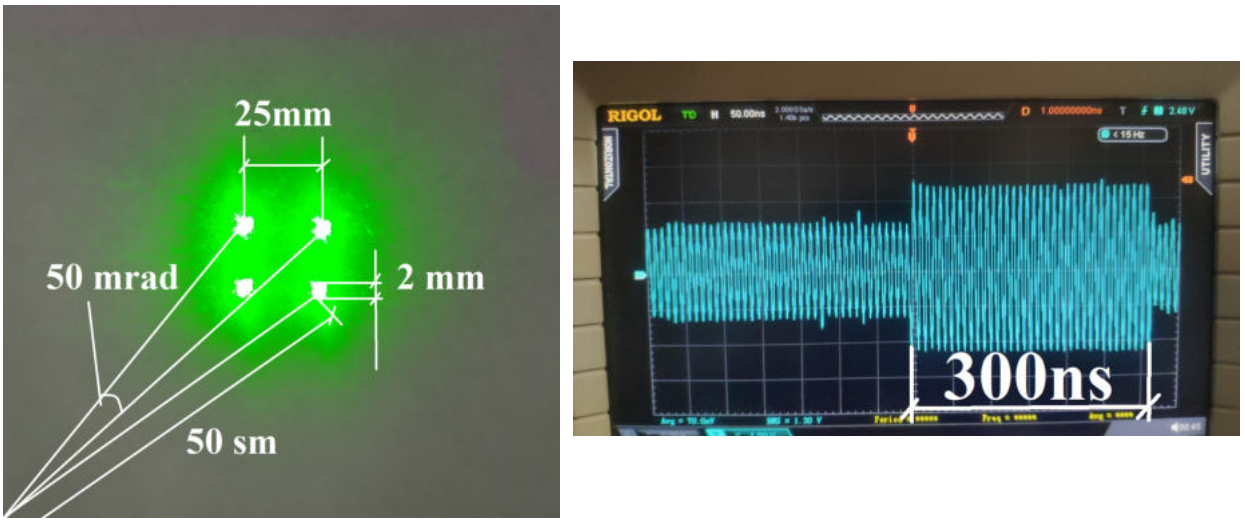

a) b)

Figure 4. a) Acousto-optic deflector radiation pattern. b) 1 pixel playback duration of AOD

Figure 5 shows the resonance of the SRR cell in the absence of photodiode illumination and at illumination of 4,000 lux, in the next month all figures will be replaced with normal ones.

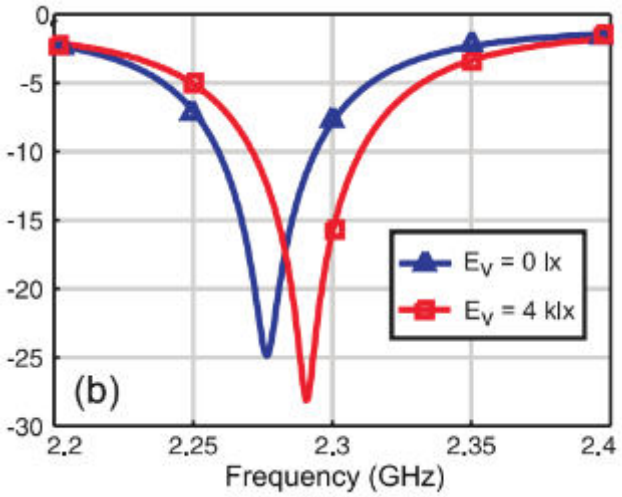

Figure 5. SRR cell resonance.

The rise time of the photodiode and the switching time of the meta-atom SRR are shown in Figure 6. We observe a time delay between the rise time of the photodiode and the switching time of the meta-atom due to the reactance of the system.

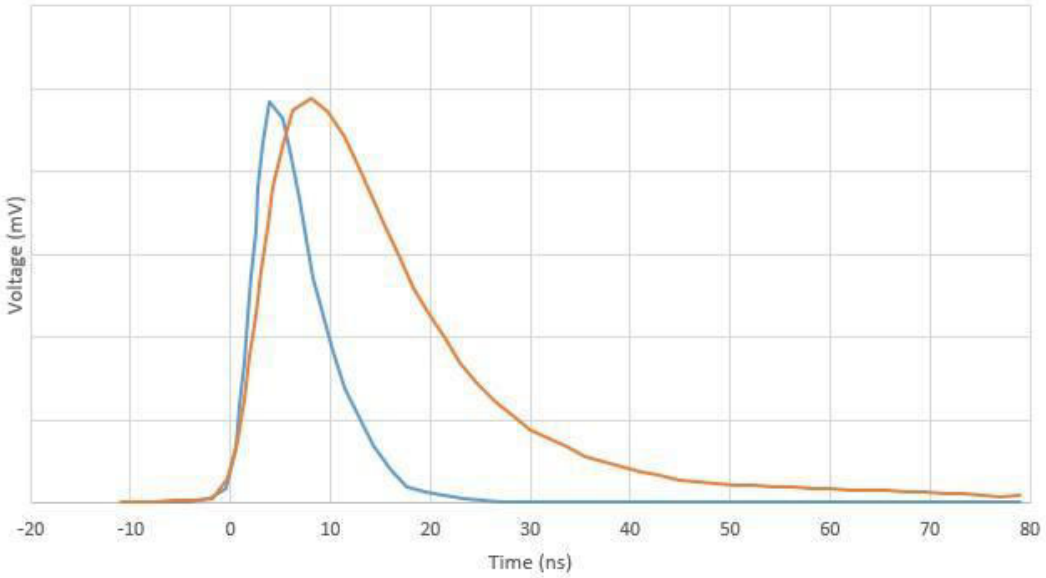

Figure 6. The rise time of the photodiode and the switching time of the meta-atom SRR.

3. Conclusion

We have developed and experimentally realised the setup consisting of a laser, acousto-optic deflector with periphery equipment, and a 4-element SRR array. The implemented setup allows investigating tunability of SRR arrays with the aid of photodiodes operated in photovoltaic mode. First experimental studies of the setup reveal the capability to traverse between optical patterns with characteristic time of 1200 ns. Impedance switching of an individual element occurs at 2,27MHz. Those results confirm the hypothesis that microsecond latency requirements can be met.

Acknowledgments

The research was supported by the federal academic leadership program Priority 2030 and the experimental part of the work was supported by the Outdoor Lasers, ltd.

References

[1] Shadrivov I, Morrison S and Kivshar Y, 2006 Tunable split-ring resonators for nonlinear negative-index metamaterials *Optics Express* **14** 9344
[2] Boardman A 2010 Active and tunable metamaterials *Laser & Photonics Rev.* **5(2)** 287
[3] Kapitanova P, Maslovski S, Shadrivov I, Voroshilov P, Filonov D, Belov P and Kivshar Y 2011 Controlling split-ring resonators with light *Appl. Phys. Lett.* **99** 251914
[4] Filonov D, Kozlov V, Schmidt A, Steinberg B and Ginzburg P 2018 Resonant metasurface with tunable asymmetric reflection *Appl. Phys. Lett.* **113** 094103
[5] Bait-Suwailam M and Ramahi O 2010 Simultaneous switching noise mitigation in high-speed circuits using complementary split-ring resonators *Electr. Lett.* **46(8)** 563
[6] Bait-Suwailam M and Ramahi O 2012 Ultrawideband Mitigation of Simultaneous Switching Noise and EMI Reduction in High-Speed PCBs Using Complementary Split-Ring Resonators *IEEE Transactions on Electromagnetic Compatibility* **54(2)** 389
[7] Gallacher T, Søndenå R, Robertson D and Smith G 2013 Dynamic beam steering at submm- and mm-wave frequencies using an optically controlled lens antenna *Passive and Active Millimeter-Wave Imaging* **XVI** 8715
[8] Mikhailovskaya A, Yusupov I, Dobrykh D, Krasikov S, Shakirova D, Bogdanov A, Filonov D, and Ginzburg P 2021 Omnidirectional miniature RFID tag *Appl. Phys. Lett.* **119** 033503

The effect of mesa-stripe design parameters on the 975 nm laser diode output characteristics

A V Fomin, E M Filonenko, S A Kryukov, S H Nazhmetov

FSUE «RFNC – VNIITF named after Academ. E. I. Zababakhin», Snezhinsk 456770, Russia

E-mail: dep5@vniitf.ru

Abstract. The present work is devoted to evaluating the effect of mesa-stripe design parameters on the output characteristics of 975 nm InGaAs/GaAs/AlGaAs laser diodes with the emitting stripe width W = 100 μm and the cavity length L = 4 mm.

1. Introduction

Today, high-power laser diodes (LDs) emitting at 975 nm are widely used for fiber laser pumping. Optical confinement of LD radiation in the vertical direction is formed directly during epitaxial growth of laser heterostructure waveguide layers, while the formation of a waveguide necessary to create a lateral direction of LD radiation is considered to be one of the crucial design problems, solved in the course of post-stage operations of high-power LD technology along with the development of optical and contact coatings.

Lateral confinement of radiation in a laser heterostructure can be attained by creating an effective refractive-index step Δn_{eff} at the boundary with the region of radiation or be achieved by a difference in the gain in this direction [1]. An appropriate LD design in the first case can be formed by etching the heterostructure down to the n-type cladding thus defining the LD emitting mesa-stripe with the walls of the etch profile and providing optical confinement of the radiation in the lateral direction. A gain step Δg can be similarly achieved by forming a LD mesa-stripe by etching the heterostructure, yet with the etch front reaching only the p-type cladding. In this case, the concentration of charge carriers is high enough only in a limited region under the stripe, which creates conditions for overcoming optical losses.

This work was aimed at considering the above-mentioned design solutions and was devoted to evaluating the effect of the etching depth of the grooves forming the mesa-stripe on the output parameters of LDs emitting at 975 nm in order to determine the optimal mesa-stripe geometry for the existing construction of InGaAs/GaAs/AlGaAs laser heterostructure.

2. Experiment details

The InGaAs/GaAs/AlGaAs heterostructure samples to be studied were grown by the MOCVD epitaxy method. The topology of the produced LDs was a mesa-stripe structure with different depths of etched grooves defining mesas, denoted further as deep and shallow ones. In the first case, the etch front reached the n-cladding region. In the second case, the etch front reached the p-cladding without affecting the laser heterostructure waveguide and the active region.

3. Results

The output characteristics of two groups of LDs without applied cavity mirrors (emitting stripe width W=100 μm and cavity length L=4 mm) with different mesas for the QCW mode at the current of 3 A are shown in Figure 1. A larger scatter in the values of spectral characteristics (central wavelength λ and FWHM), as well as values of output power, are observed within the group of LDs with deep mesa design, while the scatter in the threshold current values is identical for both groups (Fig. 1a, b).

The output characteristics were also measured in the CW mode for LDs with deposited mirrors. Typical values of FWHM for deep mesa LDs at the current of 12 A reached 10 nm on the condition of the several local maxima presence in the spectrum. At the same time, typical values of FWHM for LDs with shallow mesa at the current of 12 A made up 3,7-5 nm. Conclusions about the cause of the spectrum broadening for the deep mesa LDs were made in the work. On the basis of the conducted studies, the optimum value of the etching depth for the formation of the mesa-stripe structure was proposed.

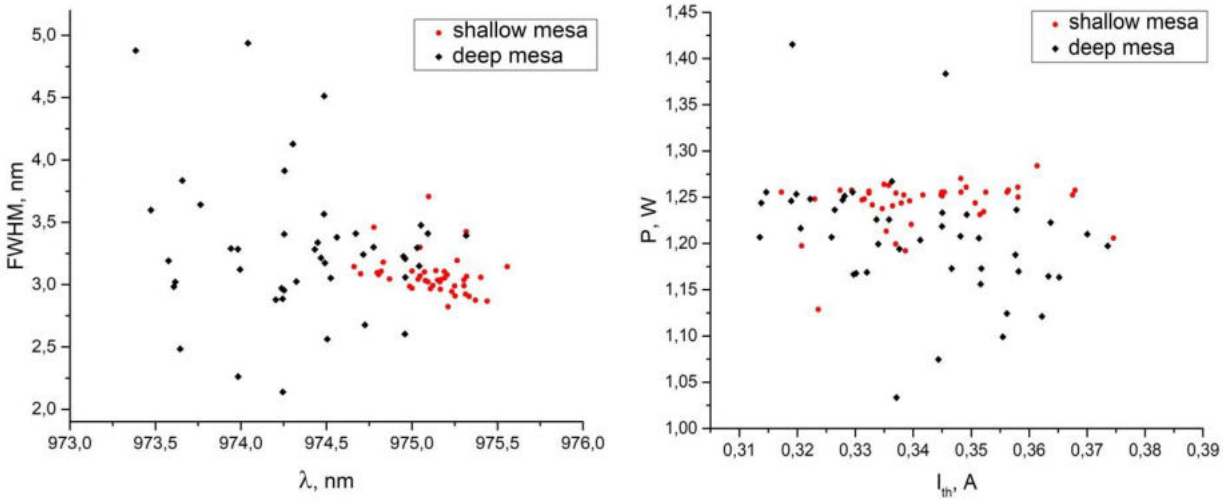

a) b)

Figure 1. Correlation plots of a) - FWHM and central wavelength λ and b) - LDs output power and threshold current for two groups of LDs with shallow and deep mesas.

References

[1] Diehl R. High-Power Diode Lasers: Fundamentals, Technology, Applications with Contributions by Numerous Experts. 2000 *Applied Physics* **78**

Measurement of the internal quantum efficiency of emission in the local region of the LED chip

I V Frolov, O A Radaev, V A Sergeev

Ulyanovsk Branch of Kotel'nikov Institute of Radio-Engineering and Electronics of Russian Academy of Sciences, Ulyanovsk 432071, Russia

e-mail: ilya-frolov88@mail.ru

Abstract. A method for measuring the internal quantum efficiency of InGaN LED emission in a local region of the chip is presented. The method is based on registration by a digital CMOS camera of the brightness and 3dB frequencies distribution profiles of the LED luminescence at two small pulsed currents and a pixel-by-pixel calculation of the internal quantum efficiency. The method has been tested on commercial green InGaN LEDs. The method can be used to diagnose defects in local regions of light-emitting heterostructures.

1. Introduction

The internal quantum efficiency (IQE) of emission is the most important parameter of LEDs, which determines the efficiency of converting electric current into optical emission. According to the ABC model of charge carrier recombination in a heterostructure, the IQE is defined as the ratio of the radiative recombination rate to the sum of the radiative and nonradiative recombination rates. Since the rate of nonradiative recombination is directly related to the defects density in the heterostructure, the IQE can be used as a parameter characterizing the quality of the structure. Heterostructure defects and indium concentration fluctuations in InGaN-based light-emitting heterostructures are responsible for the inhomogeneous distribution of electroluminescence parameters over the chip area. The presence in the structure of local regions with an increased defects density can cause accelerated degradation of the LED characteristics. In this regard, the development of new methods and means for measuring the electro-optical parameters of local regions of LED chips is an actual task from the point of view of increasing the efficiency of detecting and rejecting defective and potentially unreliable LEDs.

The purpose of the work was to develop and experimentally test a method for measuring the IQE of emission from local regions of the InGaN LED chip.

2. Description of the measurement method and experimental testing

The method for measuring the IQE of emission presented in [1] was used as a basis. The method consists in measuring the emission power and 3dB frequencies of the electroluminescence of the LED at two low currents, and calculating the value of the IQE η at the LED current I from the functional dependence

$$\eta(I)=\frac{1-\frac{f_{3\partial Б}(I_1)}{f_{3\partial Б}(I)}\left(1-\frac{f_{3\partial Б}(I_2)/f_{3\partial Б}(I_1)-1}{\sqrt{P(I_2)/P(I_1)}-1}\right)}{1+\frac{f_{3\partial Б}(I_1)}{f_{3\partial Б}(I)}\left(1-\frac{f_{3\partial Б}(I_2)/f_{3\partial Б}(I_1)-1}{\sqrt{P(I_2)/P(I_1)}-1}\right)}, \quad (1)$$

where $f_{3дБ}(I_1)$ and $f_{3дБ}(I_2)$ is 3dB frequencies of LED electroluminescence measured at current I_1 and I_2, respectively; $P(I_1)$ и $P(I_2)$ is LED emission power at current I_1 and I_2, respectively.

To measure the IQE of emission from a local region of the LED chip, a hardware-software complex [2] was used, which makes it possible to measure the distribution profiles of 3dB frequencies and emission brightness with a resolution of up to 0.65 μm. Approbation of the method was performed on a commercial green InGaN LED TO-3216BC-PG. The profiles of $f_{3dB}(I)$ and $P(I)$ were measured at currents I_1 = 20 μA and I_2 = 50 μA. The results of measurements of the IQE in a local region of the chip with dimensions of 25 × 25 μm are shown in Fig. 1.

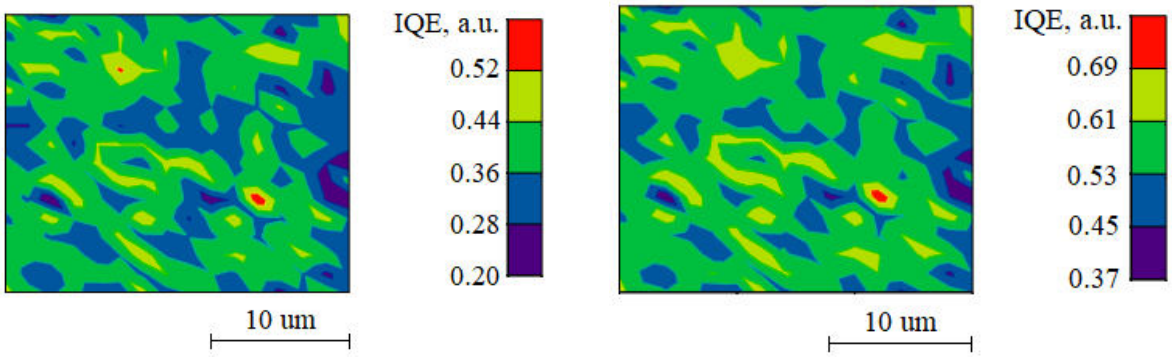

a) b)

Figure 1. Distribution of the IQE value over the local region of the chip, measured at a current of 20 μA (a) and 50 μA (b).

At a current of 20 μA, the average value of the IQE is 0.33, the standard deviation is 0.024. At a current of 50 μA, the average value of the IQE is 0.51, the standard deviation is 0.026. The average value of the coefficient of variation is 6%, which indicates a high degree of homogeneity of the distribution of the IQE value over the local region of the chip.

3. Conclusions

The presented measurement method can be used to diagnose defects in local regions of light-emitting heterostructures.

Acknowledgments

The work was carried out within the framework of the state task and partially was supported by the Russian Foundation for Basic Research and Ulyanovsk region, project number 19-47-730002.

References

[1] Frolov I V, Sergeev V A, Radaev O A 2021 A *Technical Physics* **66(8)** 1230

[2] Frolov I V, Sergeev V A, Radaev O A 2021 *Instruments and Experimental Techniques* **64(2)** 259

Peculiarity of electron density calculation during interaction of ultrashort laser pulse with nitrogenous base of DNA molecule adenine

A A Kharlamova and D N Makarov

Department of Fundamental and Applied Physics, Northern Arctic Federal University named after M V Lomonosov, Severnaya Dvina Embankment 17, Arkhangelsk 163002, Russia

Kharlamova.anastasya2015@yandex.ru

Abstract. Today, ultrashort laser pulses are used to study and analyse biomolecules. Their advantages over X-rays are the rapidity of capturing the state of a molecule, and the accuracy. However, the practical possibility of studying chemical and biological processes in facilities using existing and promising X-ray free-electron lasers requires the development of a theory of interaction of laser pulses with matter. In this article we will consider the interaction of ultrashort laser pulse (USPs) with the base of DNA molecule - adenine. We will consider in detail the calculation of photon generation probability and propose a method for calculating electron density for the case when the substance has different elemental composition.

1. Introduction

Imaging techniques from diffraction data obtained using ultrashort laser pulses are being actively developed for applications in nanotechnology and structural biology. In this case the scattering spectrum moves into the femto and atto-second time range, which is poorly understood up to now[1-2]. The use of (USPs) to analyse the structure of molecules is a very promising area of research. As noted, ultrashort laser pulses (USPs) operate on a small time scale. This is very convenient for the description of organic structures, as such materials can be both stationary and non-stationary. Non-stationary objects, such as DNA, for example, can only be studied using (USPs), because the characteristic time in such systems is smaller or comparable to the femtosecond time scale. In order to analyse the experimentally obtained data, theoretical descriptions of the interaction processes between (USPs) and biostructures are urgently needed [3-5].

In this paper we will consider the DNA molecule as a promising and poorly studied biomolecule at the atomic level. The molecule stores biological information in the form of a genetic code consisting of a sequence of nucleotides. Consequently, a defect on a nucleotide can indicate the presence of a defect in the molecule. In [6] we considered the interaction of an ultrashort laser pulse with a DNA molecule in a simplified form, considering each nucleotide as a separate unit of matter, within the whole molecule. We now focus in detail on a single nucleotide with the nitrogenous base adenine. The difficulty of the new calculation is that now it is necessary to take into account the elemental composition of the molecule. It is possible to take it into account through the electron density of the molecule, which we will consider in this work.

2. Results and Discussion

A nucleotide is a compound of a phosphate group, a carbohydrate, and a nitrogenous base – adenine. Let us imagine it as an arbitrary polyatomic system, on which the (USPs) falls in the direction n_0. The duration of such a pulse will be considered much less than the characteristic atomic time. To simulate the spectra of the interaction of radiation with a molecule, it is necessary to consider the probability of the birth of a photon. The Dirac-Hartree-Fock-Slater model is used for this calculation.

$$\frac{d^2W}{d\omega d\Omega} = \frac{1}{(2\pi)^2}\frac{1}{c^3\omega}(N_a N_b G(\omega,\mathbf{n},\mathbf{n_0}) + \delta_N(\mathbf{p})(N_b - 1)F(\omega,\mathbf{n},\mathbf{n_0}), \quad (1)$$

We will use the Dirac-Hartree-Fock-Slater model $\rho(\mathrm{r}) = \frac{N_e}{4\pi r}\sum_{i=1}^{3} A_i \alpha_i^{\,2} e^{-\alpha_i \mathrm{r}}$ [20], where $A_i, \alpha_i -$ are the table coefficients giving the electron density in the atom [7]. In our case we cannot use this form of electron density since the base of the molecule consists of different elements. Let us present a 3D model of the nucleotide. Using the given distances of 1.372 A between the elements and their coordinates in space we will find the electron density.

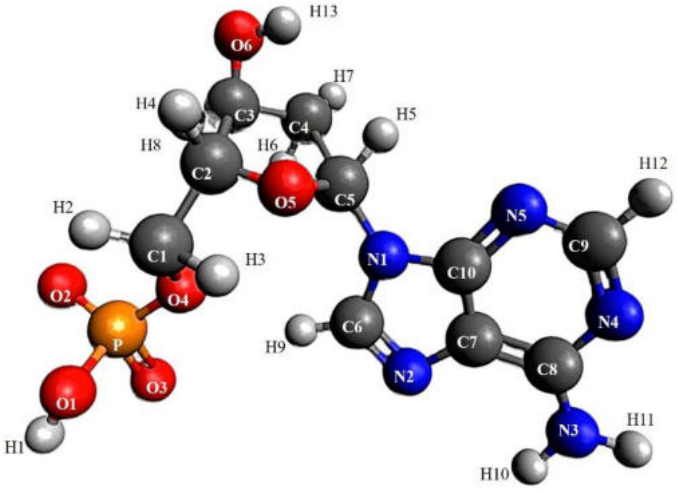

Figure 1. Arrangement of atoms in a nucleotide: C - carbohydrate, N - nitrogen, O - oxygen, P - phosphorus, H – hydrogen, the model by which the electron density is calculated

Acknowledgments

The work was supported by Russian Science Foundation grant № FSRU-2021-0008.

References

[1] V. A. Astapenko *J. Exp. Theor. Phys.* **130**, 56–61(2020)
[2] Dmitry N. Makarov *Optics Express* **27**(22), 31989-32008 (2019).
[3] Scapin G *Current Pharmaceutical Design* **12** (17), 2087–2097 (2006).
[4] Ahmed H. Zewail *J. Phys. Chem. A,* **104** (24), 5660–5694 (2000).
[5] Suryanarayana C., Norton M. Grant (2013-06-29) *Springer Science & Business Media*. ISBN 9781489901484
[6] D. N. Makarov,A. A Kharlamova *AIP Conference Proceedings* **2313**, 030070 (2020).
[7] F. Salvat, J. D. Martinez, R. Mayol, and J. Parellada *Phys. Rev. A* **36** (2), 467-474 (1987)

Temperature rate equations for a semiconductor laser

S Hydyrova[1,2,3], M Puplauskis[1], R Shakhovoy[1,4,5]

[1]QRate, Novaya av. 100, Moscow, Russia
[2]Russian Quantum Center, 45 Skolkovskoye shosse, Moscow, Russia
[3]Bauman Moscow State Technical University, Moscow, Baumanskaya 2-ya, 5/1, 105005, Russian Federation
[4]NTI Center for Quantum Communications, National University of Science and Technology MISiS, 4 Leninsky prospekt, Moscow, Russia
[5]Moscow Technical University of Communications and Informatics, 8A Aviamotornaya, Moscow, Russia

s.hydyrova@goqrate.com

Abstract. We propose a new approach to follow the temperature dynamics in the active layer of a semiconductor laser based on the substitution of a partial differential equation by the system of ordinary differential equations, which we refer to as *temperature rate equations*. Such an approach allows taking into account the Joule heat released in the volume of a laser diode as well as the bi-exponential behavior of the temperature relaxation process.

Temperature rise in the active layer of the semiconductor laser caused by dissipation of radiative power leads to the frequency shift of the lasing field. Such a shift can have a significant impact on the interference of laser pulses and is essential in applications such as direct phase modulation via optical injection [1].

There are several models describing transient temperature rise in the active layer of the semiconductor laser [2]-[3]; however, these models are not very convenient to use in the context of laser dynamics, inasmuch as they require to solve a partial differential equation with time dependent boundary conditions. In [1], we proposed a simple approach to substitute partial differential equation by an ordinary rate equation for the temperature accompanied by the modification of the laser rate equation for the phase. Although this approach allows us to take into account the most significant features of the temperature dynamics, some important features are left out. Thus, following the assumptions made in [2]-[3] we neglected the contribution from the Joule heat P_J, which, however, could make a significant impact on the temperature evolution. Moreover, we did not take into account that time evolution of the temperature exhibits a noticeable deviation from the mono-exponential behavior and should be rather approximated by a bi-exponential function.

The proposed system of *temperature rate equations* is as follows:

$$\begin{aligned} d(\Delta T_J)/dt &= -\Delta T_J \tau_J^{-1} + r_h P_J \tau_J^{-1}, \\ d(\Delta T_{R1})/dt &= -(\Delta T_{R1}(t) - r_h P)\chi_1 - k_{12}(\Delta T_{R1} - \Delta T_{R2}), \\ d(\Delta T_{R2})/dt &= -(\Delta T_{R2}(t) - r_h P)\chi_2 - k_{12}(\Delta T_{R2} - \Delta T_{R1}). \end{aligned} \qquad (1)$$

where r_n is a thermal resistance between the laser active layer and the heat sink, and the coefficients k_{12}, r_1 and r_2 are related to the specific mass r, specific heat capacity C and thermal conductivity k of the semiconductor material as follows: $k_{12} = 11.03k/(rCl^2)$, $r_1 = 22.54k/(rCl^2)$, $r_2 = -4.64k/(rCl^2)$, where l is the thickness of the passive semiconductor layer between the laser active layer and the heat sink. The radiative power dissipated in the active layer can be defined for the 1.55 μm laser as $P = 0.8I(1-h)$, where h is the differential quantum output and I is the injection current. The overall temperature rise DT of the active layer can be defined as a sum of two contributions: $DT = DT_R + DT_J$, where $DT_R = (DT_{R1} + DT_{R2})/2$ is the contribution from the radiative power P, and DT_J is the contribution from the Joule heat P_J.

We calculated the temperature rise for a gain-switched 1.55 μm semiconductor laser with the same parameters as in [1] and for the three cases: with the single rate equation model from [1] and using the system (1) with $P_J = 0$ and $P_J = 0.5P$ (figure 1). To demonstrate the effect of the temperature rise, we used laser rate equations from [1] and simulated the interference of laser pulse train with itself shifted by one pulse repetition period (figure 2).

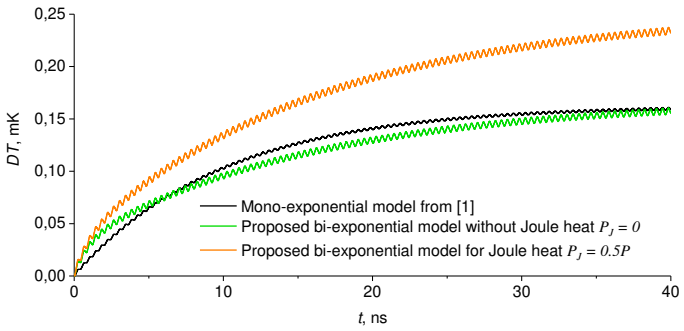

Figure 1. Temperature rise in the laser active layer.

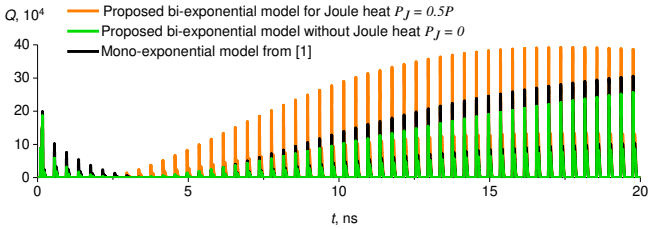

Figure 2. Simulated laser pulse interference.

References

[1] Shakhovoy R, Puplauskis M, Sharoglazova V, Duplinskiy A, Zavodilenko V, Losev A and Kurochkin Y 2021 *Optics Express* **29**(6) 9574-9588

[2] Nakwaski W 1983 *Optical and Quantum Electronics* **15**(4) 313-324

[3] Engeler W and Garfinkel M 1965 *Solid-State Electronics* **8**(7) 585-604

Hollow-core antiresonant optical fiber activated with YAG:Yb^{3+}

D N Shurupov[1,2], G A Pchelkin[2,3], V V Demidov[2], V V Davydov[1]
[1]Peter the Great Saint-Petersburg Polytechnic University, Saint Petersburg, Russia, 195251
[2]JSC "Research and Production Association Vavilov State Optical Institute", Saint Petersburg, Russia, 192171
[3]The Bonch-Bruevich Saint Petersburg State University of Telecommunications, Saint Petersburg, Russia, 193232
e-mail: shurupoff.dm@yandex.ru

Abstract. This article presents a method for modifying the structure of an antiresonant optical fiber with a hollow core, which allows the formation of active substance layers without the use of technologically complex and expensive CVD processes. To obtain luminescence centers, a hollow antiresonant fiber was filled with a solution of a YAG:Yb^{3+} composite and dimethylformamide. This procedure was followed by several post-processing steps, including drying the impregnated preform under normal conditions and its heat treatment at a temperature of 1000 °C. As a result, thin films based on YAG:Yb^{3+} were formed inside the capillaries. The resulting luminescence peaks correspond to the main and one of the additional peaks for YAG:Yb^{3+}.

1. Introduction

Nanosized lanthanide-activated phosphors are widely used as base materials for the manufacture of fluorescent labels, contrast effects, upconverting media, lighting elements, and displays [1]. The practical cellular oxidation of phosphors involves the presence of radiation in visible and infrared (IR) form, increased lifetime, increased progress, acceleration to photobleaching, obtaining low toxicity, as well as simple and affordable availability of raw materials.

The proposed study is aimed at revealing the activity of a quartz optical fiber with nanosized YAG:Yb^{3+} phosphors found distributed (in the transverse and extended directions) inside the fibers. The main criteria for the development of preforms were the limited number and internal diameter of the capillaries.

2. Optical system and research methodology

The design of a hollow antiresonance fiber should ensure ease of filling with a modifying solution, and the fiber should also have transmission windows in the spectral regions close to the photoluminescence excitation wavelengths of 940 and 975 nm and the emission wavelength of 1030 nm. For these purposes, a fiber with four capillaries with an external diameter of 310 μm, an internal diameter of 200 μm and internal capillaries with a diameter of 48 μm and a wall of 8 μm perfectly suited.

The raw material for the synthesis of the modifying solution was a composite based on YAG:Yb^{3+} dissolved in dimethylformamide at a ratio of 1 part solid to 3 parts solvent.

The formation of homogeneous luminescent coatings on the inner surfaces of the capillaries was carried out in several stages. They included a sequence of operations, the first of which was the impregnation of the workpiece. To simplify the procedure for impregnating the workpiece with a modifying solution, the air pressure in the channels was deliberately reduced. This approach made it possible to evenly fill the air channels.

The second stage included convective drying of the impregnated preform at a temperature of 150°C for 4 hours. To prevent uneven distribution of the substance, the excess of the modifying solution was removed before drying, which made it possible to form composite layers on the inner surfaces of the preform capillaries.

To form a sufficient layer of substance, the first and second stages were repeated 2 times before proceeding to the last stage.

At the last stage, the dried billet was subjected to heat treatment at a temperature of 1000°C for 2 hours. As a result of this operation, the chemical decomposition (combustion) of the entire solvent and metal salts occurred, followed by the formation of thin films based on YAG:Yb^{3+} inside the capillaries.

3. Result of experimental investigations

To experimental study the spectral and luminescent properties of the resulting fiber, a setup was used that included a 64642 HLX halogen lamp (Osram) as a light source, an MDR-23 monochromator for feeding a signal with a wavelength of 975 nm to the fiber input, an AQ-1212B spectrophotometer (Ando Electric Corporation), a germanium photodiode for the 900-1700 nm spectral range, an eLockIn 204 optical amplifier (Anfatec Instruments), and an AQ-1135E optical power meter (Ando Electric Corporation). A fiber sample ~150 cm long was used to transmit radiation from the monochromator. Dependence is shown in Figure 2.

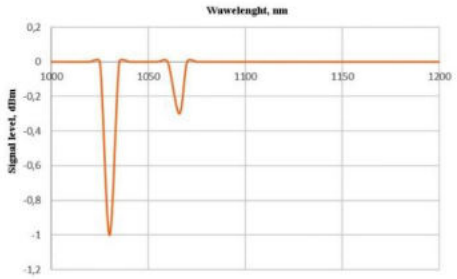

Figure 2. The dependence of the signal level on the wavelength when applying to the input wavelength of 975 nm.

The resulting luminescence peaks correspond to the main and one of the additional peaks for YAG:Yb^{3+}.

4. Conclusion

To obtain luminescence centers, a hollow antiresonant fiber was filled with a solution of a YAG:Yb^{3+} composite and dimethylformamide. This procedure was followed by several post-processing steps, including drying the impregnated preform under normal conditions and its heat treatment at a temperature of 1000 °C. As a result, thin films based on YAG:Yb^{3+} were formed inside the capillaries. The resulting luminescence peaks correspond to the main and one of the additional peaks for YAG:Yb^{3+}. The presented method for modifying the structure of an antiresonant hollow-core optical fiber makes it possible to form active silica layers several hundred nanometers thick without using conventional CVD processes, which are usually technologically complex and expensive.

References

[1] Das, G.K., Heng, B.C., Ng, S.-C., White, T., Loo, J.S.C., D'Silva, L., Padmanabhan, P., Bhakoo, K.K., Selvan, S.T., Tan, T.T.Y., Langmuir, 26(14), 11631-11641 (2010).

Study of the vortex modulation effect on the characteristics of a quantum key distribution system in free space

Daniil A. Yashin[3], Iurii A. Adam[2], Aleksei V. Chernykh[1], Boris A. Nasedkin[1,2]

[1]Laboratory of Quantum Processes and Measurements, ITMO University, St. Petersburg, 197101 Russia

[2]Laboratory of Quantum Communications, ITMO University, St. Petersburg, 197101 Russia

[3]Faculty of Photonics and Optical Information, ITMO University, St. Petersburg, 197101 Russia

dayashin@itmo.ru, iaadam@itmo.ru, chernykh_a@itmo.ru, banasedkin@itmo.ru

Abstract. In the present work, the effect of use of vortex radiation beams (vortex modulation) as an information carrier in a quantum key distribution (QKD) system in free space is investigated. A simulation of vortex beams propagation in turbulent atmospheric channel is conducted by using multiple random phase screen method. A calculation of secret key generation rate and quantum bit error rate of the studied QKD system is made.

Introduction

Quantum communications i.e., quantum key distribution, with the use of atmospheric channel is one of the advanced areas of quantum technologies.

Now, there are many protocols of quantum key distribution that implement information encoding using various radiation parameters. Thus, the mostly used protocols for quantum key distribution in an atmospheric channel are based on encoding information using radiation polarization [1]. However, this approach has several significant drawbacks. First, it is necessary in these systems to use elements that ensure conservation of radiation polarization, which reduces commercial potential of such systems [2]. Secondly, systems with polarization coding do not provide invariance to spatial orientation of transmitting and receiving telescopic devices, thereby inducing additional methods for compensating polarization rotation to be used, which complicates the system and limits its parameters [3]. As an alternative to this approach, it is proposed to use phase-modulated radiation, which removes the presented limitations and is used, for example, in a subcarrier wave quantum key distribution system [4].

An important feature of all protocols using an atmospheric communication channel is the influence of scattering particles and atmospheric turbulence, which reduce the maximum signal transmission range and limit the secret key generation rate. To solve this problem, vortex beams, such as Laguerre-Gaussian modes, can be used, which show greater stability when propagating through turbulent atmospheric channel in comparison to ordinary Gaussian beams [5].

Methodology and Results

The theoretical model of the propagation of a quantum signal in the form of a vortex beam in free space is based on the developed model of subcarrier wave quantum key distribution, however, it considers the use of an atmospheric communication channel and applying vortex radiation beams by numerically calculating their propagation in the communication channel (it is proposed to use the well-known convolution method).

To simulate the effect of negative atmospheric factors on the transmitted signal, Rayleigh and Mie scattering on particles of various types of air precipitation (haze, fog, rain, snow) are considered. In addition, elements of von Karman turbulence model are applied. We implement multiple random phase screen method to simulate the negative effect of turbulence on beam propagating through the atmosphere [6].

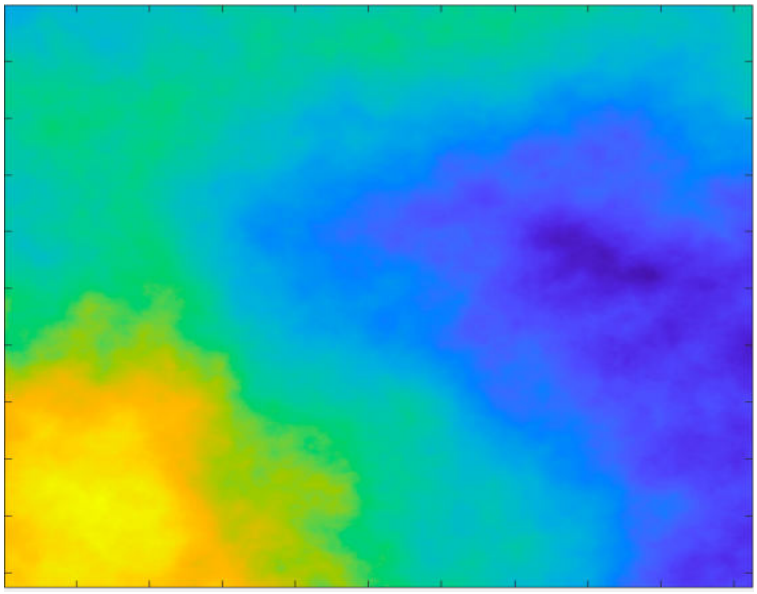

Figure 1. An example of random phase screen generated using discrete Fourier transform (DFT) method

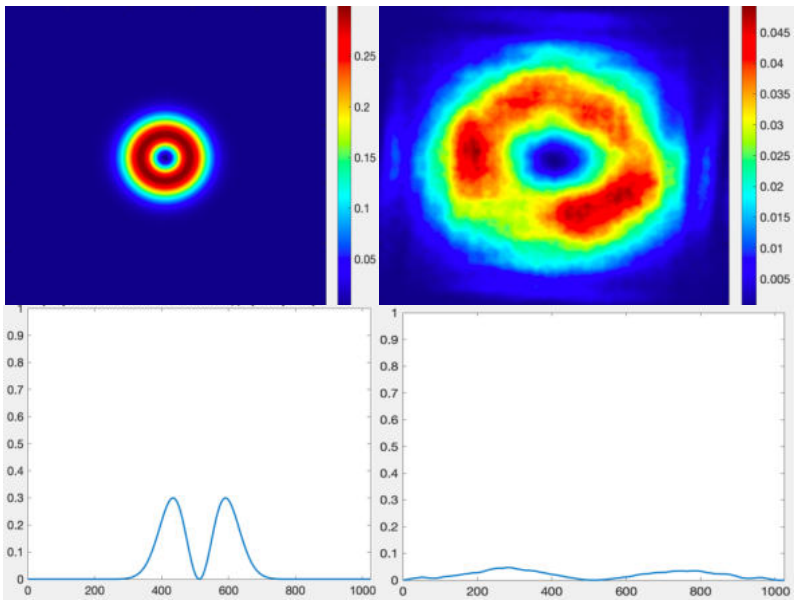

Figure 2. Intensity distributions (Top) and intensity profiles (Bottom) of Laguerre-Gaussian beam before (Left) and after (Right) propagation on 500m through turbulent scattering atmosphere (5 random phase screens applied)

Relative Intensity Change = 85.2020 %

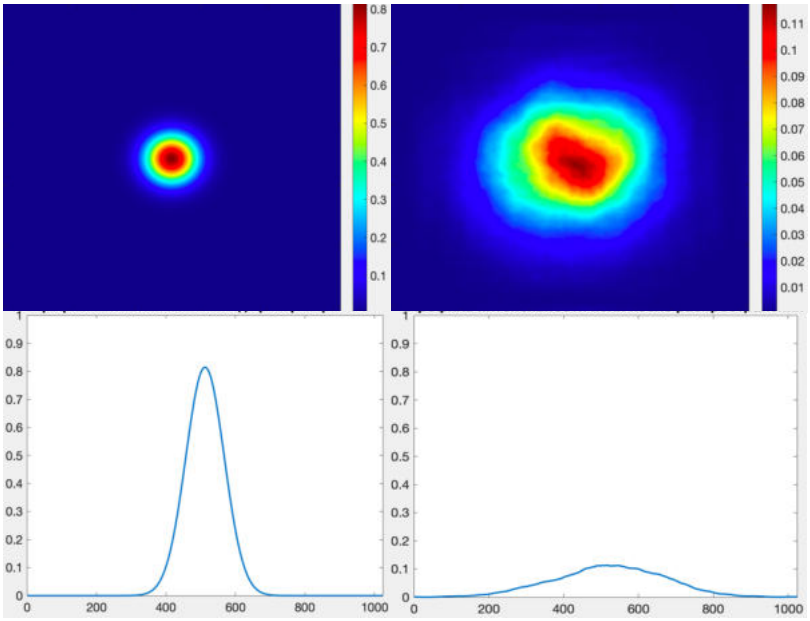

Figure 3. Intensity distributions (Top) and intensity profiles (Bottom) of Gaussian beam before (Left) and after (Right) propagation on 500m through turbulent scattering atmosphere (5 random phase screens applied)

Relative Intensity Change = 85.5139 %

Based on developed theoretical model for subcarrier wave quantum key distribution, given in [4], results for quantum key generation rate and quantum bit error rate of studied QKD system were obtained. Results show that vortex beams can be potentially used in free space communications to reduce negative factors of atmosphere. It is worth noting that results of numerical experiment are obtained using classical description of given QKD system.

Acknowledgments

The study is funded by RPMA grant of School of Physics and Engineering of ITMO University

References

[1] Schmitt-Manderbach T. et al. Experimental demonstration of free-space decoy-state quantum key distribution over 144 km //Physical Review Letters. – 2007. – Т. 98. – №. 1. – С. 010504.

[2] Ko H. et al. Experimental filtering effect on the daylight operation of a free-space quantum key distribution //Scientific reports. – 2018. – Т. 8. – №. 1. – С. 1-7.

[3] Liao S. K. et al. Satellite-to-ground quantum key distribution //Nature. – 2017. – Т. 549. – №. 7670. – С. 43-47.

[4] Gleim A. V. et al. Secure polarization-independent subcarrier quantum key distribution in optical fiber channel using BB84 protocol with a strong reference //Optics express. – 2016. – Т. 24. – №. 3. – С. 2619-2633.

[5] Liu X., Pu J. Investigation on the scintillation reduction of elliptical vortex beams propagating in atmospheric turbulence //Optics express. – 2011. – Т. 19. – №. 27. – С. 26444-26450.

[6] Martin J. M., Flatté S. M. Intensity images and statistics from numerical simulation of wave propagation in 3-D random media //Applied Optics. – 1988. – Т. 27. – №. 11. – С. 2111-2126.

Automated setup for testing Single-Photon Detectors countermeasures with bright-light attacks

Polina Acheva[1,2*], Konstantin Zaitsev[1,3], Vadim Makarov[1,3,4]
[1]Russian Quantum Center, Skolkovo, Moscow 121205, Russia
[2]Moscow State University of Geodesy and Cartography, 105064 Moscow, Russia
[3]NTI Center for Quantum Communications, National University of Science and Technology MISiS, Moscow 119049, Russia
[4]Shanghai Branch, National Laboratory for Physical Sciences at Microscale and CAS Center for Excellence in Quantum Information, University of Science and Technology of China, Shanghai 201315, People's Republic of China

*achevap17@yandex.ru
Abstract. Quantum key distribution (QKD) is a novel technology that has developed from idea to growing industry in a part 30 years. Although the most QKD problems are shown both theoretically and experimentally, the lack of certification standards slows down industry growth. In the recent work we show an approach of automated QKD component testing. We have chosen Single-Photon Detector (SPD) as the most vulnerable element for QKD scheme. We test it with bright-light attacks. Also, we update setup for testing photocurrent flow as SPD countermeasure.

1. Introduction

The idea of quantum key distribution was first announced 1983 by Bennet and Brassard [1] and first proof-of-principle was shown in 1992 [2]. But increasing interest to technology was obtained after Shor has shown the threat of classical cryptography by quantum computer concept [3]. Now a lot of companies suggest QKD realizations on the market.

However real implementations often have distinctions with perfect devices in theory. For example, Single-Photon Detectors (SPD) were shown to be totally controlled with bright light more than 10 years ago [4]. For the past decade a lot of ideas to close this loophole were suggested [], however their efficiency is still a debate matter. Here we present an automated setup to test SPDs with or without countermeasures. We show setup in Section 2 and discuss results in the next section.

2. Setup

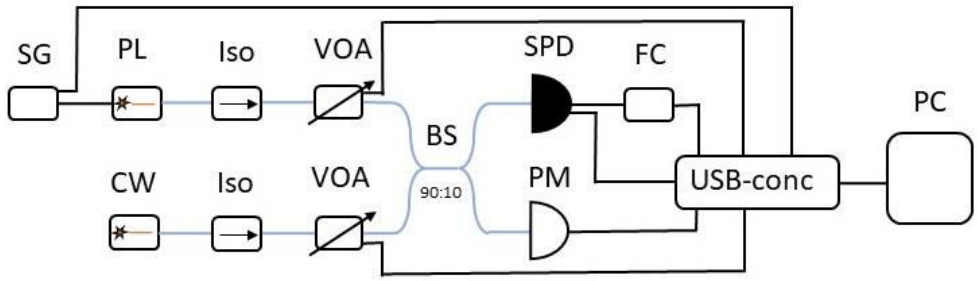

Fig.1 Experimental setup. SG – signal generator, PL – pulse laser, CW – continuous laser, Iso – isolator, VOA – variable optical attenuator, BS – beamsplitter, SPD – single-photon detector, PM – power meter, FC – frequency counter, USB-conc – USB concentrator, PC – personal computer.

The automated setup is shown on the fig. 1. We apply continuous wave laser to blind detector and apply pulse laser to control it. Variable optical attenuators allow to control lasers power, that is observed with power meter. SPD outputs are observed with frequency counter and personal computer. A Labview program varies attenuation, collects data, builds graphs and prepares a report on SPD safety automatically.

3. Results

Fig. 2 shows SPD behavior under bright-light attack. Subplot (a) shows that detector can be blinded, while subplot (c) shows SPD countermeasure response. Subplot (b) shows that detector can be controlled by bright pulses and subplot (d) shows SPD countermeasure response on bright pulses. It can be seen that SPD countermeasure reacts on bright-light attack.

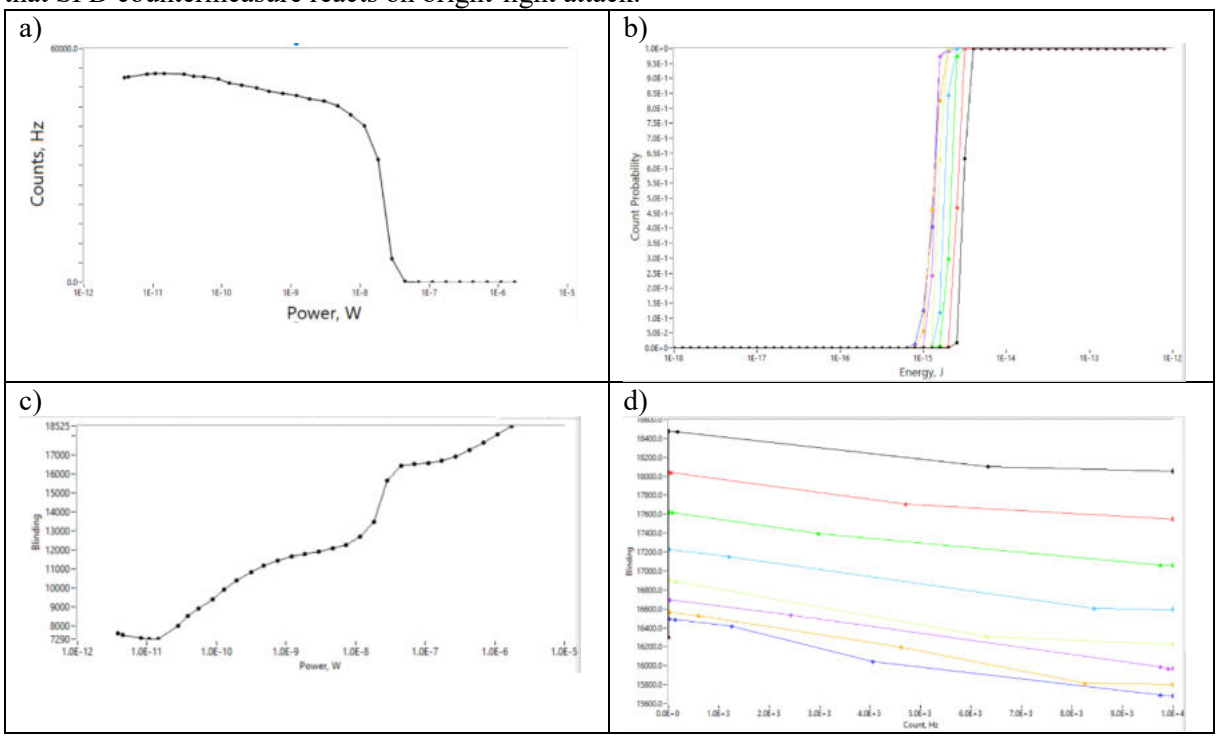

Fig. 2. Graphs obtained by automated testbench. a – SPD counts vs continuous laser power; b – SPD counts probability vs pulse energy; c – SPD countermeasure value (arbitrary units) vs continuous laser power; d - SPD countermeasure value (arbitrary units) vs SPD counts.

Acknowledgments

This work was supported by Russian Science Foundation (project № 21-42-00040).

References

[1] Bennett C H and Brassard G 1984 Proc. IEEE International Conf. on Computers, Systems, and Signal Processing (Bangalore, India)(New York: IEEE Press) pp 175–9.

[2] Bennett, C. H., F. Bessette, G. Brassard, L. Salvail, and J. Smolin, 1992, ‘‘Experimental quantum cryptography,’’ J. Cryptology 5, 3–28.

[3] P. Shor, Proc. 35th Ann. Symp. Found. Comp. Sci. (IEEE Comp. Soc. Press, Los Alamitos, California, 1994), p. 124.

[4] Lydersen, L., Wiechers, C., Wittmann, C. et al. Hacking commercial quantum cryptography systems by tailored bright illumination. Nature Photon 4, 686–689 (2010).

[5] Z. L. Yuan, J. F. Dynes, and A. J. Shields, “Resilience of gated avalanche photodiodes against bright illumination attacks in quantum cryptography,” Appl. Phys. Lett. 98, 231104 (2011).

[6] Yong-Jun Qian, De-Yong He, Shuang Wang, Wei Chen, Zhen-Qiang Yin, Guang-Can Guo, and Zheng-Fu Hans, “Robust countermeasure against detector control attack in a practical quantum key distribution system,” Optica 6, 1178–1184 (2019).

Development of technological methods for fabrication high-density luminescent structures based on up-conversion $NaYF_4:Yb^{3+},Er^{3+}$ particles.

N Vovk[1,2], I Asharchuk[1], E Timofeeva[1], I Filipov[1], E Zenova[1], K Smirnov[2] and M Tarkhov[1]

[1] Institute of Nanotechnologies of Microelectronics, Russian Academy of Sciences, 119991, Russia

[2]Higher School of Economics - National Research University, 101000, Russia

email: navovk_1@edu.hse.ru

Abstract. In this paper, we present a technological method for creating high-density luminescent structures based on up-conversion $NaYF_4$ particles and experimentally demonstrate the possibility of their creation. This technology is applicable for large-scale fabrication of patterned media with a level of filling with microparticles of more than 96% for the fabrication of planar structures applicable in photonics and optoelectronics.

1. Introduction

Up-conversion nanoparticles doped with lanthanides are capable of converting excitation in the near infrared region into visible and ultraviolet radiation [1]. Their unique optical properties are a promising class of materials for a wide range of applications such as fluorescence microscopy, deep tissue bioimaging, nanomedicine, optogenetics, security labeling, and volumetric imaging. When microparticles are pumped with IR radiation at a wavelength of 980 nm, a pixel for a display can be obtained, the luminescence wavelength of which will depend on the chemical element with which $NaYF_4$ particles are doped [2].In this work, methods have been developed that make it possible to deterministically place $NaYF_4:Yb^{3+},Er^{3+}$microparticles in a patterned environment matrix with a high filling density. The small dispersion of microparticles by size allows filling the patterned environment with a high fill rate of >96%.

2. Experimental technique

The method of forming high-density luminescent structures is based on the principle of filling with $NaYF_4:Yb^{3+},Er^{3+}$ particles pre-prepared arrays of holes on arbitrary substrates. To demonstrate the possibilities of creating luminescent structures, silicon wafers with thermal oxide 100 mm in diameter were chosen as substrates. At the first stage of creating a high-density luminescent structure, a pattern of the patterned environment was formed in the AZ4999 photoresist using a Heidelberg DWL 2000 laser lithograph, followed by development in a 0.7% KOH solution. When applying the photoresist, the thermal oxide plate was processed in GMDS to improve the adhesion characteristics during the process of applying the photoresist by spin coating. The thickness of the photoresist was 600 nm. Next, the thermal oxide was etched through the formed mask by plasma-chemical etching in C_4F_8 gas. To further fill the wells formed in thermal silicon oxide, an aqueous suspension of $NaYF_4:Yb^{3+},Er^{3+}$ particles. The next step in the formation of a high-density luminescent

structure was to place a 100 mm plate with holes formed in thermal oxide into the suspension and keep it there for several hours. Due to the natural settling of particles on the surface, a uniform layer was formed, the technology is similar to the deposition of carbon nanotubes [3]. Particles that got into the holes due to surface forces are kept in them, and the rest of the particles are removed. Figure 1(a,b) shows the SEM image of the surface and particles located in the wells. It is clearly seen that the filling is of sufficient quality, almost all the particles ended up in the formed wells.

3. Results

Figure 1(c) shows the photoluminescence map of $NaYF_4:Yb^{3+},Er^{3+}$ up-conversion microparticles in pre-prepared well arrays. The paper also shows that the method using plasma-chemical etching of thermal oxide as the creation of high-density luminescent structures has a significantly higher filling index with microparticles than the method using a photoresist mask with holes as a patterned environment.

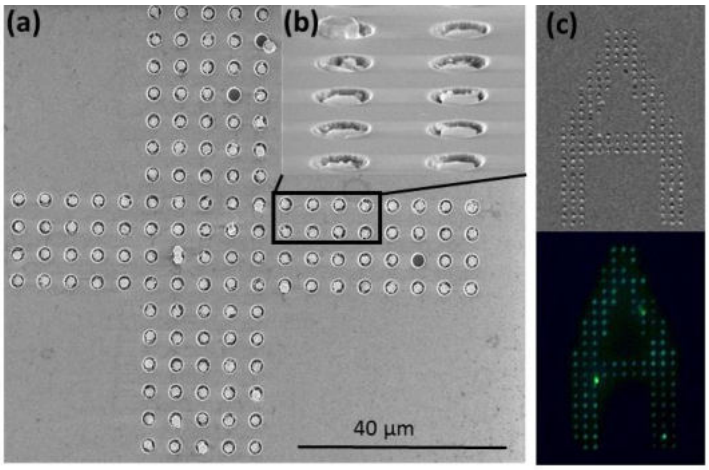

Figure 1. a) Demonstration by scanning electron microscopy of the entry of microparticles into the patterned environment. b) Magnified view of (a) the surface of the patterned environment at an angle. c) Photoluminescence of up-conversion microparticles based on $NaYF_4:Yb^{3+},Er^{3+}$ at a laser wavelength of 980 nm.

4. Conclusion

The technology of particle deposition by suspension deposition into patterned media produced by plasma-chemical etching is a universal technology for deposition of particles of different sizes and geometries. This allows for scalable technology and the possibility of deterministic placement of different particles over a large area. Such possibilities are an advantage over technologies using a polymer as a layer for recesses [4], using probes of an atomic force microscope to create a patterned environment [5].

Acknowledgments

The work was supported by project 1021061509690-0-1.2.1. Ministry of Education and Science of the Russian Federation.

References

[1] Wen S *et. al.* 2018 *Nature Communications* **9**, 2415
[2] Nie Z *et. al.* 2019 *The Journal of Physical Chemistry* **123**, 22959–22970
[3] Bishop M 2020 *Nature Electronics* **3**, 492–501
[4] Rose M *et. al.* 2018 *Journal of Materials Chemistry C* **1**, 12031-12037
[5] Rosenberger M 2019 *ACS Nano* **1**, 904–912

Evaluation of the operational parameters of single-photons detectors in quantum key distribution devices

V. V. Zavodilenko*[1,2], A. V. Losev[1,2,3], A. A. Filyaev[1,2], A. A. Koziy[1,2], Y. V. Kurochkin[1,2,3]

[1]"QRate" LLC, St. Novaya, d. 100, Moscow region, Odintsovo, Skolkovo, 143026, Russia.
[2]NTI Center for Quantum Communications, National University of Science and Technology MISiS, Leninsky prospekt 4, Moscow, 119049, Russia
[3]National University of Science and Technology MISIS, Leninsky prospect, 4, Moscow, 119333, Russia.

E-mail: v.zavodilenko@goqrate.com

Abstract. Automated measuring stand for evaluation of the operational parameters of single-photons detectors (SPD) are developed. The graphical interface of software is presented, which allows to form recommendations for configuration the mode of operation of the detector and subsequent integration these devices into the quantum key distribution (QKD) system.

1. Introduction

A device that is sensitive to one photons with a certain wavelength is single-photon detector (SPD). Such devices have many applications [1, 2]. One of the promising use of SPDs is their implementation in the quantum key distribution (QKD) system [3]. One of the most important task at the stage of production of SPDs is the measurement and evaluation of their operational parameters for configuration the mode of operation of the detector and subsequent integration these devices into the QKD system.

2. Automated measuring stand for evaluation of the operational parameters of single-photons detectors

We have developed a custom automated stand to measure the SPD's operational parameters. This setup includes a synchronization system, laser source (HF laser driver), beam splitters system, a system of controlled optical attenuators with output power control, measured SPD, a frequency meter, and oscilloscope. All elements of this system are controlled with the software created in the LabVIEW program.

Laser source emits optical pulses. These pulses are generated in the same frequency grid as the gating signal. The phase between gating signal and optical pulses is controlled with the synchronization system. Our synchronization system is a programmable logic device (PLD) used as a reference frequency generator for the high-frequency laser driver and our SPD.

Optical pulses arrive at the input of a 90/10 beam splitter, and then they are split into two beams with different intensities. We use this element to have a possibility to control our laser

pulses shape, duration, and repetition rate.

A beam with a lower intensity arrives at the two series-connected controlled attenuators system input. Due to the possibility of measuring the power of light radiation after the first attenuator and a fixed attenuation coefficient of the second attenuator, it is possible to adjust and maintain the power of laser pulses at the output of about 0.1 photons per pulse, which arrives at the input of SPD.

The output signal from the detector incidents simultaneously to a frequency counter and an oscilloscope using an electric power divider. Indications of the frequency counter determine PDE and DCR. The oscilloscope displays a time histogram of triggers that determines the dead time and the afterpulsing probability AP.

3. Description of software for evaluation of the operating parameters of single-photons detectors

We have developed a technique for estimating the efficiency parameters of single-photons detectors according to experimental data obtained by the results of an automated stand. Software has been developed according to this technique. The software interface is shown in Figure 1.

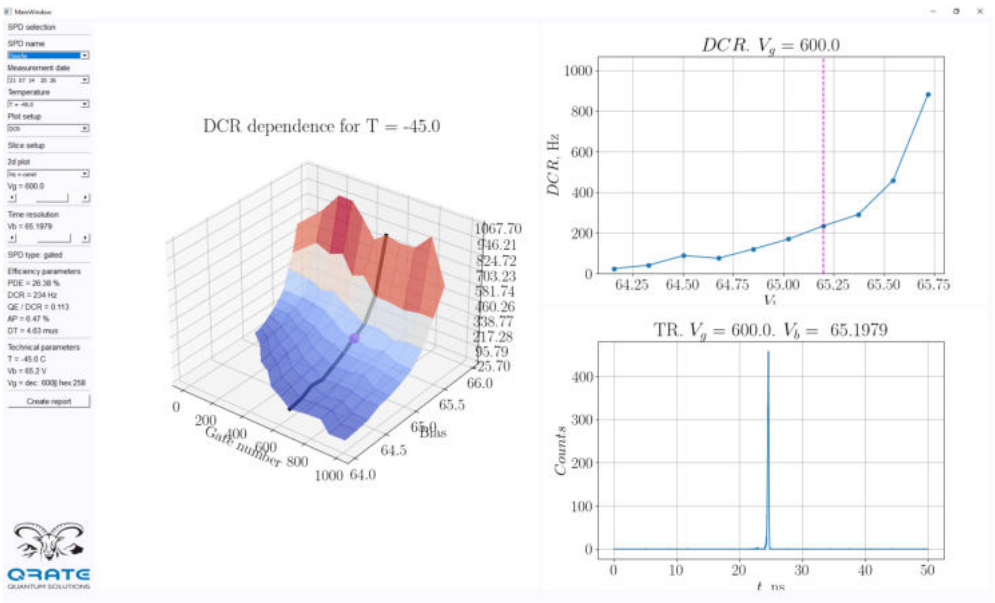

Figure 1. Software for evaluating operating parameters of SPD.

4. Conclusion

The developed automated stand allows parallel measurements of the operational parameters of two SPDs of various types. Developed software allows to evaluate the operational parameters for the formation of recommendations for configuration the mode of operation of the detector and subsequent integration these devices into the QKD system in the form of generated reports.

References

[1] Bruschini C, Homulle H, Antolovic I M, Burri S and Charbon E 2019 *Light: Science and Applications* **8**(1) 1-28

[2] Heide F, Diamond S, Lindell D B and Wetzstein G 2018 *Scientific reports* **8**(1) 1-8

[3] Yuan Z et al. 2018 *Journal of Lightwave Technology* **36**(16) 3427-3433

Тезисы
(Дата: 30 марта 2022 г.)

I. Тезисы

Afterpulse effects simulation of InGaAs/InP single-photon avalanche diodes for applying in quantum key distribution systems

A. A. Filyaev*[1,2], A. V. Losev[1,2,3], V. V. Zavodilenko[1,2], A. A. Koziy[1,2], Y. V. Kurochkin[1,2,3]

[1]"QRate" LLC, St. Novaya, d. 100, Moscow region, Odintsovo, Skolkovo, 143026, Russia.
[2]NTI Center for Quantum Communications, National University of Science and Technology MISiS, Leninsky prospekt 4, Moscow, 119049, Russia
[3]National University of Science and Technology MISIS, Leninsky prospect, 4, Moscow, 119333, Russia.

E-mail: alex.filyaev.98@gmail.com

Abstract. The measurement technique and a probabilistic model for estimating the afterpulse based on the recursive nature of this effect in InGaAs/InP single-photon avalanche diodes are developed. It will allow us to obtain valid internal afterpulsing parameters, which response to a single triggering of detector with such diodes in its composition. We showed the advantages of our approach to other models, widely used for quantum key distribution systems.

1. Introduction

Single-photon avalanche diode (SPAD) in the composition of single-photon detector (SPD) have been widely used for applications in quantum key distribution (QKD) systems. One of the big problems of the QKD is the difficulty of determining the secrecy of the generated key. In contrast to classical cryptographic algorithms, in which applied mathematical transformations strictly determine confidentiality of the key, quantum cryptography depends on the installation's physical parameters. Thus, calculated key secrecy can be selected pessimistically, which will significantly reduce key generation rate or optimistically, which will endanger security of subsequently encrypted data. For this reason, development of methods for accurate determination of the parameters of SPD like the afterpulse probability in SPAD is an actual task that can significantly increase the efficiency of the QKD installation as a whole.

2. Analysis of approaches to afterpulse effects simulation

There are the most popular methods for determining of afterpulsing: Bethune method [1], subharmonic-clock-rate pulse injection method [2], coincidence method [3].

The Bethune, subharmonic-clock-rate pulse injection and coincidence methods are pretty similar; however, they differ in histogram collections and postprocessing approaches. We need to collect two histograms in each method: with and without light illumination. As we can see, all of these models describe the afterpulsing to varying degrees of accuracy. Also we can observe the dependences of the afterpulse probability from external parameters (Figure 1).

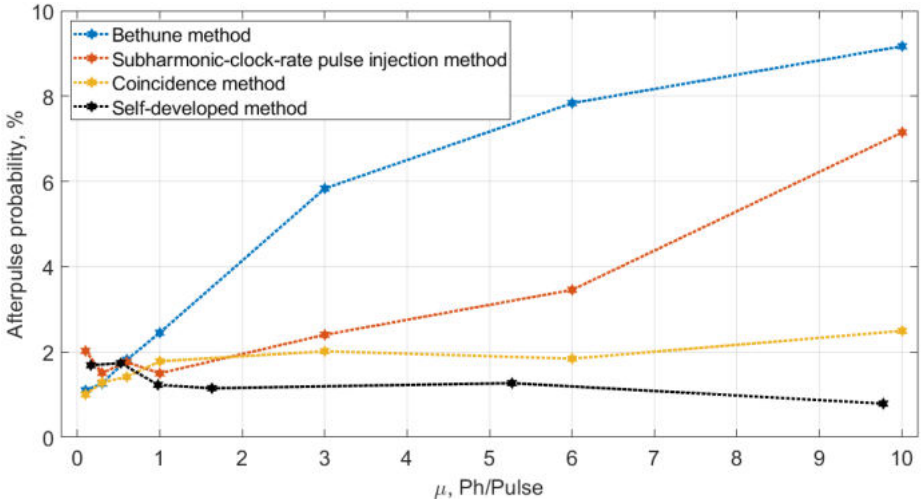

Figure 1. The comparison of the afterpulse probability for different methods to laser pulse energy.

The afterpulsing is an internal SPD parameter, and it should not depend on external factors, like laser pulse repetition rate or average energy per laser pulse. Nevertheless, the afterpulsing is a non-markovian process, and its probability, obtained with standard methods, will strongly depend on the count rate. It means that each of described methods does not allow us to obtain actual internal afterpulse probability.

3. Self-developed afterpulse model

In our work we create the model of afterpulsing measurement, that based on recursive nature of this effect, and which will allow us to obtain true internal afterpulsing parameter. If we know true internal parameter, it means, that we can model our device at any external parameters, like laser pulse frequency or average laser pulse energy.

Two different models: "Simple" and "Complex" are developed. The advantage of the simple model is its simplicity and possibility of easy p_{ap} calculation from the statistics. The advantage of the complex model is that it is an accurate statistical description of afterpulse processes in the diode.

4. Conclusion

We present the measurement technique and a probabilistic model for estimating the afterpulse based on the recursive nature of this effect. It will allow us to obtain valid internal afterpulsing parameters. We can model our device at any external parameters if we know valid internal parameters, like laser pulse frequency or average laser pulse energy. We have compared our afterpulsing measurement approach with other commonly used models like Bethune method, subharmonic-clock-rate pulse injection method, and coincidence method. We have shown that the afterpulse probability obtained with our method is less sensitive to the laser pulses power changes.

References

[1] Bethune D S, Risk W P and Pabst G W 2004 *Journal of modern optics* **51**(9-10) 1359-1368
[2] Yuan Z L, Kardynal B E, Sharpe A W and Shields A J 2007 *Applied Physics Letters* **91**(4) 041114
[3] Zhang Y, Zhang X, Shi Y, Ying Z and Wang S 2014 *Optical Engineering* **53**(6) 067102

Investigation of interference patterns by scanning near-field optical microscopy

T V Mikhailova[*1], E V Skorokhodov[2], S A Gusev[2], I V Dzedolik[1]

[1]V.I. Vernadsky Crimean Federal University, Simferopol 295007, Russia
[2]Institute for Physics of Microstructures of the Russian Academy of Sciences (IPM RAS), Nizhny Novgorod 603087, Russia

*taciamikh@gmail.com

Abstract. This paper presents the results of investigation of optical properties of perforated structures made in Au films using aperture polarization near-field optical microscopy.

1. Introduction

Synthesis and study of various plasmonic nanostructures are relevant for the purpose of creating micro-sized optical isolators, modulators and switches, elements of integrated photonics and plasmonics devices controlled by magnetic or electric field, magnetic field sensors and biosensors [1]. The subject of intensive attention of researchers is two-dimensional interference patterns of surface plasmon polaritons (SPPs) in structures consisting of nanosized slits of various configurations made in thin films of Au [2, 3]. Interest in such structures is due to their potential application in information processing and storage devices.

2. Experimental

In order to form and observe interference states due to the excitation of SPPs, samples with slits of various configurations in Au films were synthesized. Au films of thicknesses 20 and 50 nm were deposited using magnetron sputtering. Nanoslits in the form of arcs and lines were obtained by electron beam lithography. The slit width varied from 156 to 260 nm. The lengths of the linear slits and the radii of the arcs used to form the structures were 10 and 5 μm (structure I) and 20 and 10 μm (structure II), respectively.

Measurements of the near-field optical fields at the air-gold interface of structures were carried out by scanning near-field optical microscopy (НТ-МДТ, Ntegra). A focused laser beam with a wavelength λ of 532 or 633 nm illuminated the structure from the side of substrate using an aspherical lens with a low NA = 0.3 and polarizer. Optical radiation was collected from above the structure from the air-gold interface through an aperture probe SNOM_NC with typical diameter of (120 ± 25) nm and lens (NA = 0.7, 100x).

The registered SNOM images are shown in Figure 1. The observed interference pattern depends on the polarization of the incident radiation and its wavelength. The direction of polarization relative to the structure is shown in the figures by arrows. This fact confirms that SPPs are involved in the formation of the interference pattern.

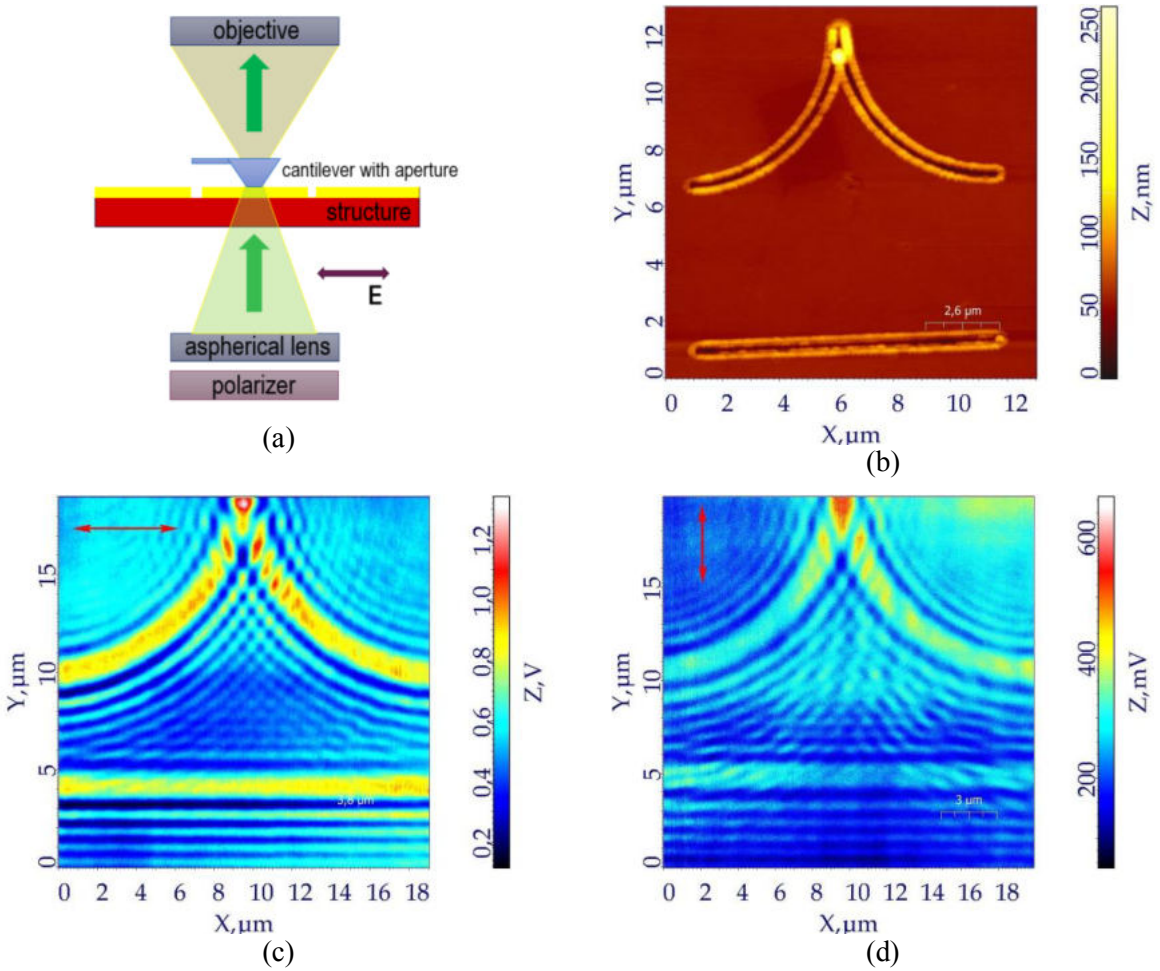

Figure 1 (a, b, c, d). Schematic diagram of SNOM-measurements **(a)**. Atomic force microscopy image of structure I **(b)**. Scanning near-field optical microscopy image of structure II depending on the direction of beam polarization with a wavelength of 633 nm 0° **(c)** and 90° **(d)**. Thickness of Au is 50 nm.

Acknowledgments

The development of technique of electron beam lithography, synthesis and complex diagnostics of the structural properties of the samples was carried out using technological and analytical equipment of the Common Research Center "Physics and Technology of Micro- and Nanostructures" of the Institute for Physics of Microstructures RAS. The authors acknowledge support by Russian Science Foundation (project no. 19-72-20154).

References

[1] Armelles G, Cebollada A, García-Martín A, González M 2013 Magnetoplasmonics: Combining Magnetic and Plasmonic Functionalities *Adv. Optical Mater* 1 10.

[2] Dvořák P, Édes Z, Kvapil M, Šamořil T, Ligmajer F, Hrtoň M, Kalousek R, Křápek V, Dub P, Spousta J, Varga P, Šikola T 2017 Imaging of near-field interference patterns by aperture-type SNOM – influence of illumination wavelength and polarization state *Optics Express* 25(14) 16560.

[3] Minovich A, Klein A E Janunts N, Pertsch Th, Neshev D N, Kivshar Yu S 2011 Generation and Near-Field Imaging of Airy Surface Plasmons *Phys. Rev. Lett.* 107, 116802.

Precision formation of hybrid Au/Si nanoantennas by STM lithorgaphy

Shkoldin V.A.[1,2], Lebedev D.V[1,3,4], Permyakov D.V.[2], Golubok A.O.[3], Mozharov A.M[1], Samusev A.K.[2], Mukhin I.S.[1,4,5]

[1]St. Petersburg Academic University, 8/3 Khlopina str., St. Petersburg, 194021 Russia
[2]ITMO University, 9 Kronverksky pr., St. Petersburg, 197101 Russia
[3]St. Petersburg State University, 7/9 Universitetskaya nab., St. Petersburg, 199034 Russia
[4] Institute for analytical instrumentation RAS, 26 Rizhskii pr., St. Petersburg, 190103 Russia
[5]Peter the Great St.Petersburg Polytechnic University, Polytechnicheskaya, 29, St.Petersburg, 195251 Russia

shkoldin@spbau.ru

Abstract. The modern electronics is need in miniature electrically driven sources for utilization all benefits of optical links in integrated circuits. Light emitting tunnel junction is a good candidate, but they has small quantum efficiency. We develop technique, with allow to create CMOS-compatible nanoantennas by the STM-Lithography. This nanoantennas can increase the quantum efficiency of such tunnel junctions.

1. Introduction

Modern optical communication lines transmit enormous amounts of information between continents, and every year this amount is growing by 20-30%[1]–[3]. This growth is directly related to the increasing availability of information, the development of information technology and microprocessor technology. Fiber optic type of communication prevails over the classical copper lines when transmitting information at distances from a meter to thousands of meters (intercontinental distances). However, with data transmission at scales comparable to the size of devices and/or integrated circuits (IC), signal is mainly transmitted by means of electrons moving along traditional metal wires

A good solution for integration photonic source in ICs is a light emitting tunnel junction[4], [5]. But its quantum efficiency is about 10^{-7}-10^{-5} photons per electron, and it isn't enough for application in ICs.

One of the way for solution of this problem is usage of optical nanoantennas for increasing of local density of states, which amplifies an quantum efficiency of tunnel junctions[5], [6].

2. Experiment

We developed a technique for creating optical hybrid nanoantennas. It was realizing on thin 10 nm film which coat a think 100 nm gold film. The studies showed that by the methods of applying short pulses of 10-100 ms with disabling the feedback system and continuous current exposures with varying voltages with the feedback switched on, features are formed on the surface of the sample. These features can be characterized as "nanoknobs". Typical dimensions of nanoknobs start at 60 nm in diameter. The

dependence of the lateral dimensions of the features on the exposure time on the surface was determined. Also, this technique allows to do modificated regions moreover single nanoknobs.

The tunnel emission was study for that nanoknobs. The estimated calculation based on experimental data showed more than ten times amplification of light emission intensity on nanoknobs in comparing atomic flat gold surface.

3. Conclusion

The STM-lithography allow to create light sources based on hybrid Au/Si nanoknobs. Also, gold and silicon are good materials for CMOS technology, which is most used in nowadays. Additionally, the tunnel junction light sources solve size mismatches problem between light source and modern semiconductors devices.

Acknowledgments

This work was supported by the Russian Science Foundation (project no. 21-79-10346 of the Russian Science Foundation)

References

[1] J. Hecht, "The bandwidth bottleneck that is throttling the Internet," *Nature*, vol. 536, no. 7615, pp. 139–142, Aug. 2016, doi: 10.1038/536139a.

[2] Cisco, "Cisco Annual Internet Report (2018–2023) White Paper," 2020. https://www.cisco.com/c/en/us/solutions/collateral/executive-perspectives/annual-internet-report/white-paper-c11-741490.html (accessed May 24, 2021).

[3] D. V. Lebedev *et al.*, "Scanning Tunneling Microscopy-Induced Light Emission and I(V) Study of Optical Near-Field Properties of Single Plasmonic Nanoantennas," *J. Phys. Chem. Lett.*, vol. 12, no. 1, pp. 501–507, Jan. 2021, doi: 10.1021/acs.jpclett.0c03039.

[4] S. L. McCarthy and J. Lambe, "LEIT effect in metal-insulator-semiconductor tunnel junctions," *Appl. Phys. Lett.*, vol. 33, no. 10, pp. 858–860, Nov. 1978, doi: 10.1063/1.90214.

[5] M. Parzefall and L. Novotny, "Optical antennas driven by quantum tunneling: a key issues review," *Reports Prog. Phys.*, vol. 82, no. 11, p. 112401, Nov. 2019, doi: 10.1088/1361-6633/ab4239.

[6] F. Bigourdan, J.-P. P. Hugonin, F. Marquier, C. Sauvan, and J.-J. J. Greffet, "Nanoantenna for Electrical Generation of Surface Plasmon Polaritons," *Phys. Rev. Lett.*, vol. 116, no. 10, 2016, doi: 10.1103/physrevlett.116.106803.

Modulation and demodulation process of the vortex beam under the condition of additional phase modulation

I A Adam, D A Kargina, D A Yashin, B A Nasedkin

ITMO University, Department of Photonics and Optical Information, St. Petersburg, 197101, Russian Federation

E-mail: iuriiadam@yandex.ru

Abstract. In the presented thesis, the possibility of conservation the phase modulation of a Gaussian light beam with its additional modulation and demodulation into vortex beam were studied. The results obtained can be used in optical information transmission systems with an atmospheric communication channel.

1. Introduction

Currently, optical information systems with an atmospheric communication channel are widely used. As a rule, such systems use classical Gaussian beams, which experiences additional amplitude, phase or other types of modulation to transmit information. One of the most important limitations of this approach is the influence of atmospheric turbulence on the propagated light, which limits the maximum range of signal transmission. In turn, a number of researches [1-2] have shown that optical vortex, light with an orbital angular momentum, is less influenced by the atmosphere turbulence compared to Gaussian beams. It is possible to obtain a vortex beam by modulating Gaussian beam [3]. However, the possibility of preserving the phase modulation of the beam during the transition from Gaussian radiation to vortex optical beam and vice versa has not been demonstrated before. This condition is necessary for the integration of an atmospheric communication channel into a single-mode fiber-optic communication line. Thus, this work is aimed at studying the conservation of phase modulation with additional modulation and demodulation of vortex beams from light described by the Gaussian function using a fork-shaped diffraction grating.

2. Methods and experimental results

In order to generate vortex beams, or light emission with orbital angular momentum, different methods are used. The most common ones are spiral phase plates [4], fork-gratings [5] and spatial light modulators (SLM) [6]. In considered study the fork-grating method is used due to the research focus of this work and its advantages such as the control of vortex beam parameters and low cost. Fork-grating is a diffraction grating in the middle of which a spatial singularity with the form of a fork is located. Mathematically it is obtained as an interference pattern of a vortex beam and an inclined plane wave. As a result of the interaction of a Gaussian beam with a fork-grating, vortex beams are generated in side diffraction orders, the topological charge of which coincides with the such orders. Demodulation of the vortex beam in this case is provided by using a symmetrical fork-grating. The Gaussian beam will be restored in the opposite diffraction order with the respect to initial modulation order.

To study the possibility of conservation phase modulation with additional modulation and demodulation of optical vortex, a classical Mach-Zehnder interferometer was used. In one of its optical

paths, light was phase-delayed using an electro-optical phase modulator. Next, the Gaussian beam was modulated into a vortex beam using a fork-grating. After 50 cm, the reverse process of demodulation into the Gaussian beam were employed using a similar fork-grating. Finally, the two optical paths of the interferometer were combined on a beam splitter, in one of the outputs of which a registration camera was placed. The results obtained are shown in Figure 1. It can be seen that the stripes of the interference pattern are shifted in accordance with the introduced phase delay in one of the optical paths, which indicates the preservation of phase modulation with additional modulation and demodulation of the optical vortex.

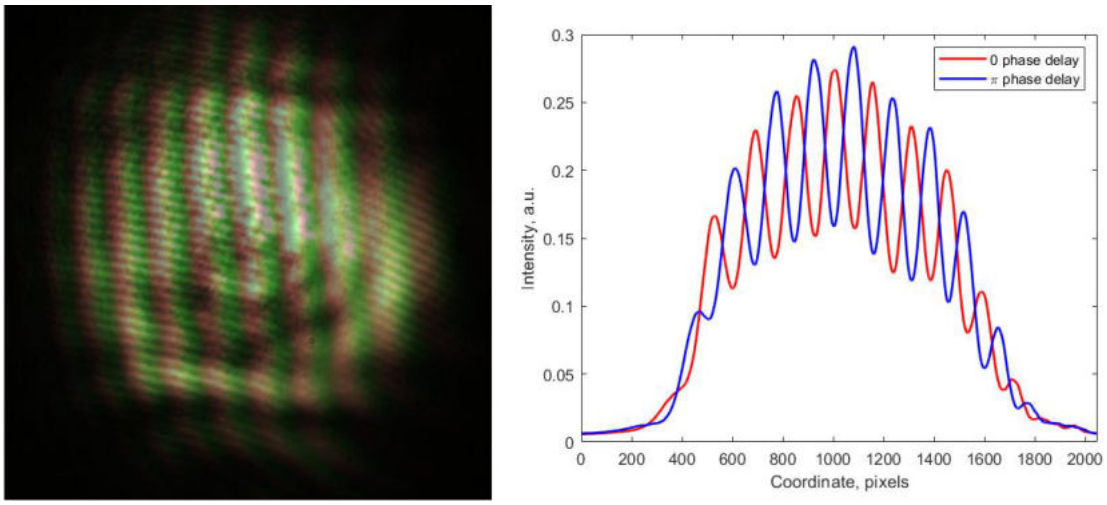

Figure 1. The interference pattern, where red is responsible for 0 phase delay, and green for π phase delay (a), interference pattern cross section averaged over 30 frames (b).

3. Conclusion

Thus, this research demonstrates the possibility of conservation phase modulation with additional modulation and demodulation of the optical vortex.

Acknowledgments

The authors of this research express their gratitude to Aleksey Viktorovich Chernykh from ITMO University for help in conducting the experimental results and to the Centre for Reprography at the Russian National Library for the production of the fork-gratings.

The study is funded by RPMA grant of School of Physics and Engineering of ITMO University.

References

[1] Chen, Z.Y., Cui, S.W., Zhang, L., Sun, C.Z., Xiong, M.S. and Pu, J.X., 2015. Optoelectronics Letters, **11(2)**, 141-144.

[2] Liu, X. and Pu, J., 2011. Optics express, **19(27)**, 26444-26450.

[3] Vallone, G., D'Ambrosio, V., Sponselli, A., Slussarenko, S., Marrucci, L., Sciarrino, F. and Villoresi, P., 2014. Physical review letters, **113(6)**, 060503.

[4] Hui, X., Zheng, S., Hu, Y., Xu, C., Jin, X., Chi, H. and Zhang, X., 2015. IEEE Antennas and Wireless Propagation Letters, **14**, 966-969.

[5] Topuzoski, S., 2016. Optical and Quantum Electronics, **48(2)**, 1-6.

[6] Pradhan, P., Sharma, M. and Ung, B., 2018. IEEE Photonics Journal, **10(1)**, 1-10.

Optical absorption and Raman scattering mapping of nanoparticles patterns formed in glass by nanosecond laser in UV, VIS and IR

E S Babich[1,2*], V P Kaasik[1,2], A V Redkov[3] and A A Lipovskii[1,2]

1 Alferov University, 8/3 Khlopina, St. Petersburg, 194021, Russia
2 Peter the Great St. Petersburg Polytechnic University, 29 Polytechnicheskaya, St. Petersburg, 195251, Russia
3 Institute of Problems of Mechanical Engineering RAS, 61 Bolshoj prosp. V. O., St. Petersburg, 199178, Russia

*Correspondence: babich_es@spbstu.ru

Abstract. The paper is devoted to optical and surface enhanced Raman scattering study of silver nanoparticles formed in a glass enriched with silver ions upon irradiation with nanosecond laser. The impact of laser wavelength, fluence and pulse frequency on the arrangement and optical properties of the nanoparticles is revealed.

1. Introduction

Metal nanoparticles (NPs) are known for their extraordinary optical properties. Their resonance light absorption at wavelength of localized surface plasmon (LSPR) is accompanied by giant enhancement of electric field nearby metal surface. This enhancement intensifies light-matter interaction allowing, in particular, detection of single molecules via surface enhanced Raman scattering (SERS) [1]. The developing approach to the formation of NPs is reduction of metal ions, which are embedded into a glass, by irradiation of UV-IR short pulse lasers [2]. One of the advantages of this approach is patterning of NPs distribution according to a given template, which opens up possibilities to integrate NPs in microfluidic chips and create lab-on chip devices based on SERS. In this study, we reveal impact of laser wavelength, fluence and pulse frequency on spatial arrangement, SERS-activity and optical properties of silver NPs formed upon ns-laser irradiation of a glass enriched with silver ions.

2. Experimental

In the experiments we used soda-lime silicate glass and introduced silver ions in the subsurface layer of the glass via $Na^+ \leftrightarrow Ag^+$ ion exchange [3]. The glass was irradiated with Nd:YAG ns-laser at 1.06, 0.53 and 0.35 μm wavelength in 5-13 J/cm^2 laser fluence range. Using the computer-driven platform, which moved the glass in the plane perpendicular to the laser beam, and varying laser pulse frequency from 0.5 to 3 Hz we patterned NPs to draw “lines” (pulses overlapping on the glass surface) and “spots” (individual pulses). Both patterns had characteristic yellowish coloration induced by optical absorption at ~450 nm (silver NPs LSPR). To reveal NPs arrangement we mapped the absorption intensity distribution in the glass subjected to the laser irradiation and additional chemical etching. We also mapped SERS signal obtained from few monolayers of test molecules adsorbed at the etched and

non-etched glass surface. Typical optical and SERS maps are presented in figure 1(a) and (b), respectively.

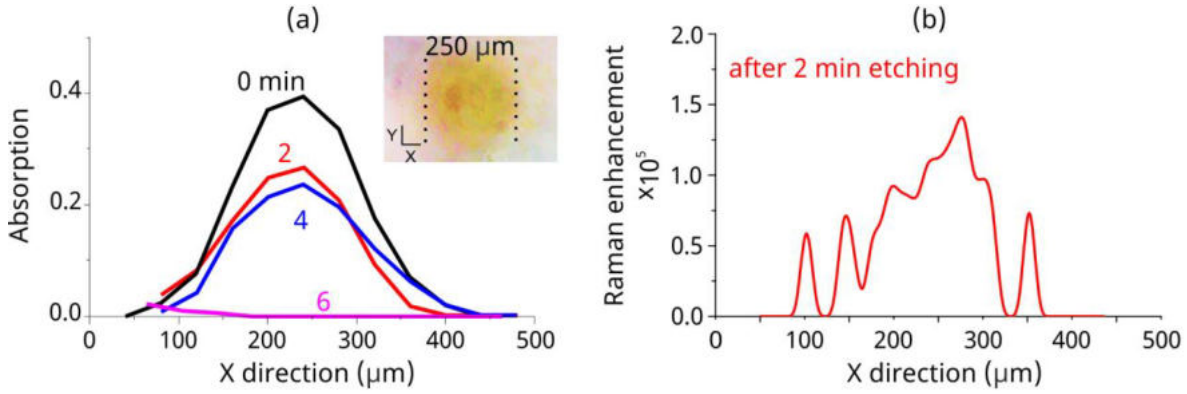

Figure 1. (a) Optical absorption intensity distribution across silver NPs pattern before and after chemical etching of glass (etching rate 23 nm/min, etching time is denoted). (b) Raman enhancement distribution across the same pattern after 2 min etching. Inset: optical image of the studied pattern formed via 1.06 μm laser irradiation at 12.8 J/cm^2 laser fluence and 0.5 Hz pulse frequency.

3. Result and discussion

Optical mapping combined with the chemical etching demonstrates that under ns-laser irradiation of the silver-ions-enriched glass NPs form within a thin, hundreds of nanometers, subsurface glass layer. The thickness of the NPs-containing layer, as well as concentration of NPs, increases with the increase of the laser fluence and pulse frequency. Besides, NPs are covered with ~20 nm of glass and SERS signal is detectable only after removal of this covering layer. The average Raman enhancement provided by silver NPs patterns after the etching is ranged from $3{\cdot}10^4$ to $3{\cdot}10^5$, being maximal for the "lines" drawn at 0.35 μm laser wavelength. Distribution of SERS signal across NPs patterns is relatively uniform for the patterns formed under 0.35 and 0.53 μm laser irradiation, the relative standard deviation of SERS signal is about 50% and it decreases down to 30% with the increase of the laser fluence.

Acknowledgments

E Babich thanks the Council for Grants of the President of the Russian Federation (project SP-1491.2021.4). V Kaasik and A Lipovskii thank the Ministry of Science and Higher Education of the Russian Federation (project FSRM-2020-001).

References

[1] Li C, Huang Y, Li X, Zhang Y, Chen Q, Ye Z, Alqarni Z, Bell S E J and Xu Y 2021 *J. Mater. Chem.* C **9** 11517–52

[2] Babich E, Kaasik V, Redkov A, Maurer T and Lipovskii A 2020 *Nanomaterials* **10(9)** 1849

[3] Varma R S, Kothari D C and Tewari R 2009 *J. Non-Cryst. Solids* **355** 1246–51

Adaptive eavesdropping on the BB84 quantum key distribution protocol with distinguishable photons

D. Babukhin[1,2,3], D. Kronberg[4,5,6] and D. Sych[7]

[1] QRate LLC, Novaya av. 100, Moscow 121353, Russia
[2] NTI Center for Quantum Communications, National University of Science and Technology MISiS, Leninsky prospekt 4, Moscow 119049, Russia
[3] Sirius University of Science and Technology, 1 Olympic Ave, 354340, Sochi, Russia
[4] Department of Mathematical Methods for Quantum Technologies, Steklov Mathematical Institute of Russian Academy of Sciences, Gubkina str. 8, Moscow 119991, Russia
[5] Terra Quantum AG, St. Gallerstrasse 16A, CH-9400 Rorschach, Switzerland
[6] Moscow Institute of Physics and Technology, 141700, Institutskii Per. 9, Dolgoprudny, Moscow Distr., Russian Federation
[7] P.N. Lebedev Physical Institute, Russian Academy of Sciences, 53 Leninskiy Prospekt, Moscow 119991, Russia

Corresponding author: dv.babukhin@gmail.com

Abstract. In theory, photon sources in quantum key distribution (QKD) produce photons with controllable modes. In practice, uncontrollable difference in non-operational modes leads to additional opportunities for eavesdropping. Here we show adaptive eavesdropping strategy on a BB84 QKD protocol with distinguishable photons. We show, that difference in non-operational photon modes allows for a quantum-memory-free attack, which can be as effective as the most efficient theoretical attack on the BB84 procotol. We provide estimates for hardware parameters, which allow for this adaptive attack efficiency.

1. Introduction

Quantum cryptography promises unconditional security for secret key distribution due to no-cloning theorem [1]. However, when a QKD protocol is implemented in hardware, difference in theoretic models and real devices introduce additional opportunities for eavesdropping, rather than attacking only the protocol. This leads to decrease of the quantum security promise.

One of the main parts of QKD system is a photons source. A transmitting side (Alice) uses the source of photons to encode a secret bit into the quantum state and to send in through the quantum channel. For security of QKD protocol, the source must produce photons with fully controllable modes. For example, if Alice uses polarization of photons to encode secret bits, then the source must produce photons with a chosen polatization and with all other modes completely coinciding among each other. If there is any uncontrollable difference in the non-operational modes (side channel of information leakage), then an eavesdropper (Eve) can use this difference to make a more powerful attack on the QKD process comparing to the attack on the protocol without side channels.

2. Adaptive eavesdropping

In this section we provide an explicit example of eavesdropping the BB84 protocol with a photon distinguishability side channel. We demonstrate performance of this eavesdropping strategy for sources with different degrees of photons distinguishability in comparison with a most effective attack on the theoretic side-channel-free BB84 protocol.

2.1. An eavesdropping strategy

The proposed eavesdropping strategy is based on the intercept-resend attack, but with included actions which adapt it to the use of photons distinguishability. In particular, the ensemble of BB84 states with the photon distinguishability after side channel state measurement has a following form:

$$\{\tfrac{1-q}{4}\colon |0_z\rangle\langle 0_z| \otimes \rho^{\Delta}_{z,0}, \tfrac{q}{4}\colon |1_z\rangle\langle 1_z| \otimes \rho^{\Delta}_{z,1}, \tfrac{q}{4}\colon |0_x\rangle\langle 0_x| \otimes \rho^{\Delta}_{x,0}, \tfrac{1-q}{4}\colon |1_x\rangle\langle 1_x| \otimes \rho^{\Delta}_{x,1}\} \quad (1),$$

Then, Eve applies a filtering to the state of the photon in the quantum channel, which probabilistically makes two most probable state more orthogonal to each other, while making the other two less distinguishable [2]. Finally, Eve uses an optimal measurement of two most probable states to find a value of the secret bit and a basis choice of Alice and resends the measured state towards Bob.

2.2. Calculation results

On Figure 1 we provide calculation results of the proposed eavesdropping strategy for several values of the Hong-Ou-Mandel (HOM) visibilities of the photons, produced with Alice photon source. We use HOM visibility to characterize photon distinguishability side channel with an experimentally-available physical value [3]. We see, that for sources with V = 0.335 or less, the proposed eavesdropping strategy allows Eve to obtain the eavesdropping efficiency of the most effective theoretical attack on the BB84 protocol. The theoretical-limit attack requires Eve to possess a quantum memory to make a collective measurement over all eavesdropped quantum states. In contrast, the proposed eavesdropping strategy does not require a quantum memory, which makes this strategy easier to implement with technologies of the nearest future.

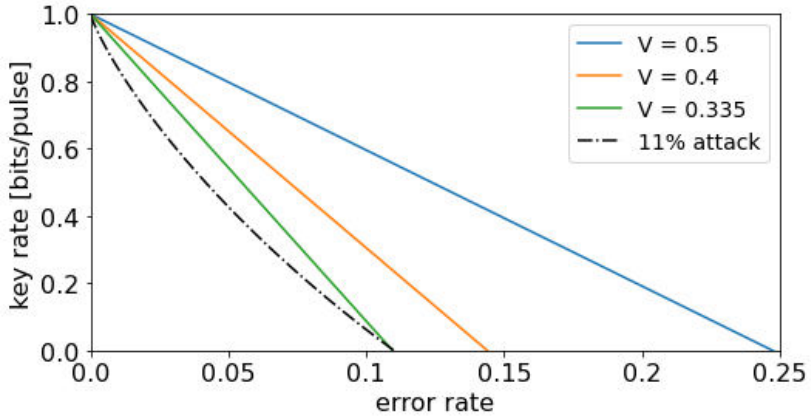

Figure 1: key rate for adaptive eavesdropping with different photon source HOM visibilities

Acknowledgments

Danila Babukhin acknowledges funding by RFBR, Sirius University of Science and Technology, JSC Russian Railways and Educational Fund "Talent and success", project number 20-32-51004, all authors acknowledge support by the Russian Science Foundation under grant 20-71-10072

References

[1] Shor P W and Preskill J 2000 *Phys. Rev. Lett.* **85** 441-444
[2] Kronberrg D A 2021 *Proc. Steklov Inst. Math*. **313**
[3] Duplinskiy A and Sych D V 2021 *Phys. Rev. A* **104** 012601

X-ray spectral studies of doped bismuth-magnesium and bismuth-zinc tantalates

K.A. Bakina[1], N.A. Zhuk[2], S.Yu. Kovalenko[2], O.V. Petrova[1], D.V. Sivkov[1], R.N. Skandakov[1], V.N. Sivkov[1], S.V. Nekipelov[1,2]

[1]Institute of Physics and Mathematics, Komi Science Centre of the Ural Branch of the Russian Academy of Sciences, Syktyvkar 167982, Russia
[2]Pitirim Sorokin Syktyvkar State University, Syktyvkar 167001, Russia

E-mail: tylxen@gmail.com

Abstract. Solid solutions of bismuth-magnesium tantalates and bismuth-zinc tantalates doped with 3d-metal atoms were studied by XPS and NEXAFS spectroscopy. Based on spectral studies, it was shown that the atoms of bismuth, magnesium and zinc in all the compounds under consideration have the charge state Bi^{3+}, Mg^{2+} and Zn^{2+}, respectively, and the tantalum atoms, in turn, have an effective charge of +(5-δ).

1. Introduction

Complex bismuth-containing tantalates are characterized by their excellent dielectric properties. In this case, the doping of bismuth tantalates with atoms of various metals can lead to a significant change in their electrophysical properties, which can depend both on the type of doped atoms and on the degree of doping.

This work shows the results of NEXAFS and XPS spectroscopy studies of the electronic state and nature of interatomic interactions of 3d-metal atoms in bismuth-magnesium and bismuth-zinc tantalates doped with copper and nickel atoms at different degrees of doping $Bi_2Ta_2Mg_{1-x}Cu(Ni)_xO_9$ and $Bi_2Ta_2Zn_{1-x}Cu(Ni)_xO_9$ (x = 0.1–0.9).

2. Results

Based on spectral studies it has shown that the atoms of bismuth, magnesium and zinc in all observed compounds have a charge state Bi^{3+}, Mg^{2+} and Zn^{2+}, respectively. The tantalum atoms, in turn, have an effective charge of +(5-δ). Doped nickel atoms mainly have a charge state of +2. Copper atoms are in the univalent Cu (I) and divalent Cu (II) states, or they have the Cu^+ and Cu^{2+} charge states, respectively.

It was also shown that when pairs of copper-magnesium and copper-zinc atoms are added, the charge state of the copper atom changes with a change in its concentration. On the other hand, when doping nickel-magnesium and nickel-zinc substitution pairs the charge state of the nickel atom is preserved at various concentrations of this atom and remains equal to +(2+δ).

Acknowledgments

The study was funded by the Grant of the President of the Russian Federation (MK 3796.2021.1.2), the RFBR and the Komi Republic within the framework of research projects number 19-32-60018 and 20-42-110002 r-a. The study was supported by the Ministry of Science and Higher Education of Russia under Agreement No. 075-15-2021-1351 in part of research on NEXAFS spectroscopy.

Silicon nanoantenna for efficient control of single-photon source emission

Olga Sergaeva[1], Kseniia Baryshnikova[1]

[1]School of Physics and Engineering, ITMO University, St. Petersburg, Russia

k.baryshnikova@metalab.ifmo.ru

Abstract. Recently the control of standalone quantum sources emission attracted interest of scientific community due to growth of technological abilities to create and locate these emitters on demand. Here we report a silicon-of-insulator nanoantenna design providing strong dependence of its radiation on the quantum emitter position inside the system. Results are useful for controlling of light at nanoscale and potentially for creating of quantum computers.

1. Introduction

Resonant dielectric and semiconductor (silicon, germanium, etc.) nanostructures have attracted scientific interest in recent years due to the possibility of efficient light control at the nanoscale by excitation of optical modes of both electric and magnetic Mie-type resonances. Moreover, for these materials it is easy to find regions of transparency in the near-IR range, where light absorption losses are negligible.

The creation of effective compact sources of single photon emission has a wide range of potential applications, first of all, in optical communication lines and information processing systems, including quantum computers. Here we study silicon nano-islands with embedded germanium quantum dots, whose growth technology is compatible with silicon integrated technology. Emission extraction from such systems is often a difficult task [1]; this work aimed at solving this problem. We performed theoretical modelling of high-efficiency dielectric nanoresonators for controlling near-infrared emission of single-photon sources.

Conventional Yagi-Uda nanoantenna consists of one larger reflector nanoparticle and one or several smaller director nanoparticles with the light emitter placed in free space between the nanoparticles [2, 3]. Here we propose silicon-on-insulator design inspired by the Yagi-Uda nanoantenna made of one reflector and one director with a light emitter embedded inside of it for efficient control of the single-photon source emission directivity. Placing a quantum emitter in a bright spot of electromagnetic field inside a semiconductor nanoparticle allows its emission to be resonantly enhanced through the Purcell effect [4]. Multipole decomposition is commonly used for analysing the optical properties of subwavelength nanostructures [5]. We chose using silicon cylindrical nanoparticles of the same height as the building blocks of our structure, since the planar technology for

their fabrication is well established in standard nanofabrication platforms [6]. Also, crystalline silicon has low material losses at wavelengths of interest (1300 nm).

2. Results and discussion

We carried out numerical calculations of the characteristics of the proposed nanosystem on a substrate in the COMSOL Multiphysics. The emitter was modelled as a point dipole oriented parallel to the substrate's surface and located inside the Si director nanoparticle at different positions. The geometry of the structure and calculated radiation patterns are shown on Figure 1.

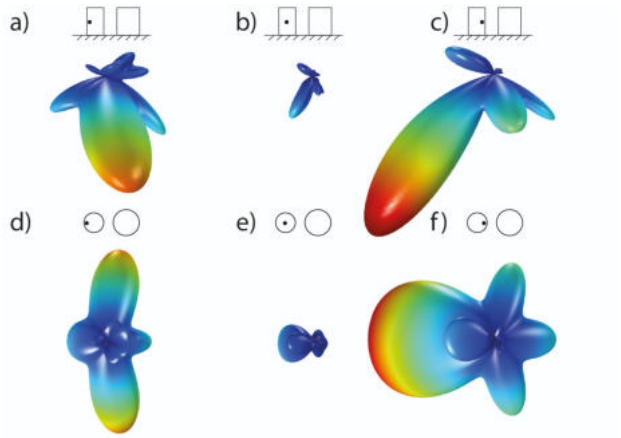

Fig. 1. Far-field radiation patterns calculated for a nanoantenna composed of silicon cylinder director of 230-nm radius and 680 nm height and cylinder director of 260-nm radius and same height as director, quantum emitter is located inside of director nanoparticle, its location were varied to show the dependence of radiation pattern (shown schematically). (a-c) Patterns for different location of emitter in plane perpendicular to surface of substrate. (d-f) Patterns for different location of emitter in plane parallel to surface of substrate.

In result, we proposed silicon nanoantenna made of two cylindrical nanoparticles used as reflector and director with a light emitter embedded inside of it for efficient control of the single-photon source emission directivity. Thorough analysis of eigenmodes as well as multipole decomposition helped us to find adequate geometrical parameters of the nanostructure.

Acknowledgments

The work was supported by the Russian Science Foundation (project No. 21-72-20184).

References

[1] A.F. Koenderink, *Nano Lett.* (2009) 9, 4228.

[2] A. Krasnok, I. Maksymov, A. Denisyuk, P. Belov, A. Miroshnichenko, C. Simovski, and Y. Kivshar, *Phys. Usp.* 56 (2013), 539 .

[3] W. Liu, A. Miroshnichenko, D. Neshev, and Y. Kivshar, *ACS Nano* 6 (2012), 5489.

[4] O.N. Sergaeva, V.V Yaroshenko., I.A. Volkov, D.A. Zuev, R.S. Savelev, *Semiconductors* 53 (14), (2019), 1942.

[5] N. Ustimenko, K. Baryshnikova, R. Melnikov, D. Kornovan, V. Ulyantsev, B. N. Chichkov, A. B. Evlyukhin, *JOSA B* 38 (2021) 3009.

[6] D. G. Baranov, D. A. Zuev, S. I. Lepeshov, O. V. Kotov, A. E. Krasnok, A. B. Evlyukhin, and B. N. Chichkov, *Optica* 4 (2017), 814.

Generation of correlated photons and single photon detection processes in an array of qubits in a microwave transmission line

M.V. Bastrakova*, D.S. Pashin

Lobachevsky State University of Nizhny Novgorod, Nizhny Novgorod 603022, Russia

*bastrakova@phys.unn.ru

Abstract. It has been shown that an array of qubits connected to bifurcation Josephson amplifiers can act as sensitive tunable single-photon detectors. The process of generation and propagation of correlated photons in a transmission line through an array of qubits with sensors is studied.

1. Introduction

Systems based on Josephson contacts operating in the parametric amplifier mode or in the bifurcation amplifier mode have recently been widely used as detectors for selective measurements of the states of superconducting [1] and semiconductor qubits [2]. The main advantage of such a measurement is to minimize noise when detecting states. The state of the resonator can thus be determined reliably without being limited by qubit relaxation, thereby providing a high-fidelity single-shot qubit readout [3].

In this paper, we study a model of a sensitive single-photon sensor based on an array of qubit connected to a measuring sensitive detector, which is a Cavity Bifurcation Josephson Amplifier (CJBA) of high quality. Array of the qubits with such detectors can be connected to each other via a microwave transmission line, which in turn can be used both for initialization and for reading the state of qubits. We have analytically and numerically investigated the transport of a microwave signal in this system. The processes of generation of correlated photons and their detection are studied in detail.

2. Discussion of the results

Firstly, we studied the influence effect of the CJBA on the probability of excitation of the qubit state by a single-photon in a transmission line. For this purpose, the non-Hermitian Hamiltonian method [4] was used, which allows, in addition to the probability of excitation, to calculate the coefficients of transmission, reflection and the scattering wave function. At the same time, we have demonstrated that the measuring oscillator can shift the effective frequency of the qubit, at which the probability of its excitation is maximal, which coincides with the known results. Due to the fact that when calculating the array of qubits associated with JBA detectors, the analytical method of the non-Hermitian Hamiltonian quickly becomes cumbersome. We propose a generalized method for calculating the excitation probabilities, taking into account the phase surge of the wave during propagation from one qubit to another.

Secondly, we have studied the process of spontaneous emission of photons into the transmission line. In this case, correlated photons are generated, which can be detected by CJBA means of single-shot readout.

3. Conclusion

Our calculations show that the array of qubits with CJBA can act as a highly sensitive single-photon sensor of microwave photons. Based on the method of single reading of qubit states using a bifurcation amplifier, it is possible to determine which qubit from the array emitted or absorbed a photon into the transmission line by shifting the resonant frequency CJBA. In addition, we can trace the process of formation of correlated photonic statistics.

Acknowledgments

The work was supported by the grant of the President's program no.MK-2740.2021.1.2.

References

[1] Schmitt V et al. 2014 *Phys. Rev. A* **90** 062333
[2] Schaal S et al. 2020 *Phys. Rev. Lett.* **124** 067701
[3] Mallet F et al. 2009 *Nat Phys* **5** 791
[4] Greenberg Ya S and Shtygashev A A 2015 *Phys. Rev. A* **92** 063835

Investigation of graphene photodetectors for next generation telecommunication systems

P Bondareva[1], K Shein[1,2], M Rybin[3] , I Gayduchenko[2*] and G Goltsman[1,2]

[1]Moscow Pedagogical State University, Moscow, 119435, Russia;

[2]National Research University Higher School of Economics, Moscow, 101000, Russia;

[3]Prokhorov General Physics Institute, RAS, Moscow, 119991, Russia

[*]igorandg@gmail.com

Abstract. The aim of this study is to develop technology for manufacturing photodetectors based on graphene, optimize the device design and characterize the fabricated detectors. We report on our recent efforts towards development of photodetector based on a single layer graphene sheet on a silicon substrate. The bandwidth of measured devices exceeds 10 GHz, signal/noise ratio equals 45 dB.

1. Introduction

Currently, there has been found an urgent need of fast photodetectors operating in a wide spectral range in various fields of science, technology, medicine, as well as everyday life. Data traffic is increasing every day and thus, in turn, one requires the development of an ultra-fast element base. Graphene, due to its unique properties, is considered as a promising material for the creation of ultrafast photodetectors [1]. In this paper, we investigate ways to create graphene photodetectors in two practically important frequency bands for data transmission: 140 GHz (atmosphere transparency windows for wireless data transmission) and 1.55 microns data transmission over optical fiber.

2. Development of manufacturing process

Our detectors are two-electrode devices in which graphene acts as a conduction channel and has contact with two different metals (V and Au) on opposite sides. The first reported studies on measuring the performance of graphene detectors with asymmetric metallization have shown the promising results in use of such approach [1]. However, the sensitivity of such detectors is still more inferior to commercially available ones. Our detectors are made in the following way. At the first stage, metal marks were formed by standard methods of photolithography and electron beam sputtering. Then graphene was synthesized by the CVD method and transferred on the silicon substrate. Next contact electrodes were formed using positive electron lithography in a two-layer MMA 6% and PMMA 4% electronic resistor and e-beam evaporation of V/Au. To create the asymmetry of the device necessary for detecting radiation, we manufactured the electrodes in two different ways: one electrode was made with thin adhesion layer of

vanadium (1 nm) and another one with thick (10 nm). At the last stage we formed graphene channel using lithography and plasma etching in O_2.

Figure 1. THz photodetector based on graphene, designed with an antenna for coupling the sensing element with radiation.

Figure 1 shows a photo of a typical graphene-based THz detector equipped with an antenna. The chosen geometry of the electrodes allows one to create devices with a resistance close to 50 ohms, which is important for matching the sensor element to the incident radiation.

3. Results

The first measurements of the characteristics of manufactured photodetectors demonstrate the prospects of using graphene as a universal platform for the development of a new generation microwave device: the bandwidth exceeds 10 GHz, signal/noise ratio is 45 dB. Graphene is considered as a promising material for creating ultrafast photodetectors in a wide spectral range: from visible to terahertz.

Acknowledgments

The reported study was funded by RSF, project number 21-79-20084 21

References

[1] Koppens, F., Mueller, T., Avouris, P. *et al.* Photodetectors based on graphene, other two-dimensional materials and hybrid systems. *Nature Nanotech* **9,** 780–793 (2014).

Laser microscopy of periodic holographic structures with quantum dots

L N Borodina[1], V N Borisov[1], I A Vovk[1], A U Dubavik[1], A V Veniaminov[1] and A O Orlova[1]

[1] ITMO University, 14, Birzhevaya line, St.Petersburg, 199034 Russia
e-mail: lborodina141@gmail.com

Abstract. The results on luminescent properties of a polymer layer with periodic structure comprised of quantum dots studied with steady-state and time-resolved laser scanning microscopy demonstrate the absence of quantum dot aggregation, basing on luminescence mapping and luminescence decay analysis.

1. Introduction

Semiconductor colloidal quantum dots (QDs) are prominent for such their outstanding properties as high photoluminescence quantum yield, photostability, refractive index. Photopolymerizable compositions comprising QD help create efficient holographic structures including distributed feedback lasers and sensors. Any aggregation of QDs would deteriorate the luminescence efficiency and the accuracy of fine structure. In this contribution, surface stabilization by monomer molecule is used to prevent aggregation, and laser scanning microscopy is used to prove its absence.

2. Materials and methods

The semiconductor colloidal CdSe/ZnS QDs were synthesized in our lab. The composition comprised of 2-carboxyethyl acrylate (Aldrich № 552348) monomer, QDs, and Irgacure784 photoinitiator was placed between a microscopic glass slide and a cover slip. Spatially nonuniform polymerization of the composition layer was provided by holographic recording of a transmission grating with spatial period of 2.5μm using 532 nm Nd:YAG DPSS laser. The local transmittance and luminescence were visualized and measured using LSM 710 confocal laser scanning microscope (Carl Zeiss) with 405 nm diode laser. The luminescence decay of QDs in the holographic grating was monitored using a MicroTime 100 (PicoQuant) laser scanning microscope.

3. Results

To ensure the compatibility of QDs with the surrounding medium, monomer molecules were applied as stabilizer identical to those polymerized in the course of recording. A periodical structure (Figure 1) of luminescent layers without any noticeable aggregates was formed by holographic recording. Figure 2 shows the respective intensity profiles of photoluminescence and transmitted light along the grating vector, in which maxima and minima respectively manifest the areas of high QD concentration originating from photoinduced diffusion.

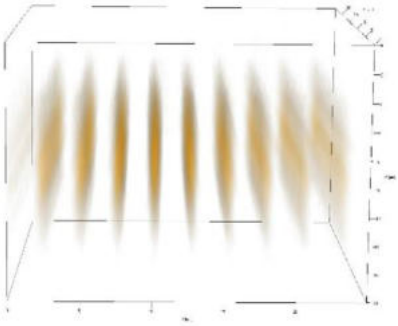

Figure 1. Volumetric image of a 10 μm-thick grating with QDs obtained using LSM 710 laser scanning microscope when scanning in three coordinates with laser radiation at a wavelength of 405 nm.

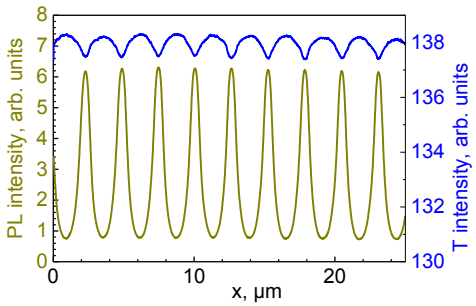

Figure 2. Photoluminescence and transmitted light (405 nm) intensity profiles along the holographic grating vector.

The spatial distribution of luminescence decay times shaped slightly different from the luminescent view of the grating (Figure 3) implies the difference in decay dynamics in the regions of high and low QD concentration, hence energy transfer and aggregation. However the apparent long-time contribution is more likely due to relatively high noise in darker areas, and the absence of significant wavelength dependence of decay times regardless of the QD concentration (Figure 4) evidences for negligible efficiencies of Förster energy transfer, hence aggregation.

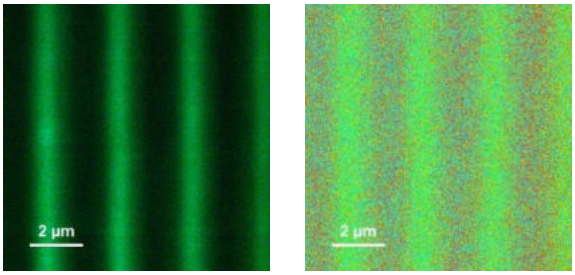

(a) (b)

Figure 3. Luminescence image (a) and fluorescence lifetime image (b) of a grating with QDs.

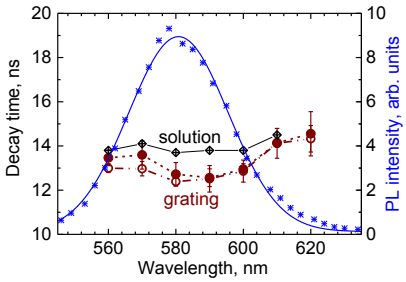

Figure 4. Dependence of the average luminescence decay times on the detection wavelength within the luminescence band.

4. Conclusion

Using steady-state and time-resolved luminescent laser scanning microscopy, we studied the polymer film with regular spatial distribution of QDs that originated from exposure to an interference pattern, photopolymerization, and photoinduced diffusion. The same substance was used both as a surface stabilizer and a monomer to be photopolymerized, thus making QDs fully compatible with the surrounding. The microscopic luminescence visualization of the periodic structure indicates the absence of micrometer-scale aggregates, while the absence of spectral dependence of luminescence decay time evidences against any aggregation of QDs in the regions of either high or low concentration.

Acknowledgments

This work was supported by the Ministry of Science and Higher Education of the Russian Federation: state contracts no. 2019-1080 (L. Borodina, A. Dubavik, A. Veniaminov, A. Orlova) and RPMA grant of School of Physics and Engineering of ITMO University (L. Borodina, I. Vovk).
The authors are grateful to Dr. Elena Ushakova of ITMO University for sharing her knowledge.

Hybrid Tamm-microcavity optical modes with tunable Q-factor

D. S. Buzin[1,2], P. S. Pankin[1,2], G. A. Romanenko[1,3], A. I. Krasnov[1,2], V. S. Sutormin[1,2], S. V. Nabol[1,2], I. A. Tambasov[1], F. V. Zelenov[4,3], A. N. Masuygin[4,3], S. Ya. Vetrov[2,1], I. V. Timofeev[1,2]

[1]Kirensky Institute of Physics, FRC KSC SB RAS, Krasnoyarsk 660036, Russia
[2]Siberian Federal University, Krasnoyarsk 660041, Russia
[3]Siberian State University of Science and Technology, Krasnoyarsk 660037, Russia
[4]AO NPP Radiosvyaz, 660021 Krasnoyarsk, Russia

daniil.buzin.00@mail.ru

Abstract. Bound states in the continuum (BICs) have been investigated in systems of various physical origin. One of them is photonics. BICs can be found in microcavities based on one-dimensional photonic crystal with anisotropic layers. High Q-factor of the microcavity corresponds to narrow spectral lines observed in the vicinity of BIC. By changing the orientation of the optical axis of the anisotropic layer, one can control the Q-factor of the microcavity without changing its geometrical parameters. The paper paves the way to control the Q-factor of the microcavity, using voltage, heating or mechanical rotation of the microcavity.

1. Introduction

Bound state in the continuum (BIC) is a localized state in an open system. The state energy lies in the continuous energy spectrum, but the state is completely decoupled from the continuum [1]. Wigner and von Neumann in 1929 for the first time discovered special oscillating potentials for a localized particle with an energy in the continuous spectrum above the potential barrier. BIC have also found applications in photonic devices, lasers, solar cells and sensors [1].

2. Model

The structure under study (Fig. 1, left) is a photonic crystal (PhC) bounded by a golden layer on one side. A PhC has a defect layer filled with anisotropic material, such as liquid crystal (LC). At this layer the microcavity modes can be excited. The anisotropic layer is located between two ITO conductive layers, which make it possible to control the LC director orientation by external voltage. The PhC structure consists of periodically arranged layers of silicon nitride (Si_3N_4) and silicon oxide (SiO_2). At the interface between the PhC and the golden layer, the Tamm plasmon polariton (TPP) can be excited [2]. The number of periods of the PhC structure between the LC and golden layer is chosen to provide the optimal coupling coefficient between the TPP and the microcavity mode.

3. BIC in the PhC structure

If the radiation is introduced into the structure at the Brewster angle, the TM-polarized wave passes through the PhC and is not localized in the defect layer. On the contrary, the TE-polarized wave

diffracts on the periodic PhC structure. This Bragg reflection allows it to be localized in the defect layer. Such localized modes are called symmetry-protected BICs. The anisotropic layer makes it possible to mix the TM and TE polarizations and shift the mode in the vicinity of the BIC position. When the LC director rotates relative to the plane of incidence, a channel for energy relaxation into the continuum opens due to the transition of the TE polarization to the TM polarization. Figure 1 (right) shows the reflection spectrum of the structure under study depending on the angle of rotation of the optical axis of the defect layer relative to the plane of incidence of the TM-wave. One can see the collapses of the spectral linewidth at the rotation angles equal to 0 and $\pi/2$. Narrow spectral lines can be seen in the vicinity of these points, which indicates a high Q-factor of the microcavity. At some angles φ other than 0 and $\pi/2$, the collapse of the spectral lines also occurs, which indicates the realization of the Friedrich-Wintgen BIC type [3]. By changing the orientation of the optical axis of the defect layer, one can control the Q-factor of the microcavity. The LC material response is extremely sensitive to external influences. By applying an external electric field to it, or by heating it, one can control its effective refractive index. This leads to a change in the coupling value between the TM- and TE-waves, and as a result, to a change of the Q-factor of the microcavity.

The structure under study can be considered as two coupled resonators in which the TPP and the microcavity mode are separately excited. Figure 1 (right) shows the splitting of the resonance lines in the 600 nm region due to the coupling between the TPP and the microcavity mode. This leads to the formation of hybrid Tamm modes. The value of the spectral splitting can be controlled by changing the number of PhC periods between the defect layer and the golden layer.

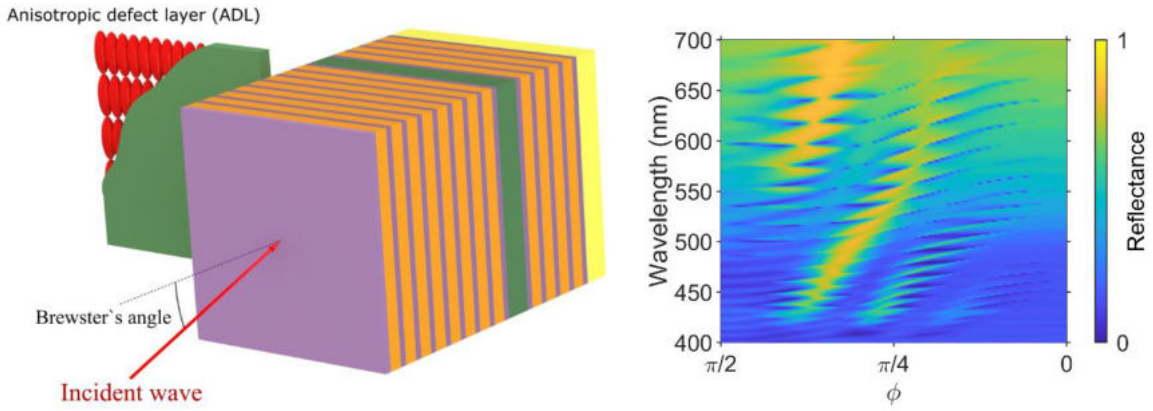

Fig.1. Left: Schematic model of the structure under study. Right: Reflectance spectrum of the PC structure depending on the optical axis rotation angle of the LC layer relative to the wave incidence plane.

Acknowledgments

This research was funded by the Russian Science Foundation (project no. 22-22-00687).

References

[1] Hsu, C. W., Zhen, B., Stone, A. D., Joannopoulos, J. D., & Soljačić, M. (2016). Bound states in the continuum. Nature Reviews Materials, 1(9), 1-13. number)' style.

[2] Kaliteevski, M., Iorsh, I., Brand, S., Abram, R. A., Chamberlain, J. M., Kavokin, A. V., & Shelykh, I. A. (2007). Tamm plasmon-polaritons: Possible electromagnetic states at the interface of a metal and a dielectric Bragg mirror. Physical Review B, 76(16), 165415.

[3] Pankin, P. S., Wu, B. R., Yang, J. H., Chen, K. P., Timofeev, I. V., & Sadreev, A. F. (2020). One-dimensional photonic bound states in the continuum. Communications Physics, 3(1), 1-8.

Luminescent properties of carbon dots from o-phenylenediamine under excitation at 800 nm

A A Vedernikova[1], **A A Arefina**[1], **A O Ismagilov**[1], **E V Ushakova**[1]

[1]ITMO University, 197101 Saint Petersburg, Russia

E-mail: vvedernikova.anna@gmail.com, iaarefina@itmo.ru

Abstract. In recent years, attention to carbon dots (CDs) has increased due to their unique properties, which can find applications in many fields from bioimaging to optoelectronics. In this study, the CDs based on o-phenylenediamine are obtained by solvothermal method. The change in absorption and luminescence spectra for CDs from o-phenylenediamine and various additional precursors were studied in detail. In addition to the expected emission under ultraviolet excitation (400 nm), this CDs are able to show a specific up-converted photoluminescence signal under near-infrared excitation.

1. Introduction

Carbon dots (CDs) can be an excellent candidate as a fluorescent agent for bioimaging, because of their unique optical properties such as low cost, biocompatibility, high chemical stability, and variety of functionalization [1]. The CDs optical properties can be controlled by using various precursors and solvents together with varying synthesis parameters, as temperature, reaction time, and pH of the medium [2]. Thus, it is possible to «tune» the luminescence for specific tasks. The key aspect for bioimaging is that the emissive probes should be excited and capable to emit light in the infrared region of the spectrum. Up-converted photoluminecence (PL) offers special advantage for bioimaging such as deeper penetration, lower photodamage and autofluorescence [3].

In this work, by varying additional precursors, solvents and their ratio, CDs with upconversion PL are obtained by solvothermal synthesis. As a main precursor an o-phenylenediamine (o-pd) is chosen because of it has molecular structure that can produce large conjugated sp^2-domains. Furthermore, o-pd can play role of a nitrogen source due to amine groups; this may result in narrow-bandgap CDs with longer-wavelength emission.

2. Methods

2.1. Sample synthesis

The CDs were synthesized by the solvothermal synthesis method described in.[4]. The o-pd was chosen as the main precursor, additional precursors were added to study their impact on CDs optical properties. Four samples of CDs were obtained: o-pd in water (CD-1), o-pd with benzoic acid (0.56 g) in ethanol (CD-2), o-pd with thiourea (0.7 g) in water (CD-3), and o-pd with thiourea (0.7 g) in ethanol (CD-4). The mixture of precursors was solvothermally heated to 180°C and kept in autoclave for 6 h. After the reaction, the autoclave was naturally cooled down to room temperature. The colloidal solutions were purified from large particles and agglomerates using a filter with a 0.22 μm membrane. Then CDs were dialyzed for 24 h against water to purify from unreacted precursors and molecular fluorophores.

2.2. Characterization

The absorption and PL spectra of the solutions were measured on a spectrophotometer UV-3600 (Shimadzu, Kyoto, Japan) and spectrofluorometer Cary Eclipse (Varian, Australia), respectively.

3. Results

The abortion (a) and PL spectra under excitation at 400 (b) and 800 (c) nm for all samples are shown in Figure 1. The broad absorption band (420 - 450 nm) might be assigned to surface groups. The bands at 230 – 250 nm and 270 – 290 nm should be ascribed to the π→π* and n→π* transitions. An additional absorption peak at 350 nm is observed for sample CD-4.

Form the PL spectra, the PL band is almost independent from the excitation wavelength and is observed at 540, 570, and 460 nm for CD-1, CD-2, and CD-3. The addition of benzoic acid (sample CD-2) results in the redshift of the PL band by 30 nm. On the contrary, the addition of thiourea (sample CD-3) results in the PL blueshift by almost 80 nm. Besides, the thiourea in the synthesis leads to the increased PL intensity under 400 and 800 nm excitation. Compare CD-3 and CD-4, the change of the solvent from water to ethanol results in the redshift of the PL band to 540 nm together with a widening and further 20 nm redshift of the PL band excited at 800 nm.

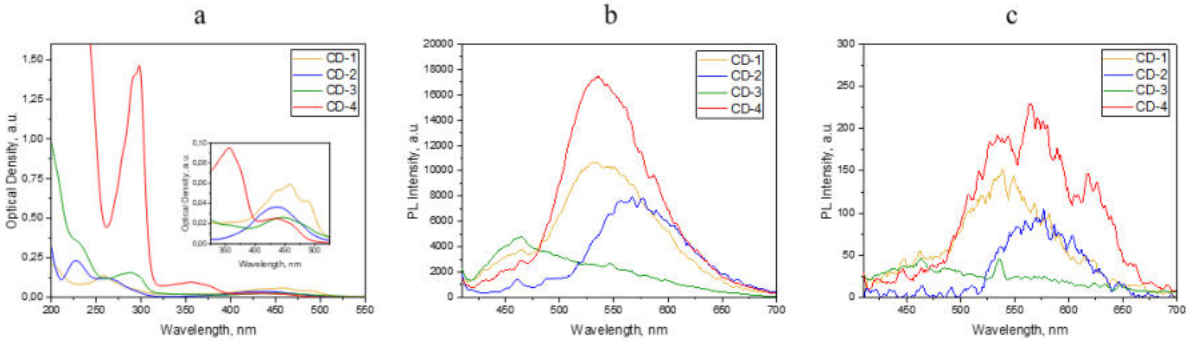

Figure 1 (a,b,c). (a) Absorption spectra of CDs; **(b)** PL spectra of CDs under 400 nm excitation, normalized to absorption; **(c)** PL spectra of CDs under 800 nm excitation.

Acknowledgments

The study is funded by RPMA grant of School of Physics and Engineering of ITMO University.

References

[1] Pan L, Sun S, Zhang L, Jiang K and Lin H 2016 Near-infrared emissive carbon dots for two-photon fluorescence bioimaging *Nanoscale* 8 17350–6

[2] Li D, Jing P, Sun L, An Y, Shan X, Lu X, Zhou D, Han D, Shen D, Zhai Y, Qu S, Zbořil R and Rogach A L 2018 Near-Infrared Excitation/Emission and Multiphoton-Induced Fluorescence of Carbon Dots *Advanced Materials* 30 1705913

[3] Mehta V N, Desai M L, Basu H, Kumar Singhal R and Kailasa S K 2021 Recent developments on fluorescent hybrid nanomaterials for metal ions sensing and bioimaging applications: A review *Journal of Molecular Liquids* 333 115950

[4] Lin S, Lin C, He M, Yuan R, Zhang Y, Zhou Y, Xiang W and Liang X 2017 Solvatochromism of bright carbon dots with tunable long-wavelength emission from green to red and their application as solid-state materials for warm WLEDs *RSC Advances* **7** 41552–60

Fabrication of diffraction gratings for generation of OAM light.

I O Venediktov[1,2], K O Sedykh[2,3], P I Zolotov[1,2], N S Kaurova[2], E S Lebedeva[2], G N Goltsman[1,2,3,4] and D V Sych[1,5,6]

[1]National Research University Higher School of Economics, Moscow 101000, Russia
[2]Department of Physics, Moscow Pedagogical State University, Moscow 119435, Russia
[3]NTI Center for Quantum Communications, National University of Science and Technology MISiS, Moscow 119049, Russia
[4]Russian Quantum Center, Skolkovo 143025, Moscow, Russia
[5]P. N. Lebedev Physical Institute, Moscow 119991, Russia
[6]Sirius University of Science and Technology, 1 Olympic Ave, 354340, Sochi, Russia

Ilia1999ven@gmail.com

Abstract. In this work we describe fabrication of diffraction gratings for generation of light with orbital angular momentum (OAM). OAM light characterized by topological charge l and modes with different l are orthogonal, which makes OAM light useful in quantum communication and tomography. We demonstrate fabrication route of diffraction gratings with computer generated hologram pattern on sapphire substrate and niobium reflective coat for generation of OAM light of visible spectrum.

1. Introduction

Light has 2 angular momentum characteristics - spin angular momentum and orbital angular momentum. Usually light has only spin angular momentum, because wave vector $\boldsymbol{k}$ has no component perpendicular to the direction of propagation. Light with non zero orbital angular momentum has linear phase dependence on azimthal angle through constant l, which leads to apperance of $\boldsymbol{k}$ component tangent to phase plane. Mode with defined l can be described in terms of generalized Laguerre polinimial of order l. Those modes are orthogonal which makes modes with different l perfectly distinguishable and allows us to use OAM light for quantum communication and quantum tomography. There are several ways of generating OAM light such as spiral phase plates [1], cylindrical mode converters [2], Q-plates [3], pitch-fork holograms [4]. The last method is using diffraction gratings for generating OAM light. Pattern for this holograms can be obtained by computing interference pattern of OAM light and plane wave. Then we can load those patterns on SLM and use it as diffraction grating, which allows to change patterns very fast. But also we can just make solid diffraction gratings out of some transperent material with reflective coat material. This method has advantages over SLM because of accuracy of produced gratings.

2. Fabrication route of diffraction grating

Firstly we need to compute pattern for diffraction grating. For this we need to calculate interference pattern of OAM light and plane wave. OAM and plane wave must be represented just by their phase terms, not taking into account spatial amplitude distibution (2).

$$I(x,y) = \left| (e^{il\theta} + e^{i\vec{k}\cdot\vec{r}}) \right|^2 \tag{2}$$

The plane wave must be at some angle relative to OAM light to form strip structure. Amplitudes of OAM and plane wave must be equal for high contrast of the pattern. As substrate for gratings double polished sapphire was used and NbN was used as reflective coat. Width of sapphire is 400 μm (±5%) and width of NbN is 60 nm. NbN was deposed by magnetron deposition in nitrogen atmosphere and then was etched in SF_6/Ar plasma forming diffraction pattern. The darkest parts of interference picture on figure 1 were etched, therefore gratings were designed for transmision diffraction.

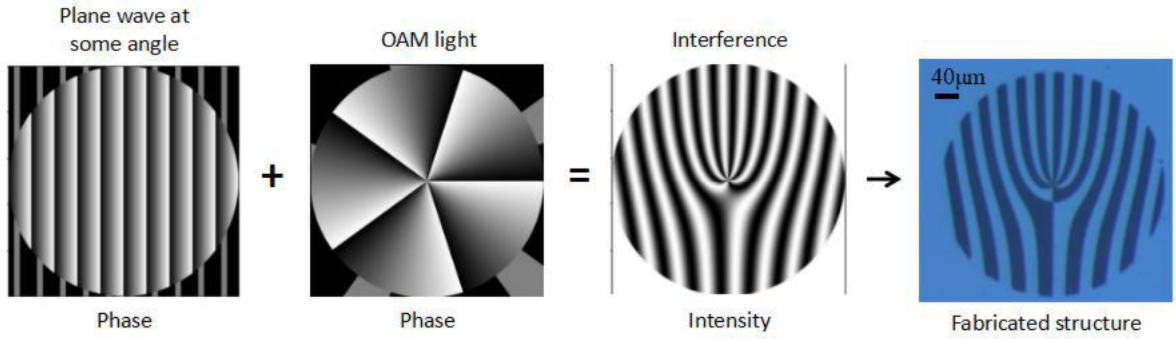

Figure 1. Computing of hologram pattern and fabricated diffraction grating for *l*=5

3. Fabricated stucture

We fabricated array of diffraction gratings on sapphire plate. On the structure we arrange 12 fork-diffraction gratings for different number of *l* and with different grating period. Periods of 20μm and 30μm represented. Several periods were made for testing how it will affect generation of OAM. From the micropicture on figure 1 it can be seen that pattern was produced accurately and all irregularities are order of wavelenght and can't affect diffraction pattern.

4. Conclusion

We fabricated array of diffraction gratings for generation of OAM light. Different grating periods and topological charges were represented. Our work has a great potential for developing a structure for generating of light with angular momentum.

Acknowledgments

We thank Dr. Ledesma and Mr. Pabon for sharing program for CGH generating and also useful literature. We acknowledge support of the Russian Foundation for Basic Research Project No. 21 72 10117.

References

[1] Beijersbergen, M W, Coerwinkel R P C, Kristensen, M, Woerdman, J P, *Optics Communications* **112** (5–6): 321 (1994)

[2] Allen, L.; Beijersbergen, M.; Spreeuw, R.; Woerdman, J. (1992). . *Phys. Rev.* A **45** (11): 8185–8189 (1992)

[3] Marrucci L, Manzo C, Paparo D *Physical Review Letters* **96** (16): 163905 (2006)

[4] Heckenberg N R, McDuff R, Smith C P, White A G *Optics Letters* **17** (3): 221 (1992)

Modulation of quantum beat signals upon photoionization of Xe isotopes

E A Viktorov[1*], P Yu Serdobintsev[1], N N Bezuglov[1,2] and K Miculis[2,3]

[1] Department of Optics, Faculty of Physics, St. Petersburg State University, 198504, St. Petersburg, Russia
[2] University of Latvia, Institute of Atomic Physics and Spectroscopy, LV-1586 Riga, Latvia
[3] Moscow Engineering Physics Institute, 115409, Moscow, Russia

*eaviktorov@yandex.com

Abstract. Photoionization processes involving Xe atoms in the presence of an external magnetic field were analyzed in our previous studies. It was shown that the modulation of quantum beats in the observed electronic photo signals could not be explained by the Paschen-Back effect accounting for fine-structure levels only. In the current work, ionized Xe^+ isotopes are used as the output channel of photoionization. By comparing the temporal partial signals in the mass spectra of the Xe^+ isotopes, it was possible to explain the modulation of quantum beats in ion fluxes as a consequence of the presence of the hyperfine structure in the Zeeman components of the ^{129}Xe isotope.

1. Introduction

Excitation of polarized states of atoms by polarized light along with accompanying analysis of fluorescence signals allows one to significantly expand the possibilities of both optical diagnostics of gaseous media [1] and its applied aspects [2]. The use of bound-free transitions gives, due to almost 100% registration of photoelectrons, the series of benefits, greatly increasing the likelihood of observing subtle physical effects [3]. In the current work, the «pump-probe» experiment is used to study the $5p^5(^2P_{3/2})6p[^3/_2]_2$ ($79212{,}5 cm^{-1}$) state of the Xe isotopes in a supersonic beam. Previously, using a similar scheme, we observed the modulation of the quantum beat signals upon Xe photoionization and revealed that the nature of this modulation cannot be due to the quadratic Paschen-Beck effect. The last one turns out to be powerless amid a fine splitting of quantum states for the external magnetic field of the magnitude about 1 Tesla [4]. Here we experimentally demonstrate the occurrence of the collapse of atomic polarized states, which is due to the hyperfine structure of the Xe isotopes atomic levels.

2. Experimental setup

The monokinetic beam of Xe atoms is created by using a supersonic nozzle. This atomic beam is exposed to a two-photon excitation (252.5nm) and a two-photon ionization (795nm) applying the horizontal polarization light. The two-photon ionization was chosen based on the requirement that the ionization by the probe pulse should not be overshadowed by the three-photon ionization of the pump laser. Such a condition is associated with the registration of the ion fluxes intensities integrated over

all channels. The horizontal polarization leads to beats at twice the Larmor frequency, which makes it possible to increase the number of periods in the scanning time interval. Time-of-flight mass spectrometer determines the isotopic composition of the appearing ions during the photoionization process. The corresponding mass spectra are displayed in figure 1 (a).

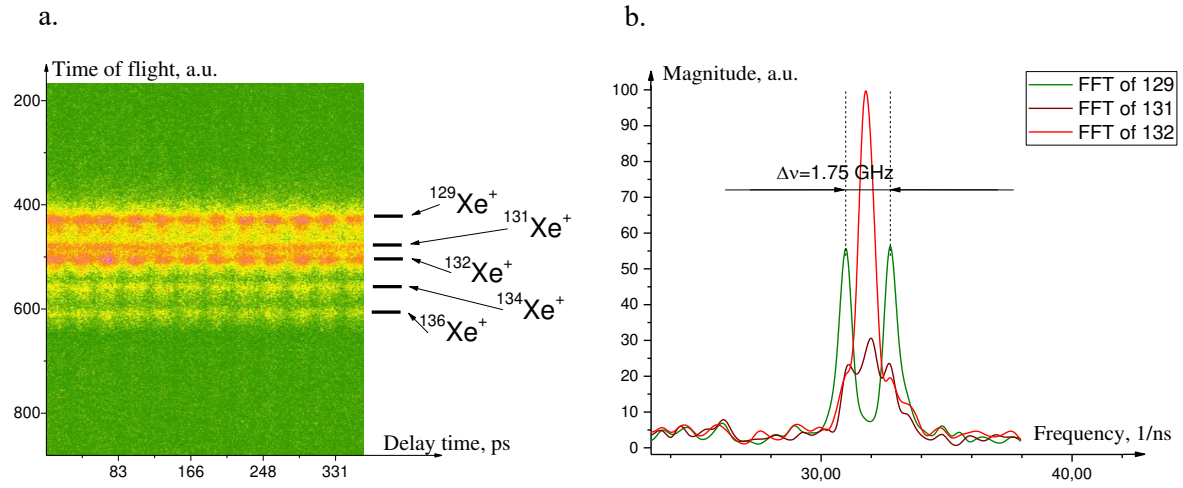

Figure 1. (a) Mass spectra of ionized Xe^+ isotopes depending on the delay time. (b) Fourier spectra of signals from ionized Xe^+ isotopes.

Fourier spectra of partial signals from each isotope provide the ability to determine both the frequency of the quantum beats and the modulation frequencies for various Xe isotopes. (Figure 1.b).

3. Conclusion

The experimentally observed modulation of the quantum beats signals manifests itself in the integral signal of Xe^+ isotopes with odd masses 129, 131. In contrast, there is no such signal modulation for isotopes with even masses 132, 134, 136. Note that the most pronounced modulation structure is inherent in the ^{129}Xe isotope case.

Acknowledgments. This work was supported by the Latvian Science Council Grant No lzp-2019/1-0280. The equipment of the Resource Center "Physical Methods of Surface Investigation" of the St. Petersburg State University was used in experiments.

References

[1] Auzinsh M, Budker D and Rochester S 2010 Optically Polarized Atoms. Understanding light atom interactions (New York: Oxford University Press)

[2] Aleksandrov E B, Chaika M P and Khvostenko G I 1993 Interference of Atomic States. Springer Series on Atoms and Plasmas vol 7 (Berlin: Springer-Verlag)

[3] Porfido N, Bezuglov N N, Bruvelis M, Shayeganrad G, Birindelli S, Tantussi F, Guerri I, Viteau M, Fioretti A, Ciampini D, Allegrini M, Arimondo E, Ekers A and Fuso F 2015 Phys. Rev. A 92 043408

[4] Viktorov E A, Dimitrijević M S, Srećković V A, Bezuglov N N, Miculis K, Pastor A A and Serdobintsev P Yu 2021 Eur. Phys. J. D 75 13 174003

State preparation intensity fluctuations in QKD

Arina Gavrilovich[1,2,3,4] **and Andrey Tayduganov**[1,4]

[1] QRate, Skolkovo, Moscow 143025, Russia
[2] Russian Quantum Center, Skolkovo, 143026, Russia
[3] Moscow Institute of Physics and Technology, Dolgoprudny, 141700, Russia
[4] NTI Center for Quantum Communications, National University of Science and Technology MISiS, Moscow 119049, Russia

E-mail: gavrilovich.aa@phystech.edu

Abstract. Quantum key distribution (QKD) is a state-of-the-art technology for secure communication. QKD is proven to be unconditionally secure against any attacks allowed by quantum physics. However, the realistic device imperfections create a mismatch between theoretical model used in proofs and practical setup which potentially compromises the security of the system. Here we investigate the dependence of the key generation rate on pulse intensity fluctuations. We show that the deviation from ideal case is not significant if the integral output power control is precise enough.

1. Introduction

The security of QKD relies on fundamental laws of physics and is proven mathematically [1]. However, any implementation of QKD differs from an ideal mathematical model due to various real-life imperfections. Although in the QKD framework we do not calculate explicitly what happens in the quantum channel between users, it is crucial to accurately model the outgoing pulses. Any gap between theoretical assumptions and a real setup can be exploited by an eavesdropper to gain additional information and compromise the protocol.

In this work, we develop a straightforward approach for including the intensity fluctuations during Alice's state preparation into the BB84 decoy-state protocol model [2] and derive a refined estimation of the secret key rate.

2. Methods

Our experimental setup for weak coherent state preparation on Alice's side is depicted in Fig. 1. The MZI output intensity is modelled as function of the modulation voltage U,

$$I(U) = I_0 \cos^2\left(\frac{\pi U}{2U_\pi}\right), \tag{1}$$

where I_0 is the input intensity, and U_π is some fixed constant. The desired signal and decoy intensities $\alpha = \{\mu, \nu_1, \nu_2\}$ are set by applying the appropriate voltage U_α and fixing the attenuation ξ of ATT such that $I(U_\alpha) \times 10^{-\xi/10} = \alpha$.

To monitor and control the intensities in time, the photodetector PD that measures the integral output power W during one second is used. The relative deviation δW due to intensity fluctuations can be expressed as

$$\frac{\sum_\alpha p_\alpha \big[I(U_\alpha + \delta U) - I(U_\alpha)\big]}{\sum_\alpha p_\alpha I(U_\alpha)} = \frac{\delta W}{W} \tag{2}$$

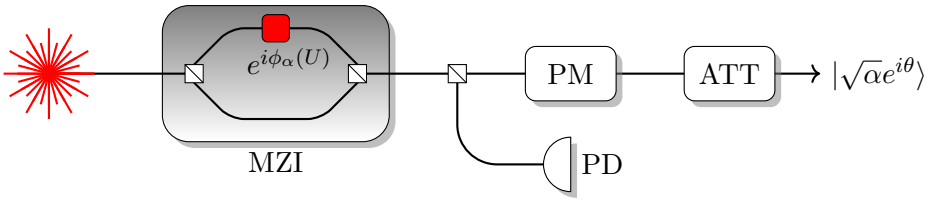

Figure 1: Weak coherent state preparation scheme: Mach–Zehnder interferometer (MZI), photodetector (PD), phase modulator (PM) for bit and basis choice, and fixed attenuator (ATT)

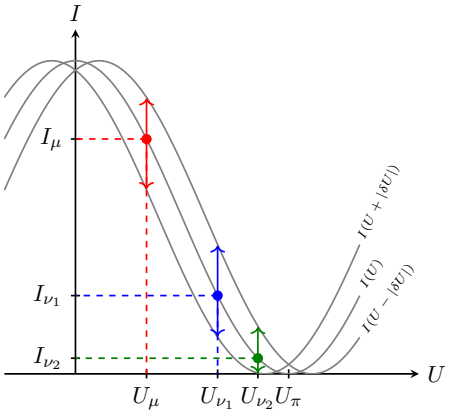

Figure 2: Dependence of light intensity after Mach–Zehnder interferometer on phase modulator voltage.

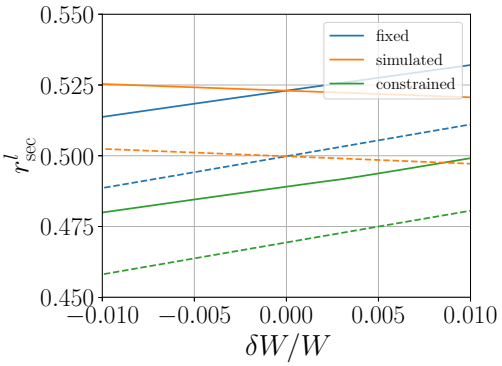

Figure 3: Secret key rate (per bit) as function of wattage deviation for fixed, simulated and constrained intensities. Solid (dashed) lines correspond to 50(100) km line length.

where p_α is the α–pulse generation probability. Using the measured $\delta W/W$ one can determine δU by solving Eq. (2) and correct the voltage and hence the floated intensities.

We simulate the intensity fluctuations as functions of $\delta W/W$ using Eqs. (1) and (2), and compute the secret key rate (per bit) $r^l_{\rm sec}$ in various scenarios (see Fig. 3) : for fixed initial (in blue), true shifted (in orange), and unknown but constrained (in green) intensities. The later is the most conservative estimation and is defined as

$$r^l_{\rm sec} = \min_{I_\alpha \in [I^{\rm min}_\alpha, I^{\rm max}_\alpha]} r^l_{\rm sec}(\{I_\alpha\})\,, \tag{3}$$

where $I^{\rm min}_\alpha$ and $I^{\rm max}_\alpha$ are determined for realistic experimental value $|\delta W|/W \leq 0.01$.

3. Results and discussion

The calculated secret key rate for the described cases is shown in Fig. 3. From the results of the simulation one can see that for $|\delta W|/W \leq 0.01$ the key rate drops insignificantly and the key generation is still possible. Thus, we demonstrate that the refined analysis confirms practicability of QKD under condition that we monitor and control the light power W within few percents.

References

[1] Shor P W and Preskill J 2000 *Physical Review Letters* **85** 441–444
[2] Ma X, Qi B, Zhao Y and Lo H K 2005 *Physical Review A* **72**

On whispering gallery mode crystalline microresonators polishing techniques

M.L. Galkin[1,2], A.N. Danilin[1,3], I.K. Gorelov[1], K.N. Minkov[1]

1 Russian Quantum Center
2 Skolkovo Institute of Science and Technology
3 Moscow State University

galkinmax1997@gmail.com

Abstract. In this work we compared techniques that are exploited in high Q-factor crystalline whispering gallery mode (WGM) microresonators fabrication. Among the other processing approaches chemico-mechanical polishing apparently seems as the time-saving and effective.

1. Introduction

WGM microresonators have the highest quality factor [1] in comparison with all other types of optical microresonators and have a broad range of applications in modern photonics (narrow-bandwidth lasers, frequency standards, optical combs). The Q-factor of a WGM microresonator is in directly dependence on its surface roughness [2, 3], so the purpose of this work is comparison of existing methods of treating surface of crystalline whispering gallery mode (WGM) microresonators and suggestion of a new one.

2. Comparison of Polishing Techniques

For optical surfaces the following treatment methods are widely used: chemical polishing (CP) [3], electrochemical polishing (ECP), mechanical polishing (MP) [4], thermomechanical polishing (TMP) [2], laser polishing [5], electron-beam polishing (EBP) and ion-beam polishing (IBP) [3].

These processing types find their applications in treatment of various optical components, however, considering their usage for microresonators polishing each of these methods exhibits certain drawbacks. CP does not allow to uniformly control the etching depth over the entire sample area, which is especially critical for cylindrical objects. During MP particles of diamond suspension scratch the surface with their edges, which cannot be eliminated by reducing the particle size and seems to be the fundamental limitation of this method. EHP is only suitable for conductive materials such as steels. TMP method includes MP followed by several quite long (more, than 24 hours) cycles of high-temperature annealing for reduction of crystal structural defects, which can result in appearance of mechanical stresses in the crystal. Particular attention in MP must be paid to isolation from air, humidity and contamination of any kind, in addition, special expensive equipment is required. LP implies glass surface heating with a laser beam so that its viscosity decreases and the surface is smoothed by surface tension forces [5]. Crystalline materials are for this reason obviously not treatable by LP. EBP and IBP [6] involve evaporation (atomization under the action of a beam) of a target of the same material from which the processed surface is made, with subsequent deposition of the atomized substance on it. This method is not suitable for the treatment of single crystals, which microresonators are made of.

3. Proposed Technique

An alternative method is chemico-mechanical polishing (CMP) [6]. CMP method do not suffer from the above disadvantages, especially in comparison with mechanical polishing, because CMP polishing suspension consists of liquid oxidizer and nanometer-size round solid amorphous silicon dioxide (SiO_2) particles, which have no shock impact on the surface. The particles remove only the layers that are prepared by the etchant. Crystals undergo CMP treatment without tension, compression, torsion or scratching and the simultaneous chemical dissolution reduces or removes mechanically stressed areas of the crystal. The CMP method has several advantages over other methods: allowance for less surface roughness due to the use of amorphous particles; reduction of cleaning stages number and easy resonator surface quality control; significant polishing time reduction; polishing process automatization availability; applicability to a wide range of crystalline materials.

4. Experimental Results

In the experiment we have compared chemico-mechanical polishing (CMP) with mechanical polishing (MP) by diamond suspension. The surface roughness after CMP was about RMS = 0.6 nm, when polishing with diamond suspensions the roughness value was about RMS = 0.8 nm, with comparable quality factors of the resonators. In case of CMP the measured quality factor of not lower than $4 \cdot 10^8$ can be obtained.

5. Discussion

CMP method turns out to be suitable for fabrication of high-frequency crystalline WGM microresonators with quality factor not lower than $4 \cdot 10^8$. Application of CMP method contributes to significant reduction of polishing time and improvement of surface quality of structures with complex shape and will allow in future to automate the process of microresonators manufacturing.

Acknowledgments

The work was performed using the equipment of the Center for Collective Use VNIIOFI (ckp.vniiofi.ru). Work supported by the Russian Science Foundation (project No. 21-72-00132).

References

[1] Microresonators with giant quality factor / M.L. Gorodetsky. M., 2011. 415 p.

[2] Matsko A.B., Savchenkov A.A., Strekalov D., Ilchenko V.S., Yu N. and Maleki L., "Fabrication, Characterization and Applications of Crystalline Whispering Gallery Mode Resonators," 2007 9th International Conference on Transparent Optical Networks, 2007, pp. 50-54.

[3] Maia J.M., Amorim V.A., Viveiros D. et al. Femtosecond laser micromachining of an optofluidics-based monolithic whispering-gallery mode resonator coupled to a suspended waveguide. Sci Rep 11, 9128 (2021).

[4] Min'kov K.N., Likhachev G.V., Pavlov at al. Manufacturing of high-quality crystalline whispering gallery mode microresonators using single point diamond turning. // Journal of Optical Technology, 2021, Vol. 88, pp. 84-92.

[5] A. Krishnan and F. Fang, "Review on mechanism and process of surface polishing using lasers", Frontiers of Mechanical Engineering, vol. 14, no. 3, pp. 299-319, 2019.

[6] Stognij A. I., Novitski N. N., Stukalov O. M. Ion Beam Polished Nanodimensional Relief on the Surface of Optical Materials //Technical Physics Letters. – 2002. – Т. 28. – №. 1

[7] Artemov, A.S. Chemicomechanical polishing of material. Nanotechnol. Russia 6, 419 (2011).

[8] Shitikov A.E., Galiev R.R., Kondratiev N.M., Lobanov V.E., Min'kov K.N., Matsko A.B. and Bilenko I.A., "Optimization of the self-injection locking and resonator characterisation in this regime", Laser Resonators, Microresonators, and Beam Control XXIII, 2021.

Atomic force lithography for fabrication of high-Q planar perovskite polaritonic cavities

N. Glebov[1], M. Masharin[1], A. Samusev[1]

[1]ITMO University, School of Physics and Engineering, St. Petersburg, 197101, Russia

nikita.glebov@metalab.ifmo.ru

Abstract. Halide perovskites are currently of great interest due to their strong room-temperature excitonic response. Coupling exciton resonance in a perovskite material to a high-Q optical cavity may give rise to half-light half-matter quasiparticles – exciton-polaritons. Their ability to both couple with light and interact with each other opens the way to realization of various highly nonlinear and energy-efficient devices such as all-optical switches, transistors, etc. Until recently, such systems were based on bulk vertical Bragg cavities. In this work, we demonstrate that atomic force lithography applied to a thin quazi-2D perovskite $(PEA)_2PbI_4$ (PEA - phenylethylammonium, Pb - plumbum, I - iodine) film is a powerful tool for highly controllable and precise fabrication of planar polaritonic cavities. Using angle-resolved optical reflectance and photoluminescence measurements, we confirm the realization of strong coupling between exciton resonance and leaky optical modes supported by fabricated periodic structure at room temperature. Our results open new path towards realization of planar high-quality perovskite-based polaritonic devices.

1. Introduction

Photonics deals with the fundamental and applied aspects of operation with optical signals, as well as the creation of future energy-efficient optical computing devices. In order to realize such devices, where light is controlled by light, one should design systems with strong optical nonlinearity. Searching for new simple materials that are easy to fabricate and are compatible with the planar geometry is one of the most important tasks of modern photonics. In this regard, systems that support strong light-matter coupling and exciton-polariton modes are very attractive as their nonlinear response can be 3-4 orders of magnitude higher than in alternative materials where photons and electronic excitations are coupled weakly [1]. First pioneering devices based on this principle have been fabricated with GaAs. However, such structures are characterized by a highly complex fabrication process and low (cryogenic) working temperature range. Currently, quazi-2D halide perovskites are considered as promising materials due to their easy and low-cost fabrication along with their outstanding excitonic properties, which allow for realization of room-temperature polaritons [2]. In this work, we for the first time demonstrate a unique method of perovskite atomic force lithography allowing to fabricate high-quality planar polaritonic cavities based on thin 2D perovskite films.

2. Results

To synthesize a thin $(PEA)_2PbI_4$ film, a solution was prepared from PEAI and PbI_2 salts in a ratio of 2:1 to maintain the stoichiometry of the final solution with a molarity of 0.3 M. The salts were hung in a vial in a dry atmosphere of a glove box. The mass of PEAI salts was 149.5 mg, and PbI_2= 138.3 mg.

The salts in the vial were dissolved in 1 ml of the DMSO solvent, after which they were stirred on a magnetic stirrer for more than a day. The spincoating method was chosen as the method for synthesizing 2D perovskite. The synthesis took place in a glove box with a dry nitrogen atmosphere. After that, a substrate from a 12x12 mm glass slide was loaded onto a spincoater, 20 μl of the prepared perovskite solution was deposited on it, then the spincoater was started, the solvent dries and forms perovskite film. Then it is necessary to evacuate the sample in order to slowly remove the solvent from the film and start slow crystallization, and then anneal it on a plate in order to evaporate the solvent and form the desired perovskite phase.

For the procedure of atomic force lithography, cantilevers with a single-crystal diamond tip (TipsNano DRP-IN) with a resonant frequency of 500–1000 kHz, a force constant of 100–600 N/m, and a tip curvature radius of 25-35 nm were used. At the first stage of the work, $(PEA)_2PbI_4$ perovskite films with a thickness of about 100–150 nm were structured. Before lithography, the area of the sample, on which it was planned to fabricate a planar resonator, was characterized by atomic force microscopy in the semi contact mode. The measured surface roughness of the films should not exceed 15 nm. The produced resonator was a grating up to 50x50 um^2. The parameters of the lithography process controlled the grating period, the filling factor (the ratio of the width of the uncut part of the grating to the period), and the depth of the relief modulation. For the manufacture of resonators of this type, the mode of vector lithography with a constant force was used. The main parameter of the process, which determines the geometry of the future structure, is the deviation of the probe from the initial position during lithography. It is this parameter that characterizes the force of pressure on the sample, which, in turn, determines the modulation (depth) of cutting through the film by the probe. It was experimentally found that the working force F required to achieve modulation of 20-60 nm on $(PEA)_2PbI_4$ perovskite films is about 5-30x10^3 nN. Another important parameter in the fabrication of a planar resonator is the speed of the probe. It turned out that at a sufficiently high scanning speed (more than 3 um/s), the probe begins to pull out perovskite grains. The optimal rate for structuring perovskite and $(PEA)_2PbI_4$ films was found to be 1 um/s. The final nanostructured samples were also studied by atomic force microscopy. The lattice geometry was chosen based on the results of numerical simulations. The period was 280 nm, the modulation depth was 50 nm, and the filling factor was 0.5.

In order to confirm realization of strong light-matter regime in the fabricated samples, angular dependence of the optical reflectance and photoluminescence spectra of the nanostructured samples was measured. A polariton mode fitting was performed using a two coupled oscillator model in order to estimate the Rabi splitting, which reached the values as high as 173 meV. An exciton resonance energy of 2361 meV and width of 2.35 meV were also obtained from the fitting.

To summarize, a perovskite atomic force lithography technology has been developed, which allows to fabricate nanostructured planar cavities based on $(PEA)_2PbI_4$ perovskite. The main advantage of this approach to fabricate planar resonators based on perovskites is the precise control of the geometric parameters of the nanostructure, which makes it possible to control the final dispersion of exciton-polaritons. The fabricated planar periodic resonators support optical modes with both TE and TM polarizations with quality factors of larger than 100. Due to the large binding energy of the exciton, we expect that the proposed geometry would allow not only to study exciton-polariton nonlinearities, but also to realize a room-temperature polariton condensate.

Acknowledgments

This work was supported by Russian Science Foundation, grant #21-12-00218.

References

[1] Bélanger N., Villeneuve A., Aitchison J. S. Solitonlike pulses in self-defocusing AlGaAs waveguides //JOSA B. – 1997. – T. 14. – №. 11. – C. 3003-3012.

[2] Makarov S. et al. Halide-Perovskite Resonant Nanophotonics //Advanced optical materials. – 2019. – T. 7. – No. 1. – C. 1800784.

The research of laser radiation direction change in the time it dissemination to Anderson differential cuvette

A A Goldberg[1], I D Kochetkov[1] and V V Davydov[1, 2, 3]
[1]Peter the Great Saint-Petersburg Polytechnic University, Saint Petersburg, Russia, 195251
[2]The Bonch-Bruevich Saint-Petersburg State University of Telecommunications, Saint Petersburg 193232, Russia
[3]All-Russian Research Institute of Phytopathology, Moscow Region 143050, Russia

e-mail: artemiy.goldberg@mail.ru

Abstract. The necessity of studying the nature of the propagation of laser radiation in the Anderson differential cuvette is substantiated in order to determine the optimal design parameters of a small-sized differential type refractometer. The construction of the Anderson differential cuvette is considered. A new method for studying the nature of the propagation of laser radiation in the differential Anderson cuvette is proposed. The trajectory of movement of the maximum of the laser radiation directive pattern in the cuvette, as well as beyond it (up to the sensor of the photodiode ruler on which the registration takes place) is plotted. An equation is obtained to study the changes in the nature of the propagation of laser radiation from various parameters of the differential cuvette, the reference liquid medium and the investigated liquid medium. A polynomial of the 12th degree is formed to obtain an analytical solution of the equation from the refractive index of the investigated medium.

1. Introduction

In the modern world, when conducting scientific research, producing various liquid mediums and much more, reliable express control becomes an important element. The use of express control is necessary to get reliable information about the state of the medium at the test site in order to make an adequate decision [1, 2]. In addition, it is necessary to obtain confirmation of the detected deviation in the sample on high-resolution devices later [2]. One of the devices that allows express control of the state of liquid mediums with high precision at the sampling site is a refractometer.

High requirements for conducting experiments, the manufacture of complex mediums, for example, medical suspensions or medicaments for injection into veins, requires measurements of the refractive index n_m with high precision over a large range of values. The last statement is related to various applications of the refractometer. A differential refractometer based on an Anderson cuvette, for measurements in which a calibration liquid is used, is one of the possible solutions to express control problems. The problem of measuring n_m with an error of 0.0001 is related to the lack of relations between different parameters in the design of the refractometer and the Anderson cuvette.

2. Anderson cuvette design and profile of laser radiation propagation

On figure 1 is shown the propagation of laser radiation in the Anderson cuvette and after exiting it to the sensor of the photodiode ruler (the sensor is located at a distance y from the wall of the cuvette).

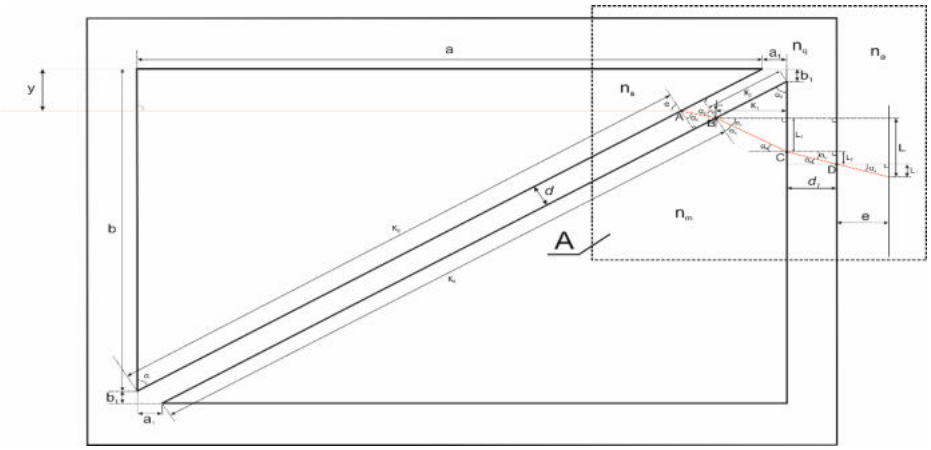

Figure 1. Anderson cuvette and the direction of laser radiation propagation

To determine the change in the measurement error n_m, it is necessary to establish the dependence of the change in the displacement of the maximum laser radiation L on the photodiode ruler on the parameters of the Anderson cuvette, the distance e, and the values n_m and n_s.

3. The equation for research of laser radiation direction change in the time it dissemination in optical part of refractometer

To derive the equation and verify it at control points, the description of the nature of the change in the propagation of laser radiation was divided into 4 parts (L_1, L_2, L_3 and L_4). This allowed us to obtain the following equality:

$$L = L_1 + L_2 + L_3 + L_4 = \frac{ad}{\sqrt{a^2+b^2}}\left(1 - \frac{n_s b}{\sqrt{n_q^2\left(a^2+b^2\right) - n_s^2 a^2}}\right) + a\left(\sqrt{n_m^2\left(a^2+b^2\right) - n_s^2 a^2} - n_s b\right) * \left(\frac{e}{\sqrt{n_a^2\left(a^2+b^2\right)^2 - a^2\left(n_m^2\left(a^2+b^2\right) - n_s^2 a^2 + n_s^2 b^2 - 2n_s b\sqrt{n_m^2\left(a^2+b^2\right) - n_s^2 a^2}\right)}} + \right.$$

$$\left. + \frac{d_1}{\sqrt{n_q^2\left(a^2+b^2\right)^2 - a^2\left(n_m^2\left(a^2+b^2\right) - n_s^2 a^2 + n_s^2 b^2 - 2n_s b\sqrt{n_m^2\left(a^2+b^2\right) - n_s^2 a^2}\right)}} + \frac{\left(y - b_1 + \frac{ad}{\sqrt{a^2+b^2}}\left(1 - \frac{n_s b}{\sqrt{\left(a^2+b^2\right)n_q^2 - a^2 n_s^2}}\right)\right) tg\frac{a}{b}}{b\sqrt{n_m^2\left(a^2+b^2\right) - n_s^2 a^2} + n_s a^2}\right) \quad (1)$$

In the situation when $n_m = n_s$, only one term remains in equality (1). When the beam exits the Anderson cuvette, it shifts by a distance of L_4 (Fig. 1) and retains its original direction of propagation.

4. Conclusion

The obtained results show that the equality (1) cannot be solved explicitly without transformations to determine the extremum points of the function $L(n_m)$. Therefore, in the future, equation (1) will need to be represented as a polynomial (exclude n_m from the relations connected with the root).

It is necessary to notice that the obtained equality (1) allows us to estimate the possibility of measuring the n_m value with an error of 0.0001 when changing the distance L on the photodiode ruler corresponding to the distance between photosensitive sensors (the ruler design contains 1024 sensors).

References

[1] Karabegov M A 2004 *Measurement Techniques* **47(11)** 1106-1112
[2] Marusina M Y, Bazarov B A, Galaidin P A, Marusin M P, Silaev A A, Zakemovskya E Y and Mustaev Y N 2014 *Measurement Techniques* **57(5)** 580-586

Photoluminescence from lead halide perovskite superlattices

Pavel Tonkaev, Evgeniia Grechaninova, Anatoly Pushkarev, Sergey Makarov

ITMO University, Kronverksky av. 49 197101 St. Petersburg, Russia

E-mail: pavel.tonkaev@metalab.ifmo.ru

Abstract. Lead halide perovskites are a new class of materials with promising optoelectronic properties. Colloidal perovskite nanocrystals have shown high efficiency of photoluminescence. We studied photoluminescence properties of $CsPbBr_3$ superlattices at room temperature and 6 K. We demonstrated that the photoluminescence spectra of perovskite nanocrystals are preserved in superlattices.

1. Introduction

Lead halide perovskites are a class of new materials with outstanding properties that have been applied in the field of photovoltaics [1] and light-emitting diodes [2]. Moreover, due to relatively high refractive index, perovskite nanoparticle supports Mie resonances in optical and near-infrared range which enhance photoluminescence [3] and lower the lasing threshold [4]. Meanwhile, perovskite nanocrystals with quantum confinement have high photoluminescence quantum yield [5]. Assembling perovskite nanocrystals in an ordered 3D array or superlattice allows controlling of additional properties of optical nanosources. Herein we aim to study photoluminescence of single CsPbBr3 superlattices with linear dimensions of several microns at room temperature and 6 K.

2. Results and discussion

The CsPbBr3 perovskite nanocrystals were obtained by the hot injection method. The resulting nanocrystals were separated by centrifugation and dispersed in toluene to obtain a colloidal solution. Superlattices were formed from these colloidal nanocrystals. The CsPbBr3 superlattices were fabricated on a silicon substrate. The transverse dimensions of individual superlattices ranged from 1 μm to 10 μm, while some of them agglomerated to form clusters of superlattices, and some remained spatially isolated, which made it possible to measure photoluminescence for individual objects.

Experimental measurements of photoluminescence spectra revealed that the photoluminescence maximum of the CsPbBr3 superlattice is located at the wavelength of 517 nm, whereas the maximum of the bulk thin film is 526 nm. Perovskite nanocrystals demonstrated slightly different results compared to superlattice, the maximum is shifted and located at 518 nm. Therefore, we can conclude that perovskite superlattices have good quality and quantum confinement is preserved. Perovskite superlattices exhibited similar behavior in optical experiments at the temperature of 6K. The maximum of photoluminescence spectra shifted to a long wavelength region and was 530 nm for superlattice and 538 nm for thin film.

3. Conclusion

We have studied photoluminescence properties of superlattices assembled from CsPbBr3 nanocrystals at room temperature and 6K. Our study reveals that photoluminescence spectra of perovskite superlattices are similar to emission spectra of initial colloidal nanocrystals. These structures allow modification of optoelectronic properties of perovskite nanocrystals at 3D level. In addition, perovskite superlattices are promising structures for micro- and nanolasers and photodetectors.

Acknowledgments

This work was supported by the Russian Science Foundation (project № 22-22-20077)

References

[1] Snaith H. J. 2018 *Nature materials* **17** 372-376
[2] Lin K. et al 2018 *Nature* **562** 245-248.
[3] Tiguntseva E. et al 2018 *Nano Letters* **18** 1185–1190
[4] Tiguntseva E. et al 2020 *ACS Nano* **14** 8149-8156.
[5] Protesescu L. et al 2015 *Nano Letters* **15** 3692-3696.

Development of compact NMR relaxometer for express control of the state of liquid media

M N Davydov[1] and V V Davydov[1, 2]
[1]Peter the Great Saint-Petersburg Polytechnic University, Saint Petersburg, Russia, 195251
[2]All-Russian Research Institute of Phytopathology, Moscow Region 143050, Russia

e-mail: davydov.mn@edu.spbstu.ru

Abstract. As rises the consumption of petroleum products, so rises the demand to quality control of those products. Matter of cost is significant. Therefore, work is constantly underway to develop devices that meet this requirement and allow for express control "on the spot" to detect the presence of undesirable impurities. Compact NMR relaxometer pattern is suggested and measurements taken. Experimental data are given.

1. Introduction

At present, there are many instruments available for on-site measurements, but these instruments are quite expensive, which prevents their large-scale use.

We propose a simple solution – qualitative express analysis of the state of the media. This approach allows to identify impurities at the sampling site. If an impurity Is detected, a laboratory analysis is carried out with the identification of this contamination.

2. Measurement technique and pattern of NMR relaxometer

The principle of operation of the proposed device is based on the measurement of relaxation constants. Modulation technique is used, because it allows to provide the smallest weight and size characteristics of the device and allows to determine the percentage of impurities in the media [1, 2].

The carbon compounds of interest to us are liquids, the Block equations are not satisfied, therefore, in the work a modification of Bloch equation special to modulation technique is proposed, which makes it possible to describe the NMR signal (and relaxation constants) with an error of less than 1% [2].

$$\begin{cases} \dfrac{du(t)}{dt} + \dfrac{u(t)}{T_2} + \gamma H_m \sin(\omega_m t)\, \upsilon(t) = 0 \\ \dfrac{dv(t)}{dt} + \dfrac{v(t)}{T_2} - \gamma H_m \sin(\omega_m t) u(t) + \gamma H_1 M_z(t) = 0 \\ \dfrac{dM_z(t)}{dt} + \dfrac{M_z(t)}{T_1} - \chi_0 \dfrac{H_0 + H_m \sin(\omega_m t)}{T_1} - \gamma H_1 \upsilon(t) = 0 \end{cases} \quad (1)$$

Figure 1 shows pattern of suggested device.

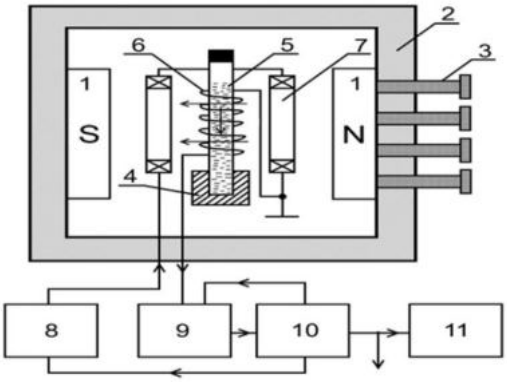

Figure 1. NMR relaxometer pattern. 1 – magnet, 2 – neutral for placing and centering magnets, 3 – adjusting screws, 4 – fixing device for the container with the test medium, 5 – container with the investigated medium, 6 – NMR signal registration coil, 7 – modulation coils, 8 – radio frequency generator, 9 – autodyne detector, 10 -processing and control device, 11 - oscilloscope

This design makes it possible to measure the relaxation times of liquid media outside the laboratory (for example, in the field, on the banks of rivers and bays, on the territory of industrial enterprises, etc.).

3. Experimental results and discussion

As an example, table 1 contains the results of measuring the longitudinal relaxation time T_1 and transverse relaxation time T_2 of relaxation of various grades of gasoline at temperature of T = 291 K. The measurements were carried out using the developed design of a small-sized NMR relaxometer and an industrial NMR relaxometer Minispec mq 20.

Table 1. NMR relaxation constants of liquid media.

Medium	Compact NMR relaxometer		Industrial NMR relaxometer Minispec mq 20	
	T_1, s	T_2, ms	T_1, s	T_2, ms
Soviet Petrol standard A – 76	1.432 ± 0.007	146.05 ± 0.73	1.4266 ± 0.0029	145.35 ± 0.29
Soviet Petrol standard “Nefras C2-80/120”	1.333 ± 0.006	207.51 ± 1.04	1.3403 ± 0.0027	206.38 ± 0.42

An analysis of the obtained values of the relaxation times by two devices shows that they coincide within the measurement error.

4. Conclusion

The obtained results confirm the possibility of monitoring the state of liquid media with a small-sized NMR relaxometer developed by us. Using the obtained values of the relaxation times T_1 and T_2, we can draw a conclusion about the quality of gasoline with high accuracy. The developed device allows express control of the state of any liquid media containing protons.

References

[1] Marusina M Y, Bazarov B A, Galaidin P A, Marusin M P, Silaev A A, Zakemovskya E Y and Mustaev Y N 2014 *Measurement Techniques* **57(5)** 580-586
[2] Kashaev R S and Gazizov E G 2010 *Journal of Applied Spectroscopy* **77** 321–328

Development of compact NMR relaxometer for express control of the state of liquid media

M N Davydov[1] and V V Davydov[1, 2]
[1]Peter the Great Saint-Petersburg Polytechnic University, Saint Petersburg, Russia, 195251
[2]All-Russian Research Institute of Phytopathology, Moscow Region 143050, Russia

e-mail: davydov.mn@edu.spbstu.ru

Abstract. The consumption of petroleum products rises, so rises the demand to quality control of those products. Matter of cost is significant. Therefore, there is a need to develop devices that meet low-cost requirement and allow for express control "on the spot" to detect the presence of undesirable impurities. Compact NMR relaxometer pattern for express control of the liquid medium at the sampling site has been developed. Experimental data are presented. The obtained values were compared with the values obtained using an industrial NMR relaxometer.

1. Introduction

There are many pollutions of liquid medium, both in water bodies and in laboratory samples or in industrial production [1,2]. It is important in these cases to have reliable express control of the state of the medium at the sampling site [1-3]. Very often, it is only necessary to establish the presence of a deviation in the medium from the standard state (further studies of the sample will be carried out in a laboratory). Express control methods require that the measurements taken should not introduce irreversible changes in the composition and structure of the medium [2,3]. Method of express control based on the phenomenon of NMR is one of the most preferable in given situation.

In weak magnetic fields, it is extremely difficult to obtain the NMR spectrum. This problem can be solved by using a modulation technique for recording the NMR signal. Control of the state can be done with the measurement of the longitudinal T_1 and transverse T_2 relaxation times. By shift of the values of T_1 and T_2 from the standard, the presence of a deviation in the medium is determined.

2. Measurement technique and pattern of NMR relaxometer

In the device developed by us, the registration of NMR signal will be carried out at the resonant frequency of protons, The Bloch equations are used to describe the process of registering an NMR signal at the resonant frequency. Their use in some cases makes it possible to determine the composition of the medium. In Figure 1 pattern of suggested device is shown.

$$\begin{cases} \dfrac{du(t)}{dt} + \dfrac{u(t)}{T_2} + \gamma H_m \sin(\omega_m t)\, v(t) = 0 \\ \dfrac{dv(t)}{dt} + \dfrac{v(t)}{T_2} - \gamma H_m \sin(\omega_m t) u(t) + \gamma H_1 M_z(t) = 0 \\ \dfrac{dM_z(t)}{dt} + \dfrac{M_z(t)}{T_1} - \chi_0 \dfrac{H_0 + H_m \sin(\omega_m t)}{T_1} - \gamma H_1 v(t) = 0 \end{cases} \quad (1)$$

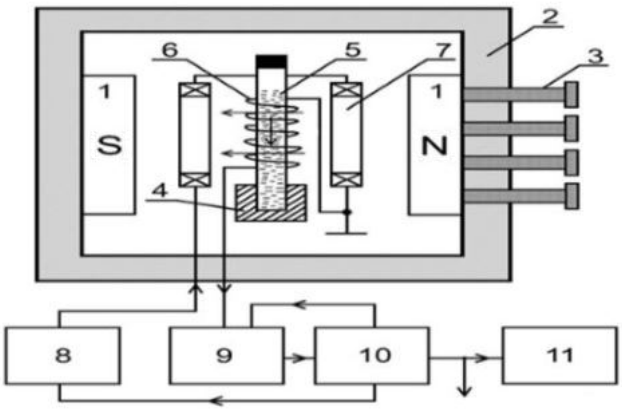

Figure 1. NMR relaxometer pattern. 1 – magnet, 2 – neutral for placing and centering magnets, 3 – adjusting screws, 4 – fixing device for the container with the test medium, 5 – container with the investigated medium, 6 – NMR signal registration coil, 7 – modulation coils, 8 – radio frequency generator, 9 – autodyne detector, 10 -processing and control device, 11 - oscilloscope

This design makes it possible to measure the relaxation times of liquid media outside the laboratory: for example, in the field, on the banks of rivers and bays, on the territory of industrial enterprises, etc..

3. Experimental results and discussion

As an example, table 1 contains the results of measuring the longitudinal relaxation time T_1 and transverse relaxation time T_2 of relaxation of various grades of gasoline at temperature of T = 291 K. The measurements were carried out using the developed design of a small-sized NMR relaxometer and an industrial NMR relaxometer Minispec mq 20.

Table 1. NMR relaxation constants of liquid media.

Medium	Compact NMR relaxometer		Industrial NMR relaxometer Minispec mq 20	
	T_1, s	T_2, ms	T_1, s	T_2, ms
Soviet Petrol standard A – 76	1.432 ± 0.007	146.05 ± 0.73	1.4266 ± 0.0029	145.35 ± 0.29
Soviet Petrol standard “Nefras C2-80/120”	1.333 ± 0.006	207.51 ± 1.04	1.3403 ± 0.0027	206.38 ± 0.42

An analysis of the obtained values of the relaxation times by two devices shows that they coincide within the measurement error.

4. Conclusion

The obtained results confirm the possibility of monitoring the state of liquid media with a small-sized NMR relaxometer developed by us. Using the obtained values of the relaxation times T_1 and T_2, we can draw a conclusion about the quality of gasoline with high accuracy. The developed device allows express control of the state of any liquid media containing protons.

References

[1] D’yachenko S V, Kondrashkova I S and Zhernovoi A I 2017 *Technical Physics* **62(1)** 1602-1604
[2] Marusina M Y, Bazarov B A, Galaidin P A, Marusin M P, Silaev A A, Zakemovskya E Y and Mustaev Y N 2014 *Measurement Techniques* **57(5)** 580-586
[3] Kashaev R S and Gazizov E G 2010 *Journal of Applied Spectroscopy* **77** 321–328

New design of a waveguide integrated photon number resolving superconducting detector with micron-wide strips

M Dryazgov[1,2], Yu Korneeva[2], A Korneev[1,2,3]
[1]Higher School of Economics - National Research University, 101000, Russia
[2]Institute of Nanotechnology of Microelectronics of the Russian Academy of Sciences, 119991, Russia
[3]Department of Physics, Moscow State Pedagogical University, 119992, Russia

e-mail: mdryazgov@hse.ru

Abstract. We report on the development of a design for a waveguide integrated photon number resolving superconducting detector with micron-wide strips. The planarize operation is used to place a micron-wide superconducting strip. The detector resolves the number of photons in an optical pulse by matching the impedance with a Klopfenstein taper.

1. Introduction

Superconducting Single Photon Detectors (SSPD) have proven to be excellent for detecting single photons [1]. However, the challenges of quantum optics require detectors capable to resolve the number of photons (PNR) [2]. Moreover, present development of quantum computers is directed towards integrated circuits [3]. All this suggests that superconducting PNR detectors should be compatible with the integration on a photonic chip [4].

Traditionally, SSPDs are made as nanometer-wide strips, which does not allow them to effectively absorb the radiation from the waveguide. There is also the problem of the location of the contacts, since they cause the back-reflection of the radiation in the waveguide. All of the above problems can be solved using micron-wide superconducting strips [5], planarized [6] and integrated with impedance matching Klopfenstein tapers [7].

The planarization makes it possible to cover the waveguide and the entire area around it with a dielectric layer, producing a flat surface for the superconductor deposition. Then a micron-wide superconducting strip can be placed above the waveguide, even if the strip is wider than the waveguide. The use of impedance matching Klopfenstein tapers makes it possible to distinguish the resistances of several hot spots, that is, to distinguish the number of absorbed photons.

We propose a new design of the PNR detector matching with a Klopfenstein taper on the waveguide and determine its parameters for manufacturing.

2. Design concept

On a dielectric substrate of SiO_2 ($n = 1.444$) there is a silicon nitride (Si_3N_4) waveguide (n=1.9894), which is single mode for a wavelength $\lambda = 1550$ nm: $w_{wg} = 1.68\ \mu m$, $d_{wg} = 0.5\ \mu m$ (Fig. 1b). Such waveguide parameters have already been used in research, and the results of modeling in the COMSOL environment have shown their effectiveness in the task at hand. The waveguide is covered with a dielectric layer (SiO_2) with subsequent planarization, which will allow placing a detector on top with impedance matching transformer in the form of a Klopfenstein taper. The thickness of the dielectric layer (d_{diel}) between the waveguide and superconductor is assumed to be as small as possible: for

example, the maximum absorption of 1.4 dB/μm is $d_{diel} = 0\ nm$, while $d_{diel} = 100\ nm$ the absorption is only 0.7 dB/μm (Fig. 1c).

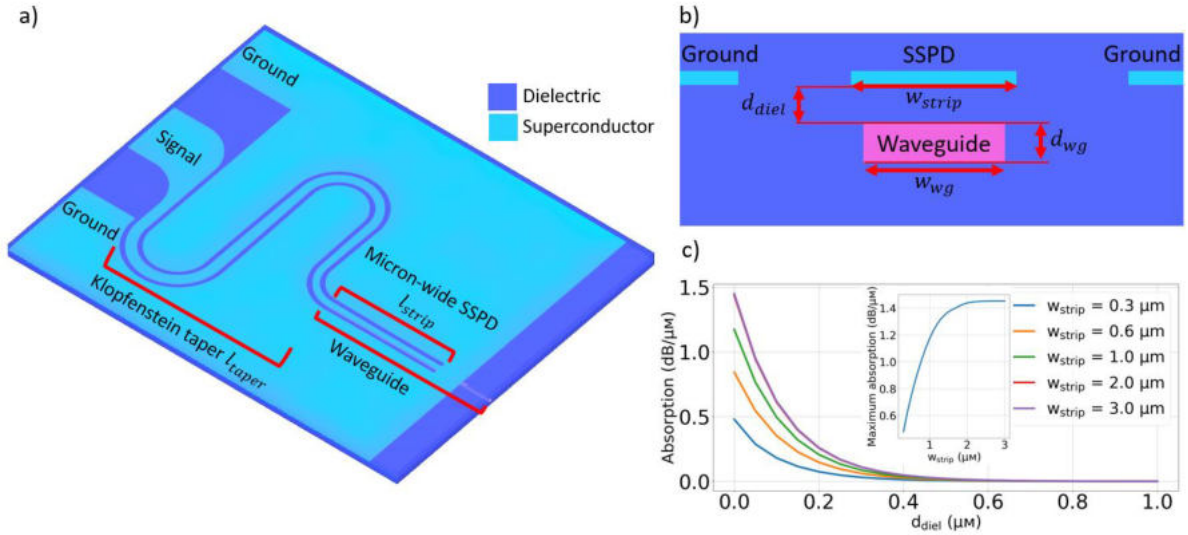

Figure 1. a) The design concept of the PNR-SSPD with a Klopfenstein taper integrated on the optical waveguide (not to scale). b) A 2D slice showing the waveguide under a planarized dielectric layer with an SSPD on top. c) Dependence of absorption on the thickness of the dielectric layer above the waveguide. In insert: dependence of the maximum absorption (at zero thickness of the dielectric above the waveguide) on the width of the superconducting strip.

The detector is made in the form of a straight 2-μm-wide strip of NbN ($n = 5.20685 - 5.82i$), the width is obtained by the simulation and is optimal for absorbing the largest fraction of radiation per unit length. The length of the superconducting strip required to absorb 99% of the radiation in this case is $l_{strip} = 14\ \mu m$.

One end of the superconducting strip goes to the Klopfenstein taper, which parameters are also obtained by the simulation: a coplanar line with a constant dielectric gap of 20 μm and changing width of the signal contact from 2 μm to 20 μm over $l_{taper} =$ 51 cm, thereby providing a smooth impedance matching of the 50 Ω coaxial line with 1 kΩ impedance of the superconductor in the normal state. The other end of the superconducting strip is grounded through a junction above the waveguide (Fig. 1a). After all, the structure is covered with a dielectric layer to prevent radiation scattering.

3. Conclusion

We have proposed a design for a waveguide integrated PNR superconducting detector with micron-wide strips connected to Klopfenstein taper. The optimal parameters were calculated for absorbing 99% of the radiation and matching the impedance of the coaxial line and the superconductor in the normal state: $w_{strip} = 2\ \mu m$, $l_{strip} = 14\ \mu m$, $w_{wg} = 1.68\ \mu m$, $d_{wg} = 0.5\ \mu m$, $l_{taper} =$ 51 cm.

4. Acknowledgments

This work was supported by the Russian Science Foundation (RSF) Grant No. 20-12-00287.

References

[1] You L 2020 *Nanophotonics* **9**, 2673–2692
[2] Cattaneo M *et al* 2018 *Phys. Rev. A* **98**, 012333
[3] Peter S *et al* 2019 *Nano Lett*. 19 **10**, 7164–7172
[4] McDonald C *et al* 2019 *Appl. Phys. Lett.* **115**, 081105
[5] Korneeva Yu *et al* 2018 *Phys. Rev. Appl.* **9**, 064037
[6] Hiroyuki Sh *et al* 2019 *Supercond. Sci. Technol.* **32**, 034001
[7] Zhu D et al 2020 Nano Lett. 20 **5**, 3858–3863

Investigation of optical waveguide properties of SOI integrated circuits

A. A. Ershov, D. V. Ryaykkenen, A. A. Nikitin, and A. B. Ustinov

email: aaershov@stud.etu.ru

Abstract. In the present work, optical properties of an SOI integrated circuit have been investigated and described. The investigated circuit is comprised of the following elements: a straight waveguide, directional coupler, Mach-Zehnder interferometer, and micro-ring resonator. Optical properties, namely, the dispersion characteristic, coupling coefficient, damping decrement, Bragg grating coupler efficiency have been obtained experimentally. The obtained values and dependencies are used to describe the transfer function of the Mach-Zehnder interferometer theoretically. Experimental data is in a good agreement with theoretical predictions. It is shown that by using the aforementioned elements as reference, it is possible to characterize optical waveguide properties of other elements present in the integrated circuit.

1. Introduction

To date, the silicon-on-insulator (SOI) technology has become prevalent in the field of photonics and optoelectronics. The SOI technology for photonic integrated circuits exhibits the following advantages: high index contrast, small bending radius, as well as low propagation losses [1, 2]. These advantages have allowed SOI technology to achieve a high degree of compatibility with CMOS, which promises full integration of electronic and optical elements on a single chip. Low propagation losses (2-3 dB/cm at 1550 nm [2]) and high index contrast between silicon and silicon dioxide enable high density of elements, which leads to smaller chip size and lower production costs. As such, SOI technology is a promising platform for research and development of photonic integrated circuits [1-3]. However, it is well known that large scale integrated circuits demonstrate small variation of material parameters (thickness, roughness, refractive index) not only between different wafers but between chips from the same wafer.

2. Optical waveguide properties

The aim of the present work is to investigate the optical properties of a commercially available SOI chip as well as to propose a method of accounting for the possible discrepancies in waveguide properties by using reference elements. The investigated chip consists of the following reference elements: a straight waveguide, directional coupler, and micro-ring resonator (MRR), as well as Mach-Zehnder interferometer (MZI) serving as a benchmark. The reference elements enable us to measure the dispersion characteristic $n_{\text{eff}}(\lambda)$, coupling coefficient κ, and damping decrement α, Bragg grating coupler efficiency $T(\lambda)$. The elements consist of silicon waveguides with a cross section of 220×550 nm^2. The measurement is carried out as follows. First, fiber-to-fiber insertion loss of a straight waveguide (see Fig. 1a-I) is experimentally observed. The following approximation which describes

Bragg grating coupler efficiency is found: $T_W(\lambda) = -27556.66 + 35288 \cdot \lambda - 11305.81 \cdot \lambda^2$. Theoretical and experimental dependencies are shown in Fig. 1b. Second, the directional coupler, which consists of a half-ring and a straight waveguide (see Fig. 1a-II) is used to determine the power coupling coefficient of $\kappa = 1.045 \cdot 10^{-3}$. Third, the MRR (Fig. 1a-III) transfer function is experimentally measured. Dispersion relation and propagation losses are extracted from the best fit of experimental data to the theoretical dependence obtained with an original theoretical model (see left graph in Fig. 1c) [4]. In accordance with this method the following value of damping decrement of $\alpha = 2$ dB/cm and the expression for the effective refractive index $n_{eff}(\lambda) = 4.115 - \lambda - 0.04\lambda^2$ are obtained.

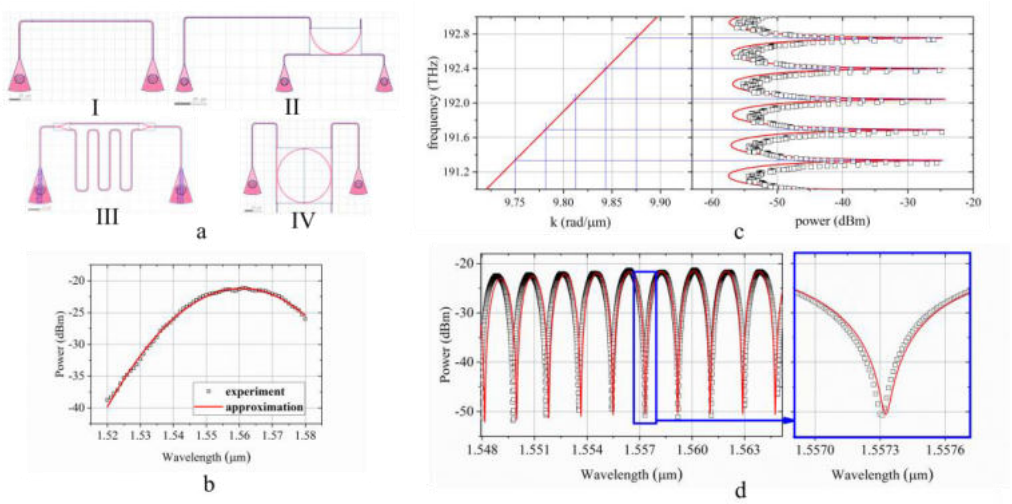

Fig. 1. The topologies of the investigated elements (a); transfer function of the straight waveguide (b); MRR transfer function (c), MZI transfer function (d)

In order to check the adequacy of obtained parameters the theoretical transfer function of MZI (Fig. 1a-IV) is modelled. As it is seen in Fig. 1d, the obtained transfer function is in good agreement with the experimental data.

3. Conclusion

In conclusion, the waveguide properties of integrated circuits have been described using a straight waveguide, directional coupler, and MRR. The obtained optical waveguide parameters are used for the modelling of the MZI. The modelling results show good agreement with measurement data. Thus, using the developed approach it is possible to describe the waveguide properties and account for the local differences in characteristics of various elements in different parts of a single chip.

Acknowledgements

The authors acknowledge the support of Ministry of Education and Science of Russian Federation (Project “Goszadanie”)

References

[1] S. Pathak, *Nanoelectronics*. Elsevier, 219-270 (2019).

[2] Chrostowski L., Hochberg M., (2015). *Silicon photonics design: from devices to systems*. (Cambridge University Press, 2015)

[3] W. Bogaerts, et al. *Laser & Photon. Rev.* **6**, 47-73 (2012).

[4] A. Nikitin, et al. *Results in Physics* **18,** 103279 (2020).

Light modulation by semiconductor metasurfaces upon electric injection of free carriers

A.A. Ibragimov[1], N.D. Masharov[1], A.S. Shorokhov[1], A.A. Fedyanin

[1]Faculty of Physics, Lomonosov Moscow State University, Moscow 119991, RUSSIA

Email: ibragimov@nanolab.phys.msu.ru

Abstract. Metasurfaces of dielectric nanostructures — subdiffractive arrays of nanoantennas made of transparent materials — can enhance the interaction of light with matter, which has applications in many applications, including metasurfaces, holograms and optical filters [1]. However, these devices are almost always passive in the sense that their optical properties are fixed at the production stage and cannot be modified afterwards. The free carrier injection mechanism into the nanoantenna material, either by using optical emission pulses [2] or by applying an external electric field [3], can be used to solve this problem. It is the second approach that will be considered in this research work. Metasurfaces with the possibility of modulation of their optical properties by external forces can become an effective technique in applied photonics.

1. Methods

In this research, we numerically and experimentally study the optical response of a subwavelength array of cylindrical holes etched in a p-AlGaAs/i-GaAs/n-AlGaAs-type heterostructure under the electrical injection of free carriers into the sample. This structure has a feature in the reflection spectrum in the spectral region near $\lambda = 580$ nm. This feature appears as a pronounced diffraction peak in the reflection spectrum and is determined by the geometric parameters of the sample, which were selected using the numerical finite difference method in the time domain in the Lumerical FDTD software package.

The experimental sample according to numerically selected optimal parameters was fabricated using a combination of molecular-beam epitaxy (MBE), sequential optical ultraviolet lithography in multiple layers with overlapping, plasma-enhanced chemical vapour deposition (PECVD) to create insulating layers of Si3N4, and magnetron sputtering followed by annealing. Focused ion beam (FIB) atomization was used to create holes in the obtained samples according to a given template meeting the design parameters. The choice of nanocylinders as elements of these structures was caused by the comparative simplicity of their production, and the use of GaAs as the main material of the heterostructure by significant changes in its optical properties in the process of carrier injection.

2. Conclusion

The results obtained can be used in the future to create tunable optical metasurfaces for photonics applications. In future work, it is also planned to consider a different geometry of the structure to achieve more significant changes in optical response [4]. In addition, this will allow control not only over the integral magnitude of the reflected electromagnetic wave energy but also over its distribution in space, which may be relevant for applications such as laser beam scanners in lidars.

References

[1] Jie Hu, Sankhyabrata Bandyopadhyay et al., "A Review on Metasurface: From Principle to Smart Metadevices", Front. Phys. 8, 586087 (2021)

[2] Lu Ding, Dmitry Morits et al., "All-optical modulation in chains of silicon nanoantennas", ACS Photonics, 7, 1001–1008 (2020)

[3] Weifeng Zhang1 and Jianping Yao, "A fully reconfigurable waveguide Bragg grating for programmable photonic signal processing", Nat. Commun. 9, 1396 (2018);

[4] Mark Lawrence, David R. Barton III et al., "High quality factor phase gradient metasurfaces", Nat. Commun. 15, 956–961 (2020).

Broadband light absorber based on a multilayer metal-insulator-metal structure

A I Kashapov[1,2], E A Bezus[1,2], D A Bykov[1,2], N V Golovastikov[1,2] and L L Doskolovich[1,2]

[1] Image Processing Systems Institute of RAS — Branch of the FSRC "Crystallography and Photonics" RAS, 151 Molodogvardeyskaya St., Samara 443001, Russia
[2] Samara National Research University, 34 Moskovskoe shosse, Samara 443086, Russia

E-mail: ar.kashapov@outlook.com

Abstract. Broadband absorption of electromagnetic waves can be used for solving a number of practical problems and, in particular, can find application in photovoltaics and in optical sensing. In the present work, we investigate the possibility of achieving ultra-broadband absorption by adding additional layers to a simple three-layer metal-insulator-metal structure.

1. Introduction

In recent years, broadband absorbers of electromagnetic radiation have been a subject of great research interest. Such photonic devices can be used in photovoltaics and optical sensors, among other applications [1]. One of the promising types of absorbers is the metal-insulator-metal (MIM) structure consisting of a homogeneous dielectric layer enclosed between two metal layers [2–4]. In our recent work [5], we rigorously proved the existence of a zero in the reflectance spectrum of the MIM structure and discussed its application for analog optical computing [5]. In the present work, we demonstrate that by using a slightly more complex configuration of such a structure, namely, by adding two additional insulator layers with a metal layer between them, and by numerically optimizing the layer thicknesses, the width of the absorption band can be significantly increased.

2. Numerical simulation results and discussion

Let us first consider a simple three-layer structure on a quartz substrate (SiO_2), consisting of a silicon dioxide layer between two chromium (Cr) layers. The medium over the structure has a unit refractive index. Figure 1(a) shows the absorption spectrum of this structure at normal incidence and angles of incidence of 30 and 60 degrees. The geometry of the structure is shown schematically in the inset. The layer thicknesses are: 5 nm (Cr), 166 nm (SiO_2), and 80 nm (Cr). These thicknesses were obtained from the zero-reflectance condition [5] at the wavelength of 1100 nm.

Next, we make the structure slightly more complex by adding two insulator layers with a metal layer between them (thus, the configuration of the structure layers takes the form SiO_2-Cr-SiO_2-Cr-SiO_2-Cr). By numerically maximizing the merit function $F(h) = \int_{\lambda_1}^{\lambda_2} A(h,\lambda)d\lambda$, where A is the absorption and h is the array of structure layer thicknesses, we maximize total absorption in the selected wavelength range.

For the case of $\lambda_1 = 400\,\text{nm}$ and $\lambda_2 = 1.2\,\mu\text{m}$, we obtained a structure with the following thicknesses: $h = (91,7,96,16,95,80)\,\text{nm}$. As Figure 1(b) shows, the introduction of the additional layers makes it possible to obtain a broadband absorber over the selected design wavelength range. It is also worth noting that the structure has a high tolerance to a change in the angle of incidence.

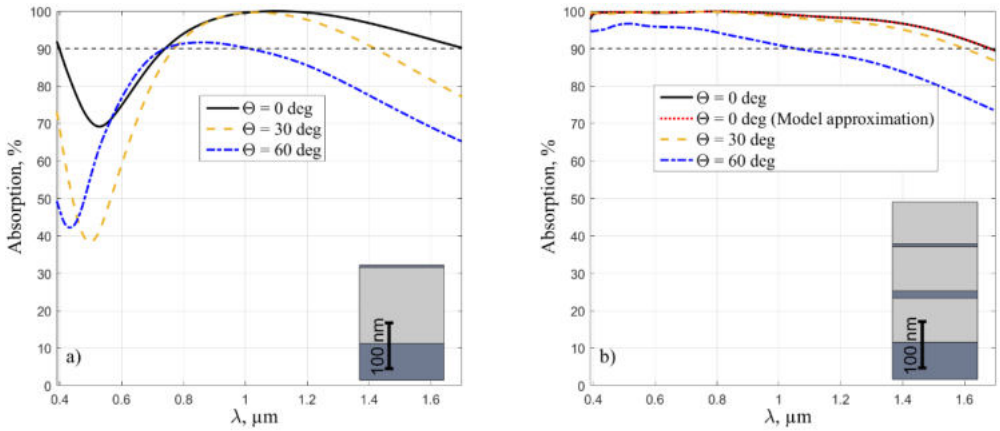

Figure 1. Absorption spectra of a three-layer structure (a) consisting of chromium (dark gray) and quartz (light gray), and an optimized structure with the addition of two quartz layers and a chromium layer (b) for the angles of incidence $\theta = 0^\circ$ (black solid lines), $\theta = 30^\circ$ (yellow dashed lines), and $\theta = 60^\circ$ (blue dotted lines). The red dotted line shows the "resonant" approximation [Eq. (1)] of the absorption spectrum at normal incidence. Geometry of the structures with scale bars is shown inset.

It should also be noted that the obtained broadband absorption effect has a resonant nature and is associated with the excitation of the eigenmodes of the structure. The red dotted line in Figure 1(b) shows the "resonant" approximation of the spectrum of the structure with the additional layers by expression (1), which confirms the assumption about the resonant nature of the above mentioned effect:

$$A(\lambda) = 1 - |r(\lambda)|^2 = 1 - \left| \rho \sum_{i=1}^{3} \frac{\lambda - \lambda_{i,z}}{\lambda - \lambda_{i,p}} \right|^2, \qquad (1)$$

where ρ is the non-resonant reflection, and $\lambda_{i,z}$ and $\lambda_{i,p}$ are the complex values corresponding to zeros and poles (eigenmode wavelengths) of the reflection coefficient $r(\lambda)$, respectively.

In conclusion, we proposed and investigated a broadband absorber based on the metal-insulator-metal structure. We demonstrated that a properly optimized structure can provide absorption exceeding 90% in a more than 1 μm - wide wavelength range and has low sensitivity to the angle of incidence.

Acknowledgments

This work was funded by the Ministry of Science and Higher Education of the Russian Federation (state assignment for research to Samara University (laboratory "Photonics for Smart Home and Smart City", project FSSS-2021-0016), design and investigation of multilayer metal-dielectric-metal structures; and state assignment to the FSRC "Crystallography and Photonics" RAS (agreement 007-GZ/Ch3363/26), implementation of the numerical simulation software).

References

[1] Yu P, Besteiro L, Huang Y, Wu J, Fu L, et al 2019 *Adv. Optical Mater.* **7** 1800995
[2] Yan M 2013 *J. Opt*. **15** 025006
[3] Zhongyang L, Butun S, Aydin K 2015 *ACS Photonics* **2** 183–188
[4] Wesemann L, Panchenko E, Singh K, Gaspera E, Gómez D, et al 2019 *APL Photonics* **4** 100801
[5] Kashapov A I, Doskolovich L L, Bezus E A, Bykov D A, Soifer V A 2021 *J. Opt.* **23** 023501

Experimental study of all-van-der-Waals waveguide polaritons at room temperature

V. I. Kondratiev, T. Ivanova, M. D. Tiugaev, A. K. Samusev, V. Kravtsov

School of Physics and Engineering, ITMO University, Saint-Petersburg, Russia

Email: valeriy.kondratiev@metalab.ifmo.ru

Abstract. In this work, we experimentally investigate waveguide polaritons utilizing only 2D materials, with hBN as the waveguide layer and WS_2 monolayer as the excitonic medium. We place the WS_2 monolayer at the maximum of the waveguide mode electromagnetic field, therefore reaching optimal conditions for the strong coupling between the exciton resonance and waveguide mode. To excite and detect the non-radiating waveguide polariton modes, we use the back focal plane microscopy approach with a solid immersion lens. Polaritons in such all-van-der-Waals structures observed in ambient conditions reveal new possibilities for studying quantum physics and provide strong advantages in terms of miniaturization and integrability.

1. Introduction

Over the last several years, polaritonics has attracted substantial attention as a promising approach to developing non-linear optical and opto-electronic devices. Polaritons arise from strong coupling between light and resonance transitions in matter and manifest themselves in the energy spectrum as Rabi splitting between the transition and optical mode. One promising class of materials for polaritonics is the family of transition metal dichalcogenides (TMDCs). In the monolayer limit, TMDCs are direct bandgap semiconductors [1], and their optical response is dominated by the excitonic resonance. Excitons in TMDCs have large oscillator strengths and large binding energies; moreover, they are stable in ambient conditions, which makes monolayer TMDCs ideal candidates for room-temperature polaritonic devices [2].

The most common way to achieve strong light-matter interaction utilizing excitonic resonances in TMDCs is to couple them to resonant optical modes supported by stand-alone resonators, such as distributed Bragg reflector mirrors [3], plasmonic nanoparticles [4], or subwavelength gratings [5]. Despite the associated chip-compatible planar geometries, such systems require complicated fabrication processes, which creates challenges for applications in real devices.

Here, we study excitons in monolayer WS_2 strongly interacting with a waveguide mode in a subwavelength hBN waveguide. To excite and detect intrinsically non-radiating polaritons propagating below the light line, we use the back focal plane microscopy approach with a high-index solid immersion lens [6]. The complete device can be fabricated in a straightforward way with the dry transfer technique. The geometry of the studied structure allows us to put the WS_2 monolayer precisely at the maximum of the waveguide mode's electromagnetic field by controlling the thickness of the hBN layers. Our results provide a basis for future investigations of waveguide polaritons in devices fabricated entirely from van der Waals 2D materials.

2. Results

The fabricated all-van-der-Waals polariton waveguide is schematically shown in Figure 1 (a). A WS_2 monolayer and hBN flakes were mechanically exfoliated from bulk crystals, then dry transferred onto a SiO_2/Si substrate. The SiO_2 layer introduces additional mode leakage into the substrate; therefore, in order to place the WS_2 monolayer at the maximum field strength of the waveguide mode, the bottom hBN layer had a thickness of ~30 nm, and the top layer had a thickness of ~70 nm. The black solid curve in Figure 1 (a) represents the electromagnetic field distribution in the sample. We used atomic force

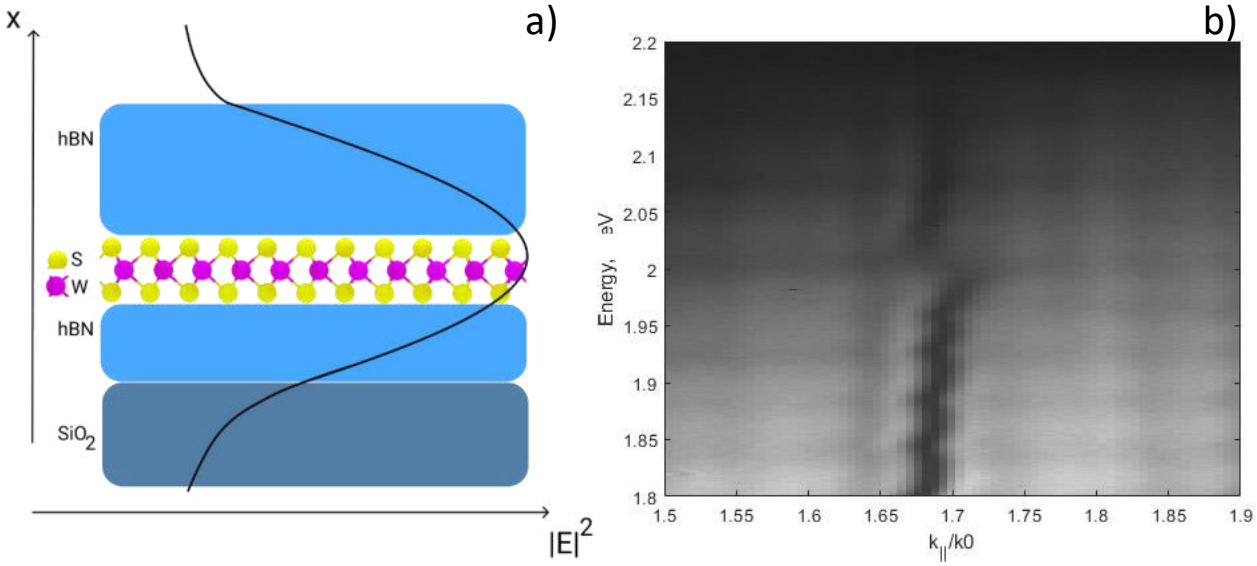

Figure 1. a) Schematic representation of the sample. The thicknesses of the top and bottom hBN layers are 70 nm and 30 nm, respectively. The thickness of SiO_2 is 1 um. (b) Angle-resolved reflectance map observed in the experiment using the back focal plane microscopy approach with a high-index solid immersion lens.

microscopy to determine the thickness of the hBN layers and the assembled device.

In Figure 1 (b) one can see the experimentally observed mode anticrossing at ~2.01 eV that arises from the strong coupling between the excitonic resonance in monolayer WS_2 and the waveguide mode in hBN. To support the experimental observations, we performed a numerical simulation of the angle-resolved reflectivity from the fabricated structure using the transfer-matrix method. The experimental results agree quite well with the numerical simulations and show Rabi splitting values on the order of tens of meV.

3. Conclusion

We experimentally demonstrate waveguide polaritons in an hBN waveguide with an embedded TMDC monolayer in ambient conditions. Our results pave the way towards miniature and chip-compatible room-temperature polaritonic devices based entirely on 2D materials.

Acknowledgments

The research is supported by grant of the Russian Science Foundation (Project №22-22-00663).

References

[1] Mak, K. F. and Shan, J.. "Photonics and optoelectronics of 2D semiconductor transition metal dichalcogenides." Nature Photonics 10.4 (2016): 216-226.

[2] Akinwande, D., et al. "Graphene and two-dimensional materials for silicon technology." Nature 573.7775 (2019): 507-518.

[3] Dufferwiel, S., et al. "Exciton–polaritons in van der Waals heterostructures embedded in tunable microcavities." Nature Communications 6.1 (2015): 1-7.

[4] Munkhbat, Battulga, et al. "Electrical control of hybrid monolayer tungsten disulfide–plasmonic nanoantenna light–matter states at cryogenic and room temperatures." ACS Nano 14.1 (2020): 1196-1206.

[5] Kravtsov, V., et al. "Nonlinear polaritons in a monolayer semiconductor coupled to optical bound states in the continuum." Light: Science & Applications 9.1 (2020): 1-8.

[6] Permyakov, D. V., et al. "Probing Optical Losses and Dispersion of Fully Guided Waves through Critical Evanescent Coupling." JETP Letters 113.12 (2021): 780-786.

Investigation of luminescence in colloidal solutions of zinc aluminate

I. Y. Konstantinova, V. I. Borisov, O. V. Seraya, V. V. Ivanov

Functional Materials Testing Center, Moscow Institute of Physics and Technology, Dolgoprudny, 141701, Russia

Abstract. The purpose of this work is to study luminescence in colloidal solutions of zinc aluminate. During the work, zinc aluminate was synthesized in a gas discharge. The sizes of agglomerates were determined by the method of dynamic light scattering: 110 - 211 nm. The absorption peak of zinc aluminate was determined using a spectrophotometer. The peak was observed at a wavelength of 203 nm.

1. Introduction

In 1980, plasmonic properties were discovered in aluminum nanostructures, but only in recent years has the direction of aluminum plasmonic begun to actively develop. Aluminum is one of the most common materials on Earth, having plasmon resonance in the UV region. Near metal nanoparticles, the intensity of the electromagnetic field increases significantly, the lifetime of the excited state of the emitter changes, which is used to enhance fluorescence [1]. This effect is actively used in improving LED systems, data storage devices, and bio-diagnostics [2,3]. Zinc aluminate is a reflective pigment used for painting lighting fixtures.

2. Methods and materials

Three samples of nanoparticles were obtained in a pulse-periodic spark discharge generator under the following synthesis conditions for AlZnO I: the discharge frequency was 200 Hz, the battery voltage was 1.5 kV, the pressure in the chamber was 1.5 atm, the capacitor capacity was 38 nF, Al was used as the cathode (Zn - anode). For ZnAlO II: the discharge frequency was 200 Hz, the battery voltage was 1.5 kV, the pressure in the chamber was 1.5 atm, the capacitor capacity was 107 nF, Al was used as the cathode (Zn - anode). AlZnO III: the discharge frequency was 200 Hz, the battery voltage was 1.5 kV, the pressure in the chamber was 1.5 atm, the capacitor capacity was 38 nF, ballast resistance - 5 ohms, Al was used as the cathode (Zn - anode). The particles are formed in an inert atmosphere (Ar. 4.8) and are collected on a fixed cellulose filter and a Cu-mesh with a carbon coating. Further, to control the dimensional characteristics of zinc aluminate nanoparticles in suspension, ultrasonic treatment of dispersions (UZD2-0,1/22 dispersant) was used for 30-40 minutes. The dimensional parameters were studied using a transmission electron microscope (TEM) on a JEOL JEM-2100 device with an accelerating voltage of 200 kV and using dynamic light scattering (DRS) on a particle size meter Zetasizer Nano ZS from Malvern. The absorption intensity of zinc aluminate was obtained using a Jasco V770 spectrophotometer. The study of particle luminescence was carried out on a fluorimeter FP-8300 (Jasco) at excitation wavelengths of 260 nm.

3. Results

The elemental composition of the three samples of AlZnO I (weight percentages): Al = 1.4, Zn = 0.7, O = 97.9. For AlZnO II: Al = 2.2, Zn = 72.0, O = 25.8. AlZnO III has an elemental composition: Al = 2.2, Zn = 57.7, O = 36.8. The average hydrodynamic diameter of AlZnO I obtained by DSR is 158 nm, AlZnO II – 112 nm, AlZnO III – 211 nm. The TEM image of zinc aluminate nanoparticles in a large agglomerate and the corresponding electron diffraction pattern are shown in the Figure.1. The maximum absorption of zinc aluminate nanoparticles occurred at wavelengths in the range from 201 to - 205 nm. Luminescence of AlZnO was observed at a wavelength of 260 nm Figure 1.

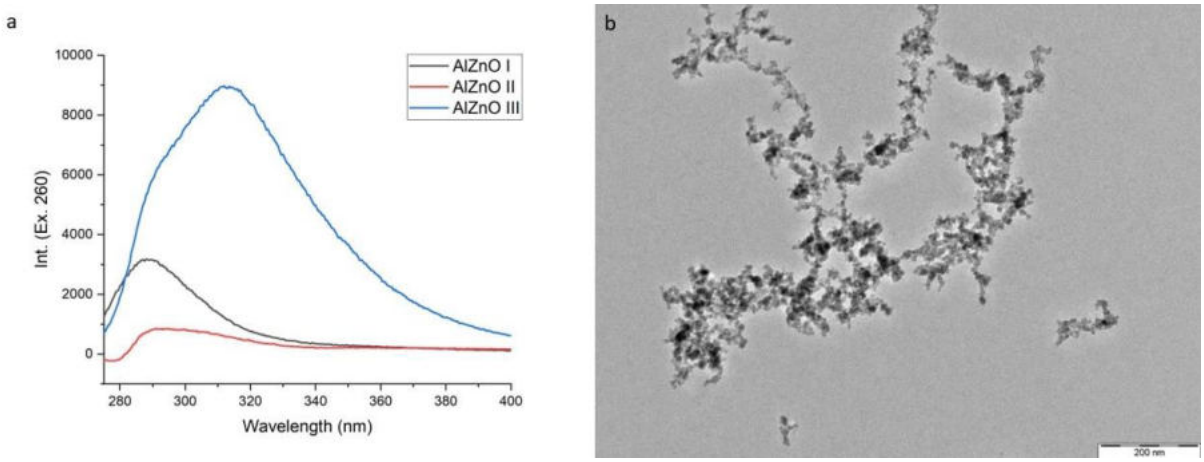

Figure 1(a-b): (a) Luminescence at an absorption wavelength of 260 nm, (b) TEM image.

Reference

[1] A.A. Zvekov, A.V. Kalensky, B.P. Aduyev, M.V. Ananyev. Optics and spectroscopy: Features of plasmon resonance in nanoparticles of various metals, Kemerovo. 2015.
[2] D.V. Guzatov, S.V. Gaponenko. Dokl. NAS of Belarus: The use of plasmon amplification of luminescence to improve the characteristics of LED systems. 2016. - Vol. 60, No. 6. - pp. 37-42
[3] S.N. Gorbov, I.S. Sazykin, O. S. Bezuglova. Dokl. Southern Federal University: Using plasmon luminescence amplification to improve the characteristics of LED systems. Rostov-on-Don. 2016. pp.97-99

Ultraviolet luminescence in colloids of zinc aluminate nanoparticles produced by spark discharge

I. Y. Konstantinova, A.A. Lizunova, V. I. Borisov, O. V. Seraya, V. V. Ivanov

Functional Materials Testing Center, Moscow Institute of Physics and Technology, Dolgoprudny, 141701, Russia

Abstract. The purpose of this work is to study the peculiarities of synthesis of zinc aluminate ($ZnAl_2O_4$) nanoparticles in spark discharge by simultaneous erosion of zinc and aluminum electrodes and investigate their size, element composition, absorption and luminescence properties in colloidal solutions. Three different conditions of spark discharge were used to produce agglomerates of primary nanoparticles with the sizes from 4 to 12 nm. The sizes of agglomerates in isopropyl alcohol determined by dynamic light scattering were in the range from 110 to 160 nm. The photoluminescence peaks of three samples of zinc aluminate nanoparticles were observed in ultraviolet (UV) range at different wavelengths from 290 to 320 nm.

1. Introduction

In recent years, aluminum plasmonic has been developing for different photonics applications due to unique Plasmon properties of metal aluminum nanoparticles in ultraviolet range. In the presence of metal nanoparticles, the intensity of the electromagnetic field increases significantly, the lifetime of the excited state of the emitter changes, which is used to enhance fluorescence of phosphors [1]. This effect is actively used in improving LED systems, data storage devices, and bio-diagnostics [2,3]. Zinc aluminate is a promising material with predicted luminescence in mid-deep UV range that can be used to create cathodoluminescence bactericidal light sources.

2. Methods and materials

Three samples of nanoparticles were obtained in a pulse-periodic spark discharge generator under the following synthesis conditions for AlZnO I: the discharge frequency was 200 Hz, the battery voltage was 1.5 kV, the pressure in the chamber was 1.5 atm, the capacitor capacity was 38 nF, Al was used as the cathode (Zn - anode). For ZnAlO II: the discharge frequency was 200 Hz, the battery voltage was 1.5 kV, the pressure in the chamber was 1.5 atm, the capacitor capacity was 107 nF, Al was used as the cathode (Zn - anode). AlZnO III: the discharge frequency was 200 Hz, the battery voltage was 1.5 kV, the pressure in the chamber was 1.5 atm, the capacitor capacity was 38 nF, ballast resistance - 5 ohms, Al was used as the cathode (Zn – anode). The particles were formed in an inert atmosphere (Ar. 4.8) and collected on a cellulose filter and a Cu-mesh with a carbon coating for microscopy measurements. Further, to control the dimensional characteristics of zinc aluminate nanoparticles in suspension, ultrasonic treatment of dispersions (UZD2-0,1/22 dispersant) was used for 30-40 minutes. The dimensional parameters were studied using a transmission electron microscope (TEM) on a JEOL JEM-2100 device with an accelerating voltage of 200 kV and dynamic light scattering (DLS) on a particle size analyzer Zetasizer Nano SZ (Malvern, USA). The absorption intensity of zinc aluminate was

obtained by Jasco V770 spectrophotometer. The study of particle photoluminescence was carried out on a fluorimeter FP-8300 (Jasco) at the excitation wavelength of 260 nm.

3. Results

The average elemental composition of the three samples of zinc aluminate obtained by energy dispersive X-ray spectrometry in the TEM were the following: AlZnO I: Al = 1.4, Zn = 0.7, O = 97.9 Wt.%., for AlZnO II: Al = 2.2, Zn = 72.0, O = 25.8 Wt.%; for AlZnO III: Al = 2.2, Zn = 57.7, O = 36.8 Wt.%. The average hydrodynamic diameter of AlZnO aluminate nanoparticles measured using the dynamic light scattering method were in the range from 110 to 160 nm for three samples. The maximum absorption of zinc aluminate nanoparticles occurred at wavelengths in the range from 201 to 205 nm. Photoluminescence spectra shown in a Figure 1a confirm UV luminescence for all samples with the peak position from 290 to 320 nm. Typical TEM image of zinc aluminate nanoparticles presented in Figure.1b show that primary nanoparticles with the sizes from 4 to 12 nm formed large agglomerates.

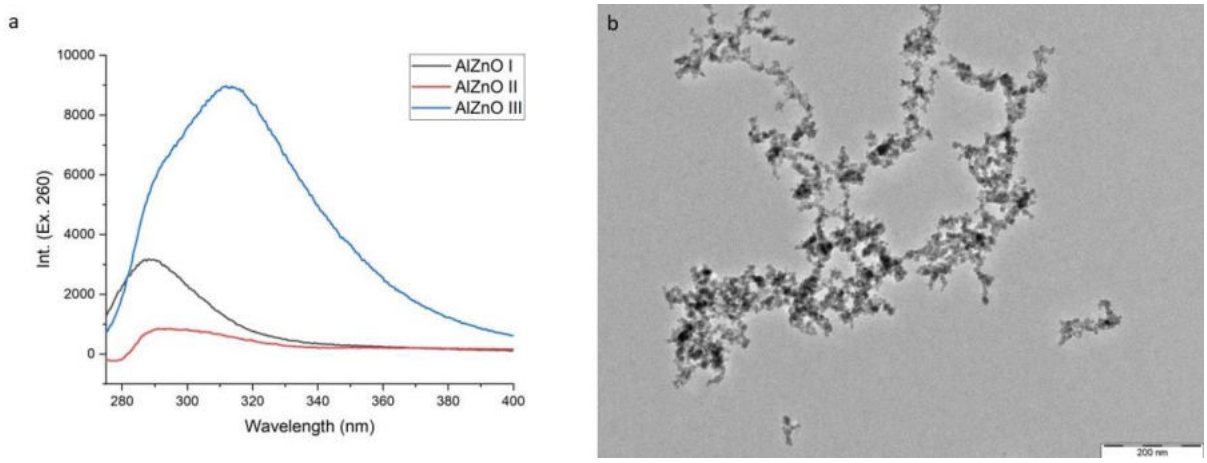

Figure 1(a-b): Optical and size properties of zinc aluminate nanoparticles: (a) Luminescence spectra of the three samples at an extinction wavelength of 260 nm, (b) typical TEM image of an agglomerate.

Acknowledgments

This research was funded by the Ministry of Science and Higher Education of the Russian Federation (state contract no. 075-03-2021-095, project identifier 0714-2021-0007, project title: “Development of functional materials with controlled electrical, chemoresistive and catalytic properties for manufacturing sensor microsystems by using methods of printed electronics”).

Reference

[1] A.A. Zvekov, A.V. Kalensky, B.P. Aduyev, M.V. Ananyev. Optics and spectroscopy: Features of plasmon resonance in nanoparticles of various metals, Kemerovo. 2015.
[2] D.V. Guzatov, S.V. Gaponenko. Dokl. NAS of Belarus: The use of plasmon amplification of luminescence to improve the characteristics of LED systems. 2016. - Vol. 60, No. 6. - pp. 37-42
[3] S.N. Gorbov, I.S. Sazykin, O. S. Bezuglova. Dokl. Southern Federal University: Using plasmon luminescence amplification to improve the characteristics of LED systems. Rostov-on-Don. 2016. pp.97-99

Ultraviolet luminescence in colloids of zinc aluminate nanoparticles produced by spark discharge

I. Y. Konstantinova, A.A. Lizunova, V. I. Borisov, O. V. Seraya, V. V. Ivanov

Functional Materials Testing Center, Moscow Institute of Physics and Technology, Dolgoprudny, 141701, Russia

Abstract. The purpose of this work is to study the peculiarities of synthesis of zinc aluminate ($ZnAl_2O_4$) nanoparticles in spark discharge by simultaneous erosion of zinc and aluminum electrodes and investigate their size, element composition, absorption and luminescence properties in colloidal solutions. Three different conditions of spark discharge were used to produce agglomerates of primary nanoparticles with the sizes from 4 to 12 nm. The sizes of agglomerates in isopropyl alcohol determined by dynamic light scattering were in the range from 110 to 160 nm. The photoluminescence peaks of three samples of zinc aluminate nanoparticles were observed in ultraviolet (UV) range at different wavelengths from 290 to 320 nm.

1. Introduction

In recent years, aluminum plasmonic has been developing for different photonics applications due to unique Plasmon properties of metal aluminum nanoparticles in ultraviolet range. In the presence of metal nanoparticles, the intensity of the electromagnetic field increases significantly, the lifetime of the excited state of the emitter changes, which is used to enhance fluorescence of phosphors [1]. This effect is actively used in improving LED systems, data storage devices, and bio-diagnostics [2,3]. Zinc aluminate is a promising material with predicted luminescence in mid-deep UV range that can be used to create cathodoluminescence bactericidal light sources.

2. Methods and materials

Three samples of nanoparticles were obtained in a pulse-periodic spark discharge generator under the following synthesis conditions for AlZnO I: the discharge frequency was 200 Hz, the battery voltage was 1.5 kV, the pressure in the chamber was 1.5 atm, the capacitor capacity was 38 nF, Al was used as the cathode (Zn - anode). For ZnAlO II: the discharge frequency was 200 Hz, the battery voltage was 1.5 kV, the pressure in the chamber was 1.5 atm, the capacitor capacity was 107 nF, Al was used as the cathode (Zn - anode). AlZnO III: the discharge frequency was 200 Hz, the battery voltage was 1.5 kV, the pressure in the chamber was 1.5 atm, the capacitor capacity was 38 nF, ballast resistance - 5 ohms, Al was used as the cathode (Zn – anode). The particles were formed in an inert atmosphere (Ar. 4.8) and collected on a cellulose filter and a Cu-mesh with a carbon coating for microscopy measurements. Further, to control the dimensional characteristics of zinc aluminate nanoparticles in suspension, ultrasonic treatment of dispersions (UZD2-0,1/22 dispersant) was used for 30-40 minutes. The dimensional parameters were studied using a transmission electron microscope (TEM) on a JEOL JEM-2100 device with an accelerating voltage of 200 kV and dynamic light scattering (DLS) on a particle size analyzer Zetasizer Nano SZ (Malvern, USA). The absorption intensity of zinc aluminate was

obtained by Jasco V770 spectrophotometer. The study of particle photoluminescence was carried out on a fluorimeter FP-8300 (Jasco) at the excitation wavelength of 260 nm.

3. Results

The average elemental composition of the three samples of zinc aluminate obtained by energy dispersive X-ray spectrometry in the TEM were the following: AlZnO I: Al = 1.4, Zn = 0.7, O = 97.9 Wt.%., for AlZnO II: Al = 2.2, Zn = 72.0, O = 25.8 Wt.%; for AlZnO III: Al = 2.2, Zn = 57.7, O = 36.8 Wt.%. The average hydrodynamic diameter of AlZnO aluminate nanoparticles measured using the dynamic light scattering method were in the range from 110 to 160 nm for three samples. The maximum absorption of zinc aluminate nanoparticles occurred at wavelengths in the range from 201 to 205 nm. Photoluminescence spectra shown in a Figure 1a confirm UV luminescence for all samples with the peak position from 290 to 320 nm. Typical TEM image of zinc aluminate nanoparticles presented in Figure.1b show that primary nanoparticles with the sizes from 4 to 12 nm formed large agglomerates.

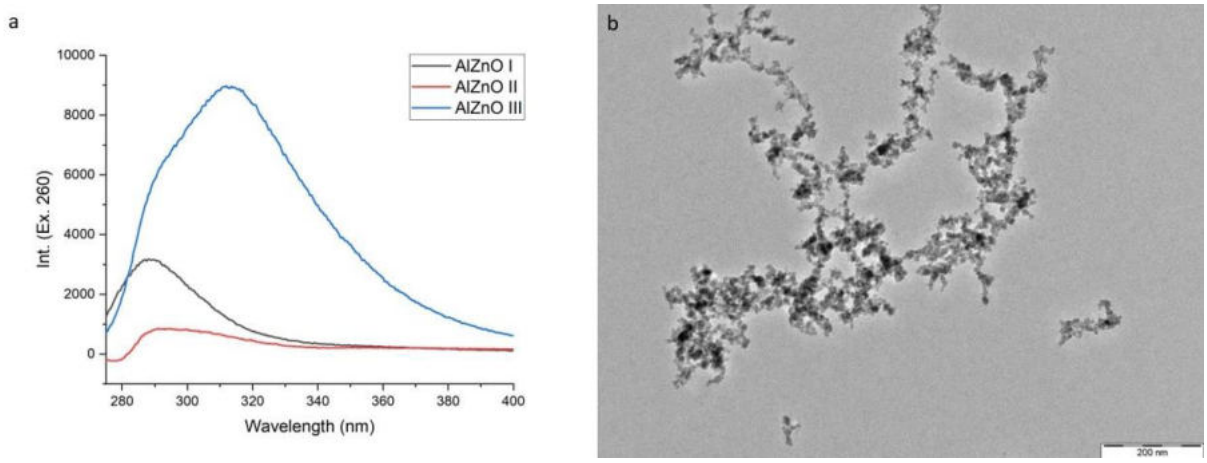

Figure 1(a-b): Optical and size properties of zinc aluminate nanoparticles: (a) Luminescence spectra of the three samples at an extinction wavelength of 260 nm, (b) typical TEM image of an agglomerate.

Acknowledgments

This work was financially supported by Russian Science Foundation (project № 22-19-00311).

Reference

[1] A.A. Zvekov, A.V. Kalensky, B.P. Aduyev, M.V. Ananyev. Optics and spectroscopy: Features of plasmon resonance in nanoparticles of various metals, Kemerovo. 2015.

[2] D.V. Guzatov, S.V. Gaponenko. Dokl. NAS of Belarus: The use of plasmon amplification of luminescence to improve the characteristics of LED systems. 2016. - Vol. 60, No. 6. - pp. 37-42

[3] S.N. Gorbov, I.S. Sazykin, O. S. Bezuglova. Dokl. Southern Federal University: Using plasmon luminescence amplification to improve the characteristics of LED systems. Rostov-on-Don. 2016. pp.97-99

Enhancement of luminescent efficiency of α-$NaREF_4$:Er^{3+} (RE= Y, Yb, Lu) nanocrystals through multi-doping strategy

A V Koshelev[1,2], N A Arkharova[1], K V Khaydukov[1], and D N Karimov[1]

[1]FSRC «Crystallography and Photonics» of Russian Academy of Sciences, 59, Leninskiy Prospekt, Moscow, 119333 Russia

e-mail address:avkoshelev03@gmail.com

Abstract. One of the effective approaches to improve the low photoluminescence efficiency of rare-earth doped fluoride nanoparticles is doping modification. Effect of Zn^{2+} and Ce^{3+} ions on the luminescence characteristics of cubic α-$NaREF_4$ (RE = Y, Yb, Lu) nanoparticles doped with Yb^{3+} and Er^{3+} ions was studied in the visible and IR spectral ranges. Nanocrystals with chemical composition α-$NaYbF_4$:$Er_{0.02}Ce_{0.02}Zn_{0.1}$ demonstrate the most intense luminescence in the region of 400-1600 nm due to up- and down-conversion energy transfer, which offers great opportunities for applications of these materials in nanophotonics and biotechnologies.

1. Inroduction

Photoluminescent (**PL**) fluoride nanoparticles (**NPs**) doped with rare-earth elements (**REE**) attract considerable interest for modern photonics and biotechnologies. The practical significance of these materials is due to their unique chemical and luminescent properties (chemical stability, large shifts in fluorescence peaks, high signal-to-noise ratio, photobleaching absence), which makes these NPs a potential candidate for various nanophotonic applications: biomedicine, photocatalysis, nanosensors, anti-counterfeiting, etc. [1-3]. However, despite the advantages described above, the low PL efficiency significantly limits their opportunities, therefore the luminescence efficiency enhancement for design of nanophosphors, capable intensively luminesce in a wide spectral range, is a very essential. One of the effective approaches to comprehensive improve the PL efficiency of these NPs is ion-doping, which permits to control the fluorescence of nanocrystals by the manipulation of the local crystal field symmetry around optically active ions [4,5]. In this study, effect of host chemical composition and dopants (Zn^{2+}, Ce^{3+} ions) on the PL characteristics of cubic α-$NaREF_4$ (RE = Y, Yb, Lu) NPs in the visible and IR spectral ranges is demonstrated.

2. Experimental details and discussion

Cubic α-$NaREF_4$:$Er_{0.02}$ (RE= Y, Yb, Lu) fluoride NPs synthesized by thermal decomposition were used as prototypes. Size, morphology, composition, and photoluminescence properties of prepared NPs were characterized by transmission electron microscopy, X-Ray diffraction analysis (XRD), and fluorescence spectroscopy. The synthesized nanoparticles with "core-shell" architecture were crystallized in the fluorite-type structure (sp. gr. *Fm*-3*m*) and were an average size of 40 nm. Cubic α-$NaYbF_4$ host doped with 2 mol.% Er^{3+} ions exhibit the most intense PL among all studied α-$NaREF_4$ (RE=Y, Yb, Lu) nanocrystals.

The strategy of additional doping of α-$NaYbF_4$:$Er_{0.02}$ NPs with homo- (Ce^{3+}) and heterovalent (Zn^{2+}) ions for PL properties improvement was applied. The concentration of Ce^{3+} and Zn^{2+} doping

ions varied from 0 to 12 mol.%. These dopants incorporate isomorphically in the α-$NaYbF_4$ crystal host over the entire range of studied concentrations, which was confirmed by XRD analysis, and without affecting the NPs dimensional characteristics. The optimal dopant Ce^{3+} concentration is 2 mol.% and composition α-$NaYbF_4$:$Er_{0.02}Ce_{0.02}$ exhibit intense PL in both the visible (400–800 nm) and IR (1500–1700 nm) spectral ranges due to up- and down-conversion energy transfer (Fig. 1). An increase in the Zn^{2+} content to 10 mol.% leads to an enhancement of PL intensity of multi-doped α-$NaYbF_4$:$Er_{0.02}Ce_{0.02}Zn_{0.1}$ NPs in the visible and IR spectral ranges up to 340% and 66% respectively.

The excellent PL properties in visible and NIR-II spectral regions makes studied NPs as potential candidate for bioimaging applications.

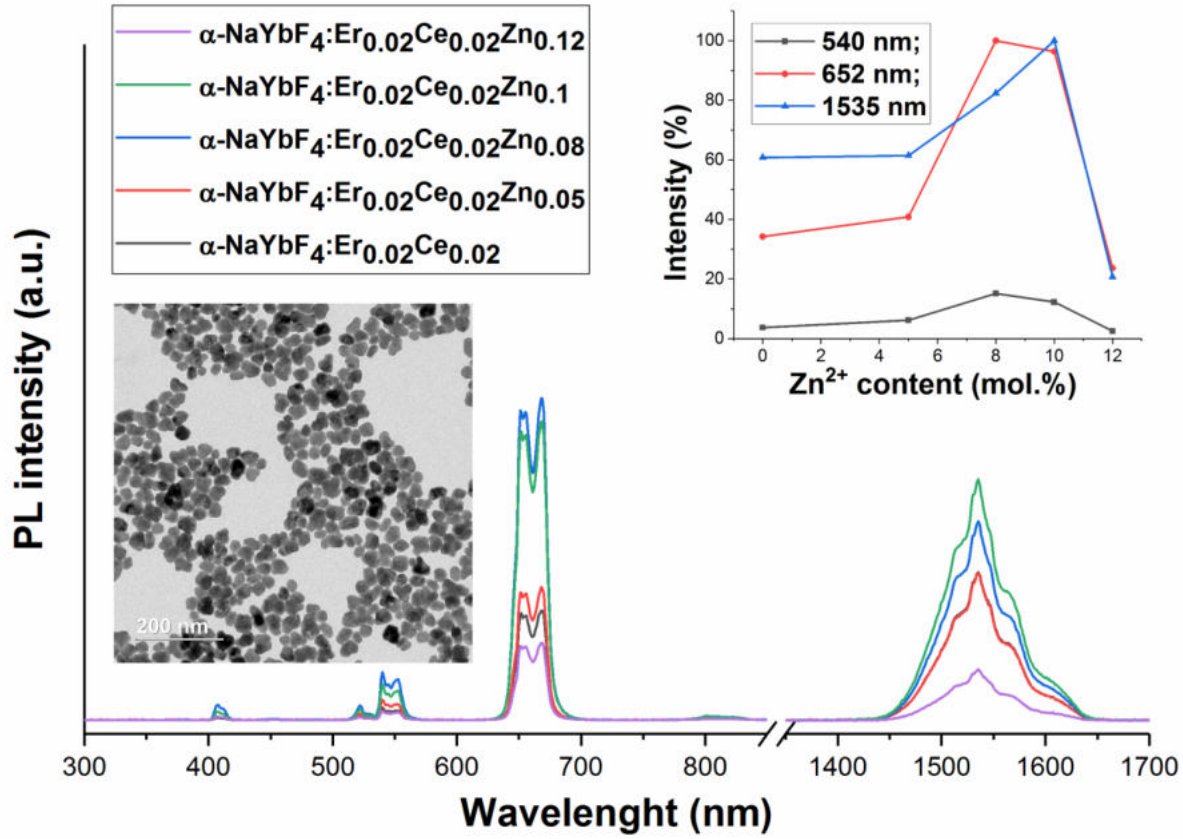

Figure 1. The PL spectra of α-$NaYbF_4$:$Er_{0.02}Ce_{0.02}Zn_x$ (x = 0 - 0.12) NPs upon IR excitation (λ=975 nm); TEM image of α-$NaYbF_4$:$Er_{0.02}Ce_{0.02}Zn_x$ NPs is shown as insert.

Acknowledgments

This research was funded by the Russian Foundation for Basic Research (project No. 20-52-56017) and Iran National Science Foundation (project No. 99004620).

References

[1] J M Meruga, W M Cross, P S May et al. *Nanotechnol.* **2012,** *23*(39), 395201.
[2] S P Tiwari, S K Maurya, R S Yadav et al. *J. Vac. Sci. Technol. B Nanotechnol. Microelectron.* **2018**, *36*(6), 060801.
[3] D N Karimov, P A Demina, A V Koshelev et al. *Nanotechnol. Russ*. **2020,** *15,* 655-678.
[4] D Chen, Y Wang. *Nanoscale* **2013**, *5*(11), 4621-4637.
[5] W You, D Tu, W Zheng et al. *J. Lumin.* **2018**, *201*, 255-264.

Neuromorphic photoelectric synapses based on metal oxides nanocrystallites

V. V. Krasnikov[1], A. A. Chezhegov, I. S. Balashov[1], A. S. Chizhov[2], A. A. Grunin[1], A. A. Fedyanin[1]

[1] Faculty of Physics, Lomonosov Moscow State University, Moscow 119991, Russia
[2] Faculty of Chemistry, Lomonosov Moscow State University, Moscow 119991, Russia

Email: krasnikov@nanolab.phys.msu.ru

Abstract. This work present the implementation of a photoelectric synapse based on semiconductor nanocrystallite (ZnO, In2O3, WO3). By choosing the type of nanocrystallite and manufacturing parameters, we obtain neuromorphic elements with variable properties. In the form of a synaptic signal, light pulses are used at a wavelength of 405 nm. The change in the conductivity of a nanocrystallite upon irradiation with light corresponds to the change in the resistance on the postneuron.

1. Introduction

Nowadays, the big data processing is one of the main areas of science and technology. The problem of image recognition and classification is solved by artificial neural networks (ANN). ANN are traditionally supported by classical computers based on the von Neumann architecture. This architecture is suitable for executing a single sequence of instructions at high speed. But ANN problems require highly parallel and multi-threaded computations with the transfer of a large amount of data between the processing unit and the memory unit by the data bus. Due to the finite size of the data bus and throughput, multi-threaded calculations on the von Neumann architecture have limitations, which leads to a decrease in the learning rate at the problems in recognition, prediction, optimization, and control [1,2]. One possible path for the future computing paradigm is to move towards brain-inspired neuromorphic photovoltaic circuits.

An artificial synapse is one of the main elements of a neuromorphic computer. The synapse communicates between the preneuron and postneuron [3]. The biological synapse has the properties of synaptic plasticity, which lead to the emergence of short-term memory (STM) and long-term memory (LTM) and is responsible for the learning of neurons [4].

2. Experiment

This work describes the implementation of a photoelectric synapse based on semiconductor nanocrystals (ZnO, In2O3, TiO2, WO3). The approach to creating an artificial synapse is cheap and easy to implement. The choice of the type of nanocrystallite and the choice of manufacturing parameters make it possible to obtain neuromorphic elements with different characteristics. Light pulses at a wavelength of 405 nm are used as a neural pre-signal for the photoelectric synapse. The change in the conductivity

of the nanocrystallite structure upon irradiation with light is used as the output signal of the postneuron, which is measured in the experiment (Fig. 1).

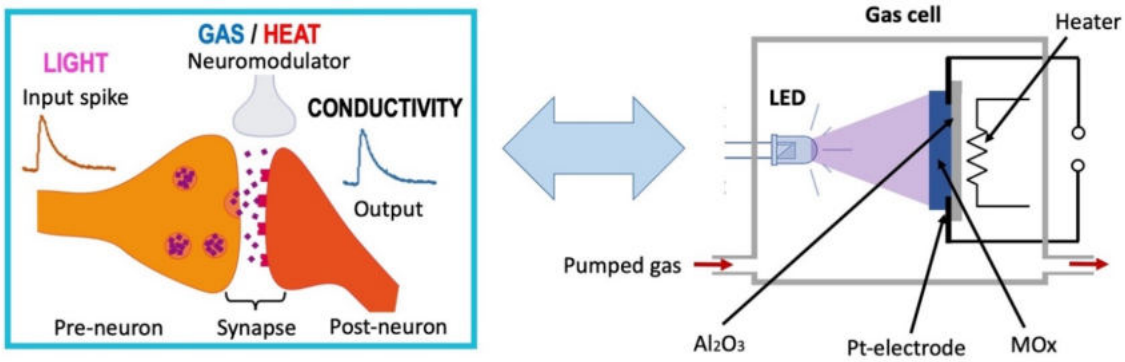

Figure 1. Biological synapse (left) and bioinspired photoelectric synapse (right) based on a nanocrystallites semiconductor film with atmosphere gas composition and temperature as an additional control parameters.

3. Results

The studied photoelectric synapses based on semiconductor nanocrystals perfectly demonstrate biologically similar synaptic properties of plasticity. The analysis of the obtained results showed that the spike frequencies and temporal following of spikes affects the dynamics of synaptic plasticity (STM, LTM). The photoelectric synapse has demonstrated a transition from STM to LTM with increasing spike frequency, synaptic spike weight, and number of spikes received. The basic method of neuromorphic learning was demonstrated in the form of pair-impulse fasciillation (PPF index) [5].

A promising direction in the search for control parameters that act as neuromodulators has been found that the gas composition of the atmosphere and temperature changes play this role. The studied photoelectric synapses based on ZnO, In2O3, TiO2, WO3 have a wide range of parameters that differ in the temporal characteristics of STM and LTM. Additional channels for changing the composition of the gas and the temperature of the structures act as neuromodulators, which have a high potential for implementation as a large class of components of photovoltaic neuromorphic schemes.

References

[1] del Valle, Javier, et al. "Challenges in materials and devices for resistive-switching-based neuromorphic computing." Journal of Applied Physics 124.21, 211101 (2018).

[2] Nahmias, Mitchell A., et al. "Neuromorphic photonics." Optics and Photonics News 29.1, 34-41 (2018).

[3] Kotseruba, Iuliia, and John K. Tsotsos. "40 years of cognitive architectures: core cognitive abilities and practical applications." Artificial Intelligence Review 53.1, 17-94 (2020).

[4] Lee, Minkyung, et al. "Brain-inspired photonic neuromorphic devices using photodynamic amorphous oxide semiconductors and their persistent photoconductivity." Advanced Materials 29.28, 1700951 (2017).

[5] Hu, S. G., et al. "Emulating the paired-pulse facilitation of a biological synapse with a NiOx-based memristor." Applied Physics Letters 102.18, 183510 (2013).

All-dielectric photonic crystal microcavity with electrically tunable Q-factor

A. I. Krasnov[1,2], P. S. Pankin[1,2], D. S. Buzin[1,2], G. A. Romanenko[1,3], V. S. Sutormin[1,2], S. V. Nabol[1,2], F. V. Zelenov[4,3], A. N. Masyugin[4,3], S. Ya. Vetrov[2,1], I. V. Timofeev[1,2]

[1]Kirensky Institute of Physics, FRC KSC SB RAS, Krasnoyarsk 660036, Russia
[2]Siberian Federal University, Krasnoyarsk 660041, Russia
[3]Siberian State University of Science and Technology, Krasnoyarsk 660037, Russia
[4]AO NPP Radiosvyaz, 660021 Krasnoyarsk, Russia

E-mail: krasnov04850@mail.ru

Abstract. At the moment, the problem of external control of resonances, namely their spectral position and Q-factor, remains open. External control of the spectral position of the modes is carried out either by changing the thickness of the resonant layer or by changing the refractive index of the material. The concept of bound states in the continuum allows to control the Q-factor of the microcavity. The paper presents the design of a photonic crystal microcavity with a tunable Q-factor.

1. Introduction

Bound state in the continuum (BIC) is the non-radiative eigenstate in an open system. BICs are usually divided into three types [1]. The first type of BIC, firstly proposed by Wigner and von Neumann, occurs when a particle is scattered at an oscillating potential. As a result of destructive interference of scattered waves, the wave function of a particle is localized in a potential well, despite the fact that its energy is greater than the potential barrier. The second type of BIC occurs when the system parameters are changed. It includes Fabry-Perot BIC and Friedrich-Wintgen BIC. The last type is symmetry-protected BIC which arises due to differences in the symmetry of localized and propagating waves [1]. BICs have found application in lasers, nonlinear optical effects enhancement, in generation of optical beams with special properties, such as vortex beams [2,4].

2. Results and discussion

The model of the optical microcavity is shown in Figure 1 (left). The microcavity consists of two glass substrates with dielectric layers of silicon nitride and silicon dioxide deposited on them. The layers alternate with a period comparable with the wavelength of visible light, forming a one-dimensional photonic crystal (PhC). The PhC contains a defective layer is filled by liquid crystal (LC) 5CB which is an anisotropic material. Technological layers of ITO and PVA are also included. The ITO layer is required for the application of the external electric field, and the PVA is used for the planar alignment of the LC molecules.

Figure 1 (right) shows the reflection spectrum of the microcavity, calculated by the Berreman method, depending on the rotation angle φ of the LC optical axis. When light is incident at Brewster angle, the TE-wave is reflected, due to the photonic bandgap. The TM-wave passes through the PhC without a reflection. When the LC optical axis is rotated, TM-waves are transformed into TE-waves that are localized in the microcavity. A number of resonant lines corresponding to microcavity modes can be seen in the spectrum. It can be seen from the figure that at the angles φ equal to 0 and $\pi/2$, a collapse of the resonance linewidth is observed, indicating the realization of BIC protected by symmetry. They are realized because at these values of φ, TE localized modes are

not coupled with propagating TM waves. It can be seen that when the angle φ changes, the width of the resonant lines is changed, which makes it possible to control the Q-factor of microcavity modes.

At some intermediate angles φ, a collapse of resonant lines is also observed, indicating the realization of Friedrich–Wintgen-type BIC. These BICs are formed by destructive interference of ordinary and extraordinary waves, when they leak out of the LC layer [5].

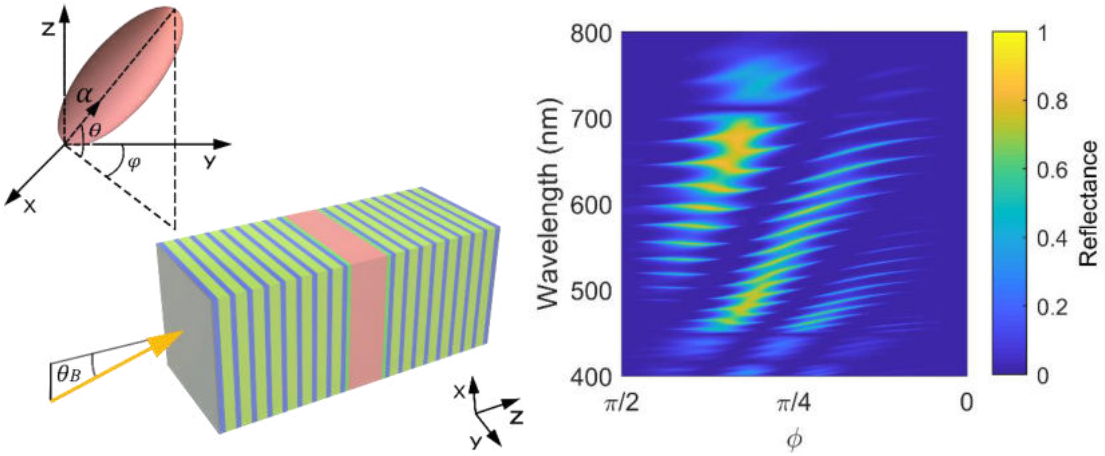

Fig. 1. Schematic model of the optical microcavity and liquid crystal (LC) optical axis orientation (left). The reflection spectrum of the microcavity versus the rotation angle of the LC layer (right)

Liquid crystal is sensitive to external influences. By applying an external electric field to it, or by heating it, one can control its effective refractive index. This leads to a change in coupling coefficient between TM- and TE-waves, and as a consequence, to a change in the Q-factor of the resonances.

3. Conclusion

The spectral properties of a microcavity consisting of two PhC mirrors with an anisotropic LC layer between them are investigated. The possibility of control of the spectral properties by external influence on the LC layer is shown. The obtained results can be useful for creating optical microcavities with tunable Q-factor.

Acknowledgments

This research was also funded by the Russian Science Foundation (project no. 22-22-00687).

References

[1] Azzam, S. I., & Kildishev, A. V. (2021). Photonic bound states in the continuum: from basics to applications. Advanced Optical Materials, 9(1), 2001469.

[2] Hsu, C. W., Zhen, B., Stone, A. D., Joannopoulos, J. D., & Soljačić, M. (2016). Bound states in the continuum. Nature Reviews Materials, 1(9), 1-13.

[3] Sadreev, A. F. (2021). Interference traps waves in open system: Bound states in the continuum. Reports on Progress in Physics.

[4] Joseph, S., Pandey, S., Sarkar, S., & Joseph, J. (2021). Bound states in the continuum in resonant nanostructures: an overview of engineered materials for tailored applications. Nanophotonics.

[5] Pankin, P. S., Wu, B. R., Yang, J. H., Chen, K. P., Timofeev, I. V., & Sadreev, A. F. (2020). One-dimensional photonic bound states in the continuum. Communications Physics, 3(1), 1-8.

Integrated optical transceiver based on III-V microdisk laser and photodiode

Natalia V. Kryzhanovskaya[1,2], Eduard I. Moiseev[1,2], Anna S. Dragunova[1,2], Mikhail V. Maximov[2], Nikolay A. Kaluzhnyy[3], Sergey A. Mintairov[3], Fedor I. Zubov[2], Marina M. Kulagina[3], Julia A. Guseva[3], Alexey I. Likhachev[3], Alexey E. Zhukov[1]

[1] International Laboratory of Quantum Optoelectronics, HSE University, St Petersburg, Russia

[2] Nanophotonics lab, Alferov University, St. Petersburg, Russia

[3] Ioffe Institute, St. Petersburg, Russia

E-mail: nataliakryzh@gmail.com

Abstract. In this work, we study III-V p-i-n photodetectors and disk microlasers in terms of their static and small-signal modulation frequency response. InGaAs/GaAs quantum well-dots (QWDs) are used as the active region of devices to provide operation wavelength around 1.1 μm, high optical and frequency response and temperature stability of characteristics. 30 μm-in-diameter microdisk lasers revealed CW output power level of 15-22 mW and error-free 10 Gbit/s data transmission at 30ºC without temperature stabilization. The microdisk laser and the p-i-n photodiode were heterogeneously integrated on a silicon substrate by Au-Au thermocompression bonding to form a compact transceiver. Detection of microlaser emission by the closely placed p-i-n photodiode is studied. The absolute value of the responsivity of the waveguide detector as high as 0.68 A/W for unbiased device is demonstrated. The efficiency of the optical link at the level of 1.4% is achieved. Approaches to obtain higher efficiency of the optical link are discussed.

1. Introdusction

Semiconductor resonators with disk geometry supporting whispering gallery modes (WGMs) are a promising basis for creating energy-efficient and small-sized coherent light sources suitable for various applications [1]. For a number of practical applications, it is desirable to combine a semiconductor WGM microlaser with a photodetector to form an optocoupler. For example, such optocouplers with an open optical channel available for external action can be used as various types of microsensors (biosensor, nanoparticle detection), for galvanic isolation, for contactless control, etc [2]. Such optical components that includes a laser source and a photodetector, and any passive element (optical waveguide) should be fabricated on silicon-on-insulator substrates using complementary metal–oxide–semiconductor (CMOS) technologies for further signal processing. Formation of photonic waveguides and optical modulators integrated over CMOS circuits have been demonstrated already [3, 4]. Compound III–V semiconductor lasers have been grown directly on silicon substrate

[5], but rather high growth temperature (above 500°C) is not compatible with CMOS processing. Direct bonding of III–V active devices on silicon platform offers an acceptable low temperature process that is compatible with CMOS fabrication. In this work, we report on the design, fabrication and characterization of an optical transceivers based on III-V microdisk lasers and photodetector bonded onto silicon substrate.

2. Structure design and fabrication

In this work we use semiconductor microdisk (MD) laser as a light source for a compact transceiver. MD lasers demonstrate low energy-to-data ratio (1.5 pJ/bit for the 10-μm in diameter laser) and in the plane output emission, which facilitates the integration of such microlasers with other planar optoelectronic elements even in the far field. For light detection we used a waveguide p-i-n photodiode. Metal-organic vapor phase epitaxy was used to grow the epitaxial structures of the p-i-n photodiode and the laser on an n^+-GaAs substrate misoriented by 6° toward [111] direction. The active region of the photodiode consists of ten stacked InGaAs/GaAs quantum well-dots structures, with a plane quantum dot density in excess of 1×10^{11} cm^{-2}. MD laser with a mesa diameter D of 31 μm were formed by photolithography and dry etching (STE ICPe68). The photodiode was made in the form of a parallelepiped cleaved along {110} crystallographic planes. The length and the width of the photodiode were 200 μm and 50 μm, respectively. Top p-contact was formed using a 0.1 μm thick AgMn/Ni/Au alloy. As an n-contact, we used the metallization of the AuGe and Ni alloy, deposited by thermal evaporation on the back side of the substrate. The light-absorbing edges of the photodiode structures were formed by cleaving crystals without applying additional anti-reflective coatings.

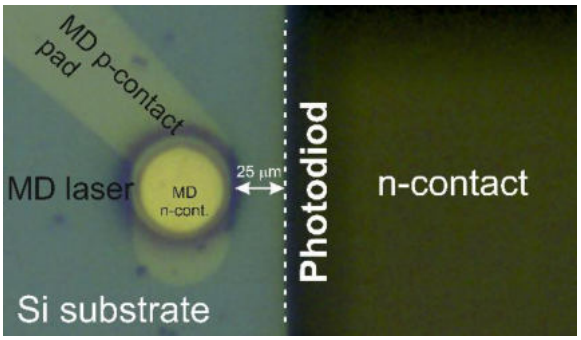

Figure 1. Photo of the microlaser and photodiode bonded onto the Si substrate.

Microlaser and photodiode were bonded onto Si substrate using Au-Au thermocompressive bonding (Figure 1). The distance between the MD sidewall and the PD was as small as 25 μm.

3. Results

First, the microdisk laser and the p-i-n photodiode were fabricated and studied separately. The microlaser demonstrates single-mode emission near 1.1 μm. As detected by an external Ge power meter, the free space output optical power increases almost linearly up to 12 mW limited by the thermal roll-over at 120 mA (Figure 2). In 31 μm in diameter bonded microdisk laser the maximum -3-dB modulation frequency of 8.2 GHz was found. The InGaAs/GaAs QWDs p-i-n photodiodes with low dark current (2.1 μA/cm2) and sensitivity up to 1.12 μm spectral range were demonstrated.

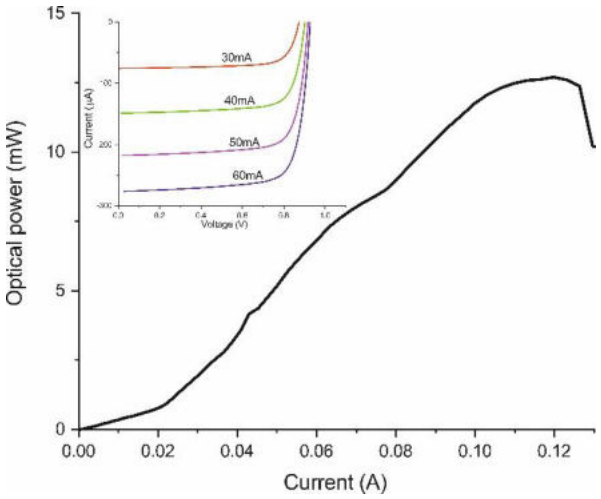

Figure 2. Light-current characteristic of the bonded 31 μm in diameter disk microlaser obtained at 20°C. Inset: photocurrent of the photodiode integrated with microlaser at different laser pumping current.

Next, microlaser and photodetector were integrated onto Si substrate using Au-Au thermocompressive bonding. Epi-side down bonding of the microdisk laser to a silicon substrate significantly (~2 times) decreases the thermal resistance and improves continuous-wave and dynamic characteristics. The photocurrent of the photodiode integrated with microlaser versus the MD pumping current and PD reverse bias were studied (inset in Figure 2). The maximum link efficiency determined as the ratio of the photodiode photocurrent increment to the increment of the microlaser bias current was up to 1.4%.

Acknowledgments

This work was supported by the Russian Science Foundation grant 18-12-00287, https://rscf.ru/project/18-12-00287/.

References

[1] W. W. Wong, C. Jagadish and H. H. Tan, "III-V Semiconductor Whispering-Gallery Mode Micro-Cavity Lasers: Advances and Prospects," in IEEE Journal of Quantum Electronics, doi: 10.1109/JQE.2022.3151082.

[2] Toropov, N., Cabello, G., Serrano, M.P. et al. Review of biosensing with whispering-gallery mode lasers. Light Sci Appl 10, 42 (2021)

[3] Y.A. Vlasov, S.J. McNab, Opt. Express 12, 1622–1631 (2004)

[4] A. Liu, R. Jones, L. Liao, D. Samara-Rubio, D. Rubin, O. Cohen R. Nicolaescu, M. Paniccla, Nature 427, 615–618 (2004)

[5] Victoria Cao, Jae-Seong Park, Mingchu Tang, Taojie Zhou, Alwyn Seeds, Siming Chen, Huiyun Liu, Recent Progress of Quantum Dot Lasers Monolithically Integrated on Si Platform, Front. Phys., Vo. 10 (2022)

Thermo-optical effect in a Mach-Zehnder interferometer on a silicon nitride platform for quantum photonic applications

A Kuzin[1,2,*], A Lyubchak[2,3], A Golikov[2], P An[2,4,5], V Kovalyuk[2,4,5], G Goltsman[2,3]

[1]Skolkovo Institute of Science and Technology, Russia, 121205

[2]Department of Physics, Moscow State Pedagogical University, Russia, 119992

[3]National Research University Higher School of Economics, Russia, 101000

[4]NTI Center for Quantum Communications, National University of Science and Technology MISiS, Russia, 119049

[5]Russian Quantum Center, Skolkovo, Russia, 143025

*Corresponding author: Aleksei.Kuzin@skoltech.ru

Abstract. Here we study the experimental dependence of the Mach-Zehnder interferometer transmission spectrum on the thermo-optical effect for cases of a microheater and a stage with temperature control. The results of this work can be used to create precision phase modulators for quantum photonic applications.

1. Introduction and operation device principle

The Mach-Zehnder interferometer (MZI) with a phase shifter is a wide spread technique for building receivers for signal-to-noise operation [1]. It is related with necessary to achieve phase stabilization and low optical losses. Due to low optical losses in C-Band and CMOS-compatible route [2], the technology of creating photonic integrated circuits on a silicon nitride (Si_3N_4) platform becomes promising. However, the contribution of bouth internal (microheaters) and external (hot plate) temperature sources on the phase change for one device based on Si_3N_4 platform still not studied.

Figure 1(a,b) shows microphotographs of the MZI on a Si_3N_4 platform with Ti/Au phase modulators.

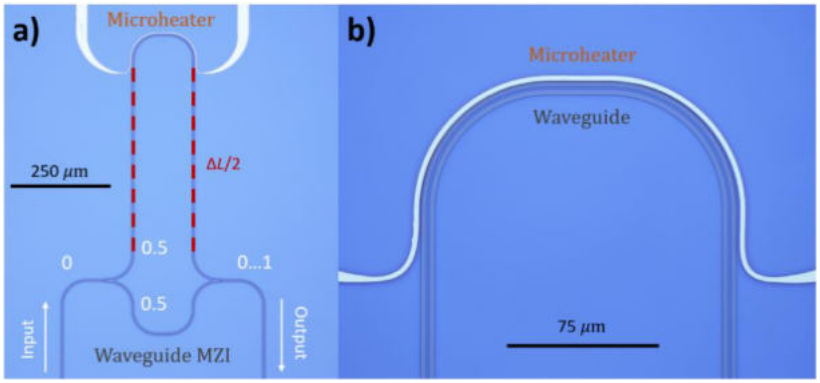

Figure 1. (**a**, **b**) Microphotos of the MZI with microheater.

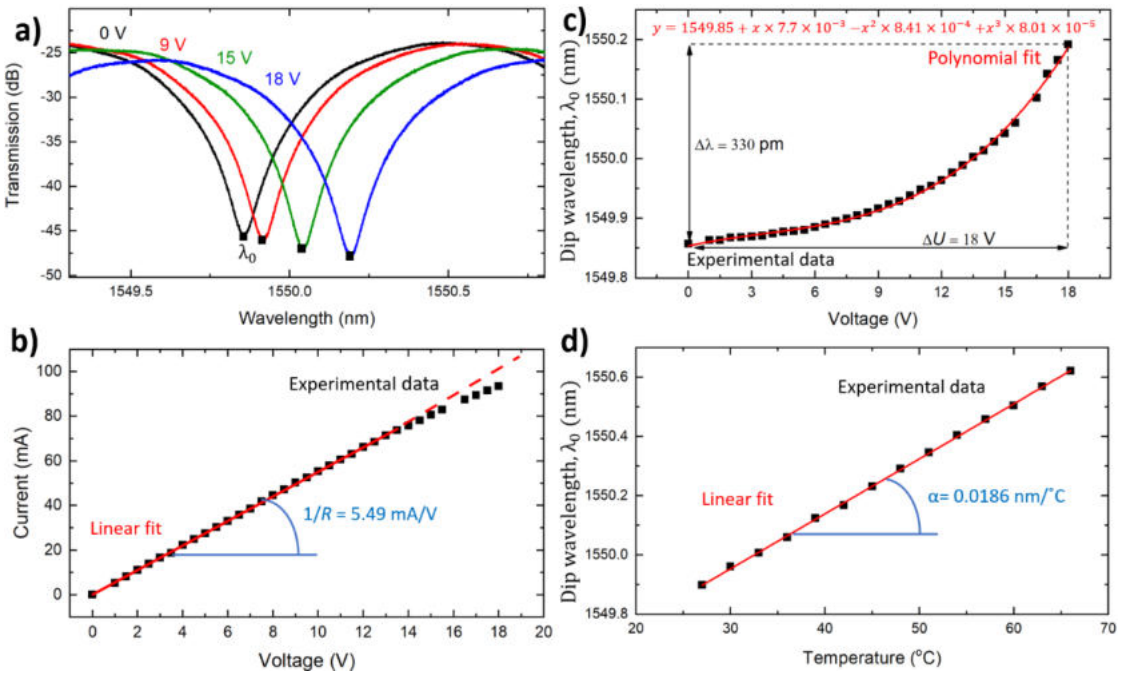

Figure 2. **(a)** Zoomed section of the transmission spectrum at the central wavelength close to 1550 nm at different voltage values; **(b)** IV-curve of the microheater; **(c)** The dependence of dip wavelength on the microheater voltage; **(d)** Dependence of dip wavelength on 3D stage temperature.

Optical radiation input/output from the chip by using focusing grating couplers (FGCs) [3]. The geometric difference between the length of the arms (ΔL) for the MZI was 952 μm to provide a free spectrum range approximately 1 nm. The microheater with width equal 4 μm and thickness 230 nm was located at 4.5 μm from the waveguide.

2. Results and Discussion

Firstly, a fixed voltage value was applied to the microheater, and the current was measured. Voltage values were changed from 0 V to 18 V with 0.5 V steps, every 2 minutes (Fig 2 (b)). Under the influence of Joule heating, the effective refractive index changed, which affected on the optical path and further on the phase difference in the MZI arms (Fig 2 (a)). The results of the experiment by using a microheater are demonstrated in Figure 2 (c). The maximum change in dip wavelength (λ_0) with increasing voltage from 0 to 18 V was 0.33 nm. Secondly, the phase shift was controlled by changing the 3D stage temperature. Figure 2 (d) shows the linear dependence of the λ_0 on the stage temperature. The slope of the straight line was 18.57±0.11 pm/°C. Thus, in instance to shift λ_0 by 0.33 nm, it is necessary to increase the temperature of the entire structure by 18°C or apply a voltage of 18 V to the microheater.

Conclusion

The results obtained make it possible to evaluate the thermo-optical effect due to microheaters on a chip relative to external sources of temperature adjustment. These data are promising for creation precision phase modulators for quantum photonic applications.

Acknowledgments

We acknowledge support of the Russian Science Foundation, grant No. 19-72-10156.

References

[1] Sych, D., and Gerd, L. Phys. Rev. letters 117.20: 200501, 2016.
[2] Venediktov, I. O., et al. Journal of Physics: Conf. Series. Vol. 1695. No. 1. IOP Publishing, 2020.
[3] Kuzin, A., et al. Journal of Physics: Conf. Series. Vol. 1410. No. 1, 2019.

Synthesis and properties of nanostructure composites based on barium titanate and 3d metal

A.V. Kurilova*[,1], A.L. Sukhachev[2], K.V. Bogdanov[1], I.V. Nemtsev[2,3], K. Shulga[3], A.E. Sokolov[2,3] and A.Yu. Dubavik[1]

[1] ITMO University, Kronverksky 49, Saint Petersburg 197101, Russia
[2] Kirensky Institute of Physics SB RAS, FRC KSC SB RAS, Akademgorodok 50/38, Krasnoyarsk 660036, Russia
[3] Siberian Federal University, Svobodny 79, Krasnoyarsk 660041, Russia

ankurilova@niuitmo.com

Abstract. The synthesis, optical and magneto-optical properties of hybrid nanocomposites based on BaTiO3 nanoparticles and nanoalloy cobalt-iron are presented. The influence of ferroelectric properties on the effect of magnetic circular dichroism in the obtained nanocomposites, as well as the manifestation of the Stark effect in them, is considered.

1. Introduction

Multiferroics are materials and multiphase heterostructures with several coexisting order parameters. They have great potential for practical use in magneto- and optoelectronics, spintronics as elements of various sensors, tunable optical elements, and memory devices with magnetic reading or electrical recording [1, 2].

The BTO nanoparticles are the most studied perovskite-type ferroelectrics because of their excelling optical and electrical properties. The spontaneous polarization of barium titanate crystals at room temperature range between 0.15 C/m^2 and 0.26 C/m^2 and its Curie temperature is between 120 and 130 °C [3]. The Fe–Co alloys demonstrate the high saturation magnetization M_s (often more than 100 emu/g) with soft magnetic properties and the high curie temperatures Tc ≈ 900 °C that make them great potential candidates for the high-temperature applications [4].

In our work, we investigated an artificial multiferroic composite that coincides with a combination of lead-free ferroelectric perovskite, $BaTiO_3$ (BTO), and nanoparticles of cobalt and iron nanoalloy.

In a report [5], analogy structure (CoFe films on BTO substrates) shows significant change properties during structural phase transitions of BTO. Starting from 300 K, cooling through the tetragonal to orthorhombic phase transition leads to a sharp 90° magnetic switching in the magnetic strip domains, an increase in magnetoelastic anisotropy while preserving the overall structure of the magnetic domains. But the influence of morphology and the ratios of BTO to FeCo and Fe to Co on the current processes is not yet known.

2. Samples

The first step of creating of our composite was based on article [6]. BTO nanoparticles were synthesized by hydrothermal method from barium chloride dihydrate, oxalic acid and butyl titanate in distilled water. In following step, as in paper [7], we expected to obtain nanocrystal with the formula $Fe_{45}Co_{55}$ for shell $BaTiO_3$. The binding of BTO and FeCo particles was caused by high-temperature heating.

3. Experiments

The morphology of samples at all stages of synthesis was studied using a desktop scanning electron microscope Hitachi TM-3000. In a result, the mean size of the completed sample is 290 nm. Its form and dimensions can be explained by agglomeration during heat treatment. Another reason is the specifics of hydrothermal processing of synthesis of $BaTiO_3$ nanotorus. The optical and magneto-optical properties of the samples were measured on a Jasco J-1500 circular dichroism spectrometer with an attachment for magnetic circular dichroism, in a magnetic field range of ±1.5 T and a spectral range from 300 to 800 nm. There are reported in study [7] that the charge of iron is 3+ and cobalt is 2+. It's confirmed our research. The spectrum MCD of FeCo/C nanoalloy demonstrate transitions on 330, 440, 565 nm for ion Fe^{3+} and 290, 370, 475 nm for ion Co^{2+}. The spectrum of composite $BaTiO_3$-FeCo/C show redistribution of the intensity of long-wave transitions with additional splitting line CD on 730 nm in magnetic field. So, it can be called a manifestation of the Stark effect.

4. Conclusion.

A comprehensive study $BaTiO_3$ nanoparticles and nanoparticles based on cobalt-iron alloy showed that as a result of the synthesis, nanocomposites with an average size of 290 nm were obtained.

The study of the magnetic circular dichroism of the obtained samples showed that since the magnetic nanoparticles are in the field of residual polarization, a larger ferroelectric particle, weaker effects associated with the Stark effect appear on the spectra of magnetic circular dichroism (MCD). The study of the magnon-polariton interaction of these samples remains an interesting task from the point of view of fundamental physics

Acknowledgments

The electron microscopy investigations were conducted in the Krasnoyarsk Regional Center of Research Equipment of Federal Research Center «Krasnoyarsk Science Center SB RAS».

References

[1] A. M. Kalashnikova, R. V. Pisarev, L. N. Bezmaternykh, V. L. Temerov, A. Kirilyuk, Th. Rasing. JETP Letters **81.9** (2005) 452
[2] A. P. Pyatakov, A. G. Zhdanov, A. K. Zvezdin. ICONO 2005: Nonlinear Optical Phenomena **6259** (2006)35
[3] J. Shieh, J. H. Yeh, Y. C. Shu, J. H. Yen,. Materials Science and Engineering: **B 161** (2009)50
[4] C. W. Kim, Y. H. Kim, H. G. Cha, D. K. Lee, Y. S. Kang. J. Nanosci. Nanotechnol. ***6*.11**(2006)3417
[5] T. H. E. Lahtinen, S.van Dijken .Applied Physics Letters **102.11**(2013)112406
[6] H. Jiao, K. Zhao, L. Ma, Y. Tang. Inorganic and Nano-Metal Chemistry **47.5**(2017)647
[7] V. Tzitzios, G. Basina, D. Niarchos, Wanfeng Li, G.Hadjipanayis (2011). Synthesis of air stable FeCo nanoparticles, 109(7), 7–0.

Detection of orbital angular momentum by forked diffraction method.

E S Lebedeva[1], K O Sedykh[1, 3], I O Venediktov[1, 4], G N Goltsman[1, 2, 3] and D V Sych[4, 5]

[1]Department of Physics, Moscow State Pedagogical University, Moscow, 119992, Russia
[2]Russian Quantum Center, Skolkovo 143025, Moscow, Russia
[3]NTI Center for Quantum Communications, National University of Science and Technology MISiS, Moscow 119049, Russia
[4]National Research University Higher School of Economics, Moscow, 101000, Russia
[5]P. N. Lebedev Physical Institute, Russian Academy of Sciences, Moscow, 119991, Russia

narniyall02@gmail.com

Abstract. Orbital angular momentum (OAM) is a characteristic of wave describing its spiral phase front. These waves can be applied in various fields such as quantum communications and computations, hence, there is a need for a compact and simple method of its generation and detection. Here we describe an experiment proving efficiency of forked diffraction method.

1. Introduction

There are several methods for generation and detection of OAM light beams. Forked diffraction method distinguishes its flexibility, simplicity in execution as well as possibility to generate several OAM beams at once, which will simplify working with them in future.

2. Theoretical background

The wave vector of initial Gauss beam is directed straight with respect to the direction of propagation. In OAM carrier beams, this vector is directed tangentially to the propagation plane and at some angle along the vertical axis, so wave has a spiral phase front [3]. The degree, direction and size and symmetry of the swirl determines the topological charge - l. Its value depends on the number of torsions per wavelength of the wave and sign – on the direction of torsions (clockwise – $l < 0$, counterclockwise – $l > 0$) [2]. Grating with $+l$ (figure 1(a)) transforms initial Gauss beam into a diffracted one, where central order remains with l of initial beam, first right order will have the same l as grating, left one – $(-l)$, with each subsequent order $|l|$ will increase by l of the grating. To prove that obtained pattern is an OAM carrier, it should be transformed back into the Gauss beam. For that it is necessary to select the near-right order with $+l$ and let it pass through the plate with a charge equal to $-l$, in other words, inverted one [1]. Topological charge of resultant beam will become 0, which means it will turn into Gauss beam back. Since the plate is made of reflective material, the pattern formed by the slotted lattice can be considered as inverted at the reflection.

3. Experiment.

The necessary masks with a size of 0.2 mm were cut on the niobium plates on a sapphire substrate. The source of the Gaussian beam was a red CW laser. The first grid which generated OAM and through which the light passed had a charge of +1. On the obtained picture first right order is selected and guided through the pinhole to cover all other orders and then was focused by converging lens and completely reflect from the second grid which detected OAM.

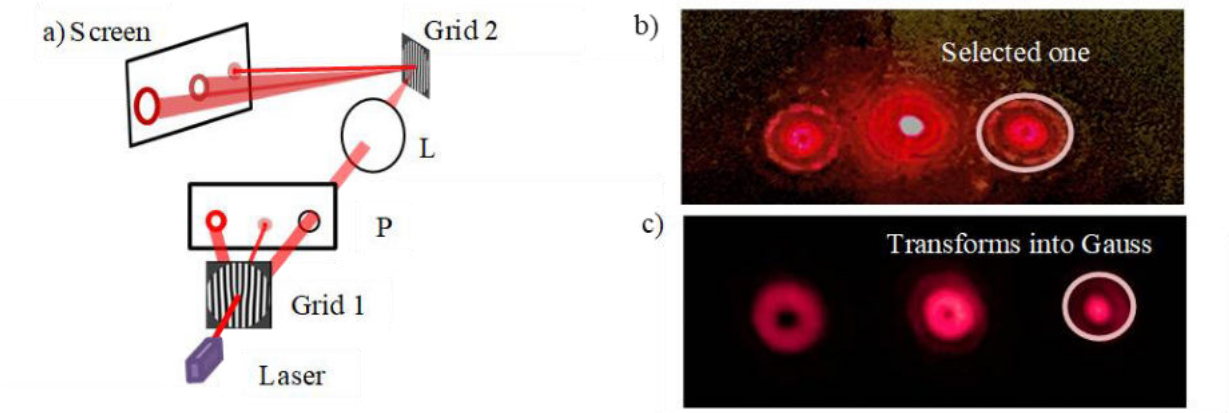

Figure 1. a) Set up. Laser – free space CW laser (wavelength - *650 nm),* GRID 1 – first grating (*l = 1*) generates OAM, P - pinhole, L – converging lens (*F = 40 mm*), GRID 2 – second grating (*l = (-1))* at the reflection), detects OAM. b) Picture at the output of the first grid. Left order – *l = (-1),* central – *l = 0,* right (the chosen) – *l = 1.* c) Picture on the reflection of the second grid. Left order – *l = (-2),* central – *l= (-1),* right – *l = 0.*

Passing through the first grating (figure 1(c)), the Gauss beam transforms into required diffraction pattern: at the central order *l = 0,* the right has *+l,* the left has *-l* and the intensity decreases from the central order. When detecting (figure 1(c)), *l* of the selected order became 0, the central one has *l = (-1)* and the left one has *l = (-2).* Intensity is distributed in the same way. This fact established the presence of OAM in the beam obtained during generation.

4. Conclusions

Results of this experiment proves the possibility of generation and detection of OAM light beams with high efficiency level. The use of special diffraction gratings significantly simplifies the study and the use of OAM beams, which can be used in many fields of optics.

Acknowledgments

We acknowledge Natalia Kaurova and Philip Zolotov for gratings fabrication, Dr. Ledesma and Mr. Pabon for sharing program for diffraction masks generating.

References

[1] André B Cunha et all. November 2015 CONF TELE 2015, Aveiro, **108**

[2] Rui Chen, Hong Zhou, Marco Moretti et all November 2019 *IEEE Communication Surveys & Tutorials* **22** p 840-868

[3] L Allen, M B Beijersbregen et all. June 1992 *Physsical Review A* **45** 11

Method for constructing NMR signal spectra using the discrete Fourier transform

S S Makeev[1] and V V Davydov[1, 2, 3]
[1]Peter the Great Saint-Petersburg Polytechnic University, Saint Petersburg, Russia, 195251
[2]The Bonch-Bruevich Saint Petersburg State University of Telecommunications, Saint Petersburg, 193232, Russia
[3]All-Russian Research Institute of Phytopathology, Moscow Region 143050, Russia

e-mail: st_makeev@mail.ru

Abstract. This article is devoted to the study of the structure of the nuclear magnetic resonance signal, which is recorded using the modulation technique. As a result of this study, the influence of the properties of the medium on the possibility of registering an NMR signal in a weak magnetic field was determined. A new methodology for recording the NMR signal using the contributions of absorption and dispersion signals is proposed. The features of the use of spectral analysis in the study of the NMR signal from liquid media are determined. The results of theoretical calculation and experimental studies are compared.

1. Introduction

In recent years, various methods of express control of the state of condensed matter have become increasingly in demand. The results of express control are used during various physical and chemical experiments, as well as for environmental control of hard-to-reach reservoirs and water protection zones. They are also relevant for quality control of products of the hydrocarbon industry, at all stages of its production (for example, gasoline, motor oils, etc.).

The main condition for a qualitative study of liquid media is the preservation of the physical structure and chemical composition of the medium under study [1, 2]. The fulfillment of this condition in the case of express control of a liquid can be achieved only with the help of devices whose operation is based on the phenomenon of nuclear magnetic resonance. Other types of devices for express monitoring of the state of a liquid, such as optical, ultrasonic and X-ray devices, can fulfill this condition only when they work with a certain class of media [2].

In the course of the work, experimental studies were carried out, which showed that in a small-sized magnetic system, the NMR signal is recorded based on the modulation technique. The main disadvantage of the modulation technique is the absence of a practically applicable theoretical model. Therefore, the purpose of this work is to develop a technique for processing NMR signals in the express control of condensed media in order to expand the functionality of the method.

2. Features of recording the nuclear magnetic resonance spectrum of a condensed medium during express control of its state

One of the features of the application of spectral analysis is that the registered NMR signal is a non-periodic oscillation in the form of damped peaks. Therefore, it is advisable to use the discrete Fourier transform to describe the NMR signal:

$$y_k = \sum_{n=0}^{N-1} x_n e^{-j2\pi kn/N} \quad (1)$$

where n = 0, 1, 2, …, N–1; xn - input data sequence; N is the number of elements of the input data sequence x_n.

In the course of the study, it was determined that the spectral components of the amplitude and phase spectrum can be expressed in terms of the spectral components of the amplitude and phase spectra of signals υ(t) and u(t). The coefficients that determine this relationship will be the contribution of these signals to the recorded NMR signal. For these signals, the amplitude and phase spectra are calculated. Next, the amplitude and phase spectra of the NMR signal are plotted. On fig. 1 shows the amplitude and phase spectra of the NMR signal for oil.

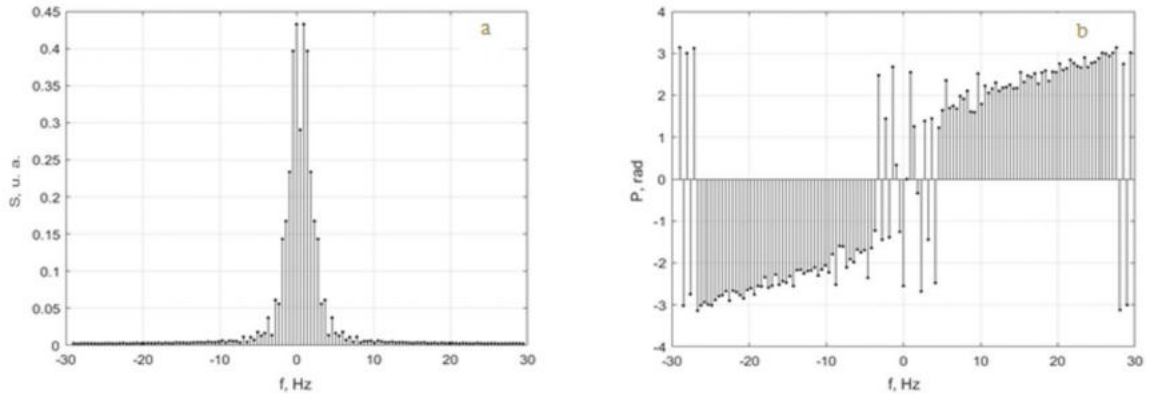

Fig. 1. Spectra from the calculated NMR signal for oil: a) amplitude; b) phase

The new method proposed by us, developed on the basis of our own theoretical model, makes it possible to obtain information on the composition of the medium under study at the sampling point during express control with a small-sized NMR spectrometer and make an informed decision on its further use without additional sample studies in a stationary laboratory. Previously obtained during the express control of the condensed medium at the sampling site, they only provided information about the presence of a deviation from the standard state in it, and additional studies were required in a stationary laboratory to make a reliable decision on the further use of the medium.

3. Conclusion

As a result, it was found that the proposed spectral research method has no restrictions on its use. To use it, it is necessary to register the NMR signal from a medium containing nuclei with magnetic moments, for example, at the resonant frequency of protons (more than 99% of liquid media contain protons) and measure the relaxation constants T1 and T2 to calculate absorption and dispersion signals.

References

[1] Marusina M Y, Bazarov B A, Galaidin P A, Marusin M P, Silaev A A, Zakemovskya E Y and Mustaev Y N 2014 *Measurement Techniques* **57(5)** 580-586

[2] Kashaev R S and Gazizov E G 2010 *Journal of Applied Spectroscopy* **77** 321–328

Chemical Stability of the SERS Substrate Based on Gold Nanoparticles Self-Assembling Films

K A Maleeva[1*], K V Bogdanov[1]

[1]Center of Information Optical Technologies, ITMO University, Saint Petersburg 197101, Russia

e-mail:*khnykina.kseniya@mail.ru

Abstract. Signal-reproducing and high-enhancement substrates are essential for surface enhanced Raman spectroscopy (SERS) for many studies in various area of science. In addition to the reproducibility and efficiency of SERS, the substrate must be resistant to various aggressive media in the study of liquid analytes. In this work, we consider the chemical stability of a SERS substrate based on self-assembling films of gold nanoparticles in a polymer matrix (SPF-PS).

1. Experiments

1.1. Materials

Chloroauric acid (99.995%); trisodium citrate; tetraoctylammonium bromide (TOABr); pseudoisocyanine iodide (97%); polystyrene (PS) Mw 192,000; were purchased from Aldrich. Toluene, trichloromethane ($CHCl_3$), acetone, acetonitrile (ACN), ethanol, isopropyl alcohol (iPA), hexane sodium hydroxide, hydrochloric acid and nitric acid were purchased from Vekton, Russia. All chemicals were used without additional purification. Ultrapure water (Milli-Q) was used throughout the experiments.

Organic and inorganic contaminants were removed from the glassware before the syntheses. All glassware was washed in ethanolic potassium hydroxide to remove any organic impurities and then cleaned with aqua regia. Finally, the glass was thoroughly rinsed twenty times with deionized water.

1.2. Preparation of SPF-PS

Obtaining SPF-PS takes place in two stages. The scheme for obtaining a self-assembled gold film without a polymer matrix is described in [1,2]. An aqueous colloid of gold particles is synthesized to obtain SPF-PS. The approximate size of gold nanoparticles is ~20 nm. Self-assembly of a film of gold nanoparticles is carried out from the resulting aqueous colloid. For this, a solution of TOABr and PS in toluene is prepared. The toluene solution of the polymer and the self-assembling agent is then mixed with the aqueous colloid of the gold particles. A gold film is observed in the tube a few seconds after shaking. The reaction mixture is poured onto a polytetrafluoroethylene (Teflon) flat substrate. The resulting SERS substrate is separated from the Teflon substrate. The area of the resulting substrate was 5 cm^2. The substrate was cut into equal parts for further research.

2. Results and Discussion

2.1. Different solvents

The resulting SERS substrates were placed in various solvents. SPF-PE samples were dissolved in toluene, $CHCl_3$, acetone, ACN. The SPF-PE sample placed in hexane partially dissolved after 2 hours. SPF-PE samples are placed in ethanol, iPA, water did not dissolve in after 2 days. A reproducibility study of preferences for SPF-PS samples showed that SPF-PE parameters did not deteriorate. The study of enhancement factors and reproducibility parameters was carried out similarly to the works [1 - 3]

2.2. Different pH

Solutions were prepared with different pH values to study the stability of SPF-PE. The values of the studied pH are 3, 5, 7, 9, and 11. The greatest changes in the enhancement factors were observed for pH 3. The intensity of the signal for pseudoisocyanine iodide decreased by 17 times. At the same time, the reproducibility of the signal was preserved and changed only by 3%.

Acknowledgments

This work was supported by the Russian Science Foundation (Agreement 20-72-00114)

References

[1] Khnykina K.A. et al 2021 *J. Phys.: Conf. Ser.* **1984** 012020
[2] Maleeva K. A. . et al 2022 *J. Phys.: Conf. Ser.* **2172** 012007
[3] Khnykina K. A. et al 2021 *Optics and Spectroscopy* **129** 495-504.

Aluminum nanostructures produced by aerosol dry printing for ultraviolet photoluminescence enhancement

D Malo[1,2], A A Lizunova[1], M Nouraldeen[1,3], V I Borisov[1], and V V Ivanov[1]

[1]Moscow Institute of Physics and Technology, National Research University, Institutsky lane 9, Dolgoprudny, Moscow region, 141700, Russia
[2]Biomedical Engineering Department, Faculty of Mechanical and Electrical Engineering, Damascus University, Damascus, Syria
[3]Physics Department, Faculty of Science, Tartous University, Tartous, Syria

Corresponding author's e-mail: malo.dana@mail.ru

Abstract. This work demonstrates metal-enhanced luminescence in the ultraviolet (UV) region of zinc oxide nanoparticles deposited on films of aluminum nanoparticles formed by dry aerosol printing. Two different conditions of metal aluminum nanoparticles (Al NPs) production in spark discharge method were used to obtain Al NPs with an average size 9.5± 5.6 and 15.5 ± 8.9 nm. At an excitation wavelength of 325 nm, the enhancement factor at 377 nm was about 1.3 for zinc oxide nanoparticles with mean size 26.6 ± 7.4 nm.

1. Introduction

The luminescence enhancement is considered one of the most intense research fields at the present time, especially in ultraviolet region. Aluminum nanoparticles have plasmon resonance in the UV region [1] that make this metal as a promising material for creating plasmonic structures with enhancing luminescence in the UV region of the spectrum for many applications in medicine and technology. Here, we presented the metal-enhanced luminescence of ultraviolet phosphor, namely zinc oxide nanoparticles, in presence of aluminum nanoparticles produced by spark discharge and deposited on quartz substrate by dry aerosol printing.

2. Methods and Materials

Suspension of zinc oxide was prepared from a dispersion of ZnO Sigma Aldrich (40 wt. %) by dilution, ultrasonic treatment and centrifugation to get suspension with concentration 2.2 g/l. To obtain Al NPs, the spark discharge generator [1] was used in atmosphere of argon of purity 6.0 with aluminum electrodes, capacitor 40 nF, discharge voltage 1.5 kV, pulse repetition rate 0.5 kHz and gas flow 1 L/min, for Al_I sample, 7 degrees of bevel of the electrodes were used, while for Al_{II} sample additional in-flow thermal treatment (600 ^oC) of NPs in tube furnace was applied. To form thin films, Al NPs were deposited (4x4 mm^2) on (2x2 cm^2) a quartz substrate by dry aerosol printing [2]. For studying the luminescence enhancement, the ZnO NPs (2.2 g/l) were disposed on Al NPs film.

The size and crystal structure of primary nanoparticles was received by transmission electron microscope (TEM) Jeol JEM 2100 (200 kV). The UV-vis-NIR spectra and luminescence emission of films were obtained using JASCO V–770 and JASCO FP–8300 spectrometers correspondingly.

3. Results and Discussion

TEM and electron diffraction images show that the Al nanoparticles have spherical shape and crystal structure, the average primary particle size synthesized with 7 degrees of bevel of the electrodes (Al_I) were 9.5 ± 5.6 nm while 15.5 ± 8.9 nm for particles synthesized at 600 ºC (Al_{II}). ZnO NPs were with mean size 26.6 ± 7.4 nm. (figure 1). The measurements of the Al NPs films absorption spectra showed the presence of absorption peak in the UV region with peak position approximately at 245 nm for Al samples and for ZnO approximately at 360 nm (figure 2a). As shown on figure 2b luminescence enhancement was achieved on quartz substrate using two of Al NPs samples and the peak position was at 377 nm at an excitation wavelength of 325 nm.

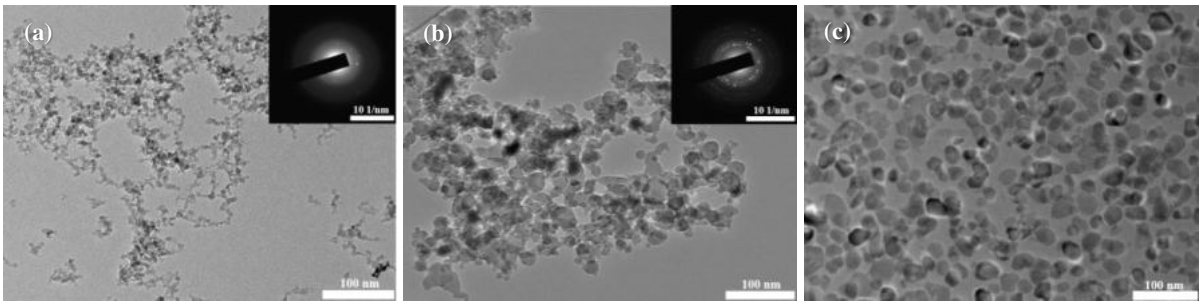

Figure 1. TEM images and corresponding SAED patterns (on the insert) for **(a)** Al_I, **(b)** Al_{II}, **(c)** ZnO.

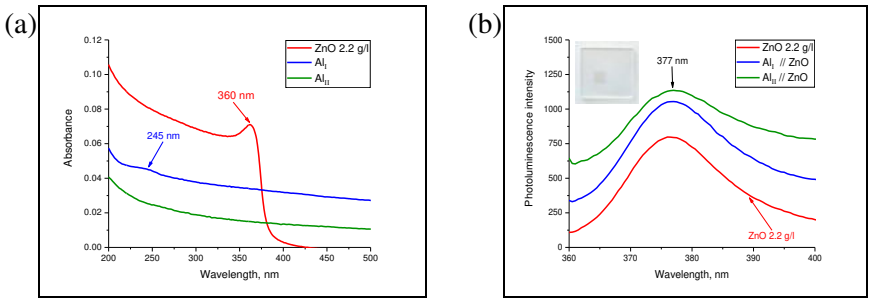

Figure 2. (a) Absorption spectra of films: ZnO 2.2 g/l, Al_I and Al_{II}; **(b)** Photoluminescence emission spectra of films: ZnO 2.2 g/l, Al_I layer followed by ZnO layer and Al_{II} layer followed by ZnO layer at an excitation wavelength 325 nm.

Thus, the photoluminescence intensity of ZnO NPs in the UV region increased by 30 % in presence of Al film based on metal NPs synthesized by spark discharge method and deposited on quartz substrate by dry aerosol printing when compared to bare ZnO film was shown. This promising result can be used for many applications in catalysis and UV photonics.

Acknowledgments

This research was funded by the Ministry of Science and Higher Education of the Russian Federation in part of development of spark discharge modification (state contract no. 075-03-2021-095, project identifier 0714-2021-0007, project title: “Development of functional materials with controlled electrical, chemoresistive and catalytic properties for manufacturing sensor microsystems by using methods of printed electronics”).

References

[1] Borisov V I, Lizunova A A, Mazharenko A K, Malo D, Ramanenka A A, Shuklov I A and Ivanov V V. 2020 *J. Phys.: Conf. Ser.* **1695** 012021

[2] Khabarov K M, Nouraldeen M, Lizunova A A, Urazov M N, Ivanov V V. 2021 *J. Phys.: Conf. Ser.* **2086** 012147

Aluminum nanostructures produced by aerosol dry printing for ultraviolet photoluminescence enhancement

D Malo[1,2], A A Lizunova[1], M Nouraldeen[1,3], V I Borisov[1], and V V Ivanov[1]

[1]Moscow Institute of Physics and Technology, National Research University, Institutsky lane 9, Dolgoprudny, Moscow region, 141700, Russia
[2]Biomedical Engineering Department, Faculty of Mechanical and Electrical Engineering, Damascus University, Damascus, Syria
[3]Physics Department, Faculty of Science, Tartous University, Tartous, Syria

Corresponding author's e-mail: malo.dana@mail.ru

Abstract. This work demonstrates metal-enhanced luminescence in the ultraviolet (UV) region of zinc oxide nanoparticles deposited on films of aluminum nanoparticles formed by dry aerosol printing. Two different conditions of metal aluminum nanoparticles (Al NPs) production in spark discharge method were used to obtain Al NPs with an average size 9.5± 5.6 and 15.5 ± 8.9 nm. At an excitation wavelength of 325 nm, the enhancement factor at 377 nm was about 1.3 for zinc oxide nanoparticles with mean size 26.6 ± 7.4 nm.

1. Introduction

The luminescence enhancement is considered one of the most intense research fields at the present time, especially in ultraviolet region. Aluminum nanoparticles have plasmon resonance in the UV region [1] that make this metal as a promising material for creating plasmonic structures with enhancing luminescence in the UV region of the spectrum for many applications in medicine and technology. Here, we presented the metal-enhanced luminescence of ultraviolet phosphor, namely zinc oxide nanoparticles, in presence of aluminum nanoparticles produced by spark discharge and deposited on quartz substrate by dry aerosol printing.

2. Methods and Materials

Suspension of zinc oxide was prepared from a dispersion of ZnO Sigma Aldrich (40 wt. %) by dilution, ultrasonic treatment and centrifugation to get suspension with concentration 2.2 g/l. To obtain Al NPs, the spark discharge generator [1] was used in atmosphere of argon of purity 6.0 with aluminum electrodes, capacitor 40 nF, discharge voltage 1.5 kV, pulse repetition rate 0.5 kHz and gas flow 1 L/min, for Al_I sample, 7 degrees of bevel of the electrodes were used, while for Al_{II} sample additional in-flow thermal treatment (600 ^oC) of NPs in tube furnace was applied. To form thin films, Al NPs were deposited (4x4 mm^2) on (2x2 cm^2) a quartz substrate by dry aerosol printing [2]. For studying the luminescence enhancement, the ZnO NPs (2.2 g/l) were disposed on Al NPs film.

The size and crystal structure of primary nanoparticles was received by transmission electron microscope (TEM) Jeol JEM 2100 (200 kV). The UV-vis-NIR spectra and luminescence emission of films were obtained using JASCO V–770 and JASCO FP–8300 spectrometers correspondingly.

3. Results and Discussion

TEM and electron diffraction images show that the Al nanoparticles have spherical shape and crystal structure, the average primary particle size synthesized with 7 degrees of bevel of the electrodes (Al_I) were 9.5 ± 5.6 nm while 15.5 ± 8.9 nm for particles synthesized at 600 ºC (Al_{II}). ZnO NPs were with mean size 26.6 ± 7.4 nm. (figure 1). The measurements of the Al NPs films absorption spectra showed the presence of absorption peak in the UV region with peak position approximately at 245 nm for Al samples and for ZnO approximately at 360 nm (figure 2a). As shown on figure 2b luminescence enhancement was achieved on quartz substrate using two of Al NPs samples and the peak position was at 377 nm at an excitation wavelength of 325 nm.

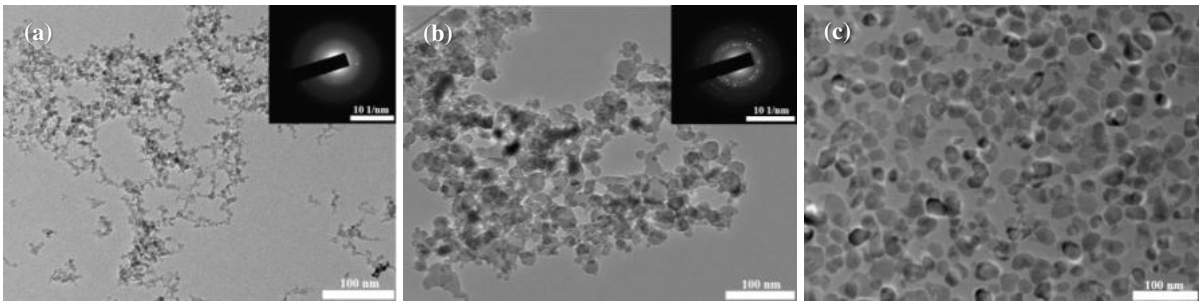

Figure 1. TEM images and corresponding SAED patterns (on the insert) for **(a)** Al_I, **(b)** Al_{II}, **(c)** ZnO.

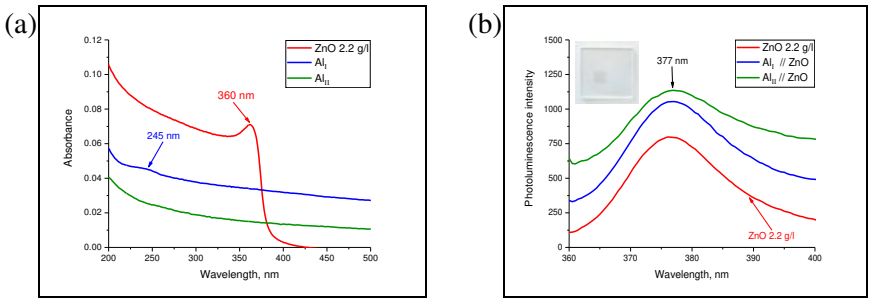

Figure 2. (a) Absorption spectra of films: ZnO 2.2 g/l, Al_I and Al_{II}; **(b)** Photoluminescence emission spectra of films: ZnO 2.2 g/l, Al_I layer followed by ZnO layer and Al_{II} layer followed by ZnO layer at an excitation wavelength 325 nm.

Thus, the photoluminescence intensity of ZnO NPs in the UV region increased by 30 % in presence of Al film based on metal NPs synthesized by spark discharge method and deposited on quartz substrate by dry aerosol printing when compared to bare ZnO film was shown. This promising result can be used for many applications in catalysis and UV photonics.

Acknowledgments

This research was funded by the Ministry of Science and Higher Education of the Russian Federation in part of development of spark discharge modification (state contract no. 075-03-2021-095, project identifier 0714-2021-0007, project title: “Development of functional materials with controlled electrical, chemoresistive and catalytic properties for manufacturing sensor microsystems by using methods of printed electronics”).

References

[1] Borisov V I, Lizunova A A, Mazharenko A K, Malo D, Ramanenka A A, Shuklov I A and Ivanov V V. 2020 *J. Phys.: Conf. Ser.* **1695** 012021

[2] Khabarov K M, Nouraldeen M, Lizunova A A, Urazov M N, Ivanov V V. 2021 *J. Phys.: Conf. Ser.* **2086** 012147

Aluminum nanostructures produced by aerosol dry printing for ultraviolet photoluminescence enhancement

D Malo[1,2], A A Lizunova[1], M Nouraldeen[1,3], V I Borisov[1], and V V Ivanov[1]

[1]Moscow Institute of Physics and Technology, National Research University, Institutsky lane 9, Dolgoprudny, Moscow region, 141700, Russia
[2]Biomedical Engineering Department, Faculty of Mechanical and Electrical Engineering, Damascus University, Damascus, Syria
[3]Physics Department, Faculty of Science, Tartous University, Tartous, Syria

Corresponding author's e-mail: malo.dana@mail.ru

Abstract. This work demonstrates metal-enhanced luminescence in the ultraviolet (UV) region of zinc oxide nanoparticles deposited on films of aluminum nanoparticles formed by dry aerosol printing. Two different conditions of metal aluminum nanoparticles (Al NPs) production in spark discharge method were used to obtain Al NPs with an average size 9.5± 5.6 and 15.5 ± 8.9 nm. At an excitation wavelength of 325 nm, the enhancement factor at 377 nm was about 1.3 for zinc oxide nanoparticles with mean size 26.6 ± 7.4 nm.

1. Introduction

The luminescence enhancement is considered one of the most intense research fields at the present time, especially in ultraviolet region. Aluminum nanoparticles have plasmon resonance in the UV region [1] that make this metal as a promising material for creating plasmonic structures with enhancing luminescence in the UV region of the spectrum for many applications in medicine and technology. Here, we presented the metal-enhanced luminescence of ultraviolet phosphor, namely zinc oxide nanoparticles, in presence of aluminum nanoparticles produced by spark discharge and deposited on quartz substrate by dry aerosol printing.

2. Methods and Materials

Suspension of zinc oxide was prepared from a dispersion of ZnO Sigma Aldrich (40 wt. %) by dilution, ultrasonic treatment and centrifugation to get suspension with concentration 2.2 g/l. To obtain Al NPs, the spark discharge generator [1] was used in atmosphere of argon of purity 6.0 with aluminum electrodes, capacitor 40 nF, discharge voltage 1.5 kV, pulse repetition rate 0.5 kHz and gas flow 1 L/min, for Al_I sample, 7 degrees of bevel of the electrodes were used, while for Al_{II} sample additional in-flow thermal treatment (600 ^oC) of NPs in tube furnace was applied. To form thin films, Al NPs were deposited (4x4 mm^2) on (2x2 cm^2) a quartz substrate by dry aerosol printing [2]. For studying the luminescence enhancement, the ZnO NPs (2.2 g/l) were disposed on Al NPs film.

The size and crystal structure of primary nanoparticles was received by transmission electron microscope (TEM) Jeol JEM 2100 (200 kV). The UV-vis-NIR spectra and luminescence emission of films were obtained using JASCO V–770 and JASCO FP–8300 spectrometers correspondingly.

3. Results and Discussion

TEM and electron diffraction images show that the Al nanoparticles have spherical shape and crystal structure, the average primary particle size synthesized with 7 degrees of bevel of the electrodes (Al_I) were 9.5 ± 5.6 nm while 15.5 ± 8.9 nm for particles synthesized at 600 ºC (Al_{II}). ZnO NPs were with mean size 26.6 ± 7.4 nm. (figure 1). The measurements of the Al NPs films absorption spectra showed the presence of absorption peak in the UV region with peak position approximately at 245 nm for Al samples and for ZnO approximately at 360 nm (figure 2a). As shown on figure 2b luminescence enhancement was achieved on quartz substrate using two of Al NPs samples and the peak position was at 377 nm at an excitation wavelength of 325 nm.

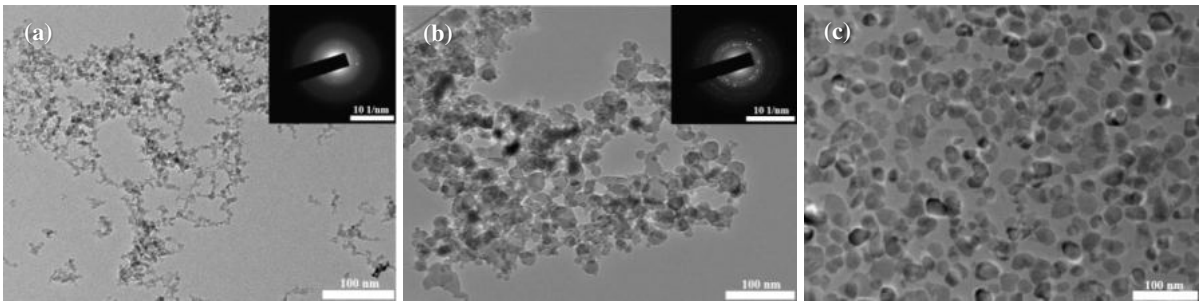

Figure 1. TEM images and corresponding SAED patterns (on the insert) for **(a)** Al_I, **(b)** Al_{II}, **(c)** ZnO.

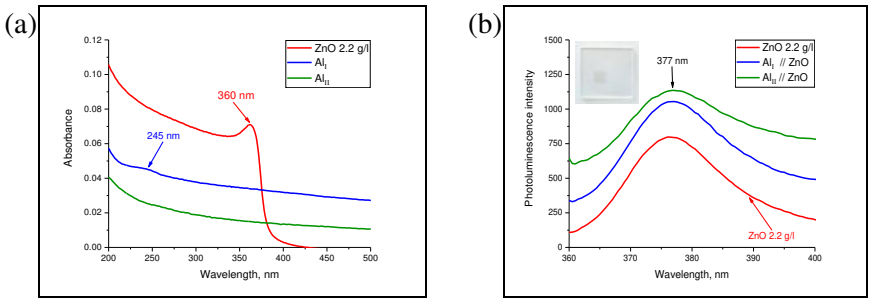

Figure 2. (a) Absorption spectra of films: ZnO 2.2 g/l, Al_I and Al_{II}; **(b)** Photoluminescence emission spectra of films: ZnO 2.2 g/l, Al_I layer followed by ZnO layer and Al_{II} layer followed by ZnO layer at an excitation wavelength 325 nm.

Thus, the photoluminescence intensity of ZnO NPs in the UV region increased by 30 % in presence of Al film based on metal NPs synthesized by spark discharge method and deposited on quartz substrate by dry aerosol printing when compared to bare ZnO film was shown. This promising result can be used for many applications in catalysis and UV photonics.

Acknowledgments

This research was funded by the Ministry of Science and Higher Education of the Russian Federation in part of development of spark discharge modification (state contract no. 075-03-2021-095, project identifier 0714-2021-0007, project title: “Development of functional materials with controlled electrical, chemoresistive and catalytic properties for manufacturing sensor microsystems by using methods of printed electronics”).

References

[1] Borisov V I, Lizunova A A, Mazharenko A K, Malo D, Ramanenka A A, Shuklov I A and Ivanov V V. 2020 *J. Phys.: Conf. Ser.* **1695** 012021

[2] Khabarov K M, Nouraldeen M, Lizunova A A, Urazov M N, Ivanov V V. 2021 *J. Phys.: Conf. Ser.* **2086** 012147

Aluminum nanostructures produced by aerosol dry printing for ultraviolet photoluminescence enhancement

D Malo[1,2], A A Lizunova[1], M Nouraldeen[1,3], V I Borisov[1], and V V Ivanov[1]

[1]Moscow Institute of Physics and Technology, National Research University, Institutsky lane 9, Dolgoprudny, Moscow region, 141700, Russia
[2]Biomedical Engineering Department, Faculty of Mechanical and Electrical Engineering, Damascus University, Damascus, Syria
[3]Physics Department, Faculty of Science, Tartous University, Tartous, Syria

Corresponding author's e-mail: malo.dana@mail.ru

Abstract. This work demonstrates metal-enhanced luminescence in the ultraviolet (UV) region of zinc oxide nanoparticles deposited on films of aluminum nanoparticles formed by dry aerosol printing. Two different conditions of metal aluminum nanoparticles (Al NPs) production in spark discharge method were used to obtain Al NPs with an average size 9.5± 5.6 and 15.5 ± 8.9 nm. At an excitation wavelength of 325 nm, the enhancement factor at 377 nm was about 1.3 for zinc oxide nanoparticles with mean size 26.6 ± 7.4 nm.

1. Introduction

The luminescence enhancement is considered one of the most intense research fields at the present time, especially in ultraviolet region. Aluminum nanoparticles have plasmon resonance in the UV region [1] that make this metal as a promising material for creating plasmonic structures with enhancing luminescence in the UV region of the spectrum for many applications in medicine and technology. Here, we presented the metal-enhanced luminescence of ultraviolet phosphor, namely zinc oxide nanoparticles, in presence of aluminum nanoparticles produced by spark discharge and deposited on quartz substrate by dry aerosol printing.

2. Methods and Materials

Suspension of zinc oxide was prepared from a dispersion of ZnO Sigma Aldrich (40 wt. %) by dilution, ultrasonic treatment and centrifugation to get suspension with concentration 2.2 g/l. To obtain Al NPs, the spark discharge generator [1] was used in atmosphere of argon of purity 6.0 with aluminum electrodes, capacitor 40 nF, discharge voltage 1.5 kV, pulse repetition rate 0.5 kHz and gas flow 1 L/min, for Al_I sample, 7 degrees of bevel of the electrodes were used, while for Al_{II} sample additional in-flow thermal treatment (600 ^oC) of NPs in tube furnace was applied. To form thin films, Al NPs were deposited (4x4 mm^2) on (2x2 cm^2) a quartz substrate by dry aerosol printing [2]. For studying the luminescence enhancement, the ZnO NPs (2.2 g/l) were disposed on Al NPs film.

The size and crystal structure of primary nanoparticles was received by transmission electron microscope (TEM) Jeol JEM 2100 (200 kV). The UV-vis-NIR spectra and luminescence emission of films were obtained using JASCO V–770 and JASCO FP–8300 spectrometers correspondingly.

3. Results and Discussion

TEM and electron diffraction images show that the Al nanoparticles have spherical shape and crystal structure, the average primary particle size synthesized with 7 degrees of bevel of the electrodes (Al_I) were 9.5 ± 5.6 nm while 15.5 ± 8.9 nm for particles synthesized at 600 ºC (Al_{II}). ZnO NPs were with mean size 26.6 ± 7.4 nm. (figure 1). The measurements of the Al NPs films absorption spectra showed the presence of absorption peak in the UV region with peak position approximately at 245 nm for Al samples and for ZnO approximately at 360 nm (figure 2a). As shown on figure 2b luminescence enhancement was achieved on quartz substrate using two of Al NPs samples and the peak position was at 377 nm at an excitation wavelength of 325 nm.

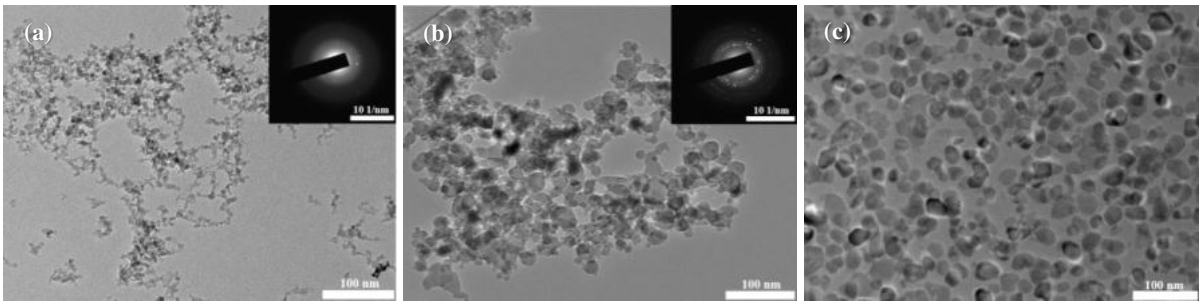

Figure 1. TEM images and corresponding SAED patterns (on the insert) for **(a)** Al_I, **(b)** Al_{II}, **(c)** ZnO.

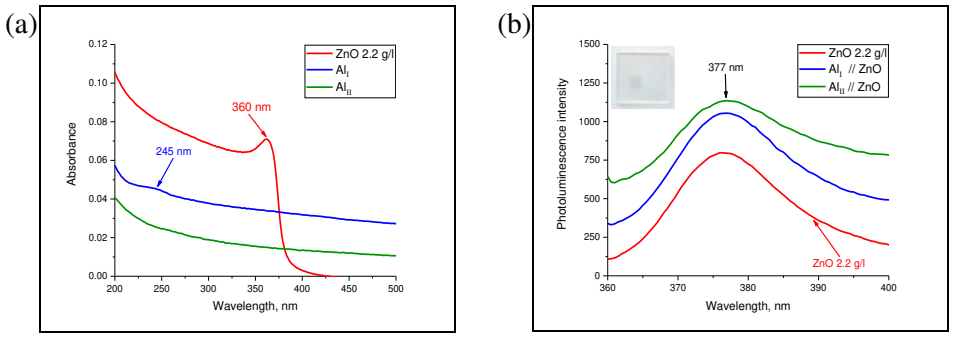

Figure 2. (a) Absorption spectra of films: ZnO 2.2 g/l, Al_I and Al_{II}; **(b)** Photoluminescence emission spectra of films: ZnO 2.2 g/l, Al_I layer followed by ZnO layer and Al_{II} layer followed by ZnO layer at an excitation wavelength 325 nm.

Thus, the photoluminescence intensity of ZnO NPs in the UV region increased by 30 % in presence of Al film based on metal NPs synthesized by spark discharge method and deposited on quartz substrate by dry aerosol printing when compared to bare ZnO film was shown. This promising result can be used for many applications in catalysis and UV photonics.

Acknowledgments

This work was financially supported by Russian Science Foundation (project № 22-19-00311).

References

[1] Borisov V I, Lizunova A A, Mazharenko A K, Malo D, Ramanenka A A, Shuklov I A and Ivanov V V. 2020 *J. Phys.: Conf. Ser.* **1695** 012021

[2] Khabarov K M, Nouraldeen M, Lizunova A A, Urazov M N, Ivanov V V. 2021 *J. Phys.: Conf. Ser.* **2086** 012147

Aluminum nanostructures produced by aerosol dry printing for ultraviolet photoluminescence enhancement

D Malo[1,2], A A Lizunova[1], M Nouraldeen[1,3], V I Borisov[1] and V V Ivanov[1]

[1]Moscow Institute of Physics and Technology, National Research University, Institutsky lane 9, Dolgoprudny, Moscow region, 141700, Russia
[2]Biomedical Engineering Department, Faculty of Mechanical and Electrical Engineering, Damascus University, Damascus, Syria
[3]Physics Department, Faculty of Science, Tartous University, Tartous, Syria

Corresponding author's e-mail: malo.dana@mail.ru

Abstract. This work demonstrates metal-enhanced luminescence in the ultraviolet (UV) region of zinc oxide nanoparticles deposited on films of aluminum nanoparticles formed by dry aerosol printing. Two different conditions of metal aluminum nanoparticles (Al NPs) production in spark discharge method were used to obtain Al NPs with an average size 9.5± 5.6 and 15.5 ± 8.9 nm. At an excitation wavelength of 325 nm, the enhancement factor at 377 nm was about 1.3 for zinc oxide nanoparticles with mean size 26.6 ± 7.4 nm.

1. Introduction

The luminescence enhancement is considered one of the most intense research fields at the present time, especially in ultraviolet region. Aluminum nanoparticles have plasmon resonance in the UV region [1] that make this metal as a promising material for creating plasmonic structures with enhancing luminescence in the UV region of the spectrum for many applications in medicine and technology. Here, we presented the metal-enhanced luminescence of ultraviolet phosphor, namely zinc oxide nanoparticles, in presence of aluminum nanoparticles produced by spark discharge and deposited on quartz substrate by dry aerosol printing.

2. Methods and Materials

Suspension of zinc oxide was prepared from a dispersion of ZnO Sigma Aldrich (40 wt. %) by dilution, ultrasonic treatment and centrifugation to get suspension with concentration 2.2 g/l. To obtain Al NPs, the spark discharge generator [1] was used in atmosphere of argon of purity 6.0 with aluminum electrodes, capacitor 40 nF, discharge voltage 1.5 kV, pulse repetition rate 0.5 kHz and gas flow 1 L/min, for Al_I sample, 7 degrees of bevel of the electrodes were used, while for Al_{II} sample additional in-flow thermal treatment (600 ^oC) of NPs in tube furnace was applied. To form thin films, Al NPs were deposited (4x4 mm^2) on (2x2 cm^2) a quartz substrate by dry aerosol printing [2]. For studying the luminescence enhancement, the ZnO NPs (2.2 g/l) were disposed on Al NPs film.

The size and crystal structure of primary nanoparticles was received by transmission electron microscope (TEM) Jeol JEM 2100 (200 kV). The UV-vis-NIR spectra and luminescence emission of films were obtained using JASCO V–770 and JASCO FP–8300 spectrometers correspondingly.

3. Results and Discussion

TEM and electron diffraction images show that the Al nanoparticles have spherical shape and crystal structure, the average primary particle size synthesized with 7 degrees of bevel of the electrodes (Al_I) were 9.5 ± 5.6 nm while 15.5 ± 8.9 nm for particles synthesized at 600 ºC (Al_{II}). ZnO NPs were with mean size 26.6 ± 7.4 nm. (figure 1). The measurements of the Al NPs films absorption spectra showed the presence of absorption peak in the UV region with peak position approximately at 245 nm for Al samples and for ZnO approximately at 360 nm (figure 2a). As shown on figure 2b luminescence enhancement was achieved on quartz substrate using two of Al NPs samples and the peak position was at 377 nm at an excitation wavelength of 325 nm.

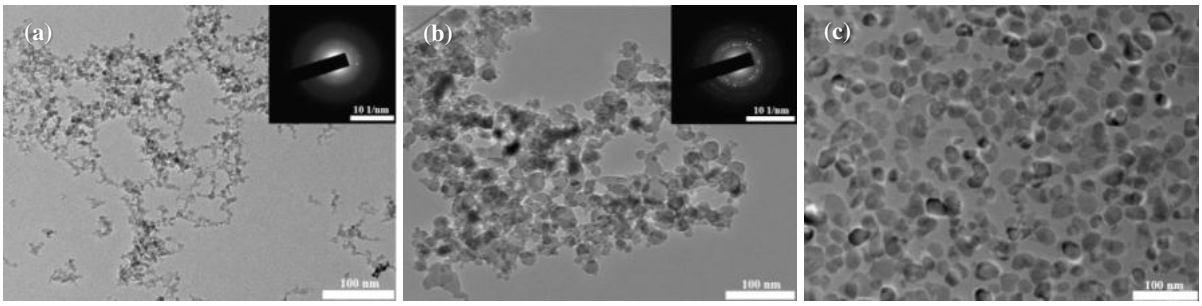

Figure 1. TEM images and corresponding SAED patterns (on the insert) for **(a)** Al_I, **(b)** Al_{II}, **(c)** ZnO.

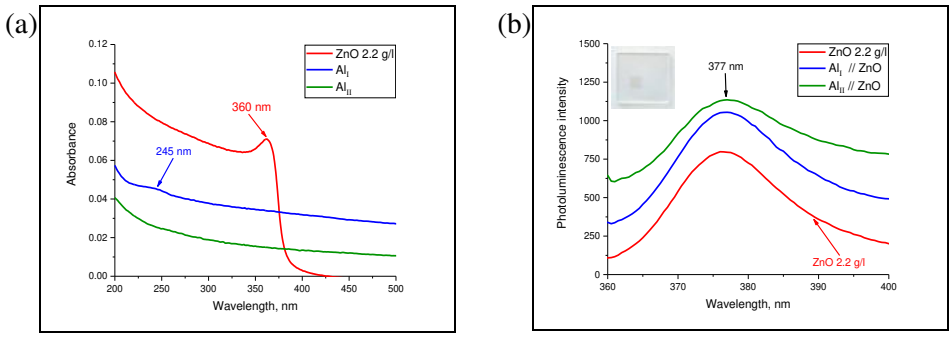

Figure 2. (a) Absorption spectra of films: ZnO 2.2 g/l, Al_I and Al_{II}; **(b)** Photoluminescence emission spectra of films: ZnO 2.2 g/l, Al_I layer followed by ZnO layer and Al_{II} layer followed by ZnO layer at an excitation wavelength 325 nm.

Thus, the photoluminescence intensity of ZnO NPs in the UV region increased by 30 % in presence of Al film based on metal NPs synthesized by spark discharge method and deposited on quartz substrate by dry aerosol printing when compared to bare ZnO film was shown. This promising result can be used for many applications in catalysis and UV photonics.

Acknowledgments

This work was financially supported by Russian Science Foundation (project № 22-19-00311).

References

[1] Borisov V I, Lizunova A A, Mazharenko A K, Malo D, Ramanenka A A, Shuklov I A and Ivanov V V. 2020 *J. Phys.: Conf. Ser.* **1695** 012021

[2] Khabarov K M, Nouraldeen M, Lizunova A A, Urazov M N, Ivanov V V. 2021 *J. Phys.: Conf. Ser.* **2086** 012147

Aluminum nanostructures produced by aerosol dry printing for ultraviolet photoluminescence enhancement

D Malo[1,2], A A Lizunova[1], M Nouraldeen[1,3], V I Borisov[1], and V V Ivanov[1]

[1]Moscow Institute of Physics and Technology, National Research University, Institutsky lane 9, Dolgoprudny, Moscow region, 141700, Russia
[2]Biomedical Engineering Department, Faculty of Mechanical and Electrical Engineering, Damascus University, Damascus, Syria
[3]Physics Department, Faculty of Science, Tartous University, Tartous, Syria

Corresponding author's e-mail: malo.dana@mail.ru

Abstract. This work demonstrates metal-enhanced luminescence in the ultraviolet (UV) region of zinc oxide nanoparticles deposited on films of aluminum nanoparticles formed by dry aerosol printing. Two different conditions of metal aluminum nanoparticles (Al NPs) production in spark discharge method were used to obtain Al NPs with an average size 9.5± 5.6 and 15.5 ± 8.9 nm. At an excitation wavelength of 325 nm, the enhancement factor at 377 nm was about 1.3 for zinc oxide nanoparticles with mean size 26.6 ± 7.4 nm.

1. Introduction

The luminescence enhancement is considered one of the most intense research fields at the present time, especially in ultraviolet region. Aluminum nanoparticles have plasmon resonance in the UV region [1] that make this metal as a promising material for creating plasmonic structures with enhancing luminescence in the UV region of the spectrum for many applications in medicine and technology. Here, we presented the metal-enhanced luminescence of ultraviolet phosphor, namely zinc oxide nanoparticles, in presence of aluminum nanoparticles produced by spark discharge and deposited on quartz substrate by dry aerosol printing.

2. Methods and Materials

Suspension of zinc oxide was prepared from a dispersion of ZnO Sigma Aldrich (40 wt. %) by dilution, ultrasonic treatment and centrifugation to get suspension with concentration 2.2 g/l. To obtain Al NPs, the spark discharge generator [1] was used in atmosphere of argon of purity 6.0 with aluminum electrodes, capacitor 40 nF, discharge voltage 1.5 kV, pulse repetition rate 0.5 kHz and gas flow 1 L/min, for Al_I sample, 7 degrees of bevel of the electrodes were used, while for Al_{II} sample additional in-flow thermal treatment (600 ^oC) of NPs in tube furnace was applied. To form thin films, Al NPs were deposited (4x4 mm^2) on (2x2 cm^2) a quartz substrate by dry aerosol printing [2]. For studying the luminescence enhancement, the ZnO NPs (2.2 g/l) were disposed on Al NPs film.

The size and crystal structure of primary nanoparticles was received by transmission electron microscope (TEM) Jeol JEM 2100 (200 kV). The UV-vis-NIR spectra and luminescence emission of films were obtained using JASCO V–770 and JASCO FP–8300 spectrometers correspondingly.

3. Results and Discussion

TEM and electron diffraction images show that the Al nanoparticles have spherical shape and crystal structure, the average primary particle size synthesized with 7 degrees of bevel of the electrodes (Al_I) were 9.5 ± 5.6 nm while 15.5 ± 8.9 nm for particles synthesized at 600 ºC (Al_{II}). ZnO NPs were with mean size 26.6 ± 7.4 nm. (figure 1). The measurements of the Al NPs films absorption spectra showed the presence of absorption peak in the UV region with peak position approximately at 245 nm for Al samples and for ZnO approximately at 360 nm (figure 2a). As shown on figure 2b luminescence enhancement was achieved on quartz substrate using two of Al NPs samples and the peak position was at 377 nm at an excitation wavelength of 325 nm.

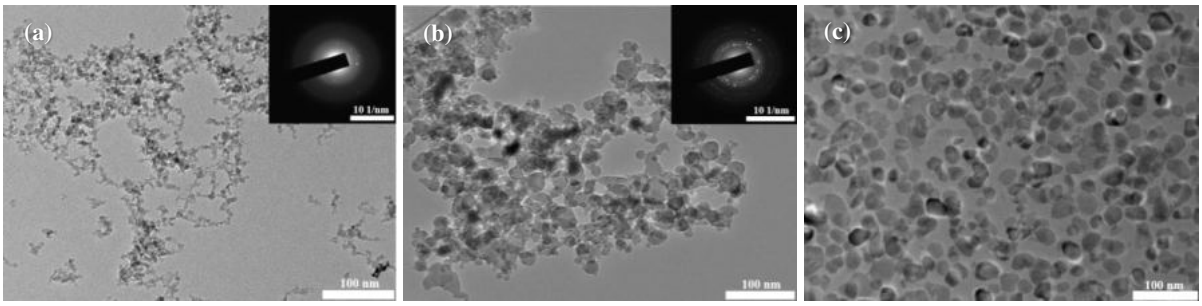

Figure 1. TEM images and corresponding SAED patterns (on the insert) for **(a)** Al_I, **(b)** Al_{II}, **(c)** ZnO.

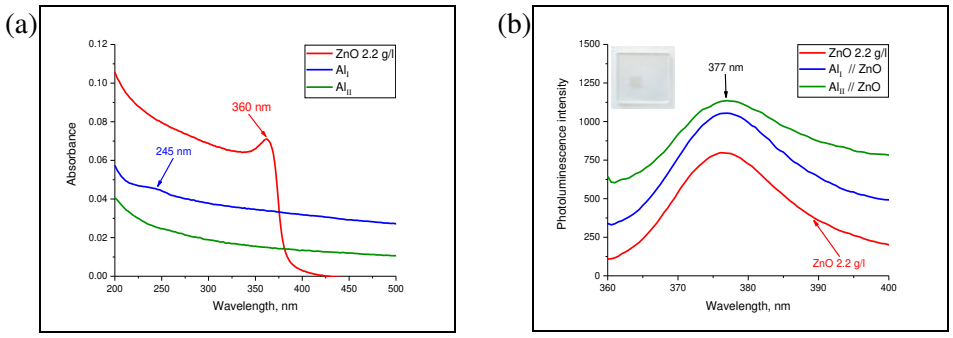

Figure 2. (a) Absorption spectra of films: ZnO 2.2 g/l, Al_I and Al_{II}; **(b)** Photoluminescence emission spectra of films: ZnO 2.2 g/l, Al_I layer followed by ZnO layer and Al_{II} layer followed by ZnO layer at an excitation wavelength 325 nm.

Thus, the photoluminescence intensity of ZnO NPs in the UV region increased by 30 % in presence of Al film based on metal NPs synthesized by spark discharge method and deposited on quartz substrate by dry aerosol printing when compared to bare ZnO film was shown. This promising result can be used for many applications in catalysis and UV photonics.

Acknowledgments

This work was financially supported by Russian Science Foundation (project № 22-19-00311).

References

[1] Borisov V I, Lizunova A A, Mazharenko A K, Malo D, Ramanenka A A, Shuklov I A and Ivanov V V. 2020 *J. Phys.: Conf. Ser.* **1695** 012021

[2] Khabarov K M, Nouraldeen M, Lizunova A A, Urazov M N, Ivanov V V. 2021 *J. Phys.: Conf. Ser.* **2086** 012147

FPGA-Based Time-to-Digital Converter for Time-of-Flight Photon Counting LiDAR measurement

Mazen Makhlouf[1], **M S Elezov**[2,3,4], **M L Shcherbatenko**[2,4], **D V Sych**[6] **and G N Goltsman**[1,2,3,4]

[1]HSE University (National Research University Higher School of Economics)
[2]Moscow State Pedagogical University, Moscow 119992, Russia
[3]Russian Quantum Center, Skolkovo 143025, Moscow, Russia
[4]NTI Center for Quantum Communications, National University of Science and Technology MISiS, Moscow 119049, Russia
[6]P.N. Lebedev Physical Institute, Russian Academy of Sciences, Moscow, 119333, Russia

E-mail: mazenmakhlouf@gmail.com

Abstract. We have developed a FPGA-based time-to-digital converter (TDC) that can be used for a TOF (Time-of-Flight) - LiDAR block detector based on superconducting nanowire single photon detector (SNSPD)[1]. The tapped delay line (TDL) method implemented with a dedicated carry chain structure was used to measure short time intervals. The proposed TDC system, implemented in a DLP Discovery 4100 Development Platform (Virtex-5 FPGA family), consists of a TDC unit and Test unit. The Test unit generates start and stop pulses which allows us to test the functionality of the TDC unit while TDC measure time interval between start and stop pulses.

1. Introduction

Development of LiDAR system based on SNSPD detector requires acquisition methods for obtaining ToF which is a method for measuring the distance from object, based on the time difference between the emission of a laser and its return from detector, after being reflected by an object. FPGA-TDCs have less cost, unlimited reconfigured signal processing compared to ASIC-TDCs [2].

2. Implementation of TDC system

The TDC unit consists of coarse counter, two fine counters and an encoder. The figure 1 illustrates the block diagram of this unit. The coarse counter calculates the number of cycles n_c between the start and the stop pulses. However, the fine counter measures, in term of number of taps T_{Delay}, the time difference between the rising edge of the input pulse n_{fstr} and the nearest rising edge of the clock clk. Two fine counters are used, one for the start pulse and the other for the stop pulse n_{fstp}. Therefore, the time delay T_{out} (in picoseconds) between the rising edge of the start pulse and the rising edge of the stop pulse could be given as follows:

$$T_{out} = n_c * clk + (n_{fstr} - n_{fstp}) * T_{Delay} \quad (1)$$

The coarse counter is based on a finite state machine, at first the start and stop pulses are passed through a pulse generator to restrict each pulse duration to one clock period. The state machine detects

the arrival of the start pulse and start counting until the arrival of the stop pulse. After which the number of cycles n_c is valid at the output. The fine counter was implemented using carry chains technique where the input pulse passes through a delay chain constructed of carry logics. Each output of a carry logic is connected to a register. When a delayed pulse reaches the carry logic output, it will be latched at the register output. The number of latched registers corresponds to the delay to be measured.

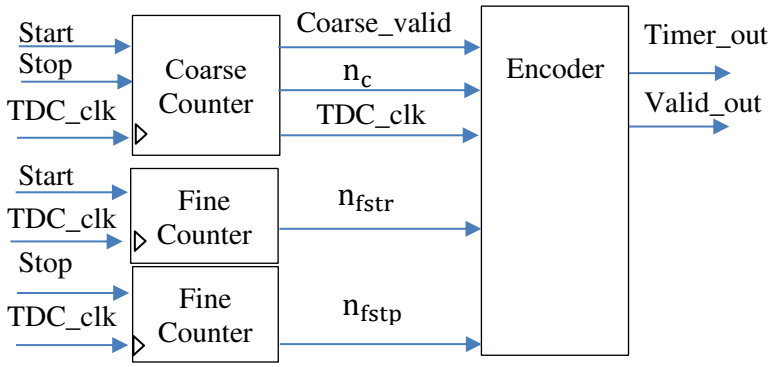

Figure 1. Block diagram of TDC system

The time regulation depends on delay element, each delay element (tap) corresponds to the MUXCY (Multiplexer for Carry Logic) element of a CARRY4 block [3]. These delays are dependent on the device selected and its speed grade. In our case, a Virtex-5 FPGA device has a maximum of 100 ps for a speed grade type. Since each block has 4 MUXCY elements, the average delay for one element is about 25 ps. The timing measurements at the output of the TDC unit are saved in a histogram which is refreshed every one second. The histogram bin equals 25 ps and number of bins equals 40000, which allows us to measures times between 0 and 1 μs with a resolution of 25 ps figure 2.

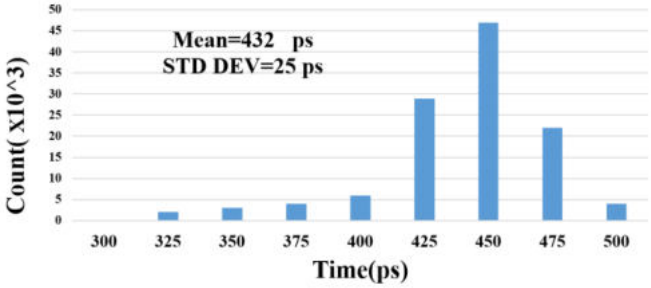

Figure 2. Measurement histogram of a constant time interval

3.Conclusion

We have designed and simulated an FPGA-based TDC architecture delivering high performance with low resource usage, the Virtex-5 FPGA family capabilities have been tested. It has been implemented with a 200MHz clock frequency. That will be investigated in ToF measuring for LiDAR system.

Acknowledgments

We acknowledge support of the Russian Foundation for Basic Research Project No. 20-32-51004.

References

[1] Gol'Tsman, G. N., et al. 2001 *Applied physics letters*, **79(6)**, 705-707.
[2] J. Torres et al. 2014 *IEEE Transactions on Nuclear Science*, **61(1)**,107-114
[3] Parsakordasiabi, M. et al, 2021, *Sensors*, **21(1)**, 308.

Temperature-dependent exciton-polaritons in perovskite photonic crystal slab

Masharin M.A.[1], Makarov S.V.[1], Samusev A.K.[1]

[1]ITMO University, School of Physics and Engineering, St. Petersburg, 197101, Russia

mikhail.masharin@metalab.ifmo.ru

Abstract. Strong light-matter coupling regime allows studying unique phenomena, combining exciton and photon features, which can be used in all-optical logical elements. Until recent years exciton-polaritons were demonstrated only in semiconductor quantum wells embedded in vertical Bragg cavities in cryogenic temperatures. However, thanks to the last studies about new materials and photonic designs, it becomes possible to realize room-temperature exciton-polaritons without any vertical Bragg resonators. In this work for the first time, we experimentally demonstrate a strong light-matter regime in planar perovskite photonic crystal slab from $MAPbBr_3$ at room temperature. We also demonstrate the main characteristics of exciton-polaritons in this system and how they depend on temperature.

1. Introduction

Exciton-polaritons are hybrid part-light, part-exciton bosonic quasiparticles. These quasiparticles appear in optically resonant systems under strong light-matter coupling regime. Thanks to the hybrid nature, exciton-polaritons possess small effective mass, long decoherence time and exhibit strong optical nonlinearities. All of this allows to study a variety of quantum collective phenomena such as polariton solitons and realize low threshold polariton lasers, polariton all-optical transistors. First exciton-polariton designs and further polariton devices were realized at cryogenic temperatures with quantum wells inside Bragg resonators and were based on currently well-studied materials such as GaAs [1] and CdTe [2]. However, due to the low binding energy of exciton in these materials, polaritonic phenomena are limited to cryogenic temperatures, therefore, for realizing of realistic designs for real-world applications new materials are demanded.

Now there exist systems, which have been proven to support room temperature strong light-matter coupling regime: GaN- and ZnO-based quantum well cavities, transition metal dichalcogenides, some polymer compounds and halide perovskites [3-7]. The latter have become very popular materials due to their unique physical properties such as tunable bandgap, defect tolerance, huge optical gain, long carrier lifetime and others. Moreover, perovskites are relatively easy to fabricate and structure, which allows using them in various photonic designs.

The most common optical microcavity employed to realize exciton-polaritons is vertical Bragg resonator, however, fabrication of it is labour intensive, hard to scale and difficult to use it in further planar optical chips. Recent works have shown that perovskite-based planar photonic designs can maintain photonic states with high quality factor, allowing to realize the strong exciton-photon coupling regime [7]. In this work, we experimentally study exciton polaritons in planar periodic structure based on $MAPbBr_3$ perovskite.

2. Results

Less than 150 nm thick perovskite thin films can maintain visible-range guided waves in a single-mode regime. Thanks to the high exciton binding energy in $MAPbBr_3$, and high exciton oscillator strength, waveguide cavity photon mode couples with the exciton resonance enabling exciton-polariton. To prove this, we first nanoimprint perovskite thin film using a periodic stamp and then measure the leaky mode dispersion using angle-resolved spectroscopy approach.

In the experiment, we obtain dispersion of only lower polariton brunch since the upper one is suppressed due to strong bandgap absorption of perovskite. We implement two coupled oscillator model to extract temperature dependence (in the range of 7-290 K) of all the system parameters, including exciton transition energy and Rabi splitting of exciton-polaritons. The latter reaches an exceptional value of 107 meV at room temperature.

3. Conclusion

To summarize, in this work we for the first time experimentally demonstrate room temperature $MAPbBr_3$ exciton-polaritons realized in a photonic crystal slab. We also experimentally show the strong dependance of exciton resonance energy and polariton dispersion on temperature.

Acknowledgments

The work was supported by Russian Science Foundation, grant #21-12-00218.

References

[1] Bajoni, D. et al. Polariton laser using single micropillar gaas- gaalas semiconductor cavities. Phys. review letters 100, 047401 (2008).

[2] Kasprzak, J. et al. Bose–einstein condensation of exciton polaritons. Nature 443, 409–414 (2006).

[3] Liu, X. et al. Strong light–matter coupling in two-dimensional atomic crystals. Nat. Photonics 9, 30–34 (2015).

[4] Li, F. et al. From excitonic to photonic polariton condensate in a zno-based microcavity. Phys. review letters 110, 196406 (2013).

[5] Kravtsov, V. et al. Nonlinear polaritons in a monolayer semiconductor coupled to optical bound states in the continuum. Light. Sci. & Appl. 9, 1–8 (2020).

[6] Betzold, S. et al. Coherence and interaction in confined room-temperature polariton condensates with frenkel excitons. ACS Photonics 7, 384–392 (2019).

[7] Masharin, M. A., et. al, (2022). Polaron-enhanced polariton nonlinearity in lead halide perovskites. arXiv preprint arXiv:2201.10265.

Dynamics of the uncertainty value of quadratures for bosonic quantum states

Svetlana Medvedeva [1*], Andrei Gaidash [1,2], George Miroshnichenko [3], Alexei Kiselev [2,3,4], and Anton Kozubov [1,2]

[1]Laboratory of Quantum Processes and Measurements, ITMO University, Saint Petersburg, Russia

[2]Department of Mathematical Methods for Quantum Technologies, Steklov Mathematical Institute of Russian Academy of Sciences, Moscow, Russia

[3]Faculty of Laser Photonics and Optoelectronics, ITMO University, Saint Petersburg, Russia

[4]Faculty of Photonics and Optoinformatics, ITMO University, Saint Petersburg, Russia

[5]Faculty of Physics, St. Petersburg State University, St. Petersburg, Russia

*E-mail: ss_medvedeva@itmo.ru

Abstract. We consider the time evolution of the mean values of the first and second moments of the quadrature operators for an arbitrary quantum state in a single mode transmitted through an optical fiber channel. Utilizing the density matrix formalism and the quantum optics theory we derive expressions for the dynamics of mentioned field observables for such prominent quantum states as squeezed vacuum state, squeezed coherent state and superposition of coherent states.

1. Introduction

One of the main constraints on the technological utilization of the unique quantum features such as superposition or squeezing lies in decoherence: the detrimental influence of environment leads any quantum system to the loss of its beneficial quantum features [1]. A theory that may be employed to investigate the evolution of quantum systems considering decoherence is open quantum systems approach [2]. Within this theory different methods are being used, in our research we focus on solving a master equation for a density matrix of a quantum state.

2. Method

In order to give a description of a nonunitary dynamics of a bosonic quantum state study the Liouville master equation that is a special case of the Gorini–Kossakowski–Sudarshan–Lindblad (GKSL) master equation equation [3]. The explicit solution to this equation may be found, for example, with the use of SU(1,1) algebra formalism [4], Jordan mapping [5]. In this investigation we act by an operator of

interest on the master equation, apply the trace operation and then solve the resulting equation to obtain the time-dependence of a mean value of an operator [6, 7].

3. Results

Utilizing the method presented above We obtain the expressions of time evolution for the first and second moments of the quadrature operators [8] for an arbitrary bosonic quantum state in a single mode transmitted through an optical fiber channel. Moreover, we derive an expression of the dynamics of the uncertainty value of the quadrature operators for an arbitrary bosonic quantum state. We perform a numerical simulation of the obtained time evolution for squeezed vacuum state, squeezed coherent state and superposition of coherent states,investigating the dependence of the dynamics on the squeezing parameter and other characteristics of quantum states.

Acknowledgments

This work was supported by the Ministry of Science and Education of the Russian Federation (Passport #2019-0903).

References

[1] H.-P. Breuer, F. Petruccione, The theory of open quantum systems. Oxford University Press on Demand. (2002).

[2] E. Joos,H. D. Zeh, C. Kiefer, D. J. Giulini, J. Kupsch, I. O. Stamatescu , Decoherence and the appearance of a classical world in quantum theory. Springer Science & Business Media. (2013).

[3] H. Carmichael, An open systems approach to quantum optics: lectures presented at the Université Libre de Bruxelles, October 28 to November 4, 1991. Springer Science & Business Media. 18, (2009).

[4] A.A. Gaidash, A.Kozubov. Kozubov, G.P. Miroshnichenko, Dissipative dynamics of quantum states in the fiber channel. Physical Review A 102, 2, 023711 (2020).

[5] A.A. Gaidash, A.V. Kozubov, G.P. Miroshnichenko, A.D. Kiselev, Quantum dynamics of mixed polarization states: effects of environment-mediated intermode couplings. Optical Society of America 38, 9, 2603-2611 (2021).

[6] A.A. Gaidash, A.V. Kozubov, S.S. Medvedeva, G.P. Miroshnichenko, The Influence of Signal Polarization on Quantum Bit Error Rate for Subcarrier Wave Quantum Key Distribution Protocol. Multidisciplinary Digital Publishing Institute 22, 12, 1393 (2020).

[7] S.S. Medvedeva, A.A. Gaidash, A.V. Kozubov, G.P. Miroshnichenko, Dynamics of field observables in quantum channels. IOP Publishing 1984, 1, 012007 (2021).

[8] M. O. Scully, M. S. Zubairy, Quantum optics. American Association of Physics Teachers. (1999).

Fabrication of SERS-Active Structures *via* Electrostatic Deposition of Colloidal Gold Nanoparticles on Polymer Microspheres

M A Miropoltsev[1], A P Tkach[1], K A Maleeva[1], K V Bogdanov[1]

[1]Center of Optical Information Technologies, ITMO University, St. Petersburg 197101, Russia

miropoltsev_m@niuitmo.ru

Abstract. In this work, the fabrication of SERS-active structures *via* electrostatic deposition of colloidal gold nanoparticles on polymer microspheres was demonstrated. Commercially available polystyrene microspheres were pre-coated with charged polyelectrolytes and treated with gold nanoparticle solutions. By varying the coating parameters, we found the best conditions for successful preparation of the nanoparticle-coated microspheres. The proof-of-concept measurements revealed that the enhancement in our system had similar values as in more complex SERS structures.

1. Introduction

Surface-Enhanced Raman Scattering (SERS) is a promising tool for the analysis of chemical composition and structural features of molecular and crystalline materials. The effect of SERS is based on the resonant amplification of exciting radiation by plasmonic nanostructures. The latter are usually made in the form of thin films, ordered arrays, or single nanoparticles of noble metals [1].

A unique way of creating SERS-active media is immobilization of gold nanoparticles (AuNPs) in various polymer matrices, including self-assembly on polymer microspheres (PMS). To immobilize AuNPs on the microsphere surface, the so-called layer-by-layer deposition can be used. In this method, alternatively charged polyelectrolytes are applied to prepare a smooth charged covering on the PMS surface that electrostatically attracts nanoparticles. This technique has already been successfully used to assemble the arrays of quantum dots on microspheres [2]. However, just a few publications mentioned the possibility of assembling such arrays of plasmonic nanoparticles.

In the present work, we have filled the gap by fabricating SERS-active structures from polymer microspheres and colloidal gold nanoparticles *via* electrostatic deposition. The PMS were coated with several layers of polyelectrolytes and treated with the AuNP solutions at different PMS:AuNP ratios. By varying the coating parameters, we found the best conditions for successful assembly of AuNPs on the PMS surface. The proof-of-concept measurements of the organic dye Raman spectra revealed that the enhancement by our AuNP-coated PMS was comparable to that of more complex SERS structures.

2. Results and Discussion

Stable colloidal gold nanoparticles were synthesized by the well-known citrate reduction method [3]. The as-prepared AuNPs were 20 nm in diameter as determined by SEM and had a plasmonic peak at 525 nm. The hydrodynamic diameter and zeta-potential measurements revealed that the nanoparticles

were well-dispersed and possessed a strong negative charge due to the surface-bound citrate ions. Commercial carboxylate-modified polystyrene microspheres, 4 μm in size, were used as-provided.

At first, we tested the layer-by-layer deposition technique for creation of a smooth charged covering on the PMS surface that would further be applied to electrostatically attract AuNPs. We used a well-known couple of positive and negative polyelectrolytes: poly(allylamine hydrochloride) (PAH) and poly(sodium 4-styrenesulfonate) (PSS). Zeta-potential measurements have demonstrated that 11 layers of polyelectrolytes retain a stable positive charge on the PMS for more than three weeks.

Next, we deposited the AuNPs on the PMS surface pre-covered with several layers of polyelectrolytes. We varied the PMS:AuNP ratio and the number of polyelectrolyte layers and monitored the morphology of the AuNP coatings by the means of optical and scanning electron microscopy (SEM). Interestingly, the stability and morphology of the fabricated structures strongly depended on the number of polyelectrolyte layers. The SEM images that are presented in Figure 1 show the difference between the AuNP coatings for 5 and 11 pre-coated layers.

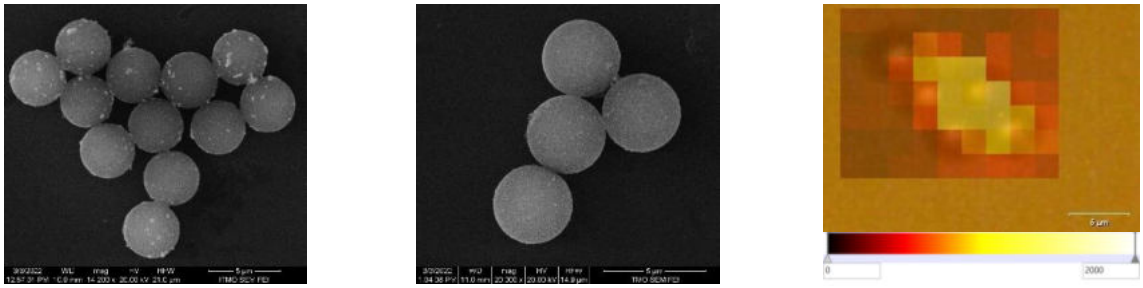

(a) (b) (c)

Figure 1. SEM images of the AuNP-coated PMS that were pre-coated with 5 (a) and 11 (b) layers of polyelectrolytes. (c) A Raman scattering map indicating the intensity enhancement close to PMS.

As follows from Figure 1a,b, thicker polyelectrolyte pre-coating results in a smoother and more homogeneous distribution of AuNPs over the PMS surface. For the sample with better coating morphology, the proof-of-concept Raman scattering measurements were performed with the help of a common organic dye, pseudoisocyanine iodide. The Raman scattering map presented in Figure 1c indicates the intensity enhancement of the 1365 cm^{-1} dye band. This demonstrates the possibility of using our fabricated AuNP-coated PMS as the SERS-active component for material analysis.

3. Conclusions

In this work, we have fabricated SERS-active structures *via* electrostatic deposition of colloidal gold nanoparticles on polymer microspheres. The PMS were coated with several layers of polyelectrolytes and treated with the AuNP solutions at different PMS:AuNP ratios. At first, we studied the stability of polyelectrolyte coatings on the PMS. Then, we deposited the AuNPs on the PMS surface at different parameters to find the best assembly conditions. The proof-of-concept measurements revealed that our system induced enhancement comparable to more complex SERS structures and hence can be used as the SERS-active component for material analysis.

Acknowledgments

The study is funded by RPMA grant of School of Physics and Engineering of ITMO University.

References

[1] Han, X. X., et al., Nat Rev Methods Primers 1, 1 (2022)

[2] Sukhanova, A., and Nabiev, I., Crit. Rev. Oncol. Hematol. 68, 39 (2008)

[3] Lee, P. C., and Meisel, D., J. Phys. Chem. 86, 3391 (1982)

Collective states with high quality factors in chains of dielectric resonators

M S Mikhailovskii[1], M S Sidorenko[1], R S Savelev[1], Z F Sadrieva[1], A A Bogdanov[1], M I Petrov[1]

[1]School of Physics and Engineering, ITMO University, St. Petersburg, 197101, Russia

E-mail: m.mikhailovskii@metalab.ifmo.ru

Abstract. In this work we investigate the interference of the collective modes in the chain of dielectric particles that lead to the increase of the qualiy factor of one of the modes for a properly chosen geometrical parameters. We have performed eigenmode simulations of the chain of ceramic particles which revealed that the maximal *Q*-factor for a chain consisting of 6 particles reaches almost 10^5 for the optimal value of the period. Experimental measurements of the scattering parameters of the chain of ceramic particles in a microwave spectral range under excitation by a dipole antenna confirmed the presence of high quality factor resonance with values similar to the calculated ones.

1. Introduction

All-dielectric optical resonant structures supporting resonances with high quality factors and allowing to localize electromagnetic fields in a small volume are of both fundamental and applied interest due to significant increase of light-matter interaction strength. One type of such structures are ensembles of coupled dielectric subwavelength resonators [1,2]. Due to the interference of radiation from individual elements, such structures support collective resonant oscillations, characterized by suppressed radiative losses and consequently high quality factors. It has been experimentally shown that such systems allow to enhance the nonlinear response of the material of which they are made [2], to enhance the photoluminescence intensity of the quantum dots integrated into them [3], and to achieve regime of laser generation [4].

Besides destructive interference between radiation from individual particles in an ensemble, coupling between two or more modes via radiation continuum can occur under variation of the parameters of such structures. In this case the quality factor of one of the eigenmodes can be substantially increased. For example, this can be achieved by precision control of the gap between individual resonators in the chain [5]. This mechanism can be explained by a change of the dispersion curve of the corresponding infinite chain of particles, namely, by the appearance of an inflection point near the edge of the Brillouin zone. However, this effect has been predicted only theoretically and not investigated experimentally.

2. Results and discussion

In this work we investigate the influence of the gap size between individual subwavelength resonators in a chain on the quality factor of the collective resonant states. Ceramic cylinders with characteristic sizes of the order of a centimetre were chosen as resonators, which greatly simplifies the experimental

verification of the results; scheme of the structure is shown in the inset in Fig.1(a). First, we have calculated the dispersion properties of an infinite chain for different values of the gap between the cylinders. The results plotted in Fig. 1(a) show that for the critical value of the gap g_{cr} ~ 7.3 mm the sign of the group velocity changes sign at the edge of the Brillouin zone. The dispersion branch under study corresponds to the coupled magnetic dipole resonances in the individual cylinders, oriented along the cylinder axis. According to the theory, a finite chain of the particles should exhibit the maximum of the Q-factor of the eigenmode of the chain approximately for the critical value of the period. Calculations of the finite chain of 6 cylinders confirmed this, as shown in Fig.1(b). For realistic values of the losses in ceramic material Im(ε) ~ 0.005, the maximal Q-factor reaches almost 100 000, which is almost one order larger than for non-optimal periods. Further, we have calculated the experimentally measurable S21-parameters by placing electrically small dipole antennas at both sides of the chain. The results are shown in Fig. 1(c). The Q-factor and the eigenfrequency extracted from the scattering spectrum well agrees with those obtained from the eigenmode simulations.

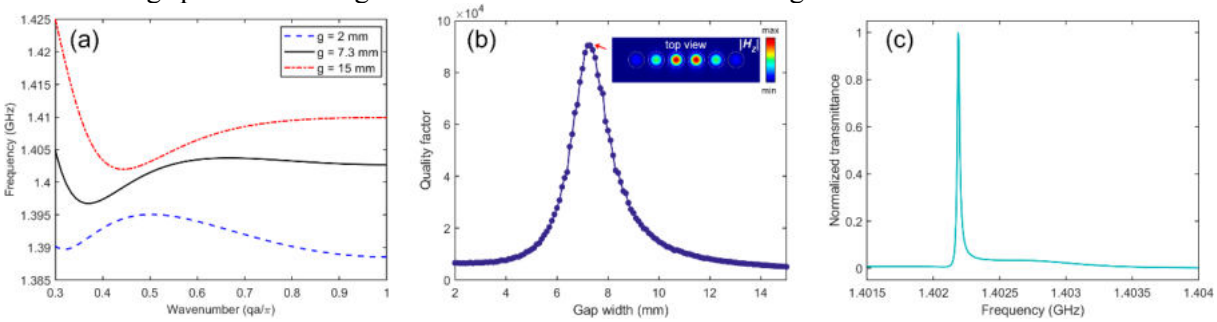

Figure 1. (a) Dispersion diagrams of an infinite chain for different gap sizes, (b) Q-factors vs gap width of the finite chain for N = 6 cylinders, the inset shows the distribution of the out-of-plane component of the magnetic field at the maximum value of the Q-factor, (c) Transmission spectrum of the 6-disk chain for the critical value of the gap.

We have also studied the dependence of the Q-factor on the number of the cylinders in the chain. The simulations revealed that the mode with the highest quality factor is characterized with the growth rate $Q \propto N^{6.3}$, when the ceramic material is transparent, which is much higher than N^3 growth rate, observed in conventional band-edge collective modes. In a more realistic case, if the loss tangent is in the range 10^{-5}-10^{-4}, one can observe a significant decrease in quality factor, which imposes a limit on the maximum possible quality factor regardless of the number of the cylinders. Preliminary experimental measurements of scattering parameters of the chain of ceramic cylinders excited by an electric or magnetic dipole antenna confirmed the presence of high quality factor resonance with values similar to the calculated ones.

Acknowledgments
This work was supported by the Russian Foundation for Basic Research, No. 20-52-12062.

References

[1] Blaustein G. S. et al., Guiding optical modes in chains of dielectric particles, Optics Express, 15 (25), 17380-17391, 2007
[2] Ding L. et al., All-optical modulation in chains of silicon nanoantennas, ACS Photonics, 7 (4), 1001-1008, 2020
[3] Rutckaia V. et al., Coupling of Germanium Quantum Dots with Collective Sub-radiant Modes of Silicon Nanopillar Arrays, ACS Photonics, 8 (1), 209-217, 2020
[4] Hoang T. X. et al., Collective Mie resonances for directional on-chip nanolasers, Nano Letters, 20 (8), 5655-5661, 2020
[5] Kornovan D. F. et al., High-Q localized states in finite arrays of subwavelength resonators, ACS Photonics, 8 (12), 123627-3632, 2021

On improvements of nuclear magnetic resonance magnetometer to study magnetic mid-fields variations

N S Myazin[1], **V V Davydov**[1]
[1]Peter the Great St. Petersburg Polytechnic University, St. Petersburg 195251, Russia

e-mail: myazin.n@list.ru

Abstract. The necessity to develop a magnetometer for variations research in the mid-fields magnetic strength with a relative error of 10^{-6} is justified. A new design of nuclear magnetometer with using to maser with flowing liquid is proposed. The block diagram of the magnetometer is presented, and the principle of its operation is described. The results of experimental investigations of various variations of magnetic fields are presented.

1. Introduction

In the modern world, data on the magnetic field characteristics are in demand in many areas of science and technology [1]. In most cases, it is necessary to control of magnetic field parameters with high accuracy. These problems are successfully solved using the quantum magnetometers based on nuclear magnetic resonance (NMR), which are highly accurate in time measuring of magnetic field variations [2]. There are several types of quantum NMR magnetometers. The most widely used magnetometers are based on a nuclear resonance filter [1] with a phase or frequency self-tuning of the external generator frequency to the frequency of the passive NMR line and the spin generator [2]. The first one has high requirements for the tracking system due to the very narrow NMR line. This creates several measurement problems. For example, significant dynamic errors occur in the case of temperature variations. Existing solutions of this problem significantly complicate the magnetometer design. Therefore, the upper limit of magnetic field induction measurement in most models of industrial quantum NMR magnetometers is 100 μT. To solve special tasks, laboratory versions of quantum NMR magnetometers with an upper measurement limit of up to 200 μT have been developed. These values of magnetic field induction B refer to low magnetic fields. The commissioning of new particle accelerators and tokamaks for research, the development of magnetic starting mechanisms for high-speed objects, new tasks for determining the coordinates of an underwater object at a depth with a remanent magnetization of 12 mT and much more have determined the need to control the magnetic field parameters in the range from 0.2 to 200 mT with a relative measurement error no worse than 10^{-6}.

2. Experiment and theory

Currently, the Hall effect magnetometers are used to measure mid-field magnetic strength ($0.2\ \text{mT} < B < 1000\ \text{mT}$). One of the best magnetic induction meters DX-180 has a relative measurement error of $5\cdot(10^{-5}\div10^{-4})$ in the measurement range from 10^{-5} to 0.3 T with a resolution of $10\div100$ nT. Therefore, the development of a new design of a magnetometer for measuring variations with a relative error no worse than 10^{-6} is extremely urgent.

Figure 1 shows the block diagram of the developed magnetometer. In its development, the data on the Benoit maser [3] were used. A solution of filtered tap water with alcohol is used as a liquid.

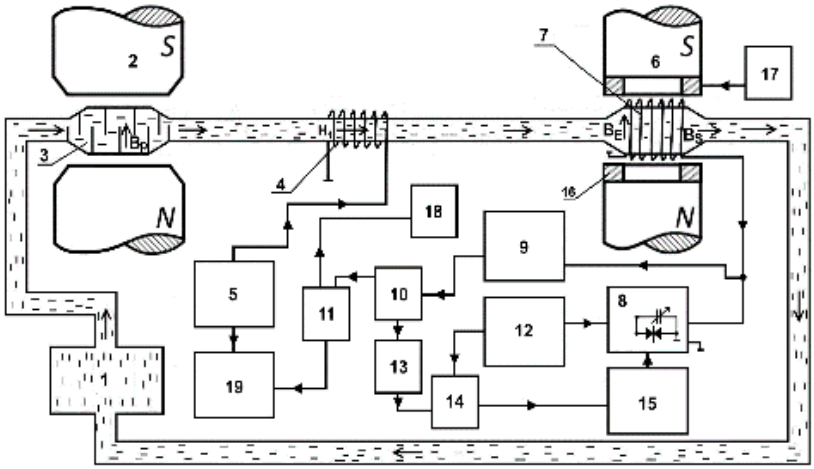

Figure 1. Block diagram of a nuclear magnetic magnetometer. Magnetometer consists of a centrifugal pump (1), polarizer magnet (2), polarizer vessel (3), pulse coil of water proton magnetization inversion (4), radiofrequency generator (5), electromagnet (6), measuring sensor (7), receiving circuit (8), regenerator (9), resonance amplifier (10), registration device (11), low-frequency generator (12), low-frequency amplifier (13), synchronous detector (14), control circuit (15), excitation coils (16), pulse radiofrequency generator (17), oscilloscope (18) and frequency meter (19).

In our nuclear magnetometer design, the transverse relaxation time T_2 is determined in two ways:

1. Using the decay time of the free induction signal when the spin system is excited by a π/2 pulse;
2. Using the decay time of the NMR signal recorded during the modulation of the magnetic field when switching the regenerator to self-excitation mode and disconnecting generator 5 from nutation coils 4 (Figure 1)

Using the relaxation time value, it is possible to evaluate variations of the magnetic field strength:

$$\Delta\omega_{\max} = 1/\left(T_2\sqrt{Q_c/Q_0 - 1}\right)$$

where Q_0 is the threshold quality factor at zero detuning, Q_c is the quality factor of the receiving circuit.

3. Results and discussion

The experiments results show that there is a wide range of variation of the expenditure q, in which the signal-to-noise ratio of the recorded NMR signal is high (more than 20). Specifically, this range is from $q_1 = 1.59 \pm 0.02$ ml/s to $q_2 = 4.74 \pm 0.05$ ml/s. In this case, a change in expenditure q (even by 10 %) will not have a significant impact on the error of measurement of physical quantities a during operating in the center of this range q.

The transverse relaxation time T_2 was determined in two ways for fluid flow $q = 3.06 \pm 0.03$ ml/s. Using free induction decay, $T_2 = 23.21 \pm 0.18$ ms was measured. Using magnetic field modulation, $T_2 = 23.04 \pm 0.23$ ms was measured. Measurements for both cases were repeated 10 times to average the data and estimate the measurement error according to standard methods.

In addition, the same solution at T = 295.3 K was studied on a Minispec mq 20M stationary NMR relaxometer (made by BRUKER company). The measured value is $T_2 = 23.198 \pm 0.065$ ms. All obtained values of T_2 coincided within the measurement error.

References

[1] Ledbetter M P, Pustelny S, Budker D, Blanchard J W and Pines A 2012 *Phys. Rev. Lett.* **108(24)** 243001
[2] Xu S, Crawford C W, Rochester S, Budker D and Pines A 2008 *Phys. Rev.* A **78(1)** 013404
[3] Benoit H, Friver P and Guibe L 1958 *Comptus Rendus* **246** 3608-14

Optical properties of nanoporous alumina activated by pseudoisocyanine molecular nanoclusters

R D Nabiullina, I Y Nikitin, E O Soloveva, I A Gladskikh, A A Starovoytov

Center of Information optical technology, ITMO University, St. Petersburg 197101, Russia

e-mail: rezida2105@mail.ru

Abstract. The hybrid nanomaterials based on inorganic matrix and organic compound with customizable properties have practical potential in the field of new developments in biological and chemical sensors, photonic and solar cell devices, as well as laser media. The optical properties of molecular clusters so called J-aggregates embedded in nanoporous aluminum oxide in presence of silver plasmonic nanoparticles were studied. The unique technique for obtaining nanoporous aluminum oxide on the island silver film was proposed. The optimal parameters of the impregnation of nanopores in the ethanol solution of pseudoisocyanine dye for the molecular nanoclusters formation have been studied. The resonant transfer of optical energy from the oxygen vacancy in aluminum oxide to organic molecules was observed in the resulting hybrid films.

1. Introduction

Photonic nanostructured composite materials combine the current advances in material science of matrix at the nanoscale with multiple functionalities, outstanding performances, and tailored architectures of organic molecules [1]. For optical applications, non-absorbing templates in the optical range are important, so anodic aluminum oxide as the self-organized matrix with honeycomb-like structure formed by close-packed arrays parallel cylindrical nanopores, seems promising. Such template with plasmonic nanoparticles can be the basis of advanced optical sensors for atoms and molecules due to free access of the detected molecules through the nanoporous structure [2]. On the anodic aluminum oxide matrix activated with dye monomolecules of Rhodamine 6G, random lasing was realized [3].

The pore diameter and the pore spacing can be varied by changing the conditions of aluminum anodizing and allows the formation of oriented organic molecules, as well as highly organized molecular aggregates and nanoclusters with unique spectral-optical properties, such as narrower luminescence and absorption spectra in comparison with monomeric forms of dye.

2. Results

In this work the optical properties of nanoporous aluminum oxide formed on an island silver film and activated by molecular clusters of pseudoisocyanine dye were studied. The influence of the current strength and anodizing time on the properties of hybrid Al_2O_3/Ag film was considered. With an increase in the anodizing time, a decrease in reflection is observed, which is associated with an increase in the amount of aluminum oxide. An increase in the current strength leads to an increase in the pore size in alumina and an increase in scattering in the short-wave region (Fig.1).

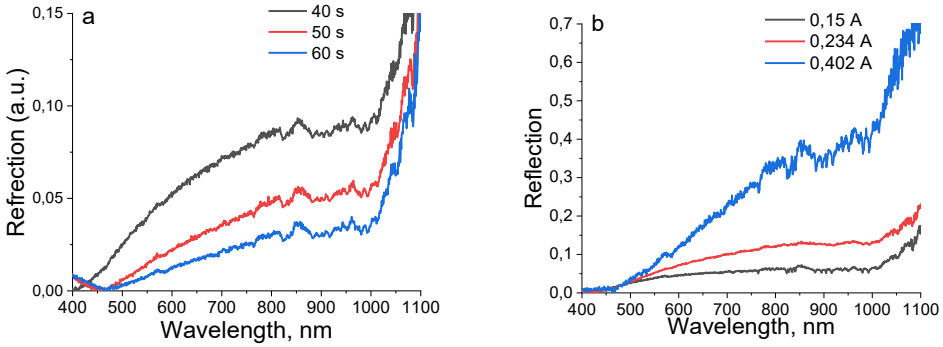

Figure 1. Reflection spectra of hybrid films depending on the time (a) and current strength (b) of anodizing of Al/Ag film

The optimal conditions for obtaining molecular nanoclusters are as follows, the saturated solution should be heated to temperatures close to the boiling point of ethanol (T) and carry out impregnation of sample for a certain time (t). After that, the sample should be removed from solution and dried, prolonged impregnation of the sample leads to a decrease in aggregation (Fig. 2).

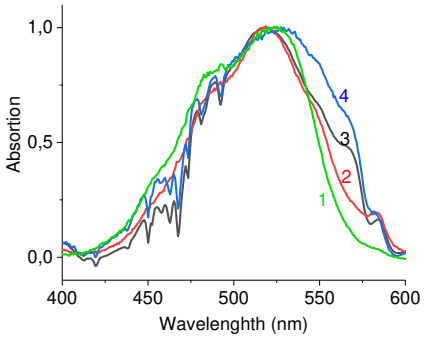

Figure 2. Normalized absorption spectra of dye molecules embedded in alumina membrane. (a) dependence on impregnation process: 1 – T = 75 °C, t = 60 min, then sample stay cooling in solution for 2 days; 2 – T = 75 °C, t = 60 min; 1 – T = 75 °C, t = 30 min; 1 – T = 60 °C, t = 60 min

In a hybrid film activated with dye molecules, luminescence of molecular clusters was observed with excitation at 405 nm. Non-resonant luminescence occurred due to resonance energy transfer from oxygen vacancy of alumina to organic molecules.

Acknowledgments

Mr. Nikitin, Ms. Nabiullina and Ms. Solovieva are grateful to RPMA grant of School of Physics and Engineering of ITMO University; Prof. Starovoytov and Dr. Gladskikh are grateful to Russian Science Foundation (Project 21-72-10098).

References

[1] Feng S and Ji W 2021 *Front. Nanotechnol.* **3** 1–18
[2] Wang X G, Wang J, Li J-F, Tao D-W, Zhou W-M, Li Y and Wang C-W 2021 *Appl. Surf. Sci.* **544** 148881:1- 9
[3] Lyubas G A 2017 *Nanotechnologies Russ.* **12** 276–284

Fabry-Perot type bound state in the continuum in an anisotropic photonic crystal

S V Nabol[1,2], P S Pankin[1,2], D N Maximov[1,2], I V Timofeev[1,2]

[1]Kirensky Institute of Physics, FRC KSC SB RAS, Krasnoyarsk 660036, Russia
[2]Siberian Federal University, Krasnoyarsk 660041, Russia

Abstract. In the present work, we consider an anisotropic photonic crystal containing two anisotropic defect layers. For y-polarized waves, the structure is completely transparent, while for x-polarized waves, there is a photonic bandgap. By varying the orientation of the optical axis of the anisotropic defect layers, it is possible to couple the localized mode and the propagating wave, which have orthogonal polarizations. Thus, it becomes possible to control the quality factor of the localized modes.

1. Introduction

Bound state in the continuum (BIC) is the nonradiative eigenstate in an open system. The BIC eigenenergy is embedded into the continuum of propagating waves [1]. Theoretically, BIC has an infinite Q-factor, since it does not radiate into the surrounding space. Consequently, its excitation or detection is impossible, unless the BIC becomes coupled with propagating waves. This coupling immediately turns the BIC into a quasi-BIC with finite Q-factor [2]. BICs have found many applications in photonics, including low-threshold lasers, high-precision optical sensors and narrow-band filters [3].

The model under study is a photonic crystal (PhC) consisting of alternating isotropic and anisotropic layers with two anisotropic defect layers (fig.1, a). We assume that y-polarized light falls normally on the structure. Anisotropic PhC is transparent for y-waves, and it is opaque for x-waves. So, the latter waves can be localized in the defect layers. By rotating the optical axis of the defect layers, a destructive interference can be achieved for the waves leaking from the defect layers. The resulting BIC is called a Fabry-Perot type BIC (FP-BIC), because the defects act like a pair of cavity mirrors [4].

2. Result

Figure 1(b) shows the reflectance spectrum of the structure, calculated using the Berreman's method, depending on the optical axis azimuthal angle φ_1 of the first defect layer. The red horizontal line shows the position of the defect mode, in the case when there is only one defect in the structure, which rotation angle is fixed. Another red line shows the position of the defect mode, in the case when there is only one defect in the structure, which rotation angle is changed. It can be seen that the resonances in the structure with two defects demonstrate avoided crossing behavior, which is characterized by the repulsion of eigenmodes (in yellow) while the partial mode lines cross each other. The avoided crossing arises due to the coupling of two localized modes.

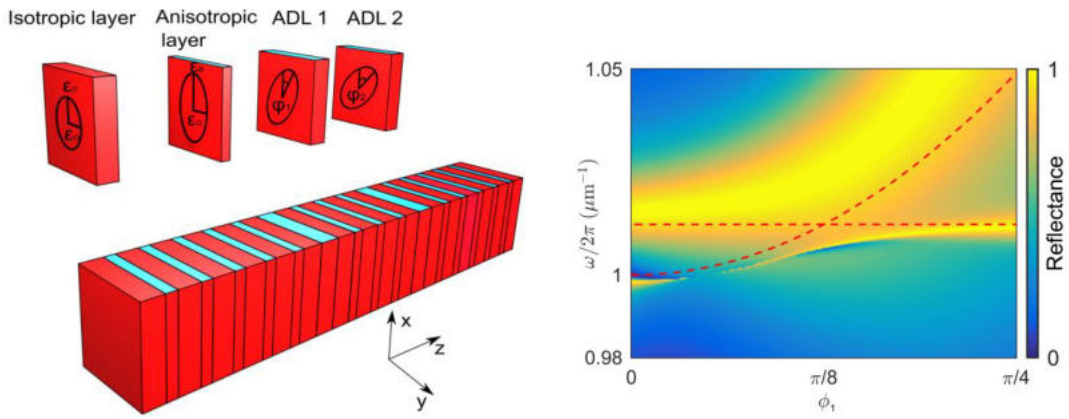

Figure 1. (a) Schematic model of the structure under study. (b) Reflectance spectrum of the structure for y-polarized light.

The coupling also produces FP-BIC, which manifests itself spectrally as the resonance linewidth collapse. FP-BIC occurs due to destructive interference of waves leaking from defect layers. It can be seen that, in the vicinity of the BIC, one can effectively control the width of the resonance lines, i.e. the quality factor of the resonant mode. The obtained spectral features can be explained within the framework of the temporal coupled-mode theory [5].

3. Conclusions

In this work, a Fabry–Perot type BIC was found in a PhC structure with alternating isotropic and anisotropic layers containing two anisotropic defect layers. The obtained results can be useful for the construction of optical microcavities with tunable Q-factor.

Acknowledgments

This work was supported by the Council on Grants of the President of the Russian Federation (MK-4012.2021.1.2).

References

[1] Hsu, C. W., Zhen, B., Stone, A. D., Joannopoulos, J. D., & Soljačić, M. (2016). Bound states in the continuum. *Nature Reviews Materials*, *1*(9), 1-13. Another reference

[2] Pankin, P. S., Maksimov, D. N., Chen, K. P., & Timofeev, I. V. (2020). Fano feature induced by a bound state in the continuum via resonant state expansion. Scientific reports, 10(1), 1-10.

[3] Joseph, S., Pandey, S., Sarkar, S., & Joseph, J. (2021). Bound states in the continuum in resonant nanostructures: an overview of engineered materials for tailored applications. *Nanophotonics*.

[4] Sadreev, A. F. (2021). Interference traps waves in open system: Bound states in the continuum. *Reports on Progress in Physics*.

[5] Fan, S., Suh, W., & Joannopoulos, J. D. (2003). Temporal coupled-mode theory for the Fano resonance in optical resonators. JOSA A, 20(3), 569-572.

A new method of processing measurement results of tissue oxygen saturation abnormalities

V V Naumova[1] and V V Davydov[1, 2, 3]

[1]Peter the Great Saint-Petersburg Polytechnic University, Saint Petersburg, Russia, 195251
[2]The Bonch-Bruevich Saint-Petersburg State University of Telecommunications, Saint Petersburg 193232, Russia
[3]All-Russian Research Institute of Phytopathology, Moscow Region 143050, Russia

e-mail: naumova.vv@edu.spbstu.ru

Abstract. A noninvasive intelligent blood filling control complex for lower limb ischemia using a multisensory system based on optical sensors and machine learning methods is presented. The results are presented, indicating the possibility of automated detection of deviations from the norm of the parameters of blood filling of the extremities.

1. Introduction

Every year the issue of noninvasive diagnostic methods application in medicine becomes more and more actual all over the world. Non-invasive methods include optical devices, which do not violate the integrity of tissues and structures of the human body. Methods of optical detection became widespread due to many developments in scientific and medical spheres. Their main advantages are ease of use, high performance, and most importantly, the possibility of performing diagnostics outside a medical institution [1]. One of the significant trends is the development of optical methods of human limb blood-flow control using multichannel spectrum analyzer [2]. Deviations in blood flow status in limb vessels detected by optical methods can be associated with the development of dangerous pathologies such as diabetes mellitus, atherosclerosis and others.

The aim of this study is to create a prototype of an intelligent diagnostic optical system for noninvasive monitoring of human lower limb tissue oxygen saturation abnormalities. The method is based on a combination of the use of machine-learning methods and optical methods for recording spectra by a multichannel analyzer having operating wavelengths in the range from 410 to 940 nm. The groups of subjects at different risk of blood supply disorders were formed using a mathematical analysis of the results obtained using the principal component method.

2. Method

The multisensor optical system contains two modules. The first module - optoelectronic - is an eighteen-channel integral optical analyzer of visible and near-infrared spectra and is intended for carrying out blood-flow studies of human lower limbs by noninvasive method. The second module - information-computer module - performs displaying of the obtained measurements and processing of the obtained data array.

Registration of optical system readings was performed under conditions of rest, low-intensity physical activity (3 metabolic units (MET)), as well as in the process of the subject's recovery after physical activity. Physical activity causes significant changes in limb blood flow and disturbances in hemodynamics, due to which pathophysiological conditions can be more clearly expressed, detection of which helps to diagnose latent diseases such as diabetes mellitus, atherosclerosis and others.

The performed mathematical analysis of the results of measurements registered by the optical system of lower limbs, healthy and affected, of the subject with diabetes mellitus at rest and during physical activity revealed different trends in changes in the blood flow of the limbs before and after the exercise test. Using the principal component method we obtained groups of subjects with different response to physical exercise, visualization of the ranking results was performed, which allowed us to identify hidden patterns in changes of limb blood flow according to the readings of optical sensors at different moments of the experiment.

3. Results

In Figure 1 shows the measurement results of the patient's healthy leg. The graph shows that in the resting state in the standing position, as well as during exercise, the sensor readings vary in the same range of values, but in the recovery process the readings go down.

(a) (b)

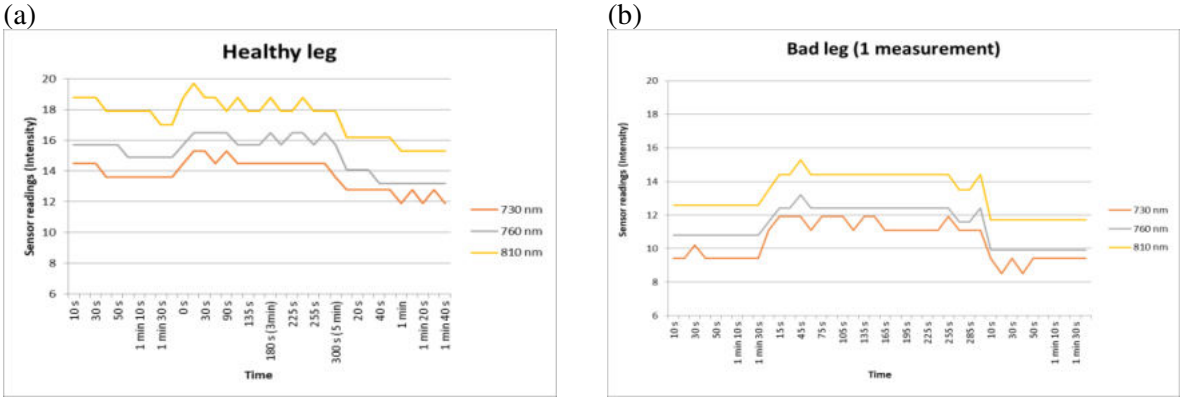

Figure 1 The sensor readings (intensity) depending on the time at rest, physical activity and the process of restoring the patient's healthy (a) and bad (b) legs for wavelengths of 730,760, 810 nm.

The optical system was then moved to the other leg (the affected limb). The optical sensor was not repositioned and remained in place during the patient's two physical tests.The results of the measurements of the affected leg are shown in Figure 1 (b). Compared with the "Healthy leg" graph, we can see a clearly different trend in the change of sensor readings. First, the range of values at rest is several values lower in the affected leg than in the healthy leg. Secondly, with the beginning of physical activity we see a sharp jump upwards, similarly, with the end of the exercise a sharp drop in values.

4. Conclusion

The results obtained testify to the possibility of intelligent automated detection of tissue oxygen saturation abnormalities in human lower limb ischemia and allow medical personnel to make a preliminary decision on the presence or absence of pathology.

References

[1] Zaitceva A Yu, Kislyakova L P, Kislyakov Yu Ya, Avduchenko S A 2019 *Journal of Physics: CS*. **1400** 033022.

[2] Mazing M S, Zaitceva A Yu, Kislyakov Yu Ya, Kondakov N S, Avdushenko S A, Davydov V V 2020 *International Journal of Pharmaceutical Research*. **12(2)** 1974-1978.

Nonlinear circular dichroism in dielectric nanoparticle dimers and trimers

Anastasia Nikitina[1], Anna Nikolaeva[1], Kristina Frizyuk[1]

[1]The School of Physics and Engineering, ITMO University, St. Petersburg, 197101, Russia

E-Mail: anastasia.nikitina@metalab.ifmo.ru

Abstract. We performed the theoretical study of circular dichroism (CD) in the second harmonic (SH) signal from nanostructures with different symmetries. Using the apparatus of group theory, we compared dimer and trimer structures, and explained the absence of nonlinear response in AlGaAs trimers.

1. Introduction

Circular dichroism is a relevant phenomenon in nanophotonic that allows for the exploration of many properties of media. There are a lot of studies devoted to nonlinear circular dichroism that also finds applications in different fields [1-5].

One of the recent works on CD in the SH signal considered a structure that consists of two identical AlGaAs cylinders irradiated by circularly polarized light [5]. The crystal lattice has a specific orientation [100]‖x, and the structure can be rotated around z-axis. The study revealed that CD exists only if the dimer's axis is rotated with the respect to the [100] crystalline axis. An erroneous conclusion can be drawn, that this is due to the low total symmetry of the structure with lattice.

We demonstrated that the existence of CD in the SH signal depends on the symmetry in a tricky way, and one should always consider the symmetry of the induced nonlinear polarization and the nanostructure's eigenmodes. To show, that the total symmetry does not play a major role, we compared the nonlinear response of dimers and C3v symmetric trimers and received and explained via the group theory the total absence of CD in the trimer. All our results were also verified using numerical modeling in COMSOL Multiphysics™.

2. Results and discussion

Considering the dimer, i.e., two identical AlGaAs cylinders, we obtain the nonvanishing nonlinear CD for majority of angles. To provide the theory of the appearance of the nonlinear CD, we should assess nonlinear polarization $\vec{P}^{2\omega}(\vec{r}')$, which is related to the nonlinear susceptibility of the crystal lattice and the symmetry group of the sample. The contribution of each eigenmode $\vec{E}_n(\vec{r})$ to the SH is described by an overlap integral: $D_n = \int_V dV' \vec{E}_n(\vec{r}')\vec{P}^{2\omega}(\vec{r}')$.

SH polarization for AlGaAs contains two terms: $\vec{P}^{2\omega}(r,\phi,z) \propto \vec{P}_0^{2\omega}(r,z) + \vec{P}_4^{2\omega}(r,z)e^{\pm 4i(\phi-\beta)}$, where β is the angle between the crystalline x-axis and sample x′-axis, ϕ is an angle in cylindrical coordinates, and $\pm$ stands for two different circular polarizations. The symmetry group of the dimer is C2v [6]. Its eigenmodes with multipolar indexes m=0 and m=4 correspond to the same irreducible

representations (irreps) of the symmetry group. In this case, the eigenmodes that contribute to one radiation channel give nonzero overlap integral with both parts of nonlinear polarization. It leads to the existence of nonlinear CD. In contrast symmetry group of the trimer is C3v. Its eigenmodes with m=0 and m=4 belong to different irreps. Due to this fact, these eigenmodes contribute to SH intensity independently. As a result, in trimers, nonlinear CD cannot be observed. The main results are shown in Figure 1.

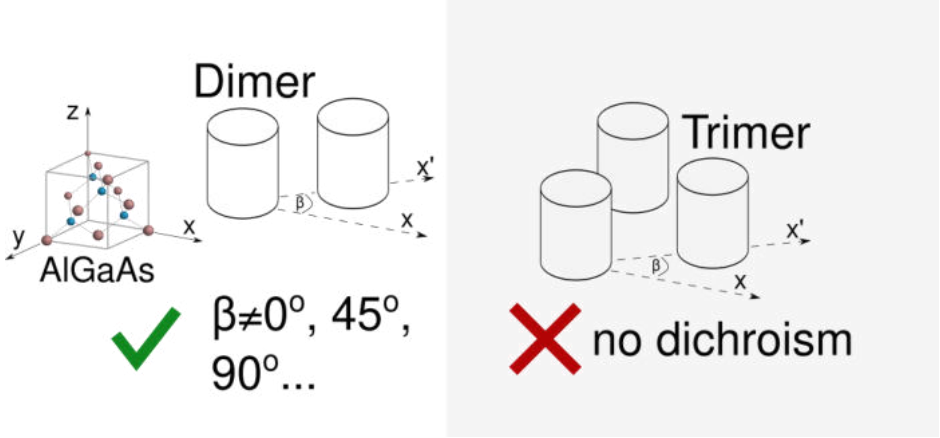

Figure 1. It is the main result of the study of CD in SH signal in AlGaAs nanoparticles. On the left side of the Figure, we considered a dimer, where we can observe a nonvanishing nonlinear CD. It exists only if $\beta \neq Z\pi/4$, where β is the angle between the crystalline x-axis and sample x'-axis. On the right side of the Figure, we considered a trimer. SH-CD never appears here for any lattice orientation.

Conclusions

In summary, we provide the theoretical description of SH-CD. We describe, how the symmetry of crystal lattice and the structure together affect nonlinear response.

Acknowledgments

This research was supported by Priority 2030 Federal Academic Leadership Program. K.F. acknowledges support from the Foundation for the Advancement of Theoretical Physics and Mathematics "BASIS" (Russia).

References

[1] Berova, N.; Nakanishi, K.; Woody, R. W. Circular Dichroism: Principles and Applications, 2nd ed.; Wiley−VCH: Hoboken, NJ, 2000.

[2] Wang, Z., Cheng, F., Winsor, T., & Liu, Y. (2016). Optical chiral metamaterials: a review of the fundamentals, fabrication methods and applications. Nanotechnology, 27(41), 412001.

[3] Slocik, J. M., Govorov, A. O., & Naik, R. R. (2011). Plasmonic Circular Dichroism of Peptide-Functionalized Gold Nanoparticles. Nano Lett., 11(2), 701–705.

[4] Belardini, A., Larciprete, M. C., Centini, M., Fazio, E., Sibilia, C., Chiappe, D., ...Buatier de Mongeot, F. (2011). Circular Dichroism in the Optical Second-Harmonic Emission of Curved Gold Metal Nanowires. Phys. Rev. Lett., 107(25), 257401.

[5] Frizyuk, K., Melik-Gaykazyan, E., Choi, J.-H., Petrov, M. I., Park, H.-G., & Kivshar, Y. (2021). Nonlinear Circular Dichroism in Mie-Resonant Nanoparticle Dimers. Nano Lett., 21(10), 4381–4387.

[6] Gladyshev, S., Frizyuk, K., & Bogdanov, A. (2020). Symmetry analysis and multipole classification of eigenmodes in electromagnetic resonators for engineering their optical properties. Phys. Rev. B, 102(7), 075103.

Förster resonance energy transfer in thin layers of indium phosphide quantum dots

D.N. Pevtsov [1,2], S.A. Tovstun [1,2], A. V. Aybush [3], V. F. Razumov [1,2]

[1]Institute of Problems of Chemical Physics, Russian Academy of Sciences, Chernogolovka, Moscow oblast, 142432 Russia
[2] Moscow Institute of Physics and Technology (National Research University), Dolgoprudny, Moscow Region 141701, Russia
[3]N.N. Semenov Federal Research Center for Chemical Physics RAS, Moscow 119991, Russia

e-mail: pevtsov.dn@phystech.edu

Abstract. Colloidal quantum dots (CQDs) of indium phosphide with a zinc sulfide shell have been synthesized. They were used to fabricate thin CQD films. For solutions and films, the spectra of absorption, stationery and time-resolved luminescence were measured. The spectra are analyzed and the parameters of the Förster energy transfer and the distance between the nearest particles in the layer are estimated. The dimensionless rate constant of transfer between particles of the same size was 21, and the Foerster radius was 6.2 nm.

1. Introduction

Colloidal quantum dots (CQDs) are successfully used in solar cells, light emitting diodes, and photodetectors. To achieve maximum performance of photovoltaic devices based on CCPs, it is necessary to understand the mechanism and main parameters of excitation and charge carrier transfer processes.

CQDs in layers have a size distribution and are located at small distances from each other. In such systems, the Förster nonradiative resonant energy transfer (FRET) process is effective. The excitation created by light is transferred from small particles to large ones i.e., the luminescence of donors (small CQDs) is quenched when that of acceptors (large CQDs) increases. Because of this, the luminescence spectrum of an ensemble of close-packed particles turns out to be shifted to the red region relative to the luminescence spectrum of an ensemble of free particles.

The efficiency of FRET is directly determined by the distance between particles, which can be controlled by the size of the CQD ligand shell. From the analysis of the luminescence spectra of the layers, it is possible to estimate the FRET parameters and from them to estimate the average distance between the particles. [1].

2. Experiments

Thin InZnP CQD films on glass substrates were prepared as follows. The glass slide was soaked in potassium dichromate for at least two hours and washed in an ultrasonic bath: first in acetone for five minutes, and then in deionized water also for five minutes. Next, the glass substrate was placed on a spin coater, the rotation speed of which was then set to 4000 rpm. The solution of nanoparticles was applied using a dispenser. The applied volume was 35 μl. After that, the glass was placed for 30 seconds in a 4% solution of ethanedithiol in acetonitrile, and then washed in pure acetonitrile also for 30 seconds. The procedure for applying layers on the spincoater was repeated 10 times.

3. Results and discussion

The resulting films were examined for homogeneity by confocal luminescent microscopy. Figure 1 shows micrographs of films at various magnifications. The inhomogeneity of the film is clearly seen: nonluminescent regions and brightly luminescent clusters are visible.

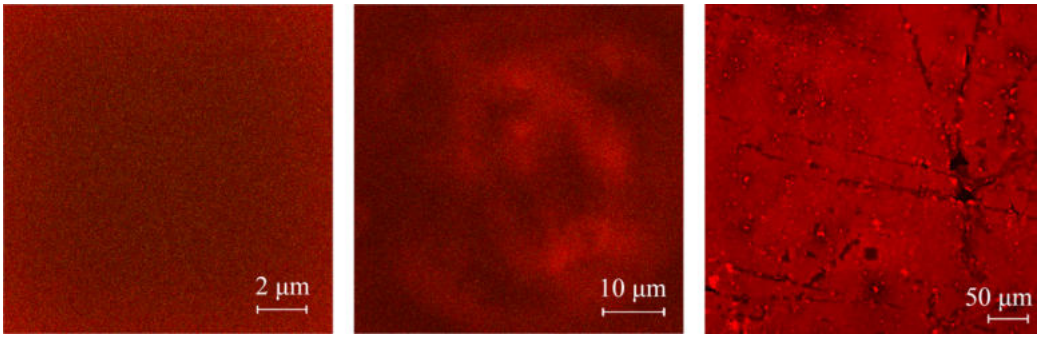

Figure 1. Images of films from InZnP nanoparticles obtained by confocal luminescence microscopy.

To quantitatively measure the FRET efficiency, time-resolved luminescence spectra of solutions and layers of InZnP CQDs were recorded (Fig. 2).

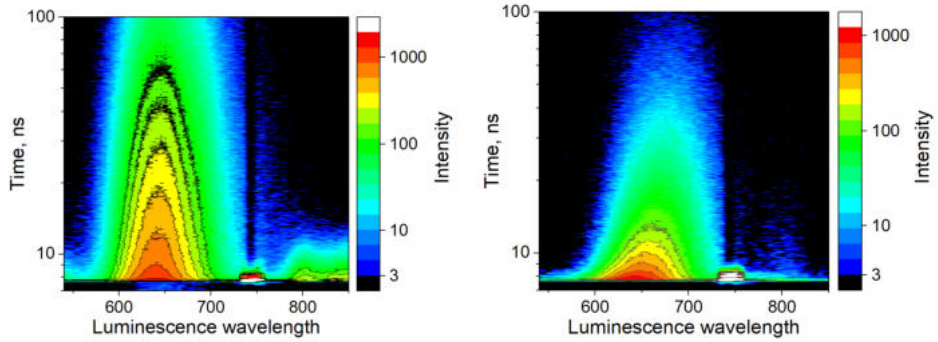

Figure 2. Time-resolved fluorescence decay kinetics upon pulsed excitation at a wavelength of 372 nm for InZnP nanoparticles. Left: for nanoparticles in hexane. Right: for nanoparticles in a film on a glass substrate. Peak at 744nm - monochromator artifact (twice the excitation wavelength).

Next, we determined the absorption cross section averaged over the ensemble as a function of the wavelength, the magnitude of the homogeneous and inhomogeneous broadenings, and calculated the uniform shapes of the lines of the luminescence spectrum and the overlap integrals of donors and acceptors according to [2, 3].

As a result of processing, the value of the dimensionless rate constant of transfer between particles was obtained - 21. This constant characterizes the efficiency of FRET - in the film under consideration, all the nearest neighbors of a certain particle have the same size as itself, then the rate constant of excitation transfer from it to these neighboring particles 21 times greater than the radiative constant outside the film. Substituting this constant into the Foerster formula gave a Foerster radius of 6.2 nm. This value characterizes the average distance between the centers of the nearest particles.

Acknowledgments

This work was supported by the Russian Science Foundation Grant No. 21-73-20245

References

[1] Brichkin S.B., Tovstun S.A., Spirin M.G., Razumov V.F. High Energy Chemistry. 2017. Vol. 51. № 6. pp. 455-461.

[2] Tovstun, S. A.; Ivanchikhina, A. V.; Spirin, M. G.; Martyanova, E. G.; Razumov, V. F., J. Chem. Phys., 2020, 153, 084108.

[3] Tovstun, S. A.; Razumov, V. F. Theoretical analysis of nonradiative energy transfer in nanoclusters of quasi-monodisperse colloidal quantum dots. High Energ. Chem. 2015, 49, 352– 360.

Experimental Study of Luminescent Properties and Band Structure of Two-Dimensional Photonic Crystals with Ordered Ge(Si) Nanoislands

Peretokin A.V.[1,2,*], Stepikhova M.V.[1], Novikov A.V.[1,2], Smagina Zh.V.[3], Dyakov S.A.[4]

[1] Institute of Physics of Microstructures RAS, st. Akademicheskaya, 7, 1 Afonino, Kstovsky district, Nizhny Novgorod region, Russia
[2] UNN them. N.I. Lobachevsky, Gagarin Ave., 27, Nizhny Novgorod, Russia
[3] Institute of Semiconductor Physics A.V. Rzhanov SB RAS, 13 Lavrentiev Ave., Novosibirsk, Russia
[4] Skolkovo Institute of Science and Technology, st. Nobelya, 3, Moscow, Russia

*aperetokin@ipmras.ru

Abstract. The paper presents the results of experimental studies of two-dimensional photonic crystals (PhC) with a square lattice of holes, formed on silicon structures with ordered Ge(Si) nanoislands. The ordering of nanoislands in such structures is treated by the formation of seed pits on the substrate, which also play the role of holes forming the PhC. The phenomena of considering the PL signals of nanoislands in such structures for the interaction of their interaction with the modes of a photonic crystal are discussed. The band structure of a PhC with a square lattice of holes is experimentally obtained, and the modes that make the main contribution to the detection of the PL signal are revealed.

To solve the problem of creating near-IR radiation sources on silicon, structures with self-forming Ge(Si) nanoislands are of interest. To increase the micro-PL signal, two-dimensional photonic crystals (PCs) formed on such structures are used. As will be shown in this work, the increase in the intensity of the PL signal occurs due to the interaction of nanoislands with PC modes. A greater enhancement of the PL signal can be expected with precision embedding of nanoislands into the maxima of the PC mode field [1]. This paper will present the results of experimental studies of the band structure of such photonic crystals by micro-photoluminescence spectroscopy, and consider the observed amplification phenomena of the nanoislands related PL and their relationship with the lattice parameters of photonic crystals.

We have studied PhCs with a square lattice of holes formed on silicon structures with Ge(Si) nanoislands. Initially, the holes in silicon structures were formed in order to arrange the nanoislands in the growth plane, however, as the results of our studies have shown, these holes can also play the role of PhC's holes, leading to the effects of PhC modes interaction with the medium and the amplification of the PL signal [2]. In this work, a lattice of holes with the periods varied from 0.5 to 2 μm was studied. Depending on the period, the depth of the holes and the growth parameters, the islands in such structures are formed in the holes, between them and around them forming a specific "sunshine" pattern.

To analyze the luminescence properties of these structures and the band structure of photonic crystals, the following methods were used: 1) - the standard micro-PL method, which allows us to measure the luminescence response with a high spectral (up to 0.01 cm-1) and spatial (up to 2 μm) resolution, and 2) - the method for the directional diagram studies [3]. The essence of the latter method consists in analysis of the angular distribution of PhC's emission with a geometrical reference of the observed PL signal to the reciprocal lattice of photonic crystal.

The performed series of studies showed the presence of a significant (by more than an order of magnitude) amplification of the PL signal related with Ge(Si) nanoislands in PhCs with the lattice periods of 0.7-0.8 μm. A specific modes pattern that is responsible for this amplification was revealed. The experimental results obtained are in good agreement with the data of the theoretical simulation scarried out for these structures by the scattering matrix method [4].

References

[1] R. Jannesari, M. Schatzl, F. Hackl et al. // Opt. Express, V. 22, 25426 (2014).

[2] A.V. Novikov, Zh.V. Smagina, M.V. Stepikhova et al. // Nanomaterials, V. 11, 909 (2021).

[3] S.A. Dyakov, M.V. Stepikhova, A.A. Bogdanov et al. // Laser Photonics Rev.,V. 15, 2000242 (2021).

[4] S.G. Tikhodeev, A.L. Yablonskii, E.A. Muljarov et al. //Phys. Rev. B, V. 66, 045102 (2002).

Phase-time-encoding MDI QKD tolerant to detector imperfections

Ivan Petrov[1,2,3,4*], **Daniil Menskoy**[1,2,3,5*] **and Andrey Tayduganov**[1,3]

[1]QRate, Skolkovo, Moscow 143025, Russia
[2]Moscow Institute of Physics and Technology, Dolgoprudny, Moscow Region 141701, Russia
[3]NTI Center for Quantum Communications, National University of Science and Technology MISiS, Moscow 119049, Russia
[4]Russian Quantum Center, Skolkovo, Moscow 143025, Russia
[5]Institute for Information Transmission Problems RAS, Moscow 127051, Russia

E-mail: *{i.petrov, d.menskoy}@goqrate.com

Abstract. Measurement-device-independent quantum key distribution (MDI QKD) allows to eliminate the single-photon detector (SPD) vulnerabilities, increase the communication distance limits, and construct a multiple users key distribution network. Nevertheless, detector imperfections are able to decrease the secret key rate and maximum distance by orders of magnitude. In this work we propose a model of large SPD's dead time for the phase-time-encoding MDI QKD. We also propose a modified measurement device (Charlie) scheme with four detectors which is able to partially restore the sifted key loss caused by dead time.

1. Successful events

In this work we consider the phase-time-encoding MDI QKD protocol with decoy-state technique. The theoretical model [1] is used to predict probabilities of successful events (gain) after the Bell measurement of a joint Alice-Bob state. Events of the form $A_i \cap A_j$ are considered successful, where A_i, A_j denote detector's click in the corresponding time and space mode $i \in \{c_E, d_E\}$, $j \in \{c_L, d_L\}$ (E and L stand for "Early" and "Late"). As far as standard measurement scheme (see Fig. 1a) contains only one SPD at each beam splitter (BS) output, the events like $A_{c_E} \cap A_{c_L}$ cannot be detected in the case of dead time $\tau \sim T_{\text{tot}}$, where $T_{\text{tot}} = 1/f\eta_{\text{ch}}$ is the average period of detection rate, η_{ch} is the overall channel transmission probability (taking into account detector quantum efficiency). We analytically demonstrated that the signal gain decreases by the factor $1/2$ if states in one basis are chosen with equal probabilities. The proposed scheme (see Fig. 1b) contains two detectors at every BS output. As a result, approximately one half of the previously discarded events can be detected, which gives 25% restore of the sifted key rate in comparison with the classical scheme.

2. Sifted key generation rate

The above result is valid for the sifted key rate correction only in the case when the dead time overlaps every second pulse ($\tau \simeq T_{\text{tot}}$). Otherwise the result, obtained in the limit $\tau \gg T_{\text{tot}}$ and

under condition of synchronous dead time, is additionally applied [2] :

$$R_{\text{sift}}^{\tau\neq 0} = \frac{R_{\text{sift}}^{\tau=0}}{1+\tau R_{\text{tot}}}, \tag{1}$$

where R_{tot} is the overall rate when at least one detector clicks. The simple estimation that takes into account the dark counts and multi-photon pulses is $R_{\text{tot}}^{(1)} = f(2\text{Pr}(n_{ph} > 0) + 4p_{\text{dc}})$, where $\text{Pr}(n_{ph} > 0) = 2(1-e^{-\mu'}) - (1-e^{-\mu'})^2 \simeq 4\mu'$ is a probability of generation nonzero-photon pulses, $\mu' = \mu\eta_{\text{ch}}$, μ - mean photon number per signal pulse. In general, for the decoy-state MDI protocol all events have to be taken into account, and one has to sum up the click probabilities of at least one detector: click from two incoming coherent states, prepared in different bases and of different intensities, and clicks due to dark counts. This estimation is referred to as $R_{\text{tot}}^{(2)}$.

In order to predict the sifted key rate in the new scheme, one can use the approximation of Eq. (1), but instead of $R_{\text{sift}}^{\tau=0} = r(\eta_d)$ we consider $R_{\text{sift}}^{\tau=0} = r(\eta_d) + r(\eta_d/2)$, η_d - detector quantum efficiency. Here $r(\eta_d) = fp_Z^2 p_\mu^2 Q^Z_{\mu_a\mu_b}$ drawn out of signal gain $Q^Z_{\mu_a\mu_b} = q(\eta_d)$ calculated in [1], $p_\mu = 0.5$ and $p_Z = 0.5$ are signal pulse and basis choice probabilities respectively. In Fig.1c we compare the computed secret key generation rate for two presented detection schemes as function of detector's dead time. The ratio $R(4D)/R(2D) \simeq 1.26$ does not depend on τ and scheme and remains constant for parameters from Tab. 2.

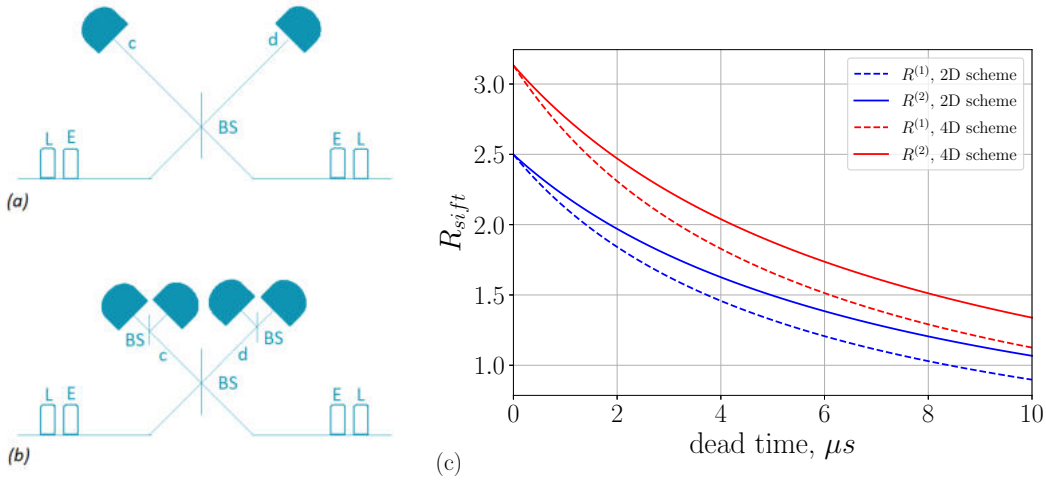

Figure 1. Measurement scheme for phase-time encoding: (a) two detectors, (b) four detectors. Plot (c) of sifted key rate vs. detector's dead time. $R^{(1)}$ - naive estimation, $R^{(2)}$ - our result based on model from [1].

μ	L_{ab}	η_d	p_{dc}	f
0.1	160 km	10%	10^{-6}	3×10^8

Table 1. Key model parameters.

References

[1] X. Ma, and M. Razavi. Alternative schemes for measurement-device-independent quantum key distribution. *Phys. Rev. A*, 86:062319, 2012.

[2] V. Burenkov, B. Qi, B. Fortescue, and H.-K. Lo. Security of high speed quantum key distribution with finite detector dead time. arXiv:1005.0272, 2010.

Lensed optical fiber production technology using optical glue

R S Ponomarev, V S Kozhevnikov, A I Shmyrova, A S Pankov

[1]Perm State University, integrated photonics laboratory, Perm 614990, Russia

Email: rsponomarev@gmail.com

Abstract. The technology of creating optical microlenses at the end of a fiber light guide using optical glue is considered. A method for dispensing and positioning an adhesive microdrop has been implemented, which makes it possible to place an adhesive volume of about 0.2 pl with an error of no more than 1 μm at the end of an optical fiber in the region of the core. The selection of an optical adhesive that satisfies the requirements of the technological process and the physicochemical properties of microlenses as much as possible has been carried out. It is shown that the microvibrations makes possible to control the shape of a drop, the polymerization of which allows to obtain a lensed fiber with a given shape and focal length. The results of measuring the focal length and mode field diameter of the resulting lens are presented.

1. Introduction

Fiber light guides with microlenses at the end, also called lensed fibers, are widely used in integrated and fiber optics to change the parameters of transmitted radiation [1]. Such fibers are used to increase the efficiency of the input/output of radiation into optical integrated circuits [2, 3] with channel waveguides of small diameter (less than 3 μm) based on InP, SOI, Si_3N_4, to optimize the output of optical radiation from laser diodes (LED, PUMP, DFB , SLD) to fiber optic networks [4], etc.

In this paper, we present an alternative method for creating microlenses at the end of an optical fiber using an optical adhesive used in integrated photonics. In particular, we are talking about an optical adhesive with ultraviolet curing with a refractive index equal to the refractive index of the fiber core. For such an adhesive, due to the variations in density, surface tension, kinematic viscosity and polymerization parameters, it becomes possible to manufacture lenses of any required geometry.

2. Technique for creating a microlens

The creation of a microlens at the end of the optical fiber comes in several stages: 1. selection of optical glue, 2. application of optical glue to the intermediate element and its transfer to the end of the optical fiber, 3. putting a drop of a given shape under the action of a high-frequency vibration field, 4. polymerization of the optical glue.

Optical glue is the basis for the manufacture of microlenses. So special attention should be paid to the dynamic viscosity before glue hardens and to the refractive index, hardness and temperature characteristics of the material after polymerization.

To create a hemispherical microlens with the chosen size of the fiber core (9 μm), it is necessary to apply a volume of optical glue about 0.2 pl to the fiber end. A sharpened metal needle was used for taking such a small amount of glue and transferring it to the optical fiber, an intermediate element. Next, the needle with the help of a three-axis positioner was smoothly brought to the fiber until they

touched. The same time, a certain amount of glue dropped onto the fiber surface in the core area. Before that the protective coating was already removed and the fiber was cleaved at a right angle.

Then the acoustic vibrations form and shape drop of glue.

Fixing the shape of the microdroplet surface is the final stage of the technological process. A 60 W ultraviolet lamp located perpendicular to the end of the optical fiber at a distance of 20 cm polymerize optical glue.

3. Qualitative assessment of the microlens

The main optical parameters of fiber lenses are the mode field diameter (MFD) - the minimum diameter of the optical beam in the waist region, and the focal length of the lens.

The measurement of MFD of fabricated lint fibers was carried out by the transverse shear method [5]. The method is based on measuring the power of radiation emitted from two successively coupled single-mode fibers during their mutual radial displacement at the junction. MFD was defined as the distance between the points of the Gaussian distribution of the fundamental mode of the optical fiber, at which the signal power drops by a factor of e^2. The measurements show that the value of the MFD of the optical fiber before the formation of an adhesive microlens at its end is 9.8 μm, and after - 4.1 μm.

The focal length of lensed fibers was determined using a Fabry-Perot interferometer [5-6]. It turned out to be 36.4 μm. This method is useful for many reasons. Firstly, the method avoids the problem of adjusting the optics and the need for precise positioning of the main optical planes. Secondly, the single-mode optical fiber used as the main element in the optical scheme as a light source, an object, and a micrometer-sized receiver at the same time. And this fiber is also highly sensitive to the spatial shift of the focused emission back reflection. Thirdly, the optical circuit diagram is simple, compact and easy to implement.

Acknowledgments

The work was carried out within the framework of the state task of the Ministry of Science and Higher Education of the Russian Federation No. 121101300016-2.

References

[1] Piccirillo F, Giaquinto M, Ricciardi A et al. 2021 *Results in Optics* **6** 100203.
[2] Yang L, Dai D, Yang Bo et al. 2009 *Applied optics* **48** 672.
[3] Ounnas B, Sauviac B, Takakura Y et al. 2015 *IEEE Transactions on Antennas and Propagation* **63(12)** 5612.
[4] Song J H, Roycroft B J, Corbett B et al. 2010 *Optical Engineering* **49** 014301.
[5] Li E 2006 *Optics Letters* **31(2)** 169.
[6] Karnaushkin P V, Ponomarev R S 2017 *Bulletin of Perm University, Series: Physics* **1(35)** 54.

Model of a photon neuron based on multilayer structures with films of phase-change materials

Egor Pritotskii and Mikhail Pankov
Institute on Laser and Information Technologies of Russian Academy of Sciences - Branch of FSRC «Crystallography and Photonics» RAS, Shatura, Russia

Corresponding author (Egor M Pritotskii): pritotsky@bk.ru

Abstract. The function of threshold filtration was investigated according to the Leaky Integrate-and-Fire model for the implementation of a photonic neuron based on thin films of phase-changing materials. A model of an optical artificial neuron is proposed. In the model, C-band laser pulses change phase of the GST film, which becomes transparent (activated) and transmits pulse to the input synaptic layer of the next neurons.

A neuron integrates input signals from other neurons through synapses and generates output signals known as impulses ("action potentials", "bursts", "spikes") when the integrated input signal exceeds a threshold value ("membrane potential"). The Leaky Integrate-and-Fire (LIF) neuron model is one of the most widely used models of biological neurons in modern theoretical neurobiology.

The behavior of artificial networks according to this model provides the greatest similarity with the work of biological neurons, but is limited to a small set of basic operations: weighting and delay at the input from the synapse, summation, time integration, and threshold filtering in a neuron. Generation of impulses by a neuron is a natural hybrid of analog and digital processing, where the output signal of a neuron is binary in amplitude, while the processing in the neuron itself is analog. It is this type of processing that has evolved in biological systems to overcome the noise accumulation problem common in analog computing. Thus, all information transmitted to the next neuron is contained only in the presence or absence of an impulse, but not in its shape or amplitude.

The development of semiconductor technologies and technologies of non-volatile memory offers many new approaches to the hardware implementation of the basic functions of a neuron. One of the variants of an array of synapses and neurons is implemented in the IBM TrueNorth, where the weights of the trained network are written in integers in one artificial synapse from an array of semiconductor transistors, and the neuron is implemented according to the LIF model. Another variant of the impulse system with learning on a chip is presented in the development of Intel in the Loihi processor.

Impulse neural networks are based on local learning rules that are more promising in terms of computing power and required volumes of labeled data, using only information about neuron activity to update synapse weights. The functions of summation and temporal integration are considered in some detail and there are various examples of technical implementation, but the interpretation of threshold filtering in a neuron comes down to processing digital signals using software algorithms and special architectures that imitate the neuron LIF model. LIF neurons are powerful primitives in terms of computational processes and complexity. New approaches and methods are needed to implement the function of nonlinear activation of a neuron upon receipt of input weighted signals.

An additional advantage of the computational model of neurons with impulses is its ability to naturally include learning and adaptation using the mechanisms of plasticity, depending on the impulse time. A LIF neuron has inputs, a membrane potential, and one activation output state. The input data is a continuous time series of bursts or analog signals. At the moment when the time-integrated signal exceeds the membrane potential, the neuron emits an impulse, so the output of the neuron consists of a continuous time series of impulses.

The development of neuromorphic systems is possible due to the transition to pulsed optical neural systems. Optical synapses and neurons are technologically realized on fibers or planar waveguides, where the main principle of the device is a high-speed change in the optical signal.

It is possible to recreate the activation function according to the LIF model due to the rapid change in the extinction coefficient of the $Ge_2Se_2Te_5$ (GST) film in the C-range. The main criterion for optimizing the parameters of a multilayer structure is an increase in absorption during a phase transition. We use quarter-wavelength layers of transparent oxides to increase the transmission contrast and effective antireflection in two phase states of the GST film. The absorption of the multilayer structure increases by an order of magnitude during the phase transition, which makes it possible to implement threshold filtering of input pulses and transmit one output pulse.

The GST film is initially in a crystalline state and absorbs low-intensity optical pulses without reamorphization. Reamorphization occurs when the energy density of the weighted input pulses simultaneously reaches a threshold value. The impulses travel by reducing the absorption of the film, thus generating an output neural impulse. Upon exposure to the following pulses, the top layer of the GST film crystallizes with increased reflection. The duration of the multipulse crystallization of the film will depend on the combined effect of excitatory or inhibitory synapses (Figure 1).

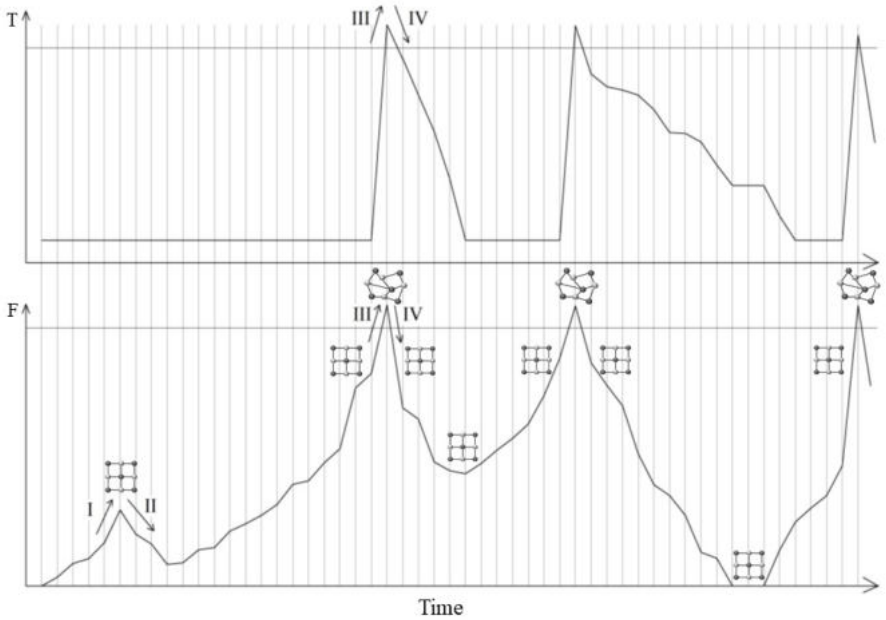

Figure 1. Model of the implementation of the threshold filtering function and activation of a photonic neuron, where the upper solid line shows the membrane potential, T – transmittance, F – fluence of energy, I - the combined effect of excitatory synapses, II - the combined effect of inhibitory synapses, III - achieving the fluence of reamorphization, IV - multi-pulse crystallization

The model structure simulates a biological neuron according to the principle of integration and activation, with the only difference that an artificial neuron integrates optical power at a fixed time, in contrast to its biological analog, which integrates incoming impulses in time. A photonic neuron can act as the main computational element in multilevel photonic neural networks suitable for scalable implementation of neurosynaptic systems.

A new technique for monitoring the state of liquid media by the optical method in express control

D S Provodin[1] **and V V Davydov**[1, 2]
[1]Peter the Great Saint-Petersburg Polytechnic University, Saint Petersburg, Russia, 195251
[2]All-Russian Research Institute of Phytopathology, Moscow Region 143050, Russia

e-mail: provodindanya@gmail.com

Abstract. The necessity of express control of the state of liquid media in real time is substantiated. Various methods of express control of the state of liquid media are considered. The basic requirements for these methods are determined. An optical method for monitoring the state of liquid media using the phenomenon of refraction is presented. The use of a small-sized differential-type refractometer for express control of the state of liquid media is substantiated. Its design has been developed and a new principle for measuring the refractive index of the investigated liquid has been proposed. The results of experimental studies are presented.

1. Introduction

The development of scientific and technological progress has set a large number of tasks for scientists. One of which is the express control of the state of liquids in real time [1]. Its role in the modern world is very difficult to assess, since the number of negative factors that worsen the state of liquid media is constantly increasing [1, 2]. Express control is especially in demand when conducting environmental monitoring, monitoring the state of various environments during experiments or in production, where there are no automated control systems, etc. In these cases, the use of expensive high-resolution instruments that require special operating conditions is inappropriate to use. To solve such problems, compact, reliable equipment with an autonomous power source is required [2]. In addition, ongoing studies of the state of the medium during express control should not change its physical structure and chemical composition [2]. This is necessary to obtain confirmation of the detected contamination in the environmental sample on high-resolution instruments in a stationary laboratory. One of the methods that satisfies these requirements is based on the phenomenon of refraction. The refractive index of the medium n and the temperature T are measured, and the value of n is compared with the value of n corresponding to the standard state of the medium.

2. Design of a differential refractometer and the principle of measuring the refractive index of a liquid

On Figure 1 shows the design of the Anderson cuvette and the path of laser beams in it for the design of a differential refractometer. In the designs of differential refractometers developed earlier, a technique based on detecting a change in the angle of laser radiation between beams 1 and 2 was used. Beam 1 corresponds to the case of equality $n_s = n_m$. In the case of a change in n_m, the laser radiation beam is deflected and exits the cuvette at a certain angle β. Using various optical elements, this angle was measured and the refractive index n_m was determined. For measurements in the field, this measurement

method turned out to be difficult to implement, since it is necessary to provide accurate measurements of the rotation of optical elements to determine the angle β. When transferring the device, misalignment of the structure is possible. In addition, changes in ambient temperature T will affect the operation of the optical elements when measuring the angle β. This will lead to a large measurement error. In addition, with this principle of measurement, it is quite difficult to ensure the small size of the design of the refractometer.

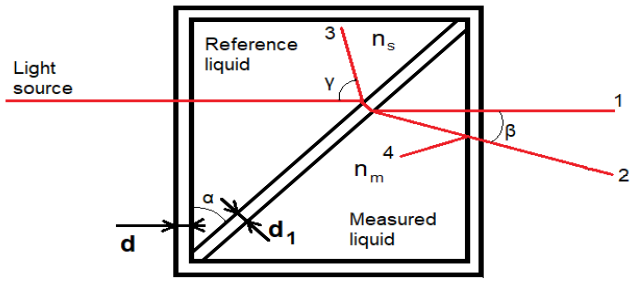

Figure 1. Structural diagram of the optical part of the differential refractometer and the path of the rays in the Anderson differential cuvette.

Therefore, we have developed another principle for measuring the refractive index n_m. To register laser radiation, a photodiode array consisting of 1024 photosensitive sensors is used. The position of the maximum laser radiation is recorded on one of the photosensitive sensors (for this, a semiconductor laser with a narrow radiation pattern is used). The shift of the position of beam 2 relative to the position of beam 1 on the photodiode line is calculated taking into account the parameters of the Anderson cuvette, the refractive index n_s and n_m, and the distance L between the cuvette and the photodiode line.

3. Results of experimental studies of various media and discussion

On Figure 2 shows the results of a study on the effect of impurities on condition control of Rheinol 5W-30 engine oil as an example. Engine oil very often needs to be tested before use for various reasons.

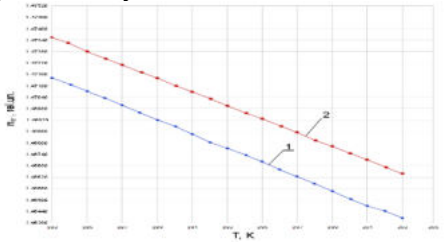

Figure 2. Dependence of the change in the refractive index nm of engine oil on temperature T. The graphs correspond to the state of the engine oil: 1 - standard, 2 - the presence of AI-80 gasoline in the oil

Analysis of the obtained data in figure 2 shows the reliability of the differential refractometer we have developed.

4. Conclusion

The results obtained allow us to consider that the design of the differential type refractometer proposed by us can be used to solve problems of express control of the state of liquid media in various situations. In the case of registering the maximum laser radiation on one photosensitive sensor of the photodiode array, it is possible to provide a measurement range n of the order of 0.8 with a measurement error of 0.001. This is enough for express control.

References

[1] Grebenikova N M 2019 *Journal of Physics: Conference Series* **1326(1)** 012012
[2] Karabegov M A 2004 *Measurement Techniques* **47(11)** 1106-1112

Perfect absorption of a focused beam by a single nanoparticle

Alexey Proskurin[1]*, Andrey Bogdanov[1], and Denis G. Baranov[2]

[1] School of Physics and Engineering, ITMO University, St. Petersburg, 197101, Russia
[2] Center for Photonics and 2D Materials, Moscow Institute of Physics and Technology, Dolgoprudny, 141700, Russia

* alexey.proskurin@metalab.ifmo.ru

Abstract. The absorption of electromagnetic energy plays an essential role in many processes of light-matter interaction. Increased absorption efficiency is key to the performance of devices in areas such as molecular sensing, photodetection, photovoltaics. In this work, we theoretically demonstrate the possibility to absorb all the incoming energy with a single nanoparticle located above a conducting plane. Our model suggests analytical expressions for the required shape of the illumination beam and the required material parameters of the particle. We confirm our calculations with the full-wave numerical simulation.

The light-matter interaction is a promising area of research, resulting in a plethora of possible practical applications. An essential part of such processes is the absorption of electromagnetic radiation. An increased absorption rate allows the development of efficient devices in photovoltaics, photodetection, photocatalysis, and molecular sensing.

A perfect absorber is an object absorbing all the incoming energy. Traditional examples of perfect absorbers involve infinite structures absorbing energy delivered through a trivial channel. Moreover, it might be difficult to create the proposed systems since the incident field contains both far-field and near-field components.

Confined objects are usually not a useful platform for perfect absorption. Because their absorption cross-section is limited, they cannot absorb the infinite amount of energy carried by a plane wave.

Our work aims to deal with both limitations mentioned above. We suggest an elegant setup allowing an analytical solution for the required incident field's shape that does not contain any decaying components. It consists of the dipole particle above the PEC substrate. Incident illumination is composed of a set of propagating plane waves forming a focused beam. Exploiting the theory of Fredholm equations, we obtained expressions for the particle's dipole polarizability and the field profile required for perfect absorption. We verified the analytical results with full-wave numerical simulations. For realistic materials and a fixed-size particle, we achieved absorption rates > 99.5%.

Acknowledgments
This research was supported by Priority 2030 Federal Academic Leadership Program. D.G.B. acknowledges support from the Russian Science Foundation (21-72-00051).

References

[1] Proskurin, A., Bogdanov, A., & Baranov, D. G. (2021). Perfect absorption of a focused light beam by a single nanoparticle. *Laser & Photonics Reviews*, 15(8), 2000430.

Electron-spectrum and transport phenomena in two-dimensional Dirac Semimetals

G R Rakhmanova[1, 2] **and I V Iorsh**[1]

[1]School of Physics and Engineering, ITMO University, Saint Petersburg 197101, Russia
[2]gulnaz.rahmanova@metalab.ifmo.ru

Abstract. We consider two-dimensional (2D) Dirac semimetals where nonsymmorphic crystal lattices possess symmetry-enforced Dirac-like band dispersion around certain high symmetry momenta in the presence of spin-orbit coupling. Here we calculated linear optical conductivity and show that electronic state supports plasmons with quasi-linear anisotropic dispersion.

1. Introduction

The discovery of graphene with Dirac cones at the Fermi energy attracted intense interest in the field of two-dimensional (2D) materials. In the absence of spin-orbit coupling the Dirac points in graphene are protected by symmetry, while spin-orbit coupling opens a gap at the Dirac spectrum. There was introduced symmetry-protected 2D Dirac semimetals, where Dirac cones at high-symmetry points are not gapped by spin-orbit interactions [1]. These are of interest because they are symmetry tuned to the boundary between topological and trivial insulating phases. Dirac-like band dispersions have recently been observed in the nonsymmorphic monolayer film, α-bismuthene [2]. The lattice is invariant under a glide mirror reflection that leads to band degeneracy at the high symmetry momentum points of the Brillouin zone. In this paper, we will investigate the new features that nonsymmorphic symmetry brings to the optical conductivity.

2. Model

We have taken the example of α-bismuthene (α-Bi) that is nonmagnetic and centrosymmetric material, so the time-reversal and inversion symmetries are preserved [2]. Also, it has glide mirror symmetry that helps us to decompose the Hamiltonian in the form [3]:

$$\widehat{H} = v_x k_x \left(\sigma_x \cos\alpha + \sigma_y \sin\alpha\right) + v_y k_y \sigma_z, \tag{1}$$

where σ_i are Pauli matrices for the spin degree of freedom, $v_y = v$ and $v_x = \rho v$. The anisotropy factor ρ refers to the mismatch in the Fermi velocity along x and y-direction. The angle α is the "mixing angle," which is an intrinsic parameter of the model.

Eigenvalues are:

$$E = \pm v\sqrt{\rho^2 k_x^2 + k_y^2} \tag{2}$$

The coupling to electromagnetic field is introduced via the gauge transform $k \rightarrow k - e\mathcal{A}$,where $\mathcal{A}$ is the vector potential of the perturbing field.

3. Linear conductivity

Linear conductivity can be obtained within the formalism based on the density matrix approach, where the average current is given by:

$$\langle \boldsymbol{J}(t) \rangle = \mathrm{Tr}[\boldsymbol{J}\rho(t)] = \sum_n \frac{e^{-\beta E_n}}{Z} \langle n(t)|\hat{\boldsymbol{J}}(t)|n(t)\rangle, \tag{3}$$

where $\boldsymbol{J}$ is the current operator, $\rho(t)$ is the density matrix operator, E_n and $|n(t)\rangle$ are the eigenvalues and eigenfunctions written in the interaction picture, respectively. The time-dependent eigenstates in the interaction picture are $|n(t)\rangle = exp\left(-i/\hbar \int^t dt'\ \hat{V}(t')\right)\ |n\rangle$, where the interaction term is given by $\hat{V}(t) = \boldsymbol{J}(t,r)\,\mathcal{A}(t,r')$.

The current operator is introduced as $J = \frac{\partial H}{\partial A}$. Then, components of current operator are given by:

$$I_x = -\rho v\big(\sigma_x \cos\alpha + \sigma_y \sin\alpha\big), \qquad I_y = -v\sigma_z \tag{4}$$

Linear conductivity can be found as

$$\langle \boldsymbol{J}(w) \rangle = \sigma(w,q)\mathbf{E}(\omega) \tag{5}$$

We assume that $T \to 0$ and wave vector of plasmon is much smaller than Fermi wave vector. The expression for conductivity is:

$$\sigma = \frac{1}{\rho} \frac{\omega\tilde{q}}{v_F^2\tilde{q}^2 - \omega^2}, \tag{6}$$

where $\tilde{q} = \sqrt{\rho^2 q_x^2 + q_y^2}$.

The result of eq. (6) describes 2D plasmon with quasi-linear anisotropic dispersion $\omega = \pm v_F\sqrt{\rho^2 q_x^2 + q_y^2}$.

4. Conclusion

In conclusion, we demonstrate that 2D Dirac semimetals show anisotropic electronic transport properties due to strong in-plane anisotropy. We calculated linear optical conductivity and show that electronic state supports plasmons with quasi-linear anisotropic dispersion**.**

References

[1] Young S M and Kane C L 2015 *PRL* **115** 126803
[2] Kowalczyk P J , *et al* 2020 *ACS Nano* **14** 1888
[3] Chakraborty A, *et al* 2022 *Phys. Rev. B* **105** 085101

Metal-dielectric optical microcavity with tunable Q-factor

G A Romanenko[1,2], P S Pankin[1,3], D S Buzin[1,3], A I Krasnov[1,3], V S Sutormin[1,3], S V Nabol[1,3], I A Tambasov[1], F. V. Zelenov[4,2], A N Masyugin[4,2], I V Timofeev[1,3]

[1]Kirensky Institute of Physics, FRC KSC SB RAS, Krasnoyarsk 660036, Russia
[2]Siberian State University of Science and Technology, Krasnoyarsk 660037, Russia
[3]Siberian Federal University, Krasnoyarsk 660041, Russia
[4]AO NPP Radiosvyaz, 660021 Krasnoyarsk, Russia

E-mail: gavriil21romanenko@mail.ru

Abstract. The article shows numerical calculation of the spectra for a metal-dielectric microcavity. The microcavity consists of a photonic crystal mirror, metallic mirror and a liquid crystal layer between them. It is shown that the system supports both symmetry-protected and Friedrich-Wintgen types of bound states in the continuum. The quality factor and position of resonant modes are effectively controlled by changing the system parameters or applying an external electric field to the liquid crystal layer.

1. Introduction

Bound state in the continuum (BIC) is a non-radiative state with an infinite Q-factor, although it is localized in an open system. The BIC is realized when the bound state inside the resonator is decoupled from the continuum of waves propagating in waveguides. Microcavities supporting symmetry-protected BICs (SP-BIC) and Friedrich-Wintgen BICs (FW-BIC) were previously proposed in one-dimensional photonic crystals (PhCs) [1].

By definition, the BIC is decoupled from the environment. Coupling of the BIC with the continuum of propagating waves makes it excitable and detectable quasi-BIC. The Q-factor of the quasi-BIC is controlled by changing the coupling coefficient. The real BIC does not achieve an infinite Q-factor since the absorption is unavoidable in real systems with account of material losses. The BIC and quasi-BIC concepts have been proposed for novel lasers, LEDs, solar cells [2] and for magnetophotonic applications [3].

2. Results and discussion

In this article, we consider a BIC localized in a liquid crystal (LC) layer, located between two mirrors: – a one-dimensional PhC and a metal layer (Fig. 1, a). The PhC mirror consists of periodically arranged Si_3N_4 and SiO_2 layers. The first and last PhC layers are made of Si_3N_4 material with a high refractive index. A transparent conducting ITO layer is located in front of the PhC mirror. The defect layer is filled by uniaxial nematic LC 5CB. The optical axis orientation depends on LC director (the averaged orientation of LC molecules). Vector $\boldsymbol{a}$ shows the LC director inside the layer. The spectral features of the microcavity are changed with the LC effective refractive index when the director is rotated. The polyvinyl alcohol (PVA) layer is deposidet at the PhC surface and rubbed to align the LC director relative to the incident light polarization. The last layer of the microcavity is an opaque golden mirror.

The microcavity spectra were calculated by the Berreman numerical method for TM-polarized light incident at Brewster angle. The reflectance spectra are shown in figure 1 (b) as a three-dimensional colormap versus the rotation angle φ of the LC director. At an angle φ = 0 the propagating TM-wave is not coupled with an orthogonal TE-wave, which cannot propagate in a PhC mirror due to the presence of a photonic band gap. In this case, the LC director is oriented along the y axis and the TE-mode with the electric field component E_y does not contribute to the propagating TM-wave. The resonant linewidth collapse is observed in the reflectance spectrum, indicating the implementation of SP-BIC, marked with a red cross on the left edge of some resonant line. At the angle φ = π/2, the LC director is oriented along the x axis, and the localized TE-mode again does not contribute to the propagating TM-wave (red cross on the right edge of in figure 1 (b)). The position of the resonant mode shifts to the short-wave region, and its width increases with increasing of angle φ. The collapse of the resonant mode is observed for some other values of the angle φ, indicating the FW-BIC, due to the destructive interference of ordinary and extraordinary waves outgoing from the LC layer. The FW-BIC positions are marked with red circles (Fig. 1, b).

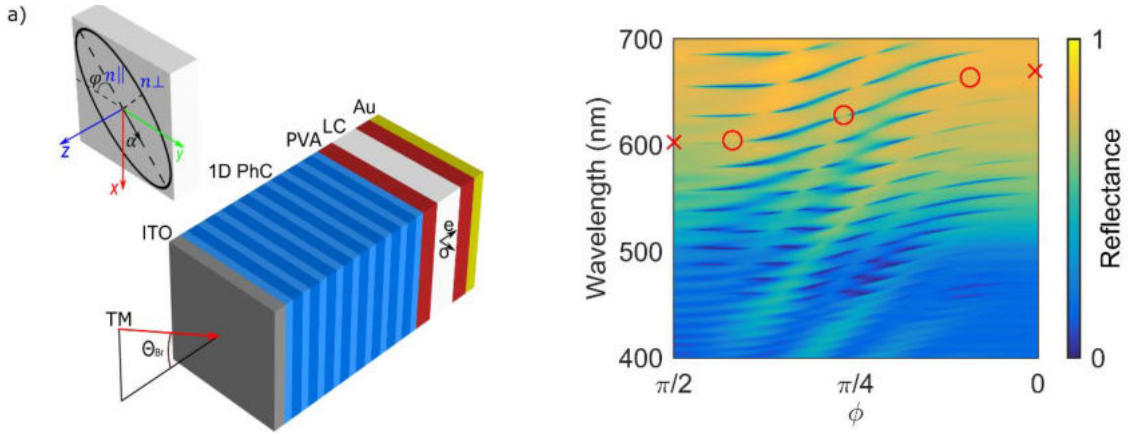

Figure 1. a) Optical microcavity scheme. b) Reflectance spectrum depending on the rotation angle φ of the LC director and optical axis.

3. Conclusions

The article shows the possibility of realization of SP-BIC and FW-BIC in a metal-dielectric microcavity. The position and width of the resonant lines change when the angle of rotation of the optical axis of the LC layer is changed. It is also possible to control spectral characteristics by applying an external electric field to the LC layer. The obtained results can be used to create microcavity with tunable Q-factor.

Acknowledgments

This research was funded by the Russian Science Foundation (project no. 22-42-08003).

References

[1] Pankin P S, Wu B-R, Yang J-H, Chen K-P, Timofeev I V and A F Sadreev 2020 *Commun. Phys.* 3(91),

[2] Joseph S, Joseph J, Pandey S and Sarkar S 2021 *Nanophotonics*, 10(17), 4175-4207

[3] Ignatyeva D O and Belotelov V I 2020 *Optics Letters* 45(23), 6422-6425

Towards Passive Silicon Micro-Ring Memories Using Nonlinear Free Carrier Dispersion Effect

I. A. Ryabcev[1], A. A. Nikitin[1], D. A. Konkin[2], A. A. Kokolov[2], L. I. Babak[2], A. B. Ustinov[1]
[1]St. Petersburg Electrotechnical University "LETI", St. Petersburg, Russia
[2]Tomsk State University of Control Systems and Radioelectronics "TUSUR", Tomsk, Russia

Author e-mail address: ryabcev.ilya@gmail.com

Abstract. The present work focuses on experimental investigation of a silicon-on-insulator (SOI) micro-ring resonator (MRR). The resonator exploits a bistability phenomenon induced by the free-carrier dispersion effect. We demonstrate a stable hysteresis response of transfer characteristics. Flipping the optical input power provides a convenient mechanism for a switching of the MRR output characteristics between two steady states. Obtained results show an application of the passive SOI MRR as an all-optical memory.

1. Introduction

Silicon micro-ring resonators (MRR) are a promising platform for the study of nonlinear dynamics due to exhibition of several competing nonlinear effects. The first is the relatively slow thermo-optic effect which takes place when light is absorbed in the silicon MRR as a result of both linear and nonlinear damping. The damping provides heating of the resonator, which leads to a change in the refractive index of the MRR core. The second is the relatively fast free-carrier dispersion (FCD) effect which causes change in the refractive index due to the generation of the free carriers induced by the two-photon absorption. The competition of these effects causes a mutually opposite change in the refractive index which results in the negative or positive resonant frequency shift. The bistability phenomenon appears as soon as the hysteresis loop occurs in the frequency response characteristics [1]. An application of the thermo-optic effect for silicon-on-insulator (SOI) memories is limited by the high thermal dissipation time [2]. This effect usually dominates over the FCD. It hinders the realization of high speed memories on a passive MRR. Recently, carrier-induced optical bistability in the silicon micro-ring resonators under continuous wave pumping has been experimentally demonstrated [3]. This phenomenon paves the way to sufficient improvement of the switching time of the nonlinear MRR required for high performance optical memories [4].

The present work focuses on the study of the FCD-induced bistability and demonstrates robust operation of the passive SOI MRR as an optical memory.

2. Experiments and results

The structure under investigation consists of straight waveguides and a ring with a diameter of 256 μm fabricated using SOI SG25PIC technology [5]. The thickness of the BOX and cladding layers are 2 μm and 14 μm respectively. The waveguide cross section is 500×220 nm^2. The distance between the ring and waveguides is 250 nm. The experimental setup is described in detail in [6].

The MRR frequency response is measured at input optical power of -9.97 dBm (see Fig. 1a). The resonator demonstrates a free spectral range of 88.8 GHz and a loaded Q-factor of 45000. An increase of the input power up to 14.87 dBm leads to the FCD-induced positive frequency shift as well as a decrease in the transmission coefficient due to the TPA-induced nonlinear damping (see Fig.1b). In order to provide a more detailed view of the bistable loop, Fig. 1c shows the output power taken at various input power levels at frequency 191.818 THz (shown by black dotted line in fig. 1b). These characteristics are measured for increasing (see red line in Fig. 1c) and decreasing (see blue line in Fig. 1c) input powers. The measured characteristic has a form of a counterclockwise hysteresis loop with a width of 0.48 a.u. As it is seen when the input power exceeds 0.7 a.u., the resonator switches to the high stable state. The MRR holds this state while the input power is higher than 0.22 a.u. After that the MRR stays in low state so long as the input is less than 0.7 a.u. Such nonlinear behavior paves the way to implementing a memory cell based on the SOI MRR. Finally, the temporal responses of the MRR output power are measured. For this purpose, an optical signal shown in Fig. 1d with a pulse repetition frequency of 100 kHz is fed to EOM port. As it is seen in Fig. 1e the MRR output is switched between two stable states in accordance with hysteresis loop discussed above.

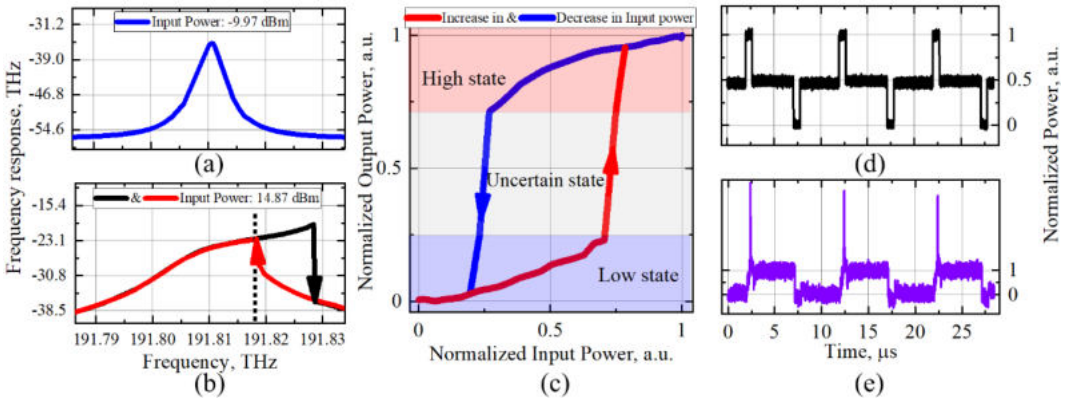

Figure 1. Linear (a) and nonlinear (b) frequency responses of the MRR; dependence of the output power versus the input power (c); input optical signal (d); temporal responses of the MRRs (e).

3. Conclusion

In conclusion, we show FCD-induced bistable characteristics of the SOI MRR. The observed power hysteresis paves the way to memory implementation.

Acknowledgments

The work of St. Petersburg Electrotechnical University was supported by the Ministry of Science and Higher Education of the Russian Federation (grant number No. FSEE-2020-0005).

References

[1] V. R. Almeida and M. Lipson, "Optical bistability on a silicon chip," Opt. Lett. 29, 2387 (2004).
[2] Q. Xu and M. Lipson, "Carrier-induced optical bistability in silicon ring resonators," Opt. Lett. 31, 341 (2006).
[3] A. A. Nikitin et al. "Carrier-induced optical bistability in the silicon micro-ring resonators under continuous wave pumping," Optics Communications 480, 126456 (2021).
[4] T. Alexoudi, G. T. Kanellos, and N. Pleros, "Optical RAM and integrated optical memories: a survey," Light Sci Appl 9, 91 (2020).
[5] IHP – innovations for high performance microelectronics, 2022, https://www.ihp-microelectronics.com/services/research-and-prototyping-service/mpw-prototyping-service/sigec-bicmos-technologies. (Accessed 04 April 2022).
[6] A. A. Nikitin et al. "Optical bistable SOI micro-ring resonators for memory applications," Optics Communications 511, 127929 (2022).

The investigation of the optical vortices diffraction on silicon ring gratings with variable height using high-performance computer systems

D A Savelyev[1,2]

[1]Samara National Research University, Moskovskoye Shosse 34, Samara, Russia
[2]Image Processing Systems Institute - Branch of the Federal Scientific Research Centre "Crystallography and Photonics" of Russian Academy of Sciences, Molodogvardeyskaya str. 151, Samara, Russia

dmitrey.savelyev@yandex.ru

Abstract. The diffraction of Laguerre-super-Gaussian modes of the first order on subwavelength silicon ring gratings was investigated in this paper. It is shown that varying the height of the even and odd rings of subwavelength gratings significantly affects the diffraction pattern in the near zone.

1. Introduction

Silicon and its compounds are used in various fields of human activity [1], in particular, its use is well known for solving problems of photonics [2], in medicine [3], and for the manufacture of semiconductor devices [4]. It is also known to use silicon diffractive axicons to reduce the size of the laser beam focal spot [5].

Among structured laser beams [6], considerable attention is paid to optical vortices [7], which is associated with their use for a number of applications [8], including increasing the throughput of optical communication systems [9], as well as optical manipulation [10]. It is also possible to achieve a redistribution of energy between the components of the electric field by introducing a vortex phase singularity into the laser beam [11].

The diffraction of the Laguerre-superGaussian (1,0) modes on silicon subwavelength optical elements (ring gratings and a diffractive axicon) studied in this paper. For numerical calculations (3D) of the propagation of laser radiation, the method of finite differences in the time domain (FDTD) was used using high-performance computer systems [12].

2. Diffraction of optical vortices on silicon ring gratings

A silicon diffractive axicon with a numerical aperture (NA) of 0.95 (lattice period 1.05λ) is considered, as well as silicon subwavelength annular gratings with the same period. The height of individual gratings rings h_i, where i changed from 0 (center) to 5 (extreme ring).

Modeling parameters: radiation wavelength $\lambda = 1.55$ μm, size of the computational domain x, y, z was in the range [–5.7λ; 5.7λ]. Spatial sampling step: λ/30, time sampling step: λ/(60c), where c is the speed of light. The thickness of the absorbing layer PML from all sides surrounding the computational domain is equal to λ. The Laguerre-superGauss (1,0) [13] mode of degree 6 with circular polarization

was considered as the input beam. The silicon refractive index n is 3.47. In this case, the height of the binary element relief, corresponding to the phase π radians, is equal to 0.2λ [5].

The results of propagation of the considered laser radiation through a diffractive axicon and ring gratings with relief height hi equal to 0.2λ, 0.5λ and λ are shown on Figure 1. The size of the focal spot on the optical axis was estimated as the full width at half maximum (FWHM), and the size of the longitudinal light segment was estimated by half the intensity (depth of focus – DOF). The FWHM values were taken at the maximum intensity on the optical axis.

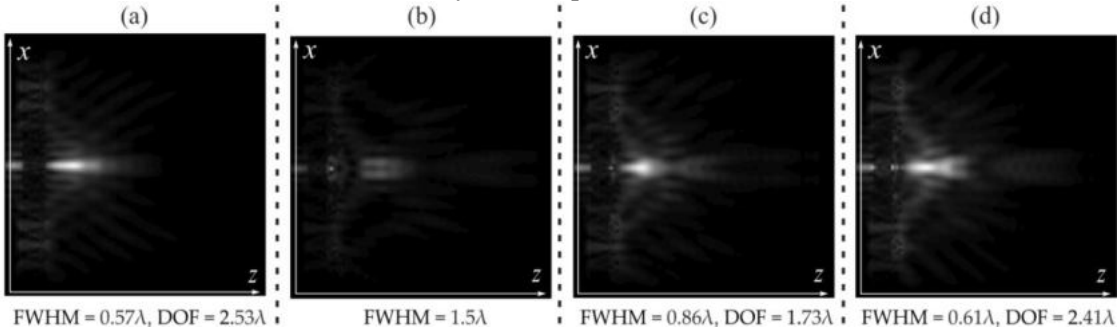

Figure 1. The longitudinal cross section (xz) of optical vortices propagation: (a) the diffractive axicon, $h_i = 0.2\lambda$, and the ring grating with (b) $h_0 = h_2 = h_4 = 0.5\lambda$, $h_1 = h_5 = \lambda$, $h_3 = 0.2\lambda$,(c) $h_0 = h_2 = h_4 = 0.2\lambda$, $h_1 = h_3 = h_5 = 0.5\lambda$, (d) $h_0 = h_2 = h_4 = 0.5\lambda$, $h_1 = h_3 = h_5 = 0.2\lambda$.

It is clearly seen that a change in the height of individual zones of ring gratings significantly affects the diffraction pattern. It should be noted that the main maximum was formed outside the optical element, except for the case of Figure 1b, but for this case a focal spot FWHM = 0.32λ was obtained at a distance of 0.8λ from the element. In the immediate vicinity of the element in the case of Fig. 1d, the size of the focal spot was FWHM = 0.4λ.

3. Conclusion

In this paper, the FDTD method was used to study the propagation of optical vortices on a silicon diffractive axicon and subwavelength annular gratings with a change in the height of the even and odd rings of the gratings. It was shown that the change in the heights of the even and odd rings of subwavelength gratings significantly affects the diffraction pattern in the near zone. The smallest size of the focal spot outside the element was FWHM = 0.32λ.

Acknowledgments

This research was funded by the Russian Science Foundation (project No. 20-72-00051) in the parts «Diffraction of optical vortices on silicon ring gratings», «Conclusion» and scholarship of the President of the Russian Federation SP-1173.2022.5 in the parts «Introduction».

References

[1] Cheng L, Mao S, Li Z, Han Y and Fu H Y 2020 *Micromachines* **11** 666
[2] Butt M A, Khonina S N and Kazanskiy N L 2019 *Computer Optics* **43** 1079
[3] Xu Y et al. 2019 *Sensors* **19** 2908
[4] Hwang S-W et al. 2012 *Science* **337** 1640
[5] Savelyev D and Kazanskiy N 2021 *Sensors* **21** 1973
[6] Rubinsztein-Dunlop H et al. 2016 *Journal of Optics* **19** 013001
[7] Tkachenko G, Chen M, Dholakia K and Mazilu M 2017 *Optica* **4** 330
[8] Zhu L and Wang J 2019 *Frontiers of Optoelectronics* **12** 52
[9] Ma X et al. 2015 *Scientific Reports* **5** 1
[10] Zhan Q 2009 *Advances in Optics and Photonics* **1** 1
[11] Khonina S N and Savelyev D A 2013 *Journal of Experimental and Theoretical Physics* **117** 623
[12] Khonina S N and Savelyev D A 2015 *Radiophysics and Quantum Electronics* **57** 650
[13] Savelyev D A 2021 *Computer Optics* **45** 214

Describing topological transitions in subwavelength metamaterials via effective material parameters

L. Shaposhnikov, D. Sakhno, D. Bobylev, and M. Gorlach

School of Physics and Engineering, ITMO University, Kronverksky Pr. 49, bldg. A, St. Petersburg, 197101, Russia

denis.sakhno@metalab.ifmo.ru

Abstract. We present the approach to examine the topological transitions in subwavelength photonic structures in terms of their effective material parameters and illustrate the proposed technique on the example of a breathing honeycomb lattice. To verify our conclusions, we do an independent check by calculating the complex band structure and examining the behavior of the evanescent modes within the bulk bandgap.

1. Introduction

Topological insulators are artificially created structures that support localized edge modes (topological states) [1] that are resilient to the various types of disorder and are protected by the global symmetries of the system.

The complexity of existing approaches to the study of topological structures significantly slows down the search for new geometries with desired topologically nontrivial properties. Nevertheless, theoretical works [2, 3] indirectly suggest the possibility of describing topological structures using the effective medium approach, and this idea provides the starting point for the present study. This approach involves only the retrieval of the scattering coefficients, which allows us to simplify the analysis of topological transitions.

The main idea of our method is to observe a synchronous sign change for the effective material parameters extracted via the Nicholson-Ross-Weir (NRW) method [4] during a topological transition. Since the topological transition is accompanied by closing and reopening of a bandgap prohibiting wave propagation, the effective refractive index must remain negative. In our work, we apply this consideration to the classical breathing honeycomb lattice [5] and compare the retrieved refractive indices with those determined from the dispersion of the evanescent modes inside the band gap. An important condition for this method is the subwavelength periodicity of the structure under consideration.

2. Results

We consider a well-celebrated breathing honeycomb structure with six dielectric cylinders ($\varepsilon_c = 81$) in the unit cell (Fig. 1(a)). The topological properties of this metamaterial are determined by the geometry parameter a/R [5]. A topological transition with the degeneracy of the dispersion curves at the Γ point is observed at $a/R = 3$, since this configuration separates the topological ($a/R < 3$) and trivial ($a/R > 3$) cases from each other. The difference between those two cases originates from the frequency order of the dipole and quadrupole modes (highlighted with red and blue colors in Fig. 1, respectively) near Γ-point.

The dispersion of the evanescent modes within the bulk bandgap (Fig. 1) can be calculated using the Weak Form PDE interface of COMSOL Multiphysics software

package [6]. The resulting extended mode pattern, which includes decaying modes (with a purely imaginary or complex wavenumbers), makes it possible to extract the effective refractive index for further verification of the proposed method: $n_{eff}^2 = \varepsilon\mu = -(ck''/\omega)^2$, where k'' is an imaginary part of the wave number of the dominant mode.

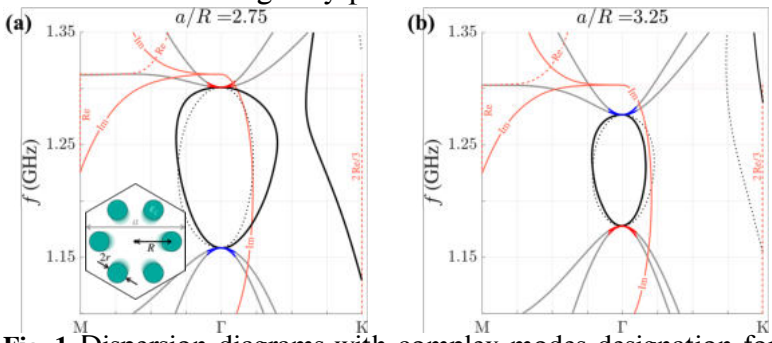

Fig. 1 Dispersion diagrams with complex modes designation for a/R parameter value of (a) 2.75 (topological case) and (b) 3.25 (trivial case). Purely imaginary modes are shown by solid black lines. Complex modes – by orange solid (imaginary part) and dashed (real part) lines. Unit cell geometry is shown in subfigure (a) (a = 5 cm, r = 0.5 cm).

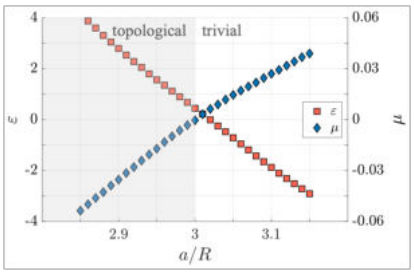

Fig. 2 The dependencies of effective parameters ε and μ obtained via NRW method on the geometry parameter a/R at frequency 1.225 GHz.

The extraction of material parameters by the NRW method at normal incidence makes it possible to independently obtain the values of ε and μ in the chosen direction of propagation (this direction determines the choice of the metamaterial boundary) at the chosen frequency within the bandgap. In Fig. 2 we depict the retrieved (in ΓM direction) dependence of ε and μ on the geometric deformation parameter a/R. As expected, the results demonstrate the simultaneous change in the sign of the parameters at the topological transition point ($a/R = 3$), while the sign of the effective refractive index inside the band gap naturally remains negative.

3. Conclusion

The proposed method to test topological transitions is feasible from the experimental point of view and can simplify the experimental verification of topological transitions. Moreover, it fills a gap between the two views on topological metamaterials: one that exploits the periodic nature of the structure and another relying on the effective medium description.

Acknowledgments

This work was supported by the Russian Science Foundation (Grant No. 20-72-10065).The authors acknowledge partial support by RPMA grant of School of Physics and Engineering of ITMO University.

References

[1] Ozawa, Tomoki, et al. "Topological photonics." Reviews of Modern Physics 91.1 (2019): 015006.

[2] Silveirinha, Mario G. "Chern invariants for continuous media." Physical Review B 92.12 (2015): 125153.

[3] Silveirinha, Mario G. "Z2 topological index for continuous photonic materials." *Physical Review B* 93.7 (2016): 075110.

[4] Nicolson, A. M., and G. F. Ross. "Measurement of the intrinsic properties of materials by time-domain techniques." *IEEE Transactions on instrumentation and measurement* 19.4 (1970): 377-382.

[5] Wu, Long-Hua, and Xiao Hu. "Scheme for achieving a topological photonic crystal by using dielectric material." *Physical Review Letters* 114.22 (2015): 223901.

[6] Davanзo, Marcelo, Yaroslav Urzhumov, and Gennady Shvets. "The complex Bloch bands of a 2D plasmonic crystal displaying isotropic negative refraction." *Optics Express* 15.15 (2007): 9681-9691.

Multimode interference splitter based on silicon metamaterial for sub-THz range

Sergey Svyatodukh[1,2], Sergey Seliverstov [1], Aleksey Prokhodtsov[1], and Gregory Goltsman[1,2]

[1]Moscow State Pedagogical University, Moscow, Russian Federation
[2]National Research University Higher School of Economics, Moscow Institute of Electronics and Mathematics, Moscow, Russian Federation

sergey.svetodux@gmail.com

Abstract. THz photonics range is a rapidly developing field of science with many practical applications in medicine, telecommunications, imaging, and others. From practical point of view many applications requires compact and multifunctional solutions, with a property of scalability. Such as in visible and infrared ranges photonic integrated circuits could solve given problem. In this work we are working on enlarging element base of purely silicon THz photonic integrated circuits. We consider 1x2 splitter based on multimode interferometer on silicon integrated platform. Design simplicity and an opportunity to get any splitting ratio with minor changes in design implies practicality of our study.

1. Introduction

The terahertz range, which lies in the frequency range from 0.1 to 10 THz, is promising for many different applications, such as spectroscopy, telecommunications, medicine, security systems, and others [1–2]. This is due to the fact that the spectrum of the terahertz range is energetically equivalent to many physical, chemical and biological processes [3-4]. However, even though many results have already been obtained, the implementation of such systems is hampered by the lack of available and powerful sources, sensitive and fast detectors, as well as the lack of a platform with low losses and high functionality (such as a silicon platform in infrared photonics [5-6]).

Over the past five years, much attention has been paid to the development of THz photonic integrated circuits [7-8]. The most promising from them is a purely silicon integrated platform based on metamaterial – effective medium [7]. Main advantages of this platform are – low losses, broadband, design simplicity and high fabrication tolerance, compared to its counterpart – photonic crystals [8]. In this work we consider a modeling of one of the most important passive element of a photonic integrated circuit – a splitter based on multimode interferometer. Design simplicity and an opportunity to get any splitting ratio with minor changes in design implies practicality of our study.

Results and Discussion

In this work we consider a modeling of multimode interference (MMI) splitter on effective medium silicon platform. Effective medium in this work consists of circular holes in silicon substrate of thickness 400 μm arranged in square lattice. Figure 1 a), demonstrates considered platform. For our study we choose an effective refractive index of the medium equal to 2. This choice was based of the requirement of compactness and big fabrication tolerance. All calculation in this work were done in Lumerical simulation software. In next two sections, we give a design consideration of MMI 1x2 splitter and finally present simulation results of a designed MMI splitter and compare an effective medium approximation with a full structure consisting of circular holes in silicon substrate.

1.1. MMI splitter design

Firstly, we simulate simple waveguide for an effective medium approximation for 150 GHz frequency – it consists of a central waveguide structure, with a refractive index of silicon, equal to 3.41, surrounded with an effective medium with a refractive index 2. To obtain a single mode regime of a waveguide, a

geometric dispersion was calculated – a dependance of a propagation constant (equivalent modal effective index) on a width of central waveguide. Calculation results are presented on Figure 1 b), from that we choice a waveguide width equal to 300 µm. Next up, MMI splitter was considered, it consists of an input waveguide, which is connected to a wide multimodal area, which is connected to two output waveguides. We designed MMI splitter as followers, firstly we chose a width of a multimodal region equal to 3000 µm. After that we calculated a power density field distribution for an quasi-infinite structure (which is given on Figure 1 c) and finally placed two output waveguides at the point of multimodal part, where the power splits on two parts (this part is highlighted green on Figure 1 c)).If ones want to obtain different splitting ratio, for example 1x4, it only requires to move four output waveguides at a position of multimodal area, where power splits in four equal parts (highlighted as red on Figure 1 c)). Considered principle is called – self-imaging principle [9] Design parameters obtained for an MMI 1x2 splitter are – MMI width – 3000 µm, MMI length – 8000 µm, distance between output waveguides – 1800 µm.

1.2. Results

Lastly, we simulated transmission characteristics of designed MMI splitter. Two calculated simulations are presented on Figure 2 a,b) – simulation for an effective medium approximation and full structure consisting of circular holes in silicon substrate, respectively. Transmission spectrum for both simulations in range from 100 GHz to 200 GHz are presented on Figure 2 c). From it one can see that an effective medium approximation coincides with a full structure. Obtained power on the output port for 150 GHz is equal to 3.18 dB. 3dB bandwidth of modelled structure is equal to 100 GHz (from 100 to 200 GHz). To obtain higher transmission for MMI coupler (nearly 3dB), tapered structures for input and output waveguide, should be considered, to minimize reflections – main source of losses for MMI splitter.

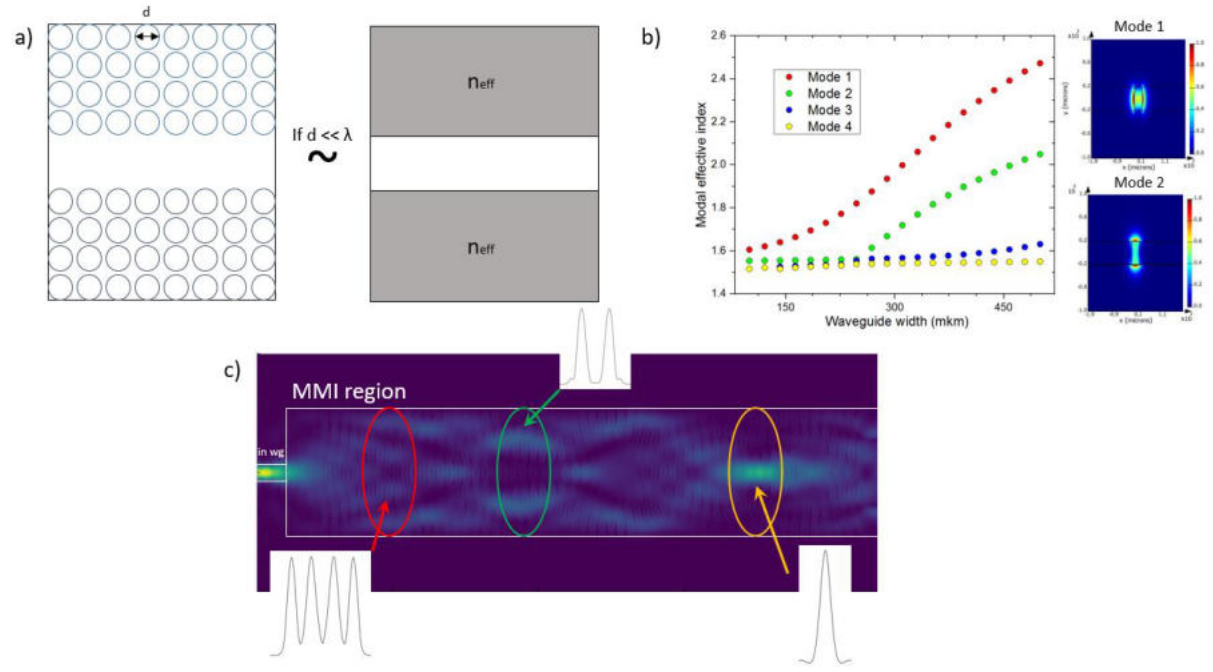

Fig. 1. a) Metamaterial silicon photonic integrated platform and its equivalence with effective medium approximation. b) Geometric dispersion of a waveguide, considered in this work. c) MMI splitting ratio design.

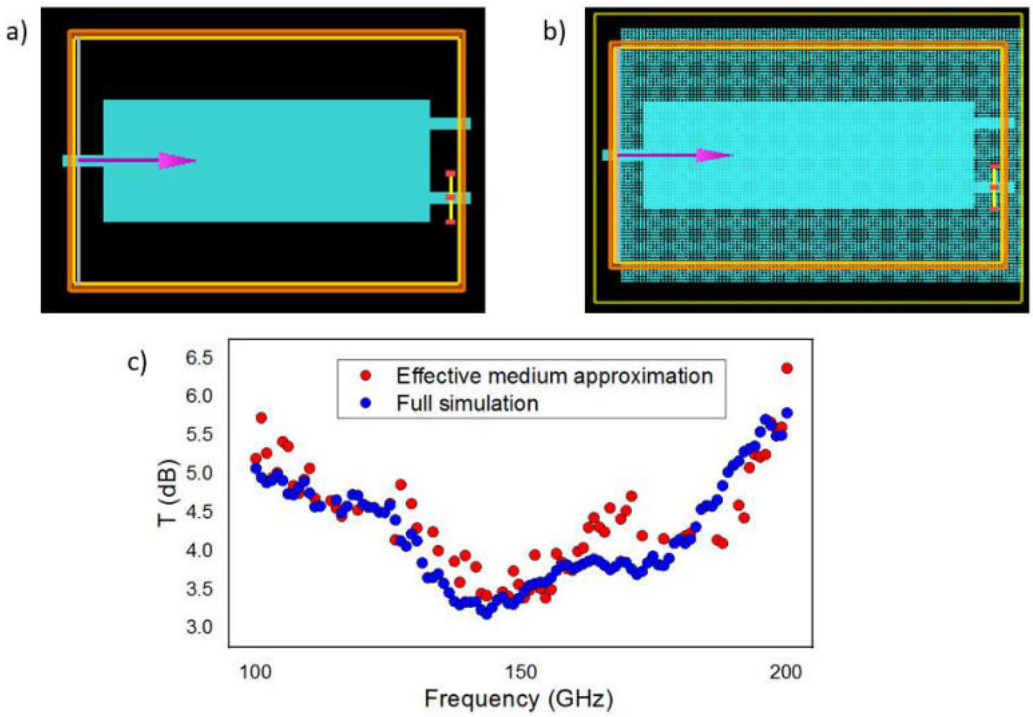

Fig. 2. a) Simulation for an effective medium approximation b) Simulation for the full structure. c) Transmission spectrum for both simulations in range from 100 GHz to 200 GHz

Acknowledgments

The study was supported by a grant from the Russian Science Foundation No. 21-72-10119, https://rscf.ru/project/21-72-10119/.

References

[1] Zhou J. et al. Temperature dependent optical and dielectric properties of liquid water studied by terahertz time-domain spectroscopy //AIP Advances. – 2019. – Т. 9. – №. 3. – С. 035346.

[2] Raddo T. R. et al. Transition technologies towards 6G networks //EURASIP Journal on Wireless Communications and Networking. – 2021. – Т. 2021. – №. 1. – С. 1-22.

[3] Chen T. et al. Analysis of Intermolecular Weak Interactions and Vibrational Characteristics for Vanillin and Ortho-Vanillin by Terahertz Spectroscopy and Density Functional Theory //IEEE Transactions on Terahertz Science and Technology. – 2020.

[4] Hou L. et al. Probing trace lactose from aqueous solutions by terahertz time-domain spectroscopy //Spectrochimica Acta Part A: Molecular and Biomolecular Spectroscopy. – 2021. – Т. 246. – С. 119044.

[5] Hao Y. et al. Recent progress of integrated circuits and optoelectronic chips //Science China Information Sciences. – 2021. – Т. 64. – №. 10. – С. 1-33.

[6] Kazanskiy N. L., Butt M. A., Khonina S. N. Silicon photonic devices realized on refractive index engineered subwavelength grating waveguides-a review //Optics & Laser Technology. –

[7] Gao W. et al. Effective-medium-cladded dielectric waveguides for terahertz waves //Optics Express. – 2019. – Т. 27. – №. 26. – С. 38721-38734.

[8] Yu X. et al. Simultaneous low-loss and low-dispersion in a photonic-crystal waveguide for terahertz communications //Applied Physics Express. – 2019. – Т. 12. – №. 1. – С. 012005.

[9] Soldano L. B., Pennings E. C. M. Optical multi-mode interference devices based on self-imaging: principles and applications //Journal of lightwave technology. – 1995. – Т. 13. – №. 4. – С. 615-627.]

Generation of different orbital angular momentum modes via array of computer-generated holograms.

K O Sedykh[1, 2], I O Venedictov[1, 3], E S Lebedeva[1], G N Goltsman[1, 2, 3, 4] and D V Sych[2, 5, 6]

[1]Department of Physics, Moscow State Pedagogical University, Moscow 119992, Russia
[2]NTI Center for Quantum Communications, National University of Science and Technology MISiS, Moscow 119049, Russia
[3]National Research University Higher School of Economics, Moscow, 101000, Russia
[4]Russian Quantum Center, Skolkovo 143025, Moscow, Russia
[5]Sirius University of Science and Technology, 1 Olympic Ave, 354340, Sochi, Russia
[6]P. N. Lebedev Physical Institute, Moscow 119991, Russia

kseniaolegovna98@gmail.com

Abstract. Orbital angular momentum (OAM) is discrete property of light which can be explained as characteristic of the twisting of spiral phase front. The amplitude of the vortex wave field is zero along the centre of the axis, so that there is a "dark" core at the site of the phase singularity. Here we present a scheme for generation such beams with different topological charges via array of computer-generated holograms (CGH) method deposed on a double polished sapphire substrate by means of electron lithography.

1. Introduction

In 1992, L. Allen and colleagues combined the concept of orbital angular momentum (OAM) with the idea of an optical vortex [1]. After that, the study of optical vortices took on a new form, since the creation of such rays in the laboratory turned out to be quite simple [2]. OAM beams have found their application in various fields such as particle manipulation, optical tweezers, optical imaging. They are used in quantum communications: the creation of superposition states, quantum entanglement. It is also known that such multidimensional quantum systems increase the level of security in quantum cryptography in the presence of noise and are required by some quantum protocols and quantum computing schemes.

The wavefront of electromagnetic waves during propagation will twist due to the phase singularity. Thus, vortex waves are formed, in which the planes of the constant phase of the electric and magnetic vector fields form a helicoid moving in the direction of propagation. That is, the center of the vortex is the position of zero intensity, phase singularity, no energy or momentum transferring. OAM rays are described by the phase component $\exp(il\phi)$, where l is the topological charge, ϕ is the azimuthal angle. The topological charge or OAM mode, as it is also called, is discrete and determines the chirality and the number of vortices per wavelength, a multiple of 2π.

2. Generation of vortex beams

There are several ways to create OAM beams. The common technique is to share a Gaussian beam into converter [3]. Such converters can be: spiral phase plates, phase holograms, SLM DMD, metamaterials or q-plates. In our experiment, we consider to use holograms method. Computer-generated hologram (CGH) is a superposition of two waves, from which a lattice pattern is obtained. For the first wave, the phase changes from the coordinate modulo 2π. For the second, the phase change depends on the topological charge. The given waves interfere on the pattern, obtaining in an l-fold bifurcated grating image (Figure 1 (b)). For the experiment we use CGH array sample with diffraction gratings of different modes. Fabrication of diffraction grating includes NbN film deposition and film patterning with electron-beam lithography (Figure 1 (a)).

If a laser beam falls on l-fold bifurcated diffraction grating, then a vortex beam with a topological charge nl can be obtained in the n-th order of diffraction. The scheme of the experimental setup is presented in Figure 1 (c). So, when laser source was passed through CGHs array sequentially with each topological charge, different diffraction orders was obtain (Figure 2).

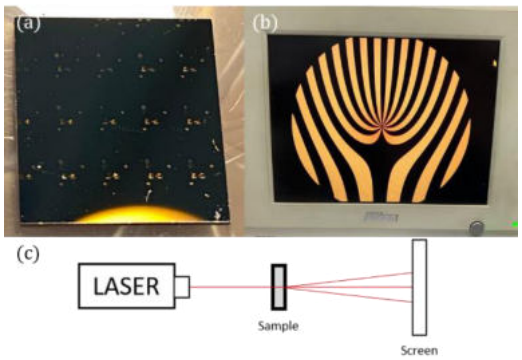

Figure 1. (a) CGH array sample with diffraction gratings of different modes (double polished sapphire substrate, 60 nm NbN film), (b) microscope image of CGH with $l = 1$, (c) experimental setup.

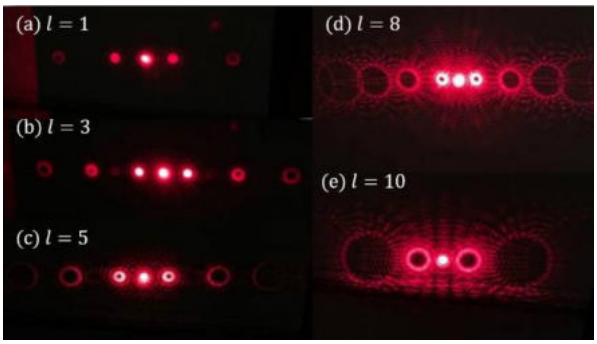

Figure 2. Measured pattern of vortex beams with different modes via CGH's.

3. Conclusion

In this work, we consider generation of vortex beams by computer-generated holograms method. CGHs array was used for obtaining OAM beams with different topological charges. Characteristic phase singularities inside OAM rings was clearly visible on the screen. The diameter of the output vortex beam is directly proportional to the root of the OAM's mode: the larger the topological charge, the larger the diameter of the doughnut-shaped beam. Next step for this work is detection vortex beams with different topological charges.

Acknowledgments

The reported study was funded by RFBR, Sirius University of Science and Technology, JSC Russian Railways and Educational Fund "Talent and success", project number 20-32-51004. We also thank Philipp Zolotov and Natalia Kaurova for NBN film fabrication and NbN pattering respectively; Dr. Ledesma and Mr. Pabon – for sharing program for CGH generating and useful literature.

References

[1] Allen L, Beijersbergen M W, Spreeuw R J C, and Woerdman J P 1992 *Phys. Rev. A* **45** 8185

[2] Andrews D L 2008 Structured Light and Its Applications: An Introduction to Phase-Structured Beams and Nanoscale Optical Forces (1st ed.). *Academic Press*.

[3] Chen R et al. 2020 *IEEE Commun. Surv. Tutor.* **22(2)** 840–68

Control of color centers charge states in crystals by using X-Ray radiation

Eduard S. Sektarov[1, 2], Vadim V. Sedov[3], Kirill N. Boldyrev[1]
[1]Institute of spectroscopy, Russian Academy of Sciences, Fizicheskaya 5, Troitsk, Moscow, Russia
[2]Department of Physics, National Research University Higher School of Economics, Myasnitskaya 20, Moscow, Russia
[3]Prokhorov General Physics Institute, Russian Academy of Sciences, Vavilov 38, Moscow, Russia

sektarov_es@mail.ru

Abstract. Crystals with color centers are widely used in various fields of industry and science. X-Ray radiation can be used as the instrument of study and manipulating of color centers in diamonds. The research illustrates experimental results of X-Ray interaction with color centers and changing of charge states. Diamonds with NV (nitrogen-vacancy), SiV (silicon-vacancy) and GeV (germanium-vacancy) centers were investigated in experiments. This work includes experimental infrared absorption spectra and calculations of defect concentrations in diamonds with NV and SiV. The paper concludes that X-Ray can affect color centers and their charges.

1. Introduction

Color centers in crystals are unique optical elements. Crystal impurities are widely used in various fields of industry and science. Impurities in diamonds can be applied in optical quantum memory, quantum sensorics, lasers and quantum computing. Color centers are defects in the crystal lattice that absorbs and/or radiates in the wavelength range outside the intrinsic absorption of the crystal. Due to color centers characteristics, they are researched actively, but there much of unknown physics and effects connected with interactions of centers with crystal structure and electromagnetic waves. One of that area is an interaction of color centers with X-Ray radiation. The purpose of this work is to illustrate that X-Ray can influence on color centers.

2. Methodology

2.1. Crystal samples

The subjects of the study were diamonds with NV, SiV and GeV impurities. These color centers were chosen, because they are well-studied, and techniques of their growth allows to create new diamond samples in short times. CVD (chemical vapor deposition) method are used for the growth of samples.

2.2. Experimental installation

The study of color centers in the X-Rays was carried out on a Bruker IFS 125HR high-resolution Fourier spectrometer with a cryogenic attachment. The instrument allows to provide experiments in visible and infrared diapasons from 5 to 50000 cm^{-1} (2×10^{-6} to 200 nm) and high optical resolution up to 0.001 cm^{-1}. Special module was developed on a base of X-ray tube BSV-30 with a copper anode,

with a nominal power of 500 W and a characteristic radiation Cu Kα 8027 eV. The results of the research were absorption spectra, obtained at a temperature of 5 K.

2.3. Absorption method

The absorption method allows to obtain a well-resolved structure of lines in the spectra, which makes it possible to quantify the concentration of color centers. Integral intensities will be obtained from the absorption spectra of impurities spectral lines for calculations of defects concentrations changing.

3. Results

3.1. Absorption spectra of color centers

The spectra obtained after exposure of X-rays, the absorption line intensities change at wavelengths of 946 nm (SiV^0), 737 nm (SiV^-), 575 nm (NV^0), 637 nm (NV^-) and 602 nm (GeV^-), corresponding to color centers. The appearance of new lines was observed, which can be associated with GeV^0 and/or GeV^+ centers in the sample with GeV. A change in the SiV and NV centers was noted, the increase in the concentration of SiV^0 is proportional to the decrease in SiV^-. Furthermore, more complex interaction is observed between NV^0 and NV^-. Other charge states such as NV^+, NV^{2+} or unknown states may be involved in the process, since the appearance of new lines after irradiation was found.

3.2. Concentrations of defects

Changes in defect concentrations (x) were calculated by using formula (1) from [1] for samples with NV and SiV. Calibration coefficients k_{zpl} are presented in [1] for SiV and [2] for NV, the integral intensity I_{zpl} of absorption lines was calculated using the OPUS™ software.

$$I_{zpl} = k_{zpl} \bullet x \quad (1)$$

The result of research demonstrates that X-rays radiation can affect absorption spectra of diamonds impurities. Moreover, study reveals that X-Ray can be used to control the charge states of color centers in diamonds.

Acknowledgments

The work was supported financially by the Russian Science Foundation (synthesis and processing of samples - grant no. 21-72-10153, spectroscopic studies - grant no. 19-72-10132).

References

[1] D'Haenens-Johansson U. F. S. et al., Phys. Rev. B. 2010, 82, 155205.
[2] Davies G., Physic: Condensa. Matter 1999, 273, 15.

Simulation of terahertz photonic integrated antenna

Sergey Seliverstov[1], Sergey Svyatodukh[1,2], Aleksey Prokhodtsov[1], and Gregory Goltsman[1,2]

[1]Moscow State Pedagogical University, Moscow, Russian Federation
[2]National Research University Higher School of Economics, Moscow Institute of Electronics and Mathematics, Moscow, Russian Federation

seliverstovsv@mail.ru

Abstract. The rapid development of wireless devices, that take place over the last decade, is associated with an increase in the need to achieve a higher data transfer rate. To achieve this goal, it is necessary to use the terahertz range. The vast majority of terahertz devices (no matter bulk or integrated) require fast, non-mechanical beam shape control, which is generally defined as the ability to manipulate the shape of the radiation pattern in the desired way. But it's hard to implement without the use of photonic integrated antennas. In this paper, the possibility of the creation of photonic integrated antenna which is a basic element of such a system is investigated and confirmed. The antenna is based on a platform of metamaterial silicon with perforations, the dimensions of which are in the deep subwavelength region, which makes it possible to provide a wide bandwidth with low dispersion.

1. Introduction

In recent years, there has been a significant increase in the need to achieve a higher data rate. It can be done by the transition to a higher frequency range. In particular, the transition to terahertz (THz) radiation is currently seen as the most promising. The first such laboratory prototypes of transceiver systems with a data rate of up to 1 Tbit per second have already been demonstrated [1]. At the same time, the transition to THz radiation as the basis for promising new generation communication systems is associated with a number of difficulties. First of all, this is the high absorption of THz radiation in the atmosphere, which limits the use of such systems over long distances, as well as large signal losses during radiation propagation in metal waveguides (of the order of several dB per cm [3]). The solution to this problem can be the use of dielectric waveguides, which are characterized by much lower values of absorption of THz radiation [2].

A number of leading scientific teams around the world are working on their development, and some success has been achieved [4, 5]. At the same time, it should be noted that the current approaches, based primarily on the use of microstrips as well as photonic crystals, limit the bandwidth of waveguides as well as show relatively high dispersion. This problem greatly complicates the use of such waveguide technology in real practical applications. In addition, the development of THz communication systems is associated with the need for a rapid (non-mechanical) change in the radiation pattern of THz emitters. But it's hard to implement without using of phased antenna arrays in which this change is carried out due to phase adjustment. The basic element of such a system is a photonic integrated antenna. In this article the possibility of creation of the photonic integrated antenna based on a platform of metamaterial silicon with perforations is studied. The dimensions of the perforations are in the deep subwavelength region which makes it possible to provide a wide bandwidth with low dispersion.

2. Results and Discussion

The boundaries of the waveguide and horn antenna were formed by a periodical structure of cylindrical perforations in the high-resistance silicon substrate. A square lattice was used as the periodic structure. The permittivity of the obtained effective medium for TE and TM polarizations in the case of filling the space inside the perforations with air with a permittivity equal to 1 was calculated based on a theory presented in [6].

In the simulation, the TE polarization of the radiation was studied. The substrate thickness was 400 μm. The radius of the sphere filled with air was 4000 μm. The frequency was 150 GHz. A single TE1 mode was implemented for the given configuration of the antenna with these set of parameters. The power of radiation supplied to the incoming ports was equal to 1 W. The boundary conditions were defined at the edge of the substrate where the input ports are located and specified on the sphere bounding the model in such a way that it completely scatters the radiation incident on it. The given model was divided into finite elements (tetrahedra). After that, the Maxwell's equations were numerically solved for the obtained mesh of elements to obtain distribution of the electric field vector. Iterations of discretization into a smaller elements and recalculations were carried out until the required accuracy was achieve.

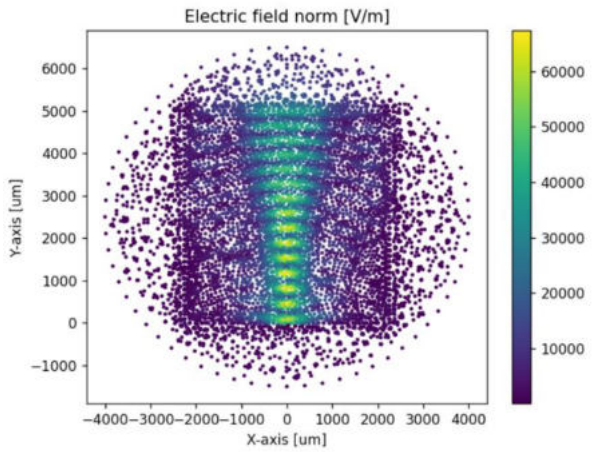

Fig. 1. Electric field distribution in a silicon horn at a radiation frequency of 150 GHz.

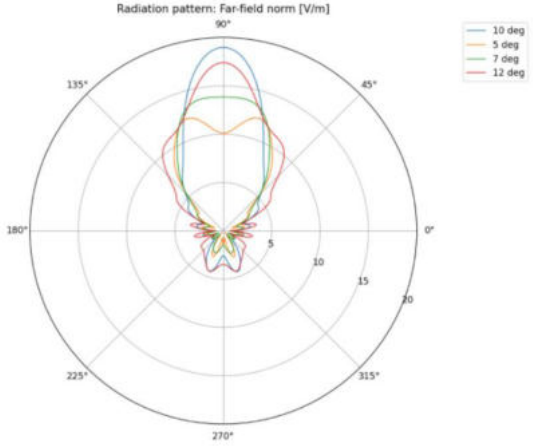

Fig. 2. The radiation pattern of a horn antenna at various values of the horn's half-angle.

During the simulation of the horn antenna radiation pattern, the length of the input waveguide was fixed at 1000 μm and the half-opening angle of the horn was varied. One can see from the Fig. 2 that the half-opening angle of about 10 degrees turned out to be optimal for providing the required shape of the radiation pattern. The field distribution in the horn at a given angle is shown in the Fig. 1.

The presented results of simulation confirm the possibility of practical implementation of the proposed concept of integrated horn antennas on a perforated high-resistance silicon substrate platform. These antennas will be used to create devices for controlling the parameters of the output THz radiation beam, which will be the main components for next-generation communication systems.

Acknowledgments

The study was supported by a grant from the Russian Science Foundation No. 21-72-10119, https://rscf.ru/project/21-72-10119/.

References

[1] Corre, Y., , et al. (2019, March). Sub-THz spectrum as enabler for 6G wireless communications up to 1 Tbit/s. In 6G Wireless Summit.

[2] Gao, W., , et al. (2019). Effective-medium-cladded dielectric waveguides for terahertz waves. Opt. exp., 27(26), 38721-38734.

[3] Frankel, M. Y., et al. Terahertz attenuation and dispersion characteristics of coplanar transmission lines. IEEE Transactions on microwave theory and techniques 39.6 (1991): 910-916.

[4] Malekabadi, Ali, et al. High-resistivity silicon dielectric ribbon waveguide for single-mode low-loss propagation at F/G-bands. IEEE Trans. on Terahertz Sc. and Tech. 4.4 (2014): 447-453.

[5] Yu, Xiongbin, et al. Simultaneous low-loss and low-dispersion in a photonic-crystal waveguide for terahertz communications. Applied Physics Express 12.1 (2019): 012005.

[6] Subashiev, Arsen V., and Serge Luryi. Modal control in semiconductor optical waveguides with uniaxially patterned layers. Journal of lightwave technology 24.3 (2006): 1513.

Synthesis of silver nanoparticles by spark discharge

O V Seraya[1], A A Lizunova[1], K M Khabarov[1], M Nouraldeen[1], V V Ivanov[1]
[1]Research Center for Functional Materials, Moscow Institute of Physics and Technology, Dolgoprudny, 141701, Russia

Abstract. The article is devoted to the study of the processes of interaction of nanosecond laser radiation of different power (0, 230 and 460 mW) and wavelength (527 and 1054 nm) with the flow of aerosol agglomerates of silver nanoparticles synthesized in a spark discharge, and the assessment of the effect of pulsed radiation power on the morphology of silver nanoparticles. Silver nanoparticles of different sizes and morphology were obtained in a pulsed spark discharge and modified by laser radiation. It was shown that spherical of nanoparticles was formed at the maximum laser radiation power of the wavelength of the green part of the visible spectrum (527 nm), close to the plasmon resonance peak for silver.

1. Introduction

At the moment, there are several options for manufacturing volumetric micro-sized structures from nanoparticles that are used in electronics, photonics and biomedicine [1]. For example, such structures are obtained by lithography, inkjet printing using nanoinks or by dry aerosol printing with nanoparticles obtained in a pulsed spark discharge. The urgency of manufacturing and modifying particles in the flow for dry aerosol printing of plasmon structures is associated with ensuring a more environmentally friendly process, in contrast to the use of nanoinks, which entails environmental pollution, and also requires the subsequent removal of component residues from the obtained structures from nanoparticles and cleaning the nozzles from large microdrops. Moreover, the method of obtaining nanoparticles in a pulsed spark discharge is economically advantageous for obtaining nanoparticles of various metals, oxides and semiconductors and is devoid of difficulties associated with the synthesis, transportation and storage of components, and provides a lower electrical resistivity of sintered lines of silver nanoparticles than when sintering particles obtained from nanoinks as well [2].

2. Materials and Methods

An aerosol with silver nanoparticles was produced in a spark discharge (1,5 kV) in a flow of argon working gas (Ar 6.0) of 10-400 ml/min, then it was processed by laser radiation with a wavelengths of 527 and 1054 nm at pulse energies up to 900 μJ and pulse repetition rate up to 500 Hz directly in the gas stream. The resulting aerosol was transported to a nozzle to focus it on a substrate to form various plasmon nanostructures. A more detailed description of the installation is provided in [3]. During the project, the study of particle size parameters and phase composition was carried out using a set of methods, namely: transmission electron microscopy (TEM) on a JEOL JEM-2100 device with an

accelerating voltage of 200 kV, aerosol NP analyzer SMPS 3936 (TSI Inc., Shoreview, MN, USA) for measuring the agglomerates sizes, Jasco V770 spectrophotometer, ImageJ image analysis software, for constructing a statistical distribution of the sizes of silver nanoparticles, as well as information for analyzing diffraction patterns from the American Mineralogist Crystal Structure Database.

3. Results and Discussion

A typical TEM image of large agglomerate of primary nanoparticles obtained in a spark discharge without laser interaction and the corresponding electron diffraction pattern are presented on Figure 1. The average size was 16±4.5 nm for primary silver nanoparticles, and 160±132 nm for agglomerates (TSI data). Most of the nanoparticles' sizes were detected to be from 6 to 30 nm, a few single particles with sizes of 35 - 43 nm were observed. Pursuant to SAED pattern we had concluded that all nanoparticles were crystallized in the silver phase of the Fm3m space group. As a result of the conducted research, it turned out that the power value of pulsed laser radiation affects the size of nanoparticles and the shape of their agglomerates: smaller sizes were observed in nanoparticles that did not interact with laser radiation. The energy required for modification depends on the size, material and extinction/absorption coefficient of nanoparticles at the laser wavelength. It is known that the maximum absorption coefficient of silver at a wavelength of 527 nm, that's why better modification by green laser than red was assumed. Absorption spectra analysis of silver nanoparticles showed the maximum intensity peak of absorption energy in the green part of visible spectrum. Shape changing by green laser impact to spherical was confirmed by TEM results (fig.1, c). A decrease in the flow of nanoparticles from 50 to 10 ml/min affects the quality of sintering: individual spherical silver particles of average sizes 24.7±23 nm (λ = 1054 nm) and 55.8±31 nm (λ = 527 nm) were observed.

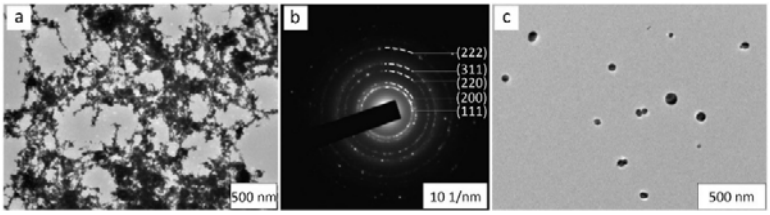

Figure 1(a-c). (a) TEM image of primary agglomerates (no laser); **(b)** SAED pattern taken from primary agglomerates area; **(c)** Modified silver nanoparticles (laser radiation: 527 nm, 100% power, gas flow: 10 ml/min).

4. Acknowledgments

This research was funded by the Ministry of Science and Higher Education of the Russian Federation (State Contract No. 075-03-2021-095, Project Identifier 0714-2021-0007, Project Title: 'Development of functional materials with controlled electrical, chemoresistive and catalytic properties for manufacturing sensor microsystems by using methods of printed electronics').

References

[1] V V Ivanov, A A Efimov, D A Mylnikov, A A Lizunova 2018 *Russian Journal of Physical Chemistry A* **92** 607

[2] V V Ivanov, A A Efimov, D A Mylnikov D.A., A A Lizunova, A V Bagazeev, I V Beketov, S V Shcherbinin 2016 *Tech. Phys. Lett*. **42** 876

[3] K M Khabarov, M N Urazov, A A Lizunova, E I Kameneva, A A Efimov, V V Ivanov 2021 *Appl. Sci.* **11** 4147

Förster Resonance Energy Transfer from colloidal quantum dots to xanthene dye in polymer film

N Slyusarenko, E Slyusareva
Siberian Federal University, Krasnoyarsk 660041, Russia

E-mail: sci_box@mail.ru

Abstract. In the work, a system with effictive (up to 80%) Förster resonance energy transfer is implemented. The system includes thin gelatin films with embedded CdTe quantum dots (donors) and rose bengal xanthene dye (acceptor). The energy transfer mechanism revealed to be possible due to the high local concentration of fluorophores (~10^{-3} M) as well as careful selection of donor and acceptor spectral characteristics. The energy transfer was confirmed by the quenching of the donor photoluminescence in both steady-state and time-resolved measurements. It was shown that the photoluminescence spectrum of the system can be drived by changing the ratio of the donor-to-acceptor concentration.

Creation of light sources with adjustable spectral properties is of high interest in medicine [1], sensing [2], design of optoelectronic devices [3], lasers, photocatalysis and photopatterning [4]. The semiconductor quantum dots (QDs) are very promising for implementation of the ideas since they have a wide and intense absorption spectrum in the UV region and tunable photoluminescence (PL) spectra. Adding a suitable acceptor to the quantum dots for the implementation of Förster Resonance Energy Transfer (FRET) [5] allows adjusting the emission of the system. As well as the efficiency of this process is specific to series of parameters, it is possible to use a FRET systems as sensors for temperature, pressure, radiation etc. We investigated the efficiency of FRET in thin gelatin films with embedded CdTe quantum dots (donors) and rose bengal (acceptor) under variation of the donor-to-acceptor concentration ratio.

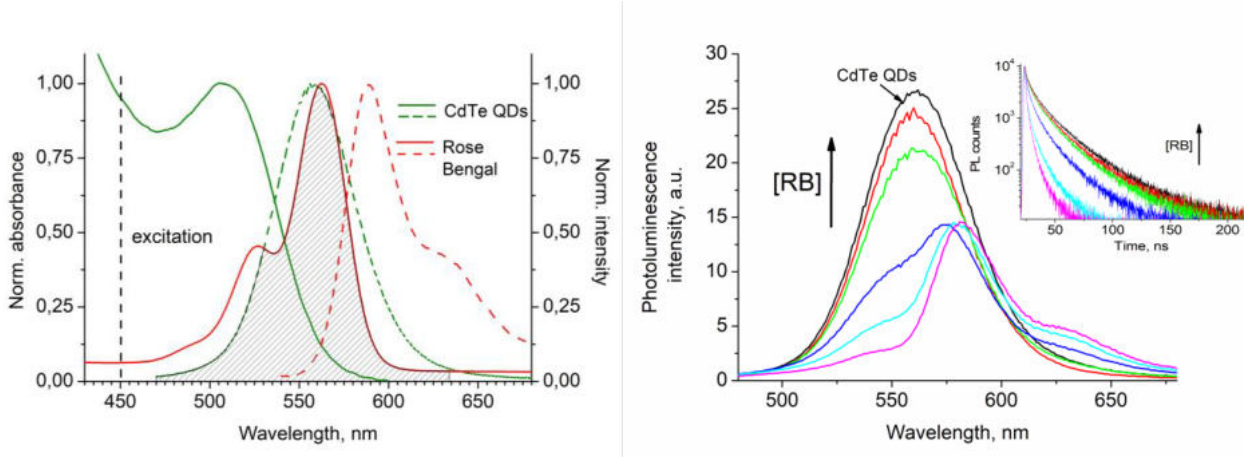

(a) (b)

Figure 1. (a) Absorption and PL spectra of CdTe QDs (donor) and rose bengal (acceptor) in gelatin film. (b) The fluorescence steady-state spectra and time-resolved decays (insert) of CdTe QDs in gelatin films with increasing of the rose bengal concentration

The water dispersible semiconductor quantum dots CdTe with a wavelength of PL maximum of ~ 550 nm and rose bengal dye (RB) were used as a donor-acceptor pair with Förster radius of 6 nm (**Figure 1a**). We

provide a high concentration (~10^{-3} M) of fluorophores in gelatin film in order to meet this criterion. The absorption and fluorescence spectroscopy (both steady-state and time-resolved) was applied to analyze the efficiency of energy transfer (**Figure 1b**).

The Förster's model [5] was used for FRET analysis. Estimated FRET efficiency reached to 80%. An increase in the acceptor concentration leads to a rise in the efficiency of FRET and a change in the emission spectrum of the system. The possibility of adjusting the PL spectrum of the system by varying the donor-to-acceptor concentration ratio is shown. The total change in the gravity center (taking the change in the position of the maximum and the shape of the spectrum into account) revealed to be more than 30 nm. The presented approaches and objects are promising for the creation of low-cost systems with tunable spectra.

Acknowledgments
This research was supported by the Ministry of Science and Higher Education of the Russian Federation (Grant MK–995.2022.1.2).

References
[1] Xing J, Gong Q, Akakuru O U, Liu C, Zoua R, and Wu A 2020 *Nanoscale* **12** 24311
[2] Slyusarenko N V, Gerasimova M A, Slabko V V, and Slyusareva E A 2017 Russ. Physs. J. **60** 477
[3] Shu Y, Lin X, Qin H, Hu Z, Jin Y, and Peng X 2020 Int. Ed. **59** 22312
[4] Devatha G, Rao A, Roy S, and Pillai P P 2019 *ACS Energy Lett*. **4** 1710
[5] Förster T 1960 *Radiat. Res. Suppl.* **2** 326

Edge states and modulation instability in nonlinear photonic topological lattices

Ekaterina O. Smolina[1,2], **Lev A. Smirnov**[1,2], **Daria A. Smirnova**[3]

1. Institute of Applied Physics, Russian Academy of Science, Nizhny Novgorod 603950, Russia

2. Nizhny Novgorod State University, Gagarin Av. 23, Nizhny Novgorod, 603950 Russia

3. Research School of Physics, Australian National University, Canberra ACT 2601, Australia

smolinakate@outlook.com

Abstract. We study self-action effects in topological photonic lattices with local nondispersive Kerr nonlinearity. We show that in the continuum limit, the nonlinear evolution of a spinor wavefunction in such systems is governed by the generic nonlinear Dirac equations allowing for instructive analytical considerations. It is demonstrated that the nonlinear evolution of finite wavepackets propagating along the valley-Hall domain wall in a staggered honeycomb lattice is accompanied by steepening of the trailing wavefront up to the effect of a gradient catastrophe. The development of modulational instability of nonlinear Bloch waves in a chiral square lattice leads to nonlinear wave mixing and further spontaneous creation of wave polarization singularities determined by the band Chern number. To distinguish different topological phases in slowly driven Floquet lattices, we apply the same approach along with a study of the nonlinear dynamics of nonstationary superposition states, which enables the anomalous Floquet phases to be distinguished from the trivial phase.

Photonic topological insulators are a novel class of crystalline structures supporting robust propagation of light along edges and interfaces [1]. They show great potential for numerous applications in optical communications and computing technologies due to the exceptional topological protection of their transport properties against disorder, including the ability of electromagnetic pulses to overcome structural imperfections without back-reflection. Since optical nonlinearity is an inherent feature of materials employed in topological photonics, the wave processes in such structures can be accompanied by a variety of nonlinear effects, including harmonic generation [2], self-action effects [3], and modulational instability [4].

In this work, we study both analytically and numerically nonlinear effects in topological photonic lattices of different geometries. First, we focus on the propagation of slowly-varying wavepackets along the topological domain walls in nonlinear photonic valley-Hall insulators [5]. As a specific example, we consider a dimerized graphene lattice composed of single-mode dielectric waveguides with local nondispersive Kerr nonlinearity. We show that in the continuum limit, the nonlinear evolution of a spinor wavefunction in such a system is governed by the nonlinear Dirac equations. It is analytically demonstrated that the evolution of finite wavepackets propagating along the domain wall is accompanied by steepening of the trailing wavefront up to the development of a gradient catastrophe. To illustrate this key effect, we also perform numerical modeling of the temporal

dynamics of edge wavepackets. Taking the weak spatial dispersion into account stipulates then the formation of stable edge quasi-solitons. Our results are validated by full-wave numerical modeling of beam propagation along a valley-Hall domain wall in realistic staggered honeycomb lattices of laser-written waveguides.

Next, we consider the nonlinear instabilities, developing in the presence of intense laser pulses in a topological photonic lattice [4]. We show that scenarios of the development of modulation instability in a chiral square lattice with the Kerr-type nonlinearity are determined by the topological properties of its energy bands. An analysis of the modulation instability makes it possible to distinguish the topology of the band structure (whether it is trivial or nontrivial). The number of vortex formations resulting from instability is quantized, which can be directly used to extract the topological invariant.

Finally, we study how to utilize the nonlinear propagation dynamics of bulk states to distinguish topological phases of slowly driven Floquet lattices [6]. Following to the methodology developed in [4], we show how to measure the Chern number using singularities emerging in nontrivial polarization textures. Moreover, we propose a scheme to identify dynamical symmetry inversion points using the nonlinear dynamics of nonstationary superposition states and, thereby, distinguish the anomalous Floquet phases from the trivial phase. These approaches may be readily implemented using light propagation in nonlinear waveguide arrays.

Beyond the specific examples we considered, our findings are instructive for other emerging experimental studies of nonlinear dynamic phenomena in a variety of topological platforms spanning from metamaterials to optical lattices and exciton-polariton condensates.

Acknowledgments

This work was supported by the Russian Foundation for Basic Research (Grant No. 19-52-12053).

References

[1] T. Ozawa, H.M. Price, A. Amo, N. Goldman, M. Hafezi, L. Lu, M.C. Rechtsman, D. Schuster, J. Simon, O. Zilberberg, and I. Carusotto, “Topological photonics,” Reviews of Modern Physics 91, 015006 (2019).

[2] D. Smirnova, S. Kruk, D. Leykam, E. Melik-Gaykazyan, D.Y. Choi, and Y. Kivshar, “Third-harmonic generation in photonic topological metasurfaces,” Physical Review Letters 123, 103901 (2019).

[3] D.A. Smirnova, L.A. Smirnov, D. Leykam, and Y.S. Kivshar, “Topological edge states and gap solitons in the nonlinear Dirac model,” Laser & Photonics Reviews 13, 1900223 (2019).

[4] D. Leykam, E. Smolina, A. Maluckov, S. Flach, and D.A. Smirnova, “Probing band topology using modulational instability,” Physical Review Letters 126, 073901 (2021).

[5] D. A. Smirnova, L. A. Smirnov, E. Smolina, Dimitris G. Angelakis, and D. Leykam. "Gradient catastrophe of nonlinear photonic valley-Hall edge pulses." Physical Review Research 3, 043027 (2021).

[6] A. Maluckov, E. Smolina, D. Leykam, S. Gundogdu, D. G. Angelakis, and D.A. Smirnova, “Nonlinear signatures of Floquet band topology”, Physical Review B 105, 115133 (2022).

Ion-beam-induced formation of gold nanostructures on polymethyl methacrylate film.

Vitaly M. Studzinsky[1], **Konstantin V. Karabeshkin**[2,3], **Maxim V. Mishin**[4], **Anastasia S. Kondrateva**[4], **Platon A. Karaseov**[1]

[1]Peter the Great Saint-Petersburg Polytechnic University, St. Petersburg, Russia
[2]St. Petersburg Academic University, St. Petersburg, Russia
[3] JSC "Research and Production Enterprise "ELAR", St. Petersburg, Russia
[4] Alferov University, St. Petersburg, Russia

Abstract. In this work, we study the behavior of a thin gold layer on the surface of a polymethyl methacrylate (PMMA) film under irradiation with keV atomic P and molecular PF_4 ions. It was found that the behavior of both the gold layer and the PMMA film depends on the kind of ions used. Small doses of molecular ions flattens the gold layer. As the dose increases, it quickly decomposes into nanoparticles. Monatomic P ion irradiation converts the gold layer into nanoparticles at any of the doses used. Th gold nanoparticle formation proceeds less efficiently than in case of the ion-beam dewetting of the Au layer on the SiO_2 substrate. The formation of nanostructured regions in the polymer bulk was also established.

1. Introduction

Nanocomposite materials are of widespread use in various fields from catalysis to sensing and more. Noble metal nanoparticles exhibit tunable plasmon resonances over VIS-NIR spectral band. Incorporation of nanoparticles into bulk matrix could increase its rigidity, strength, wear resistance and other mechanical properties. One can also tailor electrical conductivity, optical transmission and reflection, antimicrobial properties, temperature response characteristics, and many others. Noble metal, especially gold, nanoparticles have attracted attention, primarily due to their unique electronic, optical, thermal, chemical and biological properties, and, accordingly, promising potential applications in various fields, including biology and medicine, chemistry, photonics, materials science, and other interdisciplinary areas.

One of dry low-temperature gold nanoparticle synthesis techniques is heating of a few nanometer thick metallic gold layer [1], or its irradiation with accelerated ions [2]. This layer can be either deposited on a substrate, or buried ten to hundred nanometers deep. Moreover, implantation of metal ions has been used to fabricate [3] and control the size, shape, and distribution of metal nanoclusters in various matrices. Indeed, stopping ion shifts target atoms from their places thus enforcing various processes, among which is radiation-stimulated diffusion resulting in nanoparticle formation. Carbon-based polymer matrices are of interest due to possible biocompatibility of a resulting composite [4]. The influence of the substrate material on the process of particle formation can play a decisive role in the formation of nanoparticles. Besides a lot of efforts, there are still a number of unanswered questions; in particular, role of the density of collision cascades formed in the target by a fast ion during its stopping [5] is not clear. Local density of collision cascades formed by a stopping ion affects all radiation-related phenomena.

This work is devoted to study the modification of a 5 nm thick gold layer deposited on polymethylmethacrylate (PMMA) film under bombardment with accelerated molecular and monatomic ions. Overlapping of collision sub-cascades formed by atomic constituents of a molecular ion gives rise to an increase in the density of the cumulative cascade formed by molecular ion. This fact let us study the effect of collision cascade density on formation of gold nanoparticles. Ion doses were taken the same in the units of gold atom displacements (DPA) in order to compare the effects of molecular and atomic ion bombardment

2.Results

The samples obtained were studied by AFM, SEM and FTIR. Formation of inhomogeneous nanosized regions occurs as revealed in the SEM image of the unirradiated sample, in contrast to Au on silicon where a flat layer is obtained at a given thickness of the gold film. The shape of the gold islands is nonuniform. The gold film on poly(methyl methacrylate) is initially formed with a large number of small islands. Ion irradiation induces surface modification with some notable trends. It can be seen that at the initial stage of irradiation, fine particles become much smaller, and the gold coverage even slightly increases. Thus, at small ion doses the gold film distribution over the surface is more even, while small islands merge and almost one large gold layer is formed. It also follows from the analysis that a large film breaks down into smaller nanostructures with the dose increase. Particle size distributions were derived on the base of brightness analysis of SEM images obtained from samples. The area occupied by gold structures decreases with an increase in the radiation dose. Surface modification with P ions requires a higher dose compared to PF_4 molecular ions. The resulting nanoparticles differ significantly from each other in size. It can be seen from the figure that to achieve the same size of nanoislands, a higher dose of atomic ions is required compared to molecular ions PF_4. Since the total number of displacements of gold atoms is the same, we conclude that the formation of nanoislands on poly(methyl methacrylate) is more pronounced in the case of molecular ion bombardment, i.e. a molecular effect in Au nanoparticle formation is found. A similar situation was observed in tha casde of ion beam formation of gold nanoparticles on silicon [5]. The AFM images show that surface nanostructures are formed on the surface. PMMA is also affected by ion irradiation. All effects will be discussed in the talk.

Acknowledgments

The work was partially supported by the Russian Ministry of Science and Higher Education (project № FSRM-2020-00011).

References

[1] Bespalova P., Enns Y., Kunkel T., Balanov V., Speshilova A., Vorobyev A., Mishin M., Karaseov P. Gold Nanoparticle Array Formation by Low-Temperature Annealing, in E. Velichko et al. (eds.), International Youth Conference on Electronics, Telecommunications and Information Technologies, Springer Proceedings in Physics 255, 2020, p.34.

[2] LoSavio R., Repetto L., Guida P., Angeli E., Firpo G., Volpe A., Ierardi V., Valbusa U., Control of the micrometric scale morphology of silicon nanowires through ion irradiation-induced metal dewetting. Solid State Communications, 240, 2016, p. 41-45.

[3] A. N. Mikhaylov, A. B. Kostyuk, D. S. Korolev, I. Yu. Zhavoronkov, I. A. Chugrov, A. I. Belov, V. A. Burdov, A. V. Ershov & D. I. Tetelbaum, Formation of gold nanoparticles in single-layer and multi-layer ensembles of light-emitting silicon nanocrystals using ion implantation, Bulletin of the Russian Academy of Sciences: Physics 76, (2012) 214–217.

[4] J. Prakash, A. Tripathi, V. Rigato, J.C. Pivin, J. Tripathi, K.H. Chae, S. Gautam, P. Kumar, K. Asokan and D. K. Avasthi, Synthesis of Au nanoparticles at the surface and embedded in carbonceeous matrix by 150 keV Ar ion irradiaion, J. Phys. D: Appl. Phys. 44, 2011, 125302.

[5] M.S. Tuzhilkin, P.G. Bespalova, M.V. Mishin, I.E. Kolesnikov, K.V. Karabeshkin, P.A. Karaseov, A.I. Titov, Formation of Au Nanoparticles and Features of Etching of a Si Substrate under Irradiation with Atomic and Molecular Ions, Semiconductors 54(1), 2020, 137-143

Thermal relaxation mechanisms in CVD monocrystalline boron-doped diamond microstructures

Titova, N.[2*], Kolbatova, A.[1,2], Baeva E.[1,2], Semenov, A.[2], Goltsman, G.[1,2], Eon, D.[3], Bustarret, E. [3], Khrapai, V.[1,4]
(1) National Research University Higher School of Economics, Russia;
(2) Moscow Pedagogical State University, Russia;
(3) Univ. Grenoble Alpes, CNRS, Institut Néel, France;
(4) Institute Solid State Physics RAS, Russia
*titovana@mail.ru

Abstract. In this paper, we study thermal relaxation in a superconducting single-crystal boron-doped diamond (C:B) film with a thickness of 130 nm using the noise thermometry. We demonstrate that the experimental dependences of the noise temperature (T_N) on the heating power (P_J) of the C:B samples with different length are well described by the dependence $P_J \sim \Sigma_{e\text{-}ph}(T_N^5 - T_b^5)$, where T_b is the bath temperature. Based on these dependencies for long samples, we determine the electron-phonon coupling constant ($\Sigma_{e\text{-}ph}$).

1. Introduction

Diamond is one of the prospective materials for realization of optical integrated circuits, including waveguides, single-photon sources and single-photon detectors on a single chip [1,2]. The complete realization of the so-called 'diamond platform' requires an efficient single-photon detector, which is technologically compatible with the platform. Single-photon detectors that are used in such hybrid circuits are currently based on disordered superconducting NbN films [1,2]. These detectors' performance depends strongly on the structural uniformity, which is determined by the smoothness of the diamond platform. Development of a superconducting single-photon detector based on a boron-doped diamond (C:B) enables fabrication of a monolithic diamond platform hence studying thermal transport in this material is required. For this investigation, we fabricated samples of various lengths and widths from a C:B film and study thermal relaxation transport.

2. Result

We expand the methods of our studies of nonequilibrium processes occurring in superconducting boron-doped single-crystal diamond films [3] to understand better energy relaxation of electrons (holes) in this material. We used noise thermometry for measure the rate of energy transport between the electrons and lattice at low temperatures [4]. We fabrication sample from superconducting 130-nm thick C:B epilayer on IIa-(100)-oriented diamond substrate. The epilayer was also characterized with a critical temperature Tc =1.7 K and a carrier density of $1.46 \cdot 10^{21}$ cm^{-3} measured at 20 K. The studied samples were structured into wires with a length varied from 2.5 to 330 μm and a width from 150 nm to 30 μm respectively. For fabricated wires we used e-beam lithography and plasma chemical etching through Al mask (Fig.1a).

The samples were fixed in a holder placed in a cryostat for dissolving He3 in He4. A resonant circuit with frequencies of 40 and 22 MHz was also located there. The whole circuit was supplemented by a

chain of low-noise amplifiers and filters located at room temperature. The signal from the sample was measured by a power detector (Fig.1a).

We measured noise spectral power in the samples at low heating (joule) powers and low bath temperature (0.5 K) and observed that the heat flow rate is associated either with electrons diffusion into reservoirs or with electron-phonon interaction and is described thermal balance equation [5]:

$$-\frac{d}{dx}\left(k(x)\frac{dT_e(x)}{dx}\right) = \frac{I^2R}{\Omega} + \Sigma_{e-ph}(T_N^n - T_b^n) \qquad (1)$$

where Ω is the sample volume, T_N is the noise temperature, $\Sigma_{e\text{-}ph}$ is the electron-phonon coupling constant, n is fitting parameters, here is n=5, k is the thermal conductivity. Also T_N can be determined from the Johnson–Nyquist relation $S_I = 4k_BT_N/R$. In the shortest samples (L=2.5 μm), we observed diffusion transport into contacts (Fig.1b). In longer samples, however, thermal transport is observed, which is characterized only by electron-phonon relaxation. The obtained value for $\Sigma_{e\text{-}ph}$ = 0.028 nW/(K^{5}μm^3) is lower than conventional metals have (Au-2.4, Al-0.3 nW/(K^{5}μm^3)), but close to values for P-doped Si – 0.04 nW/(K^{5}μm^3) [6]. Also the solution of equation (1) allows to determine the length of the electron-phonon interaction: $l_{e-ph} = (\sigma\pi^2k_B^2/3e^2n\sum_{e-ph}T^{n-2})^{0.5}$.

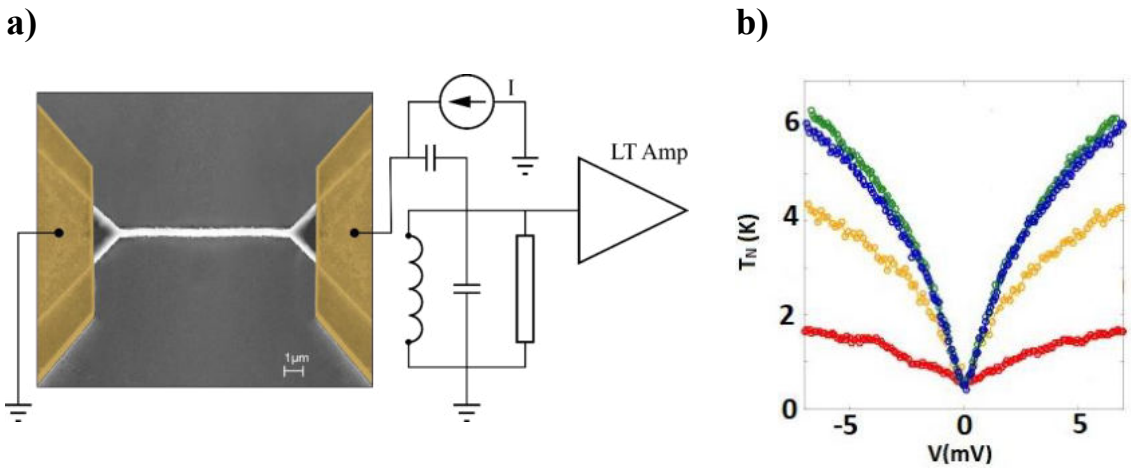

Figure 1. (a) Schematic diagram of the noise thermometry and SEM image of a typical device. (b) Dependence of the noise temperature versus voltage for four sample with a length of 2.55 μm (blue and green circle), 7.7 μm (orange) and 98 μm (red).

Conclusion

We have studied thermal transport between the electron and phonon subsystems in the normal state for a superconducting boron-doped diamond film. The results obtained for samples with bridge lengths exceeding the electron-phonon interaction length ($l_{e\text{-}ph}$) make it possible to estimate the electron-phonon coupling parameter.

Acknowledgments

This work was supported by the RSF project No.19-72-10101

References

[1] P.Rath et.al, Light:Science&Applic., 4, 2015
[2] Lenzini, et al, Adv. Quantum Technol. 2018
[3] A. Kardakova et. al, Phys.Rev B 93, 2016
[4] M. Roukes, et al, Phys.Rev.Lett.55, 1985
[5] B. Huard, et al, Phys. Rev. B 76, 2007
[6] Giazotto et.al, Rev. Mod. Phys. 78, 2006

Investigation of crystallinity degree for $Ge_2Sb_2Te_5$ films by reflection and transmission photometry

N M Tolkach[1, *], N V Vishnyakov[2], V G Litvinov[2], A O Yakubov[1], E S Trofimov[2] and A A Sherchenkov[1]

[1] National Research University of Electronic Technology (MIET), ld. 1, Shokin Square, Zelenograd, Moscow, 124498, Russian Federation
[2] Ryazan State Radio Engineering University named after V.F. Utkin, 59/1, Gagarina Street, Ryazan, 390005, Russian Federation

[*] n.m.tolkach@gmail.com

Abstract. To assess the crystallinity degree for $Ge_2Sb_2Te_5$ (GST) films the method of reflection and transmission photometry and the approximation of an effective medium of the Brueggemann type were used. It was found that the changes in the energy and duration of the laser pulse lead to the change in the ratio of crystalline and amorphous fractions and change in crystallinity degree. It was found that an increase of crystalline fraction leads to an increase of refractive index and extinction coefficient at telecommunication wavelength of 1550 nm, which also leads to changes of reflectivity and transmissivity of the GST film and can be used to perform modulation and switching of signals.

1. Introduction

Semiconductor materials with first kind phase transition (Phase Change Material - PCM), in particular, chalcogenide glassy semiconductors, have found their application in non-volatile radiation-resistant memory elements for creating dynamic storage devices. Currently, PCM material $Ge_2Sb_2Te_5$ (GST) is actively used for this purpose. GST has a fast and low-energy phase transition, which can be excited by both an electric and a laser pulse [1]. In addition to the main phase states (amorphous and crystalline) of GST, there can be additional intermediate states due to the presence of nanosized fractions of the material in both these states. Controlling the ratio of the amorphous and crystalline fractional composition (crystallinity degree) of GST opens up wide possibilities in fine-tuning its optical parameters, but at the same time, it requires studying the processes and peculiarities that occur when laser radiation is applied to the GST material. Therefore, the aim of the work is to investigate in the GST thin films the amorphous and crystalline fraction ratio, which is characterized by the crystallinity degree.

2. Methods and experiments

To estimate the crystallinity degree of GST films in this work, we used the method of reflection and transmission photometry and the approximation of an effective medium of the Brueggemann type. Such approximation represents a medium in the form of amorphous matrix with growing quantity of spherical crystallites. Fraction of crystals in the matrix (crystallinity degree) is equal to [2]:

$$C = (\bar{n}^2 - \bar{n}_a^2)\,(2\bar{n}^2 + \bar{n}_c^2) \,/\, (3\bar{n}\,(\bar{n}_c^2 - \bar{n}_a^2)), \quad (1)$$

where $\bar{n}$, $\bar{n}_a$ and $\bar{n}_c$ are the complex refractive index of GST film in the current, amorphous and crystalline state respectively. The complex refractive index $\bar{n}$ is found from the model expressions determined by the Airy formulas for reflectivity $\Re$ and transmissivity $\Im$ of the GST structure taking into account processes of multiple re-reflection of electromagnetic waves in the film and their interference.

The GST thin film with the thickness of 24 nm were deposited by magnetron sputtering. The measurement setup based on the NTEGRA Spectra (NT-MDT SI, Russia) was used and allowed to carry out investigations using methods of Raman spectroscopy, atomic force microscopy, optical microscopy, photometry, laser modification. Laser modification of the GST film has been performed by radiation with the 405 wavelength, with the focused spot diameter of about 1 μm and with various duration values τ (from 4 ns to 1 microseconds), repetition intervals T (from 20 ns to 1 microseconds) and radiant exposures (from 0.02 nJ/μm^2 to 20 nJ/μm^2) of the pulse. Photometry was used to measure the reflectivity and transmissivity of the GST film at 405, 638 and 1550 nm wavelengths.

3. Research results

Crystallinity degree of the local film area was determined using the obtained values of the complex refractive index at the wavelengths of 405, 638, and 1550 nm. As can be seen from figure 1, when films are exposed to laser pulses with wavelength of 405 nm at energy exposure of pulse from 2.92 to 3.26 nJ/μm^2, the crystallinity degree changes from 1 to 0.

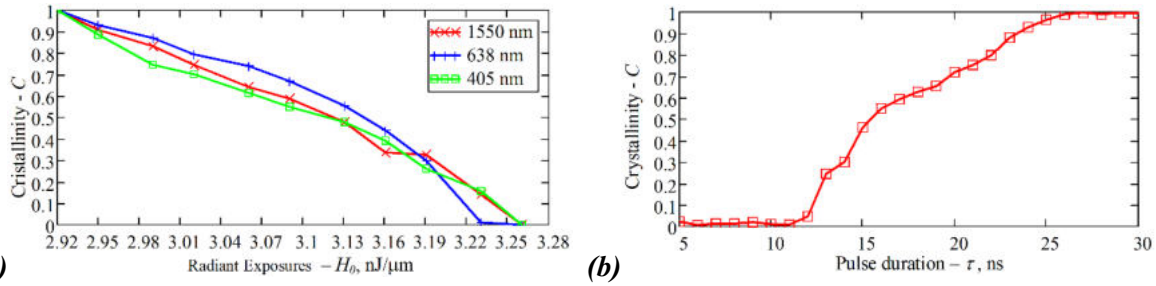

Figure 1. Changes in the crystallinity degree of the local region in the GST film: depending on the energy exposure of the 405 nm laser pulse ***(a)***; depending on the laser pulse duration τ ***(b)***

The evaluation of crystallinity degree showed that amorphization of the film is observed when exposed to laser pulses with wavelength of 405 nm at energy exposure of pulse from 3.26 to 3.37 nJ/μm^2, with pulse durations up to 12 ns. Partial crystallization of amorphous GST at these energy exposures is observed at the pulse durations from 12 to 25 ns, while full crystallization is observed at the pulse durations from 25 to 78 ns. An increase in the proportion of crystalline fractions leads to an increase of refractive index and extinction coefficient at telecommunication wavelength of 1550 nm, which also leads to changes of reflectivity and transmissivity of the GST film and can be used to perform multilevel recording, and amplitude modulation or routing of signals.

Thus, it was found that a change in the energy and duration of a laser pulse leads to a change in the crystallinity degree and, so, to a change in the ratio of crystalline and amorphous fractions.

Acknowledgments

The reported study was funded by RFBR according to the research project # 19-37-60023 “A study of optical switching processes in alternating structures based on crystal-amorphous materials of Ge-Sb-Te system for optical switches” and used the equipment of Region Centre of probe microscopy of Ryazan State Radio Engineering University named after V.F. Utkin.

References

[1] Zhang Y, Chou J B, Li J, Li H, Du Q, et al 2019 *Nat. Commun.* **10** 4279

[2] Kim D H, Merget F, Laurenzis M, Bolivar P H, Kurz H 2005 *J. Appl. Phys.* **97(8)** 83538

Photoluminescence from lead halide perovskite superlattices

Pavel Tonkaev, Evgeniia Grechaninova, Anatoly Pushkarev, Sergey Makarov

ITMO University, Kronverksky av. 49 197101 St. Petersburg, Russia

E-mail: pavel.tonkaev@metalab.ifmo.ru

Abstract. Lead halide perovskites are a new class of materials with promising optoelectronic properties. Colloidal perovskite nanocrystals have shown high efficiency of photoluminescence. We studied photoluminescence properties of $CsPbBr_3$ superlattices at room temperature and 6 K. We demonstrated that the photoluminescence spectra of perovskite nanocrystals are preserved in superlattices.

1. Introduction

Lead halide perovskites are a class of new materials with outstanding properties that have been applied in the field of photovoltaics [1] and light-emitting diodes [2]. Moreover, due to relatively high refractive index, perovskite nanoparticle supports Mie resonances in optical and near-infrared range which enhance photoluminescence [3] and lower the lasing threshold [4]. Meanwhile, perovskite nanocrystals with quantum confinement have high photoluminescence quantum yield [5]. Assembling perovskite nanocrystals in an ordered 3D array or superlattice allows controlling of additional properties of optical nanosources. Herein we aim to study photoluminescence of single CsPbBr3 superlattices with linear dimensions of several microns at room temperature and 6 K.

2. Results and discussion

The CsPbBr3 perovskite nanocrystals were obtained by the hot injection method. The resulting nanocrystals were separated by centrifugation and dispersed in toluene to obtain a colloidal solution. Superlattices were formed from these colloidal nanocrystals. The CsPbBr3 superlattices were fabricated on a silicon substrate. The transverse dimensions of individual superlattices ranged from 1 μm to 10 μm, while some of them agglomerated to form clusters of superlattices, and some remained spatially isolated, which made it possible to measure photoluminescence for individual objects.

Experimental measurements of photoluminescence spectra revealed that the photoluminescence maximum of the CsPbBr3 superlattice is located at the wavelength of 517 nm, whereas the maximum of the bulk thin film is 526 nm. Perovskite nanocrystals demonstrated slightly different results compared to superlattice, the maximum is shifted and located at 518 nm. Therefore, we can conclude that perovskite superlattices have good quality and quantum confinement is preserved. Perovskite superlattices exhibited similar behavior in optical experiments at the temperature of 6K. The maximum of photoluminescence spectra shifted to a long wavelength region and was 530 nm for superlattice and 538 nm for thin film.

3. Conclusion

We have studied photoluminescence properties of superlattices assembled from CsPbBr3 nanocrystals at room temperature and 6K. Our study reveals that photoluminescence spectra of perovskite superlattices are similar to emission spectra of initial colloidal nanocrystals. These structures allow modification of optoelectronic properties of perovskite nanocrystals at 3D level. In addition, perovskite superlattices are promising structures for micro- and nanolasers and photodetectors.

Acknowledgments

This work was supported by the Russian Science Foundation (project № 22-22-20077)

References

[1] Snaith H. J. 2018 *Nature materials* **17** 372-376
[2] Lin K. et al 2018 *Nature* **562** 245-248.
[3] Tiguntseva E. et al 2018 *Nano Letters* **18** 1185–1190
[4] Tiguntseva E. et al 2020 *ACS Nano* **14** 8149-8156.
[5] Protesescu L. et al 2015 *Nano Letters* **15** 3692-3696.

Phase-change periodic surface structures for engineering of excitonic photoluminescence in WS2 monolayers

Pavel I. Trofimov[1], Tatyana Ivanova[1], Ivan S. Sinev[1]

[1]Department of Physics and Engineering, ITMO University, St. Petersburg, Russia

p.trofimov@metalab.ifmo.ru

Abstract. Due to their two-dimensional nature, transition metal dichalcogenide monolayers exhibit extremely strong sensitivity of their excitonic response to the permittivity of the surrounding medium. Here, we show that the intensity and wavelength of the excitonic photoluminescence can be spatially modulated by periodic structures induced by laser pulses in phase change material films.

1. Introduction

The class of two-dimensional transition metal dechalcogenides (TMD) has attracted a lot of attention in photonics due to its strong excitonic effects, flexibility and tunability. Large exciton binding energy, strong absorbance and short radiative lifetime found in such materials already established them as a strong candidates for excitation of strong-coupled exciton polaritons, lasing and creation of single photon emmiters [1]. Moreover, the optical response of such systems can be changed by applying voltage and tuning coupling constants in polariton systems [2], wavelength of single photon emitters [3] and the handedness of circularly polarized electroluminescence [4].

Another way to control exciton binding energy in TMD is to tune its dielectric environment, in particular the refractive index of surrounding media which affects exciton screening. This can be implemented using various methods [5] but the family of so called phase-change materials (PCM) is of particular interest [6]. First, these materials have two different metastable phase states at normal conditions - amorphous and crystalline - with high contrast of optical and electrical properties between them. Moreover heating and subsequent meltquenching of these materials applying optical or electrical pulses results in rapid nanosecond-scale switching between its phase states [7]. Finally the irradiation of PCM thin films with femtosecond laser pulses results in formation of the periodic surface structures with period and direction defined by wavelength and polarization of the emitted light [8].

In this work we studied how laser induced periodic surface structures (LIPSS) formed in GST thin films which is in direct contact with WS_2 monolayer affects its optical properties, in particular the wavelength and intensity of the excitonic response.

2. Results & Discussion

To fabricate WS_2-GST LIPSS heterostructure we first irradiate 50 nm GST film on W substrate to imprint LIPSS-based GST gratings of different type and period using procedure, described in our previous work [9]. After that we mechanically exfoliate large area of monolayer of WS_2 from commercial bulk crystals and dry transferred the obtained monolayer onto laser-processed GST thin

film. The optical images of the reflection and integral photoluminescence excited with ultraviolet lamp, from the structure is shown in figure 1 (a, b). Here we observed the modulation of photoluminescence signal above GST grating there its maximum corresponds to amorphous GST lines. Such result is in consistent with the fact that GST static dielectric constant is higher for the crystalline state which result in more efficient screening of the exciton and its damping above crystalline GST lines in comparison with amorphous ones.

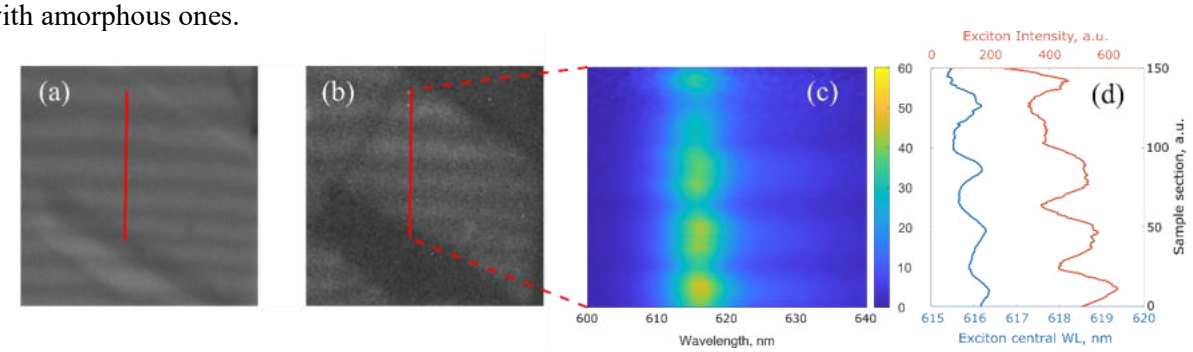

Figure 1. (a) Reflection and (b) integral photoluminescence from WS_2 monolayer on LIPSS formed in GST thin film. The optical response of the sample along its section (red line on (a, b)): (c) photoluminescence map, (d) graphs of spectral position (blue) and intensity of the exciton (red).

To further investigate the optical properties of the fabricated heterostructure we performed photoluminescence spectroscopy using reflection optical scheme coupled to a liquid-nitrogen-cooled imaging CCD camera using TORUS solid state continues wave laser as a pump source. As a result we obtained maps of WS_2 photoluminescence signal (Fig. 1c). After that spectral position and intensity of the excitonic response was calculated fitting the measured photoluminescence spectra to Cauchy line shape. We observed blue shift and damping of the excitonic photoluminescence above the crystalline GST lines (Fig. 1d). The small values of modulation in the exciton spectral position on the contrast with high exciton intensity modulation is a result of two effects of different sign: renormalization of the band gap of the WS_2 monolayer and change in its binding energy.

To conclude we studied the optical properties of the WS_2-GST heterostructure. We showed that the photoluminescence response of the WS_2 monolayer, in particular its spectral position and intensity can be controlled by imprinting periodic phase structures in the underlying GST film. These results shows the potential of phase-change – TMD platform to dynamically control the excitonic response, as the process of formation of phase-change GST gratings is fast and reversible in nature.

Acknowledgments

The reported study was funded by RFBR according to the research project № 20-31-70001

References

[1] Mak K.F.; Shan J. Photonics and optoelectronics of 2D semiconductor transition metal dichalcogenides. Nature Photonics 2016, 10, 216–226.

[2] Weisbuch, et al. Observation of the coupled exciton-photon mode splitting in a semiconductor quantum microcavity. Phys. Rev. Lett. 1992 69, 3314–3317

[3] He, M. et al. Single quantum emitters in monolayer semiconductors. Nature Nanotech. 2015, 10, 497–502.

[4] Zhang, et al. Electrically Switchable Chiral Light-Emitting Transistor. Science, 2014, 344, 6185, 725-728.

[5] Cui et al. Tunable Metasurfaces Based on Active Materials. Adv. Funct. Mater. 2019, 29, 1806692

[6] Wuttig, M.; Taubner, T. Phase-change materials for non-volatile photonic applications. Nature Photonics 2017, 11, 465-476.

[7] Au Y-Y et al. Phase-change devices for simultaneous optical-electrical applications. Sci. Rep. 2017, 7, 9688
[8] Kozyukhin S. et al. Specific Features of Formation of Laser-Induced Periodic Surface Structures on Ge2Sb2Te5 Amorphous Thin Films under Illumination by Femtosecond Laser Pulses. Phys. Status Solidi B 2020,257, 1900617
[9] Trofimov P. et al. Rewritable and Tunable Laser-Induced Optical Gratings in Phase-Change Material Films. ACS Appl. Mater. Interfaces 2021, 13, 27, 32031–32036

The Investigation of Optical Coupling of Microlasers with Tapered Fiber

N A Fominykh[1,2], E I Moiseev[1], I S Makhov[1], K N Min'kov[3], Yu A Guseva[4], M M Kulagina[4], S A Mintairov[4], N A Kalyuzhnyy[4], N V Kryzhanovskaya[1,2], A E Zhukov[1]

[1]National Research University Higher School of Economics, 16 Soyuza Pechatnikov, St. Petersburg 190008, Russia
[2]St. Petersburg Academic University RAS, Khlopina 8/3, St. Petersburg, 194021, Russia
[3]Russian Quantum Center, Novaya 100, Moscow, 143026, Russia
[4]Ioffe Physical Technical Institute of RAS, Politehnicheskaya 26, St Petersburg, 194021, Russia

E-mail: fominy-nikita@yandex.ru

Abstract. We present an investigation of optical coupling of injection microdisk and microring lasers with different diameters with a tapered fiber. We studied the dependences of the laser dominant mode intensity on the distance between the tapered fiber and the microlaser's sidewall. For every studied laser a sharp intensity growth by 2-3 orders of magnitude was observed when the tapered fiber came in contact with the microlaser. We compared lasing spectra received by the tapered fiber and by the microobjective. Though the intensity of the electroluminescence signal received by the tapered fiber was lower than that coupled by the microobjective, the ratio of the dominant (lasing) mode intensity to spontaneous emission was noticeably higher for the case of the tapered fiber.

1. Introduction

Currently, semiconductor microdisk (MD) and microring (MR) lasers attract a lot of interest due to their potential use as building blocks in future microphotonic and nanophotonic devices [1]. Microlasers of this design support whispering gallery modes (WGM) with high quality factor and, accordingly, low output losses [2]. Lateral light output of WGM microlasers makes them promising for optically coupled systems. Coupling of microlaser emission by tapered fiber has already been investigated for the cases of passive WGM microresonators [3] and WGM microlasers with optical pumping [4]. In this work we study the optical coupling of injection semiconductor MD and MR lasers with different diameters (15-50 μm) with tapered fiber.

2. Methods

The studied microlasers were fabricated from a laser epitaxial heterostructure synthesized on an n+-GaAs substrate by MOCVD with an active region representing a 6-layer array of InGaAs/GaAs quantum well-dots. The mesa diameters varied in range from 15 μm to 50 μm. More detailed description of the epitaxial structure and fabrication details may be found elsewhere [5].

The tapered fiber was fabricated by adiabatic stretching method [6]. The tapered section of the fiber with its ends fixed on movable supports was positioned above the heating system. The tapered fiber was cleaved in the thinned part. The smallest diameter of the thin part of the tapered fiber was 2 μm. The tapered fiber was mounted on a 3-dimentional translation stage for more careful positioning near microlaser (figure 1).

3. Results and discussion

The lasing spectra of the studied microlaser with 40 μm diameter received by the tapered fiber and by the microobjective are shown in figure 1. The tapered fiber was located near the active region of the structures as shown in the inset to figure 1. To determine a threshold current we studied the evolution of the emission spectra received by the tapered fiber and by the microobjective with increasing injection current. We didn't observe any difference in the threshold currents of the microlasers determined by two methods. The lasing spectra received by the tapered fiber have lower intensity compare to that received by the microobjective. However, the ratio of the dominant mode intensity to spontaneous emission was noticeably higher for the case of the tapered fiber. The reason of the higher resonant mode intensity can be lasing mode coupling to the tapered fiber. Also, we studied the dependences of the dominant mode intensity on the distance between the tapered fiber and the microlaser's side wall (x). For the studied lasers a sharp intensity growth by 2-3 orders of magnitude was observed when the tapered fiber came in contact with the microlaser (figure 2). Any changes of the resonant line full width at half maximum were not found at the contact of the microlaser with fiber probably due to the low spectral resolution of the optical spectrum analyser used.

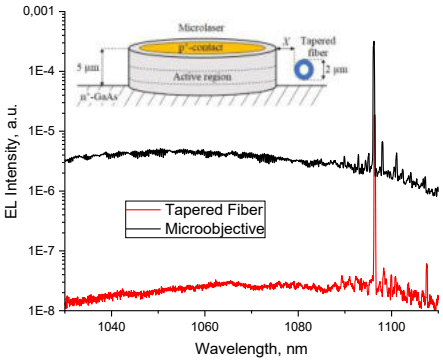

Figure 1. EL spectra of 40 μm MD laser at 10 mA current received by the tapered fiber and by the microobjective, an inset shows the coupling scheme.

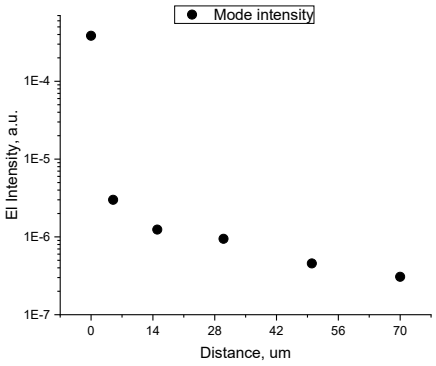

Figure 2. The dependence of the dominant mode intensity on the distance between the tapered fiber and the 20 μm MR laser.

Thus, for the first time, we realize the outcoupling of the lasing emission from an injection microdisk laser into a tapered fiber without the evidence of the lasing parameters deterioration.

Acknowledgments

This study was supported by Russian Foundation for Basic Research, project #20-02-00334. The tapered fiber was fabricated using the equipment of the Center for Collective Use VNIIOFI (ckp.vniiofi.ru).

References

[1] C Schmidt et al. 2009 *Physical Review A* **80** 4 043841
[2] N V Kryzhanovskaya et al 2019 *Journal of Applied Physics* **126** 6 063107
[3] K Srinivasan, O Painter 2007 *Physical Review A* **75** 2 023814
[4] M Cai et al 2000 *Optics letters* **25** 19 1430-2
[5] M V Maximov et al. 2020 Applied Sciences **10** 3 1038
[6] A D Ivanov, K N Min'kov, A A Samoilenko 2017 *Journal of Optical Technology* **84** 7 500-3

Luminescent properties of mixed $CsPb(Br_xI_{1-x})_3$ perovskite nanocrystals in borogermanate glass

R D Kharisova, A N Babkina, A S Pavliuk, K S Zyryanova

Research Center for Optical Material Engineering, ITMO University, Saint Petersburg 199034, Russia

e-mail: harisovarufina@gmail.com

Abstract. A series of borogermanate glasses with mixed $CsPb(Br_xI_{1-x})_3$ perovskite nanocrystals is synthesized. With the equimolar replacement of bromine by iodine ions, the intense luminescence shifts to the red region. By adjusting the Br/I ratio in the nanocrystals, it is possible to obtain a material with tunable luminescent properties in the range from 520 to 700 nm. The perovskite glass-ceramics obtained can be used as the adjustable radiation source.

1. Introduction

Optical materials based on cesium lead halide perovskite nanocrystals are promising due to their unique optical [1], optoelectronic [2], and photovoltaic [3] properties. Wide color gamut liquid crystal displays (LCDs) with quantum dot LEDs as backlight require narrow-FWHM and intense emission to achieve high system optical efficiency [4]. The convenience of using perovskite nanocrystals in this application lies in their ability to smoothly tune the luminescence location depending on the halogen ions ratio, obtaining the so-called mixed nanocrystals.

Herein, a series of borogermanate glasses with mixed $CsPb(Br/I)_3$ perovskite nanocrystals was synthesized and its luminescent properties under Br/I ratio were studied.

2. Material and methods

The initial glass matrix had the following composition: 6.67 ZnO-5.81 Na_2O-31.3 B_2O_3-50.53 GeO_2 mol. %. The perovskite nanocrystals were nucleated in a borogermanate network via spontaneous volume crystallization during glass annealing and additional heat treatment at temperatures above glass transition temperature (470°C). The synthesis was carried out in air atmosphere at a temperature of 950°C using quartz crucibles. A series under study contained glasses with different Br/I ratios in $CsPb(Br_xI_{1-x})_3$ nanocrystals, where x=1; 0.5; 0.4; 0.3; 0.2; 0 according to the batch composition.

The glass optical density spectra were measured by a Lambda 650 spectrophotometer (Perkin Elmer) in the spectral range of 200–900 nm with a step of 1 nm at room temperature. For the luminescence and excitation spectra recording, the LS-55 spectrofluorimeter (Perkin Elmer) was used. Absolute quantum yield was measured on an Absolute PL Quantum Yield Measurement System C9920-02G, -03G (Hamamatsu) consisting of multichannel analyzer with InGaAs sensor, integrating sphere unit, a Monochromatic light source with a 150 W Xenon light source and remote-controlled monochromator.

3. Experimental results

The luminescence spectra of the obtained glass-ceramics under 410 nm excitation and different heat treatment temperatures are shown in Figure 1. The luminescence band of purely bromide perovskite nanocrystals is in the region of 517-520 nm, depending on the heat treatment conditions, and of purely iodide - in the region of 684-692 nm. Almost no dependence of the luminescence location on the heat treatment temperature was observed since crystals were already isolated in the initial glasses, thus, during heat treatment only an additional increase in the crystal size occurred without nucleation.

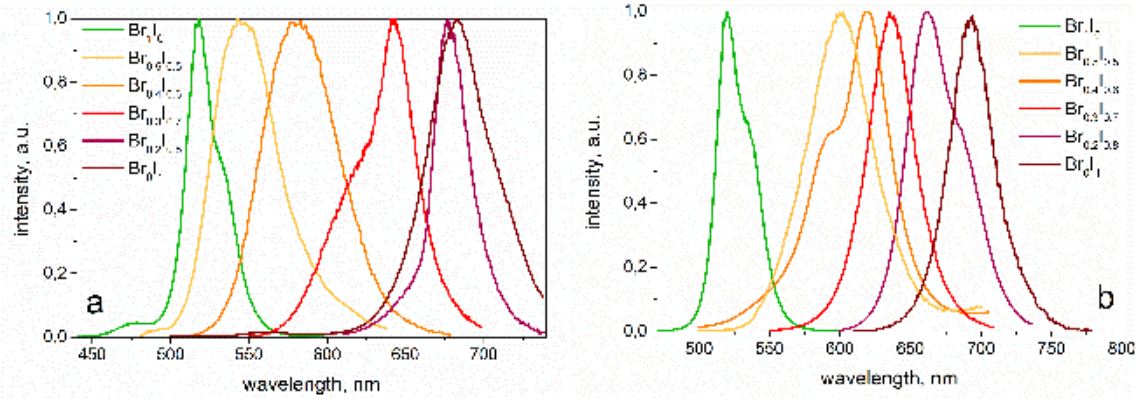

Figure 1. The luminescence spectra of the glass-ceramics with perovskite nanocrystals obtained after 470°C (a) and 550°C (b) heat treatment.

Figure 1 shows that with an increase of iodine content in the composition of perovskite nanocrystals, the luminescence band systematically shifts to the red region. However, the shift is not proportional to the change in the Br/I ratio. Since the current ratio was calculated based on the batch composition, during the synthesis, some of the halogens were volatilized, and their final ratio in the glass will be different. Most of the studied compositions of mixed perovskite crystals demonstrated a sufficiently high quantum yield, thus borogermanate glass-ceramics with $CsPb(Br_xI_{1-x})_3$ are a promising material for the development of adjustable radiation sources.

Acknowledgments

Optical measurements were funded by RPMA grant of School of Physics and Engineering of ITMO University. Glass synthesis was supported by the grant of the President of the Russian Federation for young PhD scientists No. MK-4235.2021.1.3.

References

[1] Kolobkova E, Kuznetsova M and Nikonorov N 2021 *J. Non. Cryst. Solids* **563** 120811

[2] Nam J K, Jung M S, Chai S U, Choi Y J, Kim D and Park J H 2017 *J. Phys. Chem. Lett.* **8** 2936–40

[3] Swarnkar A, Marshall A R, Sanehira E M, Chernomordik B D, Moore D T, Christians J A, Chakrabarti T and Luther J M 2016 *Science.* **354** 92-95

[4] Wang D, Wu D, Dong D, Chen W, Hao J, Qin J, Xu B, Wang K and Sun X 2016 *Nanoscale* **8** 11565–70

Classification and multipolar content of the eigenmodes of acoustic resonators with different symmetries

M. Tsimokha, V. Igoshin, A. Nikitina, I. Toftul [*], K. Frizyuk[+], and M. Petrov

The School of Physics and Engineering, ITMO University
{[*]itoftul@itmo.ru, [+]k.frizyuk@metalab.ifmo.ru}

Abstract. Acoustic resonators and their eigenmodes serve a grand role in analysing complex acoustic systems, such as acoustic metamaterials, phononic crystals, and topological structures. In this work, using group theory methodology we classified the eigenmodes for various resonator shapes and predicted the multipolar content of scattered fields. Results are supported by numerical simulations.

1. Introduction

The most important characteristics of any resonator are its eigenmode spectrum and field structure. Analytical solutions have been provided for a number of simple resonator shapes (e.g. a sphere) [1], but struggles for more complex shapes. Thereby the unified description of eigenmodes of an acoustic resonator is yet to be made. We use a powerful method from group theory analysis that has been utilized in many diverse domains of physics, such as optics, quantum chemistry, and solid-state physics [2–5]. The mode structure of a resonator is *defined by its symmetry* and can be classified by irreducible representations (irreps) of the symmetry group. In this work we show classification and multipole expansion of eigenmodes of acoustic resonators of different shape, and apply it to predict acoustic scattering content. We focuse solely on longitudinal waves in the monochromatic domain.

2. Results and discussion

2.1 Multipole expansion. Eigenmodes of a spherical resonator are solely defined by scalar spherical harmonics (one mode — one harmonic). Next, eigenmodes of any finite resonator can be decomposed in series of spherical harmonics, however this time each mode contains a particular set of harmonics or multipoles. This multipole content can be revealed from Wigner's theorem [6,7], which essentially states that only symmetry is responsible for the content of such decomposition.

We consider any finite resonator as a perturbation of a spherical one [8, 9]. That being so, the quasinormal modes of that resonator would have been composed of spherical eigenmodes. In other words, assessing the complex pressure amplitude, which describes an eigenmode of an acoustic resonator, we decompose it in a series of scalar spherical harmonics [7]. According to Wigner's theorem (W.T.), this eigenmode is transformed under a particular irrep, thus only spherical functions transformed under the same one will be present in that decomposition:

$$p_{mode}(\vec{r},\,\omega) \;=\; \sum_{p\,=odd,\,even}\;\sum_{l=0}^{\infty}\;\sum_{m\,=\,-l}^{l} b_{plm}(r,\omega)Y_{plm}(\theta,\phi) \;=\; \sum_{(p,l,m)\in irrep} b_{plm}(r,\omega)Y_{plm}(\theta,\phi)$$

2.2 Reducing the symmetry. We have classified resonators of various symmetry groups and also focused on multipole content of the resonator in case of decreased symmetry[7]. In Fig. 1 the case of the pyramid resonator of the C_{4v} symmetry group lowering its symmetry to C_{2v} is shown. With decreasing symmetry a number of irreps is lessening, namely two one-dimensional representations (A_2 and B_2) have merged together forming another one (A_2). In addition, some of the degeneracies that come out of a rotational symmetry along the vertical axis have been cancelled with its destruction: two-dimensional representation E has produced two one-dimensional ones — B_1 and B_2.

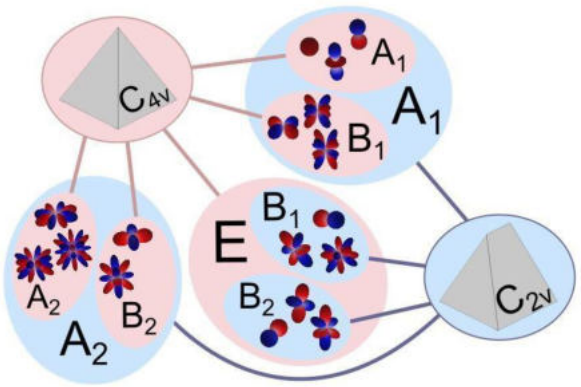

Fig. 1. Change of modes and multipole content due to the symmetry reduction of the scatterer.

2.3 Acoustic wave scattering. We consider the scattering process, with the incident wave propagating along the z-axis. In our case as the incident wave contains only spherical functions with m = 0, so the excited modes would also contain a spherical function with m = 0, but also admixed m due to the low symmetry of the nanoparticle. We confirmed all the results by numerical modelling in COMSOL Multiphysics™ software and provide the similarities and dissimilarities with optics [7, 8].

Conclusion

Our results draw a parallel between optics and acoustics, showing that the similarities in mode analysis and scattering processes.

Acknowledgments

This work was supported by Russian Science Foundation (project 20-72-10141) and by Priority 2030 Federal Academic Leadership Program

References

[1] V. C. Anderson, The Journal of the Acoustical Society of America 22, 426 (1950).
[2] G. Ma and P. Sheng, Science Advances 2, 10.1126/sci- adv.1501595 (2016).
[3] L. Landau and E. Lifshitz, Quantum Mechanics: Non-Relativistic Theory, Course of Theoretical Physics (Elsevier Science, 1981).
[4] E. L. Ivchenko and G. Pikus, Crystal symmetry, in Superlattices and Other Heterostructures: Symmetry and Optical Phenomena, Springer Series in Solid-State Sciences, (Springer, 1995) p. 9–38.
[5] M. S. Dresselhaus, G. Dresselhaus, and A. Jorio, Group Theory. Application to the Physics of Condensed Matter (Springer, 2008).
[6] A. Piroth and J. Solyom, Fundamentals of the Physics of Solids (Springer, Berlin, 2007).
[7] Tsimokha, M., Igoshin, V., Nikitina, A., Petrov, M., Toftul, I., & Frizyuk, K. (2021). arXiv, 2110.11220.
[8] S. Gladyshev, K. Frizyuk, and A. Bogdanov, Phys. Rev. B 102, 075103 (2020).
[9] M. B. Doost, W. Langbein, and E. A. Muljarov, Phys. Rev. A 90, 013834 (2014).

Simple expressions for the quantum entanglement of non-monochromatic photons on a waveguide beam splitter

Yu V Tsykareva and D N Makarov

Northern Arctic Federal University named after M V Lomonosov,
Arkhangelsk 163002, Russia

E-mail: aisonoka@gmail.com

Abstract. Simple expressions for the quantum entanglement of monochromatic and non-monochromatic photons on a waveguide beam splitter were found and analysed using von Neumann entropy. It will be shown the great difference between both cases, which can be used to create large quantum entanglement.

1. Introduction

Studying beam splitters as sources of entangled photons is a relevant topic in modern physics. The interest towards them appears mainly due to the fact that such sources of entangled photons could be used in many applications of quantum and nonlinear physics such as: quantum metrology [1], quantum computers [2] etc. One of the most promising beam splitter types for quantum technologies is the linear beam splitter. This beam splitter consists of two coupled waveguides on a substrate, where photon entanglement happens at the point of maximum waveguide contact due to the magnetic field overlay. This beam splitter type is actively used in creating integrated circuits based on quantum optics technologies [3] and in building optical quantum computers [2].

2. Results and discussion

Simple expressions that characterize quantum entanglement with a single parameter - reflectance R - have already been obtained for monochromatic photons previously in work [4]. Reflectance itself is determined by the parameters of the original photons presented as harmonic oscillators. In this work we explore a case of non-monochromatic photons [5] with a linear beam splitter, obtain simple expressions for the quantum entanglement of these photons and complete a comparative analysis of cases with monochromatic and non-monochromatic photons using the von Neumann entropy. It is demonstrated that the obtained expressions can be applied in quantum optics, particularly, in quantum metrology to create a large source of quantum entanglement.

Acknowledgments

The work was supported by Russian Science Foundation grant № 20-72-10151.

References

[1] Pezze L, Smerzi A, Oberthaler M K, Schmied R and Treutlein Ph 2018 *Rev. Mod. Phys.* **90** 035005

[2] Ladd T D, Jelezko F, Laflamme R, Nakamura Y, Monroe C and O'Brien J L 2010 *Nature* **464** 45–53

[3] He Y M, Clark G, Schaibley J et al 2015 *Nature Nanotech* **10** 497–502
[4] Makarov D N 2020 *Phys. Rev.* E **102** 052213
[5] Makarov D N and Tsykareva Yu V 2022 *Entropy* **24** 49

Terahertz response in superconducting niobium diselenide

K V Shein[1,3,5], E V Zharkova[2], P I Bondareva[1], I A Gayduchenko[3], D A Bandurin[2], IM Charaev[1],and G N Goltsman[1,3]

[1] Moscow Pedagogical State University, Moscow, 119435, Russia
[2] Programmable functional materials lab, Brain and Consciousness Research Center, Moscow 121205, Russia.
[3] National Research University Higher School of Economics, Moscow, 101000, Russia
[5] Author to whom any correspondence should be addressed

sheinkv97@gmail.com

Abstract. Here we report the terahertz response of thin $NbSe_2$ flakes in a superconducting state under the 140 GHz radiation. The $NbSe_2$ flakes with thickness of 15-20 nm were measured, in which a superconducting transition with a critical temperature in a range from 6.5 to 7.25K, respectively, was observed. The dependence of the response on the generator power and the bias current was also measured.

.

1. Introduction

Thin superconducting films are used as the basis of various quantum detectors, such as SSPD[1] and HEB[2], which are in demand in various fields such as astronomy and quantum communications. The most significant parameter of these detectors is the thickness of the superconducting film, which affects the detector. Therefore, using of two-dimensional superconducting materials is attractive since the possibility of obtaining films with a thickness of 1-2 atomic layers.

2. Materials and fabrication

The detector fabrication technology included the following steps. We used a silicon substrate(Si) with a 285 nm silicon oxide(SiO_2). On the following step, two Ti/Au(5/20 nm) electrical contacts were fabricated using the e-beam lithography technique. A 75-Ohm logarithmic-spiral antenna was made in contact with them for better matching of terahertz radiation to the detector [3] (Figure 1). $NbSe_2$ flakes have tendency to degrade [4] in air atmosphere, therefore, to avoid this effect the flakes were encapsulated in hexagonal boron nitride (hBN).

3. Results

We use a tuning backward-wave oscillator (BWO) in frequency range from 129 to 140 GHz as a radiation source. The terahertz radiation was modulated by 20-kHz frequency for direct-detection method. The response dependence on the generator power and the bias current change was also measured.

Figure 1. Optical image of the $NbSe_2$ detector integrated with a logarithmic spiral.

4. Conclusion

We have demonstrated a THz response in thin $NbSe_2$ film in a superconducting state. According to accomplished results, we suggest that material can be used in terahertz superconducting HEB (hot electron bolometers).

Acknowledgments

Acknowledgments The reported study was funded by RSF, project number 21-79-20084 21

References

[1] G. N. Gol'tsman, O. Okunev, G. Chulkova, A. Lipatov, A. Semenov, K. Smirnov, B. Voronov, A. Dzardanov, C. Williams and R. Sobolewski, Appl. Phys. Lett. 79, 705 (2001).

[2] D. Cunnane et al., "Characterization of MgB2 Superconducting Hot Electron Bolometers", IEEE Trans. Appl. Supercond., vol. 25, no. 3, pp. 2300206, Jun. 2015.

[3] Tretyakov I, Ryabchun S, Finkel M, Maslennikova A, Kaurova N, Lobastova A, Voronov B and Gol'tsman G ,2011 Low noise and wide bandwidth of NbN hotelectron bolometer mixers Appl. Phys. Lett. 98 033507

[4] M. S. El-Bana, D. Wolverson, S. Russo, G. Balakrishnan, D. M. Paul and S. J. Bending, Supercond. Sci. Tech. 26, 125020 (2013).

Optical second-harmonic response of an axially-symmetric medium under radially polarized excitation

S A Scherbak[1], **I V Reshetov**[1]
[1]Department of Physics and Technology of Nanostructures, St. Petersburg Academic University RAS, St. Petersburg 194021, Russia

Abstract. We simulated optical second harmonic (SH) response, both surface and bulk, of axially symmetric media excited by tightly focused radially polarized fundamental beams. The calculations performed showed a highly localized character of SH generation (SHG). Radiation patterns of SH waves were compared for surface and bulk SH responses. The model developed is applicable for SHG by interfaces, films and poled glasses.

1. Introduction

It is known that radially polarized light waves focused with a high numerical aperture (NA) objective acquire a significant longitudinal component of electric field near the focal plane [1]. This peculiar distribution of electric field can provide a nonlinear optical response that differs significantly from that characteristic of trivially polarized excitations. Particularly, this allows measurements of second order nonlinearity of highly symmetrical (e.g., axial) structures under normal incidence. In this study, we developed a model that describes both surface and bulk second harmonic response of an axially symmetric medium under tightly focused radially polarized excitation.

2. Theory

We consider a radially polarized light beam falling normally (along z-axis) to a focusing lens and then to the interface between two media with indices n_1 and n_2. Resulting equations for components of the second harmonic electric field in the far-field zone in the direction defined by the polar angle θ are:

$$E_\rho^{2\omega}(\theta) = P_1 \sin\theta\cos\theta - P_2 \sin^2\theta + P_2, \tag{1}$$

$$E_z^{2\omega}(\theta) = P_1 \cos^2\theta - P_2 \sin\theta\cos\theta - P_1. \tag{2}$$

where parameters P_1 and P_2 are:

$$P_1 = 2\pi \int_0^{+\infty} rdr \int_{z_0}^{z_1} dz P_\perp(r,z) J_0(Kr\sin\theta) e^{iKz\cos\theta}, \tag{3}$$

$$P_2 = 2\pi i \int_0^{+\infty} rdr \int_{z_0}^{z_1} dz P_\parallel(r,z) J_1(Kr\sin\theta) e^{iKz\cos\theta}, \tag{4}$$

z_0 is a coordinate of an interface of the sample, z_1 is a coordinate of a rare side of the nonlinear layer, K – wave vector of the second harmonic wave. Components of nonlinear polarizability **P** are connected with components of the fundamental field via nonlinear constitutive equations. For an axially symmetric medium, these are:

$$P_\perp = \chi_{\perp\perp\perp} E_z^2 + \chi_{\perp\parallel\parallel} E_r^2, \tag{5}$$

$$P_{\parallel} = \chi_{\perp\perp\parallel} E_z E_r , \tag{6}$$

where $\chi_{\perp\perp\perp}$, $\chi_{\parallel\perp\parallel}$ and $\chi_{\perp\parallel\parallel}$ are nonzero components of the second order susceptibility tensor $\boldsymbol{\chi}$. Surface nonlinearity can be considered using substitution $\boldsymbol{\chi} \to \boldsymbol{\chi}^{surf} \delta(z - z_0)$, where $\delta(z\text{-}z_0)$ is the Dirac δ-function. Expressions for distribution of a fundamental electric field of a radially polarized light wave, E_z and E_r, near the focal plane are presented in Ref.[2]. Squared modulus of SH field, which component are described by Eqs. (1-2), integrated over all θ is the total intensity of the radiated SH signal.

3. Results

In calculations, we considered fundamental wavelength of 1064 nm, the objective NA=0.9, n_1=1, n_2=1.51, $\chi_{\perp\perp\perp} = 3\chi_{\parallel\perp\parallel} = 3\chi_{\perp\parallel\parallel}$. This relation between the components of $\boldsymbol{\chi}$ is a so-called "1/3 rule" which is common for poled glasses [3]. In the case of only surface nonlinearity, we calculated SH signal depending on focus shift z_f relatively to the nonlinear surface. This dependence, which is presented in Figure 1a, demonstrates a symmetric peak with a half-width of ~2 μm, i.e. 1-μm focus shift from the surface results in two-fold decrease of SH signal. For 3-μm focus shift, the decrease is 10-fold. Note, for smaller NAs this dependence is broader and the SH signal – lower.

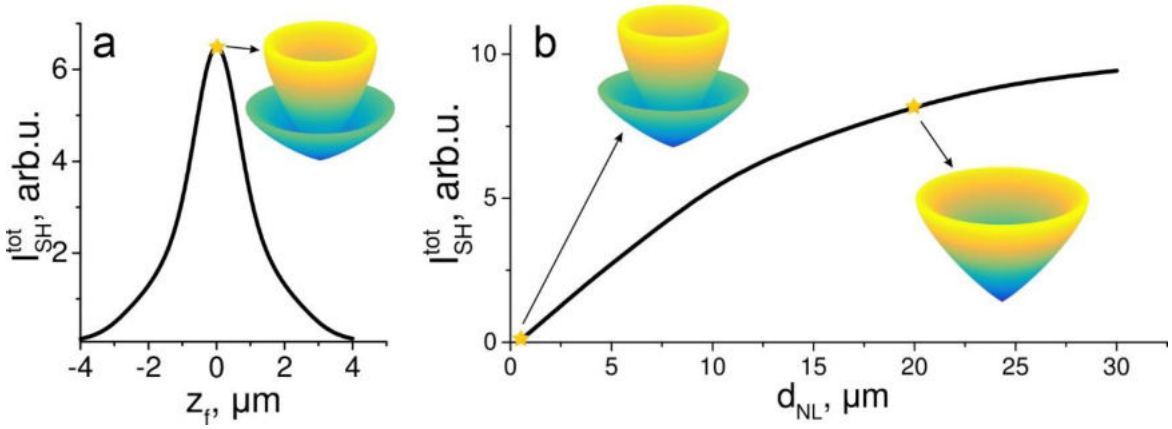

Figure 1. a) Total signal of surface SH generation vs focus shift from the surface. b) Total signal of bulk SH generation vs thickness of nonlinear layer. Insets: radiation patterns of SH waves.

In Figure 1b we demonstrate total SH signal for nonlinear layer vs thickness of the layer, d_{NL}. The signal expectedly increases with the thickness. The dependence saturates, since excitation is localized. Note, for non-localized regime of SHG under weakly focused excitation, total SH signal depends on the thickness of nonlinear layer quadratically. Also, in the insets in Figure 1 we schematically present radiation patterns of SH waves. They are expectedly axially symmetric. Moreover, they are similar in the cases of surface nonlinearity and thin (0.5 μm) nonlinear layer – two enclosed empty cones, whereas for thicker nonlinear layer (20 μm) the pattern represents a single empty cone. This transformation occurs because of different dependence of transverse and longitudinal components of fundamental field on z-coordinate and of different impact of $\boldsymbol{\chi}$ components in SHG patterns.

This study was funded by RSF according to the research project № 21-72-00048

4. References

[1] Hao B and Leger J 2007 Experimental measurement of longitudinal component in the vicinity of focused radially polarized beam *Opt. Express* **15** 3550

[2] Biss D P and Brown T G 2001 Cylindrical vector beam focusing through a dielectric interface *Opt. Express* **9** 490

[3] Kazansky P G and Russel P S J 1994 Thermally poled glass: frozen-in electric field or oriented dipoles? *Opt. Commun.* **110** 611–4

Nanoscale waveguide beam splitter in quantum technologies

Makarova K.A.[1,*], Tsykareva Yu.V.[1], Kapustin S.N.[1], Goshev A.A.[1], Kharlamova A.A.[1], Makarov D.N.[1]

[1]Northern (Arctic) Federal University, Arkhangelsk, 163002, Russia

[*]E-mail: ksenya931408@yandex.ru

Abstract. It is shown that a nanosized waveguide beam splitter has a significant difference from a similar device, but on a larger scale. The results are important for quantum technologies which use such beam splitter.

1. Introduction

It is well known that the waveguide beam splitter is one of the main devices in quantum technologies [1,2]. This device has a great prospect of application due to its small size. This, in turn, leads to the fact that at small sizes new phenomena can arise that are not inherent in similar devices, but on a large scale. It is usually considered that the main characteristics of a waveguide beam splitter are the reflection coefficients R and transmission coefficients T are constant values. This means that by setting these parameters one can always obtain the required characteristics at the output ports of the beam splitter. It was shown in [3,4] that using a beam splitter based on coupled waveguides, i.e. waveguide beam splitters Hong-Ou-Mandel (HOM) effect may not be performed even if R=T=1/2 and the photons used are identical. It was also pointed out in these papers [3,4,5] that in the main such changes in the example of the HOM effect appear for sufficiently small waveguide beam splitters.

Here we show that this problem is inherent not only for the HOM effect, but also for a waveguide beam splitter in general, which has sufficiently small dimensions, and this is a micro and nano scale. Undoubtedly, the results obtained are important primarily for quantum technologies, since the use of micro and nanosized beam splitters is one of the prospects that is already beginning to be realized today.

2. Result

It has been shown in [3,5] that the reflection coefficient R and the transmittance T for a waveguide beam splitter are

$$R = \frac{\sin^2\left(\Omega t_{BS}/2\sqrt{1+\varepsilon^2}\right)}{(1+\varepsilon^2)};\ T = 1 - R;\ \ \varepsilon = \frac{\omega_2 - \omega_1}{\Omega}, \tag{1}$$

where Ω is a certain frequency characterizing the BS; $t_{BS} = L/v$ is the time of interaction of photons in the BS (L is the length of the coupled region of the waveguide, v is the speed of wave propagation in the waveguide); ω_1 and ω_2 are the photon frequencies in the first and

second ports, respectively. It should be added that the greater the coupling in the waveguides, the greater the value of Ω and vice versa. Thus, we can regulate the coupling in the waveguide by changing Ω.

The final wave function of the photons at the beam splitter outputs is

$$\Psi_{out} = \sum_{k=0}^{s_1+s_2} \int \phi(\omega_1, \omega_2) c_{k,p} |k, s_1 + s_2 - k\rangle d\omega_1 d\omega_2, \quad (2)$$

where $|k, s_1 + s_2 - k\rangle = |k\rangle|p\rangle$ is the state of the photons at the output ports of the BS, $c_{k,p}$ these are some coefficients, see [5], $\phi(\omega_1, \omega_2)$ is the joint spectral amplitude (JSA) of the two-modes wavefunction ($\int |\phi(\omega_1, \omega_2)|^2 d\omega_1 d\omega_2 = 1$).

In Eq. (2) the coefficient $c_{k,p}$ depends on R and T. Analysis and numerical calculations show that if we consider the photons to be monochromatic, the Ψ_{out} wave function at the output ports of the beam splitter has the same form at small and large dimensions of the beam splitter. If one assumes that the incoming photons are non-monochromatic (this is usually the case), then at small and large dimensions of the beam splitter the wave functions of photons at the output ports have a different form.

3. Conclusion

Thus, it was shown that the wave function of photons at the output ports of a beam splitter can depend significantly on the dimensions of the waveguide beam splitter. First of all, this dependence is determined by the non-monochromaticity of photons incident on the input ports of the beam splitter. There is also a dependence on the material from which the beam splitter is made, since the coefficients R and T depend on Ω.

The results obtained are important for beam splitters with micro and nanometer scales.

Acknowledgments

The study was supported by the Russian Science Foundation, project No. 20-72-10151

References

[1] J. W. Pan, Z.B. Chen, C. Y. Lu, H. Weinfurter, A. Zeilinger and M. Zukowski, 2012, Rev. Mod. Phys. 84, 777.

[2] P. Kok, W. J. Munro, K. Nemoto, T. C. Ralph, J. P. Dowling, G. J. Milburn, 2007, Rev. Mod. Phys. 79, 135

[3] D.N. Makarov, Optics Letters, 2020, 45(22) 6322–6325.

[4] D.N. Makarov, Scientific Reports, 2020, 10(1) 20124.

[5] D.N. Makarov, E.S. Gusarevich, A.A. Goshev, K.A. Makarova, S.N. Kapustin, A.A. Kharlamova, Yu.V. Tsykareva, 2021, Scientific Reports, 11, 10274.

Исследование устойчивости серебряных зеркал с защитными покрытиями к условиям высокой влажности и термоциклирования

Терещенко И. Б.[1,2], Самсонов Д.С.[1,2], Мухин Е.Е.[1,2], Губаль А.Р.[3], Марчий Г.В.[1], Комаревцев И.М.[4]
[1]ФТИ им. Иоффе
[2]АО "Спектрал-Тех"
[3]Институт химии СПбГУ
[4]Политехнический университет

Собирающие системы оптических диагностик ИТЭР должны обеспечить долговременную оптическую стабильность в условиях значительных эксплуатационных (вибрация), радиационных, тепловых и прочих нагрузок. Для многих диагностических систем, собирающие системы содержат значительное количество отражений, что предъявляет высокие требования к коэффициенту отражения каждого зеркала.

На состояние поверхности внутривакуумных зеркал, находящихся не в прямой видимости плазмы, в первую очередь влияет аварийный выброс пара. При таком выбросе зеркало продолжительное время находится под воздействием высокой влажности, а также несколько часов при температуре более 250°C. Это может приводить к снижению отражательной способности зеркал вследствие химического взаимодействия материала поверхности с водой и растворенными в ней веществами.

Известно, что материалом, наиболее стойким к воздействию пара, является Rh. Однако имеющий коэффициент отражения R<86% в видимой области спектра не удовлетворяет требованиям отражательной способности зеркал R>90%. Таким образом, наиболее подходящим материалом является Ag. Однако Ag легко подвержено коррозии под воздействием S, Cl, O, присутствующих в паре [1,2].

В качестве способа защиты отражающего слоя Ag выбран барьерный, механизм работы которого заключается в том, чтобы создать механическое препятствие (защитный слой) на пути коррозионных агентов к слою Ag. Конструкции защитного покрытия состоят из одного SiN_x или трех чередующихся слоев SiN_x и SiO_x общей толщиной не более 30 нм. В качестве адгезионного слоя в интерфейсе между подложкой SS 316L(N)-IG и слоем Ag выбран NiV, а в интерфейсе между защитным покрытием и слоем Ag тонкий слой $NiVN_x$ или NiV, толщина которого составляет менее 1 нм.

Толщины слоев, входящих в защитное покрытие, а также тонкого адгезионный слоя, должны быть достаточно тонкими, чтобы не снижать не значительно отражательную способность серебра и обеспечивать минимальные механические напряжения [3,4] с одной стороны и достаточно толстыми, чтобы эффективно препятствовать механизму коррозии с другой стороны. Наличие нескольких слоев в защитном покрытии позволяет компенсировать дефекты, возникающие при формировании слоев, а также скорректировать спектральную характеристику за счет интерференции.

Литература.

[1]. Jobst, P. J., Stenzel, O., "Optical properties of unprotected and protected sputtered silver films: Surface morphology vs. UV/VIS reflectance," Adv. Opt. Technol. 3, 91–102 (2014).
[2]. Vargas, O. L. Valdez, S. B., "The corrosion of silver in indoor conditions of an assembly process in the microelectronics industry," Anti-Corrosion Methods Mater. 56, 218–225 (2009).
[3]. Grigoriev F.V., Sulimov V.B., “Atomistic simulation of stresses in growing silicon dioxide films”, Coatings 10(3), 220, (2020)
[4]. Schwinde S., Shurmann M., “Protected silver coatings for reflectors”, CEAS Space Journal, 11, 579-587, (2019)

Up-conversional luminescence particles based on $NaYF_4$ matched with passive optical devices

Asharchuk I. M.[1], Vovk N. A[1], Sokolov V.I.[2], Gorychuk I. O.[2], Minaev N.V. [2] and Tarkhov M. A. [1]

[1] Institute of Nanotechnology of Microelectronics of the Russian Academy of Sciences, Moscow 119991,Russia
[2] Institute of Photon Technologies, Federal Scientific Research Centre 'Crystallography and Photonics', Russian Academy of Sciences, Troitsk, Moscow 108840, Russia

e-mail: ilyaasharchuk@gmail.com

Abstract. The work is aimed at creating matching passive elements with optical planar devices. A three-dimensional structure-interface was made to match the position of the center of the optical fiber with active optical elements. NaYF4 microparticles doped with rare-earth ions Yb3+, Tm3+, Er3+ with a diameter of 2.2 μm and 1.1.65 μm were synthesized. The formation of hemispherical lenses with radii from 0.75 to 25 μm has been demonstrated for optical matching with optical fiber by IR (infrared) photopolymerization.

1. Introduction

Today, the directions for creating single-photon radiation sources necessary for quantum computing, quantum cryptography, etc. are relevant [1]. However, an equally important problem is the manufacture of matching elements for detecting and delivering radiation to single-photon sources and detectors, respectively [2]. Up-conversion nano particles (UCNPs) doped with Er^{3+}, Tm^{3+}, Yb^{3+} lanthanides can serve as single-photon emitters; they have anti-Stokes emission, manifested by the generation of high-energy photons through multiphoton absorption of low-energy photons [1]. Compared to traditional phosphors such as fluorescent dyes and quantum dots, UCNPs are resistant to photobleaching, they are photostable and have real intermediate energy levels [3–6]. Such features of UCNP with matching technology become attractive for the development of single-photon radiation sources necessary for quantum computing.

2. Materials and techniques

To obtain fluoride microcrystals of the composition $NaY_{0.78}F4$: $Yb_{0.2}$, $Er_{0.02}$, $NaY_{0.78}F_4$: $Yb_{0.2}$, $Tm_{0.006}$ with a hexagonal crystal lattice (β-form), commercial reagents were used: oxides of yttrium, ytterbium, erbium, sodium carbonate , oleic acid 90%, 1-octadecene 90% (Sigma-Aldrich), and trifluoroacetic acid 99% (PanReac). Synthesis was carried out by thermal decomposition of trifluoroacetates of rare earth elements and sodium in an oxygen-free environment in a mixture of oleic acid and 1-octadecene. To determine the phase of the crystals, X-ray diffraction analysis (XRD - X-Ray Diffractometry) was used. The electron microscopy (SEM) method was used to analyze the shape and size of the particles. To form polymer microlenses, we used an original approach, NIR photopolymerization [7] based on lanthanide-doped up-conversion microparticles (UCMP) NaYF4:Yb,Tm. UCMPs convert NIR light into ultraviolet (UV) or visible (VIS) light, which in turn triggers the photopolymerization reaction in Dental Clear photopolymer (HARZLabs, Russia). The microparticles were deposited on the substrate by centrifugation at a speed of 1800 min-1 for 30 s. For the photopolymerization process, a continuous

laser with a wavelength of 975 nm (PL980P330J, Thorlabs) and an incident power of 50 mW was used. The radiation was focused using an Olympus UPlanSApo 60x/1.2 NA objective. W.

The concept of the formation process is shown in the figure 1. Determination of the morphology of microlenses with a radius of 1.55 μm was carried out using atomic force microscopy in the contact mode of the probe. The NFOL process was used to create the microadapter. Polymethyl methacrylate (PMMA) 495K A2 is used as a spin-coated resistive material[8].

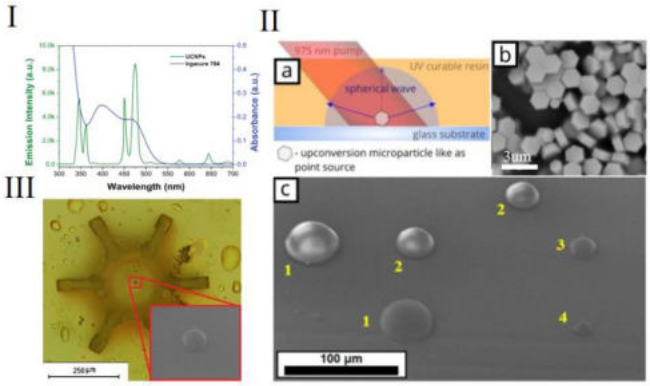

Figure. 1. I. Luminescence spectra of an up-inverting $NaYF_4$ microparticle: Yb^{3+}, Tm^{3+} (green curve) and absorption spectra of the Irgacure 784 photoinitiator (blue curve). II. a) Schematic representation of the principle of IR photopolymerization, b) SEM photograph of hemispherical microlenses formed by IR photopolymerization with different exposure times by 980 nm radiation, c) SEM inset shows $NaYF_4$: Yb^{3+}, Tm^{3+} particles III. Three-dimensional structure of the optical fiber interface formed above the microlens.

Results

Synthesized microparticles with a hexagonal crystal lattice and low dispersion of diameter d = 1.65 - 2.2 μm for $NaYF_4$:$Yb^{3+}Er^{3+}$ and $NaYF_4$:Yb^{3+}, Tm^{3+}, respectively. Hemispherical microlenses with radii from 0.75 to 25 μm were obtained. A microadapter for standard single-mode and multimode fibers was fabricated by two-photon photopolymerization.

Conclusion

The developed technological approach to the creation of a microoptical holder for standard single-mode and multimode fibers is demonstrated. This type of holder can be used to manufacture an optical matching unit for optical fibers with sensitive optical elements. Which allows you to combine the position of the center of the optical fiber with active optical elements. The resulting interface unit can be used in planar integrated optical microdevices.

Acknowledgments

The work was supported by project 1021061509690-0-1.2.1. Ministry of Education and Science of the Russian Federation.

References

[1] Sarah Thomas & Pascale Senellart 2021 *Nature Nanotechnology* **12**, 367–368
[2] Henrik Mäntynen *et. al* 2019 *Nanophotonics*; **8(5)** 747–769
[3] Zhou, B., *et. al*. 2015 *Nature Nanotechnolgy.* **10**, 924–936
[4] Liu, Y. *et. al.* 2017 *Nature* **543**, 229–233
[5] Karimov D.N. et. al. 2020 *Nanotechnologies in russia*.. **15**, P. 655-678
[6] Demina P . *et. al.* 2019 *Molecules **24***, 2476
[7] Minaev N. V. *et. al*. 2018 *Laser Phys. Lett.***15,** 1–6

Optimization of gating signal parameters of sine-gated single-photon detector based on InGaAs/InP single-photon avalanche diodes

A. V. Losev[*1,2,3], **V. V. Zavodilenko**[1,2], **A. A. Filyaev**[1,2], **A. A. Koziy**[1,2], **Y. V. Kurochkin**[1,2,3]

[1]"QRate" LLC, St. Novaya, d. 100, Moscow region, Odintsovo, Skolkovo, 143026, Russia.
[2]NTI Center for Quantum Communications, National University of Science and Technology MISiS, Leninsky prospekt 4, Moscow, 119049, Russia
[3]National University of Science and Technology MISIS, Leninsky prospect, 4, Moscow, 119333, Russia.

E-mail: a.losev@goqrate.com

Abstract. The research object of this work is a self-developed sine wave gated single-photon detector (SPD) for 1550 nm wavelength primary for quantum key distribution (QKD) usage. The development of a simple and effective algorithm for optimizing the signal parameters was carried out on the basis of an analysis of the influence of DC bias voltage and AC gate amplitude on the SPD's functional parameters. Such optimization showed practical benefits while SPD was set up on the QKD device. We admitted that the dark count rate decreases with an increase in gating voltage with fixed photon detection efficiency.

1. Introduction

Single-photon detector (SPD) is a device, that is sensitive to single photons with a specific wavelength. SPDs have many applications, such as quantum key distribution (QKD) [1], 3D imaging systems (LIDAR) [2], biomarker tomography [3] etc. SPD's structure is not universal, it's designed for a specific application and operating parameters and is based on various physical principals. The optimal device for creating a miniature SPD and compact QKD device as a whole is InGaAs/InP single-photon avalanche diode (SPAD).

InGaAs/InP SPAD control electronics for performing sine-gating has a set of important for effective diode's work parameters, such as DC bias voltage, AC bias voltage (gating signal), the shape of gating signal, and dead time. It's quite an important but a laborious task to find the optimal parameters list to make photon detection efficiency (PDE) high enough (10 – 20 %), dark count rate (DCR) low enough (< 200 Hz) and afterpulse probability (AP) low enough too (< 1 %). In this paper, we explore the influence of gating parameters on PDE, DCR, and AP to make some recommendations about tuning the InGaAs/InP SPAD biasing scheme to increase the efficiency of a whole QKD device.

2. Result and discussion

This work determines the effective operation mode of sine-gated InGaAs/InP SPAD as ensuring the minimum DCR value at a given PDE. The afterpulse probability AP is also essential, but

it's a secondary parameter in our optimization criteria. If we have a similar DCR with constant PDE with different operational parameters, we will choose the optimal point according to AP. Such optimization criteria are suitable for long-distance QKD, where the count rate is not so much higher than DCR. Also, we offer one more optimization criteria – the minimum of $SNR = PDE/DCR$ $[\%/Hz]$, but the main disadvantage of such approach is that the optimal point usually has low PDE (< 5 %). This point will not be optimal for QKD as a whole.

We investigate nine commercially available InGaAs/InP SPADs with similar back-illuminated structures with a diameter of the active region $D \approx 25$ μm. The measurement results for one of the investigated SPD are presented in Figure 1.

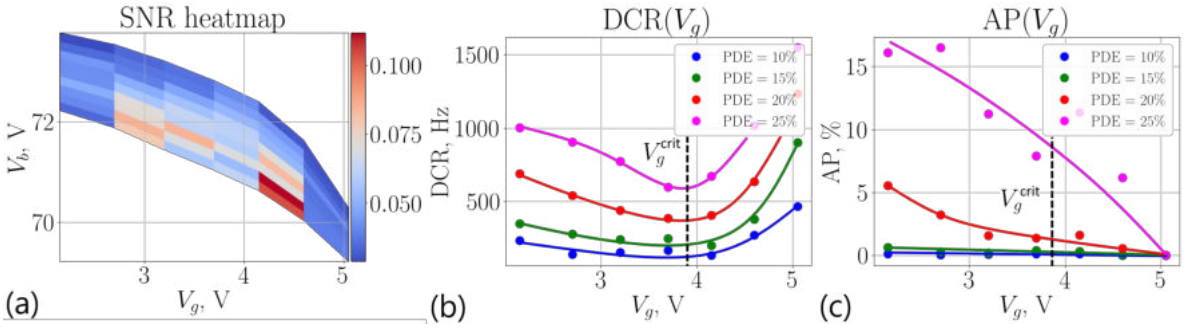

Figure 1. SNR (a), DCR (b) and AP (c) dependencies for one of the investigated SPD with parameters: $V_{br} = 73.73$ V, $T = -50$ $^\circ C$.

After analyzing the measurement results, we received the following important conclusions: approach with SNR based optimization is not so good because, in practice, we need to set up two SPDs with similar PDE parameters for effective QKD device work (we desire that DCR and AP parameters have coincided too, but this is not a critical requirement); increasing the gate voltage for a lot of SPDs to decrease the DCR with fixed PDE, up to fast DCR growing, due to the charge-persistence effect; increasing gate amplitude V_g with fixed PDE helps decrease afterpulse probability AP, and the charge-persistence effect leads to incorrectly determining its actual value.

3. Conclusion

In this work, we have studied the influence of the gating signal parameters on the main operational parameters of the SPD: PDE, DCR, and AP.

We proposed universal recommendations for increasing the performance of the SPD with sinusoidal gating. Recommendations are based on the established relationship of DCR and AP decrease with increasing gate amplitude. Using the described dependence has made it possible to reduce the DCR up to three times and AP up to 7 times for one of the measured SPDs. Other SPDs have lower optimization impacts, but are still very significant. The proposed simple optimization algorithm has shown practical use at the QKD device.

References

[1] Kiktenko E O, Pozhar N O, Anufriev M N, Trushechkin A S, Yunusov R R, Kurochkin Y V, Lvovsky A I and Fedorov A K 2018 *Quantum Science and Technology* **3**(3) 035004

[2] Yu C, Shangguan M, Xia H, Zhang J, Dou X and Pan J W 2017 *Opt. Express* **25**(13) 14611–14620

[3] Al-Rawhani M A et al. 2019 *Optical Engineering* **67**(2) 614-623 *Physical Review Applied* **13**(5) 054027

Modification of the optical and electrical properties of NiO films by thermal annealing

Y Enns[1,2], A Kazakin[1,2], I Komarevtsev[1,2], E Vyacheslavova[1], M Mishin[1]

[1]Alferov University, St. Petersburg, Russia
[2]Peter the Great Saint-Petersburg Polytechnic University, St. Petersburg, Russia

Abstract. This paper presents the results of studying the effect of thermal annealing on the optical and electrical characteristics of NiO films. The influence of thermal annealing on the characteristics of NiO films was studied on films obtained by DC magnetron sputtering. The results of optical and electrical studies have shown that annealing at 550°C leads to an increase in transparency from 5% to 80% at a wavelength of 700 nm and increase in resistivity from 0.2 Ω cm to 1460 Ω cm.

1. Introduction

There is an increase in attention to transition metal oxides such as TiO_2, MoO_3, WO_3, CuO, ZnO, NiO and others. These materials can be used both for manufacturing power diode structures [1] and for optoelectronic applications [2]. Nickel oxide (NiO) is the most prominent representative of this class of substances. At the moment, there are several models for the conductivity of semiconductor nickel oxide, but all of them are based on the fact that NiO is a direct-gap material, has its own hole conductivity, and has a band gap of 3.6–4.0 eV. Thus, this oxide semiconductor has a high prospect in optoelectronic devices.

NiO films can be synthesized by various methods, among which the method of magnetron sputtering is highly promising, due to the high quality of the film, low cost, and high speed of coating formation. Films are deposited using both RF magnetrons and targets made of high-purity Ni or stoichiometric NiO [3] and DC magnetrons with Ni targets [4]. In both cases, deposition occurs by adding O_2 to the working gas mixture. A high concentration of acceptors can be obtained due to spontaneously formed Ni vacancies [5], which is achieved by choosing the reactive sputtering technological parameters. At the same time, it is rather difficult to achieve a high quality of NiO films after magnetron sputtering, where films can mainly have low crystallinity, low mobility, and low transparency. This is due to the high concentration of point defects inside the film due to the high oxygen content [6]. The simplest method for modifying the resulting film coatings is high-temperature annealing. Annealing can lead to an increase in the structural perfection of the material and, as a consequence, to a decrease in the concentration of point defects inside the film, an increase in the width of the optical band gap, and an increase in resistivity.

In this work, we study in detail the effect of high-temperature annealing on the optical and electrical characteristics of magnetron sputtered NiO films.

2. Results

In the study, NiO films were formed on a glass substrate using DC magnetron sputtering from a Ni (99.95%) nickel target. Magnetron sputtering was carried out in a mixture of working gases

25% O2 / 75% Ar at a working pressure of 3 mTorr. The thickness of the NiO layer was 150 nm. The resulting NiO films had high conductivity and low transparency.
After deposition, the NiO films were subjected to thermal annealing in an oxygen-containing controlled environment. A series of annealings were carried out in the temperature range of 200–550°C with a duration of 5–120 min.
The optical and electrical parameters of the resulting films were measured. Optical transmission and reflectance spectra were measured using an AvaSpec-ULS2048XL-EVO-RS spectrometer in the wavelength range of 300 nm - 1100 nm. Electrical measurements were carried out using a probe station to determine the current-voltage characteristics.
The results obtained showed an increase in the transparency of the films with an increase in the temperature and duration of the annealing of the films. Thus, after annealing at 550°C, the transmission of the films increased from 5% to 80% at a wavelength of 700 nm. In addition, it has been found that an increase in the transparency of the films is accompanied by a significant increase in resistivity from 0.2 Ω cm to 1460 Ω cm.

3. Acknowledgments
The work was done as a part of the state assignment (№FSRM-2020-0011) of the Ministry of Education.

References
[1] Mistry B. V. et al.. 2011 *Thin Solid Films* **519** 3840–3843
[2] Warasawa, M. et al. 2013 *J. Appl. Phys.* **52** 021102
[3] Ren Y, Li L, Liu N, Zhang K, Li Ch, Chen Zh, Zhang B 2020 *Vacuum* **182** 109784
[4] Li L, Wang X, Liu Y, Ao J-P 2016 *J. Vac. Sci. Technol. A* **34** 02D104
[5] Lany S, Osorio-Guill´en J, Zunger A 2007 *Phys. Rev. B Condens. Matter* **75** 1–4
[6] Kim S-K, Yang H, Kim Y-S 2020 *J Mater Sci* **55** 17046–170606

Application of a broadband Josephson parametric amplifier

A.E. Dorogov[1,3*], A.Yu. Dmitriev[1], G.P. Fedorov[1,2,3], D.A. Kalacheva[4,1,2], A.N. Bolgar[1], N.N. Abramov[2], O.V. Astafiev[4,1]

[1] Moscow Institute of Physics and Technology, 141701 Dolgoprudny, Russia
[2] National University of Science and Technology MISIS, 119049 Moscow, Russia
[3] Russian Quantum Center, National University of Science and Technology MISIS, 119049 Moscow, Russia
[4] Skolkovo Institute of Science and Technology, 121205 Moscow, Russia

[*]Dorogov.AE@phystech.edu

Abstract. Detecting single-photon level signal – carrying both classical and quantum information – is particularly challenging for low-energy microwave frequencies. Here we introduce a quantum-limited Josephson-junction-based parametric amplifier, the SNAIL Parametric Amplifier, which uses an array of SNAILs (Superconducting Nonlinear Asymmetric Inductive eLements) and leverages broadband impedance engineering.

1.Fabrication

The fabrication of the device starts with the aluminum evaporation on a silicon substrate followed by etching of a patterned optical resist mask in Cl_2 plasma. To minimize the amount of native oxide on silicon substrate, piranha solution and buffered HF treatment were implemented [2]. The Josephson junctions for the device were fabricated using electron lithography and the aluminum was evaporated using Dolan bridge technique [3].

2.Characterization

The experimental characterization of the device was performed in a dilution refrigerator with a base temperature about 20 mK. The maximum gain 20 dB in a bandwidth 600 MHz was achieved. Further, the amplification performance was found to be greatly dependent on both the bias magnetic flux and pump power.

In order to find the appropriate parameters, one has to tune the pump frequency near the double frequency of the signal he wants to amplify. In most cases, the best gain-bandwidth products are achieved for large pump powers between -50 and -35 dBm. The bias magnetic flux should be chosen near the resonance.

3.Saturation power

The saturation power, or 1-dB compression point, depends on the bias flux and pump power as well. It varies in a range between -105 and -115 dBm which outperforms many other realizations (for example, see [1], [6])

4.Application

The parametric amplifier was used for transmon qubits dispersive readout. It proved to be a useful device for multi-qubit measurements with 20 dB amplification for 4 qubits simultaneously.

The signal-to-noise ratio (SNR) was also improved due to the usage of the amplifier, being increased by 15%. Although such an improvement allows to speed up the measurements, this result is still worse than the anticipated doubling the SNR. The discrepancy might have been caused by a not optimal regime which does not provide the lowest noise level. Further developments are to be done in order to increase SNR and automate the choice of the parameters.

Aknowledgements

The work was done in the frame of the Roadmap for the development in the Russian Federation the high-tech field of "Quantum Computation" for the period up to 2024.

References

[1] N.E. Frattini, V.V. Sivak, A.Lingenfelter, S.Shankar, and M.H. Devoret, Optimizing the nonlinearity and dissipation of a SNAIL Parametric Amplifier for dynamic range, Phys. Rev. Applied **10**, 054020 (2018)

[2] D. Kalacheva, G. Fedorov, A.Kulakova, J. Zotova, E. Korostylev, I. Khrapach, A.V. Ustinov, and O.V. Astafiev, Improving the quality factor of superconducting resonators by post-process surface treatment, AIP Conference Proceedings **2241**, 020018 (2020)

[3] G. J. Dolan, Offset masks for lift-off photoprocessing, Appl. Phys. Lett. **31**, 337 (1977)

[4] A.A. Clerk, M.H. Devoret, S.M. Girvin, Florian Marquardt, and R.J. Schoelkopf, Introduction to Quantum Noise, Measurement and Amplification, Rev. Mod. Phys. **82**, 1155 (2010)

[5] Tanay Roy, Suman Kundu, Madhavi Chand, A.M. Vadiraj, A. Ranadive, N. Nehra, Meghan P. Patankar, J. Aumentado, A.A. Clerk, and R. Vijay, Broadband parametric amplification with impedance engineering: Beyond the gain-bandwith product, Appl. Phys. Lett. **107,** 262601 (2015)

[6] C. Eichler, Y. Salathe, J. Mlynek, S. Schmidt, and A. Wallraff, Quantum-Limited Amplification and Entanglement in Coupled Nonlinear Resonators, Phys. Rev. Lett. **113**, 110502 (2014)

Cross-bar memristor nanostructures array for neural network layout

Avilov V.I., Tominov R.V., Zhavoronkov L.G., Hahulin D.A., Ilin O.I., Smirnov V.A.

Southern Federal University, Institute of Nanotechnologies, Electronics and Equipment Engineering, Taganrog, 347922, Russia

avilovvi@sfedu.ru

Abstract. In the work, a technological process was developed, and a neural network layout was made in the form of 4×4 artificial synapses crossbar array based on memristor nanostructures. Endurance and retention research of the obtained memristor nanostructures based on electrochemical titanium oxide has been carried out.

1. Introduction

Robotics is one of the promising areas for the development of modern electronics and microsystem technology. At the same time, its development is inextricably linked with the use of neural networks and artificial intelligence systems that repeat the principles of the human brain, in which information is processed and transmitted through neurons and synapses. At the same time, in most cases, the implementation of neural network algorithms is carried out on the classical von Neumann architecture, which negatively affects the performance and energy efficiency of autonomous robotic systems. The use of hardware implementation of neural networks will allow not only to solve these problems, but also to implement various functions of robotic systems on separate replaceable neural processors, by analogy with the parts of the brain responsible for speech, vision, coordination, etc. The most promising material for the manufacture of artificial synapses of neuromorphic devices are memristors that can change their resistance over a wide range of values. Memristor structures based on electrochemical titanium oxide have high speed and neuromorphic plasticity.

Thus, an urgent task is to manufacture and study the resistive switching parameters of artificial synapses based on electrochemical titanium oxide.

2. Experiments and methods

For experimental studies, a neural network model was made in the form of a crossbar structure of titanium oxide nanostructures (Fig. 1). To do this, a titanium film about 30 nm thick was formed on a semiinsulating silicon substrate by magnetron sputtering on a multifunctional Auto 500 facility (BOC Edwards, England). Then the titanium film was lithographed to form structures of the lower contact electrodes, which act as preneurons of the neural network. At the next stage, local anodic oxidation of the lower contact electrodes was carried out using a Solver P47 Pro scanning probe microscope, as a result of which titanium oxide nanostructures about 5 nm thick were formed on their surface, which acted as artificial synapses in the neural network. Then, using a Nova NanoLab 600 scanning electron

microscope (FEI Company, The Netherlands), the ion-stimulated deposition of tungsten upper contact electrodes corresponding to the postneurons of the neural network was performed.

To confirm the operation of the developed layout, the electrical parameters of the formed artificial synapses were studied using the Keithley 4200-SCS measuring complex. The endurance study was carried out for 100 cycles of switching between the states LRS (U_{set}=0.4V) and HRS (U_{reset}=-0.2V), while the readout voltage was 0.04V. For the retention study, the structure was switched to the LRS state, and then every second reading was carried out for 3000 seconds.

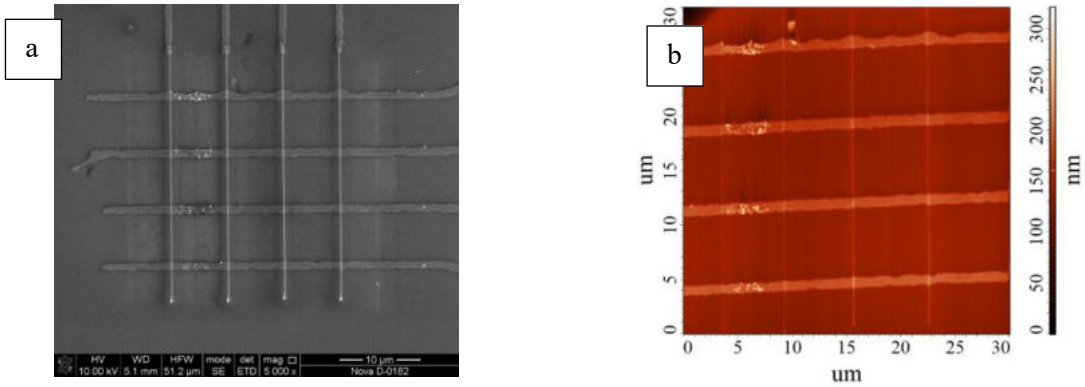

Figure 1. Titanium oxide nanostructure cross-bar array: a) – SEM image; b) – AFM image

3. Results and Discussion

The study of the electrical parameters of artificial synapses showed that titanium oxide nanostructures located between the corresponding upper and lower electrodes exhibit a memristor effect and switch between resistances of 864 ± 56 Ω in the LRS state and 1214 ± 51 Ω in the HRS state during 100 switching cycles (Fig. 2,a).

Then a study on the retention of the state of the artificial synapse was carried out. It was shown that for 3000 seconds the resistance of the structure in the LRS state was 742 ± 177 Ω (Fig. 2b).

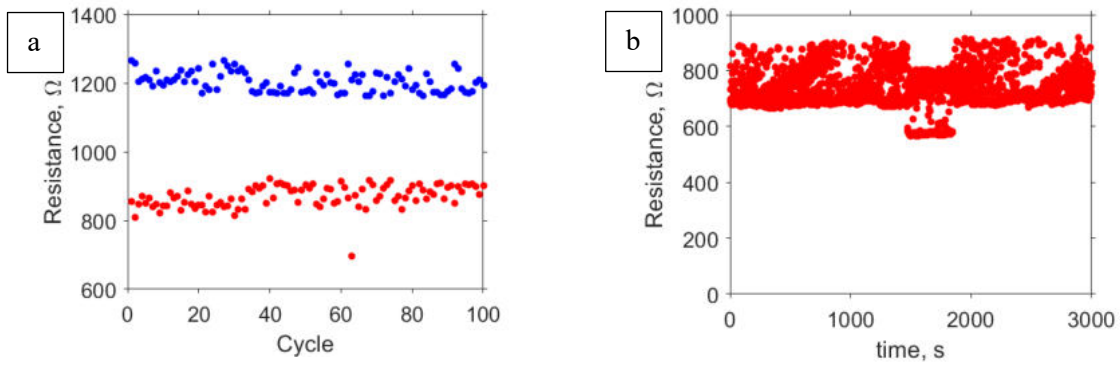

Figure 2. Study of cross-bar memristor nanostructure: a) – endurance; b) – LRS retention

4. Conclusion

The results obtained can be used in the development of technological processes for the manufacture of neural processors and artificial intelligence systems in robotics.

Acknowledgments

This work was supported by RFBR according to the research project No. 19-29-03041 mk, by grant of the President of the Russian Federation No. MK-2290.2022.4 and with the financial support of the Ministry of Science and Higher Education of the Russian Federation within the framework of a state task in the field of scientific activity No. FENW-2022-0001.

Optical properties of carbon dots covalently bonded with plasmonic nanoparticles

I A Arefina[1], D A Kurshanov[1], A A Vedernikova[1], A V Fedorov[1], E V Ushakova[1], A L Rogach[2,3]

[1] Center of Information Optical Technologies, ITMO University, Kronverksky pr. 49, 197101 Saint Petersburg, Russia;
[2] Centre for Functional Photonics (CFP), Department of Materials Science and Engineering, City University of Hong Kong, Hong Kong SAR 999077, China; andrey.rogach@cityu.edu.hk
[3] Shenzhen Research Institute, City University of Hong Kong, Shenzhen 518057, China

iaarefina@itmo.ru, elena.ushakova@itmo.ru

Abstract. In this paper we study optical properties of complexes consist of carbon dots (CDs) and metal nanoparticles (MNPs) in two different regimes of resonance. Carbodiimide chemistry was used to form amide bond between CDs and MNPs and to enhance PL of fluorophore.

1. Introduction

Carbon dots (CDs) are fluorescent nanoparticles with outstanding optical properties, and they have a great potential in many applications. Modification of CDs is an interesting field of research since it allows control of their physical and chemical properties in a wide range. Carbodiimide chemistry, e.g. via N-(3-Dimethylaminopropyl)-N′-ethylcarbodiimide hydrochloride (EDC) and N-Hydroxysuccinimide (NHS), is a universal tool that can be used to bond the CDs with different nanoparticles. The interaction of fluorophores with metal nanoparticles (MNPs) can have several useful effects such as increased quantum yields, photostability, resonance energy transfer efficiency, and decreased lifetimes. In this work, complexes of CDs with two types of MNPs were comprehensively investigated, the optimization of weight ratio results in CDs emission enhancement reaching 5.4 times.

2. Experimental

CDs were synthesized by solvothermal method from o-phenylenediamine and benzoic acid by procedure adopted from [1]. Gold NPs (AuNPs) and silver NPs (AgNPs) stabilized by cysteamine were synthesized according to the procedure previously reported in [2] and [3], respectively. Conjugation of the CDs with Ag or AuNPs was performed by carbodiimide chemistry (EDC/NHS reaction).

FTIR spectra were recorded on a Tenzor II infrared spectrophotometer (Bruker). DLS measurements were performed on a Zetasizer Nano ZS (Malvern Panalytical). Absorption and photoluminescence (PL) spectra were collected on a spectrophotometer UV-3600 (Shimadzu) and a spectrofluorometer FP-8200 (Jasco), respectively. PL decay was measured on a MicroTime 100 system (PicoQuant) with excitation at 405 nm.

3. Results

Optical properties of the complex's components are shown in Figure 1a. The MNPs were chosen in such a way for approbation two different enhancement regimes where plasmon peak is in resonance with (i) CDs absorption band or (ii) both CDs absorption and PL bands. FTIR spectra of complexes confirm formation of amide group after conjugation via EDC/NHS. It is worth noting that since CDs has amines on the surface, after EDC/NHS treatment aggregates corresponding to the agglomerate of 2-3 CDs were formed. Thus, CDs-MNPs complexes can be formed both from individual particles and from CDs' agglomerates bonded to MNPs. To probe the influence of CDs amount bonded to MNPs on optical responses of the complexes the set of samples with different CDs to MNPs weight ratio varied from 0.1 to 10 was prepared.

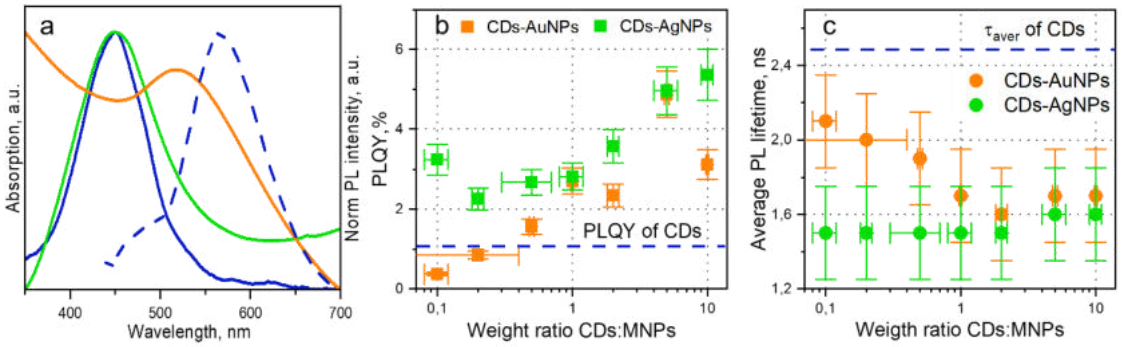

Figure 1. (a) Absorption spectra of CDs (blue), AgNPs (green), and AuNPs (orange) vs PL spectrum of CDs excited at 405 nm (blue dashed). (b) QY and (c) average PL lifetime vs weight ratio CDs:MNPs.

To estimate the PL enhancement on CDs to MNPs weight ratio, the PL quantum yield (QY) was calculated (Figure 1b). For all CDs-AgNPs complexes the PLQY is larger than that of pure CDs sample (PLQY=1%). A drop of PLQY for complexes with AgNPs can be attributed to the interaction of CDs within aggregates of complexes shown by dynamic light scattering (DLS) measurements. The highest PL enhancement of 5.4 was achieved at the size of CD-AgNP complexes corresponding to the formation of stable colloid. At low CDs amount per AuNPs the PL is quenched while the size of CDs-AuNPs complexes from DLS measurements corresponds to that expected for colloidal complex. This is caused by effective energy transfer from CDs to AuNPs since the PL band is overlapped with absorption band of AuNPs (regime (ii)). With increase of CD to MNP weight ratio above 0.2, the PL enhancement is observed with maximum reached 4.9 at CDs/MNPs=5. The PL lifetime of all CDs-MNPs complexes (Figure 1c) is shorter than that for pure CDs sample of 2.5 ns which indicates on the increased radiative rate of CDs relaxation in the presence of MNPs.

Acknowledgments

This work was financially supported by Priority 2030 Federal Academic Leadership Program.

References

1. Lin S. et al. Solvatochromism of bright carbon dots with tunable long-wavelength emission from green to red and their application as solid-state materials for warm WLEDs // RSC Advances. Royal Society of Chemistry, 2017. Vol. 7, № 66. P. 41552–41560.
2. Liu X. et al. Extinction coefficient of gold nanoparticles with different sizes and different capping ligands // Colloids and Surfaces B: Biointerfaces. Elsevier, 2007. Vol. 58, № 1. P. 3–7.
3. Oliva J.M. et al. Solvent-assisted in situ synthesis of cysteamine-capped silver nanoparticles // Advances in Natural Sciences: Nanoscience and Nanotechnology. IOP Publishing, 2017. Vol. 9, № 1. P. 015001.

Formation of Pb-Sn Janus particles on the surface of lead-tin telluride films during ion-plasma sputtering

Y D Belov[1], S P Zimin[1, 2], I I Amirov[1], V V Naumov[1], E Abramof [3], P H O Rappl [3]

[1]Valiev Institute of Physics and Technology of Russian Academy of Sciences, Yaroslavl Branch, Yaroslavl, Russia
[2]P.G. Demidov Yaroslavl State University, Yaroslavl, Russia
[3]Laboratório Associado de Sensores e Materiais, Instituto Nacional de Pesquisas Espaciais, São José dos Campos, Brazil

yadbelov@gmail.com

Abstract. The formation of Janus-like particles of Pb-Sn during ion-plasma treatment of the surface of lead-tin telluride films was found. $Pb_{0.6}Sn_{0.4}Te$ films 2 μm thick were grown on (111) BaF_2 substrates by molecular beam epitaxy. The ion-plasma treatment of the samples was carried out in a high-density low-pressure radio frequency (RF) inductively coupled plasma at an ion energy of 75 eV and 25 eV. The duration of the sputtering process is 240 s. The evolution of the film surface morphology and the formation of Pb-Sn Janus particles with nano- and submicron sizes have been studied.

1. Introduction

A solid solution of lead-tin telluride $Pb_{1-x}Sn_xTe$ is actively used in the manufacture of infrared photodiodes, lasers, optoelectronic pairs, thermoelectric devices, multilayer systems with quantum wells and superlattices [1,2]. In recent years, the problem of nanostructuring the surface of lead-tin telluride has become topical, and one of the effective methods of nanostructuring is the method of ion-plasma treatment [3]. By varying the sputtering conditions, it turned out to be possible to implement the self-formation of nanostructures by the vapor-liquid-solid (VLS) mechanism without the use of an external metal catalyst. The aim of this work was to study the role of lead and tin atoms in the processes of realization of the VLS mechanism.

2. Experimental details and results

Single-crystal $Pb_{0.6}Sn_{0.4}Te$ films were grown by molecular beam epitaxy on a Riber 32 P setup (INPE, Brazil) on (111) BaF_2 substrates. The film thickness was 2 μm; the properties of the layers in the initial state are described in detail in [3]. The argon plasma was ignited by applying RF power of 800 W (frequency 13.56 MHz) to the inductor. The energy of Ar+ ions (E_i) was 75 eV and 25 eV, the treatment time was 240 s. The ion current density is 5.2 $mA \cdot cm^{-2}$. The surface morphology was studied by scanning electron microscopy (SEM) on a Supra 40 Carl Zeiss microscope; local chemical analysis was carried out on an INCA attachment.

Fig. 1 shows SEM images of catalyst metal droplets on the tops of vertical nanostructures (E_i=75 eV) in different imaging modes. The diameter of the quasi-spherical cap at the top is from 40 to 100 nm. On fig. 1b in the backscattered electron mode clearly shows the two-phase structure of the drop, showing the self-formation of Pb-Sn Janus nanoparticles at the top of the vertical nanostructures. Figure 2 shows SEM images of metallic Janus droplets up to 0.5 μm in size after two-step processing (75 eV, 240 s+25 eV, 240 s). In backscattered electrons, the phase boundary of droplets formed after treatment with ions is clearly visible. The dark part (fig.1b, fig.2b) consists of a lighter element. Accordingly, in the dark parts contain is more tin than lead. Local chemical analysis allowed these areas to be identified as areas consisting of lead or tin.

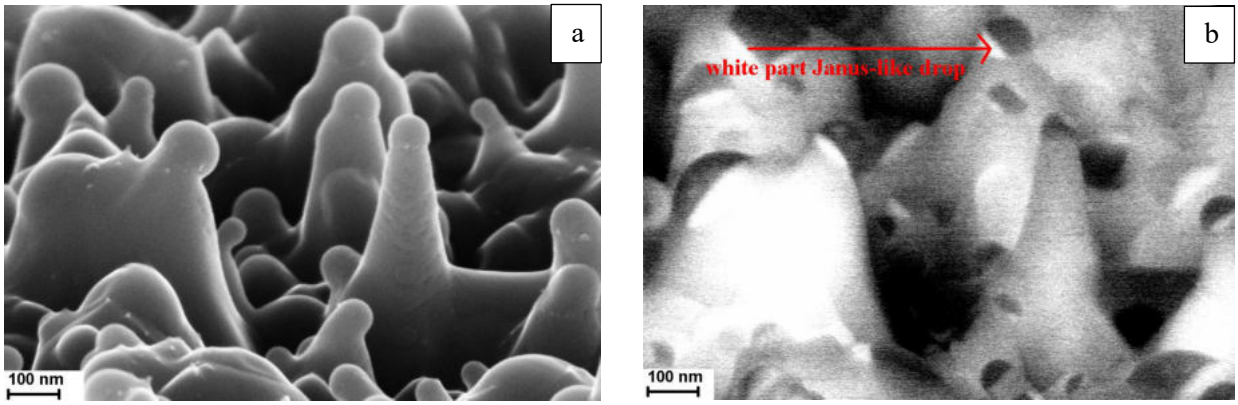

Fig.1. SEM images of the $Pb_{0.6}Sn_{0.4}Te$ film surface after treatment with argon ions E_i=75 eV for 240 s in the secondary electron mode (a) and in the backscattered electron mode (b).

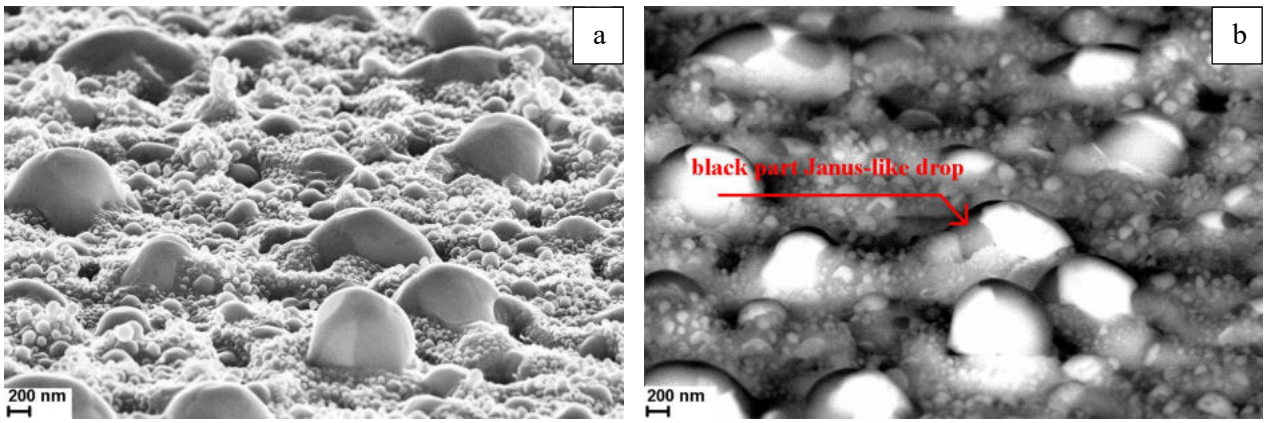

Fig.2. SEM images of the $Pb_{0.6}Sn_{0.4}Te$ film surface after two-step processing in the secondary electron mode (a) and in the backscattered electron mode (b).

3. Conclusions

The results of the work showed that self-forming droplets of the metal-catalyst of the VLS mechanism in the case of lead-tin telluride films with x = 0.4 are Pb-Sn Janus nanoparticles. Further ion-plasma treatment leads to the formation of submicron Pb-Sn Janus droplets on the surface.

Acknowledgments

The investigation was supported by the Program no. FFNN-2022-0017 of the Ministry of Science and Higher Education of Russia for Valiev Institute of Physics and Technology of RAS and within the framework of the initiative research work of the P.G. Demidov Yaroslavl State University. SEM studies were carried out at the Center for Collective Use “Diagnostics of Micro- and Nanostructures” with the financial support of the Ministry of Education and Science of the Russian Federation.

References

[1] Nimtz G and Schlicht B 1983 *Springer Tracts in Modern Physics*. **98** 1
[2] Xu E, Li Z, Acosta J A, Li N, Swartzentruber B, Zheng S, Sinitsyn N, Htoon H, Wang J and Zhang S 2016 *Nano Research.* **9** 820
[3] Zimin S P, Gorlachev E S, Amirov I I, Naumov V V, Juskenas R, Skapas M, Abramof E and Rappl P H O 2019 *Semicond. Sci. Technol*. **34** 095001

Gas-sensitive properties of cobalt oxide films formed by RTA

***V V Bespoludin[1], V V Polyakov[1], V V Petrov[1], Yu N Varzarev[1] and Z E Vakulov[2]**

[1]Southern Federal University, Taganrog, Russia

[2]Federal research Centre the southern scientific Centre of the Russian academy of sciences, Rostov-on-Don, Russia

*vladislaw.bespoludin@yandex.ru

Abstract. In this study, cobalt oxide films were formed by rapid thermal annealing (RTA) at temperatures of 500°C, 600°C and 700°C on a pre-cleaned sitall substrate. It was found that at a low heating temperature, cobalt oxide films show a low response to gases such as C_3H_6O, C_3H_8O and $NH_3 \cdot H_2O$. The response of cobalt oxide films increases significantly at heating temperatures of 300°C, 350°C and 400°C to gases C_3H_6O, C_3H_8O and $NH_3 \cdot H_2O$. The influence of the response value and heating temperature on the recovery time of cobalt oxide films after gas injection was also analyzed.

1. Introduction

Cobalt oxide has many potential applications and is an important p-type semiconductor. One of the areas of application of cobalt oxide films are gas sensors. Cobalt oxide has great potential as a gas sensitive layer [1,2].

2. Experiment details

Cobalt films were formed on a pre-cleaned sitall substrate by vacuum thermal evaporation (UVN-72). After that, the obtained cobalt films for the formation of cobalt oxide films were subjected to rapid thermal annealing (RTA) by halogen lamps in the air at temperatures of 500°C, 600°C and 700°C. Cobalt metal contacts were deposited on the surface of cobalt oxide films by vacuum thermal evaporation to measure the electrical parameters of the samples [1]. At room temperature, the resistance of cobalt oxide films formed by RTA at 500°C, 600°C and 700°C was 12.4 MOhm, 83.3 MOhm and 9.04 MOhm, respectively. The dependence of the response of cobalt oxide films on the heating temperature to gases such as C_3H_6O (acetone), C_3H_8O (isopropyl) and $NH_3 \cdot H_2O$ (25% ammonia solution) was investigated. The measurements were carried out in the temperature range from 100°C to 400°C with a step of 50°C.

3. Results and discussion

Figure 1 shows the dependence of the response of cobalt oxide films formed by RTA at temperatures of 500°C, 600°C and 700°C on the heating temperature (figure 1a,c,e), and also the dependence of the recovery time on the heating temperature (figure 1b,d,f). The gas sensitivity coefficient S (%) was determined by the following equation: $S=|(R_{gas}-R_{air})/R_{air}|*100$, where R_{gas} - film resistance in the presence of gas, R_{air} - film resistance in the air. Thus, at low temperatures, cobalt oxide films show an insignificant response to all three gases. With an increase in temperature, the response of cobalt oxide films increases. Thus, the reaction of cobalt oxide films increases significantly starting from the

heating temperature of 300°C. The sample formed by RTA at 600°C shows the highest response among the three samples. Also, at a temperature of 400°C all three samples show a decrease in the recovery time for all three gases.

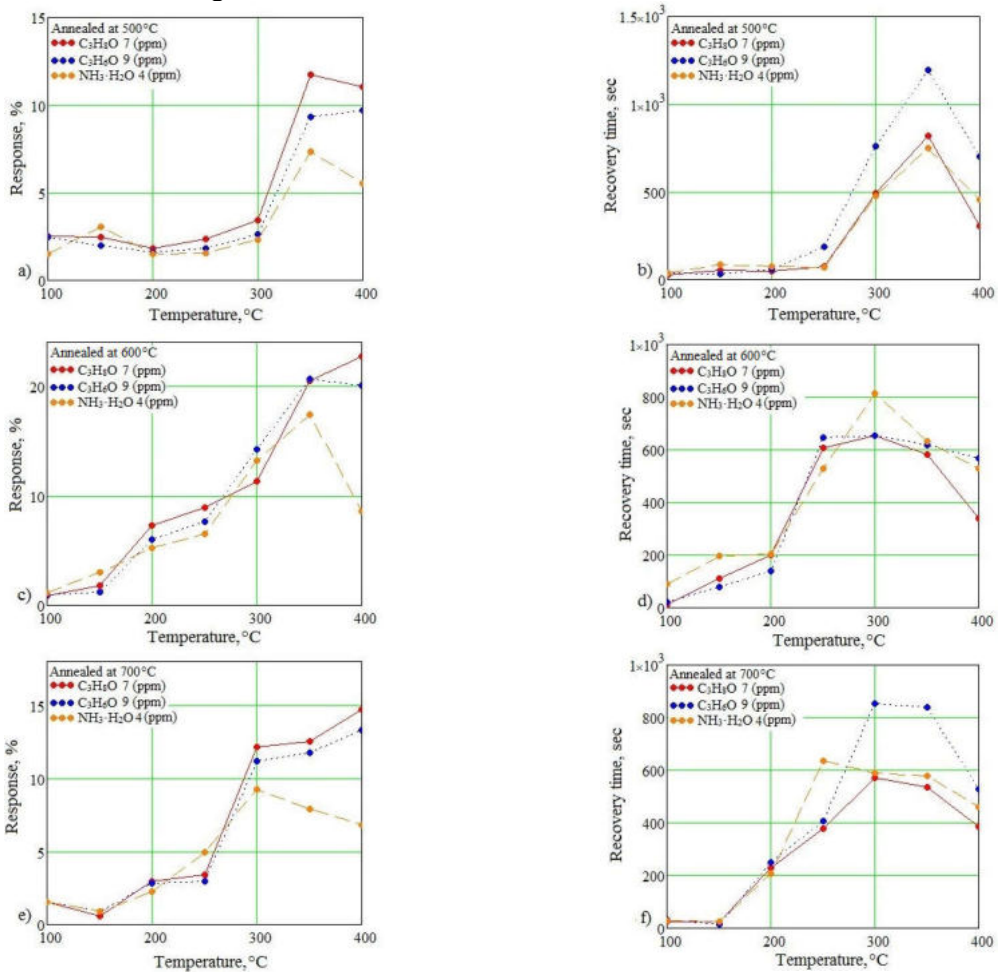

Figure 1. Dependence of the response and recovery time of cobalt oxide films on the heating temperature formed by RTA at temperatures of 500°C (a,b), 600°C (c,d) and 700°C (e,f)

4. Conclusion

As a result of the study, it was found that the heating temperature significantly affects the response of cobalt oxide films to such gases as C_3H_6O, C_3H_8O and $NH_3 \cdot H_2O$. It was found that at a low heating temperature, cobalt oxide films formed by RTA at temperatures of 500°C, 600°C and 700°C show a low response to C_3H_6O, C_3H_8O and $NH_3 \cdot H_2O$ gases. The response of cobalt oxide films increases significantly at heating temperatures of 300°C, 350°C and 400°C. It was found that the recovery time of cobalt oxide films after gas injection depends on both the response value and the heating temperature. The recovery time of cobalt oxide films formed by RTA at temperatures of 500°C, 600°C and 700°C decreases at a heating temperature of 400°C to all three gases, which can be explained by an increase in evaporation due to heating.

References

[1] Bespoludin V V, Polyakov V V, Petrov V V, Nesterenko A V, Vakulov Z E 2021 IOP Conf. Ser.: Mater. Sci. Eng. **1035** 012006

[2] Bhargava R, Khan S, Ahmad N, Ansari M M N 2018 AIP Conf. Proc. **1953** 030034

Design of LEDs based on GaN/InGaN nanowires on Si substrates

D N Bondarenko[1,2*], V O Gridchin[1,2], K P Kotlyar[1,2], R R Reznik[1,2,3], A S Dragunova[1,4], N V Kryzhanovskaya[4] and G E Cirlin[1,2,3,5]

[1] Alferov University, Saint-Petersburg, 194021, Russia
[2] Saint-Petersburg State University, Saint-Petersburg, 199034, Russia
[3] ITMO University, Saint-Petersburg, 197101, Russia
[4] Higher School of Economics, 199034, St. Petersburg, Russia
[5] Ioffe Institute, Saint-Petersburg, 194021, Russia

E-mail: * bondarenko.dariya.spb@gmail.com

Abstract This work is devoted to study the structural and optoelectronic properties of n-GaN/i-InGaN/p-GaN nanowires on n-Si substrate and p-GaN/i-InGaN/n-GaN nanowires on p-Si substrate. Both samples demonstrate photoluminescence spectra from InGaN insertions in the green-yellow region at room temperature. Study of the electrical properties of grown nanostructures shows typical diode dependencies. The results can be benefit for creation of light-emitting diodes on Si substrates.

1. Introduction

InGaN ternary compounds are attractive for creation of light-emitting devices [1] and renewable energy sources [2] due to the direct band gaps and ability to tune the emission wavelength from the near UV to near IR by changing the chemical composition [1]. However, the synthesis of InGaN ternary compounds in a wide chemical range is limited due to the “miscibility gap” problem [3]. Also, the synthesis of InGaN layers with high crystalline quality is complicated by the lack of lattice-matched substrates. One of the possible approaches to overcome these difficulties is the synthesis of nanowires (NWs). It was shown that it is possible to grow NWs with a low number of defects on substrates with lattice mismatch, in particular on silicon [4]. In these regards, a number of studies are aimed at creating of light-emitting devices based on GaN/InGaN NWs, where InGaN is used as the active region [5,6]. The present work is devoted to a comparative analysis of the structural and optoelectronic properties of n-GaN/i-InGaN/p-GaN NWs on n-Si with p-GaN/i-InGaN/n-GaN NWs on p-Si.

2. Samples and method

Samples were grown by plasma-assisted molecular-beam epitaxy using a Riber Compact 12 setup. We used n-Si(111) with 0.002-0.004 Ω·cm electrical resistivity and p-Si(111) with 0.0035-0.0065 Ω·cm electrical resistivity as substrates for the growth. Before the growth, substrates have been treated in diluted hydrofluoric acid to remove native silicon oxide layer. Next, the substrates were thermally treated directly in the growth chamber at a temperature of 900°C. Conceptually, the growth process consisted of several stages. On the first stage the GaN NWs doped with Si for n-type conductivity

were synthesized at a temperature of 850°C. Then the InGaN active region was formed at a temperature of 655°C. Finally, top part of GaN NWs doped with Mg for p-type conductivity was formed at the same temperature.

The structural properties of the grown samples were studied by scanning electron microscopy (SEM). The optical properties of grown nanostructures were studied by photoluminescence (PL) methods at room temperature. In this case, a helium-cadmium (He-Cd) metal vapor laser with a wavelength of 325 nm at 15.5 mW was used for excitation. Electrical properties were characterized by current-voltage curves (I-V).

3. Results and discussion

The results of grown NWs morphological properties showed that the morphology of both samples is a close-packed array of cone-shaped NWs with an average length of about 1.5 μm. Both samples exhibit PL spectra in the visible region (400 – 600 nm) at room temperature. For the n-i-p NWs grown on the n-Si substrate, the PL maximum corresponds to 570 nm. For the p-i-n NWs grown on the p-Si substrate, two PL maxima are observed: at 400 nm and 520 nm. We attribute the PL maxima at 520 and 570 nm to emission from the InGaN insertions and the PL peaks at 400 nm to emission from p-GaN heavily doped with magnesium impurity [7]. To measure the I–V curves, light emitting device structures based on grown NWs coated with SU8 polymer were created. The I–V curves of the samples show typical diode characteristics for both samples. An analysis of the results of the current-voltage curves will be presented in the work**.**

Acknowledgements

The samples were grown under support of Ministry of Science and Higher Education of the Russian Federation (state task № 0791-2020-0003). The electrical properties were studied under financial support of St. Petersburg State University under research grant N◦ 92591131.

References

[1] Bui H Q T, Velpula R T, Jain B, Aref O H, Nguyen H D, Lenka T R, Nguyen H P T 2019 *Micromachines* **10 (8)** 492

[2] Ramanujam J, Verma A, Gonz´alez-D´ıaz B, Guerrero-Lemus R, del Ca˜nizo C, Garc´ıa-Tabar´es E, Rey-Stolle I, Granek F, Korte L, Tucci M, Rath J, Singh U P, Todorov T, Gunawan O, Rubio S, Plaza J L, Di´eguez E, Hoffmann B, Christiansen S, Cirlin G E 2016 *Prog. Mater. Sci.* **82** 294

[3] Ho I., Stringfellow G. B. Solid phase immiscibility in GaInN 1996 *Applied Physics Letters* **69(18)** 2701-2703

[4] Dubrovskii V G, Cirlin G E, Ustinov V M 2009 *Semiconductors* **43** 1539

[5] Nami M, Stricklin I E, DaVico K M, Mishkat-Ul-Masabih S, Rishinaramangalam A K, Brueck S R J, Brener I, Feezell D F 2018 *Scientific Reports* **8** 501

[6] Gridchin V O, Kotlyar K P, Reznik R R, Dragunova A S, Kryzhanovskaya N V, Lendyashova V V, Kirilenko D A, Soshnikov I P, Shevchuk D S and Cirlin G E 2021 *Nanotechnology* **32** 335604

[7] Reshchikov M A, Morkoç H 2005 *J. Appl. Phys.* **97** 061301

Ferroelectric films for renewable energy

Z Vakulov[1], R Tominov[2], D Dzuba[2], D Khakhulin[3], V A Smirmov[2], O A Ageev[2]
[1]Federal Research Centre The Southern Scientific Centre of the Russian Academy of Sciences (SSC RAS), Rostov-on-Don 344006, Russia
[2]Institute of Nanotechnologies, Electronics, and Equipment Engineering, Southern Federal University, 347922 Taganrog, Russia
[3]Research Laboratory of Functional Nanomaterials Technology, Southern Federal University, 347922 Taganrog, Russia

zvakulov@sfedu.ru

Abstract. This paper shows the results of the development of an energy harvester based on hybrid carbon nanostructures. SiO_2/TiN/$LiNbO_3$ and SiO_2/TiN/$BaTiO_3$ samples were fabricated by pulsed laser deposition to study the piezoelectric effect. It is shown that the obtained nanocrystalline ferroelectric films exhibit a stable piezoelectric effect, which weakly depends on the nanoscale structure. An energy harvester architecture based on hybrid carbon nanostructures is developed. The obtained results can be used to create promising lead-free energy harvesters based on ferroelectric films for renewable energy and IoT devices.

1. Introduction

Today energy harvesting is considered as one of the alternatives to electrochemical batteries and can be applied as an autonomous power supply for portable IoT devices and wireless sensors [1, 2]. Energy harvesting is prospective to minimize the harmful anthropogenic impact on nature. In [3] has been shown that piezoelectric nanowires, composites, ferroelectric films, and hybrid carbon nanostructures are promising materials for mechanical energy harvesting. The study of the ferroelectric materials synthesis process is urgent since it determines the parameters of fabricated piezoelectric energy harvesters [4, 5]. A large number of piezoelectric materials studies make it possible to design prototypes of energy harvesters, while the manufacture of commercial converters requires a comprehensive solution of a number of technical issues related to the optimization of the fabrication process [6]. Thus, the purpose of the work is to study the synthesis process of ferroelectric films by pulsed laser deposition and develop a mechanical energy harvester based on hybrid carbon nanostructures.

2. Experiment

SiO_2/TiN/$LiNbO_3$ and SiO_2/TiN/$BaTiO_3$ samples were fabricated by pulsed laser deposition to study the piezoelectric effect. The growth of $LiNbO_3$ and $BaTiO_3$ films was carried out in Pioneer 180 PLD module (Neocera LCC, USA). The substrate temperature varied from 300 °C to 600 °C. Ntegra probe nanolaboratory (NT-MDT Spectrum Instruments, Russia) in the piezoresponse force microscopy (PFM) was used for piezoelectric effect study. It was established that the PFM signal amplitude in 7×7 μm^2 area is less than the amplitude in of 3×3 μm^2 the area with the phase (φ) in 7×7 μm^2 area of is equal to $\varphi = -180°$, and $\varphi = 0°$ in of 3×3 μm^2 area, respectively (Figure 1).

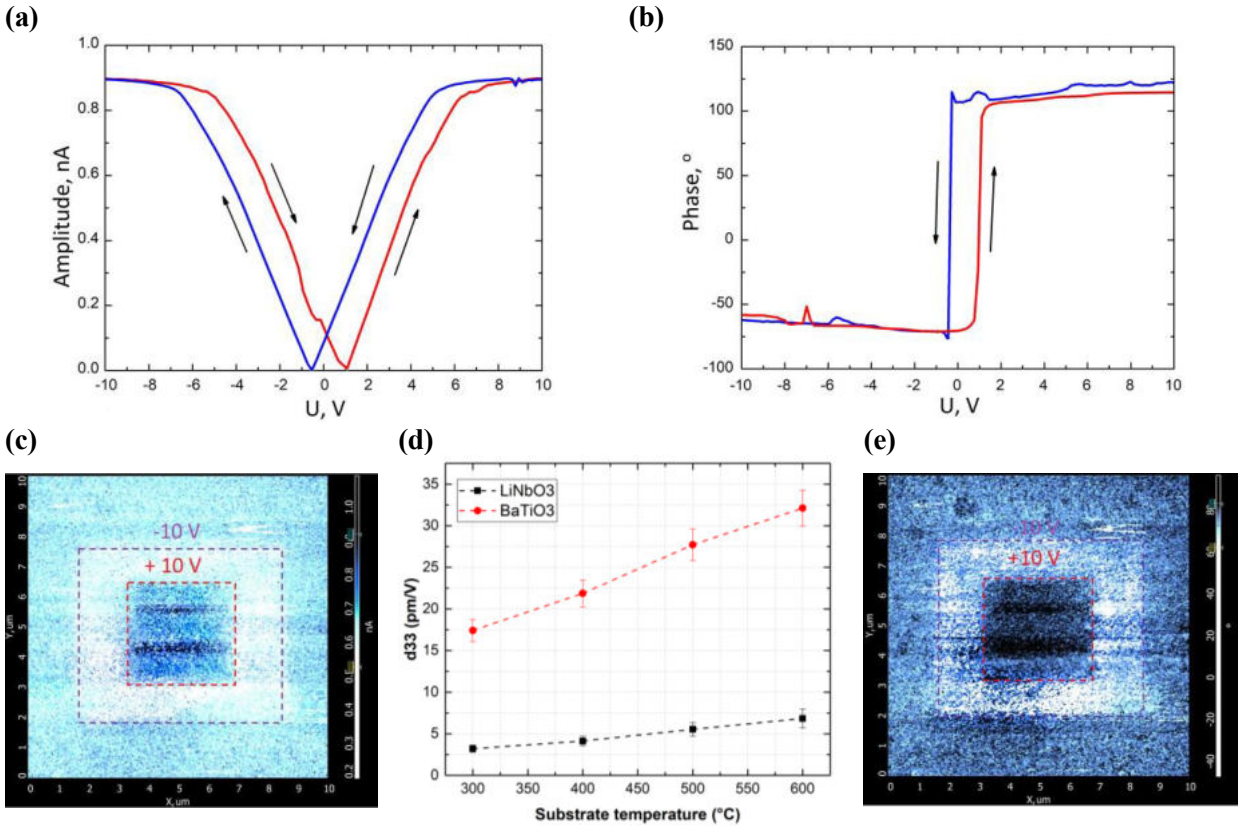

Figure 1 (a, b, c, d, e). The results of PFM study: amplitude **(a)**, phase **(b)**, PFM amplitude **(c)** and phase **(e)** images, dependences of d_{33} piezoelectric coefficient on the substrate temperature under PLD: $LiNbO_3$ and $BaTiO_3$ **(d)**

The piezoelectric coefficient d_{33} (Figure 1 (d)) was determined from the slope of the PFM amplitude vs. bias voltage curves measured between the probe and the sample. We used the curve of the approach of the probe to the sample obtained on single-crystal silicon to calculate d_{33}. An increase in the substrate temperature under PLD from 300 °C to 600 °C leads to an increase in the piezoelectric coefficient d_{33} from (3.22±0.41) pm/V to (6.84±1.13) pm/V for films $LiNbO_3$, and from (17.42±1.32) pm/V to (32.12±2.17) pm/V for $BaTiO_3$ films. The obtained result can be explained by the different growth kinetics of oxide films: the higher mobility of adatoms $LiNbO_3$ and $BaTiO_3$, with an increase in the substrate temperature, favors more oriented film growth and the increase in d_{33}. The obtained results can be used to create next-generation lead-free energy harvesters based on ferroelectric films for renewable energy and IoT devices.

Acknowledgments

The reported study was funded by the Russian Foundation for Basic Research, projects numbers 19-38-60052 and 19-29-03041 mk, and partially supported by Grant of the President of the Russian Federation MK-6252.2021.4.

References

[1] Irzaman H, Jenie R P 2018 *Ferroelectrics and Their Applications* (London: IntechOpen)
[2] Shih W C, Wang T L, Sun X Y and Wu M S 2008 *Jpn. J. Appl. Phys.* **47** 4056
[3] Takigawa R, Higurashi E and Asano T 2018 *Jpn. J. Appl. Phys.* **57** 06HJ12
[4] Tomar M, Gupta V, Mansingh A and Sreenivas K 2001 *J. Phys. D: Appl. Phys.* **34** 2267
[5] Blank D H A, Dekkers M and Rijnders G 2013 *J. Phys. D: Appl. Phys.* **47** 034006
[6] Christen H M, Eres G 2008 *J. Phys. Condens. Matter* **20** 264005

1/f noise characteristics of polyvinyl alcohol films with magnetic-sensitive multi-wall carbon tubes

S V Vasin[1*], I V Frolov[1,2], V A Sergeev[1,2] and M S Efimov[2]

[1] Kotel'nikov Institute of Radio Engineering and Electronics of Russian Academy of Sciences, Ulyanovsk Branch, Ulyanovsk, 432071 Russia
[2] Ulyanovsk State Technical University, Ulyanovsk, 432027 Russia

[*]E-mail: svasin@ulireran.ru

Abstract. A technique for obtaining polymer films with magnetically sensitive multi-walled carbon nanotubes cured in a magnetic field and in its absence is described. The effect of a magnetic field during polymer curing on the electrophysical and noise characteristics of thin films made from this nanocomposite has been studied

1. Introduction

Alignment of carbon nanotubes (CNTs) is the most efficient way to transfer their unique mechanical and electrical properties to the surrounding matrix [1]. The use of a magnetic field seems to be one of the most convenient ways to align CNTs; however, a significant magnetic field strength (15–25 T) is required to align ordinary CNTs [2]. To solve this problem, one can use CNTs decorated with various magnetic nanoparticles, for example, iron oxide Fe_3O_4. Such CNTs exhibit a much higher magnetic susceptibility and can align in magnetic fields not exceeding 0.2–0.3 T [3].

Electrical noise can serve as an additional source of information about the mechanisms of charge carrier transport in nanocomposites. The presence of $1/f$ noise in CNTs arrays has been noted by many researchers [4], but not many works have been devoted to studying the noise characteristics of thin-film nanocomposite structures based on CNTs, decorated with magnetic nanoparticles.

In this work, based on multi-walled CNTs (MWCNTs), we have obtained magnetically sensitive MWCNTs (M-MWCNTs). Based on M-MWCNTs and polyvinyl alcohol (PVA) as a matrix, a nanocomposite polymeric material was obtained. The effect of a magnetic field during polymer curing on the electrophysical and noise characteristics of thin films made from this nanocomposite has been studied.

2. Materials and methods

The preparation of M-MWCNTs with a magnetic coating from Fe_3O_4 nanoparticles was performed according to the procedure described in [3]. We used MWCNTs with a diameter of 40 – 80 nm, synthesized by the MOCVD method on an experimental laboratory setup developed at the Ulyanovsk State Technical University [5]. On the basis of M-MWCNTs and polyvinyl alcohol (PVA) as a matrix, nanocomposite polymer films were obtained by the method described in [6]. During polymerization, one group of samples (hereinafter referred to as the “m-film”) was subjected to a magnetic field of 0.3 T directed perpendicular to the surface of the films, and the second group of samples (hereinafter referred to as the “c-film”) was polymerized without exposure to a magnetic field. The low-frequency noise characteristics were measured at room temperature using a hardware-software complex [7].

3. Results and discussion

The results of measurements of the conductivity of PVA films with the addition of M-MWCNTs showed that the conductivity acquires a nonlinear barrier character, while the electrical conductivity of "m-films" in the direction perpendicular to the film surface is approximately 2 orders of magnitude higher than that of "c-films", without changing the character of the conductivity [6].

Noise current spectra $S_I(f)$ of "c-film" and films cured in a magnetic field "m-film", 10 μm thick and with an M-MWCNT concentration of 1% and 4% at a current of 200 μA in the range 10^2–10^4 Hz (Figure 1) have the character of low-frequency noise $S_I \sim 1/f^{\gamma}$, with the spectral shape index γ increasing with increasing M-MWCNT concentration. At an M-MWCNT concentration of 1%, the γ value of both films is practically the same, and at 4%, γ of the films cured in a magnetic field is 0.86, while for c-film it is noticeably higher, γ = 1.5.

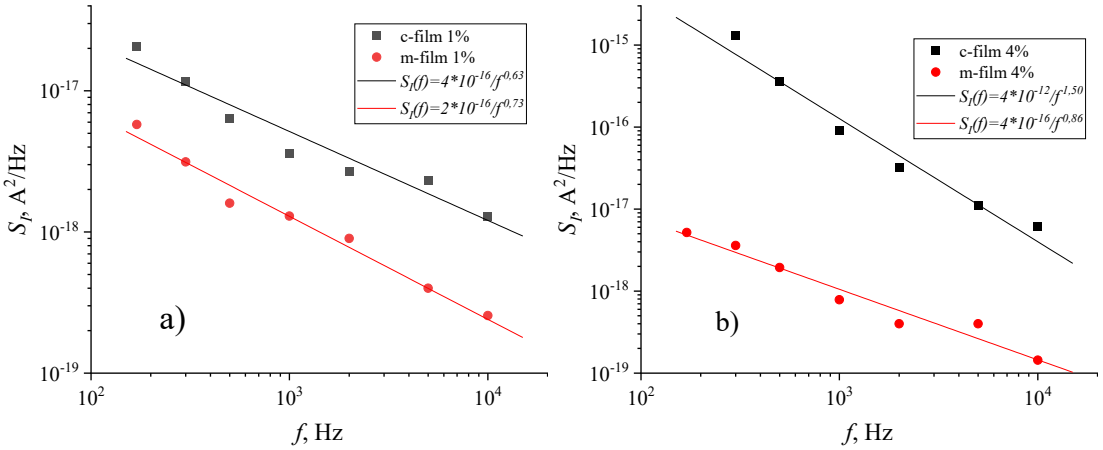

Figure 1. Low-frequency noise spectra at 200 μA of "c-film" and "m-film" film thickness 10 μm; M–MWCNT concentration 1% (a) and 4% (b).

The dependence of the level of low-frequency noise at a frequency of 1 kHz on the current for the same films has the form $S_I \sim I^{\alpha}$. The values of the index α at a concentration of 1% MWCNTs for films of both types are almost the same (1.48 and 1.55), and at a concentration of 4% they differ markedly: for "c-film" α increases to 2.27, and for "m-film" - decreases to 1.32.

Thus, an analysis of the noise characteristics can indirectly indicate the nature of the distribution and the degree of orientation of MWCNTs in the polymer medium.

Acknowledgments

This study was performed as part of a state assignment with financial support from the Russian Foundation for Basic Research and the Government of Ulyanovsk Region, Project No. 19-42-730011.

References

[1] Wang Y, Desroches G J and Macfarlane R J 2021 *Nanoscale* **13** 426–43

[2] Kimura T, Ago H, Tobita M, Ohshima S, Kyotani M and Yumura M 2002 *Adv. Mater.* **14** 1380–3

[3] He H and Gao C 2011 *J. Nanomater.* **2011** 1–10

[4] Sergeev V A, Klimov E S and Frolov I V 2019 *Tech. Phys.* **64** 1155–60

[5] Klimov E S, Buzaeva M V., Davydova O A, Makarova I A, Svetukhin V V., Kozlov D V., Pchelintseva E S and Bunakov N A 2014 *Russ. J. Appl. Chem.* **87** 1109–13

[6] Vasin S V, Efimov M S, Nizametdinov A M and Sergeev V A 2021 *J. Phys. Conf. Ser.* **2103** 012108

[7] Sergeev V A, Frolov I V and Shirokov A A 2012 *Prom. ASU Kontrollery* **11** 46

Lattice reconstruction in finite-size $MoSe_2$-WSe_2 heterostructures

I A Vovk[1], A S Baimuratov[2], S Yu Kruchinin[3], A Högele[2,4]

[1]Center of Information Optical Technology, ITMO University, Saint Petersburg 197101, Russia
[2]Fakultät für Physik, Munich Quantum Center, and Center for NanoScience (CeNS), Ludwig-Maximilians-Universität München, Geschwister-Scholl-Platz 1, 80539 München, Germany
[3]Center for Computational Materials Sciences, Faculty of Physics, University of Vienna, Sensengasse 8/12, 1090 Vienna, Austria
[4]Munich Center for Quantum Science and Technology (MCQST), Schellingtraße 4, 80799 München, Germany

E-mail: ilia.a.vovk@itmo.ru

Abstract. We have developed a theoretical approach for calculation the crystal lattice reconstruction that occurs under the action of van der Waals and elastic forces in a finite-size two-dimensional heterostructure. The developed approach was applied to study the reconstruction in the MoSe2-WSe2 heterostructures near their boundaries.

1. Introduction

Transition metal dichalcogenides monolayers with the chemical formula MX_2 (M = Mo, W and X = S, Se, Te) represent a new class of semiconductor compounds that can be widely used in nanophotonics. They can be assembled into two-dimensional heterostructures coupled by van der Waals interaction. The presence of the twist angle or the lattice mismatch between the layers leads to the formation of a nanoscale moiré pattern [1] that modulates the excitonic properties of such van der Waals heterostructures [2]. In some cases, the interpretation of experimental results requires the improvement of the infinitely rigid crystal lattice approximation. The reason is that the crystal lattice of transition metal dichalcogenides in moiré heterostructures undergoes a reconstruction that minimizes the total mechanical energy of the system [3]. Under ideal conditions, reconstruction in moiré heterostructures leads to a periodic domain structure [4]. Despite the mechanical stresses and presence of boundaries have a strong effect on the reconstruction pattern and optical properties of heterostructures based on two-dimensional transition metal dichalcogenides, there is still a lack of its consistent theoretical studies.

2. Results and discussion

Here we developed a model for the crystal lattice reconstruction for finite-size two-layer heterostructures at a triangular tip. Then the numerical optimization of the crystal lattice reconstruction in $MoSe_2$-WSe_2 heterostructures based on the developed model were carried out. In a series of calculations, the initial conditions and parameters of the heterostructure were varied, and the local energy minima and the spatial picture of the reconstruction were determined. We confirmed the

formation of large domains at the boundaries of the $MoSe_2$-WSe_2 heterostructure and traced the dependence of the reconstruction pattern on the twist angle between the layers of the heterostructure. The results obtained are in agreement with the data obtained by scanning electron microscopy for $MoSe_2$-WSe_2 heterostructures. The results of the study can be used for designing the exciton properties of van der Waals heterostructures on the nanoscale.

Acknowledgments
The study is funded by RPMA grant of School of Physics and Engineering of ITMO University.

References
[1] C. Zhang et al., Interlayer couplings, Moiré patterns, and 2D electronic superlattices in MoS_2/WSe_2 hetero-bilayers, Sci. Adv. 3, e1601459 (2017).
[2] N. P. Wilson et al., Excitons and emergent quantum phenomena in stacked 2d semiconductors, Nature 599, 383 (2021).
[3] S. Carr et al., Relaxation and domain formation in in commensurate two-dimensional heterostructures, Phys. 10 Rev. B 98, 224102 (2018).
[4] A. Weston et al., Atomic reconstruction in twisted bilayers of transition metal dichalcogenides, Nat. Nanotechnol. 15, 592 (2020).

The effect of the seed layer on the TiO_2 nanotubes coatings quality grown on the glass substrates by hydrothermal synthesis

M G Volkova[1], A P Ivanishcheva[2], V V Petrov[2], E M Bayan[1]

[1]Department of Chemistry, Southern Federal University, Rostov-on-Don, 344090, Russia,
[2]Research and Education Centre "Microsystem technics and multisensor monitoring systems", Southern Federal University, Taganrog, 347922, Russia

mvol@sfedu.ru

Abstract. The influence of the seed layer synthesis method on the TiO_2 nanotubes coatings quality obtained by hydrothermal synthesis was deeply investigated. in this work It was shown that the synthesized materials are nanoscale and have a mixture of anatase and rutile modification.

1. Introduction

Nanostructured titanium dioxide is one of the promising multifunctional inorganic materials due to its unique physical and chemical properties. TiO_2 coatings can be used in a wide range of applications, including catalysis, self-cleaning surfaces, gas sensors, solar cells, etc. [1]. There are various methods for TiO_2 films synthesis. However, hydrothermal synthesis allows one to obtain high-purity nanostructures with a given morphology. The growing of high-quality nanotubes coatings is possible on the seed layer without pores and cracks [2]. The most common used methods of seed layer synthesis are pyrolysis methods and sol-gel technology, as the simplest and most cost-effective. Therefore, the main aim of this work was to study the effect of the seed layer synthesis method on the quality of TiO_2 nanotubes coatings obtained by hydrothermal synthesis.

2. Experiment

Nanostructured film coatings were obtained in two stages. The first stage included the preparation of a seed layer using sol-gel method or solid-phase low-temperature pyrolysis technique. In the first case, the$TiCl_4$ hydrolysis product was applied to pre-prepared soda-lime glass substrates. In the second case, the seed layer was synthesized from a organic titanium salt solution as described for other oxide materials in [3]. The substrates with the applied solutions were annealed in a muffle furnace for two hours at a temperature of 550 ° C. At the second stage, TiO_2 nanotubes were obtained by hydrothermal synthesis. To complete this, the substrates with the applied seed layer were placed in a teflon tube for hydrothermal synthesis, a solution of 10 M NaOH and TiO_2 powder were added (the cell load did not exceed 80%). Hydrothermal treatment was carried out for 24 hours at a temperature of 160 ° C. After that the samples were washed with distilled water to a neutral pH and dried in the air. The synthesized materials were investigated by X-ray phase analysis (ARLX'TRA diffractometer, Thermo ARL, Cu

Kα radiation) and scanning electron microscopy (SEM, scanning electron microscope Nova Nanolab 600, at 10 keV).

3. Results and discussion

According to the XRD analysis of film materials obtained by low-temperature pyrolysis, a mixed structure of anatase and rutile was shown. Calculations of the crystallite sizes using the Scherrer equation showed that the average size was 9 and 13 nm for the anatase and rutile phases, respectively. When film materials after hydrothermal treatment were investigated, the phase composition did not change.

According to SEM data, nanostructured TiO_2 coatings obtained by hydrothermal method (the seed layer was applied by pyrolysis technique) are nanotubes with a 10 nm diameter and several microns length; the tubes are extended, sometimes curved, rolled into balls of 3-5 microns in size (Figure 1a). For nanostructures with a seed layer applied by sol-gel technology, a slightly different nature of the nanotubes growth was shown. The resulting structures are thin nanotubes with a several nanometers tens diameter, extended, curved, with a length of several microns. On the tubes surface there are agglomerates consisting of tubes tangles (Figure 1b), which may be due to the rough application of the seed layer as a result of an imperfect synthesis method.

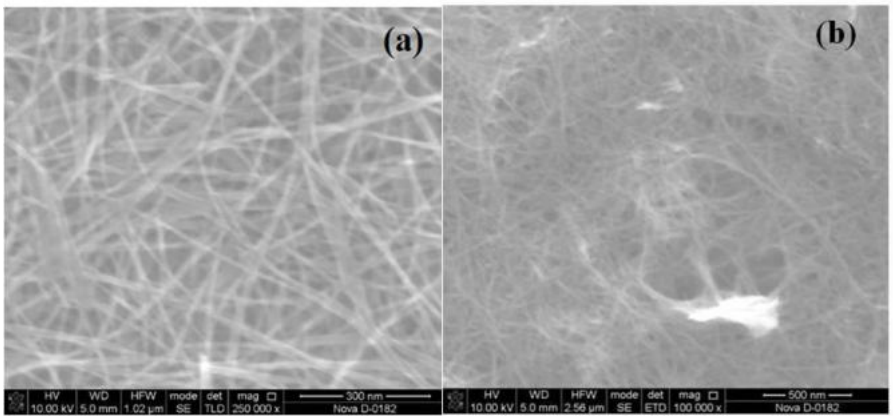

Figure 1. SEM images of TiO_2 films (seed layer was obtained by low-temperature pyrolisys technique (a) and by sol-gel method (b)).

4. Conclusion

Coatings from TiO_2 nanotubes were obtained by hydrothermal method. It was shown that when the seed layer was obtained by low-temperature pyrolysis technique, it is possible to obtain nanotubes of smaller diameter that do not form agglomerates in contrast to situation, when the seed layer was obtained by the sol-gel method.

Acknowledgments

This work was financially supported by the RFBR, project 20-07-00653 A. The authors are grateful to the Laboratory for Technology of Functional Nanomaterials of the Institute of Nanotechnology, Electronics and Equipment Engineering of the Southern Federal University for SEM studies conducting.

References

[1] G.Varshney, et al. Nanoscale TiO_2 films and their application in remediation of organic pollutants, *Coordination Chemistry Reviews* **306**, 43-64 (2016).

[2] B.Pant, et al., Recent advances in TiO_2 films prepared by sol-gel methods for photocatalytic degradation of organic pollutants and antibacterial activities, *Coatings*, **9(10)**, 613 (2019).

[3] V.V.Petrov, et al. Synthesis, characterization and gas sensing study of ZnO-SnO_2 nanocomposite thin films, *Chemosensors*, **9(6)**, 124 (2021).

Research of microresonator characteristics with carbon nanotubes

I.K. Gorelov[1,3], A.A. Mkrtchan[2], Yu.G. Gladush[2], A.E. Shitikov[1], V.E. Lobanov[1] I.A.Bilenko[1,3]

1 Russian Quantum Center

2 Skolkovo Institute of Science and Technology

3 Moscow State University

ilia19981@yandex.ru

Abstract. Nonlinearity of carbon nanotubes significantly exceeds nonlinearity of the materials of crystal microresonators and waveguides. Deposition of carbon nanotubes to the surface of the microresonator may enhance its nonlinearity. In this paper, the characteristics of high-quality factor microresonators with whispering gallery modes with single-layer carbon nanotubes deposited on the surface are experimentally investigated.

1. Introduction

High quality factor optical dielectric resonators with whispering gallery modes (WGM) are widely used nowadays, both for basic research and for manufacturing of advanced devices for microwave photonics. Their advantages are small size (from tens of microns to several millimeters), high quality factor, reaching values of 10^11 [1], high field concentration in a small volume and, as a consequence, low thresholds for observing nonlinear effects. This allows to create on their basis lasers with narrow linewidth, photonic microwave oscillators, narrowband optical filters, fast optoelectronic modulators [1].

One promising area of research is the use of nanomaterials to improve the characteristics of microresonators [2, 3]. A perspective nanomaterial is single-walled carbon nanotubes (SWCNTs), as they have a number of unique features, in particular, their nonlinearity significantly exceeds the nonlinearity of microresonator and waveguide materials. Cubic nonlinearity coefficient of SWCNTs is 10^{-12}-10^{-13} m^2/W, which is 7 orders of magnitude higher than the non-linearity of MgF_2 - 10^{-20} m^2/W. SWCNTs can be transferred to the surface of both crystal and integral microresonators.

2. Experimental results

The aim of this work is to study experimentally the characteristics of the microresonator after the deposition of SWCNTs, in particular, the Q-factor and the nonlinearity coefficient of the resulting hybrid structure. In the experiment a crystal microresonator made of MgF2 with Q-value Q=6*10^8 and carbon nanotubes with semiconductor interband transition at 1550 nm were used. The thickness of the SWCNTs layer was 4 nm, and the coating area was 2x2 mm^2. The deposition of SWCNTs occurred without the use of special devices: a film with nanotubes was brought to the resonator, pressed to the side surface

of the resonator, then it was moistened with acetone, after which the nanotubes were transferred from the nitrocellulose filter to the resonator. Immediately after the above described procedure, the quality factor of the resonator deteriorated to Q=3*10^5. Then a cleaning procedure was carried out. I was demonstrated that cleaning procedure does not damage the surface of the resonator and the nanotube film from the nitrocellulose filter residue. Washing of the resonator was performed with acetone, isopropanol, distilled water, followed by blowing the resonator with nitrogen. After all stages of cleaning procedure the Q-factor of clean resonator with nanotubes was measured: Q=10^7. Next, the nanotubes were removed from the side surface of the resonator using lint-free cloths moistened with isopropanol. The measured Q-factor after this procedure was Q= 6*10^8, which coincided with the Q-factor value before applying the nanotube film.

As a result of this study the technique of applying SWCNTs to the crystal microresonator was developed, as also a technique of cleaning the resonator after applying nanotubes. The Q-factor limit of the resonator with nanotubes was determined and it was shown that after removing nanotubes the Q-factor of the resonator is restored.

References

[1] Microresonators with giant quality factor / M.L. Gorodetsky. M., 2011. 415 p.

[2] Tomoki S. L., et al, "Design of a passively mode-locking whispering-gallery-mode microlaser," J. Opt. Soc. Am. B 38, 3172-3178 (2021).

[3] Yamashita, Shinji. "Nonlinear optics in carbon nanotube, graphene, and related 2D materials." Apl Photonics 4.3 (2019): 034301.

Surface modification of the quantum dots for applications in analytical systems.

Goryacheva Olga

Saratov State University, 83 Astrakhanskaya Street, Saratov, 410012, Russian Federation

goryachevaoa@sgu.ru

Semiconductor nanoparticles - quantum dots (QDs) have a big number of applications in different areas of science and technology. In the parallel with the biggest sites of optoelectronics and renewable energy, QDs are widely used in the development of analytical system for healthcare and food control industry. Crystal structure of QDs with different types of surface modification allows to replace organic dyes with improvements of physical and chemical stability and plenty options of emission colour and uniform peak of fluorescence. Different kinds of QDs can be used for analytical methods. Water solubility or surface modification methods affect further use. The silanized sheath can be used for various types of QDs. The method of ligand exchange on the QD surface, as a rule, leads to a change in the fluorescent properties. In most cases, the fluorescence quantum yield suffers. Such changes are associated with damage to the crystal surface as a result of ligand exchange between oleic acid and silica. Various parameters affect the strength of the process, and as a result, a drop in the quantum yield. We have considered some of them as part of their further use in analytical systems for the determination of low molecular weight substances. The inverse microemulsion method was used to silanize the QDs of the composition CdSe/CdS and CdSe/CdS/ZnS with different CdS and ZnS thickness[1]. The parameters of microemulsion such as the composition of the surfactant have been studied. The silanization reagent and its amount were also considered in order to obtain the optimal size for bioconjugation and use in lateral flow immunoassay[2].

Acknowledgments

This research was funded by the Russian Science Foundation, grant number 21-73-10046.

References

[1] O.A.Goryacheva, K D. Wegner, A. M. Sobolev, I. Häusler, N. Gaponik, I.Y. Goryacheva, U. Resch-Genger, Influence of particle architecture on the photoluminescence properties of silica-coated CdSe core/shell quantum dots, Anal. Bioanal. Chem. 2022. (2022) 1–13.

[2] O.A. Goryacheva, C. Guhrenz, K. Schneider, N. V. Beloglazova, I.Y. Goryacheva, S. De Saeger, N. Gaponik, Silanized Luminescent Quantum Dots for the Simultaneous Multicolor Lateral Flow Immunoassay of Two Mycotoxins, ACS Appl. Mater. Interfaces. 12 (2020) 24575–24584.

InGaN nanostructures on Si substrate: PA-MBE growth and properties

V O Gridchin[1-3], R R Reznik[1-3], K P Kotlyar[2], S D Komarov[1,5], A S Dragunova[1,5], D A Kirilenko, N V Kryzhanovskaya[1,5], G E Cirlin[1-4]
[1]Alferov University, St. Petersburg 194021, Russia
[2]Saint-Petersburg State University, Saint-Petersburg, 198504, Russia
[3]IAI RAS, St. Petersburg 198095, Russia
[4]Ioffe Institute, St. Petersburg 194021, Russia
[5]Higher School of Economics, 199034, St. Petersburg, Russia

e-mail: gridchinvo@gmail.com

Abstract. In the work, we study the influence of substrate temperature on the physical properties of InGaN nanostructures grown by plasma-assisted molecular beam epitaxy (PA MBE). We show that InGaN ternary alloys with a chemical composition within the miscibility gap can be synthesized under N-rich growth conditions at substrate temperatures from 600 to 670 °C. An InGaN ternary alloy with non-uniformly distributed In from 30 to 50% is grown at 600 °C. InGaN nanowires with a high In content and core-shell structure are grown at substrate temperature range from 650 to 660 °C. An InGaN layer with a chemical composition corresponding to almost pure GaN is grown at 670 °C. The results can be benefit to grow InGaN core-shell NWs and create of optoelectronic devices on Si substrates.

1. Introduction

InGaN alloys with their band gaps (0.7-3.37 eV) are among the most promising semiconductor materials for solid-state lighting and renewable energy sources [1-3]. However, the growth of InGaN alloys with high In content (x_{In} > 30 %) is an extremely challenging task caused by the large difference in interatomic spacing between InN and GaN and, as a consequence, the wide miscibility gap of the alloy [4]. Besides, the growth of high crystal quality InGaN layers is complicated by the lack of lattice-matched substrates. Three-dimensional structures such as nanowires (NWs) based on InGaN ternary alloys have recently attracted particular attention. One of the main features of NWs in terms of InGaN growth is the possibility of miscibility gap's circumventing [5]. Another advantage of NWs is the formation of them with high crystal and high optical qualities on lattice-mismatched substrates, for example on Si [6]. In these regards, this work is focused on the study of the growth condition influence on the physical properties of InGaN ternary alloys synthesized by PA MBE on Si substrates.

2. Experimental

The InGaN nanostructures were grown directly on p-type Si(111) substrates using Riber Compact 12 MBE setup, equipped with Ga, In effusion cells, and a nitrogen plasma source. The growth experiments were performed with equal each other Ga and In fluxes, under N-rich growth conditions, at substrate temperatures from 600 to 670 °C.

The morphology of the samples was studied by scanning electron microscopy (SEM Supra 25 Zeiss). Photoluminescence of the samples was excited with a helium–cadmium (He-Cd) metal-vapor laser

with a wavelength of 325 nm at 15.5 mW. The PL signal was detected using a DK480 Spectral products monochromator and a single-channel silicon detector using synchronous detection (SRS 510 "Stanford Research Systems"). The measurements were performed at room temperature.

3. Results and discussion

The SEM results show that the InGaN ternary alloy at substrate temperature of 600 °C is synthesized in a complex structure, consisting of a nanotubes layer near the substrate and three-dimensional nanostructures formed above. The average height of the nanostructures is about 4.8 μm. In the contrast, the separated InGaN NWs are grown at the substrate temperature of about 650 °C. The average height of the NWs is 2.9 μm and their average diameter is 100 nm. At higher substrate temperature the InGaN layer with an average height of 1.6 μm is formed. As can be seen, the average height of the nanostructures decreases monotonically with increasing the substrate temperature. This is explained predominantly by the In desorption from the growth surface.

The TEM studies show that the InGaN ternary alloy with non-uniformly distributed In from 30 to 50% is grown at 600 °C. InGaN NWs consist of a spontaneously formed core-shell structure with an average In content in the core of about 40% and in the shell of about 0-4%. An InGaN layer with a chemical composition corresponding to almost pure GaN is grown at 670 °C. All samples demonstrate photoluminescence at room temperature in the visible spectral range.

4. Conclusion

To conclude, we have investigated the influence of the substrate temperature on the physical properties of InGaN ternary alloys and determined the upper temperature for the PA MBE growth of InGaN ternary alloy. The results can be useful for creation RGB optoelectronics devices based only on InGaN on Si substrates.

Acknowledgments

The work was done under support of Ministry of Science and Higher Education of the Russian Federation (state task № 0791-2020-0003).

References

[1] H. Q. T. Bui, H. Q. T. 2019 Micromachines **10** 492
[2] Gridchin, V. O. et al. 2021 Nanotechnology **32** 335604
[3] Chu, S. 2017 Nano Futures **1**, 022001
[4] Karpov, S. Y.1998 MRS Internet Journal of Nitride Semiconductor Research **3** 1
[5] Roche, E. 2018 Nanotechnology **29**(46) 465602
[6] Dubrovskii, V. G. 2009 Semiconductors **43**(12) 1539

The plasma assistant cathodic electro-chemical exfoliation of graphite.

E Grushevsky[1], D Savelyev[1], N Savinsky[2], M Smirnova[1], D Pukhov[2] and R Selyukov[2]

[1] The Basic Department of Nanotechnology in Electronics of the P.G. Demidov Yaroslavl State University, Sovetskaya Street 14, 150003, Yaroslavl, Russia.
[2] Valiev Institute of Physics and Technology of Russian Academy of Sciences, Yaroslavl Branch, 150007, Universitetskaya Street 21, Yaroslavl, Russia.

yaregor@mail.ru

Abstract: The method of anodic electrochemical exfoliation of graphite has established itself as a promising ecological industrial method for producing nanographite with subsequent grinding of ultrasound into few-layered graphene (FLG). In this paper, a method of cathodic electrochemical exfoliation is proposed, accompanied by a plasma discharge of 200 V DC, in a solution of various electrolytes. The process features make it possible to obtain exfoliation products doped with oxygen and sulfur.

1. Plasma assistant electrochemical exfoliation

The graphite exfoliation products attract the attention of researchers, as a method of doping by substitution and (or) addition of graphene carbon with oxygen, nitrogen, sulfur, phosphorus atoms [1-3]. Cathodic exfoliation was carried out in a two-electrode cell in aqueous solutions of electrolytes 0.2 M ammonium sulfate, 0.3M hydrazine sulfate, hydrazine hydrate, hydroxylamine sulfate and their mixtures. The 0.5 mm graphite foil "Graflex" RF was used as the cathode, pressed graphite foil was used as the anode of 5 mm thickness. Commercial graphite foil "Graflex" (produced in the Russian Federation) 0.5 mm thick, having a carbon content of 99.5%, sulfur $\leq$ 0.12, chlorine $\leq$ 50ppm, was used after drying at 100^0C for 5 hours. The DC source creates a potential of 200V on the electrodes, when immersed in the electrolyte, the current density reaches more than 30A/cm^2, which obviously leads to instantaneous evaporation of water, the formation of a vapor-gas shell and plasma discharge.

In contrast to anodic electrochemical exfoliation, carbon products are not adapted to a large part by oxygen due to the minimal effect of oxidation by hydroxyl radicals. According to the data of elemental analysis, the atomic oxygen content in nanographite powders is 1.52 at. % and sulfur 1.5 at %, which indicates a rather low degree of its functionalization. The study of graphite exfoliation products was carried out using the following methods: X-ray phase analysis DRON7, IR-Fourier spectroscopy, Raman spectroscopy EnSpectr R532, SEM and energy dispersion X-ray fluorescence method FIB-SEM system Quanta 3D 200i. Figure 1a shows the IR spectra of the initial foil (bottom) and the graphite exfoliation product (top) in a 0.3M solution of ammonium sulfate and 0.2 hydrazine hydrate. Intense bands in the region above 3600 cm^{-1} are attributed with vibrations bond O-H of free water, 3600-2700 cm^{-1} with O-H hydroxyl-containing compounds with intermolecular hydrogen bonds, 1700 -1660 cm^{-1} valence vibrations of C=O carbonyl groups. A number of additional bands can be

attributed as methylene fragments -CH_2-2921cm^{-1}, sulphonyl groups SO^{-2} 1424cm^{-1}[4]. Graphite is characterized by the same absorption bands, with the exception of oxygen and sulphonyl. Figure 1c shows a diffractogram of the initial foil and the exfoliation product. The determination, according to the method [5], of the number of graphene layers in the crystallite from the diffractogram data was 15. This makes it possible to classify the product as a nanographite. Figure 1b shows the raman spectrum of the foil and the exfoliation product of the nanographite at a wavelength of 532 nm. According to the method [6], the defect nd/nc expressed in millionths of ppm is an insignificant value of 18 ppm/μ^2, which characterizes the process as low-defect.

2. Conclusion

Thus, cathodic exfoliation of graphite in aqueous-alkaline solutions of electrolyte b at 200V leading to the formation of electrolyte plasma allows the exfoliation of graphene into nanographite with low oxygen and sulfur doping and low defectiveness.

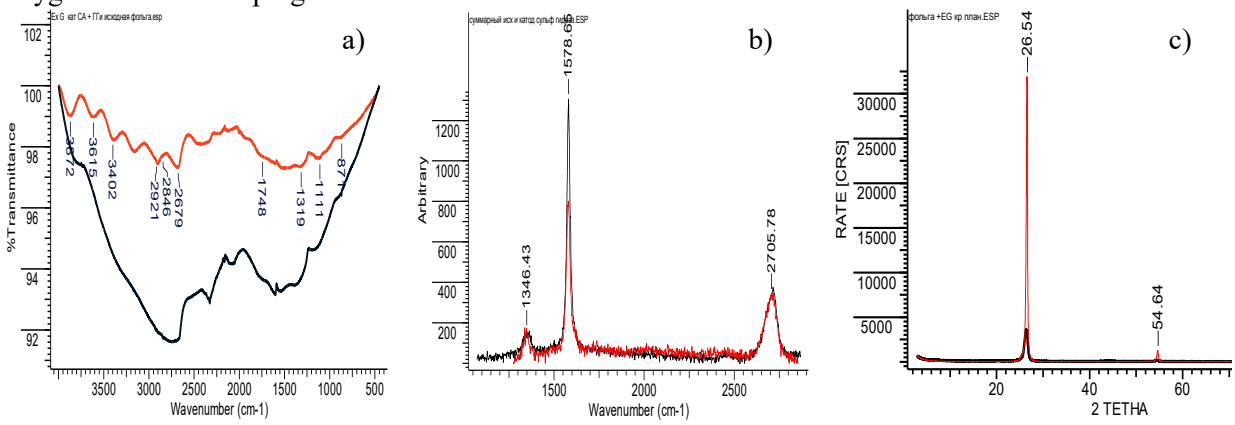

Figure 1. a)FT-IR spectra, b) KR spectrum of the initial graphite and nanographite after the process, c) Diffractogram of foil and nanographite.

Acknowledgements

This research was financially supported within the framework of the state assignment of the Valiev Institute of Physics and Technology of the Russian Academy of Sciences Yaroslavl Branch of the Ministry of Education and Science of the Russian Federation on the topic No. 0066-2019-0003. Some experimental results were obtained on the equipment of the Center for Collective Use "Diagnostics of Micro-and nanostructures" with the support of the Ministry of Education and Science of the Russian Federation.

References

[1] Komarova N S, Konev D V, Kotkin A S, Kochergin V K, Manzhos R A and Krivenko A G 2020 Mendeleev Commun. **30** 472–473.

[2] Krivenko A G, Manzhos R A, Komarova N S, Kotkin A S, Kabachkov E N and Shul'g Yu M 2018 Russian journal of electrochemistry **54** N 11 825-834.

[3] Grushevski E A, Savelyev D N, Mazaletsky L A, Savinski N G and Puhov D E 2021 Journal of Physics: Conference Series **2086** 012014.

[4] Solov'ev M E, Raukhvarber A B, Savinskii N G and Irzhak V I 2017 Russian journal of general chemistry **87** N 4 805-811

[5] Savinsky N G, Melesov N S, Parshin E O, Vasiliev S V, Bachurin V I and Churilov A B 2020 *Bulletin of the Russian Academy of Sciences: Physics* **84** N 6 732–735.

[6] Savelyev D N, Grushevski E A, Savinski N G, Smirnova M A, Mazaletsky L A, V. I. Bachurin V I and Churilov A B 2022 *Bulletin of the Russian Academy of Sciences: Physics* **86** N 5 667–673

The effects of epitaxial strain on the thermodynamic parameters of III-V bismuth-containing alloys

E M Danilina and A S Paschenko
[1]Federal research centre the Southern Scientific Centre RAS, 41, Chekhov st., Rostov-on-Don, 344006, Russia

Abstract. The work is devoted to the study of the effect of epitaxial deformation on the thermodynamic stability of III–V bismuth alloys. The thermodynamic limitations characterizing the possibilities of synthesis of $Ga_xIn_{1-x}Bi_yAs_{1-y}$, $Ga_xIn_{1-x}Bi_yP_{1-y}$ alloys on GaAs, GaSb, S substrates are determined based on delta lattice parameter (DLP) model. It has been found that elastic stresses lead to a decrease in the miscibility gap, a decrease in the critical temperature. The $Ga_{0.75}In_{0.25}Bi_{0.03}As_{0.97}/GaAs$ epitaxial alloy obtained by ion-beam epitaxy.

1. Introduction

The epitaxial films of III-V semiconductor alloys with Bi have been interested as promising materials for infrared optoelectronic applications [1,2].

The introduction of bismuth into the crystal lattice makes it possible to achieve a decrease in the mismatch between the lattice periods of the epitaxial layer and the substrate, as well as to reduce the band gap [3]. On the other hand, such alloys are prone to spinodal decomposition due to increase in internal stresses, which leads to phase separation and inhomogeneity of layer composition.

Thus, the thermodynamic stability analysis for the Bi-containing semiconductors is of fundamental importance and may provide guidelines for alloy growth leading to a relatively high Bi concentration at a low defect density.

2. Materials and Methods

For the thermodynamic description semiconductor alloys, we will consider the Gibbs free energy in accordance with the approximation based on semi-empirical delta lattice parameter (DLP) model [4]

$$G = \Delta H_{mix} - T\Delta S_{mix} + E_{st},$$

where

ΔH_{mix} – the enthalpy of mixing;

ΔS_{mix} – the entropy of mixing;

T – the absolute temperature;

E_{st} – the epitaxial strain energy.

The miscibility gap and the unstable region of relatively infinitesimal compositional fluctuations for a quaternary alloy system can be determined based on the Prigogine-Defey criterion [5]. Thus, the spinodal isotherms are founded by solving equation

$$\frac{\partial^2 G}{\partial x^2}\frac{\partial^2 G}{\partial y^2} - \left(\frac{\partial^2 G}{\partial x \partial y}\right)^2 = 0.$$

Fig. 1 - 2 exhibits the calculated binodal and spinodal isotherms for $Ga_xIn_{1-x}Bi_yAs_{1-y}$ in strained states.

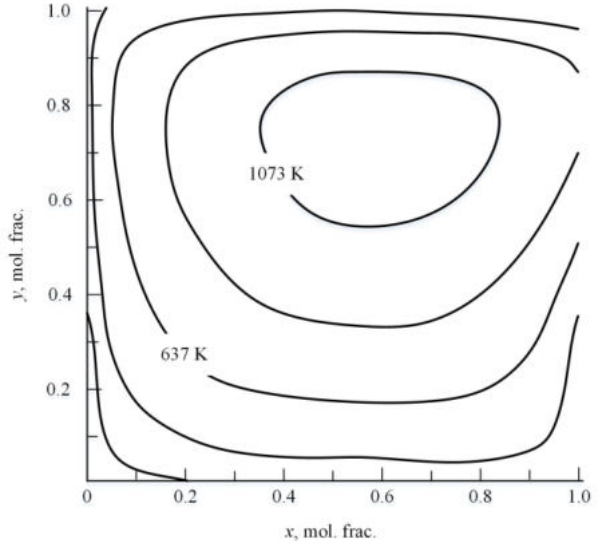

Figure 1. Binodal isotherms for $Ga_xIn_{1-x}Bi_yAs_{1-y}$ alloy on {100} GaAs substrate with strain effect

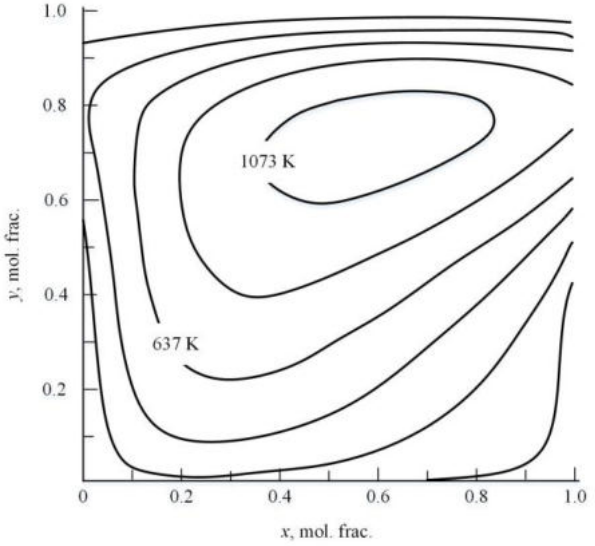

Figure 2. Spinodal isotherms for $Ga_xIn_{1-x}Bi_yAs_{1-y}$ alloy on {100} GaAs substrate with strain effect

3. Discussion and Conclusions

The isotherms of chemical and coherent binodal and spinodal decompositions were calculated for quaternary $Ga_xIn_{1-x}Bi_yAs_{1-y}$, $Ga_xIn_{1-x}Bi_yP_{1-y}$ alloys on GaAs, GaSb, S substrates. The results revealed that elastic stresses during epitaxial growth lead to an expansion of the region of thermodynamic stability, a decrease in the miscibility gap, a decrease in the critical temperature for $Ga_xIn_{1-x}Bi_yAs_{1-y}$ alloy up to 1163 K on the GaAs substrate and to 763 K on the GaSb substrate. An increase in the substrate lattice parameter leads to a decrease in the binodal and spinodal temperatures for all compositions of $Ga_xIn_{1-x}Bi_yAs_{1-y}$ and $Ga_xIn_{1-x}Bi_yP_{1-y}$ alloys.

The proposed semi-empirical model has shown good agreement with experimental data for $Ga_{0.75}In_{0.25}Bi_{0.03}As_{0.97}$ epitaxial semiconductor alloy growth on the GaAs substrate at 693 K by ion beam epitaxy, a lattice-mismatched composition by 3.6 %.

Acknowledgments

This work was funded by as a part of a state order to the Southern Scientific Center of the Russian Academy of Sciences, projects nos. 122020100254-3. This work was carried out with financial support by the Russian Science Foundation grant 19-79-10024.

References

[1] Svensson J, Chen Y, Anttu N, Pistol M-E and Wernersson L-E 2017 *Appl. Phys. Lett.* **110**
[2] Elyukhin V A 2018 *Journal of Applied Physics* **123**
[3] Samajdar D P, Das T D, Dhar S 2016 *Computational Materials Science* **111**
[4] Stringfellow G B 1972 *J. Phys. Chem. Solids* **33**
[5] Prigogine I, Defay R 1954 *Chemical Thermodynamics* (London: Longmans Green and Co)

Effect of pregrowth annealing temperature on the subsequent epitaxial growth of GaAs on Si

M M Eremenko[1], S V Balakirev[1], N E Chernenko[1], N A Shandyba[1], M S Solodovnik[1] and O A Ageev[1,2]

[1]Institute of Nanotechnologies, Electronics and Equipment Engineering, Southern Federal University, Taganrog 347922, Russia
[2]Research and Education Center "Nanotechnologies", Southern Federal University, Taganrog 347922, Russia

Email: eryomenko@sfedu.ru

Abstract. In this work, we studied the effect of the pregrowth annealing temperature on the epitaxial growth of GaAs on modified Si areas. It is shown that an increase in the annealing temperature leads to a decrease in the selectivity of GaAs epitaxial growth and also to a transition from two-dimensional like growth to the growth of nanowires. At 1-10 FIB beam passes and an annealing temperature of 600°C, no epitaxial growth was observed on the modified areas. An increase in the annealing temperature to 800°C followed by growth of GaAs leads to the activation of parasitic growth outside the modification areas.

1. Introduction

With its high-speed data processing capability, outstanding thermal performance, and low cost, silicon technology is the world leader in modern micro and nanoelectronics. On the other hand, the indirect band nature of silicon does not allow using it as a basis for creating information transmission devices based on light sources and optical detectors. For these purposes, III-V semiconductors are used because of their outstanding optical properties. Therefore, in recent years, the task has been to find approaches for integrating III-V semiconductors on silicon, which would make it possible to combine the advantages of both technologies [1]. However, the formation of high-quality III-V structures on silicon is still an unsolved problem. In this work, we investigated the effect of the annealing temperature of silicon modified with a focused ion beam (FIB) on the subsequent epitaxial growth of GaAs. The effect of annealing on the structural characteristics of the FIB-modified silicon areas is shown in our previous work [2].

2. Experiment

Experimental studies of GaAs epitaxial growth were carried out on FIB-modified Si(100) substrates. FIB-modification was carried out by processing 5×5 μm areas of the substrate with a Ga^+ beam with an accelerating voltage of 10 kV and a different number of beam passes. Then the samples were placed in a growth chamber and annealed followed by epitaxial growth. The annealing temperature varied from 600 to 800°C, the annealing time was 60 minutes. Next, GaAs 200 nm thick buffer layer was deposited at a growth temperature of 600°C, and the growth rate was 0.25 ML/s.

3. Results and discussion

The results of experimental studies have shown the possibility of achieving high selectivity of GaAs growth on FIB-modified samples annealed at 600°C. A comparative analysis of structures formed in areas with different FIB treatment modes (Figure 1a, b) allows us to conclude that the selectivity of the growth process is determined by the number of passes (implantation dose). Thus, after deposition of 200 nm GaAs, the structures were not formed only in the areas processed at the lowest value of the number of passes. We attribute this behavior to the fact that, as shown earlier [2], with such a number of passes, the formation of nanosized holes on the silicon surface during annealing begins, which act as localization and nucleation centers for epitaxially grown structures.

An increase in the annealing temperature to 800°C (Figure 1c, d) followed by growth of GaAs under similar conditions leads to the activation of parasitic growth outside the modification areas, which reduces the selectivity of the growth process. This change is due to the formation of pores in the native oxide at a high annealing temperature. It should be noted that the growth of GaAs on the modified areas is accompanied by the formation of nanowires oriented in directions perpendicular to each other.

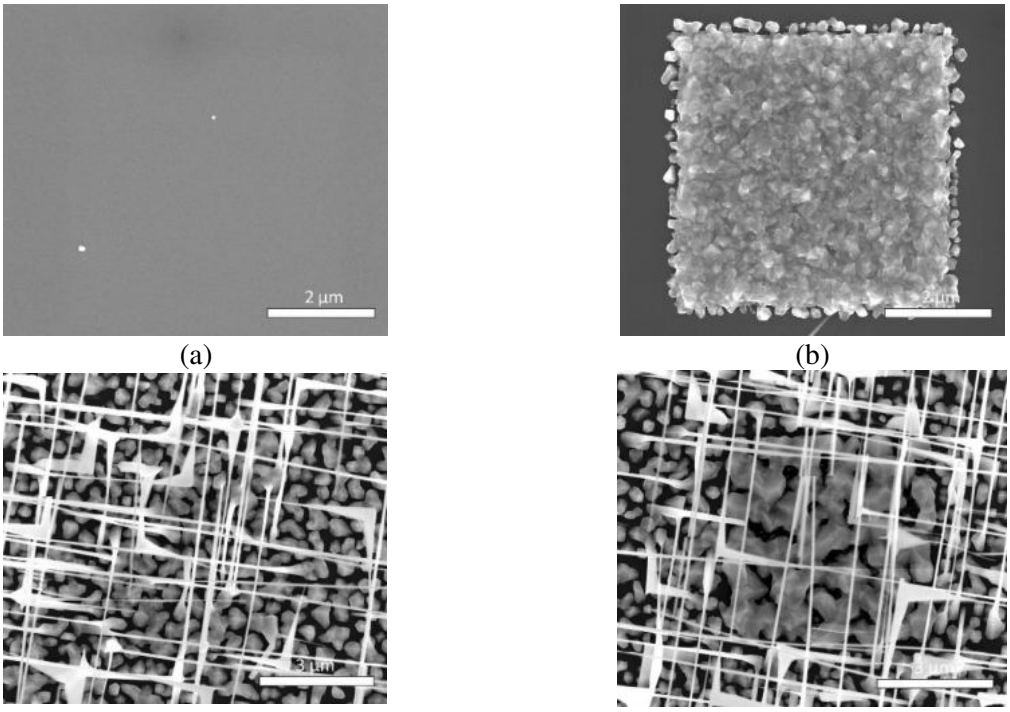

Figure 1. SEM images of FIB-modified Si areas after annealing at temperatures of (a), (b) 600°C and (c), (d) 800°C followed by deposition of 200 nm GaAs at 600°C. (a), (c) 1 beam pass, (b), (d) 200 beam passes.

Acknowledgments

This work was supported by the Russian Science Foundation Grant No. 20-69-46076 in the Southern Federal University.

References

[1] Tang M, Park J S, Wang Z, Chen S, Jurczak P, Seeds A Liu H 2019 *Prog. Quant. Electr.* B **66** pp 1–18

[2] Eremenko M M, Shandyba N A, Chernenko N E, Balakirev S V, Nikitina L S, Solodovnik M S and Ageev O A 2021 J. Phys.: Conf. Ser. **2086** 012027

Self-assembly of recyclable semiconductor nanowires from lutetium bis-phthalocyanine on solids

A. I. Zvyagina[1], A. E. Aleksandrov[1], A. G. Martynov[1], A. R. Tameev[1], A. E. Baranchikov[2], A. A. Ezhov[3], Yu. G. Gorbunova[2], M. A. Kalinina[1]

[1] A. N. Frumkin Institute of Physical Chemistry and Electrochemistry RAS

[2] N. S. Kurnakov Institute of General and Inorganic Chemistry RAS

[3] Moscow State University, Department of Physics

e-mail: zvyagina.ai@gmail.com

Abstract. Herein we report a new strategy for fabricating extended conductive nanowires through self-assembly of double-decker tetra-15-crown-5-substituted lutetium phthalocyaninate (LuL_2) via crown-assisted coordination with potassium ions. We showed that this type of organization of phthalocyanines leads to the maximum conductivity among phthalocyanine-based semiconductors. The field-assisted method is developed to deposit aligned conductive K^+-LuL_2 assemblies on solids. The solid-supported nanowires can be disintegrated into starting components in a good aprotic solvent for further recycling.

1. Introduction

Fabrication of processable one-dimensional (nano)semiconductors and their arrangement on solids are among major challenges for organic electronics. Phthalocyanines are electron-rich polyaromatic molecules with a remarkable ability to form ordered structures through aromatic stacking. This ability makes them exceptionally attractive for fabrication of conductive nanowires for organic electronics. However, the efficient overlapping of electron densities between molecules to form conductive band is not enough for having good electric properties in such structures. The size of monocrystalline domains is principally important because the efficiency of charge transfer drops sharply at domain boundaries. This is why the assembly of phthalocyanines through aromatic stacking alone most often leads to the formation of small aggregates with very low electrical conductivity. Their electric properties can be enhanced only after doping or partial oxidation of phthalocyanines.

To solve this problem we suggest a new supramolecular strategy that makes it possible to obtain long conductive nanowires from phthalocyaninces without doping. Our method exploits the coordination bonding between pre-designed organic ligands and metal clusters conventionally used for fabrication of metal-organic frameworks.

2. Results and discussion

Herein, we describe cooperative self-assembly of lutetium crown-substituted double-decker phthalocyaninate (LuL_2) via crown-assisted coordination with K^+ for fabricating supramolecular

nanowires with an average length up to 50 μm, thickness down to 5 nm. The conductivity of the film obtained with deposition of nanowires from the dispersion in chloroform under slow evaporation of the solvent is 11.4 $S \cdot cm^{-1}$. This value is the highest measured in non-doped phthalocyanine assemblies. The ability of crown-groups of the LuL_2 complex to interact with K^+ ions dictate the full conjugation of macrocyclic rings of phthalocyanine complexes in 1D aggregate and the efficiency of charge transfer along the nanowires.

The high sensitivity of K^+-LuL_2 assemblies to the electric field makes it possible to use field-assisted method for the arrangement of the already prepared nanowires on solid supports. The voltage applied between the electrodes guides the oriented deposition of the already formed nanowires from their solution onto the surface. The nanowires are oriented along the field lines from anode to cathode immediately after field switch on. The deposition proceeds within 20 minutes yielding the continuously ordered layer of nanowires on the support. The packing density of the nanowires within the layer can be tuned by varying the concentration of K^+-LuL_2 dispersion.

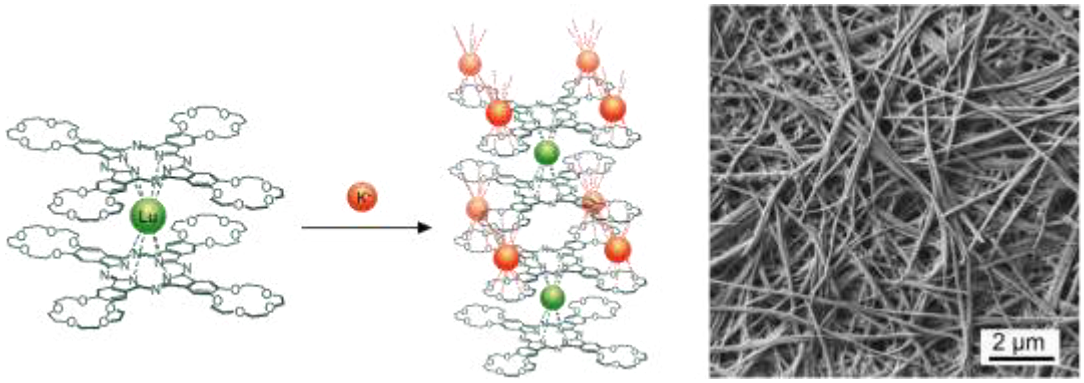

Fig. 1 Scheme of nanowires formation and SEM photo of nanowires deposited onto solid support

The recyclability of the self-assembled nanowires is a significant advantage over conventional covalently linked polymers for fabricating organic-based devices for a next-generation "green" electronics. The K^+-LuL_2 nanowires, otherwise stable in water and most organic solvents, can be easily disintegrated into starting components in acetonitrile and then separatied for further re-application without adding any other chamicals.

3. Conclusion

Our results demonstrate the potency of supramolecular strategy based on self-assembly for fabricating semiconductor nanowires with high electric properties from organic molecules with large aromatic system, such as phthalocyanines. Cooperative process involving weak intermolecular oordination bonds provide full conjugation of electronic systems of phthalocyanines for efficient charge transfer along nanowires. Although the cooperative binding provides stability to the as-formed structures, the bond weakness makes it possible to desintegrate these nanowires in a good aprotic solvent for further recycling.

Acknowledgments

The work is supported by Russian Science Foundation (N◦ 20-13-00279).

References

[1] Zvyagina, A.I., Aleksandrov, A.E., Martynov, A.G., Tameev, A.R., Baranchikov, A.E., Ezhov, A.A., Gorbunova, Y.G. and Kalinina, M.A.. *Inorganic Chemistry*, 2021, *60*(20), pp.15509-15518.

A method for measuring the resistance of transparent conducting oxides based on the four-probe method

T O Zinchenko, E A Pecherskaya, P E Golubkov, V S Alexandrov, G V Kozlov, J V Shepeleva

Penza State University, Russia, Penza, Krasnaya 40, 440026

scar0243@gmail.com

Abstract. A scheme of the developed installation for measuring the surface resistance of transparent conducting oxides synthesized by the spray pyrolysis method is presented. A technique for indirect measurement of surface resistance using the example of tin dioxide samples with different levels of doping with antimony, obtained at different values of technological regimes, is described. The achieved results allow to select technological regimes in the synthesis of transparent conducting oxides with the given properties, including those having the required value of surface resistance, by spray pyrolysis.

1. Introduction

Among electrophysical characteristics, surface resistance (Ohm/□) is the main parameter characterizing the TCO quality. The most common method for measuring the surface resistance of semiconductor materials is the four-probe method, the use of which is due to its high metrological performance and simple design of measuring instruments, the possibility of automating measurements and calculations [1, 2].

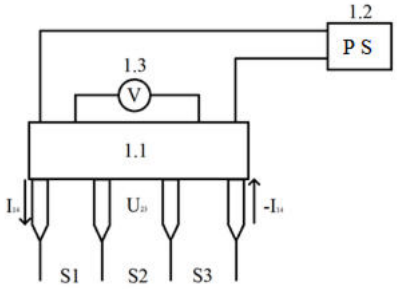

Figure 1. Scheme of four-probe installation.

1.1. Head with four linearly arranged probes (interprobe distance S=(1.60±0.01) mm).

1.2. Power supply APS-3203, providing obtaining currents of the set values from 1 to 5 mA with the help of a resistor with a resistance R=1 kOhm.

1.3. Digital multimeter DT890B allowing to determine the voltage between the probes.

2. Indirect resistance measurement by the four-probe method

Measurements of the surface resistance values were carried out on TCO samples obtained by the previously presented method by the spray- pyrolysis method [3]. The measurements were carried out at a fixed temperature (23±2) °C. The experiment scheme was assembled according to Figure 1. The sample under study was installed on the platform under the probes of the measuring head. The probes were smoothly lowered onto the sample surface. The current value I_{14} (from 1 to 5 mA) flowing through the sample was set, and the electric potential difference between the internal probes U_{23} was measured.

Below we consider the calculation of resistance on the example of sample № 4. Let's take current values I_{14} in the range from 1 to 3 mA. In this case, the corresponding results of measuring the voltage U_{23} were 391 mV, 773 mV, 1160 mV. Sample length was 16 mm and sample width was12 mm. The surface resistance values of the studied samples were calculated by the formula (given for the 4th sample, by analogy, the calculation is made for other samples):

$$R_S(4) = f\left(\frac{a}{b}, \frac{b}{s}\right)\frac{U_{23}}{I_{14}} = 1556 \ , \qquad (1)$$

where a is the sample length, b is the sample width, f is the correction function, which can be determined according to [4].

Among all the obtained samples, the sample No. 1 in the third batch has the smallest value of R_S = 32 Ohm/□ is (see Table 1). Table 1 shows the values of technological parameters χ - the impurity concentration, V - the sprayed solution volume, d - the coating thickness, as well as the results of calculating the surface resistance R_S. This value is only three times the surface resistance of commercially available ITO coatings (tin-doped indium oxide), which are today the market leader in transparent conductors [4, 5].

Table 2. Values of TCO resistance based on tin dioxide with different levels of antimony doping.

№	χ, %	V, ml	d, nm	R_S, Ohm/□
1	0	20	337	647
2		15	230	675
3		10	173	761
4		5	150	1556
5	0.05	20	346	32
6		15		57
7		10	168	98
8		5		208
9	0.1	15	250	60
10		10		132
11		5		262

The obtained results make it possible to select the technological regimes of the spray pyrolysis method to obtain transparent conducting oxides with these properties, in particular, with the required value of surface resistance.

Acknowledgments

The study was carried out with the financial support of the Russian Foundation for Basic Research within the framework of scientific project № 20-38-90044.

References

[1] T O Zinchenko, V I Kondrashin, E A Pecherskaya, A S Kozlyakov, K O Nikolaev, J V Shepeleva 2017 Electrical properties of transparent conductive ATO coatings obtained by spray pyrolysis *IOP Conference Series: Materials Science and Engineering* 225(1) 012255

[2] T O Zinchenko, Y A Pecherskaya, V I. Kondrashin, A S Kozlyakov, Y V Shepeleva 2017 Analysis of Research Methods of Electro-Physical Properties of Transparent Conducting ATO Coatings Received by Spray Pyrolysis *International Conference of Young Specialists on Micro/Nanotechnologies and Electron Devices EDM* 320–323 7981764

[3] T Zinchenko, E Pecherskaya, D Artamonov 2019 The properties study of transparent conductive oxides (TCO) of tin dioxide (ATO) doped by antimony obtained by spray pyrolysis *AIMS Materials Science* 6 (2) 276-287

[4] L Kerkache, A Layadi, E Dogheche, D 2006 Remiens Physical properties of RF sputtered ITO thin films and annealing effect J. *Phys. D: Appl. Phys*. 39 184-189

[5] L J Meng, M P Santos 1997 Properties of indium tin oxides films prepared by r.f. reactive magnetron sputtering at different pressures *Thin solid films* 303 151-155.

A method for measuring the resistance of transparent conducting oxides based on the four-probe method

T O Zinchenko, E A Pecherskaya, P E Golubkov, V S Alexandrov, G V Kozlov, J V Shepeleva

Penza State University, Russia, Penza, Krasnaya 40, 440026

scar0243@gmail.com

Abstract. A scheme of the developed installation for measuring the surface resistance of transparent conducting oxides synthesized by the spray pyrolysis method is presented. A technique for indirect measurement of surface resistance using the example of tin dioxide samples with different levels of doping with antimony, obtained at different values of technological regimes, is described. The achieved results allow to select technological regimes in the synthesis of transparent conducting oxides with the given properties, including those having the required value of surface resistance, by spray pyrolysis.

1. Introduction

Among electrophysical characteristics, surface resistance (Ohm/□) is the main parameter characterizing the TCO quality. The most common method for measuring the surface resistance of semiconductor materials is the four-probe method, the use of which is due to its high metrological performance and simple design of measuring instruments, the possibility of automating measurements and calculations [1, 2].

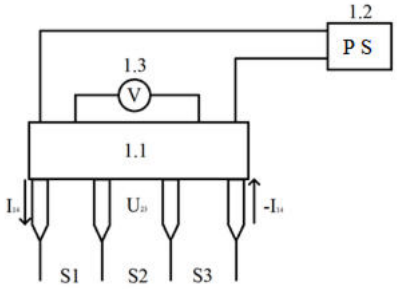

Figure 1. Scheme of four-probe installation.

1.1. Head with four linearly arranged probes (interprobe distance S=(1.60±0.01) mm).

1.2. Power supply APS-3203, providing obtaining currents of the set values from 1 to 5 mA with the help of a resistor with a resistance R=1 kOhm.

1.3. Digital multimeter DT890B allowing to determine the voltage between the probes.

2. Indirect resistance measurement by the four-probe method

Measurements of the surface resistance values were carried out on TCO samples obtained by the previously presented method by the spray- pyrolysis method [3]. The measurements were carried out at a fixed temperature (23±2) °C. The experiment scheme was assembled according to Figure 1. The sample under study was installed on the platform under the probes of the measuring head. The probes were smoothly lowered onto the sample surface. The current value I_{14} (from 1 to 5 mA) flowing through the sample was set, and the electric potential difference between the internal probes U_{23} was measured.

Below we consider the calculation of resistance on the example of sample № 4. Let's take current values I_{14} in the range from 1 to 3 mA. In this case, the corresponding results of measuring the voltage U_{23} were 391 mV, 773 mV, 1160 mV. Sample length was 16 mm and sample width was12 mm. The surface resistance values of the studied samples were calculated by the formula (given for the 4th sample, by analogy, the calculation is made for other samples):

$$R_S(4) = f\left(\frac{a}{b}, \frac{b}{s}\right)\frac{U_{23}}{I_{14}} = 1556 \ , \qquad (1)$$

where a is the sample length, b is the sample width, f is the correction function, which can be determined according to [4].

Among all the obtained samples, the sample No. 1 in the third batch has the smallest value of R_S = 32 Ohm/□ is (see Table 1). Table 1 shows the values of technological parameters χ - the impurity concentration, V - the sprayed solution volume, d - the coating thickness, as well as the results of calculating the surface resistance R_S. This value is only three times the surface resistance of commercially available ITO coatings (tin-doped indium oxide), which are today the market leader in transparent conductors [4, 5].

Table 2. Values of TCO resistance based on tin dioxide with different levels of antimony doping.

№	χ, %	V, ml	d, nm	R_S, Ohm/□
1	0	20	337	647
2		15	230	675
3		10	173	761
4		5	150	1556
5	0.05	20	346	32
6		15		57
7		10	168	98
8		5		208
9	0.1	15	250	60
10		10		132
11		5		262

The obtained results make it possible to select the technological regimes of the spray pyrolysis method to obtain transparent conducting oxides with these properties, in particular, with the required value of surface resistance.

Acknowledgments

The study was carried out with the financial support of the Russian Foundation for Basic Research within the framework of scientific project № 20-38-90044.

References

[1] T O Zinchenko, V I Kondrashin, E A Pecherskaya, A S Kozlyakov, K O Nikolaev, J V Shepeleva 2017 Electrical properties of transparent conductive ATO coatings obtained by spray pyrolysis *IOP Conference Series: Materials Science and Engineering* 225(1) 012255

[2] T O Zinchenko, Y A Pecherskaya, V I. Kondrashin, A S Kozlyakov, Y V Shepeleva 2017 Analysis of Research Methods of Electro-Physical Properties of Transparent Conducting ATO Coatings Received by Spray Pyrolysis *International Conference of Young Specialists on Micro/Nanotechnologies and Electron Devices EDM* 320–323 7981764

[3] T Zinchenko, E Pecherskaya, D Artamonov 2019 The properties study of transparent conductive oxides (TCO) of tin dioxide (ATO) doped by antimony obtained by spray pyrolysis *AIMS Materials Science* 6 (2) 276-287

[4] L Kerkache, A Layadi, E Dogheche, D 2006 Remiens Physical properties of RF sputtered ITO thin films and annealing effect J. *Phys. D: Appl. Phys*. 39 184-189

[5] L J Meng, M P Santos 1997 Properties of indium tin oxides films prepared by r.f. reactive magnetron sputtering at different pressures *Thin solid films* 303 151-155.

AlGaN/GaN heterostructures grown on hybrid SiC/porSi substrates

P Seredin[1], A Lenshin[1], D Goloshchapov[1], D Zolotukhin[1], V Kashkarov[1], N Builov[1], I Arsentiev[2] and I Kasatkin[3]

[1]Voronezh State University, Universitetskaya pl. 1, 394018, Voronezh, Russian Federation
[2]Physico-technical institute named after A.F. Ioffe RAS, Polytekhnicheskaya ul. 26, St. Petersburg, Russian Federation
[3]St. Petersburg state university, Universitetskaya nab-aya, 7/9, St. Petersburg, Russian Federation

E-mail: paul@phys.vsu.ru

Abstract. Employing a set of microstructural and spectroscopic methods of analysis the effect of the etching modes and their combination on the design, microstructural and optical properties of the compliant substrates on the basis of porous silicon was investigated in the work.

1. Introduction

Integrated light sources combining advantages of silicon technology and unique optical and electro-physical properties of the promising semiconducting materials of GaAs group and AIII-N nitrides in the common device are an important component in the wide area of photonics applications [1]. The main problem of such integration us the large difference in lattice parameters and thermal expansion coefficients between III-nitrides and commonly used silicon wafers. It can lead to the generation of high number of dislocations and defects in the films. One of the methods of AIII-BV integration with Si is the use of compliant porous substrate involving several porous layers with a variable porosity in each of sub-layers. The main issue that should be solved here is the study of the effect of staging etching modes and their combination on the design, structural and optical properties of the compliant substrates based on porous silicon. Our work is concerned just with this problem.

2. Materials and methods

Porous silicon layers were formed by electrochemical etching applying our tailored technique [2,3] in a solution of hydrofluoric acid and dimethylformamid with an admixture of hydrogen peroxide and sulfuric acid. Silicon wafers (as substrates) were utilized doped with phosphorus (0.3 Ohm·cm, n-type conductivity). Modes of single-staged (A and B) and double-staged (AB and BA) etching were selected that represented successive combination of single-staged modes.

The obtained samples were studied using a set of structural, spectroscopic and microscopic methods of analysis and they involved high-resolution X-ray diffractometry, Raman spectroscopy and electron microscopy.

3. Results and discussion

The type and consequence of the etching modes for silicon plates impacts on the structure of the formed porous layer. Experiments demonstrated that the selected etching modes provided formation of porous layer with a thickness of no less than ~10-15 □m for all of the samples. Scanning electron microscopic (SEM) images show formation of the pillars perpendicular to the surface of the sample. Diameter of pores in the samples varied in a dependence of the etching mode and is at the average: for sample A ~270 nm, B ~350 nm, BA ~410 nm, AB ~240 nm. The distance between the pillars also depends on the sequence of etching stages and takes the following values for sample A ~210 nm, B ~140 nm, BA ~370 nm, AB ~140 nm.

In order to determine the value of crystallinity for porous substrates symmetric 004 rocking curves with a high resolution were obtained. Since etching resulted in appearance of crystal mosaic structure, and crystallites are slightly disoriented relative to each other, the rocking curve is a function of mosaic crystal structure. Hence, its angular width $\Delta\omega$_RC is determined by the swivel angle of the blocks relative to each other, i.e. by mosaic structure η. Analysis of the calculated value of disorientation for mosaic blocks in the porous layer η demonstrated that an increase of porosity determined from the analysis of SEM images attained including combination of the etching modes, correlated with mosaic structure of the crystals.

Employing Raman micro-spectroscopy and measuring the value of the shift of silicon LO mode in the etched silicon layers with different porosity relative the position of LO mode in single-crystalline substrate made it possible to estimate residual stresses. Our calculations showed that the value of residual stresses is within the limits of 525-800MPa, that is in agreement with the data of [4] for single-layer structures with similar values of porosity. However, it should be noted that according to the work by Kang Yilan et al. [5] residual stresses are distributed all over porous silicon structure in a rather complicated manner. And since the depth of analysis for Raman spectroscopy is of about 600-700 nm, an accurate determination of the stresses, their distribution and gradient require performing of the local micro-mapping of the lateral facet for porous layer; and this is a separate problem.

Conclusions

Using of single-stage etching modes and their combinations enabled to form silicon porous layers of approximately the same thickness. At the same time, they demonstrated different structural, morphological and optical properties. Basing on the results of a set of structural, spectroscopic and microscopic methods of analysis it was shown that for the invariable crystal lattice parameters the value of residual stresses, crystallite size as well as reflectance and the energy of direct transitions in the porous layer of silicon depend on the combination of etching modes, however, these parameters do not always correlate with the value of porosity in the layer calculated from the analysis of SEM images.

Acknowledgments

X-ray studies were performed with the use of equipment of the resource center "X-ray diffraction investigations" at St-Petersburg state university.

The work was made under financial support of Russian scientific foundation (grant № 19-72-10007). and the Ministry of science and higher education of Russian Federation (grant № FZGU-2020-0036).

References

[1] Kim H, Lee W-J, Farrell A, Morales J, Senanayake P, Prikhodko S, Ochalski T and Huffaker D 2017 *Nano Lett.* **17** 3465–70

[2] Lenshin A, Seredin P, Agapov B, Minakov D and Kashkarov V 2015 *Mater. Sci. Semicond. Process.* **30** 25–30

[3] Lenshin A, Kashkarov V, Seredin P, Minakov D, Agapov B, Kuznetsova M, Moshnikov V and Domashevskaya E 2012 *Semiconductors* **46** 1079–84

[4] Manotas S, Agulló-Rueda F, Moreno J, Ben-Hander F and Martínez-Duart J 2001 *Thin Solid Films* **401** 306–9
[5] Kang Y-I, Qiu W and Lei Z 2007 *Optoelectron. Lett.* **3** 126–8

AlGaN/GaN heterostructures grown on hybrid SiC/porSi substrates

P Seredin[1,2], A O Radam[1], D Zolotukhin[1], D Goloshchapov[1], A Lenshin[1,3], V Kashkarov[1], N Builov[1], A Mizerov[4], S Timoshnev[4] and I Kasatkin[5]

[1]Voronezh State University, Universitetskaya pl. 1, 394018, Voronezh, Russia
[2]Ural federal university named after the first President of Russia B.N. Yeltsin, Yekaterinburg, ul. Mira, 19, 620002, Russian Federation
[3]Voronezh state university of engineering technologies. Voronezh. Prospekt Revolutsii, 19, Russian Federation
[4]St. Petersburg National Research Academic University named after Zh.I. Alferov RAS Khlopina street, 8, 194021, St. Petersburg, Russia
[5]St. Petersburg state university, Universitetskaya nab-aya, 7/9, St. Petersburg, Russian Federation

E-mail: paul@phys.vsu.ru

Abstract. Structural and spectroscopic studies of the epitaxial AlGaN/GaN layers were performed in the work. The layers were grown by molecular-beam epitaxy technique using plasma-activated nitrogen on the hybrid SiC/porSi substrate involving the layers of silicon carbide and porous silicon. The incensement in PL intensity was observed and less residual stress level was measured in the samples.

1. Introduction

Among the most promising techniques for improving of the characteristics of newly designed devices and increasing their efficiency is the integration of the optical functional elements on the basis of nitrides of III-elements with traditional silicon chips. An idea of combining of AIII-BV semiconductor systems and Si is not enough new. However, solution of this problem until now is not known.

One of the promising technological ways of integration is based on the use of "compliant structured silicon substrate", comprised of porous silicon and a layer of silicon carbide. Therefore, the main issue of our work was the study of AlGaN/GaN heterostructures grown on the hybrid SiC/porSi substrates.

2. Materials and methods

Epitaxial AlGaN layers were grown by molecular beam epitaxy technique with plasma-activated nitrogen in Veeco Gen 200 chamber [1]. To do this compliant substrate was formed on the basis of Si(111) silicon plate, obtained by electrochemical etching, and a layer of silicon carbide SiC, formed according to the technique of the matched replacement of the atoms [2,3]. After nitridizing procedure nucleation layer of AlN with a thickness of ~10 nm was grown, and, next, heterostructures of AlGaN (15 nm)/GaN (160 nm) were formed. Structural and spectroscopic studies of heterostructure involved high-resolution X-ray diffractometry, Raman and photoluminescence spectroscopy

3. Results and discussion

Using results of X-ray diffractometry and applying elasticity theory [4] for the layers with wurtzite lattice we have calculated not only the lattice parameters but the residual stresses in the epitaxial layers of heterostructures as well. It was shown that the residual stresses in the growth plane of GaN epitaxial layer are of about ~110 MPa, that is comparable with the values for the bulk thick films obtained on the transition buffer layers. These data are confirmed by the results of calculations on the basis of Raman and photoluminescence spectroscopy data. The value of residual stresses σ_xx in the epitaxial layer of GaN calculated from Raman scattering spectra is of about ~250 MPa, while the values determined from the photoluminescence band shift were near ~150MPa.

It should be noted that only one peak with the energy of ~3.42 eV is present in the photoluminescence spectrum of AlGaN/GaN heterostructure grown on the hybrid SiC/porSi substrate that corresponds to the band-to-band emission of wurtzite-type GaN. No additional yellow fluorescence was observed in the spectrum (it is not presented in figure 3), characteristic for n-type gallium nitride [5], associated with formation of the defects of Ga-O. Note that the width of the photoluminescence band was of about ~ 0.12 eV.

Conclusions

Structural and spectroscopic studies of the epitaxial AlGaN/GaN layers grown by molecular beam epitaxy technique under plasma activation with nitrogen on the hybrid SiC/porSi substrate comprised of the layers of silicon carbide and porous silicon were performed in our work. With the use of X-ray diffractometry technique, Raman and photoluminescence spectroscopy methods it was shown that thin films obtained on the hybrid substrate are characterized by the minimal residual stresses and rather intensive photoluminescence

Acknowledgments

The work was performed under financial support of the grant of Russian scientific foundation 19-72-10007.

The work was partly supported by the Ministry of Education and Science of the Russian Federation (grant № FZGU-2020-0036 and № FSRM-2020-0008).

In a part of access to scientific equipment and methodology this study was supported by the Ministry of Science and Higher Education of Russia under Agreement N 075-15-2021-1351

References

[1] Mizerov A, Timoshnev S, Sobolev M, Nikitina E, Shubina K, Berezovskaia T, Shtrom I and Bouravleuv A 2018 *Semiconductors* **52** 1529

[2] Kukushkin S and Osipov A 2014 *J. Phys. Appl. Phys.* **47** 313001

[3] Kukushkin S and Osipov A 2021 *Inorg. Mater.* **57** 1319

[4] Seredin P, Leiste H, Lenshin A and Mizerov A 2020 *Appl. Surf. Sci.* **508** 145267

[5] Specht P, Ho J C, Xu X, Armitage R, Weber E, Erni R and Kisielowski C 2005 *Solid State Commun.* **135** 340

Heteroepitaxial growth of κ-Ga_2O_3 films by halide vapor phase epitaxy

A Yu Ivanov[1], **Y N Kovach**[1], **A E Ageev**[1], **A A Petrenko**[1], **Kremleva A V**[1]

[1] ITMO University, St. Petersburg, 197101, Russia

E-mail: aapetrenko@itmo.ru

Abstract. Results are presented on heteroepitaxial growth of κ-Ga_2O_3 films by halide vapor phase epitaxy and their subsequent structural properties investigations. The growth conditions for films with a rocking curve width 91'' are described.

1. Introduction

Gallium oxide (Ga_2O_3) is a wide band gap semiconductor with significant potential in ultraviolet optoelectronics [1] and power electronics [2] for gas sensors, Schottky barrier diodes, photodetectors and transistors manufacturing [3]. Five Ga_2O_3 stable and metastable polymorphs are currently known: α-, β-, γ-, δ- and κ-Ga_2O_3 [3]. Among all Ga_2O_3 polymorphs κ-phase is a promising material for high electron mobility transistors (HEMT) design due to predicted spontaneous polarization value up to 23–26 μC/cm^2 that is larger than GaN [4]. The large spontaneous polarization is expected to achieve high 2DEG density contributed to low on-resistance – the essential condition to high efficient HEMT manufacturing.

Despite the fact that a number of investigations have been carried out on κ-Ga_2O_3 films obtained by various methods [5], the heteroepitaxial growth of the individual κ-Ga_2O_3 is not completely understood. In this paper we describe the conditions for κ-Ga_2O_3 growth on sapphire substrates by halide vapor phase epitaxy (HVPE) to obtain samples with high crystalline quality.

2. Experimental section

κ-Ga_2O_3 films were grown on sapphire substrates by HVPE. The growth area was a hot-wall type horizontal reactor, which comprises of 75 mm diameter quartz tube with induction heating. HCl and air were used as precursors, Ar as a carrier gas. The maximum HCl flow was limited by the range of the flow regulator – 0,6 L/min. The air precursor was obtained by liquidizing and evaporating atmospheric air and consisted mainly of oxygen (20%), argon (79%), nitrogen and other gases (1%). The concentration of impurities such as water, carbon dioxide, hydrocarbons, etc., did not exceed 1 ppm. GaCl gas was obtained *in situ* as a result of the metallic gallium (99.9999%) and HCl gas (99.999%) at 600–700 °C reaction. The GaCl release fraction was more than 80%. After all preparatory processes, the gases were sent to the reactor deposition zone, where they were mixed with air to obtain Ga_2O_3. The growth time was 4 min. After growth, the substrate was cooled to room temperature in an Ar flow.

The crystal structure of κ-Ga_2O_3 samples was analyzed by X-ray diffraction (XRD, DRON-8 diffractometer) by θ- θ and ω scan. The film thicknesses were measured by scanning electron microscopy (SEM, Tescan MIRA 3) as well as surface morphology analysis. Figure 1a shows the

results of samples characterization. Grown κ-Ga_2O_3 films rocking curve on reflection from the (006) plane is uniform and narrow (with 91'' width) indicating that obtained samples possessed high quality. Thickness and surface of κ-Ga_2O_3 films are shown on figure 1b (the degree of the surface smoothness can be judged of at the level of the utilized scanning electron microscope resolution, additional surface studies, for example, by atomic force microscopy, have not been carried out to date).

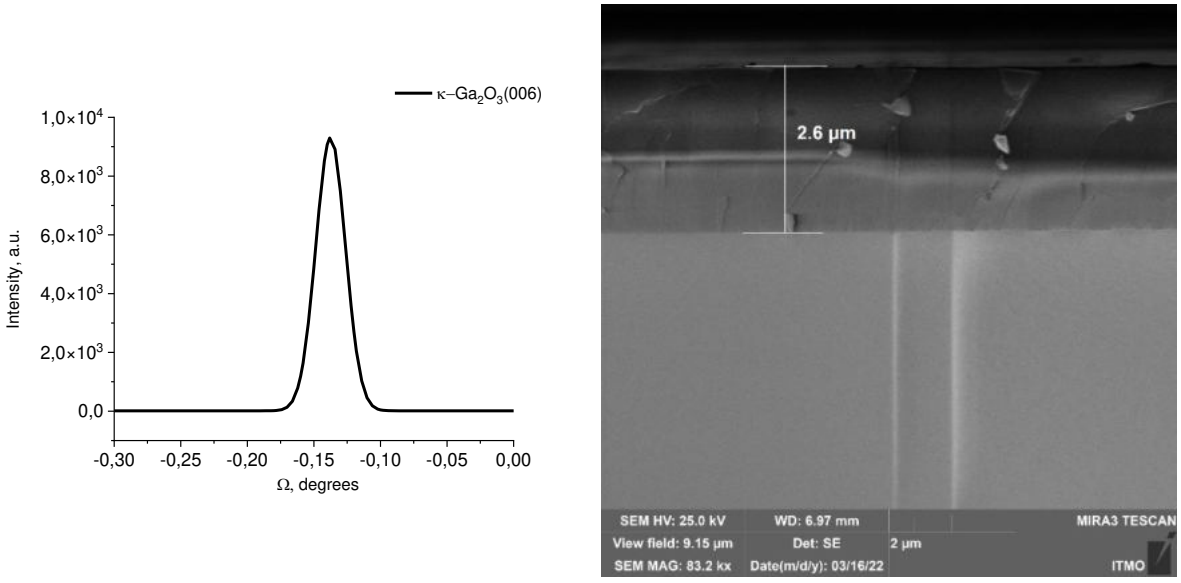

Figure 1. Rocking curve on reflection from the (006) plane (left) and SEM image of transverse cleave surface (right) for κ-Ga_2O_3 sample grown on sapphire substrate

3. Conclusion

The results of 2.6 μm thick κ-Ga_2O_3 films growth and structural properties investigations have been presented. The growth conditions are described for high crystalline quality κ-Ga_2O_3 heteroepitaxy on sapphire substrates by HVPE. For the samples obtained the rocking curve width is 91'' for (006) plane, surface morphology is smooth without any roughness.

Acknowledgements

This study was supported by the Russian Science Foundation (project no. 21-79-00211).

References

[1] Chen X, Ren F, Gu S and Ye J 2019 *Photon. Res.* **7** 381-415.
[2] Pearton S J, Yang J, Cary P H, Ren F, Kim J, Tadjer M J and Mastro M A 2018 *App. Phys. Rev.* **5** 011301.
[3] Playford H Y, Hannon A C, Barney E R and Walton R I 2013 *Chem. Europe. Jour.* **19** 2803-13.
[4] Nishinaka H, Ueda O, Tahara D, Ito Y, Ikenaga N, Hasuike N and Yoshimoto M 2020 *ACS Omega* **5** 29585-92.
[5] Bosi M, Mazzolini P, Seravalli L, Fornari R. 2020 *J. Mater. Chem.* **8** 10975.

Study of hydrothermal zinc oxide nanostructures photovoltaic properties

S A Kadinskaya[1], V M Kondratev[1], I K Kindyushov[1], A Kusnetsov[1], A I Lihachev[2], A V Nashchekin[2] and A D Bolshakov[1,3,4]

[1]Alferov University, St. Petersburg, 194021, Russia
[2]Ioffe Institute, St. Petersburg, 194021, Russia
[3]ITMO University, St. Petersburg, 197101, Russia
[4]Moscow Institute of Physics and Technology, Dolgoprudniy, 117303, Russia

E-mail: skadinskaya@bk.ru

Abstract. The electrical properties of zinc oxide were studied in terms of changes in the total electrical resistance (impedance) of the synthesized structures under infrared (IR), red, green, blue, and ultraviolet (UV) illumination. A physical interpretation of photoabsorption in ZnO is given, and the prospect of using the synthesized structures as photosensitive elements is shown.

1. Introduction

Zinc oxide (ZnO) is a wide-gap semiconductor material with band gap 3.37 eV at room temperature [1]. In addition, ZnO is inexpensive, widespread, chemically stable, easy to synthesize, and non-toxic material. Based on this material, it is possible to create light-emitting devices, nanoelectromechanics devices, sensors and others [1].

Most of the current research on ZnO is associated with the production of defective nanostructures. Defects are most often understood as zinc and oxygen vacancies [2], which create levels of nonradiative recombination in ZnO, which can be used to produce photoabsorbing devices operating in the IR, visible, and UV wavelength ranges. However, the presence of oxygen and zinc vacancies also indicates a low crystalline perfection of the synthesized structures. This work is devoted to the development of protocols for the control of the morphology of ZnO structures synthesized using hydrothermal method and the study of their photoelectric characteristics.

2. Synthesis

Hydrothermal synthesis is a method of growing various materials and compounds, based on the use of physical and chemical processes that take place in aqueous solutions at slightly elevated temperatures often used to obtain ZnO nanostructures [3].

In our work, silicon substrates Si (111) are used for the hydrothermal synthesis of ZnO nanostructures since this material is known to be the most often used in nanoelectronics. Zinc acetate is used as a seed layer material. The growth solution consists of equimolar aqueous solutions of $Zn(NO_3)_2$ and hexamethylenetetramine (HMTA). Samples #2 and #3 were synthesized using sodium citrate and polyethylenimine (PEI) respectively.

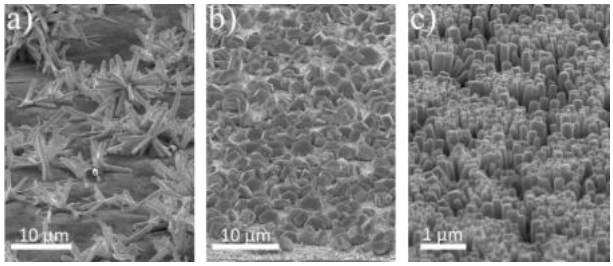

Figure 1. Scanning electron microscopy (SEM) images of a) sample #1 (branched NWs); b) sample #2 (hexapods); c) sample #3 (vertical NWs).

3. Impedance spectroscopy

The electrical properties of the prepared samples were studied using a Z500P impedance meter (Elins, Chernogolovka, Russia) in the frequency range from 100 Hz to 500 kHz by impedance spectroscopy. During the experiment, the impedance spectra were recorded under dark conditions, as well as when the sample was illuminated with IR (850 nm), red (650 nm), green (570 nm), blue (470 nm), and UV (390 nm) LEDs. The spectra of samples under different conditions are presented in Nyquist coordinates - the dependence of the imaginary part of the electrical impedance on the real one (figure 2).

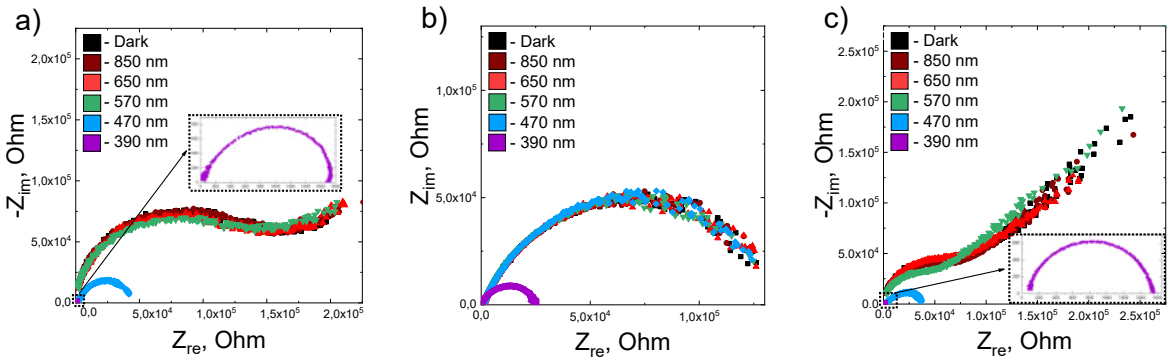

Figure 2. Impedance spectra of a) sample #1; b) sample #2; c) sample #3.

All samples show high absorption when exposed near the absorption edge (390 nm). Samples #1 and #3 show photoconductivity under blue light (λ = 470 nm). This behavior may be due to the presence of defective levels – zinc vacancies [2] in the restricted area. The absence of absorption at a wavelength of 470 nm in the sample #2 indicates a low defectiveness of the structures. Sample #3 PEI also exhibits absorption at a wavelength of – 570 nm, which may be due to the presence of oxygen vacancies and interstitial Zn atoms [2]. Thus, the zinc oxide structures synthesized in the course of this work are promising for their use as photosensitive elements.

Acknowledgments

Authors thank the Ministry of Science and Higher Education of the Russian Federation (Grant FSRM-2020-00011) for support of the nanostructures synthesis and study.

SEM characterization were performed using equipment owned by the Federal Joint Research Center "Material science and characterization in advanced technology".

References

[1] Özgür Ü, Alivov Ya I, Liu C, Teke A, Reshchikov M A, Doğan S, Avrutin V, Cho S-J and Morkoç H 2005 *Journal of Applied Physics* **98** 041301

[2] Galdámez-Martinez A, Santana G, Güell F, Martínez-Alanis P R and Dutt A *Nanomaterials* 2020 **10(5)** 857

[3] Xu H Y, Wang H, Zhang Y C, He W L, Zhu M K, Wang B, Yan H 2004 *Ceramics International* **30(1)** 93-7

Multistage droplet epitaxy for the fabrication of InAs/GaAs quantum dots with ultra-low density

D V Kirichenko, N E Chernenko, N A Shandyba, M M Eremenko, S V Balakirev and M S Solodovnik

Institute of Nanotechnologies, Electronics and Equipment Engineering, Southern Federal University, Taganrog 347922, Russia

Email: dankir@sfedu.ru

Abstract. In this paper, we present a novel droplet epitaxial technique for the fabrication of InAs/GaAs quantum dots with a very low surface density. In contrast to the traditional two-stage approach, we introduce an additional stage of exposure to the ultra-low arsenic flux which enables reduction of In droplets to appropriate sizes. At the following stages of crystallization and annealing, In droplets are converted to low-density InAs quantum dots with a diameter below 30 nm and a surface density below 10^8 cm^{-2}.

1. Introduction

In order to be used in promising electronic and photonic devices, semiconductor quantum dots (QDs) must be well-isolated from each other and have an appropriate size to exhibit quantum effects. In this paper, we demonstrate a technique of multistage droplet epitaxy that allows formation of low-density small-sized InAs/GaAs nanostructures due to an additional stage of the exposure to the ultra-low As flux.

2. Experiment

At the first stage, 1.5 equivalent monolayers (ML) of In were deposited on the surface of epitaxially prepatterned GaAs(001) substrate at 300 °C. At the next stage, droplets formed on the surface were exposed to an As_4 flux of various values (P/P_0 where $P_0 = 7 \cdot 10^{-8}$ Pa) and with various periods t between exposure to the ultra-low flux (ULF) and heating in a large As_4 flux ($P > 3.5 \cdot 10^{-5}$ Pa).

3. Results and discussion

Exposure of droplets to the As flux leads to the formation of various nanostructure complexes [1] (Fig. 1a). A reduction of the droplet size from 98 to 18 nm with the formation of InAs ring at a boundary of three phases (Fig. 1b) occurred in a range of the relative arsenic pressures P/P_0 from 1 to 2.9. The ring diameter indicates the original droplet boundaries and does not change significantly with increasing P.

An increase in the As flux P/P_0 from 4 to 10 induces droplet etching of the surface leading to the formation of a hole under the initial droplet position. A significant increase in the As flux (P/P_0 from 70 to 929) allows a clear observation of the disk formation with an average diameter ranging from 674 to 885 nm around the crystallized InAs rings (Fig. 1c). A transition to exposure at T = 500 °C leads to a qualitative change in the growth system (Fig. 1d). The average diameter of nanostructures obtained after the high-temperature As exposure without a pause between the As supply and substrate heating (t = 0 s) is 102 nm. An increase in this time period from 0 to 60 and 180 seconds leads to a decrease in the diameter of nanostructures from 102 to 87 nm and to 38 nm, respectively (Fig. 2).

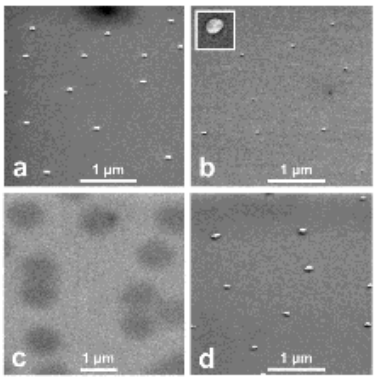

Figure 1. SEM images of nanostructures obtained after deposition of 1.5 ML of In and further exposure to the ultra-low As flux P/P_0: a) 1, b) 1.4, c) 500, d) 714. Inset area is 150×150 nm^2.

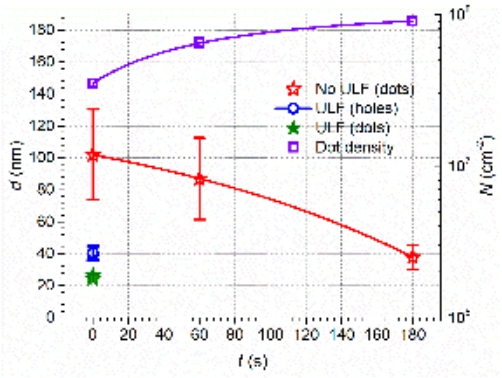

Figure 2. Heating expectation time dependences of the diameter and surface density of 1.5-ML In nanostructures and their further exposure to the ultra-low As flux.

To obtain small-sized QDs with a value of the initial droplet density, we implement the two-stage exposure in the As flux. At the first stage, the droplet volume is reduced to an optimal value under the influence of the ultra-low As flux. At the final stage, a droplet with required parameters is crystallized into an InAs semiconductor QD. As a result, arrays of nanostructures with a density of $3 \cdot 10^7$ cm^{-2} (Fig. 3) and an average diameter of 27 ($P/P_0 = 2$) and 24 nm ($P/P_0 = 2.9$) were obtained (Fig. 2, 4). An average height of the nanostructures is 2.8 nm and 2.5 nm at $P/P_0 = 2$ and $P/P_0 = 2.9$, respectively (Fig. 4).

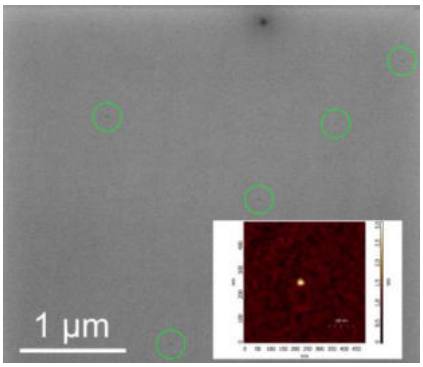

Figure 3. SEM and AFM (inset) images of nanostructures obtained after deposition of 1.5 ML of In and further two-stage As exposure.

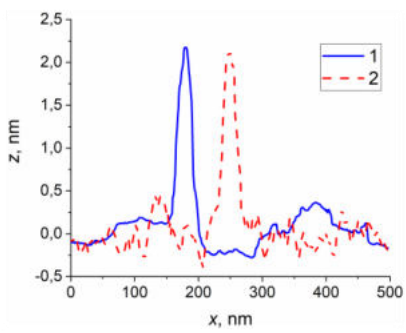

Figure 4. AFM sections of typical nanostructures from Figure 3: 1) $P/P_0 = 2.0$, 2) $P/P_0 = 2.9$.

4. Conclusion

Using the multistage droplet epitaxial technique, we demonstrated the possibility of fabrication of low-density arrays of droplets that can be reduced in size and then transformed into semiconductor QDs. In contrast to the one-stage crystallization in the arsenic vapor, nanostructures obtained after the pre-exposure to the ultra-low As flux have a small size and can be used for the fabrication of low-density InAs QDs.

Acknowledgments

This work was supported by the Russian Science Foundation Grant No. №19-79-10099 at the Southern Federal University.

References

[1] Balakirev S V, Chernenko N E, Eremenko M M, Ageev O A and Solodovnik M S 2021 *Nanomaterials* **11** 1184

Effect of noble metal nanoparticles in transition metal oxide magnetron sputtering

A Kondrateva[1], I Komarevtsev[1,2], Y Enns[1,2], A Kazakin[1,2], P Karaseov[1], M Mishin[1]

[1]Alferov University, St. Petersburg, Russia
[2]Peter the Great Saint-Petersburg Polytechnic University, St. Petersburg, Russia

Abstract. The purpose of this work is to study the transition metal oxides with metal nanoparticles structures formation features. A design technology is proposed, consisting of the oxide matrix magnetron sputtering, Au nanoparticles thermal evaporation and dewetting, and covering it with oxide. Catalytic growth of nickel and titanium oxides on gold nanoparticles has been found. It is shown that the top layer being formed has a pronounced texture. The optical and electrical characteristics of the formed coatings were studied. The results obtained indicate a broad prospect of using the formed structures in the field of integrated optoelectronic devices.

1. Introduction

For the last decades there is a growing need for functional layers with tailored optoelectrical properties, however the bare materials does not usually provide the required characteristics [1, 2]. Thereat, a mixture of materials with precisely guided organization in order to enhance the device features is required. In this respect the noble metal nanoparticles (NPs) dispersed inside semiconductor matrices have recently been under extensive study as high-performance active layers material in numerous integrated optoelectronic devices [3]. Generally, active layers are formed in thin film configuration by using chemical deposition (wet chemistry [4] or CVD [5]), and physical (magnetron deposition [6]). The former are convenient in that they allow the matrix and a filler formation in one process, the latter are more technologically applicable. A wide range of chemical and physical techniques are also used to obtain noble metal nanoparticles [7]. However, despite each of physical techniques requiring expensive deposition equipment, they produce films with sufficient control of NP size, size distribution, and spatial distribution within the layer.

This paper is focused on the the metal oxide film (MOF) deposition on AuNPs research for potential enhancement of properties for optoelectronic devices. The purpose of this work is to study the transition metal oxides with metal nanoparticles structures formation features using nickel and titanium oxides as an example and to investigate the optical and electrical properties of the formed functional coatings.

2. Results

In this work, TiO_2 films were obtained by reactive magnetron sputtering (DC) with a Ti target in an O/Ar gas mixture on amorphous quartz and Si substrates. The gas ratio varied in the range 0.2-1 at an operating pressure of 1.8 mTorr. NiO films were obtained by reactive magnetron sputtering (DC) with a Ni target in an O/Ar gas mixture on amorphous quartz and Si substrates. The gas ratio varied in the

range 0.2-1 at an operating pressure of 1.8 mTorr. The film's thicknesses were controlled by ellipsometry and stands at 50-100 nm. The technique described in [8] were used for AuNP formation. The structure of the samples were analyzed by scanning electron microscopy (SEM), using a JEOL JSM-7001F equipped with Energy Dispersion Spectroscopy (EDS) attachment Bruker XLash 6/30. Top-view and cross-sectional images were obtained using both secondary and backscattered electrons, respectively for morphology studies and atomic weight contrast of the Au NPs. The behavior of TiO_2 and NiO on gold nanoparticles were investigated in terms of texturing and crystallinity. The technique described in [8] were used for electrical and optical experiments.

SEM images of cleavages show two oxide layers, between which there is a clearly defined boundary. In both cases, the formation of an oxide layer with a pronounced structure was observed above the boundary. At the boundary, there are Au nanocrystallites, the average grain size of 50 ± 1 nm. In the case of Si/NiO/AuNP/NiO (SNAN), the EDS results show the presence of O, Si, Ni and Au. In the case of SNAN, the average size of bunsenite crystallites in the lower and upper layers was 35 ± 2 nm and 45 ± 1 nm. The layers differ in the predominant orientation of crystallites (200) and (111), respectively. It was supposed that Au particles acted as a catalyst for the formation of nickel oxide textured in the (111) direction. The EDS results for $Si/TiO_2/AuNP/TiO_2$ (STAT) indicate the presence of O, Si, Ti, and Au. In the case of STAT, the average size of anatase crystallites was 70 ± 1 nm, and for rutile, 100 ± 5 nm. That is, the presence of Au particles also contributed to the formation of texture. That is, the presence of gold nanoparticles on the oxide surface provokes the formation of a textured oxide layer. In addition, the formed structures showed a significant increase in the electrical response when illuminated with visible light, which indicates the prospects for the use of these materials as optically active layers in devices for various purposes.

3. Acknowledgments

Authors wishing to acknowledge the Ministry of Education foundation for financial support assistance (№ FSRM-2020-0011).

References

[1] Lad R J 1995 *Surf. Rev. Let*. **2** 109-126
[2] Mallah A R, Zubir M N M, Alawi O A, Kazi S N, Ahmed W, Sadri R, Kasaeian A 2022 *Renewable Energy* **187** 1204-1223
[3] Kumar A, Choudhary P, Kumar A, Camargo P H, Krishnan V 2022 *Small* **18** 2101638
[4] Tamm A, Acik I, Arroval T, Kasikov A, Seemen H, Marandi M, Krunks M, Mere A, Kukli K, Aarik J 2016 *Thin Solid Films* **616** 449-455
[5] Kulczyk-Malecka J, Donaghy D, Delfour-Peyrethon B, Werner M, Chalker P R, Bradley J W, Kelly P J 2020 *J. Vac. Sci. Technol. A: Vac. Surf. Fil.* **38**(3) 033410
[6] Proença M, Borges J, Rodrigues M, Meira D, Sampaio P, Dias J, Pedrosa P, Martin N, Bundaleski N, Teodoro O, Vaz F 2019 *Appl. Surf. Sci*. **484** 152-168
[7] Bigall N, Eychmüller A 2010 *Philos. Trans. Royal Soc. A: Math. Phys. Engin. Sci.* **368**(1915), 1385-1404
[8] Enns Y, Kondrateva A, Komarevtsev I, Kazakin A, Vyacheslavova E, Kuznetsov A, Andreeva V, Mishin M 2021 *IOP J. Phys. Conf.Ser.* **2103**(1) 012106
[9] Enns Y, Kondrateva A, Mishin M 2020 *J. Phys. Conf. Series* **1695**(1) 012115

Surface modification of magnetron sputtered metal oxide films with plasmonic nanoparticles

A Kondrateva[1], I Komarevtsev[1,2], Y Enns[1,2], A Kazakin[1,2], A Speshilova[1], P Karaseov[1], M Mishin[1]

[1]Alferov University, St. Petersburg, Russia
[2]Peter the Great Saint-Petersburg Polytechnic University, St. Petersburg, Russia

Abstract. The purpose of this work is the plasmonic activators on the transition metal oxides surface formation technology development. The paper demonstrates the main regularities of the plasmonic gold nanoparticles formation on the surfaces of nickel and titanium oxides, and shows that one of the key parameters is the wetting angle. The optical and electrical characteristics of the formed coatings are studied.

1. Introduction

It is well known that the material functional properties are determined not only by its chemical nature, but also by its structure [1]. In this regard, in recent years, the method of the functional coatings properties modification by introducing various nanoobjects into it, in particular, metal nanoparticles, has gained wide popularity. In addition to the obvious change in the structure of the material, resonant absorption at the plasmon frequency, which is characteristic of metal nanoparticles, is manifested [2]. Thus, it is possible not only to reduce the optical band gap of the material, but also to significantly increase the efficiency of the functional coating vs. light interaction. This approach makes it possible to effectively fabricate optically active structures based on virtually any matrix material, and can be used to fabricate functional layers of various optoelectronic products [1–3].

Silver, platinum, palladium and gold are promising materials for distributed arrays of NPs [4]. An important parameter of an plasmonic nanoparticles array is their shape and size, which determine the resonance characteristics [2–4]. In addition, the matrix material also affects the efficiency of radiation conversion. For this reason, despite the presence of a certain number of publications on the features of the formation of nanoparticles on the surface of silicon and materials based on silicon oxide, the transfer of the obtained dependences is impossible.

Thus, The purpose of this work is the plasmonic activators on the transition metal oxides surface formation technology development, using the various phases of nickel and titanium as matrix material.

2. Results

In this work, TiO_2 films were obtained by reactive magnetron sputtering (DC) with a Ti target in an O/Ar gas mixture on Si substrates. The gas ratio varied in the range 0.2-1 at an operating pressure of 1.8 mTorr. NiO films were obtained by reactive magnetron sputtering (DC) with a Ni target in an O/Ar gas mixture on Si substrates. The gas ratio varied in the range 0.2-1 at an operating pressure of 1.8 mTorr. The thickness of the films was controlled by ellipsometry and stands at 43-70 nm. Film structure was investigated using the Scanning Electronic Spectroscopy (SEM) with Gwyddion 2.58

softwear. The optical properties of the films were obtained from the transmission and reflection spectra. On the basis of obtained parameters, behavior of gold nanoparticles on the formed TiO_2 and NiO surfaces were investigated. For electrical and optical examinations, the technique described in [5] were used.

It was found that in the case of bunsenite (cubic nickel oxide), the following regularity is observed: with an the initial gold layer thickness increase from 3.5 to 8 nm, the average diameter of the formed particles and the degree of surface filling with particles decrease from 25 to 25 nm and from 32 to 25%, respectively. According to the SEM data, a layer of hemispherical particles is formed. In the case of titanium oxide (both rutile and anatase), the opposite pattern is observed: the average size of the formed gold particles is retained and amounts to 27 nm, the degree of filling increases from 23 to 29%. According to SEM data, a layer consisting of faceted particles is formed. It is assumed that the features of metal folding on oxide surfaces are determined by the lyophilicity of the latter. Thus, in the case of nickel oxide, the contact angle for water is about 56° [6], which provides a more significant spreading than the surface of titanium oxide, which contact angle is about 82° [7]. The obtained results are consistent with the published experimental data for particles with a diameter of 20 nm [8].

3. Acknowledgments

Authors wishing to acknowledge the Ministry of Education foundation for financial support assistance (№ FSRM-2020-0011).

References

[1] Lad R J 1995 *Surf. Rev. Let*. **2** 109-126
[2] Mallah A R, Zubir M N M, Alawi O A, Kazi S N, Ahmed W, Sadri R, Kasaeian A 2022 *Renewable Energy* **187** 1204-1223
[3] Kumar A, Choudhary P, Kumar A, Camargo P H, Krishnan V 2022 *Small* **18** 2101638
[4] Goswami L, Aggarwal N, Shibin K, Singh M, Vashishtha P, Govind G 2020 *ACS Omega* **5** 14535−14542
[5] Enns Y, Kondrateva A, Mishin M 2020 *J. Phys. Conf. Series* **1695**(1) 012115
[6] Zhang E, Cheng Z, Lv T, Li L, Liu Y 2015 *Nanoscale* **7**(45) 19293-19299
[7] Farichah I, Wahyuningsih S, Ramelan A H 2019 *IOP Conf. Series: Mater. Sci. Eng.* **578** 012030
[8] Kondrateva A, Enns Y, Kazakin A, Morozov I, Karaseov P, Mishin M 2020 *Semiconductors* **54**(14) 1885–1888

Control of optical properties by change in surface chemistry of carbon dots based on citric acid and ethylenediamine

K D Kosolapova[1], A A Vedernikova[1], S A Cherevkov[1], A V Koroleva[2], E V Zhizhin[2] and E V Ushakova[1]

[1] Department of Photonics, ITMO University, St. Petersburg, 197101 Russia
[2] Centre for Physical Methods of Surface Investigation, Saint Petersburg State University, St. Petersburg, 199034 Russia

e-mail: kosolapova@niuitmo.ru

Abstract. A detailed study of optical and electrical properties of carbon dots in dependence on the type of the shell formed on their surface is presented. It was found that the greater the amount of the additives, the more the degree of nanoparticle's surface oxidation. Another set of different additives showed the emission redshift due to graphitic nitrogen doping, that was confirmed by carbon dots morphology studies.

1. Introduction

Carbon dots (CDs) possess several distinct merits such as low toxicity, superior optical properties, and biocompatibility, which makes them attractive for various applications in sensorics, photonics, and biomedicine. However, methods for control of electronic structure and optical properties of CDs need to be expanded which remains an intense research topic [1]. The introduction of new molecules on the CDs surface usually leads to changes in the physicochemical properties determined by switching the surface charge or introducing n orbitals, thus, varying CDs bandgap [2].

In this work, special attention is paid to the study of the CDs optical properties and their morphology depending on the type of added moieties and their quantity, among which were hydrogen peroxide (H_2O_2), ethylenediamine (EDA), citric acid (CA), o-phenylenediamine (o-pd), and urea. A study of the CDs surface chemistry has also been conducted providing additional information about the electronic subsystem of such nanoparticles.

2. Methods

2.1. Synthesis

CDs were synthesized using the solvothermal method, where CA and EDA were selected as precursors in a molar ratio of 1:0.33. Water was used as a solvent. The resulting solution of precursors was heated in an autoclave at a temperature of 190 °C for 8 h. The final colloidal solution was purified from large particles and agglomerates using a syringe filter and further purified from small organic molecules using dialysis with a cut-off by weight of 6-8 kDa.

To establish the effect of the surface oxidation degree on the CDs optical properties, a different amount of H_2O_2 (5 - 40 μL) was added to 200 μL of the stock sample. For the second set of samples, EDA was used as an additive in the same proportions.

To estimate the influence of precursors (urea, CA, and o-pd) on optical and electrical properties of CDs three other samples were prepared: to 1 mL of CDs (1 mg/mL) a 2 g of each precursor, the mixtures were dissolved in 9 mL of water. The solutions were transferred into autoclaves, heated at 180 °C for 6 h and cooled down to room temperature. Then colloidal solutions were purified from residual precursors via dialysis with a cut-off by weight of 6-8 kDa.

2.2. Samples characterization

Absorption and photoluminescence spectra of samples were recorded with a spectrophotometer UV-3600 (Shimadzu) and a spectrofluorometer Cary Eclipse (Agilent). A Fourier-transform infra-red (FTIR) spectrophotometer Tenzor II (Bruker) was used to study the chemical composition of the CDs surface. The elementary composition of CDs was obtained using the method of X-ray photoelectron spectroscopy (XPS) using an ESCALAB 250Xi photoelectron spectrometer (Thermo Fisher Scientific) at the Resource Center "Physical Methods of Surface Research", Scientific Park of St. Petersburg State University.

3. Results

Optical measurements showed that in the absorption spectra of CDs with a different proportion of H_2O_2, there is a blueshift shift of the absorption band with further the additive's amount increase. Similarly, there are changes in the absorption spectra of CDs with different EDA amounts. The photoluminescence (PL) spectra of the samples showed a decrease in the intensity with the amount of additives. FTIR spectroscopy indicated the appearance of new molecular groups on the surface, which results in changes in the CDs chemical composition depending on the type of additive.

CDs samples prepared by solvothermal treatment with urea, CA, and o-pd were found to have a redshift in emission as the content of graphitic nitrogen increased. CA and urea, under hydrothermal conditions, form molecular fluorophores of the pyridine family (and other heterocyclization products), which usually dominate the CDs optical properties [2].

As a result, it was shown that the oxidation of the CDs surface affects the optical properties of the obtained samples, and the study of the CDs surface chemistry depending on the type of additive indicates the appearance of new molecular groups on the surface. Thus, it is possible to control the electrical and optical properties of such nanostructures by change in their morphology.

Acknowledgments

The work was financially supported by the Ministry of Science and Higher Education of the Russian Federation under the GZ 2019-1080, under the grant NIRMA PT MF ITMO University. XPS studies were conducted with financial support from St. Petersburg State University (project No 93021679).

References

[1] Zhu J, Bai X, Chen X, Shao H, Zhai Y, Pan G, Zhang H, Ushakova E V, Zhang Y, Song H and Rogach A L 2019 Spectrally tunable solid state fluorescence and room-temperature phosphorescence of carbon dots synthesized via seeded growth method *Adv. Opt. Mat.* **7** 1801599

[2] Dordevic L, Arcudi F, Cacioppo M and Prato M 2022 A multifunctional chemical toolbox to engineer carbon dots for biomedical and energy applications *Nat. Nan.* **17** 112-130

New bismuth titanates heterostructures as Vis-photocatalysts: DFT and experimental insight

A.G. Krasnov[1], M.S. Koroleva[1], I.V. Piir[1], I.R. Shein[2],

[1] Institute of Chemistry, Federal Research Center Komi Science Center UB RAS, Syktyvkar, 167982, Russia
[2]Institute of Solid State Chemistry, UB RAS, Ekaterinburg, 620990, Russia.

alexey-krasnov@rambler.ru

Abstract. Photocatalytic properties of bismuth titanates with pyrochlore, sillenite, and layered perovskite structures are examined via the *ab initio* calculation and experiment. In situ heterojunction formation was performed for each pair of the compounds. The DFT and experimentally determined characteristics suggest high photocatalytic activity of the single-phase and heterojunction photocatalysts. The ability to decompose organic dye RhB and paracetamol as the modeling pollutants in aqueous solutions was revealed during the photocatalytic tests under visible light irradiation.

1. Introduction

The heterogeneous photocatalysis process with semiconductors is one of the preferable purification methods. The possibility of applying natural and renewable solar energy to purify water, air, and surfaces from organic pollutants (including drugs) makes photocatalysis environmentally friendly and economical cost. Bismuth titanates with various structural types are stated to be perspective photocatalysts[1,2]. Several strategies are known to enhance the photocatalytic activity of the photocatalysts in visible light, e.g., the optimization of crystal structure, surface area, and morphology; the manipulation of native defects; doping to adjust the optoelectronic properties, heterojunction construction.

2. Experiments and methods

Bismuth titanates $Bi_2Ti_2O_7$, $Bi_4Ti_3O_{12}$, and $Bi_{12}TiO_{20}$ were prepared in the form of nanopowders by using a simple coprecipitation method[2–4]. In situ heterojunction formation was performed for each pair of the compounds e.g., $Bi_2Ti_2O_7$/$Bi_4Ti_3O_{12}$, $Bi_2Ti_2O_7$/$Bi_{12}TiO_{20}$, and $Bi_4Ti_3O_{12}$/$Bi_{12}TiO_{20}$. A comprehensive certification of the obtained samples by physicochemical methods (XRD, SEM, TEM, DSC, dynamic light scattering method, BET, diffuse reflectance spectroscopy) was carried out. The ability to decompose organic dye RhB and paracetamol as the modeling pollutants in aqueous solutions was estimated during the photocatalytic tests under visible light irradiation.

DFT calculations of the bismuth titanates models were conducted using the PAW method as implemented in VASP software. The GGA-PBE formalism was used to describe exchange-correlation effects during geometry optimization. We employed the screened Coulomb hybrid exchange-correlation functionals to accurately predict the optoelectronic properties.

3. Results and Discussion

We carefully detected phase formation temperature of single-phase samples $Bi_2Ti_2O_7$, $Bi_4Ti_3O_{12}$, and $Bi_{12}TiO_{20}$ using XRD method. Pure $Bi_2Ti_2O_7$ and $Bi_4Ti_3O_{12}$ could be crystallized after one annealing stage at 500 °C, when $Bi_{12}TiO_{20}$ required the annealing temperature 100 degrees higher. The in-situ heterojunction photocatalysts were performed according this annealing conditions. The SEM analysis of each sample reveals only one phase, in which element ratios are almost identical to the initial ones. The estimated crystallite size is 30–40 nm with noticeable agglomerates of about 100–500 nm according to scanning electron microscopy (SEM) and with the formation of particles (300-600 nm) in the aqueous medium. The isoelectric points of the nanopowders seem to be shifted to the strongly acidic region, resulting in the formation of negative surface particle charges at pH in distilled water.

The excellent agreement between DFT calculated and experimental structural parameters of the bismuth titanates is found. The screened Coulomb hybrid HSE03 functional is the most appropriate for describing the optoelectronic properties. Single-phase bismuth titanates and their heterojunctions are wide-gap semiconductors with the strong abilities to be active photocatalysts under Vis irradiation. The optical E_g values for direct/indirect transitions are in good agreement with DFT/HSE03 predicted values and are in the visible light. The calculated low effective masses of the charge carriers and suitable band edges positions confirm the ability of the bismuth titanates to act as Vis-photocatalysts. The photocatalytic activity is evaluated through the decomposition of the rhodamine B and paracetamol water solutions under Vis irradiation.

Acknowledgments

The research was done using the equipment of Center for Collective Use «Khimiya» of Russian Academy of Sciences Ural Branch Federal Research Center Komi Science Center Institute of Chemistry; Center for Collective Use of IMM UrB RAS "Supercomputer Center URAN IMM UrB RAS." This work was supported by the Council on grants of the President of the Russian Federation (MK-310.2021.1.3).

References

[1] Noureldine, D.; Lardhi, S.; Ziani, A.; Harb, M.; Cavallo, L.; Takanabe, K. Combined Experimental-Theoretical Study of the Optoelectronic Properties of Non-Stoichiometric Pyrochlore Bismuth Titanate. *J. Mater. Chem. C* **2015**, *3* (46), 12032–12039. https://doi.org/10.1039/c5tc03134f.

[2] Krasnov, A. G.; Napalkov, M. S.; Vlasov, M. I.; Koroleva, M. S.; Shein, I. R.; Piir, I. V. Photocatalytic Properties of Bi2-XTi2O7-1.5 x(x = 0, 0.5) Pyrochlores: Hybrid DFT Calculations and Experimental Study. *Inorg. Chem.* **2020**, *59* (17), 12385–12396. https://doi.org/10.1021/acs.inorgchem.0c01472.

[3] Ishchenko, A. V.; Koroleva, M. S.; Vlasov, M. I.; Istomina, E. I.; Piir, I. V. Synthesis and Luminescent Properties of Bismuth Titanates Bi1.6HoxTi2O7 – δ and Bi1.6Mg0.1HoxTi2O7 – δ. *Phys. Solid State* **2019**, *61* (5), 867–873. https://doi.org/10.1134/S1063783419050111.

[4] Krasnov, A. G.; Koroleva, M. S.; Vlasov, M. I.; Shein, I. R.; Piir, I. V.; Kellerman, D. G. Ab Initio and Experimental Insights on Structural, Electronic, Optical, and Magnetic Properties of Cr-Doped Bi2Ti2O7. *Inorg. Chem.* **2019**, *58* (15), 9904–9915. https://doi.org/10.1021/acs.inorgchem.9b01057.

Efficiency of GaO_x nanoclusters formation in SiO_2 and Al_2O_3 dielectric layers subjected to O^+ and Ga^+ ion implantation

R N Kriukov*, S Yu Zubkov, D E Nikolichev, D S Korolev, A A Nikolskaya, A V Zdoroveyshchev, V K Vasiliev

Lobachevsky State University of Nizhni Novgorod, 23/3, Gagarina pr., Nizhni Novgorod, 603950 Russia

* email: kriukov.ruslan@yandex.ru

Abstract. It is shown that successive irradiation of SiO_2 and Al_2O_3 dielectric films with O^+ and Ga^+ ions is accompanied by the formation of gallium oxides and elemental Ga inclusions. The distribution profiles of these chemical compounds depend on the sequence of implantation of O^+ and Ga^+ ions.

1. Introduction

The task to create ultraviolet photodetectors is dictated by a wide range of possible practical problems from engine diagnostics to the study of the Earth's ozone layer [1, 2]. This requires the sensors that could register light with a wavelength of less than 280 nm. For such purposes, the Ga_2O_3 semiconductor is suitable, because of its wide band gap of 4.8 eV [3], which corresponds to a maximum wavelength of 260 nm. Since now, there is no technology for creating high-quality gallium oxide layers on semiconductor substrates, that is why the possibility of creating Ga_2O_3 nanoclusters in a dielectric matrix by ion implantation becomes relevant [4]. At the same time, there is a problem of optimizing the technology and evaluating the efficiency of the inclusions formation. To study the features of the creation of nanoclusters in the framework of the work, the method of X-ray photoelectron spectroscopy (XPS) with ion profiling is used.

2. Methods

The structures synthesized by a two-stage technology. At the first stage, Al_2O_3 and SiO_2 films with the thicknesses of 200 and 350 nm, correspondingly, were grown on a Si substrate by electron-beam evaporation. At the second stage, successive implantation of O^+ (23 keV, 6×10^{16} cm^{-2}) and Ga^+ (80 keV, 5×10^{16} cm^{-2}) ions was performed. XPS spectra were measured using an Omicron Multiprobe RM ultrahigh vacuum complex (Germany). Photoemission was excited by MgKα radiation. The analysis area diameter was 3 mm. Layer-by-layer profiling was carried out by etching with Ar^+ ions with an energy of 1 keV. The limiting detectable concentration of elements which was determined by the signal-to-noise ratio of the photoelectron spectra was 0.1-1 at.%. To determine the concentration of chemical elements, photoelectron lines O 1*s*, C 1*s*, Ga $2p_{3/2}$, Al 2*p*, Si 2*s* were recorded. The spectra were recorded at an analyzer transmission energy of 30 eV and an energy step of 0.2 eV. Mathematical processing of the spectra was carried out using the SDP v. 4.3 software according to the method [5].

3. Results

It has been found that the irradiation of SiO_2 and Al_2O_3 films with O^+ and Ga^+ ions is accompanied by the formation of gallium oxides (GaO_x) compounds and elemental Ga^0. The concentration maxima of these compounds are separated in depth. After the first ion implantation, an oxygen-enriched region, in which oxygen is not chemically bound to aluminum, is formed deep inside the layer. At the second stage, after Ga^+ implantation, a significant part of it is at an oxygen-enriched layer, and, accordingly, gallium oxide compounds are formed.

The differences in the distribution profiles of GaO_x and Ga^0 for different matrices can be explained as follows. Presumably, in Al_2O_3 layers, which are more radiation-resistant, it is more difficult to break chemical bonds and deform the crystal lattice. This leads to the possible out-diffusion of implanted Ga and O atoms, which did not chemically interact in the film, to the surface. A similar picture was observed earlier during ion implantation of In into Al_2O_3 [6].

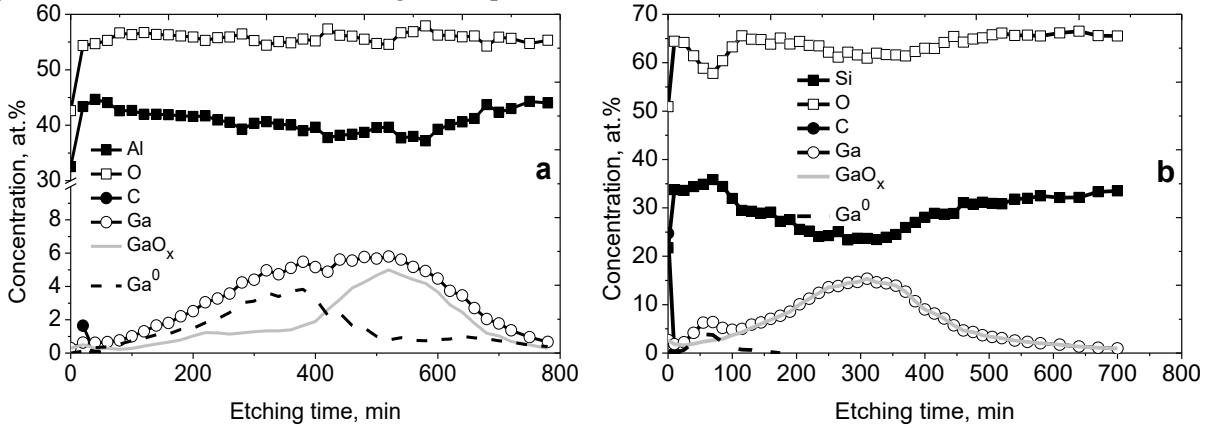

Figure 1. Distribution profiles of chemical elements in a) Al_2O_3 and b) SiO_2 layers subjected to sequential ion implantation of O^+ and Ga^+.

The results of the investigation of depth profiles in Al_2O_3 and SiO_2 dielectric layers implanted sequentially with O^+ and Ga^+ ions show that the technological process of solid-state synthesis of GaO_x nanoclusters in such matrices requires a more accurate selection of irradiation regimes to increase the fraction of oxidized gallium.

Acknowledgments

The study was supported by a grant from the Russian Science Foundation № 21-79-10233, https://rscf.ru/en/project/21-79-10233/.

References

[1] Monroy A E, Omnes F, Calle F, 2003 *Semicond. Sci. Technol.* **18 (4)** R33.

[2] Tsai D, Lien W, Lien D, Chen K, Tsai M, Senesky D G, Yu Y, Pisano A P, He H, 2013 *Sci. Rep.* **3** 2628.

[3] Hu G C, Shan C X, Zhang N, Jiang M M, Wang S P, Shen D Z, 2015 *Opt. Express.* **23 (10)**, 13554.

[4] Rajamani S, Arora K, Belov A, Korolev D, Nikolskaya A, Usov Yu, Pavlov D, Mikhaylov A, Tetelbaum D, Kumar M, Kumar M, 2018 *IEEE Sensors Journal* **18 (10)** 4046.

[5] Boryakov A V, Surodin S I, Kryukov R N, Nikolichev D E, Zubkov S Yu, 2018 *J. of Electron Spectr. and Rel. Phenomena* **229** 132.

[6] Mouritz A P, Sood D K, St John D H, Swain M V, Williams J S, 1987 *Nuc. Instr. and Meth. in Phys. Research* **B19/20** 805.

SIMLAD: A General Simulation Program For Semiconductor Laser Dynamics

Igor Kudryashov[1,2,3], **R Shakhovoy**[1,4,5]
[1]QRate, Novaya av. 100, Moscow, Russia
[2]Russian Quantum Center, 45 Skolkovskoye shosse, Moscow, Russia
[3]Moscow Institute of Physics and Technology, National Research University, Institutsky lane 9, Dolgoprudny, Moscow region, 141700, Russia
[4]NTI Center for Quantum Communications, National University of Science and Technology MISiS, 4 Leninsky prospekt, Moscow, Russia
[5]Moscow Technical University of Communications and Informatics, 8A Aviamotornaya, Moscow, Russia

E mail i.kudryashov@goqrate.com

Abstract. We present here a simulation program for semiconductor laser dynamics, which was developed as a user-friendly window program for visualizing laser output at various laser parameters and configurations.

Semiconductor laser rate equations are a very convenient and powerful tool for analysing the dynamics of lasers including its stochastic properties [1, 2]. Here, we present a simulation program for semiconductor laser dynamics – SIMLAD. The program was conceived as a user-friendly window program for visualizing laser output at various laser parameters and configurations.

The program allows the user to set the values of various laser parameters: threshold and transparency carrier number, the Henry factor, the gain compression, the confinement factor, etc. The user also has the opportunity to set pump current parameters, including the form of the injection current (sinusoidal or square pulses), to change the pulse repetition rate, the values of the modulation and bias currents, the pulse width and even the bandwidth of the "electric path". The user can "switch-on" and "switch-off" the spontaneous emission noise; corresponding stochastic rate equations are solved using Euler-Maruyama [3] method. In addition, the user can "switch-on" and "switch-off" temperature effects related to the dissipation of optical power in the active layer of the laser.

The program allows setting the properties of the photodetector, which is simulated by applying a signal filtering (the user can choose a type of the filter and its cutoff frequency). One can also simulate the interference of the output light in the Mach-Zehnder interferometer, and the user can choose the delay line and control the phase shift in the interferometer.

The program can calculate spectra of a solitary single-mode semiconductor laser in pulsed and continuous mode. One can also simulate bandpass spectral filtering setting variable parameters (filter type, bandwidth, filter order, central frequency, etc.). Moreover, the program allows simulating transfer functions and response functions of linearized semiconductor laser model.

In addition to a solitary semiconductor laser, the user can simulate the output of an optically injected laser. The user can set up the parameters of both slave and master lasers, enable/disable stochastic and temperature effects on both lasers.

The user can set up plots that are shown by the program and export simulated data in different formats.

References

[1] K. Petermann 1988 *Laser Diode Modulation and Noise* (Tokyo Kluwer Academic Publishers)

[2] Govind P. Agrawal, Niloy K. Dutta 2001 *Semiconductors Lasers* (Kluwer Academic Publishers)

[3] Peter E. Kloeden, Eckhard *Platen* 1995 *Numeerical Solution of Stochastic Differential Equations* (Springer-Verlag Berlin Heidelberg)

Method of Ge_xSi_{1-x} doping with phosphorus in the spark plasma sintering process

Yu M Kuznetsov[1,2], M V Dorokhin[2], P B Demina[2], I V Erofeeva[2], A V Zdoroveyshchev[2], A Yu Zavrazhnov[3], M V Ved[2], D A Zdoroveyshchev[1,2] and A V Voronin[1]

[1]Lobachevsky state university, 603950, Russia, Nizhny Novgorod, Gagarin av. 23 b.3
[2]Scientific Research Institute of Physics and Technology of Lobachevsky State University, 603950, Russia, Nizhny Novgorod, Gagarin av. 23 b.3
[3]Voronezh state university, 394018, Russia, Voronezh, University Square 1

E-mail: yurakz94@list.ru

Abstract. The paper proposes a new method for doping a germanium-silicon solid solution with phosphorus during synthesis by spark plasma sintering: silicon phosphide is used as a dopant source. A study of the thermoelectric characteristics of of n-type conductivity samples depending on the technological conditions and composition are discussed. The sintering parameters providing the highest thermoelectric figure of merit were obtained.

1. Introduction

Thermoelectrics are materials that convert thermal energy into electrical one. The efficiency of conversion is determined by the expression:

$$ZT = \alpha^2 T/\rho\lambda, \quad (1)$$

where α is the Seebeck coefficient, ρ is the resistivity, λ is the thermal conductivity. The trends of recent years are aimed at studying the *ZT* of GeSi semiconductor ceramics formed by sintering nanopowders with low thermal conductivity [1].

2. Experimental technique

A feature of this work is the use of non-toxic silicon phosphide as a dopant for a germanium-silicon solid solution. Such an approach makes it possible to avoid the use of toxic phosphorus for doping, thereby significantly facilitating work with the powders to be sintered. We have investigated a series of samples in which the dopant concentration and the heating rate of the powder mixture were varied. The samples were sintered in a DR-SINTER SPS-625 Spark Plasma Sintering System at a pressure of 70 MPa and a temperature of 1040 °C.

Measurement of the temperature dependence of α was carried out during the generation of a controlled temperature gradient with subsequent measurement of the thermo-voltage signal. The value of ρ was measured using a standard four-probe technique. The temperature dependence of λ was obtained by the method of stationary heat flux. The value of *ZT* was calculated using formula (1). Measurement techniques are described in [2].

3. Results

The temperature dependences of the thermoelectric parameters of the studied samples were obtained.

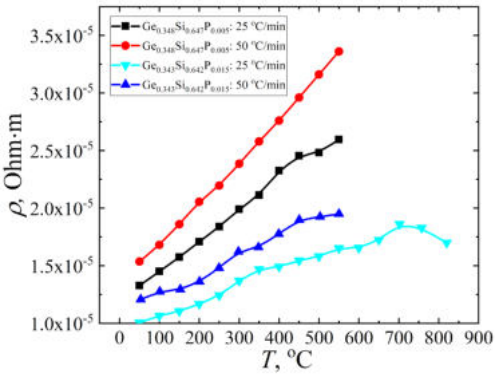

Figure 1. Temperature dependence of resistivity

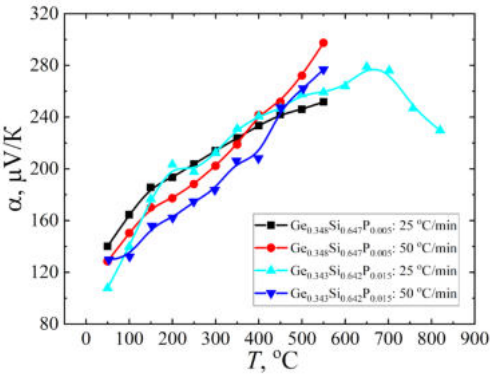

Figure 2. Temperature dependence of the Seebeck coefficient

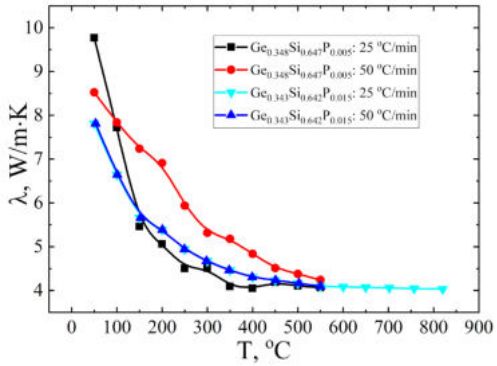

Figure 3. Temperature dependence of the thermal conductivity

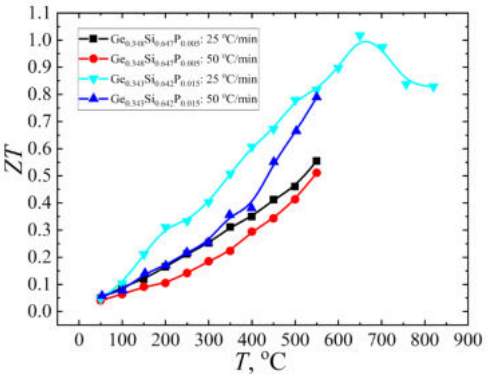

Figure 4. Temperature dependence of *ZT*

All samples demonstrate rather low resistivity and high ZT values. The largest *ZT* in the entire measured temperature range is revealed for a sample fabricated at a sintering rate of 25 °C/min. This sample was additionally investigated up to temperatures of 850 °C. The value *ZT* = 1.03 was obtained at a temperature of 690 °C, which is in good agreement with world analogues [3].

4. Conclusion

The paper shows a new method of phosphorus doping of nanostructured thermoelectric materials based on a germanium-silicon solid solution in the process of synthesis by spark plasma sintering. The optimal technological parameters, as well as the level of doping, at which high values of thermoelectric figure of merit are achieved, have been established.

Acknowledgement

The work was supported by the RFBR grant (20-32-90032) and by the support of the federal academic leadership program «Priority 2030» of the Ministry of Science and Higher Education of the Russian Federation.

References

[1] Mao J, Chen G and Ren Z 2021 *Nature Materials* **20** 454

[2] Murugasami R, Vivekanandhan P, Kumaran S, Suresh K R and Tharakan J 2019 *Bull. Mater. Sci.* **118** 110483
[3] Romanjek K, Vesin S, Aixala L, Baffie T, Bernard-Granger G and Dufourcq J 2015 *J. Electron. Mater.* **44** 2192

Optimizing deposition regimes to fabricate vanadium dioxide film for active metasurfaces

M.E. Kutepov[1], I.K. Domaratskiy[2], S.S. Zhukov[2], E.M. Kaidashev[1], I.V. Lisnevskaya[3], K.G. Abdulvakhidov[4] and V. E. Kaydashev[1]

[1]Laboratory of Nanomaterials, Southern Federal University, Stachki Ave. 200/1, 344090, Rostov-on-Don, Russia
[2]Center for Photonics and 2D Materials, Moscow Institute of Physics and Technology (MIPT), Institutskiy Per.9, 141701, Dolgoprudny, Russia
[3]Department of Chemistry, Southern Federal University, Zorge 7, 344090, Rostov-on-Don, Russia
[4]The Smart MaterialsResearch Institute, Southern Federal University, Sladkova 178/24, 344090, Rostov-on-Don, Russia

kaydashev@gmail.com

Abstract. Several deposition protocols to prepare epitaxial VO_2 films for active metasurfaces were studied. The optimization of properties was done by analysing electrical, structural properties, lattice vibrations and reflection in middle IR range of prepared films.

1. Introduction

THz/middle IR imaging techniques for biology and medicine as well as sixth generation (6G) of mobile communication systems urgently need new tools to in-situ manipulate a front of a plane wave in sub-THz range of 0.1-1 THz and middle IR range of 10-60 THz. By exploiting "static" metasurfaces made of metallic antenna array one may already fabricate a great variety of devices to filter mid-IR/THz waves, modulate its intensity or manipulate a wavefront, i.e. focus radiation, obtain beam steering to a given angle, alter polarization, filter wavelength or achieve ultrafast modulation. Due to use of metallic elements the functions of these devices are pre-defined by their design. VO_2-based metasurfaces whose mid-IR/THz transmission/reflection are dynamically altered due to isolator-to-metal transition (IMT) do offer a great flexibility in programming device characteristics by local heating, electric current or laser light exposure. Some progress in this direction has already been achieved recently [1,2]. However, to obtain an advanced performance of a metasurface several characteristics of VO_2 film should be engineered in proper manner. These properties of VO_2 film should be simultaneously optimized, namely, isolator-to-metal state resistance alteration ratio, abruptness of a resistance versus temperature characteristics, lower phase transition temperature and reduced photo- and/or electrically induced switching times. We study the effect of pulsed laser deposition regimes on properties of the deposited epitaxial vanadium oxide film on c-Al_2O_3 substrates to optimally apply them in desired metasurfaces. The influence of oxygen pressure and incident laser fluence on the properties of the deposited VO_2 films were characterized by temperature dependent electric measurements, XRD, Raman spectroscopy and mid-IR absorption/reflection spectroscopy.

2. Experimental

VO_2 films were prepared by pulsed laser deposition method. KrF laser beam (248 nm, 15ns, 10 Hz) was focused on the surface of rotating VO_2 or metallic vanadium target to give a fluence of 2 J/cm^2. The c-Al_2O_3 substrate was positioned at 5 cm from the target. The epitaxial films were deposited in oxygen ambient for 4000 laser pulses as shown in Figure 1b.

The samples in the first series were obtained from VO_2 target at different oxygen pressure in the range of 1.5×10^{-2} – 5×10^{-2} mbar. The substrate temperature was maintained at 550°C. VO_2 film shows the greatest resistance reduction for 2.4×10^3 times and the a minimal hysteresis width of ΔT=4.5 °C due to heat induced IMT in samples deposited at oxygen pressure of 4×10^{-2} mbar as shown in Figure 1a. The drop of resistance is accompanied with structural transition from monocline (M1+M2) to rutile and monocline (R+M2) phase mixture in VO_2 lattice (Figure 1c) and significant increase of film reflectance in broad mid-IR range (Figure 1d).

The samples in the second series were obtained at varied laser fluence in the range of 2-3 J/cm^2. The oxygen pressure and the substrate temperature were maintained at 1.5×10^{-2} mbar and 550°C, correspondingly. The hysteresis width of *R(T)* characteristics was narrowest and resistance shows a maximal decrease at fluence of 2.5 J/cm^2.

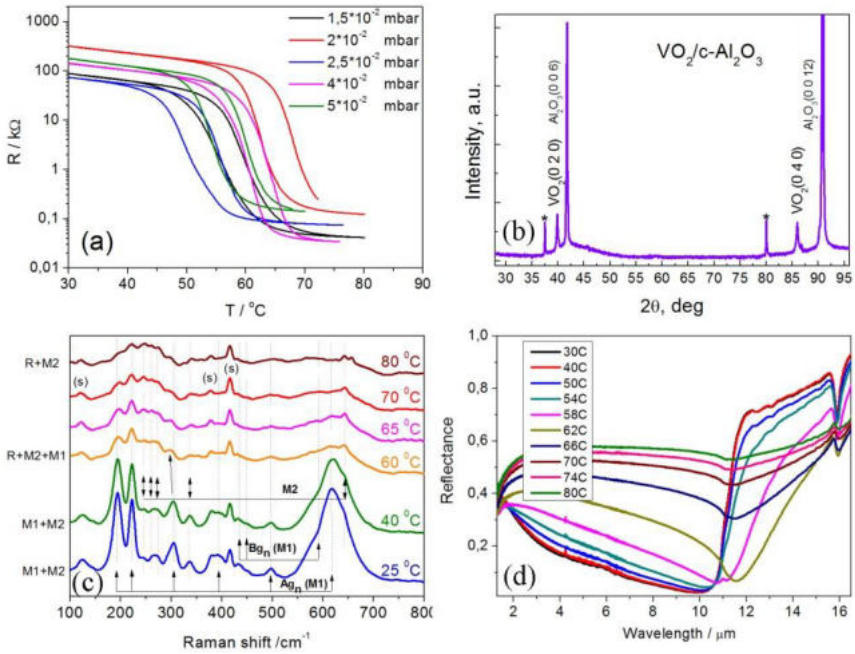

Figure 1 Temperature dependent resistance of VO_2 film on c-Al_2O_3 substrate deposited at various oxygen pressure in the range of 1.5×10^{-2} – 5×10^{-2} mbar (a); XRD of typical VO_2 film (b);. Raman (c) and middle IR reflection spectra (d) of typical VO_2 film as function of temperature.

Acknowledgments

Deposition of VO_2 films was supported by project No.07/2020-06-MM at SFU, mid-IR reflection study was supported by RSF project No.21-79-00209 at MIPT, electrical measurements and Raman study were supported by RSF project No.22-29-01037 at SFU

References

[1] S. Cueff, J. John, Z. Zhang, J. Parra, J. Sun, R. Orobtchouk, S. Ramanathan, P. Sanchis, "VO2 nanophotonics," APL Photon., vol. 5, no.11, pp. 110901, Nov. 2020

[2] J. He, T. Dong, B. Chi, Y. Zhang, "Metasurfaces for Terahertz Wavefront Modulation: a Review," J. Infrared, Millimeter, and Terahertz Waves, vol. 41, pp. 607-631, Feb. 2020.

Independent control of size and shape of GaAs nanostructures during droplet epitaxy using ultra-low arsenic flux

E. A. Lakhina, D. V. Kirichenko, H. E. Chernenko, H. A. Shandyba, M. M. Eremenko, S. V. Balakirev, M. S. Solodovnik

Institute of Nanotechnologies, Electronics and Equipment Engineering, Southern Federal University, Taganrog 347922, Russia

Email: lakhina@sfedu.ru

Abstract. In this paper, we first reveal a possibility to reduce a size of Ga droplets using ultra-low arsenic flux. The control of size and shape of droplets is implemented independently of their surface density that enables formation of low-density arrays of small-sized quantum dots. Based on droplet arrays with bimodal size distribution, we demonstrate that droplets with larger sizes are less influenced by the low arsenic flux whereas smaller droplets may reduce in volume or decay completely.

1. Introduction

The importance of zero-dimensional GaAs/AlGaAs nanostructures is increasingly growing because of their applicability to promising nanoelectronic and quantum photonic devices [1]. However, it is still difficult to fabricate small-sized GaAs quantum dots with a low density (less than 10^8-10^9 cm^{-2}) and control their size and shape independently.

In this paper, we demonstrate a possibility to reduce a size of Ga droplets using an ultra-low arsenic flux (ULF) before their total arsenization and study its effect on the droplets with various diameters.

2. Experiment

At the first stage, 3 Ga monolayers (ML) were deposited on GaAs substrate at $T = 500$ °C followed by exposure in a low As_4 flux of different values at $T_{ULF} = 300$ °C to decrease the initial droplet size by the outflow diffusion of Ga atoms from the droplet. An additional exposure at $T_{ULF} = 400$ °C was carried out on the following samples.

3. Results and discussion

An increase of the arsenic pressure increment ΔP from $3 \cdot 10^{-8}$ to $5 \cdot 10^{-7}$ Pa leads to a decrease in the average diameter of droplets obtained after deposition of 3 ML Ga on GaAs surface from 71 nm to 56 nm (Fig. 1, 2). A further increase in the pressure increment ΔP to 1 10^{-6} leads to a larger change in the droplet diameter as a percentage of the original droplet diameter (26% for the sample with $\Delta P = 1 \cdot 10^{-6}$ and 24% for the sample with $\Delta P = 5 \cdot 10^{-7}$), determined by the droplet boundaries or the diameter of the crystallized ring retained around the droplet. Therefore, the droplet size can be significantly controlled by the ultra-low As flux.

It is also worth noting that the average diameter of droplets obtained after deposition of 3 ML of Ga and exposed to the ultra-low As flux $\Delta P = 6 \cdot 10^{-8}$ Pa at $T_{ULF} = 300$ °C have a bimodal distribution (Fig. 3a,c) implying the presence of the secondary nucleation.

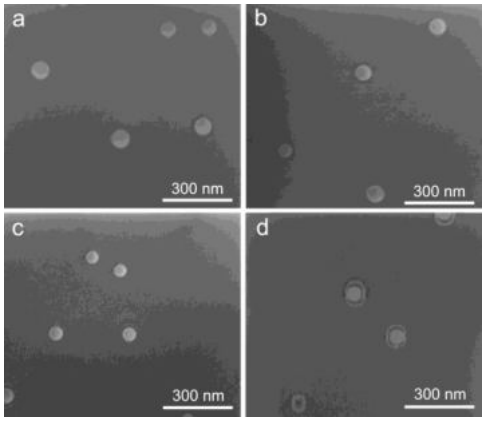

Figure 1. SEM images of nanostructures obtained after deposition of 3 ML Ga on the GaAs surface and subsequent exposure to the low As flux ΔP: *a*) $3 \cdot 10^{-8}$ Pa, *b*) $6 \cdot 10^{-8}$ Pa, *c*) $5 \cdot 10^{-7}$ Pa, *d*) $1 \cdot 10^{-6}$ Pa.

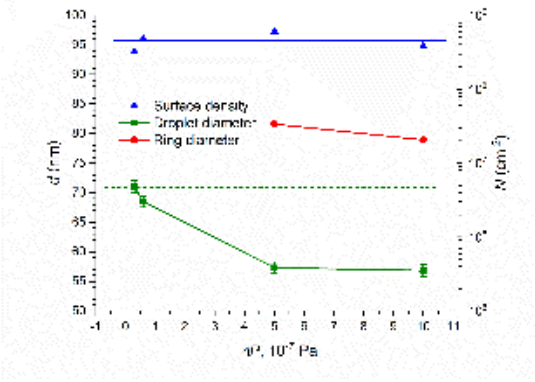

Figure 2. Arsenic pressure dependences of the average diameter of nanostructures obtained after the deposition of 3.0 ML Ga on the GaAs surface at $T = 500$ °C.

The exposure at a higher temperature of 400 °C leads to the complete decay of smaller droplets and retention of larger droplets (Fig. 3b) which indicates that near-critical droplets are more influenced by the As flux. Besides the possibility of droplet size control, the low-flux As exposure opens up opportunities for a decrease of the surface density of nanostructures after initial formation of high-density droplet arrays.

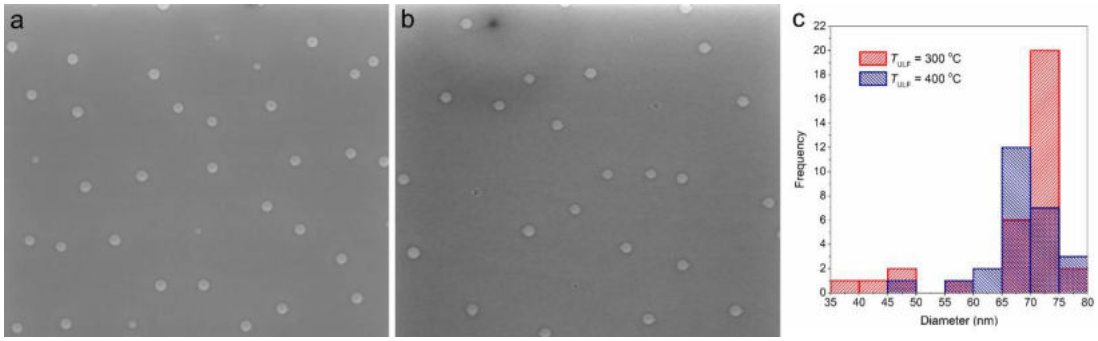

Figure 3. SEM images of nanostructures obtained after deposition of 3 ML Ga and exposure to the low As flux $\Delta P = 6 \cdot 10^{-8}$ Pa: *a*) $T_{ULF} = 300$ °C, *b*) $T_{ULF} = 400$ °C, *c*) histograms of the droplet size distribution.

4. Conclusion

We reported, for the first time, the possibility of reducing the Ga droplet size using an ultra-low As flux to obtain low-density arrays of small-sized nanostructures. The droplet diameter decreases with increasing As flux whereas the surface density remains approximately at the same value. Droplet arrays obtained after deposition of 3 ML of Ga at $T = 500$ °C with subsequent exposure to the As flux are shown to have a bimodal size distribution. We revealed that Ga droplets of smaller sizes exposed to the As flux at $T_{ULF} = 400$ °C etch the surface and then decay completely.

Acknowledgments

This work was supported financially by the Russian Science Foundation (Project № 19-79-10099) at the Southern Federal University.

References

[1] Balakirev S V, Solodovnik M S, Eremenko M M, Chernenko N E and Ageev O A 2020 *Nanotechnology*, **31** 485604

InAs quantum dots in Si: MBE growth and optical properties

V V Lendyashova[1,2,3*], I V Ilkiv[1,2], V G Talalaev[1], B R Borodin[3], R R Reznik[1,2], G E Cirlin[1,3]

[1] Alferov University, St. Petersburg, 194021, Russia
[2] St. Petersburg State University, St. Petersburg 199034, Russia
[3] Ioffe Institute, St. Petersburg 194021, Russia

E-mail: * erilerican@gmail.com

Abstract. Owing years, Si-based nanocomposite materials with optically active quantum dots (QDs) is of great interest due to potential prospects for their integration with conventional silicon electronics. In this study, we present the direct growth of InAs QDs on Si and fabrication of nanocomposite material by molecular beam epitaxy (MBE). Photoluminescence spectra study of samples with InAs quantum dots showed emission in the third telecommunication window near 1.6 μm region.

1. Introduction

Nowadays, the development of new optical integrated circuits (ICs) is one of the most important directions because the use of such ICs can significantly increase the performance of computing systems and reduce their energy consumption [1,2]. The most promising approach to do so is based on the integration of traditional ICs with active A3B5 semiconductor photonics devices. Despite the great effort have being paid toward the transfer A3B5 devices applying wafer bonding approach, monolithic growth of A3B5 nanostructures, including quantum wells, dots etc., still remains more relevant from technological point of view. It is well known, that that direct growth of planar structures typically accompanied with the formation of dislocations due to the mismatch of the parameters of crystal lattices and different coefficients of thermal expansion. In turn, quantum dots are known to be more tolerant to dislocations [3]. Therefore, direct growth of A_3B_5 quantum dots on silicon is of considerable scientific interest. Here we report on the fabrication of InAs QDs in silicon matrix by molecular beam epitaxy (MBE) and the study of optical properties of such composite material.

2. Experiments and results

The samples were synthesized by molecular beam epitaxy at 21EB200 Riber MBE system equipped with solid-state As, In effusion cells and e-beam evaporator for deposition of Si. Prior the growth, Si(100)4° substrates were prepared by wet chemical processing using modified Shiraki method followed with annealing step at 950°C in MBE set-up. Then the substrate temperature was reduced to 600℃ for deposition of 50 nm Si buffer layer. Afterwards, the substrate temperature was reduced to 400℃ and the growth of 0.7-3 ML InAs QDs was performed.

Morphological properties of the samples were investigated by atomic force microscopy (AFM). Interestingly, AFM-study revealed nonlinear dependence of the size of quantum dots on the duration of growth. For instance, deposition of 0.3 ML InAs led to the formation of cylindrical InAs QDs with diameter of about 20-30 nm, 2-4 nm height and density of $5 \cdot 10$ μm^{-2}. In turn, deposition InAs more

than 0.7 ML led to formation bigger InAs QDs, which had bimodal size distribution. In detail, QDs with bigger size had 100-140 nm and 8-17 nm height, while smaller QDs had diameter and height of 40-60 nm and 2-5 nm. In addition, low temperature photoluminescence (PL) study of InAs QDs capped with 30 nm Si layer revealed emission at 1.6 μm. It should be note here, that PL intensity of samples with small QDs was 2-3 times higher than that of samples with bigger sizes InAs QDs.

3. Conclusion

In conclusion, we demonstrated the fabrication InAs QD embedded in Si by molecular beam epitaxy. Optical study of such composite material revealed emission at 1.6 um. Thus, it opens up the possibilities for the fabrication of novel type Si-based optoelectronic devices.

Acknowledgments

This work has been supported by the grant of St. Petersburg State University No. 75746688. The samples were grown under the support of the Ministry of Science and Higher Education of the Russian Federation (No. 0791-2020-0003).

References

[1] Thomson D et al 2016 *J. Opt.* **18**(7) 073003
[2] Chen X et al 2018 *Proceedings of the IEEE* **106**(12) 2101–2116
[3] Dhingra P, Fan S, Sun Y, Hool R D, Eng B, Lee M L 2020 *Appl. Phys. Lett.* **117**(18) 181102

Plasma Deposited Indium Phosphide and its Electrophysical Properties

Maksimova A.A. [1], Baranov A.I. [2], Uvarov A. V. [2], Vyacheslavova E.A.[2] and Gudovskikh A.S. [1,2]
[1]Department of Photonics, Saint Petersburg Electrotechnical University "LETI", St. Petersburg, 197376 Russia
[2]St. Petersburg Academic University, St. Petersburg 194021, Russia

E-mail: maksimova_alina@spbau.ru

Abstract. For the first time using the method of plasma-chemical atomic layer deposition were indium phosphide (InP) layers are grown. Trimethyllindium (TMI) acted as a source of indium, and phosphine (PH_3) as a source of phosphorus. Properties of InP layers were evaluated, such as electrical conductivity, type of conductivity and carrier concentration to integrate them into a c-Si-based solar cell. The composition of the InP layers according to the energy dispersive X-ray spectroscopy (EDX) was close to stoichiometric within measurement errors. Thus, the possibility of using InP-based layers for solar cells was evaluated.

1. Introduction

Indium phosphide is a promising material for applications in various areas of electronics due to its distinctive properties such as high electron mobility (higher than that of silicon, germanium and gallium arsenide) and high band gap value (1.3 eV). In this regard, InP has found application in power and high-frequency electronics. InP-based solid solutions are widely used to create LEDs, laser diodes, and avalanche photodiodes. InP has good optical and electronic properties, it is also a direct-gap semiconductor, due to which it has found application in the creation of photonic integrated circuits. The above properties also make indium phosphide an attractive material in solar cells. According to [1], the efficiency of SCs based on InP under standard conditions reaches 21.9%.

Recently, research has been actively conducted on the creation of solar cells based on the integration of A_3B_5 compounds with silicon in order to reduce the cost and increase the efficiency of solar cells. Thus, it is possible to create solar cells based on the InP/Si heterojunction.

2. Experiment details

The phosphide layers are grown by plasma enhanced chemical vapor deposition technique using the Oxford Plasmalab 100 PECVD setup. This is a reliable, industry-relevant technique that allows one to grow electronic-quality films at low temperature on large areas. Plasma-chemical deposition methods make it possible to form layers several nanometers thick, which play the role of both passivating and highly doped layers at relatively low temperatures on an industrial scale. Recently was developed low-temperature (250-380 °C) plasma-chemical synthesis technology of thin GaP layers on Si [2], and possibility of their donor doping [3].

Deposition of InP films was carried out on p-type silicon and quartz substrates at a temperature of 380°C. Trimethyllindium (TMI) will act as the indium source and phosphine (PH_3) as the phosphorus

source. The decomposition of TMI occurred due to temperature, and the decomposition of phosphine due to RF plasma power of 200 W. The growth rate was 0.17 nm/cycle, which corresponds to growth of 0.7 monolayer per cycle. The stoichiometry of the composition of the InP layers was evaluated using energy dispersive X-ray spectroscopy (EDX). The composition of the InP layers according to EDX was close to stoichiometric within measurement errors.

The structural properties of the resulting layers were studied using Scanning Electron Microscopy (SEM) and Raman spectroscopy. Layers InP have a fairly rough surface root-mean-square roughness at the level of 3-5 nm, which is due to their microcrystalline structure. Use of intermediate annealing in Ar plasma after the step of deposition of a monolayer of phosphorus immediately before the deposition of indium leads to a significant decrease in roughness to the level of fractions of nanometers. Using of additional annealing in Ar plasma does not lead to an increase in growth rate.

To study the electrical properties of the resulting InP/Si heterojunctions to InP layers and silicon substrates were formed metal contacts and the current-voltage characteristics of the obtained structures were measured. Ohmic contact to n-Si (10^{15} cm^{-3}) was formed by sequential deposition of highly doped layer of n-GaP with a thickness of 5 nm and the deposition of indium, and p-Si (10^{16} cm^{-3}) was simply deposited indium without additional layers. On the front side of the InP layers indium dots were applied.

As a result, the I–V characteristic through the InP/n-Si heterojunction has a linear behavior characteristic of a resistance with a low value, and not a diode: this means, that the resulting InP layer has a donor type of conductivity with a high concentration free electrons. On the contrary, IV InP/p-Si obtained in the dark has asymmetric behavior: low reverse bias current and exponential growth current at forward bias, which proves the presence of a p-n junction and confirms donor type of conductivity of InP layers. Next, the I–V characteristics of InP/p-Si were measured at illumination with the spectrum of solar radiation, as a result of which Voc=0.48 V was obtained, which confirms the possibility of using InP-based layers for solar cells. The surface resistance of InP layers on silicon and quartz substrates was $8.82 \cdot 10^3$ ohm/□ and $1.66 \cdot 10^6$ ohm/□ respectively. Thus, the possibility of using InP-based layers for solar cells will be evaluated.

Acknowledgments

This work was supported by Ministry of Science and Higher Education of the Russian Federation (research project 0791-2020-0004)

References

[1] Green M.A. et al. Solar cell efficiency tables (version 27) // Prog. Photovolt.: Res. and Appl. 2006.Vol. 14. P. 45-57.

[2] Gudovskikh, A. S., Morozov, I. A., Uvarov, A. V., Kudryashov, D. A., Nikitina, E. V., Bukatin, A. S., … Kleider, J.-P. (2018). Low temperature plasma enhanced deposition of GaP films on Si substrate. Journal of Vacuum Science & Technology A: Vacuum, Surfaces, and Films, 36(2), 021302. doi:10.1116/1.4999409

[3] Gudovskikh, A. S., Uvarov, A. V., Morozov, I. A., Baranov, A. I., Kudryashov, D. A., Zelentsov, K. S., … Kleider, J.-P. (2018). Interface Properties of GaP/Si Heterojunction Fabricated by PE-ALD. Physica Status Solidi (a), 1800617. doi:10.1002/pssa.201800617

Effect of thermal annealing on catalytic properties of Ge-Co nanostructure obtained by electrochemical deposition

I.K. Martynova[1], I.M. Gavrilin[1]

[1]National Research University of Electronic Technology (MIET), Bld. 1, Shokin Square, Zelenograd, 124498, Moscow, Russia

e-mail: irina.martynova.miet@gmail.com

Abstract. This work is devoted to the study of changes in the catalytic properties of oxygen release of nanostructures Ge-Co under the influence of various annealing temperatures (300 °C, 450 °C, 600 °C). The one-dimension Ge-Co nanostructures have been prepared by electrochemical deposition. Catalytic properties of the samples have been tested in solution of 1 M NaOH. The nanostructures after at an annealing temperature of 600 °C show the best properties as oxygen evolution catalyst.

1. Introduction

Due to the development of various industries, the negative impact on the environment increases, there is a greater release of hydrocarbons that pollute the environment. That is why more and more research is being conducted to develop environmentally friendly energy, which would also be cheaper than it is now. One of the ways to obtain ecological fuel is producing hydrogen [1].

Hydrogen gas is extracted from water by a technique known as electrolysis, which involves running a high electric current through water to separate hydrogen and oxygen atoms. however, this technology is still ineffective due to the slow reaction rate on conventional electrodes. To eliminate this problem, various types of catalysts are being investigated, which would accelerate the reactions of hydrogen evolution reaction (HER) or oxygen evolution reaction (OER) [2]. Cobalt-based compounds are one of the possible catalysts for accelerating OER because of their stability, selectivity and they also provide a high reaction rate [3].

In this work we investigate effect of thermal annealing on catalyst activity of one-dimension nanostructure Ge-Co obtained by electrochemical deposition.

2. Experiment

In the synthesis of Ge-Co nanostucture the 50 μm-thickness titanium foil has been used as a substrate. On the substrate an array of spherical indium nanoparticles has been deposited by vacuum-thermal evaporation at the residual pressure of $1 \times 10{-}5$ Torr of material weighed portion of 35 mg.

Ge-Co structures have been formed on the substrates by electrochemical deposition in a three-electrode cell. A platinum plate has been used as a counter electrode, and a standard silver chloride electrode has been used as a reference one. The solution contained 0.05 M of germanium (IV) oxide GeO_2, 0.5 M of potassium sulfate Na_2SO_4 and 0.1 M of tartaric acid with the addition of 0.05 g $CoCl_2$.

The solution pH has been brought to 6.5 by adding NH_4OH. Deposition has been performed at constant voltage -1,3 V for 1 min at the solution temperature of 85 °C.

The catalytic properties of the samples have been investigated in a solution of 1 M NaOH using Autolab PGSTAT302N.

3. Results and discussion

Graphics of current density-voltage curve (CV curve) based on the results of testing catalytic activity of the samples with and without annealing are shown in Figure 1. Figure 1 also shows a graph for a pure titanium substrate, it can be observed that there are no electrochemical processes on it. Accordingly, titanium substrate does not participate in the oxygen evolution reaction.

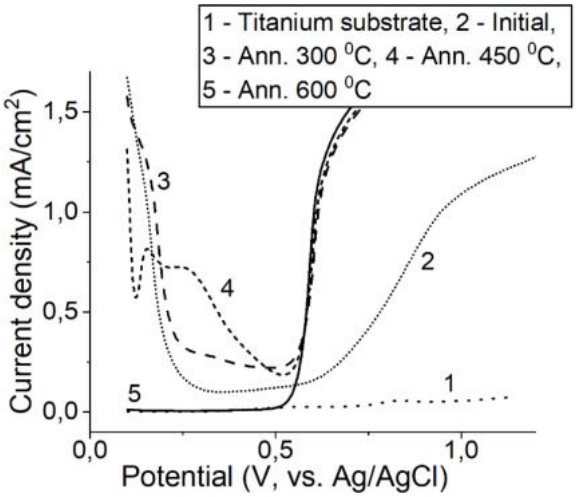

Figure 1. CV curve of initial/annealing Ge-Co samples and titanium substrate

For all annealed samples, there is a change in current density starting from 0.5 V. This change is associated with the beginning of the oxygen release process. The faster the current density increases, the faster the reaction proceeds and the catalyst works more efficiently, therefore, according to the graphic, the sample without annealing shows less catalytic activity.

After the annealing temperature at 300 °C and 450°C, there is also an increase in the current density in the range from 0.2 V to 0.5 V which is caused by additional oxidation reactions of germanium and cobalt. It is an indicator of a less selective process oxygen release than for the sample after annealing at 600 °C, where electrochemical processes are only related to reactions with the release of oxygen.

4. Conclusions

In the present work nanostructures Ge-Co have been prepared by electrodeposition. Their catalytic properties were investigated after various different temperature annealing. It can be concluded that the annealing temperature at 600 °C is the most optimal temperature for the formation of an oxygen evolution catalyst based on Ge-Co nanostructure.

Acknowledgments

The work is supported by the Grant of the President of the Russian Federation №МК 5839.2021.1.3 and by the State assignment 2020-2022 № FSMR-2020-0018.

References

[1] Chen X, Li S 2012 *Chem. Soc. Rev*. **41** 7909.

[2] She Z, Kibsgaard J, Dickens C 2017 *Science* **355** 6321.

[3] Xu Z, Li W, Wang X 2018 A*CS Applied Materials & Interfaces* **10** 30357.

Titanium oxide nanotubes for high capacity systems

I O Yavtushenko[1], A A Adamovich[1,2], M Yu Makhmud-Akhunov[1,2]

[1]Laboratory of Diffusion Processes, Ulyanovsk State University, 432017 Ulyanovsk, Russia
[2]Department of Physical Materials Science, Faculty of Engineering and Physics of High Technologies, Ulyanovsk State University, 432017 Ulyanovsk, Russia

maratmau@mail.ru

Abstract. The features of the formation of supercapacitors based on nanotubes of anodic titanium oxide and a conducting polymer are considered. The structure of the formed electrodes was estimated by scanning electron microscopy (SEM). Based on the analysis of the read in voltammograms, the capacitance of the systems under study was determined, which reached ~10^{-3} F.

1. Introduction

Nanoporous materials are characterized by specific physicochemical properties. The highly developed surface of such materials opens up prospects for their use in the creation of lithium-ion batteries [1], in catalysis [2], sensors [3], etc. Nanoporous materials, including metals, can be obtained by various methods, for example, by dealloying [4], dynamic hydrogen bubble template [5], etc. As for dielectric materials and coatings, a simple and most common method of their formation is the method of electrochemical anode treatment. Such treatment of, for example, titanium leads to the formation of a layer of ordered oxide nanotubes. In this work, we consider the features of the use of such films for the formation of systems with extended capacity.

2. Experimental

Layers of titanium oxide nanotubes were formed by anodic oxidation of titanium foil in an ethylene glycol solution containing 0.8 wt. % NH_4F and 10 wt. % H_2O at 60 V for 60 min. Each electrode was coated with a layer of emeraldine form of polyaniline (PANI). The interlayer between the electrodes was a solution of polyvinyl alcohol with 3.4 M phosphoric acid. The parameters of the system under study were estimated by cyclic voltammetry on a pulsed potentiostat-galvanostat P-45X in the range from –0.5 to 0.5 V at a potential sweep rate of 20 and 100 mV/s.

3. Results and discussion

Titanium oxide nanotubes were obtained in a solution based on ethylene glycol. Compared to aqueous solutions, the use of this type of solvent in systems with a low water content or anhydrous leads to the formation of thicker films with a slight increase in the diameter of the nanotubes. Figure 1 shows a typical image of a titanium surface after anodic oxidation. It can be seen that the surface consists of regions with an ordered arrangement of nanotubes, the average diameter is ~80-100 nm.

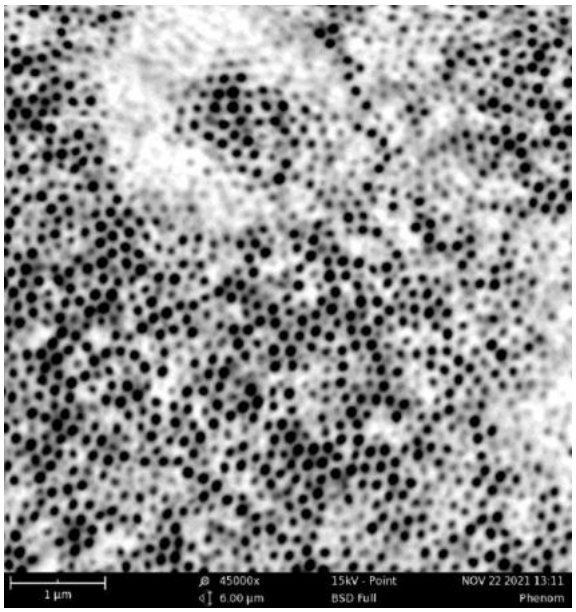

Figure 1. SEM image of titanium surface after anodic oxidation at 60 V for 60 min.

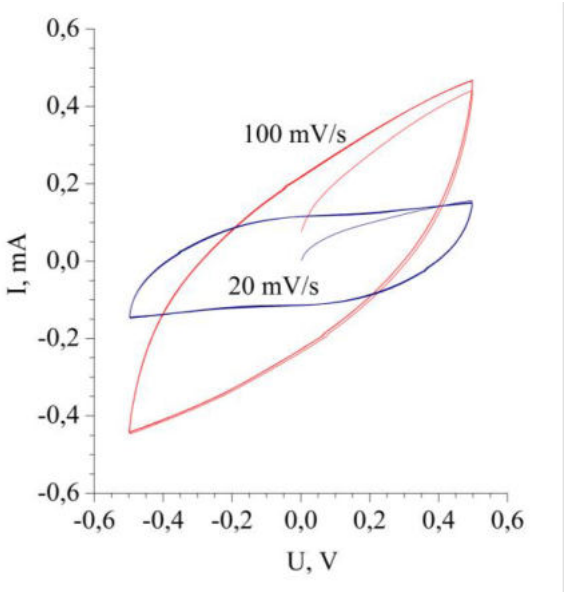

Figure 2. Cyclic voltammograms of supercapacitors based on titanium oxide nanotubes.

Large film thickness and tube diameter increase the effective area of such electrodes, which is a positive factor in the development of capacitive systems such as supercapacitors. Figure 2 shows typical voltammograms (VAGs) of systems based on titanium oxide nanotubes. It can be seen that the VAG has a shape close to an ideal capacitor, and the calculated capacitance is ~ 10^{-3} F.

4. Conclusions

In this work, we show the special feature of using titanium oxide nanotubes for the formation of supercapacitors. Based on the voltammetry data, the capacitance of the systems under study was estimated to be ~ 10^{-3} F.

Acknowledgments

This work is supported by the Russian Science Foundation (project no. 19-71-10063).

References

[1] Madian M, Eychmüller A and Giebeler 2018 *Batteries* **4** 7
[2] Parlett C M, Wilson K and Lee A F 2013 *Chem. Soc. Rev.* **42** 3876.
[3] Sun YF, Liu SB, Meng FL, Liu JY, Jin Z, Kong LT and Liu JH 2012 *Sensors.* **12** 2610
[4] Nam S, Jo H, Choe H, Ahn D and Choi H 2014 *Mater. Trans.* **55** 1414
[5] Li Y, Song YY, Yang C and Xia XH 2007 *Electrochem. Commun.* **9** 981

Creation of a sensitive element of a gas sensor based on a graphene-like film

J V Morozova[1], Z E Vakulov[2], and V S Klimin[1]

[1]Southern Federal University, Department of Nanotechnology and Microsystems, Taganrog 347922, Russia
[2]Southern Scientific Center of the Russian Academy of Sciences, Rostov-on-Don, 344000, Russia

ulamrzv@dmail.com

Abstract: This paper presents the creation of a sensitive element of a gas sensor based on a graphene-like film. The formation of the sensitive area occurs by a combination of methods of focused ion beams and plasma chemical etching. According to experimental data, the structure has a depth of 900 nm, a height of 860 nm and a minimum size of 280 nm. Breakdown voltage values for the methane-air mixture (ratio 5:1) the U_{CH4} = 1.5 V and Ut_{air} = 4.4 V were made, which indicates an increase in the value of the ionization current.

1.Introduction

Modern electronics imposes more stringent requirements on precision methods for creating micro- and nanoelectronics elements, which makes it relevant to search and develop new methods of nanoscale profiling. The combination of focused ion beam (FIP) and plasma chemical etching methods makes it possible to increase the efficiency of the formation of nanoscale structures when creating gas sensors [1-3]. The precision action of the ion beam on the substrate surface in the FIP method provides a modification of the surface with a nanometer resolution, the advantages of the plasma chemical etching method are high performance, minimal side-etching effect, as well as high resolution. This makes it possible to ensure better selectivity of the sensitive element of the gas sensor to various gas molecules [4].

2.Materials and methods

Silicon carbide was used as the substrate material when forming the sensitive element of the gas sensor. The SiC substrates were previously chemically cleaned. The pointed structures were formed by the method of focused ion beams. Modeling has shown that gallium ions in these modes of formation by the FIP method are located at a depth of 5-10 atomic layers. Defective atomic surface layers were removed by layer-by-layer plasma chemical two-stage etching. On the formed nanoscale defect-free silicon carbide structures, a graphene coating was formed by plasma chemical etching in a fluoride low-temperature ICP discharge plasma by removing silicon atoms from the SiC lattice.

The operation of the gas sensor is based on the principle of changing the ion current, which appears in the process of gas ionization in the graphene-gas-graphene system due to the formation of a glow discharge. The gas under study is passed through technological openings, a voltage sufficient for the flow of emission currents from the graphene surface is applied to the contacts, gas ions passing through

the sensitive area of the sensor contribute to the voltage value being removed. Each gas has a characteristic voltage change that allows it to be identified.

3.Results

As a result of experimental studies, a combination of focused ion beams and plasma-chemical etching methods formed the structures of a sensitive element with a depth of 900 nm, a height of 860 nm and a minimum structure size of 280 nm.

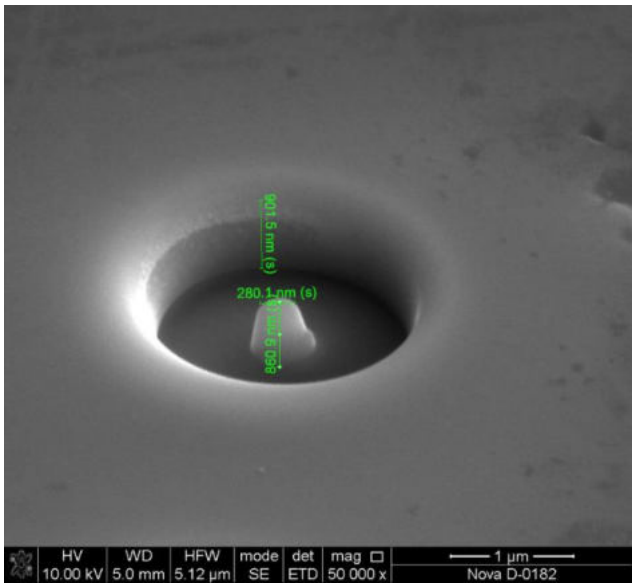

Figure 1 – SEM is an image of a graphene gas-sensitive element formed by plasma chemical deposition and focused ion beams on the SIC surface.

In the course of the study in air, two increases in the current value were observed at voltages associated with the fact that air is a complex mixture of gases (O_2, CO_2, N_2, Ar, etc.) in different concentrations. For a mixture of methane: air in a ratio of 5:1, the increase in current is fixed at two values of the initial breakdown voltage U_{CN4} = 1.5 V and U_{air} = 4.4 V.

The sensor is characterized by increased selectivity to such gas molecules as NH_3, CO, NO_2, and H_2O vapors.

4.Acknowledgments

The reported study was funded by the Russian Foundation for Basic Research, project number 19-38-60052.

5.References

[1] Vakulov, Z., Khakhulin, D., Geldash, A., Tominov, R.V., Klimin, V.S., Smirnov, V.A., Ageev, O.A. Impact of laser pulse repetition frequency on nucleation and growth of LiNbO3 thin films \\ Journal of Advanced Dielectrics, 2021, No. 2160019.

[2] Kots, I.N., Kolomiitsev, A.S, Lisitsyn, S.A., Polyakova, V.V, Klimin, V.S., Ageev, O.A. Studying the Regimes of Silicon Surface Profiling by Focused Ion Beams // Russian Microelectronics, 2019, Vol. 48, No. 2, pp. 72-79.

[3] Hwanyeol Park, Ho Jun Kim Theoretical Analysis of Si2H6 Adsorption on Hydrogenated Silicon Surfaces for Fast Deposition Using Intermediate Pressure SiH4 Capacitively Coupled Plasma // Coatings, 2021, Vol. 11(9), No.1041.

[4] V S Klimin, A A Rezvan, O A Ageev Research of using plasma methods for formation field emitters based on carbon nanoscale structures // J. of Phys: C.S,2018. V.1124. – P. 071020.

Cetyltrimethylammonium bromide as a soft template for the synthesis conductometric gas sensor active substance

G R Nizameeva[1,2], R R Gainullin[1], I R Nizameev[1]

[1] FRC Kazan Scientific Center, Russian Academy of Sciences, Lobachevsky Str. 2/31, Kazan 420111, Russian Federation
[2] Kazan National Research Technological University, Kazan 420015, Russia

E-mail: guliya.riv@gmail.com

Abstract. This paper presents the results of a study of the processes of self-organization of molecules of cetyltrimethylammonium bromide (CTAB), which is used as a micellar template in the synthesis of transparent conductive coatings based on metal nanonetworks. The free surface energy of glass, which is used in the work as a substrate, and the free energy of the glass-CTAB interface, on which the micellar template is formed, are calculated.

1. Introduction

The most promising materials for creating transparent conductors today are metal nanonetworks due to their high electrical conductivity, mechanical strength, and low cost [1,2]. Metal nanonetworks can be obtained by various methods, but from the point of view of economy and scalability, the most promising is the synthesis of metal nanonetworks by chemical deposition from a liquid phase using a "soft" micellar template. Molecules of surface-active substances (surfactants) act as such a template, which, as a result of self-organization, form cylindrical micelles at the "solid-liquid" interface. These cylinders can be used as a template in the synthesis of metal nanonetworks. In this regard, studies of the properties of a micellar template formed at the "solid-liquid" interface are of great practical importance.

In this work, we study the processes of self-organization of CTAB molecules at the glass–surfactant solution interface and the micellar template of CTAB on the surface of a glass substrate made of silicate glass. The obtained data on the processes of self-organization of STAB at the interface "solid body - liquid" allow more efficient control of the chemical deposition of oriented metal networks.

2. Results and discussion

As is known, the functional characteristics of optically transparent, conductive coatings largely depend on the quality of the working optical surfaces, that is, on the quality of the substrate surface. To assess the quality of the substrate surface, a parameter such as roughness is used. To determine the roughness, the surface morphology of the selected glass substrate was examined by atomic force microscopy (AFM). The surface morphology of the glass substrate and the topographic histogram are shown in Figure 1. According to the obtained data, the surface roughness Ra (arithmetic mean deviation from the absolute values of the profile deviations within the baseline) of the glass substrate is approximately 3.24 nm. For a more detailed understanding of the processes of self-organization of

CTAB molecules at the “glass-liquid” interface, we studied the wetting angles of the glass used in the work as a substrate with water and aqueous solutions of CTAB at various concentrations.

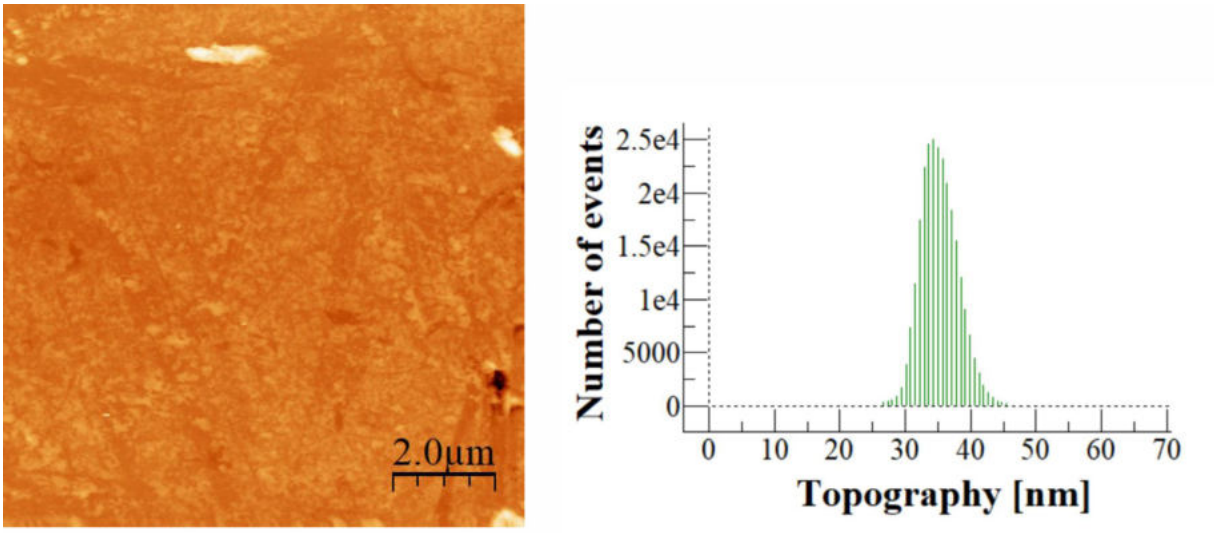

Figure 1. AFM image of a small area of the glass substrate and a topography histogram

As a result of the research, it was found that the contact angle of wetting the glass substrate when wetted with water is 19.30. In the course of studying the contact angle of glass wetting with aqueous solutions of CTAB, it was revealed that wetting inversion is observed for the glass substrate. At a CTAB concentration of 1 mM, a transition from hydrophobicity to hydrophilicity is observed, and the formation of a micellar pattern is observed at the glass-solution CTAB interface. In addition, the free energy of glass was calculated and found to be 69.1 mJ/m^2. Using this value, according to the Young equation, the interfacial energy of the glass-surfactant solution was calculated and it turned out to be 32 mJ/m^2.

Acknowledgments
The reported study was funded by the government assignment for FRC Kazan Scientific Center of RAS.

References
[1] Hecht D S, Hu L, Irvin G 2011 *Adv. Mater.* **23** 1482-1513.
[2] Shengrong Y, Rathmell A R, Chen Z, Stewart I E, Wiley B J 2014 *Adv. Mater.* **26** 6670-6687.

Study of FIB-modified silicon areas by AFM

L S Nikitina[1], E A Lakhina[1], M M Eremenko[1], S V Balakirev[1], N E Chernenko[1], N A Shandyba[1], M S Solodovnik[1] and O A Ageev[1,2]

[1]Institute of Nanotechnologies, Electronics and Equipment Engineering, Southern Federal University, Taganrog 347922, Russia
[2]Research and Education Center "Nanotechnologies", Southern Federal University, Taganrog 347922, Russia

Email: larnikitina@sfedu.ru

Abstract. This paper presents the results of AFM studies of the effect of high-temperature annealing on the height/depth parameters of silicon areas modified by a focused ion beam (FIB). It is shown that the FIB treatment with 5 beam passes leads to swelling of the surface of the modified silicon areas. It has been established that high-temperature annealing leads to the formation of deepening at those processing parameters, when swelling was observed before annealing. An increase in the number of passes in both cases led to an increase in the depth of the FIB-treated areas.

1. Introduction

To date, one of the key tasks of micro and nanoelectronics is to find solutions for the formation of high-quality III-V structures on silicon in a single technological cycle. Although there are certain successes in this direction, the defects density in the grown structures is not comparable with the growth on native substrates. Therefore, in our work, AFM studies of silicon area modified by a focused Ga ion beam in modes from amorphization to etching are carried out, which can contribute to a potential decrease in the defectiveness of subsequent growing layers.

2. Experiment

In this work, AFM studies of the effect of high-temperature annealing on the height parameter of FIB-modified silicon areas were carried out. The modification of the silicon substrates was carried out by treating the areas of 5×5 μm with a focused Ga^+ ion beam. The processing parameters were: accelerating voltage - 30 kV, current - 30 pA, the number of beam passes varied from 5 to 200. After FIB processing, the substrates were studied by AFM. Next, the samples were subjected to thermal annealing in an MBE chamber at 800°C for 60 minutes. Then they were removed from the MBE chamber and examined by AFM to compare the resulting parameters.

3. Results and discussion

AFM studies of samples without annealing showed that when processing silicon areas with a small number of beam passes, these areas swell (Figure 1a). A further increase in the number of beam passes resulted in etching and a gradual increase in the depth of the modified areas (Figure 1c). It should be noted that with such FIB processing parameters (section 2), the height of the processed area was compared with the substrate level with the number of beam passes equal to 10.

The situation changes in the AFM study of samples after high-temperature annealing at 800°C. With a small number of beam passes, there is no swelling of the surface and a deepening of the modified areas is immediately observed (Figure 1b). This suggests that during annealing, the implanted material emerges on the surface, followed by its evaporation and/or etching of the modified area, which leads to the formation of a deepening. The subsequent increase in the number of passes led to an ever-greater increase in the depth of the modified areas (Figure 1c). Moreover, the change in the height/depth of the modified areas is not the same if we compare the cases of samples with and without annealing. Apparently, this is due to the fact that when FIB-processing with large values of the beam passes, high damage to the modified areas and, accordingly, high defectiveness occur, which contribute to a more intensive throw off of the implanted material and its evaporation.

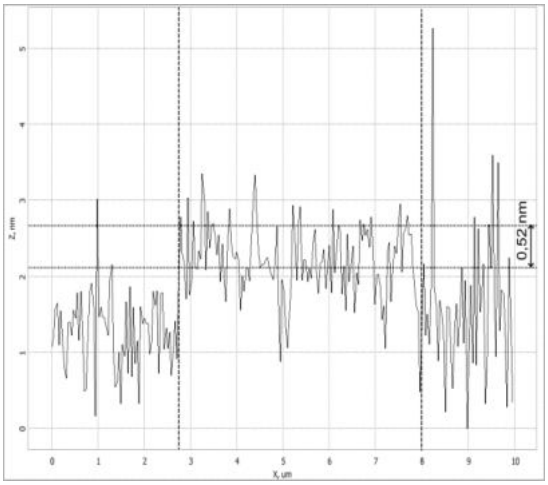

(a)

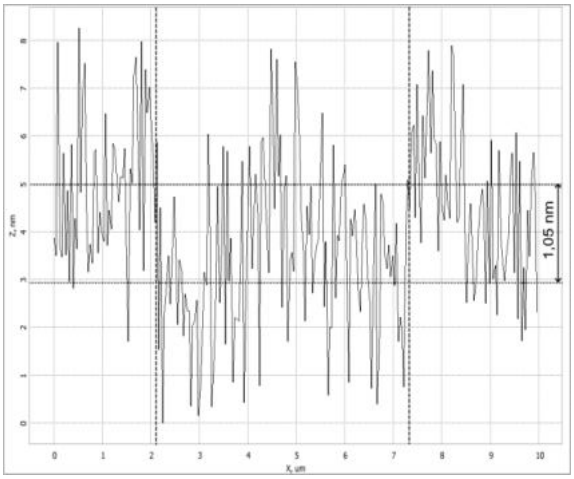

(b)

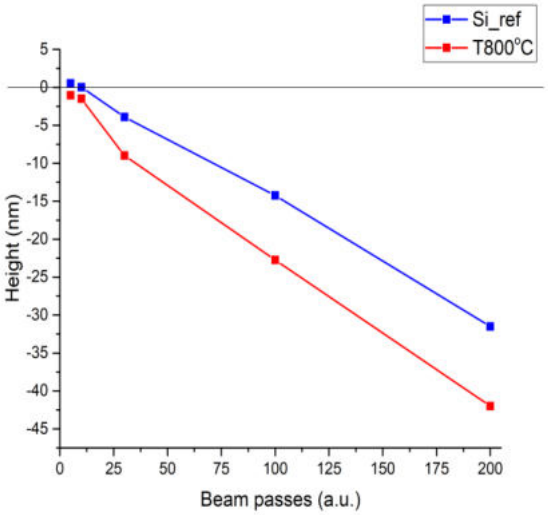

(c)

Figure 1. AFM profiles of FIB-modified silicon areas treated with 5 beam passes: (a) without annealing, (b) after annealing at 800°C. (c) Height of FIB-modified areas before and after annealing (negative height values indicate etch depth).

Acknowledgments
This work was supported by the Russian Science Foundation Grant No. 20-69-46076 in the Southern Federal University.

III-V hybrid nanostructures on silicon: molecular-beam epitaxy growth and physical properties

R R Reznik[1-4], K P Kotlyar[1,2], V O Gridchin[1,2], I V Ilkiv[1,2], A I Khrebtov[1], Yu B Samsonenko[1,4], I P Soshnikov[1,4,5], A S Dragunova[6], N V Kryzhanovskaya[6], L Lorenzo[7], N Akopian[7] and G E Cirlin[1-4]

[1]Alferov University, Khlopina 8/3, 194021, St-Petersburg, Russia
[2]St. Petersburg State University, 199034 St. Petersburg, Russia
[3]ITMO University, Kronverkskiy pr. 49, 197101, St. Petersburg, Russia.
[4]Institute for Analytical Instrumentation RAS, Rizhsky 26, 190103, St-Petersburg, Russia
[5]Ioffe Institute, 194021 St. Petersburg, Russia
[6] Higher School of Economics, 199034, St. Petersburg, Russia
[7]DTU Fotonik, 2800 Kongens Lyngby, Denmark

E-mail: moment92@mail.ru

Abstract. III-V semiconductor nanostructures of combined dimensionalities were synthesized by molecular-beam epitaxy technique on silicon substrates. Morphological, structural and optical properties of grown nanostructures were studied. Research results have shown that synthesized objects are promising for optoelectronic applications, in particular, sources of single photons.

1. Introduction

III-V semiconductor nanostructures of combined dimensionalities are promising building blocks for future optoelectronic devices, in particular, single-photon emitters. For example, the size, shape, and density of self-assembled Stranski-Krastanow quantum dots (QDs) can be controlled by changing of the growth parameters such as substrate temperature, growth rate and growth time, but in the end it is a self-organized strain induced process and controlling the properties of the array independently is a challenging task. QDs in nanowires (NWs) have, in contrast, shown great potential as a highly controllable system. The diameter, height, and density of the QDs are defined by the NW diameter, the growth time, and the NW density, respectively, and can be chosen more predictable. Due to a very efficient strain relaxation on the free sidewalls, coherent growth can be much easier realized in the NW geometry, where a small footprint is dictated by a metal catalyst particle assisting the NW growth via the vapor-liquid-solid (VLS) mechanism [1]. Moreover, it has recently been shown that [111] grown nanowires, especially heterostructured, are ideal candidates for the generation of entangled photon pairs [2].

Experimentally, all the samples in the present work were grown by molecular-beam epitaxy (MBE). For GaAs/AlGaAs, InGaAs/AlGaAs and InAsP/InP material systems, different growth conditions were applied, but the strategy was the same: we have used Au-assisted growth of the NWs on Si(111) substrate, firstly we grew the AlGaAs and InP base of the NW, secondarily, the GaAs, InGaAs or InAsP nanoinsertion with lower bandgap, or QD, was formed and we end the structure with the core with the same material as the base. In case of AlGaAs NWs it was found that during the growth spontaneous, independently on the Al fraction, core-shell structures with lower aluminum content in the cores are formed. Optically, our growth method results in the formation of GaAs QD in a AlGaAs NW having very narrow spectral linewidth (< 10ueV), single-photon emission in the wavelength range 750 – 820 nm in dependence on the QD growth recipe. Moreover, the emission wavelengths al-lows one to design light emission devices in a red range by simply changing of the Al fraction in AlGaAs NWs. In case of InAsP/InP NWs it was found that using a special procedure of substrate preparation immediately before

the growth made it possible to obtain a nanowire coherency with the substrate of nearly 100%. A high-intensity emission from nanostructures was observed at a wavelength of ~1.3 μm at room temperature. In addition, the physical properties of InGaAs/AlGaAs NWs were investigated and shown to be promising for quantum cryptography and other applications.

2. Acknowledgements

The samples were grown under support of Ministry of Science and Higher Education of the Russian Federation (state task № 0791-2020-0003). Structural properties of grown samples were studied under financial support of St. Petersburg State University under research grant № 92591131. Optical properties of grown samples were studied under financial support of the Russian Science Foundation Grant № 21-72-00099

References

[1] Wagner R S, Ellis W C 2011 *Appl. Phys. Lett.* **4** 89
[2] Singh R, Bester G 2009 *Phys. Rev. Lett.* **103** 063601

Thermal and mechanical properties of a metal-matrix composite with ceramic inclusions

V V Rybin[1], A A Solovyev [1], A D Zuev[1]

[1]Department of Physical Materials Science, Faculty of Engineering and Physics of High Technologies, Ulyanovsk State University, 432017 Ulyanovsk, Russia

vlad_rib@mail.ru

Abstract. Al/Nd_2O_3 composite was a blend of fine aluminum powder serving as a matrix while neodymium oxide as an inclusion. Powder metallurgy was used to manufacture samples of the desired shape. This study was conducted to know microhardness, density, porosity, thermal conductivity and SEM analysis. The results show that the properties of composite with 10% Nd_2O_3 volume fraction comparable with Al-10%Al_2O_3 composite.

1. Introduction

The mechanical and thermal properties of metal matrix composites make it possible to use such materials for the production of the most critical parts and assemblies. Powder metallurgy methods are possible to obtain the required composition by simply mixing the components. This method is used in the nuclear industry to obtain transuranium elements [1]. We used in this work a model composite based on aluminum powder and neodymium oxide, similar in its properties to the plutonium and curium oxides. Therefore, the aim of this work was to study the mechanical and thermophysical properties of the material used.

2. Experimental

Al-Nd_2O_3 MMC composite was obtained by adding nano-sized Nd_2O_3 powder at a volume ratio of 10% to Al matrix using powder metallurgy. Al powder having an average size of 30-μm as the matrix and Nd_2O_3 powder having an average size of 100-nm as the reinforcement were used in the experiments. In order to provide a homogeneous mixture of the powders, they were mixed at a speed of 180 rpm over a 2 h using a Y-type machine tool. The prepared powder mixtures were put in cylinder-shaped mold and pressure was made at 5 tons. Press process is on hold for 15 minutes to obtain specimens with uniform density and pressure. The sample size was 1.3 cm in diameter and 4 mm high. Each cold compacted was sintered in a furnace at 550 °C for 30 min in argon atmosphere.

3. Results and discussion

The microhardness of the studied composite, in comparison with cast, sintered aluminum and a material containing 10% alumina [2], is shown in Figure 1. An increase in the hardness of the composite can be associated with a homogeneous and uniform distribution of inclusions in the aluminum matrix.

The measurement results presented in Figure 2 showed that in the temperature range of 300–340 K the material has a thermal conductivity of 3.6–4.2 W/(m·K), which is significantly lower than the values

for cast and sintered powder aluminum (220 and 200 W/(m·K) at room temperature, respectively) and even aluminum oxide (37 W/(m·K) at room temperature [3]).

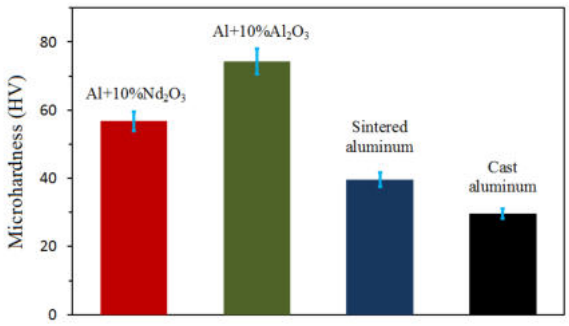

Figure 1. Microhardness of composite and pure Al.

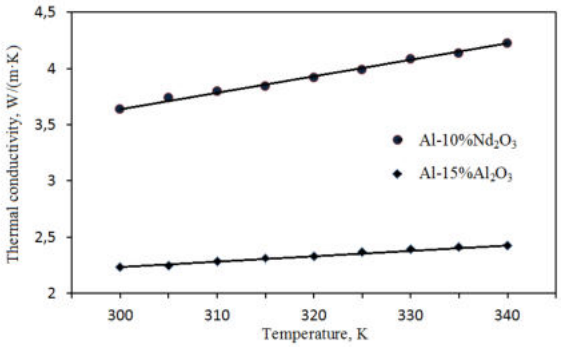

Figure 2. The thermal conductivity of composite with inclusions neodymium oxide and alumina.

Such low values of the thermophysical properties of the composite indicate poor thermal contact of various phases in its structure, a large volume of internal pores with zero thermal conductivity. In addition, aluminum powder particles are easily oxidized in air and covered with a thin oxide film with low thermal conductivity.

4. Conclusions

Microhardness and thermal conductivity of aluminum matrix composite with neodymium oxide inclusions was investigated. The parameter values turned out to be low and comparable to aluminum hardened by its own oxide. The low thermal conductivity of the material under study must be taken into account when choosing the thermal modes of operation of products made from it.

References

[1] Washington J, King J and Shayer Z 2017 Nucl. Eng. Des. **313** 53
[2] Garbiec D, Jurczyk M, Levintant-Zayonts N and Moscicki T 2015 Arch. Civ. Mech. Eng. **15** 933
[3] Saheb N, Khan M S 2018 Sci. Sinter. **50** 1

Studies of the plasma effect on the properties of tin dioxide-based nanomaterials synthesized by sol–gel dip coating

A P Sigaev[1], I A Pronin[1], A A Karmanov[1], N D Yakushova[1]

[1]Department of Nano- and Microelectronics, Penza State University, 440026, Penza, Russia

Abstract. We have developed the method of synthesis of SnO_2-based nanomaterials by sol-gel dip coating. We have studied the effect of exposure of both nitrogen and oxygen plasma on the qualitative composition and morphology of SnO_2-based nanomaterials synthesized according to the developed method using Fourier-transform infrared spectroscopy and scanning electron microscopy, respectively. The scanning electron microscopy has confirmed that with an increase in the energy of the ions involved in the plasma treatment process, the degree of morphological features of the surface manifested in the transformation of the initial structure to autonomous aggregates increases.

1. Introduction

The introduction of additional plasma treatment of the formed nanomaterials is one of the possible ways to modify their properties [1-3]. In this work, we investigate the effect of various plasma modes in both nitrogen and oxygen environments on the qualitative composition and morphology of SnO_2-based nanomaterials obtained by sol-gel dip coating method.

2. Experiment

The synthesis of SnO_2-based film-forming sol was carried out by the sol-gel method [4]. Then the film-forming sol was applied to silicon substrates by the dip-coating method in compliance with the following parameters: dip rate to sol is 10 mm/min, wet time in sol is 30 seconds, lift rate of sample is 10 mm/min and drying time in air is 30 seconds. The final stage of the formation of nanomaterials is combination of pre-drying at a temperature of 65°C for 20 minutes in air and thermal annealing at a temperature of 575°C for 50 minutes in air.

The treatment of the obtained nanomaterials was performed in inductively coupled plasma under various modes and process gases (nitrogen or oxygen).The main variable parameters were the power of inductively coupled plasma source P_1 and the power of supplementary high-frequency source P_2, which allowed us to control the energy and density of the plasma as well as the ion flow intensity and direction, respectively.

The IR transmission spectra of nanomaterials was measured on an FSM 1201 Fourier transform infrared (FTIR) spectrometer (OOO Infraspek, Russia) using a specular reflectance attachment (10° angle of incidence).

3. Results and Discussion

The analysis of the IR transmission spectra presented in Figure 1 (the spectra are additively shifted for convenience of perception) showed that identical bands and absorption peaks are characteristic of SnO_2-based nanomaterials prior to and after plasma treatment [4]. This allowed us to conclude that the

effect of nitrogen and oxygen plasma does not lead to a pronounced change in the qualitative composition. At the same time, depending on the modes of plasma exposure, there is a change in the intensity of the vibrational mode at 2360 cm^{-1}, which corresponds to deformation vibrations of the C=O bonds of atmospheric carbon dioxide, and in a wide absorption band 3100-3700 cm^{-1}, corresponding to valent symmetric vibrations of OH groups associated with the surface of SnO_2. In particular, the effect of oxygen plasma at P_1 = 250 W and P_2 = 0 W leads to a significant decrease in the intensity of these bands, which become weakly expressed. This can be used, for example, to create gas sensors whose characteristics are weakly dependent on the humidity of the environment.

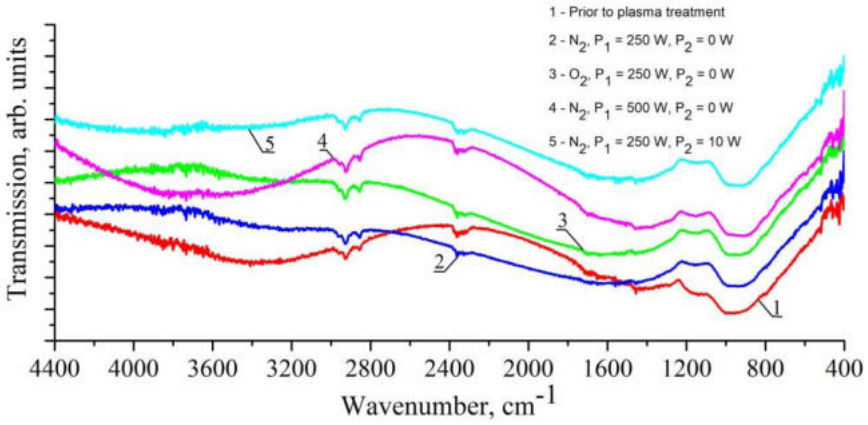

Figure 1. IR transmission spectra of SnO_2-based nanomaterials prior to and following plasma treatment

The analysis of the SEM image (Figure 2, a) showed that a structure consisting of a lot of combined quasi-spherical aggregates of various sizes, which are typical for nucleophilic increase in sol-gel systems, is identified on the surface of synthesized SnO_2-based nanomaterials.

During plasma treatment two main mechanisms of interaction of samples with the ions of low-temperature nitrogen or oxygen plasma are possible: 1) bombardment of the surface of samples with partial removal of nanomaterial particles of relatively small size; 2) introduction of plasma ions within the near-surface layer of the nanomaterial. After plasma treatment the surface structures are modified, acquiring the appearance of many separate autonomous aggregates (Figure 2, b, c, d). Moreover, with an increase in the energy of the ions involved in the process these morphological features become more pronounced.

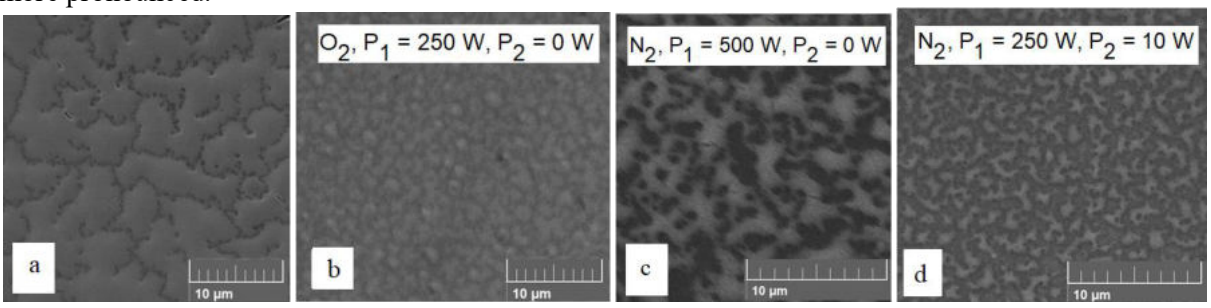

Figure 2 (a, b, c, d). SEM images of the surface of SnO_2-based nanomaterials prior to (**a**) and following (**b, c, d**) plasma treatment

Acknowledgments

The study was carried out with the financial support of the Russian Foundation for Basic Research (project No. 20-38-90155) and the grants from the President of the Russian Federation (grants No. MD-172.2021.4, MK-3541.2021.12).

References

[1] Dao H T and Makino H 2019 *Materials Science in Semiconductor Processing* **96** 46–52

[2] Sigaev A P, Averin I A, Karmanov A A, Pronin I A and Yakushova N D 2020 *Physical and chemical aspects of the study of clusters, nanostructures and nanomaterials* **12** 162–9

[3] Danilova M N, Pylinina A I, Platonov E A and Yagodovskii V D 2015 *Russian Journal of Physical Chemistry A* **89** 1339–42

[4] Averin I A, Karmanov A A, Moshnikov V A, Pronin I A, Igoshina S E, Sigaev A P, Terukov E I 2015 *Physics of the Solid State* **57** 2373-81

Investigation of the properties of quantum dots depending on the nature and number of additional semiconductor layers

Troshkina N., Novikova S., Nasirov P., Volobueva M., Mukhina I., Popova A., Gribova E.

141982, Moscow region, Dubna, st. Universitetskaya, 19, Dubna State University

e-mail: tnn.18@uni-dubna.ru

Abstract. The present study aims to investigate the properties of quantum dots depending on the nature and number of additional semiconductor layers. The analysis of spectral data showed that when CdTe-QDs are coated with a ZnS shell, a bathochromic shift of the exciton peak and maximum of fluorescence is observed due to the restriction of charge carriers in the nucleus. However, the build-up of the additional shell leads to a decrease in the quantum yield, which may be due to the difference in the parameters of the crystal lattices to CdS and ZnS and the occurrence of defects in the crystal structure. In contrast, CdTe-QDs coated with a CdS shell increased the quantum yield and shifted the peak of fluorescence to a longer wavelength region.

1. Introduction

Currently, semiconductor nanostructured materials are much in demand due to their unique properties. Nanostructured materials exhibit specific optical and electronic properties when their size changes in the range of 1-100 nm. Depending on the dimension, they can be classified as two-dimensional (thin films or quantum wells); one-dimensional (quantum wires); zero-dimensional (quantum dots) ones [1]. Thus, a quantum dot (QD) is a zero-dimensional system and has a limited number of atoms forming discrete energy states. Quantum dots have a surface effect and a quantum restriction which affect their atomic-like properties. The quantum restriction results in specific size- and shape-dependent optoelectronic properties.

As the size of nanocrystals decreases, the ratio of their surface to the volume increases, which is a surface effect. A large number of atoms on the surface greatly affects the optical properties of the entire particle. The external environment interacts with the surface of the nanoparticle, which increases the number of defects on the surface – broken atomic bonds, electronic traps are formed. Therefore, QDs must be passivated or coated to increase the luminescence and stability of nanoparticles. One of the methods of surface passivation of QDs is to build up an inorganic layer, for example, a semiconductor one, which involves complete passivation of the states of surface traps [3]. Such a QD structure is called a "core/shell" structure. Additional shell build-up significantly improves the fluorescence quantum yield and photostability of quantum dots. The proper choice of the shell material and its thickness are important factors affecting the overall properties of QDs. If the core and shell structures have a huge lattice mismatch, this leads to lattice deformation and defective states occur inside or at the core/shell interface. In addition, a thicker semiconductor shell creates mismatch dislocations, which also reduces the fluorescence quantum yield due to the non-radiative process.

2. Results and discussion

The present study aims to investigate the properties of quantum dots depending on the nature and number of additional semiconductor layers. QDs with a CdTe core and additional semiconductor shells were synthesised in the study. The material of the semiconductor shells is selected so that the difference between the crystal lattices of the core-shell-shell is minimal. The layer size is controlled by the synthesis time. As the size of the semiconductor layer increases, the quantum yield increases to a certain size, then decreases sharply with a further increase in the layer size, which is demonstrated in [4]. In order to increase stability, additional shells from wider-band ZnS and CdS semiconductors were built up on CdTe-QDs. The analysis of spectral data showed that when CdTe-QDs are coated with a ZnS shell, a bathochromic shift of the exciton peak and maximum of fluorescence is observed due to the restriction of charge carriers in the nucleus. However, the build-up of the additional shell leads to a decrease in the quantum yield, which may be due to the difference in the parameters of the crystal lattices to CdS and ZnS and the occurrence of defects in the crystal structure. In contrast, CdTe-QDs coated with a CdS shell increased the quantum yield and shifted the peak of fluorescence to a longer wavelength region.

Acknowledgments
This research was carried out with the financial support of The Foundation for Assistance to Small Innovative Enterprises in Science and Technology (No. 16271ГУ/2021)

References

[1] Ramalingam G. et al. Quantum confinement effect of 2D nanomaterials //Quantum Dots-Fundamental and Applications. – IntechOpen, 2020.
[2] Kumar D. S., Kumar B. J., Mahesh H. M. Quantum nanostructures (QDs): an overview //Synthesis of Inorganic Nanomaterials. – 2018. – С. 59-88.
[3] Xia M. et al. Surface passivation of CdSe quantum dots in all inorganic amorphous solid by forming Cd1− xZnxSe shell //Scientific reports. – 2017. – Т. 7. – №. 1. – С. 1-9.
[4] Smith A. M., Mohs A. M., Nie S. Tuning the optical and electronic properties of colloidal nanocrystals by lattice strain //Nature nanotechnology. – 2009. – Т. 4. – №. 1. – С. 56.

A new MoS_2 exfoliation method for metal-organic frameworks fabrication

Konstantin A. Tumbinskiy[1,2], Maksim R. Sokolov[1,2], Maria A. Kalinina[2]

[1]Moscow State University, Moscow, Russia

[2]A. N. Frumkin Institute of Physical Chemistry and Electrochemistry, Russian Academy of Sciences, Moscow, Russia

tumbinskiyk@gmail.com

Abstract. In this work, we describe synthesis of new metal-organic framework (MOF) material based ultra-thin MoS2 nanoflakes, obtained by novel method of liquid phase exfoliation in the saturated solution of 2-methylimidazole. We show that the intercalation of this small electron-rich heterocyclic compound between the MoS2 planes induces rapid disintegration of the pristine material into the dispersion with a large fraction of single-sheet nanoflakes with comparatively narrow size distribution in a range 50 ± 25 nm. The method allows to obtain large quantities of as-prepared dispersions with relatively high concentrations of nanoparticles within 2–4 h. The as-prepared MoS2 nanoflakes were characterised by a combination of methods (UV–vis absorption, fluorescence, infrared and Raman spectroscopies, X-ray powder diffraction and energy-dispersive X-ray spectroscopy, transmission electron, atomic force and confocal fluorescence microscopies, 4-probe electric measurements) to investigate their composition, structure and morphology. The spin-coated and dip-coated films of the as-prepared nanoflakes were deposited on solids to study their optical and electric properties. Obtained nanoscale particles were used to fabricate functional materials based on a zinc complex of 5,10,15,20-tetrakis(4- carboxyphenyl)-porphyrin-zinc(II) (ZnTCPP). Catalytic, compositional and structural properties of MOFs were studied.

1. Fabrication of MoS2 nanosheets using new 2-methylimidazole-assisted exfoliation

Transition-metal dichalcogenides (TMD) form a family of functional layered materials, with a unique combination of optical, chemical and semiconductor properties which are revealing at nanoscale. TMD-based materials are useful for potential sensing applications, electro and photocatalysis, energetics and biomedicine.Due to the growing interest in molybdenum disulfide-based nanomaterials, many methods of producing MoS2 nanoflakes have been developed. These methods can be categorised as bottom-up or top-down approaches. However, both of these methods have major drawbacks that limit their application. Mechanical exfoliation does not produce nanoparticles in high amounts. Chemical exfoliation with intercalated metal atoms generates excess charge on the particles surface, and surface-active substances aggregate on nanoflakes and cannot be purified. We suggest a new

technique of producing nanoscaled MoS_2 using 2-methylimidazole, this method provides a size-controlled and perfectly pure product.

2. Synthesis of MoS_2/ZnTCPP functional materials

Nowadays there are no attempts in fabrication of composite functional materials based on MoS_2 nanosheets and porphyrin derivatives. ZnTCPP, being a metal-organic complex, demonstrates good charge separation and coordination properties. This makes ZnTCPP perfect substrate for materials applied in the fields of catalysis and photoelectronics. ZnTCPP/MoS_2 materials were synthesised using hydrothermal method. Collided with a solid semiconductor template of MoS_2 nanoflakes, ZnTCPP/zinc acetate MOF forms composite material with new catalytic properties. Obtained material was characterised with spectral methods (Raman, IR and UV-vis spectroscopy), X-ray powder diffraction and scanning electron microscopy, catalytic activity was studied.

Growth of nanostructured cobalt film at oblique angle deposition

I S Fattakhov[1], OS Trushin[2], A A Popov[2]and L A Mazaletsky[2]

[1]Department of Nanotechnology in Electronics, P.G. Demidov Yaroslavl State University,Sovetskaya Street 14, Yaroslavl, 150003, Russia
[2]Valievinstitute of physics and technology of RAS, Yaroslavl Branch, Universitetskaya, 21, Yaroslavl, 150007, Russia

33ychenikan@mail.ru, otrushin@gmail.com

Abstract. Nanocolumnar Co thin films growth by oblique angle deposition on Si substrate is experimentally studied. Formation of regular arrays of vertical Co nanocolumns has been observed at incidence angles more than 80 degrees with rotation of substrate. Such films might be perspective material for applications as a magnetic recording media for next generations of hard disks.

1. Introduction

Magnetic thin films with easy axis normal to the substrate surface are of considerable interest as a promising material for ultrahigh density magnetic recording. However thin film growth at standard conditions leads to magnetization vector oriented in the plane of the surface. A promising method for the formation of films with special properties is their nanostructuring during growth. One of the known technological methods allowing the growth of nanostructures is oblique angledeposition[1,2]. It is well known that by varying the angle of incidence one can change the direction of magnetic anisotropy[3].Besides that chiral nanostructured thin films can be produced through precise control of the angle of incidence of a vapor flux concurrent with substrate rotation[4].Main goal of this work was finding optimal conditions for the formation of perpendicular magnetic anisotropy in Co films using this method.

2. Experiment

Experiments on the deposition of Co films on an inclined substrate were carried out on an Oratoria-9 electron beam evaporation unit. The deposition conditions were as follows: base vacuum 4 10^{-6}Torr, electron beam voltage 8 kV, current 0.5 A. A standard single-crystal silicon wafer with a thermal oxide layer 300 nm thick was used as a substrate. During deposition substrate inclination angle was fixed to be equal to 85°. Besides that the substrate was rotating around its vertical axis with average rate of 30 rpm. The growth rate of the film was equal to 1 nm/s. The surface morphology of as deposited films was investigated by scanning electron microscopy (SEM) (Supra 40).

3. Results

Cross-section of the film deposited at incidence angle $\varphi=85^{o}$ and rotation rate of 30 rpm is shown at fig,1a. One can see that vertical fibrous microstructure is formed at this conditions. More complete

information about the morphology of the film is obtained from the analysis of top view on its surface shown at fig.1*b*. One can see that separate Co fibers have shape of nanocolumns extending upwards with the width less than 70 nm.

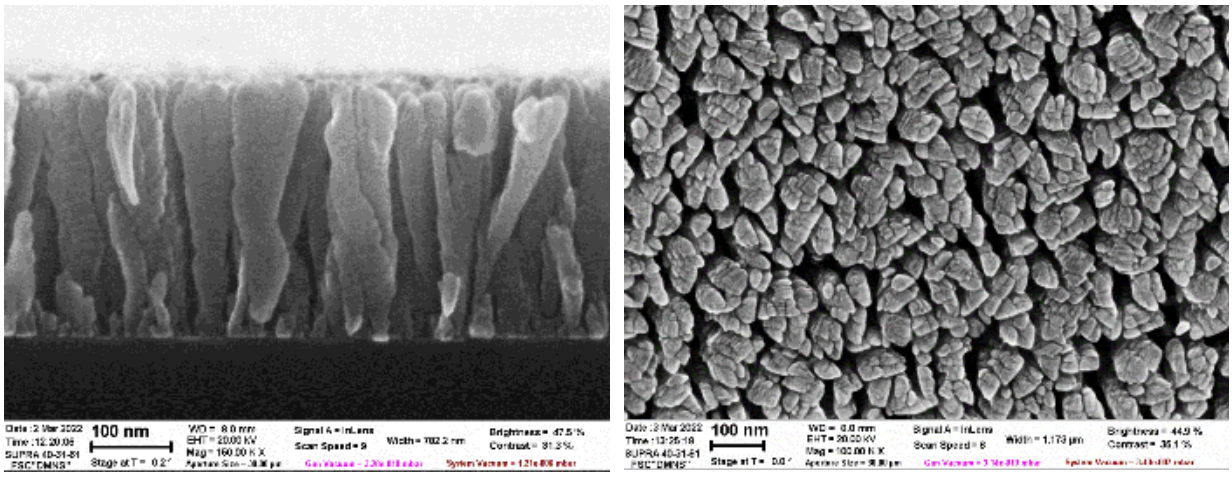

A B

Fig.1: Cross-section of the Co film (A) and top view on its surface (B). The images were obtained using electron scanning microscopy (SUPRA-40).

4. Conclusion

In summary, as the results of experimental studies of the growth of Co thin films by oblique angle deposition with rotation of substrate it was found that optimal conditions for nanostructuring are achieved at the angle of 85°. Studies of magnetic properties of the films are currently in progress. Such films might be perspective for application in ultrahigh density magnetic recording.

Acknowledgments

This work was carried out on the equipment of the centre for collective use of scientific equipment "Diagnostics of micro- and nanostructures" within the framework of the State assignment of the P.I. K.A. Valiev RAS Ministry of Education and Science of the Russian Federation on topic No. FFNN-2022-0018 "Fundamental and applied research in the field of creating promising instrument nanostructures for storing information on new physical principles."

References

[1] Barranco A, Borras A, Gonzalez-Elipe A and Palmero A 2016 *Perspectives on oblique angle deposition of thin films: From fundamentals to devices* (*Progress in Materials Science* vol 76)pp 59–153

[2] Hawkeye M, Taschuk M and Brett M 2014 *Glancing Angle Deposition of Thin Films*(UK: John Wiley &Sons Ltd) pp 1-299

[3] Akulov A A, Trushin O S, Popov A A, Pestova A N and L A Mazaletsky 2021 Nanostructuring at oblique incidence deposition of cobalt, J. Phys. Conf. Ser., 2086, 012001

[4] Liu F., Umlor M. T., Shen L., Weston J., Eads W., Barnard J. A., and Mankey G. J. 1999 The growth of nanoscale structured iron films by glancing angle deposition, Journal of Applied Physics 85, 5486

Grain structure of LPCVD polycrystalline silicon

A V Fedotov[1, 2, 3], N A Kolobov[2]

[1] National Research University Higher School of Economics, Moscow, 101000, Russia
[2] Dephan LCC, Skolkovo, 121205, Russia
[3] Author to whom any correspondence should be addressed

avfed05@mail.ru

Abstract. In the report, we present the grain structure of LPCVD polycrystalline silicon. SEM method was used for thin polysilicon film surface analysis. Grain size distribution is discovered and intergranular space volume is determined. Grain structure influence on conduction of polysilicon is also demonstrated.

1. Introduction

Polysilicon is an important material for semiconductor microelectronics. It can be used for various applications. It serves as a conductive material, gate electrode in MOS transistors, insulating material or resistive material. Consequently, it is very important to research polysilicon technological and electrophysical characteristics [1].

Behavior of polysilicon electrophysical characteristics are mostly determined by its grain structure [2]. Polysilicon is a polycrystalline material that consists of a large amount of grains, which have the same structure as a crystalline silicon, separated by intergranular space. This space has an amorphous structure and, therefore, serves as an insulating barrier for charge carriers. Intergranular space provides a large amount of traps in a zone diagram of polycrystalline materials. Such traps determine charge carrier transport in the volume of the material and at its contacts with other materials. Thus, polysilicon structure analysis is an important task for semiconductor device fabrication.

2. Method

Polysilicon thin films were deposited on n^+-silicon substrate. For polycrystalline silicon films formation LPCVD (low-pressure chemical vapor deposition) method at temperature T = 650ºC and pressure P = 12 mTorr was used. For further contact metallization molybdenum films were deposited and photolithography method was used.

Polysilicon structure was analyzed via scanning electron microscopy (SEM). SEM photos of structure with different angles were taken. Polysilicon grain size distribution was received as a result of SEM photo analysis with different angles. An example of SEM photo is presented on figure 1.

Doping of films was carried out by ion implantation of arsenic method. Electrical properties of polysilicon films were determined via IV measurements.

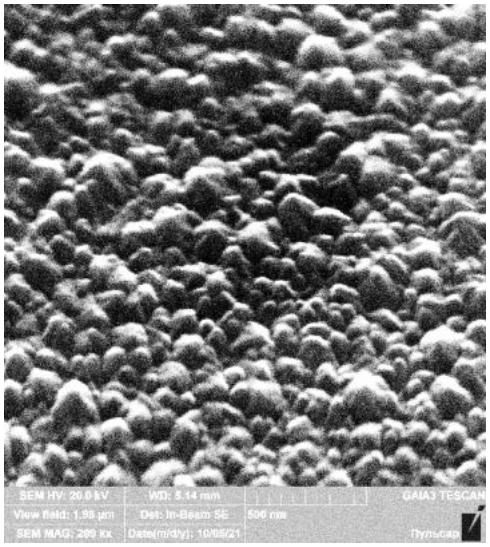

Figure 1. SEM photo of polysilicon surface

3. Results

The result of the experiment provides an important information about polysilicon grain structure. The structure determines electrophysical characteristics of films. Moreover, the information is important for further technological processes optimization: it can be defined which share of doping impurities is collected in intergranular space and is electrically inactive.

Acknowledgments

The research was supported by scientific and production enterprise “Pulsar”.

References

[1] Robert Doering, Yoshio Nishi – Handbook of Semiconductor manufacturing technology – 2007;
[2] A A Glushko, V A Shahnov – Parameters of resistive structures on pollycristalline silicon – 2010.

Electrochemical investigation pyrrolidinofullerene

A A Nekrasov,[1] N V Nekrasova,[1] M A Savel'ev,[2] A A Khuzin,[3]*
V A Barachevsky,[2,4] A R Tuktarov[3]
[1]A.N. Frumkin Institute of Physical Chemistry and Electrochemistry RAS, Leninskii prospect 31, Moscow, 119071, RU
[2]Interdepartmental Center of Analytical Research of the Russian Academy of Sciences, Moscow, Profsouyznaya Str., 65, Bl.6, Moscow, 117997, RU
[3]Institute of Petrochemistry and Catalysis of RAS, Ufa 450075, RU
[4]Photochemistry Center of FSRC "Crystallography and Photonics" of the Russian Academy of Sciences, Novatorov Str.,7a, Bl.1, Moscow, 119421, RU

*e-mail: artur.khuzin@gmail.com

Abstract. The thesis reports on the first experiments on reversible transformations of a hybrid molecule based on [60]fullerene and spiropyran under conditions of combined photo- and electrochemical exposure. The results of an electrochemical study of a solution of a hybrid molecule prove the possibility of electrical control of the rate of discoloration of the photoinduced form.

Introduction

Photochromic transformation implying reversible transformation of molecules between two forms with different absorption spectra, induced by electromagnetic radiation, represent area of emerging interest to the researchers all over the world. To date, spirocyclic compounds (spiropyrans and spirooxazines) are some of the most studied photochromic systems.[1-5] In the compounds of this type, the spirocyclic form absorbs in the UV region of the spectrum, while the photoinduced merocyanine form absorbs in the visible region of the spectrum.

Recently,[6-14] we have synthesized a wide range of hybrid photochromic and acidochromic molecules based on fullerenes and spiropyrans or dithienylethenes. The studies revealed great potential of the synthesized photochromic hybrid molecules as light-regulating semiconductor layers for organic field-effect transistors.[15-17] In this case, in contrast to the initial spiropyrans, hybrid molecules exhibited high resistance to photodegradation during repeated switching and prolonged exposure to UV light.

As a follow-up to our research work on developing synthesis approaches and studying the properties of new hybrid molecules based on fullerenes and spiropyrans,[6-10] and taking into account the prospects of photochromic compounds and fullerenes for various areas of science and technology, we conducted for the first time electrochemical studies of pyrrolidinofullerene containing a spiropyran fragment.

Results and Discussion

Photochromic pyrrolidinofullerene 1 and its precursor, spiropyran 2, were selected as objects of study:

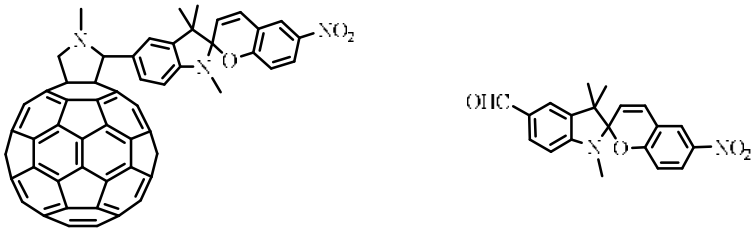

1 2

Fig. 1. Objects under study

The synthesis, structure, and photochromic properties of compounds 1 and 2 are detailed in the paper.[6] The method for measuring CV curves was applied to study the differences in the electrochemical behaviour of spiropyran in the initial colourless and UV-induced colored forms.

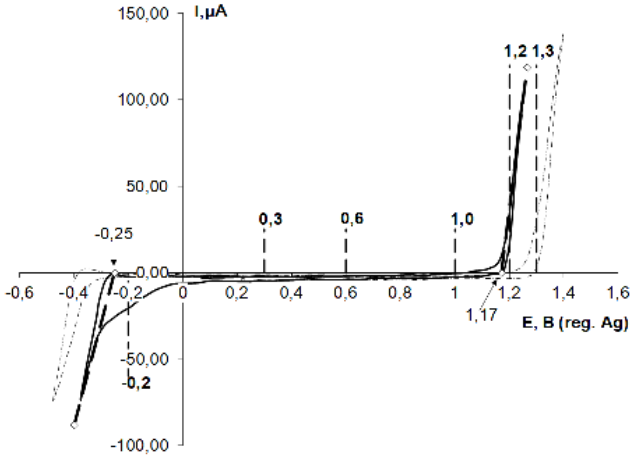

Fig. 2. Cyclic voltamperograms of pyrrolidinofullerene 1 (C = 1.10^{-3} M) in o-dichlorobenzene containing NBu_4BF_4 (C = 0.1 M), measured in a three-electrode photoelectrochromic cell before (dashed curve) and under constant UV irradiation (solid curve). The potential sweep rate was 50 mV/s

Based on the analysis of the CV curve obtained under UV irradiation, it is possible to select the potential regions in which electrochemical action can lead to discoloration of the colored product. Vertical dashed lines in Figure 2 show these regions indicating the values of the potential. These potentials can be used to decolorize the photoinduced form of spiropyran.

Acknowledgments

This work was supported by the Ministry of Science and Higher Education within the State Assignments of the Institute of Petrochemistry and Catalysis of RAS in the part of synthesis spiropyrane and his hybrid molecule with [60]fullerene (FMRS-2022-0075), the Photochemistry Center of FSRC "Crystallography and Photonics" of RAS in the part of spectral kinetic studies, the Interdepartmental Center of Analytical Researches of RAS in the part of measurements, the Institute of Physical Chemistry and Electrochemistry RAS in the part of electrochemical and spectroelectrochemical studies.

References

[1] Minkin V.I. *Chem. Rev.*, 2004, 104, 2751

[2] Lukyanov B.S., Lukyanova M.B. *Chem. Heterocycl. Compd.,* 2005, 41, 281–311

[3] Minkin V.I. *Molecular Switches*, 2011, 1, 37
[4] Klajn R. *Chem. Soc. Rev.,* 2014, 43, 148-184
[5] Kortekaas L., Browne W.R. *Chem. Soc. Rev.*, 2019, 48, 3406-3424.
[6] Tuktarov A.R., Khuzin A.A., Tulyabaev A.R., Venidictova O.V., Valova T.M., Barachevsky V.A., Khalilov L.M., Dzhemilev U.M. *RSC Advances*, 2016, 6, 71151.
[7] Pomogaev V.A., Barachevsky V.A., Tuktarov A.R., Avramov P.V., Artyukhov V.Ya. *J. Phys. Chem. A,* 2018, 122, 505-515.
[8] Galimov D.I., Tuktarov A.R., Sabirov D.Sh., Khuzin A.A., Dzhemilev U.M. *J. Photochem. Photobiol. A: Chemistry*, 2019, 375, 64-70.
[9] Tuktarov A.R., Khuzin A.A., Dzhemilev U.M. *Mendeleev Commun.*, 2019, 29, 229.
[10] Khuzin A.A., Tuktarov A.R., Barachevsky V.A., Valova T.M., Tulyabaev A.R., Dzhemilev U.M. *RSC Advances*, 2020, 10, 15888-15892.
[11] Tuktarov A.R., Khuzin A.A., Akhmetov A.R., Barachevsky V.A., Venidiktova O.V., Dzhemilev U.M. *Tetrahedron Lett.*, 2015, 56, 7154-7157
[12] Tuktarov A.R., Khuzin A.A., Khalilov L.M., Tulyabaev A.R., Akhmetov A.R., Dzhemilev U.M. *Mendeleev Commun.,* 2015, 25, 470
[13] Tuktarov A.R., Khuzin A.A., Akhmetov A.R., Khalilov L.M., Tulyabaev A.R., Barachevsky V.A., Venidiktova O.V., Dzhemilev U.M. *Mendeleev Commun.,* 2016, 26, 143-145.
[14] Tuktarov A.R., Khuzin A.A., Akhmetov A.R., Venidiktova O.V., Barachevsky V.A., Dzhemilev U.M. Russ. J. Org. Chem., 2017, 53 (6), 891
[15] Khuzin A.A., Tuktarov A.R., Venidiktova O.V., Barachevsky V.A., Mullagaliev I.N., Salikhov T.R., Salikhov R.B., Khalilov L.M., Khuzina L.L., Dzhemilev U.M. *Photochemistry and Photobiology, 2021, DOI:10.1111/php.13539*
[16] Tuktarov A.R., Salikhov R.B., Khuzin A.A., Safargalin I.N., Mullagaliev I.N., Venidiktova O.V., Valova T.M., Barachevsky V.A., Dzhemilev U.M. *Mendeleev Commun.,* 2019, 29, 160.
[17] Tuktarov A.R., Salikhov R.B., Khuzin A.A., Popod'ko N.R., Safargalin I.N., Mullagaliev I.N., Dzhemilev U.M. *RSC Advances*, 2019, 9, 7505-7508

Experimental study of nanoholes formation using local droplet etching of FIB-modified GaAs (001) surface

N E Chernenko, D V Kirichenko, N A Shandyba, S V Balakirev, M M Eremenko and M S Solodovnik

Institute of Nanotechnologies, Electronics and Equipment Engineering, Southern Federal University, Taganrog 347922, Russia

Email: nchernenko@sfedu.ru

Abstract. In this work, we study of the effect of focused ion beam (FIB) and local droplet etching (LDE) techniques combination on the regular nanohole array formation on GaAs (001) surface, which can act as template for selective quantum dot formation. The results of the influence of the regimes of method combination on the nanohole shape and size are presented. The possibility of obtaining highly symmetrical nanoholes of various diameters and depths in one technological cycle is shown.

1. Introduction

To date, problem of controlling the quantum dots (QD) size, along with the density, shape and their position on the surface is an important challenge. This problem can be solved with using surface pre-structuring, that is, by forming symmetrical holes on it. Controlling the position and geometrical characteristics (size and shape) of holes on the surface will make it possible to control the geometrical characteristics of QDs formed in these holes. Obtaining ordered highly symmetric QDs with low characteristics dispersion is one of the key problems on the way to creating a promising element base for quantum communications (single- and entangled photon sources), quantum computing (QD based registers) and nanoelectronics (single QD based transistors). In this paper we present the results of experimental studies of holes formation on GaAs (001) surface using combination of FIB-modification and LDE techniques. The obtained results show the promise of this combination for obtaining ordered and highly symmetric holes for QD formation.

2. Experiment

FIB-modification of GaAs (001) surface was carried out using a Nova NanoLab 600 scanning electron microscope (SEM) equipped with a FIB system (with a Ga^+ ion source) at accelerating voltages of 10 kV. We used FIB-modification point arrays of 5×5 μm with distance between point of 1.0 μm and number of beam passes (N): from 5 to 300. Then we used LDE technique in SemiTEq STE 35 MBE setup to obtain arrays of local nanoholes at FIB-modification points on the GaAs (001) substrate. The obtained samples were studied by the SEM, AFM, and Raman spectroscopy.

3. Results and discussion

The modified regions were studied by AFM immediately after FIB-modification. It was found that hole diameter varies from 64 nm at $N = 5$ to 160 nm at $N = 300$, and the hole depth from 4.8 nm to 65.1 nm,

respectively. Raman spectroscopy shows a decrease in the intensity of the LO-GaAs peak (294 cm^{-1}) by 2.5 times, which is due to crystal structural damage by the ion beams. An analysis of the obtained SEM images shows that, after LDE, holes with different geometric characteristics form at FIB-modification points. Figure 1 shows how, depending on the number of FIB passes *(N)*, the hole faceting, size and shape change. It can be seen how, with an increase in the number of passes (dose), the symmetry of the formed holes improves, and their faceting also changes (Figure 1): faceting with (111) planes is replaced by faceting with a system of (111) and (110) planes.

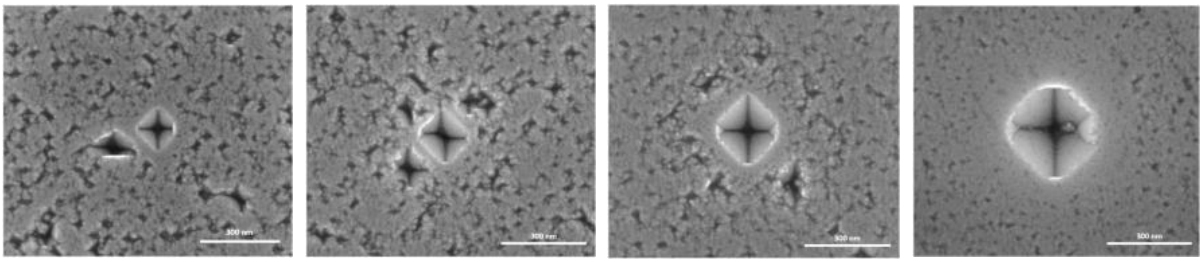

(a) *(b)* *(c)* *(d)*

Figure 1. SEM images of the GaAs (100) surface with holes formed in the areas effect of FIB at different number of FIB passes *N*: 5 (*a*), 10 (*b*), 40 (*c*), 300 (*d*).

The dependences of the hole diameter on the number of passes *N* are also shown (Figure 2*a*). The diameter of the holes gradually increases from 128 to 240 nm. Disks begin to form from $N = 5$ with diameter of 222 nm, then gradually grows to $N = 300$ with diameter of 500 nm. Figure 2*b* shows the dependence of the hole depth on the number of passes. A gradual increase in the depth of the pits from 20 to 100 nm is observed.

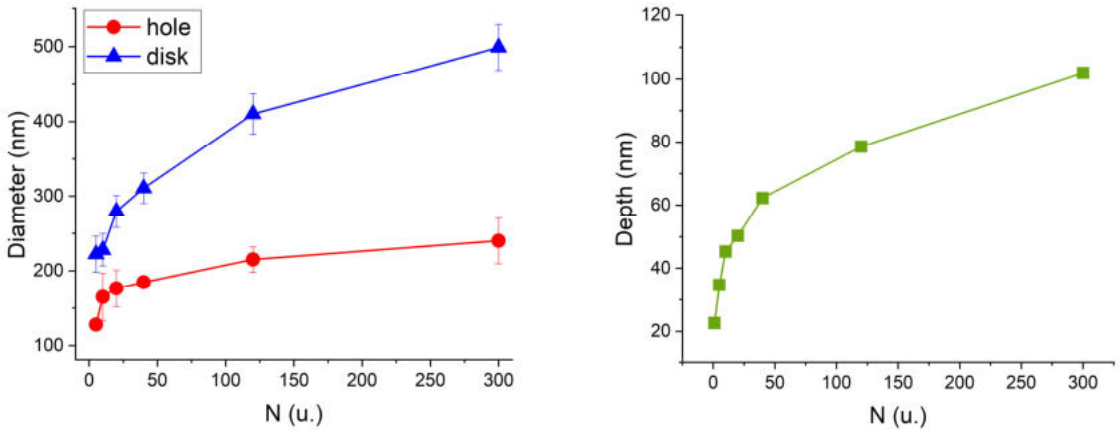

(a) *(b)*

Figure 2. Dependences of the diameter of the holes on the number of passes (*a*), the depth on the number of FIB passes *N* (*b*).

Thus, the results of experimental studies allow us to conclude that the use of a combination of the FIB and LDE methods is promising for creating ordered and highly symmetric holes for obtaining regular arrays of quantum dots of a given shape, size, and density. In addition, we have shown the possibility of obtaining holes of various shapes in a single technological cycle.

Acknowledgments
This work was supported by the Russian Science Foundation Grant No. №21-79-00310 in the Southern Federal University.

Effect of FIB-modification of Si(111) surface on GaAs nanowire growth

N A Shandyba, N E Chernenko, M M Eremenko, D V Kirichenko, S V Balakirev and M S Solodovnik

Institute of Nanotechnologies, Electronics and Equipment Engineering, Southern Federal University, Taganrog 347922, Russia

Email: shandyba@sfedu.ru

Abstract. The paper presents the results of experimental studies of GaAs nanowire growth on Si(111) substrate with Ga^+ focused ion beam modified areas with different treatment doses. We observed a significant difference between the parameters of nanowires arrays formed on modified and unmodified areas. It is shown that changing the dose of Ga^+ ions from 52 fC/μm^2 to 1×10^4 fC/μm^2 allows to form nanowire arrays with a different set of parameters in a single technological cycle with a high selectivity. The effect of the focused ion beam surface treatment on the key characteristics of GaAs nanowires (density, diameter, length and orientation) have been experimentally established.

1. Introduction

To date, the synthesis of nanowires (NWs) is one of the actively developing technologies due to the presence of unique electronic, optical, mechanical and magnetic properties of materials and structures based on these objects. But the problem associated with effective control of various NW parameters (length, diameter, density, etc.), incl. through pre-growth surface preparation, remains relevant to this day. The use of traditional technological processes based on the optical lithography operations, chemical wet and plasma etching do not provide the required parameters of the obtained structures and (or) are poorly compatible with growth processes. Also, some methods are characterized by a high cost of pre-growth treatment. At the same time, the technology of focused ion beams (FIB) makes it possible to carry out the operation of local ion-beam etching with high spatial resolution under high vacuum conditions, without the need to use resists, masks, and chemical etchants.

The aim of this work is to study the effect of the Si(111) surface treatment with different Ga^+ ion doses on the GaAs nanowire growth.

2. Experiment

For experimental studies we formed a squares template 5x5 μm with different Ga^+ implantation dose varying from 52 fC/μm^2 to 1×10^4 fC/μm^2 by ion-beam treatment of the Si(111) surface with an accelerating voltage of 30 kV. Then the modified sample was annealed, and GaAs NWs growth was performed using MBE. NWs formation was carried out at substrate temperature of 600°C with an effective gallium deposition rate of 0.25 ML/s and an equivalent GaAs deposition thickness of 200 nm.

3. Results and discussion

The analysis of the obtained images from scanning electron microscope (Figure 1) shows a sharp difference between the NWs formed on modified and unmodified Si areas. We also detected a nonlinear dependence of the NWs key parameters on the Ga^+ ions dose (Figure 2).

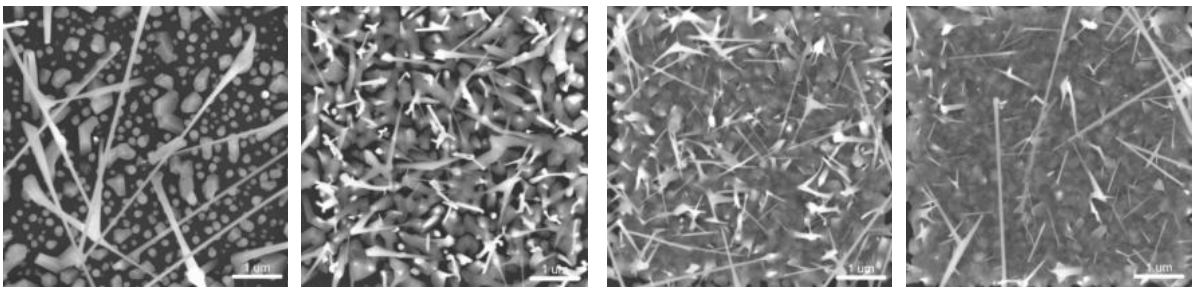

(a) (b) (c) (d)

Figure 1. SEM images of modified areas after GaAs nanowires growth for Ga^+ ion dose of 52 fC/μm^2 (a), 260 fC/μm^2 (b), 1.56×10^3 fC/μm^2 (c), 1×10^4 fC/μm^2 (d).

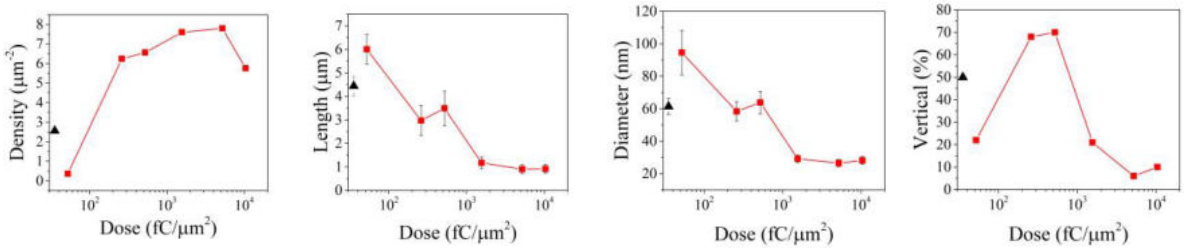

(a) (b) (c) (d)

Figure 2. Dependences of density (a), length (b), diameter (c) and vertical orientation of NWs (d) on Ga^+ ion dose (▲ – values for unmodified areas).

So, NWs growth is completely suppressed on area with ion dose of 52 fC/μm^2 (Figure 1, a). We assume that this may be caused with the swelling effect on the treated surface due to Ga ions (atoms) implantation. This process accompanied by defects generation, and it makes difficult for embedded Ga ions to reach the surface. All of this leads to suppressing the formation of Ga catalyst droplets (nucleation centers of GaAs NWs) from FIB implanted ions (atoms).

Increasing the dose to 260 fC/μm^2 (Figure 1, b) leads to the beginning of active NWs growth on the modified region, which corresponds to a sharp raising of NWs density while reducing their length and diameter (Figure 2, b, c). We think that such dose increment provides to the increasing of the near-surface layer defectiveness on modified region. This leads to an intensification of the crystal lattice reduction processes at the annealing stage and accompanying segregation of embedded Ga ions (atoms) on the Si surface. Consequently, it promotes to the formation of additional catalyst droplets.

A further dose increases the leads first to raising of NWs density (Figure 2, a) with a peak value of 7.8 μm^{-2} (5.2×10^3 fC/μm^2) and then to a slight decrease to 5.76 μm^{-2} (Figure 1, d). We suggested that such behavior may be caused by formation of a polycrystalline base due to intensification of GaAs parasitic crystallites growth on the modified areas. This process starting from a dose of 1.56×10^3 fC/μm^2 (Figure 1, c) and fundamentally change the conditions of the NWs nucleation and growth in these regions. Accordingly, this greatly effects on the key NWs parameters.

The largest percentage of NWs verticality is 70 % in area with the dose of 520 fC/μm^2 (Figure 2, d).

Acknowledgments

This work was supported by the Ministry of Science and Higher Education of the Russian Federation; the state task in the field of scientific activity No. FENW-2022-0001 in Southern Federal University.

Formation of porous silicon layers in a «universal» type electrochemical cell

I A Shishkin[1], D A Shishkina[1]

[1]Samara National Research University, Samara 443086, Russia

Email: shishkinivan9@gmail.com

Abstract. The paper presents a solution to the problem of determining the main parameters of obtaining porous silicon by creating a physical and mathematical model. To compare the simulation results, it was necessary to create an electrochemical bath for etching silicon substrates of optimal design. To create an electrochemical bath, a Makerbot Replicator 3D printer was required, and the COMSOL Multiphysics package was used to describe physical processes.

1. Introduction

The most common method of creating porous silicon is anodic electrochemical treatment of silicon in HF:C_2H_5OH (1:1) solution. The anode and cathode sometimes are graphite electrodes. The appearance of pores begins on the surface of the silicon substrate, with the passage of time of anodic treatment, the ends of the pores move further and further into the crystal. Most of the developed models of pore formation do not take into account the effect of microrelief on the surface of a silicon wafer, where the anode-electrolyte interface is usually considered flat [1-3]. In this paper, we solved the problem of constructing a three-dimensional physical and mathematical model describing the distribution of the field in an electrochemical cell of vertical type and on the surface of the sample, and also constructed the distribution of the electric field and potential in the process of electrochemical etching.

The process of creating porous silicon should be well reproducible, so an effective and universal method is needed. Thus, using variations in the composition of the electrolyte, the anodizing current density from 5 - 30 mA/cm^2 and the anodizing time of 1-5 minutes, layers of porous silicon from 0.01 - 50 microns are created with the possibility of forming all major morphological types of structures from nano- to macroporous. The new type of electrochemical cell created will allow working with 8 samples simultaneously, where each substrate is different in its configurations.

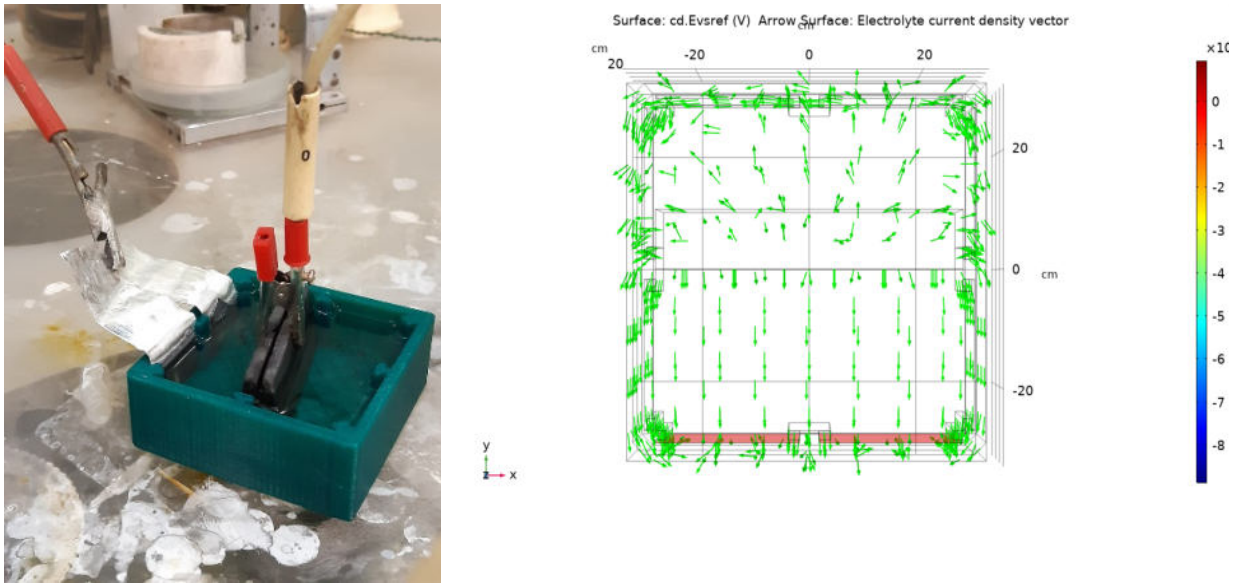

Figure 1. Electrochemical cell for the production of porous silicon and the result of simulation an electric field in Comsol Multiphysics

2. Experiment

The electrochemical cell is made for substrates with a size of 2.5x2.5 cm. On each wall of the cell in which the samples are placed, two grooves are provided for inserting samples and anodes in the form of 0.25 mm thick aluminum foil films. Up to 8 samples can be placed in total, but this design is only a prototype and can be increased in size for large silicon wafers (Fig. 1). Studies of the dependence of the electric field on the location of the cathode have been carried out.

The results showed that with such an arrangement of the cathode (Fig. 1), the pyramidal surface is etched, while it is observed that the pore sizes exceed 2-3 microns (macropores). With an increase in the current density, the process switches to the polishing mode of silicon substrates.

3. Conclusion

Simulation of the etching process in Comsol Multiphysics present that in order to obtain high-quality nanocrystalline silicon layers, the cathode must be located near the cell wall, otherwise, with long etching times or high currents, the substrate is destroyed or porous silicon is formed to the entire depth of the substrate.

Acknowledgments

This work was supported by the Foundation for Assistance to Small Innovative Enterprises, grant № 12980GU/2018.

References

[1] Conebeer G, Green M, Corkish R, Cho Y, Cho E-C, Jiang C-W, Fangsuwannarak T, Pink E, Huang Y, Puzzer T, Trupke T, Richards B, Shalav A, Lin K-L 2006 *Thin Solid Films* **511-512** 654-662

[2] Loni A 2014 *Handbook of Porous Silicon. Springer*, *Cham.* 12-22

[3] Canham L 2014 *Handbook of Porous Silicon. Springer*, *Cham*. 85-91

Semiconductor metasurfaces for Fourier filtering of an optical signal

Iushkov Viacheslav, Shorokhov Alexander, Fedyanin Andrey

iushkov@physics.msu.ru
shorokhov@nanolab.phys.msu.ru
fedyanin@nanolab.phys.msu.ru

Abstract. We have proposed and numerically tested a method for fully optical image processing based on Fourier analysis using a semiconductor metasurface. Designed metasurface is composed of silicon nanodisks embedded into silica and can be fabricated by well-established fabrication techniques. This study opens up new possibilities in various real-time image processing applications.

1. Introduction

Over the past couple of decades, metastructures have aroused considerable interest in the scientific community. Such objects are arrays of scattering particles of a given shape, designed and arranged in such a way that the resulting device has a given specific response, for example, close to zero or a negative effective refractive index. Two-dimensional analogs of metamaterials - metasurfaces, are much easier to manufacture and design than their three-dimensional counterparts. The properties of such structures mainly depend on the mutual arrangement of nanoparticles relative to each other, their size and shape. Changing these parameters makes it possible to correct the radiation wavefront on a subwavelength scale. Based on this, many devices such as metaholograms [1], metalens [2], or vortex beam generators [3] have been demonstrated over the past ten years. One of the most commonly used materials for metasurfaces are semiconductors and dielectrics due to low losses in the visible and near IR range.

Among the promising applications of metasurfaces, one can single out the implementation of mathematical operations on an optical signal [4,5,6]. The easiest way to implement such operations is in the form of Fourier filtering of an optical signal, where the metasurface acts as a filter. However, in such a situation, there is a problem associated with the static response of such a filter. To solve this problem, one can use fully optical pumping to change the profile of the complex transmittance of the nanostructure material [7].

The purpose of this work is to create and study metasurfaces operating in the near-IR range of the radiation spectrum for the implementation of the method of all-optical image analysis. One of the key tasks is to study the change in the optical response of the structure under the action of laser pumping and the subsequent uneven absorption of light by the nanoantennas that form it.

2. Results

During the work, metasurfaces were modeled from semiconductor (silicon, gallium arsenide) disks immersed into glass to realize a given response. The choice of material and design is justified by the

ease of manufacture and the availability of materials. The metasurface is divided into zones called pixels, each pixel contains identical disk-shaped nanoparticles. Using the configuration for reflection or transmission, the operations of convolution and taking the derivative along the selected axis over the incident image were numerically simulated using a metasurface. The question of the possibility of creating a tunable metasurface using optical pumping was analyzed, a suitable material was proposed, and a simulation of changes in its optical properties was performed.

The results obtained can be used to create compact optical signal processing devices with subpicosecond time resolution.

Acknowledgments

References

[1] Katie E. Chong et al., «Efficient polarization-insensitive complex wavefront control using Huygens' metasurfaces based on dielectric resonant meta-atoms», *ACS Photonics* **3**, 514-519 (2016).

[2] Mohammadreza Khorasaninejad, Federico Capasso, «Metalenses: Versatile multifunctional photonic components», *Science* **358**, 1146 (2017).

[3] Gregorius C. G. Berkhout et al., «Efficient Sorting of Orbital Angular Momentum States of Light», *Phys. Rev. Lett.* **105**, 153601 (2010)

[4] Junxiao Zhou et al., «Optical edge detection based on high-efficiency dielectric metasurface», *Proc. Natl. Acad. Sci. U.S.A.* **116**, 11137 (2019)

[5] Ata Chizari et al., «Analog optical computing based on a dielectric meta-reflect array», *Opt. Lett.* **41**, 3451-3453 (2016)

[6] Tariq Manzur, John Zeller, and Steve Serati, «Optical correlator based target detection, recognition, classification, and tracking», *Appl. Opt.* **51**, 4976 (2012)

[7] Shcherbakov, M.R., Liu, S., Zubyuk, V.V. et al. «Ultrafast all-optical tuning of direct-gap semiconductor metasurfaces», *Nat. Commun.* **8**, 17 (2017)

The properties of magneto-luminescent nanocomposites in a liquid flow

A. Dadadzhanova[1], I. Reznik[1], A. Kurilova[1], A. Dubavik[1], A. Orlova[1]

[1]ITMO University, Saint Petersburg, Russia

E-mail: fadeeva.antonina95@gmail.com

Abstract. This paper presents the move of magneto-luminescent nanocomposites Fe3O4@SiO2-CdTe in a liquid flow simulating blood flow in vessels when a magnetic field is applied.

1. Introduction

One of the promising applications of Fe_3O_4 nanoparticles is the formation of magneto-luminescent platforms for conducting local therapeutic effects [1].

Obviously, the ability to monitor the effectiveness of magnetic nanoparticles' penetration by the luminescent response makes development these systems is promising. However, the formation of nanocomposites based on the Fe_3O_4 core and a semiconductor luminescent shell leads to deterioration of the luminescent properties. In the overwhelming majority of cases, the deterioration of the properties of the luminescent component of the system is due to the efficient transfer of energy/charge to Fe_3O_4 [2]. The using an insulating layer on the magnetic component allows to solve this problem. For example, a mesoporous silica coating can be used, because it is sufficiently stable, non-toxic, and biocompatible. The insulating layer from SiO_2 prevents charge/energy transfer while maintaining magnetic and luminescent properties. To use magneto-luminescent nanocomposites for targeted drug delivery using an applied magnetic field, it is necessary to study the magnetic properties of such nanocomposites in a liquid flow simulating blood flow in vessels.

In this work we investigated the magneto-luminescent properties of nanocomposites with diameter 90 nm based on Fe_3O_4 covered by SiO_2 shell and CdTe quantum dots covalent attached to the Fe_3O_4@SiO_2 surface in a liquid flow simulating blood flow in vessels. A glass tube with an inner diameter of 1 mm was used as a model vessel for the human body. A liquid with magneto-luminescent nanocomposites was passed through a glass tube at a rate of 1 ml/s. An electromagnet with a field strength of 0.3 T was used as a magnetic field affecting the flow of magneto-luminescent nanocomposites in a glass tube.

2. Results and Discussion

The nanocomposite solution was fed into the glass tube at maximum speed until its internal volume was filled. After that, images were automatically recorded on the microscope in the luminescence recording mode at a rate of 62.5 frames per second. 20 seconds after the start of image recording, the electromagnet was turned on at maximum power (0.37 T) for 30 seconds. Figure 1 shows a series of images of a Fe3O4@SiO2-CdTe nanocomposite solution obtained on a fluorescent microscope before and after turning on the magnetic field.

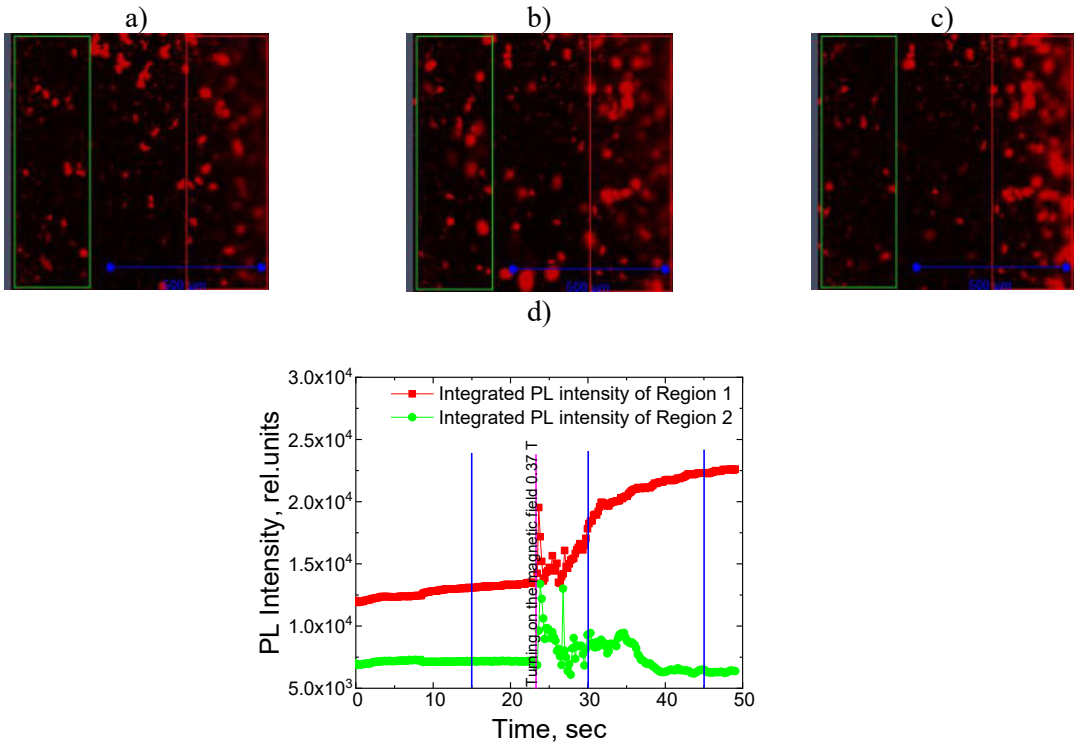

Figure 1. Luminescent images of Fe3O4/SiO2/CdTe nanocomposites solution obtained before turning on a magnetic field with a strength of 0.37 T (a), after 15 seconds (b), 30 seconds (c). d) Time dependence of the integrated luminescence intensity taken from the area in the center of the viewing cell (green curve) and near the magnetic field source (red curve) before and after switching on the magnetic field with a strength of 0.37 T (marked with a purple vertical line on the graph). The blue vertical lines correspond to the timestamps of the images (a), (b) and (c)

As can be seen from Figure 1, the magnetic field is turned on lead to the active migration of nanocomposites to the walls of the cuvette occurs for ~ 15 seconds, which confirms that they have magnetic properties.

3. Conclusion

The study of magneto-luminescent nanocomposites showed the synthesized nanocomposites retain their magnetic and luminescent properties. The movement and luminescence of nanocomposites upon application of a magnetic field in a liquid flow indicates their promising use for targeted drug delivery.

Acknowledgments

This work was supported by the Ministry of Science and Higher Education of the Russian Federation, GOSZADANIE No. 2019-1080

References

[1] Liu Y. L. et al. A review of magnet systems for targeted drug delivery //Journal of Controlled Release. – 2019. – T. 302. – C. 90-104.

This reference has two entries but the second one is not numbered (it uses the ‘Reference (no number)’ style.

[2] Tong L. et al. Luminescent and magnetic properties of Fe3O4@ SiO2@ Y2O3: Eu3+ composites with core–shell structure //The Journal of Physical Chemistry C. – 2012. – T. 116. – №. 12. – C. 7153-7157

Influence of the applied voltage on electrophysical properties of conductive hydrogel studied by Raman spectroscopy

D S Bolshin[1,2], P M Gotovtcev[2] and P K Kashkarov[1,2]

[1] Department of General Physics and Molecular Electronics, Faculty of Physics, M.V.Lomonosov Moscow State University. Moscow 119991, Russia
[2] National Research Center «Kurchatov institute», 1, Akademika Kurchatova pl., Moscow, 123182, Russia

e-mail: ds.boljshin@physics.msu.ru

Abstract. In such spheres as applied medicine, tissue engineering, soft electronics, smart materials, particular emphasis is given to hydrogels, especially conductive ones. Passing from a dry state to a swollen one, hydrogel can acquire new properties. An applied voltage to a conductive hydrogel swollen in physiological NaCl solution caused a change in its electrophysical properties. In this paper the mechanism of these electrophysical changes was described and confirmed with an analysis method based on Raman spectroscopy.

1. Introduction

Hydrogel is a stable polymer matrix capable of absorbing and retaining a much greater mass of water than the mass of the matrix itself. Hydrogel can provide immobilization of other objects, such as conductive polymers. The resulting properties of semiconductors or supercapacitors arise the practical interest in hydrogels in the fields of soft electronics and applied medicine.

The research object of this work is hydrogel based on crosslinked polyvinyl alcohol and xanthan matrix with the addition of PEDOT:PSS (poly(3,4-ethylenedioxythiophene) polystyrene sulfonate), a polymer with high electrical conductivity, stability, and biocompatibility [1]. This hydrogel swollen in physiological NaCl solution (8.4 g/L) has two types of conductivity: hole conductivity due to PEDOT:PSS [2] and ionic one. The same hydrogel swollen in distilled water has only hole conductivity.

2. Residual potential difference

For 30 seconds the constant voltage in the range from -0.3 to 0.3 V was applied to the hydrogel swollen in saline solution. After turning off the applied voltage and relaxation, a residual potential difference, that monotonically depended on the magnitude of the applied voltage, was observed in hydrogel. It has been hypothesized, that this effect is caused by a change in the state of PEDOT:PSS.

3. Raman spectroscopy

In the following experiment, the voltage of 0.3 V was applied to the hydrogels swollen in saline and distilled water for 30, 90, and 300 seconds. Raman spectra were measured along the sample after the voltage had been turned off. The laser wavelength in Raman spectrometer is 638 nm.

4. Results

The findings from the work [3] demonstrated that the decomposition of the obtained spectra makes it possible to estimate the oxidation state of the PEDOT chain from the integral intensities of the lines of oxidized and reduced PEDOT normalized to the integral intensity of Cα=Cβ vibrations. In current research, this approach was exploited as a main analysis method. In addition to qualitative changes in the spectra for the gel in saline, an increase in the difference in the oxidation state of the conductive polymer from the cathode to the anode was recorded along with the increase of the voltage application time. In the case of the gel in distilled water, the applied voltage caused no changes in the spectra.

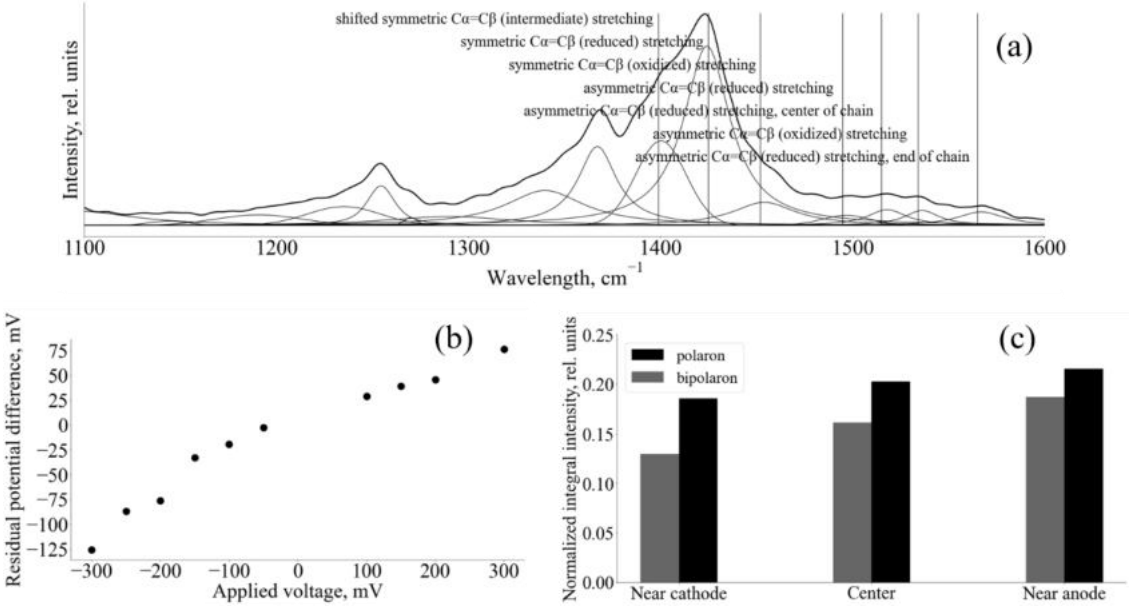

Figure 1. The decomposition of the Raman spectrum of the swollen hydrogel for the evaluation of the oxidation state of PEDOT:PSS (a); the dependence of the residual potential difference in the hydrogel after relaxation on the magnitude of the applied voltage for 30 sec (b); normalized integral intensities of PEDOT chain after 300 seconds that represent PEDOT:PSS oxidation state differences along the gel induced by the applied voltage (c).

5. Conclusion

The experiments conducted in this research showed, that the residual potential difference observed in the gel swollen in saline solution is caused by the hole conductivity gradient along the gel from the cathode to the anode. The applied voltage induces a redistribution of Na^+ and Cl^- ions. Na^+ binds to the acceptor chain of PSS, provoking the reduction of the PEDOT chain. On the other hand, an increase in the concentration of Cl^- triggers the oxidation of the PEDOT chain. Eventually, after the voltage is turned off, the concentration of mobile ions becomes uniform, but PEDOT:PSS continues to be in different states. In distilled water, the hydrogel absorbs more water [3], the polymer matrix expands more, the PEDOT and PSS chains are shielded by water molecules, which causes a stronger PEDOT:PSS reduction than in saline. The absence of a difference in the spectra for the hydrogel in water corresponds to the proposed mechanism of changing the hole conductivity.

Acknowledgments

The work was financially supported by Russian Foundation for Basic Research grant № 20-32-90221.

References

[1] Boehler C, Aqrawe Z and Asplund M 2019 *Bioelectron. Med.* **2** 2

[2] Garreau S, Louarn G, Buisson J P, Froyer G and Lefrant S 1999 *Macromolecules* **32** 6807

[3] Bolshin D S, Kashkarov P K 2022 *Nanobiotechnology Reports* **17** (3)

Investigation of the surface properties of thin nanocomposite films of TiO_2-SnO_2 composition

I A Gulyaeva[1], A P Ivanishcheva [1], M G Volkova[2], E M Bayan[2], V V Petrov[1]

[1] Research and Education Centre "Microsystem technics and multisensor monitoring systems", Southern Federal University, Taganrog, 347922, Russia
[2] Department of Chemistry, Southern Federal University, Rostov-on-Don, 344090, Russia

E-mail: tenirka@mail.ru

Abstract. Thin nanocomposite films based on pure tin dioxide with a low content of titanium oxide (0, 5 mol. %) were obtained by solid-phase low-temperature pyrolysis. The thickness of the films obtained was up to 200 nm. The particle size of the TiO_2-SnO_2 nanomaterial is in the range of 7-13 nm. Atomic force microscopy (AFM) has shown that the films have a granular structure with a height difference of 11-34 nm. The method of Kelvin probe force microscopy (KPFM) revealed a surface potential showing the existence of a high surface electric field.

1. Introduction

Inorganic oxide nanomaterials based on tin and titanium dioxides are currently being intensively studied, since such materials are widely used to create electronic devices, photocatalysts, solar cell electrodes and gas sensors [1]. The purpose of this work was to study the surface morphology and surface electrical potential of synthesized tin dioxide thin films doped with titanium by solid-phase low-temperature pyrolysis.

2. Experiment

Tin ($SnCl_4$ $5H_2O$) and titanium ($(C_4H_9O)_4Ti$) salts were used as precursors to obtain TiO_2–SnO_2 thin film materials by solid-phase low-temperature pyrolysis. The resulting salts were dissolved in 1,4-dioxane and applied three times onto prepared silicon and polycor substrates. Each layer was dried in air and in an oven at a temperature of 120°C. The final thermal treatment was carried out in a muffle furnace at a temperature of 600°C for two hours.

The surface morphology and surface potential of the obtained films were studied using the Ntegra probe nanolaboratory (NT-MDT SI, Russia). An NSG10/Pt cantilever was used in the study by AFM and KPFM methods. To process the results of AFM measurements, the Image Analysis (NT-MDT) program was used. Based on the KPFM measurements, the values of the surface potential $\Delta\Phi_B$ were determined.

3. Results and discussion

Figure 1 shows the AFM scans of the studied samples of TiO_2-SnO_2 films with a Ti:Sn ratio of 0:100, 1:99 mol.% with a size of 3×3 μm^2.

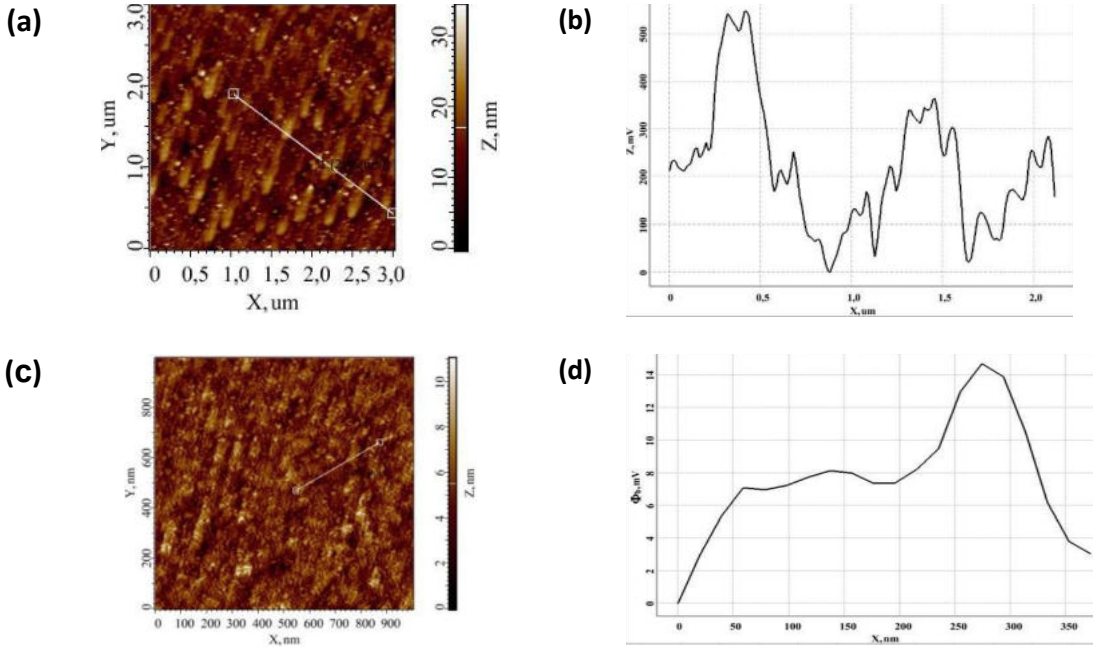

Figure 1. AFM scans of the relief (a, c) and the corresponding surface potential distribution (b, d) over the surface of films with a molar ratio of tin and zinc Ti:Sn equal to 1:99(a, b) and 0:100 (c, d) mol. %

AFM studies have shown that the films have a granular structure with a "Peak to peak" (Sy) height difference. In general, when 1% titanium is added, the height difference increases from 11 to 34 nm. However, the surface of the film with a Ti concentration of 1 mol% has a higher roughness than the surface of the films with the ratio of titanium and tin Ti:Sn =0:100 mol.%. Studies of the KPFM showed that the lowest average value of the surface potential of about 4 mV is typical for a tin oxide film - Fig. 1 d. However, for a film with a Ti:Sn molar ratio of 1:99 mol.%, a peak value of the surface potential is observed, the value of which reaches 1325 mV. The latter indicates the existence of a strong (up to 10^7 V/cm) electric field on the surface of such a film, which can significantly affect the transfer of charge carriers in it and the processes occurring on its surface [3].

4. Conclusion

Nanosized films of the composition TiO_2-SnO_2 of controlled thickness were formed by the method of solid-phase low-temperature pyrolysis. The surface potential was found on their surface by the KPFM method, which indicates the existence of a high surface electric field. The resulting TiO_2-SnO_2 films can be used as solar cell electrodes and as gas-sensitive materials for gas sensors.

Acknowledgments

This work was financially supported by the RFBR, project 20-07-00653 A. We would like to express our gratitude to the staff of the Laboratory for Technology of Functional Nanomaterials of the Institute of Nanotechnology, Electronics and Equipment Engineering of the Southern Federal University for their help in conducting AFM and KPFM studies.

References

[1] Bayan E M, Lupeiko T G, Pustovaya L E, Volkova M G 2020 Synthesis and photocatalytic properties of Sn–TiO2 nanomaterials *J Adv. Dielectr.* **10** 01n02 2060018

[2] Petrov V V 2007 Investigation of the gas molecules interaction features with the oxide gas-sensitive materials surface, Nano- and microsystem technology 1 24-27

Study of photoconductivity of thin films Co_3O_4 – ZnO

I A Gulyaeva[1], I O Ignatieva[2], E M Bayan[2], V V Petrov[1]

[1]Southern Federal University, Institute of Nanotechnologies, Electronics, and Equipment Engineering, Taganrog, 347922, Russia.
[2] Department of Chemistry, Southern Federal University, Rostov-on-Don, 344090, Russia

E-mail: tenirka@mail.ru

Abstract. In this work, the photoconductivity parameters of Co_3O_4 – ZnO thin films formed on polycor substrates are studied. Co_3O_4 – ZnO nanocomposite films were deposited on substrates by solid-phase pyrolysis with a Co:Zn molar ratio of 10:90, 5:95, 3:97, 1:99 and annealed at a temperature of 600°C. The film thickness was 150 – 200 nm. The crystal structure of the films was studied. After applying the contact metallization, the photoconductivity parameters were measured under the action of light from an LED with a peak wavelength of 400 nm.

1. Introduction

The development of new materials for alternative energy sources is attracting more and more attention from researchers. Efficient use of sunlight opens great opportunities for energy savings. That is why much attention is paid to obtaining new materials with the necessary photosensitivity for solar and photocells. In this work, thin films of Co_3O_4 – ZnO were synthesized by a new method of solid-phase pyrolysis [1-3], in which the structural and photoelectric properties were studied.

2. Experiment

When forming thin Co_3O_4 – ZnO films by solid-phase pyrolysis, zinc (II) acetate dihydrate $Zn(CH_3COO)_2$ $2H_2O$, cobalt (II) acetate tetrahydrate $Co(CH_3COO)_2$ $4H_2O$, and organic acid were used. The two-stage synthesis procedure made it possible to obtain the required precursor compositions. During the first stage, an intermediate product, a mixture of organic salts of zinc and cobalt, was obtained. During the second stage, a solution of the resulting product in an organic solvent was applied to preliminarily prepared substrates. The substrates were calcined for two hours at 600°C. The phase composition of the obtained materials was studied by XRD. Based on the results of the XPA, it was established that the material obtained is two-phase, which is confirmed by the presence of peaks characteristic of ZnO and Co_3O_4. It is noted that the intensity of the peaks of zinc oxide wurtzite is much more pronounced than the peaks of cobalt oxide.

In the future, a counter-pin V-Ni metallization was applied to the Co_3O_4-ZnO film by the method of thermal vacuum evaporation through the mask and a flat photoresistor with an initial "dark" resistance R_0 was formed.

There was a direct change in photoconductivity under the action of light from an LED with a peak wavelength of 400 nm with a light level of 525 lux. There was no ultraviolet component. Radiation parameters were measured using the CENTER 532 ultraviolet intensity meter (China) and the CENTER 530 illumination meter (China). When the LED was turned on, a photoresistance was observed in all film samples. the measurement was carried out before the beginning of the "unfolding" of the dependencies. Subsequently, the time constant for the generation of charge carriers under the action of light was calculated.

Figure 1 shows a timeline of the time change in normalized photoresistance under the action of light for films with a molar ratio of Co:Zn of 10:90, 5:95, 3:97, 1:99.

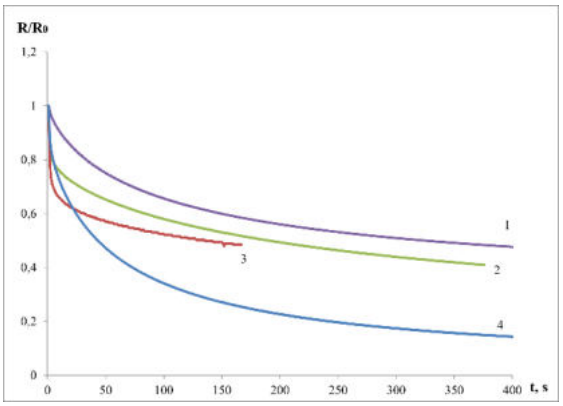

Figure 1. Graph of the temporal change in normalized photoresistance under the action of light for films with a molar ratio Co:Zn of 10:90 (1),5:95 (2),3:97 (3),1:99 (4).

Studies have shown that a film with an additive of 1% cobalt has the longest constant time equal to 70 s. Adding cobalt oxide of 3% and 10% drastically reduces the constant duration to 37-60 s. The fastest response time of 25 s was found in a sample with a Co:Zn ratio of 5:95. This behavior of photoconductivity parameters is associated with the nanocomposite structure of the film material, and lower values of the constant time are associated with a higher concentration of charge carrier generation centers at the Co_3O_4 – ZnO interface at a Co:Zn ratio of 5:95. It can also be noted that the response kinetics for all films were similar, which indicates the same generation mechanisms - recombination of charge carriers in ZnO sol-gel films with the addition of CoO.

3. Conclusion

Thus, in this work, thin films of Co_3O_4 - ZnO were synthesized by a new method of solid-phase pyrolysis, in which the phase composition and the measured kinetics of photoconductivity were investigated. The Co_3O_4– ZnO film with a Co:Zn ratio of 5:95 has the lowest value of the time constant (25 s).

Acknowledgments

The study was supported by the Russian Science Foundation grant No. 22-29-00621, https://rscf.ru/en/project/22-29-00621/ at the Southern Federal University.

References

[1] Bayan E M, Petrov V V, Volkova M G, Storozhenko V Yu, Chernyshev A V, SnO_2–ZnO nanocomposite thin films: The influence of structure, composition and crystallinity on optical and electrophysical properties 2021 *J. Adv.d Dielectr.* **11 (4-5)** 2160008

[2] Petrov V V, Sysoev V V , Starnikova A P , Volkova M G , Kalazhokov Z Kh , Storozhenko V Yu, Khubezhov S A, Bayan E M, Synthesis, Characterization and Gas Sensing Study of ZnO-SnO_2 Nanocomposite Thin Films *Chemosensors* **9(6)** 124 (2021)

[3] Volkova M G, Storozhenko V Yu, Gulyaeva I A, Starnikova A P, Petrov V V and Bayan E M TiO_2-SnO_2 films: Synthesis by low-temperature pyrolysis and electrophysical properties *Materials Today: Proceedings* **52 (2)** 187-190 (2022)

Study of narrow-band UV radiation sources based on zinc oxide

I K Kindyushov[1], S A Kadinskaya[1], M E Labzovskaya[2], B V Novikov[2], I V Shtrom[1,2], A I Lihachev[3], A V Nashchekin[3] and A D Bolshakov[1,4,5]

[1]Alferov University, St. Petersburg, 194021, Russia
[2]Saint Petersburg State University, St. Petersburg, 199034, Russia
[3]Ioffe Institute, St. Petersburg, 194021, Russia
[4]ITMO University, St. Petersburg, 197101, Russia
[5]Moscow Institute of Physics and Technology, Dolgoprudniy, 117303, Russia

E-mail: kindyushow@gmail.com

Abstract. The structures of zinc oxide synthesized by hydrothermal method on a silicon substrate with orientation (111) are investigated in this paper. An efficient protocol for the synthesis of zinc oxide microstructures with a low aspect ratio of the characteristic longitudinal to transverse size has been demonstrated. The optical properties of the resulting structures were studied by photoluminescence spectroscopy (PS). The possibility of synthesizing low-defect hydrothermal zinc oxide microstructures suitable for creating narrow-band sources of UV radiation, as well as laser sources of radiation based on whispering gallery modes is shown.

1. Introduction

Zinc oxide (ZnO) has been widely established as the material of modern electronics. There are piezonanogenerators, gas sensors and optical devices based on a zinc oxide [1-5]. Zinc oxide in the geometry of hexagonal microcrystals has its own resonator structure and can be used to create a whispering gallery mode based laser.

Many methods are suitable to produce zinc oxide especially - hydrothermal. The advantages of hydrothermal synthesis include wide possibilities for controlling growth conditions, the ability to carry out synthesis at relatively low temperatures (less than 100°C), which leads to a significant reduction in energy consumption and makes the method quite economical [6].

Even though there are many light-emitting devices based on various materials [7–9], low-defect ZnO microstructures synthesized by a hydrothermal method have great prospects for solving problems of modern photonics and electronics.

2. Synthesis

To synthesis of zinc oxide microstructures zinc acetate as the seed layer material and zinc nitrate ($Zn(NO_3)_2$) and hexamethylenetetramine (HMTA) as a precursors were used. The main growth parameters are given in previous works [1, 5].

Two type of zinc oxide based microstructures are synthesized via hydrothermal synthesis using spin coating and silar technics for seed layers formation. As a result of the synthesis, hexagonal microcrystals with a diameter of about 7–10 μm for the first sample and 3–5 μm for the second were obtained. The volume of ZnO on the sample's №2 surface is higher than that of sample № 1.

3. Experiment

Zinc oxide is characterized by PL emission in all spectral regions from UV to IR [10]. Peaks outside the UV region are due to the presence of defects and impurities in the ZnO structure [9]. The absence of a PL response in the long-wavelength region indicates a high crystalline perfection of the synthesized hydrothermal microstructures. In the spectral region of the short-wavelength PL band at low temperatures, radiation containing lines of excitons coupled to shallow neutral and ionized donors (D^0X) enters. In the long-wavelength region of the spectrum, an emission band is observed, which includes bands due to transitions of a free electron of the conduction band - an acceptor, emission of donor-acceptor pairs during transitions of a localized electron to a shallow acceptor and the first LO-phonon repetition of a free exciton

4. Conclusion

In this work, we synthesized high crystal quality hydrothermal ZnO microstructures. The PL spectra of the synthesized structures at low temperature have been studied, indicating the presence of a narrow emission band near 370 nm, as well as the absence of a PL response in the visible region of the spectrum. It is shown that interband recombination is suppressed due to the high crystallinity of the structures.

It has been established that the PL intensity is mainly determined by the volume and morphology of the ZnO on the substrate surface, which can be control via growth conditions and seed layers variation.

References

[1] V M Kondratev, A D Bolshakov and S S Nalimova 2021 *IEEE Conference of Russian Young Researchers in Electrical and Electronic Engineering (ElConRus)*, 2021, 1163.

[2] E A Levkevich, A I Maksimov, S A Kirillova, S S Nalimova, V M Kondrat'ev and A. A. Semenova 2020 *IEEE Conference of Russian Young Researchers in Electrical and Electronic Engineering* (EIConRus), 2020, 984.

[3] S S Nalimova, V M Kondratev, A A Ryabko, A I Maksimov and V A Moshnikovl *J. Phys.: Conf. Ser*., 2020, 1658 012033.

[4] S S Nalimova, A A Bobkov, V M Kondrat'ev, A A Ryabko, V A Moshnikov and Z V Shomakhov 2020 *IEEE Conference of Russian Young Researchers in Electrical and Electronic Engineering* (EIConRus), 2020, 991.

[5] S S Nalimova and V M Kondrat'ev 2020 *IEEE Conference of Russian Young Researchers in Electrical and Electronic Engineering* (EIConRus), 2020, 987.

[6] Жуков А Е, Моисеев Е И, Надточий А М и др. *Письма в ЖТФ*, 2020, **46(16)**, 783-786.

[7] Bolshakov A D, Shishkin I, Machnev A, Petrov M, Kirilenko D A, Fedorov V V, Mukhin I S, Ginzburget P *Nanoscale* 2022, **14(3)**, 993.

[8] Kuznetsov A, Roy P, Kondratev V M, Fedorov V V, Kotlyar K P, Reznik R R, Vorobyev A A, Mukhin I S, Cirlin G E, Bolshakov A D *Nanomaterials* 2022, **12(2)**, 241.

[9] P Roy, A D Bolshakov *Physica Status Solidi (RRL) – Rapid Research Letters* 2021, **15(6)**, 2000579.

[10] Galdámez-Martinez, A., Santana, G., Güell, F., Martínez-Alanis, P. R., & Dutt, A. (2020). *Nanomaterials*, **10(5)**, 857. doi:10.3390/nano10050857

Optical studies of InP nanostructures monolithically integrated in Si (100)

I A Melnichenko[1], N V Kryzhanovskaya[1], Y Berdnikov[1], E Moiseev[1], I S Makhov[1]

[1]National Research University Higher School of Economics, 16 Soyuza Pechatnikov, St. Petersburg 190008, Russia

E-mail: imelnichenko@hse.ru

Abstract. We present a photoluminescence study of InP nanostructures monolithically integrated to Si (100) substrate. The InP nanostructures were grown in pre-formed pits in the silicon substrate using an original approach, based on selective area growth and driven by a molten alloy in metal–organic vapor epitaxy method. The obtained InP/Si nanostructures have submicron size above Si substrate. Individual InP/Si nanostructure was investigated by photoluminescence spectroscopy in temperature range 5-300K at different pump power. The room temperature photoluminescence spectra of the studied structures exhibit the peak corresponding to zinc blende InP band gap. The obtained results show high crystalline quality of the InP material.

1. Introduction

Creation of efficient A3B5 light sources on silicon, suitable for device applications, remains challenging [1]. New generation of compact and low-power light sources are expected to expand the frequency band of the modern electronics and should be compatible with the well-developed scalable silicon processing technologies [2, 3]. The A3B5 materials have high electron mobility and direct band gap. However, integration the A3B5-based light emitting devices with Si platform is difficult because of the lattice mismatch between most of A3B5 materials and silicon, as well as the difference in thermal expansion coefficients, which typically lead to high defect density in the structures. ~~Large~~ Low number of defects and dislocations is critical for various optical devices due to the detrimental impact of non-radiative recombination of charge carriers on the efficiency of light emission.

In this work we study InP nanostructures epitaxially grown in the pits of in Si(001) substrates using the recently developed technique, described previously in the work [4]. The molten alloy-driven method of selective area growth by metal–organic vapor phase epitaxy allows obtaining InP/Si nanostructures with low crystal defect density and sharp interfaces between the grown InP and hosting Si. Here we study the optical properties of the formed InP/Si nanostructures. PL spectra were measured for the obtained structures and surface maps were made using confocal microscopy and scanning electron microscopy.

2. Methods

InP nanostructures were formed in the arrays of 200 nm wide and 200 nm pits in Si (100) substrate. Scanning electron microscopy image of the sample with InP/Si nanostructures with 800 nm pitch between the preliminary formed pits is shown in Figure 1(a). Photoluminescence (PL) 3D maps were

obtained using an Integra Spectra (NT-MDT) confocal microscope at room temperature. A Nd:YLF laser was focused using a 100x objective for excitation. The same objective collected the PL of a single of InP/Si structure. Low temperature measurements were performed using a closed-cycle optical cryostat Montana Instruments Cryostation s50 with temperatures down to 5 K.

3. Results and discussion

Photoluminescence at room temperature is observed from almost every single nanostructure, indicating the formation of the InP material. PL scanning over the depth of each nanostructure shows homogeneous of the InP material along the growth axe. Also, we observed significant variation of the PL intensity from different nanostructures, that may be due to the different amount of InP material inside each pit.

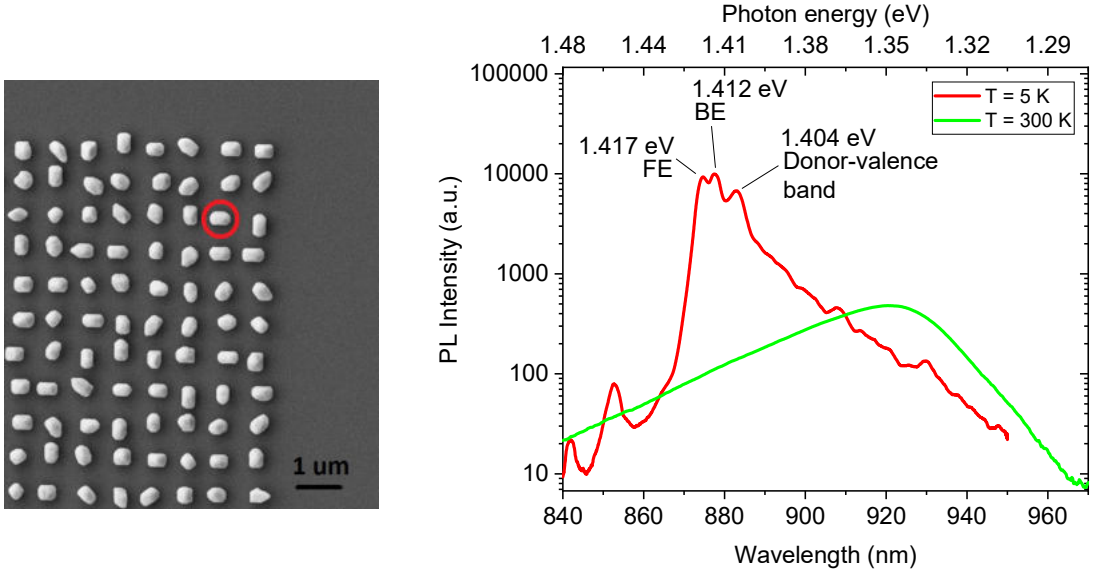

Figure 1.(a) SEM image and (b) PL spectrum from highlighted InP nanostructure, measured at room temperature and 5 K.

Next we studied low temperature photoluminescence spectra of the nanostructure (Figure 1 (b)). At the temperature of 5K we observe three spectral lines assigned to zinc blende InP free exciton (FE) at 1.417 eV, bound exciton (BE) at 1.412 eV and donor-valence band transition (1.404 eV) [5]. Shorter-wavelength series of lines (840-860 nm or 1.48-1.44 eV) caused by twinning defects in InP/Si nanostructure, that were observed on TEM images in small amount [4].

Acknowledgments

This work was supported by the Russian Science Foundation (grant № 22-22-20057, https://rscf.ru/project/22-22-20057/). The authors are thankful to E. Semenova and D.Viazmitinov for the structures provided.

References

[1] Luxmoore I J, Toro R, Pozo-Zamudio O Del, Wasley N A, Chekhovich E A, Sanchez A M, Beanland R, Fox A M, Skolnick M S, Liu H Y and Tartakovskii A I 2013 *Sci. Rep.* **3** 1

[2] Bettotti P 2014 *Adv. Opt.* **2014** 1

[3] Roelkens G *et al.* 2015 *Photonics* **2** 969

[4] Viazmitinov D V et al 2020 *Nanoscale* **12** 23780

[5] Heim U, Röder O, Queisser H J and Pilkuhn M 1970 *Jour. of Luminescence* **1** 542

Topological features of nanoplasmonic structures based on Bi-substituted iron garnets

S V Osmanov[*1], T V Mikhailova[1], E V Skorokhodov[2], S A Gusev[2], A L Kudryashov[1], A G Shumilov[1], A V Karavainikov[1], A S Nedviga[1], A I Dolgov[1], and A N Shaposhnikov[1]**

[1]V.I. Vernadsky Crimean Federal University, Simferopol 295007, Russia
[2]Institute for Physics of Microstructures of the Russian Academy of Sciences (IPM RAS), Nizhny Novgorod 603087, Russia

[*]osmanovfti1@mail.ru; [**]taciamikh@gmail.com

Abstract. Magneto-optical metal-dielectric structures based on Bi-substituted iron garnet and Au films were proposed and synthesized. The structural and morphological features of the structures were demonstrated.

1. Introduction and motivation

Magneto-optical metal-dielectric structures are effectively used in modern devices. Elements of plasmonic circuits, optical modulators, insulators and switches were created on their basis [1]. Technologies for formation of nanoscale elements, including one- and two-dimensional structures, can significantly improve the operational characteristics of such devices [2, 3]. The creation of magneto-optical structures is a rather expensive and multi-stage project [3]. This research presents the technology of formation and study of morphological features of nanostructures based on Bi-substituted iron garnet (Bi:IG) nanofilms and metallic gold coating. The determining the features of formation of magneto-optical metal-dielectric nanostructures is an important step in investigation of their basic optical properties and their further purpose during operation in high-performance devices.

2. Methods of formation and characterization

In order to form magneto-optical metal-dielectric structures, three types of Bi:IG samples were selected with nanoscale thickness. Single layer films of composition $Bi_{0.9}Lu_{2.1}Fe_5O_{12}$ with thickness $h(Bi_{0.9}Lu_{2.1}Fe_5O_{12})$ = 140 nm were synthesized by liquid-phase epitaxy on monocrystalline substrates of gadolinium gallium garnet (GGG) of crystallographic orientation (111) according to the technology described in [4]. Such films exhibit a monocrystalline structure and low surface roughness. Root mean square roughness is *RMS* = 3 nm. Polycrystalline iron garnet films double-layer $Bi_{2.8}Y_{0.2}Fe_5O_{12}$ / $Y_3Fe_5O_{12}$ with layer thicknesses, respectively, $h(Y_3Fe_5O_{12})$ = 85 nm and $h(Bi_{2.8}Y_{0.2}Fe_5O_{12})$ = 100 nm and single layer $Bi_{2.3}Dy_{0.7}Fe_{4.2}Ga_{0.8}O_{12}$ with thickness $h(Y_3Fe_5O_{12})$ = 100 nm were synthesized by magnetron and ion-beam sputtering on GGG substrates, accordingly. The deposition of target material of these compositions was carried out in vacuum in an oxygen-argon medium on a cold substrate. The formed amorphous films were annealed at temperatures from 650 to 710 ºC in order to obtain a crystal structure (polycrystalline) [5]. *RMS* of samples ranged from 6 to 10 nm with an average size of crystallites *AGS* from 40 to 136 nm.

Electron beam lithography was used to form the nanostructures on film surface. Arrays of nanoholes and nanorhombuses were chosen as nanostructure templates. Height of nanostructure elements on Bi:IG surface was about 50 nm. After nanostructuring of Bi:IG films, Au film with design thickness $h(Au)$ = 30 nm was deposited on the surface of structures by magnetron sputtering. Figure 1 shows images of a magneto-optical metal-dielectric nanostructure array obtained by SEM and AFM. Au rings were formed on perforated surface of the garnet. The height of rings on Au varies from 50 to 120 nm.

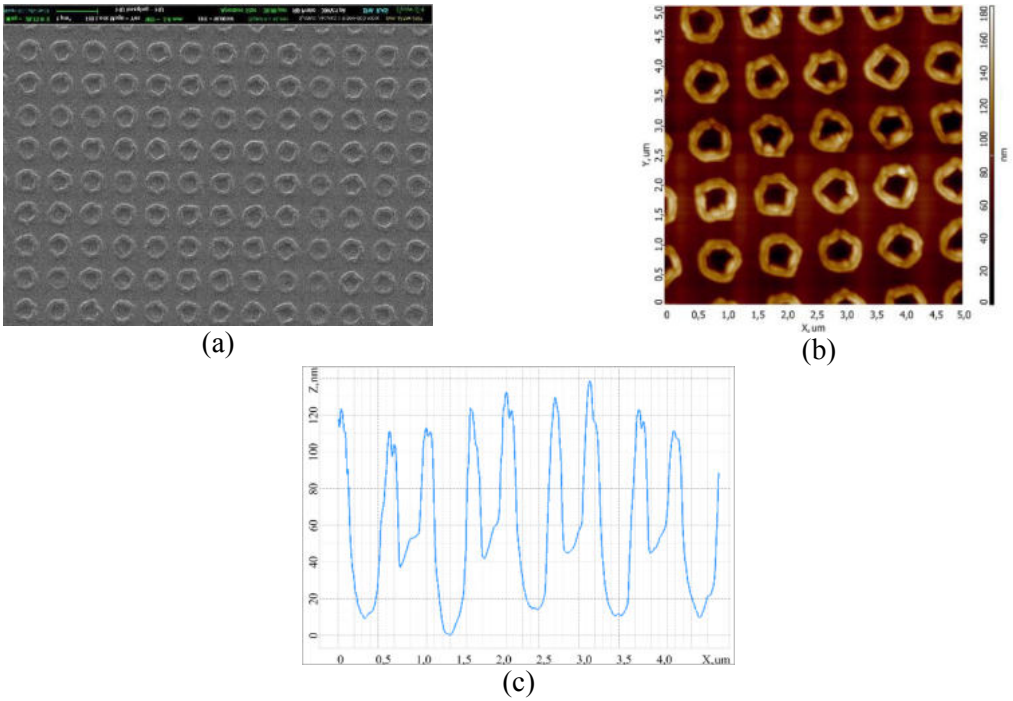

Figure 1 (a, b, c). Images of a pattern of magneto-optical metal-dielectric nanostructure Au / $Bi_{0.9}Lu_{2.1}Fe_5O_{12}$ / GGG: SEM (a), AFM (b) and AFM cross-section (c). Structure period is 1000 nm.

Acknowledgments

The development of technique of electron beam lithography in order to obtain the gratings on Bi:IG surface was carried out using technological and analytical equipment of the Common Research Center "Physics and Technology of Micro- and Nanostructures" of the Institute for Physics of Microstructures RAS. The authors acknowledge support by Russian Science Foundation (project no. 19-72-20154).

References

[1] Zvezdin A K, Kotov V A 1997 Modern Magnetooptics and Magnetooptical Materials (IOP Publishing Ltd, London).

[2] Inoue M, Baryshev A V, Goto T, Baek S M, Mito S, Takagi H and Lim P B 2013 Magnetophotonic Crystals: Experimental Realization and Applications *Magnetophotonics* eds. Inoue M, Levy M, Baryshev A V (Springer-Verlag Berlin Heidelberg) chapter 7 p. 163

[3] Ignatyeva D O, Karki D, Voronov A A, Kozhaev M A, Krichevsky D M, Chernov A I, Levy M, Belotelov V I 2020 *Nature communications* **11** 1

[4] Polulyakh S N., Berzhanskii V N., Semuk E Yu., Belotelov V I., Vetoshko P M., Popov V V, Shaposhnikov A N, Shumilov A G & Chernov A I 2021 *Journal of Experimental and Theoretical Physics* **132(2)** 257–263

[5] Prokopov A R, Mikhailova T V, Danishevskaya E V, Shaposhnikov A N, Berzhansky V N, Karavainikov A V, Nedviga A S, Nauhatsky I A, Milyukova E T 2019 *Technical Physics* **64(11)** 1709–1715

Development of the design of a THz radiation source based on tunnel-coupled quantum wells

Kharin N.Yu., Vinnichenko M. Ya., Firsov D.A.

Peter the Great St. Petersburg Polytechnic University, 29 Politekhnicheskaya str., St. Petersburg, 195251, Russia

E-mail: kharin.nikita66@gmail.com

Abstract. The electron wave functions and energy spectrum are calculated for a structure with a pair of GaAs/AlGaAs tunnel-coupled quantum well designed to develop a source terahertz radiation. The problem of maximizing the matrix element of terahertz optical transitions between subbands is solved. This study is the basis for further experimental study of THz photoluminescence related to intersubband electron transitions under interband optical pumping.

1. Introduction

Terahertz (THz) radiation is a high-promising object for investigations due to its wide range of applications in various fields [1]. For example, THz emission can be obtained by the optical transitions of nonequilibrium carriers in semiconductor with shallow impurities [2]. However, approach based on intersubband electron transitions in nanostructures is more promising due to the ability to control energy distance between subbands. When designing a THz radiation source, it should be taken into account that the radiation intensity depends on the population of the final state of optical transition. It was proposed that for THz radiation based on intersubband transitions the final state can be depopulated by interband radiative recombination of carriers from the first electron subband to the first heavy hole subband. This process is significantly enhanced under conditions of stimulated radiative recombination [3].

In this work, we are theoretically analyzing the intersubband optical transitions between electron levels in tunnel-coupled quantum wells (TCQW).

2. Results and discussion

The final aim of this work is to suggest a better design of structure in which THz radiation can be observed due to optical transitions between lowest subbands in quantum well (QW). The object of research is a pair of GaAs/$Al_xGa_{1-x}As$ quantum wells with a tunnel-transparent $Al_xGa_{1-x}As$ barrier between them. First, it is necessary to exclude the possibility of a nonradiative transitions between lowest subbands with the emission of optical phonon, which is equal to 36 meV for GaAs. So we designed quantum wells with the energy distance between the first and second subbands taken equal to 15 meV which corresponds to the THz range.

The THz photoluminescence spectra of the designed structure are planned to be observed with interband optical pumping. Under such conditions, levels 1 and 2 are populated by electron transitions from the barrier. This process is most efficient if the distance between the second level and the barrier bottom is equal to the optical phonon energy.

The absorption coefficient in a QW depends on the matrix element of the optical transition, which is determined by the expression [4]:

$$\overrightarrow{p_{if}} = \int_{\Omega} \psi_f^* \cdot \hat{\vec{p}} \cdot \psi_i d\vec{r}$$

where ψ_i, ψ_f – wave functions of the initial and final states respectively, $\overrightarrow{e_\omega}$ – unit polarization vector, $\hat{\vec{p}}$ – momentum operator, Ω – normalization volume.

The energy position of the subbands in TCQW is determined by a set of geometric parameters — the widths of the wells and barrier, and the height of the barriers. The envelope wave functions of the subbands in TCQW for each set of parameters will have a different shape and as a consequence, transition matrix elements will be different. Thus, it is necessary to solve the problem of maximizing the value of the optical matrix element.

The calculation of the wave functions and subband energies was carried out by the transfer matrix method with taking into account the nonparabolic of the dispersion law. The calculation showed that the maximum value of the matrix element is observed for a pair of TCQW with equal width and depth. Comparison of TCQW with a single well at the same energy distance between subbands showed that single well have more levels at given conditions. For example, for the Al composition $x = 0.3$ and for a given energy gap between the first and second subbands (15 meV), there are 7 levels in a single well. However, if there are more than two levels in a quantum well, then the oscillator strength decreases for transitions between the first and second subbands. In TCQW we can design different number of levels for a given composition. This confirms the interest in the design of the THz source on TCQW.

Based on the performed calculations, an optimal structure was designed for the experimental study of THz photoluminescence under conditions of interband optical pumping. It is a pair of GaAs/$Al_{0.1}Ga_{0.9}As$ QWs with 80 nm wide that separated by a 26 nm wide $Al_{0.1}Ga_{0.9}As$ barrier. The next step of our work will be to grow this structure and to investigate the THz photoluminescence using experimental technique described in [3].

Acknowledgments

This work was supported by the Russian Science Foundation (grant 22-22-00105, https://rscf.ru/project/22-22-00105/).

References

[1] Tonouchi M. 2007 Cutting-edge terahertz technology. *Nature photonics*, 1(2), 97-105.

[2] Altukhov I. V., Kagan, M. S., Korolev, K. A., Sinis, V. P., Chirkova, E. G., Odnoblyudov, M. A., Yassievich, I. N. (1999). Resonant acceptor states and terahertz stimulated emission of uniaxially strained germanium. *Journal of Experimental and Theoretical Physics*, 88(1), 51-57.

[3] Makhov, I. S., Panevin, V. Y., Sofronov, A. N., Firsov, D. A., Vorobjev, L. E., Vinnichenko, M. Y., Vasil'ev A. P., Maleev, N. A. 2017 The effect of stimulated interband emission on the impurity-assisted far-infrared photoluminescence in GaAs/AlGaAs quantum wells. *Superlattices and Microstructures*, 112, 79-85.

[4] Vorob'ev, L. E., Firsov, D. A., Shalygin, V. A. 2007 Optical properties of semiconductors: textbook.

Colloidal core/shell silver nanoparticles to enhance the PL of InGaN nanowires

T M Shugabayev[1,*], V O Gridchin[1-3], A S Kulagina[1,4], K P Kotlyar[1-3], R R Reznik[1-3], S D Komarov[1,5], L N Dvoretskaya[1], N V Kryzhanovskaya[1,5], G E Cirlin[1-4]

[1]Alferov University, St. Petersburg 194021, Russia
[2]Saint-Petersburg State University, Saint-Petersburg, 198504, Russia
[3]IAI RAS, St. Petersburg 198095, Russia
[4]Ioffe Institute, St. Petersburg 194021, Russia
[5]Higher School of Economics, 199034, St. Petersburg, Russia

E-mail: * talgashugabaev@mail.ru

Abstract. In this work, we propose a method for enhancing the photoluminescence (PL) of InGaN nanowires using colloidal silver nanoparticles (NPs). Based on the modified Stober method, the possibility of obtaining nanoparticles with an Ag/SiOx core/shell structure with a controlled oxide thickness is shown. The results of the study showed that the deposition of silver NPs and Ag/SiOx core/shell NPs on an array of InGaN nanowires leads to a significant change in the PL and increases the main PL peak.

1. Introduction

InGaN NWs are promising solids for creating new generation light emitting diodes. The main advantage of these nanostructures is the possibility to grow with a small number of structural defects on Si substrates [1]. Also, InGaN NWs can be synthesized with different In content, which makes it possible to obtain light-emitting nanostructures in the entire visible range. [2]. NWs have a developed lateral surface, which enables to deposit various NPs on them with high efficiency, forming NW/NP hybrid nanostructures.

On the other hand, the internal quantum efficiency of InGaN NWs is not ideal [3], and the mechanisms of this problem are an urgent challengies for modern research. Due to the difference in the refractive indices of InGaN and the environment, it is not possible to obtain an ideal light extraction efficiency. All of this reduce the radiation from InGaN NWs. Thus, different approaches to enhance light extraction efficiency in particular by using the localized plasmon resonance (LPR) of metal NPs are investigated [4]. It was shown that direct contact between a metal NPs and an emitting semiconductor nanostructure results in PL quenching. Therefore, for the amplification effect, dielectric gap between NPs and the emitter should be used [5]. In this work, we propose a cheap and simple method for amplifying the PL at room temperature of an array of InGaN NWs using silver NPs with SiOx shell's. To synthesis SiOx on NPs modified Stober method was used [6].

2. Experiments

The initial silver NPs (cores) were synthesized by the colloidal method in an aqueous medium based on [7]. Cl^- ions were used to give NPs a spherical shape. The synthesis temperature was 95°C. The

optical density of the colloidal solution of NPs was obtained using a spectrophotometer. The size of silver NPs was determined by the dynamic light scattering (DLS).

The InGaN NWs were grown using Riber Compact 12 MBE system equipped with In and Ga effusion cells and a nitrogen source. The growth was performed at a substrate temperature at 660 °C [2].

Silver NPs (cores) and Ag/SiOx core/shell NPs were deposited onto an array of InGaN NWs with further thermal annealing and treatment in heated acetone. This procedure was necessary to remove the remnants of the reaction products after the formation of silver NPs.

Morphological properties of the samples were examined using a SUPRA 25 C. Zeiss scanning electron microscope (SEM). The optical properties of the samples were studied using the photoluminescence method at room temperature. A helium-cadmium (He-Cd) metal vapor laser with a wavelength of 325 nm at 15.5 mW was used for excitation.

3. Results

The synthesized silver NPs (cores) have λ_{LPR} = 400 nm, and the full width at half maximum **(**FWHM**)** value of the optical density spectrum is 53 nm. The average NPs size is 32 nm with a polydispersity index (PDI) of 25%.

To form nanoparticles with the Ag/SiOx core/shell structure, we used the modified Stober method [6], in which the source of silicon atoms is tetraethoxysilane (TEOS). In order to form an oxide shell of a given thickness, it was necessary to estimate the added volume of TEOS. For this, a formula was obtained taking into account the extinction cross section of silver NPs (cores) and their concentration, as well as the yield of the chemical reaction. As a result, Ag/SiOx NPs with h ≈ 15 nm and λ_{LPR} = 422 nm were obtained. By applying the shell, the FWHM of the optical density spectrum increases and amounts to 92 nm.

InGaN nanowires were grown at a substrate temperature of 660 °C. The resulting sample is a dense NW array with a height of ≈ 400 nm. The NW diameter is not constant: it increases from the substrate surface to the middle, and decreases from the middle to the top of the NW. The initial PL spectrum of NWs has two photoluminescence peaks that might be explained by the phase decomposition effect [8]. The first PL peak corresponds to λ = 439 nm, the second PL peak (the PL maximum) corresponds to λ = 484 nm. After deposition of Ag NPs on the NWs, we obtained an enhancement of the main PL peak in both cases, upon depositing NPs with and without shells.

4. Conclusion

In summary, we have obtained the conditions for the formation of silver NPs with a silicon oxide shell of a given thickness. The deposition of these NPs on InGaN NWs leads to a strong change of the PL spectrum, including an increase in the main PL peak by 17%. The obtained hybrid nanostructure of InGaN NWs/silver NPs is promising for the creation of high-efficiency light-emitting diodes.

Acknowledgements

The work was carried out under support of Ministry of Science and Higher Education of the Russian Federation (state task № 0791-2020-0003).

References

[1] Dubrovskii V. G., Cirlin G. E., Ustinov V. M. 2009. **43** 1539.
[2] Gridchin, V O et al. 2021 Nanotechnology **32** 335604
[3] Ebaid M. et al. 2015 Scientific reports **5** 1
[4] Yao, Yung-Chi, et al. 2016 Scientific reports **6** 1
[5] Gu X. et al. 2011 Nanoscale research Lett. **6** 1
[6] Matyushkin L. B., Pertsova A., Moshnikov V. A. 2018 Technical Physics Lett. **44** 331
[7] Li H. et al. 2013 Langmuir **29** 5074
[8] Karpov S. Y.1998 MRS Internet Journal of Nitride Semiconductor Research **3** 1

Study of narrow-band UV radiation sources based on zinc oxide

I K Kindyushov[1], S A Kadinskaya[1], M E Labzovskaya[2], B V Novikov[2], I V Shtrom[1,2], A I Lihachev[3], A V Nashchekin[3] and A D Bolshakov[1,4,5]

[1]Alferov University, St. Petersburg, 194021, Russia
[2]Saint Petersburg State University, St. Petersburg, 199034, Russia
[3]Ioffe Institute, St. Petersburg, 194021, Russia
[4]ITMO University, St. Petersburg, 197101, Russia
[5]Moscow Institute of Physics and Technology, Dolgoprudniy, 117303, Russia

E-mail: kindyushow@gmail.com

Abstract. The structures of zinc oxide synthesized by hydrothermal method on a silicon substrate with orientation (111) are investigated in this paper. An efficient protocol for the synthesis of zinc oxide microstructures with a low aspect ratio of the characteristic longitudinal to transverse size has been demonstrated. The optical properties of the resulting structures were studied by photoluminescence spectroscopy (PS). The possibility of synthesizing low-defect hydrothermal zinc oxide microstructures suitable for creating narrow-band sources of UV radiation, as well as laser sources of radiation based on whispering gallery modes is shown.

1. Introduction

Zinc oxide (ZnO) has been widely established as the material of modern electronics. There are piezonanogenerators, gas sensors and optical devices based on a zinc oxide [1-5]. Zinc oxide in the geometry of hexagonal microcrystals has its own resonator structure and can be used to create a whispering gallery mode based laser.

Many methods are suitable to produce zinc oxide especially - hydrothermal. The advantages of hydrothermal synthesis include wide possibilities for controlling growth conditions, the ability to carry out synthesis at relatively low temperatures (less than 100°C), which leads to a significant reduction in energy consumption and makes the method quite economical [6].

Even though there are many light-emitting devices based on various materials [7–9], low-defect ZnO microstructures synthesized by a hydrothermal method have great prospects for solving problems of modern photonics and electronics.

2. Synthesis

To synthesis of zinc oxide microstructures zinc acetate as the seed layer material and zinc nitrate ($Zn(NO_3)_2$) and hexamethylenetetramine (HMTA) as a precursors were used. The main growth parameters are given in previous works [1, 5].

Two type of zinc oxide based microstructures are synthesized via hydrothermal synthesis using spin coating and silar technics for seed layers formation. As a result of the synthesis, hexagonal microcrystals with a diameter of about 3–5 μm were obtained. The volume of the active medium on the substrate surface is higher than that of sample № 1.

3. Experiment

Zinc oxide is characterized by PL emission in all spectral regions from UV to IR [11]. Peaks outside the UV region are due to the presence of defects and impurities in the ZnO structure [9]. The absence of a PL response in the long-wavelength region indicates a high crystalline perfection of the synthesized hydrothermal microstructures. In the spectral region of the short-wavelength PL band at low temperatures, radiation containing lines of excitons coupled to shallow neutral and ionized donors (D^0X) enters. In the long-wavelength region of the spectrum, an emission band is observed, which includes bands due to transitions of a free electron of the conduction band - an acceptor, emission of donor-acceptor pairs during transitions of a localized electron to a shallow acceptor and the first LO-phonon repetition of a free exciton

4. Conclusion

In this work, we synthesized high crystal quality hydrothermal ZnO microstructures. The PL spectra of the synthesized structures at low temperature have been studied, indicating the presence of a narrow emission band near 370 nm, as well as the absence of a PL response in the visible region of the spectrum. It is shown that interband recombination is suppressed due to the high crystallinity of the structures.

It has been established that the PL intensity is mainly determined by the volume and morphology of the ZnO on the substrate surface, which can be control via growth conditions and seed layers variation.

References

[1] V M Kondratev, A D Bolshakov and S S Nalimova 2021 *IEEE Conference of Russian Young Researchers in Electrical and Electronic Engineering (ElConRus)*, 2021, 1163.

[2] E A Levkevich, A I Maksimov, S A Kirillova, S S Nalimova, V M Kondrat'ev and A. A. Semenova 2020 *IEEE Conference of Russian Young Researchers in Electrical and Electronic Engineering* (EIConRus), 2020, 984.

[3] S S Nalimova, V M Kondratev, A A Ryabko, A I Maksimov and V A Moshnikovl *J. Phys.: Conf. Ser*., 2020, 1658 012033.

[4] S S Nalimova, A A Bobkov, V M Kondrat'ev, A A Ryabko, V A Moshnikov and Z V Shomakhov 2020 *IEEE Conference of Russian Young Researchers in Electrical and Electronic Engineering* (EIConRus), 2020, 991.

[5] S S Nalimova and V M Kondrat'ev 2020 *IEEE Conference of Russian Young Researchers in Electrical and Electronic Engineering* (EIConRus), 2020, 987.

[6] Жуков А Е, Моисеев Е И, Надточий А М и др. *Письма в ЖТФ*, 2020, **46(16)**, 783-786.

[7] Bolshakov A D, Shishkin I, Machnev A, Petrov M, Kirilenko D A, Fedorov V V, Mukhin I S, Ginzburget P *Nanoscale* 2022, **14(3)**, 993.

[8] Kuznetsov A, Roy P, Kondratev V M, Fedorov V V, Kotlyar K P, Reznik R R, Vorobyev A A, Mukhin I S, Cirlin G E, Bolshakov A D *Nanomaterials* 2022, **12(2)**, 241.

[9] P Roy, A D Bolshakov *Physica Status Solidi (RRL) – Rapid Research Letters* 2021, **15(6)**, 2000579.

[10] Pathan, H. M., & Lokhande, C. D. (2004). *Bulletin of Materials Science*, **27(2)**, 85–111. doi:10.1007/bf02708491

[11] Galdámez-Martinez, A., Santana, G., Güell, F., Martínez-Alanis, P. R., & Dutt, A. (2020). *Nanomaterials*, **10(5)**, 857. doi:10.3390/nano10050857

The development of the method for temperature-resolved measuring of local Raman and photoelectric response

I.E. Chistikov, A.V. Redkov

Institute for Problems in Mechanical Engineering RAS

chisilia12@gmail.com

Abstract. In this work, a technique was developed and implemented, which allows local mapping of the Raman and photoelectric response of the sample at different temperatures. The technique was approved on the GaN film sample and it was shown, that both types of responses demonstrate high correlation.

1. Introduction

The semiconductor thin films are actively used in electronics, optics, aerospace and other fields of industry. For the growth of high-quality thin films and heterostructures deep understanding of the growth processes and analysis of the properties of grown samples are needed, which requires the use of different measurement techniques. One of such powerful techniques is Raman spectroscopy [1] of the samples, which allows one to get a lot of information about the properties of the sample. The use of a confocal microscope together with a movable piezo table for Raman measurements, in turn, makes it possible to study all these properties locally, with a resolution of several hundred nanometers. In this work, we proposed and developed a new measurement technique, based on the simultaneous measurement of the local Raman response of the sample to the excitation laser beam and its photoelectric response, carried out at different temperatures. This makes it possible to obtain new information about the samples (especially semiconductors), such as information about interrelation between the local chemical composition, the crystalline perfection of the sample, elastic stresses and many other properties, and the magnitude of the generated photocurrent. In this work a module was developed based on Raspberry Pi 3B+, which implements this technique onto the serial confocal Raman spectroscope Witec Alpha 300R equipped with scanning piezo-table.

2. Proposed technique

A standard Raman spectroscope consists of a laser and a system of lenses that project the exciting beam into the objective, a sample on a movable piezo-table, and a detector that captures the reflected light. n our new technique, a heating element was added to these components and a module which measures photocurrent. It is located between the sample and piezo table. The control of the heating element, and hence the temperature of the sample, and measurement of the photocurrent is performed via Raspberry Pi 3B+. The laser passes through the lens system and hits the sample, exciting both local Raman and photoelectric response in it, the detectors pick up the responses and save it along with the point coordinate. Then the piezo table changes the coordinate. Once the local mapping of certain area is completed, the thermoelectric cooler changes the temperature, and the scanning is performed again. After that all the obtained maps can be compared with each other.

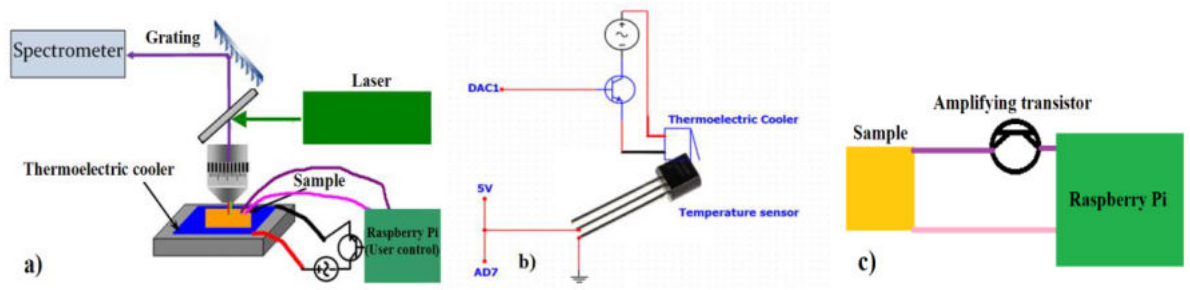

Figure 1. Simplified model of Raman spectroscope with developed module (a), scheme of temperature module based on Raspberry Pi 3 Model B+ (b), scheme of photoelectric measurement module (c).

Based on the Raspberry Pi 3 Model B+ - single board computer, a circuit diagram was developed that implements various temperature conditions for the sample, makes measurements of the photoelectric response of the sample synchronously with Raman mapping, and converts the received signal into color maps, which then can be compared with data obtained from Raman spectroscopy. Also, a program was created in Python. It is responsible for passing information between the user and the scheme. The user can adjust the desired sample temperature, or even certain temperature dependencies. The technique was tested on a gallium nitride (GaN) film sample grown on silicon substrates with a SiC buffer layer [2]. The figures show the results of measurements of the area containing cracks on the surface. One can see a strong correlation between the photoelectric response and bright areas on the Raman maps, reflecting various information (elastic stresses, composition, defectiveness).

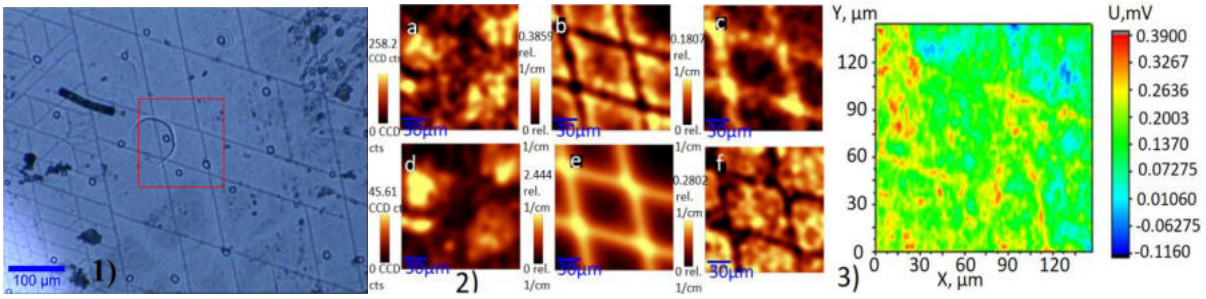

Figure 2. Optical image (1), Raman maps (50*50 dots, 150*150 µm) of the area, taken by intensity (2a), spectral position (2b), width (2c) of silicon line (520 cm^{-1}) and similar properties (2d, 2e, 2f of the gallium nitride line (568 cm^{-1}). Photoelectric response map of the same area, measured using the proposed technique at room temperature (3)

3. Conclusions

In conclusion, the new method for temperature-resolved analysis of the properties of the samples and a hardware module for its implementation were developed based on Raspberry Pi 3 B+. The technique was verified on the samples of GaN and shown that high correlation of the Raman spectra and the measured photoelectric response indeed can be seen. The authors are grateful for the Council for Grants of the President of Russian Federation (grant #MK-201.2021.1.2).

References

[1] Smith E., Dent G. (2019). *Modern Raman spectroscopy: a practical approach*. John Wiley & Sons.
[2] Kukushkin S. A., Osipov A. V. (2014). *Journal of Physics D: Applied Physics*, *47*(31), 313001.

Resistive type gas sensor based on carbon nanotubes

N N Rudyk[1], O I Il'in[1], Yu Y Jityaeva[1] and M V Il'ina[1]
[1]Southern Federal University, Institute of Nanotechnologies, Electronics and Equipment Engineering, Taganrog, 347922, Russia

Abstract. In this research, a resistive-type gas sensor based on carbon nanotubes was fabricated. The sensor was tested for sensitivity to ammonia, carbon monoxide and nitrogen dioxide. The sensitivity was found to be 3.7%, 3.2% and 23.9% for NH_3, CO and NO_2, respectively. The average response time and the nature of the conductivity of CNTs under the action of oxidizing and reducing gases are determined.

1. Introduction

Currently, in conditions in a complex technogenic environment, the actual direction in the development of sensors is the creation of energy-efficient gas sensors for environmental monitoring, detection of explosives, and early diagnosis of diseases [1].

Carbon nanotubes (CNTs), due to their structure, electrical and chemical properties, are a promising material for creating sensitive elements of gas sensors [2]. Control of the CNT parameters, as well as the topology of the sensor structure, allows to control such parameters of the gas sensor as selectivity, sensitivity, energy efficiency and service life. At the same time, the design of the sorption-type sensor is the simplest and cheapest to manufacture, but it is associated with a number of disadvantages: high power consumption, low sensitivity, and degradation of the sensitive element.

2. Experiments and methods

To create the sensor, we used a Si (100) substrate, on which an insulating SiO_2 layer 2 μm thick was formed by plasma-chemical deposition. TiN was used as a contact layer, and Ni 10 nm thick was used as a catalyst, which were deposited by magnetron sputtering. An array of CNTs network was grown by plasma enhanced chemical vapor deposition at a temperature of 660°C in an atmosphere of acetylene and ammonia.

The resistive sensor was made on the basis of an array of interdigital electrodes, on the surface of which was grown a sensitive layer based on CNTs network, which have a developed surface and good electrical contact with the metal electrodes.

Experimental studies of the gas sensor were carried out using the MICROGAZ-FM gas analytical equipment (NTPO Ekopribor, Russia). NH_3, CO and NO_2 were used as analyzed gases, synthetic air was used as diluent and purge gas. The initial resistance of the sensor without exposure to target gases was 902 Ohm. The sensor sensitivity was assessed by the relative change in resistance:

$$S = \frac{R - R_0}{R_0} * 100\ \%,$$

where R_0 is the initial resistance when blowing with air, R is the resistance when exposed to the analyzed gas.

3. Results and Discussion

The average diameter of the grown CNTs in the array was 56±14 nm. Figure 1 shows the dependence of the sensing element response of a CNT-based resistive sensor to NH_3 and CO at a concentration of 500 ppm, and to NO_2 at a concentration of 20 ppm.

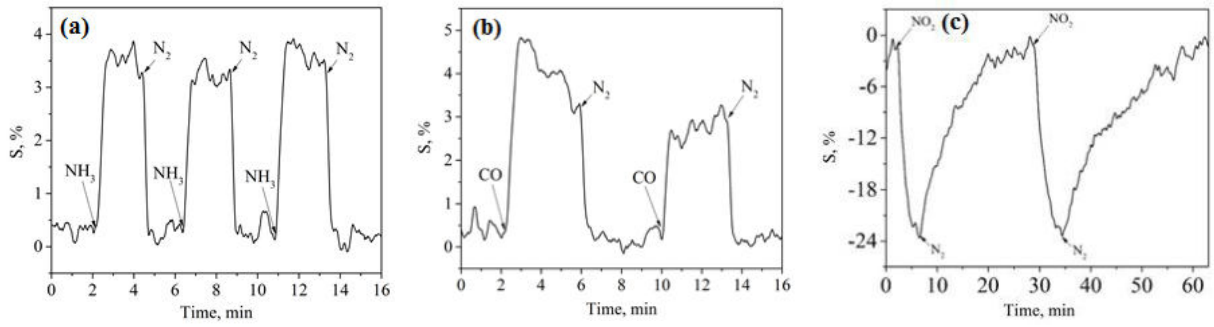

Figure 1(a,b,c). Sensor response to **(a)** NH_3, **(b)** CO and **(c)** NO_2

The sensitivity of the sensor was 3.7% for NH_3, 3.2% for CO and 23.9% for NO_2. The average response time T_{90} (time required to indicate 90% gas concentration) of the sensor element for ammonia, carbon monoxide and NO_2 was 35 sec, 28 sec and 125 sec, respectively, and the recovery time was 42 sec, 25 sec and 690 sec, respectively. Figure 1 a,b shows that when exposed to ammonia, the resistance of the sensor increases, and when exposed to nitrogen dioxide, it decreases. This character of the dependence indicates that CNTs are p-type semiconductors. As a result of the adsorption of NH3 molecules, which are electron donors, electrons are injected into the surface layers, and the conductivity of p-type semiconductor CNTs decreases. The reverse situation is observed during the adsorption of NO2 molecules, which are acceptors.

Thus, the proposed gas sensor showed high sensitivity to NO2, which is achieved when operating at room temperature. The results obtained can be used in the development of promising sensors based on CNTs.

4. Acknowledgments

The creation of the sensor topology, the manufacture of contact electrodes and conduct of photolithographic processes was supported by the Russian Science Foundation under grant No. 22-29-01124.

References

[1] Valle M. D 2021 Current Opinion in Green and Sustainable Chemistry **31** 100501.

[2] Zhuohao Xiao 2018 Sensors and Actuators B S0925-4005(18)31277-2

Ruthenium as an electrode material for the fast electrochemical actuator

P S Shlepakov[1,2]**, I V Uvarov**[1,2] **and V B Svetovoy**[1,3]
[1]Valiev Institute of Physics and Technology RAS, Yaroslavl Branch,
Universitetskaya 21, 150007 Yaroslavl, Russia
[2]P.G. Demidov Yaroslavl State University, Sovetskaya 14, 150003 Yaroslavl, Russia
[3]A.N. Frumkin Institute of Physical Chemistry and Electrochemistry RAS,
Leninsky pr. 31, 199071 Moscow, Russia

Abstract. Electrolysis of water performed by alternative polarity (AP) voltage pulses increases the operating frequency of the electrochemical actuator by several orders of magnitude due to the fast recombination of the produced gas. The gas is located in nanobubbles (NBs) that disappear quickly due to the spontaneous combustion of hydrogen and oxygen. However, this type of electrolysis damages the electrodes and the actuator performance reduces with time. Platinum electrodes suffer from mechanical action of nanobubbles, while titanium electrodes are oxidized. A promising material for electrodes is ruthenium because it is chemically inert and mechanically strong. In this work Ru, Pt and Ti electrodes are tested in the AP electrolysis. The degree of wear, current flowing through the cell, and threshold voltage are analyzed and compared.

1. Introduction

Electrochemical production of gas in a closed chamber provides extra pressure that pushes a flexible membrane. This phenomenon is used as a working principle of the electrochemical actuators, which are good candidates for various microfluidic systems. Conventional actuators based on the DC electrolysis suffer from a long response time due to slow recombination of the produced gas. Usage of microsecond AP voltage pulses instead of the DC voltage is a possible solution of the problem. The chamber is filled with NBs of about 100 nm in diameter, which disappear in milliseconds due to the spontaneous combustion of hydrogen and oxygen. A fast electrochemical actuator was demonstrated, which works several orders of magnitude faster than the conventional devices [1]. However, the electrodes of the actuator have a limited lifecycle because of the two factors. The first one is a strong mechanical action of NBs on the electrode surface, while the second factor is the oxidation of the electrode material. Platinum electrodes are not oxidized, but they are destroyed quickly by NBs due to a relatively low hardness of Pt (3.5 units in Mohs scale) [2]. Titanium is a harder material (6 units), but the oxidation reduces the current flowing through the electrolyte and suppresses the gas production [3]. Ruthenium is a promising electrode material, which has a hardness of 6.5-7 units and its oxide is conductive. In this work, we investigate the degradation of Ru electrodes as compared with Pt and Ti structures.

2. Methods

The electrodes of a circular shape are fabricated on an oxidized silicon wafer. The sample is placed in a Petri dish filled with the electrolyte, which is a molar solution of Na_2SO_4 in distilled water. A layer of SU-8 protects the signal lines from the electrolyte. Square AP voltage pulses are applied to the working

electrode, while the other one is grounded. The frequency of the pulses is 500 kHz. The samples are tested in two regimes. In the first one the pulses with an amplitude of 11 V are applied continuously during 15 min. The voltage is not large enough to produce explosions of microbubbles. The mechanical destruction due to the action of NBs is investigated and compared for 100 nm thick Pt and Ru electrodes. The current flowing through the electrochemical cell is recorded every 10 s and the average absolute value I_{av} is calculated. In the second regime, a series of pulses with the duration of 0.5 s is applied to the electrodes every 2 s. The amplitude is adjusted to the threshold level U_{th}, at which the concentration of NBs in the electrolyte reaches a critical value. For this critical concentration the nanobubbles merge into a microbubble, which explodes with the release of a large amount of energy. The experiment lasts until the electrodes are destroyed or U_{th} reaches 19 V. The lifecycle and durability are investigated for Al/Ti and Al/Ru electrodes with a thickness of 500/100 nm.

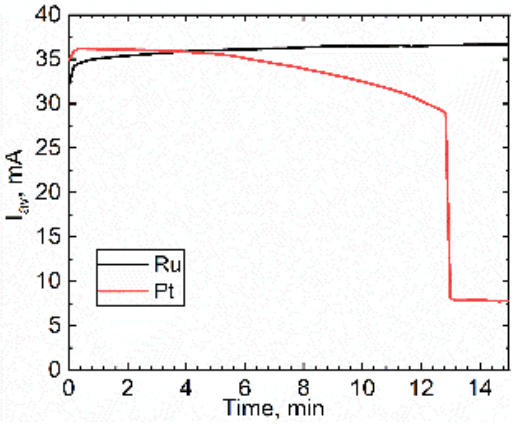

Figure 1. Time dependence of I_{av} in the continuous test.

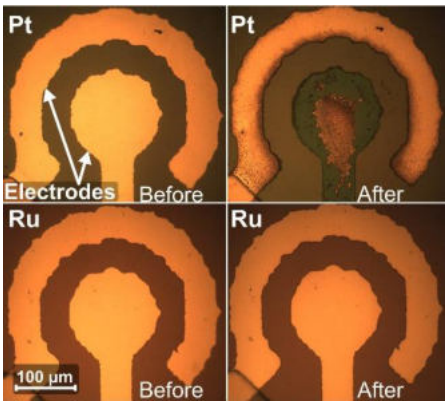

Figure 2. Top view of the electrodes before and after the continuous test.

3. Results and discussion

Time dependence of the current is shown in figure 1. At the beginning of the test, Pt and Ru electrodes demonstrate similar values of I_{av} (35.0 and 32.5 mA, respectively) due to close values of electrical resistivity. Then I_{av} for Pt decreases because of the electrode damage. At the 13th minute the central electrode is almost completely destroyed as shown in figure 2, which is accompanied by a drop of the current. At the same time, Ru electrodes demonstrate a slight increase of the current until the end of the test. A probable reason is the heating of the electrolyte. Ru electrodes do not demonstrate any visible wear, as one can see in figure 2. In the second regime, Ti and Ru electrodes have initial threshold voltage of 12-13 and 10-11 V, respectively. Ti electrodes are oxidized during the test, and U_{th} reaches the maximum value in 18 min. Ruthenium structures are able to generate explosions up to 2 hours, and U_{th} does not exceed 12 V. Thus, Ru electrodes ensure high and stable current in the continuous regime without noticeable wear and generate explosions several times longer than Ti electrodes. These properties make ruthenium a preferable material for the fast electrochemical actuators.

Acknowledgments

This work is supported by the Russian Science Foundation, Grant No. 18-79-10038.

References

[1] Uvarov I V, Lokhanin M V, Postnikov A V, Melenev A E and Svetovoy V B 2018 *Sensor Actuat. B: Chem.* **260** 12

[2] Uvarov I V, Shlepakov P S, Postnikov A V and Svetovoy V B 2021 *J. Colloid Interface Sci*. **582** 167

[3] Shlepakov P S, Uvarov I V, Naumov V V, Mazaletskiy L A and Svetovoy V B 2019 *Int. J. Electrochem. Sci.* **14** 5211

Improving the electrical characteristics of a frequency standard based on cesium atoms

K G Arinushkina[1], A P Valov[2], V E Istominskij[1]and V V Davydov[1, 3]
[1]Peter the Great Saint-Petersburg Polytechnic University, Saint Petersburg, Russia, 195251
[2] The Bonch-Bruevich Saint Petersburg State University of Telecommunications
[3]All-Russian Research Institute of Phytopathology, Moscow Region 143050, Russia

e-mail: k-arinushkina@mail.ru

Abstract. The necessity of constant modernization of quantum frequency standards (QFS) - atomic clocks, which are used in satellite navigation and telecommunication systems to solve new problems in terms of the speed of transmission of large amounts of information, etc., is substantiated. It is noted that among all atomic clocks, cesium QFSs occupy a special place. These standards are the primary frequency reference upon which the international time scale is based. The main goal of all QFS upgrades is to improve the metrological characteristics. In the case of its use on moving objects, its dimensions, weight and power consumption also become important characteristics. The article presents one of the options for reducing the influence of negative factors on the stability of the QFS. The problem of modernizing the cesium frequency standard by including a device for monitoring and stabilizing the temperature regime of its operation is considered.

1. Introduction

Frequency standards (FS) are used in GLONASS and GPS systems as synchronizing generators. The accuracy of the GLONASS system at the moment is about 0.4-0.5 m. Such accuracy values for a number of areas are no longer enough. One way to improve the accuracy of geolocation is to improve the synchronization of the time scales of the satellites of the navigation system. So, if long-term instability of master oscillators in the system is ensured at the level of $3 \cdot 10^{-14}$, then the error in matching satellite time scales will be 10 nanoseconds, which can reduce the geolocation error to 0.2-0.3 m. In this paper, we consider the problem of modernizing the cesium frequency standard by including a device for monitoring and stabilizing the temperature regime of its operation [2].

2. Auto frequency system

The error in measuring the delays between the clock signals of spacecraft (SC) at the receiving point, which determines the accuracy of calculating the coordinates of the object, is determined by the error in the formation of time scales and the frequency stability of the reference oscillators (RO). The required data for new applications of AVAR $< 1 \cdot 10^{-13}$ of daily instability are not provided by the existing FS. To improve the characteristics of the FS, it is necessary to reduce the influence of a number of destabilizing factors, first of all, to reduce the instability of the magnetic field in the region of interaction between atoms and the electromagnetic field (long-term drift of the current source, its temperature dependence, the influence of an external magnetic field). This problem can be solved not only by creating new types of FSs, but also by modernizing existing ones. At the same time, a

reduction in weight and dimensions, a reduction in energy consumption, and an improvement in their metrological characteristics can be achieved at the same time. In the auto frequency system (AFS) system of the quantum frequency standard, the source of the reference signal is a quartz oscillator, and the control device performs the functions of a frequency discriminator.

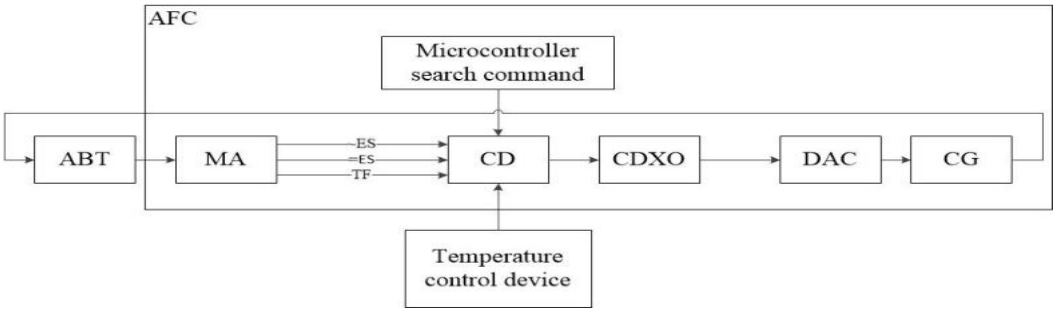

Figure 1. Scheme of the AFC of the quantum frequency standard: ABT - atomic beam tube, MA - matching amplifier, CD - control device, QO - quartz oscillator, ES - error signal.

The ambient temperature determines the voltage applied to the control device in the automatic frequency control circuit (Figure 1), and, consequently, the voltage applied to the crystal oscillator. This leads to a mismatch between the frequencies of the microwave signal and the atomic transition, which leads to errors in the matching of satellite time scales. On figure 2 shows the dependence of the change in the values of the Allan variance $\sigma_y(\tau)$ on time τ for the modernized and previous QFS design. The results obtained show an improvement in the Allan variance $\sigma(\tau)$ by 5%. Studies of the operation of the QFS were carried out for 12 days in a temperature chamber.

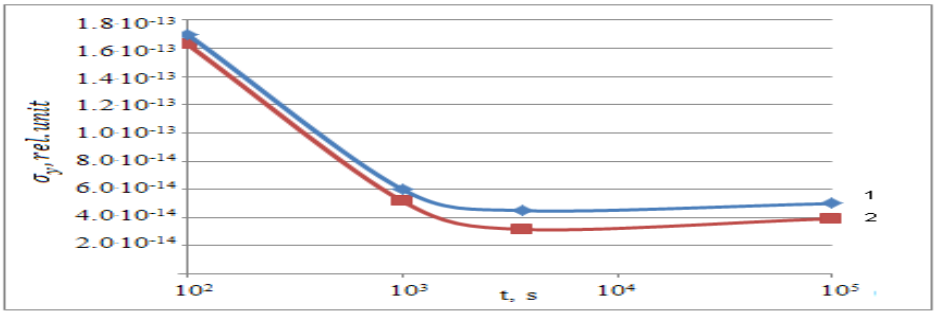

Figure 2. Plot of the Allan variance σy versus time t. Graphs 1 and 2 correspond to the previously used AFC system in the QSC and developed by us.

3. Conclusion

The conducted experiments have shown the efficiency of using automatic frequency control systems with the thermal compensation device developed by us. As a result of using the device for compensating the temperature coefficient of frequency, the temperature sensitivity of the AFS system decreased by a factor of 1.3, which improves the synchronization of satellite time scales for spacecraft with Earth remote sensing systems.

References

[1] F. Riehle, Frequency standard. Basic and applications. WILEY-VCH Verlag CmbH Co. KGaA: New-York, 2008.

[2] A. A. Petrov, V. E. Shabanov, D. V. Zalyotov, A. L. Bulyanitsa, and D. V. Shapovalov, “Modernization of the frequency synthesizer of cesium atomic clock,” IEEE International Conference on Electrical Engineering and Photonics, EExPolytech 2018, vol. 8564389 pp. 52-55, Saint-Petersburg, 2018.

Magnetic field in a magneto-optical system of solenoids and magnetic quadrupole lenses

I.V. Vasiliev, A.V. Bagrov,

Samara National Research University, Samara 443084, Russia

E-mail: sinisterevil163@gmail.com, bagrov_00@internet.ru

Abstract. Calculations of the system of magnetic fields and modeling of these fields in the Mathematica package were performed to estimate the confinement of a beam of charged particles and the formation of a dynamic target for the subsequent fusion reaction on colliding beams in a magneto-optical system, which is a 4-cycle synthesis chamber of alternating solenoids and quadrupole lenses.

Introduction

The development and design of magnetic traps for confining charged particles and, in particular, plasma have been going on for a long time. Since then, various configurations of magnetic fields have been proposed that allow particles to be contained by a magnetic field. An example of such devices can be called a “probkotron”, where regions with a strong magnetic field are formed on the sides of the trap with the help of solenoids, which reflect the flow of charged particles, therefore, such elements are also called magnetic mirrors. In this paper, we calculate and simulate the magnetic field for the synthesis chamber of an electronically controlled plasma generator [1] in the Mathematica package.

Methods and principles

The magneto-optical system in the synthesis chamber of an electronically controlled plasma generator is a system of alternating solenoids and magnetic quadrupole lenses with a discrete change in the field in the solenoids [1]. Using known formulas for the magnetic field of a finite-dimensional solenoid [2] and solving these equations numerically, it is possible obtain the distribution of the magnetic field for a system of solenoids. Performing a similar calculation for magnetic quadrupole lenses, it is possible calculate the superposition of a system of such fields, thereby obtaining the general picture of the magnetic field inside the synthesis chamber presented in [1].The magneto-optical system, which is a 4-cycle chamber for the synthesis of variable solenoids and quadrupole lenses and for which calculations and modeling of fields for estimating the retention of a charged particle beam are presented, is shown in Figure 1.The magnetic fields in the first and fifth solenoids remain constant. The variables are 2-4 solenoids,thanks to which the beam is delayed and the subsequent collision occurs.

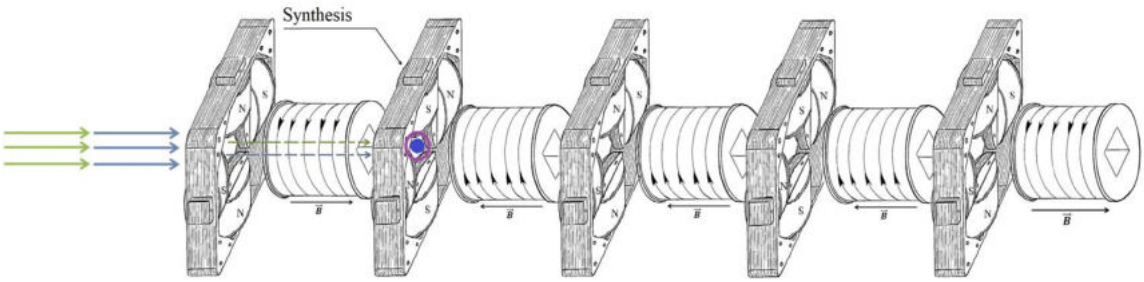

Figure 1. Magneto-optical system

Discussion

Knowing the high probability of propagation of charged particles in a weakly nonhomogeneous magnetostatic field [3]. It is necessary to know this when solving the problem of thermonuclear fusion reaction, which is realize in the results of [1]. Alternating-gradient focusing makes it possible to control a beam of charged particles well [4], so the calculation of magnetic fields makes it possible to estimate this effect that will have a positive effect on the estimate of intra-chamber synthesis reaction.

References

[1] Dolgopolov M.V., Radenko V.V., Zanin G.G. etc. 2022 Electronically Controlled Plasma Power Devices for Sustainable and Environmentally Friendly Electric Energy Technologies // Advances in Engineering Research. Issue 210. P. 197-205

[2] Callaghan E. E., Maslen S. H. 1960 NASA Technical Note D-465

[3] Belomytsev S.Y., Pegel I.V. 2008 Publishing House of the Tomsk Polytechnic University, 115p.

[4] Feynman R.Ph. 1963 The Feynman Lectures on Physics, volume 2, chapter 29

Performance optimization of the cantilever-based MEMS switch

I A Belozerov[1, 2] **and I V Uvarov**[1]
[1]Valiev Institute of Physics and Technology of Russian Academy of Sciences, Yaroslavl Branch, Universitetskaya 21, 150007 Yaroslavl, Russia
[2]P.G. Demidov Yaroslavl State University, Sovetskaya 14, 150003 Yaroslavl, Russia

Abstract. Microelectromechanical system (MEMS) switches combine advantages of electromagnetic and semiconductor relays. However, a number of problems prevent the widespread use of these devices. One of them is high actuation voltage. In this work, voltage reduction is achieved by optimizing the shape of the electrodes. The switch is simulated by the finite element method. Dependences of the actuation voltage on the geometric parameters are obtained. The proposed shape of the electrodes reduces the voltage by almost 2 times compared to conventional design without deterioration of other working characteristics.

1. Introduction

MEMS switches are tiny devices, typically less than 100 μm in length. They combine advantages of electromagnetic relays and switches based on silicon transistors, namely, low insertion loss, good isolation, low power consumption, and small size [1]. In addition, MEMS switches are compatible with CMOS circuits. These facts necessitate the development and improvement of MEMS switches. A typical MEMS switch contains a cantilever suspended above a metal transmission line at a distance of about one micron. A driving electrode is also located under the cantilever. When voltage is applied to it, the cantilever bends under the electrostatic force and comes in contact with the line. This design is simple and reliable, but it has a high actuation voltage of several tens and hundreds of volts [2]. Such a voltage complicates the use of MEMS switches in modern electronic circuits with a typical voltage level of 3-5 V. There are several ways to reduce the actuation voltage: increasing the overlap area of the cantilever with the electrode, reducing the gap between them, and reducing the elasticity of the structure. In this work, we use the first method and optimize the shape of the electrodes.

2. Design of the switch

The conventional switch is shown schematically in figure 1. The aluminum cantilever has a length L = 50 μm, a width W = 10 μm and a thickness t = 2 μm. The end with the coordinate x = 0 is fixed. The gap between the cantilever and the electrodes is g = 1.5 μm. The driving electrode has an area of 18×12 μm^2 and a thickness of 100 nm. The switch is simulated by the finite element method using verified software. The model consists of about 10^5 tetrahedral elements. The cantilever is grounded, while the electric potential is applied to the driving electrode. The potential gradually increases until the pull-in instability. The potential for which the computer is able to calculate the cantilever position is considered as the actuation voltage.

3. Results and discussion

The actuation voltage of the conventional switch is 146 V. This value can be reduced by increasing the width of the electrode and cantilever, as shown in figure 2. Increasing the width from 12 to 22 µm reduces the voltage to 107 V. Further widening may lead to a situation where even a slight asymmetry in the position of the cantilever and electrode creates a significant torque, rotating the cantilever around its axis. The cantilever may touch the driving electrode, and a short circuit may happen. Therefore, the further reduction in the actuation voltage is achieved by extending the electrode along the x axis and surrounding the transmission line, see the bottom inset in figure 2. This design has the actuation voltage of 82 V, which can be provided by a built-in charge pump with a 3.3V power supply [3]. The simulation shows that the optimization does not deteriorate the response time, restoring force and other working characteristics of the switch, because the bending part of the cantilever does not change size and the structure does not lose elasticity. Thus, optimizing the electrode shape provides an almost twofold voltage reduction and makes the switch implementable in common electronic devices.

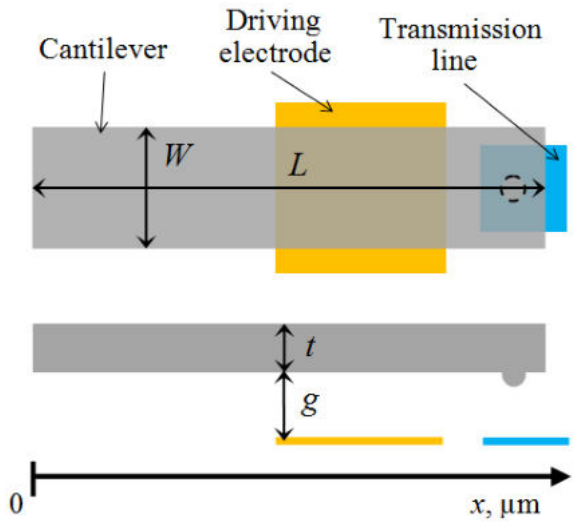

Figure 1. Schematic illustration of the MEMS switch.

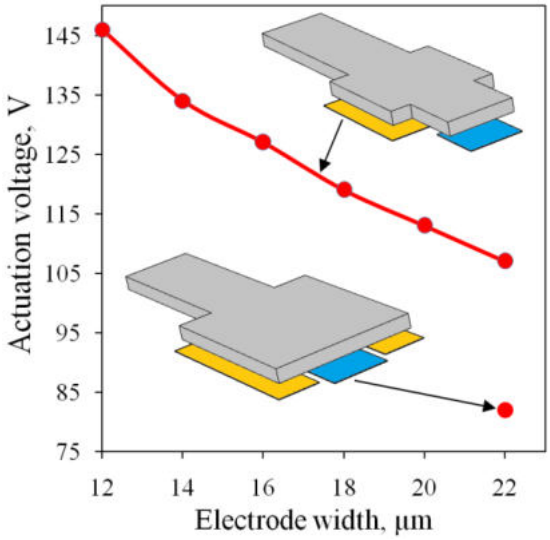

Figure 2. Dependence of the actuation voltage on the electrode width.

4. Acknowledgments

This work is supported by the grant of President of the Russian Federation № MK-945.2021.4 and the program no. FFNN-2022-0017 of the Ministry of Science and Higher Education of Russia for Valiev Institute of Physics and Technology of RAS.

References

[1] Rebeiz G M 2003 *RF MEMS: Theory, Design, and Technology* (Hoboken, New Jersey: John Wiley & Sons)

[2] Patel C D and Rebeiz G M 2011 *IEEE MTT-S Int. Microw. Symp. Dig.*, vol. 59, № 5, pp. 1230-1237

[3] Goggin R, Fitzgerald P, Stenson B, Carty E and McDaid P. *2015 IEEE MTT-S Int. Microw. Symp.*, 2015, pp. 1-4

Synchronization systems of time scales and frequencies in polar latitudes by meteor radio channel

A A Briushinin[1] **and V V Davydov**[1, 2]
[1]Peter the Great Saint-Petersburg Polytechnic University, Saint Petersburg, Russia, 195251
[2]All-Russian Research Institute of Phytopathology, Moscow Region 143050, Russia

e-mail: anatoliyb2000@mail.com

Abstract. The necessity of using a meteor communication channel as a backup system for determining the coordinates of moving objects in polar latitudes and transmitting information is substantiated. The necessity of using a time scale synchronization system in the meteor communication channel has been established. The reasons that cause a failure in the transmission of information in the meteor communication channel are presented. A model for calculating the shift of time scales in the meteor communication channel is proposed. A method has been developed to reduce random errors and increase the noise immunity of the meteor communication channel.

1. Introduction

Today, the task of developing polar regions rich in oil and gas is urgent [1]. Vessels serving the extraction of minerals use navigation systems to determine their location within the Northern Sea Route (NSR). However, in the polar regions, GLONASS is blocked by ionospheric disturbances arising under the influence of magnetic anomalies (for example, the Northern lights). Moreover, the performance of satellites is limited to approximately 70 degrees north latitude, while the NSR passes much higher.

Under these conditions, navigation is carried out by ground-based pulse-phase radio navigation systems (PPRNS) emitting radio pulse navigation signals [2, 3]. The coordinates of the transmitting stations of the PPRNS are known in advance. The stations serve a certain area of the earth's surface. Transmitting stations work in groups forming a single chain. Each chain includes a master station and several slave stations, whose radio pulse emissions are synchronized with the signals of the master station. The emissions of the leading station of the chain are synchronized, for example, by signals of the exact time.

2. Meteor synchronization

In northern latitudes, it is advisable to use the meteor radio channel as a backup channel for transmitting the exact time signal. The principle of meteor radio communication is based on the ability of ultrashort waves (VHF) to mirror the ionized traces formed as a result of the combustion of meteoroids in the Earth's atmosphere (Fig. 1) [4].

The advantages of meteor radio communication are a small transmitter power (from 0.5 to 2 kW), simple «wave channel» type antennas, increased communication secrecy and a wide frequency band.

It is known that the radiometric communication channel is intermittent. The ionized trace is formed on average for 1 second, then it dissipates due to the process of bipolar (ambipolar) diffusion and it is

necessary to wait for the formation of the next meteor trail. This disadvantage limits the scope of the radiometric communication channel.

Due to the random location of the meteor trail in the synchronization systems of spatially remote time scales and frequencies on the meteor radio channel, the time of signal propagation is not known in advance, therefore, it is necessary to use two-way information transmission - the method is called active (two-way, duplex).

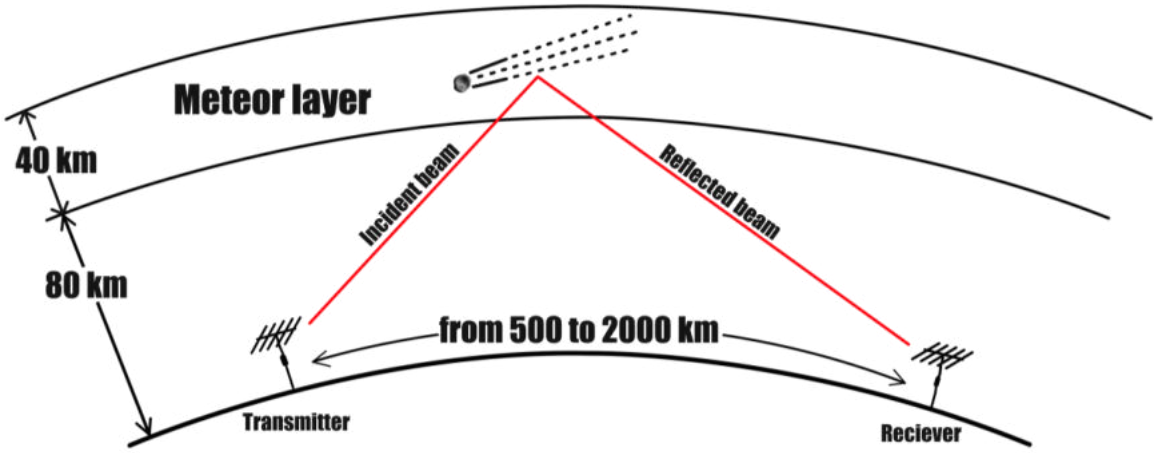

Figure 1. The principal model of the meteor communication channel.

To calculate the shift of the time scales ΔT, it is necessary to calculate the propagation time of the signal t_p, for this, in addition to fixing the timestamp $t^{<2>}_R$ by the receiver, the time $t^{<1>}_T$ is fixed by the transmitter, after exchanging this information, a system of two equations is compiled:

$$\begin{cases} t_R^{<2>} = t_T^{<1>} + \Delta T + t_p \\ t_R^{<1>} = t_T^{<2>} - \Delta T + t_p \end{cases}$$

In total, we solve a system of two equations with two unknowns:

$$\Delta T = \frac{1}{2}[(t_R^{<2>} - t_R^{<1>}) + (t_T^{<2>} - t_T^{<1>})]$$

In this case, both simultaneous transmission of the timestamp (counter method) and alternate transmission is possible. Alternate transmission is suitable for a communication range of less than 500 km.

3. Conclusion

Transmission as a timestamp of the m-sequence allows to increase the noise immunity and secrecy of the meteor radio communication system, as well as to reduce the random error. The use of highly stable quantum generators (frequency standards) in meteor communication channels makes it possible to further reduce the random error during channel synchronization [5].

References

[1] Kondratov N A 2017 *Arctic Evironmental Research* **1** 120-126.

[2] Davydov R and Kulikova M 2020 *Proceedings of the 2020 IEEE International Conference on Electrical Engineering and Photonics (EExPolytech 2020)*, Saint-Petersburg **9244003**, p. 38–41

[3] Davydov R and Nagornaya A 2020 *Proceedings of the 2020 IEEE International Conference on Electrical Engineering and Photonics (EExPolytech 2020)*, Saint-Petersburg **9243977** 145–148

[4] Ryabov I V, Tolmschev S V and Lebedeva A A 2016 *Modern High Technologies* **7** 312-319

[5] Petrov A and Grebenikova N 2018 *Journal of Communications Technology and Electronics* **63(11)** 1159–1164

RFID-based sensor for insect detection

Nikita Bulatov[1, a)], Tatyana Vosheva[1], Anton Khudykin[2], Dmitry Filonov[1]

[1]*Center for Photonics and 2D Materials, Moscow Institute of Physics and Technology, Dolgoprudny 141700, Russia*

[2]*Telecom R&D Center, Moscow Institute of Physics and Technology, Dolgoprudny 141700, Russia*

a) nikita.bulatov@phystech.edu

Abstract. Real-time monitoring of insects is an important objective across many life-science disciplines. Here we demonstrate the first of its kind RFID-based disposable insects detector. We developed a new type of biodegradable antenna, based on caramel mixtures with metal powders. As the result, the structures are conductive on one hand, i.e., can serve electromagnetic functions, and attractive to insects on another. Electrical connection, being broken after an interaction with insects, makes changes in RFID circuit impedance matching, leading to a wireless readout. We fabricated and characterized the first generation of sensors, which were found to be well-fitted with numerical modelling.

1. Introduction

Real-time monitoring of the distribution, migration, and population of insects provides valuable information in ecology, agriculture, and other life science disciplines. Quite a few methods have been developed, including optical, acoustic, acousto-optic, chemical, radiofrequency-based, and others [1]–[3]. The main fundamental challenge, faced by radiofrequency approaches, is the small size of insects relative to operational wavelengths. A probable solution is shifting operation frequencies towards the sub-terahertz region. However, the penalty of this approach is a high atmospheric decay, making the wireless detection extremely short-range and not practical.

Here we propose a sensor, based on well-established RFID technology. There are studies that show the fundamental possibility of such an approach using the example of detecting bee and bumblebee by applying radio frequency tags to them [4], [5]. The solution proposed in this paper is based on indirect indicators of the speed of insects eating the sugar melt - caramel.

2. Geometry and design

The basic structure of the proposed RFID sensor is PCB meander whose configuration and parameters is shown in Figure 1. The proposed design is printed on 1 mm FR-4 substrate with 36 μm copper metal layer. Chosen geometry of tag reduced overall size (40 x 40 mm^2) related to UHF RFID wavelength (370 – 330 mm) and increase thickness homogeneity of caramel layer during manual crafting. Lumped port with 20-ohm impedance replaces IC chip. Dielectric properties of caramel are $\varepsilon=3$ (without dispersion) and $tg\delta = 0$ (in the model loss in caramel is neglected). Numerical simulation of sensor shows its high sensitivity to caramel layer thickness as a resonant structure.

3. Results and discussion

Three samples were numerically simulated, made and measured (S_{11}-parameters of magnetic loop). One of them hasn't caramel layer, another has 2 mm thickness superstrate and third has 5 mm thickness layer. Results of experiments and comparison with simulations are shown in Figure 2. The results show good convergence of simulation and experiment at small caramel layer thickness. Inadequate results at thick superstrate can be explained by a slight discrepancy between the dielectric characteristics (loss tangent probably) of caramel and those stated in the model. Curvature of the caramel at the edges of the board can also be an additional error factor.

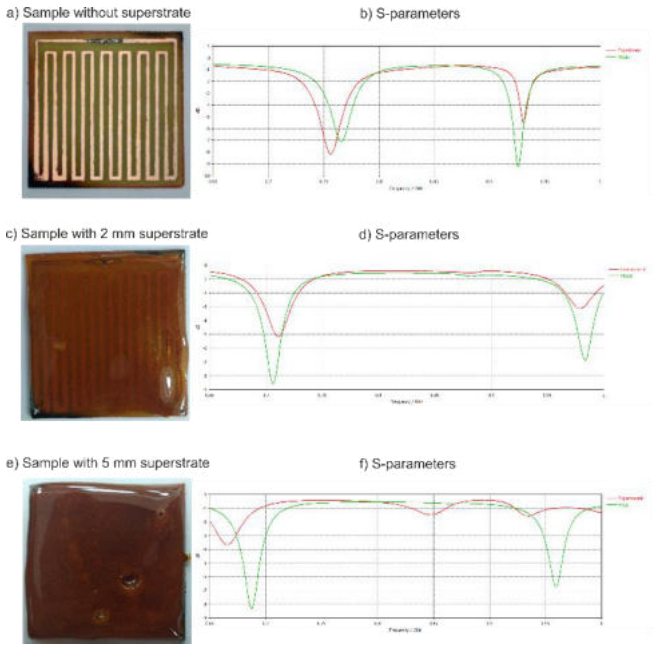

Figure 1. RFID tags a) without caramel superstrate, c) with 2 mm and e) 5 mm of caramel thickness and their S-parameters.

In continuation of this study, it is required to measure dielectric characteristics of caramel and obtain precise convergence of model and experiments. The current task is to make additional samples and increase the homogeneity of caramel thickness. By the date of the conference, it is expected to receive and summarize all the planned data, prepare the final version of this proceeding and update it.

Acknowledgments

The research was supported by of the federal academic leadership program Priority 2030

References

[1] "Monitoring of Flying Insects using a Dual-Wavelength CW Lidar System | IEEE Conference Publication | IEEE Xplore." https://ieeexplore.ieee.org/document/8988954 (accessed Apr. 01, 2022).

[2] K. Izumi, S. Ishibashi, and T. Tsujimura, "Exploring of gas source location using behavioral model of insects," *2017 56th Annual Conference of the Society of Instrument and Control Engineers of Japan, SICE 2017*, vol. 2017-November, pp. 180–181, Nov. 2017, doi: 10.23919/SICE.2017.8105747.

[3] W. Pan, X. Kong, J. Xu, and W. Pan, "Measurement and analysis system of vibration for the detection of insect acoustic signals," *2016 Asia-Pacific International Symposium on Electromagnetic Compatibility, APEMC 2016*, pp. 1090–1092, Jul. 2016, doi: 10.1109/APEMC.2016.7522953.

[4] P. de Souza *et al.*, "Low-Cost Electronic Tagging System for Bee Monitoring," *Sensors 2018, Vol. 18, Page 2124*, vol. 18, no. 7, p. 2124, Jul. 2018, doi: 10.3390/S18072124.

[5] S. E. Barlow, M. A. O'Neill, and B. M. Pavlik, "A prototype RFID tag for detecting bumblebee visitations within fragmented landscapes," *Journal of Biological Engineering*, vol. 13, no. 1, Feb. 2019, doi: 10.1186/S13036-019-0143-X.

Wireless power transfer using a higher-order eigenmode of a birdcage coil in MRI-bore

Oleg Burmistrov[1], Pavel Seregin[1]

[1]ITMO University, 197101 Saint Petersburg, Russia

E-mail: oleg.burmistrov@metalab.ifmo.ru

Abstract. In this work, we consider wireless power transfer with a higher order eigenmode of a birdcage coil within a magnetic resonance imaging scanner. Numerical simulations of electric and magnetic field, specific absorption rate in human voxel model, output voltage at receive antennas inside the birdcage coil are presented. Moreover, optimal eigenmode for wireless power transfer has been established. Finally, possible applications of the proposed concept are analysed.

1. Introduction. Wireless power transfer (WPT) in magnetic resonance imaging (MRI) is a highly demanded field presently. Local coils power supply inside MRI-bore carried out using large radiofrequency (RF) cables. It decreases patient placing speed and his comfort. Local coils can be powered wirelessly by energy harvesting from the B1 field [1, 2] or an additional transmit antenna [3]. However, if a birdcage coil is used, which is already an integral part of many MRI scanners, an extra transmit antenna for WPT isn't needed. Moreover, more energy can be transferred compared with energy harvesting from the B1 field without his homogeneity violations.

2. Methods. Numerical simulations produce in the program package CST Microwave Studio. Two orthogonal loop coils using for receiving energy (FIG. 1a). It lets to receive a circular polarization of magnetic field. The numerical model of the birdcage coil with a screen is equivalent to the body coil from a clinical MRI scanner Siemens Avanto 1.5 T. A cylindrical phantom placed in the birdcage coil isocenter (FIG. 1b). Liquid parameters in the model are equivalent to parameters in phantoms for clinical MRI scanners by Siemens. The receive antennas system is at 50 mm from the surface of the cylindric phantom (FIG, 1b) and the detailed voxel human model (FIG. 1c).

3. Results. Saturation parameters are got during numerical simulation of the birdcage coil with screen and phantom. Then five eigenmodes with different frequencies are selected for research based on the S-parameters. Electric and magnetic fields of eigenmodes on different frequencies are orthogonal therefore the mutual influence of fields is minimum. That is, MR images quality isn't getting worse during the WPT on no Larmor frequency. Further, the receive antennas system was added to the numerical model (FIG. 1b) and every eigenmode of the birdcage coil is researched independently of each other. Wherein the receive antennas system is tuning to resonance frequency the birdcage eigenmode is under research. The maximum sum voltage on receive antennas system is got on eigenmode with resonance frequency equal 44.2 MHz. This eigenmode has circular polarization of the magnetic field. The research of an electric field on different frequencies (FIG. 1d – 1e) is shown that

the WPT on 44.2 MHz frequency is safer because the electric field is less concentrated in the phantom. This leads to less heating of a research object from a conducting current during the scan. The research of the specific absorption rate with the human body voxel model (FIG. 1c) is represented what research object heating is minimum and this the WPT system is safety. Numerical simulation of magnetic field (FIG. 1f – 1g) is shown that this field concentrated outside the phantom (FIG. 1g) whereby the WPT is more effective compared to energy harvesting on the Larmor frequency since less loss in a phantom. A significant modification of the present MRI scanners with field-level 1.5 T during the WPT on 44.2 MHz frequency doesn't need because an extra transmit antenna doesn't use. This system lets power supply devices within MRI-bore.

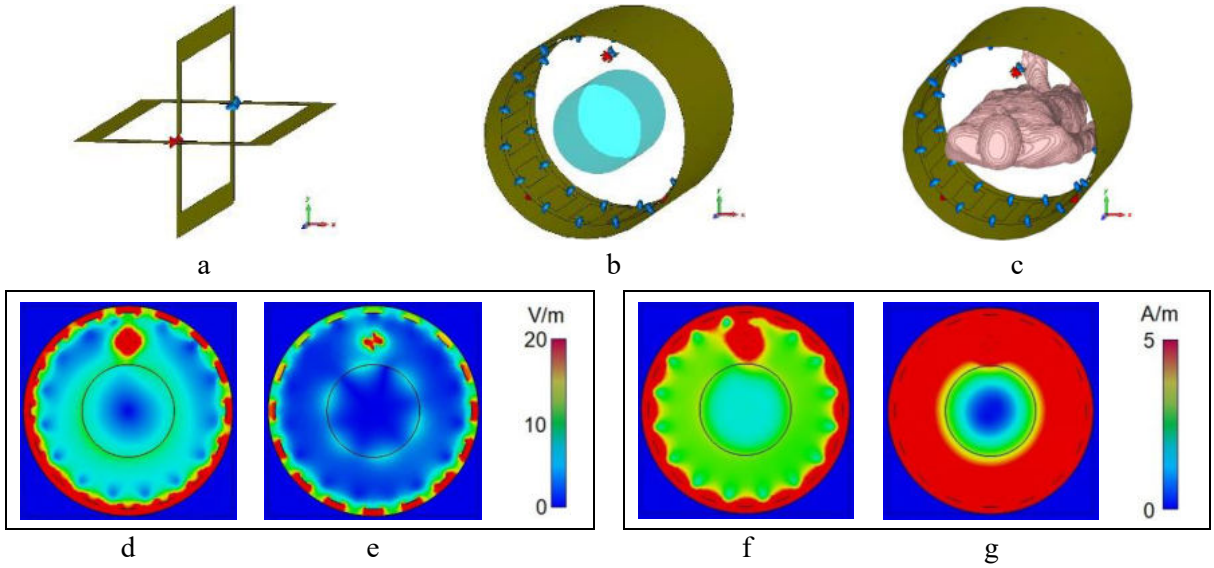

Figure 1. Numerical simulations of the WPT system in MRI: the receive antennas system (a); the birdcage coil with the screen, the receive antennas system and cylindric phantom (b) or human body voxel model (c); the electric field distribution in a axial surface on 63.6 MHz (d), 44.2 MHz (e) frequencies; the magnetic field distribution in a axial surface on 63.6 MHz (f), 44.2 MHz (g) frequencies

4. Conclusion. The optimal eigenmode for the WPT inside the birdcage coil has the frequency of 44.2 MHz featuring electric and magnetic fields concentrated on the surface of the phantom. As a result, the WPT system is more efficient, demonstrating lower ohmic losses as well as safe for a patient. Moreover, the fields at 44.2 MHz and Larmor frequencies are orthogonal. Thus, MR images quality does not decrease. The WPT system at the frequency of 44.2 MHz can be implemented in clinical MRI scanners without a significant modification of the scanner and allows realizing a power supply for devices in MRI-bore.

Acknowledgments
This work was supported by the Russian Science Foundation (Project No.21-79-30038).

References
[1] P. Seregin, O. Burmistrov, G. Solomakha, E. Kretov, N. Olekhno and A. Slobozhanyuk, *In Journal of Physics: Conference Series*, **1**, 012134 (2021)
[2] M. Venkateswaran, M. Kurpad, J. Brown, S. Fain and D. van der Weide, *42nd Annual International Conference of the IEEE EMBC*, 1469-1472 (2020)
[3] A. Ganti, J. Lin, T. Wynn, and T. Ortiz, *Wireless Power Transfer*, **6**, 138–153 (2019)

Additive Manufacturing of An Antenna Array

Vladimir Burtsev[1, a)], Kirill Rogozhkin[1], Tatyana Vosheva[1], Anton Khudykin[2], Dmitry Filonov[1]

[1]Center for Photonics and 2D Materials, Moscow Institute of Physics and Technology, Dolgoprudny 141700, Russia

[2]Telecom R&D Center, Moscow Institute of Physics and Technology, Dolgoprudny 141700, Russia

[a)] burtsev.vd@phystech.edu

Abstract. Antenna arrays are essential elements in modern wireless communication technologies. Capabilities to perform real-time beamforming with millisecond-scale latencies enable supporting frontier 5G communication protocols. Being based on standard lithography methods, printed board antenna arrays are two-dimensional by design. However, exploration of the third dimension allows for obtaining new capabilities, including wide-angle scanning, broadband impedance matching, higher directivity, and several others. Here we demonstrate an additively manufactured volumetric antenna array, where each individual element is 3D-printed and subsequently metalized with the aid of electrochemical deposition. The manufactured array is compared with its planar counterpart (the same number of elements and area on a printed board) and demonstrated better gain characteristics. Additive manufacturing is foreseen to provide capabilities of a complete production cycle, including electronics and peripheries, being fabricated within the same machine. Here, the full potential of volumetric antenna arrays will be revealed.

1. Introduction

The development of various additive technologies has been gaining momentum recently [1]. Additive technologies serve science in various industries. A bright example of an additive technology is three-dimensional metal printing [2], [3]. Also, there already exists a set of developments in the field of printing with conductive ink [4]. The scope of applicability of additive manufacturing methods extends in the field of radio engineering and data transmission. There are a number of works devoted to obtaining electrodynamic structures using laser sintering [5], [6], drawing with conductive ink [7]–[9], polymer deposition [10], and others [11]–[13]. Some researchers use electrically conductive plastic to make antennas [14], [15]. Such antennas are well predicted using numerical modeling [16].

In this paper, we are going to highlight the possibility of assembling antenna arrays based on additively manufactured antennas.

2. Geometry and designs

Figure 1 (a) shows the general geometry of the printed circuit board (PCB) layout. All the dimensions are given in millimeters. The thickness of the metallization is about 0.1 mm. The thickness of PCB is 1.5 mm.

Fig. 1 (b) shows the reflection coefficient of this antenna array in the computer simulation environment CST Studio Suite. It is noticeable that at a frequency of 2 GHz, the antenna has a better matching of about -23 dB. Studies have shown that at the same frequency of 2 GHz, the antenna array has realized gain equal to 9.21 (inset (c) shows 3D-diagram of the realized gain and its exact value) and scanning angle equal to 34...36 degrees (Fig.1 (d and e)).

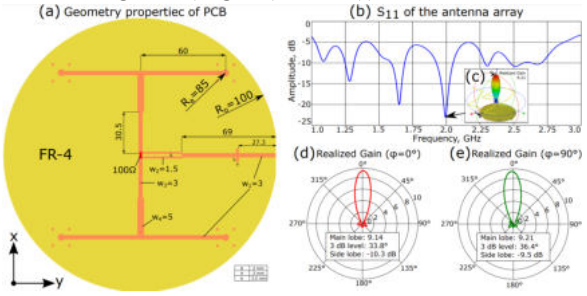

Fig. 1. Geometry properties of an antenna array and its radiation properties in the numerical simulation package CST Studio Suite.

The last stage of the experiment is aimed at implementing this structure using the proposed additive algorithm.

3. Discussion

By the date of the conference, it is expected to receive and summarize all the planned data, prepare the final version of this proceeding and update it.

4. Acknowledgements

The research was supported by of the federal academic leadership program Priority 2030.

5. References

[1] U. M. Dilberoglu, B. Gharehpapagh, U. Yaman, and M. Dolen, "The Role of Additive Manufacturing in the Era of Industry 4.0," *Procedia Manuf.*, vol. 11, pp. 545–554, Jan. 2017, doi: 10.1016/J.PROMFG.2017.07.148.

[2] J. P. Kruth, M. C. Leu, and T. Nakagawa, "Progress in Additive Manufacturing and Rapid Prototyping," *CIRP Ann.*, vol. 47, no. 2, pp. 525–540, Jan. 1998, doi: 10.1016/S0007-8506(07)63240-5.

[3] N. K. Roy, D. Behera, O. G. Dibua, C. S. Foong, and M. A. Cullinan, "A novel microscale selective laser sintering (μ-SLS) process for the fabrication of microelectronic parts," *Microsystems Nanoeng. 2019 51*, vol. 5, no. 1, pp. 1–14, Dec. 2019, doi: 10.1038/s41378-019-0116-8.

[4] R. Pandey *et al.*, "Highly Conductive Copper Film on Inkjet-Printed Porous Silver Seed for Flexible Electronics," *J. Electrochem. Soc.*, vol. 165, no. 5, p. D236, Apr. 2018, doi: 10.1149/2.1331805JES.

[5] M. Ferrando-Rocher, J. I. Herranz-Herruzo, A. Valero-Nogueira, and B. Bernardo-Clemente, "Selective Laser Sintering Manufacturing as a Low Cost Alternative for Flat-Panel Antennas in Millimeter-Wave Bands," *IEEE Access*, vol. 9, pp. 45721–45729, 2021, doi: 10.1109/ACCESS.2021.3067637.

[6] H. Sigmarsson, E. Kinzel, W. Chappell, and X. Xu, "Selective laser sintering of patch antennas on FR4," *IEEE Antennas Propag. Soc. AP-S Int. Symp.*, vol. 1 A, pp. 280–283, 2005, doi: 10.1109/APS.2005.1551303.

[7] I. Kazani *et al.*, "Performance study of screen-printed textile antennas after repeated washing," *Autex Res. J.*, vol. 14, no. 2, pp. 47–54, 2014, doi: 10.2478/V10304-012-0049-X.

[8] S. L. Merilampi, T. Bjorninen, A. Vuorimaki, L. Ukkonen, P. Ruuskanen, and L. Sydanheimo, "The effect of conductive ink layer thickness on the functioning of printed UHF RFID antennas," *Proc. IEEE*, vol. 98, no. 9, pp. 1610–1619, 2010, doi: 10.1109/JPROC.2010.2050570.

[9] D. Kim and J. Moon, "Highly conductive ink jet printed films of nanosilver particles for printable electronics," *Electrochem. Solid-State Lett.*, vol. 8, no. 11, p. J30, Sep. 2005, doi: 10.1149/1.2073670/XML.

[10] R. Olejník, S. Goňa, P. Slobodian, J. Matyáš, R. Moučka, and R. Daňová, "Polyurethane-Carbon Nanotubes Composite Dual Band Antenna for Wearable Applications," *Polym. 2020, Vol. 12, Page 2759*, vol. 12, no. 11, p. 2759, Nov. 2020, doi: 10.3390/POLYM12112759.

[11] D. Maurya *et al.*, "3D printed graphene-based self-powered strain sensors for smart tires in autonomous vehicles," *Nat. Commun. 2020 111*, vol. 11, no. 1, pp. 1–10, Oct. 2020, doi: 10.1038/s41467-020-19088-y.

[12] M. Ferrando-Rocher, J. I. Herranz, A. Valero-Nogueira, and B. Bernardo, "Performance Assessment of Gap Waveguide Array Antennas: CNC Milling vs. 3D Printing," *IEEE Antennas Wirel. Propag. Lett.*, vol. 1225, no. c, pp. 1–1, 2018, doi: 10.1109/LAWP.2018.2833740.

[13] M. Liang, C. Shemelya, E. MacDonald, R. Wicker, and H. Xin, "3-D Printed Microwave Patch Antenna via Fused Deposition Method and Ultrasonic Wire Mesh Embedding Technique," *IEEE Antennas Wirel. Propag. Lett.*, vol. 14, pp. 1346–1349, 2015, doi: 10.1109/LAWP.2015.2405054.

[14] V. Kyovtorov, I. Georgiev, S. Margenov, D. Stoychev, F. Oliveri, and D. Tarchi, "New antenna design approach – 3D polymer printing and metallization. experimental test at 14–18 GHz," *AEU - Int. J. Electron. Commun.*, vol. 73, pp. 119–128, Mar. 2017, doi: 10.1016/j.aeue.2016.12.017.

[15] J. Thévenard, D. Lo Hine Tong, A. Louzir, C. Nicolas, C. Person, and J. P. Coupez, “3D multi-sector vivaldi antennas based on metallized plastic technology,” *IEEE Antennas Propag. Soc. AP-S Int. Symp.*, pp. 5849–5852, 2007, doi: 10.1109/APS.2007.4396882.

[16] D. Filonov, S. Kolen, A. Shmidt, Y. Shacham-Diamand, A. Boag, and P. Ginzburg, “Volumetric 3D-Printed Antennas, Manufactured via Selective Polymer Metallization,” *Phys. status solidi – Rapid Res. Lett.*, vol. 13, no. 6, Jun. 2019, doi: 10.1002/PSSR.201800668.

Possibility of using atomic clocks on mercury-199 ions in satellite navigation systems

Wang Ding[1] and V V Davydov[1, 2, 3]
[1]Peter the Great Saint-Petersburg Polytechnic University, Saint Petersburg, Russia, 195251
[2]The Bonch-Bruevich Saint-Petersburg State University of Telecommunications, Saint Petersburg 193232, Russia
[3]All-Russian Research Institute of Phytopathology, Moscow Region 143050, Russia

jssdwang06@mail.ru

Abstract. The necessity of developing atomic clocks with high long-term stability for space exploration and improving the operation of satellite systems is substantiated. The problems that arise in the operation of existing models of atomic clocks are considered. The prospects of using atomic clocks on mercury-199 ions for solving these problems are noted. The state of research on improvement of the design for atomic clocks on mercury-199 ions for space applications and data on Allan deviation for different models of the atomic clock on mercury-199 ions are presented. The directions for further research are determined.

1. Introduction

Atomic clocks as high-precision devices, provide timekeeping for positioning satellite navigation systems, the accuracy of positioning and synchronization of satellite navigation and positioning in outer space depends on the reliable operation of atomic clocks [1-4]. With the development of satellite navigation systems and deep space exploration technologies, the characteristics of traditional space satellite atomic clocks no longer meet the requirements, and atomic clocks with better characteristics are needed as time standards.

The atomic clocks on mercury-199 ions are microwave atomic clocks, that went into space after cesium, rubidium and hydrogen atomic clocks, compared with them, this new generation of atomic clocks has the highest hyperfine energy level transition frequency [1], can provide very high frequency stability, adapts to space conditions under conditions of long-term operation and a large number of interferences (for example, solar wind, magnetic storms, etc.), can improve by an order of magnitude the determination of the coordinates of a spacecraft in deep space exploration [3]. The main problem in the development of atomic clocks on mercury-199 ions is related to reducing the size and weight of the Pauli ion trap, as well as reducing the power consumption while maintaining the metrological characteristics that are obtained for atomic clocks on mercury-199 ions ground applications.

2. Principles of trapped mercury-199 ions to ensure the required accuracy characteristics

One of the main elements of the atomic clocks on mercury-199 ions is the Pauli ion trap, which uses an electromagnetic field to trap a certain number of charged ions in a certain area of space, effectively reducing collisions with the wall of the vessel, the trajectory of mercury ions obtains by solving the Mathieu equation. The trapped mercury-199 ions interact with wavelength λ = 194 nm (usually a lamp with mercury-202 ions) and microwave field, whose frequency is formed according to the transition

with a frequency equal to c/λ. When the frequencies coincide exactly, the maximum fluorescence signal is produced, which is registered by a photodetector. If the frequencies do not match, an error signal is generated and the frequency of the crystal oscillator is adjusted to the transition frequency. The main problem is associated with keeping the required number of charged ions in a fixed zone while reducing the size of the trap. For the use of these frequency standards in space systems, there are severe restrictions on the weight of the design.

3. Analysis of metrological characteristics of quantum standard frequencies

Frequency stability is frequently used as an indicator of atomic clock performance, usually described by Allan deviation. Figure 1 shows the Allan deviation data for different models of atomic clocks placed on satellites.

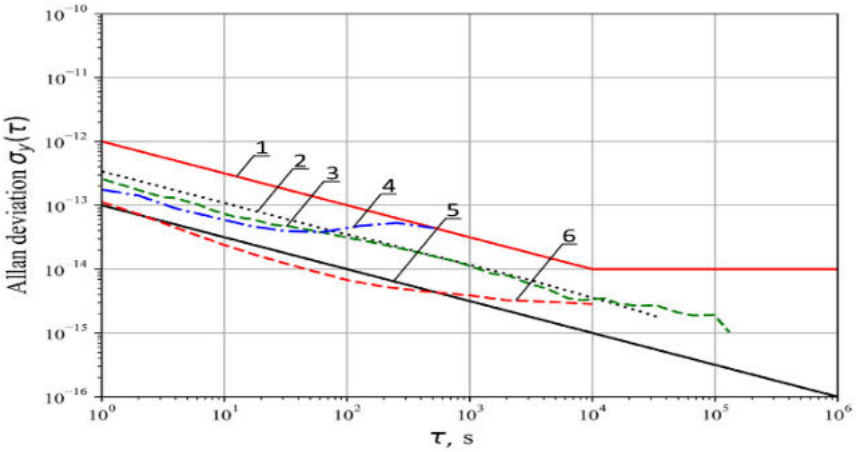

Figure 1. The Allan deviations of different current space atomic clocks and station communication on Earth. Graphs 1, 2, 3, 4, 5, and 6 correspond to the following atomic clock: Cs-133 – Glonass; PHM and RAFS – GPS; JPL 199Hg ion – GPS experimental; Leonardo RAFS – Galileo; PHM – ship communication station; PHM – communication station on Earth [2].

Analysis of the Allan deviation data for different models of atomic clocks shows that atomic clocks on mercury-199 ions have characteristics that, in some cases, are better than those of other models of atomic clocks.

4. Conclusion

Atomic clocks on mercury-199 ions as the first ion clock sent into space, the experimental satellite showed good performance with a daily drift about $3.0 \cdot 10^{-16}$ [3], which is the best choice for future satellite navigation systems.

References

[1] Jaduszliwer B and Camparo J 2021 *GPS Solutions* **25 (1)** 27

[2] Batori E, Almat N, Affolderbach C and Mileti G 2021 *Advances in Space Research* 68 (12) 4723-4733

[3] Burt E A, Prestage J D, Tjoelker R L, Enzer D G, Kuang D, Murphy D W, Robison D E, Seubert J M, Wang R T and Ely T A 2021 *Nature* **595 (7865)** 43-47

[4] Petrov A A, Shabanov V E, Zalyotov D V, Bulyanitsa A L and Shapovalov D V 2018 IEEE International Conference on Electrical Engineering and Photonics, EExPolytech 2018 (Saint-Petersburg, 2018) **8564389** 52-55

Modelling of ion transfer processes in ion-plasma generator with discrete flow compaction

A.V. Bagrov, I.V. Vasiliev

Samara University, Samara 443084, Russia

E-mail: sinisterevil163@gmail.com

Abstract. The experimental electronically controlled plasma power system is analysed in the mathematical model, the operation of which is based on the reaction of thermonuclear fusion on colliding beams. The physical aspects of retention ion flows are considered in magneto-optical system, models for describing the dynamics of flows, and the principles of compaction of ion and plasma flows with the discrete change are presented. The dependences of ion current distribution and concentration for initial energy values from 250 to 350 keV are investigated.

1. Introduction

Thermonuclear fusion is the process by which two light nuclei combine to form the heavier core. During the thermonuclear process, the huge amount of energy is released in the form of fast-moving particles. Since atomic nuclei are positively charged due to the protons contained in them, an electrostatic or Coulomb repulsive force arises between them. In order for two nuclei to enter into the thermonuclear reaction, it is necessary to overcome this barrier of repulsion, which happens if two nuclei are brought close enough to each other, where the shortrange nuclear forces become sufficient to overcome the Coulomb force and start the process of thermonuclear fusion of these nuclei. The energy required for the nuclei to overcome the Coulomb barrier is provided by their thermal energy, which must be very high. The purpose of this work in the above-mentioned perspective is to obtain electronically controlled ion-plasma flows for the initialization of the thermonuclear fusion, followed by the retention of electronically controlled thermonuclear fusion in linear magnetic traps.

2. Methods and principles

The operation of an electronically controlled plasma electric generator [1] is based on the reaction of nuclear fusion in ion flows [2–5] obtained as the result of evaporation of lithium hydride in the cartridge-evaporator. Highlights of the installation system works according to the following principles: 1) acceleration of ions, 2) variable compression of successive discrete ion fluxes by a magnetic lens, 3) ensuring quasi-stability by converting ”outgoing fluxes” into rotation, 4) braking of the frontal current, which becomes the target, and collision with new particle fluxes (in fact, synthesis on oncoming beams), 5) ensuring ”multi-passability” of ion currents through the active zone chamber, 6) external electrical synchronization of the system, due to which point 5) above is also provided

The possible types of nuclear reactions supported in the considered electronically controlled plasma generator are indicated in the Table 1.

Reaction	Energy release, Mev	Бmax in the energy range of 1 Mev	Energy of the incident particle Бmax, Mev
$p + {}^{6}Li \rightarrow {}^{4}He + {}^{3}He$	4,0	10^{-4}	0,3
$p + {}^{7}Li \rightarrow 2{}^{4}He + \gamma$	17,3	$6 \cdot 10^{-3}$	0,25
$p + {}^{9}Be \rightarrow 2{}^{4}He + d$	0,56	0,46	0,33
$p + {}^{9}Be \rightarrow {}^{6}Li + {}^{4}He$	2,1	0,35	0,33
$p + {}^{11}Be \rightarrow 3{}^{4}He$	8,7	0,6	0,675
$p + {}^{15}N \rightarrow {}^{12}C + {}^{4}He$	5,0	0,69 (at 1,2 MeV)	1,2

Table 1: Fusion reactions supported in the considered generator

3. Discussion

The plasma dynamics inside the synthesis chamber can be described using the equations of magnetohydrodynamics. In our case, the plasma moves in a magnetostatic field, but which varies discretely. Calculations have been made for individual magnetic quadrupole lenses consequence for charged particle flows compacting in strong magnetic fields, including pulsed ones, and their advantages have been well studied and known [6–8]. Ion fluxes are considered as an ideal gas when describing particle velocities and describe them by Maxwell's equation. By changing the parameters of the magnetic lens, it is possible to change the parameters of the currents inside the synthesis chamber, which just affect the distribution of particles in space, which leads to a more structured target for more accurate further analysis bombardment by other streams.

As the result of the work, graphical dependences of the distribution of microcurrents and concentrations in the optimal sequence of solenoid and quadrupole magnetic fields are obtained.

References

[1] Dolgopolov M.V., Radenko V.V., Zanin G.G. etc. 2022 Electronically Controlled Plasma Power Devices for Sustainable and Environmentally Friendly Electric Energy Technologies // Advances in Engineering Research. Issue 210. P. 197-205

[2] Brown J G 2004 The Physics and Technology of Ion Sources (Wiley & Sons, Incorporated, John) 396 p

[3] Mecyach G A 2004 Pulsed power engineering and electronic (Moscow: Nauka) 704 p

[4] Forrester A T 1988 Large Ion Beams (New York: Wiley–Interscience) 325 p

[5] Akimchenko A et al. 2017 EPJ Web of Conferences 158 06004

[6] Watterson J I W, 2000 International Atomic Energy Agency 31 P. 5-14

[7] Dolgopolov M V et al., 2019 EPJ Web of Conferences 222 02014

[8] Tyrsa V E, Burtseva L P, 2003Technical Physics 48(7) P. 807-812

Analysis of electrical models of electronic components used in measuring technology

A V Volik[1], E A Pecherskaya[1], D E Tuzova[1], V A Listyuhin[1], A E Shepeleva[1] and D V Artamonov[1]

[1]Department of Information and measuring equipment and metrology, Penza State University, Penza 440026, Russia

pea1@list.ru

Abstract. The metrological analysis of the inverting integrator used in many devices for measuring the electrical parameters of materials and electronic components based on them is performed. Electrical models of resistors and capacitors, taking into account the presence of parasitic capacitances and inductances at different frequencies of the measuring signals, which leads to the occurrence of methodological measurement errors are considered. The results of the parasitic parameters analysis were used in the development of methods and techniques for compensating errors in measurements of hysteresis loops B (H) of magnetically soft materials using the measuring system proposed by the authors.

1. Introduction

Modern devices that measure the electrical and magnetic parameters of electronic materials are developing towards the widespread use of digital signal processing in various ways and methods [1, 2]: using general-purpose microcontrollers, FPGA circuits, signal controllers, DSP controllers. Methods of digital signal processing are the most effective, as they provide more stable temperature and time parameters, allow to change the transfer function coefficients. Digital signal processing methods have less impact on the output parameters of the signals under study. This is due to the absence of parasitic parameters inherent in passive components, including capacitors and resistors - one of the most common components of analog integrator circuits.

Integrating circuits are used in various functional units: voltage-frequency converters, frequency-voltage converters, analog-to-digital converters, control units in automatic control systems, pulse generators, active analog filters [3]. During the device operation, in the integrating circuit, it is necessary to change its parameters, namely the time constant, that is, to rebuild it. In this case, there are transient processes that affect the result of integration.

2. Structure and function of the inverting integrator transformation

The use of analog methods of integrating signals in measuring technology is accompanied by the occurrence of an error at the output of integrating circuits. The integration error is associated primarily with parasitic phenomena in the passive circuit elements. Below is an analysis of the electrical integrator model, which includes an operational amplifier, a resistor and a capacitor in the feedback circuit.

The integrator circuit allows the integration of the input signal over the frequency range. For example, it is advisable to use such an integrator as part of a channel for measuring the magnetic induction of soft magnetic materials; the generalized structure of the measuring system is presented in [1]. The main characteristics of the integrator depend on the time constant of the electrical circuit and the bandwidth of the operational amplifier. The input signal is applied to the inverting input of the amplifier, so the output voltage has the reverse polarity of the input signal. The scheme of an inverting integrator based on an operational amplifier is shown in Figure 1.

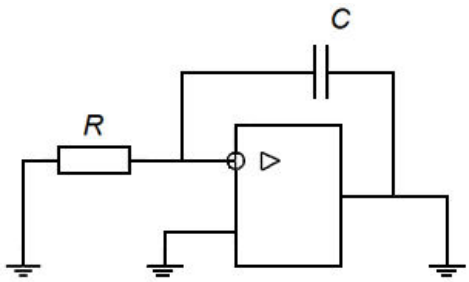

Figure 1. Basic circuit of an inverting integrator based on an operational amplifier

The input current U_{in}/R flows through capacitor C. Since the inverting input is potential-grounded, the output voltage is determined as follows:

$$U_{вых} = \frac{1}{RC}\int U_{вх}dt \quad (1)$$

Analysis of expression (1) allows to conclude that the determining factors in the operation of the integrated circuit are the parameters of the resistor R and capacitor C, which set the value of the integration time constant. In turn, the resistor and capacitor models can be represented as equivalent circuits shown in Figures 2 and 3, respectively. These models are simplified resistor and capacitor equivalent circuits showing the main parasitic parameters. It should be noted that parasitic parameters depend on the design and manufacturing technology of the electronic component [4].

3. Electrical Models of Resistor and Capacitor with Parasitic Elements

The equivalent circuit of the resistor includes, in addition to the resistance R, parasitic reactive elements - its own inductance L_0 and capacitance C_0, which distort the properties of the resistor at high frequencies, starting from a few MHz. The influence of parasitic oscillatory circuits, which represent the equivalent circuit of the resistor, are manifested when pulsed and high-frequency signals are transmitted through the resistor.

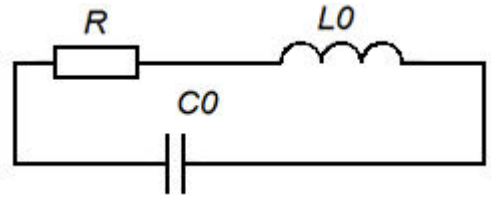

Figure 2. Simplified resistor equivalent circuit

The capacitor equivalent circuit takes into account the losses in the non-ideal dielectric resistor RC, and L is the parasitic inductance of the supply contacts. As with a resistor, the manifestation of parasitic quantities in a capacitor has an effect when operating at high frequencies.

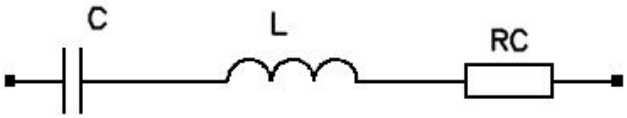

Figure 3. Simplified Capacitor Equivalent Circuit

For a surface mount capacitor (SMD or chip capacitor), the equivalent circuit shown in Figure 3 is complemented by an infinite resistor between the plates (RD) and two capacitors - parallel capacitances (CP) between pads on the PCB and the earth plane. The equivalent circuit for the SMD capacitor is shown in Figure 4.

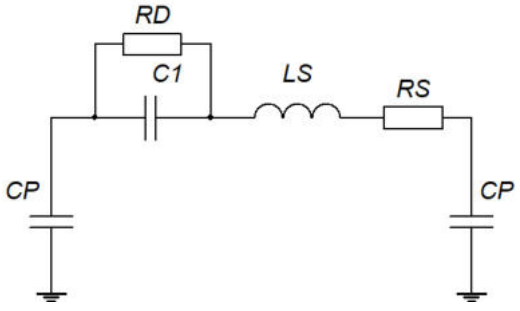

Figure 4. Equivalent circuit diagram of an SMD capacitor

At high signal frequencies, the inductance has the greatest non-linearity. In an ideal capacitor, the impedance (complex impedance) decreases infinitely with increasing frequency, but the presence of parasitic inductance causes the dependence of the impedance on frequency to behave non-linearly, dropping to the resonant frequency and then increasing. Figure 5 shows the capacitor impedance dependence on frequency.

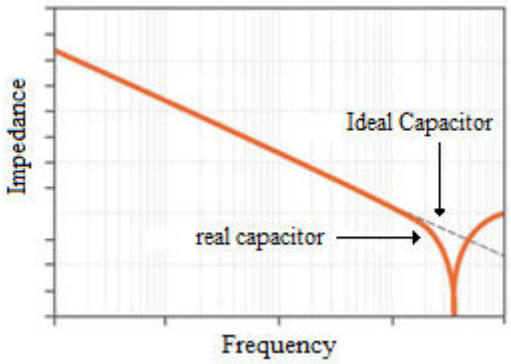

Figure 5. Capacitor impedance dependence on frequency

Conclusion

It is advisable to use the considered basic equivalent circuits of a resistor and a capacitor in the development of methods and techniques for compensating errors in measuring electrical parameters by means of measuring instruments, which include integrators. The measuring installation also becomes more complicated due to the introduction of capacitor discharge circuits in the measuring paths, which is also analyzed by the authors from a metrological point of view.

The proposed circuit design solution for the measurement installation of magnetic parameters includes a digital integrator based on a programmable logic integrated circuit (PLIC). The PLIC also performs the functions of a central processor that exchanges data with a personal computer via the RS232 interface, as well as setting measurement modes. The use of an PLIC-based digital integrator improves the measurement accuracy of *B*(*H*) hysteresis loops compared to an analog integration circuit.

References

[1] A V Volik, E A Pecherskaya, Y A Varenik, T O Zinchenko, D V Artamonov, O A Timohina 2021 Metrological aspects of an automated method for measuring electrophysical parameters of soft magnetic materials *Journal of Physics: Conference Series* **2086**(1) 012072

[2] P Golubkov, E Pecherskaya, O Karpanin, M Safronov, J Shepeleva, A Bibarsova 2019 Intelligent automated system of controlled synthesis of MAO-coatings *Conference of Open Innovation Association, FRUCT* 96–103, 8711874

[3] L He, J Sun, Z Lin, B Cheng 2021 Capacitor-Voltage Self-Balance Seven-Level Inverter with Unequal Amplitude Carrier-Based APODPWM IEEE Transactions on Power Electronics **36**(12) 9456989 14002-14013

[4] H Zhu, Y Y Zhao, J Ouyang, K Wang, H Cheng, Y Su 2022 Achieving a Record-High Capacitive Energy Density on Si with Columnar Nanograined Ferroelectric Films *ACS Applied Materials and Interfaces* 14 (6), 7805 - 7813

Analysis of electrical models of electronic components used in measuring technology

A V Volik[1], E A Pecherskaya[1], D E Tuzova[1], V A Listyuhin[1], A E Shepeleva[1] and D V Artamonov[1]

[1]Department of Information and measuring equipment and metrology, Penza State University, Penza 440026, Russia

pea1@list.ru

Abstract. The metrological analysis of the inverting integrator used in many devices for measuring the electrical parameters of materials and electronic components based on them is performed. Electrical models of resistors and capacitors, taking into account the presence of parasitic capacitances and inductances at different frequencies of the measuring signals, which leads to the occurrence of methodological measurement errors are considered. The results of the parasitic parameters analysis were used in the development of methods and techniques for compensating errors in measurements of hysteresis loops B (H) of magnetically soft materials using the measuring system proposed by the authors.

1. Introduction

Modern devices that measure the electrical and magnetic parameters of electronic materials are developing towards the widespread use of digital signal processing in various ways and methods [1, 2]: using general-purpose microcontrollers, FPGA circuits, signal controllers, DSP controllers. Methods of digital signal processing are the most effective, as they provide more stable temperature and time parameters, allow to change the transfer function coefficients. Digital signal processing methods have less impact on the output parameters of the signals under study. This is due to the absence of parasitic parameters inherent in passive components, including capacitors and resistors - one of the most common components of analog integrator circuits.

Integrating circuits are used in various functional units: voltage-frequency converters, frequency-voltage converters, analog-to-digital converters, control units in automatic control systems, pulse generators, active analog filters [3]. During the device operation, in the integrating circuit, it is necessary to change its parameters, namely the time constant, that is, to rebuild it. In this case, there are transient processes that affect the result of integration.

2. Structure and function of the inverting integrator transformation

The use of analog methods of integrating signals in measuring technology is accompanied by the occurrence of an error at the output of integrating circuits. The integration error is associated primarily with parasitic phenomena in the passive circuit elements. Below is an analysis of the electrical integrator model, which includes an operational amplifier, a resistor and a capacitor in the feedback circuit.

The integrator circuit allows the integration of the input signal over the frequency range. For example, it is advisable to use such an integrator as part of a channel for measuring the magnetic induction of soft magnetic materials; the generalized structure of the measuring system is presented in [1]. The main characteristics of the integrator depend on the time constant of the electrical circuit and the bandwidth of the operational amplifier. The input signal is applied to the inverting input of the amplifier, so the output voltage has the reverse polarity of the input signal. The scheme of an inverting integrator based on an operational amplifier is shown in Figure 1.

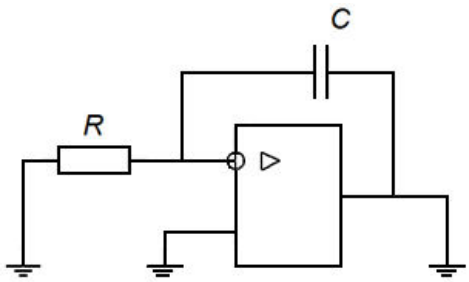

Figure 1. Basic circuit of an inverting integrator based on an operational amplifier

The input current U_{in}/R flows through capacitor C. Since the inverting input is potential-grounded, the output voltage is determined as follows:

$$U_{вых} = \frac{1}{RC}\int U_{вх}dt \quad (1)$$

Analysis of expression (1) allows to conclude that the determining factors in the operation of the integrated circuit are the parameters of the resistor R and capacitor C, which set the value of the integration time constant. In turn, the resistor and capacitor models can be represented as equivalent circuits shown in Figures 2 and 3, respectively. These models are simplified resistor and capacitor equivalent circuits showing the main parasitic parameters. It should be noted that parasitic parameters depend on the design and manufacturing technology of the electronic component [4].

3. Electrical Models of Resistor and Capacitor with Parasitic Elements

The equivalent circuit of the resistor includes, in addition to the resistance R, parasitic reactive elements - its own inductance L_0 and capacitance C_0, which distort the properties of the resistor at high frequencies, starting from a few MHz. The influence of parasitic oscillatory circuits, which represent the equivalent circuit of the resistor, are manifested when pulsed and high-frequency signals are transmitted through the resistor.

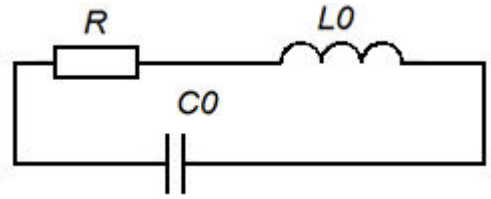

Figure 2. Simplified resistor equivalent circuit

The capacitor equivalent circuit takes into account the losses in the non-ideal dielectric resistor RC, and L is the parasitic inductance of the supply contacts. As with a resistor, the manifestation of parasitic quantities in a capacitor has an effect when operating at high frequencies.

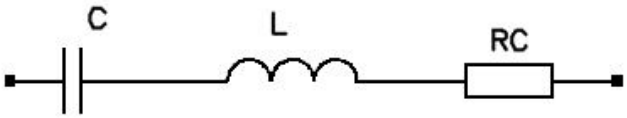

Figure 3. Simplified Capacitor Equivalent Circuit

For a surface mount capacitor (SMD or chip capacitor), the equivalent circuit shown in Figure 3 is complemented by an infinite resistor between the plates (RD) and two capacitors - parallel capacitances (CP) between pads on the PCB and the earth plane. The equivalent circuit for the SMD capacitor is shown in Figure 4.

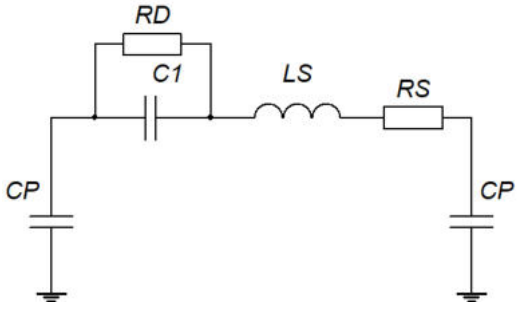

Figure 4. Equivalent circuit diagram of an SMD capacitor

At high signal frequencies, the inductance has the greatest non-linearity. In an ideal capacitor, the impedance (complex impedance) decreases infinitely with increasing frequency, but the presence of parasitic inductance causes the dependence of the impedance on frequency to behave non-linearly, dropping to the resonant frequency and then increasing. Figure 5 shows the capacitor impedance dependence on frequency.

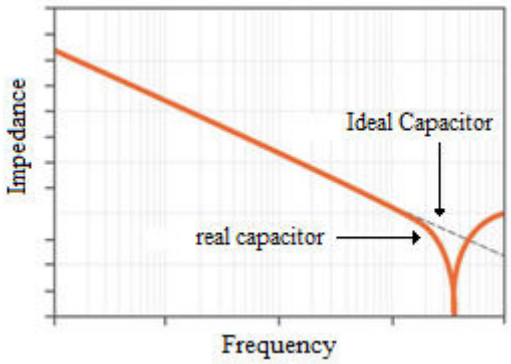

Figure 5. Capacitor impedance dependence on frequency

Conclusion

It is advisable to use the considered basic equivalent circuits of a resistor and a capacitor in the development of methods and techniques for compensating errors in measuring electrical parameters by means of measuring instruments, which include integrators. The measuring installation also becomes more complicated due to the introduction of capacitor discharge circuits in the measuring paths, which is also analyzed by the authors from a metrological point of view.

The proposed circuit design solution for the measurement installation of magnetic parameters includes a digital integrator based on a programmable logic integrated circuit (PLIC). The PLIC also performs the functions of a central processor that exchanges data with a personal computer via the RS232 interface, as well as setting measurement modes. The use of an PLIC-based digital integrator improves the measurement accuracy of *B*(*H*) hysteresis loops compared to an analog integration circuit.

References

[1] A V Volik, E A Pecherskaya, Y A Varenik, T O Zinchenko, D V Artamonov, O A Timohina 2021 Metrological aspects of an automated method for measuring electrophysical parameters of soft magnetic materials *Journal of Physics: Conference Series* **2086**(1) 012072

[2] P Golubkov, E Pecherskaya, O Karpanin, M Safronov, J Shepeleva, A Bibarsova 2019 Intelligent automated system of controlled synthesis of MAO-coatings *Conference of Open Innovation Association, FRUCT* 96–103, 8711874

[3] L He, J Sun, Z Lin, B Cheng 2021 Capacitor-Voltage Self-Balance Seven-Level Inverter with Unequal Amplitude Carrier-Based APODPWM IEEE Transactions on Power Electronics **36**(12) 9456989 14002-14013

[4] H Zhu, Y Y Zhao, J Ouyang, K Wang, H Cheng, Y Su 2022 Achieving a Record-High Capacitive Energy Density on Si with Columnar Nanograined Ferroelectric Films *ACS Applied Materials and Interfaces* 14 (6), 7805 - 7813

Higher spectral harmonics generation in an unamplified fiber ring resonator with electro-optical phase modulator

V S Gerasimenko, N D Gerasimenko and V M Petrov

ITMO University, Kronverksky 49, St. Petersburg, 197101, Russia

lyagacruz@gmail.com

Abstract. In this work, we studied the generation of high order spectral harmonics in an unamplified ring resonator with an electro-optical phase modulator. A phase modulator with electro-induced additional optical delay has been proposed. The system makes it possible to the fine-tune optical path length and, as a result, obtain relatively stable resonant spectra.

1. Introduction

The opportunities of higher spectral harmonics usage are very wide. In particular, they are used in modern communication systems. The most common methods for their generation exploit the eigenmodes of a passive ring microcavity with Kerr nonlinearity or work with the spectra of mode-locked lasers. However, both of these methods have significant limitations in the output spectrum parameters adjustment. Another method, that will be discussed in this paper, is the usage of electro-optical modulators, which output spectrum parameters can be changed by the control radio frequency (RF) source tuning[1].

The first works describing the use of electro-optical modulators for higher spectral harmonics generation were published in the mid-90s and were theoretical[2]. They considered ring fiber resonators or Fabry-Perot cavities using Bragg mirrors[3]. Both types of circuits had significant losses and therefore assumed the use of erbium amplifiers. Later experimental confirmation and development of these studies made it possible to significantly improve the results obtained, but still used amplifiers that produce significant noise at the eigenfrequencies of the resonator. Further research made it possible to abandon amplifiers due to the use of cascades of modulators (both phase and amplitude modulators were used in the circuits), however, such circuits required the use of complex systems for supplying and synchronizing control signals[4]. In the past few years, a lithium niobate thin films on a silicon oxide substrate modulators tecnology makes it possible to obtain a greater number of higher order harmonics in the spectrum at the same electrical power, but now this technology is still far from mass application[5].

Last few years, ITMO University produced the first samples of its own integrated electro-optical modulators on lithium niobate substrates[6]. Experiments on obtaining higher spectral harmonics with these modulators have demonstrated their great promise for this task. However, the performed work used standard phase modulators, which made it impossible to fine-tune the optical path length. Because of this, it was impossible to achieve optical and microwave resonance simultaneously in the experiment, which led to the instability of the output spectrum in time[7].

2. Experiment

Several samples of electro-optical phase modulators with the opportunity of additional optical delay controll were proposed and manufactured. This was realized through the use of capacitive electrodes with feeding scheme similar to an amplitude modulator one.

The scheme of the experiment (Figure 1, a) contains a laser source, a 99/1 X directional coupler, the phase modulator, and an optical spectrum analyzer (OSA). The light from the laser is divided on the coupler, and 1% of its power is looped in the fiber resonator with the modulator, so sidebands on the OSA are about 40 dB weaker than the unmodulated light (Figure 1, b).

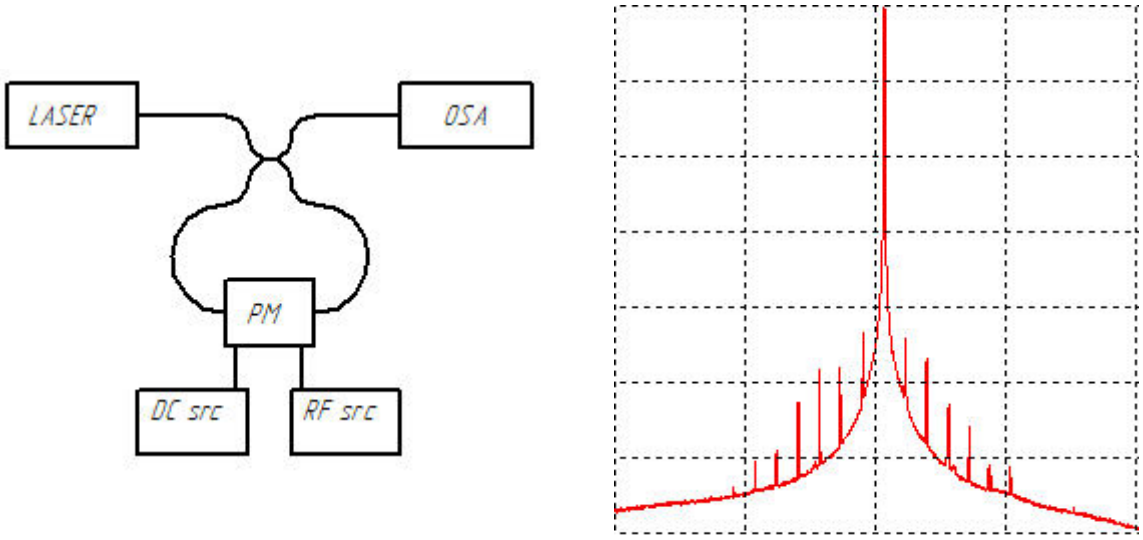

Figure 1. a) Scheme of experiment: LASER – laser source, OSA – optical spectrum analyzer, PM – phase modulator, DC src – source of control voltage for capacitive electrodes, RF src – source of harmonic RF signal. b) An example of output spectrum.

The performed experiments demonstrate increase in a number of sidebands for both RF and optical resonances. Also, when the optical resonance is reached the stability of output spectral comb increases too. However, even weak thermal changes can break the resonant conditions, and either a thermal stabilization or a fast electrical adaptation must be performed to further increase of the output spectrum stability.

3. Results and conclusion

The results obtained already show that the output spectrum generated in the fiber ring resonator with the modified electro-optical phase modulator is more stable and efficient than that obtained with a conventional one, but experiments in this area are still ongoing.

References

[1] Petrov V, Shamrai A *Interference and Diffraction for Information Photonics.* – SPb.: Lan'. 2019. 460 pp.
[2] Ho K and Kahn J 1993 *IEEE photonics technology letters* **5**(6) 721-725
[3] Kogahara S et al. 2007 *IEEE Photonics Technology Letters* **19**(19) 1565-1567
[4] Metcalf A J et al. 2013 *IEEE Journal of Selected Topics in Quantum Electronics* **19**(6) 231-236
[5] Ren T et al. 2019 *IEEE Photonics Technology Letters* **31**(11) 889-892
[6] Petrov V, Shamrai A et al 2020 *Photonics Russia* **14**(5) 414-423
[7] Petrov V, Shamrai A et al 2020 *Photonics Russia* **14**(7) 570-585

Features of the formation of the frequency of the microwave excitation signal in the quantum frequency standard

R A Dmitriev[2], A S Grevtseva[1] and V V Davydov[1, 3, 4]
[1]The Bonch-Bruevich Saint Petersburg State University of Telecommunications, Russia, Saint Petersburg
[2]Russian Institute of Radionavigation and Time, Russia, Saint Petersburg, 192012
[3]All-Russian Research Institute of Phytopathology, Moscow Region 143050, Russia
[4]Peter the Great Saint-Petersburg Polytechnic University, Saint Petersburg, Russia, 195251

e-mail: Rusher.official@gmail.com

Abstract. The article discusses the need to modernize the quantum frequency standard**.** The different navigation systems and them main characteristics are considered. An analysis of the characteristics of various designs of quantum frequency standards has been carried out. A solution is proposed to improve the design of the rubidium standard. A scheme of the upgraded part is presented.A forecast for improving its metrological characteristics is presented.

1. Introduction

In modern navigation systems, without determining the exact time and frequency, it is impossible to achieve the required accuracy in determining the coordinates. Data on the coordinates of the object is necessary for solving problems of environmental monitoring, carrying out various works, etc.. The operating satellite navigation constellations (Russian GLONASS, European GALILLEO, American (USA) GPS and Chinese BSD) actively use quantum frequency standards (QFS) to determine the exact time [1]. Among quantum standards in satellite communication systems, rubidium QFS's are most widely used due to their small size and low cost in comparison with other types of standards.

At present, with the development of electronic equipment, the requirements for the accuracy of satellite navigation systems are constantly increasing, which makes the task of their modernization especially urgent [2, 3]. This paper discusses one of the possible solutions for modernizing the design of a quantum frequency standard based on rubidium-87 atoms.

2. Modernization a part to design of the rubidium frequency standard

The principle of the QFS operation is based on automatic tuning of the crystal oscillator (CO) frequency to the value of the quantum transition frequency in optically oriented Rb-87 atoms. To implement the tuning of the CO frequency, the working cell of the atomic discriminator (DA) is irradiated with a microwave signal, the frequency of which corresponds to the frequency of the quantum transition of excited rubidium-87 atoms. In the case of a deviation of the frequency of the microwave signal from the value of the frequency of the resonant transition, an error signal (ES) is generated, according to which the CO is adjusted. Therefore, one of the important points in the functioning of the QFC is the formation of a microwave signal.

In this paper, a microwave signal with a frequency of 6834.7 MHz is proposed to be synthesized using a two-ring phase locked loop (PLL) system. New shaping circuitry includes a 6.8 GHz voltage controlled oscillator. To reduce the weight and size characteristics, the use of a VCO with a PLL in the form of a compact microwave module was chosen. An electrical circuit was developed for its operation and control. This scheme is shown in Figure 1.

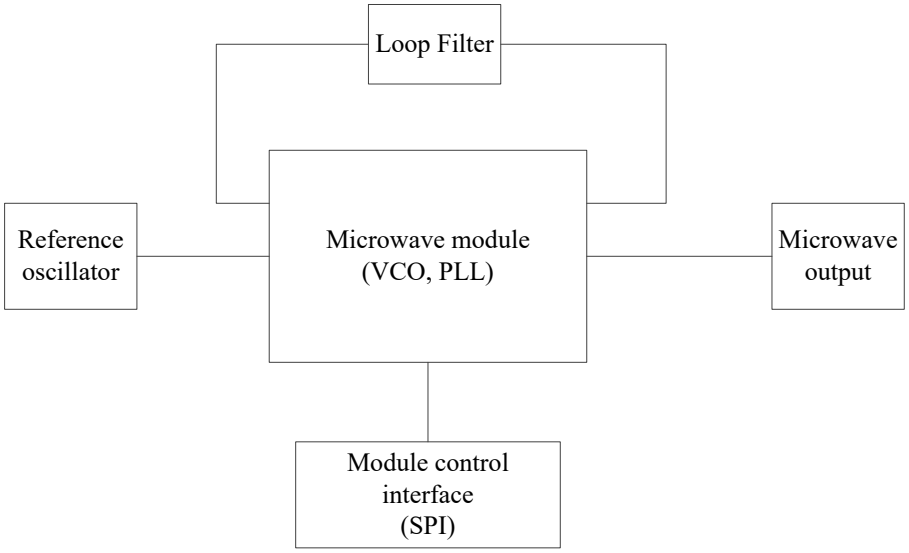

Figure 1. The frequency converter circuit for quantum frequency standard based on rubidium-87 atoms.

The developed design of the QFS has several significant advantages. First, the use of an indirect synthesis method, namely a phase-locked loop system, allows a cleaner spectrum of the output signal to be obtained. Secondly, the formation of the microwave signal at all stages of the new circuit is controlled; it is possible to precisely adjust the signal frequency to the frequency of the quantum transition of rubidium-87 atoms.

3. Conclusion

The developed design of the QFS has several significant advantages. First, the use of an indirect synthesis method, namely a phase-locked loop system, allows a cleaner spectrum of the output signal to be obtained. Secondly, the formation of the microwave signal at all stages of the new circuit is controlled; it is possible to precisely adjust the signal frequency to the frequency of the quantum transition of rubidium-87 atoms. This makes it possible to reduce the error in establishing the actual value of the frequency of the output signal of the rubidium RFS, which improves the stability of the device.

References

[1] Riechle F 2004 Frequency Standards. Basics and Applications (Wiley-VCH, New Jersy)
[2] Petrov A A, Shabanov V E, Zalyotov D V, Bulyanitsa A L and Shapovalov D V 2018 IEEE International Conference on Electrical Engineering and Photonics, EExPolytech 2018 (Saint-Petersburg, 2018) **8564389** 52-55
[3] Petrov A, Davydov V and Grebenikova N 2018 *Journal of Communications Technology and Electronics* **63(11)** 1159–1164

Lithium ions with energy 250-360 keV in the system of solenoidal and quadrupole magnetic fields

Elisov M.V.[1]

[1]Samara University, 34, Moskovskoye shosse, Samara, 443086, Russia

kovalski20031@mail.ru

Abstract. This publication considers the analysis and modeling of the motion of a stream of charged particles in magnetic fields, as well as in their various variations and combinations. The initial data are taken directly for the operating linear accelerator.

1. Introduction

Nowadays, the issue of electricity generation is extremely acute, it is aggravated by the gradual abandonment of fossil fuels and the transition to "green" methods of energy production, however, they are very expensive to use, and produce a relatively small amount of electricity. Research is being actively carried out on the industrial possibilities of thermonuclear fusion, however, the fusion of nuclei at millions of degrees Kelvin is still too complicated a process for mass industrial use, so now thermonuclear fusion in linear installations seems to be an urgent solution. In order for two nuclei to enter into a thermonuclear reaction, it is necessary to overcome the repulsion barrier, which happens if two nuclei are brought close enough to each other to overcome the potential barrier and start the process of thermonuclear fusion of light nuclei. This is possible with the help of acceleration and compaction of flows of charged particles by magnetic fields. The paper considers the control of particle flows with the help of a system of sequentially arranged solenoidal and quadrupole magnetic fields.

2. System Description and Graphical Modeling

We assume that the ion flux injected into the magnetic field is uniform, entering at an angle α to the direction of the central lines of force. We also accept that the initial velocities of the ions obey a uniform distribution, that is, in the range of initial velocities, any of them is equiprobable.

In this research, we consider particles with initial velocities of 9000 m/s - 11000 m/s, mass 10^{-24} kg, charge $3.2 \cdot 10^{-19}$ C, the mathematical package Mathcad is used as a modeling environment.

As follows from the obtained model, the particle beam with the given initial conditions does not exceed 5–6 mm in radius.

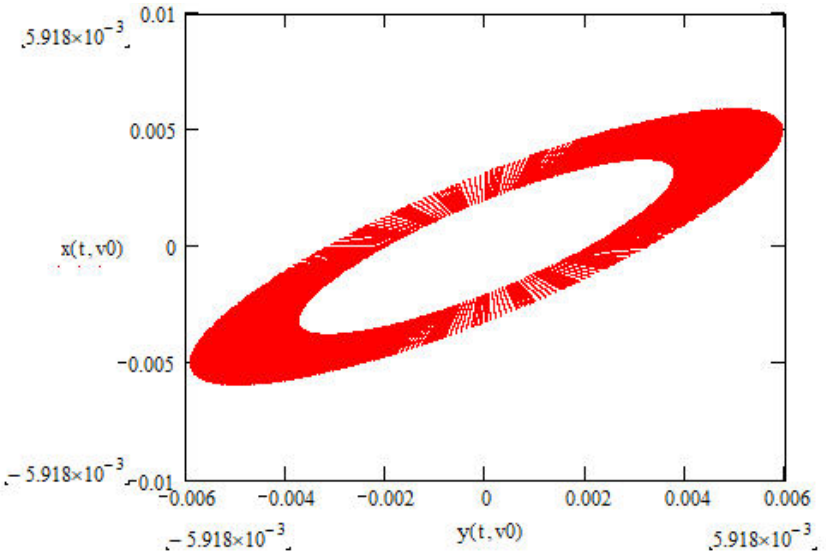

Figure 1. Transverse emittance of an ensemble of particles with different initial velocities

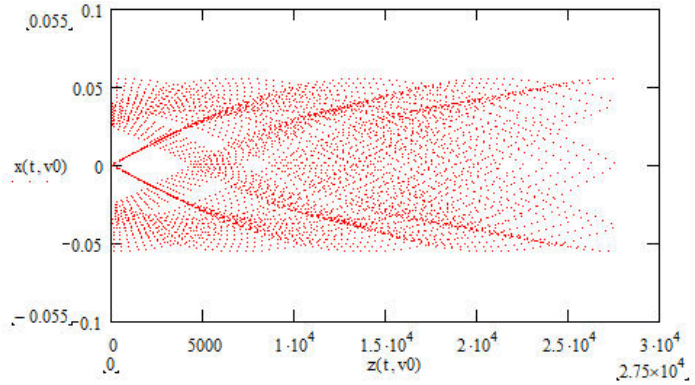

Figure 2. Longitudinal emittance of an ensemble of particles with different initial velocities

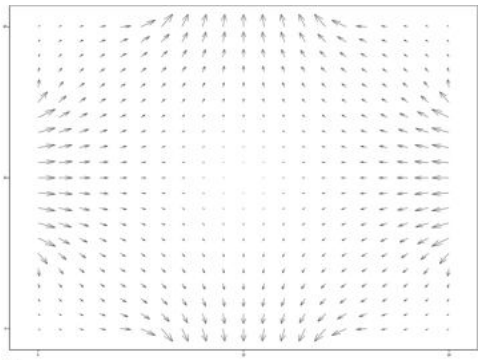

Figure 3. Magnetic quadrupole field strength distribution

3. Conclusion

The law of motion of charged particles in a magnetic field was obtained, with the help of which images of the distribution of charged particles in the phase space were constructed. Qualitative and quantitative characteristics of the movement of ions were obtained.

References

[1] Morozov A.I. Introduction to plasma dynamics, Moscow: FIZMATLIT, 2006.

[2] Paul W. Electromagnetic traps for charged and neutral particles // Uspekhi fizicheskikh nauk. - 1990. - T. 160, No. 12. — pp. 109–127.

[3] Dolgopolov M.V., Radenko V.V., Zanin G.G. etc. Electronically Controlled Plasma Power Devices for Sustainable and Environmentally Friendly Electric Energy Technologies // Advances in Engineering Research 2022. — Issue 210. — P. 197-205

Study of the "peak effect" at approach-retraction curves in a scanning ion-conductance microscopy

M V Zhukov, S Yu Lukashenko, I D Sapozhnikov, M L Felshtyn, O M Gorbenko, and A O Golubok

Laboratory of scanning probe microscopy and spectroscopy, Institute for Analytical Instrumentation RAS, St. Petersburg 198095, Russia

E-mail: cloudjyk@yandex.ru

Abstract. Using the direct current scanning ion-conductance microscope (DC-SICM) the dependence I(z) of ion current trough nanopipette from distance to surface of a soft polyethylene sample immersed in electrolyte have been studied. The borosilicate glass capillaries with an internal diameter of 100 nm and taper angle of ~ (3-5)° at the pointed end have been fabricated and used as SICM probes. In addition to the usual decreasing of the ion current the dependences I(z) with an increasing and decreasing branches of the current with point of maximum current as the nanopipette approaches the sample were also observed. We called this phenomenon the "peak effect". The peak effect was studied at various aqueous NaCl buffer concentration, nanopipette aperture sizes, applied voltages and saturation currents away from the sample.

1. Introduction

In the direct current scanning ion-conductance microscope (DC-SICM) the ion current through glass nanopipette (NP) probe filled with electrolyte decreases as NP approaches to the sample immersed in electrolyte because the surface of the sample blocks the flow of ions. This dependence makes it possible to use a feedback loop for surface topography visualization according to the principle of scanning probe microscopy (SPM). This method based on the simple geometric model of ion current decreasing near the sample surface was first described by Paul Hansma in 1989 [1]. However, the behaviour of the ion current flowing through the NP near the sample surface is not so simple. Thus, contrary, at the [2, 3] the effect of ion current elevation when NP approaches to the sample was demonstrated. At the same time, the authors of [2,3] focused on the area with a monotony current increasing , but do not study the peak on the I(z) dependency when NP approaches the sample surface which we'll call the “peak effect”.

The aim of the work was to study the "peak effect" on the current/distance curves between the pipette and the sample I(z) at various ionic strength of the electrolyte and polarity of the applied voltage.

2. Experimental setup

Borosilicate glasses NP have been fabricated by thermal melting and rupture at PMP-107 (Micro data instrument inc., USA). A “hand-made” SICM measuring head and a control/data acquisition unit have been used based on SPM Nanotutor (NT-SPb, Russia). The quality of the NP has been controlled using a scanning electron microscope Inspect (FEI, USA). The inner diameter of the pipette tip was

~100 nm with a tip taper angle of ~3-5˚, resistance of the NP of about 100 MOhm. Chlorinated silver filaments AgCl were used as electrodes, and aqueous saline solutions of NaCl (0.1; 0.9 and 10% wt.) were used as a buffer.

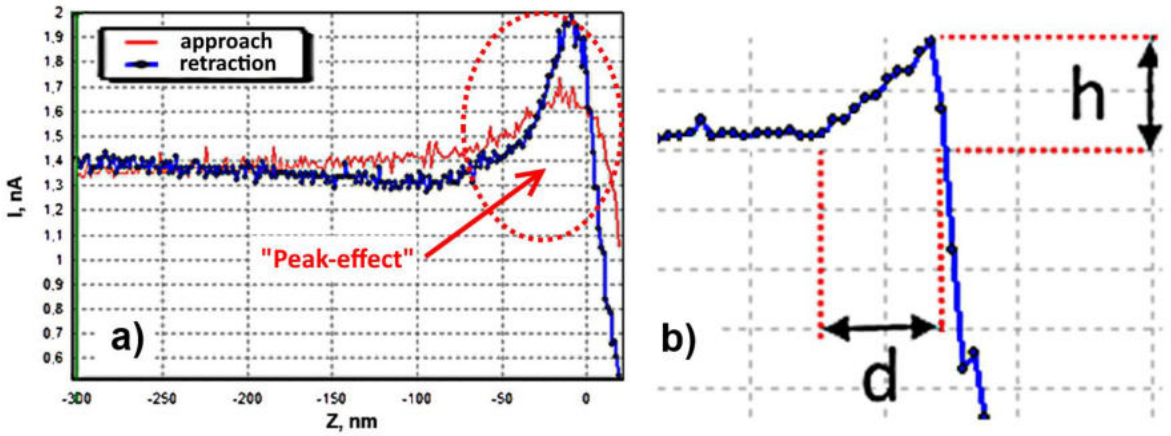

Figure 1. I-Z curve of approaching/retracting NP to the sample with a "peak effect" (a) and shape of the peak (b) on a retraction curve as an example: height (h, nA/%) and width (d, nm). Zero point (Z=0 nm) - near the sample.

3. Results and Discussions

We studied the features of the current-distance (I-Z) curves at different interaction parameters (I from 1 to 9 nA, U from 0,3 to 1 V) and NaCl buffer concentration (0,1%, 0,9%, 10%). With a decrease in the buffer concentration, due to a decrease in conductivity, the capture current decreases, and the applied voltage has to be increased. It was found that under our conditions, the peak is more noticeable on the removal curve for NaCl buffer concentrations of 0.1 and 0.9% (standard saline solution). The maximum value of the peak was about 80% from the saturation current at a width of about 50 nm (at 1.4 nA and 1 V). Peak height and width for 0.9% NaCl buffer decrease when decrease U and I, specifically peak height ~15% and width ~50-120 nm at 0.5V (current 8 nA) to ~10% and ~20-40 nm at 0.3V (current 5 nA). In some cases, there is a large hysteresis in the approach and retraction curves, which, as a rule, is strongly manifested when measuring from an array of points. When working with 10% NaCl buffer, a small "peak-effect" in the centre and bottom of the I-Z curve was revealed, the height from the saturation current ~7% at a width ~50 nm. In mixed mode (0.1% NaCl buffer in a pipette, 10% NaCl buffer in a bath), the current-voltage characteristic is unstable and changes with time, a "smoothed" peak appears ~2-5% at a width ~200 nm. In the mixed mode, an inverse peak (to the other side) is detected with a height ~ 18% and a width ~50 nm. Distance from the beginning of the current drop to the sample: 0.1% NaCl buffer - 20-50 nm, 0.9% NaCl buffer - 50-150 nm, 10% NaCl buffer - 200-300 nm, mixed mode 0.1-10% NaCl buffer - 50-300 nm. Thus, the largest peak effect is seen at 0.1%, the smallest and inverted peaks in mixed mode, at 10% there is peak phenomena in the centre and bottom of the I-Z curve. It should be noted that the effect does not always appear, and when measuring from an array of points, the probability of finding a peak effect is about 50%. It follows from the data that, with a high degree of probability, a peak effect appears when an I(V) dependence of nanopipette has a diode-like form [4]. It should be noted that the peak appeared at one polarity (when Cl^- ions flows out of the NP) and NP outlet radius not more than ~100–150 nm.

In conclusion, we note that the appearance of a peak on the approach curve can be the reason for the unstable operation of the scanning probe microscope in the DC SICM mode. Indeed, the servo system in the DC SICM mode is tuned to decrease the ion current as the probe approaches the sample. If the reference value of the current in the DC SICM mode has a value that falls into the area of increasing current when the nanopipette approaches the sample surface, instabilities and noise will appear on the SICM image.

Acknowledgments
Work carried out with the support of the state assignment № FFZM-2022-0008 (theme № 22 542,089) of the Ministry of education and science of the Russian Federation.

References
[1] P. K. Hansma, B. Drake, O. Marti , et al. 1989 *Science* **243(4891)** 641–643.
[2] Richard W. Clarke, Alexander Zhukov, et al. 2013 *J. Am. Chem. Soc.* **135(1)** 322–329.
[3] Kim McKelvey, Sophie L. Kinnear, et al. 2014 *J. Am. Chem. Soc.* **136 (39)** 13735–13744.
[4] M V Zhukov, S Yu Lukashenko, et al. 2020 *J. of Phys.: Conf. Ser.* **1695** 012167.

Rail condition monitoring using LSTM recurrent neural networks

M A Denisenko[1], A S Isaeva[1], I N Kots[1]
[1]Southern Federal University, Taganrog, 347922, Russia

isaevaas@sfedu.ru

Abstract. In this paper the solution of the multiclass classification problem of the events recognition during the movement of a bogie model along rails containing defects is described. The problem was solved using LSTM recurrent neural networks and implemented by Python programming language. The method of the data collection and the description of the test stand is given. Conclusions about the efficiency of event recognition from a given set are made.

1. Introduction

Improving the efficiency of detecting defects in the railway track is an urgent task for any state that implements railway communication on its territory. The large length of railway tracks (more than 85 thousand kilometers of general-purpose tracks in the Russian Federation) makes it difficult to regularly inspect them and detect defects. All over the world, systems for diagnosing the condition of railway tracks are being actively developed, including the use of artificial intelligence systems [1-3]. Development of monitoring systems installed on existing railway cars and (or) trains, transfer and aggregation of the received data, analysis and identification of places of possible defects sems to be a good strategy. Data from a microphone, an accelerometer, a gyroscope, a photos of a railway tracks, etc. could be analyzed. In this paper we used information about accelerations that a vehicle moving on rails is subjected to.

2. Test bench development

A model of a railway bogie was designed and manufactured for this experiment. Bogie is complected with an NVIDIA Jetson module, a Bluetooth/WiFi wireless data transmission module, sensitive elements - an inertial accelerometer module, and a power bank.

The rail track model consists of two metal L-shaped (3 × 3 cm) profiles 4 mm thick and 2 m long, fixed on wooden bars. The bogie rolls along the top edge of the profile. There are two such structures, so we have a total track length of 4 m and a joint that imitates a non-welded butt rail joint. The model was leveled and fixed on a solid base. A defect imitating rail spalling was applied to the working surface.

3. Data collection and processing

For the task of multiclass classification solving six variables were used: activity, user, timestamp, x-axis, y-axis, z-axis. Activity is the target variable and its takes three values: 1 (corresponds to the event "driving on rails"), 2 (corresponds to the event "non-welded joint of the rail track detected") and 3 (corresponds to the event "defect detected "). The x-axis, y-axis, z-axis are accelerations along the x, y, z axes. Numeric variables were normalized and converted to binary features, i.e., to a unitary code (one-hot encoding). In total, the training sample included 1957111 acceleration measurements, the test sample

included 489275 measurements, that is, 80% and 20%, respectively, of the entire data set: 840,536 acceleration measurements were collected when a bogie model traveled on rails that did not contain defects, 775,118 acceleration measurements when a bogie model traveled along a joint, and 830,735 acceleration measurements when a bogie model traveled along a defect. Accelerations were taken at a sampling rate of 400 Hz.

4. Neural network training and classification

To implement the event recognition algorithm, a network of long short-term memory (LSTM) was used. It is a one of recurrent neural networks. The LSTM network is well adapted to learning on the problems of classification, processing and forecasting of time series in cases where important events are separated by time lags with indefinite duration and boundaries. To improve the performance of the model, a bidirectional LSTM network (Bidirectional LSTM) was used. Unlike a conventional LSTM network, a bidirectional LSTM network is trained on both the direct and external side of the input data [4].

The LSTM neural network was implemented using the Keras library. It consists of one layer of 128 neurons. The model was trained for 20 epochs, batch size = 32. During the training of the neural network, frames of 200 and 500 values of the timestamp feature were used.

5. Conclusion

The neural network determines the event with an accuracy of 91%. The largest number of errors occurs due to the fact that the model cannot distinguish between the events “non-welded track joint detected” and “defect detected”.

Acknowledgments

The work was carried out at the expense of funds, task No. FENW-2020-0022 for the implementation of scientific research carrying out scientific research at the expense of the Federal budget, in terms of scientific activities on the topic "Development and research of methods and means of monitoring, diagnostics and forecasting state of engineering objects based on artificial intelligence".

References

[1] X. Giben, V. M. Patel and R. Chellappa. Material classification and semantic segmentation of railway track images with deep convolutional neural networks // 2015 IEEE International Conference on Image Processing (ICIP). – 2015. – PP. 621-625.

[2] X. Gibert, Xavier, P. Vishal, R. Chellappa. Robust Fastener Detection for Autonomous Visual Railway Track Inspection // Proceedings - 2015 IEEE Winter Conference on Applications of Computer Vision. – 2015.

[3] C. Yang, Y. Sun, C. Ladubec, Y. Liu. Developing Machine Learning-Based Models for Railway Inspection // Applied Sciences. – 2021. – Vol. 11(1):13.

[4] Ralf C. Staudemeyer, Eric R. Morris. Understanding LSTM - a tutorial into Long Short-Term Memory Recurrent Neural Networks // ArXiv. –2019.

Improvement of the characteristics of the frequency synthesizer in the quantum frequency standard on caesium atoms

E V Isupova[1], A S Budnikov[1], S Y Shvetsov[2] and V V Davydov[1, 3, 4]
[1]Peter the Great Saint-Petersburg Polytechnic University, Saint Petersburg, Russia, 195251
[2]Russian Institute of Radionavigation and Time, Saint Petersburg, 192012, Russia
[3]The Bonch-Bruevich Saint Petersburg State University of Telecommunications, Saint Petersburg, 193232, Russia
[4]All-Russian Research Institute of Phytopathology, Moscow Region 143050, Russia

e-mail: isupova.e24@mail.ru

Abstract. A new circuit of a frequency synthesizer is presented, which is an important functional node in the quantum frequency standard on caesium atoms. The advantages and disadvantages of the new signal synthesis method are considered in detail. By increasing the bit depth of the accumulating adder, it was possible to reduce the step of tuning the output frequency by several orders of magnitude. This method meets all the requirements for the parameters of frequency synthesizers.

1. Introduction

The first frequency standard on ^{133}Cs atoms was developed in the middle of the 20th century. It is this standard, unlike others, that has an exact unit of time and a uniform time scale. Since that time, the quantum frequency standard (QSF) on caesium atoms has been modified, due to the development of electronics, materials and much more. The block diagram of the quantum frequency standard on ^{133}Cs atoms is shown in Fig. 1.

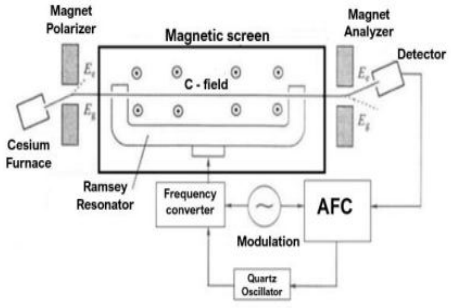

Figure 1. The structure scheme of the atomic clock.

One of the important functional units of the quantum frequency standard is the frequency synthesizer. The synthesizer is a source of stable vibrations in devices that require tuning to different frequencies in a wide range and high stability of the selected frequency [1].

Currently, the signal synthesis method has exhausted the possibilities for increasing accuracy [2]. Since the accuracy of the frequency generated by the synthesizer affects the accuracy of the resonant transition frequency and other characteristics of the CSF output signal, a large resolution is required.

2. Method and description of the improved synthesizer

The new design of the digital frequency synthesizer uses the method of direct digital synthesis. This solution is due to some advantages in comparison with other methods of frequency synthesis. Digital systems synthesize a signal with precise specified characteristics. Output signal parameters such as frequency, amplitude, and phase are precisely known and continuously controlled by the system. High frequency and phase resolution, fast switching to another frequency and high tuning speed in the absence of outliers or other distortions that may occur due to the establishment time, a wide range of generating frequencies are also advantages of this method.

The synthesizer circuit based on this method includes only one unstable element - a digital-to-analog converter. This instability is characteristic of all analog circuits.

Modern synthesizers use an updated version of direct digital synthesis. For this reason, the ROM address counter has been replaced with an accumulating adder. The accumulating adder is a register, at each clock cycle, of which the device is rebooted. Also, for each clock cycle of the device, the value obtained earlier is summed and the constant summand is summed with accumulation. The final scheme of the synthesizer is shown in Fig. 2.

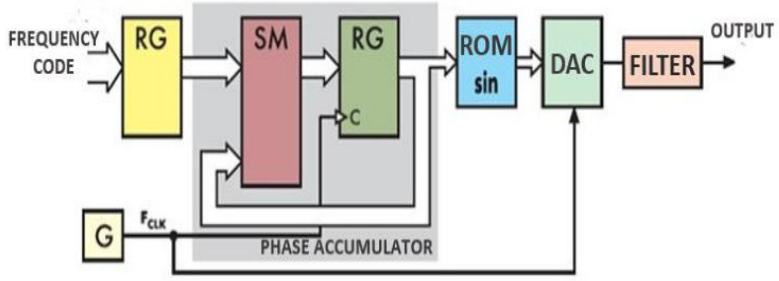

Figure 2. Digital synthesizer circuit.

3. Results and conclusion

The parameters of the frequency synthesizer are extremely important for communication devices and frequency standards. It is the synthesizer that sets the characteristics of each specific device, since it is the main unit of the system. The parameters of the synthesizer based on the DDS ("direct digital synthesis") method meet most of the technical and economic requirements. In addition, most of the parameters of such a synthesizer are controlled by the program. All the above features define DDS synthesizers as very promising devices.

During the research, a new design of a frequency synthesizer based on the direct digital synthesis method was developed. The main difference between the new model and the previous one was an increase in the bit depth of the accumulating adder, which is a phase accumulator. The bit depth of the adder increased from 32 bits to 40, which led to a decrease in the step of tuning the output frequency by several orders of magnitude.

References

[1] Riechle F 2004 Frequency Standards. Basics and Applications (Wiley-VCH, New Jersy)
[2] Petrov A, Davydov V and Grebenikova N 2018 *Journal of Communications Technology and Electronics* **63(11)** 1159–1164

Low-induction integral heater for temperature control of MEMS vapor cell

R Kenesbay[1], Y Enns[1,2], A Kazakin[1,2], I Komarevtsev[1,2], Y Akulshin[1]

[1]Peter the Great Saint-Petersburg Polytechnic University, St. Petersburg, Russia
[2]Alferov University, St. Petersburg, Russia

kenesbaj.r@edu.spbstu.ru

Abstract. This paper describes a solution to the problem of temperature control and the occurrence of a magnetic field created by a resistive heater in a vapor cell of an atomic clock. A low-induction integral heater was developed in the form of a two-layer metallization system that mutually compensates for each other's magnetic fields. Numerical simulation was carried out, based on the results of which a prototype of a low-induction integral heater was developed using precision photolithography and technologies for applying thin-film conductive and dielectric coatings.

1. Introduction

Atomic frequency standards based on the absorption of alkali metal vapors (Cs or Rb) are the most precision standards of frequency and time. The development of microelectronics and microsystem technology provides technical opportunities for their integrated production, miniaturization, reduction of power consumption and cost. These devices include a cell in the form of a sealed capsule filled with alkali metal vapors. However, the disadvantage of reducing the overall sizes of the atomic clock cell is a decrease in the optical path, and therefore a decrease in the intensity of the output signal. An increase in the temperature of alkali metal vapors (80-200°C), leading to an increase in the atomic density of vapors, is a key aspect of increasing the intensity of the output signal [1]. In addition, thermal stabilization has a high value, since temperature fluctuations can lead to changes in atomic density, relaxation rate and polarization [2]. Thus, the system of temperature setting and controlling is one of the key components of the atomic clock system.

Typical power for atomic clock cells is approximately 1 mW - 50 W, depending on the size and materials of the cell, as well as the casing [3], [4]. However, the use of typical resistive heaters leads to the formation of a parasitic magnetic flux density, due to the flowing current of the heater. The use of traditional heaters is impossible due to the extreme sensitivity of atomic cells to magnetic flux.

One of the ways to create a non-inductive heating and thermal stabilization is the using of hot air flow [5]. This method of heating the vapor cell is non-magnetic and allows to achieve high heating power. But its application requires high power consumption and has a low integration ability. An alternative method is the sequential combination of two parallel resistive heaters in the form of meanders [2]. This arrangement leads to compensation of the magnetic flux density, which is generated by each heater. However, the distance between the metal lines is on the order of a millimeter and its reduction is necessary to enhance the effect of magnetic flux suppression [6].

This project is aimed at solving the problem of creating a low-induction integral heater and a resistive thermometer for atomic clock cells. The solution of the problem is based on the formation of a two-layer metallization system mutually compensating magnetic fields of each other. In the course of the work, numerical modeling methods will be used to optimize the thermal stabilization system and the following production of prototypes using thin-film conductive and dielectric coating technologies, and also will be used precision photolithography.

2. Results

The results of numerical simulation showed the possibility of reducing the magnetic field density to 10^{-12} T. Based on the obtained results, the construction of the integral low-induction integral heater was designed and produced. The construction includes a two-layer metallization system of a heater and a thermistor. The heater and thermistor were made by magnetron sputtering of Cr and SiO_2 layers on a LK-5 type glass substrate. The thickness of the metallization layer and the SiO_2 insulation layer was 100 nm and 400 nm, respectively.

A fabricated low-induction integral heater was placed at the bottom of the vapor cell. The temperature of the vapor cell was controlled by an additional platinum microthermometer mounted on top of it. The resulting assembly was mounted on a ceramic suspension to reduce heat leakage. The ceramic suspension was made by laser scribing.

The static and dynamic characteristics of the integral heater were determined as a part of the work in the test unit. The received measurements showed a low-inertia nature and the possibility of thermal stabilization of the cell temperature in the range up to 100°C with a power consumption of up to 0.7 W.

Acknowledgments

This work was carried out in Peter the Great St.Petersburg Polytechnic University and was supported by a grant of Russian Science Foundation (project № 20-19-00146).

References

[1] Seltzer S J 2008 *Princeton University*
[2] Wyllie R 2012 *University of Wisconsin-Madison*
[3] Shah V, Knappe S, Schwindt P D D, Kitching J 2007 *Nature Photonics* **11** 649-652
[4] Vasilakis G 2011 *Princeton University*
[5] Allred J C, Lyman R N, Kornack T W, Romalis M V 2002 *Physical Review Letters* **13** 130801
[6] Schwindt P D D, Lindseth B, Knappe S 2007 *Applied Physics Letters* **8** 081102

The kinetic simulation in vacuum electronics: uncovering the fundamental nature of non-Maxwellian distribution function effects

Vasily Kozhevnikov, Andrey Kozyrev, Aleksandr Kokovin, Natalia Semeniuk, Aleksey Sitnikov

Institute of High Current Electronics SB RAS, 2/3 Akademichesky ave., 634055 Tomsk, Russian Federation

Vasily.Y.Kozhevnikov@ieee.org

Abstract. This paper presents main theoretical results obtained in vacuum explosive-emission electronics by using of the numerical methods aimed to the direct solution of Vlasov-Poisson kinetic equations. It was shown that computational physical kinetics makes it possible to explain a number of important physical laws occurring in vacuum diodes unlike widely used Particle-in-Cell or hydrodynamic simulation. The kinetic approach makes it possible to take into account nonequilibrium non-Maxwellian effects mainly associated with the "tails" of distribution functions. The advantages of kinetic simulation are shown on two highly relevant problems of vacuum electronics are considered in details.

Here we demonstrate the advantages of a fundamental theoretical approach based on the application of the physical kinetics principles to the vacuum electronics. This approach differs from hydrodynamic and particle-in-cell simulation modeling. Namely, it is based on the calculation of nonstationary nonequilibrium distribution functions for ensembles of charged particles.

Two important fundamental problems of vacuum electronics are considered as subjects of research. The first one is devoted to the appearance of electrons having anomalously high kinetic energies ε (significantly exceeding the maximum value of the voltage drop across the diode, i.e. $\varepsilon > qU_{\max}$) in vacuum diodes. It was shown that such fraction of electrons exists in diodes with an unrestricted electron emission only if the anode voltage rise front is sufficiently short comparing to the electron beam transition time. In such case the space-charge relaxation oscillations arise. The resulting anode current also oscillates with an amplitude exceeding the known Child-Langmuir value. It was discovered in terms of physical kinetics that the maximum current amplitude is delivered by high-energy electrons with energies ε greater than $qU_{\max}$.

Another actual problem is connected to the phenomenon of the "anomalous" ion transportation that plays key role during the initial stage of a vacuum breakdown stage in vacuum diodes with a quasi-continuous cathode plasma emission. We provide a self-consistent explanation of the phenomenon in terms of one-dimensional collisionless plasma kinetic model based on Vlasov-Poisson set of equations for the charged particles ensembles. The derived numerical solution of the model non-stationary equations shows that the "anomalous" transport has an electrodynamic nature connected with dynamics of the electric potential minimum ("virtual cathode") arising self-consistently. Also, the role of collisional processes

on the electrodynamic nature of the "anomalous" transport of cathode plasma ions is clarified in the work.

References

[1] Kozhevnikov VY, Kozyrev AV, Kokovin AO. 2021 Journal of Physics: Conference Series **2064** 012025

[2] Kozhevnikov V, Kozyrev A, Kokovin A, Semeniuk N. 2021 Energies **14** 7608

[3] Kozhevnikov VY, Kozyrev AV, Semeniuk NS. 2017 IEEE Transactions on Plasma Science **45** 2762

Monitoring of overhead power lines parameters in real time

V A Listyuhin, E A Pecherskaya, P E Golubkov, O V Karpanin, V S Alexandrov, D V Artamonov

Department of Information and measuring equipment and metrology, Penza State University, Penza 440026, Russia

Corresponding author: nauka-fpite@mail.ru

Abstract. Using quality control methods, an analysis of the technological disturbances (accidents) causes on overhead power lines with a voltage of 0.4 to 110 kV AC was made. The main causes of accidents on overhead lines are systematized. The need to control the operational parameters of overhead lines that affect the sustainable functioning of electric power systems has been proved. The structure of the information-measuring system for monitoring the parameters of overhead power lines, the purpose of which is to ensure reliable power supply to consumers, improve the level of operational and technological control of networks and reduce the economic costs of eliminating the consequences of accidents in electrical networks.

1. Introduction

Due to their design, overhead power lines (OL) are the most vulnerable element of electric power systems, which has the greatest impact on the reliability of power supply to consumers [1]. A lot of research has been directed to solving the problems of ensuring the stable functioning of overhead lines. For example, in [2], the authors propose to monitor the position of the overhead line wire according to the following parameters: ambient air temperature and power transmitted through the conductor. In [3], the author assesses the reliability of overhead lines depending on the impact of natural factors (ambient air temperature and wind loads). The studies presented in [4] are aimed at creating a system for controlling the wire sag by an optical-mechanical system using an optical fiber that is resistant to electromagnetic fields and ambient temperature. Based on the analysis of statistical data of the causes and consequences of accidents on overhead lines, the authors propose the development and implementation of an information-measuring system for monitoring parameters that affect the stable operation of power lines.

2. Materials and methods

Based on the analysis of the number and causes of technological disturbances (accidents) in electrical networks with a voltage in the range from 0.4 to 110 kV AC, the main causes of overhead line failures were identified, namely: untimely detection of defects (44.43% of the total number of accidents); impact of climatic events (31% of the total number of accidents); unsatisfactory technical condition of the equipment caused by aging, changes in the properties and the material structure (23% of the total number of accidents).

In order to reduce the number of technological disturbances at the facilities of the power grid complex, improve the efficiency of monitoring the network, as well as improve the quality indicators of services provided to consumers for the transmission of electrical energy, the authors propose the

development and implementation of an information-measuring system for monitoring the power lines parameters [5].

3. Characteristics and functionality of the developed information-measuring system

During the operation of overhead lines, the information-measuring system monitors the parameters that affect its stable operation, namely: the wire sag control; ambient temperature control; wind load speed control; indication of the damage location (short circuit) on the line. Table 1 presents the characteristics of the measuring IMS channels.

Table 1. Characteristics of the measuring IMS channels.

Channel name	Measuring device name	Measured value	Measurement range	Limits of permissible absolute error
Distance measurement channel	Laser distance meter	Distance	0.5-35 m	±0.1
Ambient temperature measurement channel	Thermal anemometer	Ambient temperature	-45–+45 °C	±0.5
Channel for measuring the wind loads speed	Thermal anemometer	Speed	0-30 m/s	±1
Fault location	Fault indicator	Short circuit direction	20 - 120 A	±1

Conclusion

The introduction of the proposed information-measuring system will ensure the reliability of the electrical networks operation and improve the quality of services provided to consumers for the electrical energy transmission due to the timely detection of defective sections, by detecting the stage of the initial formation of a defect and timely preparation of preventive measures to ensure uninterrupted power supply. The use of an information-measuring system is advisable for the operational maintenance and management of electrical networks.

References

[1] H Zangl, T Bretterklieber, G Brasseur G 2009 A feasibility study on autonomous online condition monitoring of high-voltage overhead power lines *IEEE Transactions on Instrumentation and Measurement* **58**(5) 1789-1796

[2] S D Gupta, S Kundu, A Mallik 2012 Monitoring of sag & temperature in the electrical power transmission lines *International Journal of Recent Technology and Engineering (IJRTE)* **1**(4) 43-45.

[3] S R Khasanov et al. 2020 Reliability modeling of high-voltage power lines in a sharply continental climate *E3S Web of Conferences* **178** 01051.

[4] M Wydra et al 2018 Overhead transmission line sag estimation using a simple optomechanical system with chirped fiber bragg gratings. Part 1: Preliminary measurements *Sensors* **18**(1) 309.

[5] V A Listyuhin, E A Pecherskaya, O A Timokhina, V V Smogunov 2021 System for monitoring the parameters of overhead power lines *Journal of Physics: Conference Series* **2086**(1) 012059.

Algorithm and installation for measuring the current lacing voltage in high-power RF and microwave bipolar and heterojunction bipolar transistors

K A Litvinov[1], O A Radaev[2], I S Kozlikova[2], V A Sergeev[2], A A Kulikov[1]

[1]Ulyanovsk State Technical University, Ulyanovsk 432027, Russia
[2]Ulyanovsk Branch of Kotel'nikov Institute of Radio-Engineering and Electronics of Russian Academy of Sciences, Ulyanovsk 432071, Russia

sva@ulstu.ru

Abstract. Methods of measuring the current lacing voltage in high-power bipolar (BT) and heterojunction bipolar (HBT) RF and microwave transistors are considered. A method and installation for determining the current lacing voltage in a transistor without introducing the device into the hot spot mode by the steepness of the dependence of the variable component of the voltage at the emitter junction on the collector voltage at a given emitter current and the supply of the sum of linearly increasing and small alternating voltage to the collector is described.

1. Introduction

It is known that current distribution in high-power bipolar (BT), including heterojunction bipolar (HBT), RF and microwave transistors loses stability at certain values of collector current and voltage and the so-called «current cord» and «hot spot» (HS) are formed in the structure of the device [1, 2]. The line of mode parameters in current-voltage coordinates corresponding to current lacing defines one of the boundaries of the safe operation area (SOA) of BT and HBT, going beyond which, even for a short time, leads either to irreversible destruction of the instrument structure and catastrophic failure of the device, or to degradation of the device [3].

A critical drawback of the known methods [4, 5] for determining the voltage of the U_{KL} localization in BT and HBT is that the devices enter the HS mode.

2. Description of the algorithm and measuring installation

According to the model presented in [6], for the case of defects of an electrophysical nature in the BT structure, the dependence of the variable voltage component $\tilde{U}_{EB}$ on emitter junction from the collector voltage is described by the formula:

$$\tilde{U}_{EB}(U_K) = \tilde{U}_{EB}(0)\left[1 + \frac{b}{\left(1 - U_K / U_{KL}\right)^2}\right], \quad (1)$$

where $\tilde{U}_{EB}(0)$ is the amplitude of the alternating voltage at the emitter junction at a collector voltage U_{K0} close to zero; b – is a dimensionless parameter depending on the magnitude of the defect in the BT structure, and, as a rule, $b << 1$.

Based on this model, in [7] a non-destructive method and in [8] the installation are proposed for determining the U_{KL} at a given emitter current by three counts of the alternating voltage at the emitter at three collector voltages U_{K1}, U_{K2}, of a transistor included in a circuit with a common base, when the sum of a linearly increasing voltage and a small sinusoidal voltage is applied to the collector:

$$U_{KL} = \frac{U_{K2} - mU_{K1}}{1-m}, \tag{2}$$

where $m = \sqrt{\frac{a1-1}{a2-1}}$, $a1 = \tilde{U}_{\text{EB}}(U_{K1}) / \tilde{U}_{EB}(U_{K0})$, $a2 = \tilde{U}_{\text{EB}}(U_{K2}) / \tilde{U}_{EB}(U_{K0})$.

The accuracy of this method strongly depends on the choice of collector voltage values, while there is a possibility of the device entering the HS mode. In order to exclude the devices from entering the GP mode and to increase the accuracy of determining the U_{KL} when setting the transistor mode according to the method [7], the new method proposes to measure the amplitude of the alternating emitter voltage at a low collector voltage; then measure the values of the collector voltage and, at which the amplitude becomes equal to (1+k1) and (1+k2) , respectively, where k1 and k2 are the given coefficients, and the voltage U_{KL} is calculated by the formula:

$$U_{KL} = \frac{\sqrt{k2/k1}U_{K2} - U_{K1}}{\sqrt{k2/k1} - 1}. \tag{3}$$

Figure 1 shows a characteristic type of BT dependence with current localization with specified levels, and Figure 2 shows a block diagram of the device implementing the method.

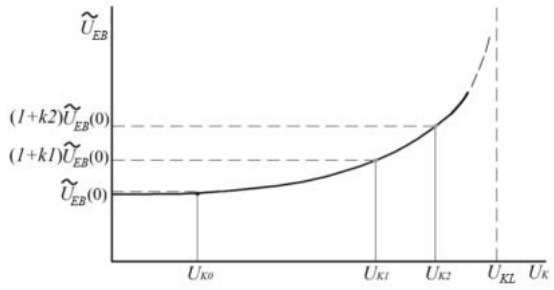

Figure 1. Type of BT dependence with current localization and preset levels.

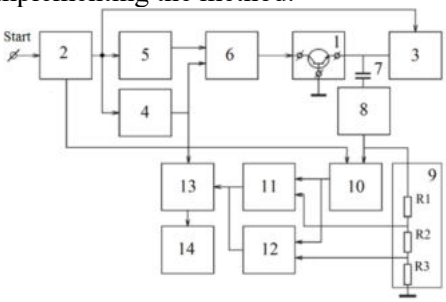

Figure 2. Block diagram of the device implementing the method.

The device implementing the method contains a block 1 for connecting a transistor; a control device 2; a current source 3; a linearly increasing voltage generator 4; a low frequency generator 5; a power amplifier adder 6; a separating capacitor 7; an envelope extraction device 8; a resistive divider 9; a sampling and storage device 10; comparators 11 and 12; logger13 and computer 14. An experimental sample of the device is implemented on the basis of an Arduino debugging board. The algorithm and device have been tested on several samples of domestic and foreign BT and HBT transistors.

Acknowledgments

The work was supported by the Russian Science Foundation, the project No. 22-29-01134

References

[1] Sergeev V A 1997 *St. Petersburg Journal of Electronics*, **2**, 40-42
[2] Sinkevich V F 2003 *Electronic industry*, **2**, 232
[3] Liu W 1996 *IEEE Trans. on Electron Devices*, **2**, 220
[4] Ladbrooke P et al 2008 *Patent US* 20080228415
[5] Gusev V A, Kapranov I Yu 2008 *Vestnik SevSTU. Ser. Informatics, electronics, communications : collection of scientific tr.*, **93**, 106
[6] Sergeev V A, Dulov O A, Kulikov A A 2009 *News of universities. Electronics*, **2**, 10
[7] Sergeev V A, Dulov O A, Kulikov A A 2015 *Patent Russia*, 2537519
[8] Sergeev V A et al 2017 *Automation of control processes*, **3**, 96

New optic system for low mass ^{199}Hg ion clock

N A Lukashev[1] and V V Davydov[2, 3]

[1]The Bonch-Bruevich Saint-Petersburg State University of Telecommunications, Saint Petersburg 195251, Russia
[2]Peter the Great Saint-Petersburg Polytechnic University, Saint Petersburg, Russia, 195251
[3]All-Russian Research Institute of Phytopathology, Moscow Region 143050, Russia

n-lukash@list.ru

Abstract. Newly developed optic system has been applied to low mass ion clock prototype. With its help it has become possible to significantly take up short term stability and temperature coefficients. The prospects for using this design in various moving objects are considered.

1. Introduction

The use of high speeds, both in the movement of objects and in the transmission of data, requires the determination of time with high accuracy [1, 2]. Despite the fact that atomic clocks are the most reliable timekeepers on the world, them nonetheless contain instabilities that can produce a small lag, or "offset," between the clock's time and the real time. If left untreated, these offsets will accumulate and cause substantial positional inaccuracies. Fractions of a second might spell the difference between reaching Mars safely and missing it entirely.

There are several uses for ultra-stable clocks in space and on Earth that necessitate a tiny package size. Deep-space vehicles, for example, have strong physical size limits for onboard instruments; total spacecraft mass (unfueled) is frequently less than 400 kg, with projected trends toward even less mass.

2. New design atomic clock

We have developed a high-performance ^{199}Hg+ trapped-ion clock with frequency stability near $2 \cdot 10^{-16}$. The ion-trapping technologies developed for this clock are critical to achieving this level of stability. The ion trap design for the liter clock is be based on "ion-shuttling" between a linear quadrupole and a linear multipole, similar to what is utilized in ground clocks [1, 3]. However, improvements and redesigns in the vacuum and optical systems are required to achieve the 1- to 2-liter size requirement.

The optical system that collects appropriate ultraviolet (UV) fluorescence from the trapped Hg ions is crucial for achieving the desired short-term stability. The apparatus depicted in Fig. 1 was conceived and built by us, and it is utilized for both concentrating the source light from a ^{202}Hg lamp onto the trapped ions and capturing fluorescence from these ions. The dielectric-coated folding mirror acts as a dichroic reflector, reflecting 194-nm ion fluorescent light with >95 percent reflectance and parasitic 254-nm light from a neutral Hg transition with just 10 % reflectance. Because stray light limits the stability, it is critical to remove the 10 stronger 254-nm light from the beam because it is situated inside the UV-sensitive photomultiplier tube's detection band.

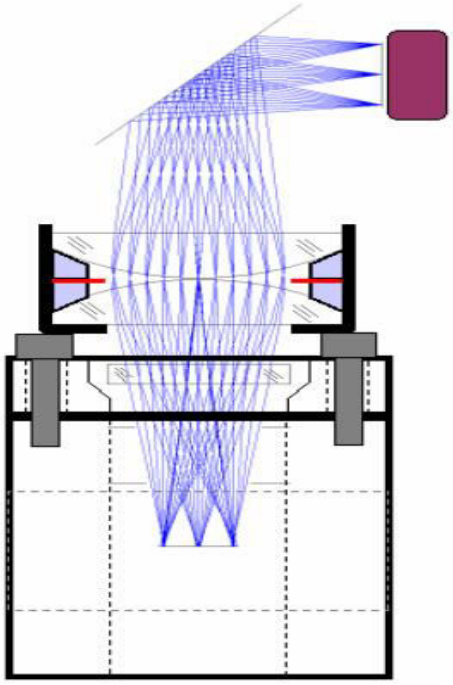

Figure 1. UV Optical system

This system is integrated with the ion trap assembly. The electronics modules that control the photomultiplier tubes, pulse amplifier–discriminator, and discharge lamp are housed in the same enclosure as the lens, mirrors, and detectors/source. The ground clock used three independently movable optics modules to optimize ion fluorescence, but the single-module approach to the optical package here is different. The three identical optical arms of the integrated optical system described here may be placed on the bench such that their focuses fall in the same place. Since the production and assembly of the optical package have been recently completed, the optical alignment process is just getting started.

3. Conclusion

With the newly implemented optical system it has been possible to achieve the increase in short term stability by 7% to the previously developed prototype. Furthermore, the temperature coefficients of this technique are quite modest, a few times 10^{-15} per degree Celsius change. The clock physics and electronic packages were not thermally shielded when these figures were calculated. To achieve 10^{-15} clock stability, very minor thermal shielding would be necessary.

Acknowledgments

References

[1] Petrov A, Davydov V and Grebenikova N 2018 *Journal of Communications Technology and Electronics* **63(11)** 1159–1164

[2] Riechle F 2004 Frequency Standards. Basics and Applications (Wiley-VCH, New Jersy)

[3] *Lukashev N A, Petrov A A, Grebenikova N M and Valov A P 2018 Proceedings of 18th International conference of Laser Optics ICLO-2018 (Saint-Petersburg),* vol. 8435889 (IEEE), p. 271

A mmWave Rod Antenna Array Compatible with a PCB Prototyping Technology

A Lyubchak[1,2], A Prikhodko[1,2], V Andreev[1,2], S Antipov[2], A Shurakov[2,3], G Goltsman[1,2]

[1]National Research University Higher School of Economics, Moscow 101000, Russia
[2]Moscow Pedagogical State University, Moscow 119435, Russia
[3]National University of Science and Technology MISiS, Moscow 119049, Russia

anlyubchak@miem.hse.ru

Abstract. A mmWave communication is becoming a reality. Nowadays, 5G networks are at the stage of commercial implementation while numerous studies around the world are devoted to investigating practical issues of switching to the 6G standard. Next generation communication systems should rely on highly directive transceivers, which potentially suffer from a micromobility issue. In this paper we report on the design of a mmWave rod antenna array compatible with a PCB prototyping technology. The array makes use of a dielectric multimode power splitter equipped with four weakly coupled rods at its output. It is cheap to fabricate and has a FWHM of 11° with a side lobe level of -11 dB at 135 GHz. Thus, the proposed design seems suitable for prototyping mmWave transceivers within lab studies of a micromobility issue in 6G networks.

1. Introduction

Nowadays, millimeter waves (mmWaves) attract close attention of both the scientific community and the communication industry. The society needs for fast and reliable data transfer eminently grew in the coronavirus pandemic era. A mmWave communication is becoming a reality. 5G networks are at the stage of commercial implementation while numerous studies around the world are devoted to investigating practical issues of switching to the 6G standard. Next generation communication systems should rely on transceivers equipped with high directivity antennas [1] causing potential loss of connection upon slight displacement of a mobile device. This is referred to as a micromobility issue and is of high practical importance [2].

Conventional way to implement a high directivity input optics of a receiver/transmitter is to use an antenna array. Since there is a variety of antenna array technologies, the choice is always a trade-off between performance of the array and its fabrication complexity. In this paper we report on the design of a mmWave rod antenna array compatible with a PCB prototyping technology. The design is inspired by that of a W-band fully dielectric rod antenna array with integrated power divider [3], but it relies on a low-cost PCB laminate (FSD255G series, 1 mm thick [4]). Fabrication details and outcome of performance tests are provided further in the text.

2. Fabrication and evaluation details

Referring to figure 1(a), the proposed antenna array is fully dielectric and makes use of a multimode power splitter integrated with four weakly coupled rods at its output. The geometry is implemented

with the aid of a MITS Eleven Lab PCB prototyping machine [5], metallization on both sides of the PCB laminate is removed via wet etching. The array is designed for operation at 135 GHz where it has a full width at half maximum (FWHM) of 11° and a side lobe level of -11 dB. Outcome of the beam profile measurements is provided in figure 1(b).

During the beam profile measurements, we used a membrane-integrated planar Schottky diode (PSD) [6] as a core of direct-detection receiver (Rx). The PSD WR6.5 input was loaded by the proposed antenna array. Transmitter (Tx) made use of a backward wave oscillator (BWO) providing CW AM signal over the frequency range of 126.5-145.5 GHz. Tx was equipped with input optics identical to that of Rx. The measurements were conducted at the Tx-to-Rx distance of 35 cm. Despite noticeable absorption loss in the array elements, we observed peak value of a signal-to-noise ratio (SNR) of ~670 during all the measurements. This SNR was achieved for the Rx time constant of 100 ms. Given that power at the array input can be increased from 1.5 to 100 mW if BWO is replaced by a commercially available solid state mmWave source, insertion loss of the array is acceptable from a practical point of view.

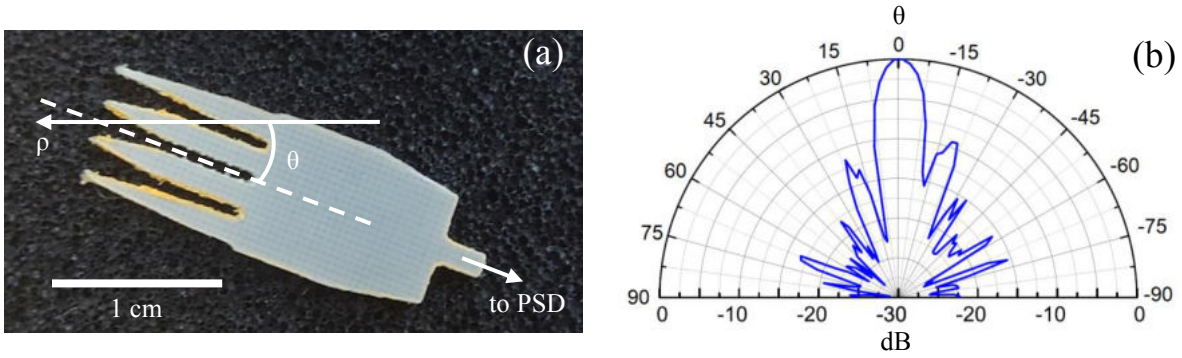

Figure 1(a, b). (a) Geometry of the proposed array in H-plane; **(b)** Measured H-plane beam profile.

The proposed design is adaptable for high permittivity laminates. Switching to a material with relative permittivity of 4.4 provides reduction in the array dimensions by ~50% [7]. Thus, we plan to further reduce aperture size of the array via switching to FSD1020T series laminate [8]. In addition to shortening a Fraunhofer distance, this aids to minimize propagation losses due to absorption in the array elements. Remaining compliant with a 2D PCB machinery, the design becomes even more attractive for implementation of highly directive mmWave transceivers as part of a lab measurement equipment.

Acknowledgments

The study was supported by a grant from the Russian Science Foundation No. 21-72-10119, https://rscf.ru/project/21-72-10119/.

References

[1] B. Ning et al. 2021 arXiv preprint arXiv:2107.03032
[2] N. Stepanov et al. 2021. *IEEE Trans. Veh. Technol.* 71(1) 725-738
[3] H. Tesmer et al. 2019 *Frequenz* 73(11-12) 367-377
[4] Online: http://www.eltm.ru/attach/catalog/v_2464_253.pdf
[5] Online: http://www.mitspcb.com/edoc/11lab.htm
[6] A. Shurakov et al. 2021 *Microwave & telecommunication technology* 3 34
[7] R. Reese et al. 2019 *In proc. of the 12th Ger. Microwave Conf. (GeMiC)* 13-16
[8] Online: http://www.eltm.ru/attach/catalog/v_2464_349.pdf

Transmission of Electromagnetic Waves Through Disordered Multiphase Composite Media

P.A. Makarov[1], V.A. Ustyugov[2], S.V. Nekipelov[1]

[1]Institute of Physics, Mathematics, Komi Science Center Ural Division of the Russian Academy of Sciences, 167982, Oplesnina, 4, Syktyvkar, Russia
[2]Syktyvkar State University named after Pitirim Sorokin, 167001, Oktyabrsky 55, Syktyvkar, Russia

makarovpa@ipm.komisc.ru

Abstract. This research presents an algorithm for numerical simulation of the transmission of electromagnetic waves through disordered multiphase composite media. Developed algorithm is suitable for analysing the main features of the propagation of various types of signals in disordered layered systems in three modes: simplex, duplex and half-duplex regimes.

1. Introduction

Study of electrodynamics properties of the stochastic composite media and disordered systems is such an impressive problem, both in fundamental science and in applied research and engineering applications [1-5]. There are specific problems of condensed matter physics, radiophysics, electronics and communications, in which this problem plays an major role. Because of this, there is important to improving the methods that make it possible to analyse, visually and simply represent the process of electromagnetic signal propagation in specific stochastic multiphase composites [2-5].

At the same time, the development of these methods is far from being complete. For example, there is not many researches with detailed description and model of the electromagnetic signals propagation in the disordered inhomogeneous composites formed by heterogeneous phases: dielectrics and magnetic materials [5].

2. Results and Discussion

In this research an algorithm for the simulation of the electromagnetic waves propagation through stohastic multiphase composite media by the FDTD method has been developed. That algorithm is suitable for analysing time delays, shape distortion, amplitude attenuation and another features of the different types signals, transmitted through the complex structures.

The numeric experiments of simulation the single pulses, series of pulses, sine signal and square waves propagation in stochastic disordered multiphase composite media with various types of phase contrast is carried out. Further, mix of random-ordered dielectric and magnetic scatterers over the background of an inhomogeneous medium with different profiles of inhomogeneity are considered.

On top of that, in this investigation revealed influence concentration of inhomogeneities and the type of their distribution on the characteristics of the transmitted and reflected signals.

Acknowledgments
The authors are grateful to V.S. Vlasov (Syktyvkar State University) for his stimulating attention to the work and numerous helpful comments.

References

[1] Torquato S., Kim J., Nonlocal Effective Electromagnetic Wave Characteristics of Composite Media: Beyond the Quasistatic Regime, Phys. Rev. X, v. 11, 021002, 2021, DOI: 10.1103/PhysRevX.11.021002

[2] Kantartzis N.V., Zygiridis T.T., Antonopoulos C.S., Kanai Y., Tsiboukis T.D., A generalized domain-decomposition stochastic FDTD technique for complex nanomaterial and graphene structures, IEEE Trans. Magn., v. 52, 7203804, 2016, DOI: 10.1109/TMAG.2015.2477280

[3] Codecasa L., Di Rienzo L., Stochastic finite integration technique formulation for electrokinetics, IEEE Trans. Magn., v. 50, 7014104, 2014, DOI: 10.1109/TMAG.2013.2280522

[4] Chilton R.A., Lee R., The Lobatto cell: Robust, explicit, higher order FDTD that handles inhomogeneous media, IEEE Trans. Ant. Prop., v. 56, 2167-2177, 2008, DOI: 10.1109/TAP.2008.926758

[5] Makarov P., Ustyugov V., Kotov L., Nekipelov S., Sivkov V., Simulation of Electromagnetic Wave Propagation in Magnetic Randomly Inhomogeneous Magnetic Media, IEEE Magn. Let., v. 13, 2101305, 1-5, 2022, DOI: 10.1109/LMAG.2021.3132857

Millimeter Wave Photonic Crystal Waveguides Fabricated via Direct Machining

A Prikhodko[1,2], I Belikov[1,2], A Lvov[1], A Shurakov[1,3], G Goltsman[1,2]

[1]Moscow Pedagogical State University, Moscow 119435, Russia
[2]National Research University Higher School of Economics, Moscow 101000, Russia
[3]National University of Science and Technology MISiS, Moscow 119049, Russia

anatprikh1995@yandex.ru

Abstract. At the moment millimeter waves attract close attention not only of the scientific community, but also of the communication industry. Number of studies worldwide are currently focused on finding efficient solutions for the transceiver technologies compatible with beamforming and carrier frequencies beyond 100 GHz. It was recently demonstrated that the technology of integrated silicon photonic crystals provides decent propagation loss and low fabrication complexity upon implementation of waveguide components for the sub-mmWave band. In this paper we report on the millimeter wave photonic crystal waveguides fabricated from high permittivity laminate by the means of direct machining. The photonic crystals are designed for operation at frequencies 130-160 GHz. The design considerations, including justification of the laminate choice, and results of performance tests are presented in the paper.

1. Introduction

At the moment the millimeter wave (mmWave) band attracts close attention not only of the scientific community, but also of the communication industry. Progress in a mmWave communication is in line with the society needs for the speed and quality of data transfer which drastically enlarged in the coronavirus pandemic era. Next generation communication networks should rely on the transceiver technologies compatible with beamforming and carrier frequencies beyond 100 GHz [1]. This may potentially result in a fatal increase of their complexity, fabrication and operational costs. Thus, number of studies worldwide are currently focused on finding efficient software and hardware solutions.

It was recently proposed that the technology of integrated silicon photonic crystals is beneficial compared to that of conventional rectangular waveguides at sub-millimeter waves [2]. The benefits are mainly related to the reduction of propagation loss and fabrication complexity upon implementation of a single-mode waveguide and simple passive components. In this paper we report on the technology of a mmWave photonic crystal waveguide (PCWG) fabricated by the means of direct machining. PCWG utilizes high permittivity laminate [3]. The geometry of photonic crystal is implemented with the aid of a PCB prototyping machine [4]. Metallization on both sides of the laminate is removed via wet etching at the final step of the fabrication process. The waveguide is designed for a single-mode operation at frequencies 130-160 GHz. The design considerations and results of performance tests are presented further in the text.

2. Evaluation of fabricated samples

Our designs make use of FSD1020T series laminate, which attributes relative permittivity (ε_r) of 10.2 and loss tangent ($tan\delta$) of 0.002 at 10 GHz according to the manufacturer specifications. Suitability of the laminate for our task is justified by evaluation of its dielectric properties in the mmWave band. We measure $\varepsilon_r \approx 10.6$ and $tan\delta = 0.011$ at 145 GHz. This corresponds to the laminate power attenuation coefficient (α) of 0.47 dB/mm. These values are used to develop geometry of the photonic crystal intended for the implementation of a single-mode waveguide.

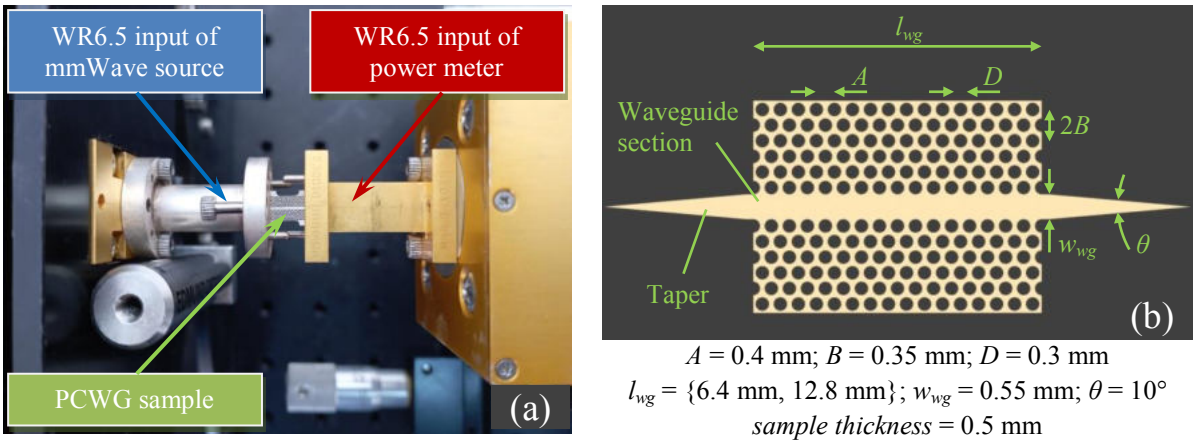

A = 0.4 mm; B = 0.35 mm; D = 0.3 mm
l_{wg} = {6.4 mm, 12.8 mm}; w_{wg} = 0.55 mm; θ = 10°
sample thickness = 0.5 mm

Figure 1(a, b). (a) Measurement setup with a PCWG sample installed; **(b)** Geometry of the samples.

We fabricate PCWG samples with waveguide sections of several lengths (l_{wg}) to evaluate insertion losses due to the energy leakage into a free space (L_{wg}) and those due to the input/output coupling elements (L_{ce}). Thus, total insertion loss (L_{tot}) can be explicitly presented as a function of l_{wg} as $L_{tot}(l_{wg}) = 2L_{ce} + (\alpha + \alpha_{wg})\ l_{wg}$ if measured in decibels. Here $\alpha_{wg} = L_{wg}\ l_{wg}^{-1}$ is the power attenuation coefficient attributed to the waveguide geometry.

Figure 1(a) provides photo of the fabricated PCWG sample installed between WR6.5 inputs of a solid state mmWave source and precision power meter. Referring to figure 1(b), PCWG section is integrated with input/output tappers, which insure coupling with the TE_{10} mode when inserted into a WR6.5 waveguide. Positioning of the sample together with the power meter with respect to the mmWave source is maintained with the aid of a precision 3D translation stage.

We measure α_{wg} = 0.02 dB/mm and L_{ce} = 0.2 dB at 145 GHz. Detailed inspection of the fabricated PCWG samples reveals no violation of the photonic crystal geometry due to the fabrication tolerances. Frequency profiles of the samples insertion loss agree well. All together proves suitability of a 2D direct machining, i.e. drilling and milling, for implementation of mmWave PCWG components.

Acknowledgments

The study was supported by a grant from the Russian Science Foundation No. 21-72-10119, https://rscf.ru/project/21-72-10119/.

References

[1] B. Ning et al. 2021 *arXiv preprint arXiv:2107.03032*
[2] W. Withayachumnankul et al. 2018 *Advanced Optical Materials* 6(16) 1800401
[3] Online: http://www.eltm.ru/attach/catalog/v_2464_349.pdf
[4] Online: http://www.mitspcb.com/edoc/11lab.htm

Monitoring of radioactive contamination in the atmosphere using radar systems

D. A. Ryzhova[1] and V. V. Davydov[1, 2, 3]
[1]Peter the Great Saint-Petersburg Polytechnic University, Saint Petersburg, Russia, 195251
[2]The Bonch-Bruevich Saint-Petersburg State University of Telecommunications, Saint Petersburg 193232, Russia
[3]All-Russian Research Institute of Phytopathology, Moscow Region 143050, Russia

e-mail: qwdarya1234@gmail.com

Abstract. The necessity of monitoring the state of the environment is justified. Various methods of environmental monitoring were analyzed. The radar method for monitoring radioactive contamination in the atmosphere was considered in detail. The monitoring data using radar stations were processed and analyzed. The efficiency of this method was estimated. Recommendations were proposed to expand the monitoring capabilities using radars to assess the environmental situation.

1. Introduction

At present, radar monitoring finds various applications both in the scientific field and for solving important tasks in everyday life. For example, the use of radar monitoring for remote control of the state of the environment [1-3].

Due to the constant increase in the number of industrial enterprises, the study of radiation formations in the air is extremely important for humans, especially in high-risk areas, such as places located in close proximity to radiation-hazardous objects. The amount of radioactive substances released into the atmosphere is also increasing every year [2-4]. These hazardous substances enter the air masses and can be transported over vast distances, and thus fall on land and water objects in the form of precipitation.

Many methods have been developed to control the radiation situation and timely response to emergencies. Over time, most of them have become obsolete, and the remaining ones have a number of disadvantages [1, 3-5]. Among the various methods, the radar method is the most optimal, since it is remote, which is important when working with radioactive particles.

2. Method

The principle of the radar method of finding radioactive particles consists of several points. Firstly, radioactive substances are released into the atmosphere. Then, a plasmoid is formed in the atmosphere, which can change locations with the help of air masses. This plasmoid can be detected using a radar station that is located at safe distance from the object under study. Radiation directed at the plasmoid is reflected from it and then enters the receiving path of the radar. Due to the fact that the reflected signal has a small power, the signal is amplified in the receiving path and transmitted to the control panel using fiber-optic communication lines. In Fig.1 presents a block diagram of the radar operation.

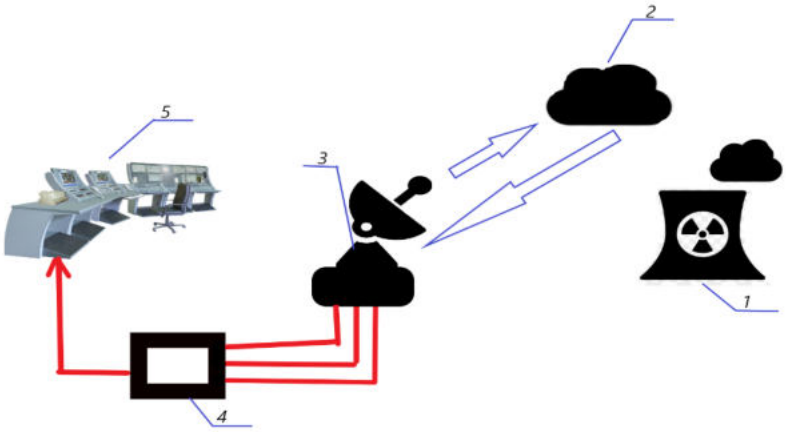

Figure 1. The structural diagram of the radar operation: 1 – radiation-hazardous object, 2 - plasmoid, 3 – radar antenna complex, 4 – radar receiving path, 5 – remote control

An important feature of the plasmoid is that the refractive index of ionization formations and the density are quite different from the parameters of air formations in the atmosphere. This fact indicates the ability of the plasmoid to reflect the microwave radiation that hits it from the radar station.

In order to determine the parameters of the plasmoid, it is necessary to describe its shape. Thus, a mathematical model is compiled. Often, radioactive contamination enters the atmosphere through pipes that have the shape of a cylinder. Therefore, the volume of the plasmoid is found using the cylinder volume formula.

In comparison with other methods for detecting radioactive substances in the atmosphere, the radar method has established itself as a method that has only one significant drawback. In the presence of a strong wind, it is difficult to detect and study the plasmoid, since the plasmoid is prone to rapid dispersion. It breaks down into smaller particles that are difficult to detect.

3. Conclusion

The use of the proposed methodology for environmental monitoring allows more efficient detection of ionization formations resulting from emissions of radioactive elements into the atmosphere. In a number of cases, the radar method has proven itself to be the best, as it is one of the safest for humans and the most accurate methods for monitoring and detecting radioactive elements.

References

[1] Fadeenko I, Fadeenko V, Reznik V, Popovskiy N, Dudkin V and Nikolaev D 2019 *IOP Conference Series: Earth and Environmental Science* **390(1)** 012022
[2] Davydov R, Antonov V and Moroz A 2019 *Proceedings - IEEE International Conference on Electrical Engineering and Photonics (EExPolytech-2019)* **8906791** p. 295 – 297
[3] Elokhin A P 2001 *Technical Physics* **46(8)** 1026 – 1036
[4] Elokhin A P 2012 *Atomic Energy* **112(4)** 269 – 280
[5] Elokhin A P 2015 *Atomic Energy* **117(3)** 206 – 215

Generator of highly stable SHF signals with low phase noise

D D Savin[1] and V V Davydov[1, 2, 3]

[1]Peter the Great Saint-Petersburg Polytechnic University, Saint Petersburg, Russia, 195251
[2]All-Russian Research Institute of Phytopathology, Moscow Region 143050, Russia
[3]The Bonch-BruevichSaint Petersburg State University of Telecommunications, Saint Petersburg, 193232, Russia

e-mail: savin.dd@edu.spbstu.ru

Abstract. The necessity and relevance of the development of high-precision multichannel microwave generators is shown. A block diagram of the device is given. The active elements providing the set level of phase noise are selected. The operation of the device for a frequency of 100 MHz is assembled and modeled.

1. Introduction

Currently, there is a large-scale development of information transfer technologies. A considerable part of them is occupied by wireless signal transmission technologies, which require highly stable oscillators - heterodynes. Time synchronization devices, such as quantum frequency standards, also play an important role in these systems [1, 2]. When implementing the designs of quantum frequency standards, low-noise generators are indispensable devices, since standards in some cases must work autonomously for a long period of time (for example, in satellites in orbit, etc.). Highly stable microwave generators are indispensable in various radio engineering systems and experimental installations.

Modern designs of highly stable SHF generators have a number of disadvantages, among which are the relatively large size of the structure and the high cost. If there is more than one block in a device, for example, in a quantum frequency standard, requiring a high-frequency signal, the dimensions of such a device will be large. This creates problems with its use on satellites and mobile objects [1]. All this ultimately leads to an increase in the cost of the design of the device in which the microwave generator is installed, and the cost of its operation. In addition, these generators will not be synchronized, which leads to a phase difference between the signals that arrive at the corresponding blocks. In most cases, this situation is unfavorable, so they try to prevent it by including a synchronization block in the scheme. This will further increase the size and cost of the device. Therefore, the development of new microwave generator circuits, which allows solving these problems, is extremely relevant.

2. Generator of highly stable SHF signals

The scheme we have developed allows us to generate three highly stable synchronized SHF signals with low noise. The block diagram of the device is shown in Figure 1. It can be divided into two parts: a highly stable SHF signal generator (a) and a splitter (b).

To ensure the generation of highly stable signals, two differential amplifiers are used in the circuit. The LMH6739 amplifier with a gain of 1 is used as a buffer. In this case, the input noise, which is 2.3

nV/(Hz)$^{1/2}$ for this amplifier, will not be particularly amplified. The LMH6629 amplifier is low-noise – its input noise is 0.69 nV/(Hz)$^{1/2}$. However, its minimum gain is 4, so the amplitude of the output signals will be greater than the input.

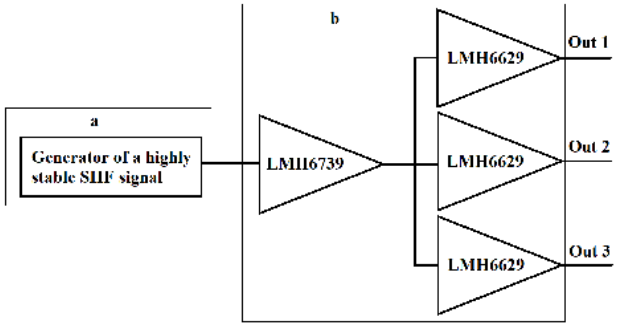

Figure 1. Scheme of highly stable SHF signals generator with low phase noise: a – generator of a highly stable SHF signal; b – splitter.

Figure 2 shows, for example, the results of modeling the operation of the microwave generator circuit.

a) b)

Figure 2. Waveforms: a) highly stable signal, b) output signals.

The analysis of the obtained results shows that the amplitudes of the three microwave signals differ from each other by less than 0.2%, which corresponds to the requirements that are imposed on these devices during experiments.

3. Conclusion

As a result of the simulation, it was confirmed that the microwave signals are generated synchronously. At the same time, the noise induced by the splitter is small. According to preliminary calculations, the dimensions of the generator being developed are 60% smaller than the circuits currently used. The electric power consumption will also decrease.

References

[1] F. Riehle, Frequency standard. Basic and applications. WILEY-VCH Verlag CmbH Co. KGaA: New-York, 2008.

[2] Petrov A, Davydov V and Grebenikova N 2018 *Journal of Communications Technology and Electronics* **63(11)** 1159–1164

On the mechanism of CNT network resistive response to NH_3

N S Struchkov, E A Kozlovskaya, K A Tsarik, A V Lashkov, D D Levin, A V Romashkin

National Research University of Electronic Technology, Moscow 124498, Russia

struchkov.nikolaj@gmail.com

Abstract. A carbon nanotube (CNT) network is a promising gas sensing material for "e-nose". However, its dominant mechanism of sensitivity remains unclear, since both the CNT body and CNT-CNT junctions can be gas-sensitive. In the current work, we simulated CNT networks with varied densities using equivalent circuits to estimate resistive response. We compared the results with the sensitivity of the P3-SWCNT spray-coated interdigital chip toward ammonia exposure. A decrease in network density results in higher sensitivity, which indicates a greater contribution of junctions than the CNT's body in low density networks.

1. Introduction

Recently, nanomaterials gain relevance as gas-sensing materials on account of the rapid development of "e-nose" technology. Key "e-nose" requirements for sensitive layers are the adjustable sensitivity to selected gas species, miniaturization and integrability. Since it is required to fit a large array of sensors with different cross-sensitivity on a single substrate to mimic the olfactory system. Carbon nanotubes (CNT) fulfil these requirements, therefore, are considered a promising gas-sensing material.

Since the pioneering works in the early 2000s, the CNT's sensitivity mechanism remains a matter of argument. A large number of studies of single CNT based field-effect transistors assert the existence of both sensitivity of CNT body (intra-CNT) and sensitivity of Schottky barrier between CNT and electrode. The apparent inconsistency of the known results rises from a large number of factors varied in selected works that determine the dominance of one of the mechanisms on the overall sensitivity. For example, the presence of defects and functional groups in CNT, the work function of the metal that determines the height of the Schottky barrier, etc. When studying CNT networks, the identification of the dominant mechanism is even more complicated, since the presence of both metallic m¬¬-CNT and semiconducting s-CNT and their junctions should be considered. Taking into account that the resistance of the junction dominates the total resistance of the network, the role of CNT-CNT (inter-CNT) junctions in gas sensitivity can be essential. The effect of CNT intersections in short CNT channels was already demonstrated by Boyd et.al [1] and others. However, a deeper understanding of inter- and intra-CNT sensitivity in large area networks is still required. in light of the relevance of heterojunctions based composite CNT-metal oxide sensors, demonstrating record sensitivity up-to-date.

In this work, we simulated the electrical response of the resistor-based model of CNT networks and experimentally measured the resistive response of the spray-coated network to ammonia exposure. We compared simulation and experimental result to evaluate which sensitivity mechanisms prevails in fabricated gas sensing layers.

2. Results and discussion

To simulate the CNT network resistive response we randomly generated a 2-D network of randomly distributed sticks of two types. Then the resulting network was converted into a SPICE model of an equivalent resistor circuit. We used the following approach: CNT was divided into segments in intersections with other CNTs and simulated by a resistors with values $R_{S,M}=\rho_{S,M}\cdot L$ where L is a segment length. Resistivity $\rho_{S,M}$ were taken of ρ_M=6 kΩ/μm and ρ_S=9 kΩ/μm for m-CNT and s-CNT, respectively. The values correspond in order of magnitude to experimental results for non-sorted HNO_3 treated single-walled CNTs in [2], while ρ_S is slightly higher than ρ_M which is observed at least for as-synthesized CNTs [3]. Since minimal resistance of CNT is limited by $1/2G_0$, where G_0 is quantum conductance, the resistors with $R_Q=1/4G_0$ were added to each junction with other CNTs. The contact resistances were simulated with $R_{M\text{-}M}$=40 kΩ, $R_{S\text{-}S}$=60 kΩ and $R_{S\text{-}M}$=200 kΩ [2,3]. The inter- and intra-CNT sensitivities were estimated as the ratio of the resulting circuit currents with $R_{S\text{-}M}$ and R_S of above given and doubled values, respectively [4].

We also spray-coated interdigital chip with a P3-SWCNT network of varied density (Fig. 1a) and measured the resistive response to ammonia exposure to compare with the simulation results. The sensitivity $S=\Delta R/R_0$ is linearly dependent on the gas concentration in the range of 50-400 ppm and increases with decreasing network density. Despite the resistance of the simulated network being several orders of magnitude less than the experimental one, the dependence of sensitivity on resistance changes in a similar way as inter-CNT sensitivity, but even more like the sum of both components (Fig. 1b). We also measured response at elevated temperatures, as well as the response to water vapour. Thus, we demonstrate that the dominant role in CNT low density network response to ammonia may be related to inter-CNT sensitivity.

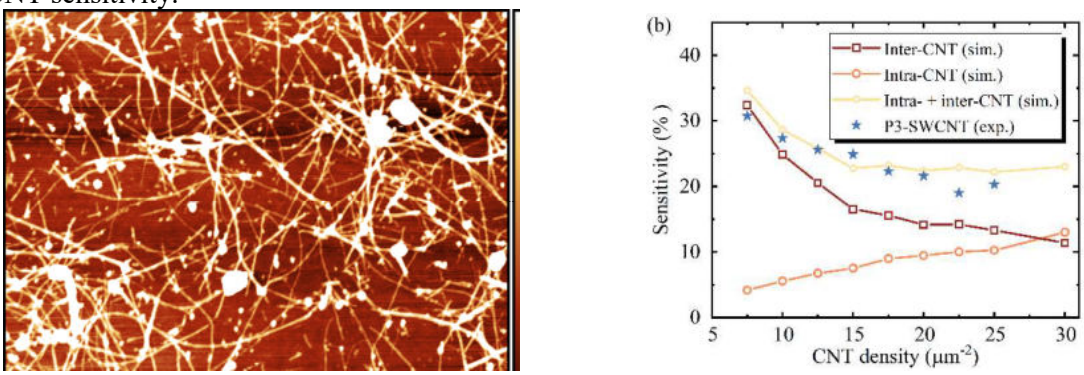

Figure 1. (a) AFM image of CNT network; (b) the dependence of simulated and experimental response to 100 ppm ammonia exposure on CNT network density

Acknowledgments

This work was supported by grant of President of the Russian Federation grant No МК-4010.2022.4 (sensors fabrication, electrical simulation) and Russian Science Foundation project number № 19-19-00401 (samples characterization, gas sensing measurement).

References

[1] Boyd, Anthony, et al. "Gas sensing mechanism of carbon nanotubes: From single tubes to high density networks." Carbon 69 (2014): 417-423.

[2] Znidarsic, Andrej, et al. "Spatially resolved transport properties of pristine and doped single-walled carbon nanotube networks." The Journal of Physical Chemistry C 117.25 (2013): 13324-13330.

[3] Lee, Eduardo JH, et al. "Spatially Resolved Potential Distribution in Carbon Nanotube Cross-Junction Devices." Adv. Mater 21 (2009): 2720-2724.

[4] Peng, Ning, et al. "Sensing mechanisms for carbon nanotube based NH3 gas detection." Nano letters 9.4 (2009): 1626-1630.

Manufacturing of the RF MEMS switch for 5G mobile network transceivers

A V Tkachenko[1], I E Lysenko[1], A V Kozlov[2]
[1]Southern Federal University, Rostov-on-Don region, Taganrog, 347922, Russia
[2]Center for Collective Design of Electronic component Base and Electronic Equipment, National Research University of Electronic Technology (MIET), Zelenograd, Moscow, 124498, Russia

Abstract. This article presents the results of manufacturing experimental sample of the developed high-performance single-pole single-throw radio-frequency microelectromechanical switch designed to operate in the frequency range 5G NR FR1, namely at the central resonant electrical frequency 3,6 GHz, based on the developed methodology for designing capacitive radio-frequency microelectromechanical switches. The projected radio-frequency micromechanical switch can potentially be used in radio-frequency front-end control interface, both for mobile communication devices and in the construction of a 5G network architecture, as well as in a complex of base stations, smart antennas, antennas with multiple-inputs and multiple-outputs, etc.

1. Introduction

In all 5G RF systems or subsystems from a hardware point of view, the radio-frequency (RF) switch is one of the most fundamental and important components that is used to route signals along RF signal transmission paths with a high degree of efficiency. Its RF characteristics, switching time, RF signal power value and reliability can directly affect the corresponding properties and performance of 5G applications.

The purpose of this work is to present the results of manufacturing experimental sample of the single-pole single-throw (SPST) RF microelectromechanical (MEMS) switch designed to operate in the frequency range of 5G NR FR1 (sub-6GHz) mobile networks, characterized by excellent electromagnetic parameters, high linearity, low insertion resistance, low control voltage and almost zero power consumption.

2. Design and analysis

The images obtained using a scanning electron microscope (SEM) of manufactured experimental sample of the SPST RF MEMS switch is shown in Figure 1, which is the capacitive shunt RF MEMS switch with a hybrid type of contact. The choice of materials and the design methodology is based on the results of the works [1-3].

Figure 2 shows the results of measuring the electromagnetic parameters or scattering parameters (S-parameters) of the manufactured experimental sample of the SPST RF MEMS switch. The measurements were carried out in a hermetic metal RF package with coaxial RF terminals, which are connected to the CPW of the manufactured experimental SPST RF MEMS switch using a micro-welding operation with a thin gold wire (Ø=50 um). Part of the technological operations and measurements are performed in Center for Collective Design of Electronic component Base and Electronic Equipment, National Research University of Electronic Technology (MIET).

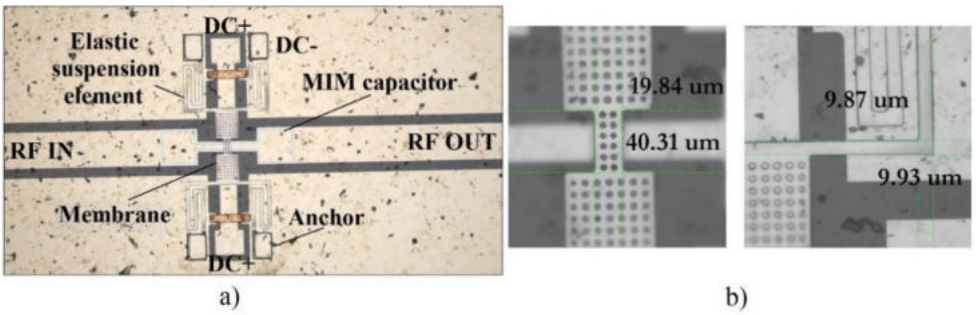

Figure 1. SEM-images of the manufactured sample of the SPST RF MEMS switch: a) topology with indication of the main elements; b) focus on the suspended membrane and elastic suspension element.

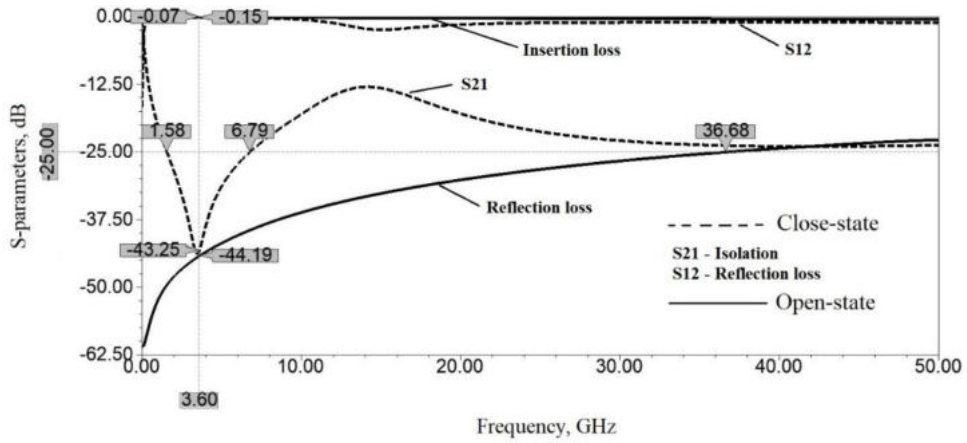

Figure 2. Results of measurement of the electromagnetic parameters.

3. Conclusion

The results obtained and the available scientific and technological potential can be used as a basis for designing complex RF MEMS devices, such as RF MEMS switches with two and more throw of RF signal transmission, multi-position attenuators, as well as additional RF signal generation functions such as attenuation and phase shift, they can be combined in the same RF MEMS device.

Acknowledgments

The work was carried out at the expense of funds, task No. FENW-2020-0022 for the implementation of scientific research carrying out scientific research at the expense of the Federal budget, in terms of scientific activities on the topic "Development and research of methods and means of monitoring, diagnostics and forecasting state of engineering objects based on artificial intelligence".

References

[1] Lysenko I E, Tkachenko A V, Sherova E V, Nikitin A V 2018 Analytical Approach in the Development of RF MEMS Switches *MDPI, Electronics J.* **7(12)** 1–23.

[2] Tkachenko A V, Lysenko I E, Denisenko M A, Ezhova O A 2021 Design and Optimization of a Shunt RF MEMS Switch with a Hybrid Contact Type *Springer: Proc. in Physics. Proc. of the Int. Youth Conf. on Electronics, Telecommunications and Information Technologies (YETI-2021)* **268** pp 281–299.

[3] Tkachenko A V, Lysenko I E, Kovalev A V, Vertyanov D V 2021 High-performance inline RF MEMS switch for application in 5G mobile networks *J. of Physics: Conf. Series. Proc. of the 8th Int. School and Conf. "Saint Petersburg OPEN-2021": Optoelectronics, Photonics, Engineering and Nanostructures (SPbOPEN-2021)* **2086 (012068)** pp 1–6.

Variation of the disorder of ultrathin NbN films

A D Triznova[2], A I Lomakin[1,2], E M Baeva[2], P I Zolotov[2,3], A V Semenov[1], A I Kolbatova[1,2], and G N Goltsman[1,2]
[1]National Research University Higher School of Economics, 20 Myasnitskaya St, Moscow, Russia
[2]Moscow Pedagogical State University, 29 Malaya Pirogovskaya St, Moscow, Russia
[3] LLC Superconducting Nanotechnology (SCONTEL), Moscow 119021, Russia

ad.triznova@mpgu.su

Abstract. We demonstrate the variation of superconducting and normal-state properties of ultra-thin NbN films. By variation of the substrate temperature, nitrogen concentration and sputtering pressure 2.5 nm films had significantly different Ioffe-Regel parameter $k_F l$ ranging from 1.6 to 6.3 and critical temperature T_c from 3.40 to 11.54

1. Introduction

Thin superconducting films, in particular NbN films, are the basis for the manufacture of various electronic devices [1-4], including single-photon detectors (SSPD) [1-2]. There is a relevant problem with optimising the efficiency of SSPD in the mid-IR spectrum range [5], which is typically solved by obtaining ultrathin films with a high degree of disorder and a small diffusion coefficient. Previously, there was less evidence that the necessary parameters could be obtained for ultrathin NbN films [6]. Our study extends the possibility of varying normal-state resistance R_{Ns} from 530 Ω/sq to 5500 Ω/sq, the electron diffusivity D in the range from 0.59 cm^2/s to 0.19 cm^2/s, and the Ioffe-Regel (disorder) parameter $k_F l$ in the range from 1.6 to 6.3 in films with a fixed thickness.

2. Samples and measurement setup

Ultrathin NbN films of 2.5 nm thickness were deposited by DC magnetron sputtering on r-cut sapphire substrates with a background pressure of 9×10^{-8} torr. The films s1-s5, deposited at an operating pressure of 3.6 mTorr and 20% concentration of nitrogen in an argon-nitrogen atmosphere are grown at the temperatures ranging from 500°C to 25°C. The most disordered samples (s6 and s7) are grown at 500°C at increased concentration of nitrogen in the mixture - 33% and 6.5 mTorr (s6) and 23% and 6.8 mTorr (s7). Films were covered with a 5 nm silicon (Si) layer to prevent oxidation.

The films were patterned into 500-μm wide and 1000-μm long Hall-bars. Electrical transport measurements were carried out with a 370 AC Lake Shore resistance bridge at a bias current less than 1 μA. Normal-state resistance Rs was measured in a four-probe configuration. The measurements were carried out in a homemade 4He cryogenic insert immersed in a dewar and performed in a wide temperature range (from 300 K to 1.7 K). The temperature dependence of the sheet resistance $R_s(T)$ and the Hall coefficient were measured for each sample.

3. Results and discussion

The metallic properties of the studied samples are presented in Table 1. Our results demonstrated that deposition regimes greatly changed their sheet resistance R_s and critical temperature T_c. An increase in the substrate temperature during film deposition is expected to lead to an increase in T_c and a decrease in R_s. The degree of disorder of the films is represented, using the k_Fl parameter, which increases with increasing substrate temperature (s1-s5). Another parameter varying the disorder of films is the partial pressure and concentration of nitrogen. An increase in the values of the latter parameters allows to obtain films with the greatest R_s and degree of disorder, but a significant decrease in T_c (s6) and even the absence of superconductivity (s7).

In line with previous studies [7] the high degree of disorder and low value of diffusion coefficient of films allow to increase the probability of a photoresponse of SSPDs. On the other hand, less disordered films give a significant advantage in the time characteristics of devices, in particular the jitter of SSPD. On this basis, we conclude that it becomes possible to vary the properties of ultrathin NbN films, which makes them a universal component for various devices.

Table 1. Parameters of NbN films

Sample	R_s^{300} (Ω/sq)	T_c (K)	R_{Ns} (Ω/sq)	k_Fl	D (cm^2/s)
s1	437	11.54	530	6.3	0.59
s2	509	10.76	645	5.5	0.57
s3	815	8.43	1210	3.5	0.36
s4	912	7.02	1420	3.2	0.35
s5	1025	6.03	1678	2.8	0.34
s6	1574	3.40	5500	2.1	0.27
s7	1950	-	-	1.6	0.19

Acknowledgments

The reported study was funded by RFBR, project number 19-32-60076

References

[1] Gol'tsman G N, Okunev O, Chulkova G, Lipatov A, Semenov A, Smirnov K, Voronov B, Dzardanov A, Williams C and Sobolewski R 2001 *Applied Physics Letters* **79** 705

[2] Divochiy A, Misiaszek M, Vakhtomin Y, Morozov P, Smirnov K, Zolotov P and Kolenderski P 2018 *Optics Letters* **43** 6085

[3] Tretyakov I, Ryabchun S, Finkel M, Maslennikova A, Kaurova N, Lobastova A, Voronov B and Gol'tsmanG 2011 *Applied Physics Letters* **98** 033507

[4] Annunziata A J, Santavicca D F, Frunzio L, Catelani G, Rooks M, Frydman A and Prober D E 2010 *Nanotechnology* **21** 445202

[5] Zolotov P I, Divochiy A V, Vakhtomin Y B, Morozov P V, Seleznev V A and Smirnov K V 2017 *Journal of Physics: Conference Series* **917(6)** 062037

[6] Noat Y, Cherkez V, Brun C, Cren T, Carbillet C, Debontridder F and Roditchev D 2013 *Physical Review B* ***88*****(1)** 014503

[7] Vodolazov D Y 2017 *Physical Review Applied* ***7*****(3)** 034014

A seesaw-type MEMS switch with Pt and Ru contacts

I V Uvarov, V V Naumov, A N Kupriyanov, M O Izyumov and I I Amirov
Valiev Institute of Physics and Technology of Russian Academy of Sciences,
Yaroslavl Branch, Universitetskaya 21, 150007 Yaroslavl, Russia

Abstract. Microelectromechanical systems (MEMS) switches have outstanding working characteristics and a wide range of possible applications. However, these devices suffer from the lack of reliability. The main reason of failure is the degradation of metal contacts, which increases the on-resistance or leads to stiction. A proper choice of the contact material may solve the problem. In this work, we investigate the performance of Pt-Pt and Ru-Ru contacts. The study is performed at the recently proposed stiction-protected MEMS switch. The contact resistance and lifecycle in the cold switching conditions are measured and compared.

1. Introduction

Wireless communication and radar systems demonstrate a significant progress in recent years. The evolution is achieved due to the use of advanced electronic components, including switches for routing of radio frequency and microwave signals. However, the development of electromagnetic and semiconductor relays has almost exhausted, and new approaches are required to support the progress. MEMS switches are a promising an alternative to conventional devices. They provide superior radio frequency characteristics in combination with small size, low power consumption and capability of integration with CMOS circuits [1]. An important characteristic of the switch is the lifecycle, which is mainly determined by the durability of contacts. Metallic surfaces degrade during operation due to friction, contamination and other phenomena [2]. The degradation is considered as the main reason for the switch failure, because it increases the contact resistance or leads to stiction. Several methods to overcome the problem are known, including the selection of contact materials. The contacts are typically made of noble metals due to their chemical inertness and low resistivity. In this work we compare working characteristics of Pt-Pt and Ru-Ru contacts. The study is performed at the recently proposed seesaw-type MEMS switch [3]. The modified design provides the enhanced contact force at the reasonable driving voltage. The on-resistance and lifecycle for both materials are analyzed and compared.

2. Design of the switch

The switch is shown in figure 1. A 100 μm long beam (source) is made of aluminium and suspended above gate and drain electrodes by torsion hinges. The gap between the beam and electrodes is of 1.5 μm. The gate and drain are located under the each arm of the beam, so the switch has the single-pole double-throw configuration. The beam has contact bumps on the bottom side. When the driving voltage is applied to the gate, the electrostatic force tilts the beam, and the bump touches the drain turning the switch on. When the voltage is removed, the beam returns to the initial state under the elastic force of the hinges. In case of stiction, the recovery voltage is applied to the opposite gate, which creates an additional force that breaks the contact. Thus, the switch has the built-in protection from stiction. The beam and electrodes have an optimised shape that ensures several times higher

contact force in comparison with the previous switch [3]. The switch is fabricated by surface micromachining on an oxidized silicon wafer. The route is described in the paper [4]. The bumps and electrodes are made of platinum or ruthenium, so the switch provides Pt-Pt and Ru-Ru contact. Each arm of the beam contains one or two contact bumps. In addition, we fabricate the switch with four beams, which are connected to each other and actuated simultaneously by the common gate. Both one- and four-beam switches are fabricated in one- and two-bump versions.

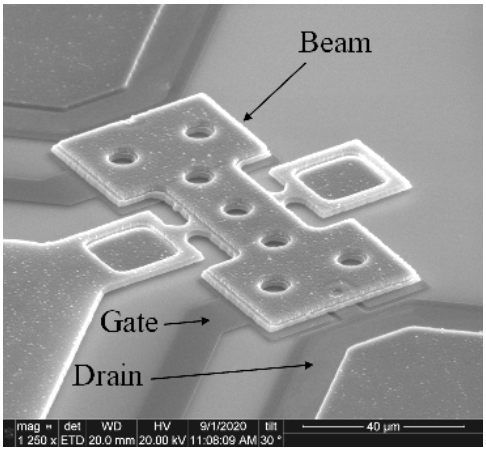

Figure 1. SEM image of the switch.

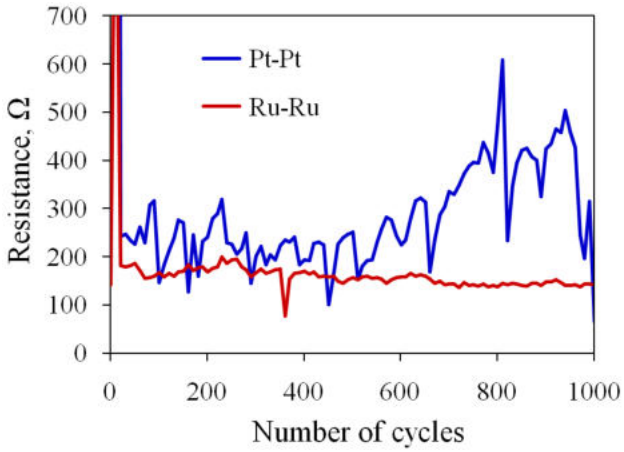

Figure 2. On-resistance of the switch during the test.

3. Testing

The switches are tested in a standard laboratory environment without packaging. Voltage pulses are applied to the gates in such a way that the arms are actuated alternately with the frequency of about 1 Hz. The switch has the pull-in voltage of 27 V. As a rule, the beam is adhered to the drain at the first actuation cycle, so the device further operates in the active contact breaking regime. In this regime, the recovery voltage V_{rec} is applied, which is considerably higher than the pull-in voltage. We use two V_{rec} values of 55 and 80 V, in order to test the contacts at various contact force. In order to avoid electric arcing, the switch operates in a cold mode. The source voltage equals to 5 V. A load resistor limits the current flowing through the switch by 1 mA, so the transmitted power is of 5 mW.

The Pt-Pt contact provides the rather high on-resistance R_{on} of about 300 Ω. The resistance varies significantly during the test, as shown in figure 2. The instability is explained by contamination that is typical for platinum contacts. Ruthenium ensures more stable and low resistance. The one-beam one-bump switch demonstrates R_{on} = 210 Ω at V_{rec} = 55 V. Increasing the voltage up to 80 V lowers the resistance to 190 Ω. The use of two bumps does not decrease R_{on}, as well as the use of four beams. The Ru-Ru contacts have several times longer lifecycle compared to the platinum ones.

4. Acknowledgments

This work is supported by the grant of President of the Russian Federation № MK-945.2021.4 and the program no. FFNN-2022-0017 of the Ministry of Science and Higher Education of Russia for Valiev Institute of Physics and Technology of RAS. The study is performed using the equipment of Facilities Sharing Centre “Diagnostics of Micro- and Nanostructures”.

References

[1] Rebeiz G M 2003 *RF MEMS: Theory, Design, and Technology* (Hoboken, New Jersey: John Wiley & Sons)
[2] Toler B F, Coutu R A and McBride J W 2013 *J. Micromech. Microeng.* **23** 103001
[3] Uvarov I V and Marukhin N V 2021 *J. Phys.: Conf. Ser.* **2086** 012069
[4] Uvarov I V 2021 *Microelectron. Reliab.* 1**25** 114372

Non-mechanical steering of GHz waves by diffraction grating

A S Usachev[1,2,*], M A Talalaev[2], K A Makhnyr[2], V V Atepalikhin[2], Tatyana Vosheva[1], Anton Khudykin[3], and Dmitry Filonov[1]

[1]Center for Photonics and 2D Materials, Moscow Institute of Physics and Technology, 141701 Moscow, Russia
[2]Outdoor Lasers, ltd., 141701 Moscow, Russia
[3]Telecom R&D Center, Moscow Institute of Physics and Technology, Dolgoprudny 141700, Russia

E-mail: * usachev.anton@phystech.edu

Abstract. Rapid change in the radiation pattern of the gigahertz range is an important task for modern data transmission networks. Here we proposed a fast-acting method for controlling the radiation pattern in three-dimensional space, new for the radio range, determined the boundary conditions and dimensions of diffraction gratings for controlling GHz radiation. We carried out a numerical simulation of the process and set up an experiment that well confirms our hypothesis.

Experimental setup

The scanning method using an auxiliary diffraction grating is a new promising non-mechanical method for pointing/correcting radio band antennas. diffraction gratings can be both amplitude and phase.

An amplitude grating Figure 1 can be implemented, for example, using a thin metal sheet on the surface of which a finely dispersed dielectric fraction is located. For control in the GHz range, diffraction gratings with a centimeter period are suitable for us. Such gratings can be created, for example, using sound waves of the kHz spectrum audible to the human ear. The sound antenna is located under a sheet of metal with a finely dispersed dielectric fraction sprinkled on top. Sound waves will create waves from the dielectric on the metal surface, and there will be both zones free from the dielectric, where the wave incident on the metal is reflected, and zones with the dielectric, where the wave is absorbed. In this case, it is only important for us that the thickness of the dielectric layer be sufficient for partial or complete absorption of the incident radio wave. For an incident radio wave frequency of 10 GHz, we use a grating with a period of 3 centimeters and a length of up to 20 periods.

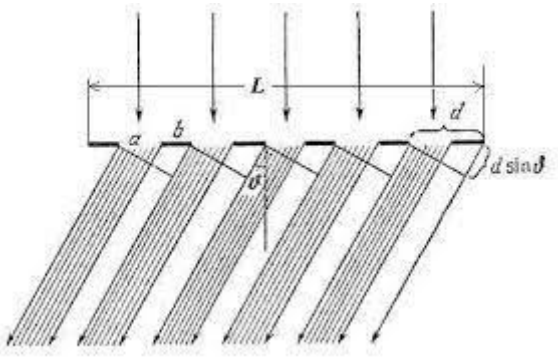

Figure 1. Amplitude diffraction grating.

The phase grating Figure 2 can be implemented both due to the periodically changing shape of the mirror, and due to periodically repeating materials with different permittivity in the operating range of radio wave lengths. A flexible mirror can be made from liquid metal or a viscous liquid with a finely dispersed metallized fraction, such as glycerin with metal filings.

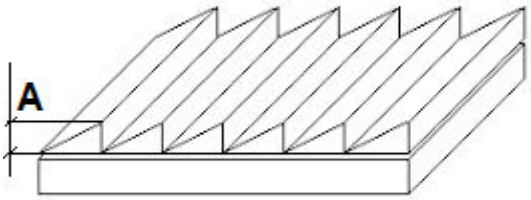

Figure 2. Phase diffraction grating.

The advantage of the phase grating is that there are no losses in the absorbing sections, which makes it possible to save on the source power from 2 to 4 times. Using a metamaterial, it is possible to realize structures with a periodically changing permittivity, for example, by illuminating them [13]. For a phase grating, the amplitude of the grating, or wave height, is critical. It can be calculated by the formula (1) H is the size of the sound field in the direction perpendicular to the direction of light and sound propagation, L is the length of the sound field along the direction of light propagation, M2 is the quality factor. The acoustic power Pak is proportional to the square of the wave amplitude A:

$$P_{ак} = \frac{\lambda_0^2 \cos^2 \theta_0 H}{2LM_2} \quad (1)$$

Power is related to intensity by formula (2):

$$I(t) = \frac{1}{T}\int_{t}^{t+T} \frac{dP}{dS}dt,$$

(2)

The dependence of the intensity (square of the amplitude) of the diffracted wave on the power Pa (square of the amplitude of the oscillation of the phase grating) is presented in formula (3).

$$I_1(\Delta k,L) = \frac{\frac{2P_{ак}M_2\pi^2L}{\lambda_0^2\cos^2\theta_0 H}}{(\Delta kL)^2 + \frac{2P_{ак}M_2\pi^2L}{\lambda_0^2\cos^2\theta_0 H}} \sin^2\frac{\sqrt{(\Delta kL)^2 + \frac{2P_{ак}M_2\pi^2L}{\lambda_0^2\cos^2\theta_0 H}}}{2}$$

(3)

Thus, the intensity of the diffracted wave in the 1st order depends on the intensity of the oscillation of the phase grating wave non-linearly and in the harmonic case in a certain frequency neighborhood has the form as in Figure 3. The color indicates the diffraction efficiency, purple is the maximum and white is no diffraction. The graph shows the measurement result of the dependence of the diffraction efficiency on the amplitude of the diffraction grating in a certain frequency neighborhood.

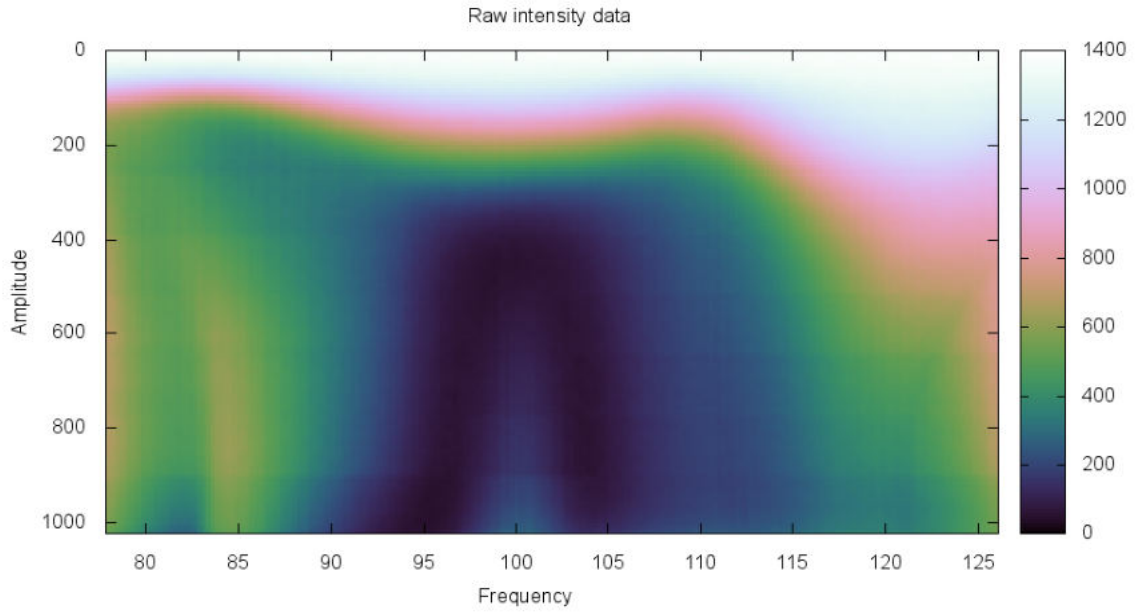

Figure 3. Frequency response of a diffraction grating with different Amplitude of grating period A.

The nature of the distribution between the diffraction maxima depends on the shape of the transition of the diffraction grating. For example, for harmonic adjustment of scattering parameters in 1 and -1 diffraction orders. In the general case, we were dealing with Raman-Nath diffraction.

Conclusion

We proposed a fast-acting method for controlling the radiation pattern in three-dimensional space, new for the radio range, determined the boundary conditions and dimensions of diffraction gratings for controlling GHz radiation. We carried out a numerical simulation of the process and set up an experiment that well confirms our hypothesis.

Acknowledgments

The research was supported by the federal academic leadership program Priority 2030 and the experimental part of the work was supported by the Outdoor Lasers, ltd.

References

[1] Waterhouse R 2003 *Microstrip Patch Antennas A Designer's Guide*, Norwell, MA: Kluwer Academic Publishers, Al-Naiemy Y 2013 *Design, Fabrication, and Testing of Microstrip Antennas*, Lambert Academic Publishing

[2] Das S, Chowdhury P, Biswas A, Sarkar P and Chowdhury S 2015 Analysis of a Miniaturized Multiresonant Wideband Slotted Microstrip Antenna with Modified Ground Plane, *IEEE Antennas and Wireless Prop. Lett.* **14** pp 60–63

[3] Asadallah F, Costantine J, and Tawk Y 2018 A Multiband Compact Reconfigurable PIFA Based on Nested Slots *IEEE Antennas and Wireless Prop. Lett.* **17(2)** pp 331–334

[4] Sim C, Chen C, Zhang X, Lee Y and Chiang C 2017 Very Small-Size Uniplanar Printed Monopole Antenna for Dual-Band WLAN Laptop Computer Applications *IEEE Transactions on Antennas and Propagation* **65(6)** pp 2916–2922

[5] Ahmad A, Tahir F and Khan F 2017 A Planar GPS/GLONASS/LTE/WWAN Antenna for Ultra-Slim Smartphones *11th European Conf. on Antennas and Prop. (EUCAP)*

[6] Ghaffar F, Yang S, Cheema H and Shamim A 2016 A 24 GHz CMOS Oscillator Transmitter with an Inkjet Printed On-Chip Antenna *IEEE MTT-S IMS* pp 1–3

[7] Tang M, Shi T and Ziolkowski R 2015 Flexible Efficient Quasi-Yagi Printed Uniplanar Antenna *IEEE Transactions on Antennas and Propagation* **63(12)** pp 5343–5350.

[8] Sabban A 2017 New Fractal Compact Printed Antennas I*EEE International Symposium on Antennas and Propagation & USNC/URSI National Radio Science Meeting* pp 2197–2198.

[9] Pandey A 2019 Practical Microstrip and Printed Antenna Design *ISBN-13: 978-1-63081-668-1*

[10] Gallacher T, Søndenå R, Robertson D and Smith G 2013 Dynamic beam steering at submm- and mm-wave frequencies using an optically controlled lens antenna *Proc. Passive and Active Millimeter-Wave Imaging XVI* **8715** 87150

[11] He, Gou, Chen, Yin, Zhan, and Wu 2019 Liquid Crystal Beam Steering Devices: Principles, Recent Advances, and Future Developments Crystals **9(6)** 292

[12] Mikhailovskaya A, Dobrykh D, Slobozhanyuk D, Filonov D and Ginzburg P 2019 Optically switchable scanning antenna *IEEE International COMCAS*

[13] Kapitanova P, Maslovski S, Shadrivov I, Voroshilov P, Filonov D, Belov P and Kivshar Y 2011 Controlling split-ring resonators with light *Appl. Phys. Lett.* **99** 251914

Optimization of heterostructural transistor parameters for the MIC of the amplifying path of a medical radiothermograph

V G Tikhomirov[1], S V Chizhikov[2], A G Gudkov[2], V D Shashurin[2], A V Nikolaenkov[1]

[1] Saint-Petersburg State Electrotechnical University "LETI", St. Petersburg 197376, Russia
[2] Bauman Moscow State Technical University, Moscow 105005, Russia

The corresponding author's e-mail address: chigikov95@mail.ru

Abstract. The amplifying path of a modern miniature medical radiothermograph should provide a gain of about 80 dB with minimal intrinsic noise levels. The construction of such a path, even on the most modern element base, requires the use of several microcircuits with a significant resulting current consumption. The existing problem can be solved by creating new active elements of specialized monolithic microcircuits - low-noise transistors, for which the requirements of high energy efficiency will be taken into account when designing heterostructures. The paper presents the results of optimizing the design of a heterostructure low-noise transistor for use in microcircuits of the amplifying path of a miniature medical radiothermograph.

1. Introduction

Very high requirements are traditionally placed on the amplifying path of a radiothermograph. In addition, radiothermographs for medical use have a number of other features (for example, the requirements for a very small error in determining body temperature, not exceeding tenths of a kelvin, a record low level of intrinsic noise in the microwave range, etc.), which further tightens the characteristics of the amplifying path. Moreover, there are additional limitations when designing a miniature medical radiothermograph. Indeed, to provide a gain of about 80 dB with minimal levels of intrinsic noise, designing of such a path even on the most modern monolithic LNAs requires several microcircuits with a total current consumption in the operating mode of the order of hundreds of milliamps. Such current consumption of amplifying stages in a miniature case of a radiothermograph leads to a significant increase in temperature inside the case with the reference noise source located there. This is a significant problem for designers of modern miniature medical radiothermographs. The existing problem can be solved by creating new active elements of specialized monolithic microwave microcircuits - low-noise transistors, for which the requirements of high energy efficiency, primarily low current consumption, low heat release into the surrounding space, low noise level and sufficient gain factor will be taken into account when designing heterostructures [1- 2].

2. Results

A promising system of materials for solving the above problem can reasonably be considered heterostructures of semiconductors of the A3-B5 group. The experience accumulated by the author of successful mathematical modeling and practical implementation of heterostructural microwave

transistors with high electron mobility allows to speak about the reasonable probability of successfully solving the above problem of creating a special low-noise microwave transistor with reduced current consumption. As a result of optimizing the transistor design based on these requirements, a calculated slope characteristic was obtained, clearly showing the good amplifying capabilities of the proposed transistor in the low current region, which directly leads to the possibility of a significant reduction in the current consumption of the entire microcircuit. The results of calculated characteristics are shown in Fig.1.

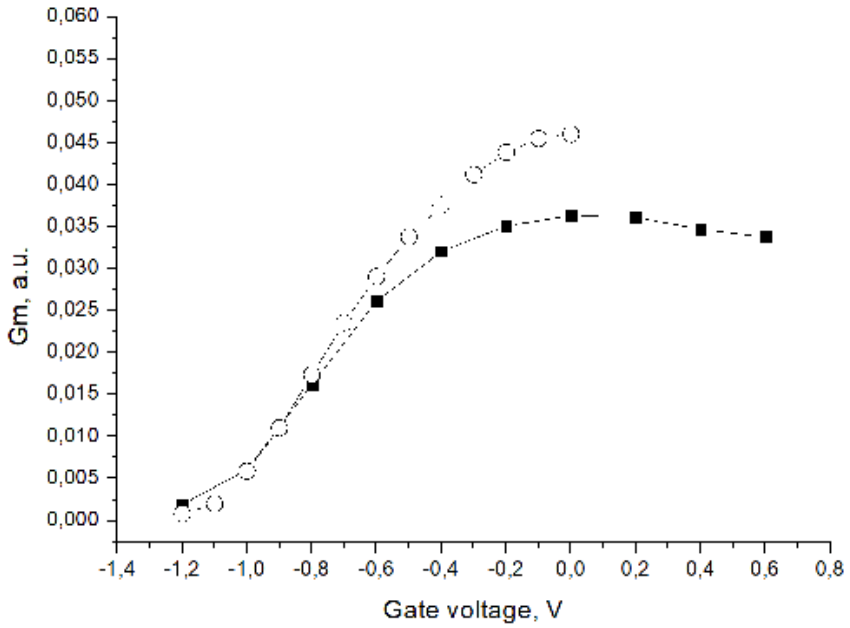

Figure 1. Calculated characteristic of the slope of the transistor transfer characteristic (squares - conventional design; circles - topology-optimized design).

3. Conclusion

Thus, the paper presents the results of optimization by numerical simulation of a low-noise p-HEMT transistor based on a domestic heterostructure. A significant increase in the steepness of the transfer characteristic of the proposed transistor design indicates the possibility of using this promising element base as part of microwave radiometers, which will allow combining the principles of multichannel, multifrequency and miniaturization in one radiometric complex and will lead to the expansion of its functionality and a significant reduction in size.

Acknowledgments

The research was carried out with the financial support of the Russian Foundation for basic research (RFBR) as part of the scientific project No. 20-37-90124 dated 24.08.2020 “Identification and research of key elements of medical radiothermometers in a monolithic integrated design that meet the high requirements for sensitivity, accuracy, broadband, noise immunity”.

References

[1] Vesnin S., Sedankin M., Leushin V., Skuratov V., Nelin I., Konovalova A. Research of a microwave radiometer for monitoring of internal temperature of biological tissues. *Eastern-European Journal of Enterprise Technologies*, 2019, Vol. 4, No. 5, pp. 6-15.

[2] Gudkov A.G., Leushin V.Y., Vesnin S.G. *et al.* Studies of a Microwave Radiometer Based on Integrated Circuits. *Biomed Eng.* **53**, 413–416 (2020).

GaN IC E-mode p-channel and n-channel transistors simulation

V A Bespalov[1], V I Egorkin[1], O B Chukanova[1], V E Zemlyakov[1], V V Kapaev[1,2], A A Zaitsev[1], M N Zhuravlev[1]
[1]National Research University of Electronic Technology, Moscow, Russia, 124498
[2]P.N. Lebedev Physical Institute of the Russian Academy of Sciences, Moscow, Russia, 119991

Email: kukhtuaeva@mail.ru

Abstract. This article demonstrates simulation of normally-off p-channel and n-channel transistors based on a p-GaN gate power platform. For n-channel transistor p-GaN critical thickness and dependence of transistor behaviour on barrier thickness and Al mole fraction in this barrier have been estimated. For p-channel device dependence of transistor behaviour on thickness p-layer and impurity concentration in it has been simulated. Also maximum drain currents in open state are 400 mA/mm and -0.9mA/mm and threshold voltages are 1.5 V and -1 V respectively.

1. Introduction

In the past time GaN-based devices have been widely used in electronics due to development of GaN technology. Many of the challenges have been decided, for example, formation of normally-off GaN transistor. But there are still problems with high inductance between the gate electrode and driver circuit and power consumption in power electronic systems and circuits. To overcome this problem monolithic integration of driver circuit and power transistor on the same chip is offered in this article.

There has been a number of articles which demonstrate GaN-based power integrated circuits (IC) [1-2], but they demonstrate integration of two types – normally-on and normally-off – n-channel transistors. These circuits have disadvantage namely static power dissipation. A complementary circuit technology is needed. The technology advantages are reduction of the circuit complexity, zero power consumption, higher noise immunity and linearity [3]. This article demonstrates simulation of epitaxial structure based on p-GaN gate GaN-on-Si platform that have many advantages, such as large wafer size and low cost.

2. Epitaxial structure and simulation

Based on [4-5] the constructions have been simulated. Simulation has been done with Sentaurus Technology Computer Aided Design (TCAD). Additional barrier layers have been excluded as they are about a half nanometers thickness. This parameter is critical and difficulty controlled in MOCVD growth. First of all p-GaN gate n-channel transistor has been simulated. The critical thickness of p-GaN layer is about 70 nm. Choosing p-GaN thickness about 100 nm dependence of type n-channel transistor on AlGaN barrier layer (t_b) and Al mole fraction (x) of this layer has been estimated (Fig.1).

The heterosctructure p-GaN (80 nm)/ $Al_{0.23}GaN$ (15 nm)/ GaN channel / AlGaN buffer/ AlN / Si has been chosen as basic. Mg concentration in p-GaN layer is about $10^{18}sm^{-2}$.These parameters provide

normally-off behavior of n-channel p-gate transistor. To form normally-off p-channel GaN FET n^+ GaN is grown on top of p-GaN layer. It's structure with two channels of different carriers. Hole-channel is basic and electron-channel is closed as this transistor works at negative voltages. Space charge region (SCR) of n^+-GaN/p-GaN junction provides normally-off behavior of the device but for certain construction. Thickness of n^+-GaN layer and its concentration weakly influence on SCR width. The n^+-GaN thickness is 50 nm and impurity concentration in it is about $10^{19}sm^{-2}$. Dependence of type p-channel device on p-layer thickness and its activated impurity concentration also has been estimated (Fig.2). Thus optimal heterostructure for complimentary pair has been choosen.

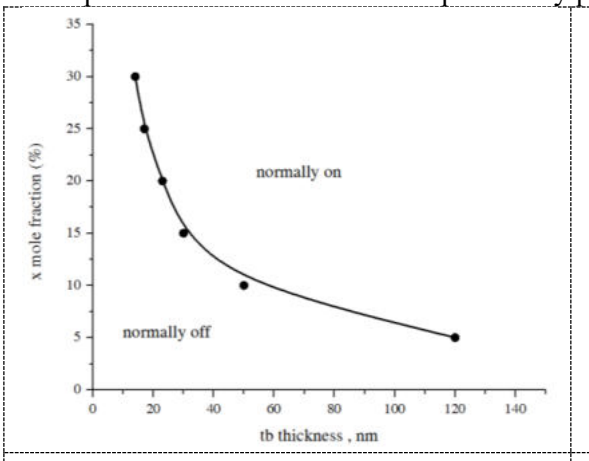

Figure 1. Dependence of type n-channel transistor on AlGaN barrier layer (t_b) and Al mole fraction (x) of this layer.

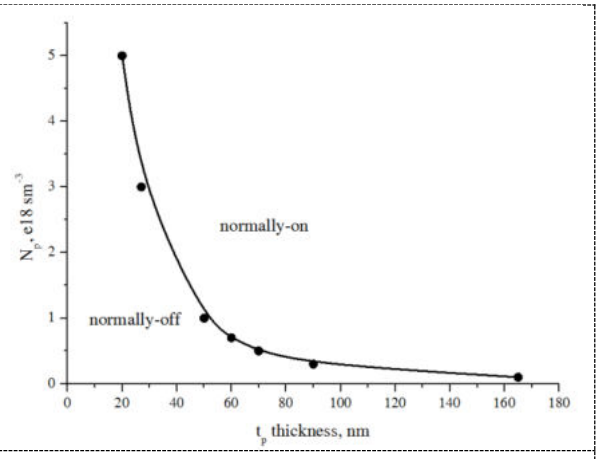

Figure 2. Dependence of type p-channel device on p-layer thickness and its activated impurity concentration.

3. Results

Simulation of normally-off p-channel and n-channel transistors based on a p-GaN gate power platform were demonstrated. The n-channel device with Lg=Lgs=1 um and Lgd=6um has threshold voltage is about 1.5 V and maximum drain current in open state is about 400 mA/mm at 4 V on the gate that doesn't contradict our previous result [4]. The p-channel device Lg=Lgs=Lgd=1 um has threshold voltage is about -1V and maximum drain current in open state is about -0.9 mA/mm at -3 V on the gate. Now we are going to develop technology of this platform, form experimental sample and verify our simulation.

References

[1] Li X, Geens K, Guo W, You S, Zhao M, Fahle D, Odnoblyudov V, Stemmer J and Groeseneken G, Decoutere S 2019 *IEEE Electron Device Lett* **40** 1499-502

[2] Reusch D, Strydom J and Glaser J 2015 *Proc Energy Convers Congr Expo 381-7*

[3] Chowdhury N, Xie Q, Yuan M, Cheng K, Then H and Palacios T 2020 *IEEE Electron Device Lett* **41** 99

[4] Kukhtyaeva O B, Egorkin V I, Zemlyakov V E, Kapaev V V, Zaitsev A A, Tsatsulnikov A F, Nikolaev A E and Sakharov A V 2019 *J Phys Conf Ser* vol. 1410 (Saint-Petersburg, Russia) p.012192

[5] Kukhtyaeva O B, Egorkin V I, Zemlyakov V E, Kapaev V V, Zaitsev A A 2021 *J Phys Conf Ser* vol. 2086 (Saint-Petersburg, Russia) p.012058

Development of automatic gain control for the rubidium-87 frequency standard

A V Shavshin[1] and V V Davydov[1, 2]
[1]Peter the Great Saint-Petersburg Polytechnic University, Saint Petersburg, Russia, 195251
[2]All-Russian Research Institute of Phytopathology, Moscow Region 143050, Russia

e-mail: shavshin2107@gmail.com

Abstract. A new scheme for automatic gain control in the optical path of a AFS based on rubidium-87 atoms is presented. The amplifier of the error signal formed on the photodetector for controlling the microwave signal is considered in detail. Experimental studies of the metrological characteristics of the atomic frequency standard based on rubidium atoms - 87 with automatic gain control are presented. The validity of the developed automatic amplification scheme for the new frequency standard based on rubidium atoms - 87 is confirmed.

1. Introduction

At present, with the advent of new technologies, the issue of accurate measurement of frequency and time is the most relevant for various areas of life [1, 2]. Atomic frequency standards are one of the main functional blocks in them that synchronize satellites with each other or synchronize a satellite with base stations on Earth. One of them is the atomic frequency standard on rubidium atoms – 87.

These frequency standards are used in GLONASS and GPS systems as synchronizing generators, as well as on moving objects in the earth's atmosphere. Each area has its own requirements for the accuracy of the data obtained. One of the main factors affecting the accuracy in sounding is the system errors introduced by the equipment of the space complex [1]. This leads to errors in the formation of a signal from the photodetector after registration of optical radiation. These errors need to be corrected.

One of the elements of their elimination is automatic gain control (AGC) for the rubidium frequency standard. When the ambient temperature changes or other external influences, the output characteristics of the frequency standard without the AGC system undergo changes that must be eliminated. Modernization of the AFS design on rubidium-87 atoms and changing the conditions of its operation require the development of new AGC systems.

2. Atomic frequency standard based on rubidium atoms - 87 and automatic gain control system

The principle of operation of the rubidium frequency standards is the resonant absorption of microwave electromagnetic waves in the beam of the rubidium atom, it is also usually called a passive atomic standard. A passive atomic frequency standard is a standard in which the frequency of absorption of electromagnetic waves of one of the energy transitions of atoms is used as a reference. The passive standard uses an atomic discriminator as a stabilizer. Atomic oscillators as part of the frequency standards produce signals with low output power, so they are first amplified using a microwave receiver, and then they stabilize the frequency of the crystal oscillator.

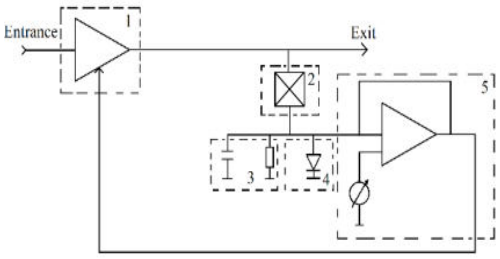

Figure 1. Scheme for automatic gain control: 1 – voltage amplifier of the microwave signal on a field-effect transistor; 2 – directional coupler; 3 – low-pass filter; 4 – detector diode; 5 – amplifier of the "error" signal, to control the power supply of the field effect transistor, the first amplifier.

A signal that is obviously attenuated in voltage is supplied to the system input, so it will need to be amplified so that the total signal power at the system output is 20 μW. For this, a field-effect transistor amplifier (1) will be used. Further, in order to form an «error» signal, part of the signal passes through a directional coupler (2) into the power supply control circuit of the field-effect transistor of the first amplifier, and part of the signal is fed to the system output. Then the future «error» signal must be detected in order to obtain the constant component of the signal. For these purposes, a detector microwave diode (4) will be used. After detection, the signal will have different amplitudes in different cases, so it is necessary to be able to adjust its amplitude to the level we need. To do this, use the «error» signal amplifier on the operational amplifier (5).

3. Results of experimental studies of the characteristics of the atomic frequency standard

As an example, the paper presents the results of a study of the characteristics of the AFS in the temperature range from 253 to 308 K in accordance with the possible technical conditions for the operation of the device. A prototype AGC was included in the structure of the AFS, whose output characteristics were measured. After processing the obtained data, plots of the dependence of the values of the Allan variance σ(τ) on time τ were plotted for the modernized and previous AFS designs Fig. 2.

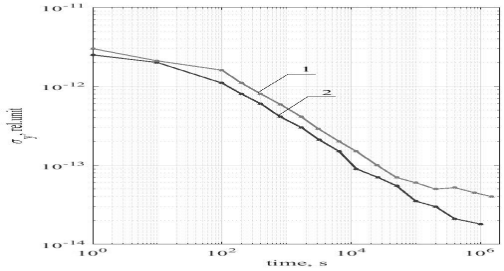

Figure 2. The dependence of change to the Allan variance. Graphs 1 and 2 correspond to AFS using the old system and the new AGC system.

The results obtained show an improvement in the Allan variance σ(τ) by 12%. Studies of the operation of the AFS were carried out for 12 days in a temperature chamber.

4. Conclusion

The results of the analysis of the prototype operation showed that the chosen implementation scheme works correctly and the introduction of an automatic gain control system improves the output characteristics of the frequency converter. The AGC system made it possible to reduce the values of the Allan variance by 12%.

References

[1] Petrov A, Davydov V and Grebenikova N 2018 *Journal of Communications Technology and Electronics* **63(11)** 1159–1164

[2] Riechle F 2004 Frequency Standards. Basics and Applications (Wiley-VCH, New Jersy)

Fabrication of a micropump based on the fast electrochemical actuator with the PDMS membrane

I V Uvarov[1,2], **P S Shlepakov**[1,2], **A M Abramychev**[1,2] **and V B Svetovoy**[1,3]
[1]Valiev Institute of Physics and Technology RAS, Yaroslavl Branch,
Universitetskaya 21, 150007 Yaroslavl, Russia
[2]P.G. Demidov Yaroslavl State University, Sovetskaya 14, 150003 Yaroslavl, Russia
[3]A.N. Frumkin Institute of Physical Chemistry and Electrochemistry RAS,
Leninsky pr. 31, 199071 Moscow, Russia

Abstract. Microfluidic devices can deliver drugs to a human body in small accurate doses. For this purpose, they have to be equipped by a compact, energy-efficient and microtechnology-compatible pump. A recently proposed micropump based on the fast electrochemical actuator meets these requirements. It contains three actuators operating in a peristaltic manner. The first version of the pump was not completely functional due to the shortcomings of the fabrication process. In this work, we propose the modified technological route. Flexible membranes of the actuators are made of PDMS instead of SiN_x, which increases the fabrication yield. The route includes the formation of the PDMS membrane on a flexible film and two steps of bonding of the membrane to a photoresist SU-8, which are the most critical operations. The details of the fabrication process are reported and optimal bonding conditions are found.

1. Introduction

Microfluidic devices are attractive for chemical, biological and medical applications including precise drug delivery to a human body. Drug delivery modules require a compact, energy-efficient and microtechnology-compatible pump. A recently proposed micropump based on the fast electrochemical actuator satisfies these criteria [1]. A main part of the pump has a size of about 3 mm, which is an order of magnitude smaller in comparison with conventional micropumps. The pump is designed to have a flow rate of 1.5 μL/min with a dosage accuracy of 0.25 nL, targeting portable drug delivery devices. The first version of the pump was not completely functional due to fabrication disadvantages. The device was equipped with the SiN_x membrane that was bonded to the channels made of SU-8 photoresist. The bonding quality was sensitive to the surface imperfections, contaminants and process conditions, which led to a rather low fabrication yield. To solve this problem, we propose to make the membrane of polydimethylsiloxane (PDMS). This soft material envelops particles and defects on the SU-8 surface, thereby preventing the leakage. Here we describe the modified fabrication process for the micropump that uses the fast electrochemical actuator. The most critical operations related to the formation of the PDMS membrane and bonding it to SU-8 are described in detail.

2. Design of the pump

The micropump contains three working chambers of 500 μm in diameter and 16 μm in height with two electrodes inside, see figure 1. The chambers are covered by a 60 μm thick PDMS membrane and filled with an electrolyte. One of the electrodes in each chamber is grounded, while a series of alternating polarity voltage pulses is applied to another electrode. Nanobubbles (NBs) of hydrogen and oxygen are

generated in the chamber and push the membrane up. The membrane blocks the channel for the liquid to be pumped, which is formed in the SU-8 layer above the chambers. When the pulses are turned off, the NBs recombine in milliseconds, and the membrane returns to the initial state. Driving signals are applied in such a way that the actuators operate peristaltically and push the liquid from the inlet to the outlet [1].

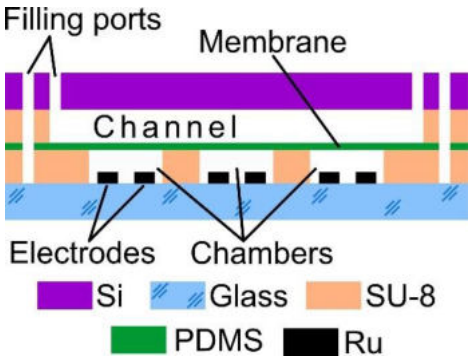

Figure 1. A schematic illustration of the micropump cross-section.

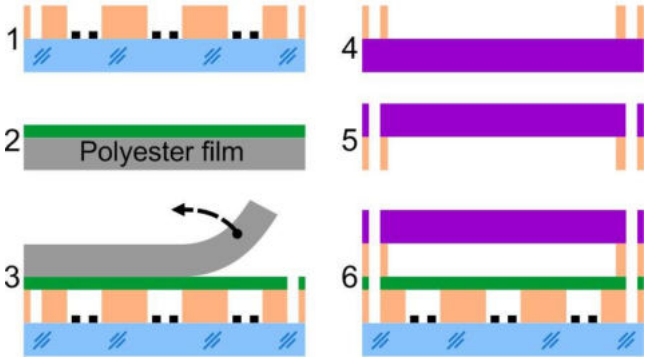

Figure 2. Fabrication process for the micropump.

3. Fabrication

The newly proposed fabrication process of the micropump is shown in figure 2. At the first step, ruthenium electrodes are deposited by magnetron sputtering on the glass substrate and the chambers are formed in the SU-8 layer. Then the PDMS membrane is formed. PDMS is spin-coated onto the polyester film (step 2) and bonded to the SU-8 surface. The film is detached from the PDMS layer, and holes for filling the chambers with the electrolyte are punched (step 3). Then a silicon wafer with the channel for the pumped liquid is prepared. The channel is made in the SU-8 layer (step 4), and the filling ports are etched using the BOSCH process (step 5). Finally, this wafer is bonded to the PDMS layer (step 6).

The proposed route includes two bonding steps. The bonding is carried out by N_2 plasma treatment of the PDMS layer followed by pressing it manually to the SU-8 surface and heating the sample to initiate the N-C bond [2]. This process is the most critical part of the fabrication. Too high pressure and high power of the plasma produce cracks in the PDMS surface, while too low values are not enough for activation of amino groups. Both cases lead to poor adhesion and leaks of the liquids. In this work, the conditions of plasma treatment are varied and the optimal parameters for the strongest adhesion are found.

Acknowledgments

This work is supported by the Russian Science Foundation, Grant No. 18-79-10038.

References

[1] Uvarov I V, Shlepakov P S, Melenev A E, Ma K, Svetovoy V B and Krijnen, G J 2021 *Actuators* **10** 62

[2] Zhang Z, Zhao P, Xiao G, Watts B R and Xu C 2011 *Biomicrofluidics* **5** 046503

Microwave Schottky diodes based on single GaN nanowires

K Yu Shugurov[1], A M Mozharov[1], V V Fedorov[1], G A Sapunov[1] and I S Mukhin[1,2]

[1] Alferov University (former St. Petersburg Academic university), 8/3 Khlopina st., St. Petersburg 194021, Russian Federation

[2] ITMO University, 49 Kronverksky pr., St. Petersburg 197101, Russian Federation

E-mail: shugurov17@mail.ru

Abstract. A series of Schottky diodes based on single GaN nanowires has been fabricated. According to the frequency response data of diode structures at various bias voltages, the parameters of the corresponding equivalent electrical circuit were determined. It is shown that the cutoff frequency of the fabricated diodes reaches 13.66 GHz.

1. Introduction

At the present stage of technical development, microwave technologies are widely implemented in various fields of science and technology - these are, first of all, mobile and satellite communications, local data transmission systems (Wi-Fi, Bluetooth), radar and navigation systems (GPS, GLONASS), medical equipment. The global trend in the development of the microwave industry is characterized by the expansion of the frequency range both to increase the data transfer rate and to create more advanced communication systems, telecommunications, equipment, etc. From the point of view of space applications, equipment that is resistant to thermal and radiation loads is needed, which will ensure a long service life of spacecraft and satellites. For example, at the moment, the estimated service life of satellites of the GLONASS system is 5-7 years, however, in reality, a large number of satellites fail earlier. To solve the existing problems and tasks of the microwave industry, a more advanced electronic component base (diodes, transistors, integrated circuits, etc.) is required, as well as the creation of new concepts of semiconductor devices.

Great prospects for the development of microwave electronics are associated with gallium nitride (GaN), which, due to economic factors, has not yet been widely used in industry. Nevertheless, microwave integrated circuits and transistors are already being produced on its basis. To date, all commercial components are made on the basis of planar structures, which in the case of GaN complicates the manufacturing technology of devices due to the lattice mismatch between the layers of the active region and the growth substrate. In this regard, of practical interest is the use of quasi-one-dimensional structures - nanowires (NWs) - which, due to their properties [1,2], can potentially not only improve the electronic characteristics of devices, but their use also represents an economic benefit.

2. Experiment

The undoped GaN NWs were synthesized on Si substrates via plasma-assisted molecular beam epitaxy (PA-MBE) technique. Then, GaN NWs were separated from the growth substrate and were dropped on a quartz wafer. As a result, GaN NWs were horizontally placed on the auxiliary substrate.

In the course of further postgrowth processing, using laser lithography and vacuum deposition of metals to single GaN NWs, electrical contacts were formed in the GSG (Ground-Signal-Ground) geometry for subsequent measurement of the frequency characteristics of the fabricated diodes. Gold was used as the metal forming the Schottky barrier. Ti (20 nm)/Au (300 nm) bilayer coating was used as ohmic contacts. During electrical measurements the current-voltage characteristics were obtained, which demonstrate a characteristic rectification, that indicates the formation of a Schottky barrier at the Au/GaN NW interface. To estimate the frequency parameters of the diodes using a vector network analyzer (VNA), the frequency dependence of the S-parameters was measured in the range of 10 MHz - 40 GHz with further approximation of the curves by an equivalent circuit.

3. Summary

In conclusion, it can be noted that a series of Schottky diodes based on single GaN NWs was fabricated. Using the VNA, the frequency dependences of the parameter S_{21} were obtained in the range of 10 MHz - 40 GHz. Approximation of experimental data was carried out using the proposed equivalent electrical circuit. It was found that the cutoff frequencies of the investigated diodes lie in the microwave range, while the highest cutoff frequency reaches 13.66 GHz.

References

[1] Dogan P, Brandt O, Pfüller C, Lähnemann J, Jahn U, Roder C, Trampert A, Geelhaar L and Riechert H 2011 Formation of High-Quality GaN Microcrystals by Pendeoepitaxial Overgrowth of GaN Nanowires on Si(111) by Molecular Beam Epitaxy *Cryst. Growth Des.* **11** 4257–60

[2] Shugurov K, Mozharov A, Sapunov G, Fedorov V, Tchernycheva M and Mukhin I 2021 Single GaN Nanowires for Extremely High Current Commutation *Phys. status solidi – Rapid Res. Lett.* **15** 2000590

Analysis of STDP characteristics of HfO2-based memristor

O O Permyakova[1, 2], **A E Rogozhin**[1], **A V Miakonkikh**[1], **E A Smirnova**[1], **K V Rudenko**[1]

[1]Laboratory of Microstructuring and Submicron Devices, Valiev Institute of Physics and Technology RAS, Moscow 117218, Russia

[2]Department of Physical and Quantum Electronics, Moscow Institute of Physics and Technology, Dolgoprudny 141701, Russia

o.permyakova@phystech.edu

Abstract. Spike-time dependent plasticity (STDP) has been commonly used as a main learning rule in computational learning models. STDP is then need to be studied in structures in order to design devices capable of unsupervised learning. In this paper we consider STDP in memristor with HfO_2/HfO_XN_Y active layer. A shift of the maximum weight update from 0.4 s to 2.4 s was found with an increase in the spike amplitude from 0.6 V to 0.8 V.

1. Introduction

A natural electronic component for the hardware implementation of artificial intelligence is a memristor [1]. The use of a memristor as a synapse is possible due to the gradual (analog) change in the resistance of the device. In this case, it is possible to associate the resistance of the device with the weight of the synapse of the neural network. The change in the resistance of the device is called resistive switching (RS). RS is possible when a voltage with an amplitude above the threshold is applied to the device. The simplest form of a memristor is a planar metal-insulator-metal structure. Due to the structure of the device, the array of memristors can be placed in the form of a crossbar array [2]. Spike-time dependent plasticity (STDP) learning is an unsupervised learning algorithm adopted from biology. STDP is based on time interval between presynaptic and postsynaptic spikes [3].

2. Device characterization

The $Pt/HfO_2/HfO_XN_Y/TiN$ structures were formed by PEALD using TEMAH and water vapor for HfO_2 layer, TEMAH and hydrogen plasma for HfO_XN_Y. Magnetron sputtering was used to deposit the electrodes. The top Pt electrode was deposited through a shadow mask. The study of device's STDP were conducted using a semiconductor characterization system Keithley-4200SCS. Pulses were applied to the upper electrode from the built-in 4205-PG2 pulse generator card while the lower electrode of the device was grounded. The signal output from the device was amplified using a transimpedance amplifier. After amplification the signal was delivered to the built-in 4200-SCP2HR oscilloscope.

STDP of $Pt/HfO_2/HfO_XN_Y/TiN$ structure are shown in figure 1. Since the pulses were applied to the one electrode, the pulses that would supplied were pre-calculated as sum of two identical spikes applied to the device to the both electrodes (Fig.1, inset). Weight update was calculated as follows: $(W_1-W_0)/W_0$, where W_0 - conductivity before spike, W_1 - conductivity after spike. Then when pre-spike follows post-spike ($dt<0$) the weight update is changed in the range (-1, 0). And when post-spike

follows pre-spike (dt>0) the weight update is changed in the range (0, ∞). Using triangle spikes STDP have form of symmetric Hebbian rule. Within negative interval between spikes weight update was similar independent of spike amplitude (0.6 V or 0.8 V). Using triangle spikes, STDP has a form of symmetric Hebbian rule. Within the negative interval between spikes, the weight update was similar regardless of spike amplitude (0.6 V or 0.8 V). However, within the positive interval between spikes, the largest weight update occurred at the spike interval of 2.4 ms at a spike amplitude of 0.8 V, in contrast to the largest weight update occurring at the spike interval of 0.4 ms at a spike amplitude of 0.6 V. This effect is currently being investigated.

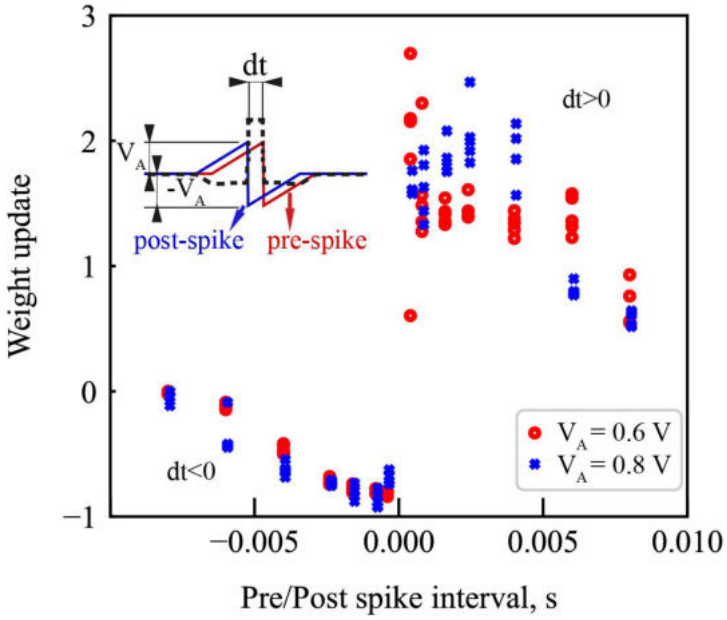

Figure 1. Experimental STDP of $Pt/HfO_2/HfO_XN_Y/TiN$ structure in range of tens milliseconds for different spike amplitudes (V_A): red circle - 0.6 V, blue cross - 0.8 V.

Acknowledgments
The reported study was funded by the Program no. FFNN-2022-0019 of the Ministry of Science and Higher Education of Russian Federation for Valiev Institute of Physics and Technology of RAS and by RFBR according to the research project no. 18-29-27029.

References
[1] Sung Hyun Jo et al. 2010 *Nano Lett.* **10** 1297
[2] Y. Zhang et al. 2020 *Appl. Phys. Rev.* **7** 011308
[3] G. Ashish and K. Takashi 2020 *Frontiers in Neuroscience* **15** 741116

Voltage noise and fluctuation mechanisms in ultrathin NbN nanowires.

M D Soldatenkova[1,2], E M Baeva[2], N A Titova[2], A D Triznova[2], P I Zolotov[2], A I Kolbatova[1,2] and G N Goltsman[1,2]

[1]Moscow State pedagogical University, Moscow 119435, Russia
[2]National Research University Higher School of Economics, Moscow 101000, Russia

soldatenkova.mariya.99@mail.ru

Abstract. Here we report on study of the voltage noise in ultrathin NbN nanowires at the resistive transition and in the normal state of superconductor. The study can be useful for understanding the detection mechanism in single-photon detectors and may reveal details for devices operating at low temperatures.

1. Introduction

Superconducting NbN nanowires have attracted interest for superconducting circuits, quantum computation and high frequency devices. For instance, single phonon detectors based on long superconducting nanowires (SNSPD) [1] are extensively used in optical and infrared technologies due to their ultimately high sensitivity and very high response speed [2]. Further development of technologies propels constant optimization of such devices. In particular, it stimulates study of the origins and control of intrinsic fluctuations in ultrathin superconducting nanowires deeper. Fluctuation phenomena may influence the main figures of merit of the SNSPD devices, such as jitter [3], dark counts [4], and latching [5]. Moreover, their study may help to reveal details about the detection mechanism in single photon detectors [6]. Here, we focus on study of the voltage noise in ultrathin NbN nanowires at the normal state above the resistive transition and at the onset of the resistive transition.

2. Sample and experimental setup

With the aim of gaining a deeper insight into the properties of NbN, we performed different experimental investigations, including DC electrical transport measurements and noise in normal state as well at the resistive transition. The measuring setup is presented in the work [7]. Ultrathin NbN film of 5 nm thickness was deposited by DC magnetron sputtering onto Si substrate and patterned to form bridges with width of 70 nm. The image of the sample in the microscope and R(T) dependence are presented in figure 1 a.

3. Results and discussion

Mechanisms of fluctuations are usually studied using *R(T)* dependencies and voltage-current characteristics (Figure 1 b). In addition, we propose to investigate the noise dependences for two different temperatures (Figure 1 c). Voltage noise at the resistive transition can be determined by the following components: the Johnson-Nyquist thermal noise, the temperature fluctuations noise, and the phase slip noise. Johnson-Nyquist thermal noise [8] is defined as $S_1 = 4k_B T R_{diff}$. We are also

considering noise contribution due to temperature fluctuations [9] $\langle \delta T^2 \rangle = \int S_T(f)df = k_B T^2/cV$, where c is the specific heat capacity, V is the sample volume, S_T is the spectral density of the temperature fluctuations. Temperature at fluctuation transition can cause the resistance fluctuations, which are in the current-biased conductor caused to the voltage fluctuations: $S_V = I^2 S_R = I^2 (dR/dT)^2 S_T$. To estimate the magnitude of this noise one can make the following assumptions: temperature fluctuations are slow, and they occur with the characteristic correlation time $\tau = c/G$, where G is the heat conductance coefficient, which is determined by the electron-phonon relaxation or escaping phonons from the film to the substrate. Thus, the spectral density of voltage fluctuations is given by $S_2 = 4k_B T_e^2 I^2 (dR/dT_e)^2 / G$. Noise due to thermally induced phase slips [10] is defined by analogy with conventional shot noise as $S_3 = 2V_{DC}\phi_0$, where ϕ_0 is magnetic flux quantum. The joule power destroy large quantities of cooper pairs and reduce the free energy barrier of phase slips, resulting in proliferation in the phase-slip events and leading to superconducting transition. The phase slip equal to 2π leads to the appearance of a voltage at the ends of the sample. According to our discussions we have the following estimations: $S_{v1} = 2.6 * 10^{-18} V^2/Hz$, $S_{v2} = 9.3 * 10^{-20} V^2/Hz$ and $S_{v3} = 4.14 * 10^{-19}\, V^2/Hz$ for ultrathin NbN nanowires with the parameters $dR/dT = 35\ kOhm/K$, $V_{DC} = 0.1\ mV$. In comparison, the experimental value of giant noise is $2.66*10^{-18}\, V^2/Hz$. In addition, we consider functional dependences of noise spectral density S_v on current I and voltage V and we have got that $S_v \sim I^2$ and $S_v \sim V$. We have estimated of the contribution of various noise mechanisms to voltage fluctuations at a superconducting transition and considered mechanisms of the occurrence of giant noise. Voltage noise in normal state is determined by the thermal relaxation limited by the Kapitza resistance. The nature of the giant noise at the superconductive transition remains an open question.

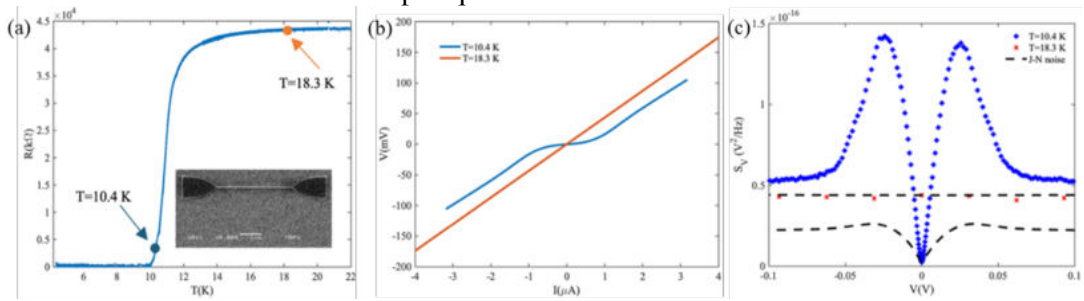

Figure 1. (a) T-dependence of resistance and image of the structure obtained in a scanning electron microscope. (b) Volt-ampere characteristics for two different temperatures T= 10.4 K и T=18.3 K. (c) The dependence of the spectral density of the voltage fluctuations on the V for the sample in comparison to the Johnson-Nyquist equilibrium noise, shown by the dashed line, where «plus symbols» - giant noise at the transition, «cross symbols» - noise in the normal state.

Acknowledgments

Authors wishing to acknowledge the RSF project 19-72-10101 for the noise measurements.

References

[1] G. Gol'tsman et al 2001 *Appl. Phys. Lett* **79** 705-707
[2] Verevkin A et al 2004 *Journal of Modern Optics* **51** 1447-58
[3] Vodolazov D et al 2020 *Phys. Rev. Applied* **14** 044041
[4] Kitaygorsky J et al 2005 *IEEE* **15** 545-548
[5] Nagaev K 1995 *Phys. Rev. B* **52** 4740
[6] Engel A, Renema J, Il'in K and Semenov A 2015 *Supercond. Sci. Technol.* **28** 114003
[7] Baghdadi et al 2020 *Phys. Rev. Applied* **14** 054011
[8] Clark J and Hsiang Y 1975 *Phys.Rev.Let.* **34** 1217-20
[9] Landau L and Lifshitz E 1980 *Statistical Physics* vol **5**
[10] Semenov A and Zaikin A 2016 *Phys. Rev. B* **94** 014512

Impact of the current pulse width on the speed of metal-insulator transition in VO_2 nanobeams

Georgy Alymov

Moscow Institute of Physics and Technology, Dolgoprudny 141700, Russia

alymov@phystech.edu

Abstract. VO_2 undergoes an insulator-metal transition at ~68 °C, making it an attractive material for the development of electrically and/or optically controlled metasurfaces and other optoelectronic devices. Applications such as wireless communications call for ultrashort transition times, which are thought to be limited by heat dissipation. We consider the possibility of improving the transition speed by using short current pulses, thereby preventing heat accumulation in the substrate. Thermal simulations for different pulse durations show that this approach can improve the transition speed by approximately two times when the pulse duration is reduced from 10 ns to 0.1 ns (for a 30 nm × 200 nm nanobeam).

1. Introduction

VO_2 undergoes a first-order insulator-metal transition (IMT) at T_c ~ 68 °C accompanied by an abrupt increase in conductivity and reflectivity. This makes it attractive for a range of applications in electronics and optoelectronics, including electrically and/or optically controlled metasurfaces [1], Mott transistors [2], and memristors [3]. Previous theoretical and experimental work has shown that the switching speed of VO_2 devices is likely to be limited by the rate of heat dissipation [4], while the "intrinsic" characteristic time of the IMT lies in the subpicosecond range [5].

Therefore, the most obvious ways of improving the transition speed in VO_2 are (i) going to the nanoscale (thin films, nanobeams, nanocrystals) and (ii) using substrates with good thermal conductivity (such as Al_2O_3). Both approaches have been successfully tested experimentally [6].

But there remains another possibility, related to the nonstationary nature of heat flow in fast-switching devices. If the device remains in the metallic (high-temperature) phase long enough, heat will accumulate in the substrate and prevent efficient cooling of the device when heating current is switched off, thereby slowing down the reverse, metal-insulator (MIT), transition. On the other hand, if VO_2 is heated by short current pulses and stays hot (metallic) only for short periods of time, the substrate will have time to cool down between the pulses, and the reverse switching will be faster. This is especially relevant for the combined optical/electrical control of VO_2 metasurfaces, when electric current is used to reduce the optical switching threshold and does not necessarily have to be pulsed [7].

2. Results

We consider an infinitely long VO_2 nanobeam of 200 nm width and 30 nm thickness grown on a 1 mm-thick single-crystal Al_2O_3 or SiO_2 substrate. It is heated by square current pulses and then cools down, switching back into the semiconducting phase. We calculate the switching time by numerically solving the heat equation, taking into account the latent heat of MIT. The switching time is defined as the interval between the end of a pulse and the moment when the whole nanobeam cools down below the transition temperature. The backside of the substrate is held at 25 °C.

The results are shown in Fig. 1. Indeed, long current pulses lead to slower switching, which is explained by the heat accumulation in the substrate (Fig. 2).

Our results indicate that pulsed heating can improve the switching speed of various optoelectronic devices based on VO_2.

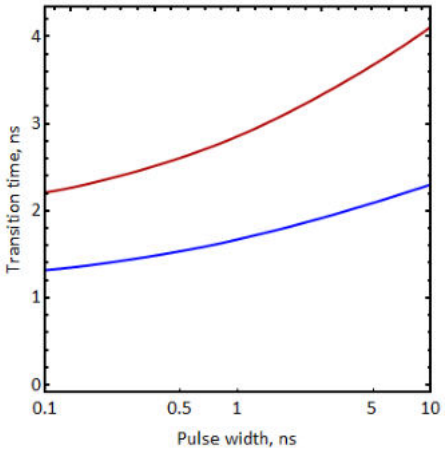

Fig. 1. Transition time in a 30 nm × 200 nm VO_2 nanobeam vs the duration of current pulses. Red curve: SiO_2 substrate, blue curve: Al_2O_3 substrate.

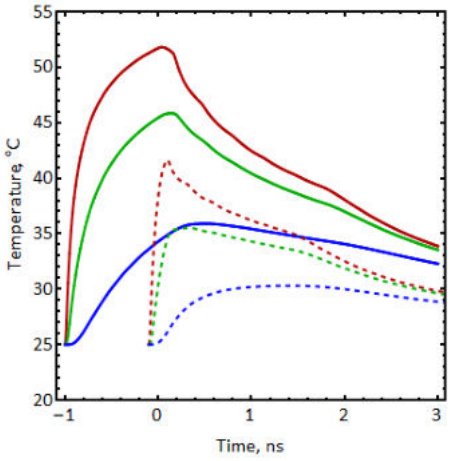

Fig. 2. Al_2O_3 temperature under the nanobeam center vs time (0 corresponds to the end of the pulse). Red, green, blue curves: 25, 50, 100 nm below the nanobeam. Solid curves: 1 ns pulse, dashed curves: 0.1 ns pulse.

Acknowledgments

This work was supported by the grant No. 21-79-00209 of the Russian Science Foundation.

References

[1] J. Shabanpour, S. Beyraghi, and A. Cheldavi. "Ultrafast reprogrammable multifunctional vanadium-dioxide-assisted metasurface for dynamic THz wavefront engineering." Sci. Rep. 10.1 (2020): 1-14.

[2] S. Sengupta et al. "Field-effect modulation of conductance in VO2 nanobeam transistors with HfO2 as the gate dielectric." Appl. Phys. Lett. 99.6 (2011): 062114.

[3] J. Lappalainen, J. Mizsei, and M. Huotari. "Neuromorphic thermal-electric circuits based on phase-change VO2 thin-film memristor elements." J. Appl. Phys. 125.4 (2019): 044501.

[4] Y. Zhang and S. Ramanathan. "Analysis of “on” and “off” times for thermally driven VO_2 metal-insulator transition nanoscale switching devices." Solid State Electron 62.1 (2011): 161-164.

[5] A. Cavalleri et al. "Evidence for a structurally-driven insulator-to-metal transition in VO_2: A view from the ultrafast timescale." Phys. Rev. B 70.16 (2004): 161102.

[6] M. Jerry et al. "Dynamics of electrically driven sub-nanosecond switching in vanadium dioxide." 2016 IEEE Silicon Nanoelectronics Workshop (SNW). IEEE, 2016.

[7] V. E. Kaydashev, S. Zhukov,M. Kutepov, I. Domaratskiy, A. Slavich, Metasurfaces based on Au and VO_2 for THz applications, Saratov Fall Meeting 2020.

Self-organization of quantum dots and porphyrin Langmuir monolayers on the surface of water subphase

A J Al-Alwani, V N Mironyuk, K A Polyakova, O A Hassoon, M V Gavrikov, E G Glukhovskoy

Saratov State University, Saratov 410012, Russia

E-mail: ammarhamlet2013@yahoo.com

Abstract. In this study, surface pressure isotherm and surface potential methods were used for studying the effect of porphyrin on the properties of semiconductor quantum dots. The presence of porphyrin with quantum dots influenced the self-organization of the Langmuir monolayer at the air-water interface. The occupied area of porphyrin has been estimated theoretically and experimentally. The stability of monolayers over time has been investigated. A significant change in the values of the surface potential was found depending on the composition ratio of monolayers. The mechanical properties of monolayers have been studied.

Introduction

Currently, Langmuir-Blodgett technology is used to create optoelectronic and photovoltaic devices such as LEDs and solar elements. The main idea of the technology is the self-organization of molecules surfactants at the water-air interface into objects with a high degree of structural perfection. One of the promising materials for creating Langmuir monolayers are the semiconductor quantum dots of CdSe/CdS/ZnS, which have found their application in various fields of science and technology. This is due to their unique optical and electrical characteristics [1] that result from the manifestation of a quantum-size effect in them, and as mixed monolayer with other components. The compound of porphyrin in quantum sots solutions use energy transfer between quantum dots and fluorescent probes and/or photosensitizers and this may increase the photodynamic therapy efficacy [2]. This work study the principal opportunities provided by using the Langmuir-Blodgett technology is to create ordered arrays of quantum dots separated from each other by the material of molecules fillers (porphyrin).

Materials, Results and discussion

Experimental study of the process of formation of mixed was carried out by the method of compression isotherms on a KSV Nima LB setup Trough KN 2002. Deionized water with specific conductivity 18 MOhm × cm, with acidity equal to 7 at a temperature of 25 °C. The surface potential isotherms were obtained by KSV NIMA Surface Potential Sensor. The solution of hydrophobic quantum dots in chloroform with a concentration of 10^{-6} M was synthesized by I.Yu. Goryacheva's group [3]. Amphiphilic porphyrin 5,10,15,20-tetrakis (4-hexadecyloxyphenyl) (Ia-16) was synthesized by Smirnova A I group [4], with concentration 10^{-4}M. The occupied area per molecule of porphyrin was found ~ 78Å^2.

Working solutions used with the following values of the quantum dots and porphyrin at ratio (1:0, 1:1, 2:1, and 3:1). By analyzing the compression isotherm of monolayers and a graph changes in its derivative, three phase states of a monolayer can be distinguished: gas phase - with areas exceeding 170 cm^2, liquid condensed - at areas from 170 to 127 cm^2 and the phase of the condensed quantum dots film - at areas less than 127 cm^2, according to the classification proposed in the works [5]. However, the isotherm of mixed at ratio of 3:1 shown a decrease in the occupied area of monolayer by 33.5% with noticeable lower shift in the value of surface potential of isotherm gas phase. An increase in the value of the compression model of mixed monolayers by 18% at ratio 3:1with respect to quantum dots monolayer.

The study of the monolayers stability was carried out according to the following method - the monolayer was compressed to a given value of the surface pressure at 20 mN/m, which corresponded to the middle of the section with the maximum angle of inclination of the tangent, after 30 minutes, the specified surface pressure value by continuously decreasing the value monolayer area. The results showed an enhancement in the stability of mixed monolayers of quantum dots and porphyrin with compare to only quantum dots monolayers. The interesting point in the result of the stability of mixed monolayers showed that the surface potential value shifts to the higher value by 3%. In this case, the results could be explain by (1) the interaction of polar group between components lead to reduces the value of surface potential, (2) the stability of monolayer during 30 minutes, a dissolution process in the components of monolayers leads to less polar interaction between the mixed component cases one direction of dipole moment and shows an increase in the value of surface potential. This study can establish a mechanism for creating heterostructure thin films with improved performance properties.

The formation of a mixed monolayer of quantum dots and porphyrin has been studied. The presence of porphyrin with quantum dots solution affects the formation and mechanical characteristics of Langmuir Langmuir monolayers. Also, enhance the stability of monolayers over time by reducing the ratio of dissolution of molecules and increase the surface potential value due to reduce the dipole interaction of a head group of the hydrophobic part. The rigidity of mixed monolayers increased by 18% at ratio 3:1.

Acknowledgments

This work is supported by a grant from the Russian Science Foundation (project No. 21-73-20057) and Saratov State University.

References

[1] Michalet X, Pinaud FF, Bentolila LA et al 2005 Science. **307** 538– 544.

[2] Allison RR, Downie GH, Cuenca R et al 2004 Photodiagn Photodyn Ther. **1** 27–42.

[3] Speranskaya, E.S. et al 2014 Biosensors, and bioelectronics. **53** 225-231.

[4] Smirnova A I 2019 Liq. Cryst. and their Appl. **19(4)**, 25–37.

[5] Adamson A.W. 1997 Physical Chemistry of Surfaces. Sixth Edition / A.W. Adamson, A.P. Gast. – New York : A wiley-interscience publication. John Wiley & Sons, Inc. 784.

Design of the Two-Axis MEMS Gyroscope-Accelerometer

I E Lysenko[1], M A Denisenko[1], A S Isaeva[1] and A V Kozlov[2]

[1]Southern Federal University, Taganrog, 347922, Russia
[2]Center for Collective Design of Electronic component Base and Electronic Equipment. National Research University of Electronic Technology, Zelenograd, Moscow, 124498, Russia

dema@sfedu.ru

Abstract. We have developed an inertial sensor, which is a functionally integrated microelectromechanical system that includes a two-mass two-axis gyroscope-accelerometer. The device is a highly sensitive multisensor that allows solving problems of object orientation in space and control of its movement parameters. The article presents the design and topology of the sensor element. The results of modeling obtained using CAD ANSYS are presented. The scope of this inertial sensor is diagnostic systems for the needs of railway transport..

1. Introduction

Inertial sensors are one of the main segments of the microelectromechanical systems market. MEMS accelerometers and gyroscopes are widely used in all high-tech areas: from children's toys and wearable electronics to the automotive and aviation industries, heavy engineering and space [1].

An important direction in the application of modern achievements in the design of inertial MEMS sensors are all kinds of diagnostic systems, systems for monitoring and controlling the parameters of engineering objects, such as railway transport facilities. Sensitive elements can be used not only to monitor the current state, but also as part of systems using machine learning methods and artificial neural networks that allow predicting the future state of research objects [2].

2. Design and simulation

The proposed design of a two-mass two-axis gyroscope-accelerometer is shown in Figure 1. The following designations are used in the figure: C1, C2, C3, C4 – capacitive accelerometer transducers; A1, A3 – gyroscope actuators; M1, M2 – inertial masses. Contacts are located as follows: 1, 5, 9, 11, 15, 19, 23, 26 – corresponding auxiliary plates of comb capacitors; 2, 4 – actuator rotors A1; 3 – main plate of actuator A1; 6, 8 – plates of capacitor C2; 10 – central plate; 12, 14 – plates of capacitor C3; 13 – capacitor rotor C3; 16, 18 – actuator rotors A3; 17 – the main plate of the actuator A3; 20, 22 – plates of capacitor C4; 21 – rotor of capacitor C4; 24 – rotor 2; 25 – rotor 3; 27, 29 – plates of capacitor C1; 28 – rotor C1.

We've developed a model of the presented micromechanical device that allows determining the movements of the inertial masses of the sensor under the action of electrostatic forces, angular velocities along two axes of sensitivity and linear accelerations along three axes of sensitivity with an error of less than 10%. Models for calculating the stiffness of the elastic suspension of the sensitive

elements of the MEMS device are also proposed, which allow calculating the natural frequencies of vibrations of the elastic suspension along the Y axis of motion, along the X and Z axes of sensitivity.

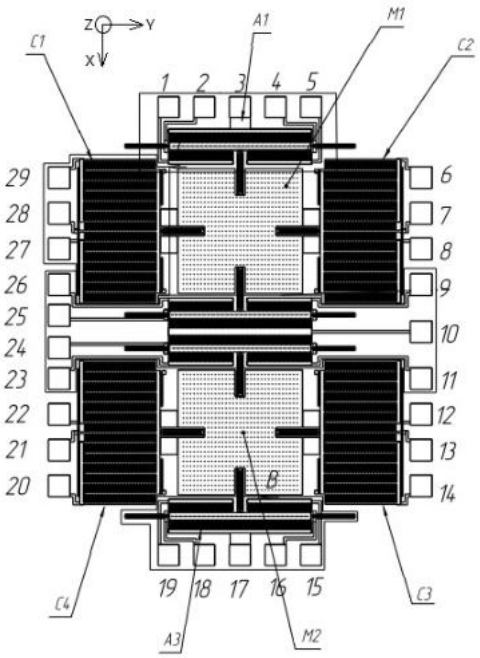

Figure 1. Integrated micromechanical inertial sensor with two sensitive axes.

The geometric model of the MEMS gyroscope-accelerometer was developed using the ANSYS Mechanical APDL software module. The sensitivity to angular velocity is 0.1 mv/deg./ s, and to the linear acceleration az - 1.5 mv / m / s2.

3. Conclusion

Thus, based on the simulation results, the final version of the design of the inertial MEMS sensor was obtained. In the Tanner L-Edit software module, a topology was developed in accordance with the rules for designing MEMS devices using the PolyMUMPs technology [3], and a test for compliance with production requirements (DRC) was carried out. The resulting project file in GDSII format was transferred to production. The results of the research have shown that when acceleration or angular velocity is applied along one of the axes, there is practically no effect on the other two axes, and the change in capacitance on the other two axes occurs within acceptable errors.

Acknowledgments

The work was carried out at the expense of funds, task No. FENW-2020-0022 for the implementation of scientific research carrying out scientific research at the expense of the Federal budget, in terms of scientific activities on the topic "Development and research of methods and means of monitoring, diagnostics and forecasting state of engineering objects based on artificial intelligence".

References

[1] Raspopov V Ya 2007 *Micromechanicheskie pribory: uchebnoye posobie* (Tula: Tulskiy gos. Universitet)

[2] Jing Y, Li S, Wang Z, Dong H, Wang J and Tang S 2020 *Using Deep Learning to Detect Defects in Manufacturing: A Comprehensive Survey and Current Challenges* Materials. **13** 1-23

[3] Koester D A, Cowen A, Mahadevan R, Stonefield M and Hardy B 2003 *PolyMUMPs Design Handbook: A MUMPsfi process*.

Electrical conductivity and optical properties of water-based graphene/AgNWs hybrid inks for flexible electronics

M A Dronova[1,2], M R Veretennikov[1] and E A Danilov[1]

[1] Research Institute for Graphite-Based Structural Materials "NIIgraphite", 111524, 2 Electrodnaya St., Moscow, Russian Federation
[2] Bauman Moscow State Technical University (BMSTU), 105005, Moscow, 5, 2nd Baumanskaya Str., Russian Federation

mariadv277@gmail.com

Abstract. The present study provides the description of water-based inks made of hybrid graphene-silver nanoparticles conductive fillers in a wide concentration range. Aqueous graphene suspensions were manufactured via ultrasonic exfoliation of pristine graphite, whereas polyol synthesis was used to obtain silver nanowires. Hybrid suspensions were centrifuged to improve transmittance while retaining electrical conductivity. As a result, conductive transparent films with transmittance up to 94% were successfully manufactured.

1. Introduction

Flexible electronics have shown great potential for applications in various areas of human life. Applications include flexible printed circuit boards, flexible electrodes for displays, antennas, wearable skin sensors, etc. [1] The growing need in printed electronics causes increased interest in manufacturing of new materials that meet optical and electrical requirements. Since the most common and simple method for flexible electronics production is inkjet printing technology, there are also specific requirements in terms of particle size, viscosity, adhesion, sintering temperature and so on.

The range of conductive inks types is very broad and includes conductive polymers, carbon nanotubes (CNTs), graphene and metal nanoparticles (MNPs) of various shapes. Currently, the most widely used inks are based on silver nanoparticles or nanowires due to their excellent electrical conductivity [2], or graphene [3]. However, both of these ink types have limitations. Specifically, high concentration of AgNPs and high sintering temperature are required to achieve desired conductivity values, or low conductivity of pure graphene ink that limits its widespread use. Moreover, high cost of Ag increases the processing cost. Combination of graphene and AgNWs solves cost-effectiveness problems by reducing the concentration of AgNWs. Simultaneously, it increases conductivity, and graphene improves the mechanical performance of AgNWs for flexible electronic applications.

2. Experimental section

The choice of solvent for graphene exfoliation can serve as a separate topic for research [4], but the use of water is most environmentally friendly and economically viable way. However, it requires the need to use surfactants. It has been experimentally confirmed that the use of 0.6 mg/mL of ZONYL

BA-L surfactant during the 7.5-hour ultrasonic exfoliation leads to a stable conductive suspension of graphene (6 mg/mL). Further sonication hardly changes particle size distributions.

Suspensions of AgNWs were made via polyol process. The main advantage of this process is the ability to vary wide number of parameters to obtain the required result [5]. In this study, we reduced silver nitrate with ethylene glycol at 178 °C in the presence of KBr, AgCl, and PVP (10^6 g/mol).

3. Results and discussion

Graphene/AgNWs hybrid inks with graphene content 0, 15, 25, 35, 50, 75, 85 and 100 wt.% were prepared and then centrifuged at 2000 rpm for 45 minutes in order to achieve satisfactory transparency and dispose of agglomerates. The resulting properties are shown in table 1. As can be readily seen from the dataset, although transparency was highest for 65 wt.% suspension, its conductivity is relatively low.

Table 1. Graphene/AgNWs hybrid inks properties

Graphene content, wt.%	0	15	25	35	50	65	75	85	100
Conductivity, μS/cm	105.9	139.2	121.8	105.8	85.8	58.7	48.1	47.7	47.0
Optical transmittance (550 nm), %	20.1	69.3	60.4	54.0	90.1	97.3	62.1	41.1	69.4

Thin films were made by drop-casting inks on glass substrate with dispenser and drying for 1 hour at 100 °C. Transparency measurements of both suspensions and thin films were performed via UV-Vis absorption spectrophotometry (Agilent Cary 60). Sheet resistance was calculated from current-voltage curves (linear region slopes) in a four point-probe cell (source/measure unit – Agilent b2901a) The best transmittance of 94.1 % was observed for the hybrid with 50 wt.% graphene content. The best sheet resistance of $3.1 \cdot 10^3$ Ω/sq is obtained for film with 35 wt.% graphene content.

4. Conclusion

In this work, water-based graphene/AgNWs hybrid inks were manufactured; their electrical conductivity and optical transmittance were measured. Transmittance after centrifugation for both liquid suspensions and thin films was above 80% for optimal concentration range. Best conductivity value of 139.2 μS/cm obtained for suspension with 15% graphene mass content whereas the best transparency was at 65 wt.% of graphene. The best sheet resistance for drop casted thin films of $3.1 \cdot 10^3$ Ω/sq is observed in the film with 35% graphene mass content.

References

[1] Htwe, Y. Z. N., Mariatti, M. Printed Graphene and Hybrid Conductive Inks for Flexible, Stretchable, and Wearable Electronics: Progress, Opportunities, and Challenges. Journal of Science: Advanced Materials and Devices. (2022) 100435.

[2] Fernandes, I. J., Aroche, A. F., Schuck, A., Lamberty, P., Peter, C. R., Hasenkamp, W., Rocha, T. L. Silver nanoparticle conductive inks: Synthesis, characterization, and fabrication of inkjet-printed flexible electrodes. Scientific reports. 10(1) (2020) 1-11.

[3] Capasso, A., Castillo, A. D. R., Sun, H., Ansaldo, A., Pellegrini, V., Bonaccorso, F. Ink-jet printing of graphene for flexible electronics: an environmentally-friendly approach. Solid State Communications. 224 (2015) 53-63.

[4] Htwe, Y. Z. N., Abdullah, M. K., Mariatti, M. Optimization of graphene conductive ink using solvent exchange techniques for flexible electronics applications. Synthetic Metals. 274 (2021) 116719.

[5] Fiévet, F., Ammar-Merah, S., Brayner, R., Chau, F., Giraud, M., Mammeri, F., ... & Viau, G. The polyol process: a unique method for easy access to metal nanoparticles with tailored sizes, shapes and compositions. Chemical Society Reviews. 47(14) (2018) 5187-5233.

TEM contrast enhancement by adsorption of erbium ions on the inner surface of micro-mesoporous silica particles

D A Eurov, D A Kirilenko, D A Kurdyukov and E Yu Stovpiaga
Ioffe Institute, 194021 St. Petersburg, Russia

Abstract. A simple and facile method is proposed for processing the inner surface of micro-mesoporous spherical particles of amorphous silica, which allows direct visualization of the porous structure by transmission electron microscopy (TEM). The method is based on the adsorption of ions of heavy elements (on the example of Er^{3+} ions) by the surface of the pores, which makes it possible to enhance the contrast in the TEM image. It is shown that the adsorption of erbium ions does not affect the internal structure of silica particles - the specific surface area, volume and pore size do not change.

Introduction

Porous silica particles are of great interest due to their inertness, biocompatibility and high adsorption capacity and are used in a wide variety of applications [1]. The porosity is one of the main characteristics of the particles in practical use. It determines the importance of the detailed study of the porous structure in order to fabricate materials with the required properties such as specific surface area, size, morphology and volume of pores. A number of methods are used to study the porous structure, in particular, adsorption porosimetry, small-angle X-ray scattering, transmission electron microscopy (TEM) [2,3]. Direct visualization of nanosize pores within the submicron particles by TEM is quite intricate due to the low contrast (because of a low atomic numbers of silicon and oxygen). In ordered channel-like materials (e.g. SBA-15) mesopores can be observed due to their regular spatial arrangement and orientation of the channels along a certain axis, while micropores in the channel walls are not visible. The introduction of a contrast agent (NaCl) into the reaction mixture during synthesis made it possible to visualize micropores in SBA-15 [4]. When studying the micro-mesoporous particles of amorphous silica synthesized earlier [5], the study of the porous structure by the TEM method becomes even more complicated due to the fact that the pores inside the particles are disordered. In this case, the interpretation of TEM images, which are, in some approximation, the projection of the density of a complex three-dimensional structure, is significantly difficult. To enhance the TEM contrast, we developed a method for the adsorption of heavy metal ions by the surface of pores, which made it possible to directly visualize their porous structure.

Results

In the present study we used monodisperse spherical micro-mesoporous silica particles (MMSP) with a diameter of 500 ± 25 nm. The particle synthesis is described in Ref.[5]. The functionalization of the inner surface with Er^{3+} ions was carried out by the method of capillary impregnation of particles with an erbium sulfate solution.

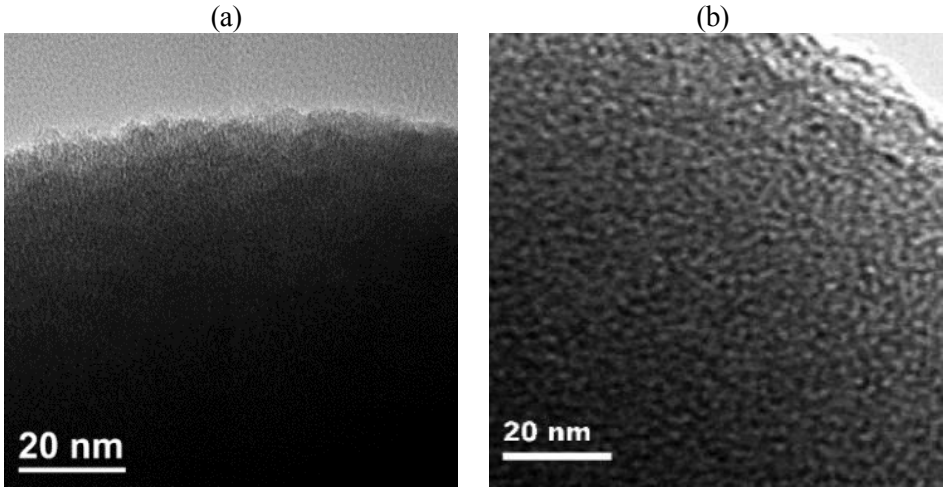

Fig.1 TEM images of micro-mesoporous silica particles before (a) and after (b) functionalization with erbium ions.

For this, a weighed portion (0.5 g) of particles was added to 5 ml of an $Er_2(SO_4)_3 \cdot 8H_2O$ solution and subjected to ultrasonic treatment for 2 h, after which the resulting suspension was left for a day. During the impregnation, erbium ions were adsorbed by active silanol groups on the surface of silica. To remove excess $Er_2(SO_4)_3$, the particles were sedimented by centrifugation, and the supernatant was separated. After that, the particles were dried in air at 60°C and then annealed at 200°C for 10 min. To remove bulk erbium compounds from the outer surface of the MMSP and nanocrystallites from their pores, the particles were immersed with a 5M HNO_3 and kept for 2 h, after which the particles were centrifuged and the supernatant was poured off. The procedure was repeated twice. The resulting particles were then washed twice with deionized water.

TEM images of MMSP before and after adsorption of erbium ions show that the size and shape of particles do not change. According to the results of adsorption structural analysis, the specific surface area and pore volume of particles before and after treatment with erbium sulfate solution also remained practically unchanged and were found to be 1630 m^2g^{-1}, 0.72 cm^3g^{-1} and 1610 m^2g^{-1}, 0.71 cm^3g^{-1}, respectively. This also agrees with the EDS (energy dispersive X-ray spectroscopy) data, which does not show significant Er content after adsorption). On the TEM images of MSSP treated with erbium sulfate, the porous structure of the particles is much more clearly visible due to the adsorbed Er^{3+} ions (fig.1). The proposed technique for processing of particles with Er^{3+} made it possible to visualize features less than two nanometers in size on high-resolution TEM images of the particles' surface region, which corresponds to the pore sizes calculated from the results of nitrogen porosimetry.

Conclusion

A method is proposed for functionalization of the inner surface of silica with Er^{3+} ions to visualize micro- and mesopores inside the particles by TEM. The proposed approach made it possible to significantly enhance the contrast in TEM images of MMSP. It was shown that the adsorption of erbium ions does not affect the particles' porous structure. The developed technique is simple, easily reproducible, inexpensive, and can be applied to most porous materials in which it is required to study the internal structure.

Acknowledgments

This work was funded by the Russian Science Foundation, project no. 22-23-20104 and by the St. Petersburg Science Foundation, agreement no. 27/2022 (14.04. 2022).

References

[1] Narayan R et al. 2018 Pharmaceutics **10** 118.
[2] Impéror-Clerc M et al. 2000 *J. Am. Chem. Soc.* **122** 11925
[3] Liu J et al. 2002 *Chem. Mater.* **14** 2536
[4] Kjellman T et al. 2013 *Chem. Mater.* **25** 4105
[5] Kurdyukov D A et al. 2016 *Micropor. Mesopor. Mater.* **223** 225

STUDY OF PIEZOCERAMIC MATERIALS POLARIZATION

A. E. Zhurina[1], E. A. Pecherskaya[1], A. V. Fimin[1], T. O. Zinchenko1[1], A. E. Shepeleva[1], G. V. Kozlov[1]

[1]Department of Information and measuring equipment and metrology, Penza State University, Penza 440026, Russia

gelya.zhurina@mail.ru

Abstract. The effect of temperature and electric field strength on the piezoceramic materials polarization has been studied. Experimental studies were carried out using the automated information-measuring system developed by the authors. It is based on the modified Sawyer-Tower method, which measures the hysteresis loops of the polarization dependences on the electric field strength in the ferroelectric phase at different temperatures. Indirectly, the calculation of the electrophysical parameters of piezoceramic materials, including the tangent of the dielectric loss angle, relative dielectric permittivity are carried out.

1. Introduction

Piezoelectric ceramics is a promising material for various applications, for example, it is used in the creation of sensors and actuators. The widespread use of piezoceramics has become possible due to high electromechanical coupling, large piezoelectric constants, high environmental and chemical stability, the ability to work at high temperatures and frequencies, a wide range of dielectric constants and low dielectric losses. Materials based on barium titanate (BaTiO3) are very popular among piezoelectric materials. It has been found that the dielectric and piezoelectric BaTiO3 properties can be improved by adding elements such as; Ca, Sr, Mg or Zr. It is stated in [1] that the BCZT ceramics, which has the composition Ba0.85Ca0.15Zr0.1ti0.9O3, has the most homogeneous microstructure. Many researchers have made great efforts to improve both the dielectric and piezoelectric properties of this material.

2. Dependence of $Ba_{0.85}Ca_{0.15}Zr_{0.1}ti_{0.9}O_3$ polarization on temperature

The study of the physical $Ba_{0.85}Ca_{0.15}Zr_{0.1}ti_{0.9}O_3$ properties, in particular, the study of the piezoceramic materials polarization is an important task. Heating ceramic samples to a glassy phase with subsequent cooling to room temperature leads to the fact that during cooling in the crystal cells a phase transition occurs, as a result of which the vectors of spontaneous piezoceramics polarization in the entire set of crystal lattices do not take the same direction, while entire regions, having the same direction of spontaneous polarization, which are domains [2] appear.

In [3], $Ba_{0.85}Ca_{0.15}Zr_{0.1}ti_{0.9}O_3$ (BCZT)ceramics were prepared using a conventional solid solution. A number of studies were carried out on the sample: the influence of temperature was studied (the sample surface was examined using a scanning electron microscope, etc.). On the basis of studies [3], a volume graph of the $Ba_{0.85}Ca_{0.15}Zr_{0.1}ti_{0.9}O_3$ polarization dependence on temperature and external electric field strength was constructed (Fig. 1).

With increasing temperature, the $Ba_{0.85}Ca_{0.15}Zr_{0.1}ti_{0.9}O_3$ polarization decreases, and with an increase in the strength of the external magnetic field- increases.

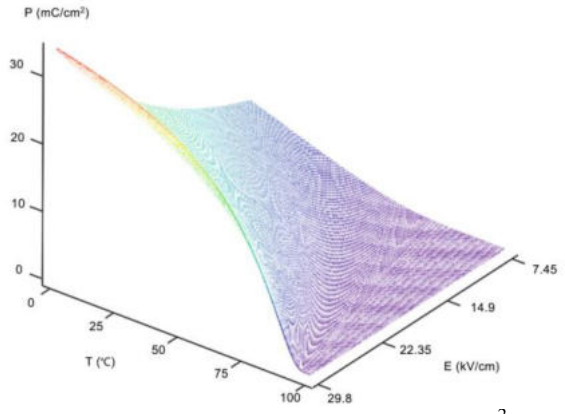

Figure 1. Dependence of $Ba_{0.85}Ca_{0.15}Zr_{0.1}ti_{0.9}O_3$ polarization P (mC/cm^2) on temperature T, °C and external electric field strength E (kV/cm).

To study the phenomenon of dielectric hysteresis of the polarization P dependence on the electric field strength E, the authors proposed an automated information-measuring system based on the modified Sawyer-Tower method [4, 5]. Fig. 2 shows the experimental dependence of the ferroelectric ceramics sample based on barium titanate polarization against tension electric field at a temperature of 80 °C.

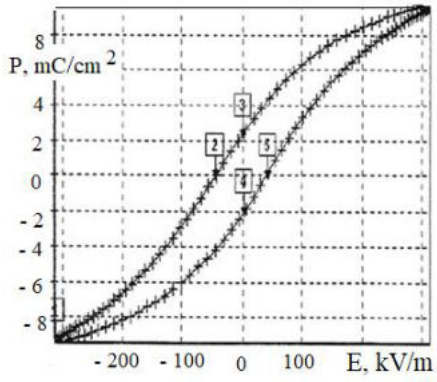

Figure 2. Experimental dependence of the ferroelectric ceramics sample based on barium titanate polarization against tension electric field at a temperature of 80 °C.

Conclusion

The proposed methods make it possible to estimate the coercive field (marked as "2" and "5" in Fig. 2) and the residual polarization (marked as "3" and "4" in Fig. 2, respectively) from the results of the dependences P (E) measurements, and also calculate the values of other electrophysical parameters, including the tangent of the dielectric loss angle, the relative permittivity.

References

[1] K I Othman, A A Hassan, A Hashim, A M Emam, E El-Kashif 2020 Synthesis and characterization of $Ba_{0.85}Ca_{0.15}Zr_{0.1}ti_{0.9}O_3$ lead-free piezoelectric ceramic materials *Technology Reports of Kansai University* **62**(11) 6535-6546.

[2] A N Soloviev, G D Vernigora 2010 Identification of effective properties of the piezocomposites on the basis of finite element method (FEM) modeling with ACELAN *Piezoceramic materials and devices* pp. 219-242

[3] A Dahri, Y Gagou, N Abdelmoula, H Khemakhem, M E Marssi 2022 The structural, dielectric, electrocaloric, and energy storage properties of lead-free Ba0.85Ca0.15Zr0.1ti0.9O3 *Ceramics International* **48** 3157–3171.

[4] S A Gurin, E A Pecherskaya, K Y Spitsyna, A V Fimin, D V Artamonov, A E Shepeleva 2020 Thin piezoelectric films for micromechanical systems *Moscow Workshop on Electronic and Networking Technologies*, *MWENT 2020 – Proceedings* 9067450.

[5] E A Pecherskaya, P E Golubkov, A V Fimin, T O Zinchenko, A V Pechersky, J V Shepeleva 2018 Intelligent system for active dielectrics parameters research Procedia Computer Science **132** 1163-1170.

Entanglement between isolated atom and Jaynes-Cummings atom in a cavity with Kerr media

R K Zakharov and E K Bashkirov

Samara University, 34, Moskovskoye shosse, Samara, 443086, Russia

rodionzhakharov@yandex.ru

Abstract. In this paper, we consider the dynamics of two dipole-coupled two-level atoms (qubits). The first of them is trapped in a lossless cavity with Kerr media and resonantly interacts with the thermal cavity field. The second qubit is outside the cavity. We obtain the exact solution of the model under consideration. On its basis we calculate the negativity as a measure of qubit-qubit entanglement. It is shown that, under certain conditions, the Kerr nonlinearity and direct dipole-dipole interaction of qubits can enhance the maximum degree of qubit-qubit entanglement induced by the thermal field and can eliminate the sudden death of entanglement.

1. Introduction

Entanglement plays a central role in quantum information, quantum computation and communication, and quantum cryptography [1]. The quantum devises require maximally entangled states. However, interactions with the environment always occur, and they will degrade the quality of the entanglement. Although the interaction between the environment and quantum systems can lead to decoherence, it can also induce entanglement. Kim et al. have investigated the atom-atom entanglement in the system of two identical two-level atoms with one-photon transition induced by a single-mode thermal field [2]. They have shown that a chaotic field with minimal information can entangle atoms prepared initially in a separable state. Later a lot of authors investigated the role of detuning, dipole-dipole interaction, Stark shift etc on the thermal entanglement between the qubits in the framework of different generalization of the two-atom Jaynes-Cummings model (see Refs. in [3]). In [4] we examined the dynamics on the entanglement between two qubits, one of which is trapped in a thermal lossless cavity, and the other is outside the cavity, taking into account the direct dipole-dipole interaction between the qubits. In this paper we continue the investigation of dynamics of the considered model taking into account the Kerr media in the cavity. In practice, Kerr nonlinearities in atomic systems are small compared to the rate of photon loss from the cavity, therefore, under such conditions, it is difficult to observe the effect of the Kerr nonlinearity on the dynamics of atoms in the cavity. At the same time, as was shown experimentally that for superconducting qubits in coplanar resonators with Kerr media, it was possible to be well within the single-photon Kerr regime [5].

2. Model and its exact solution

We consider two identical articial atoms or qubits (super-conducting Josephson circuits, spins or quantum dots) with an energy gap $\hbar\omega_0$ and one-mode quantum electromagnetic thermal field. The first atom is trapped in a lossless cavity with Kerr media and resonantly interacts with the cavity field

with frequency ω. The second atom is outside the cavity. We assume that the direct dipole-dipole interaction between qubits takes place. It's important note, that the effective dipole-dipole interaction for superconducting qubits can be much greater than the coupling between the qubit and cavity field [4]. In a frame rotating with the field frequency, the Hamiltonian for the system under rotating wave approximation can be written as

$$H = \hbar g(\sigma_1^+ a + a^+ \sigma_1^-) + Xa^{+2}a^2 + \hbar J(\sigma_1^+ \sigma_2^- + \sigma_2^+ \sigma_1^-), \quad (1)$$

where $\sigma_i^+ = |+\rangle_{ii}\langle -|$ and $\sigma_i^- = |-\rangle_{ii}\langle +|$ are the transition operators between the excited $|+\rangle_i$ and the ground $|-\rangle_i$ states in the i-th qubit ($i = 1,2$), $a^\dagger$ and a are the creation and the annihilation operators of photons of the cavity mode, g is the coupling constant between qubits and the cavity mode, X is the dispersive part of the third--order nonlinearity of Kerr medium and . J is the dipole-dipole strength. The initial qubits state is assumed to be separable such as $|\Psi(0)\rangle_A = |+,-\rangle$ or $|\Psi(0)\rangle_A = |+,-\rangle$ or Bell's type entangled state

$$|\Psi(0)\rangle_A = \cos\theta\,|+,-\rangle + \sin\theta\,|-,+\rangle \quad (2).$$

The initial cavity field state is assumed to be thermal with density matrix $\rho_F(0) = \sum_n p_n |n\rangle\langle n|$,

where $p_n = \bar{n}^n / (1+\bar{n})^{n+1}$ and $\bar{n}$ is the mean thermal photon number $\bar{n} = \left(\exp[\hbar\omega / k_B T] - 1\right)^{-1}$, k_B is the Boltzmann constant and T is the cavity equilibrium temperature.

Using the dressed state representation we obtained the exact solution of the the quantum Liouville equation for whole density matrix $\rho(t)$. . By averaging the full density matrix over the field variables, we can find the reduced qubit density matrix needed to calculate the qubit-qubit entanglement parameter $\rho_A(t) = Tr_F \rho(t)$. For a two-qubit system described by a reduced density matrix $\rho_A(t)$, Peres-Horodecki criterion or negativity can be chosen as a measure of qubit entanglement.

3. Results

We calculated the time-dependence of negativity foe separable and entangled qubits state and different values of the parameters of the models with Hamiltonian. The most interesting results is the follows. For separable initial qubits state $|+,-\rangle$ the Kerr nonlinearity greatly enhance the maximum degree of qubit-qubit entanglement. For separable initial qubits state $|+,+\rangle$ the qubit-qubit entanglement takes place only in the presence Kerr media or dipole-dipole interaction. For entangled initial qubits state (2) the inclusion of the Kerr nonlinearity and dipole-dipole interaction leads to stabilization of entanglement oscillations and the sudden death of entanglement elimination.

References

[1] Georgescu I M, Ashhab S and Nori F 2014 *Rev. Mod. Phys*. **88** 153
[2] Kim M S, Lee J, Ahn D and Knight P L 2002 *Phys. Rev*. A**65** 040101(R)
[3] Aguiar L S, Munhoz P P, Vidiella-Barranco A and Roversi J A 2005 *J. Opt*. B**7** S769
[4] Bashkirov E K 2019 *Int. J. Theor. Phys*. **58** 2346
[5] Kirchmair G, Vlastakis B, Leghtas Z, Nigg S E, Paik H, Ginossar, E, Mirrahimi M, Frunzio L, Girvin S M and Schoelkopf R J 2013 Nature **495** 205

Features of the formation Super C45-RuO_2 based planar supercapacitor structures

Yu I Kakovkina[1], Sh Sh Isokjanov[1], R M Ryazanov[2], E A Lebedev[1,2], E P Kitsyuk[2]

[1] National Research University of Electronic Technology, 124498, Zelenograd, Moscow, Russia

[2] Scientific-Manufacturing Complex "Technological Centre", 124498, Zelenograd, Moscow, Russia

Isakjanov2997@gmail.com

Abstract. The method for forming a planar supercapacitor with electrodes based on Super C45 and RuO_2 by electrophoretic deposition. Components such as cellulose and iodine were added to optimize the suspension composition in terms of its stability and deposition rate of composites, and a mixture of isopropyl alcohol and acetone was used as a solvent. The possibility of controlling the sediment composition by changing the composition of the initial suspension was demonstrated. The dependence of the specific capacity on the concentration of RuO_2 was investigated. Thus, it became possible to create powerful structures of planar supercapacitors for a wide range of applications in microelectronics. The first section in your paper.

1. Introduction

Composite materials based on various modifications of carbon with a high surface area and transition metal compounds has become quite promising due to their unique properties: high specific capacitance and power values due to the occurrence of fast redox reactions. This increases the demand for various power supplies, including supercapacitors. The main efforts of the researchers were aimed at maximizing their performance, increasing their specific capacitance and energy density. In this work, we investigated the technology for fabrication of planar supercapacitor structures with composite electrodes based on Super C45 and RuO_2, formed by electrophoretic deposition (EPD), which can form multicomponent materials and create nanostructured coatings with a given composition at room temperature.

2. Experiment

Sital plates were used as substrates, on which a nickel layer 300 nm thick was deposited by means of magnetron sputtering. For the manufacture of electrodes, as the main material, we used Super C45 and RuO_2. All components (Super C 45, RuO_2 *xH_2O, cellulose and iodine) with variations in the amount of ruthenium hydroxide were mixed in a test tube with a mixture of acetone and isopropyl alcohol prepared in a ratio of 1:1. Dispersion of the resulting solution was carried out by submersible ultrasonic disperser. The electrode material was deposited in an electrophoretic cell consisting of two electrodes: a cathode (sital with nickel coating) and an anode (gold electrode). After electrophoretic precipitation

using laser engraving on a CNC machine, a layer of the structure of a planar supercapacitor was formed, which is an interdigital comb, nested on top of each other (Figure 1).

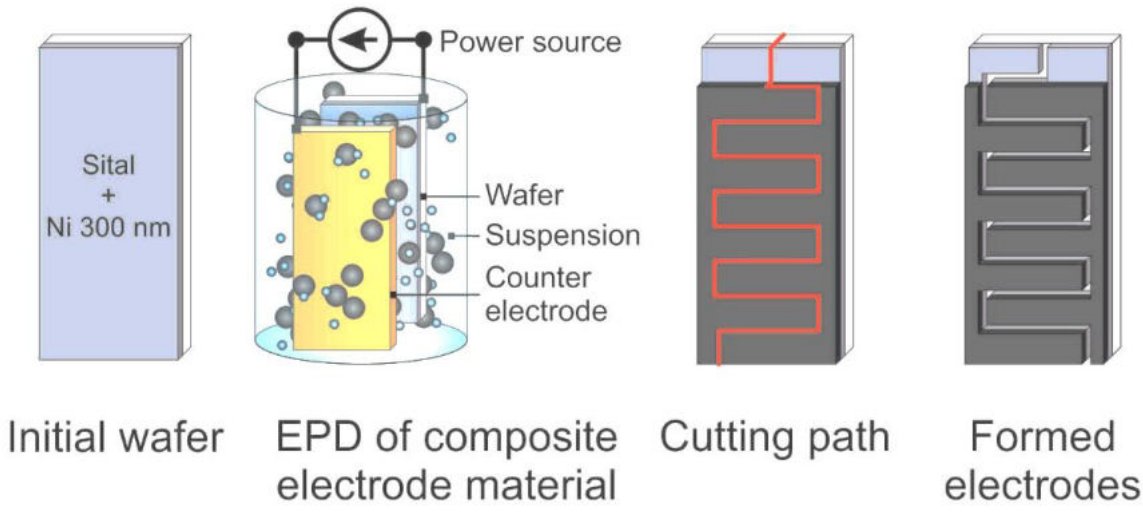

Figure 1. Schematic representation of the route for creating a planar supercapacitor with composite electrodes based on Super C45, RuO_2.

The morphology and composition of the surface of the obtained coatings were studied using energy-dispersive X-ray diffraction analysis and scanning electron microscopy. To study the electrophysical characteristics of the supercapacitors were placed in a glass with 1M KOH solution, their capacitive characteristics were measured using cyclic voltammetry (CV), galvanostatic charge-discharge (GCD), and electrochemical impedance spectroscopy (EIS) were performed to characterize the operation of the devices.

3. Results

The experiments carried out made it possible to determine the influence of the composition of the suspension on the composition of the formed layers, which, in turn, makes it possible to control and control the ratio of components in the sediment in a wide range.

The technology for manufacturing structures of planar supercapacitors was worked out, and the modes of laser engraving were optimized. The effect of topology (width and number of lines of positive and negative electrodes) on the capacitance and power characteristics of planar supercapacitors has been studied.

Acknowledgments

This work was partially supported by the Ministry of Science and Higher Education of the Russian Federation (project FNRM-2021-0002).

Investigation of the use of combined plasma to create nanostructures on the surface of semiconductor wafers

I O Kessler[1], V V Niftalieva[1], J V Morozova[1], V S Klimin[1]

[1]Southern Federal University, Department of Nanotechnology and Microsystems, Taganrog 347922, Russia
e-mail: kessler@sfedu.ru

Abstract. This article shows the results of plasma chemical treatment of silicon substrates with modified regions in fluoride plasma at accelerating voltage. The study of the obtained morphology was carried out at the atomic force microscopy (AFM) facility. As a result, the dependences of roughness, angle of inclination and height of structures on the speed and processing time were revealed.

1. Introduction

The requirement for miniaturization of semiconductor wafers is the main design trend in nanoelectronics. The advantage of plasma-chemical processing of materials in comparison with traditional chemical-technological processes lies in more environmentally friendly and less energy-intensive processes. Based on this, the study of nanostructures on substrates by micro profiling remains one of the most important issues in the field of processing solid structures. [1-3]

2. Methods and Results

The plasma-chemical treatment of the samples was carried out in a fluorine-containing plasma formed by the decomposition of sulfur hexafluoride (SF6) into SF5 radicals and fluorine atoms. The research used silicon substrates with a local modification of the 5x5 μm regions by a focused Ga + ion beam at the number of beam passes N-50, with a dose of 12.5 pCl/mm^2, the ion beams current I_{bc} – 10 pA, and the accelerating voltage U_{av} - 10 ÷ 30 keV. Plasma chemical treatment was carried out in four stages. At the first stage, the power of the inductively coupled plasma source was increased: W_{ICP} – 300÷600 W; at the second stage, the power of the capacitively coupled plasma source was changed: W_{CCP} –15 ÷ 75 W; at the third stage, the flow of fluorinated gas was changed: N_{SF6} – 2 ÷ 10 cm^3/min; at the fourth stage the processing time was changed: t – 15 ÷ 180 sec.

2.1 Results

Figure 1 shows SEM-images and AFM-images of the sample surface with a modified region at an accelerating voltage of 10 keV and a plasma-chemical etching time in the fluorinated plasma of 45 seconds. For an etching time of 15 seconds, with an increase in the accelerating voltage, the height of the structures decreases and becomes "negative" at 30 keV. The etching rate of the structures was found to be V_{Si} – 3.23 nm/sec.

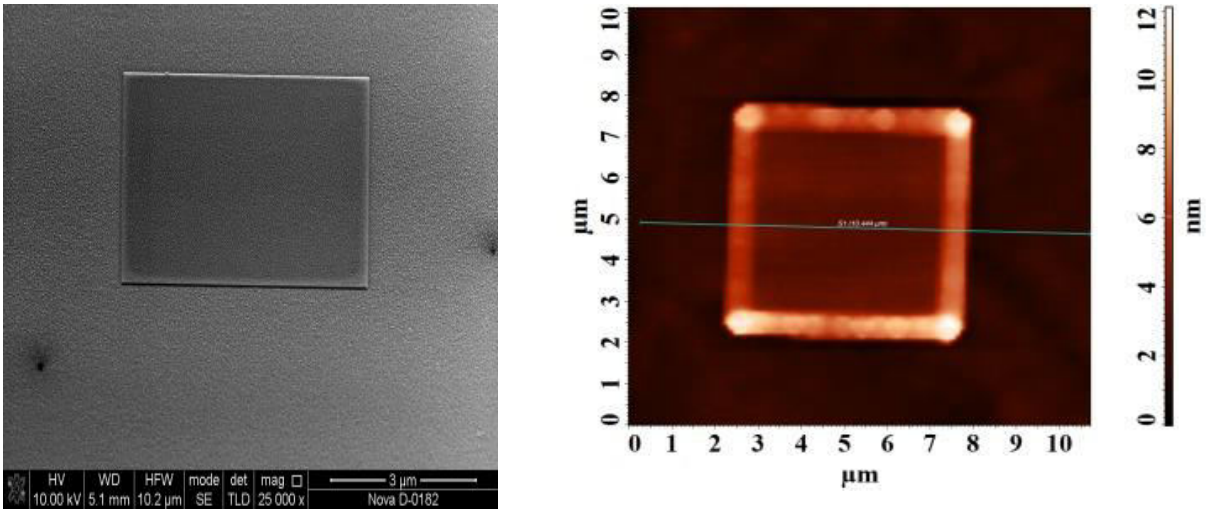

(*a*) (*b*)

Figure 1. Structure of the silicon surface after local modification by the FIB method at an accelerating voltage of 10 keV and plasma-chemical treatment in a fluorine-containing plasma for 45 seconds: (a) SEM - image; (b) AFM – image.

Experimental studies have made it possible to establish the regularities of the influence of plasma chemical treatment modes on the geometric parameters of modified silicon wafers. The modes corresponding to the minimum and maximum roughness of the etched surface were determined. To achieve maximum roughness, it is necessary to increase the values of the parameters of reactive ion etching, and for minimal roughness - to increase the values of the parameters of plasma chemical etching

Acknowledgments
This work was supported by the Grant of the Russian Science Foundation № 20-69-46076. The results were obtained using the equipment of the Research and Education Center "Nanotechnologies" of Southern Federal University.

References
[1] V S Klimin, A A Rezvan, O A Ageev Research of using plasma methods for formation field emitters based on carbon nanoscale structures // J. of Phys: C.S,2018. V.1124. – P. 071020.
[2] Giannuzzi L.A., Stevie F.A. Introduction to focused ion beams: instrumentation, theory, techniques and practice. New York: Springer, 2004. 357 p.
[3] Bhushan B. Springer Handbook of Nanotechnology (3rd edition) / ed. by Bharat Bhushan. New York: Springer, 2010. 1964 p.

Dependence of light-addressable potentiometric sensor sensitivity on photo-induced processes in Si

A V Kozlowski and S V Stetsyura

Institute of Physics, Saratov State University, Saratov 410012, Russia

E-mail: kozlowsky@bk.ru

Abstract. The effect of photoelectron processes in *n*-Si on the glucose sensitivity of a light-addressable potentiometric sensor based on electrolyte/oxide/semiconductor structure was investigated. We obtained that illumination of *n*-Si/SiO_2/polyethylenimine structure during the glucose oxidase (GOx) adsorption increases the D-glucose sensitivity by 2.5 times compare to GOx adsorption in the dark. The result is explained by a change in the density of immobilized GOx molecules induced by photoelectron processes in Si substrate during enzyme adsorption.

1. Introduction

Electrolyte/oxide/semiconductor (EOS) structures are widely used to detect nano- and bio-objects ionized in solution due to the field effect. Also, EOS-structures are used to recognize enzymatic reactions [1], viruses [2], RNA/DNA sequencing [3]. Compared to capacitive EOS-sensors, light-addressable potentiometric sensors (LAPS) have a number of advantages, such as the ability to obtain spatial and temporal charge distribution over the surface of the transducer (scanning photoinduced impedance spectroscopy), which makes it possible to visually assess the dynamics of changes in the concentration of the analyte.

In this work, we studied the effect of photo-stimulated layer-by-layer adsorption (PSA) of GOx on the glucose sensitivity of LAPS.

2. Experimental section

The sensor structures were fabricated using single-crystal (100) Si wafers (250 μm thickness) of *n*-type (ρ = 2-7 Ω cm). Initially, the wafers were boiled in a peroxide–ammonia solution and rinsed in deionized water. Afterwards, wafers were cut into substrates of 10×10 mm^2. A 300 nm aluminium layer on the rear side of the sensor structure was applied by magnetron sputtering method. The rear-side contact was partially removed to create an illumination window for the light beams. Red-LED (λ = 650-655 nm) is placed directly below the EOS-structure as a light source. An oscillator, which generates a 1 kHz rectangular signal, was provided the modulation of the red-light beam.

The glucose oxidase (GOx) form *Aspergillus niger* were used as enzyme molecules. Branched polyethyleneimine (PEI) with a molecular weight of 25 kDa was used as cationic polyelectrolyte to increase the adsorption of negatively charged GOx onto Si substrates. The organic molecules were adsorbed onto Si substrates from the aqueous solutions during 10 min followed by rinsing in deionized water (ρ ~ 18.2 MΩ cm) during 10 min and drying in nitrogen flow. The glucose solutions were prepared by dissolving D-glucose in the working buffer. As working buffer, a 0.2 mM potassium phosphate buffer solution (pH = 7.3) containing 150 mM NaCl as an ionic strength adjuster was used. The photo-

stimulated layer-by-layer adsorption technique suggested in [4] was used to adsorb GOx from aqueous solution onto Si substrates covered with PEI. The Si substrate was either in the dark or under illumination during the GOx adsorption, other things being equal. The glucose sensitivity of EOS-biosensors was studied by means of capacitance-voltage (C–V, EOS-sensor mode) and current-voltage (I-V, LAPS mode) measurements using a probe station (Cascade Microtech) controlled by a semiconductor device analyzer (Agilent B1500A). Bias voltage was applied relative to the Ag/AgCl reference electrode.

3. Results and Discussion

Figure 1 shows exemplarily a typical C–V curves of EOS-biosensor and I-V curves of LAPS structure for different pH. With increasing pH of the solution, C–V and I-V curves are shifted along the voltage axis in the direction to more positive voltage values. This is due to decrease in the H^+ concentration of on the LAPS surface.

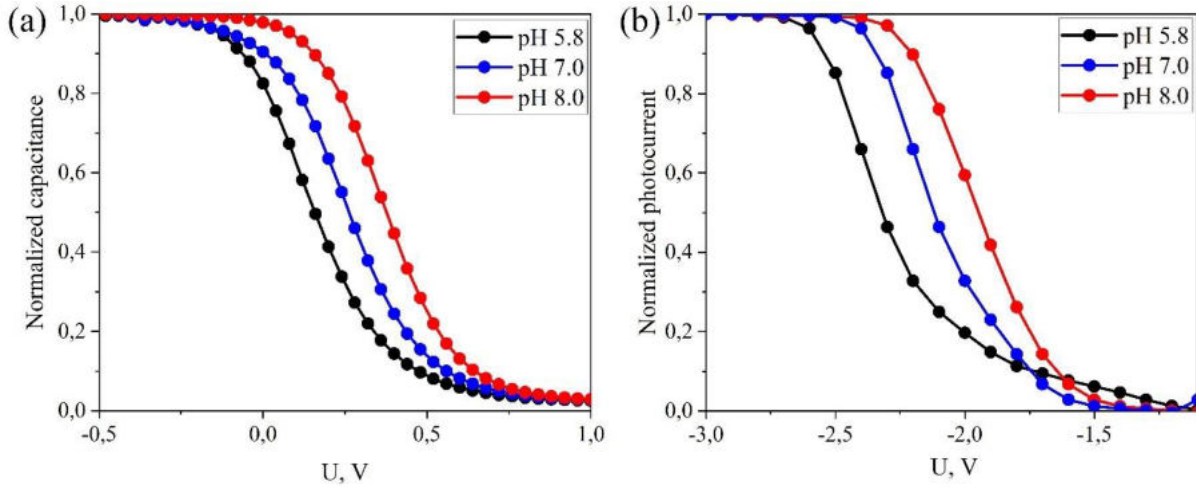

Figure 1. Typical C–V **(a)** and I-V **(b)** curves of the Si/SiO_2/PEI/GOx sensor structures measured in potassium phosphate buffer at different pH-values.

It was found that for EOS-sensor, where the GOx molecules were deposited in the dark, the sensitivity to D-glucose is 2.9 mV/mM. In the case of PSA - 5.6 mV/mM. For LAPS, the D-glucose sensitivity is 3.1 mV/mM and 7.4 mV/mM for GOx deposition in the dark and PSA, respectively.

4. Conclusion

Thus, it was shown that the white-light illumination of *n*-Si/SiO_2/PEI substrate during adsorption of GOx molecules from the aqueous solution increases the D-glucose sensitivity of LAPS. The result is explained by a change in the density of immobilized GOx molecules induced by photoelectron processes in Si substrate during enzyme adsorption.

5. Acknowledgments

The work was carried out at the expense of the Russian Science Foundation (project No. 22-22-00194, https://rscf.ru/en/project/22-22-00194/)

References

[1] S. Takenaga, et al. 2013 *Sensors and Actuators B: Chemical* **177** 745-52
[2] Giwan Seo et al. 2020 *ACS Nano* **14** 5135-42
[3] Gasparyan L, Mazo I, Simonyan V and Gasparyan F 2019 *Open Journal of Biophysics* **9** 169-97
[4] Kozlowski A V and Stetsyura S V 2021 *Journal of Physics: Conference Series* **2086** 012189

Multicomponent graphene oxide suspensions for spin-coated thin films

R V Chekin[1,2], **T S Kalyakin**[1,3] **and I A Komarov**[1]

[1] Research Institute for Graphite-Based Structural Materials "NIIgraphite", 111524, 2 Electrodnaya St., Moscow, Russian Federation
[2] Bauman Moscow State Technical University (BMSTU), 105005, Moscow, 5, 2nd Baumanskaya Str., Russian Federation
[3] Mendeleev University of Chemical Technology of Russia, 125047, 9 Miusskaya Sq., Moscow, Russian Federation

master_kom@mail.ru

Abstract. In this work, we investigate influence of different organic solvent addition on graphene oxide dispersion interaction with two different types of polymer substrates: PET and PVDF. In order to overcome the poor wettability of PET and PVDF by commercially available water graphene oxide suspensions we have manufactured series of multicomponent dispersion with different organic solvents/water/graphene oxide ratios. As additional dispersion media we used N-methylpyrrolidone, dimethylacetamide and Tamiya Laquer Thinner (diluent for enamel paints). We successfully showed the possibility to form stable multicomponent dispersions of GO in organic solvents with further film formation by spin-coating. We achieved best film uniformity on macrosize at the 50:50 GO to organic solvent ratio with ~80 nm thickness.

1. Introduction

Carbon nanomaterials, in particular graphene derivatives like graphene oxide (GO) and reduced GO are perspective materials for different application of flexible electronics, especially different sensors [1]. One of the main requirements for flexible devices is large-area uniform conductive and dielectric nanomaterials-based layers. Therefore, one of the main goals for flexible electronics is development of technology of large-area uniform layers deposition. Limitation in this case is the flexible, usually, polymer substrate, that does not allow to use conventional deposition methods.

Highly uniform films can be formed by different methods such as roll-to-roll technology [2], aerosol deposition [3]; another potential possibility of highly uniform film formation is spin-coating [4]. For the two last methods, wettability of the substrates is a critical parameter, that should be as high as possible. But most of commercially available GO forms are water suspension with poor wettability of polymeric substrates. One of the possible ways to overcome limitation of poor wettability of abovementioned substrates is to add some components to the GO solution to optimize wettability of substrates.

Additional components in the dispersion media should at least provide good dispersibility of GO. According to the data obtained from [5], GO can form long-time stable dispersions in such organic solvents (besides water) as dimethylformamide (DMF), N-methylpyrrolidone (NMP) and tetrahydrofuran (THF) and less stable in ethylene glycol, acetone and toluene. On the other hand, it is known that DMA is a good dispersion media for carboxylized carbon nanotubes [6].

In this work, we tried to form a multicomponent mixed dispersion media that contains water GO suspension and such perspective solvents as NMP, DMA and Tamiya lacquer thinner (acetone, propylene glycol and other components) with different component ratio. We also investigated interaction of these multicomponent GO dispersions with PET and PVDF substrates.

2. Results and discussion

We used 90:10, 75:25, 50:50, 25:75, 10:90 concentration ratios for mixed suspensions. Spin-coating deposition was carried out with next deposition profile: 500 rpm for 30 sec. and 5000 rpm for 180 sec.

According to the thickness measurement with AFM and optical observations, we can distinguish three different film groups. The first one contain relatively thick films with wrinkled structure typical for graphene oxide (concentrations 4.230 mg/ml (90:10) and 3.525 mg/ml (75:25)), but on the macrosize scale these films does not cover all of the substrate surface, so viscosities of these solutions are relatively high and exceed the optimal value. Second group with thicknesses of tens of nanometers has the same wrinkled structure of its surface but uniformly covers all substrate (2.350 mg/ml (50:50)). We defined this film type as optimal for further usage in flexible electronics and sensor applications.

Third group (1.175 mg/ml (25:75) and 0.470 mg/ml (10:90)) gives us island-type films with about 3 nm thickness. This means that suspensions with this ratio does not allow to further form conductive pathways and be used for electronics applications. We suggest that these films may be useful for drug-delivery applications or as platforms for biocompatible composites.

We also obtained Raman spectra from films with different concentrations. In all cases, Raman spectra confirmed presence of GO flakes or films on the substrate surface [7] with the predicted result: characteristic for GO ~0,9 to ~1,0 I_D/I_G ratio. Sharp peak at G peak vertex for 0.47; 1.175 and 3.525 mg/ml corresponds to signal from substrate.

3. Conclusion

In this work, we have investigated influence of organic solvent addition on spin-coating of GO films from mixed dispersion media. As predicted, mixed dispersion media helped to overcome poor wettability of PET substrate by water GO suspension. According to AFM and Raman spectroscopy, we achieved thin uniform films that are usable for different applications at about 50:50 component ratio, thin but non-uniform films at 90:10, 75:25 component ratios and island-type films at 25:75 and 10:90 component ratios.

References

[1] Freddi S et al. 2020 Development of a Sensing Array for Human Breath Analysis Based on SWCNT Layers Functionalized with Semiconductor Organic Molecules. *Advanced Healthcare Materials* **9** 2000377.

[2] Wells R.A. et al. 2019 Roll-to-Roll Deposition of Semiconducting 2D Nanoflake Films of Transition Metal Dichalcogenides for Optoelectronic Applications. *ACS Appl. Nano Mater.* **2** pp 7705-7712.

[3] Struchkov N.S. et al. 2020 Uniform graphene oxide films fabrication via spray-coating for sensing application. *Fullerenes Nanotubes and Carbon Nanostructures* 28 pp 214-220.

[4] Nguyen A.N. et al. 2020 Spin Coating and Micro-Patterning Optimization of Composite Thin Films Based on PVDF. *Materials* **13** 1342.

[5] Konios D et al. 2014 Dispersion behaviour of graphene oxide and reduced graphene oxide. *Journal of Colloid and Interface Science* **430,** pp 108-112.

[6] Komarov I. A., et al. 2018 Chemiresistive Sensors for Thrombin Assay Based on Nanosize Carbon Nanotube Films on Flexible Supports. *Biomedical Engineering* **51** pp 377-380.

[7] Yang S, et al. 2020 Fast Identification and Quantification of Graphene Oxide in Aqueous Environment by Raman Spectroscopy. Nanomaterials **10** 770.

Study of quasi 1-D silicon nanostructures adsorption properties

V M Kondratev[1], E A Vyacheslavova[1, 2], I A Morozov[1, 2], S S Nalimova[2], V A Moshnikov[2], A S Gudovskikh[1, 2] and A D Bolshakov[1, 3, 4]

[1] Alferov University, St. Petersburg 194021, Russia
[2] Saint Petersburg Electrotechnical University "LETI", St. Petersburg 197376, Russia
[3] ITMO University, St. Petersburg, 197101, Russia
[4] Moscow Institute of Physics and Technology, Moscow, 117303, Russia

Abstract. Hydrochloric acid and ammonia are inorganic agents found both in nature and in the human body, which is of great interest for modern sensing and diagnostic. The work is aimed at study of adsorption properties of cryogenic plasma chemical etched Si nanowires (NWs) and fabrication of precise, technological and relatively cheap gas (vapor) sensors based on which. The NWs are 10 μkm long and about 350 nm thick. Such a large aspect ratio of the length to the thinness and surface area to the volume makes it possible to call Si nanowires as quasi 1-D structures with electrical conductivity high dependents on surface adsorption properties. The correlation between Si NWs adsorption properties under H_2O, HCl and NH_3 affection and their electrical characteristic are considered via impedance spectroscopy. We demonstrate the potential of the approach for detection of both HCl and NH_3 vapors at concentrations below as 1 mmol·l^{-1} in liquid media.

1. Introduction

An important task of researchers around the globe to develop high-precision sensory devices to control human vital processes. At the same time, there are inorganic agents found both in nature and in the human body like hydrochloric acid and ammonia. In high concentrations this gases is dangerous due to irritation of respiratory system, as well as eye mucous membranes. Today, control of HCl and NH_3 contents in atmosphere becomes especially important as this gases are a common waste products of the factories and engines. From biological and medical point of view, at concentrations of about 1 mmol·l^{-1} and 20 mmol·l^{-1}, respectively, NH_3 and HCl are found in body fluids and breath and may indicate pathological changes in the body.

The concentration of various inorganic agents in human biological samples are studded via a lot of modern chemical, physical and sensory techniques for medical and biological applications. One of the ways to achieve this goal is the use of semiconductor gas sensors. Adsorption sensorics is a several decades mature technology [1]. High surface area and peculiar electronic properties compare to bulk material are the main reason for use of NWs in sensing. The existing works on Si NWs sensorics [2–3] commonly consider a small amounts of target adsorbates with the uniform nature. This paper shows the possibility of producing adsorption sensors compatible with both acidic and alkaline agents and detecting their concentrations below the "biological" level in liquid media.

2. Nanowires synthesis and study

Vertically oriented structures based on Si NWs are obtained using cryogen plasma chemical etching of Si (001) substrate in Oxford PlasmaLab System 100 ICP380 with SF_6/O_2 mixture flow and 5 mTorr pressure. The NWs morphology was investigated with scanning electron microscopy (SEM) Zeiss Supra25.

3. Sensor fabrication

The step–by–step protocol of sensor production includes the procedure for separating NWs from the growth substrate and transferring the array of NWs to the surface of the sensor platform.

Gold–NWs contacts are found to be of the Schottky type, which is proven by the voltage–current characterization obtained using Keithley 2400.

4. Sensory tests

To investigate of Si NWs adsorption properties and potential of the sensor based on them change in the sensor electrical impedance under action of the target adsorbates (vapors of HCl and NH_3 aqua solutions with concentrations about 0.125, 0.250, 0.500 and 1.000 $mmol \cdot l^{-1}$) was measured and compared with the impedance in the water vapors medium. Change in the impedance is represented in the form of Nyquist plot, which allows to selectively characterize the change in real and imaginary parts of the impedance of the sensor in the frequency range from 100 Hz to 500 kHz in the presence of H_2O, HCl and NH_3. The constant voltage of 100 mV and amplitude of the variable voltage signal is 20 mV for impedance measurement are the optimal for working with samples with an implicit active and reactive nature of resistance change.

5. Conclusion

The adsorption properties of quasi 1-D silicon nanowires are studied in terms of the dynamic range of sensitivity of the sensor based on them, the response and recovery time of the sensor, and the parameters of the optimal alternating measuring voltage.

The possibility of using impedance spectroscopy to evaluate the response of a developed sensor based on silicon nanowires when exposed to water vapor and aqueous solutions of ammonia and hydrochloric acid is shown. At the same time, the sensor impedance spectra in the presence of these media are unambiguously separable from each other with the possibility of qualitative and quantitative analysis of steam and gas media to the presence of H_2O, NH_3 and HCl. The sensor response and recovery time correspond to 600 s.

Acknowledgments

V.M.K. acknowledges financial support of the NWs manipulation from the Russian Science Foundation (Grant No. 20-72-10192).

A.D.B. thanks for support of the sensor fabrication Ministry of Science and Higher Education of the Russian Federation (grant № FSRM-2020-00011).

References

[1] Zemel J N 1988 *Thin Solid Films* **163** 189.
[2] Zhou X T, Hu J Q, Li C P, Ma D D D, .Lee C S, Lee S T 2003 *Chemical Physics Letters* **369** 220.
[3] Park I, Li Z, Pisano A P and Williams R S 2010 *Nanotechnology* **21 1** 015501.

Study of quasi 1-D silicon nanostructures adsorption properties

V M Kondratev[1], E A Vyacheslavova[1, 2], I A Morozov[1, 2], S S Nalimova[2], V A Moshnikov[2], A S Gudovskikh[1, 2] and A D Bolshakov[1, 3, 4]

[1] Alferov University, St. Petersburg 194021, Russia
[2] Saint Petersburg Electrotechnical University "LETI", St. Petersburg 197376, Russia
[3] ITMO University, St. Petersburg, 197101, Russia
[4] Moscow Institute of Physics and Technology, Moscow, 117303, Russia

Abstract. Hydrochloric acid and ammonia are inorganic agents found both in nature and in the human body, which is of great interest for modern sensing and diagnostic. The work is aimed at study of adsorption properties of cryogenic plasma chemical etched Si nanowires (NWs) and fabrication of precise, technological and relatively cheap gas (vapor) sensors based on which. The NWs are 10 μkm long and about 350 nm thick. Such a large aspect ratio of the length to the thinness and surface area to the volume makes it possible to call Si nanowires as quasi 1-D structures with electrical conductivity high dependents on surface adsorption properties. The correlation between Si NWs adsorption properties under H_2O, HCl and NH_3 affection and their electrical characteristic are considered via impedance spectroscopy. We demonstrate the potential of the approach for detection of both HCl and NH_3 vapors at concentrations below as 1 mmol·l^{-1} in liquid media.

1. Introduction

An important task of researchers around the globe to develop high-precision sensory devices to control human vital processes. At the same time, there are inorganic agents found both in nature and in the human body like hydrochloric acid and ammonia. In high concentrations this gases is dangerous due to irritation of respiratory system, as well as eye mucous membranes. Today, control of HCl and NH_3 contents in atmosphere becomes especially important as this gases are a common waste products of the factories and engines. From biological and medical point of view, at concentrations of about 1 mmol·l^{-1} and 20 mmol·l^{-1}, respectively, NH_3 and HCl are found in body fluids and breath and may indicate pathological changes in the body.

The concentration of various inorganic agents in human biological samples are studded via a lot of modern chemical, physical and sensory techniques for medical and biological applications. One of the ways to achieve this goal is the use of semiconductor gas sensors. Adsorption sensorics is a several decades mature technology [1]. High surface area and peculiar electronic properties compare to bulk material are the main reason for use of NWs in sensing. The existing works on Si NWs sensorics [2–3] commonly consider a small amounts of target adsorbates with the uniform nature. This paper shows the possibility of producing adsorption sensors compatible with both acidic and alkaline agents and detecting their concentrations below the "biological" level in liquid media.

2. Nanowires synthesis and study

Vertically oriented structures based on Si NWs are obtained using cryogen plasma chemical etching of Si (001) substrate in Oxford PlasmaLab System 100 ICP380 with SF_6/O_2 mixture flow and 5 mTorr pressure. The NWs morphology was investigated with scanning electron microscopy (SEM) Zeiss Supra25.

3. Sensor fabrication

The step–by–step protocol of sensor production includes the procedure for separating NWs from the growth substrate and transferring the array of NWs to the surface of the sensor platform.

Gold–NWs contacts are found to be of the Schottky type, which is proven by the voltage–current characterization obtained using Keithley 2400.

4. Sensory tests

To investigate of Si NWs adsorption properties and potential of the sensor based on them change in the sensor electrical impedance under action of the target adsorbates (vapors of HCl and NH_3 aqua solutions with concentrations about 0.125, 0.250, 0.500 and 1.000 $mmol \cdot l^{-1}$) was measured and compared with the impedance in the water vapors medium. Change in the impedance is represented in the form of Nyquist plot, which allows to selectively characterize the change in real and imaginary parts of the impedance of the sensor in the frequency range from 100 Hz to 500 kHz in the presence of H_2O, HCl and NH_3. The constant voltage of 100 mV and amplitude of the variable voltage signal is 20 mV for impedance measurement are the optimal for working with samples with an implicit active and reactive nature of resistance change.

5. Conclusion

The adsorption properties of quasi 1-D silicon nanowires are studied in terms of the dynamic range of sensitivity of the sensor based on them, the response and recovery time of the sensor, and the parameters of the optimal alternating measuring voltage.

The possibility of using impedance spectroscopy to evaluate the response of a developed sensor based on silicon nanowires when exposed to water vapor and aqueous solutions of ammonia and hydrochloric acid is shown. At the same time, the sensor impedance spectra in the presence of these media are unambiguously separable from each other with the possibility of qualitative and quantitative analysis of steam and gas media to the presence of H_2O, NH_3 and HCl. The sensor response and recovery time correspond to 600 s.

Acknowledgments

V.M.K. acknowledges financial support of the NWs manipulation from the Russian Science Foundation (Grant No. 20-72-10192).

A.D.B. thanks for support of the sensor fabrication Ministry of Science and Higher Education of the Russian Federation (grant № FSRM-2020-00011).

References

[1] Zemel J N 1988 *Thin Solid Films* **163** 189.

[2] Zhou X T, Hu J Q, Li C P, Ma D D D, .Lee C S, Lee S T 2003 *Chemical Physics Letters* **369** 220.

[3] Park I, Li Z, Pisano A P and Williams R S 2010 *Nanotechnology* **21 1** 015501.

```
<!DOCTYPE html>
<html xmlns="http://www.w3.org/1999/xhtml" xml:lang="ru">
<head>
<meta content="IE=edge;chrome=1" http-equiv="X-UA-Compatible" />
<meta http-equiv="Content-Type" content="text/html; charset=utf-8" />
<meta name="viewport" content="width=device-width, initial-scale=1">

<title>Вход в личный кабинет сотрудника НИУ ВШЭ : НИУ ВШЭ</title>

<link rel="stylesheet" type="text/css" href="/css/plashka.css" />
<link rel="stylesheet" type="text/css" href="/css/typo.css" />

<script src="/f/gtm/ip"></script><script type='text/javascript'><!--
(function(w,d,s,l,i){w[l]=w[l]||[];w[l].push({'gtm.start':
        new Date().getTime(),event:'gtm.js'});var f=d.getElementsByTagName(s)[0],
        j=d.createElement(s),dl=l!='dataLayer'?'&l='+l:'';j.async=true;j.src=
        'https://www.googletagmanager.com/gtm.js?id='+i+dl;f.parentNode.insertBefore(j,f);
        })(window,document,'script','dataLayer','GTM-P6DCQX');
//-->
</script>
</head>
<body >
<!-- Yandex.Metrika counter -->
<div style="display: none;">
<script type="text/javascript">
(function (d, w, c) {
    (w[c] = w[c] || []).push(function() {
        try {
            w.yaCounter15008191 = new Ya.Metrika({id:15008191, enableAll: true, webvisor:true});
        } catch(e) {}
    });
    var n = d.getElementsByTagName("script")[0],
        s = d.createElement("script"),
        f = function () { n.parentNode.insertBefore(s, n); };
    s.type = "text/javascript";
    s.async = true;
    s.src = (d.location.protocol == "https:" ? "https:" : "http:") + "//mc.yandex.ru/metrika/watch.js";
    if (w.opera == "[object Opera]") {
        d.addEventListener("DOMContentLoaded", f);
    } else { f(); }
})(document, window, "yandex_metrika_callbacks");
</script>
</div>
<noscript><div><img src="//mc.yandex.ru/watch/15008191" style="position:absolute; left:-9999px;"
alt="" /></div></noscript>
<!-- /Yandex.Metrika counter -->



<link rel="stylesheet" type="text/css" href="/css/misprint.css"/>
<script type="text/javascript" src="/js/rpc.js"></script>
    <script type="text/javascript" src="/js/dyna_loader.js"></script>
    <script type="text/javascript"><!--
    var SELECTED_TEXT;
    var validator;

    misprint_preinit(0);
    function misprint_preinit(iteration){
       var iterations = [[misprint_init,'']];
       if(!window.jQuery && iterations.length < 5){
```

```
        iterations = [[J_load, [misprint_preinit, 0]]].concat(iterations);
    }

    if( typeof(iterations[iteration]) != 'undefined' ){
        var func = iterations[iteration][0];
        var params = iterations[iteration][1];
        func.apply( null, [params] );
    }
}

function misprint_init(){
        window.misprint_init_called = true;
jQuery.noConflict();
J = jQuery;
J( function() {
                                                return;
    J('#misprint_form').hide();
    J(document).bind('textselect', function(e) { SELECTED_TEXT = e.text });
    J(document).bind('textunselect', function(e) { SELECTED_TEXT = '' });
    J(document).hot_key('ctrl enter', misprint_message);
    } );
}


function misprint_message(){
    if(SELECTED_TEXT == undefined || SELECTED_TEXT.match(/^\s*$/)){ return false; }
    var mp = J('#misprint_form');
    mp.empty();
    mp.load("/shared/misprint_form.html", function(){
        J('#misprint_form textarea.text').val(J.trim(SELECTED_TEXT));
        J('#misprint_form textarea.comment').val('');
        J('#misprint_url').val(decodeURIComponent("%2Fdb%2Fuser_login.html"));
        mp.hot_key('esc', cancel_misprint);

        mp.width('510px');
        var x = J(window).width()/2 - J('#misprint_form').width()/2;
        var y = J(window).height()/2 -J('#misprint_form').height()/2;
        mp.css( {'top':y+'px', 'left':x+'px'} );
        mp.slideDown(1000);
        J('#misprint_after textarea').focus();
    });

}


function send_misprint( rpc_url ){
    if( validator && !validator.form() ) {
        alert('Исправьте ошибки в полях и попробуйте снова!');
        return false;
    }
    var url = J('#misprint_url').val();
    var nick = J('#misprint_nick').val();
    var email = J('#misprint_email').val();
    var text_before = J('#misprint_before .text').val();
    var text_after = J('#misprint_after .text').val();
    var comment = J('#misprint_comment .comment').val();

    var captcha_image_id = J('#captcha_data').val();
    var captcha_value = J('#captcha_val').val();
    J.post(rpc_url, {
                'proc':'createMisprint',
```

```
                    'url':url,
                   'nick':nick,
                  'email':email,
              'text_before':text_before,
               'text_after':text_after,
                  'comment':comment,
                  'captcha_id':captcha_image_id,
                  'captcha_val':captcha_value
                     }, misprint_sended, 'text xml' );
  }

  function cancel_misprint(){
     var mp = J('#misprint_form');
     J('#misprint_form textarea').val('');
     J('#misprint_form :text:not(:hidden)').val('');
     mp.slideUp(1000);
  }

  function misprint_sended(data,status){
     if (status=='success'){
        var err = J(data).find('response error');
        if (err.length!=0){
           alert(err.attr('text'));
        }else{
           alert('Ваше сообщение отправлено! Спасибо за внимание и поддержку!');
           cancel_misprint();
        }
     }else{
        alert('Произошла ошибка при отсылке уведомления.');
     }
  }
  //-->
</script>

<div id="misprint_form" style="position: absolute; display:none; background:#dee7f0; padding:10px;
border:1px solid #aabbcc; z-index:15; max-width:500px">

</div>




<div id="body">
 <div style="text-align: center;" id="contenthandler">
   <div style="margin: auto;" id="content">

<style>
 html, body {
   height: 100%;
   overflow: hidden;
 }

 html {
   font-size: 62.5%;
 }

 body {
   color: #333;
   font: 1.2em/1.55 "Helvetica Neue", Helvetica, Arial, sans-serif;
 }
```

```
  :link, :visited {
    color: #4a90e2;
  }

  .grey {
    color: rgba(0,0,0,.5);
  }

  #contenthandler {
    text-align: left !important;
  }
</style>
<div class="is-page">
<style type="text/css">.mdn-modal :link,
.mdn-modal :visited,
.mdn-modal :link {
	color: #4a90e2;
	border-bottom: 1px solid #4a90e2;
	transition: all .35s ease;
	text-decoration: none;
}

.links-white :link, .links-white :visited {
	color: #fff;
	border-bottom: 1px solid rgba(255,255,255,.5);
	transition: all .35s ease;
}

.mdn-modal :link:hover, .mdn-modal :visited:hover, .mdn-modal .link:hover {
	color: #d2270b;
	border-bottom-color: rgba(210,39,11,.3);
}

.red {
	color: rgb(235,65,70);
}

.is-modal-open {
	overflow: hidden;
	padding-right: 17px;
}

.mdn-row {
	display: flex;
	word-spacing: -.43em;
	margin-left: -10px;
	margin-right: -10px;
}

.mdn-input_box {
	float: none;
	flex: 1 1 0;
	word-spacing: normal;
	padding-left: 10px;
	padding-right: 10px;
}

.mdn-input_box__label {
	display: block;
	margin-bottom: 1rem;
}
```

```
.mdn-input {
	width: 100%;
	font-size: 1.8rem;
	color: #000;
	border-color: rgba(0, 0, 0, 0.25);
	outline: none;
	border-width: 0 0 1px;
	padding-bottom: 1rem;
}

.mdn-input:-webkit-autofill,
.mdn-input:-webkit-autofill:hover,
.mdn-input:-webkit-autofill:focus,
.mdn-input:-webkit-autofill:active  {
   -webkit-box-shadow: 0 0 0 30px white inset !important;
}

.mdn-input:focus {
	border-color: #000;
}

.mdn-input_box__label {
	display: block;
	color: #1658da;
	font-size: 1.3rem;
}

.mdn-button {
	display: block;
	text-decoration: none;
	width: 100%;
	min-height: 45px;
	padding: 12px 10px;
	font: 1.6rem/1.2 'FuturaPTWebDemi', "Helvetica Neue", Arial, sans-serif;
	background: #1658da;
	border: 1px solid #1658da;
	color: #fff;
	border-radius: 5px;
	box-sizing: border-box;
	outline: none;
	text-transform: uppercase;
	letter-spacing: 1px;
	text-align: center;
	margin-top: 30px;
	cursor: pointer;
	transition: all .35s ease;
}

.mdn-modal .mdn-button:hover {
	background: #00349B;
	border-color: #00349B;
}

.mdn-button--clean, .mdn-modal .mdn-button--clean:hover {
	background: #fff;
	color: #1658da;
}

/**************************\
  Basic Modal Styles
```

```
\*************************/

.mdn-modal {
	font-family: "Helvetica Neue", Helvetica, Arial, sans-serif;
}

.mdn-modal__overlay {
	position: fixed;
	top: 0;
	left: 0;
	right: 0;
	bottom: 0;
	z-index: 10;
	background: rgba(0,0,0,0.5);
	display: flex;
	justify-content: center;
	align-items: center;
	overflow-y: auto;
}

.is-page .mdn-modal__overlay {
	background: transparent;
	overflow-y: auto;
}

.mdn-modal__container {
	max-width: 500px;
	max-height: 90vh;
	box-sizing: border-box;
	font-size: 1.4rem;
}

@media (max-width: 767px) {
	.mdn-modal__container {
		width: calc(100% - 40px);
	}
}

.mdn-modal__inner {
	box-shadow: 0 2px 50px 0 rgba(0, 0, 0, 0.25);
}

.mdn-modal__header {
	display: flex;
	justify-content: space-between;
	align-items: center;
	padding: 10px 30px;
	height: 60px;
	background: #1658da;
	color: #fff;
	box-sizing: border-box;
}

.mdn-modal__footer {
	color: #fff;
	padding: 30px;
}

.is-page .mdn-modal__footer {
	color: #000;
}
```

```
.mdn-modal__title {
	margin: 0;
	padding: 0;
	font-weight: 600;
	font: normal bold 1.6rem "Helvetica Neue", Helvetica, Arial, sans-serif;
	line-height: 1.25;
	box-sizing: border-box;
}

.mdn-modal__close {
	background: transparent no-repeat
url('data:image/svg+xml;charset=utf8,%0A%3Csvg%20xmlns%3D%22http%3A%2F%2Fwww.w3.org%
2F2000%2Fsvg%22%20width%3D%2220%22%20height%3D%2220%22%20viewBox%3D%220%200
%2020%2020%22%3E%0A%20%20%20%20%3Cg%20fill%3D%22none%22%20fill-
rule%3D%22evenodd%22%20stroke%3D%22%23FFF%22%20stroke-
width%3D%222%22%3E%0A%20%20%20%20%20%20%20%20%3Cpath%20d%3D%22M1.25%201.
25l17.678%2017.678M18.928%201.25L1.25%2018.928%22%2F%3E%0A%20%20%20%20%3C%2Fg
%3E%0A%3C%2Fsvg%3E%0A');
	border: 0;
	width: 20px;
	height: 20px;
	outline: none;
	cursor: pointer;
}

.is-page .mdn-modal__close {
	display: none;
}

.mdn-modal__content {
	padding: 30px;
	line-height: 1.5;
	color: rgba(0,0,0,.8);
	background: #fff;
}

@keyframes mmfadeIn {
    from { opacity: 0; }
      to { opacity: 1; }
}

@keyframes mmfadeOut {
    from { opacity: 1; }
      to { opacity: 0; }
}

@keyframes mmslideIn {
  from { transform: translateY(15%); }
    to { transform: translateY(0); }
}

@keyframes mmslideOut {
    from { transform: translateY(0); }
    to { transform: translateY(-10%); }
}

.micromodal-slide {
	display: none;
}
```

```
.micromodal-slide.is-open, .is-page .micromodal-slide {
	display: block !important;
}

.micromodal-slide[aria-hidden="false"] .modal__overlay {
  animation: mmfadeIn .3s cubic-bezier(0.0, 0.0, 0.2, 1);
}

.micromodal-slide[aria-hidden="false"] .modal__container {
  animation: mmslideIn .3s cubic-bezier(0, 0, .2, 1);
}

.micromodal-slide[aria-hidden="true"] .modal__overlay {
  animation: mmfadeOut .3s cubic-bezier(0.0, 0.0, 0.2, 1);
}

.micromodal-slide[aria-hidden="true"] .modal__container {
  animation: mmslideOut .3s cubic-bezier(0, 0, .2, 1);
}

.micromodal-slide .modal__container,
.micromodal-slide .modal__overlay {
  will-change: transform;
}</style><div class="mdn-modal mdn-modal micromodal-slide" id="modal-login" aria-hidden="true">
<div class="mdn-modal__overlay" tabindex="-1" data-micromodal-close="data-micromodal-close"><div
class="mdn-modal__container" role="dialog" aria-modal="true" aria-labelledby="modal-1-title"><div
class="mdn-modal__inner"><form action="/check_login.html" method="post" name="loginform">
<input type="hidden" name="goto"
value="*L3B1YnMvc2hhcmUvZm9sZGVyLzY4YTUwMDU0NGMxYWFhLzU1Njk3MzQ4Mw==/"><input
type="hidden" name="addon_name" value="default"/><script><!--
document.write('<' + 'input type="hidden" name="_r" value="' + Math.random() + '">');
//--></script><div class="mdn-modal__header"><h2 class="mdn-modal__title" id="modal-1-
title">Вход в личный кабинет сотрудника НИУ ВШЭ</h2><button class="mdn-modal__close" aria-
label="Close modal" data-micromodal-close="data-micromodal-close"></button></div><div
class="mdn-modal__content" id="modal-1-content"><div class="mdn-row"><label class="mdn-
input_box"><span class="mdn-input_box__label">Логин</span><input class="mdn-input" type="text"
value="" name="login" id="lform_login" autofocus="autofocus"/></label><label class="mdn-
input_box"><span class="mdn-input_box__label">Пароль</span><input class="mdn-input"
type="password" name="password" id="lform_password"/></label></div><input class="mdn-button"
type="submit" value="Войти"/><p class="grey">Вы можете войти с паролем от корпоративной
почты. Чтобы это работало, ваш E-Mail в домене HSE должен быть указан в Личном Кабинете.</p>
<p class="grey"> <a title="Если у вас есть логин-пароль в ЕЛК и почта в домене @hse.ru, вы
можете войти через ЕЛК" onclick="window.location.replace('https://lk.hse.ru/signin?redirecturl=https://'
+ window.location.hostname + '/mirror/co-
auth/elk/gateway.html%3Fi=*L3B1YnMvc2hhcmUvZm9sZGVyLzY4YTUwMDU0NGMxYWFhLzU1Njk3MzQ4
Mw==&systemid=27')" href="javascript:void(0)">Войти через ЕЛК</a></p><a class="mdn-button
mdn-button--clean" type="button" href="https://lk.hse.ru/">Войти в ЕЛК ВШЭ</a><p class="grey">
Авторизовавшись в Едином Личном Кабинете, вы сможете без ограничения пользоваться
автоматизированными сервисами НИУ ВШЭ</p></div></form></div><div class="mdn-
modal__footer"><p>Для успешного входа на сайт в Вашем браузере должны поддерживаться
JavaScript и Cookie.</p><p><a href="https://portal.hse.ru/help">Требуется помощь?</a></p>
<p>Личные кабинеты абитуриентов бакалавриата и магистратуры находятся здесь <a
href="https://priem.hse.ru/">https://priem.hse.ru/</a>. Контакты тех. поддержки размещены на
соответствующих <a href="https://priem.hse.ru/">страницах портала</a>.</p></div></div></div>
</div>
</div>


    </div>
  </div>
</div>
```

</body></html>

Study of the Al/CuO_x thermite material combustion initiation process using a thin film Ni/Cr heating element

E S Leonenko[1], L I Sorokina[1], R M Ryazanov[2], A V Sysa[2] and E A Lebedev[1]

[1] National Research University of Electronic Technology (MIET), 124498, Moscow, Zelenograd, Russia
[2] Scientific-Manufacturing Complex "Technological Centre", 124498, Moscow, Zelenograd, Russia

katejustkate86@gmail.com

Abstract: This study contains investigation of Al/CuO_x thermite material combustion initiation process using a thin film Ni/Cr heating element. Laser engraving modes for heating element formation were obtained. Features of Al/CuO_x thermite material electrophoretic deposition were analysed. Combustion patterns of the obtained coats were inspected in different atmospheres. In the perspective, this framework may be used as a local heat source for low-temperature joining of thermosensitive elements.

1. Introduction

Currently nanosized thermite materials are being actively studied by scientists in the field of reactive bonding. Al/CuO_x nanocomposite is one of the most popular combination among thermites due to its ability to control combustion rate through components ratio. The method of electrophoretic deposition (EPD) is considered to be a low-priced method that has the ability to deposit thin films locally. Usually initiation of self-propagating combustion wave reaction proceed with a lighter or piezoelectric element. In the course of this work, study was targeting thermite material combustion initiation process using a thin-film heating element engraved onto the sitall substrate with 400 nm Ni/Cr foil. Al/CuO_x electrophoretic deposition features were also examined. In the perspective, this framework may be used as a local heat source for low-temperature joining of thermosensitive elements.

2. Methodical

The main focus of this study was on the thin-film heating element formation. First of all, modelling of arrow-shaped heating element is needed. The arrow layout was prepared, then laser path was computed. In order to engrave the arrow, a certain mode was selected, including: laser power, focal length, and the number of laser passes. The arrow-shaped pattern was engraved by using a laser module with 450 nm wavelength for a CRONOS CNC 3018 PRO machine.

After incising the arrow, it is important to prepare suspension, which consists of the solvent - isopropyl alcohol, and nanosized powders - Al and CuO. Al to CuO ratio was 20:40 mg mixed with 50 ml isopropyl alcohol. The suspensions were dispersed in the ultrasonic disperser for 1 hour.

Electrophoretic cell for EPD process consists of two electrodes connected to a power supply and immersed into a beaker with premade suspension. Sitall substrate with Ni/Cr foil was used for main electrode, as for the counter electrode – it was stainless steel. Deposition of thermite materials was carried out at an electric field strength from 70 to 110 V/cm for 5 to 8 minutes.

Surface morphology, thickness and stoichiometry of the obtained energetic materials were investigated using scanning electron microscopy (SEM) with an attachment for analysis of energy dispersive X-ray spectroscopy (EDS). Self-propagating wave combustion process was investigated using high-velocity camera.

3. Results

Primarily, essential step is to engrave the heating element onto the substrate. It was decided to take one laser pass for time economy and the simplicity of the process. Average power value was 3,75 W. Next, the influence of the focal length on the thickness of the incised layer was examined, so that would be enough so the cut out area between the arrow and the rest of the Ni/Cr layer did not conduct current. The focal length was in the range from 3 to 5 mm of laser elevation from the original position.

Thermite coats were conformal and thick enough to initiate self-propagating reaction. SEM and EDS results showed that specimen surface is even, has little to no pores and elemental distribution is homogenous.

Combustion initiation was held in different atmospheres, specifically on air, in vacuum and argon. The initiation of on air combustion was occurred by means of probes connected to both ends of the arrow-shaped engraved heating element. The probes were also connected to a power supply. The voltage was gradually raised until the sample had burned out completely. The voltage ranges varied from 50 to 190 V, depending on the thermite material layer thickness. Vacuum needed for combustion was carried out at $7 \cdot 10^{-5}$ Torr. For combustion in the argon atmosphere, first, vacuum is needed and then the argon gas being let in until the atmosphere pressure is reached. All combustion processes were filmed with high-velocity camera at 15000 fps.

Based on the investigation results, the influence of heating element on the combustion was analysed. Optimal modes for laser engraving and electrophoretic deposition of Al/CuO_x were obtained. Combustion patterns were examined. The study of Al/CuO_x thermite material combustion by means of heating element initiation can be used as a local heat source for reactive bonding of the surfaces, and as an initiator of secondary reactions for microelectromechanical systems.

4. Acknowledgments

This work was supported by the State assignment 2020-2022 (research project FSMR-2020-0018).

Transformation of dispersed particles in a pyrotechnical flame

A N Lepaev[1], S I Ksenofontov[2], O V Vasilyeva[3]
[1]Cheboksary Institute (branch) of the Moscow Polytechnic University, Cheboksary 428000, Russia
[2]Chuvash State Pedagogical University named after I.Y. Yakovlev, Cheboksary 428000, Russia
[3]Chuvash State University named after I.N. Ulyanov, Cheboksary 428015, Russia

E-mail: [1]it@polytech21.ru, [2]ksenofontovsi@mail.ru, 3dprostokvashino@mail.ru

Abstract. In the upper layers of clouds, ice floes can form, which fall to the ground in the form of hail. Clouds are seeded with ice-forming crystalline substances to prevent the formation of large hailstones. Silver iodide is mainly used as crystalline substances. The paper studies the condensed products that are formed in the flame of a pyrotechnic composition based on ammonium perchlorate and phenol-formaldehyde resin with technological additives.

1. Introduction

Ice floes form in the upper layers of the surface atmosphere. Enlarging, they fall out in the form of hail and damage crops. The seeding of clouds with ice-forming crystalline substances makes it possible to regulate the processes occurring in the atmosphere. Ice floes form on the surface of the seed crystals. Their sizes directly depend on the concentration of the nuclei themselves. Silver iodide is used as a crystalline substance. Their crystal structure is similar to that of ice. The optimal concentration of germs is $5 \cdot 10^{12}$ per gram of the substance. To date, the study of the processes of transformation of silver iodide in pyrotechnic compositions into active centers of crystallization with maximum efficiency is an urgent task [1].

2. Results and discussion

Powders of fuel, oxidizer and target products with a particle size of 50 to 200 microns are placed in pyrotechnic compositions. The flame of the pyrotechnic composition is a reactor for the production of dispersed particles of nano- and submicron sizes, which are not capable of agglomerating into larger fractions outside the flame. It is necessary to develop a composition in which the target products, passing through the combustion zone, would turn into steam, and in the colder zones of the flame, as a result of steam condensation, the process of formation of highly dispersed crystals would begin

If the flame temperature exceeds the boiling point of silver iodide, the molecules can decompose into ions. Due to the dilution of ions by combustion products and air, their partial pressure decreases. The probability of re-formation of molecules by silver and iodine ions is extremely small.

Combustion products of fuel (phenol-formaldehyde resin) and oxidant (ammonium perchlorate) contain oxygen, chlorine and carbon. They can distort the course of the transformation of silver iodide crystals into nanoscale products with the release of silver chloride. Potassium iodide is added to the

composition in order to preserve silver iodide. The rate of conversion of potassium iodide to potassium chloride is such that silver iodide remains unchanged in the flame.

Changes in the chemical and disperse compositions in the central zones of the flame are shown in figure 1. The sampler section was processed using a Tescan electron microscope and presented as an EMF–image. Dispersed particles have a certain color to highlight the elemental composition. The list of elements in the sample is shown in the lower left corner of the image. Silver iodide crystals have a cubic shape with a size of 5 microns. Free iodine in the form of dispersed particles is located in the carbon network and on the surface of other dispersed particles.

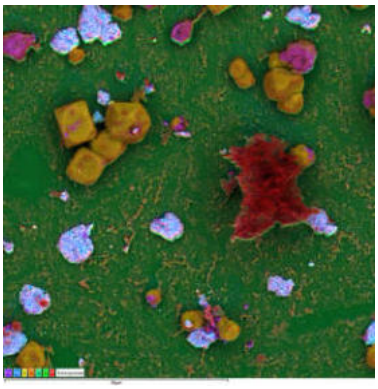

Figure 1. Electronic snapshot of the site in the EMF–image

Silver iodide in samples obtained in the peripheral zones of the flame is in the form of dispersed particles less than one micron in size (Figure 2a). Large particles larger than 10 μm are crystals of potassium chloride. The X-ray spectral analysis of these particles is shown in figure 2b.

(a)

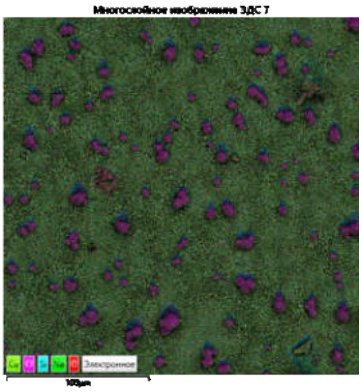

(b)

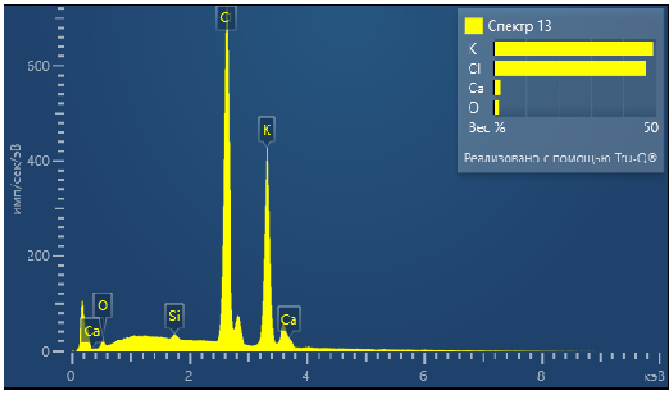

Figure 2. (a) Visual image of the sample area; (b) X-ray analysis of large particles

Cubic silver iodide particles are the α-modification of the body-centered lattice, which exists at temperatures above 420 K [1]. Another form of β-modification crystals exists at temperatures below 420 K. The type of crystal structure is similar to wurtzite [2]. The transition between the α and β forms is the melting of the silver sublattice with a melting heat of less than 14 kJ/mol.

Thus, in the flame of the pyrotechnic composition, the sizes of dispersed particles of the target products are transformed from micron size to nano- and submicron sizes. The method of chemical preservation of silver iodide makes it possible to obtain target products without loss

References

[1] Alikin V N 2004 *Charges of national economic significance* **11** 204
[2] Grigorieva I S 1991 Physical quantities (Moscow: Energoatomizdat) p 1232

Features of electrophoretic deposition of nanostructured cathode material based on NCA and Super C45

N A Litovchenko[1], L I Sorokina[1], R M Ryazanov[2], E A Lebedev[1, 2]

[1] National Research University of Electronic Technology (MIET), 124498, Moscow, Zelenograd, Russia
[2] Scientific-Manufacturing Complex "Technological Centre", 124498, Moscow, Zelenograd, Russia

E-mail: natlitovch@yandex.ru

Abstract: In this study, the features of electrophoretic deposition (EPD) of NCA- and Super C45-based cathode material were examined. Solvents and additive components were analyzed on the EPD method and the optimal suspension composition for the best layer deposition was obtained. As a result of this work, the resulting layers can be used as cathodes for microsized power sources.

1. Introduction

One of the most promising trends in micro- and nanoelectronics is microsized power supplies, their development and creation. At present, there are various symmetrical planar supercapacitors, in which the electrodes of homogeneous materials are arranged in one plane, but the main drawback is the relatively low capacitive characteristics. One way to solve this problem is to create micro-sized Li-ion batteries with dissimilar electrodes. Currently, there is no simple way to locally form two heterogeneous multicomponent materials in a single technological cycle. One approach to solving this problem is the use of the electrophoretic deposition (EPD) process, which makes it possible to form layers of cathode material on conductive substrates without expensive equipment and precisely control their composition and morphology. This work investigated the features of the deposited composite cathode material based on NCA powder ($LiNi_xCo_yAl_zO_2$), which is characterized by high specific capacitance and low cost in comparison with analogues.

2. Methodical

An electrophoretic cell which consisted of two electrodes connected to a power source and immersed in a beaker with a suspension was used to form composite materials by the EDP method. Deposition occurred on a negatively charged conductive substrate in potentiostatic mode. The electric field voltage was varied from 50 to 110 V/cm and the process duration was from 2 minutes to 5 minutes. The suspension used in this work contained NCA powdered to nanoscale and the carbon conductive additive Super C45 and was prepared on the basis of isopropyl alcohol and acetone in a 1:1 ratio. Dispersant and surfactant additives (sodium lauryl sulfate, nickel nitrate hexahydrate, cellulose, citric acid) were used to stabilize coagulating particles and improve electrophoretic mobility of the active material, each taken at a concentration of 0.25 to 0.75 g/l.

To control the composition of the obtained samples, energy dispersive X-ray spectroscopy was used. The morphology of the obtained layers was studied using a scanning electron microscope.

To study the cyclic charge-discharge characteristics, two-electrode cells were prepared in which the anode was made of lithium rolled on a nickel grid with a nickel foil current lead welded to it, and a porous polypropylene film was used as a separator; the electrolyte was 1M $LiPF_6$ solution.

3. Results

In this work, the composition of the suspension was optimized. Cellulose was added to increase stability. Nickel nitrate hexahydrate was added to increase the sedimentation rate and used as a charge. Its optimum concentration of 0.1 g/l of solution was determined based on the dependence of the density of the formed layer on its concentration.

The influence of the initial suspension composition on the formed layers was investigated, and a obtained graph presented on Figure 1.

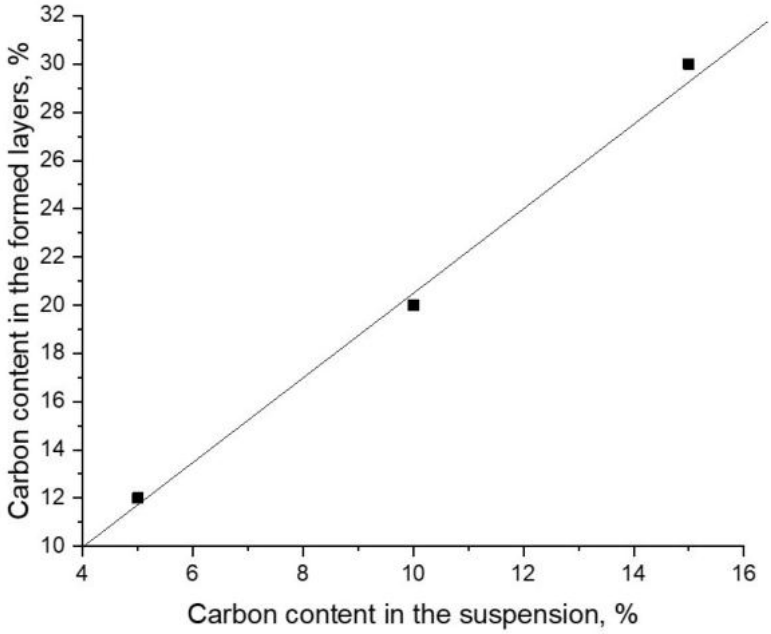

Figure 1. Dependence of the carbon concentration in the suspension on the concentration in the formed layer

This allowed precise control of the ratio of the cathode material components. The ability to vary the composition of the composite material in a wide range allows to optimize its properties in terms of specific capacitance and electrical conductivity.

The capacitive characteristics of the electrodes obtained on the basis of the formed composite cathode material were also studied. Based on the cyclic charge-discharge characteristic it was found that the specific capacitance of the obtained cathodes is 5 mAh/g.

4. Acknowledgments

This work was supported by the State assignment 2020-2022 (research project FSMR-2020-0018).

Quantum convolutional neural networks for multiclass classification

Denis Bokhan[1,2,*], Alena S. Mastiukova[2,3], Aleksey S. Boev[2], Dmitrii N. Trubnikov[1], Aleksey K. Fedorov[2,3,+]

[1] Laboratory of Molecular Beams, Physical Chemistry Division, Department of Chemistry, Lomonosov Moscow State University, Moscow 119991, Russia

[2] Russian Quantum Center, Skolkovo, Moscow 143025, Russia

[3] National University of Science and Technology "MISIS", Moscow 119049, Russia

[*] denisbokhan@mail.ru

[+] akf@rqc.ru

Abstract. Multiclass classification is of great interest for various machine learning applications, for example, it is a common task in computer vision, where one needs to categorize an image into three or more classes. Here we propose a quantum machine learning approach based on quantum convolutional neural networks for solving this problem. The corresponding learning procedure is implemented via TensorFlowQuantum as a hybrid quantum-classical (variational) model, where quantum output results are fed to softmax cost function with subsequent minimization of it via optimization of parameters of quantum circuit. Our conceptional improvements include a new model for quantum perceptron and optimized structure of the quantum circuit. We use the proposed approach to demonstrate the 4-class classification for the case of the MNIST dataset using eight qubits for data encoding and four acnilla qubits. We expect that our finding provide a new step towards the use of quantum machine learning for solving practically relevant problems in the NISQ era and beyond.

1. Introduction

Quantum computing is now widely considered as a new paradigm that by exploiting quantum physics phenomena such as superposition and entanglement, allows solving various problems, which are intractable for classical computing devices. In the quantum gate-based model, quantum algorithms are implemented as a sequence of logical operations under the qubits, which compose the corresponded quantum circuits that is terminated by qubit-selective measurements. Unlike the classical case, where a single string of n zeros and ones is sufficient to describe the state of n bits, a physical system of n qubits may require 2n complex numbers to describe its state. The use of NISQ devices in the context of the quantum-classical (variational) model has emerged as a leading strategy for their use. The workflow of variational quantum algorithms, where parameters of circuit are iteratively updated (optimized), resembles classical learning procedures. A cornerstone problem of various machine-learning-based approaches is classification, that it why it has been widely considered from the view point of potential speedups using quantum computing. In this work, we present a quantum multiclass classifier, which is based on the QCNN architecture. The developed approach use the traditional utilization of convolutional neural networks when after several convolutional layers few fully connected layers are placed. The

obtained classification results for the 4-classes of MNIST images confirms that the developed approach can be efficiently used. To the best of our knowledge, our work is the first such demonstration.

2. General scheme

At the first step, we realize amplitude encoding of input data, in our case, MNIST images. We consider MNIST images, which are rescaled from 28 by 28 to 16 by 16 pixels, and, thus, 8 qubits are required for the realization of quantum circuits. In terms of qubit states encoded images can be expressed as follows

$$\Psi_k = \sum_{m=0}^{N} C_m^k |m\rangle,$$

where k is the index of image and $|m\rangle$ is a qubit register of 8 qubits, which encode index m, and $N = 255$. Coefficients C_m^k are equal to elements of normalized flatten vectors of images.

We first employ the amplitude encoding procedure, where ancilla qubits are used for one-hot encoding of the class of target images. Preliminary analysis of encoded images is performed with 3 convolutional layers with the sizes of filters, equal to 4, 3, and 2, respectively. Each such layer consists of 2 sublayers that are needed to maintain translational invariance (at least, partially), and all the filters of the same size contain identical trainable parameters as it takes place the case for classical convolutional neural networks (CCNN).

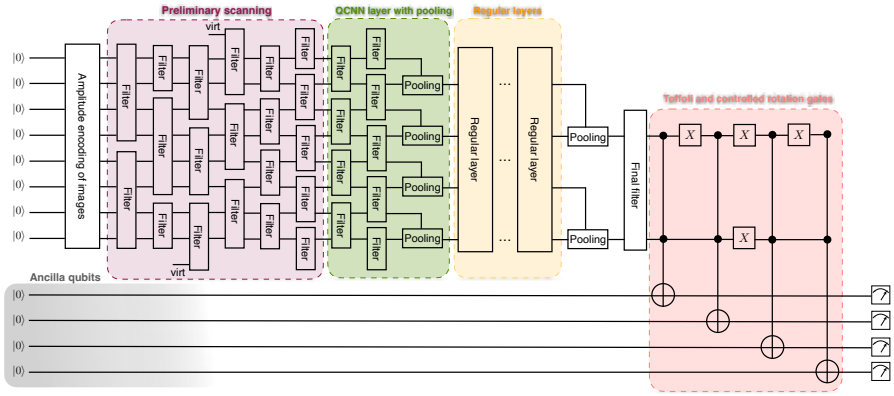

Fig. 1. General structure of the proposed quantum neural network structure consisting of several steps: Preliminary scanning using n-qubit filters, pooling, and regular layers.

3. Conclusions

Here we have demonstrated the quantum multiclass classifier, which is based on the QCNN architecture. The main conceptual improvements that we have realized are the new model for quantum perceptron and the optimized structure of the quantum circuit. We have shown the use the proposed approach for 4-class classification for the case of four MNIST. As we have presented, the results obtained with the QCNN are comparable with those of CCNN for the case if the number of parameters are comparable. Moreover, since the scheme require the use of multiqubit gates, the qudit processors, where multiqubit gate decompositions can be implemented in a more efficient manner, can be of interest for the realization of such algorithms.

Acknowledgments

A.S.M. and A.K.F. acknowledge the support of the Russian Science Foundation (19-71-10092). This work was also supported by the Russian Roadmap on Quantum Computing.

References

[1] M. Mottonen, J. J. Vartiainen, V. Bergholm, and M. M. Salomaa, Quantum Information and Computation 5, 467 (2005).

Investigation of Langmuir floating layers by capacitive methods

V N Mironyuk[1], K A Polyakova, E G Glukhovskoy[1]

[1] Education and Research Institute of Nanostructures and Biosystems, Saratov State University, Saratov, 410012, Russia

E-mail: bestblogger@yandex.ru

Abstract The paper proposes a technique for investigating floating monolayers by recording the frequency-capacitance characteristics of a planar capacitor, where the system "air gap - water subphase - floating monolayer" was used as a dielectric. Arachidic acid and liquid crystal 4-octyl-4-biphenylcarbonitrile were used as a substance for monolayer formation. The frequency-capacitance characteristics of the system containing arachidic acid show a change in capacitance depending on the volume of the injected solution and on the surface concentration of the molecules. It is shown that capacitance measurements can give information on the presence of a monolayer on the water surface and on the amount of the substance forming it. The dependence of the frequency-capacitance characteristics on the degree of compression of the ML of the liquid crystal was investigated.

1. Introduction and motivation

The molecular organization and phase state of floating monolayers (ML) are affected by many factors. Temperature, impurities, subphase pH, and ML composition can significantly affect the molecular interaction and phase transitions during ML formation [1-3]. Many methods, including non-contact methods, have been developed to control ML properties. Very often several techniques are combined and realized simultaneously in one unit. A typical technique is the simultaneous study of surface potential and surface tension depending on the area occupied by a monolayer [4], ML study by the method of isotherms of compression is accompanied by structure study using synchrotron radiation [5], or combined with spectral methods such as infra-red polarization spectroscopy [6].

The Kelvin probe method or the vibrating electrode method [7] is the basis for recording changes in the surface potential of a floating ML. This method, as a rule, operates at a single frequency and does not provide information on frequency-dependent processes. Mechanical vibrations of the upper electrode can affect the monolayer, lead to the appearance of mechanically stressed areas and increase the tendency to form defects in its structure.

In the present work, we propose a research technique based on registration of the monolayer conditioned changes in the electrical characteristics of a planar capacitor, in which the system "air gap - water subphase - floating monolayer" acts as a dielectric. The proposed development of the technique will significantly expand the spectrum of obtained data on the monolayer (including frequency dependences in a wide frequency range) and will allow obtaining data on the effects related to the phase state of the film.

2. Experimental details and results

Frequency-capacitance characteristics were measured with a semiconductor instrument parameter analyzer Agilent B1500A in the frequency range from 1 kHz to 5 MHz. The following measurement

parameters were set in EasyEXPERT software: frequency range from 1 kHz to 5 MHz; testing AC voltage - 25 mV or less. The first experimental stage was to find out whether the sensitivity of the measuring part to the presence of ML on the water surface and changes in its density was sufficient. A solution of arachidic acid (AA) diluted in chloroform 10^{-3} M was chosen as the monolayer material. A miniature circular bath was designed, the bottom of which was a metal plate and served as one of the electrodes of a flat capacitor. An upper electrode made of copper foil was placed above the trough. The volume of AA solution applied to the surface of the subphase varied from 2 µl to 20 µl in 2 µl increments.

To study the relationship between the frequency-capacitance characteristics and the degree of ML compression, the liquid crystal substance 4-octyl-4-biphenylcarbonitrile (8CB) was chosen as the monolayer material and was dissolved in chloroform to a concentration of 10^{-3} M. For this purpose, a part of the KSV NIMA Trough KN-2002, a "trough", was placed directly into the measuring box of the Cascade Microtech probe station. Thus, it is possible to form and study Langmuir ML on the surface of the aqueous subphase, with simultaneous recording of electrical characteristics and compression isotherms. A top electrode made of copper foiled textolite was attached to a movable Plexiglas frame. An electrode from the KSV NIMA Surface Potential Sensor (SPOT) was placed at the bottom of the bath. A MicroTM FM-02 sensor was used to monitor surface tension. Fifty µl of 8CB liquid crystal was added to the surface of the subphase.

From the dependencies obtained for the system with AA, it was found that the change in capacitance depends on the volume of injected solution or on the surface concentration of molecules. The relationship between the change in capacitance and the amount of injected volume is ambiguous for the frequency range under study: in the range of 1-100 kHz the capacitance decreases uniformly with the amount of injected substance, and changes are about 5% of the maximum value of capacitance (without monolayer) at high frequencies, this dependence is broken, and changes reach 80%. More detailed studies with registration of frequency-capacitance dependences on the degree of compression of the monolayer with simultaneous registration of dependences of surface tension and surface potential are needed to explain the reasons for this disturbance. Thus, it was shown that capacitive measurements can give information about the presence of the monolayer on the water surface and on the amount of substance forming it.

The dependences of the frequency-capacitance characteristics on the area per molecule (A_0) of the 8CB monolayer at the ML formation points (A_0 = 0.62; 0.57; 0.52; 0.47 nm^2) were obtained. The system capacity varied unstably in the frequency range from 1 kHz to 1 MHz and has characteristic regions for all A_0, presumably related to ML relaxation. It is worth noting that during the dependence measurements from 1 MHz to 3 MHz, the surface pressure varied discontinuously within ± 0.5 mN/m. It can be connected with reorientation of molecules of liquid crystal, under the influence of an alternating electric field and occurrence of polarization effects. In the region of high frequencies from 1 MHz to 5 MHz an increase in capacitance is observed.

Acknowledgments

The study supported by a grant of the Russian Science Foundation (project No. 21-73-20057) and Saratov State University

References

[1] Mironyuk V.N. et al. 2021 J. Phys.: *Conf. Ser*. **2086** 012195.

[2] Begletsova N.N. et al. 2020 J. Phys.: *Conf. Ser*. **1697** 012112.

[3] Begletsova N.N. et al. 2020 J. Phys.: *Conf. Ser*. **1697** 012118.

[4] Al-Alwani A.J.K. et al. 2021 Liq. Cryst. and their Appl. **21 (4)** 74–84.

[5] Erokhin, V. et al. 1998 Thin Solid Films **327** 3 636-643.

[6] Mendelsohn, R. et al. 2010 Biochimica et Biophysica Acta (BBA) – Biomembranes. 197 **2** 107-130.

[7] Hans-Jürgen, B. et al. 2003 Physics and Chemistry of Interfaces - UK. : Copyright Wiley-VCH Verlag & Co. KGaA. 373.

Modeling of thermoelectric properties of graphenylene nanotubes encapsulated with fullerenes

E.V. Morozova, D.A. Timkaeva

Ulyanovsk State University, Ulyanovsk, 432017, Russia

kat-valezhanina@yandex.ru

Abstract. Thermoelectric properties of graphenylene nanotubes with encapsulated C_{60} fullerenes are investigated by means of DFT-based calculations and the method of nonequilibrium Green functions (NEGF). Electrical and thermal conductivities, Peltier and Seebeck coefficients, thermoelectric figure of merit are calculated for various nanotube diameters and distances between fullerenes.

1. Introduction

Koch et al. [1] predicted a new family of graphenylene nanotubes (GrNTs) 'rolled' from recently synthesized two-dimensional graphenylene. It is demonstrated that the dodecagonal rings in graphenylene result in saddle-shaped pores in nanotubes, and pore diameters in the transverse direction of the tube range from 1.5 to 3.3 Å depending on nanotube chirality [1]. Recently, the computational studies of the electronic, optical and thermoelectric properties of graphenylene nanoribbons, nanotubes, and graphenylene-based van der Waals hetrostructures have been reported [2-4]. An important task of research in this area is the development of a material with a high degree of phonon scattering and low electron scattering. In the present work, the thermoelectronic properties of graphenylene nanotubes with encapsulated C_{60} fullerenes for different nanotube diameters and distances between fullerenes are investigated.

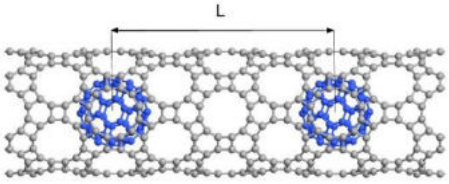

Figure 1. Structure of graphenylene nanotube (6,0) with encapsulated fullerenes C_{60} .

2. Results

The thermoelectric properties of graphenylene nanotubes with encapsulated C_{60} fullerenes were calculated at one temperature (T=300K) using the method of nonequilibrium Green functions (NEGF) of the DFT method implemented in QuantumATK.

Fig. 2 shows the results of calculations of electrical and thermal conductivities and the thermoelectric thermoelectric figure of merit for graphenylene nanotube-fullerene C_{60} systems with a distance between the centers of two neighboring fullerenes of 11.78 Å and 23.56 Å.

The thermoelectric figure of merit ZT determines the maximum efficiency of the energy conversion process in a thermoelectric material. It can be calculated using the expression

$$ZT = \frac{S^2 GT}{\lambda}, \quad (1)$$

where S is the Seebeck coefficient, G - electrical conductivity, T - absolute temperature, λ - thermal conductivity, which is equal to the sum of the electron λ_e and phonon λ_{ph} thermal conductivity.

The thermoelectric figure of merit of the CNT hybrid system (8,8) - C_{60} [5] is 6,4 times less than that of the graphenylene nanotube system (6,0) - C_{60}. For the simulated graphenylene nanopeapod (6,0) system with the distance between encapsulated fullerenes L=23.56 Å, there is a noticeable increase in the thermoelectric figure of merit. In the case of closely spaced fullerenes inside nanotubes, the conductance of the system is substantially higher, but at the same time, the electronic thermal conductivity is also increased. As a result, the ZT value is suppressed.

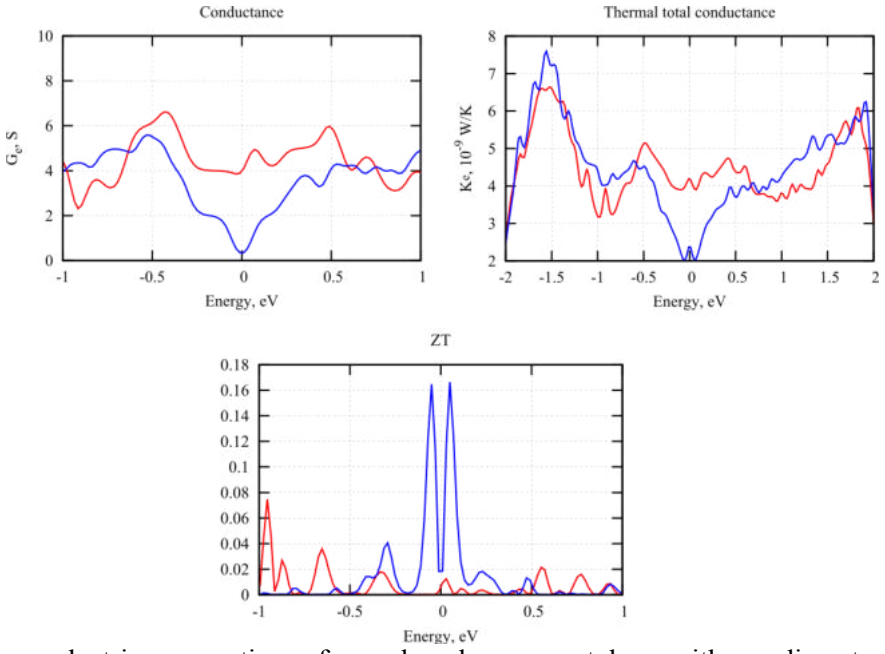

Figure 2. Thermoelectric properties of graphenylene nanotubes with a diameter D=12.99Å encapsulated with fullerenes, the distance between fullerenes L=11,78 Å (red), L=23,56 Å (blue).

Acknowledgments

This work is supported by the Ministry of Science and Higher Education of the Russian Federation (state program 0830-2020-0009).

References

[1] Koch, A.T., Khoshaman, A.H., Fan, H.D., Sawatzky, G.A. and Nojeh, A., 2015. Graphenylene nanotubes. *The journal of physical chemistry letters*, *6*(19), pp.3982-3987.

[2] Meftakhutdinov, R.M., Sibatov, R.T. and Kochaev, A.I., 2020. Graphenylene nanoribbons: electronic, optical and thermoelectric properties from first-principles calculations. *Journal of Physics: Condensed Matter*, *32*(34), p.345301.

[3] Kochaev A I, Meftakhutdinov R M, Sibatov R T, Timkaeva D A 2021 *Computational Materials Science* **186** pp 109999

[4] Meftakhutdinov R M, Sibatov R T, Kochaev A I, Evseev D A 2021 *Physical Chemistry Chemical Physics* **23 (26)** 14315.

[5] Morozova E V, Timkaeva D A 2021 *Semiconductors* pp 1-5.

Resorbable materials of complex shape based on calcium pyrophosphate for bone tissue regeneration

A.M. Murashko[1], Ya.Yu. Filippov[1]

[1]Lomonosov Moscow State University, Moscow, Russia

amur2908@gmail.com

Abstract. Calcium pyrophosphate is a promising material for bone implants. In the course of this work the possibility of using a sintering additive of mixed calcium/sodium pyrophosphate to improve the liquid phase sintering process of calcium pyrophosphate was investigated. A biocompatible pyrophosphate ceramic with sufficient compressive strength and a density close to the crystallographic density of calcium pyrophosphate was obtained at 1000 °C. Fabrication technique of macroporous ceramic without cracks and other defects based on calcium pyrophosphate with a given architecture has been developed.

1. Introduction

The most promising materials for osteoplasty are bioresorbable materials, which can perform a supporting and guiding function at the initial stages of use. Calcium pyrophosphate belongs to such materials, has good biocompatibility, bioactivity and optimal bioresorption rate. Also the implant must possess a system of macro- and micropores that promote diffusion of ions and sprouting of the forming bone. Within the framework of this study, the method of stereolithographic 3D printing is used to obtain porous materials, as traditional methods do not allow to control the final structure of the material.

Prior to that, we investigated the possibility of using a sintering additive of mixed calcium/sodium pyrophosphate with the aim to improve calcium pyrophosphate sintering, due to low-melting eutectics formation. [1] As a result, it was found out that the presence of a sintering additive allows to reduce the temperature (700 °C), required for sintering of the forming ceramics, significantly. The resulting material reaches a compressive strength of up to 140 ± 10 MPa and a density of 98 %. However, it turned out that materials obtained in this way may contain residual carbon, potentially exhibiting cytotoxic effects on body cells. Therefore, it was proposed to use powder mixtures to form ceramics based on calcium pyrophosphate at a higher temperature (1000 °C), at which residual carbon burns out.

2. Fabrication of macroporous and dense ceramics

Dense ceramics were made by molding a paste containing acetone and powder mixture of hydroxyapatite and monocalcium phosphate, followed by liquid-phase sintering at 1000 °C. Macroporous ceramics were made by stereolithographic printing. For this purpose, a powder mixture was sifted through a sieve to reduce the particle size and was mixed with a commercially available light-curing mixture of acrylic monomers and oligomers and surfactant (DISPERBYK-111) in a mass ratio of 53/45.5/1.5, respectively. To investigate the depth of polymerization, the obtained suspensions

were irradiated during different periods of time and then the thickness of the printed samples was measured. The Jacobs equation was used to approximate the dependence of polymerization depth on the irradiation dose to select the printing mode. As a result of printing, Kelvin structures with a predetermined 70 % porosity were made, which were subjected to further heat treatment according to the regime selected in line with differential curve of thermal analysis.

3. Results and discussion

Dense pyrophosphate ceramics with compressive strength 154 ± 17 MPa and Young's modulus 8.5 ± 2 GPa were obtained. The given data lies in the range of strength and stiffness values of natural bone. The density of ceramics relative to the crystallographic density of $Ca_2P_2O_7$ was 99.8 ± 0.4 %, which indicates the effectiveness of the sintering process at the selected temperature. The porosity of 3D structures was about 76 %, which is higher than the value of the predetermined porosity (70 %). This is due to the decomposition and removal of the polymer during heat treatment. According to SEM data it is clear that as a result of heat treatment of 3D structures in our proposed mode, the surface smoothing, absence of cracks and any defects formed during polymer decomposition are observed. The pH of the aqueous solution in contact with the fabricated pyrophosphate ceramics lies in the range 6.1 – 6.2, which is acceptable for biomedical applications of the material.

References

[1] Filippov, Y. Y., Murashko, A. M., Evdokimov, P. V., Safronova, T. V., & Putlayev, V. I. (2021). Stereolithography 3D printed calcium pyrophosphate macroporous ceramics for bone grafting. Open Ceramics, 8, 100185.

Characterization of MEMS gyroscope sensor by nanoindentation

I E Lysenko[1], D V Naumenko[1], O. I Soboleva[1]

[1] Southern Federal University, Taganrog 347922, Russia

Abstract. This article presents a research of a MEMS gyroscope sensor by the nanoindentation method. Nanoindentation is a modern technology for studying the mechanical properties of nanomaterials and microdevices. The stiffness of the elastic suspension of the MEMS gyroscope was studied by the finite element method, taking into account the features of the study by nanoindentation. Then the FEA simulation results were verified using a nanoindenter based on an atomic force microscope.

1. Introduction

The most common use of nanoindentation is in establishing mechanical properties such as hardness and Young's modulus. Recently there has been a significant progress in measuring also other mechanical parameters, such as the hardening exponent, creep parameters, or the residual stresses [1]. But this technique can be useful when checking the elastic properties of various devices, for example, MEMS gyroscopes. The use of physical verification helps to verify the correctness of the calculations and increases the reliability of the device.

2. FEA simulation of nanoindentation

From the point of view of nanoindentation, a MEMS gyroscope is an inertial mass and an elastic suspension, the stiffness and deformation of which must be measured.

The sample was made in a volume of silicon using SOI technology with a height of 50 μm silicon (100) using reactive ion etching. The sample of the MEMS gyroscope under study is shown in Figure 1

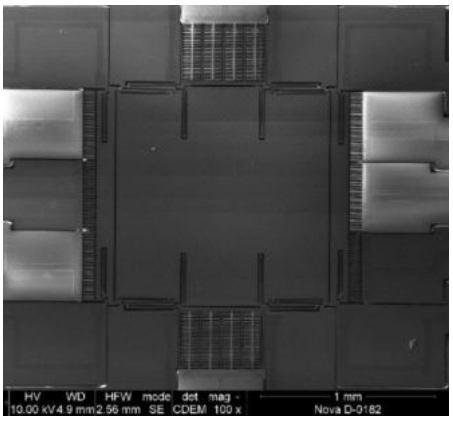

Figure 1. SEM image of the MEMS gyro

Using the FEM, a virtual tool was created to study the characteristics of a nanoindented sample [2]. Using FEM simulation, it is possible to numerically derive load (P) versus indentation depth (h) curves for various input parameters and thus obtain the resulting elastoplastic properties of the MEMS sensor. As a result of virtual studies repeating the nanoindenation process, deviations of the sample from the applied load were obtained using static analysis. Load simulation was carried out at several points on the sensor surface in order to eliminate nanoindenter positioning errors, as this was done manually. The simulation result is shown in Figure 2.

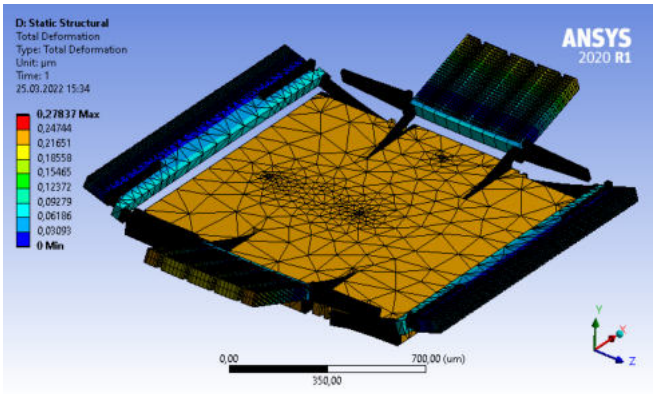

Figure 2. Results of the FEM nanoindentation

3. Experimental research

As a result of nanoindentation using AFM, a series of curves were obtained. The experimental curve P-h is shown in Figure 3.

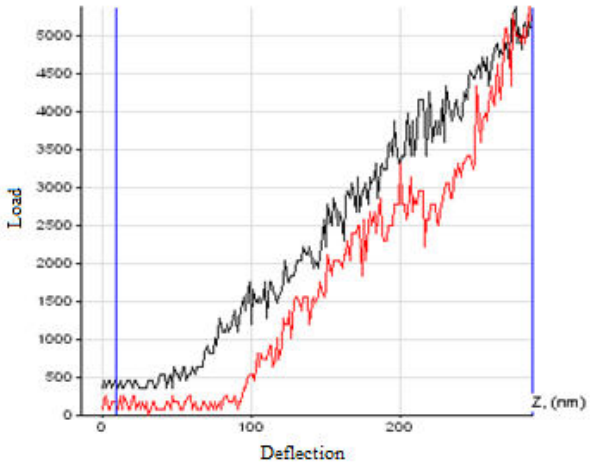

Figure 3. Experimental P-h curves.

As a result, simulation indicators and experimental data were compared. The technique showed a high convergence of research results of about 5%

4. Acknowledgments

The work was carried out at the expense of funds, task No. FENW-2020-0022 for the implementation of scientific research carrying out scientific research at the expense of the Federal budget, in terms of scientific activities on the topic "Development and research of methods and means of monitoring, diagnostics and forecasting state of engineering objects based on artificial intelligence".

References

[1] Diop, M. D., 2012, Characterization of Microdevices by Nanoindentation, Nanoindentation in Materials Science, IntechOpen, London. 10.5772/50997.

[2] Srnec Novak, J., Kamenar, E., Zelenika, 2021, Methodological correlation of finite element models to nanoindentation measurements on Si (100). U: Leach, R. & Nisbet, C. Philips, D. (ur.)Proceedings of the 21th International Conference of the European Society for Precision Engineering and Nanotechnology.

Multi-qubit gate decomposition using photonic qutrits

A S Nikolaeva[1, 2], E O Kiktenko[1, 2, 3] and A K Fedorov[1, 3]

[1]Russian Quantum Center, Moscow 143026, Russia
[2]Moscow Institute of Physics and Technology, Dolgoprudny 141700, Russia
[3]National University of Science and Technology "MISIS", Moscow 119049, Russia

anastasiya.nikolayeva@phystech.edu

Abstract. Here we describe a decomposition of a generalized N-qubit Toffoli gate with the use of $6N - 11$ two-qutrit gates, which is suitable for the implementation on a photonic quantum computing platform. The generalized Toffoli gate is a necessary element of various quantum algorithms, therefore its efficient realization is essential for realizing quantum algorithms.

1. Introduction

Photonic platforms have a great potential for quantum computing [1-3]. In addition to the progress in the implementation of the qubit gates on photonic platforms, recently, gates on d-level quantum systems, qudits, have been successfully demonstrated in various experiments [1,2]. For the photonic platforms, the realization of qubit algorithms is reduced to the implementation of a sequence of native single- and two-qubit gates. The most difficult to implement are multi-qubit gates that require a considerable number of two-qubit gates in their decomposition. However, the use of higher levels of qudits and, accordingly, qudit gates, allows implementing N-qubit Toffoli gate with a linear on N number of two-qudit gates, instead of a polynomial number of two-qubit gates required in standard no-ancilla qubit decomposition [4].

Here we describe how the generalized Toffoli gate that is in demand in a wide range of algorithms can be implemented as a sequence of native on photonic platform two-qutrit gates.

2. Results and discussion

In this work, we present an approach to generalized Toffoli gate $C^{N-1}X$ decomposition using photonic qutrits with linear on N number of two-qutrit gates. As a basic two-qutrit gate we use a generalized version of CX gate – SUM gate. For qutrits it adds the value of the control qutrit to the value of the target qutrit modulo 3 that was successfully demonstrated in recent experiment [2]. Using the sequence of three SUM gates, we construct an operation $U_{i\to j}$ that leaves qutrit i in the state $|1\rangle$ if and only if both i and j qutrits are in the state $|1\rangle$ as follows:

$$
\begin{aligned}
U_{i\to j}|00\rangle_{ij} &= |00\rangle_{ij},\\
U_{i\to j}|01\rangle_{ij} &= |01\rangle_{ij},\\
U_{i\to j}|10\rangle_{ij} &= |02\rangle_{ij},\\
U_{i\to j}|11\rangle_{ij} &= |10\rangle_{ij}.
\end{aligned}
$$

The construction of the decomposition scheme is similar to the method described in Refs. [5,6]. By applying $U_{i\to j}$ operation to $N-2$ pairs of qutrits in accordance with their coupling map graph in the photonic quantum processor, we leave the last pair of qutrits in the states $|1\rangle$ if all other qutrits, which have a path to these two qutrits, were in the state $|1\rangle$. After the sequence of $U_{i\to j}$, in order to apply phase factor -1 to the whole system, we implement CX gate on the last pair of qutrits. Then, as the third levels of qutrits were affected, we perform an uncomputation process, i.e., we apply Hermitian conjugate sequence of $U_{i\to j}$ gates in the reverse order. Thus, to implement $C^{N-1}X$ gate we employ $6N-11$ two-qutrit gates.

The proposed approach to linear on N decomposition of $C^{N-1}X$ gate allows one to reduce the complexity and, consequently, improve total fidelity of algorithms' implementation on photonic platforms. This result is of importance for realization of quantum algorithms with a considerable number of multi-qubit gates.

Acknowledgments

The work was supported by the Russian Science Foundation Grant No. 19-71-10091, LRC program on Quantum Computing (Agreement No. 014/20), and Russian Roadmap on Quantum Computing.

References

[1] Chi, Y., Huang, J., Zhang, Z. et al. A programmable qudit-based quantum processor. Nat Commun 13, 1166 (2022).

[2] Imany, P., Jaramillo-Villegas, J.A., Alshaykh, M.S. et al. High-dimensional optical quantum logic in large operational spaces. npj Quantum Inf 5, 59 (2019).

[3] Arrazola, J.M., Bergholm, V., Brádler, K. et al. Quantum circuits with many photons on a programmable nanophotonic chip. Nature 591, 54–60 (2021).

[4] Barenco, A., Bennett, C. H., Cleve, et. al. Elementary gates for quantum computation. Physical review A, 52(5), 3457 (1995).

[5] Nikolaeva, A.S., Kiktenko, E.O., Fedorov, A.K., "Decomposing the generalized Toffoli gate with qutrits" arXiv preprint arXiv:2112.14535 (2021) (accepted in PRA).

[6] Kiktenko, E. O., Nikolaeva, A. S., Xu, P., Shlyapnikov, G. V., & Fedorov, A. K. Scalable quantum computing with qudits on a graph. Physical Review A, 101(2), 022304 (2020).

Size-selective hybrid photocatalysts based on porphyrin SURMOFs and graphene oxide

Nugmanova.A.G.[1], Safonova E.A.[1], Baranchikov A.E.[2], Shkolin A.V.[1], Mitrofanov A.A.[3], Eliseev A.A.[3], Kalinina M.A.[1]

[1] A. N. Frumkin Institute of Physical Chemistry and Electrochemistry, Russian Academy of Sciences, Moscow, Russia

[2] N. S. Kurnakov Institute of General and Inorganic Chemistry, Russian Academy of Sciences, Moscow, Russia

[3] Moscow State University, Moscow, Russia

nugmanovaalsy@gmail.com

Abstract. In this work, we report on a new method to synthesize new sponge-like photocatalytic materials comprising graphene oxide (GO) and zinc porphyrin complexes ordered into surface-attached metal organic frameworks (SURMOFs). To obtain the SURMOF/GO hybrids in a powdered form, we developed a one-pot synthesis of these materials in the GO-stabilized oil-in-water Pickering emulsions. The oxidized groups on the GO sheets promote the adsorption of metal clusters followed by anchoring of porphyrins to the surface of 2D carbon [1]. The results of experimental studies involving X-ray diffraction, UV-vis spectroscopy, BET nitrogen absorption, gas chromatography-mass-spectrometry and MALDI-TOF spectroscopy. The data suggest that these mesoporous SURMOF/GO hybrids can exploit two different mechanisms yielding different products of photocatalytic degradation of model organic compounds such as rhodamine 6G (Rh6G) and 1,5-dihydroxynaphtalene (DHN). The oxidation through photoinduced generation of singlet oxygen on porphyrin centres occurs in the presence of oxygen [2]. In anaerobic conditions, the catalysts can promote reduction by a direct electron transfer to the substrates in the SURMOF pores. Their size controls the efficiency of the anaerobic process. The SURMOF/GO with the pore size of 1.6 nm can transform both Rh6G and DHN, whereas the material with 1.1-nm pores is active only with respect to the small DHN molecules. The results provide a rational basis for the substrate-selective GO-based hybrid photocatalytic materials integrated with SURMOF components with tunable porosity.

1. Synthesis of hybrid photocatalysts based on porphyrin SURMOFs and GO

The application of hybrid materials based on GO as photocatalysts is of great interest, because GO has necessary optical transparency and a low Fermi energy level, which is needed for efficient separation of the photoinduced charge. The use of porphyrins as an organic component will expand the range of optical absorption in the visible region and use the intrinsic photocatalytic properties of porphyrins. The organization of porphyrins into metal-organic frameworks (MOFs) will make it possible to create selective photocatalysts by varying functional substituents and pore size.

New photocatalysts were synthesized from GO, zinc acetate as metal cluster and zinc porphyrins, either meso-tetra(4-pyridyl)porphyrin (ZnTPyP) or meso-di(4-pyridyl)di(4-carboxyphenyl)porphyrin (ZnDPyDCPP), by non-covalent self-assembly in Pickering emulsions. X-ray powder diffraction and BET nitrogen sorption methods confirmed the formation of SURMOFs with different micropore sizes of 1.1 nm for ZnTPyP - SURMOF1/GO and 1.6 nm for ZnDPyDCPP - SURMOF2/GO.

2. Study of photocatalytic activity

The activity of materials in the photodegradation of rhodamine 6G (Rh6G) and 1,5-dihydroxynaphthalene (DHN) based on SURMOF/GO was studied by UV-Vis spectroscopy. The photocatalysts initiate aerobic oxidative photodestruction with k up to 2.3×10^{-1} min^{-1} through generation of singlet oxygen ($^1O_2$) on porphyrin centers. Generation of $^1O_2$ was confirmed by analysis of the sample with Sensor Green. Under anaerobic conditions, these materials assist photoreduction of the same dyes in the SURMOF micropores. To confirm the mechanism of the reaction in an anaerobic area, a set of methods was used - MALDI-TOF, GC-MS spectroscopy and terephthalic acid probing. The size of the SURMOF pores controls the reduction, which occur due to the effective charge separation between porphyrin SURMOFs and GO. A large pore photocatalyst, SURMOF2/GO, can destruction both Rh6G and DHN, while SURMOF1/GO is active only against small DHN molecules.

The ability of the formed SURMOF/GO photocatalysts to use two mechanisms that give different photodegradation products creates the basis for obtaining new ambivalent photocatalysts for selective transformations of target compounds in molecular mixtures.

Acknowledgments

This work was supported by the Russian Science Foundation (project No 20-13-00279).

References

[1] Meshkov I.N., Zvyagina A.I., Shiryaev A.A., Nickolsky M.S., Baranchikov A.E., Ezhov A.A., Nugmanova A.G., Enakieva Y.Y., Gorbunova Y.G., Arslanov V.V., Kalinina M.A. Langmuir. 2018, 34, 5184–5192.

[2] Meshkov I.N., Bulach V., Gorbunova Y.G., Gostev F.E., Nadtochenko V.A., Tsivadze A.Y., Hosseini M.W. Chem. Commun. 2017, 53, 9918–9921.

Membrane technology, composite films, nanostructured surface, surface modification, penta-twinned particles, hydrogen permeability, high-purity hydrogen

ILIYA PETRIEV[*;**], POLINA PUSHANKINA[*], YULIYA GLAZKOVA[*], TIMOFEY MALKOV[*], GEORGY ANDREEV[*]

[*] Department of Physics, Kuban State University, Krasnodar, 350040, Russia.
[**] Laboratory of problems of stable isotope spreading in living systems, Southern Scientific Centre of the RAS, Rostov-on-Don, 344000, Russia.

SYNTHESIS AND INVESTIGATION OF A PENTAGONALLY STRUCTURED COATING IN THE PROCESSES OF LOW-TEMPERATURE HYDROGEN PERMEABILITY

Introduction

Pd-based membranes are used to produce high-purity hydrogen. One of the ways to modify the membrane surface is to create a nanostructured layer using powdered hydrogen chemisorbing substances [1]. The aim of this study was to obtain durable Pd-containing films modified with a pentagonally structured "nanoflowers" type coating, capable of low-temperature hydrogen permeation. This will reduce energy costs in the process of obtaining high-purity hydrogen, as well as use the developed membranes to create a device for low-temperature (25-100 °C) diffusive hydrogen production.

Experimental

The modification with penta-twinned structures or "nanoflowers" of Pd-23%Ag films was carried out by following method:

Before the modification, the films were washed and degreased. Then, the prepared foil was placed on an inert holder in an electrolytic cell for anodic polarization in 0.1 M HCl, and then cathodic polarization in 0.05 M H_2SO_4. Both operations were carried out at a constant current density of 10-20 mA cm^{-2}. Next, the cell was filled with a growth solution of 2% H_2PdCl_4, and a highly dispersed palladium coating was deposited at a reduced current density of 3-4 mA cm^{-2}; after modification, the films were washed with bidistillate.

The investigation of the gas transport parameters of the developed modified samples of Pd-23%Ag membranes was carried out on a hydrogen permeability unit, according to the method described in [2].

Results and discussion

SEM images of the modified films surface were obtained in the course of the study. Microphotographs are shown in Figure 1.

After modification, these films as membranes were studied in the hydrogen transport processes. As can be seen from Figure 2, the values of the hydrogen flux for membranes modified by the "nanoflower" method are approximately 1.8 times higher than the values for membranes obtained by the classical palladium black method. Nominally, these are very small

values, but they are quite significant under low-temperature conditions, since there is practically no stable permeability in this temperature range.

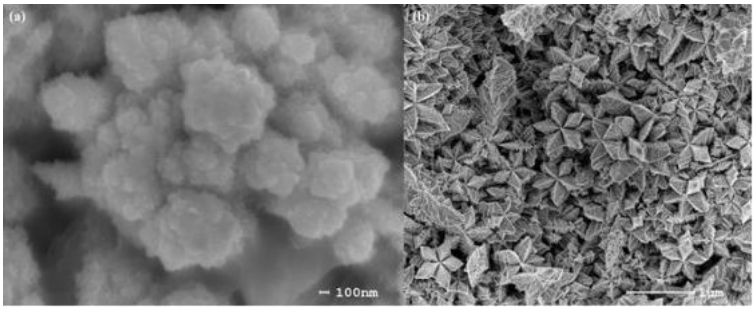

Fig. 1. SEM images of the Pd-Ag films surface with modifying coatings obtained by methods: (a) “nanoparticles” and (b)”nanoflowers”

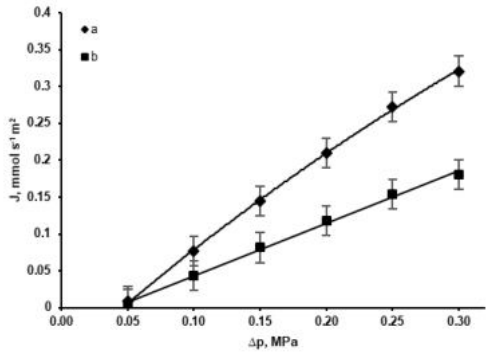

Fig. 2. Dependence of the flux density on the excess pressure of hydrogen on the inlet side of membranes modified by methods (a) “nanoflowers” and (b) “nanoparticles”

The coatings on the membrane surface formation of fundamentally new structural organizations (“nanoflowers”) increases the surface adsorption activity, which affects the catalytic activity of the material with respect to reactions involving hydrogen. In our opinion, this is the reason for the decrease in the energy barrier of hydrogen molecules dissociation and recombination processes on the membrane surface, which leads to an increase in the rate of hydrogen transport through the membrane based on the Pd-23%Ag alloy.

Conclusions

A significant feature of the experiment was the increased penetrating flux despite the reduced actual surface area. The feature was found to be inherent in membranes with lower roughness, but with a pentagonally structured surface organization. This happened contrary to the classical ideas of the acceleration of the hydrogen transport surface stages, which states that there is no alternative to an extensive increase in the complexity and specific surface area of palladium membranes.

Acknowledgment

This research was funded by Russian Science Foundation, grant number 21-72-00045, https://rscf.ru/project/21-72-00045/.

References (Times New Roman Bold 10)

[1] W. Vielstich, Brennstoffelemente. Moderne Verfahren zur elektrochemischen Energiegewinnung, Wiley-VCH Verlag GmbH & Co. KGaA., Weinheim, 1965

[2] I. Petriev, P. Pushankina, S. Bolotin, I. Lutsenko, E. Kukueva, M. Baryshev, The influence of modifying nanoflower and nanostar type Pd coatings on low temperature hydrogen permeability through Pd-containing membranes, J. Membr. Sci. 620 (2021) 118894

On the compression modulus of floating Langmuir layers

E G Glukhovskoy[1], V N Mironyuk[1], A J K Al-Alvani [1], M V Gavrikov[1], M V Pozharov[2], K A Polyakova, V.A. Kuznetsova[3], M.V. Kanevsky[3], E.V. Glinskaya[3]

[1] Education and Research Institute of Nanostructures and Biosystems, Saratov State University, Saratov, 410012, Russia
[2] Institute of Chemistry, Saratov State University, Saratov, 410012, Russia
[3] Faculty of Biology, Saratov State University, Saratov, 410012, Russia

E-mail: glukhovskoy@gmail.com

Abstract. The paper considers certain methodological issues related to the calculation of the mechanical parameters of floating Langmuir monolayers. It is shown that the values of the compression modulus and compressibility can differ significantly when using different approaches. In this case, the difference in the values obtained in calculations by various methods commensurate with the calculated values themselves. The generally accepted formulas do not allow calculating the compression modulus and other mechanical parameters as characteristic ones that have a constant value for any phase state of the monolayer. Therefore, we propose using refined formulas for calculating mechanical parameters.

1. Introduction and motivation

Floating monomolecular layers at the phase boundaries, the so-called Langmuir monolayers (MS), have attracted the attention of many scientists from various fields. From a practical point of view, such layers can become new frameworks for creating devices based on the operation of individual molecules assembled in 2D molecular systems - molecular layers and multilayer structures. Such systems can have unique pre-determined properties and characteristics due to ability to control composition of each layer of such system as well as its total structural organization, or to make multi-layer structures by alternating the layers via layer-by-layer assembly process. On the other hand, theoretical and laboratory studies have yet to reach their full prognostic potential. Monolayers serve as unique models for various system, such as biological membranes, thus, making it possible to understand structural reorganization and functioning of such systems under changing external conditions including temperature, electric fields or chemical composition. Such systems are convenient for studying processes occurring at the interfaces of two different phases (“gas-liquid”, “liquid-solid”), i.e. sorption-desorption processes, chemical reactions in low-dimensional materials, etc.

To understand the physical and chemical phenomena and processes occurring in the Langmuir layers and quantify changes in such systems, the international community has adopted common definitions and formulas.

This paper proposes a comparative consideration of the formulas used for calculating the compression modulus and compressibility of floating monolayers, and discusses the physical meaning of the calculated values.

2. Results and disscussions

Several IUPAC publications made in 1972 [1], 1985 [2], 1994 [3] and 2006 [4] have become critically important for establishing uniform definitions and rules for calculating physical quantities. In particular, one of the last ones was devoted specifically to the physics of thin films and layers - "Thin films, including layers: terminology in connection with their production and characterization: (IUPAC recommendations 1994)", that was drawn up by a large team of world-famous scientists operating in the field of surface physics [3]. These documents provide formulas for calculating the mechanical properties of MS on the water surface, including the compression modulus and compressibility for 2D objects such as thin films and layers.

It should be noted that similar formulas were originally introduced in continuum mechanics, and in their original version were used to calculate the parameters of volumetric bodies (see, for example [4,5]). Thus, such parameters as “volume (bulk) strain”, “bulk modulus or compression modulus K» and “isothermal compressibility κ_T” are defined on pages 15 and 56 of [4], respectively, as:

$$K = -V_0 \cdot \mathrm{d}p/\mathrm{d}V \qquad \kappa_T = -(1/V)(\partial V/\partial p)_T \qquad (1)$$

where V, V_0 are the volume of a rigid body at a certain point of time and the initial volume of an undeformed body, respectively, and p is the pressure.

With the development of Langmuir floating layer formation methods, the formulas for calculating the compression modulus in the 2D structures were rewritten as:

$$K_s = -A_\mathrm{s} \cdot \mathrm{d}\pi/\mathrm{d}A \qquad K_0 = -A_0 \cdot \mathrm{d}\pi/\mathrm{d}A \qquad (2)$$

where K_s, K_0 are the compression moduli and A_s, A_0 are areas occupied by a single molecule. Here, the symbol "s" means that the values of physical quantities are determined as the current experimentally recorded values, and the values with the symbol "0" are recalculated for the state of the undeformed MS. Thus, the area A_s is found as the current value of the specific area at a certain point of time during registration of the MS compression isotherm - the experimental dependence of the surface pressure on the specific area $\pi = \pi(A)$. The value of A_s depends linearly on time for a uniform motion of the barrier, i.e. , it decreases uniformly under uniform compression of the MS. The area A_0 is determined from the MS compression isotherm by finding the intersection point of the tangent to the compression isotherm with the π axis . If the tangent equation is written as $\pi = a \cdot A + b$, where a and b are some constants, then A_0 at the point of intersection (i.e. when $\pi = 0$) can be found as $A_0 = -b/a$.

It is easy to see from the experimental curves that the difference between the values for different states of the MS A_0 and A_s can be comparable with these values. As a consequence, the mechanical properties of the MS (in particular, the compression modulus) of close-packed states is not a constant value, since a changing value (A_s) is used to calculate it, and not a fixed one (A_0) (see formulas 2). In this regard, only the mechanical parameter K_0 can claim the role of a characteristic parameter for any phase state of the monolayer.

Acknowledgments

The study is supported by a grant of the Russian Science Foundation (project No. 21-73-20057) and Saratov State University.

References

[1] Everett D.H. et al. 1972 Pure and Appl. Chem. IUPAC, **31** 577-638.
[2] Ter-Minassian-Saraga L. 1985 Pure and Appl. Chem. IUPAC. **57** 621-632.
[3] Ter-Minassian-Saraga L. 1994 Pure and Appl. Chem. IUPAC and De Gruyter. **66** 1667-1738.
[4] Cohen E.R. et al. 2006 Chemistry International -- Newsmagazine for IUPAC. **28** 1-250.
[5] Cohen E.R. et al. 1987 International union of pure and applied physics. **146** 1-75.
[6]. Begletsova N.N. et al. 2020 J. Phys.: Conf. Ser. **1697** 012118

Exfoliation of h-BN for silicone-based thermal pads - effective heat management material in electronics

N S Romanov[1,2], E M Gurova[1,3] and E A Danilov[1]

[1] Research Institute for Graphite-Based Structural Materials "NIIgraphite", 111524, 2 Electrodnaya St., Moscow, Russian Federation
[2] Mendeleev University of Chemical Technology of Russia, 125047, 9 Miusskaya Sq., Moscow, Russian Federation
[3] Bauman Moscow State Technical University, 105005, 5 2nd Baumanskaya St., Moscow, Russian Federation

533west484@gmail.com

Abstract. In the present work, ultrasonic-assisted exfoliation of h-BN in isopropanol for the preparation of boron nitride nanosheets was performed. Resultant boron nitride nanosheets had lateral sizes less than 1 μm with thickness 3-4 nm. Silicone pads filled with exfoliated h-BN showed in-plane thermal conductivity of 2.65 $Wm^{-1}K^{-1}$, whereas through-plane thermal conductivity was 0.53 $Wm^{-1}K^{-1}$ (an increase of 2290% and 380% respectively, as compared to pure silicone) with thermal conductivity anisotropy 5.0 at the maximum filler content. At the same time, composites had high electrical insulating characteristics with specific volume resistance of ≈ 10^{16} Ω·cm.

1. Introduction

Layered two-dimensional (2D) materials have recently gained significant research interest owing to their huge range of outstanding properties compared to their bulk counterparts [1-5]. One of the promising 2D-materials are h-BN nanosheets (BNNS), structural analogue of graphene, which possess unique combination of mechanical, physical and chemical properties such as high thermal conductivity (TC), mechanical strength, excellent dielectric characteristics, high thermal and chemical stability [1]. Moreover, lowering h-BN thickness allows one to improve its properties, for instance, TC is reported to achieve 751 $Wm^{-1}K^{-1}$ for monolayer (as compared to 400 $Wm^{-1}K^{-1}$ for bulk BN) [2,3]. Therefore, BNNS are often utilized as filler for heat conductive polymer composites [4].

BNNS can be manufactured via either bottom-up (chemical vapor deposition, surface segregation, wet-chemical methods, etc.) or top-down approaches (ball milling, liquid-phase exfoliation). Among all these methods ultrasonic-assisted exfoliation is the most universal technique for delamination of h-BN to obtain BNNS with defect-free structure and high yields [5], as it simple, relatively fast, scalable process that does not significantly affect the in-plane structure of h-BN.

2. Experimental Section

Herein, a facile and scalable bath sonication method (duration – 30 hours, h-BN concentration – 6 g/L, media - isopropanol) was performed to obtain exfoliated BN (e-BN) for use as filler in silicone film composites. Introduction of dried e-BN into silicone resin (SR) was carried out without prior

centrifugation, as it is believed that the presence of BNNS as well as non-exfoliated h-BN, can lead to overall improvement of TC in composites, as well as facilitate manufacturing technology. Filler-matrix interaction improvement was achieved by mixing filler and low-viscous SR component (10 wt.% of e-BN) in vibrating grinder. Components were then mixed, molded, degassed and cured at 100 C. For BNNS characterization, suspension was centrifuged at 6000 rpm for 10 min.

3. Results and discussion

TEM images (Hitachi HT7800) (Fig. 1a) showed that lateral sizes of BNNS do not exceed 1 μm; suspensions are highly unstable and tend to aggregate, which is obviously related with the absence of surfactants during exfoliation. However, one can see that BNNS are highly transparent to electron beams, therefore, have low thickness, which is consistent with AFM measurements (SMART-SPM 1000) (Fig. 2b,c) – average thickness of BNNS was within 3-4 nm (which corresponds to 9-12 layers). Figure 2c shows that minimal step is 0.33 nm, as it should be for h-BN monolayers [6].

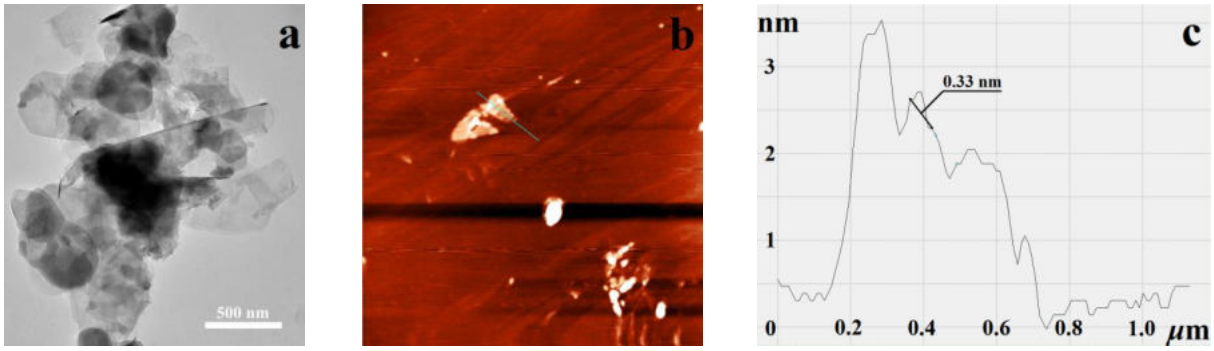

Figure 1. TEM (a) and AFM (b) images of BNNS and corresponding height profile (c)

TC of silicone composite films was measured via laser flash technique (Netzsch LFA467). TC value for neat silicone was 0.11 $Wm^{-1}K^{-1}$. Introduction of h-BN or e-BN greatly enhanced both in-plane ($\lambda_{\parallel}$) and through-plane ($\lambda_{\perp}$) TC of composites (1.20/0.81 $Wm^{-1}K^{-1}$ for h-BN/SR and 2.65/0.53 $Wm^{-1}K^{-1}$ for e-BN/SM at 50 wt.%). Higher anisotropy and average TC ($(2\lambda_{\parallel}+\lambda_{\perp})/3$) of BN/SR composite can be explained by larger average aspect ratio of e-BN as compared to h-BN.

Heat-conducting thermal pads are intended for use as thermal interface materials for electronics. Due to their high anisotropy, heat from local hotspots can be effectively dissipated. Moreover, h-BN/SR and e-BN/SR composites had excellent insulation properties (volume resistivity $\approx 10^{16}$ Ω cm).

References

[1] Rasul, M.G., Kiziltas, A., Arfaei, B., & Shahbazian-Yassar, R. 2D boron nitride nanosheets for polymer composite materials. npj 2D Materials and Applications, (2021) 5, 1-18.

[2] Zhang, K., Feng, Y., Wang, F., Yang, Z., & Wang, J. Two dimensional hexagonal boron nitride (2D-hBN): synthesis, properties and applications. Journal of Materials Chemistry C, (2017) 5, 11992-12022.

[3] Cai, Q., Scullion, D., Gan, W., Falin, A., Zhang, S., Watanabe, K., Taniguchi, T., Chen, Y.I., Santos, E.J., & Li, L.. High thermal conductivity of high-quality monolayer boron nitride and its thermal expansion. Science Advances, (2019) 5.

[4] Wang, B., Ji, H., Zhang, X., & Qu, X. Preparation of boron nitride nanosheets via polyethyleneimine assisted sand milling: towards thermal conductivity and insulation applications. RSC Advances (2021). 11, 38374

[5] Zhang, H. Ultrathin Two-Dimensional Nanomaterials. ACS nano, (2015) 9 10, 9451-69.

[6] Lin, Y., & Connell, J.W. Advances in 2D boron nitride nanostructures: nanosheets, nanoribbons, nanomeshes, and hybrids with graphene. Nanoscale, (2012) 4 22, 6908-39.

Local elastic moduli of amorphous nanostructures

A.A. Semenov*, D.A. Conyuh, Y.M. Beltukov

Ioffe Institute, Politekhnicheskaya 26, 194021 St. Petersburg, Russia

aleksandr.semenov@mail.ioffe.ru

Abstract. We have studied the local elastic properties of amorphous nanostructures within the framework of the random matrix model. Near the interface between amorphous and crystalline solids, non-affine deformations of amorphous solids lead to the formation of an interfacial layer with enhanced effective elastic properties. It is shown that the thickness of the interfacial layer is of the same order of magnitude as the length scale of non-affine deformations.

1. Introduction

In recent years, studies of the mechanical, vibrational, and heat-conducting properties of various nanostructured materials have become increasingly important. Among frequently used materials are structures containing both crystalline and amorphous components [1,2]. Recent studies show that in amorphous regions near their boundary with a more rigid body, a near-boundary region is formed, which is described by significantly higher elastic moduli compared to their values in the volume of an amorphous solid [3,4]. It was shown in [3] that an increase in the local modulus of elasticity in the near-boundary region may not be associated with a change in the local structure of the substance, but is caused by the disordered structure of the amorphous solid itself. However, the effect of disorder on local elastic properties requires a more detailed study. The purpose of this work is a more detailed study of the local elastic properties of the amorphous phase in the near-boundary region and determination of their dependence on the strength of disorder.

2. Method for describing an amorphous nanostructure

For the detailed study of deformations in the near-boundary region, we considered a three-layer nanostructure consisting of an inner amorphous layer and outer crystalline layers. To describe the nanostructure, we applied the random matrix model [5]. Such a model makes it possible to vary the strength of disorder and describe both crystals and highly disordered amorphous solids.

As an example, we considered a cubic lattice $L \times L \times L$, with a unit lattice constant $a_0 = 1$ and unit atomic masses $m_i = 1$. For numerical simulation, we use the size of the system $L = 60$ and the width of the amorphous layer $d = 30$, which is sufficient for studying non-affine deformations. We use a scalar model which assumes that the displacement of the i-th atom u_i is a scalar. To describe crystalline regions, neighboring atoms are connected by single elastic bonds, and non-zero off-diagonal elements of the dynamic matrix have the form $M_{ij}^{(c)} = -1$ for neighboring atoms i and j. To describe an amorphous phase with an arbitrary strength of disorder, we considered the dynamic matrix in the form

$$M^{(a)} = AA^T + \mu M^{(c)}.$$

Here, the dimensionless parameter μ controls the order of the amorphous phase, and the matrix elements A_{ij} are Gaussian random numbers for neighboring atoms i and j. Stresses were applied to the top and

bottom most layers of the sample $z = 0$ and $z = L - 1$, stretching the sample. Periodic boundary conditions were assumed in the x and y directions.

3. Results

We have carried out numerical simulation of an amorphous nanostructure for various values of the parameter μ. To quantitatively analyze the elastic properties of the three-layer system, we considered the equilibrium displacements u_i and the average displacement $\overline{u}(z)$ shown in Figure 1(a). The obtained compliance $S(z)$ of the three-layer structure, which is defined as

$$S(z) = \frac{1}{E(z)} = \frac{1}{\sigma}\frac{d\overline{u}}{dz}$$

is shown in Figure 1(b) for various values of μ. It can be seen that near the boundary with the crystal, an interfacial layer with reduced compliance is formed.

An analysis of the dependences $S(z)$ showed their exponential behavior far from the interfaces with a characteristic width w of the interfacial layer. The dependence $w(\mu)$ is shown in Figure 1(b). It can be seen that $w \sim \mu^{-1/4}$, which coincides with the scaling of the Ioffe-Regel length l_{IR} [6], and the non-affine length scale, on which the affine and non-affine components have the same order of magnitude.

The results of this work are of great importance for the physics of nanocomposites, since they show that an effective more rigid shell can form around nanoinclusions in a highly disordered medium. The thickness of the shell is determined by the radius of nonaffinity in such a disordered medium, which depends on the strength of disorder. The results obtained may be also applied for conductivity and other quantities of strongly disordered systems.

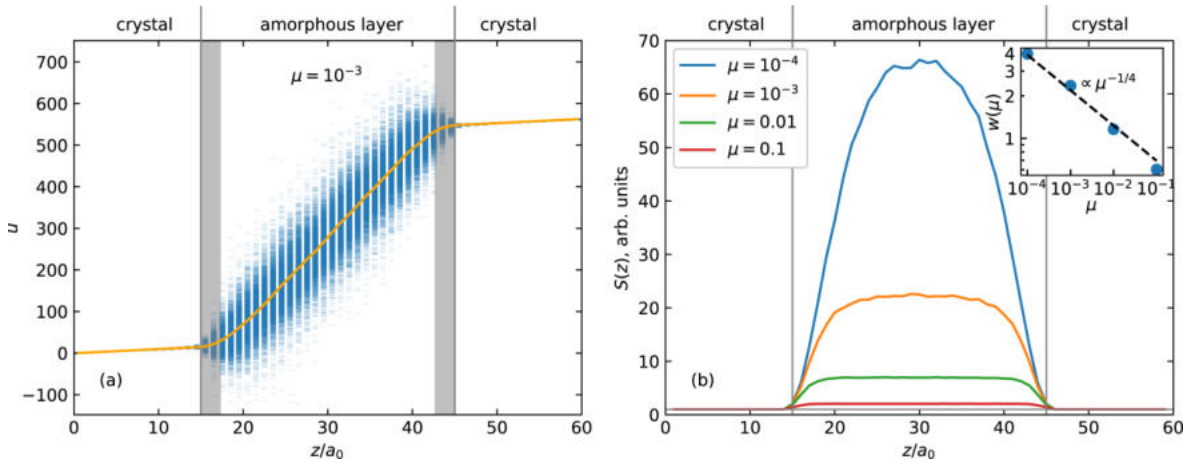

Figure 1. (a) Displacements u_i in each of the z layers (blue dashes) and their average over the x, y layers (yellow curve). The gray areas mark the interfacial layers with the width w; (b) Effective compliance for various values of μ. The inset shows the dependence of the width of the interfacial layer w on the parameter μ, corresponding to $\mu^{-1/4}$ (dashed line).

Acknowledgments

Authors thank the Russian Science Foundation (grant No. 17-72-20201) for the financial support.

References

[1] R. Jana, L. Pastewka, *Journal of Physics: Materials* **2**, 045006 (2019).
[2] Q. Wen, A. Basu, P.A. Janmey, and A.G. Yodh, *Soft matter* **8**, 8039 (2012).
[3] Y. M. Beltukov, D. A. Conyuh, and I. A. Solov'yov, *Physical Review E* **105**, L012501 (2022).
[4] J. Fankhanel, B. Arash, and R. Rolfes, *Composites Part B: Engineering* **176**, 107211 (2019).
[5] Y. Beltukov, V. Kozub, and D. Parshin, *Physical Review B* **87**, 134203 (2013).
[6] D. Conyuh and Y. Beltukov, *Physical Review B* **103**, 104204 (2021).

Influence of the initial surface state on the ripple formation induced by O_2^+ sputtering of Si

M A Smirnova, V I Bachurin and A B Churilov

P.G. Demidov Yaroslavl State University

e-mail: masha_19957@mail.ru

Abstract: Influence of the initial Si surface state on the rate of ripple nucleation under bombardment with low-energy O_2^+ ions was investigated. It was found that the creation of a defect area in the Si near-surface layer or the creation of the initial surface relief by ion bombardment with a focused Ga^+ ion beam facilitates a significant acceleration of the ripple formation of on the Si surface during subsequent irradiation with an O_2^+ ion beam.

1. Introduction

Ion beam sputtering is a powerful method for micro- and nanostructures formation on the surface of various materials. The main advantages of this method are the fairly short processing time of large areas and the possibility of metals, semiconductors, insulators nanostructuring. Moreover, the adjustment of irradiation parameters, such as angle of incidence, fluence, kinetic energy and ion beam diameter, allows generating a sized-controllable structure. Recently, a large number of works is devoted to the study of a periodic wavelike nanostructures (ripples) formation on the metal and semiconductor surfaces [1].

Bradley and Harper (BH) proposed a model of ion induced surface structure formation [2]. It took into account the dependence of the sputtering yield on the local angle of incidence and the surface atomic diffusion. The appearance of topographic instability on the surface achieved by taking into account the stochastic nature of sputtering which leads to roughening of an initial flat surface at the atomic scale. Subsequent sputtering causes an increase of topographic inhomogeneities and emergence of ripples. According to experiments, ripple nucleation on the Si surface occurs at a certain (critical) fluence, which depends on the energy and type of ions and the ion beam incidence angle [3-5]. At the moment, there is a small number of works [6, 7] which demonstrate that the creation of initial topographic inhomogeneities on the Si surface leads to a marked reduction of the critical fluence required for the sputter ripple nucleation.

In the present work, we have studied an influence of the initial Si surface state on the process of ripple nucleation and evolution under bombardment with low-energy O_2^+ ions. Initial surface is defined as the Si surface irradiated by 30 keV Ga^+ ion beam.

2. Experimental

Experiments on the formation of ripples on the Si (100) surface were carried out on the Cameca IMS 4f machine. All the samples were bombarded by separated 12,5 keV O_2^+ at an angle of 38° with respect to the surface normal. The process of ripple nucleation was determined by increasing the current of secondary Si^+ ions [8], which detected during ion bombardment of the surface. The depth of the sputtering crater where ripples nucleated was determined on a Talystep profilometer. The samples were pretreated by ion implantation of Si(100) surface with a 30 keV Ga^+ ion beam on a Quanta 3D 200i. Beams with a diameter of 4 μm were used. The dimensions of the irradiated area were 200×200 μm^2. An angles of incidence of the ion beam were $\Theta = 0°, 30°$, irradiation doses were $D = 10^{17}, 2 \cdot 10^{17}, 4 \cdot 10^{17}$ cm^{-2}. A more detailed analysis of the surface topography was carried out ex-situ using a scanning electron microscope Supra 40.

3. Results

Si samples irradiated with a Ga^+ ions were examined by the SEM method. It was found that at a fluences of $2 \cdot 10^{17}$, $4 \cdot 10^{17}$ cm^{-2} a noticeable surface relief in the form of grid-like structure and ripples occurs and Θ = 0°, 30° respectively. As the fluence increases, the surface rms rougness increases up to 30 nm at Θ = 30° and D = $4 \cdot 10^{17}$ cm^{-2}. At a fluence of D = 10^{17} cm^{-2}, an irradiated surface stays smooth at normal incidence and a small perturbations are observed at Θ = 30°.

Irradiation with O_2^+ ion beam of the virgin Si surface leads to the ripple formation at a depth of ~6.5 μm with an average wavelength of λ=460 nm, which is in good agreement with the data of [8]. The formation of ripples with wavelength λ=450±30 nm was observed on the pretreated Si samples. In this case, the depth of ripple nucleation decreased significantly: practically 1.5 times at a fluence of D = 10^{17} cm^{-2} and more than 2 times at D = $2 \cdot 10^{17}$ and $4 \cdot 10^{17}$ cm^{-2}.

As noted above, the presence of surface topographic inhomogeneities leads to decrease of the critical fluence required for ripple nucleation on the Si surface under ion bombardment [6, 7]. Present study established that the same effect is triggered by preliminary creation of a defect region in the Si near-surface layer without noticeable changes in the surface topography by implantation with Ga^+ ion beam at D = 10^{17} cm^{-2}. The apparently reason of accelerated ripple nucleation in this case is that the implanted Ga is located in the form of separate nanometer-sized precipitates lying at a depth of 10-20 nm in the Si near-surface layer (at Θ = 0°) [9]. During the sputtering of such samples with O_2^+ ion beam at depths of 10-20 nm a topographic instability may arise due to the difference in sputtering rates of Ga and Si, which will initiate the ripple nucleation process.

Acknowledgments

This study was performed with financial support from the Ministry of Education and Science of the Russian Federation within the framework of the state assignment of the P.G. Demidov Yaroslavl State University of topic no. 0856-2020-0006 and using equipment of the facilities sharing centre “Micro- and Nanostructures Diagnostics”.

References

[1] Cuerno R and Kim J-S 2020 *J. Appl. Phys.* **128** 180902

[2] Bradley R M and Harper J M E 1988 *J. Vac. Sci. Technol. A* **6** 2390

[3] Carter G, Vishnyakov V 1995 *Surf. Interf. Anal.* 1995 **23** 514

[4] Elst K, Vandervorst W J. 1994 Vac. *Sci. Technol. A* **12** 3205.

[5] Smirnov V K, Kibalov D S, Krivelevich S A, Lepshin P A, Potapov E V, Yankov R A, Skorupa W, Makarov V V, Danilin A B 1999 *Nucl. Instrum. Methods Phys. Res. B.* **147** 310

[6] Смирнов В.К., Кибалов Д.С., Лепшин, П.А. и Бачурин В.И. 2000 *Изв. РАН сер. Физ.* **64(4)** 626

[7] Karmakar P, Mollick S A, Ghose D and Chakarabarti A 2008 *Appl. Phys. Lett.* **93** 103102

[8] Smitnov V K, Kurbatov D A, Potapov E V 1992 *Izv. Acad. Nauk, Ser. Fiz.* **56(1)** 71

[9] Rommel M, Spoldi G, Yanev V, Beuer S, Amon B, Jambreck J, Petersen S, and Bauer A J *J. Vac. Sci. Technol. B* **28(3)** 595

Self-assembly of porphyrin-based symbimetic hybrid material on layered europium hydroxide

Sokolov M.R.[1,2], Enakieva Y.Y.[1], Yapryntsev A.D.[3], Shiryaev A.A.[1], Zvyagina A.I.[1], Kalinina M.A.[1]

[1]A.N. Frumkin IPCE RAS, Moscow, Russia
[2] Moscow State University, Moscow, Russia
[3]N.S. Kurnakov IGIC RAS, Moscow, Russia

sokolmax495@gmail.com

Abstract. In this work we report a new strategy for rational design of synergetic hybrid materials exploiting stabilisation of intercalated layered matrices via coordination bonding. A new hybrid material is assembled through subsequent intercalation of the surface-anchored metal–organic framework (SURMOF) components, zinc acetate and 5,10,15,20-tetrakis(4-carboxyphenyl)-porphyrin zinc(II) (ZnTCPP), into the layered europium(III) hydroxychloride (LEuH). We studied the catalytic function of the SURMOF/LEuH hybrid and its components in the model reaction of hydrolysis of bis(4-nitrophenyl) phosphate in the acidic solution. Unlike its components, the SURMOF/LEuH hybrid exhibits synergetic catalytic activity based on mutual stabilisation of the components through coordination interactions. The results provide a basis for symbimetic (mimicking the symbiotic behaviour in biological systems) hybrid materials, in which stabilisation of functional units in the intercalated structure translates into a synergy of useful properties.

1. Synthesis of the hybrid symbimetic material

In this work we studied a hybrid material comprising the components of porphyrin-based metal-organic frameworks (MOF) and europium(III) layered hydroxychloride as layered inorganic matrix.

Porphyrin-based metal-organic frameworks (MOF) are the class of coordination polymers integrating functionalized porphyrins as organic linkers and metal ions or clusters binding these linkers into the continuously ordered structure. These materials are useful for applications in separation membranes, sensors and heterogeneous catalysts though they can undergo decomposition or rearrangements in the chemically active or aggressive environment because of relatively weak coordination bonds. A possible strategy for solving this problem is the assembly of MOFs on the solid surface of layered inorganic particles. This approach makes it possible to integrate the functional properties of porphyrin MOFs with those of supporting inorganic solids in a single hybrid structure. In this work we realised this idea through the intercalation of 5,10,15,20-tetrakis(4-carboxyphenyl) zinc porphyrinate (ZnTCPP) and a binuclear complex of zinc acetate as the MOF components into the layered europium (III) hydroxychloride (LEuH) as dispersed solid matrix, that exhibits anion-exchange properties and coordination and luminescent properties of europium. Intercalation of components of porphyrin MOF into the LEuH by anion exchange mechanism makes it possible to assemble 2D-MOF in the interlayer space of LEuH, obtaining stable hybrid material with combined properties of MOF and inorganic matrix.

2. Study of catalytic activity

Zinc complexes of porphyrins show high affinity toward organic phosphates, which participate in a wide range of natural and industrial processes. Therefore, we studied the catalytic activity of the material in a course of the hydrolysis of bis(4-nitrophenyl) phosphate, which is widely used as a model reaction for DNA phosphodiesterase. The UV-vis absorption spectroscopy was used to monitor the reactions with the hybrid catalyst and the control system of pure LEuH. By studying the kinetics of the catalytic hydrolysis, we showed that the intercalated hybrid exhibits synergetic catalytic effect on the process when compared to the activity of the non-intercalated LEuH matrix and ZnTCPP-based MOF. To investigate the origin of this synergy, we studied the changes in the structure and chemistry of the hybrid materials by using a combination of analytical techniques including Raman, FTIR and UV–vis spectroscopies and the X-ray diffraction. We also pioneered the application of MALDI-TOF spectrometry for analysing the composition of the absorbed and transformed substances in the solid powders without decomposing its structure. These observations provided a basis for understanding the mechanism underlying the catalytic process in the hybrid system by separating the contributions of both components.

The obtained results suggest that the hybrid material showed symbimetic properties, that is, mimicking the behaviour of biological symbionts, due to the mutual stabilisation of the components in the reaction media. The porphyrin MOF components assembled in the interlayer space prevent splitting of the inorganic matrix in a course of the catalysed reaction and the LEuH matrix protects the unstable MOF clusters from decomposition in the acidic solution. The symbimetic properties of the hybrid materials also demonstrate themselves in the catalytic synergy since only mutually integrated porphyrin MOF and LEuH can efficiently catalyse the hydrolysis of organic phosphates. We consider that this strategy can advance rational design of the wide range of hybrid layered materials with various synergetic functions.

Acknowledgments

This work was supported by supported by the Russian Foundation for Basic Research
(grant 18-29-04026 MK)

Effect of the ratio of intensities of the reference and object beams on the performance of computer-generated holograms designed for extreme ultraviolet lithography

S N Koreshev[1], S O Starovoitov[2]

[1] Branch of JSC «Corporation «Kometa» - «Scientific and design centre of optoelectronic surveillance systems», 7 Chatelain, St. Petersburg 194021, Russia
[2] ITMO University, 49 Kronverksky, St. Petersburg 197101, Russia

s.starovoitov95@gmail.com

Abstract. Effect of the ratio of the intensities of the reference and object beams on the distribution of the intensity of the computer-generated Fresnel holograms, intended for application in extreme ultraviolet lithography, is considered. It is demonstrated that computer-generated holograms, if they have not been binarized, are always displayed and reconstructed as quantized holograms with a quantization interval depending on the parameters of the synthesis scheme. It has been established that the influence of the «overmodulation» mode on the quality of reconstructed image when using computer-generated holograms is much smaller than in the case of using traditional holograms, but is regardless determined by the dynamic range of the object beam intensity in hologram synthesis plane. It is shown that its influence is minimal in the case of computer-generated hologram recorded with a converging object beam.

1. Introduction

The continuous shrinking of transistors in microelectronic devices has been driven mostly by the advancements in photolithography. However, to reach a half-pitch smaller than 7nm, it is necessary to switch from traditional scanners which use ArF 193 nm lasers to scanners built around extreme ultraviolet 13.5 nm laser-produced plasma sources. One promising method of extreme ultraviolet lithography is based on replacing sophisticated projection optical system with computer-generated holograms (CGHs), which are capable of reconstructing large images free from aberrations [1, 2]. Out of many factors that influence the quality of images reconstructed with CGHs [3], one of the most important is the intensity ratio between the reference and object beams.

2. Methods and results

The study was carried out by analyzing the influence of intensity ratio between the reference and object beams on the intensity distribution in the hologram recording plane both for traditional holograms and CGHs. For traditional holograms, it was found that when the intensity of the object beam exceeds the intensity of the reference beam («overmodulation» mode), not only diffraction efficiency of the hologram decreases, but it becomes impossible to choose the uniform exposure time for the entire aperture of the hologram, which leads to significant nonlinear effects. However, CGHs, unless binarized, are always reconstructed as quantized holograms with a quantization interval depending on amplitudes of reference and object beams and maximal intensity of a holographic field. Thus, the influence of the «overmodulation» mode on the quality of the images reconstructed from CGHs should be less than for

traditional holograms, but it will still depend on the dynamic range of object beam intensity in hologram synthesis plane. This leads to a hypothesis that using an object beam converging at the center of CGHs instead of homocentric one would decrease the influence of «overmodulation» on image quality.

The hypothesis was verified by mathematical modeling of CGHs synthesis and reconstruction. Modelling was carried out using an amplitude object with two types of object beam described above for 5 values of ratio of the intensity of the reference beam to the intensity of the object beam: 1:1, 1:2, 1:4, 1:6 and 1:8. Two images obtained with 1:8 ratio are portrayed at figure 1a, b; figure 1c portrays results of the quality assessment of all 10 reconstructed images using numerical criterion described in [3].

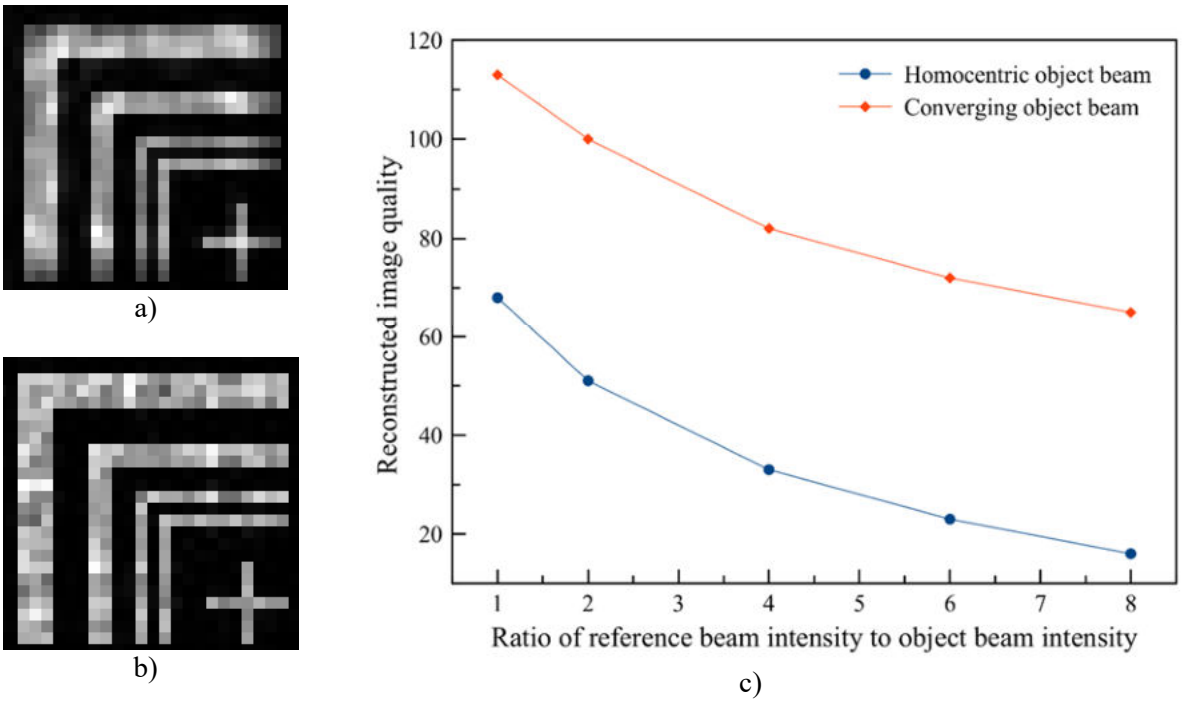

Figure 1. Reconstructed images when object beam is homocentric (a) and converging (b); dependence of image quality from the intensity ratios of beams for two object beam types (c).

Figure 1c demonstrates that while «overmodulation» leads to significant decrease in image quality, the quality of images reconstructed from CGHs obtained with converging object beam, with the coincidence of other synthesis scheme parameters, is always higher than the quality of images reconstructed from CGHs obtained with a homocentric object beam. Thus, dynamic range of object beam intensity has a major impact on the quality of images reconstructed from CGHs recorded in the «overmodulation» mode.

3. Conclusion

CGHs not subjected to binarization are reconstructed not as halftone, but as quantized holograms. The influence of «overmodulation» mode on the quality of the image for CGHs is less than for traditional holograms, and could be further minimized by using an object beam converging at the center of CGH.

Acknowledgments

The study is funded by RPMA grant of School of Physics and Engineering of ITMO University.

References

[1] Cheng Y, Isoyan A, Wallace J, Khan M and Cerrina F 2007 *Appl. Phys. Lett.* **90** 023116
[2] Fu N, Liu Y, Ma X and Chen Z 2019 *J. Microelectron. Manuf* **2**, 1–6
[3] Koreshev S, Smorodinov D and Nikanorov O 2016 *Computer Optics* **40**, 793–801

Durability silver coating for Second Mirrors optical diagnostic ITER to high humidity and thermal cycling

Tereshchenko I. B.[1,2], Samsonov D.S.[1,2], Mukhin E.E.[1,2], Gubal A.R.[3], Marchiy G.V.[1], Komarevtsev I.M.[4]

[1]Ioffe Institute, St.-Petersburg, Russia, 194021
[2]Spectral-Tech, St.-Petersburg, Russia, 194021
[3]Institute of Chemistry, St.-Petersburg State University, St.-Petersburg, 199034
[4]Peter the Great St.Petersburg Polytechnic University

i.tereschenko@mail.ioffe.ru

Abstract. This article presents the results of the experimental study optical coatings Ag based after steam ingress.

1. Introduction

Optical diagnostics is one of the most widespread and informative methods of gathering information about the processes in high-temperature plasma. The in-vessel part of the scattered light collection system (Second Mirrors) of ITER tokamak Divertor Thomson Scattering (DTS) diagnostic system consists of 7 large-scale mirrors with linear dimensions of 420 to 750 mm, assuming 5 successive reflections. The reflectance of each individual in-vessel mirror of >90% is required in the spectral range of 540-1100 nm in order to achieve desired total optical transmission of >60%. The reflectance of the DTS collecting mirrors must remain stable during the ITER life cycle of at least 15 years under significant radiation, thermal, vibration and other loads. Namely, the required reflection should retain (1) under repeated thermal cycling in the range of 70-240 °C and (2) hydrothermal action at 30-250 °C due to accidental ingress of cooling water into the ITER vacuum volume.

Highly reflective Ag-based optical coatings have been studied for many years and are successfully applied in optical instrumentation, including large-scale mirrors operating in space [1], in marine environment, near volcanoes or in deserts [2]. The listed applications are associated with the impact of high concentrations of corrosive agents on the optical coating, or thermal loads, while both factors will act simultaneously inside the ITER vacuum vessel. Such conditions are closest to those realized in solar collectors [3, 4], however, in contrast to the latter, in the corrosion in ITER occurs at high humidity.

Silver has one of the highest reflection coefficients among metals, but it is susceptible to corrosion being in contact with certain elements like S, Cl or O [5]. A barrier coating, consisting of one or more dielectric layers, is typically applied over Ag layer in order to suppress corrosion. Such a coating increases the mechanical and chemical resistance of the structure. However, corrosive agents are reported to penetrate through pores and defects [6]. In [7] a method is proposed for eliminating the specified mechanism of Ag corrosion by depositing so-called nanolaminates on a reflecting surface, which are stacks of several 5-15 nm thick dielectric layers. An increased number of layers reduces the

likelihood of superposition of defects in different layers, enabling also to reduce mechanical stress in the film, which makes precisely thin barrier layers preferable for use under cyclic thermal loads [8].

2. Materials

Thin films stack consisted of 50 nm NiV (93:7 sputtering target composition) adhesion layer, 200 nm Ag reflective layer and dielectric barrier layers. Two types of barrier coatings were applied: SiN_X monolayer (30nm) and triplex of $SiN_X/SiO_Y/SiN_X$ layers (10nm/10nm/10nm). Before depositing the barrier layers, the Ag surface was covered with NiV layer of ~0.5-1 nm thickness. Dielectric layers thickness specified was evaluated by double wavelengths optical monitor, metallic coatings were controlled by quartz crystal monitor.

3. Results

Silver-based broadband reflective mirror coating with protective $SiN_X/SiO_Y/SiN_X$ nanolaminate structure was designed for the ITER in-vessel applications. The resistance of two SiN_X-based protective structure types to the steam ingress, considered as the most critical event for mirrors in ITER, was tested. The triplex 10/10/10 nm nanolaminate coating shows advantages over the 30 nm SiN_X monolayer. Despite ~5-7% specular reflectance decrease after SI test, it remains higher than of all bulk metallic reflecting surfaces, proposed earlier. At the same time, Folgner et al. report that the reflection of the coating of similar design almost did not change after more than 200 hours of salt fog testing [9]. Thus, the revealed degradation was likely due to either different coating layers properties, or different loading conditions, e.g. at the increased temperature during the SI test, which was not the case in the mentioned investigation. Annealing of triplex samples in vacuum for 15 hours at a temperature of 250-260°C did not change the reflectivity.

Acknowledgments

The investigation of the highly reflective protected coating was supported by Ioffe Institute (Russian Federation state funding assignments 0034-2019-0001 and 0040-2019-0023).

The authors are grateful to the Interdisciplinary Resource Centre for Nanotechnology at Saint-Petersburg State University for providing access to their facilities for samples characterization.

References

[1] Sheikh D, Connell S, Dummer R 2008 *Proceeding of the SPIE Astronomical Telescopes + Instrumentation* 70104E

[2] Wolfe J, Thomas N 2000 US Patent No 6078425

[3] Alessandro A, Addonizio M, Esposito S, Ferrara M, Castaldo A, Guglielmo A, D'Angelo A 2014 *Surf Coat Technol* 255 96

[4] Gledhill S, Steyer K, Weiss Ch, Hildebrandt Ch 2019 *Coatings* 9 593

[5] Burstein T 2019 Department of Materials Science and Metallurgy University of Cambridge

[6] Schwinde S, Schürmann M, Kaiser N, Tünnermann A 2015 *Proceeding of the SPIE Optical Systems Design* 95271R

[7] Schwinde S, Schürmann M, Johannes P, Kaiser N, Tünnermann A 2015 *Appl Opt* 54 4966

[8] Grigoriev F, Sulimov V, Tikhonravov A 2020 *Coatings* 10 220

[9] Folgner A, Chu C-T, Lingley R, Kim I, Yang J-M, Barrie D 2017 *Appl Opt* 56 75-86

Probing non-Markovian dynamics of NISQ systems

A K Fedorov[1, 2]

[1] Russian Quantum Center, Moscow 143026, Russia

[2] National University of Science and Technology "MISIS", Moscow 119049, Russia

akf@rqc.ru

Abstract. In this work, we push the idea of data-driven Markovian embedding reconstruction to the limit, and present the complete framework for analysis of general case open quantum dynamics. As input data, our framework takes trajectories of a system at discrete time steps, a guess about a memory depth of the non- Markovian process, and the level of noise appeared during experimental reconstruction of trajectories. As output, our framework returns the minimum dimension of a Markovian embedding allowing prediction of dynamics, the effective dimension of the environment, eigenfrequencies of the joint system and environment quantum dynamics, and denoised trajectories of the system as a valuable by product. We note that our framework relies on linear methods of machine learning, which are known to be scalable, data efficient and admit the exact solution. We illustrate the performance of our framework on several paradigmatic examples of realistic models, such as a qubit coupled with a finite-dimensional environment, a spin-boson model, and the damped Jaynes-Cummings model.

1. Introduction

A precise understanding of the influence of an environment on quantum dynamics, which is at the heart of the theory of open quantum systems, is crucial for further progress in the development of controllable large-scale quantum systems. However, existing approaches to account for complex system environment interaction in the presence of memory effects are either based on heuristic and oversimplified principles or give rise to computational difficulties.

In practice, one can take advantage of available experimental data and replace the first-principles simulation with a data-driven analysis that is often much simpler. Inspired by recent advances in data analysis and machine learning, we suggest a data-driven approach to the analysis of the non-Markovian dynamics of open quantum systems.

2. Another section of your paper

Our method allows capturing the most important properties of open quantum systems, such as the effective dimension of the environment, eigenfrequencies of the joint system-environment quantum dynamics, as well as reconstructing the minimal Markovian embedding, predicting dynamics, and denoising of measured quantum trajectories. We demonstrate the performance of the suggested approach on various models of open quantum systems, including a qubit coupled with a finite environment, a spin-boson model, and the damped Jaynes-Cummings model [1].

A natural progression of this work is to validate the ability of the method to reconstruct interpretable Markovian embedding from incomplete data, e.g., from individual observables dynamics instead of quantum trajectories. Further research is also required to determine whether the given approach is capable to predict response of a non-Markovian system on external perturbation. The ability to predict the response on an external perturbation potentially opens a room for study new data driven quantum control methods.

Acknowledgments

The development of the data processing scheme, analysis of the spin-boson model, and analysis of the damped Jaynes-Cummings model are supported by the Russian Science Foundation (19-71-10092) and by the Leading Research Center on Quantum Computing (Agreement no. 014/20; analysis of non-Markovian processes for NISQ devices). The analysis of the finite-environment-induced non-Markovian quantum dynamics is supported by the Foundation for the Advancement of Theoretical Physics and Mathematics “BASIS” for support under Project No. 19-1-2-66-1. The authors thank A. Ryzhov and G. Semin for fruitful discussions.

References

[1] I.A. Luchnikov, E.O. Kiktenko, M.A. Gavreev, H. Ouerdane, S.N. Filippov, and A.K. Fedorov. "Probing non-Markovian quantum dynamics with data-driven analysis: Beyond “black-box” machine learning models". arXiv:2103.14490.

Measuring system for studying the dielectric parameters of piezoelectric materials

E A Pecherskaya, A V Fimin, S A Gurin, A E Zhurina, A V Pecherskiy, A V Volik
Department of Information and measuring equipment and metrology, Penza State University, Penza 440026, Russia

Annotation. The main methods for measuring the parameters (electrical, mechanical, thermal, radiation, chemical) of piezoelectric materials, which depend on their properties, are considered. A proposed scheme of a measuring installation that makes it possible to record sample parameters in dynamic and static modes. The values reliability is achieved by using a measurement algorithm in the installation, in which, in addition to determining the values, the resulting additional relative errors are taken into account.

1. Introduction

Despite many years of piezoelectric materials research , work on studying their properties, improving quality and increasing the stability of characteristics during operation is currently an urgent task.

In the field of piezoelectric materials application , the priority direction of research is the study of the used materials and their characteristics, as well as the promising substances analysis.

At the moment, two directions of piezoelectric instrumentation development can be distinguished. The first is based on obtaining new experimental materials that have piezoelectric properties, as well as improving existing structures. This direction is associated with the achievement of certain or universal characteristics of the piezomaterial, which is used in the final device. The second direction tasks are the measuring methods improvement . Such studies cover the totality of studying algorithms for controlling piezoelectric properties, methods for reliably determining parameters during the sensitive elements operation , as well as reducing errors under the influence of external influencing factors.

Methods for determining the piezomaterials parameters differ in speed and degree of reliability of the result being determined. In terminal devices, an external action on a piezoelectric assembly installed in a sensitive element changes its parameters, and the values transformation indicates the external influence degree.

It is important to note that the piezoelectric parameters registration occurs by indirect detection methods, which imposes additional errors in measurements [1, 2].

2. Basic methods for measuring the parameters of a piezoelectric material

The internal electric field of a piezoelectric material crystal under external influence on it (a piezoelectric effect appearance) can be characterized by the vector value of the electric polarization *P*. In this case, the mechanical action can affect the sample in static and dynamic modes, which is reflected in the values of various piezomaterial parameters (mechanical strength, piezoelectric modules).

Currently, the most popular method for diagnosing a material is the registration of resonant and antiresonant frequencies and piezoelectric modules using measuring installations, and the remaining

parameters (electrical, mechanical, and their combination characterizing the conversion degree of these energies into each other) are calculated using mathematical formulas [3, 4].

3. Modeling the mechanism for measuring the parameters of a piezoelectric material

To determine the parameters of a piezoelectric material, it is proposed to use a measuring installation, the block diagram of which is shown in Figure 1.

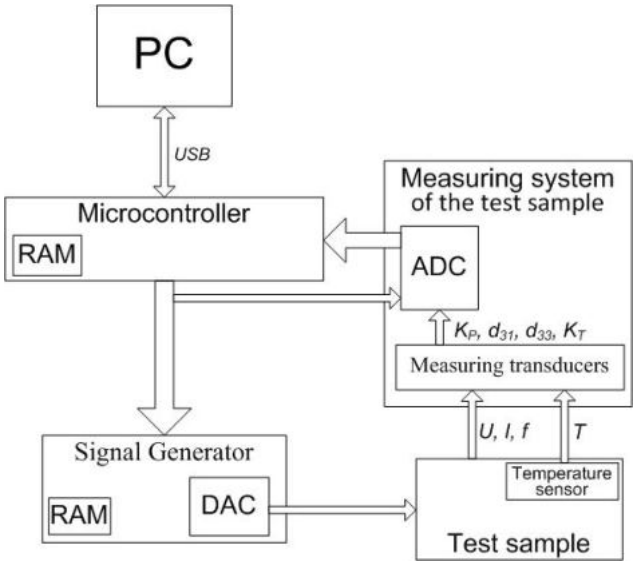

Figure 1.Structural diagram of the measuring system for recording the piezoceramic element parameters.

The installation implements a digital method for determine the piezoelectric element parameters, in which the sample is affected by a broadband signal with a certain (specified by the operator) frequency range, generated by the hardware of the generator and the software microcontroller. The generated samples are then subjected to a discrete Fourier transform. Thus, the measured analog values are converted by the recorder into the established characteristic parameters of the piezoelectric material - the coefficients of electromechanical coupling (K_P) and thermal expansion (K_T), piezomodules (d_{31}, d_{33}) and Young modules (Y_{31}, Y_{33}) in dynamic and static modes, as well as the mechanical Q factor (Q_M), the relative frequency deviation in operating temperature range from frequency ($\delta f_\theta / f_r$), relative permittivity ($\varepsilon_{33} / \varepsilon_0$) and other characteristics. The parameters are monitored in the resonant region of the frequencies generated by the generator, which corresponds to the measurement in a dynamically variable mode. If it is necessary, you can set a constant frequency value to determine the parameters in static mode.

In general terms, the installation is formed by two main basic blocks - a signal generator and an oscilloscope. However, the use of our own devices makes it possible to record sample parameters using a developed measurement technique that takes into account the influence of influencing quantities (temperature, mechanical stress, etc.), and, as a result, additional errors arising from such measurements [5].

Conclusion

The presented scheme for measuring the parameters of a piezoelectric element makes it possible to determine its characteristics with reliable accuracy when simulating operating conditions. Such an installation has significant advantages, consisting in the use of domestic element base, as well as high measurement accuracy.

Acknowledgements

The reported study was funded by RFBR according to the research project № 20-38-90151.

References

[1] M Slabki, K V Lalitha, J Rödel, J Koruza 2022 Origin of high-power drive stability in (Na1/2Bi1/2)TiO3-BaTiO3 based piezoceramics *Acta Materialia* 227 117703

[2] Fimin A V, Pecherskaya E A, Timokhina O A, Aleksandrov V S, Volik A V, Shepeleva A E 2021 Investigation of the dielectric fatigue on the example of lead titanate films PbTiO3 *Journal of Physics: Conference Series* 2086(1), 012179

[3] Fialka J, Beneš P 2012 Comparison of Methods for the Measurement of Piezoelectric Coefficients *IEEE Transactions on Instrumentation and Measurement* 62(5),6410416, pp. 1047-1057

[4] B González, F J Jiménez, J De Frutos 2020 A virtual instrument for road vehicle classification based on piezoelectric transducers *Sensors (Switzerland)* 20(16),4597, pp. 1-19

[5] Golubkov P E, Pecherskaya E A, Golovyashkin A N, Golovyashkin A A , Pecherskiy A V, Shepeleva Y V 2018 Analysis of the technological parameters influence on the reproducibility of the active dielectrics properties *19th International Conference of Young Specialists on Micro/Nanotechnologies and Electron Devices, EDM 2018Erlagol, Altai* 8435090 pp. 57 – 61.

Langmuir-Blodgett technology to obtain semi-magnetic photosensitive materials

S V Stetsyura, P G Kharitonova, E G Glukhovskoy

Institute of Physics, Saratov State University, Saratov 410012, Russia

E-mail: haritonovapg@gmail.com

Abstract. We studied and tested the technological modes of obtaining of nanoscale coatings containing a controlled number of iron atoms on a semiconductor substrate by Langmuir-Blodgett technology. The subsequent modeling of diffusion processes and precipitation of Fe atoms in a photosensitive substrate allows us to predict density, depth of the occurrence and size of nanoscale iron-containing phases to high precision. The developed material is promising for use in spintronics and optoelectronics.

1. Introduction

Of special interest are the materials whose properties can be controlled by various external effects (for example, a magnetic field and an optical range radiation). This possibility increases the functionality of devices made on the basis of these materials. Such materials are soft magnetic homogeneous and semi-magnetic heterophase materials [1], which have a perspective for use in modern industries and are interesting for science due to the variety of their properties. Previously, massive monocrystals of solid solutions were mainly investigated [2]. But in recent years, significant attention is paid to the study of the film and nanolayer [3] of soft magnetic materials and structures. Heterophase semi-magnetic photosensitive materials are not enough studied due to the lack of reproducible (proven) technology and modelling views about obtaining such material with optimal and reproducible characteristics

The aim of this work is the study and testing of technological modes and conditions for producing of nanoscale coatings containing a controlled number of iron atoms on a semiconductor substrate by Langmuir- Blodgett technology.The subsequent modeling of diffusion processes and precipitation of Fe atoms in a photosensitive substrate allows us to predict density, depth of the occurrence and size of nanoscale iron-containing phases to high precision.

2. Experimental section

Cadmium sulfide (CdS) can be used as a semiconductor matrix to create soft magnetic structures, because CdS has high photosensitivity, and its technology is well detailed for film polycrystalline forms and monocrystalline substrates. We have demonstrated [4] that the Fe-doping of CdS makes it possible to obtain heterophase structures based on a paramagnetic matrix of a solid solution CdS:Fe with ferromagnetic inclusions of FeS and Fe_2O_3, which are formed as a result of the processes of self-organization and decomposition of a supersaturated solid solution due to the limited solubility of Fe in CdS. Thus, we can control the electrophysical and optical properties of the obtained semi-magnetic

material by a magnetic field and illumination, that can be used to create semiconductor devices for photonics and spintronics.

Previously, we created a semi-magnetic heterophase material based on a CdS:Fe solid solution by thermal evaporation of all components of this material [4]. As a result, a film sample with the properties of a semi-magnetic material was obtained. However, the method of thermal evaporation does not allow us to obtaine materials with a predictable arrangement of nanoscale phases and to control the size of these phases. The Langmuir-Blodgett technology makes it possible to form multilayer nanoscale layers of surface-active substances at the liquid-gas interface with a thickness of each monolayer of one molecule. Monolayers play the role of an organic matrix, which can include various functional elements. This feature of the formation of monolayers is used for dosed transfer of metal atoms onto a solid substrate.

In our work, $FeCl_3$ was used as a source of iron, and arachic acid was used as an organic matrix. Arachic acid is a surface-active substances from the class of fatty acids. The variation of external and internal factors during the production of an iron-structured coating leads to a change in the structure and quality of the organic coating, and the number of attached iron atoms. The amount of iron and its the distribution density in the layer of a surface-active substances depend on the pH of the subphase where films were formed and the concentration of $FeCl_3$. The conditions for the transfer of monolayers onto a solid substrate were controlled by preliminary analysis of compression isotherms, calculation of the optimal surface pressure in a monolayer, and area per molecule. The quality of the organic layer transferred on the substrate was determined by atomic force microscopy (AFM).The films were transferred to a solid substrate by the Langmuir-Schaeffer method.

3. Results and Discussion

Compression isotherms obtained in acidic and alkaline media demonstrated the best results of the formation of an iron-containing film using a subphase with a pH in the range of 3.7-5.0. It follows from an analysis of $\pi - A$ isotherms that the area per molecule for a monolayer containing iron atoms increases in comparison with a monolayer of arachic acid without metal. The formation of agglomerates at high pH is observed. These results were confirmed by AFM measurements, which showed the most homogeneous distribution of iron in the film when using an acidic medium. We also observe some agglomeration of Fe atoms that it is no more than several tens of nanometers. Developed by us model of diffusion and precipitation of metal atoms in a semiconductor photosensitive substrate made it possible to estimate the number of iron arachinate monolayers required to form a heterophase material that exhibits magnetic properties. The parameters of the monolayer of iron arachinate corresponded to experimental data obtained the specified technological mode.

4. Conclusion

The researched technology allows us to obtain a heterophase nanostructured photoconductor with ferromagnetic phases. The use of organic nanoscale coatings structured by iron ions as a source of impurity makes it possible to set the required depth of formation of the ferromagnetic phase and its size.

Acknowledgments

The work was carried out at the expense of the Russian Science Foundation (project No. 22-22-00194, https://rscf.ru/en/project/22-22-00194/)

References

[1] Jindal S, Sharma P 2020 *Journal of Materials Science: Materials in Electronics* **31** 20295

[2] Ivanchik I I, Khokhlov D R and De Visser A 1996 *Semiconductors* **30 (8)** 732

[3] Nuriyev I R et al. 2019 *Journal of Surface Investigation: X-ray, Synchrotron and Neutron Techniques* **13** 1083

[4] Stetsyura S V, Kharitonova P G and Malyar I V 2020 *Applied Physics* **5** 66

Sidewall roughness model for optical losses calculation in photonic integrated circuits

[1, 2] E. S. Shamin ✉, [1, 2] A. A. Sharapov, [1, 2] I. D. Skuratov, [1, 2] S. O. Demidov

[1]MIPT (NRU), Moscow, Russia
[2]JSC «MERI», Zelenograd, Russia

✉yevgeniy.shamin@phystech.edu

Abstract. One of the key performance indicators of radiophotonic circuits is the value of optical propagation losses. Among several factors which impact these losses, the sidewall roughness is considered as the primary focus of this work. A new model of sidewall roughness based on a photolithography simulation and imitation modelling of resist exposure is presented. Simulation results, obtained using the new model, were demonstrated and an approach on their verification with experimental data was suggested. Additionally, theoretical estimations for the optical losses caused by sidewall roughness in Si waveguide are discussed.

Introduction

The research activity in the field of integrated photonics is growing steadily. As a result, some aspects of microelectronics technology which were earlier ignored, are becoming more relevant. One of such aspects is a problem of sidewall roughness, which is assumed to be one of the main components contributing to the energy efficiency of radiophotonic integrated circuits [1]. The signal, propagating along the photonic device, scatters on roughness of its element's surfaces. This decreases the output power, as well as leads to the higher heating and worse transmission characteristic, which, in its turn, increases the noise ratio and creates undesired phase deviations. This hinders the use of radiophotonic devices in radiolocation and radio transmission circuits.

Most often, due to the low availability of roughness modeling tools, as well as the high computational complexity of the algorithms used in them, the described problems are identified only at the stage of testing of the final devices. Thus, the problem of estimating losses in radiophotonic circuits caused by sidewall roughness is relevant at the design stage. In this work a highly efficient sidewall roughness model is proposed, which allows to fill this gap.

Model description

Roughness simulation, in terms of the model presented, consists of two steps. First step is a modelling of the photolithography – which allows to take the effect of photon shot noise on the formation of roughness into account. Second step is an application of the original imitational model of the resist exposure. It is assumed that the etching process used for manufacturing integrated radiophotonic elements is chosen to be highly anisotropic, which results in inheritance of roughness features from the resist to the formed structure.

Based on the photolithography modelling data, a region of "unreliable illumination" is calculated [2]. In this region there might be statistical deviations in energy, transferred to resist which may lead to local under- or over-exposures. Thus, it is assumed that sidewall roughness will be localized inside

the "unreliable illumination" region. The contribution of photoresist effects to sidewall roughness is taken into account by applying an imitational model of the resist exposure. In basic approximation, the resist polymer macromolecule can be represented as a free-jointed chain of monomers. This allows not to take into account the peculiarities of interaction of individual atoms when describing the spatial configurations of the polymer. In terms of the imitational resist exposure model, the macromolecules of the material are represented as tightly packed spheres. The resist molecules mass (and, accordingly, size) variations are taken into account. If a resist molecule is partially or completely located in "unreliable illumination" area, its activation occurs only with some probability, which contributes to the roughness of the final structure.

The proposed methodology for verification of presented roughness model consists of three steps: fabrication of test waveguide structures, measurement of numerical roughness characteristics using a scanning electron microscope, and measurement of the transmission characteristic of the devices obtained.

Results and discussion

In this work simulation results, obtained using the new sidewall roughness model, were demonstrated and an approach on their verification with experimental data was suggested. Additionally, theoretical estimations for the optical losses caused by sidewall roughness in Si waveguide are discussed.

Acknowledgments

The work was funded by a grant by the Fund for Assistance to Small Innovative Enterprises No. 075-15-2020-791 40ГУРЭС14/72785 dated Dec 26, 2021

References

[1] B. Guiana, A. Zadehgol, Characterizing THz Scattering Loss in Nano-Scale SOI Waveguides Exhibiting Stochastic Surface Roughness with Exponential Autocorrelation, Electronics, 11.3 (2022): 307.

[2] A. A. Sharapov, et al., Grounds and problem statement for software complex for photolithography optimization for minimization of losses in optical structures of photonic integrated circuits, IOP Conference Series: Materials Science and Engineering. Vol. 939. No. 1. IOP Publishing, 2020.

Features of the combustion initiation process of Al-CuO_x multilayer thermite structures

M E Shiryaev[1], E S Leonenko[1], R M Ryazanov[2], A V Sysa[2], E A Lebedev[1]

[1] National Research University of Electronic Technology, 124498, Zelenograd, Moscow, Russia

[2] Scientific-Manufacturing Complex "Technological Centre", 124498, Zelenograd, Moscow, Russia

E-mail: shiryaevme@bk.ru

Abstract: This work contains the results of studying the features of the initiation of the combustion process of Al-CuO_x multilayer thermite structures in air, in an inert atmosphere and in vacuum. Combustion was initiated using a thin-film NiCr heating element, the topological pattern of which was formed by laser engraving. Regularities were revealed and the propagation rates of the combustion front of Al-CuO_x multilayer thermite structures in vacuum, argon atmosphere and air were determined.

1. Introduction

Currently, various nanostructured thermite materials are being actively studied. Reaction bonding, which uses thin-film multilayer reaction structures that act as local heat sources, makes it possible to effectively solve a number of technological problems in microelectronics. In such structures, self-propagating exothermic reactions can occur after local initiation.

Al-CuO_x thermites are widely used due to their high specific heat of combustion. Multilayer Al-CuO_x materials can be formed using the magnetron sputtering method, which makes it possible to obtain structures with good adhesion between the layers and the substrate, and the ability to control the thickness of individual layers with an accuracy of nanometers.

Within the framework of this work, the features of the formation of Al-CuO_x multilayer structures on substrates were studied, the features of their initiation using thin-film NiCr heaters, and the nature of their combustion in various atmospheres (vacuum, argon, and air) were studied.

2. Methodical

To create thin-film heaters on glass-ceramic substrates, a 400-nm NiCr layer was formed by magnetron sputtering. Then, using the laser engraving method, various heater topologies were formed. After that, the contact pads of the heaters were masked with a layer of chemically resistant varnish to protect against further sputtering.

Next, the deposition of the Al-CuO_x multilayer structure was carried out in an argon atmosphere at the sputtering powers of Al and CuO_x targets of 500 W and 250 W, respectively. The total thickness of the structure was 2 μm, and the number of bilayers was 20. The geometric parameters of the multilayer thermite structure were controlled using a scanning electron microscope (SEM).

The study of the features of the combustion process was carried out using high-speed video recording. Investigations of combustion in vacuum and in an inert argon medium were carried out in a vacuum chamber with a transparent window, where the air was preliminarily reduced to 7×10^{-5} Torr, and then, if necessary, argon was admitted into the chamber to atmospheric pressure. The other part of the samples was studied in air at atmospheric pressure. Combustion of multilayer structures was initiated by passing an electric current through thin-film NiCr heaters. After examining the surface of the samples, they were examined using SEM.

3. Results

The initial multilayer structures and combustion products were studied using SEM and EDS. Figure 1 shows the obtained images of the initial Al-CuO_x multilayer structures (a) and combustion products (b).

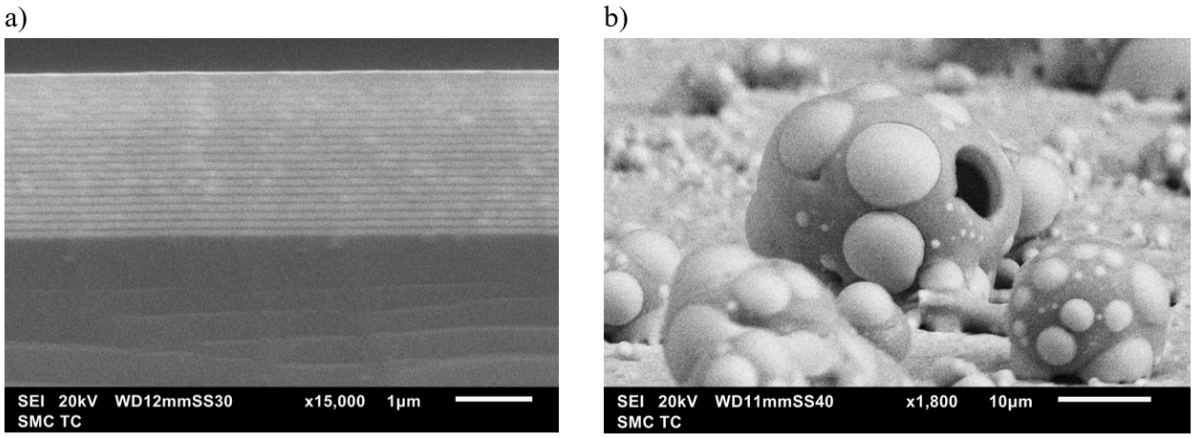

Fig 1. SEM image of the original multilayer structure Al-CuO_x (a) and combustion products (b)

The paper describes the features of the formation of multilayer thermite structures Al-CuO_x by magnetron sputtering. The obtained results of the study using SEM made it possible to draw conclusions about the features of combustion of Al-CuO_x multilayer thermite materials in various atmospheres.

Acknowledgments

The study was supported by the Russian Science Foundation grant No. 22-29-01177, https://rscf.ru/project/22-29-01177/.

Low-adhesive functionalized silicone rubbers for flexible light-emitting devices

A S Miroshnichenko,[1,2,3] K V Deriabin,[1] M Baeva,[2,3,4] F M Kochetkov,[3]

V Neplokh,[3,5] I S Mukhin,[2,3,5] R M Islamova[1]

[1] Saint Petersburg State University, 7/9 Universitetskaya Nab., 199034 St. Petersburg, Russian Federation;
[2] ITMO University, 49 Kronverksky, 197101 St. Petersburg, Russian Federation;
[3] Saint Petersburg Academic University, 8/3 Khlopina, 194021 St. Petersburg, Russian Federation;
[4] Institute of Automation and Control Processes (IACP), Far Eastern Branch of Russian Academy of Sciences, 5 Ulitsa Radio, 690041 Vladivostok, Russian Federation;
[5] Peter the Great St. Petersburg Polytechnic University, 29 Polytechnicheskaya, 195251 St. Petersburg, Russian Federation.

E-mail: anna.miroshnichenko.sergeevna@gmail.com

Abstract. In this work, phenylethyl-functionalized (SSRs) and 2-methyl-3-methoxy-3-oxopropyl-functionalized (MSRs) silicone rubbers with 25% of phenylethyl and 2-methyl-3-methoxy-3-oxopropyl (SSR25 and MSR25, respectively) were developed and employed as materials for nanowires (NWs) array encapsulation. These silicone rubbers are transparent and displays low adhesion to Si substrate. SSR25 exhibits both substantial elongation at break (ε = 45±5%) and tensile strength (σ = 1.5±0.4 MPa, Young's modulus E = 3.4±0.7 MPa). SSR25 was employed as a supporting polymer membrane for encapsulation arrays of NWs. The obtained SSR25-based membranes were used for mastering hybrid light-emitting diodes (LEDs) based on metal-halide perovskite $CsPbBr_3$ and n-doped gallium phosphide (GaP) NWs. Polyethylene oxide (PEO)–perovskite composite layer was spin-coated upon n-GaP NWs partially encapsulated into SSR25 by G-coating method. Single-walled carbon nanotubes (SWCNT) films were employed as transparent flexible electrodes for the fabricated SSR25-based LED membranes. The flexible air-stable $CsPbBr_3$:PEO/GaP/SSR25/SWCNT LED demonstrates electroluminescence in the green spectral region.

1. Introduction

Commercial polydimethylsiloxanes (PDMSs) such as Dow Corning Sylgard 182 or 184 usually being employed as supporting flexible transparent membrane for flexible NWs-based light-emitting devises[1–3] due to the transparency and relatively good elastic properties [4]. However, the commercial PDMS product Sylgard 184 demonstrate a high adhesion to a silicon substrate hampering the membrane release. These factors determine the high demand for development of new durable transparent polymer materials for manufacturing technology of thin membrane NW devices.

Modification of polysiloxanes by their reaction with various vinyl monomers leads to the increased mechanical strength and reduced adhesion [5].

2. Silicone rubbers synthesis and application

Functionalized silicone rubbers were obtained via catalytic hydrosilylation reaction between styrene (SSR) or methylmetacrilate (MSR) and polymethylhydrosiloxane (PMHS) with Karstedt's catalyst and further cross-linking with α,ω-di(dimethylvinylsiloxy)polydimethylsiloxane (v-PDMS).This method helps to avoid formation of supramolecular structures formation and consequently transparency of formed rubbers.

In addition, the presence of phenylethyl and 2-methyl-3-methoxy-3-oxopropyl substituents in the polysiloxane chains led to the reduction of membrane adhesion to the Si substrate (SSR25 – 0.55 and MSR25 – 0.66 of the Sylgard 184 adhesion value). The resulting silicone rubbers were used for encapsulation of NWs arrays to fabricate flexible and transparent membranes for optoelectronic devices. According to swelling data MSR25 poses lower polymer fraction content $\upsilon = 0.30 \pm 0.01$ and number of stiches in comparison to SSR25($\upsilon = 0.50 \pm 0.01$). Thus, MSR has shown sufficient elongation at break ($\varepsilon = 85 \pm 5\%$) along with weak tensile at break $\sigma = 0.6 \pm 0.1$ MPa and Young's modulus $E = 0.6 \pm 0.1$ MPa. SSR25 portray good mechanical properties ($\sigma = 1.5 \pm 0.4$ MPa, $E = 3.4 \pm 0.7$ MPa) and relatively sufficient elongation at break ($\varepsilon = 45 \pm 5\%$).

Due to the mentioned advantages SSR25 was chosen over MSR25 and used as supporting polymer membrane for flexible NWs-thin layer perovskite-based LED operating in the green spectral range [6]. Here, an SSR25 membrane with partially embedded GaP NWs provides both the mechanical support to all structure and excellent electrical contacting to perovskite layer owing to penetration of NW-based electrodes into perovskite; the thickness of perovskite layer can be increased in comparison with the standard perovskites-based LED architecture.

Acknowledgments

This study was supported by the Russian Science Foundation (grant 20-19-00256). Physicochemical measurements were performed at the Center for Magnetic Resonance, Center for Chemical Analysis and Materials Research, and Thermogravimetric and Calorimetric Research Center (all belonging to Saint Petersburg State University).

References

[1] Kochetkov F M, Neplokh V, Mastalieva V A, Mukhangali S, Vorob'ev A A, Uvarov A V, Komissarenko F E, Mitin D M, Kapoor A, Eymery J, Amador-Mendez N, Durand C, Krasnikov D, Nasibulin A G, Tchernycheva M and Mukhin I S 2021 Stretchable Transparent Light-Emitting Diodes Based on InGaN/GaN Quantum Well Microwires and Carbon Nanotube Films *Nanomaterials* **11** 1503

[2] Neplokh V, Fedorov V, Mozharov A, Kochetkov F, Shugurov K, Moiseev E, Amador-Mendez N, Statsenko T, Morozova S, Krasnikov D, Nasibulin A G, Islamova R, Cirlin G, Tchernycheva M and Mukhin I 2021 Red GaPAs/GaP Nanowire-Based Flexible Light-Emitting Diodes *Nanomaterials* **11** 2549

[3] Dai X, Messanvi A, Zhang H, Durand C, Eymery J, Bougerol C, Julien F H and Tchernycheva M 2015 Flexible Light-Emitting Diodes Based on Vertical Nitride Nanowires *Nano Lett.* **15** 6958–64

[4] Ren Z and Yan S 2016 Polysiloxanes for optoelectronic applications *Progress in Materials Science* **83** 383–416

[5] Neplokh V, Kochetkov F M, Deriabin K V, Fedorov V V, Bolshakov A D, Eliseev I E, Mikhailovskii V Y, Ilatovskii D A, Krasnikov D V, Tchernycheva M, Cirlin G E, Nasibulin A G, Mukhin I S and Islamova R M 2020 Modified silicone rubber for fabrication and contacting of flexible suspended membranes of n-/p-GaP nanowires with a single-walled carbon nanotube transparent contact *J. Mater. Chem. C* **8** 3764–72

[6] Miroshnichenko A S, Deriabin K V, Baeva M, Kochetkov F M, Neplokh V, Fedorov V V, Mozharov A M, Koval O Yu, Krasnikov D V, Sharov V A, Filatov N A, Gets D S, Nasibulin A G, Makarov S V, Mukhin I S, Kukushkin V Yu and Islamova R M 2021 Flexible Perovskite CsPbBr3 Light Emitting Devices Integrated with GaP Nanowire Arrays in Highly Transparent and Durable Functionalized Silicones *J. Phys. Chem. Lett.* **12** 9672–6

Multifunctional hybrid materials based on graphene oxide and organic chromophores for nanoelectronic applications

Gusarova E.A.[1,2], Zvyagina A.I..[2], Alexandrov A.E.[2], Averin A.A.[2], Kalinina M.A.[2]

[1] Lomonosov Moscow State University, Moscow, Russia

[2] A. N. Frumkin Institute of Physical Chemistry and Electrochemistry, Russian Academy of Sciences, Moscow, Russia

liisagus@mail.ru

Abstract. In this work hybrid materials based on graphene oxide and organic chromophores were obtained. It is shown that these systems exhibit non-additive increase in electrical conductivity. The obtained hybrids were integrated into cells with electron- and hole-transport layers. The photovoltaic effect as well as the properties of the ultrathin capacitor depending on the composition of the final coating were demonstrated.

1. Introduction

Due to the current trends in the development of organic nanophotonics, the design of technically simple and versatile approaches to obtain ultrathin functional coatings based on organic compounds is a relevant task. Multifunctional materials capable of exhibiting a variety of practically valuable properties depending on the modification of their assembly and environment are of particular interest. A convenient platform for the development of such systems is graphene oxide (GO), which has a unique combination of transparency, flexibility, mechanical strength and electrical conductivity of a two-dimensional carbon framework. At the same time, the unique structure of graphene oxide opens up the possibility to create hybrid materials based on GO and organic molecules using technically simple and low-cost procedures.

2. Fabrication and characterisation of hybrid materials

2.1. *GO/PDA hybrid material*

In this paper we propose a simple approach to obtain ultrathin hybrid materials with different properties based on one starting set of components - graphene oxide, aromatic chromophore, N,N'-dipropionate perylene-3,4,9,10-tetracarboxylic acid (PDI-COOH2), and surfactant, 10,12-pentacosadiynoic acid (PDA). Ultrathin hybrid GO/PDA, GO/PDI-COOH2, and GO/PDI-COOH2/PDA coatings were obtained in this work by a combination of epitaxial assembly of aromatic component domains and transfer of surfactant adsorption layers from air/water interfaces. It was demonstrated that the hybrid material GO/PDA exhibits a non-additive increase in conductivity compared to the individual components up to 46 $S \cdot cm^{-1}$ due to a reduction in the number of defects in the system and dissociation of electron-hole pairs when an electric field is applied to. It is shown that

when the material is combined with both electron-transport layers (ITO/GO/PDA/C60/BCP/Al architecture) and hole-transport layers (ITO/GO/PDA/2-TNATA/Al architecture), a photovoltaic effect is observed in the cell, which opens the possibility of using the developed hybrids in both forward and backward photodiodes.

2.2. *GO/PDI-COOH2/PDA hybrid material*

Replacing the PDA with a layer of PDI-COOH2 perylene (GO/PDI-COOH2 system) resulted in an appearance of "traps" that hindered the movement of the charge to the electrodes. In the next step of the work, these organic molecules were combined into a hybrid GO/PDI-COOH2/PDA system. It was shown that the Ferster energy transfer between the organic components is realized in the system, which is accompanied by a quenching of fluorescence peaks of perylene derivative and an increase of PDA polymer's fluorescence. The study of the volt-ampere characteristics showed that the peculiarity of the developed hybrid material GO/PDI-COOH2/PDA is its multifunctionality. It was demonstrated that when a hybrid with electron-transport layers (ITO/GO/PDI-COOH2/PDA/C60/Al architecture) is integrated, the system exhibits photodiode properties and when an assembly with hole-transport layers (ITO/ GO/PDI-COOH2/PDA/2-TNATA/Al architecture) is implemented, the system exhibits ultrathin capacitor properties.

Thus, the developed approach to obtaining hybrid materials based on GO and organic compounds opens up the possibility of creating multifunctional ultrathin coatings for a variety of nanoelectronic applications based on a single starting set of components.

Investigation of the Stability of Current Generation in Nitrogen-Doped Carbon Nanotubes

O I Soboleva[2], O I Il'in[2], M R Polyvianova[2], N N Rudyk[2] and M V Il'ina[1]
[1]Southern Federal University, Institute of Nanotechnologies, Electronics and Electronic Equipment Engineering, Taganrog, 347922, Russia
[2] Southern Federal University, Research Laboratory of Functional Nanomaterials Technology, Taganrog, 347922, Russian Federation

Abstract. The results of experimental studies of the stability of current generation in nitrogen-doped carbon nanotubes (N-CNTs) under a static load are presented. It is shown that the duration of current generation by a single N-CNT is about 5500 s when pressed with a force of 1.7 μN. The sensitivity of N-CNTs to external vibrations and noise in the form of bursts of positive current was detected. The obtained results can be used to develop energy-efficient nanogenerators based on arrays of vertically aligned N-CNTs.

1. Introduction

Recently, the development of technology has created the need to create portable energy sources for wearable electronics [1]. For this task, one of the promising materials is nitrogen-doped carbon nanotubes (N-CNTs), which have anomalous piezoelectric properties [2, 3]. Previously, we found that the occurrence of a piezoelectric response in CNTs is associated with the formation of defects in the substitution of pyrrole-like nitrogen atoms for carbon atoms and the formation of bamboo-like bridges in the nanotube cavity [2]. The aim of this work is to study the stability of current generation in N-CNTs under a static load.

2. Experimental studies

During the study, arrays of nitrogen-doped carbon nanotubes grown by the plasma-chemical vapor deposition method were used as experimental samples. Samples 1 and 2 were formed on a 100 nm thick Mo sublayer at temperatures of 645 and 630°C, respectively. Sample 3 was formed on a TiN sublayer 100 nm thick at a temperature of 645°C. The N-CNTs of samples 1 and 2 had an average diameter of 94.6±27.5 nm and 73.6±30.2 nm and a height of 6.6±0.8 μm and 9.4±0.2 μm, respectively. The N-CNTs of sample 3 were 35.8±1.3 nm in diameter and 12.9±0.5 μm in height. Scanning electron microscopy (SEM) images of these samples are shown in Figure 1.

At the same time, the analysis of the chemical composition of the samples by X-ray photoelectron spectroscopy showed that the nitrogen concentration in samples 1 and 2 was about 11% with a relative content of pyrrole-like nitrogen of about 39%, and in sample 3 about 4%, of which 17% was pyrrole-like nitrogen [4]. Experimental studies of the stability of current generation in CNT arrays were carried out using atomic force microscopy (AFM). The generated current was detected by a built-in oscilloscope when the AFM probe was statically pressed against the top of the CNT with a force of 1.7 μN. A commercial NSG10/TiN probe was used as the top electrode. Figure 2 shows the obtained dependences of the generated current on time.

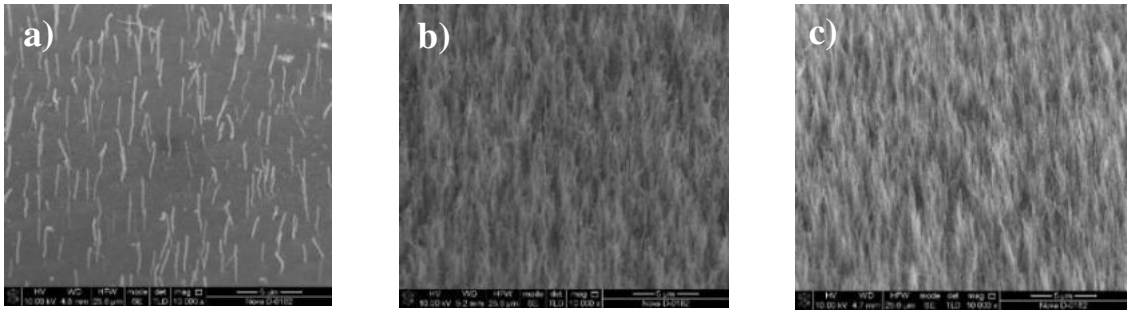

Figure 1. SEM images: a) sample 1, b) sample 2, c) sample 3.

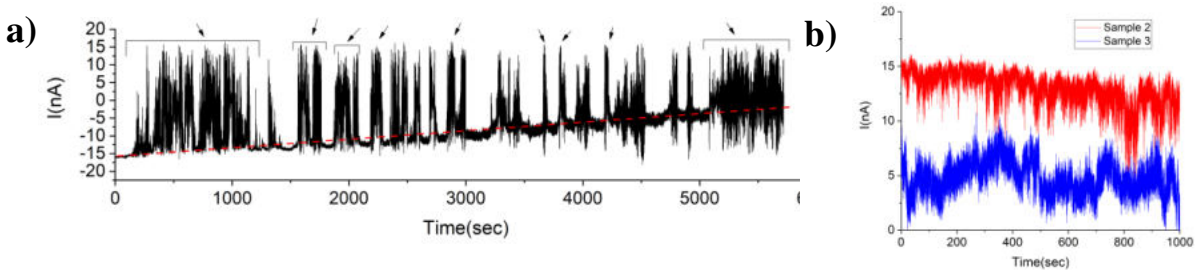

Figure 2. The dependence of the stability of the generated current on time: a) sample 1, the arrows indicate the areas during the formation of additional external noise; b) sample 2 and sample 3.

3. Results and discussion

The analysis of the obtained results showed that the current generation by the nanotube of sample 1 persisted for 5500 s (~1.5 h). The average current value changed from -16 nA to 0 (Fig. 2a). The current jumping of about 30 nA (indicated by arrows in Fig. 2a) that appear during the entire time of measurements are associated with external perturbations of the N-CNT array (steps, door opening, conversations, etc.). This dependence is related to the fact that the compression strains dominated in N-CNT and a negative current was detected when the nanotube was bent as a result of pressing the AFM probe. On the contrary, tensile strains dominated in N-CNT and a positive current under the action of external perturbations. A positive current was also detected when the N-CNTs of samples 2 and 3 were bent (Fig. 2b), which is associated with the predominant nanotube tensile strain when pressed with the AFM probe. The current decreased from ~15 nA to ~12 nA in 1000 s for sample 2 (Fig. 2b). The current was 5 nA for 1000 s for sample 3 (Fig. 2b). High stability has been associated with a larger number of N-CNTs in contact with the AFM probe. The decrease in the current value for sample 3 is associated with a decrease in the concentration of nitrogen defects and pyrrole-like nitrogen in particular [3].

Thus, nitrogen-doped carbon nanotubes under the action of a static load generate current for 5500 s with a response to external environmental perturbations. In this case, the magnitude of the generated current depends on the defectiveness and geometrical parameters of the N-CNTs. The results obtained can be used to develop energy-efficient nanogenerators based on vertically aligned N-CNTs.

Acknowledgments

This work was supported by the Russian Science Foundation (project No. 20-79-00284).

[1] Xu S., Qin Y., Xu C. Wei Y., Yang R., Wang Z. L., 2010 *Nat. Nanotechnol*. **5**, 366–373

[2] Il'ina M.V., Il'in O.I., Guryanov A.V., Osotova O.I., Blinov Y.F., Fedotov A.A. and O.A. Ageev, 2021 *J. Mater. Chem. C.* **9**, 6014–6021

[3] Il'ina M., Il'in O., Osotova O., Khubezhov S., Rudyk N., Pankov I., Fedotov A. and Ageev O. 2022 *Carbon* **190**, 348-358

[4] Il'ina M.V, Il'in O.I, Osotova O.I, Smirnov V.A. and Ageev O.A. 2022 *Diamond & Related Materials* **123**, 108858

Inelastic scattering in ultra-thin Nb films

A I Lomakin[1,2], M D Soldatenkova[1], E M Baeva[1,2], A D Triznova, P I Zolotov[1,2], A I Kolbatova[1,2], G N Goltsman[1,2]

[1]National Research University Higher School of Economics, Moscow 101000, Russia
[2]Moscow State Pedagogical University, Moscow 119435, Russia

Andrey.Lomakin.2021@mail.ru

Abstract. Here, we report on experimental study of electronic parameters and inelastic relaxation in ultra-thin superconducting Nb films with and without protective silicon (Si) layer. Measuring of magnetoconductance in the range from T_c to ~ 2-3 T_c , we observe a clear trend for the rate of inelastic scattering of electrons to increase then a film hasn't a layer. Our findings can be applied for various electronic devices operating at low temperatures.

1. Introduction

Inelastic scattering of electrons in a normal state of superconductors plays a vital role in non -equilibrium physics of superconducting detectors. For instance, rates of electron-electron (e-e) and electron-phonon (e-ph) scattering processes jointly control thermalization and cooling of nonequilibrium quasiparticles and therefore determine timing metrics (i.e. jitter, dead time) of superconducting single photon detectors (SNSPDs) and their capability to detect single photons [1–5], limit the intermediate-frequency bandwidth of hot-electron bolometers (HEB) [6], or determine scales of quasiparticle recombination rates in microwave kinetic inductance detectors (MKIDs) [7]. Thin films are a basic component of mentioned electronic devices, thereby a better understanding of inelastic scattering mechanisms is an important step in improving devices' performance.

Thin Nb films are one of the most widely used materials in superconducting electronic applications [8]. The properties of thin Nb films have been addressed by numerous studies. A predisposition of Nb films to rapid oxidization is known in ultrathin films. Besides reduction of effective film thickness, a native oxide layer, formed on the film surface, may enhance electron dephasing due to its specific properties.

In this work we study the magnetoresistance of Nb films and consider several mechanisms that may affect the electron dephasing time τ_φ in films. Analysis of the experimental data shows that a some amount of magnetic disorder can also influence on $\tau_\varphi(T)$- dependence in high-quality ultra-thin Nb films.

2. Details of sample fabrication and experimental setup.

Thin Nb films of thicknesses from 1.5 nm to 6 nm were deposed by DC magnetron sputtering onto Al_2O_3 and Si substrates. To study transport properties of Nb, we patterned the films into 500-μm wide and 1000-μm long Hall-bars. Normal-state resistance R_s was measured in a fourprobe configuration. The measurements were carried out in a homemade 4He cryogenic insert immersed in a dewar and performed in a wide temperature range (from 300 K to 1.7 K). At low temperatures we measured the magnetoresistance $R_s(B)$, the temperature dependencies of the second critical magnetic field $B_{c2}(T)$ and the Hall resistance $R_H^{20\ K}$ at 25 K by applying perpendicular magnetic field B up to 4 T. Measuring the

R(T)-dependencies at different values of B we determine the slope dB_{c2}/dT at T_c. Here, the critical temperature T_c is determined as the temperature at $R_s = R_{max}/2$.

3. Results and Discussion

The experimental data can be fitted by dependence [9]:

$$\delta\sigma(B,T) = \delta\sigma^{AL}(B,T) + \delta\sigma^{DOS}(B,T) + \delta\sigma^{MT}(B,T,\tau_\varphi)$$

where δσ is the change in the conductance of the film, σ^{AL}, σ^{MT} and σ^{DOS} quantum corrections to conductivity (the Aslamazov-Larkin (AL) term, the Maki-Thompson term and the term due to suppression in the electronic density of states (DOS)). We determine temperature-dependent electron phase-breaking rate τ_ϕ^{-1}(T) as a fitting parameter in the Maki-Thompson term. These rates of all studied samples are shown in Figure 1.

We can fit this data by the sum of the scattering mechanisms due to superconducting fluctuations τ_{SC}^{-1}, the e-e rate τ_{e-e}^{-1}, the spin-flip rate τ_s^{-1}, and the e-ph rate τ_{e-ph}^{-1} as follows: $\tau_\phi^{-1} = \tau_{e-e}^{-1} + \tau_{SC}^{-1} + \tau_s^{-1} + \tau_{e-ph}^{-1}$. But for our films τ_{e-e}^{-1} and τ_{SC}^{-1} are negligible, that is why we fit our data with the following expression: $\tau_\phi^{-1} = \tau_s^{-1} + \tau_{e-ph}^{-1}$, where $\tau_{e-ph}^{-1} = \alpha^{-1}T^p$ (α and p dimensionless parameters), τ_s^{-1} is a constant value for every film [10]. We can see that samples with a cover have a stronger T-dependence. Besides τ_ϕ^{-1}(T) for samples without a cover is higher than the time for silicon-protected samples. This may indicate that on uncovered films, there may be a hidden mechanism of enhance of electron dephasing.

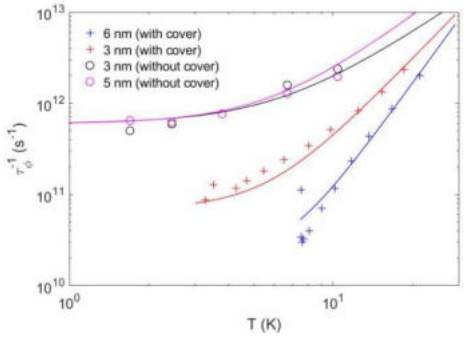

Samples	α	p	t_s^{-1}, s^{-1}
6 nm with cover	$9{,}6 \cdot 10^{-8}$	4	$2 \cdot 10^{10}$
3 nm with cover	$2{,}6 \cdot 10^{-9}$	3	$7 \cdot 10^{11}$
5 nm without cover	$7 \cdot 10^{-11}$	2	$5{,}9 \cdot 10^{13}$
3 nm without cover	$7{,}7 \cdot 10^{-11}$	2,2	$6 \cdot 10^{13}$

Figure 1. Temperature dependencies of the electron dephasing rate τ_ϕ^{-1} extracted from magnetoconductance measurements plotted in symbols on a log-log scale. The best fits of τ_ϕ^{-1} are shown with solid curves. The table shows the parameters of solid curves.

Acknowledgments

Authors wishing to acknowledge the RSF project 19-72-10101 for the transport measurements.

References

[1] A. J. Kerman et al 2006 *Appl. Phys. Lett* **88** 111116
[2] F. Marsili et al 2016 *Phys. Rev.* B **93**, 094518
[3] D. Y. Vodolazov et al 2017 *Phys. Rev. Appl* **7**, 034014
[4] S.Ferrari et al 2017 *Opt. Express* **25**, 8739
[5] B. Korzh et al 2020 *Nature Photonics* **14**, 250
[6] A. Shurakov et al 2015 *Superconductor Science and Technology* **29**, 023001
[7] J. Zmuidzinas et al 2012 *Annual Review of Condensed Matter Physics* **3**, 169
[8] C. C. Koch et al 1974 *Phys. Rev. B*, vol. 9, pp. 888–897
[9] A. L. (late) and A. Varlamov 2005 *Oxford University Press*
[10] A. Samsonova et al 2021 *IEEE* PP(99)

Thin WO_3/Pt layer with top spray deposited carbon nanotubes to form structure with heterojunctions for selective gas sensor

A V Romashkin, E V Alexandrov, N S Struchkov, A V Lashkov, D D Levin

National Research University of Electronic Technology, Moscow 124498, Russia

romaleval@gmail.com

Abstract. Structures with ontop high uniformity spray deposited CNTs on thin WO_3/Pt/W underlayer, formed in predetermined areas, and without underlayer (reference sample) on glass substrates were formed. SERS of WO_3 on island Pt layer was observed. Structures demonstrate the specific behaviour, which due to the contribution of CNT-Pt contacts: similar response to NH_3 in dry air and reduced response for the CNT-WO_3/Pt structure relative to the reference structure at 45 % humidity, which makes it possible to correctly determine the concentration of NH_3 at different humidity levels at room temperature with multisensory structures.

1. Introduction

Ammonia (NH_3) need to be measured at ~10-50 ppb level for environmental monitoring, however, the detection limit for conventional sensors based only on oxide materials is higher, and measurements are required at temperatures of ~200 ℃, they have low selectivity, however recently, structures with carbon nanotubes (CNT) and WO_3 and other nanomaterials have been actively studied to form selective high-sensitive sensors operating at room temperature (RT), while the implementation and contribution of changing the parameters of heterojunctions during gas sorption is extremely important [1]. However, due to the strong dependence of the sensor response (SR) to NH_3 on air humidity (RH), as well as due to a strong change of SR with non-optimal component ratios of such composite sensor layers [1] for gas recognition and determining the correct NH_3 concentration, it is necessary to form new multisensor structures with more tailored and controlled formation of heterojunctions in nanoscale layers (for example by photolithography) with the formation by that the specific SR behavior of the multisensor structure on different gas mixtures, which is the subject of this work.

2. Results and discussions

By magnetron sputtering of W/Pt/W layers (the thickness of each was 10 nm, fig. 1a, b, c) and lift-off photolithography, a glass substrate with 20x20 μm metallization regions with a period of 30 μm was formed. Then, by annealing in air at ~380 °C, regions with WO_3/Pt/W were formed with an increase in the layer thickness due to the formation of oxide (fig. 1b, c), and the presence of WO_3 was determined by peaks (main at 805 cm^{-1} [2]) on Raman spectra (fig. 1d), which observed only for WO_3/Pt/W and was absent on the WO_3 on glass sample, which is due to SERS [3] on a Pt island layer (R_s ~0.5 kΩ/□, ~30 times higher than the table values), formed during the oxidation of W. Then, in one process, CNTs were spray deposited (P3-SWNT, Carbon Solutions, USA) with subsequent control of the layer nonuniformity by Raman map (fig. 1e) [4] on two glass substrates: with WO_3/Pt/W regions and without (reference structure). The TCR of CNT-WO_3/Pt sample in the range of 50-100 °C was only

-0.21 %/°C, while the reference sample TCR was -0.39 %/°C, which indicates the contribution in layer resistance (R_s) of CNT-Pt contacts but not CNT-WO_3, since, firstly, the TCR of WO_3 is about -3%/°C and if it presence the layer TCR would have to higher than for reference sample, and secondly, the R_s with WO_3/Pt regions was only 140 kΩ/□ versus 1 MΩ/□ of reference, which indicates the contribution of the Pt sublayer proper in R_s. However, despite the difference in TCR, these two samples show almost identical SR to 150 ppm NH_3 at RT: 25 % for the CNT-WO_3/Pt and and 24 % for reference layer (fig. 2a). The similar SR, despite the lower TCR of the CNT-WO_3/Pt structure (and therefore lower SR from CNT layer in it, because of main contribution to SR is made by semiconductor CNTs [5]), can only be explained by the significant contribution to the SR of the CNT-Pt contacts, which significantly (additionally up to ~12 % at 150 ppm) improve the SR even in the case of use of metallic multi-walled CNTs [6]. This also explains that the measurement of a CNT layer with a similar TCR (0.24 %/°C) with R_s of ~60 kΩ/□ showed the SR to 150 ppm NH_3 was only ~8 %. But at 100 °C, the SR to 150 ppm NH_3 for CNT-WO_3/Pt decreases to 9.5 %, while a reference sample with a similar CNT network demonstrates SR of 19 % (only slightly lower than at RT, SR of another sample only with CNT layer with R_s ~3 MΩ/□ with TCR -0.6 %/°C is even slightly increased from 12 % at RT to 17 % at 100 °C). This indicates a decrease in the contribution of CNT-Pt contacts to the SR with increasing temperature (influence of the Schottky barrier at the CNT-Pt contact decrease), that is similar to the behavior of structures with other heterocontacts [7]. As a result, the specific difference in the SR of the structures at RT was realized: a similar SR to NH_3 in dry air for both, but reduced SR for the CNT-WO_3/Pt structure relative to the CNT reference structure in air with RH 45 %, which will allow to recognize correct NH_3 concentration against the background of changes in air RH (fig. 2a,b).

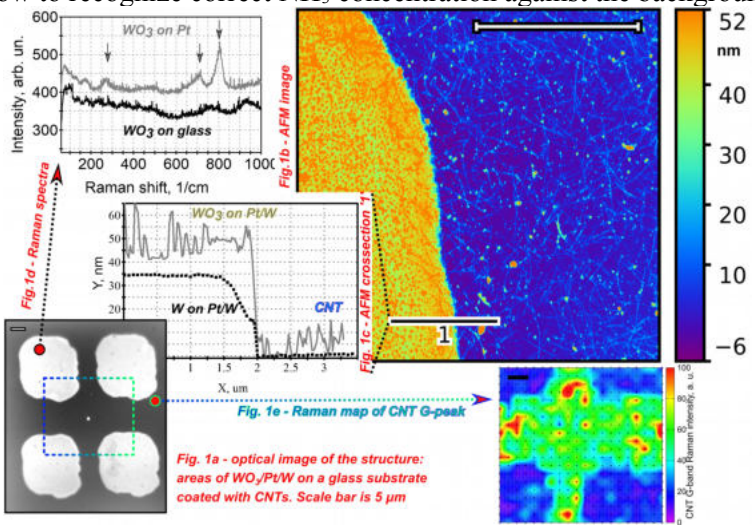

Figure 1. a) Optical image of CNT on WO_3/Pt/W structure, b,c) AFM data, d) Raman spectra of WO_3, e) Raman map of CNT G-peak. Scale bar in all images is 5 μm.

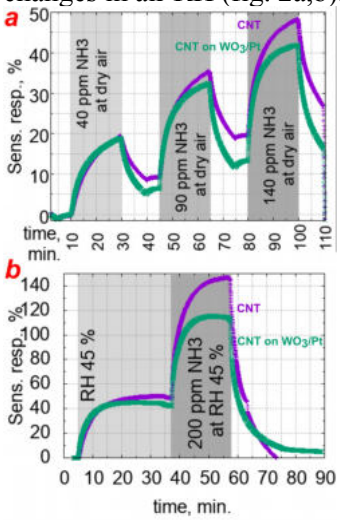

Figure 2. Sensor response to NH_3 in: a) dry air, b) in air with humidity of 45 %.

Acknowledgments

This work was supported by by RFBR, project number 19-38-60034 (development, formation, sensor response study), and grant of the President of the Russian Federation, grant No. MK-4010.2022.4.

References

[1] Duong V, Nguyen C, Luong H, Nguyen D, Nguyen, H 2021 *Solid State Sciences*, **113** 106534
[2] Manciu F, Enriquez J, Durrer W, et al 2010 *Journal of Materials Research* **25** 2401
[3] Lee C, Robertson C, Nguyen A, Kahraman M, Wachsmann-Hogiu S 2015 *Scientific reports* **5** 1
[4] Romashkin A, Polikarpov Y, Silakov G, Alexandrov E 2021 *J. Phys. Conf. Ser.* **2086** 012097
[5] Abdellah A, Abdelhalim A, Horn M, Scarpa G, Lugli P 2013. *IEEE Trans. Nanotechnol.* **12** 174
[6] Penza M, Rossi R, Alvisi M 2008 *Sensors and Actuators B: Chemical* **135** 289
[7] Nguyet QTM, Van Duy N, Manh Hung C, et al 2018 *Appl. Phys. Lett.*, **112**, 153110